Calhoun
Institutional Archive of the Naval Postgraduate School

Calhoun: The NPS Institutional Archive

Faculty and Researcher Publications | Faculty and Researcher Publications

1996-03

12th Annual Review of Progress in Applied Computational Electromagnetics at the Naval Postgraduate School, Monterey, CA, March 18-22, 1996, Conference

DUDLEY KNOX LIBRARY

Calhoun is a project of the Dudley Knox Library at NPS, furthering the precepts and goals of open government and government transparency. All information contained herein has been approved for release by the NPS Public Affairs Officer.

Dudley Knox Library / Naval Postgraduate School
411 Dyer Road / 1 University Circle
Monterey, California USA 93943

http://www.nps.edu/library

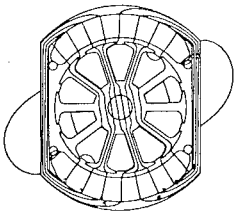

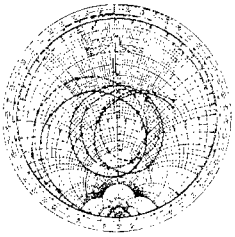

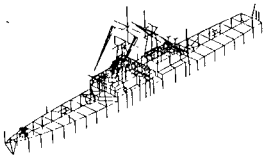

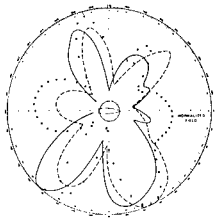

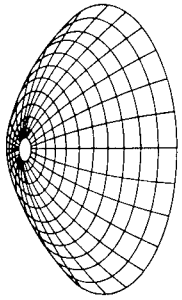

12th Annual Review of Progress in

APPLIED COMPUTATIONAL ELECTROMAGNETICS

at the

Naval Postgraduate School

Monterey, CA

March 18-22, 1996

CONFERENCE PROCEEDINGS

DISTRIBUTION STATEMENT A
Approved for public release;
Distribution Unlimited

CONFERENCE PROCEEDINGS

VOLUME I

12th Annual Review of Progress in APPLIED COMPUTATIONAL ELECTROMAGNETICS

at the

Naval Postgraduate School

Monterey, CA

March 18-22, 1996

TECHNICAL PROGRAM CHAIRMAN

Richard K. Gordon

19970910 100

Sponsored by

The Applied Computational Electromagnetics Society,

NPS, DOE/LLNL, University of Mississippi, University of Illinois

USAF, DOD AND DOE IN COOPERATION WITH IEEE, URSI, ASEE, SIAM AND AMTA

THE NAVAL POSTGRADUATE SCHOOL

DTIC QUALITY INSPECTED 4

SESSION 6: continued

SESSION 6: continued

SESSION 7:FDTD APPLICATIONS AND ENHANCEMENTS
Chair: J.H. Beggs

SESSION 8:FINITE ELEMENT AND FINITE VOLUME METHODS FOR ELECTROMAGNETIC FIELD SIMULATION
Chairs: R. D-Edlinger and R. Lee

SESSION 9:NUMERICAL ERROR ANALYSIS AND CONTROL I
Chair: J.L. Volakis

THE APPLIED COMPUTATIONAL ELECTROMAGNETIC SOCIETY

1997 CALL FOR PAPERS 1997

The 13th Annual Review of Progress in Applied Computational Electromagnetics

March 17-21, 1997

Naval Postgraduate School, Monterey, California

Share your knowledge and expertise with your colleagues

The Annual ACES Symposium is an ideal opportunity to participate in a large gathering of EM analysis enthusiasts. The purpose of the Symposium is to bring analysts together to share information and experience about the practical application of EM analysis using computational methods. The symposium offerings include technical presentations, demonstrations, vendor booths and short courses. All aspects of electromagnetic computational analysis are represented. Contact Richard Gordon for details.

Technical Program Chairman
Eric Michielssen
ECE Department
University of Illinois
1406 West Green Street
Urbana, IL 61801-2991
Phone: (217) 333-3803
FAX: (217) 333-5962
Email:michiels@decwa.ece.uiuc.edu

Symposium Administrator
Richard W. Adler
ECE Dept./Code ECAB
Naval Postgraduate School
833 Dyer Rd. Room 437
Monterey, CA 93943-5121
Phone: (408) 649-1111
FAX: (408) 649-0300
Email: rwa@mcimail.com

Symposium Co-Chairman
Jiaming Jin
ECE Department
University of Illinois
1406 West Green Street
Urbana, IL 61801-2991
Phone: (217) 244-0756
FAX: (217) 333-5962
Email:jjin@uvh.cso.uiuc.edu

Symposium Co-Chairman
Keith Whites
ECE Department
University of Kentucky
453 Anderson Hall
Lexington, KY 40506-0046
Phone: (606)-257-1768
FAX: (606)-257-3092
Email:whites@engr.uky.edu

1997 ACES Symposium
Sponsored by: ACES, NCCOSC, NPS, DOE/LLNL
In cooperation with: The IEEE Antennas and Propagation Society, the IEEE Electromagnetic Compatibility Society and USNC/URSI

THE APPLIED COMPUTATIONAL ELECTROMAGNETIC SOCIETY

CALL FOR PAPERS

The 13th Annual Review of Progress
in Applied Computational Electromagnetics

Papers may address general issues in applied computational electromagnetics, or may focus on specific applications, techniques, codes, or computational issues of potential interest to the Applied Computational Electromagnetics Society membership. Areas and topics include:

- Code validation
- Code performance analysis
- Computational studies of basic physics
- Examples of practical code application
- New codes, algorithms, code enhancements, and code fixes
- Computer hardware issues
- Partial list of applications:

antennas	wave propagation
radar imaging	radar cross section
shielding	bioelectromagnetics
EMP, EMI/EMC	visualization
dielectric & magnetic materials	inverse scattering
microwave components	**MIMIC** technology
fiberoptics	remote sensing & geophysics
communications systems	propagation through plasmas
eddy currents	non-destructive evaluation

- Partial list of techniques:

frequency-domain & time-domain techniques	
integral equation & differential equation techniques	
finite differences & finite element techniques	
diffraction theories	physical optics
modal expansions	perturbation methods
hybrid methods	moment methods

INSTRUCTIONS FOR AUTHORS AND TIMETABLE

For both summary and final paper, please supply the following data for the principal author: name, address, Email address, FAX, and phone numbers for both work and home.

October 6, 1996:	Submission deadline. Submit four copies of a 300-500 word summary to the Technical Program Chairman.
November 24, 1996:	Authors notified of acceptance.
December 22, 1996:	Submission deadline for camera-ready copy. The papers should not be more than 8 pages long including figures.

Registration fee per person for the Symposium will be approximately $245. The exact fee will be announced later.

SHORT COURSE

Short courses will be offered in conjunction with Symposium covering numerical techniques, computational methods, surveys of EM analysis and code usage instruction. It is anticipated that short courses will be conducted principally on Monday March 25 and Friday March 29. Fee for a short course is expected to be approximately $90 per person for a half-day course and $140 for a full-day course, if booked before March 3, 1997. Full details of 1997 Symposium will be available by November 1996. **Short Course Attendance is not covered by the Symposium Registration Fee!**

EXHIBITS

Vendor booths and demonstrations will feature commercial products, computer hardware and software demonstrations, and small company capabilities.

1996 Symposium Program Committee

for the

12th Annual Review of Progress in

APPLIED COMPUTATIONAL ELECTROMAGNETICS

at the
Naval Postgraduate School
Monterey, CA

Technical ProgramChairman:
Richard K. Gordon
EE Department
Univ. of Mississippi
Anderson Hall, Box 41
University, MS 38677
Phone: (601) 232-5388
FAX: (601) 232-7231
Email:eegordon@vm.cc.olemiss.edu

Co-Chair:
Eric Michielssen
ECE Department
University of Illinois
1406 West Green Street
Urbana, IL 61801-2991
Phone: (217) 333-3801
FAX: (217) 333-8986
Email:michiels@decwa.ece,edu

Co-Chair:
Jin-Fa Lee
ECE Department
Worcester Polytechnic Institute
100 Institute Road
Worcester, MA 01609
Phone: (508)831-5778
Fax: (508) 831-5491
Email:jinlee@ece.wpi.edu

Technical Asst.
Winn E. Hutchcraft
Univ of Mississippi, Dept.
EE Department
42 Midland Cove
Oxford, MS 38655
(601) 234-4912
Email:eeweh@cypress.mcsr.
olemiss.edu

Symposium Administrator
Richard W. Adler
ECE Department, Code EC/AB
Naval Postgraduate School
833 Dyer Road, Room 437
Monterey, CA 93943-5121
Phone: (408) 646-1111
FAX: (408) 649-0300
Email:rwa@mcimail.com

Short Course Chairman:
Robert Lee
Ohio State University, EE Department
2015 Neil Avenue
Columbus, OH 43210-1272
Phone: (614) 292-1433
FAX: (614) 292-7596
Email:lee@ee.eng.ohio.state.edu

Conference Secretary:
Mrs. Pat Adler

Advisory Committee:
Richard W. Adler, Naval Postgraduate School
Duncan C. Baker, University of Pretoria
Robert Bevensee, Consultant
Pat Foster, Microwave & Antenna Systems
Todd Hubing, University of Missouri-Rolla
Adalbert Konrad, University of Toronto
Ray Luebbers, Penn State University
Edmund K. Miller
Andrew Peterson, Georgia Institute of Tech.
Harold Sabbagh, Sabbagh Assoc. Inc.
W. Perry Wheless, Jr., University of Alabama

ACES

1996

March 18-22, 1996
Monterey, CA

For more information, please contact:

Technical Program Chairman
Richard Gordon
EE. Dept., University of Mississippi
Anderson Hall, Box 41
University, MS 38677
Phone: (601) 232-5388
FAX: (601) 232-7231
Email: eegordon@cypress.mcsr.olemiss.edu

Short Course Chairman
Robert Lee
Dept. Of Electrical Engineering
ElectroScience Laboratory
The Ohio State University
1320 Kinnear Road
Columbus, OH 43212
Phone: (614) 292-1433
FAX: 614-292-7596
Email: lee@ee.eng.ohio-stat.edu

Symposium Administrator
Richard W. Adler
ECE Department/Code ECAB
Naval Postgraduate School
833 Dyer Road, Room 437
Monterey, CA 93943-5121
Phone: (408) 646-1111
FAX: (408) 649-0300
Email: 5541304@mcimail.com

Conference Co-Chair
Eric Michielssen
Department of Electrical and Computer Eng.
Everitt Laboratory
1406 West Green Street
University of Illinois at Urbana-Champaign
Urbana, Illinois 61801-2991
Phone: (217) 333-3803
FAX: (217) 333-8986
Email: michiels@decwa.ece.uiuc.edu

Conference Co-Chair
Jin-Fa Lee
Department of Electrical and Computer Eng.
Worcester Polytechnic Institute
100 Institute Road
Worcester, MA 01609-2280
Phone: (508) 831-5778
Email: jinlee@ee.wpi.edu

APPLIED COMPUTATIONAL ELECTROMAGNETICS SOCIETY

The Twelfth Annual Review of Progress in Applied Computational Electromagnetics

Welcome to the 12th Annual Review of Progress in Applied Computational Electromagnetics. I want to especially thank several individuals who contributed significantly to the conference. Jin-Fa Lee arranged the advertising for the conference. Robert Lee once again did an excellent job of organizing the Short Courses. Eric Michielssen and Shirley Dipert received all the papers and put them together to produce these Proceedings. Robert Bevensee assisted in the preparation of the preliminary agenda. Elliott Hutchcraft helped me in the construction of the author database and in the preparation of an electronic mail database. And, of course, Richard and Pat Adler must be recognized for arranging for the printing of the Proceedings, for providing access to the NPGS Facilities, and for all their other contributions to the conference.

Please enjoy your time in Monterey as much as possible, whether listening to a paper being presented, catching up on the latest "gossip" in the hallways, or enjoying the sights of Monterey.

Richard K. Gordon
Technical Program Chairman
1996 ACES Conference

ACES PRESIDENT'S STATEMENT

Were it not for the ACES Annual Reviews, it would be difficult to justify being in Monterey in March. (This coming from one who spent the Winter of '95-'96 in the Midwest!) But it is time for ACES'96, so here we are in Monterey, once again. And we think that this will be the best review yet.

In addition to our regular staple of high-quality technical papers, and our world-renowned short-courses, we are adding a new feature this year --- an amateur radio session. Judging from the number of interesting questions and applications described in the NEC-LIST, amateur radio operators are a natural part, or should be, of the ACES community. Perry Wheless is to be commended for assembling this session, which appears to be well populated.

Our congratulations go to Dick Gordon, who is the Technical Program Chairman, and his colleagues, Eric Michielssen, Jin-Fa Lee, Robert Lee, W. Elliott Hutchcraft, Bob Bevensee, and Dick Adler for organizing and managing the 12th Annual Review. Their hardwork is another manifestation of the can-do spirit of dedicated volunteers in a voluntary society.

There must be more of you out there who are ready to step forward and offer your time and services to ACES. Call me! The Society, the Profession, and you will benefit enormously.

Enjoy the 12th Annual Review.

Harold A. Sabbagh
Sabbagh Associates, Inc.
4635 Morningside Drive
Bloomington, IN 47408
(812) 339-8273
(812) 339-8292 FAX
email:has@sabbagh.com

ACES 1996 SHORT COURSES

MONDAY MARCH 18 **FULL-DAY COURSES**

0830-1630 "Wavelets: Theory, Algorithms, and Applications"
by Andrew K. Chan, Texas A&M.

0830-1630 "Using Mathematical Software for Computational Electromagnetics"
by Jovan Lebaric, Naval Postgraduate School.

0830-1630 "Practical EMI/EMC Design and Modeling"
by Todd Hubing, University of Missouri-Rolla.

MONDAY MARCH 18 **HALF-DAY COURSES**

0830-1200 "An Application Oriented Introduction to the NEC-BSC Workbench"
by Ron J. Marhefka and Lee W. Henderson, The Ohio State University.

1300-1630 "Application of Modern Analytical and Hybrid Tools for Antenna Modeling and Synthesis",
by Roberto Rojas and Prabhakar Pathak, The Ohio State University.

FRIDAY MARCH 22 **FULL-DAY COURSES**

0830-1630 "Finite Element Methods for Electromagnetics"
by John Volakis, University of Michigan and
John Brauer, Mac-Neal-Schwendler Corporation.

0830-1630 "Conformal Time Domain Numerical Electromagnetics"
by Kane Yee, Lockheed.

FRIDAY MARCH 22 **HALF-DAY COURSES**

0830-1200 "Using Model-Based Parameter Estimation to Increase the Efficiency and Effectiveness of Computational Electromagnetics"
by Ed Miller.

1300-1630 "Antenna Properties in Linear and Nonlinear Environments"
by Robert Bevensee, BOMA Enterprises.

FINAL AGENDA

The Twelfth Annual Review of Progress in Applied Computational Electromagnetics

NAVAL POSTGRADUATE SCHOOL
18-22 MARCH 1996

Richard Gordon, Technical Program Chairman

Eric Michielssen, Conference Co-Chair

Jin-Fa Lee, Conference Co-Chair

Robert Lee, Short Course Chairman

W. Elliott Hutchcraft, Technical Assistant

Robert Bevensee, Assistant Conference Co-Chair

Richard W. Adler, Conference Facilitator

MONDAY MORNING 18 MARCH 1996		
0745-0830	**SHORT COURSE REGISTRATION**	**103 Glasgow Hall**
0830-1200	**SHORT COURSE (HALF-DAY)** "An Application Oriented Introduction to the NEC-BSC Workbench" R.J. Marhefka & L.W. Henderson, The Ohio State University	**102 Glasgow Hall**
0830-1630	**SHORT COURSE (FULL-DAY)** "Wavelets: Theory, Algorithms, and Applications" A.K. Chan, Texas A&M	**122 Ingersoll Hall**
0830-1630	**SHORT COURSE (FULL-DAY)** "Using Mathematical Software for Computational Electromagnetics" J. Lebaric, Naval Postgraduate School	**419 Spanagel Hall**
0830-1600	**SHORT COURSE (FULL-DAY** "Practical EMI/EMC Design and Modeling" T. Hubing, University of Missouri-Rolla	**119 Ingersoll Hall**
0900-1200	**REGISTRATION**	**103 Glasgow Hall**
MONDAY AFTERNOON		
1300-1630	**SHORT COURSE (HALF-DAY)** "Application of Modern Analytical and Hybrid Tools for Antenna Modeling and Synthesis" R. Rojas & P. Pathak, Ohio State University	**102 Glasgow Hall**
1630-1900	**REGISTRATION**	**103 Glasgow Hall**
1700-1915	**AMATEUR RADIO DINNER**	
SESSION 0:	**AMATEUR RADIO SESSION** Chair: W.P. Wheless, Jr.	**122 Ingersoll Hall**
1930	"Ground-Plane Antennas with Elevated Radial Systems"	J.S. Belrose
1950	"Review of Characteristics for HF Dipole Antennas Including the Cases Where the Dipoles are Above and Parallel to the Surface of Real-World Grounds"	G.M. Royer
2010	"HF Multi-Frequency Antennas Using Coupled Resonators"	G.A. Breed
2030	"The Optimized Wideband Antenna (OWA) and its Application"	J.K. Breakall
2050	"The Quad-Rhomb Antenna - A New All Band Antenna for Amateur Radio Applications"	R. Anders
2110	**BREAK**	
2130	"SKY-WAVES-95"	R. Anders
2150	"Using Ham Radio CEM Codes to Gain Insight to VHF Ground Plane Antennas and to Mitigate 75 Meter Mars RFI at a Naval Receiving Site"	A. Hoffman & R.W. Adler
2210	"Development of Practical Landstorfer Antennas for Amateur Use"	M.C. Tarplee
2230	"Two-Port Network Specification of Baluns for NEC Analysis and Other Applications"	W.P. Wheless, Jr., & C.S. Wheless

TUESDAY MORNING 19 MARCH 1996

0700-0800	**REGISTRATION**		**103 Glasgow Hall**
0700-0745	**CONTINENTAL BREAKFAST**		**Glasgow Hallway**
0730	**ACES BUSINESS MEETING**	President Hal Sabbagh	**102 Glasgow Hall**
0745	**WELCOME**	Richard Gordon	**102 Glasgow Hall**
SESSION 1:	**HIGH FREQUENCY METHODS (Parallel with Sessions 2, 3, 4, & 5)** Chair: R.J. Burkholder		**102 Glasgow Hall**
0800	"Physical Theory of Diffraction Analysis of Impedance Structures"		H.H. Syed & J.L. Volakis
0820	"Hybrid SBR/GTD Radio Propagation Model for Site-Specific Predictions in an Urban Environment"		J. Schuster & R. Luebbers
0840	"Analysis of Dielectric Structures Using the NEC-BSC"		R. Marhefka & L. Henderson
0900	"Hybrid MM-PO-Fock Analysis of Monopole Antennas Mounted on Curved Convex Bodies"		U. Jakobus & F.M. Landstorfer
0920	"Numerical Diffraction Coefficient for an Impedance Wedge with a Material Body Attached to its Edge"		M.F. Otero & R.G. Rojas
0940	"Reflection and Diffraction of Well-Focussed General Astigmatic EM Gaussian Beams"		G. Zogbi, H.T. Chou, P.H. Pathak, & R.J. Burkholder
1000	**BREAK**		
1020	"Polarized Scattered Light by a Semicylindrical Boss on a Conducting Flat Plane"		H.A. Yousif
1040	"Divergence of Rays in Modulated Atmospheric Ducts"		I.P. Zolotarev
1100	"Diffraction by a Weak Dielectric Wedge"		A.V. Popov
1120	"Far-field Diffraction Effects of EUV Fresnel Zone Plates"		Y.V. Kopylov, V.A.Baranov, A V.Popov, & A Vinogradov
1200	**LUNCH**		
SESSION 2:	**INVERSE SCATTERING (Parallel with Sessions 1, 3, 4, & 5)** Chairs: P.M. Goggans and L. Riggs		**Engr Auditorium**
0800	"Radar Time and Frequency-Domain Received Signals for Realistic Antennas and Scatterers"		P.M. Goggans & J.D. Pursel
0820	"The Extraction of Scattering Mechanisms from Measured Data"		H.M. Chizever & K.M. Pasala
0840	"Using the E-pulse Technique and Hypothesis Testing to Perform Radar Target Identification"		L. Riggs, J. Mooney, & C. Smith
0900	"A Boundary-Integral Code for Electromagnetic Nondestructive Evaluation"		K. Murphy & H.A. Sabbagh
0920	"The Numerical Analysis of Planar Antennas Buried in Layered Media"		J. van Tonder, J. Cloete, & D. Davidson
SESSION 3:	**RCS ANALYSIS (Parallel with Sessions 1, 2, 4, & 5)** Chair: M. El-Shenawee		**Engr Auditorium**
0940	"A Response Surface Methodology Study of Electromagnetic Data Compression and Reconstruction"		V.M. Floyd, Jr., A. Terzuoli, Jr., G.C. Gerace & P.F. Auclair
1000	**BREAK**		
1020	"Curvilinear, Isoparametric Modelling for RCS Prediction, Using Time Domain Integral Equations"		S.P. Walker, M.J. Bluck, M.D. Pocock, C.Y. Leung, & S.J. Dodson
1040	"Double Scatter Radar Cross Sections for Two Dimensional Random Rough Surfaces that Exhibit Backscatter Enhancement"		M. El-Shenawee & E. Bahar
SESSION 4:	**APPLICATIONS OF PARALLEL COMPUTING (Parallel with Sessions 1, 2, 3 & 5)** Chairs: L. Epp and K. Naishadham		**Engr. Auditorium**
1100	"Solution of Electromagnetic Eigenproblems on Multiprocessor Superscalar Computers"		M.P. Debicki, P. Jedrzejewski, J. Mielewski, P. Przybyszewski, & M. Mrozowski
1120	"Implementation of Hybrid FDTD/FVTD Conformal Algorithm on a Massively Parallel Computer"		J.S. Chen & A.A. Seidl
1140	"Parallel CARLOS-3D Code Development"		J.M. Putnam & J.D. Kotulski
SESSION 5:	**NEW DEVELOPMENTS IN TLM MODELING (Parallel with Sessions 1, 2, 3, & 4)** Chair: W.J.R. Hoefer		**122 Ingersoll Hall**
0800	"On the Advantages of ATLM Over Conventional TLM"		M. Krumpholz & P. Russer
0820	"Advanced Node Formulations in TLM - The Matched Symmetrical Condensed Node (MSCN)"		V. Trenkic, C. Christopoulos, & T.M. Benson
0840	"A General and Complete Two-Dimensional TLM Hybrid Node Formulation Based on Maxwell's Integral Equations"		N. Pena & M.M. Ney

TUESDAY MORNING 19 MARCH 1996

SESSION 5:	**NEW DEVELOPMENTS IN TLM MODELING (Parallel with Sessions 1, 2, 3, & 4) (cont)**	**122 Ingersoll Hall**
0900	"A General Formulation of a Three-dimensional TLM Condensed Node with the Modeling of Electric and Magnetic Losses and Current Sources"	N. Pena, & M.M. Ney
0920	"A Numerical Comparison of Dispersion in Irregularly Graded TLM and FDTD Meshes"	F.J. German, J.A. Svigelj, & R. Mittra
0940	"Accuracy Considerations of a Class of Frequency-Domain TLM Nodes"	S. Chen & R. Vahldieck
	BREAK	
1020	"Distributed Simulation of Planar Circuits by TLM Method in a Parallel Computing" Environment"	B. Isele, J. Schmöller, & P. Russer
1040	"Modeling Gyromagnetic Media in Symmetrical Condensed Node TLM"	L. de Menezes & W.J.R. Hoefer
1100	"A Comparative Performance Study of Absorbing Boundary Conditions in TLM and FDTD"	C. Eswarappa & W.J.R. Hoefer
1120	"Modelling of Coplanar Waveguide Discontinuities Using the Alternating Transmission Line Matrix (ATLM) Method"	B. Bader & P. Russer
1140	"Quasi-Static Correction of a Knife Edge Corner in 2D TLM Algorithm"	L. Cascio, G. Tardioli, T. Rozzi, & W.J.R. Hoefer
1200	**LUNCH**	
1200	**BOARD OF DIRECTORS MEETING/LUNCHEON**	**DelMonte Room, , Herrmann Hall**

TUESDAY AFTERNOON

1400-1800	**VENDOR EXHIBITS AND STARTING AT 1600 -1800, WINE AND CHEESE BUFFET**	**Ballroom, Herrmann Hall**
SESSION 6:	**INTERACTIVE TECHNICAL SESSION,**	**Ballroom, Herrmann Hall**
1400-1800	"Electromagnetic Visualization Using Commercial Software"	H.A. Nott
	"Performance of Multiple, Thin Layers of Lossy Dielectrics as Broadband Attenuators"	G.W. Jarriel, Jr., M.E. Baginski, & L.S. Riggs
	"Research & Engineering Framework (REF) Data Dictionary Specification for Computational Electromagnetics"	J.A. Evans
	"Development of an Electromagnetic and Mechanical Simulation Tool for the Computer Modeling of the TACAMO LF/VLF Communication System"	M.C. Longtin, R.W. Sutton, K.J. Laskey, & P.J. Morrison
	"A New Look at Antenna Traps"	P.W. Leonard
	"Imaging of Conductive and Ferromagnetic Materials Using a Magnetic Induction Technique"	J. Ferreira, F. Linhares, J. Velez, J. de Ribomar S. Oliveira, & A.R. Borges
	"Investigation of the Properties of Wavelet-Like Basis Functions in the Finite Element Analysis of Elliptic Problems"	L.A. Harrison & R.K. Gordon
	"Continuing Development of the Research and Engineering Framework (REF) for Computational Electromagnetics"	L.W. Woo, B. Hantman, K. Siarkiewicz, J. LaBelle, & R. Abrams
	"Numerical and Experimental Modelling of Liquid Dielectrics Using a Coaxial Cavity"	M. Bingle, D.B. Davidson, & J.H. Cloete
	"Hardware/Software Codesign Model for XPATCHF Optimization"	B.A. Kadrovach, T.S. Wailes, A.J. Terzuoli, Jr., & D.S. Gelosh
	"3D FDTD Simulation of EM Detection of Buried Waste"	D. Sullivan, B. Hansen & N. Skousen
	"Application of Digital Filters to the Construction of Wideband Dispersive Boundary Conditions"	M. Mrozowski, M. Niedźwiecki, & P. Suchomski
	"Note on Large Crane Coupling to Nearby AM Radio Stations"	P.W. Leonard & J.B. Hatfield
	"XPATCHF Software System Analysis and Profiling"	B.A. Kadrovach, T.S. Wailes, A.J. Terzuoli, Jr., & D.S. Gelosh
	"Theoretical Studies of Photonic Band Gap Materials"	M. Sigalas, R. Biswas, C. Chan, K. Ho, & C. Soukoulis
	"On the Use of Richardson Extrapolation in the Finite Element Analysis of Two-Dimensional Electrostatics Problems"	W.E. Hutchcraft & R.K. Gordon
	"Scattering from Chirally Coated Bodies"	R. Sharma & N. Balakrishnan

TUESDAY AFTERNOON 19 MARCH 1996

1400-1800	**VENDOR EXHIBITS AND STARTING AT 1600 -1800, WINE AND CHEESE BUFFET**	**Ballroom, Herrmann Hall**
SESSION 6:	**INTERACTIVE TECHNICAL SESSION, (cont)**	**Ballroom, Herrmann Hall**
	"A Mixed Formulation to Compute the Source Current Density in Inductors of Any Shape"	F. Robert, P. Dular, J.F. Remacle, M. Urné, & W. Legros
	"High Power Microwave Amplification for High-Intensity Relativistic Electron-Beam Storage-Rings"	R.A. Speciale
	"Real-Time Digital Signal Processor in Ionosphere Measurements"	A.L. Karpenko & V.V. Koltsov
	"High Frequency Electromagnetic Safety Analysis by Numerical and Empirical Methods on Mobile Platforms"	M.J. Packer, & R.C. Ferguson
	"Computational Modeling of Wave Plasma Interaction"	V.A. Eremenko & Y.Cherkashin
	"Attenuation of HF Radio Waves in a Forest: Results from Experiment"	I.P. Zolotarev. V.A.Popov & V.P. Romanuk
	"Statistical Reflection Properties of Electromagnetic Monopulse by Buried Object in Subsurface Random Ground Using FDTD"	Y. Miyazaki & Y. Jyonori
	"Running NEC4 on the Cray at NPS"	B. Neta
1730	**NO HOST BAR**	**Terrace Room**
1830	**AWARDS BANQUET**	**Ballroom, Herrmann Hall**

WEDNESDAY MORNING 20 MARCH 1996

0715	**CONTINENTAL BREAKFAST**	
SESSION 7:	**FDTD APPLICATIONS AND ENHANCEMENTS (Parallel with Sessions 8, 9, 10, 11 & 12)** Chair: J.H. Beggs	**102 Glasgow Hall**
0800	"UHF/VHF Propagation Model Characterization Over Irregular Terrain Using MOM/FDTD"	K.A. Lysiak, J.K. Breakall, & J. Zmyslo
0820	"Validation of FDTD Modeling of Ground-Penetrating Radar Antennas"	B.J. Zook
0840	"FDTD Analysis of Radiation from a Lens Terminated Conical TEM Antenna"	S.A. Blocher, E.A. Baca, & T.S. Bowen
0900	"FDTD Analysis of a Dipole Antenna Driven from Various Excitation Sources"	M.R. Zunoubi, N.H. Younan C.D. Taylor, & J.H. Beggs,
0920	"An Efficient Hybrid PEE-FDTD Field Modeling Technique in Cylindrical Coordinates"	M. Mrozowski, M. Okoniewski, & M.A. Stuchly
1000	**BREAK**	
SESSION 8:	**FINITE ELEMENT AND FINITE VOLUME METHODS FOR ELECTROMAGNETIC FIELD SIMULATION** Chairs: R. D-Edlinger and R. Lee **(Parallel with Sessions 9, 10, 11 & 12,**	**102 Glasgow Hall**
1020	"Local Tetrahedron Modeling of Microelectronics Using the Finite-Volume Hybrid-Grid Technique"	D.J. Riley & C.D. Turner
1040	"Full Wave Vector Maxwell Equation Modeling of Self-Limiting Effects and Optical Nonlinear Vortices"	S.V. Polstyanko & J-F. Lee
1100	"A Hybrid FEM-FMM Technique for Electromagnetic Scattering"	S. Bindiganavale & J.L. Volakis
1120	"Finite Element Method Analysis of the Celestron-8 Telescope"	R.R. DeLyser & H. Pohle
1200	**LUNCH**	
SESSION 9:	**NUMERICAL ERROR ANALYSIS AND CONTROL I (Parallel with Sessions 7 8, 10, 11, & 12)** Chair: J.L. Volakis	**122 Engersoll Hall**
0800	"Error Analysis in the Adaptive Integral Method (AIM)"	E. Bleszynski, M. Bleszynski, & T. Jaroszewicz
0820	"Using Model-Based Parameter Estimation to Estimate the Accuracy of Numerical Models"	E.K. Miller
0840	"Guidelines for Using the Fast Multipole Method to Calculate the RCS of Large Objects"	S.S. Bindiganavale & J.L. Volakis
0900	"Developments in Error Estimation for Covolume and Staggered Mesh Approximations to Maxwell's Equations"	R.A. Nicolaides & D-Q. Wang
0920	"Adaptive Methods for the Numerical Solution of Reaction-Diffusion Problems"	D.J. Estep, M.G. Larsson & R.D. Williams
0940	"Error Estimates for Subgridded FDTD Schemes"	P. Monk
1000	**BREAK**	

WEDNESDAY MORNING 20 MARCH 1996

SESSION 10:	**NUMERICAL LINEAR ALGEBRA IN COMPUTATIONAL ELECTROMAGNETICS** Chair: A.S. Hodel **(Parallel with Sessions 7, 8, 9, 11, & 12)**	**122 Ingersoll Hall**
1020	"Applications of Numerical Linear Algebra in Electromagnetics"	G.K. Gothard, J.H. Henderson, & A.S. Hodel
1040	"Multilevel Preconditioning for the Time-Harmonic Maxwell Equations"	G. Starke
1100	"Iterative Solution Methods for ill-Posed Problems"	D. Calvetti, L. Reichel, & Q. Zhang
1120	"Methods for Large Sparse Eigenvalue Problems from Waveguide Analysis"	C. Peng & D. Boley
1140	"Iterative Solution of Field Problems in Space-Decoupled Configurations"	G. Bürger, & H. Singer
1200	**LUNCH**	
SESSION 11:	**NEC APPLICATIONS (Parallel with Sessions 7, 8, 9, 10, & 12)** Chairs: M. Ney and C. Christopoulos	**Engr. Auditorium**
0800	"Numerical Investigation of Antennas for Hand-Held Radiotelephones Using NEC Code"	A.A. Efanov, M.S. Leong, & P.S. Kooi
0820	"Evaluation of the Discrete Complex-Image Method for a NEC-Like Moment-Method Solution"	G.J. Burke
0840	"The Improvement of NEC-2's Out-of-Core Operation and the Analysis of UHF Monopole Antenna Mounted on a Car Model"	K. Natsuhara, T. Suda Y. Kazama, & K. Madono
0900	"MatNEC: A MATLAB Based Graphical Interface to SuperNEC"	R.M. Cooper
1000	**BREAK**	
SESSION 12:	**VALIDATION (Parallel with Sessions 7, 8, 9, 10, & 11)** Chair: D.R. Pflug	**Engr. Auditorium**
1020	"First and Second Generation Transformable Scale Aircraft-Like Models for Code Validation: Present Results and Future Plans"	D.R. Pflug, T.W. Blocher D.E. Warren, & D.O. Ross
1040	"Software for Modeling Helix Antennas with NEC and Validation by Measurement"	C.W. Trueman, N. Sultan, S.J. Kubina, & T. Pellerin
1100	"Evaluation of the Sensitivity of Scattering Predictions to Uncertainties in Material Characteristics"	G.A. Barnhart, A.J. Terzuoli, Jr., & G.C. Gerace
1120	"Validation of the PO-based RCS Code SIGMA by Using IEM and Experiments"	E. Kemptner, D. Klement, & V. Stein
1200	**LUNCH**	

WEDNESDAY AFTERNOON

SESSION 13:	**OPTIMIZATION (Parallel with Session 15 & 16),** Chair: E. Michielssen	**Engr. Auditorium**
1320	"Optimization of Broad-Band Loaded Wire Antennas in Real Environments Using Genetic Algorithms"	D.S. Weile, E. Michielssen, & A. Boag
1340	"Genetic Algorithms Based Pattern Synthesis Approach for Arbitrary Array Designs"	Y. Lu & K.K. Yan
1400	"Speeding Convergence of Genetic Algorithms for Optimizing Antennas Arrays"	R.L. Haupt
1420	"Order Recursive Method of Moments for Iterative Design Application"	K. Naishadham & P. Misra
1500	**BREAK**	
SESSION 14:	**MULTIPOLE TECHNIQUES** Chair: P. Leuchtmann	**Engr. Auditorium**
1520	"Discrete Sources Method for the Silicon Wafers Defect Discrimination"	Y. Eremin & N.V. Orlov
1540	"Iterative Scheme of Discrete Sources Amplitudes Determination Based on D-matrix Approach"	Y. Eremin
1600	"An Improving Technique for MMP Solutions Based on Ficticious Surface Sources"	M. Gnos & P. Leuchtmann
SESSION 15:	**ANTENNA ANALYSIS (Parallel with Sessions 13 & 16)** Chairs: A.W. Glisson and A.A. Kishk	**122 Ingersoll Hall**
1320	"Accurate Design of Shaped Beam Doubly Curved Reflector Antennas for Airborne Applications"	B.S. Shridhar & N. Balakrishnan
1340	"Rapid Parametric Study of Antennas Using Moment Method Codes"	G.P. Junker, A.A. Kishk, & A.W. Glisson
1400	"A Numerical and Experimental Investigation of a Shipboard DF Antenna Array"	J.B. Knorr
1420	"Radiation Patterns of Antennas Mounted on an Attack Helicopter"	O. Givati, A. Fourie, & J. Dresel
1440	"Modelling of a Discone Antenna Mounted on a Communication Van"	J.S. Seregelyi

WEDNESDAY AFTERNOON 20 MARCH 1996

SESSION 15:	**ANTENNA ANALYSIS (Parallel with Sessions 13 & 16) (cont)**	**122 Ingersoll Hall**
1500	**BREAK**	
1520	"Dielectric Resonator Antenna Analysis and Design Using the FDTD Method"	K.P. Esselle
1540	"A Numerical and Experimental Investigation of a Semi-Loop Antenna on a Metal Box"	J.B. Knorr & D.C. Jenn
SESSION 16:	**EMI/EMC (Parallel with Sessions 13 & 15)** Chairs: T.H Hubing and J.L. Drewniak	**102 Glasgow Hall**
1320	"On the Suitability of Simple Voltage Source Models for the Study of Mutual Coupling Effects"	G.P. Junker & A.W. Glisson, & A.A. Kishk
1340	"Susceptibility Modeling for PCBs with Long Wires Attached"	B. Archambeault & H.S. Berger
1400	"Computer Modeling Tools for EMC"	T.H. Hubing & J.L. Drewniak
1420	"Electromagnetic Induced Timing Defects in CMOS Chips"	R. Perez
1440	"Finite-Difference Time-Domain Analysis of Common Mode Cable Currents"	C-W. Lam
1500	**BREAK**	
1520	"Statistical Coupling of EM Fields to Cables in an Overmoded Cavity"	R. Holland & R. St. John
1540	"Power and Ground Plane Modeling and Decoupling in High Speed Printed Circuit Board and Multichip Modules"	F. Yuan, C-W. Lam, & L. Rubin
SESSION 17:	**ARRAYS** Chair: L. Epp	**122 Ingersoll Hall**
1600	"Synthesis of Phased Arrays Aperture Distributions"	R.A. Speciale
1620	"New Results in the Synthesis of Aperture-Field Distributions for Ultra-High-Gain Phased Arrays"	R.A. Speciale
1640	"Advanced Design of Phased Array Beam-Forming Networks"	R.A. Speciale
1730	**BOARD OF DIRECTORS DINNER**	

THURSDAY MORNING 21 MARCH 1996

0715	**CONTINENTAL BREAKFAST**	
SESSION 18:	**FINITE ELEMENTS II (Parallel with Sessions 19, 20, & 21)** Chair: J.M. Jin	**102 Glasgow Hall**
0800	"Adaptive Mesh Refinement Concepts for Electromagnetics"	Z. Chen & R. Lee
0820	"Analysis of Complete Basis Sets of DivergencelessVector Expansion Functions for Finite Element Problems"	M.J. Walker
0840	"Multi-Mode S-Parameter Computation Using Finite Elements and Perfectly Matched Absorbers"	G.C. Lizalek, J.J. Ruehl, & J.R. Brauer
0900	"Characterization of MIMICs Packages Using a Parallelized 3D FEM Code"	J-G. Yook & L.P.B. Katehi
0920	"Combined PML and ABC for Finite Element Analysis of Scattering Problems"	J.M. Jin & W.C. Chew
0940	"Modeling Microstrip Patches Using the Finite Element Method"	D.B. Davidson, D.H. Malan, & C.B. Wilsen
1000	**BREAK**	
1020	"H_1(curl) Tangential Vector Finite Element Method with Additional Constraint Equation"	P. Bretchko, S.V. Polstyanko, & J-F. Lee
1040	"Extension of Higher-Order 3-D Vector Finite Elements to Curved Cells and Open-Region Problems"	J.S. Savage & A.F. Peterson
1100	"The Hybrid FEM/BEM Solution for EM Scattering from Arbitrary Cavity with Lossy and Anisotropic Material"	J. Xu, Y. Lu, & J.S. Fu
1200	**LUNCH**	
SESSION 19:	**FUTURE FIELDS FOR FDTD ANALYSIS (Parallel with Sessions 18, 20 & 21)** Chairs: D. Katz and M. Piket-May	**122 Ingersoll Hall**
0800	"FDTD Analysis of a Dielectric Leaky-Wave Antenna Using PML"	M. Chen, B. Houshmand, & T. Itoh
0820	"FDTD Analysis in Cylindrical Coordinates of a TEM Pyramidal Horn Antenna"	D. Menditto, P. Tognolatti, & F. Bardati
0840	"A Modified FDTD (2,4) Scheme for Modeling Electrically Large Structures with High Phase Accuracy"	M.F. Hadi & M. Piket-May, & E.T. Thiele
0900	"Application of the FDTD Method to Three-Dimensional Propagation in a Magnetized Ferrite"	J.W. Schuster, & R.J. Luebbers

THURSDAY MORNING 21 MARCH

SESSION 19:	**FUTURE FIELDS FOR FDTD ANALYSIS (Parallel with Sessions 18, 20 & 21) (cont)**	**122 Ingersoll Hall**
0920	"Symmetry-Aided FDTD Analysis of Finite Phased Arrays"	D. Crouch
0940	"Conformal FVTD with a Rectangular Grid for PEC Scattering Objects"	K.S. Yee & J.S. Chen
1000	**BREAK**	
1020	"Application of Recent Advances in FDTD Modeling to the Problem of Acoustic Propagation in Shallow Water"	J.B. Schneider, F.D. Hastings. & C.J. Railton
1040	"FDTD Analysis of Small Loop Antennas for Partial Exposure of Rat Head at 837 MHz"	K.W. Chan, J.A. McDougall, & C.K. Chou
1100	"Scattering from Complex Geometries Using a Parallel FVTD Algorithm"	V. Ahuja & L.N. Long
1120	"FDTD Simulation of High Frequency Devices by Using Locally Refined Meshes"	P. Thoma & T. Weiland
1200	**LUNCH**	
SESSION 20:	**NUMERICAL ERROR ANALYSIS AND CONTROL II (Parallel with Sessions 18, 19, & 21)** Chair: J.L. Volakis	**Engr. Auditorium**
0800	"A WWW-Based Data Base for Code Validation"	C.W. Trueman & S.R. Mishra
0820	"Code Scaling"	M.J. Schuh & A.C. Woo
0840	"An Overview of Numerical Dispersion Error in PDE Methods for Electromagnetics"	R. Lee
0900	"Non-rigorous CEM Error Estimates and Their Limitations"	A.F. Peterson
0920	"Comparisons of Staggered and Non-Staggered Schemes for Maxwell's Equations"	D. Gottlieb & B. Yang
0940	"Minimizing the Number of Frequency Samples Needed to Represent a Transfer Function Using Adaptive Sampling"	E.K. Miller
1000	**BREAK**	
SESSION 21:	**MODELING TOOLS FOR VISUALIZATION: PRE- AND POST-PROCESSING** Chair: J. Karty **(Parallel with Session 18, 19, & 20)**	**Engr. Auditorium**
1020	"MATLAB NEC Toolbox: The Cross Platform GUI Pre-and Post-processing Tool for NEC Applications"	Y. Lu
1040	"Computation and Graphic Visualization of Plane-Wave K-Space Spectra and Far-Field Patterns with MATLAB 4.0"	R.A. Speciale
1100	"The Intelligent Computational Electromagnetics Expert System (ICEMES)"	A.L. Drozd, T.W. Blocher, V.K. Choo, & K.R. Siarkiewicz
1120	"NECSHELL - A New Graphical User Interface for the NEC Code"	M.Y. Mikhailov, V.O. Lomtev, & A.A. Efanov
1200	**LUNCH**	

THURSDAY AFTERNOON

SESSION 22:	**FINITE ELEMENT ANALYSIS (Parallel with Session 23 & 25)** Chair: J.R. Brauer	**102 Glasgow Hall**
1320	"Finite Element Scattering and Radiation Analysis Using Prismatic Meshes and Artificial Absorbers for Conformal Domain Truncation"	M. Casciato, M. Nurnberger T. Özdemir, & J.L. Volakis
1340	"Application of Fast Multipole Method to Finite Element-Boundary Integral Solution of Scattering Problems"	N. Lu & J-M. Jin
1400	"Use of Perfectly-Matched Absorber Boundaries in Finite Element Analysis of Patch Antennas"	J.F. DeFord & G.C. Lizalek
1420	"A New Permanent-Magnet Synchronous Motor Design Configuration and Finite Element Analysis"	Q.K. Zhang, N. Ida, Y. Qiu, & Z.R. Jiang
1440	"Investigation of ABC Behavior in Axisymmetric Electrostatic Finite Element Analysis"	A. Konrad & L. Han
1500	**BREAK**	
1520	"An Efficient Scheme for Finite Element Analysis in the Frequency Domain"	M. Kuzuoglu, R. Mittra, J.R. Brauer, & G.C. Lizalek
1540	"Finite-Element Modelling of Head Coils for High-Frequency Magnetic Resonance Imaging Applications"	J.G. Harrison & J.T. Vaughan
1600	"H_1(curl) TVFEM in Conjunction with PML for Modeling 3D Waveguide Discontinuities"	S.G. Perepelitsa, R. Dyczij-Edlinger, & J-F. Lee

THURSDAY AFTERNOON 21 MARCH 1996

SESSION 23:	**METHOD OF MOMENTS APPLICATIONS (Parallel with Sessions 22 & 25** Chair: A.F. Peterson	**Engr. Auditorium**
1320	"Global Fourier-Series Basis Functions for EM Scattering"	M.H. Smith & A.F. Peterson
1340	"A Numerically Stable Method of Moments Time Domain Model"	L.B. Gravelle & J-P. Estienne
1400	"Method of Moments Analysis of the Celestron-8 Telescope"	R.R. DeLyser, P. Ensaf, & P. McDaniel
1500	**BREAK**	
SESSION 24:	**FDTD ANALYSIS AND APPLICATIONS (Parallel with Session 26)** Chair: A. Elsherbeni	**102 Glasgow Hall**
1520	"Dynamic Analysis of V Transmission Lines"	O.M. Ramahi, A.Z. Elsherbeni, & C.E. Smith
1540	"An Absorbing Boundary Condition for the FDTD Method Using Digital Filters Design Technique"	C-N. Kuo & T. Itoh
1600	"Application of the FDTD Method to the Electromagnetic Modeling of Patch Antenna Arrays"	M.F. Pasik, G. Aguirre, & A.C. Cangellaris
SESSION 25:	**MICROWAVE COMPONENTS (Parallel with Sessions 22 & 23)** Chairs: M.E. Baginski and M.M. Ney	**122 Ingersoll Hall**
1320	"Parallel Coupled Microstrip Patch Resonators on a Ferrimagnetic Layer"	J. de Ribamar S. Oliveira & A. Gomes d'Assunção
1340	"Fullwave Analysis of Circular Cylindrical Backed Slotlines"	L. Martins de Mendonça & A. Gomes d' Assunção
1400	"Properties of Tapered Microstrip Lines on Dielectric and Magnetized Ferrimagnetic Layers"	A. Gomes d' Assunção, F. de Lima, & M.R.M. Lins de Albuquerque
1420	"Frequency and Time Domain Computations of S-Parameters Using the Finite Integration Technique"	R. Schumann, M. Clemens, P. Thoma, & T. Weiland
1440	"Time Domain Analysis of Microwave Structures by MRTD"	M. Krumpholz, E. Tentzeris, R. Robertson, & L.P.B. Katehi
1500	**BREAK**	
1520	"A Parasite-Free Non-Orthogonal Finite-Difference Frequency-Domain Method for the Analysis of Inhomogeneous Lossy Waveguides"	L. Zhao & A.C. Cangellaris
SESSION 26:	**BIOMEDICAL ELECTROMAGNETICS (Parallel with Sessions 24)** Chairs: A.M. Morega and R.K. Gordon	**122 Ingersoll Hall**
1540	"A Spectral Approach to the Cardiography"	A.M. Morega, D. Mocanu, & M. Morega
1600	"Optimal Transcutaneous Pacing"	A.M. Morega, B. Ciocârlan, & M. Morega
	CLOSE	

FRIDAY MORNING 22 MARCH

0830-1200	**SHORT COURSE (HALF-DAY)** "Using Model-Based Parameter Estimation to Increase the Efficiency and Effectiveness of Computational Electromagnetics" E.K. Miller	**122 Ingersoll Hall**
0830-1600	**SHORT COURSE (FULL-DAY)** "Conformal Time Domain Numerical Electromagnetics" K. Yee, Lockheed	**102 Glasgow Hall**
0830-1630	**SHORT COURSE (FULL-DAY)** "Finite Element Methods for Electromagnetics" J.L. Volakis, University of Michigan, and J. Brauer, Mac-Neal Schwendler Corporation.	**109 Glasgow Hall**

FRIDAY AFTERNOON

1300-1630	**SHORT COURSE (HALF-DAY)** "Antenna Properties in Linear and Nonlinear Environments" R. Bevensee, BOMA Enterprises	**122 Ingersoll Hall**

SESSION 0:

AMATEUR RADIO SESSION

Chair: W. P. Wheless, Jr.

Ground-Plane Type Antennas with Elevated Radial Systems

John S. Belrose, VE2CV
Radio Sciences
Communications Research Centre
PO Box 11490 Station H
Ottawa ON K2H 8S2

Introduction

From the earliest days of radio the merits of elevated counterpoise and radial systems have been recognized because of the way in which current densities in the ground are more or less uniformly distributed over the area of the insulated counterpoise (which is in effect a large capacitance ground), c.f. **Fig. 1.** This figure shows wires running radially outwards on insulated supports without connection being made to earth plates or ground stakes at the outer ends of the system. An alternate view on the way an elevated radial system works is that it allows the collection of electromagnetic energy in the form of displacement currents, rather than conduction currents flowing through lossy earth. Certainly when only a few elevated radials are used, we cannot consider the counterpoise forming a large capacitance ground.

The development of such ground systems was, by necessity, empirical in nature, as sophisticated instrumentation and standardized antenna testing procedures were not available in the early days of radio. And, after about 1937, the use of elevated radial systems became an almost a forgotten art, because of research by Brown et. al. [1937] in favor of the buried radial system. These authors carried out a very extensive measurement program to determine the radiation efficiency of a vertical monopole as a function of ground system parameters. A result of their work leads to their recommendation that 120 radial wires each one half a wavelength long should be used to maximize antenna efficiency.

In the light of what we know today [Burke and Miller, 1989] it is surprising that empirical design, tradeoffs and optimization procedures did not emerge, since the performance of thousands of MF broadcast stations has been measured, but most stations simply used ground systems based on this recommendation. Also surprising, is that while radial systems are conventionally buried, some stations have used insulated radials, and ground conductivies are very variable from one site to another, yet radial anti-resonant effects have apparently not been found, or were missed.

VHF/UHF monopole/ground plane (GP) type antennas, e.g. a quarter wavelength vertical radiator element with four radial rods, have been used for communications for decades. Terman [1943] describes such an antenna as one of a class of flagpole antennas. Vertical antennas with a few roof top mounted quarter wavelength radial wires (a few for several bands) are a popular choice for amateur communications, particularly on the lower HF bands. These antennas are simple to erect, easy to tune, and are relatively unobtrusive.

There is still confusion between the true vertical monopole, with its 'infinite' ground plane, the real Earth, usually assisted by a number of buried radials, and the elevated ground plane with horizontal wire radials or rods sometimes described as a 'non-radiating artificial ground plane'. But four radial rods used with a monopole antenna can hardly be considered to simulate a true ground plane. Moxon, G6XN [1992] considers that the elevated ground plane antenna with two, three or four quarter wavelength wire radials needs to be considered as a form of dipole, rather than a vertical ground-plane type monopole antenna. Certainly there are a number of differences. A monopole

antenna with four horizontal radial rods at a height of several wavelengths has an input impedance of 22-ohms, and can have a vertical dipole like pattern. A ground plane antenna on a square or circular metal sheet, of sufficient size, has an input impedance of 36-ohms, and while the maximum gain can approximate that for a monopole on an infinite metal sheet, for ground planes of practical size there is a pattern null on the horizon (the plane of the finite ground-plane), c.f. Foster and Miller [1981].

One has also to be careful with GP type antennas that are at a height of a wavelengths or more, and are fed with coax. Tilson and Secord [1967] showed that the measured vertical radiation pattern VRP, of VHF/UHF ground rod antennas varies markedly with changes in element lengths and the degree to which RF currents can be kept off the outer braid of the coaxial feed line. These authors showed some typical VRPs for various ground rod antennas. The VRP that looked dipole like had 0.237λ radials and a monopole height of 0.25λ with chokes on the feedline.

Elevated counterpoise type of ground systems were extensively experimentally studied by Doty, Frey and Mills [1983]. The radial systems they used were not unlike that shown in **Fig. 1**, i.e. the counterpoise wires filled a square or rectangular area over the ground, rather than being of equal or a resonant length. Christman, KB8I [1988] was perhaps the first to show by numerical modeling that a vertical monopole with a few (four) radial wires could be at a height quite low over real ground before the radiation efficiency of the antenna was significantly degraded. Unfortunately the topic of ground mounted and elevated radials, and antennas with elevated feed, has remained clouded by controversy, e.g., recent posting on the INTERNET News Group on Radio Amateur Antenna; and, c.f. Belrose [1995].

Continuing, if four elevated radials can be used to realize performance for a monopole comparable with many buried radials, then elevated radials can be used for real antennas; and as well to simulate ground 'connection' for numerical modeling programs like NEC-2, which does not permit a wire to connect to lossy ground.

This paper briefly overviews the subject of elevated radials, and presents a few case studies for different ground plane type antennas.

Vertical Monopoles

Ground Mounted Radial Systems

NEC-2 is currently enjoying wide application by amateurs in radio, using PC based programs such as EZNEC, available from Roy Lewallen, W7EL; and NEC/Wires, available from Brian Beasley, K6STI. The ability of the NEC codes to accurately treat the air-ground interface (based on the Sommerfeld-integral formulation) is assumed to be validated by the developers of the program [Burke and Miller, 1989].

As mentioned at the outset, the most comprehensive set of experimental data is that obtained by Brown and his colleagues, who measured impedance and efficiency for several antenna heights, employing buried radial ground systems, 0.411, 0.274 and 0.137 λ long. For each length of radial system 2, 15, 30, 60, and 113 radial wires were used. While NEC-2 is not suited to model these experiments, we have used this code, by employing ground mounted radials at a height of 6.25×10^{-5} λ (5 mm at 3.75 MHz), and have achieved a rather close agreement between antenna resistances predicted and measured.

For the case studies to be reported here, we chose, initially, to model a 3.75 MHz monopole over a radial wire system where all elements were # 10 copper wire, and all wires, monopole

height and radials were 20 m long (0.25 λ long for a wavelength of 80 m).

Tom Rauch, W8JI [private communications, 1995] conducted a series of experiments with a 3.7 MHz quarter wavelength vertical wire antenna using elevated and ground mounted radials. His measured relative field strengths for the ground mounted radial systems change, as number of radials is changed, in a way closely like that predicted by NEC-2. For 4, 8 and 16 radials on the ground, his measured gain differences referenced to the relative field strength measured for 60 radials on the ground, were -5.5 dB, -2.7 dB and -1.3 dB. For an insulated radial system, height of 5 mm, with 4, 8, 16, 32 and 64 quarter-wavelength radials, EZNEC predicts gains for an antenna over average ground (σ = 3 mS/m; ε = 13) of -4.95 dBi, -2.1 dBi, -0.43 dBi, +0.21 dBi and +0.24 dBi.

Elevated Radials

All experiments that the author is aware of have used radials of a fixed length, λ/4 long (physical length) as the height of the radial system was changed. But a radial wire at a low height over finitely conducting ground needs to increasingly shortened as its height is lowered, in order to realize and maintain resonance. The length for the ground mounted radial case study described above was for a fixed length radial, λ/4 long. The resonant length of a radial wire 5 mm above average ground is 0.138 λ, and so clearly the radials were not resonant. The impedance at 3.75 MHz, according to NEC-2, of our 20 m high vertical wire antenna with 4-radials 20 m long is Z_a = 140 + j 117 ohms (which is certainly not a resonant monopole), and the gain -4.95 dBi. But, if 4-resonant radials 11.1 m long (λ/4 electrical length) are used, the antenna is more or less resonant, Z_a = 53 - j 2 ohms, and the gain - 1.4 dBi.

The reason for this can be visually seen in **Fig. 2**, where we show the wire models for these two antenna systems, and the current distribution on the wires. Since a ground system is one side of a GP antenna, its purpose is to provide a low impedance against which the antenna can be driven. Ideally this impedance should have a low resistance, and only a small reactance, since we want to maximize the current on the antenna. While the ground plane antenna can be re-dimensioned to re-establish resonance, this will change the current distribution on the radiator. Clearly the longer radials (**Fig. 2a**) do not well fulfill these requirements. Since the radials are not resonant the terminal impedance of the monopole is changed, and, since the current on the source end of the radials is not the maximum current on the radial wires, the radial system couples more current and hence more power loss to the ground beneath, then does the shorter resonant radial system (**Fig. 2b**).

In **Fig. 3** we have plotted the predicted gain for a 20 m high vertical wire antenna vs. height in wavelengths for 4-radials a quarter wavelength long (20 m); for radials of resonant length (length is a function of height and ground conductivity, which for this graph is average ground); and the gain of a half wave dipole, for reference, where height is the lower end height of the dipole.

There are only a few measured results to compare with predicted performance. Christman [1990] measured groundwave field strengths at three distances for an 8 MHz vertical monopole with various ground systems. He made measurements with four λ/4 long elevated radials for three heights, 1 m, 3 m and 5 m, using direct and isolated feed, compared with 120 ground mounted radials. In his experiment he recorded 18 field strength values, but he had to reject a block of 4 values since the results (impedance and field strength) were quite inconsistent with the full set of measurements. His measurements, in our view, illustrate the difficulty experienced in accurately measuring at a few sites on different days small differences in gain

between different antenna systems. For example, his set of measured field strengths at three sites for a quarter wavelength monopole with 4-radials at 1 m and 3 m, direct feed, compared with 120 radials on the ground, correspond to relative gain differences, of -4, -2, -1, 0, 0, and +1 dB, for a median difference between 0 and -1 dB.

Beverage [1995] determined the efficiency of an experimental 0.17λ tower with six 0.25λ radials, 0.024λ high, at the operating frequency 1580 kHz, by measuring field intensity along 12 radial directions extending out to a distance of up to 85 km. The measured RMS efficiency was 287 mV/m for 1 kW radiated at 1 km, which is the same measured value as would be expected (FCC files) for a 0.17λ tower above 120 buried radials.

In spite of this good agreement between theory and experiment, there are doubts based on measurements, concerning the realizable performance of elevated radial systems. For example, Rauch's elevated radial measurements do not agree at all with prediction. He measured a trend in change of relative gain with change in number of radials (for a radial height of 2.44 m or 0.03λ at 3.7 MHz) that is almost identical with that for radials on the ground. For 4, 8 and 16 elevated radials, referenced to 60 radials on the ground, Rauch measured relative gains of -4.17 dB, -2.28 dB and -1.08 dB. For 4, 8, 16 and 32 0.25 λ elevated radials, EZNEC predicts gains of -0.02 dBi, +0.08 dBi, +0.13 dBi and +0.16 dBi.

Further experimental work apparently has to done to resolve these apparent differences.

Direct Feed vs. Isolated Feed

There is no doubt that a coax feeder supplying power to a monopole with elevated radials can have currents induced to flow on the outer surface of the shield, if the antenna is directly fed.

Beverage [1995] noted that if he disconnected the feedline from the antenna tuning unit input to an 1160 kHz ND tower with elevated radials (radial height 0.018 λ), and installed an RF choke made up of toroidal cores around the coaxial cable, that the antenna's impedance changed by a small amount, and a slight heating of the cores indicated that an RF current path did exist along the shield of the coaxial cable. When the antenna was retuned, however, no change in field strength could be detected.

For our model with a radial height at 0.0125 λ (1 m) the shield current is insignificant. We simulated a coaxial cable feeder by dropping a wire connected to the radial system vertically down, to a height of 5 mm, and then running it horizontally (beneath a radial for maximum coupling) for 19 and 39 m, to simulate a quarter and a half wavelength feeder. The change of impedance and gain was very small. The current on the quarter wavelength feeder was 0.075 amperes, for a 1 ampere source current; 0.08 amperes for a half wavelength feeder. "Now mind you" our simulated feeder was not connected to ground at the 'transmitter end'. However, with such close coupling to ground the current on the wire would quickly decrease to zero, and in the case of an actual real antenna, the coaxial cable could be buried. We simulated the effect of a feeder for Rauch, W8JI's experimental antenna, since his radials were at a higher height, 0.03 λ (2.4 m), to see if we could explain the results he obtained (previously discussed) with elevated radials -- but again the effects were small.

Phased Array with Elevated Radials

Ground systems for directive arrays have traditionally employed non-overlapping ground systems of 120 buried radials, i.e. the ground radials are terminated at the intersections. With elevated radials current flowing on one radial wire can couple with current flowing on an adjacent radial wire

associated with the other element of the array, see **Fig. 4**, which is a directive array comprising two $\lambda/4$ radiators $\lambda/4$ apart. Four resonant radials were used, 0.2333 λ long, which corresponds to a radial wire height 0.0125λ (1 m at 3.75 MHz) over average ground. If we examine the patterns (not shown here) for equal currents, having phase differences of 0^o, 90^o and 180^o, EZNEC predicts rather ideal patterns, which change from broadside, to cardioid, to an in-line figure-of-eight pattern; horizontally polarized component less than -28 dB below maximum gain.

It is interesting to examine the currents on the radials as the phase difference in the feed currents is changed. In **Table 1** we have tabulated the currents on the radial wires (maximum current on the segment close to the junction, for a source currents of 1 ampere). Notice how these currents change as the phase difference between the source currents is changed. Whether this is important, or an interesting detail is not known. Certainly with a buried radial ground system no one worried about differences that exit between currents on the different parts of the radial wire ground system.

Ground Plane Type Loops

The author has for some fifteen years used various types of ground plane type half-loops. The loop can have various shapes, a half-quad, a half-delta or a half-diamond. The perimeter of the loop is an electrical half wavelength. The loop is grounded at one end and fed against ground at the other end.

To model GP type half loop antennas using NEC-2 we have used elevated radials, see **Fig. 5**, which is a sketch for a half diamond loop with two sets of 3 elevated resonant radials (as above 0.2333 λ long). Notice that we have also added a wire connecting the lower ends of the sloping sides. The side length for a half-diamond loop is an electrical $\lambda/4$ wavelength (0.2627 λ for our loop). The current is a maximum at the fed and ground ends of the loop, and if these currents are exactly equal and in phase, there should be little or no current on the wire connecting the lower ends of the loop. Also, whatever current there is, the phase difference between current on one end and the other end of this wire should be 180^o. For our loop, according to NEC-2, the current on each end of this wire is small, 0.12 amps (0.02 amps for a half-quad with elevated radials), compared to the source current of 1 amp; and the phase difference between current on the ends of this wire is 179^o.

The predicted gain for this antenna over average ground, frequency 3.75 MHz is - 0.69 dBi, and the impedance (a resonant antenna) is 85 ohms. Hence resonant radials do indeed simulate an effective 'ground connection', since the loop behaves like a GP type resonant half-loop. **Figure 5** also shows the current distribution on the wires. As we have noted we would not expect any current on the wire connecting the ground ends of the loop to contribute much to the radiated field. We could therefore eliminate it, see **Fig. 6a**. When we do, there is only a small change in impedance (79 - j 2 ohms) and a small change in gain (- 0.43 dBi). While the antenna now may no longler look like a half-loop, it has the characteristics of a GP loop. Continuing, since the antenna radiates dominantly in the broadside directions, perhaps we only need radials in the broadside directions, see **Fig. 6b**. Again there is a change in impedance (71 - j 13 ohms) and a change in gain (0.38 dBi). We show in **Fig. 7** the radiation patterns for Fig. 5, 6a, and 6b's antennas.

Finally, we can perhaps eliminate the radials on one of the broadside directions, see **Fig. 6c**, to realize a directive antenna system. The antenna impedance is changed (110 + j 15 ohms) and the gain is changed (0.51 dBi at a launch angle of 31^o in the direction of maximum gain). In **Fig. 8** we show the radiation patterns for Fig. 6c's antenna.

Notice that here we have a unidirectional antenna system.

The author has recently learned that one of his colleagues is using an antenna system like that sketched in **Fig. 6c**. Eldridge, VE7BS erected a half diamond loop for 160M. Since he had an inadequate ground system (rocky ground), he decided to raise the loop, cut the base wire in the middle, and swing the two ends of the wire at right angles to the plane of the loop. The apex is at 33.5 m and the wires sloping down from the apex are each 40.8 m long. The ends of the sloping wires are 4.6 m above the ground. The antenna is fed by coax, with a choke balun. The center conductor of the coax is connected to the sloping wire, the shield to the 39.6 m wire running at right angles to the loop (which is now a radial wire). Both radial wires are 4.6 m above ground where they connect with the sloping wires, and these radial wires are also sloped, end height 1.5 m. The antenna was resonant at 1.84 MHz (VSWR about 2:1). According to EZNEC the resonate frequency is 1.86 MHz, impedance 105 ohms, gain 1.4 dBi, take-off angle 27°, front/back ratio 4.2 dB.

Lifting the 'half-loop' off the ground apparently made a quieter receive antenna, the resonance was easier to establish and to maintain, and the gain definitely favored the direction toward which the radials run. VE7BS noted that amateur stations in the favored direction, Japan, were always better received than on a horizontal loop, but stations in the opposite direction (southern and southeastern USA) were usually worse.

An Inverted-L antenna with Elevated Radials

In **Fig. 9a** we show an 80M inverted-L antenna with four 20 m long radials. The vertical part of the antenna is 3 m high, and the length of the horizontal arm 17 m. We considered this an interesting case to model, since the horizontal arm of the antenna can be arranged to lie directly over a radial. One would expect that this radial would carry the most current, and that the phase of this current would be approximately 180° with respect to the source current (a transmission line effect). EZNEC tells us that this is exactly the situation. The current on the radial wire beneath the horizontal arm of the inverted-L is 0.56 amps (171°), for a source current of 1 amp (0°). EZNEC also tells us is that if I increase the number of radials to 32, I get almost exactly the same pattern, see **Fig. 9**. If for the 4-radial case we orient the horizontal arm of the antenna in a direction which is the bisector of the radial directions, the current induced on the radials is less, and the gain is significantly less (-2.24 dBi compared with -0.1 dBi). Thus, apparently, if one wants a sparse radial system to perform like a multiwire radial system, one should arrange that the antenna couples maximum current into the radial system.

Conclusions

Elevated radial ground systems have many applications: 1) to realize achievable gain for a GP type antenna over real ground with only a few radials; 2) to provide versatility, e.g. control of radiation pattern; and 3) for modeling purposes one can simulate a "connection" to ground. For the case studies that we have described, a connection to ground was necessary, since the antenna was a ground plane type. But, for purposes of modeling, a connection to ground is sometimes wanted to simulate the effect of support structures, or other grounded towers in the vicinity of the antenna system. To work well, and to not change the resonant frequency of the GP antenna, *the radials must be resonant.*

References

Admiralty Handbook of Wireless Telegraphy [1938], Volume II, His Majesty's Stationary Office, London, Section "R", p. 28.

Beasley, Brian, K6STI, 3532 Linda Vista, San Marcos, CA 92069.

Belrose, J.S. [1995], "A vertical monopole with Elevated Feed--A Full-Length Radiator", QST, January 1995, pp. 78-79.

Beverage, C.M. [1995], "New AM Broadcast Antenna Designs having Field Validated Performance", paper presented at 49th Annual Broadcast Engineering Conference of the National Association of Broadcasters, Las Vegas, Nevada, 13 April, 1995.

Brown, G.H., R.F. Lewis and J. Epstein [1937], "Ground Systems as an Factor in Antenna Efficiency". Proc. IRE, 25, pp. 753-787, June 1937.

Burke, G.J. and E.K. Miller [1989], "Numerical Modeling of Monopoles on Radial Ground Systems", IEEE AP-S International Symposium, San Jose, CA, 26-30 June, 1989.

Christman, A. [1988], "Elevated Vertical Antenna Systems", QST, August 1988, pp. 35-42.

Christman, A. [1990], "Validation of NEC-3 (Numerical Electromagnetic Code) with Application to MF and HF Antenna Technology", Ph.D. Thesis, Ohio University, June 1990, p. 215.

Doty, A.C., J.A. Frey and H.J. Mills [1983], "Efficient Ground Systems for Vertical Antennas", QST, February 1982, pp. 20-25.

Foster. P.R. and T. Miller [1981], "Radiation patterns of a quarter wave monopole on a finite ground plane", IEE Conference Proceedings No. 195, pp. 451-456.

Lewallen, Roy, W7EL, PO Box 6658, Beaverton, OR 97007.

Moxon, L.A. [1992], "Ground Planes, Radial Systems and Asymmetrical Dipoles", The ARRL Antenna Compendium Volume 3, pp. 19-27.

Terman, F.E., "Radio Engineers' Handbook", McGraw-Hill, pp. 856-857.

Tilson, W.V. and A.H. Secord [1967], "The radiation patterns of ground rod antennas", Electronics & Communications, August 1967, pp. 27-30.

Table 1

Currents on radials for a two-element phased array, see Fig. 4.

Wire Number	Phase difference source currents 0-degrees	90-degrees	180-degrees
1	0.11/148°	0.3/152°	0.36/-175°
2	0.37/170°	0.3/-162°	0.16/-160°
3	0.28/-168°	0.21/-174°	0.25/170°
4	0.28/-168	0.21/-174°	0.25/170°
6	0.32/175°	0.22/-103°	0.2/15.6°
7	0.32/175°	0.22/-104°	0.2/15.6°
8	0.17/-172°	0.22/104°	0.31/-9.8°
9	0.17/172°	0.28/-79°	0.31/-9.8°

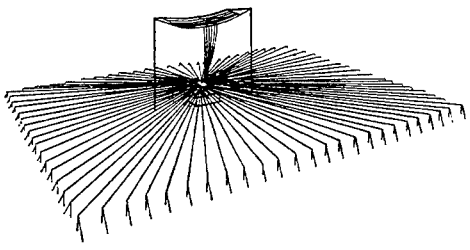

Fig. 1 T-antenna over a counterpoise earth [after Admiralty Handbook of Wireless Telegraphy, 1938].

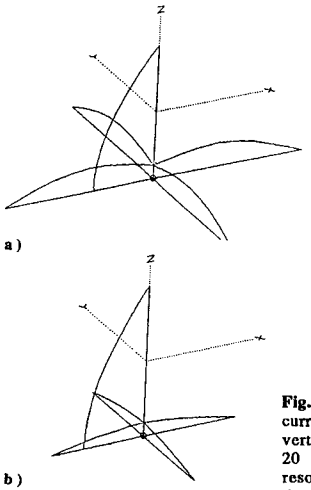

Fig. 2 Wire models, and current on the wires for a 20 m vertical wire antenna with four 20 m radials, and with four resonant radials (length 11.1 m) 5 mm above average ground.

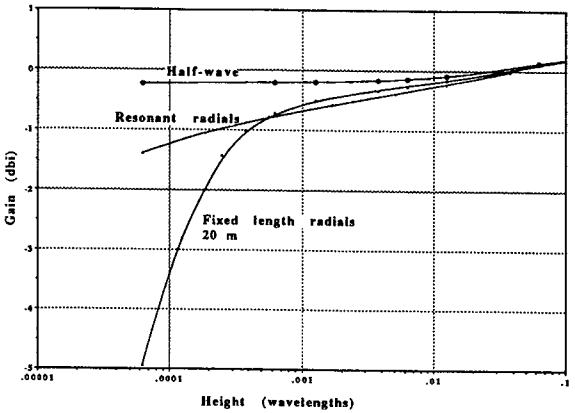

Fig. 3 Predicted gain for a $\lambda/4$ monopole with four $\lambda/4$ length radials, and with resonant radials vs. height (wavelengths) of radials over average ground; and for a half-wave dipole where height is lower end height of the dipole (frequency 3.75 MHz).

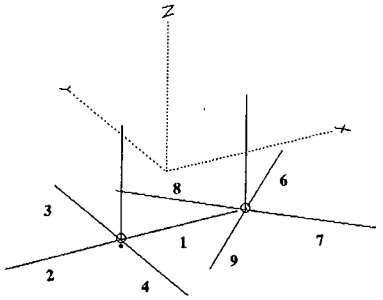

Fig. 4 Wire model for a 2-element phased array with elevated radials.

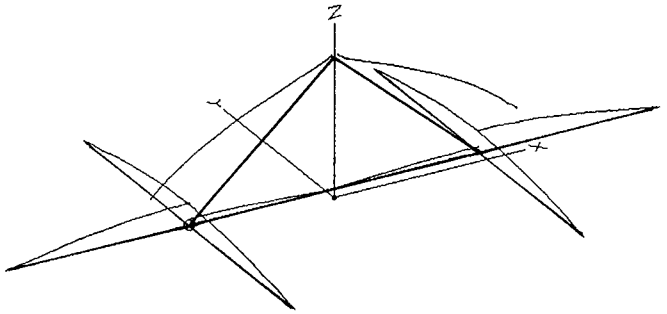

Fig. 5 Diamond ground plane type half-loop with elevated radials, and current on the wires. Note that amplitude of current is plotted without regard to phase.

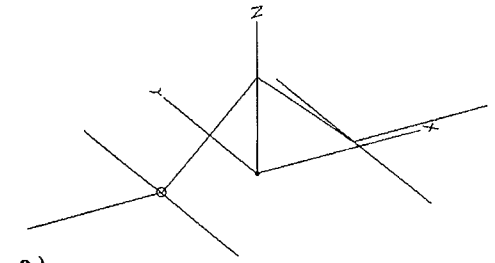

a)

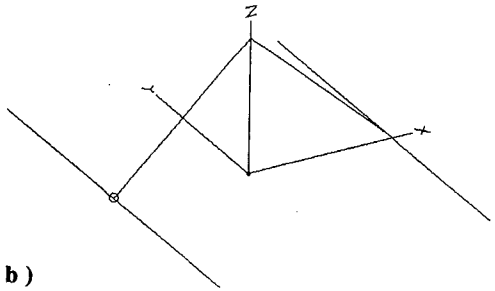

b)

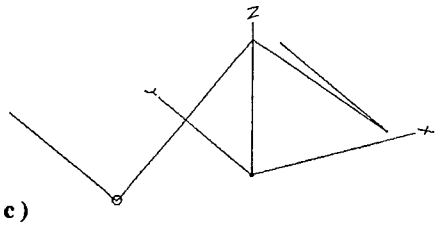

c)

Fig. 6 Figure 5's antenna with fewer radials.

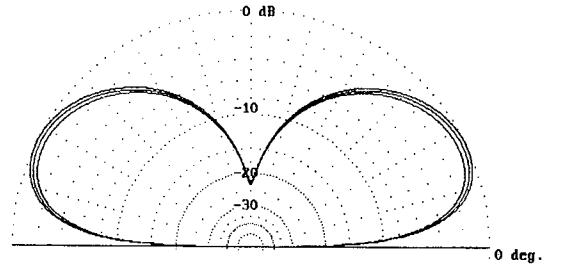

Elevation Plot
Azimuth Angle = 0.0 Deg.

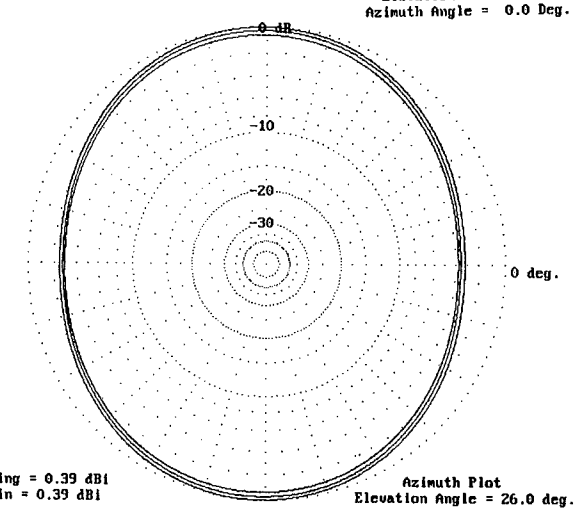

Outer Ring = 0.39 dBi
Max. Gain = 0.39 dBi

Azimuth Plot
Elevation Angle = 26.0 deg.

Fig. 7 Elevation and azimuthal patterns for Fig. 5, 6a and 6b's antenna (frequency 3.75 MHz).

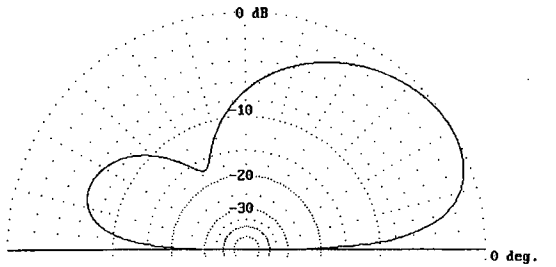

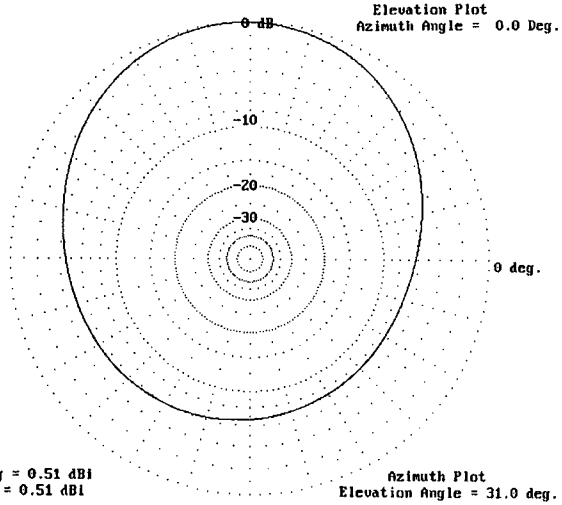

Fig. 8 Elevation and azimuthal patterns for Fig. 6c's antenna (frequency 3.75 MHz).

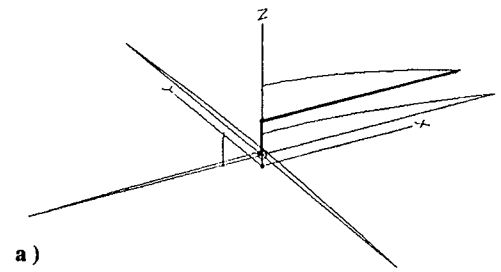

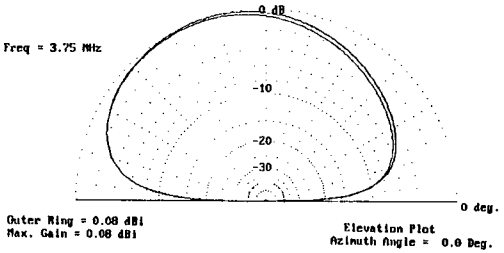

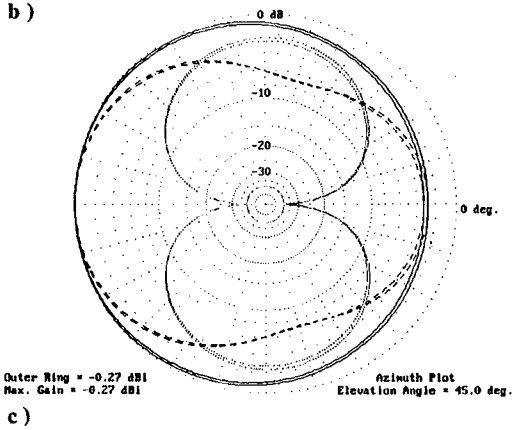

Fig. 9 a) wire model for an inverted-L antenna, and current on the wires; b) and c) elevation and azimuthal patterns for 4-radials, and for 32-radials (frequency 3.75 MHz).

REVIEW OF CHARACTERISTICS FOR HF DIPOLE ANTENNAS INCLUDING THE CASES WHERE THE DIPOLES ARE ABOVE AND PARALLEL TO THE SURFACE OF REAL-WORLD GROUNDS

by

G. M. Royer

ABSTRACT

The author has written a 95 page paper [4] which contains a comprehensive study of the characteristics for half-wave resonant HF dipole antennas, for the cases where the dipoles are: a) in free space, and b) above and parallel to the surface of a ground. The types of ground considered include those which are perfectly conducting and real-world; where real-world ground classifications range over what will be called: very dry, medium dry, and wet. The long length of [4] precludes its comprehensive presentation here; the author will therefore make available, at the conference, a number of copies of [4] for distribution among those who are interested in its contents.

1. INTRODUCTION

The computations used to obtain the characteristics contained in both this document and [4] were done with the aid of method of moments program NEC-3 (version 3 of Numerical Electromagnetic Code) [1]. Note that, although the author employed NEC-3, NEC-2 would have served as well.

Listed below are the half-wave resonant dipole chararacteristics which are investigated in [4] (see the next section for their definition): a) normalized resonant dipole length, b) input (feed gap) resistance, c) $SWR = 2$ bandwidth, d) zenith gain, and e) gain patterns. Due to length limitations on this proceedings paper, very little consideration will be given here to the chracteristics listed above under a) and e).

2. DEFINITIONS FOR VARIABLES

Figure 1 illustrates variables associated with the dipole's: a) dimensions, b) location with respect to the to surface of the ground (the XY plane), and c) orientation in the spherical (r, θ, ϕ) coordinate system.The dimensions l, g, d and h will respectively be referred to as dipole: length, feed gap width, wire diameter, and height above the ground. The frequency for the signal fed to the feed gap will be symbolized by f (Hz) (or ω (radians/sec.) where $\omega = 2\pi f$). The signal's free space wavelength is λ where $\lambda = c/f$ and c is the speed of signal propagation in free space ($c \simeq 299.8 \times 10^6$ m/sec.). The dipole's input (feed gap) impedance is expressed as $Z_a = R_a + jX_a$ in ohms(Ω)

The half-wave resonant condition for the dipole occurs when $X_a = 0$ and l is approximately equal to, but less than, $\lambda/2$. When the dipole is half-wave resonant let us symbolize f, λ and Z_a by respectively f_o, λ_o and $Z_{ao} = R_{ao} + j0$. For the case where the dipoles are half-wave resonant, the table and graphs (in both this document and [4]) will employ normalized representations for l, g, d and h; in particular we will be using: $\left(l/(\lambda/2)\right)_o$, $(g/\lambda)_o$, $(d/\lambda)_o$ and h/λ_o.

Let SWR represent the standing-wave ratio which would exist on a lossless transmission line, connected between a signal generator and the dipole's feed gap, where the transmission line's characteristic impedance is made to be the dipole's resonant feed gap resistance (R_{ao}). Subistitution of values for R_{ao} and Z_a as a function of f/f_o into eqns. (2) and (3) of [4], make it possible to compute SWR as a function of f/f_o. Figure 2 illustrates Z_a (and the resulting SWR) as functions f/f_o, for the case where the dipole is in free space and $(d/\lambda)_o = 140 \times 10^{-6}$. Let f_- and f_+ be the first frequencies encountered, as f is respectively decreased and increased from f_o, where $SWR = 2$. The dipole's $SWR = 2$ bandwiwth is defined to be $bw = ((f_+ - f_-)/f_o)100$ %. The above $SWR = 2$ type of bandwidth is mentioned (for example) on page

17-2 of [2]. Its use is justified by the observation that it becomes difficult to match a transmitter to a transmission line, at those frequencies where the *SWR* on the line is greater than 2.

We will symbolize a dipole's θ polarized gain, in the direction (θ, ϕ), by: a) $G_\theta(\theta, \phi)$, in general, and b) $G_{\theta o}(\theta, \phi)$, when the dipole is resonant. The above gains are said to be θ polarized because (see eqns. (7) and (8) in [4]) they are associated with the component of the far electric field intensity (at (r, θ, ϕ)) which is polarized parallel to the θ unit vector. $G_\phi(\theta, \phi)$ and $G_{\phi o}(\theta, \phi)$ are defined like the gains under a) and b) above, except that they are associated with the component of the far electric field intensity which is polarized parallel to the ϕ unit vector.

We are using complex notation where $exp(j\omega t)$ is understood; therefore the ground's relative permittivity can be expressed as $\epsilon_{rg} = \epsilon'_{rg} - j\epsilon''_{rg}$ where ϵ'_{rg} and ϵ''_{rg} are respectively the real and imaginary parts of the ground's relative permittivity. At HF frequencies, it is traditional to specify ground conductivity instead of ϵ''_{rg}. These two variables are related by $\epsilon''_{rg} = \sigma_g/(\omega\epsilon_o)$ where: a) σ_g in Ω^{-1}/m (mhos/m) or S/m (siemens/m), is the ground's conductivity, and b) ϵ_o is the permittivity for free space ($\epsilon_o \simeq 8.854 \times 10^{-12}$ sec./(Ωm)).

3. DIPOLE CHARACTERISTICS

For the case where the dipole is in free space, we will be content here with the presentation of the characteristics shown in Table 1. Reference [4] contains, in addition, figures which present, as functions of $(d/\lambda)_o$ (for $16 \times 10^{-6} \leq (d/\lambda)_o \leq 520 \times 10^{-6}$), the following free space dipole properties: $\left(l/(\lambda/2)\right)_o$, R_{ao}, and $SWR = 2$ frequency band properties. Note that the foregoing range for $(d/\lambda)_o$ is sufficient to include the diameters of AWG nos. 4 to 14 for frequencies across the HF band (i.e. 3 MHz to 30 MHz).

Table 1, Characteristics for Fig. 1's free space, half-wave resonant dipole, as a function of the $(d/\lambda)_o$ values shown at the top of the table.

$(d/\lambda)_o$	16×10^{-6}	140×10^{-6}	520×10^{-6}
$\left(l/(\lambda/2)\right)_o$	.9764169	.9692884	.9621924
R_{ao} (Ω)	69.7558	68.4934	67.0544
f_-/f_o	.9732212	.9660110	.9593826
f_+/f_o	1.0291353	1.0379030	1.0463694
$(f_- - f_o)/f_o$	-.0267788	-.0339890	-.0406174
$f_+ - f_o)/f_o$	.0291353	.0379030	.0463694
$(f_+ - f_-)/f_o$	.0559142	.0718920	.0869868
$G_{\theta o}(0,0)$ (dB)	2.28932	2.35642	2.44066

Figures 3 and 4 plot R_{ao} and bw for the case where Fig. 1's dipole is above and very close to a perfectly conducting ground. It is shown that, when h/λ_o is small and decreasing, both R_{ao} and bw are small and decreasing. R_{ao} behaves this way because, for a given feed gap current, as h/λ_o decreases toward a small value, the far radiated fields from the dipole and its image cancel more and more completely; resulting in a decreasing radiated power. The dipole's bw has the above discussed property because R_{ao} has this property whereas the rate of change of X_a, as a function of f, does not. In contrast to the behavior of R_{ao} and bw, Fig. 8 in [4] shows that when our dipole's normalized height (h/λ_o) above a perfectly conducting ground is small and decreasing, $\left(l/(\lambda/2)\right)_o$ is increasing and approaching 1. This is the behavior is what one would expect because as h/λ_o approaches 0, the dipole (with its image) will behave more and more like two back-to-back, non-radiating, quarter-wave resonant, transmission lines.

The reader is referred to Section 4.2 of [4] for a study of the characteristics of Fig. 1's dipole, above a perfectly conducting ground, where $.1 \leq h/\lambda_o \leq 1.6$. Included in this study are: a) $\left(l/(\lambda/2)\right)_o$, R_{ao} and bw, as functions of h/λ_o, for the cases where $(d/\lambda)_o$ are 16×10^{-6}, 140×10^{-6} and 520×10^{-6}, b) $G_{\theta o}(0,0)$ (zenith gain), as a function of h/λ_o, where $(d/\lambda)_o$ is 140×10^{-6}. Note that gain is not a sensitive function of $(d/\lambda)_o$, and c) a selection of vertical gain patterns ($G_{\theta o}(\theta, 0)$) and $G_{\phi o}(\theta, 90^\circ)$) for selected h/λ_o values and where $(d/\lambda)_o = 140 \times 10^{-6}$.

Section 5 of [4] contains an examination of resonant characteristics for Fig. 1's dipole where the ground types are real-world. Listed below are the real-world ground names, with their associated dielectric properties

(both taken from [3]), which we will be using.

a) Very dry ground. $\epsilon'_{rg} = 3$, $\sigma_g = .0001\ \Omega^{-1}/\text{m}$.

b) Medium dry ground. $\epsilon'_{rg} = 15$, $\sigma_g = .001\ \Omega^{-1}/\text{m}$.

c) Wet ground. $\epsilon'_{rg} = 30$, $\sigma_g = .01\ \Omega^{-1}/\text{m}$.

In Section 5 of [4] it was found necessary to add two independent variables (in particular, frequency and ground type) to those employed for the case where the ground was perfectly conducting. Note that frequency had to be added because (as [3] shows), while σ_g is essentially constant as a function of f, for $f \leq 30$ MHz, it follows that ϵ''_{rg} (refer to the previously given function relating ϵ''_{rg}, σ_g and ω) is not. In the interest of putting a reasonable limit on the number of graphs in the above Section 5, the author decided to present dipole characteristics for only one wire diameter. The wire diameter chosen was that for AWG no. 12 (.205 cm). This is the guage recommended on page 33-1 of [2], for long horizontal dipole wires which are expected to support their own weight, plus that of their feed lines.

Subsections 5.1 and 5.2 in [4] examine the cases where the normalized height for Fig. 1's dipole, above real-world grounds, is respectively in the following ranges: $.003 \leq h/\lambda_o \leq .1$ (when the dipole said to be close to the ground) and $.1 \leq h/\lambda_o \leq 1.6$. Both sections contain figures which plot the following dipole characteristics as functions h/λ_o: $\left(l/(\lambda/2)\right)_o$, R_{ao}, bw, and $G_{\theta o}(0,0)$. There are four plots for each of the above functions; one for each of the following values for f_o: 3 MHz, 6 MHz, 10 MHz, and 30 MHz. Each of the above figures has at least three curves; one for each of the real-world ground types. Some of the graphs, when $f_o = 6$ MHz, have an additional curve for the case where the ground is perfectly conducting. In addition to the above figures: a) Section 5.1 has a graph showing the vertical patterns $G_{\theta o}(\theta, 0)$ and $G_{\phi o}(\theta, 90^\circ)$, for the case where $f_o = 6$ MHz and $h/\lambda_o = .003$, and b) Section 5.2 has a number of plots showing the above vertical gain patterns, at $f_o = 6$ MHz, for: each of the real-world ground types, and selected values of h/λ_o.

This document's characteristics for Fig.1's dipole when above real-world grounds, are contained in Figs. 5 to 10. They plot R_{ao}, bw and $G_{\theta o}(0,0)$, as functions of h/λ_o, where $f_o = 6$ MHz. Figures 5 to 7 and 8 to 10 present characteristics for respectively the cases where h/λ_o satisfies: $.003 \leq h/\lambda_o \leq .1$ and $.1 \leq h/\lambda_o \leq 1.6$

When the dipole is close to the ground, it is shown that losses in the real-world ground make the dipole's characteristics behave much differently than they do for the case where the ground is perfectly conducting. In particular, when h/λ_o is decreased toward a small value, it is shown that:

a) when the ground is perfectly conducting: 1) $\left(l/(\lambda/2)\right)_o$ increases toward 1, 2) both R_{ao} and bw decrease toward a small value, and 3) $G_{\theta o}(0,0)$ increases toward a peak value of about 9.2 dB, whereas

b) when the ground is real-world: 1) $\left(l/(\lambda/2)\right)_o$ decreases to values between .82 and .91 at $h\lambda_o = .003$ (depending on the frequency and ground type), 2) both R_{ao} and bw increase to above free space values, and 3) $G_{\theta o}(0,0)$ decreases to values between -2 dB and -12 dB at $h/\lambda_o = .003$.

When the dipole's normalized height above real-world grounds is in the range $.1 \leq h/\lambda_o \leq 1.6$, it is shown that $\left(l/(\lambda/2)\right)_o$, R_{ao}, bw and $G_{\theta o}(0,0)$, as functions of h/λ_o, vary about their free space values. As concerns the above variations, it is shown that their; a) period is about .5, and b) amplitude increases as the ground's moisture content increases. The period of .5 for the dipole's feed gap characteristics (i.e. $\left(l/(\lambda/2)\right)_o$, Rao and bw) is explained when it is noted that the field from the dipole, to the ground, and then back to the dipole, changes phase by about 360° when h/λ_o changes through .5. The far field characteristic $G_{\theta o}(0,0)$ has a period of .5 because the zenith fields from the dipole and the ground, change in phase by about 360° when h/λ_o changes through .5. The above mentioned increase in the amplitude of variation in the dipole's characteristics, is a result of the fact that the ground's reflectivity, and hence the strength of the ground reflected signal, increases as soil moisture is increased.

4. CONCLUSIONS

The ground and its type (dry, wet,etc.) is shown to have a significant effect on the characteristics of horizontal, half-wave, HF dipole antennas. The information in [4] should make it possible for the antenna designer to estimate the magnitude of the above effects.

An example of the use of the information [4], is for the design of a system which employs an HF dipole which is close, and parallel, to a real-world ground. When compared with horizontal HF dipoles located at

greater heights above the ground, this dipole would be relatively easy to transport and erect. In addition it possesses a: a) convenient R_{ao} value, and b) relatively broad bandwidth. The designer of a system which employs this dipole should however take into consideration that: a) its resonant length changes significantly as a function of groumd type, and b) it has low gain characteristics.

5. REFERENCES

[1] G. J. Burke, "The numerical electromagnetic code (NEC)," in *Applications of Moment Methods to Electromagnetic Fields*, edited by Bradely J Straite, The SCEEE (Southeasatern Center for Electrical Engineering Education) Press, 1101 Massachusetts Ave., St. Cloud FL, 32769, 1980.

[2] *Handbook for Radio Amateurs*, American Radio Relay League, sixty-ninth edition, 1992.

[3] "Electrical characteristics of the surface of the earth," in CCIR document *Recommendations and Reports of the CCIR*, 1982, Vol. V, *Propagation in Non-Ionized Media.*

[4] G. M. Royer, "Characteristics for HF dipole antennas including the cases where the dipoles are above and parallel to the surface of real-world grounds," Sept. 1995, The author's address is: G. M. Royer, 79 Speers Cr., Kanata, Ont., Canada, K2M 1W3.

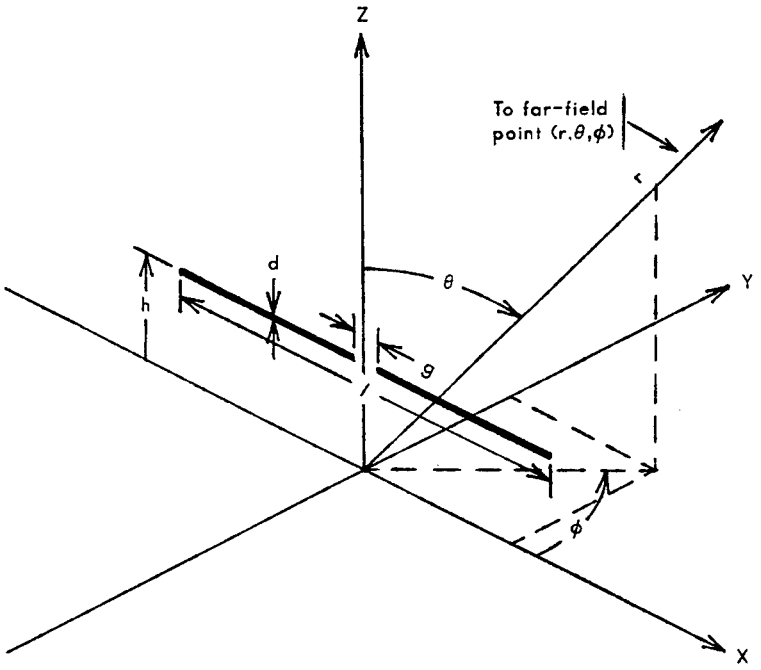

Fig. 1. Shown above, for the case where the dipole is above and parallel to a ground with a plane surface (the XY plane), are symbols associated with the dipole's: a) dimensions, and b) location in the (x,y,z) and(r,θ,ϕ) coordinate systems. The ground is homogenous and located in the region $z \leq 0$. The symbols d, g, *l* and h will be referred to as respectively dipole: wire diameter, feed gap length, length and height above the ground. In most of this paper, the above variables will be made dimensionless through their normalization wrt the signal's free space wavelength (λ). In particular we will be using d/λ, g/λ, $l/(\lambda/2)$ and h/λ (or when the dipole is resonant: $(d/\lambda)_o$, $(g/\lambda)_o$, and $(l/(\lambda/2))_o$ and h/λ_o). For all cases, we will make: a) $(g/\lambda)_o = .0052$, and b) the dipole wires to be perfectly conducting. For those cases where the ground is not perfectly conducting, d will be .205 cm (the diameter for AWG #12 wire). When the dipole is in free space: h=0, and there is no ground.

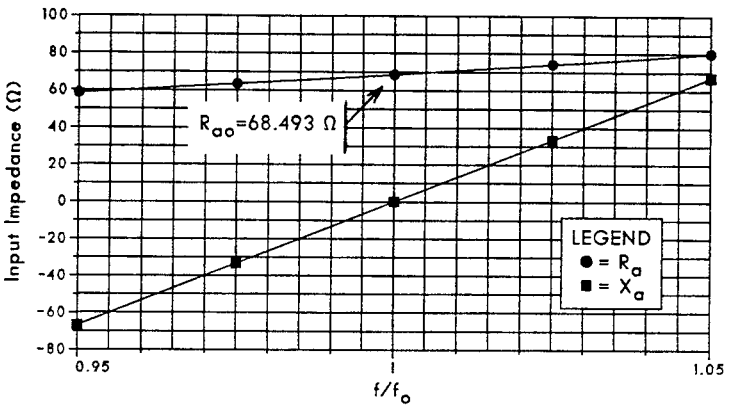

Fig. 2a. $Z_a = R_a + jX_a$ as a function of f/f_o.

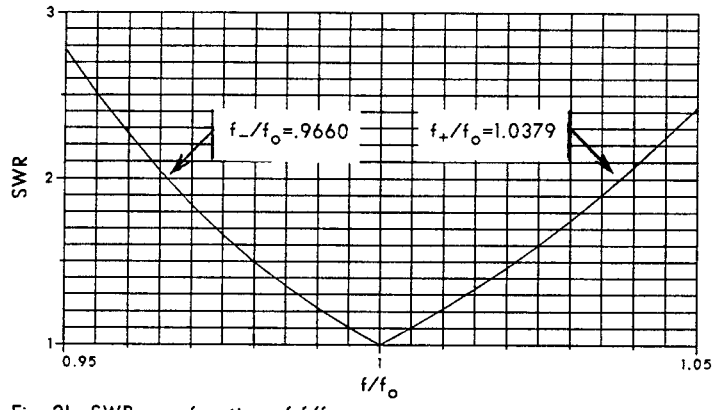

Fig. 2b. SWR as a function of f/f_o.

Fig. 2. For Fig. 1's dipole in free space (with $(d/\lambda)_o=140\times10^{-6}$), input impedance ($Z_a=R_a+jX_a$) standing-wave ratio (SWR), as functions of normalized frequency (f/f_o). Note, the dipole is resonant at $f=f_o$ (where $X_a=0$). Refer to the text for a definition of the dipole's standing-wave ratio. The normalized frequencies f_-/f_o and f_+/f_o are the values of f/f_o, respectively below and above $f/f_o=1$, where SWR=2.

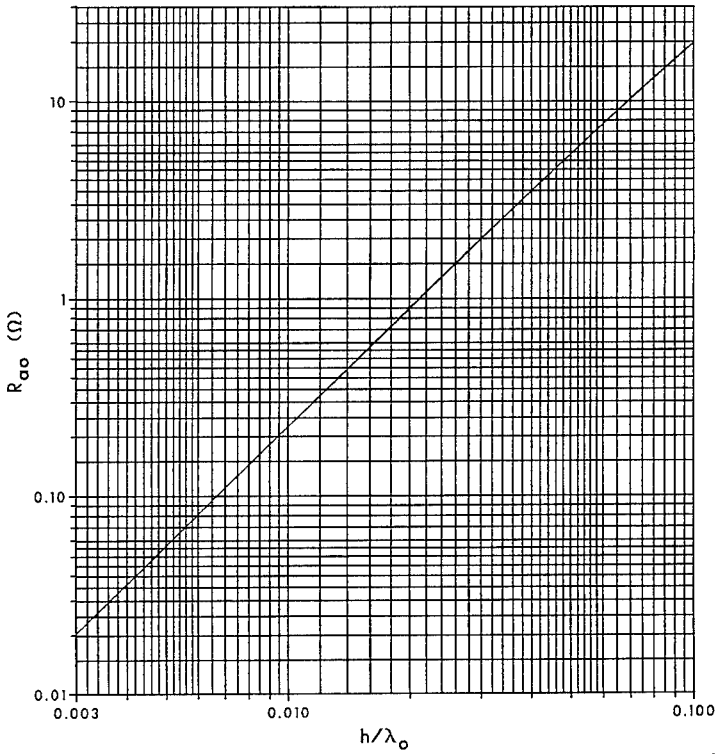

Fig. 3. For Fig. 1's dipole, the resonant input resistance as a function of normalized height above the ground plane, where: a) the ground is perfectly conducting, b) the dipole is close to the ground (i.e. $.003 \leq h/\lambda_o \leq .100$), and c) $(d/\lambda)_o = 140 \times 10^{-6}$.

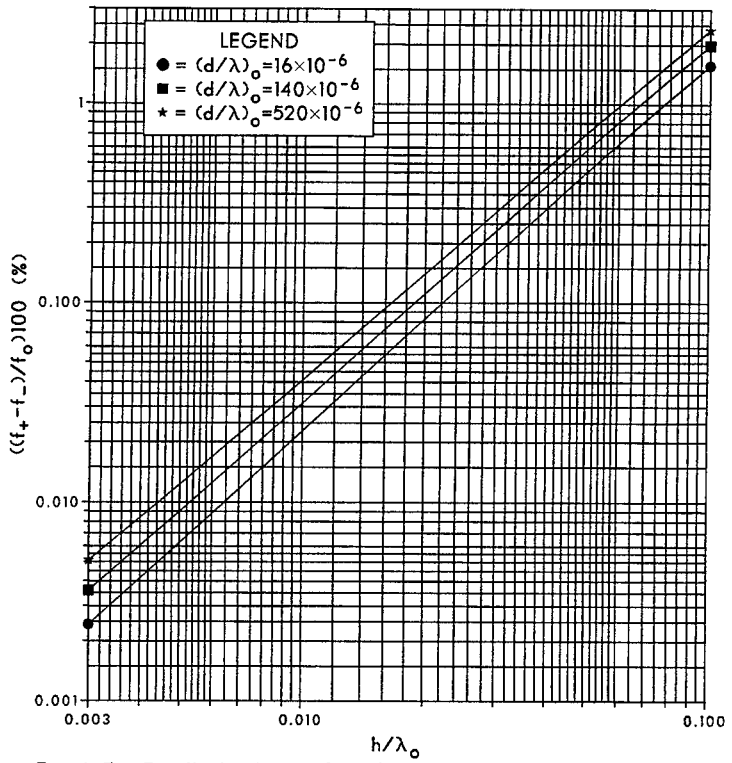

Fig. 4. For Fig. 1's dipole, the SWR=2 normalized bandwidth, as function of normalized height above the ground plane, where: a) the ground is perfectly conducting, b) the dipole is close to the ground (i.e. $.003 \leqq h/\lambda_o \leqq .100$), and c) $(d/\lambda)_o$ has the values listed in the legend.

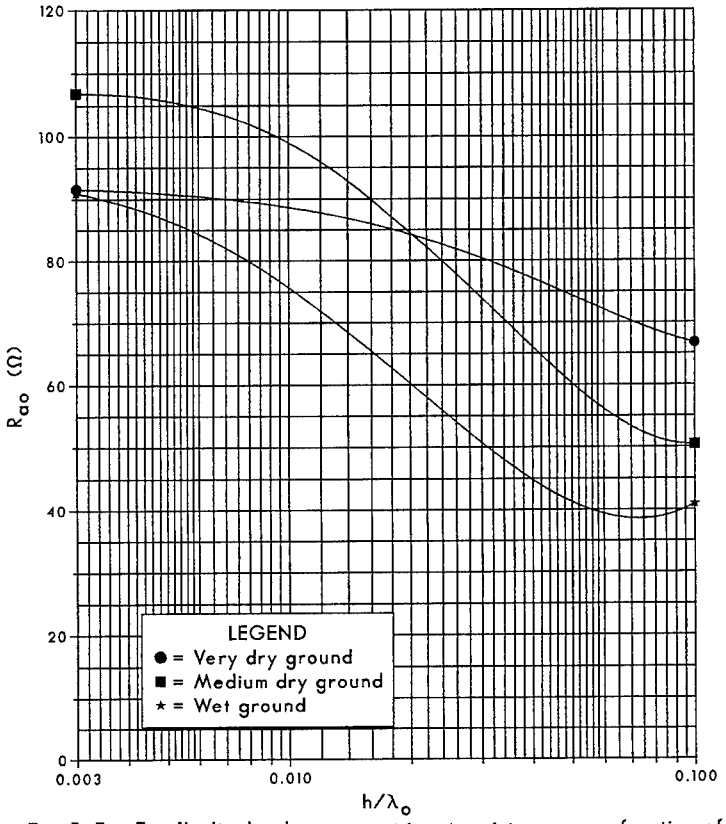

Fig. 5. For Fig. 1's dipole, the resonant input resistance, as a function of normalized height above the ground, where: a) the resonant signal frequency is 6 MHz, b) there is a curve for each of the ground types indicated in the legend, and c) the dipole is close to the ground (i.e. $.003 \leq h/\lambda o \leq .100$).

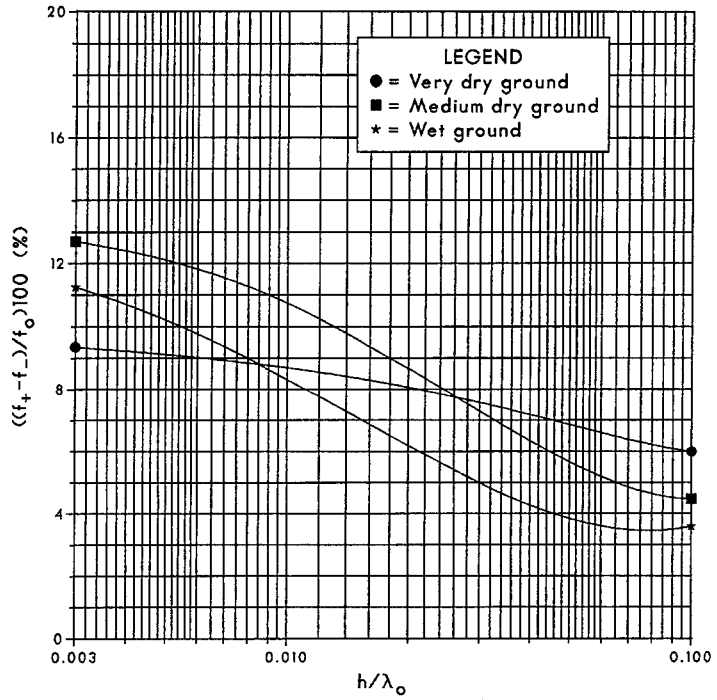

Fig. 6. For Fig. 1's dipole, the SWR=2 normalized bandwidth, as a function of normalized height above the ground, where: a) the resonant signal frequency is 6 MHz, b) there is a curve for each of the ground types indicated in the legend, and c) the dipole is close to the ground (i.e. $.003 \leqq h/\lambda_o \leqq .100$).

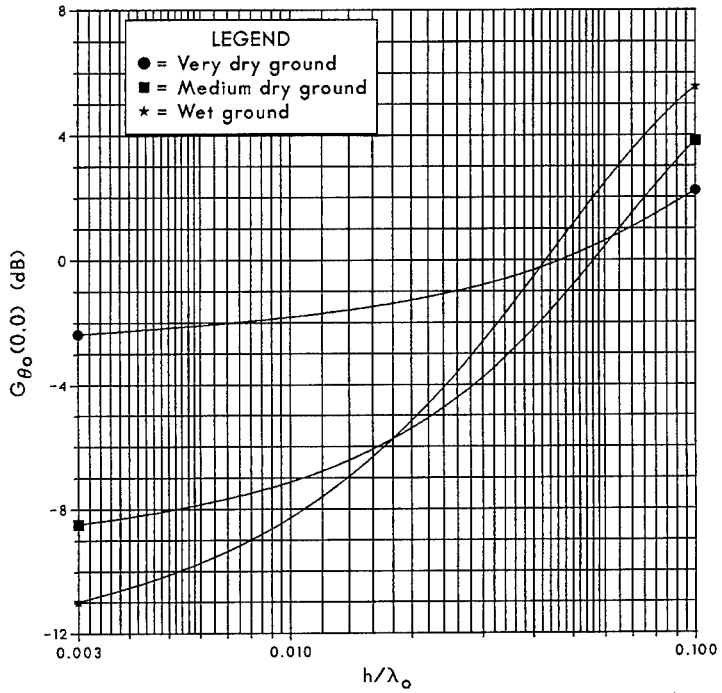

Fig. 7. For Fig. 1's dipole, the resonant zenith gain, as a function of normalized height above the ground, where: a) the resonant signal frequency is 6 MHz, b) there is a curve for each type of ground indicated in the legend, and b) the dipole is close to the ground (i.e. $.003 \leqq h/\lambda_o \leqq .100$).

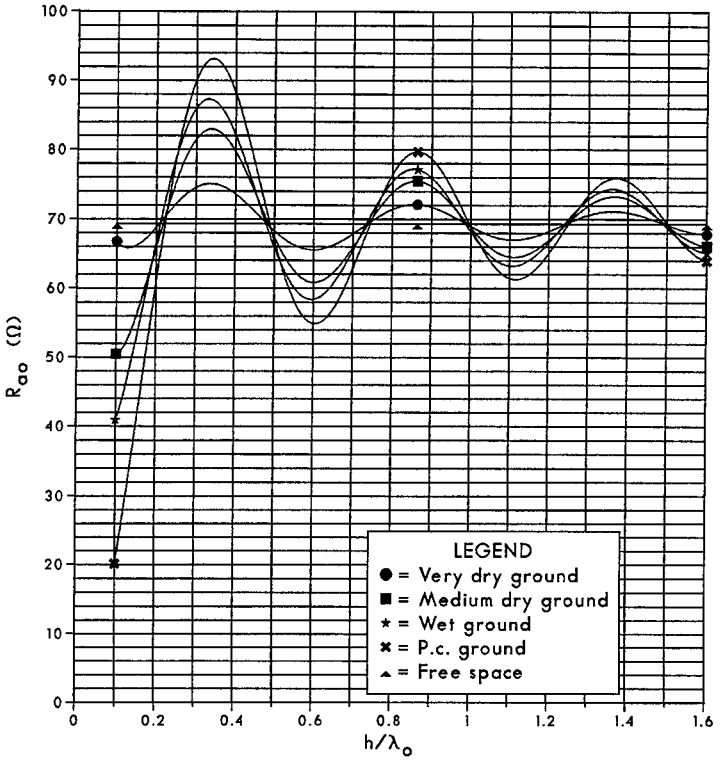

Fig. 8. For Fig.1's dipole, the resonant input resistance, as a function of normalized height above the ground, where: a) the resonant signal frequency is 6 MHz, b) there is a curve for each type of ground indicated in the legend (note that there is a curve for the case where the ground is perfectly conducting), and c) h/λ_o ranges between .1 and 1.6. Also shown, for comparison purposes, is the resonant input resistance for the above dipoles when they are in free space.

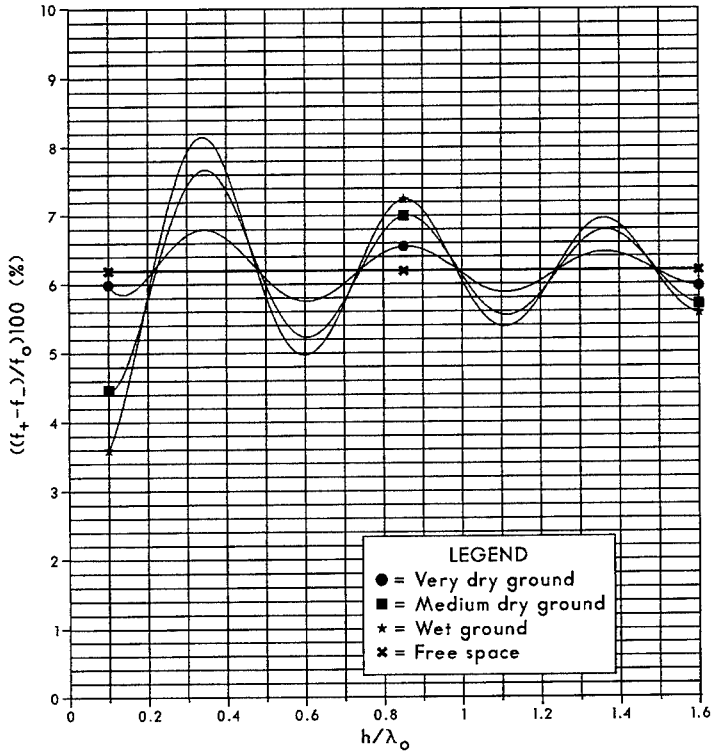

Fig. 9. For Fig.1's dipole, the SWR=2 normalized bandwidth (%), as a function of normalized height above the ground, where: a) the resonant signal frequency is 6 MHz, b) there is a curve for each type of ground indicated in the legend, and c) h/λ_o ranges between .1 and 1.6. Also shown, for comparison purposes, is the SWR=2 normalized bandwidth (%) for the above dipoles when they are in free space.

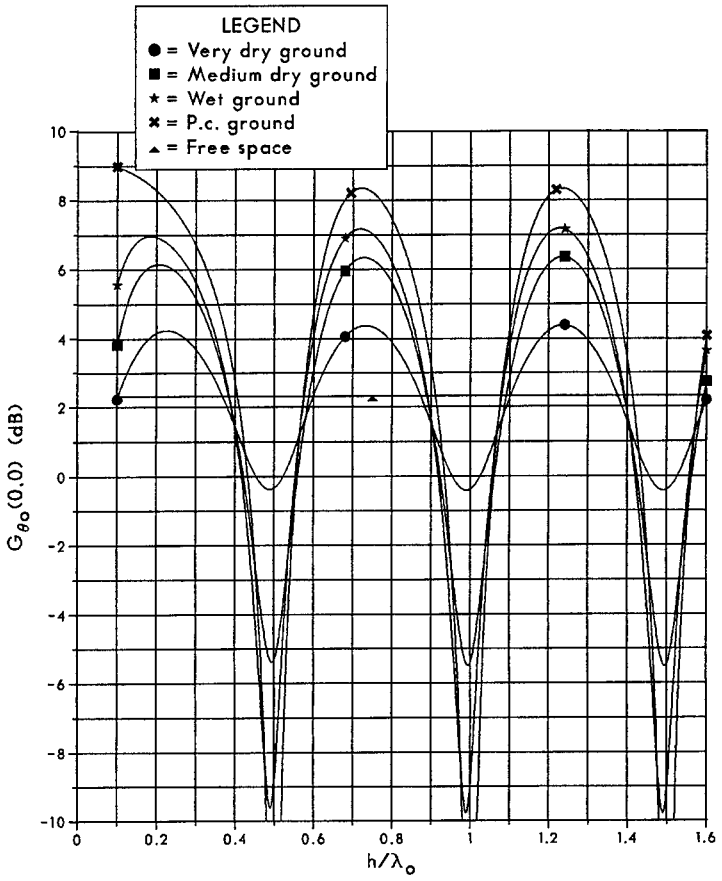

Fig. 10. For Fig. 1's dipole, the resonant zenith gain, as a function of normalized height above the ground, where: a) the resonant signal frequency is 6 MHz, b) there is a curve for each type of ground indicated in the legend, and c) h/λ_o ranges between .1 and 1.6. Also shown, for comparison purposes, is the resonant gain ($G_{\theta o}(0,0)$, (dB)) for the above dipoles when they are in free space

HF Multi-Frequency Antennas Using Coupled Resonators

Gary A. Breed
Crestone Engineering
Littleton, Colorado
and
Editor and Associate Publisher
RF Design magazine

Introduction

This paper is a continuation of material presented at the 1995 ACES Symposium [1], describing the author's work with multi-frequency antennas which use the technique of closely-spaced coupled resonators. Three practical antennas are described, which operate in several of the HF amateur radio bands.

The Coupled-Resonator Principle

The *coupled-resonator* (also called *multiple-open-sleeve*) principle is a useful technique for obtaining multi-frequency operation in dipole and monopole antenna elements. It is derived from previous work, the *coaxial sleeve antenna* and the *open-sleeve antenna*. The coaxial sleeve antenna places a cylindrical sleeve around a driven dipole (or monopole), resulting in a single structure which exhibits two resonances — that of the driven element, and of the sleeve. In the open-sleeve antenna, the sleeve is reduced to two parallel conductors which create a skeleton representation of a coaxial sleeve. Coaxial sleeve and open-sleeve techniques have been used extensively in two-frequency and broadband antennas.

Because the original work in this area involved coaxial or open-sleeve configurations, most developmental work assumed that the additional resonators were required to follow that type of construction. Relatively few antenna designers understood that only a single additional conductor is required to create a second resonance. This simpler topology allows individual conductors to be placed radially around the driven element, creating antennas with three, four, five, and more resonances. The upper limit to the number of frequencies that can be obtained in a single structure is determined by unwanted coupling among the many different conductors.

Using MININEC and NEC computer modeling, combined with several experimental antennas, the author has derived an equation that relates the conductor size, spacing, and the feedpoint impedance. The equation is based on the basic relationship:

$$\frac{\log(d)}{\log(D/4)} = 0.54$$

where,

- D is the diameter of the conductors (assumed to be equal) in wavelengths at the resonant frequency of the coupled resonator.
- d is the spacing on centers between the conductors, also in wavelengths at the resonant frequency of the coupled resonator.
- The system impedance is that of a dipole in free space, or a monopole fed against perfect ground.

- The lengths of the conductors have been adjusted for a non-reactive impedance.
- A two-frequency antenna is assumed, although the equation is a reasonable approximation for each frequency in a larger system.

Correction factors have been derived for other impedances, and for the special case where the coupled resonator approaches the driven element resonant frequency. These are described in [1] and [2], and they are combined with the above expression into a single equation: where,

$$d_{1n} = 10^{[0.54\log(D/4)]} \times \frac{Z_0 + 35.5}{109} \times \left[1 + e^{-[(((F_n/F_1)-1.1)\times 11.3)+0.1]}\right]$$

- Z_0 is the desired impedance (resistive, between 25 and 125 ohms)
- F_n is the frequency of the additional resonator
- F_1 is the frequency of the driven element
- d_{1n} is the spacing between the driven element and the desired *n*th resonator, in wavelengths at F_n
- D is the diameter of the conductors (assumed equal), in wavelengths at F_n

The above equation describes conditions for resistive impedances. The length of the elements can be adjusted to change the reactance. It is easily seen that this technique provides a wide range of control over the feedpoint impedance at a given frequency — by controlling the variables of conductor diameter, spacing and length. This flexibility in design is the principal advantage of the coupled resonator technique, and is the key to successful operation of the antenna described in Example 3 presented below.

Example 1: 10.1, 18.068, 24.89 MHz Wire Dipole

The first example is a three-frequency antenna built with #12 AWG wire conductors, operating on the 10.1, 18.068 and 24.89 MHz amateur bands. Antenna element dimensions are given in Figure 1. A free-space comparison of radiation patterns on the three bands (modeled in ELNEC) is shown in Figure 2. The radiation patterns at 10.1 and 18.1 MHz are indistinguishable from that of an ordinary dipole. At 24.9 MHz, the current in the driven element is significant, and when summed with the coupled-resonator current, results in a gain of 0.6 dB.

Feedpoint VSWR in a 50-ohm system is comparable to MININEC-calculated VSWR at the installed height of 50 feet above ground. The amateur bands covered by this antenna only

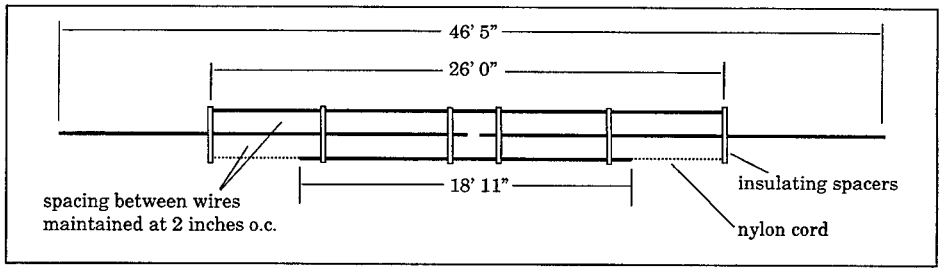

Figure 1. Dimensions of the 10.1, 18.068, and 24.89 MHz wire dipole of Example 1.

require 0.4 to 0.55 percent bandwidth, well within the bandwith provided by this antenna. The only unexpected behavior of this antenna is a greater sensitivity to height above ground than a simple dipole. This behavior had not been investigated through modeling, and it was confirmed later that modeling also predicts these impedance excursion.

On-air performance of this antenna is comparable to that expected for a dipole at each frequency.

Example 2: 14, 21, 28 MHz Aluminum Tubing Dipole

The second example antenna is also a three-frequency antenna, built for the 14, 21 and 28 MHz amateur bands, using aluminum tubing construction (dimensions in Figure 3). The 14 and 21 MHz elements taper from 1-1/4-inch diameter tubing to 5/8-inch diameter, and the 28 MHz element tapers from 1-1/8-inch diameter to 5/8-inch diameter. Spacing between the driven 14 MHz dipole and the coupled-resonator elements was fixed at 7 inches on centers.

VSWR bandwidth exceeds 4 percent at 14 MHz, and is greater than 2.5 percent at both 21 and 28 MHz. This is sufficient to cover the entire amateur band at 14 and 21 MHz, and covers the most actively-used portion of the 28 MHz band. Larger conductors were intentionally chosen for these wider amateur bands. Although operating on different frequencies than the previously-described wire antenna, a comparison shows that the larger-conductor antenna hss more than three times the percentage bandwidth for 2:1 VSWR.

The larger conductors mitigate the variations in impedance versus installed height that were first seen with the wire antenna. As with other test antennas, this version demonstrates that larger dimensions result in a less critical design, because of the inherently broader bandwidth of the larger diameter conduc-

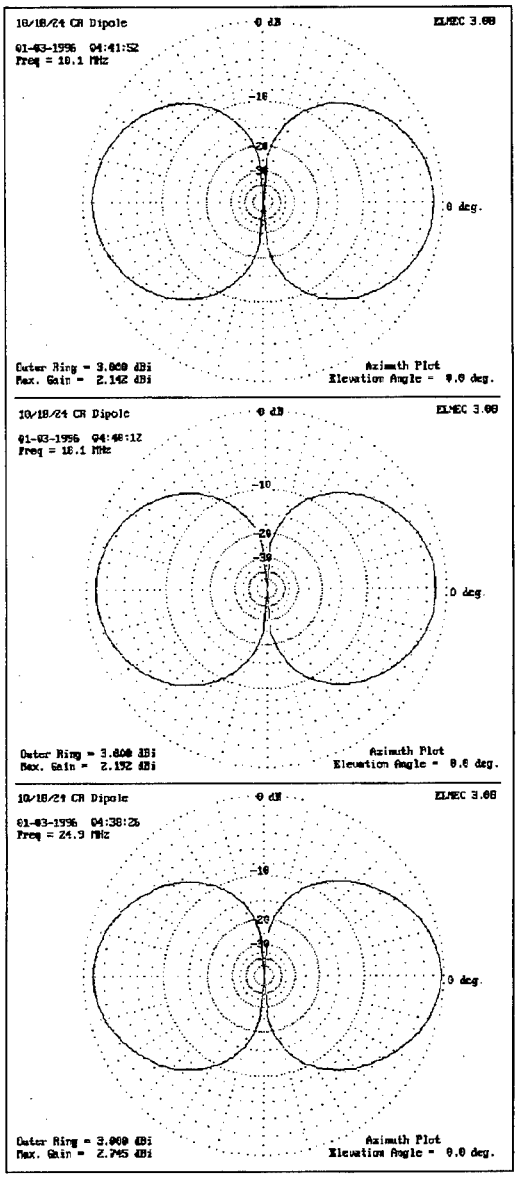

Figure 2. Radiation patterns for Example 1 — 10.1 MHz (top); 18.1 MHz (center); 24.9 MHz (bottom).

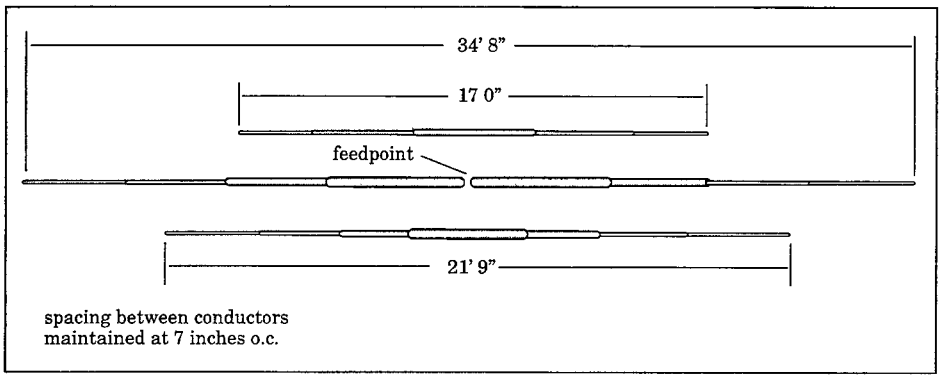

Figure 3. Dimensions of the three-frequency aluminum tubing dipole of Example 2.

tors, and the larger spacing distances for the desired feedpoint impedance. Based on modeling and experiments, the use of very small conductors (less than 0.0001 λ) is not recommended.

Example 3: A 14, 18, 21, 24, 28 MHz Vertical Dipole

The third example is a more complex antenna, a vertical dipole operating on five frequencies covering the 14, 18.068, 21, 24.89 and 28 MHz amateur bands. This antenna is illustrated in Figure 4. The driven element is a modified vertical dipole, with an inverted "T" for the lower half to reduce the overall height. The lowest conductor is installed at four feet above ground, and the vertical portion extends to 30 feet above ground. The feedpoint is eight feet above the horizontal portion, and the feedline is run inside this lower section of tubing. Above the feedpoint, the driven element tapers from 1-1/4-inch diameter to 5/8-inch diameter. Each of the additional resonators is 3/8-inch diameter tubing, mounted on fiberglass insulating spacers.

A vertical dipole installed close to ground has a feedpoint impedance in the range of 110 ohms. The inverted "T" configuration lowers this to about 90 ohms. But, operation in a 50-ohm system is desired, requiring some type of matching. A matching section of 75-ohm transmission line, 80 degrees electrical length at 14 MHz, was selected. To obtain a 50-ohm feedpoint impedance through this transmission line section, the antenna impedance should be:

14 MHz —	107.3	+j17.0 Ω
18.068 MHz —	108.2	–j15.9 Ω
21 MHz —	88.8	–j30.3 Ω
24.89 MHz —	66.6	–j27.6 Ω
28 MHz —	55.4	–j13.8 Ω

The selected line section achieves an acceptable match at 14 MHz. Using the flexibility of the coupled-resonator method, we can obtain the desired antenna impedances at the other frequencies by controlling the size, spacing and length of each resonator. This is a classic conjugate matching problem, but with the source and load reversed from the typical situation. The procedure starts by using the design equation to determine the required spacing for the resistive component of the impedance. The length of the resonator is then iteratively changed to create the inductive or capacitive reactance. Further iteration may be needed to optimize the spacing,

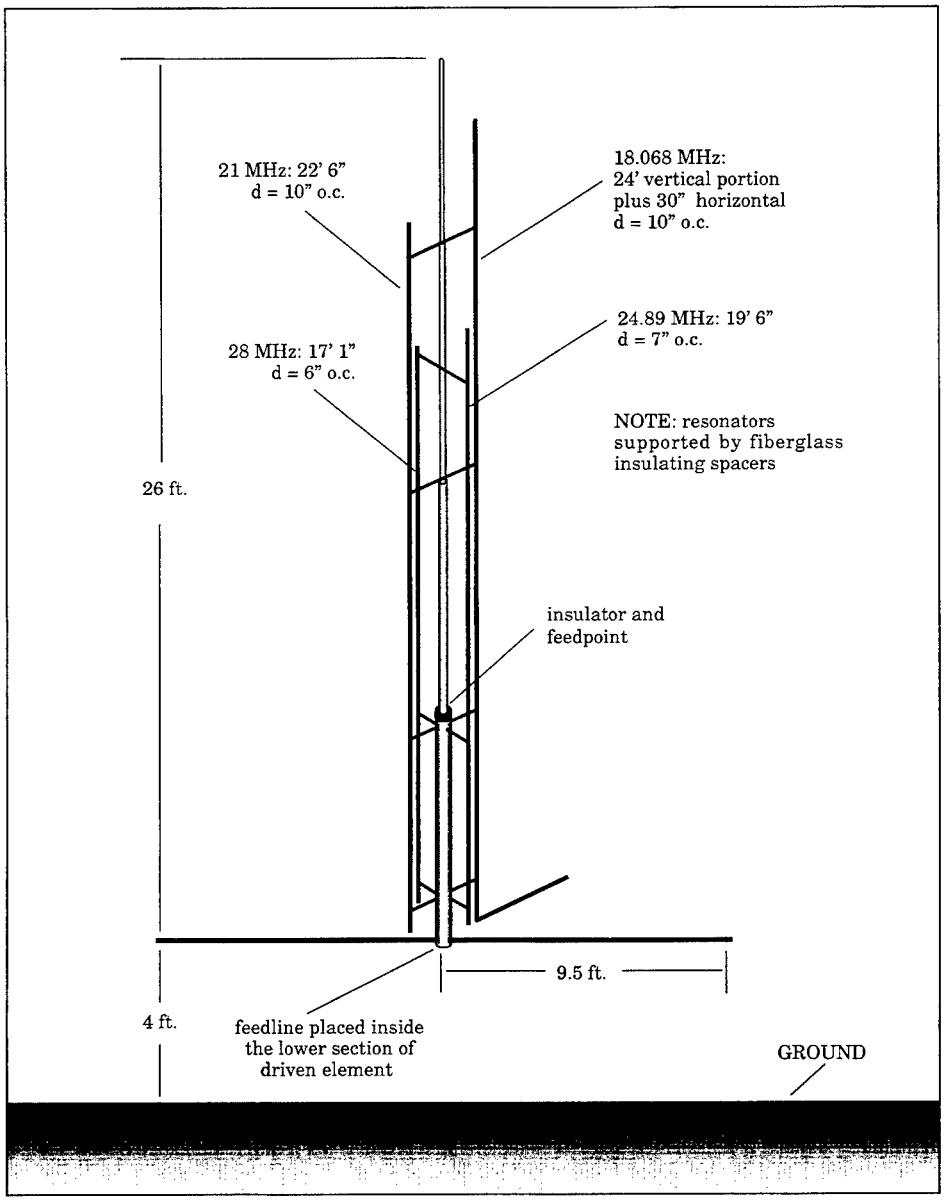

Figure 4. Diagram of the five-frequency vertical dipole antenna described in Example 3.

since the resistive component of impedance also changes with the length. As built, the finished antenna operates with a VSWR 1.2:1 or better at the five center frequencies. 2:1 VSWR bandwidths are as follows:

14 MHz —	>350 kHz (full band)
18.068 MHz —	>100 kHz (full band)
21 MHz —	≈350 kHz
24.89 MHz —	>100 kHz (full band)
28 MHz —	≈450 kHz

It is interesting to note that the bandwidth at 28 MHz is somewhat greater than expected. This is probably due to overlap with the adjacent-frequency 24.89 MHz resonator.

All coupled-resonator elements include an adjustable section at the bottom of the antenna. It should also be noted that the resonators are not symmetrical with respect to the feedpoint. This does not cause a significant variation in the required spacing, compared to a symmetrical design. Finally, the 18.068 MHz resonator is not a continuous, straight conductor; 2.5 feet of its total length is bent at 90 degrees, to maintain the desired overall height. This changes the coupling, and the required spacing was reduced from that required for a resonator coupled over its entire length.

Experimentation was needed to optimize the spacing for the 24.89 and 28 MHz resonators. MININEC modeling indicated that they should be spaced 7 and 8 inches, respectively, from the driven element. After construction, these spacings were reduced to 6 and 7 inches for best performance. The proximity to ground is the likely cause for the deviation, although the error is quite small, given the limitations of MININEC in modeling antennas near real ground.

Summary

Three antennas using the coupled-resonator antenna design technique have been described. The two three-frequency dipole examples offer a comparison of bandwidths obtained using small and large diameter conductors. The five-frequency vertical dipole antenna illustrates how this design method allows antennas to be built with arbitrary impedances at each frequency of operation. Below is a summary of the most significant characteristics of antennas designed using the coupled-resonator principle:

- Multiple frequency operation with low VSWR at each frequency
- No reactive components
- Control of impedance at each frequency
- No matching network required
- Independent fine tuning at each frequency (very little interaction)
- Some mechanical complexity
- Narrower VSWR bandwidth than a simple dipole or monopole

Although several methods are available for the construction of multi-frequency antennas, the coupled-resonator technique has flexibility as its principal advantage. Antennas built using this method are electrically simple, requiring no reactive components such as traps, stubs or matching networks. In cases where these characteristics are judged important, the technique's mechanical requirements may be deemed acceptable.

Further work is planned to develop design equations that encompass a wider range of impedances and antenna dimensions, as well as including effects of the number of resonators in the system.

References
[1] Gary A. Breed, "Development of the Coupled-Resonator Antenna Principle: A Computer Modeling Case History," *Proceedings*, 11th Annual Review of Progress in Applied Computational Electromagnetics, 1995.
[2] Gary A. Breed, "A Method of Constructing Multiple-Frequency Dipole or Monopole Antenna Elements Using Closely-Coupled Resonators," U.S. Patent application (approved, awaiting issue).

Brief Notes on the Construction of Practical Coupled-Resonator Antennas

The electrical simplicity of coupled-resonator antennas comes at the expense of mechanical complexity. Multiple conductors must be supported in a manner that maintains a consistent spacing distance.

Flexible wire conductors require either a large number of spacers, or they can be kept under tension. For end-supported dipole configurations, an equalizer assembly can be fabricated that will maintain tension on all wires, as shown in Figure A below. Swivel connections or bearings at the ends are also needed to avoid twisting. In general, wire antennas become extremely difficult to manage beyond three conductors.

Rigid conductors, such as aluminum tubing, are much easier to use. If supported at the center, typically two additional spacers are sufficient to prevent excessive motion in the wind. They should be placed about 2/3 of the distance from the center to the end of the resonator element.

Common insulating materials with sufficient strength include fiberglass and ABS plastic. Brittle materials like acrylic, or materials with insufficient insulating properties (e.g., wood), should be avoided. If the antenna is to be permanently installed outdoors, weatherproofing and ultraviolet protection should either be inherent in the material used, or accomplished with paints or other protective coatings.

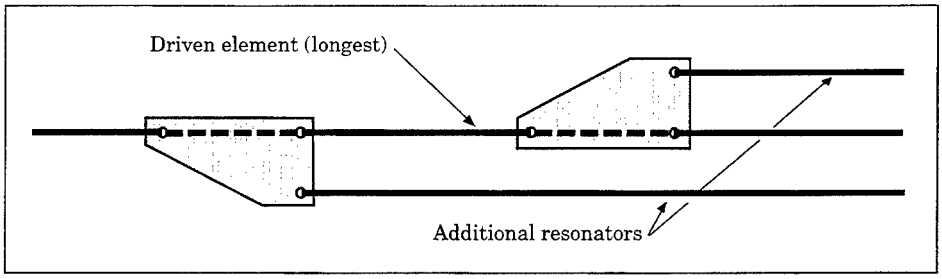

Figure A. Tension can be equalized among wire conductors using three-point spacer/insulators.

THE OPTIMIZED WIDEBAND ANTENNA (OWA) AND ITS APPLICATIONS

J. K. Breakall WA3FET
Electrical Engineering Department
The Pennsylvania State University
University Park, PA 16802

Abstract

This paper introduces a new and unique optimized wideband antenna (OWA) which has very wide bandwidth derived from optimization of the geometrical configuration of the structure. The resulting antenna looks similar to the conventional open-sleeve dipole or monopole, however, it is different in that modern computer optimization methods and algorithms were used to achieve the best globally chosen set of length and spacing parameters to achieve a minimization of the peak VSWR in a selected frequency range. This paper will show resulting designs which are far superior to past configurations of this structure, and in some cases, better than any possible known antenna configurations.

Introduction

There have been many articles and papers over the years describing different types of antennas and other techniques applied to conventional antenna structures to achieve wide bandwidth. There is a universal rule of nature called "The Law of Conservation of Difficulty" which states that if one tries to push certain intrinsic qualities e.g. antenna gain, bandwidth, smaller size, etc., another desirable parameter or characteristic will have to give (after Prof. R. Adler, K3CXZ, Naval Postgraduate School, Monterey, CA). An example is that as an antenna is made smaller, a possible desirable goal, then the bandwidth and gain may sacrifice. To achieve wider bandwidth, then the size of the antenna may have to be increased in certain of its dimensions, i.e.. cage dipole, conical monopole, discone, etc. Also, bandwidth can be increased at the expense of efficiency and gain, as in a resistively loaded antenna or an antenna close to the ground with very highly coupled earth losses. In the extreme, a dummy load can be considered a very wideband but certainly an extremely inefficient low-gain antenna.

Bandwidth as considered here will be defined as the total frequency span between some specified SWR values at each end of the range. Traditionally, the 2:1 points have been used for specifying bandwidth of antennas. One could as well specify bandwidth between the 1.5:1 SWR points or any other values appropriate to the application. In all cases, the antenna with the higher bandwidth will be that which gives a larger frequency span while insuring all SWR values in the total span are below some maximum specified level.

Some Common Broadband Antennas

It is well known that classical dipole and monopole (vertical)antennas can be made broadband by simply increasing their diameters. This becomes quite impractical at the lower HF ham bands (especially 160, 80, and 40 meters) where antennas with 1 foot or greater diameter tubing would certainly be mechanical nightmares. Fortunately, several thin wires in the form of a cage, a cone, or planar shapes (fan dipole) can actually be equivalent to solid conductors of large diameter. They can have much larger

bandwidths than just a single wire dipole with the same diameter as those of the individual wires making up the structure. These types of antennas obtain bandwidth increases due to their inherent geometrical shape and size.

The traditional open-sleeve antenna has been known and used since its invention in 1946 by Dr. J. T. Bolljahn of the Stanford Research Institute, which now is the present SRI, International[1]. The basic form of this antenna consists of a base-fed central monopole with two parallel closely spaced and coupled parasitic elements, one on each side of the central monopole, and shorted to a ground plane which the central monopole is fed against. The length of the central monopole is approximately1/4 wavelength and that of the parasitic elements is about half of the central monopole length.

All of the previous and present work which can be found in the literature on this antenna structure has been done by choosing the various geometrical lengths and spacings empirically by a trial and error or cut-and-try methods for obtaining the desired characteristics. The work to be described in this paper has used modern computer optimization methods and algorithms to achieve the best globally chosen set of length and spacing parameters to achieve a minimization of the peak SWR in a selected band. The various antenna wires or cylindrical tubing are modeled using a very sophisticated computer optimization program, NEC-OPT[2], which is based internally on NEC. As will be seen, the results have produced designs which are far superior to past configurations of this structure and in some cases better than any possible known antenna configurations. Furthermore, some of the optimized designs reported here are used in achieving extremely low SWR (less than1.1:1) over bandwidths that have never been tried to the authors' knowledge before with this open-sleeve concept.

Results

Several optimizations have been performed for some desired characteristics over some selected configurations and bands of frequencies. The first is to produce an antenna that is much wider in SWR bandwidth than the classical dipole antenna for a chosen frequency range of 6.7 to 7.6 MHz. A dipole was modeled over typical ground conditions, $\epsilon_r = 13.$ and $\sigma = .005$ Siemens/meter, and placed at a high of 35 feet above the ground. The wire gauge used was #14. The variables of the optimization were the length of the central center-fed dipole, the lengths of the two additional parasitic elements (both equal length for this optimization), and the spacing between each wire and the central dipole wire. The SWR versus frequency is shown in Figure 1 and can be seen to be under 1.5 to 1 over the complete range. In fact, it is about 1.2 to 1 from 7.0 to 7.4 MHz, or a total span of some 400 KHz. One can also see the classical dipole SWR over the same band in Figure 1 which is under 1.2 to 1 only over a 50 KHz range.

The 80 meter band is one where the bandwidth of the OWA should be very useful. A globally constrained optimization was performed from 3.5 to 4.0 MHz with three variables of length of the central wire, lengths of the two equal parasitic wires, and equal spacing between the parasitic and central wires. The diameter was wire gauge #14 which was held constant and the antenna was placed at a height of 50 feet over the same average ground conditions as above. The NEC-OPT results are shown in Figure 2 along with the results for a conventional dipole at the same 50 feet with a Z0 = 50 ohm reference. The SWR for the OWA is under 1.5 over the complete 80 meter band with fully efficient operation.

Results are shown for just a simple two wire configuration which has been optimized for the 7.0 to 7.3 MHz band of frequencies. This configuration was obtained by letting the optimizer choose the two lengths of the wires, the spacing between the wires, and the radius of the additional parasitic wire with the driven wire diameter fixed. There were 4 variables which the optimization procedure was run with. The SWR versus frequency results are shown in Figure 3 and is under 1.1 to 1 over the complete band which is a remarkable characteristic not achieved by any other known antenna with such a simple geometrical construction.

3 Element 40 Meter Yagi OWA Driven Element

One of my colleagues, Tim Duffy, K3LR, is fortunate to have a 190 foot tower and two stacked 3 element 40 meter yagis at heights of 100 and 190 feet. These were custom designs from LTA, Inc[3]. Duffy explained that the bandwidth of these yagis is pretty sharp being lucky to achieve 200 kHz bandwidth between the 2:1 SWR points.

The first step to produce a wideband yagi was to achieve a desired Front-to-Sidelobe level at the proper frequency range by adjusting the spacings and lengths of the parasitic elements of a conventional 3 element yagi. This was done with all the tools available, NEC-OPT, YO, and AO[4]. When the design was finalized for both electrical and mechanical properties, the next step was to incorporate the OWA into the yagi as an effective driven element. NEC-OPT was used to find the optimum spacing and lengths of the driven element and closely spaced parasitic element that form the OWA. The yagi really has 4 elements in this case, however, only the director and reflector at the ends of the boom affect the pattern. The extra parasitic element very close to the driven element only is used to match the impedance and widen the bandwidth as in the normal OWA.

The amazing thing about using the OWA in a yagi is that a solution can be found not only for wideband SWR results, but the impedance match can be selected for 50 ohms directly with no form of impedance transformation commonly used on yagis, such as gamma, beta, hairpin, etc. matches. All that has to be done is to use a direct connecting 1:1 current type or equivalent balun and the antenna is matched. This is really a remarkable finding and should make the other forms of matching obsolete. SWR response is shown in Figure 4 and one can clearly observe the extremely wide and unheard of bandwidth that this feed has. This is at the antenna feedpoint and even better response will be found at the end of the coax feedline at the transmitter. The Front-to-Sidelobe level of this design is greater than 15 dB across the complete 40 meter band and peaks at 37 dB at 7.05 MHz.

Other yagi designs have been optimized for 15 and 10 meters for both Front-to-Sidelobe levels and SWR bandwidth. Results of these designs are shown in Figure 5 and 6.

CONCLUSIONS

As mentioned above, there are still many more combinations which can be tried and tested. It only takes setting up the cases and performing the long computer runs.

Construction and application of the OWA is probably best suited and visualized in the high frequency (HF) and higher frequencies. The antenna can actually be made of wire or tubing with just a very

simple feeding structure. A matching transformer or other method may be required to provide the correct and best matching impedance to the feedpoint. This antenna should have application well up into the GHz regions.

REFERENCES

1. J. T. Bolljahn and J. V. N. Granger, "Omnidirectional VHF and UHF Antennas," *Antenna Engineering Handbook*, H. Jasik, ed. (New York: McGraw - Hill, 1961).

2. J. K. Breakall, J. S. Young, R. J. Bauerle, A. I. McDowell and T. A. Erdley, "Numerical Electromagnetics Code Optimization Design Software (NEC-OPT)," Tenth Annual Review of Progress in Applied Computational Electromagnetics, March 1994.

3. LTA, Inc., P.O. Box 77, New Bedford, PA 168140.

4. B. Beezley, K6STI, 3532 Linda Vista, San Marcos, CA 92069.

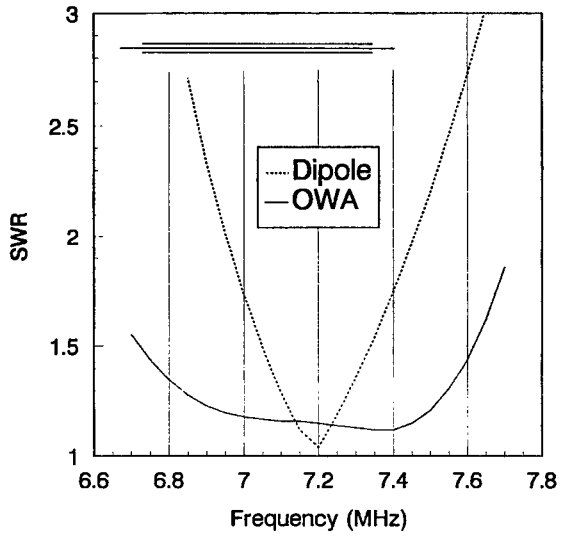

Figure 1. 40 Meter OWA vs. Dipole, #14 Wire, Height - 35 Feet

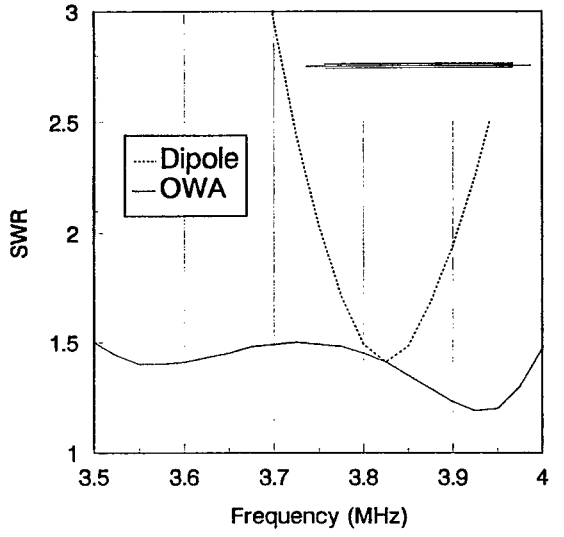

Figure 2. 80 Meter OWA, #14 Wire, Height = 50 Feet

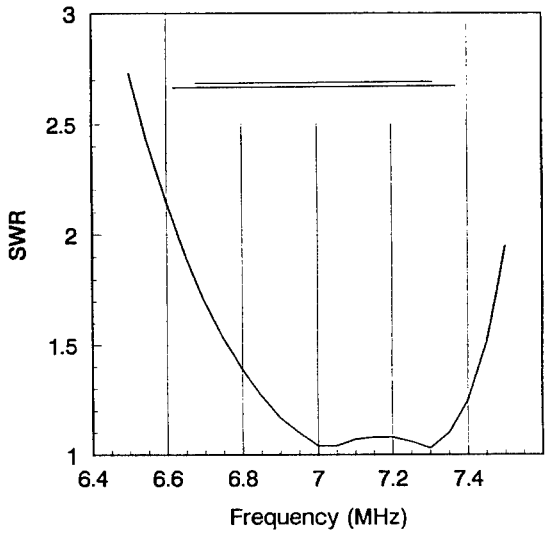

Figure 3. 40 Meter OWA Dipole, Simple 2 Wire Configuration

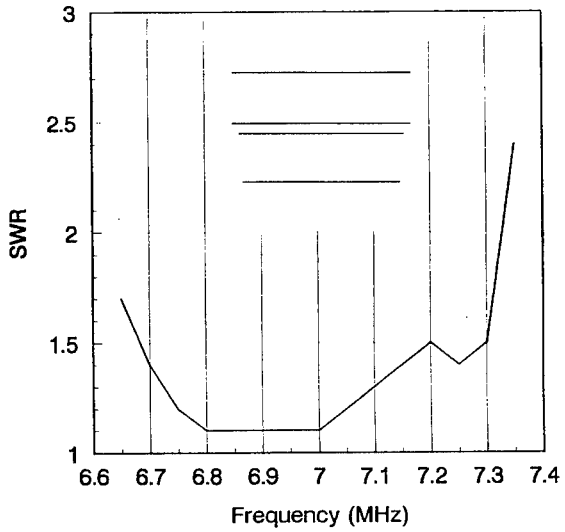

Figure 4. 4 Element 40 Meter Yagi, OWA Drive Element

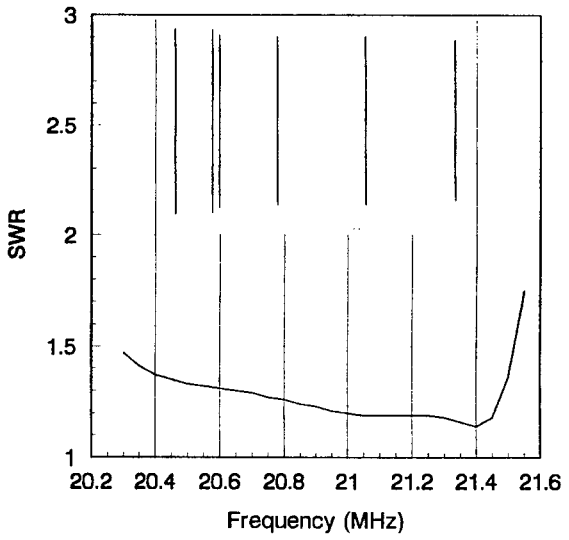

Figure 5. 6 Element 15 Meter Yagi, OWA Driven Element

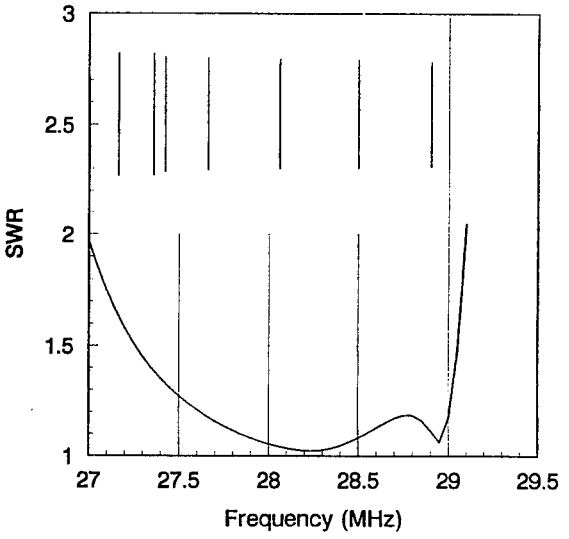

Figure 6. 7 Element 10 Meter Yagi, OWA Driven Element

The Quad-Rhomb Antenna

A New All-Band Antenna for Amateur Radio Applications

Rüdiger Anders, AA2HT
Applied Electromagentics Engineering
32 Parkgate Drive
Atlanta, GA 30328

Introduction

Covering all HF bands between 160m and 10m with only one antenna is one of the objectives of newcomers to Amateur Radio and old-timers as well. Although not easily attainable with a rotatable YAGI-UDA beam this objective can be achieved for a fixed direction, for instance working Europe from the US, while providing omnidirectional coverage for domestic and NVIS [1] operations on the low bands.

The 73m rectangular loop antenna

The Quad-Rhomb is derived from the horizontally supported 85.1m W9LZX Lazy Quad [2], which operates as a full wave- or quad loop on the 80/75m band, with similar behavior on 160m and 40m. If fed in one corner the Lazy Quad behaves like a small, non-terminated rhombus antenna on the upper HF bands, with the main lobe oriented along the diagonal through the feed point corner. Dimensions of the Lazy Quad are usually chosen such that it resonates on all of the harmonically related 160m through 10m bands. This common practice however trades ease of matching for desirable low sidelobe levels and particularly compromises the near side lobe level and gain on 10m, as shown in Fig. 1.

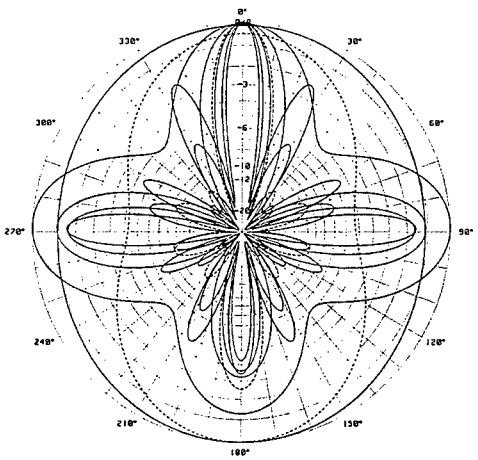

Fig. 1 Horizontal farfield (elevation 12°) of the 85.1m Lazy Loop, at 15m height over average ground

The overall sidelobe behavior can be improved considerably if the resonance requirement is dropped and the loop circumference reduced to 73.0m/239.5ft from 85.1m/279.2ft. Also, the half power beam width increases favorably on the upper HF bands and the 10m gain figure reaches that of the 12m band. The reduction of the loop side length by 3.1m to 18.25m, saves about 25% lot space, a welcome bonus for the space limited operator.

The modified 73m rectangular loop or Quad-Rhomb antenna (QR 60/30)

An even more dramatic improvement of the 73m loop can be achieved through controlling the current distribution along the loop the with a closed stub (Zl=450Ohm) that is put in-line with the loop at the corner opposite to the feed point, as depicted in Fig. 4. With a stub length of 8.9m/29.2ft (v=1.0) optimized [3] for minimum sidelobe levels on the DX bands the Quad-Rhomb features the desired horizontal radiation patterns shown in Fig. 2 with the vertical patterns for the QR 60/30 (Quad-Rhomb, approx. 60ft side length and approx. 30ft stub length) at 15.25m (50.0ft) given in Fig 3.

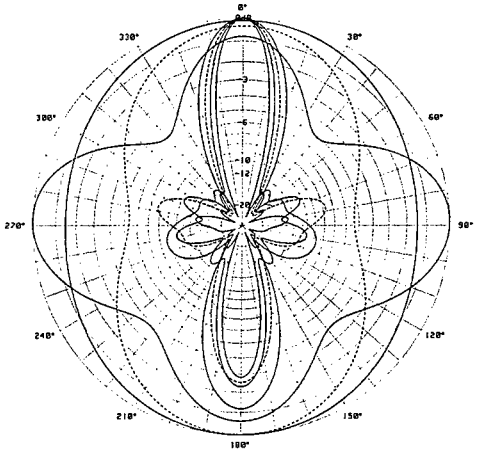

Fig. 2 Horizontal farfield (elevation 12°) of the QR 60/30, at 15m height over average ground

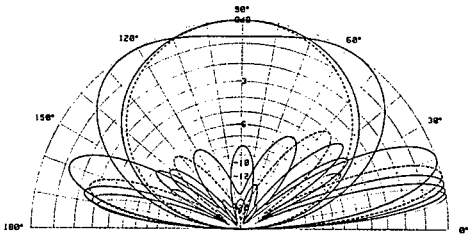

Fig. 3 Vertical farfield (azimuth 0°) of the QR 60/30, at 15m height over average ground

Lightning protection

Protection against common mode lightning discharge can easily be established by grounding the center of the stub end. Differential mode protection requires a gas discharge device across the feed point corner.

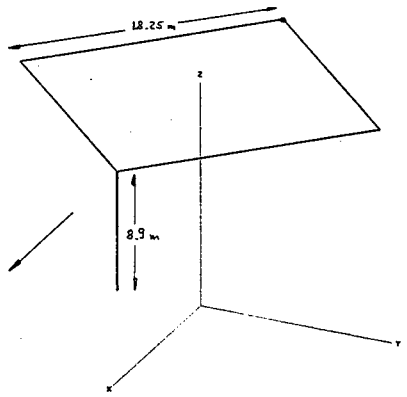

Fig. 4 Perspective view of the geometry of the QR 60/30

System Resonance and Matching

The Quad-Rhomb, if fed by a balanced transmission line of 33.85m/111ft (v=1.0) will resonate on all bands, Fig. 5, and with the exception of 160m features an input resistance around 100Ohms. A 2:1 hybrid balun at the station end of the 33.85m/111ft transmission line may be used to down-match to 50Ohms. For other line lengths an ATU is recommend.

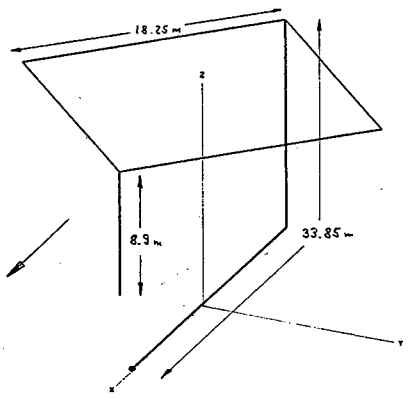

Fig. 5 Perspective view of the geometry of the QR 60/30 including 33.85m balanced feed line

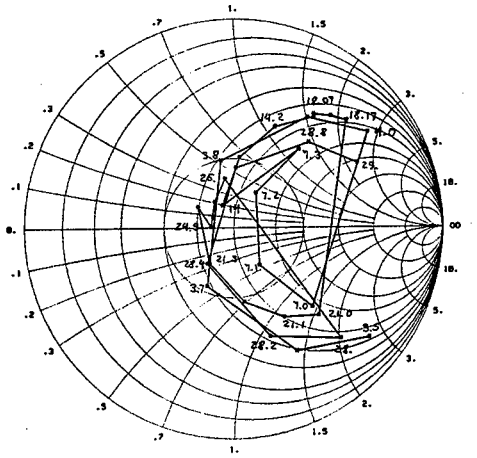

Fig. 6 Input impedance of the QR 60/30, at 15m height over average ground

For a better grasp of the farfield characteristic Fig. 7, Fig. 8, and Fig. 9 provide perspective views of the 3-D pattern at two charcteristic frequencies.

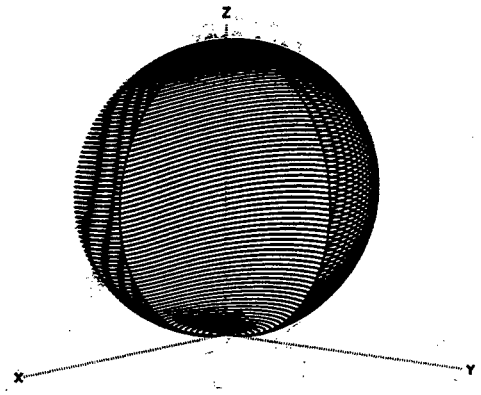

Fig. 7 3-D farfield of the QR 60/30, at 15m height over average ground, f=3.8 MHz

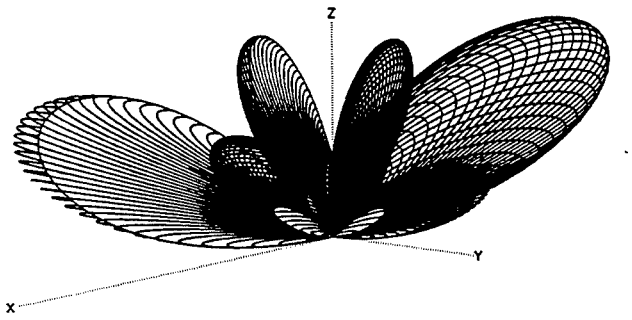

Fig. 8 3-D farfield of the QR 60/30, at 15m height over average ground, f=14.15 MHz

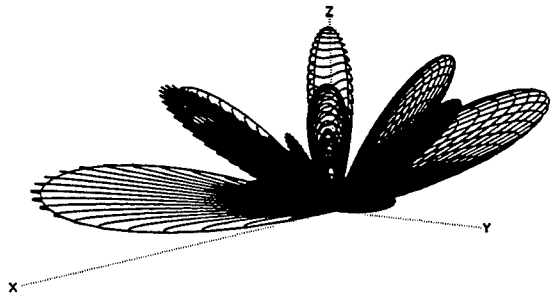

Fig. 9 3-D farfield of the QR 60/30, at 15m height over average ground, f=24.95 MHz

Conclusion

A novel all-band antenna has been presented that features quasi-omnidirectional coverage on the low ham bands (160m, 80m, and 40m) and highly directive, low sidelobe, bi-directional radiation patterns on the upper HF DX bands (30m to 10m). Due to the closed loop design which is known for an insensitivity to rain static and corona effects the Quad-Rhomb antenna presents itself as very quiet listening antenna, much appreciated among DX operators.

References

[1] E. Farmer, "A Look at NVIS Techniques", QST, January 1995, pp. 39-42.

[2] W. I. Orr, S. D. Cowan, "The W9LZX Lazy Quad for 80 or 160 Meters", The Radio Amateur Antenna Handbook, Radio Publications Inc., 1978, pp. 122-123.

[3] I-NAC-3, "Interactive Numerical Antenna Code", Version 2.0, Applied Electromagnetics Engineering, Atlanta, GA, 1996.

SKY-WAVES-95

An Educational Tool for the Exploration of HF-Skywave Propagation

Rüdiger Anders, AA2HT
Applied Electromagentics Engineering
32 Parkgate Drive
Atlanta, GA 30328

Introduction

Quite a number of software packages are currently available to help the DX enthusiast with forecasting or predicting HF skywave propagation. Why then another program? Unfortunately the majority of the software caters to the needs of the expert user who already knows the ins and outs of HF propagation, leaving the newcomer out in the cold. While these products provide reasonable results for the MUF, the traffic probability, and in some cases the signal levels to be expected, they offer very few options to systematically explore the response to the various input parameters in order to gain insight into the short- and long-term behavior of skywave propagation. It is particularly desirable for newcomers and the occasional DXer to improve the basic understanding of skywave propagation through interactively exploring the response of a computer propagation model in a much shorter time period than years of observation can do.

Objectives

SKY-WAVES-95 has been designed with the emphasis on self study by providing quick answers to common questions like:

How does the MUF fluctuate annually for the same circuit?
When does E-layer blanketing render the F2-layer ineffective?
Does the operating frequency have an influence on the MUF?
Why is there only one hop mode at band opening or closing?
How does the antenna height affect the length of a band opening?

while at the same time addressing the needs of the pros. SKY-WAVES-95 is constantly being checked and evaluated against daily propagations into various parts of the world.

Interactive variables

terminal coordinates	operating frequency
local time (or UTC)	date
solar flux	K index
probability mode(FOT, MUF, HPF)	height of antenna, stack height
bearing (range mode)	grayline (morning, evening)
path (short,long)	

Basic Model

SKY-WAVES-95 is based in part on the critical frequency f0f2 model of the improved MINIMUF-85 [1], in conjunction with the LOCKWOOD approximations for the m(d)F2 and m(d)E range factors [2], which account for an underlying ionization of the E-layer and the LOCKWOOD approximation for the mirroring height[3]. Ionospheric path incorpotates the BARGHAUSEN D-layer attenuation[4], and the DAVIS mode attenuation[5]. Rather than through control points SKY-WAVES-95 utilizes the actual location of the ionospheric refraction areas and Fresnel ground reflection regions for path evaluation. In combination with a novel iteration technique it becomes possible to account for the diurnal and geographical variations of the F2-layer mirroring height along the propagation path. As a results the takeoff the angles and the band opening and closing schedules become more accurate and the predicted relative path attenuation more realistic.

Currently SKY-WAVES-95 presents the results in tabular form Fig.1, and in terminal graphics Fig.2. In order to better and systematically understand the sun related diurnal and seasonal nature of the physics of propagation the results are represented in terms of the local mean time at the circuit terminals rather than UTC.

Examples and Output Samples

```
-------------------------------- SKY-WAVES-95 ---------------------------------
TX qth:              Atlanta  33.45°N  84.23°W  antenna bearing ->    40.24°/N
RX qth:            Dassendorf  53.32°N  10.22°E  ground distance ->  7345.18 Km
-------------------------------- (c) AA2HT 1995 -------------------------------
JAN  8 1996, LT1=varies, UTC=varies, sfx=111.00, ssn= 55, K= 0, freq= 14.00 MHz
TX boom height=  30.00 m,  TX stack height=  7.90 m,  TX take-off angle= 10.06°
RX boom height=  26.00 m,  RX stack height=  0.00 m,  RX take-on  angle= 11.53°
------------------------------ short path (MUF) -------------------------------
lt1= 0.00  utc= 5.00  lt2= 6.00   h=2  MUF=10.19 MHz  elv= 2.04°  att= 81.85 dB
lt1= 1.00  utc= 6.00  lt2= 7.00   h=2  MUF=10.18 MHz  elv= 1.46°  att= 88.34 dB
lt1= 2.00  utc= 7.00  lt2= 8.00   h=2  MUF=10.20 MHz  elv= 1.25°  att= 94.78 dB
lt1= 3.00  utc= 8.00  lt2= 9.00   h=2  MUF=10.39 MHz  elv= 1.25°  att= 60.73 dB
lt1= 4.00  utc= 9.00  lt2=10.00   h=2  MUF=10.28 MHz  elv= 1.01°  att= 68.35 dB
lt1= 5.00  utc=10.00  lt2=11.00   h=3  MUF= 9.53 MHz  elv= 6.54°  att= 51.99 dB
lt1= 6.00  utc=11.00  lt2=12.00   h=3  MUF=12.76 MHz  elv= 7.27°  att=  8.99 dB
---------vv---------vv---------vvv-----------------vv----------vv-------------
lt1= 7.00  utc=12.00  lt2=13.00   h=4  MUF=16.91 MHz  elv=12.41°  att=  2.52 dB
lt1= 8.00  utc=13.00  lt2=14.00   h=4  MUF=19.26 MHz  elv=12.36°  att=  2.43 dB
lt1= 9.00  utc=14.00  lt2=15.00   h=4  MUF=19.32 MHz  elv=12.33°  att=  5.88 dB
lt1=10.00  utc=15.00  lt2=16.00   h=3  MUF=22.21 MHz  elv= 7.10°  att=  8.47 dB
lt1=11.00  utc=16.00  lt2=17.00   h=4  MUF=17.74 MHz  elv=12.26°  att=  9.53 dB
lt1=12.00  utc=17.00  lt2=18.00   h=4  MUF=15.99 MHz  elv=12.41°  att=  9.86 dB
lt1=13.00  utc=18.00  lt2=19.00   h=3  MUF=16.11 MHz  elv= 7.28°  att=  8.68 dB
---------^^---------^^---------^^^-----------------^^----------^^-------------
lt1=14.00  utc=19.00  lt2=20.00   h=3  MUF=12.36 MHz  elv= 7.42°  att= 17.34 dB
lt1=15.00  utc=20.00  lt2=21.00   h=3  MUF=11.54 MHz  elv= 8.02°  att= 21.73 dB
lt1=16.00  utc=21.00  lt2=22.00   h=3  MUF=10.84 MHz  elv= 8.28°  att= 27.70 dB
lt1=17.00  utc=22.00  lt2=23.00   h=2  MUF=11.79 MHz  elv= 2.05°  att= 35.95 dB
lt1=18.00  utc=23.00  lt2= 0.00   h=2  MUF=11.26 MHz  elv= 2.53°  att= 36.65 dB
lt1=19.00  utc= 0.00  lt2= 1.00   h=2  MUF=10.90 MHz  elv= 2.53°  att= 42.25 dB
lt1=20.00  utc= 1.00  lt2= 2.00   h=2  MUF=10.63 MHz  elv= 2.50°  att= 50.65 dB
lt1=21.00  utc= 2.00  lt2= 3.00   h=2  MUF=10.43 MHz  elv= 2.44°  att= 59.25 dB
lt1=22.00  utc= 3.00  lt2= 4.00   h=2  MUF=10.30 MHz  elv= 2.33°  att= 67.59 dB
lt1=23.00  utc= 4.00  lt2= 5.00   h=2  MUF=10.22 MHz  elv= 2.30°  att= 73.73 dB
lt1= 0.00  utc= 5.00  lt2= 6.00   h=2  MUF=10.19 MHz  elv= 2.04°  att= 81.85 dB
-------------------------------------------------------------------------------
```

Fig. 1 Tabular form of 24 hour MUF and relative attenuation distribution

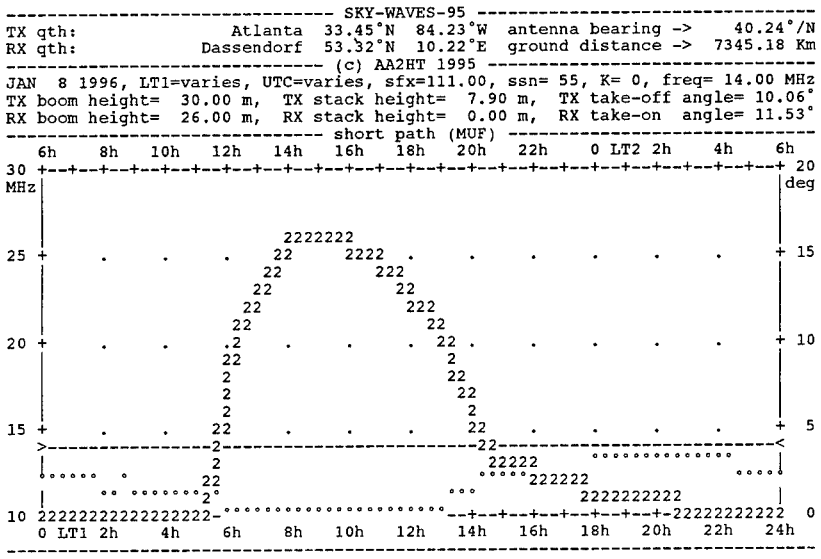

Fig. 2 Terminal graphic of 24 hour MUF distribution (winter)
numerals indicate hop numbers, ° indicate takeoff angle

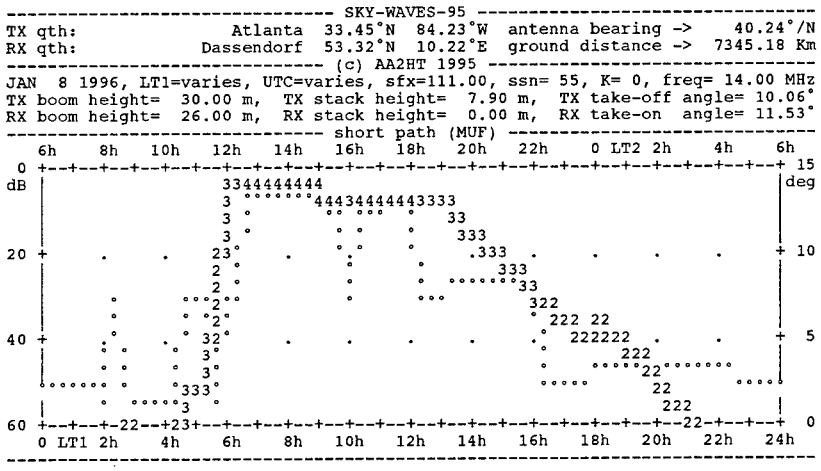

Fig. 3 Terminal graphic of 24 hour MUF distribution (summer)
numerals indicate hop numbers, ° indicate takeoff angle

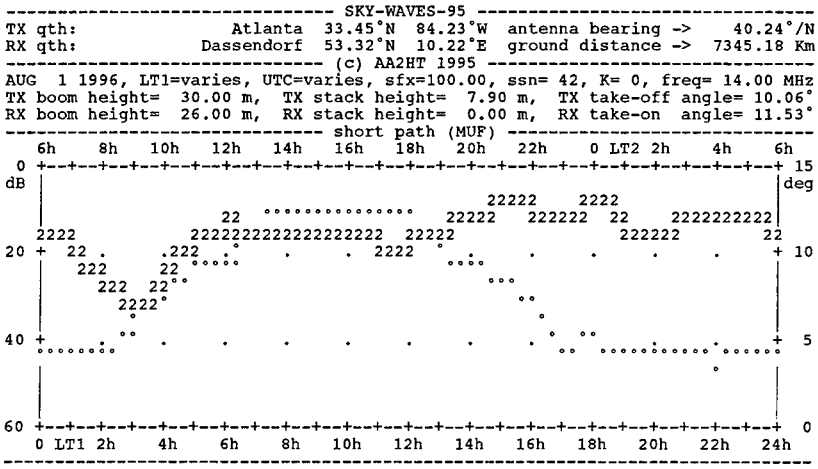

Fig. 4 Terminal graphic of 24 hour MUF distribution (summer)
numerals indicate hop numbers, ° indicate takeoff angle

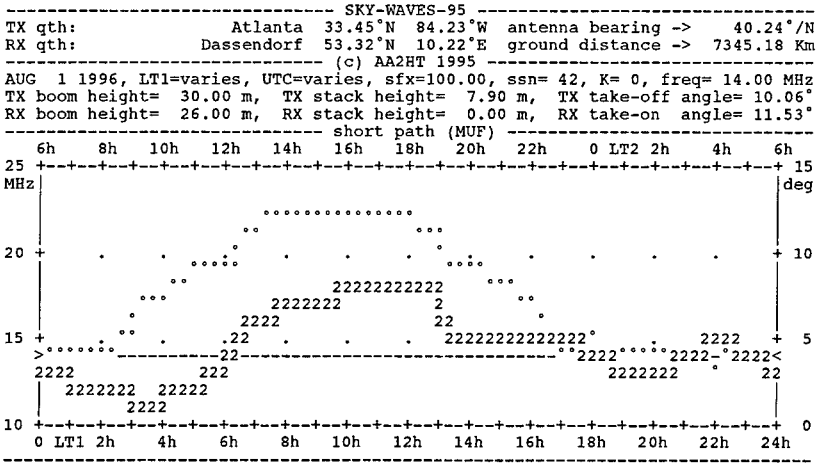

Fig. 5 Terminal graphic of 24 hour MUF distribution (summer)
numerals indicate hop numbers, ° indicate takeoff angle

```
-------------------------------- SKY-WAVES-95 ---------------------------------
TX qth:              Atlanta  33.45°N  84.23°W  antenna bearing ->    40.24°/N
RX qth:            Dassendorf  53.32°N  10.22°E  ground distance ->  7345.18 Km
-------------------------------- (c) AA2HT 1995 -------------------------------
JAN  8 1996, LT1=  8.00, UTC= 13.00, sfx=111.00, ssn= 55, K= 0, freq= 14.00 MHz
TX boom height=  30.00 m,  TX stack height=  7.90 m,  TX take-off angle= 10.06°
RX boom height=  26.00 m,  RX stack height=  0.00 m,  RX take-on  angle= 11.53°
------------------------------- short path (MUF) -------------------------------
->  2 hop(s),  MUF -> 25.34 MHz,  elevation ->  0.16°,  signal loss -> 57.18 dB
->  3 hop(s),  MUF -> 22.47 MHz,  elevation ->  7.10°,  signal loss ->  4.24 dB
->  4 hop(s),  MUF -> 19.26 MHz,  elevation -> 12.36°,  signal loss ->  2.43 dB
->  5 hop(s),  MUF -> 16.52 MHz,  elevation -> 17.27°,  signal loss -> 12.07 dB
->  6 hop(s),  MUF -> 14.54 MHz,  elevation -> 22.13°,  signal loss -> 30.28 dB
->  7 hop(s),  MUF -> 13.16 MHz,  elevation -> 27.25°,  signal loss -> 28.94 dB
->  8 hop(s),  MUF -> 12.08 MHz,  elevation -> 31.41°,  signal loss -> 82.13 dB
-------- F2-layer PENETRATION for elevations > 36.01°, signals lost in space --
--------------------------------------------------------------------------------
```

Fig. 4 Hop statistic for 14MHz operating frequency

```
-------------------------------- SKY-WAVES-95 ---------------------------------
TX qth:              Atlanta  33.45°N  84.23°W  antenna bearing ->    40.24°/N
RX qth:            Dassendorf  53.32°N  10.22°E  ground distance ->  7345.18 Km
-------------------------------- (c) AA2HT 1995 -------------------------------
JAN  8 1996, LT1=  8.00, UTC= 13.00, sfx=111.00, ssn= 55, K= 0, freq= 25.00 MHz
TX boom height=  30.00 m,  TX stack height=  7.90 m,  TX take-off angle=  5.38°
RX boom height=  26.00 m,  RX stack height=  0.00 m,  RX take-on  angle=  6.37°
------------------------------- short path (MUF) -------------------------------
->  2 hop(s),  MUF -> 25.48 MHz,  elevation ->  2.27°,  signal loss ->  9.49 dB
->  3 hop(s),  MUF -> 22.45 MHz,  elevation ->  9.13°,  signal loss -> 25.68 dB
-------- F2-layer PENETRATION for elevations > 13.59°, signals lost in space --
--------------------------------------------------------------------------------
```

Fig. 5 Hop statistic for 25Mhz operating frequency

```
-------------------------------- SKY-WAVES-95 ---------------------------------
TX qth:              Atlanta  33.45°N  84.23°W  antenna bearing ->    40.24°/N
RX qth:            Dassendorf  53.32°N  10.22°E  ground distance ->  7345.18 Km
-------------------------------- (c) AA2HT 1995 -------------------------------
JAN  8 1996, LT1=  8.00, UTC= 13.00, sfx=111.00, ssn= 55, K= 0, freq= 28.00 MHz
TX boom height=  30.00 m,  TX stack height=  7.90 m,  TX take-off angle=  5.02°
RX boom height=  26.00 m,  RX stack height=  0.00 m,  RX take-on  angle=  5.55°
------------------------------- short path (MUF) -------------------------------
->  2 hop(s),  MUF -> 25.34 MHz,  elevation ->  3.03°,  signal loss -> 15.94 dB
>>>>>>>>>>>>>>>>>>>>>>>>> antenna height less than optimal <<<<<<<<<<<<<<<<<<<<<<<
-------- F2-layer PENETRATION for elevations >  9.13°, signals lost in space --
--------------------------------------------------------------------------------
```

Fig. 6 Hop statistic for 28MHz operating frequency

```
-------------------------------- SKY-WAVES-95 ---------------------------------
TX qth:              Atlanta  33.45°N  84.23°W  antenna bearing ->    40.24°/N
RX qth:           Dassendorf  53.32°N  10.22°E  ground distance ->  7345.18 Km
------------------------------ (c) AA2HT 1995 ---------------------------------
JAN  8 1996, LT1= 17.43, UTC= 22.43, sfx=100.00, ssn= 42, K= 0, freq= 14.00 MHz
TX boom height=  30.00 m,  TX stack height=  7.90 m,  TX take-off angle=  5.02°
RX boom height=  26.00 m,  RX stack height=  0.00 m,  RX take-on  angle=  5.55°
------------------ grayline bearings -> 334.04° and 154.04° -------------------
hp=1 range= 1000.0 Km trav= 1263.7 Km   MUF= 11.35 MHz elv=33.16° att= 22.64 dB
hp=1 range= 2000.0 Km trav= 2148.4 Km   MUF= 17.67 MHz elv=13.01° att=  1.03 dB
hp=1 range= 3000.0 Km trav= 3128.4 Km   MUF= 21.48 MHz elv= 4.41° att=  8.24 dB
--------------------------------------------------------------------------------
hp=2 range= 4000.0 Km trav= 4257.5 Km   MUF= 15.42 MHz elv=11.47° att=  0.43 dB
hp=2 range= 5000.0 Km trav= 5237.0 Km   MUF= 16.11 MHz elv= 7.07° att=  2.94 dB
hp=2 range= 6000.0 Km trav= 6225.6 Km   MUF= 17.35 MHz elv= 3.45° att= 11.71 dB
hp=2 range= 7000.0 Km trav= 7225.0 Km   MUF= 18.13 MHz elv= 1.06° att= 32.23 dB
--------------------------------------------------------------------------------
hp=3 range= 8000.0 Km trav= 8329.0 Km   MUF= 15.88 MHz elv= 5.30° att=  6.17 dB
hp=3 range= 9000.0 Km trav= 9328.1 Km   MUF= 17.46 MHz elv= 3.27° att= 13.10 dB
hp=3 range=10000.0 Km trav=10326.2 Km   MUF= 17.93 MHz elv= 1.44° att= 24.49 dB
hp=3 range=11000.0 Km trav=11342.0 Km   MUF= 18.39 MHz elv= 0.17° att= 55.98 dB
--------------------------------------------------------------------------------
hp=4 range=12000.0 Km trav=12465.7 Km   MUF= 17.35 MHz elv= 3.44° att= 11.95 dB
hp=4 range=13000.0 Km trav=13441.2 Km   MUF= 17.71 MHz elv= 2.36° att= 17.82 dB
hp=4 range=14000.0 Km trav=14515.5 Km   MUF= 17.90 MHz elv= 1.29° att= 27.16 dB
hp=4 range=15000.0 Km trav=15503.1 Km   MUF= 18.33 MHz elv= 0.30° att= 45.80 dB
--------------------------------------------------------------------------------
hp=5 range=16000.0 Km trav=16651.6 Km   MUF= 17.51 MHz elv= 3.17° att= 14.03 dB
hp=5 range=17000.0 Km trav=17621.3 Km   MUF= 16.02 MHz elv= 2.24° att= 19.19 dB
hp=5 range=18000.0 Km trav=18652.3 Km   MUF= 15.01 MHz elv= 1.30° att= 26.99 dB
hp=5 range=19000.0 Km trav=19759.0 Km   MUF= 14.58 MHz elv= 1.06° att= 32.44 dB
--------------------------------------------------------------------------------
hp=6 range=20000.0 Km trav=20899.1 Km   MUF= 14.19 MHz elv= 3.17° att= 14.03 dB
--------------------------------------------------------------------------------
```

Fig. 7 grayline statistic (evening) for 14MHz operating frequency

SKY-WAVES-95 is available from the author (free of charge).

References

[1] D. B. Sailors, R. A. Sprague, W. H. Rix, "MINIMUF-85: An Improved HF MUF Prediction Algorithm", Naval Ocean System Center, San Diego, TR 1121, 1986.

[2] M. Lockwood, "Simple M-factor algorithm for improved estimation of the basic maximum usable frequency of radio waves reflected from the ionospheric F-region", IRE Proc., Vol. 130, Pt. F, No. 4, June 1983, pp. 296-302.

[3] M. Lockwood, "Simplified estimation of ray-path mirroring height for HF radio waves reflected from the ionospheric F-region", IRE Proc., Vol. 131, Pt. F, No. 2, April 1984, 117-124.

[4] A. F. Barkhausen et al., "Predicting Long-Term Operational Parameters of High-Frequency Sky-Wave Telecommunication Systems", ESSA, TR ERL 110-ITS 78, 1969, pp. 61-64.

[5] K. Davies, "Ionospheric Radio", Peter Peregrinus Ltd., 1990, p. 459.

USING HAM RADIO CEM CODES TO GAIN INSIGHT INTO VHF GROUND PLANE ANTENNA PERFORMANCE AND TO MITIGATE 75 METER MARS RFI AT A NAVAL RECEIVING SITE

Art Hoffman, WA6TVN
R. W. Adler, K3CXZ
Naval Postgraduate School

ANTENNA DESIGN

The authors have been users of the original MININEC in solving for VHF/UHF antenna performance for over 15 years. Serious use began with the release of the MININEC SYSTEM for the design of two and three-element yagis with direct coax feed for the 10 and 2-meter bands. The boom was used as a balun and was included in the model since it extended beyond the back end of the array. Designs were constructed from non-magnetic stainless steel brewery tubing or from copper water pipe. SWR measurements closely tracked the MoM results. Operational beamwidth was as predicted but the front-to-back ratio was dependent on nearby local obstructions, as expected. During this time, MN and ELNEC became available and were pressed into service.

In 1984, 2-meter activity flourished locally and new hams were in need of simple home-brew antennas for home use with their handie-talkies. The venerable standard quarter-wave (QW) 4-radial ground plane 5-wire design (Figure 1) looked like something simple to model and it could be built from inexpensive readily available materials. MININEC models correctly identified element lengths and input impedance, but radiated performance was not as satisfying as expected. It was suggested by CDR Buzz Shaw, WA1NHP, that a set of careful measurements should be made for comparison to a known basic antenna such as a vertical half-wave dipole reference antenna. (Buzz had designed a version of a J-pole antenna, for his MS thesis project in 1974, before MININEC was available, that featured a direct feed from a coax cable.) The comparison of the dipole to a 4-radial ground plane (GP) revealed a serious shortfall in gain (as much as -3 dB) of the GP. A second comparison was made to a coaxial half-wave vertical dipole. The coax dipole seemed to suffer the same degradation as the GP, showing about a 2 dB difference. The possibility of a common upset was looming.

Ten years earlier we noticed the same disappointing performance for a carefully machined aluminum GP with 12 radials, built in our machine shop. Various mounting schemes did not improve performance, but some very expensive RF absorbing material wrapped around the support mast below the feed point and down for a half wavelength did improve the observed gain. This, once remembered, lead to speculation that the mast under the radials somehow had substantial current flowing on it, contributing to the total radiated field along the horizon. And the contribution might be subtractive. Several commercial GPs were available in double-skirted (DS) versions (Figure 2). We tested one and saw definite improvement over the single-skirted (SS) designs. The MININEC models of the DSGP, however produced gains within .5 dB of the SSGP. The MININEC models contained only the upper radials, the quarter-wave vertical connecting mast below the upper radials and the lower radials. No masts nor coaxial cables were used in any of the computer models up to this point.

Efforts were then concentrated on measurements in an attempt to improve performance and especially understand what was causing the differences and disappointments. During the measurements on the QWSSGP it was observed that the loss in gain was coming from *uptilt* of the usually broadside beam. The amount of uptilt was a function of the length of the supporting mast. It was speculated that the amount of feed line that was "exposed" (not lying on the ground) and could contribute to the pattern was a factor. The coax dipole's quarter-wave sleeve is the limiting case of a QWSSGP with drooping

radials that have drooped to -90°. Up to this point, all experiments were conducted with supporting pipes that were of some arbitrary length, extending below the lower radials. A coax dipole was modified by adding a set of 4 wire radials at the bottom of the outer sleeve. An immediate increase in gain was noted, along with a nasty input impedance change. The second set of radials was added at the feed point, making the antenna electrically very close to the QWDSGP. Gain comparisons between the QWDSGP and the "radialized" coax dipole showed close difference of less than a dB.

Now it was obvious that the coax feed line outer conductor was a definite contributor to measurable amounts of radiated field at the horizon. And the MININEC modeling had NOT included the cable as a conductor because all good hams know that "transmission lines don't radiate". To test this theory, a MININEC model of a half-wave vertical dipole with a balun connected at right angles to the dipole with a coaxial cable extending a quarter-wave from the feed, then dropping straight down toward the ground was tested. Figure 3 shows the geometry of the conductors and the currents on the wires. The balun was not electrically connected to the dipole. A small gap represented the balun effect of preventing the conduction of dipole current onto the outside of the coax outer conductor. The calculated currents on the balun and coax shield are from dipole field coupling. Patterns from the "real world" dipole and a free space dipole are presented in Figure 4.

The next piece of enlightening information came by accident when some mast material was placed about a half wave from an experimental radiator. The fields near the radiator were "normal" when there was no mast within several wavelengths of the radiator. But when copper tubing was at the half-wave location, a large disturbance was noted. If a piece of Radio Shack TV mast (either their light-duty thin mast or the robust heavy-duty pipe) was placed in the same location as the copper pipe was, the disturbance was almost unmeasureable. Many other types of metallic pipe were tested, including both "el cheapo" magnetic stainless steel tubing and costly non-magnetic stainless steel conductors. The results of several tests show that magnetic steels, such as the Radio Shack mast, seem to be very lossy for RF currents at VHF. For example: a Japanese magnetic stainless steel whip became uncomfortably warm to the touch after a few minutes of being fed with 50 watts at 145 and 450 MHz.

During earlier tests on the SSGP and DSGP, the type of masts (steel, copper pipe, wooden sticks) used to support the antennas under tests was not thought to have been important. After the magnetic mast discovery, the breakthrough in showing feed line effects came when gain was proven to be dependent on the spacing between the support mast and the bottom pipe of the ground plane antennas. Clamping the GP antenna directly to the different masts gave somewhat different results, but an experiment using a short insulating mast between the GP pipe and the support mast provided the optimum mounting arrangement. A top end of a piece of insulating mast material was clamped to the bottom of the GP antenna and a quarter-wave below the bottom GP radials, a Radio Shack TV mast was clamped to the insulating support. This provided about a QW spacing below the antenna of exposed feed line coax. Then the coax was fed through the RS mast and down and away from the GP antenna. It seemed that the lossy nature of the magnetic mast eliminated RF currents that would have run down the outside of the feed line below the antenna. With the RS mast arrangement, the full expected gain of the DSGP was realized.

The next chapter in this antenna soap opera deals with the ability of MININEC to predict the coupling between the SSGP & DSGP antenna elements and the outer conductor of the coax feed line. If the fields around and the currents on the elements can induce currents on the feed line, the radiation patterns should show this. Indeed, when various lengths of conductor are attached to the basic DSGP antenna in a MININEC model, the patterns and the horizon gain does vary as observed. In fact, the notion that the first set of radials is all that is needed to isolate the radiating elements from the feed line, is shown to be completely bogus. A MININEC model of a triple-skirted GP clearly shows substantial currents on the lower radials and feed line! Patterns for an SSGP and a DSGP with coax stubs hanging down from

the bottom of the antenna are shown in Figures 5 & 6. The patterns for the original ideal GP antennas are overlaid for comparison. The SSGP with feed line included shows as much as - 4 dB gain drop along the horizon, while the DSGP with feed line suffers -3.8 dB horizon loss! This confirms the earlier measurements and validates MININEC as an analysis tool, but only after all the facts are in so a complete numerical model can be developed.

Thus, in terms of lessons learned, a design of a well-known and popular simple antenna using MININEC will yield exactly the expected results. If the modeler *verifies* the performance with careful measurements, and finds substantial differences, he might conclude that MININEC lies and that the generic antenna design is flawed. But if there is real intent and enthusiasm to discover "Mother Nature's" rules for such antennas, careful experiments and an inquisitive mind can guide one from the fog into the sunlight where the expected results can be achieved. The real fun is discovering what Mother Nature has known all along and then feeding MININEC "...the rest of the story". Once MININEC has the correct conductor lineup, the results will match observation.

Prologue: The original design of all the GP antennas came from the bare bones MININEC model. Once the need for an insulating intermediate mast was discovered, an addition glitch appeared. Using metal clamps to attach the bottom pipe of the GP (between the radial levels) to the insulated mast seems to detune the structure, wrecking the input impedance. A simple fix to restore the impedance consists of wrapping the antenna's pipe with tape, then clamping to the taped surface. A guess is that the clamp seems to increase the effective diameter of the pipe and that changes the phase difference between the two sets of radials.

MARS STATION OVERLOAD

While working at a Navy HF receiving site in Maine during the summer of 1995, we discovered an intermittent very strong local single-side-band (SSB) voice and frequency-shift keyed (FSK) radio teletype (RTTY) signal at 4.001 MHz several times each day. The signal overloaded the primary multicouplers and other components of the RF distribution system of the site. The source of the signal was traced by LCDR Andrew Parker, WV1B, to amateur station NC4B operating as a Military Affiliate Radio System (MARS) station NNNØIBM. The station was directly across Prospect Harbor at a distance of 1.8 km from the center of the vertically polarized HF receiving array as shown in Figure 7.

After contacting the station operator and explaining the nature of the problem, the antenna system was examined. (The operator was a retired Navy LCDR. She had been in charge of base housing in the old 12th Naval District which included NPS housing, and was very cooperative.) The antenna was a G5RV "all-band dipole" at 25 feet, which was oriented in-line with the receiving site. This produced a polarization match with the victim antenna. The G5RV was used in the Near Vertical Incidence SkyWave (NVIS) mode for a local Navy MARS net, and not a low angle long-haul mode. That meant that non-directional coverage was desired and reorienting the antenna by 90° would not affect the coverage, but could help the overload situation. In order to minimize the interference to the receiving site, it would have been desirable to relocate the G5RV, if it were possible to evaluate the antenna-to-antenna coupling as a function of position of the MARS antenna.

It was a stroke of good luck that I had earlier received a pre-release copy of a terrain analysis computer program from Brian Beezley, K6STI, the creator of MN and AO, which he dubbed TA. Brian had seen the results of a measurement program where the radiated fields from a collection of dipoles and monopoles located in front of, on top of and behind a small hill in central Utah. Jim Breakall, WA3FET, had been instrumental in having a version of the MOM-BSC GTD/UTD code adapted to model the terrain and antennas. The results of the measurements and numerical modeling tweeked Brian's curiosity. He studied diffraction theory and decided to try to write a simple 2-D PC code to evaluate the effects of

terrain in front of a ham antenna site. Brian asked Breakall & I to participate in the evaluation of TA. We immediately both saw its value for our students for visualizing diffraction effects. TA produces terrain modified radiation patterns from precalculated free space patterns of wire antennas. Multiple reflections and diffractions and combinations of both are supported. User defined terrain profiles can be in the form of data files or from mouse-generated terrain slopes. The upper portion of the screen contains a polar radiation pattern, with the terrain profile at the bottom. The antenna position can be mouse-adjusted "on-the-fly" to see changes in the pattern. Changes in terrain also are almost instantaneous. The user can also turn on the display of reflection, diffraction and multiple diffraction. Other tweaks add controls that are not available in the 3-D NEC-BSC code. We were pleased to see that TA runs for the Utah measurements were quite close to those of the NEC-BSC based code.

The terrain between the MARS station and the site consists of cliffs at both ends and a salt water bay between. The cliff at the transmitter was 30 feet above the water and sloped downward for 135 feet. The bay was 3350 feet across. At the receiver end of the path, the terrain rose 50 feet over a distance of 1775 feet, as shown if Figure 8. The receiving monopoles were 80 feet high. TA was used to locate the G5RV at several heights above the ground and at various distances from the edge of the cliff in back of the house. The low angle calculated gain was determined in the direction of the receiving site for the original geometry and for several new locations that was compatible with the back yard tree locations. Figure 9 is a sample of one of the runs.

Prologue: A height of 20 feet was chosen for the new location of the dipole, using a pair of trees on opposite sides of the back yard. The impedance of the G5RV remained acceptable. As soon as the relocation was completed, the NVIS performance was checked with several of the MARS net members. They all reported and increased signal with the new orientation. A phone call was then made to the receiving site where Ray Vincent, W6PUX and George Munsch, W5VPQ were waiting to measure the new signal level. The relocation and reorientation produced a 20 dB drop in signal level at the antenna terminals, enough to eliminate any trace of overload. The ray tracing display of TA showed that the new location eliminated the bounce off the bay water surface, with only cliff-edge diffractions adding to the direct rays. TA has now become part of our standard software suite we use on laptop PCs during worldwide field trips to receiver sites. Its quick solution time and revealing visualization of rays make it superior to NEC-BSC for field use.

The capability of mainframe-based batch-mode NEC-MoM and NEC-BSC codes includes solving problems like these. But the user-friendly amateur radio-based codes with their graphical interface and superior output displays are preferred over their "big brothers" for field-expedient solutions to these real-world problems. In addition, these Ham CEM codes easily fit on PC laptops that are readily available in the field.

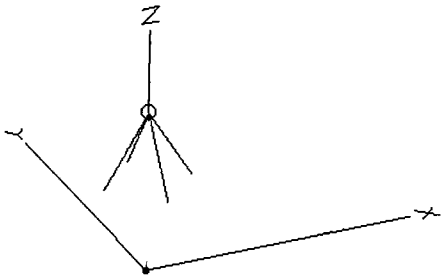

FIG. 1 SINGLE-SKIRTED GROUND PLANE

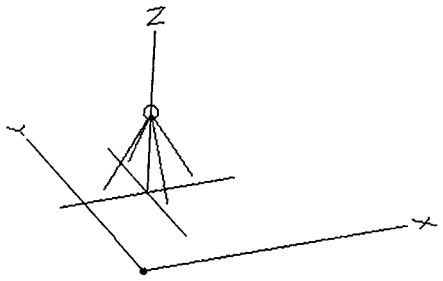

FIG. 2 DOUBLE-SKIRTED GROUND PLANE

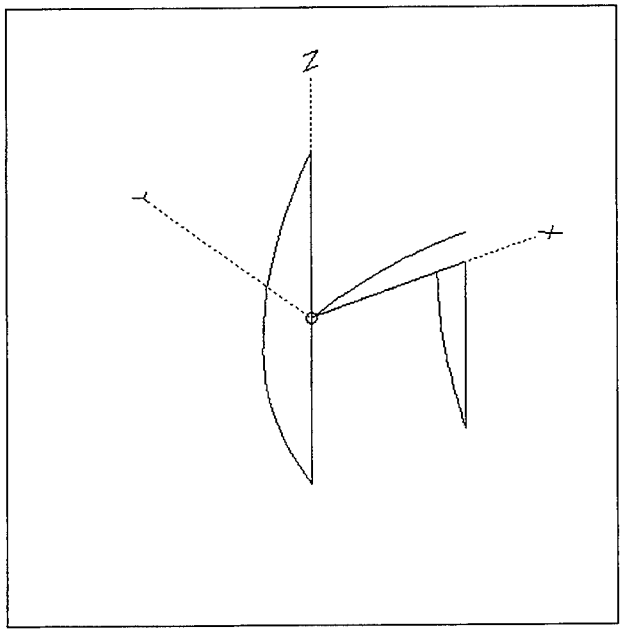

FIG. 3 HALF-WAVE VERTICAL DIPOLE, WITH BALUN AND COAX LINE, SHOWNING DIPOLE CURRENT AND INDUCED CURRENTS ON BALUN AND COAX

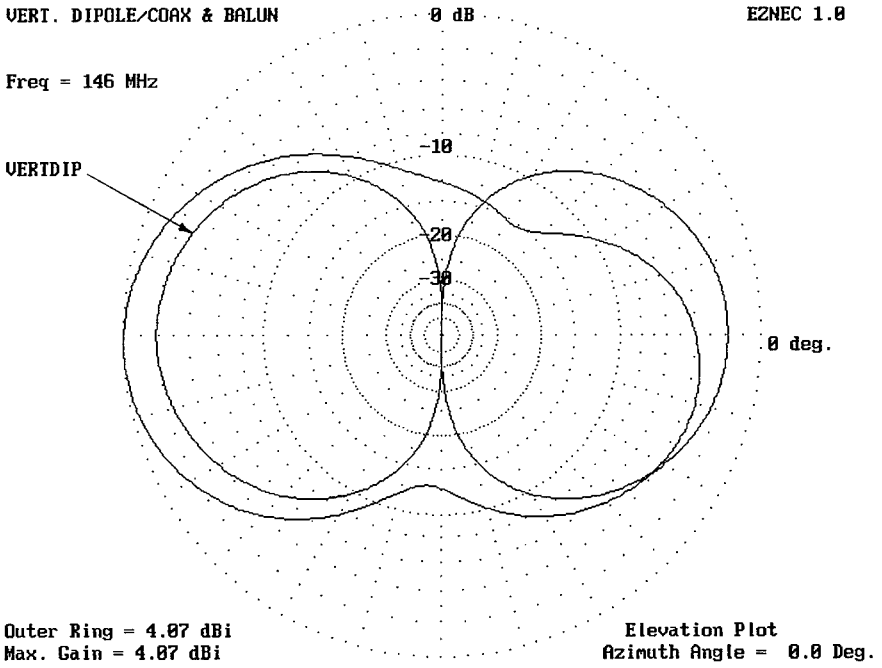

FIG. 4 PATTERNS FOR A VERTICAL DIPOLE WITH AND WITHOUT BALUN AND COAX

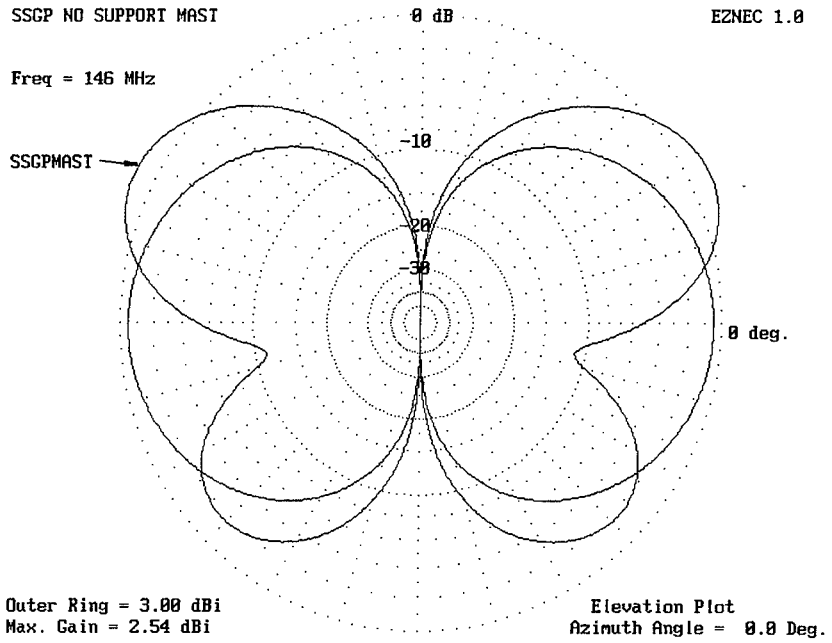

FIG. 5 SINGLE-SKIRTED GROUND PLANE WITH AND WITHOUT MAST/COAX STUBS

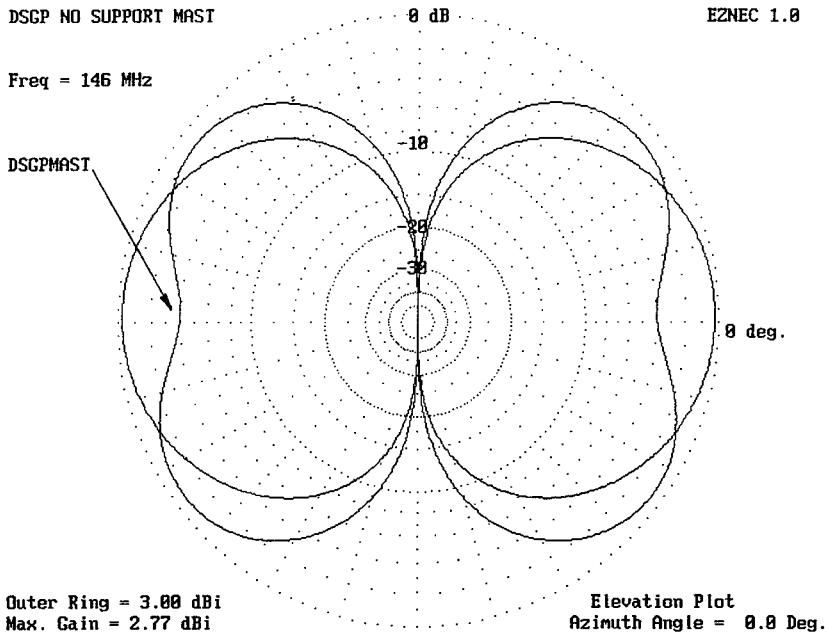

FIG. 6 DOUBLE-SKIRTED GROUND PLANE WITH AND WITHOUT MAST/COAX STUBS

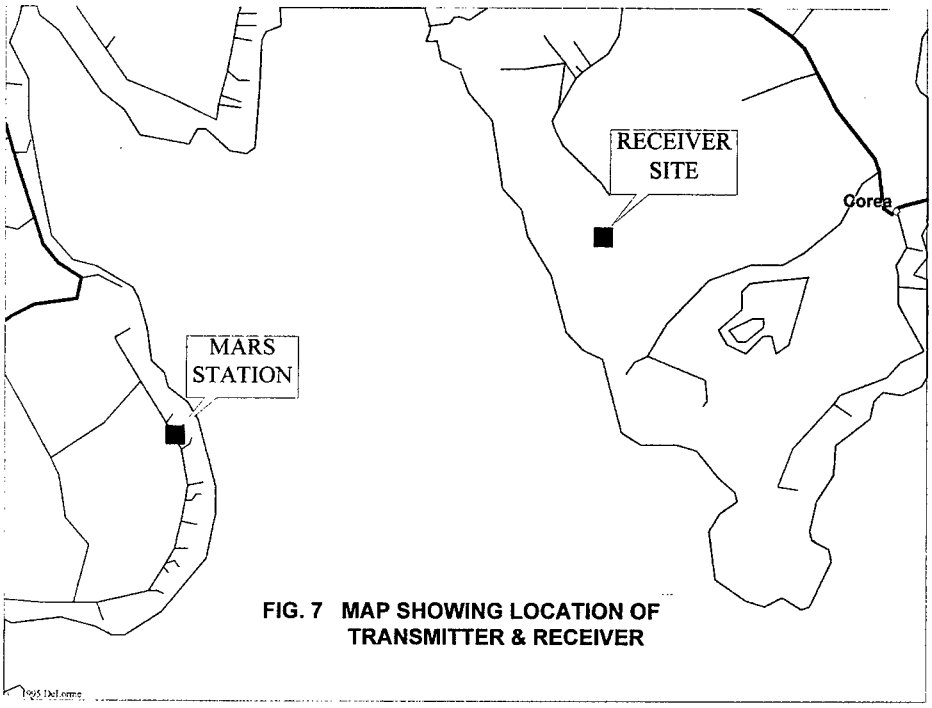

FIG. 7 MAP SHOWING LOCATION OF TRANSMITTER & RECEIVER

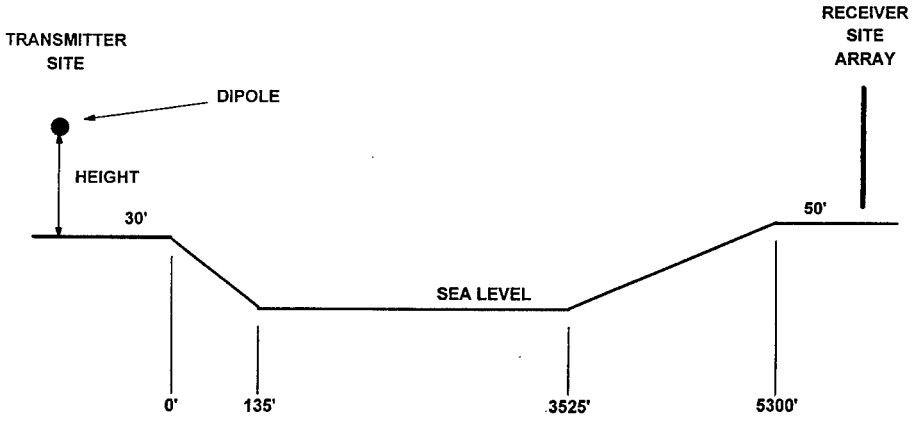

FIG. 8 TERRAIN PROFILE OF PATH

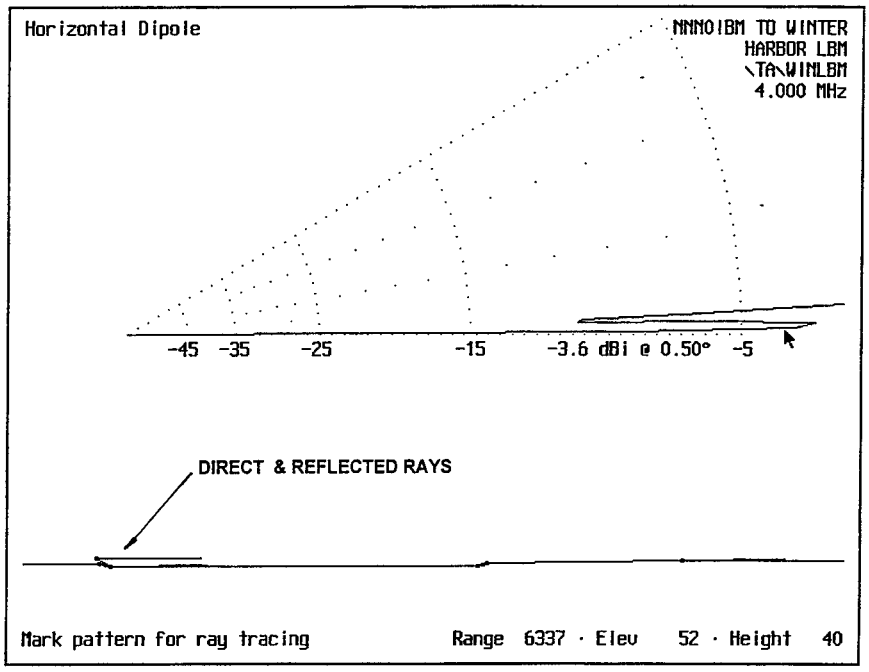

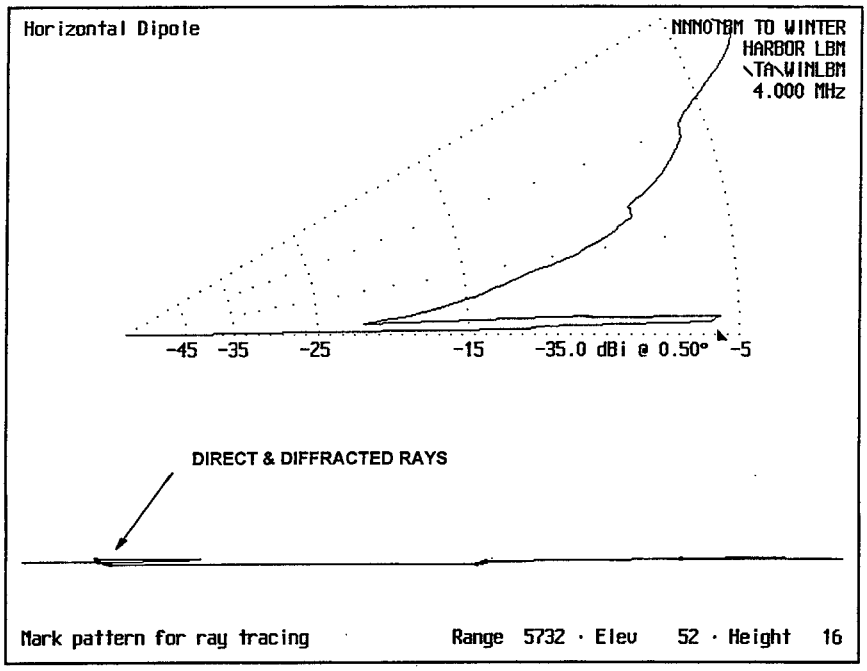

FIG. 9 LOW ANGLE RADIATION FROM A G5RV DIPOLE IN THE DIRECTION OF THE RECEIVING SITE FOR 16' AND 40' DIPOLE HEIGHT

Development of Practical Landstorfer Antennas for Amateur Use

Marc Tarplee

Landstorfer and Sacher, in 1985, considered how the performance of electrically "long" antennas (total length greater than λ/2) could be optimized. Their approach was to divide the antenna into a large number of small segments, whose positions were perturbed to optimize some aspect of the antenna's performance. They looked at ways to increase the effective height of monopoles and ways to increase the directivity of dipoles. Landstorfer and Sacher also discussed how their optimized antennas could be combined into Yagi-Uda arrays and log-periodic arrays. They tested models of Yagis and LPDA's made from their curvilinear (bent) dipoles that showed considerable promise. They did little optimization of their designs due to the limited performance of the computers available to them. [1]

Since his original work, few, if any, amateur antennas have been constructed using the principles outlined in [1]. There are probably several reasons for this. First, not many amateurs were familiar with Landstorfer's and Sacher's work. Second, computer software capable of performing the required optimizations was not available to amateur radio operators until recently. Third, Landstorfer's and Sacher's original designs are not easy to fabricate.

In this paper, I will look at three issues surrounding the Landstorfer antenna:

1. What are the properties of a "good" approximation to Landstorfer's curvilinear dipoles which is simple to fabricate ? I will try to answer questions such as: How long should the dipole be ? How many segments should it contain? What is the driving point impedance?
2. How can the Landstorfer dipole be used by amateurs?
3. How can Landstorfer dipoles be used in arrays?

All antenna analysis/optimization required for this paper will be done with AO Antenna Optimizer version 6.36 and NEC/Wires version 1.62. Prior to entering a discussion of the three issues outlined above, it is worthwhile to use AO and NEC/Wires to reproduce Landstorfer's results given in [1] as a starting point.

Review of Landstorfer's original work

Landstorfer [1] explored in some detail, the properties of a 3λ/4 monopole bent in order to optimize directivity. Below is a comparison of Landstorfer's results and my results using AO

Table 1 Comparison of calculated shapes of bent monopoles optimized for directivity

	segment angles (deg)						Directivity	Input Impedance
N	α1	α2	α3	α3	α3	α3	D (dbi)	Zin (Ω)
1	31 **(34)**						5.1 **(5.9)**	85 **(53+j11)**
2	43 **(48)**	8 **(14)**					6.9 **(6.8)**	83 **(50+j4)**
6	33 **(35)**	53 **(57)**	40 **(51)**	12 **(22)**	2 **(10)**	17**(10)**	7.1 **(6.9)**	86 **(55+j15)**

Notes:
Boldface data are results from AO; non-boldface are Landstorfer's [1]
AO was set to 10 segments per half wave with automatic tapering enabled
The antennas optimized by AO had a diameter equal to λ/1000.
All segments were the same length i.e. 3λ/4N
Directivity optimization in AO was done by modeling equivalent dipole

The agreement between Landstorfer's values and mine is fairly good. Landstorfer assumed that the current distribution in each segment is sinusoidal which would lead to slightly different results. As a further check, the directivities and input impedances were computed again using NecWires. The results appear in Table 2 below:

Table 2 Comparison of AO and NW Results

	Results from AO		**Results from NecWires**	
N	Directivity (dbi)	Zin (Ω)	Directivity (dBi)	Zin (Ω)
1	5.9	106+j22	5.9	105+j7
2	6.8	99+j8	6.7	102-j10
6	6.9	109+j29	7.0	106+j8

There is good agreement between the two programs.

Basic Properties of the Landstorfer dipole

a) Number of Segments and directivity:

A 1.5λ Landstorfer dipole was optimized for directivity using various numbers of segments. The results appear in Figure 1 below:

FIGURE 1

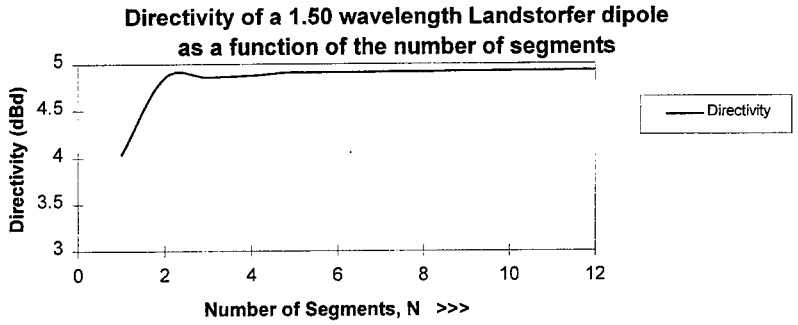

It is obvious from Fig 1 that one does not need to use a large number of segments to realize most of the directivity available from this antenna. In fact, 2 segments would be sufficient; one gains less than 0.1 dB of additional directivity by increasing to 12 segments. Note that the 2 segment antenna has a moderate advantage over a single segment antenna (which is really a resonant vee antenna). This simplifies the construction of Landstorfer curvilinear elements: one needs only one bend at the middle of each half element, as opposed to the continuously curved elements shown in [1]

b) Antenna length and directivity

For a straight dipole, the directivity increases to a maximum at $l \cong 1.28\lambda$ and decreases for longer antennas [2]. If one wishes to use a dipole as an element of a Yagi array or LPDA, it is not just the overall directivity that is important, but the directivity in the direction perpendicular to the axis of the antenna (broadside directivity, denoted by D0) that is important. D0 values for Landstorfer dipoles are much greater than those of corresponding straight wire antennas. Figure 2 below shows this variation with overall antenna length:

FIGURE 2

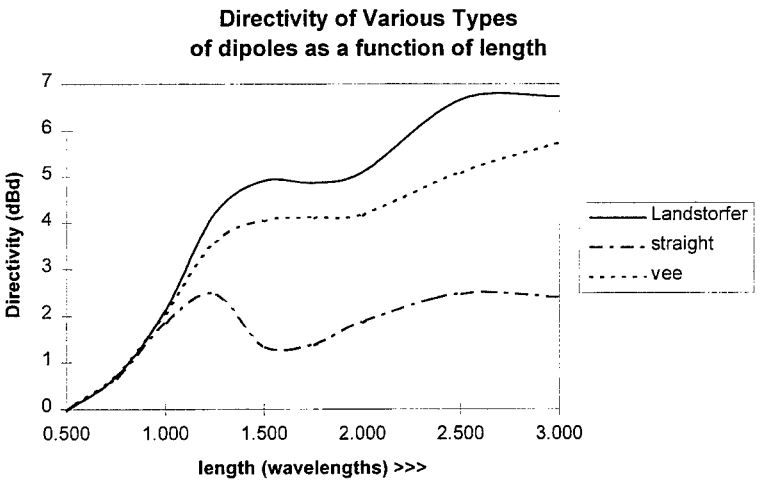

Note that the directivity of a Landstorfer dipole quickly increases to 4.9 dBd when the length reaches 1.50λ and remains almost constant to nearly 2.00λ. The next plateau comes at 2.50λ, where the directivity is approximately 6.7 dBd. It is not known if the directivity continues to increase for lengths beyond 3.00λ. It appears that a length of 1.50λ seems to be a good compromise; doubling the length to 3.00λ would add less than 2 dB to the directivity and there is no reason to believe that at some larger length that there would be a sudden increase in directivity.

c) Input Impedance

Figure 3 shows how the input impedance of a Landstorfer dipole varies with length in the range $0.50\lambda < l < 3.00\lambda$. Resonance occurs at $l = 1.47\lambda$ and 2.50λ. and there is an anti resonance at 0.84λ. The input impedance at resonance is on the order of 100 ohms, so the antenna could be fed directly with 75 ohm coax, or matched to 50 ohm coax with a 75 ohm quarter-wave matching section.

d) SWR Bandwidth

Figure 4 compares the bandwidth of a half wave dipole and a Landstorfer dipole of similar diameter ($\lambda/110$). The Landstorfer dipole has a narrower bandwidth, which is not a complete surprise. Other authors have noted that resonant vee and long wire antennas have impedances that change quite rapidly with frequency. The

explanation is that a fixed percentage change in a long antenna is much greater (in terms of a wavelength) than a short antenna [3]

Although the Landstorfer antenna is relatively narrow-band, it still has sufficient bandwidth to cover the entire 2 meter band when its diameter is relatively large (λ/100). If this antenna were scaled to 14.175 MHz and made from #12 wire (dia = λ/10000) the antenna would still have a 2:1 SWR bandwidth of about 470 kHz, enough to cover the 20 meter band.

FIGURE 3

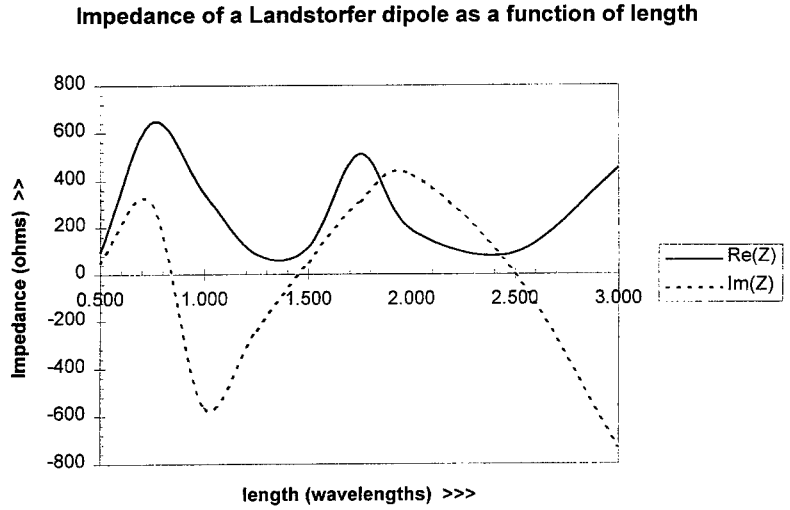

FIGURE 4

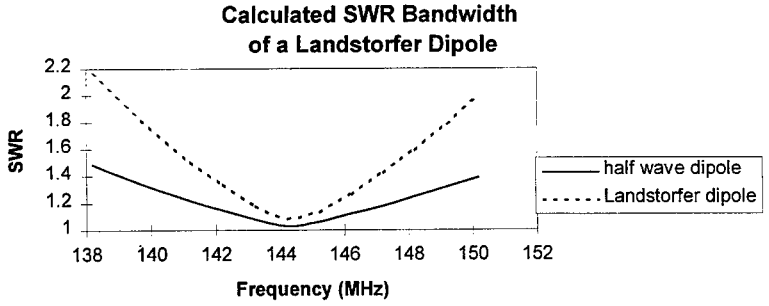

Uses of a single Landstorfer Dipole

a) Horizontally polarized gain antenna for HF

A 1.5λ Landstorfer dipole has a directivity similar to a 2 element Yagi (approximately 5 dBd),but is triple the length of a half wave dipole, which limits its use on HF. (I cannot imagine anyone erecting a 160 meter Landstorfer dipole; it would be over 800 feet long) It would require three supports, unlike a dipole which requires two, or an inverted vee, which requires one. Application on HF would probably limited to 10 and 12 meters.

b) ground-mounted HF monopole

A 2 segment 0.75λ Landstorfer monopole is about 0.6λ high. This certainly makes it possible to erect this type of antenna on the 10 through 20 meter bands. Table 3 compares the performance of 2 common types of vertical antennas ant the Landstorfer monopole:

TABLE 3

TYPE OF ANTENNA	MAX RADIATION (dBd)	ELEVATION ANGLE OF MAX (°)	EFFICIENCY (15 Ω GROUND LOSS)
0.25λ monopole	-3.96	26	60%
0.625λ monopole	-1.30	16	80%
0.75λ Landstorfer	-0.84	16	77%

Looking only at this table, one would not see much of a difference in performance between a 5λ/8 monopole and the Landstorfer monopole. These numbers are not the whole story, however. The radiation pattern of the 5λ/8 monopole has more unwanted high angle radiation than the Landstorfer antenna

c) VHF antennas

The electrically "large" dimensions of the Landstorfer antenna are not problematic on the VHF bands. A 6 meter Landstorfer dipole made from aluminum tubing is about the size of the reflector on a triband HF Yagi. I have constructed a 2 meter Landstorfer dipole which is mounted vertically and used to work local repeaters. The antenna measures about 8 feet across. While it is certainly larger than a 2 meter ground plane or dipole, it is still manageable and offers some gain.

A 6 meter Landstorfer monopole should be a good DX antenna with its gain and low angle of radiation. I am constructing one which will be ground mounted and fed against a 28 ft by 48 ft counterpoise containing 40 radial wires. It will be tested during the spring of 1996.

The Landstorfer monopole can also be used as part of a ground plane antenna. The author compared quarter wave, 5/8 wave and 3/4 wave Landstorfer ground plane antennas using AO. The ground plane consisted of 4 wires spaced at 90 degree intervals, parallel to the ground. The Landstorfer design performed better than either straight antenna. It had about 2.5 dB more gain than the quarter wave antenna and 2 dB more than the 5/8 wave design. The optimal radial length is about 0.35λ and the input impedance is around 50+j30 Ω.

Arrays of Landstorfer Dipoles

a) Log Periodic Arrays

Anyone interested in LPDA's made from Landstorfer dipoles should review chapter 5 of [1]. Landstorfer and Sacher constructed a series of UHF LPDA's and measured their properties. Their 6 element 470 - 610 MHz

design had a directivity of 10 dBd with sidelobe attenuation of at least 17 dB. It is not possible to get this kind of performance from a standard LPDA with the same number of elements and same boom length.

b) Parasitic (Yagi-Uda) Arrays

The high directivity of the Landstorfer dipole makes it the ideal building block for a parasitic array. I examined Yagis having 2 to 6 elements., I attempted to optimize each Yagi for improved directivity and F/B ratio. The antennas had resonant drivers (length = 0.738λ) and element diameters of λ/110. I used AO's optimization routine, with the following weighted constraints:

Gain	40%	no constraint
F/B	40%	F/B > 20 dB
drive resistance	20%	Re(Z) > 20 ohms

2 element Yagis

Below is an optimized 2 element design:

Reflector Length	0.743λ
Driver Length	0.711λ
Element Diameter	λ/110
Element Separation	0.122λ
Directivity	8.3 dBd
Front/Back Ratio	28 dB
Input Impedance	45+j5ohms

Lawson [4] states that the maximum directivity of a standard 2 element Yagi is 6.70 dBi or 4.6 dBd. The Landstorfer Yagi shows more than 3 dB improvement , which is equivalent to doubling one's transmitter power

I constructed a 146 MHz version of this 2 element Yagi out of 7/8 inch OD aluminum tubing. I had no way to measure the impedance of the antenna, but the SWR at resonance was 1.2, which was consistent with the model. I do not have access to an antenna range, so I had no way to verify either the F/B or gain figures produced by the model. I did mount the antenna at a height of 8 feet in by back yard and found that its performance was nearly equal to a 5 element quad array similarly mounted.

3 element Yagis

I have chosen to compare a "good" 3 element Landstorfer Yagi against an 8 element design found in [4]. The 3 element design compares quite favorably against Lawson's 8 element Yagi in all areas.

TABLE 5

PROPERTY	3-EL LANDSTORFER YAGI	8 EL LAWSON YAGI [4]
Reflector Length	0.734λ	0.4950λ
Driver Length	0.725λ	0.4726λ
Director Length	0.703λ	0.4240λ (all 6 directors)
Element Diameter	λ/110	λ/470
Element Separations	0.147λ	.184λ
Boom Length	0.294λ	1.288λ
Directivity (dBd)	10.0	9.75
Front/Back Ratio (dB)	23	29.1
Input Impedance (ohms)	17+j0	34+j0

Yagis with 4 or more elements

I have optimized 4, 5 and 6 element Landstorfer Yagi designs. (I stopped after 6 because AO would not handle any more symbols). Figure 5 compares the gain of Landstorfer and conventional Yagi arrays. Data for conventional Yagis came from [4]. Although the Landstorfer Yagi offers approximately 3 dB more gain than a conventional Yagi of similar boom length, one does not get something for nothing; the Landstorfer array has three times the width.

FIGURE 5:

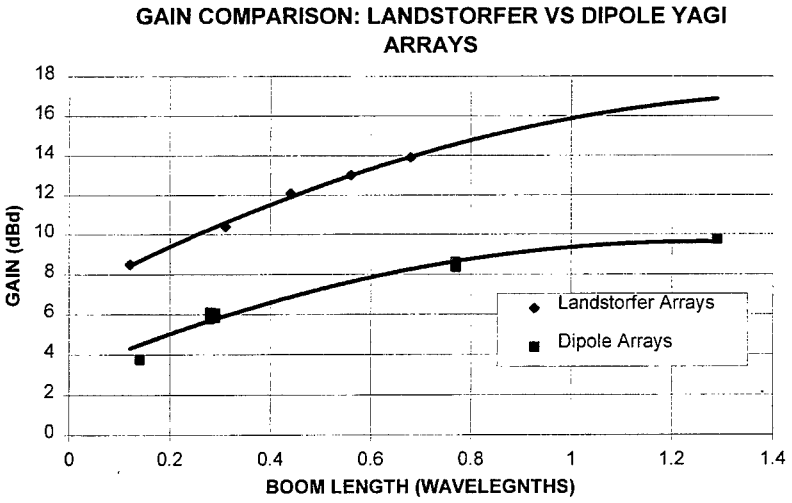

Summary

Landstorfer antennas have not seen much application in amateur circles. The computer studies that I have undertaken and the limited experiments that I have conducted indicate that this antenna has potential. The possibility of high directivity on a short boom with few elements is very appealing.

Other areas that could yield interesting results are the optimization of a Landstorfer monopole to maximize radiation at a specific elevation angle and the application of Landstorfer's ideas to traveling wave antennas such as rhombics.

Hams like to experiment with antennas and I hope that this article will spur them to begin experimentation with a new type of antenna.

REFERENCES:

[1] Landstorfer F.M and Sacher R.R , **Optimization of Wire Antennas**

[2] Balanis, **Modern Antenna Theory**

[3] Stutzman and Thiele, **Antenna Theory and Design,**p 204

[4] Lawson, **Yagi Antenna Design**

Two-Port Network Specification of Baluns for NEC Analysis and Other Applications

W.P. Wheless, Jr. and C.S. Wheless
University of Alabama, Tuscaloosa, AL 35487

Abstract - The Numerical Electromagnetics Code (NEC) provides, by means of an "NT" data file entry, for a two-port nonradiating network to be connected between any two segments in a wire antenna structure. For NEC, the electrical behavior of such a network is specified by an admittance matrix. Many wire antenna types employ baluns in their actual implementation. This paper describes a method for the characterization of baluns which allows their inclusion, as two-port networks, in NEC modeling and analysis on a routine basis. Balun characterizations from the procedure described here are also useful in other practical applications.

I. Introduction

Actual HF/VHF wire antennas often employ at least one balun for the purpose of converting an unbalanced coaxial cable input into a balanced output. These baluns vary widely in their electrical characteristics, depending on the balun type and its construction, the operating frequency, and load impedance (i.e., nature and extent of mismatch). The most common nominal balun impedance transformation ratios (output to input) are 1:1, 4:1, and 9:1, and baluns operating in close proximity to their design impedances are generally well-behaved, in the sense that they reasonably approximate ideal transformers in that case. However, practical communicators quickly learn from experience that real baluns can radically deviate from ideal transformer behavior when the load impedance varies from the design value. Under mismatched operating conditions, the matrix elements describing a particular balun are not available from 'spec sheets' or reference handbooks. The only recourse for reliable determination of the matrix elements is from actual measurements on individual baluns.

Nowadays, the instrument of preference for network characterization is the vector network analyzer. If one does not own a network analyzer, such an instrument is generally accessible at a nearby university or research laboratory, so it is fair to say that vector network analyzers for the HF (3-30 MHz) and VHF (30-300 MHz) bands are now generally available. Vector network analyzers have two ports for the connection of a Device Under Test (DUT), and can measure the four scattering parameters S_{11}, S_{12}, S_{21}, and S_{22}, which are four complex quantities as described in [1] and elsewhere. All linear two-port networks, including baluns, can be characterized fully (at a given frequency) by a 2×2 matrix of complex parameters, but the matrix type is not unique and numerous useful descriptors may be defined . For example, the network may be described by a scattering matrix, $\underline{S}$, transmission or chain matrix, $\underline{T}$, impedance matrix, $\underline{Z}$, or admittance matrix, $\underline{Y}$. There are straightforward conversion formulas among the different matrix types so that, for example, admittance element values required by NEC can be readily calculated from scattering matrix values [2].

Because the network analyzer ports are both 50Ω unbalanced, whereas one port of the balun is balanced and usually designed for a different impedance, one cannot obtain a reliable measurement of scattering parameters with the balun directly connected between the two analyzer ports.

This paper describes a method which overcomes this problem. The four s-parameters which completely characterize the balun electrically at a given operating frequency are determined from three one-port (S_{11}) measurement values with the unbalanced balun port connected to the network analyzer Port 1, and the balanced output of the balun terminated in specified loads.

II. Theoretical Basis for Procedure

The complex wave amplitudes $|a\rangle = \begin{bmatrix} a_1 \\ a_2 \end{bmatrix}$ and $|b\rangle = \begin{bmatrix} b_1 \\ b_2 \end{bmatrix}$ associated with a linear two-port network, as depicted in Figure 1, are related through the matrix equation

$$|b\rangle = \underset{\sim}{S}\,|a\rangle \tag{1}$$

where

$$\underset{\sim}{S} = \begin{bmatrix} S_{11} & S_{12} \\ S_{21} & S_{22} \end{bmatrix}. \tag{2}$$

In the context of the present problem, Port 1 represents the unbalanced balun input and Port 2 represents the balanced output, which is available for load termination changes.

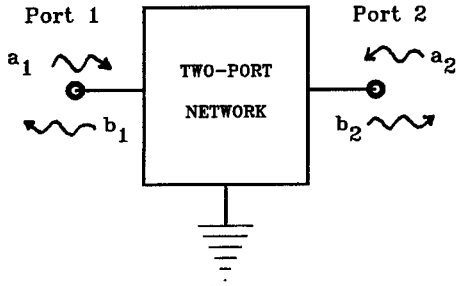

Fig. 1. Generic two-port network.

To begin, assume the balun is reciprocal, an assumption which is substantiated by measurements. This immediately gives $S_{12} = S_{21}$ and reduces the number of outstanding unknowns to three.

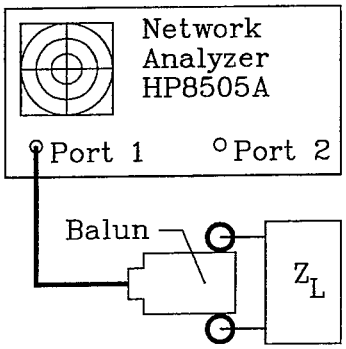

Fig. 2. Measurement setup.

One of the two linear equations contained in Eq. 1 is

$$b_1 = S_{11}a_1 + S_{12}a_2. \tag{3}$$

If Port 2 is terminated in a matched load, i.e., the balun balanced output is terminated in its design resistance, $a_2 = 0$ and $b_1 = S_{11}a_1$, or

$$S_{11} = \left.\frac{b_1}{a_1}\right|_{\text{Port 2 matched}} = \Gamma_m, \tag{4}$$

where Γ_m denotes the value of S_{11} under a matched-load condition.

If Port 2 is now terminated in a short circuit, $a_2 = -b_2$ and the equation pair embodied in Eq. 1 becomes

$$b_1 = S_{11}a_1 + S_{12}a_2 = \Gamma_m a_1 + S_{12}a_2 \tag{5}$$

and

$$(b_2 =) - a_2 = S_{12}a_1 + S_{22}a_2. \tag{6}$$

Similarly, termination of Port 2 in an open circuit causes $a_2 = +b_2$, so Eq. 5 remains valid, but now

$$(b_2 =) + a_2 = S_{12}a_1 + S_{22}a_2. \tag{7}$$

There are at least two ways to arrive at an expression for S_{12}. In the first approach, Eq. 5 divided by a_1 gives the short-circuited condition reflection coefficient

$$\left.\frac{b_1}{a_1}\right|_{\text{Port 2 shorted}} = \Gamma_s = \Gamma_m + S_{12}\frac{a_2}{a_1} \tag{8}$$

which re-arranges to

$$\frac{a_2}{a_1} = \frac{\Gamma_s - \Gamma_m}{S_{12}}. \tag{9}$$

Similarly, division of Eq. 6 by a_2, followed by re-arrangement, yields

$$\frac{a_2}{a_1} = -\frac{S_{12}}{S_{22}+1}. \tag{10}$$

Equating the Right-Hand Side (RHS) expressions of Eq. 9 and 10 produces the first result

$$S_{12}^2 = (S_{22}+1)(\Gamma_m - \Gamma_s), \tag{11}$$

where we take the angle of the complex RHS result to be restricted to $-180° \leq \Theta \leq +180°$ so that S_{12} is single-valued.

A second approach is to first obtain an expression for the open-circuited reflection coefficient through division of Eq. 5 by a_1:

$$\left.\frac{b_1}{a_1}\right|_{\text{Port 2 open}} = \Gamma_o = \Gamma_m + S_{12}\frac{a_2}{a_1}, \tag{12}$$

which re-arranges to

$$\frac{a_2}{a_1} = \frac{\Gamma_o - \Gamma_m}{S_{12}}. \tag{13}$$

Division of Eq. 7 by a_2, followed by re-arrangement, gives

$$\frac{a_2}{a_1} = \frac{S_{12}}{1 - S_{22}}. \tag{14}$$

Equation of the RHS expressions of Eq. 13 and 14 produces the second result

$$S_{12}^2 = (\Gamma_o - \Gamma_m)(1 - S_{22}). \tag{15}$$

There is no reason to prefer Eq. 11 over Eq. 15, or vice versa, as a determination of the value of S_{12} from measured data. As one might expect, the two results are very close in value, if not identical. In practice, then, it is reasonable to average the two results.

Finally, if one equates the RHS expressions of Eq. 11 and Eq. 15, and algebraically solves for S_{22}, the following expression is obtained:

$$S_{22} = \frac{\Gamma_o + \Gamma_s - 2\Gamma_m}{\Gamma_o - \Gamma_s}. \tag{16}$$

III. NEC Network (NT) Specification

At an operating frequency of interest, S_{11} is measured for a given balun terminated in three different loads: matched, open-circuit, and short-circuit. The numerical values obtained by measurement are denoted Γ_m, Γ_o, and Γ_s, respectively. A straightforward pc computer program then applies Equations 4, 11, 15, and 16 to calculate S_{11}, S_{12}, and S_{22} for the balun under test. $S_{21} = S_{12}$ by reciprocity, which completes the $\underline{S}$ matrix characterization of the balun.

Admittance parameters are required for the NEC data file. The translation from $\underline{S}$ to $\underline{Y}$, again by computer, is accomplished through the conversion relation

$$\underline{Y} = \frac{1}{D}\begin{bmatrix} E1 & E2 \\ E3 & E4 \end{bmatrix}, \tag{17}$$

where

$$D = \frac{1}{(1-S_{11})(1-S_{22}) - S_{12}S_{21}}, \tag{17a}$$

$$E_1 = \frac{(1+S_{22})(1-S_{11}) + S_{12}S_{21}}{R_{c1}}, \tag{17b}$$

$$E_2 = -\frac{2S_{12}}{\sqrt{R_{c1}R_{c2}}}, \tag{17c}$$

$$E_3 = -\frac{2S_{21}}{\sqrt{R_{c1}R_{c2}}}, \tag{17d}$$

and

$$E_4 = \frac{(1+S_{11})(1-S_{22}) + S_{12}S_{21}}{R_{c2}}. \tag{17e}$$

In the above equations, R_{c1} and R_{c2} denote the nominal characteristic impedances at Port 1 and Port 2 of the two-port balun. For example, $R_{c1} = 50\Omega$ and $R_{c2} = 450\Omega$ could be taken as appropriate values for a 9:1 balun.

IV. Another Practical Application

With the matrix $\underline{S}$ in hand, another useful application is readily available. Namely, one can predict the input reflection coefficient Γ_i, looking into Port 1 of the balun, when the output

Port 2 is terminated in an arbitrary, but known, impedance Z_L.

The chain or transmission matrix, $\underline{T}=\begin{bmatrix} A & B \\ C & D \end{bmatrix}$, is also well known as the ABCD matrix. For computer-based analysis of cascaded two-ports, an ABCD matrix description is advantageous (as discussed in reference [2]). The conversion from $\underline{S}$ to $\underline{T}$ is via

$$\underline{T}=\frac{1}{\Delta}\begin{bmatrix} \Delta_1 & \Delta_2 \\ \Delta_3 & \Delta_4 \end{bmatrix}, \tag{18}$$

where

$$\Delta=\frac{1}{2S_{21}}, \tag{18a}$$

$$\Delta_1=\sqrt{\frac{R_{c1}}{R_{c2}}}\left[(1+S_{11})(1-S_{22})+S_{12}S_{21}\right], \tag{18b}$$

$$\Delta_2=\sqrt{R_{c1}R_{c2}}\left[(1+S_{11})(1+S_{22})-S_{12}S_{21}\right], \tag{18c}$$

$$\Delta_3=\frac{1}{\sqrt{R_{c1}R_{c2}}}\left[(1-S_{11})(1-S_{22})-S_{12}S_{21}\right], \tag{18d}$$

and

$$\Delta_4=\sqrt{\frac{R_{c2}}{R_{c1}}}\left[(1-S_{11})(1+S_{22})+S_{12}S_{21}\right]. \tag{18e}$$

Nominal port characteristic impedances R_{c1} and R_{c2} are the same as in the conversion to admittance parameters.

Take the system impedance to be $Z_0 = 50\Omega$ and assume the load impedance on the balanced output side of the balun is Z_L. The calculated, or predicted, input impedance (as seen looking into Port 1 of the balun) is then

$$Z_i=\frac{AZ_L+B}{CZ_L+D} \tag{19}$$

and

$$\Gamma_i=\frac{Z_i-Z_0}{Z_i+Z_0}. \tag{20}$$

The capability to predict input impedance and mismatch for a balun with an arbitrary complex termination is of considerable interest to rf engineers concerned with practical radio communication systems at HF and/or VHF frequencies.

A. *Example of Results*

A commercially available 4:1 HF balun was characterized by the procedure described above. Because the $\underline{S}$ matrix determination is made at a specific operating frequency, one may ask how many discrete characterizations are required, as a practical matter, to cover the full 3-30 MHz HF band. Table I below shows measured S_{11} under the three conditions required for characterization for this example case, and is representative of the frequency sensitivity of typical baluns. The table contents suggest that linear interpolation between values at discrete 1 MHz intervals is acceptable (except possibly below 5 MHz).

Table I. Measured S_{11} (in dB, degrees)

Freq. (MHz)	Short	Open	200Ω Load
3	0.0∠172	0.0∠54	-10.3∠142
4	0.0∠169	0.0∠42	-11.0∠142
5	0.0∠166	0.0∠32	-11.4∠142
6	0.0∠162	0.0∠25	-11.6∠141
7	0.0∠158	0.0∠20	-11.7∠140
8	0.0∠155	0.0∠15	-11.7∠138
9	0.0∠152	0.0∠12	-11.6∠136
10	0.0∠148	0.0∠8	-11.5∠133
11	0.0∠145	-0.1∠6	-11.4∠131
12	-0.1∠142	-0.1∠4	-11.3∠129
13	-0.1∠139	-0.2∠2	-11.2∠127
14	-0.1∠136	-0.2∠0	-11.0∠125
15	-0.2∠132	-0.2∠0	-10.8∠122
16	-0.2∠130	-0.3∠ − 2	-10.7∠120
17	-0.3∠127	-0.3∠ − 3	-10.5∠118
18	-0.4∠124	-0.3∠ − 5	-10.3∠116
19	-0.4∠122	-0.3∠ − 6	-10.2∠114
20	-0.5∠119	-0.3∠ − 7	-10.0∠113
21	-0.5∠117	-0.3∠ − 9	-9.8∠111
22	-0.4∠115	-0.2∠ − 10	-9.5∠110
23	-0.4∠113	-0.2∠ − 11	-9.2∠108
24	-0.3∠110	-0.1∠ − 13	-8.9∠106
25	-0.3∠108	-0.1∠ − 15	-8.8∠104
26	-0.3∠105	-0.1∠ − 17	-8.6∠102
27	-0.3∠104	-0.1∠ − 18	-8.4∠100
28	-0.3∠101	-0.1∠ − 20	-8.2∠99
29	-0.3∠99	-0.1∠ − 21	-8.1∠97
30	-0.3∠97	-0.1∠ − 23	-7.9∠96

For purposes of illustration, the input reflection coefficient predicted by the subject characterization method is compared to measured data, for three widely different complex loads at three frequencies. The nine cases are identified in Table II below.

Table II. Test case loads.		
Case Name	Freq. (MHz)	Z_L (Ω)
3A	3.0	47 - j64.7
3B	3.0	150 - j160.8
3C	3.0	470 - 1360
9A	9.0	47 - j21.6
9B	9.0	150 - j53.6
9C	9.0	470 - j453.4
15A	15.0	47 - j12.9
15B	15.0	150 - j32.2
15C	15.0	470 - j272.1

For convenience, a definition of *error* based on the geometrical relationships of Fig. 3 is taken here. With regard to Fig. 3, let M and P denote, respectively, the lengths of the vectors connecting the origin to the measured and predicted Γ_i points. Then, if E denotes the length of the vector connecting the predicted and measured points in the Γ-plane, relative error is

$$\% \text{ Error } = \frac{E}{M} \times 100. \qquad (21)$$

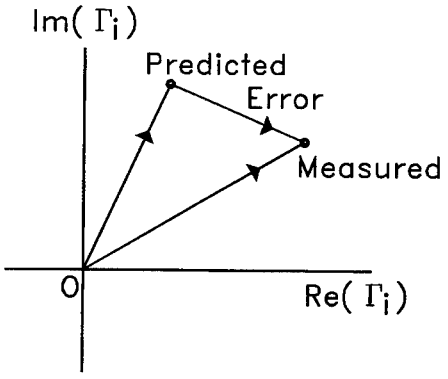

Fig. 3. Error geometry.

To emphasize the fact that rf baluns generally do not emulate ideal impedance transformation behavior well under mismatched conditions, first consider the results for Γ_i under the assumption that the balun is an ideal impedance transformer. These results are summarized in Table III.

Table III. Ideal impedance transformer.	
Case Name	Γ_i Error (see Eq. 21)
3A	25.4%
3B	108.1%
3C	83.5%
9A	51.6%
9B	92.5%
9C	33.7%
15A	74.9%
15B	99.6%
15C	93.8%
AVERAGE ERROR = 73.7%	

When the $\underline{S}$ matrix procedure described in this paper is followed, the predicted values of Γ_{in} are much closer to actual measurement values. A summary of these results is contained in Table IV.

Table IV. Results using $\underline{S}$ characterization.	
Case Name	Γ_i Error (see Eq. 21)
3A	12.2%
3B	34.7%
3C	1.9%
9A	5.6%
9B	12.1%
9C	1.2%
15A	8.4%
15B	7.0%
15C	2.5%
AVERAGE ERROR = 9.5%	

Apart from case 3B, the effectiveness of the balun characterization procedure described in this paper is apparent.

V. Conclusions

The results presented in the preceding *Example* are typical and representative of the capabil-

ity of the balun characterization procedure presented in this paper. This method provides a y-parameter description of a given balun, by means of computer-based analysis of measured S_{11} 'calibration' values, which is of sufficient accuracy for most NEC wire antenna modeling requirements.

A limitation on the accuracy and reliability of the method arises from the fact that a minimal number of load impedances is used to obtain a balun characterization. Thus, each individual S_{11} measurement strongly influences the model outcome, and the $\underline{S}$ matrix element values can be substantially incorrect as the result of just one inaccurate measurement value. Work is in progress on an extension of this procedure which utilizes more than three loads, so that the scattering matrix values follow from the solution of an overdetermined system of equations in a least squares sense. It is reasonable to believe that an overdetermined system will ameliorate the adverse effects of isolated 'calibration data' errors on the model, and so will bring analysis and predictions for arbitrary complex loads into closer agreement with actually observed balun electrical behavior.

The methodology here requires only the collection of S_{11} data, i.e., one-port measurements. Other work in progress concerns the potential for improvement in balun characterization through the use of two-port vector network analyzer measurements. It is plausible to expect that the simultaneous measurement of four complex variables (S_{11}, S_{12}, S_{21}, and S_{22}) should provide more relevant information than the measurement of just one (S_{11}), which may be applied to obtain a more reliable and accurate balun characterization.

As a result of this work, baluns can be included in NEC modeling and analysis of wire antenna structures without trepidation.

References

[1] David M. Pozar, *Microwave Engineering*, Reading, MA: Addison-Wesley Publishing Company, 1990, pp. 228-231.

[2] Darko Kajfez, *Notes on Microwave Circuits, Vol. 1*, Oxford, MS: Kajfez Consulting, 1984.

SESSION 1:

HIGH-FREQUENCY METHODS

Chair: R. Burkholder

Physical Theory of Diffraction Analysis of Impedance Structures

Hasnain H. Syed and John L. Volakis

Radiation Laboratory
Department of Electrical Engineering and Computer Science
The University of Michigan
Ann Arbor, MI 48109-2122

Abstract

Based on an approximate dyadic diffraction coefficient, equivalent currents (ECs) are derived for computing the scattering by a finite length impedance wedge of arbitrary angle. The derived equivalent currents are implemented in a standard general purpose PTD (Physical Theory of Diffraction) code and results are presented demonstrating the accuracy of the formulation for a number of impedance and (dielectrically) coated structures. These include typical shapes such as plates, finite length cones and cylinders which have been partially or fully coated.

1 Introduction

In a recent paper, Syed and Volakis [1] presented diffraction coefficients for an impedance wedge (of infinite length) illuminated at skew incidence as shown in Fig. 1. Having such a diffraction coefficient, it is now possible to consider the scattering by complex impedance structures in the context of the geometrical or physical theories of diffraction (GTD or PTD). Example applications include the scattering by non-metallic airborne structures and signal fading evaluation for mobile communication or propagation over mountainous terrain. A study of the latter was performed by Schneider and Luebbers [2] using heuristic impedance wedge diffraction coefficients.

In this paper we consider the application of the diffraction coefficients developed in [1] to scattering by impedance bodies. A key element to this application is the development of equivalent currents (ECs) or incremental length diffraction coefficients (ILDCs) for impedance wedges. The ECs were first introduced by Ryan and Peters [3] to compute the scattering by a finite edge from a knowledge of the corresponding infinite edge diffraction coefficients. They were later improved by Michaeli [4],[5] for angles off the Keller cone, and are basically fictitious currents placed at the edge of a wedge such that they generate the

far zone diffracted field of a straight infinite edge. For a finite length edge, the currents are placed over the length of that edge and are integrated to yield an approximation of the edge scattered field. In the context of PTD [6],[7],[8] the role of the ECs is played by the ILDCs introduced by Mitzner [7] (see also Butorin and Ufimtsev [9]). The ILDCs are applied to each element of the edge and generate a diffracted field which must be added to the physical optics (PO) contribution from the adjacent surfaces to produce the total scattered field.

To compute the PTD field, the PO field is calculated first by dividing the structure into, say, triangular facets or curvilinear patches and the PO current is then integrated over each facet or patch. The diffracted field or fringe wave is added by integrating the ILDC over the specified edges of the structure (see for example [10] and [11]). In the following we will first present explicit forms of the ILDCs for impedance wedges before proceeding with their application to scattering by three dimensional impedance structures. Previously, two approaches have been used for determining the ILDC or EC expressions. The one introduced by Michaeli [4],[5] and Mitzner [7] for metallic edges is more rigorous and has been extended by Pelosi et al. [12] for impedance wedges. The latter have yet to be used in practice because of a lack of skew incidence impedance wedge diffraction coefficients and could indeed be employed in our analysis in conjunction with the diffraction coefficients given in [1]. However, the resulting expressions are quite involved and their improved accuracy does not appear to be justified. Instead, we will make use of the simpler ILDCs derived using the method discussed by Knott and Senior [13].

2 ILDCs for a straight impedance wedge

Consider the plane wave

$$\mathbf{E}^{\mathrm{i}} = \hat{e}^{\mathrm{i}} e^{-jk_0 \hat{\imath}.\mathbf{r}} \tag{1}$$

illuminating the wedge shown in Fig. 1 where

$$\hat{\imath} = -\hat{x}\cos\phi^{\mathrm{inc}}\sin\theta^{\mathrm{inc}} - \hat{y}\sin\phi^{\mathrm{inc}}\sin\theta^{\mathrm{inc}} + \hat{z}\cos\theta^{\mathrm{inc}}$$

is the direction of incidence and $\mathbf{r} = x\hat{x} + y\hat{y} + z\hat{z}$.

For an infinite impedance wedge, the diffracted field can be written as

$$\mathbf{E}^{\mathrm{d}} = -\frac{e^{-jks}}{\sqrt{s}}\overline{\overline{D}}.\mathbf{E}^{\mathrm{i}} \tag{2}$$

where

$$\overline{\overline{D}} = \hat{\beta}\hat{\beta}^{\mathrm{i}} D_{\beta\beta^{\mathrm{i}}} + \hat{\beta}\hat{\phi}^{\mathrm{i}} D_{\beta\phi^{\mathrm{i}}} + \hat{\phi}\hat{\beta}^{\mathrm{i}} D_{\phi\beta^{\mathrm{i}}} + \hat{\phi}\hat{\phi}^{\mathrm{i}} D_{\phi\phi^{\mathrm{i}}} \tag{3}$$

is the dyadic diffraction coefficient for the impedance wedge given in [1], s denotes the distance between the diffraction and observation points; $\hat{s} = \hat{\beta} \times \hat{\phi}$ and $\hat{\imath} = \hat{\beta}^{\mathrm{i}} \times \hat{\phi}^{\mathrm{i}}$ with $\beta = \beta^{\mathrm{i}}$ for the infinite wedge. Note that all coordinates in (3) are with respect to the wedge (local) coordinate system illustrated in Fig. 1. In contrast to the PEC wedge, the cross-polarization elements of the dyadic diffraction coefficient matrix are non-zero and this is the reason for much of the complication associated with impedance structures. As expected, the

dyadic diffraction coefficients are functions of the local wedge coordinates ϕ, ϕ_0 and β as well as the upper(+) and lower(-) wedge impedances η_+ and η_- respectively.

To compute the diffracted field from a finite impedance wedge in the context of the method of equivalent currents we introduce the equivalent electric and magnetic currents I^e and I^m, respectively, such that

$$\mathbf{E}^{\mathrm{d}} = jk_0 \frac{e^{-jk_0 r}}{4\pi r} \int_{-\ell/2}^{\ell/2} \left\{ Z_0\, I^{\mathrm{e}}(\mathbf{r}')\, \hat{s} \times (\hat{s} \times \hat{t}) + I^{\mathrm{m}}(\mathbf{r}')\, \hat{s} \times \hat{t} \right\} e^{jk_0 \hat{s}.\mathbf{r}'}\, dz' \tag{4}$$

recovers the diffracted field (2) when $l \to \infty$. As illustrated in Fig. 1, $\hat{s}$ denotes the direction of diffraction given by

$$\hat{s} = \hat{x} \sin\theta^g \cos\phi^g + \hat{y} \sin\theta^g \sin\phi^g + \hat{z} \cos\theta^g$$

$\hat{t}$ is the vector tangent to the edge and the spherical angles (θ^g, ϕ^g) refer to the global (unprimed) coordinate system defined in Fig. 2.

It is easy to show via the stationary phase method that (4) reduces to (2) for $l \to \infty$ only when

$$\begin{aligned} I^{\mathrm{e}}(z) &= -\frac{2}{Z_0}\sqrt{\frac{2\pi}{k_0}}\, e^{-j\pi/4} \left\{ D_{\beta\beta^{\mathrm{i}}}\, E^{\mathrm{i}}_{\beta^{\mathrm{i}}}(z) + D_{\beta\phi^{\mathrm{i}}}\, E^{\mathrm{i}}_{\phi^{\mathrm{i}}}(z) \right\} \\ I^{\mathrm{m}}(z) &= 2\sqrt{\frac{2\pi}{k_0}}\, e^{-j\pi/4} \left\{ D_{\phi\beta^{\mathrm{i}}}\, E^{\mathrm{i}}_{\beta^{\mathrm{i}}}(z) + D_{\phi\phi^{\mathrm{i}}}\, E^{\mathrm{i}}_{\phi^{\mathrm{i}}}(z) \right\} \end{aligned} \tag{5}$$

These fictitious equivalent currents can in turn be used in (4) to obtain the scattered field of a finite length edge. For a straight edge, the diffraction coefficients are independent of z' and on this basis (4) and (5) simplify to

$$\begin{aligned} \hat{u}.\mathbf{E}^{\mathrm{d}} &= \frac{e^{-jk_0 r}}{r} (\overline{\overline{\mathcal{D}}}.\hat{e}^{\mathrm{i}}) \int_{-\ell/2}^{\ell/2} e^{jk_0 z'(\hat{s}-\hat{\imath}).\hat{t}}\, dz' \\ &= \frac{e^{-jk_0 r}}{r} (\overline{\overline{\mathcal{D}}}.\hat{e}^{\mathrm{i}}) \ell\, \mathrm{sinc}\left\{ \tfrac{1}{2} k_0 \ell (\hat{s}-\hat{\imath}).\hat{t} \right\} \end{aligned} \tag{6}$$

where $\hat{u}$ denotes an arbitary unit vector such that $\hat{s}.\hat{u} = 0$ as required for far zone computations. Also,

$$\begin{aligned} \overline{\overline{\mathcal{D}}}.\hat{e}^{\mathrm{i}} = \frac{1}{\sin\beta^{\mathrm{i}}}\sqrt{\frac{k_0}{2\pi}}\, e^{j\pi/4} e^{jk_0(\hat{s}-\hat{\imath}).\mathbf{r}'_0} \Big\{ &(\hat{u}.\hat{t}) \left[(\hat{t}.\hat{e}^{\mathrm{i}}) \widetilde{D}_{\beta\beta^{\mathrm{i}}} - (\hat{t} \times \hat{\imath}).\hat{e}^{\mathrm{i}} \widetilde{D}_{\beta\phi^{\mathrm{i}}} \right] \\ &+ \hat{u}.(\hat{s} \times \hat{t}) \left[(\hat{t}.\hat{e}^{\mathrm{i}}) \widetilde{D}_{\phi\beta^{\mathrm{i}}} - (\hat{t} \times \hat{\imath}).\hat{e}^{\mathrm{i}} \widetilde{D}_{\phi\phi^{\mathrm{i}}} \right] \Big\} \end{aligned} \tag{7}$$

and we have made use of the incident field components

$$E^{\mathrm{i}}_{\beta^{\mathrm{i}}}(\mathbf{r}') = \frac{\hat{t}.\hat{e}^{\mathrm{i}}}{\sin\beta^{\mathrm{i}}} e^{-jk_0 \hat{\imath}.\mathbf{r}'}, \qquad E^{\mathrm{i}}_{\phi^{\mathrm{i}}}(\mathbf{r}') = -\frac{(\hat{t} \times \hat{\imath}).\hat{e}^{\mathrm{i}}}{\sin\beta^{\mathrm{i}}} e^{-jk_0 \hat{\imath}.\mathbf{r}'}$$

The tilde in (7) was introduced in preparation for the definition of the ILDC. If we set

$$\widetilde{D}_{uv} = D_{uv} \tag{8}$$

where $\{D_{uv}\} = \overline{\overline{D}}$ is the dyadic diffraction coefficient defined in (3), then (2) gives the diffracted field in the context of the method of equivalent currents. On the other hand if we set

$$\widetilde{D}_{uv} = D_{uv} - D_{uv}^{\mathrm{po}} \tag{9}$$

where D_{uv}^{po} is the physical optics diffraction coefficient, (2) gives the fringe wave field in the context of PTD [6],[7] and $\overline{\overline{\widetilde{D}}}.\hat{e}^{\mathrm{i}}$ is the ILDC. The dyadic coefficient $\overline{\overline{D}}^{\mathrm{po}}$ then serves to remove the contribution of the physical optics current at the edge since the latter is already included in the PO field. The PO diffraction coefficient for an impedance wedge can be derived by following the procedure discussed in [4] and will be presented at the conference. Also, due to space limitations we skip the presentation of the ILDCs for curved edges. They can be derived by tessellating the curved edge into small straight edge segments and applying (8) to each segment. The total scattered field from the curved edge is subsequently obtained by summing all small edge contributions comprising the entire curved edge. This process, although simple in concept, can involve several trigonometric factors needed to transform all vector contribitions to a common coordinate system.

3 Applications

The derived equivalent currents have been implemented in a standard PTD code [14] which includes only first order high frequency fields for far zone computations. Three geometries (cone, finite cylinder and plate) were considered for validating the presented PTD formulation and diffraction coefficients for impedance structures, and in all cases the coatings were simulated by choosing $\eta_{\pm} = j\tan(k_0\sqrt{\epsilon_r\mu_r}t)$. Fig. 3 shows the backscatter RCS computations for a cone geometry whose base is 3λ in diameter. We observe that the agreement between the moment method and PTD is indeed very good in the main lobes but deteriorates slightly in the sidelobe regions. However, since the disagreements in the side lobe regions persisted for the coated and uncoated cone (results not shown), it is primarily attributed to higher order interactions and not due to the impedance simulation of the coating. Results for a partially coated cone are shown in Fig. 4 for the more challenging VV polarization with the cone's base left uncoated (i.e perfectly conducting). As expected, because the uncoated base supports multiple wave interactions, the PTD pattern for this polarization is less accurate (than the horizontal polarization) near tip-on incidences. The horizontal polarization results (not shown) were in much better agreement with the moment method data in the same region. However, when the base is illuminated, the PTD patterns for both polarizations are in excellent agreement with the moment method data. RCS calculations for other geometries will be presented at the conference.

References

[1] H. Syed and J.L. Volakis, "An approximate solution for scattering by an impedance wedge at skew incidence," *Radio Science*, pp.505-524, May-June 1995

[2] M. Schneider and R. Luebbers, "A general uniform double wedge diffraction coefficient," *IEEE Trans. Antennas Propagat.*, vol.39, pp.8-14, 1991.

[3] C.E. Ryan and L. Peters, Jr., "Evaluation of edge-diffracted fields including equivalent currents for the caustic regions," *IEEE Trans. Antennas Propagat.*, vol.17, pp.292-299, 1969.

[4] A. Michaeli, "Equivalent edge currents for arbitrary aspects of observation," *IEEE Trans. Antennas Propagat.*, vol.32, pp.252-258, 1984.

[5] A. Michaeli, "Elimination of infinities in equivalent edge currents, part I: fringe current components," *IEEE Trans. Antennas Propagat.*, vol.34, pp.912-918, 1986.

[6] P.Ya. Ufimtsev, "Method of edge waves in the physical theory of diffraction," U.S. Air Force Systems Command Foreign Technology Office Document ID No. FTD-HC-23-259-71 (translation of Russian original).

[7] K.M. Mitzner, "Incremental length diffraction coefficients," Aircraft Division Northrop Corporation Technical Report No. AFAL-TR-73-296, 1974.

[8] E.F. Knott, "The relationship between Mitzner's ILDC and Michaeli's equivalent currents," *IEEE Trans. Antennas Propagat.*, vol.33, pp.112-114, 1985.

[9] D.I. Butorin and P.Ya. Ufimtsev, "Explicit expression for an acoustic edge wave scattered by an infinitesimal edge element," *Sov. Phys. Acoust.*, **32**, pp. 283–287, 1985.

[10] E.F. Knott, J.F. Shaeffer and M.T. Tuley, *Radar Cross Section*, Artech House, Inc., Dedham MA, 1985.

[11] N.N. Youssef, "Radar cross section of complex targets," *Proc. IEEE*, **77**, pp. 722–734, 1989.

[12] G. Pelosi, S. Maci, R. Tiberio and A. Michaeli, "Incremental length diffraction coefficients for an impedance wedge," *IEEE Trans. Antennas Propagat.*, **40**, pp. 1201–1210, 1992.

[13] E.F. Knott and T.B.A. Senior, "Equivalent currents for a ring discontinuity," *IEEE Trans. Antennas Propagat.*, **AP-21**, pp. 693–695, 1973.

[14] S.W. Lee, "McPTD–1.4: a high-frequency RCS computation code based on physical theory of diffraction," DEMACO Inc., Champaign IL, 1990.

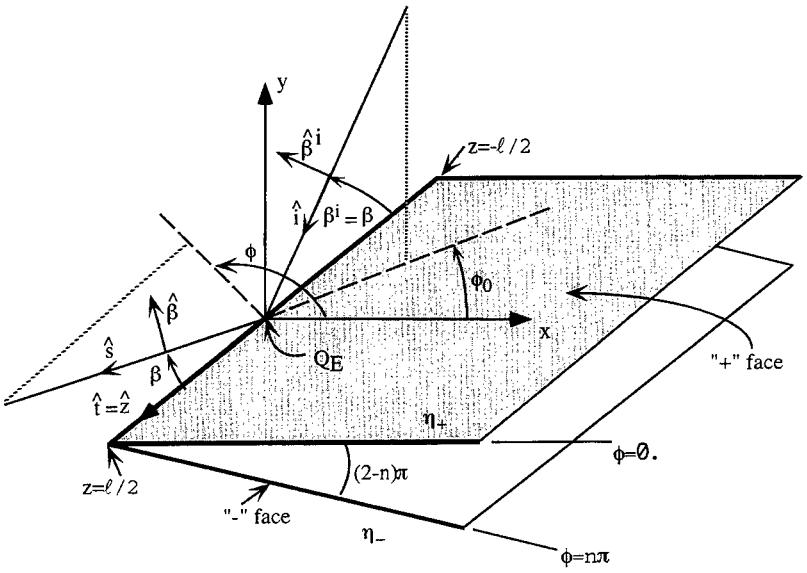

(a) Three dimensional view

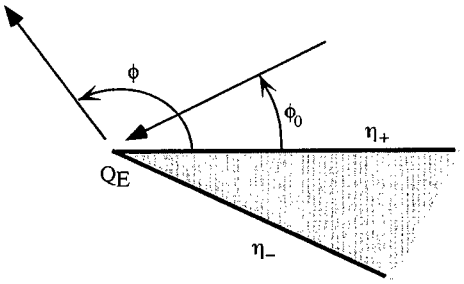

(b) xy cross section

Figure 1: Geometry and coordinate system for the impedance wedge

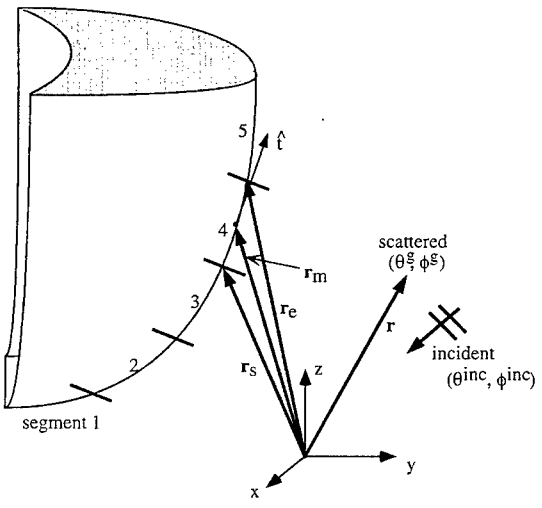

Figure 2: Curved edge illuminated by a plane wave

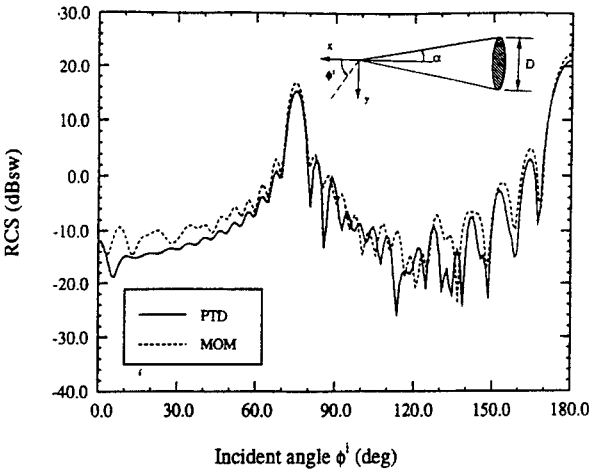

Figure 3: RCS of a flat based cone due to incident $E^i_{\phi^i}$ (HH) polarizaiton with $\alpha = 15°, D = 3\lambda, \theta^i = 90°$; Coating parameters: $\varepsilon_r = 7 - j1.5, \mu_r = 2 - j1$, thickness=$0.04\lambda$.

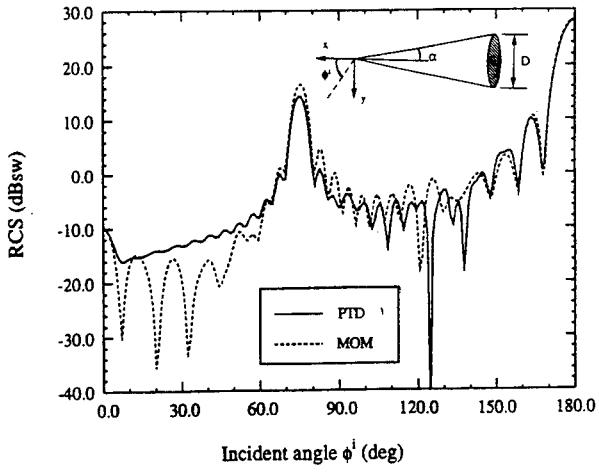

Figure 4: $E^i_{\theta^i}$ (VV) polarization RCS of a partially coated flat base cone having perfectly conducting base with $\alpha = 15°, D = 3\lambda, \varepsilon_r = 7 - j1.5, \mu_r = 2 - j1$, coating thickness=$0.04\lambda, \theta^i = 90°$.

Hybrid SBR/GTD Radio Propagation Model for Site-Specific Predictions in an Urban Environment

Joseph Schuster and Raymond Luebbers
Department of Electrical Engineering
The Pennsylvania State University

Abstract. A model which combines the Geometrical Theory of Diffraction (GTD) with an efficient ray tracing method based on the Shooting and Bouncing Ray method (SBR) is presented. The model includes ray paths with up to two diffractions and an arbitrary number of reflections in making predictions. Path loss predictions at 900 and 1900 MHz are compared to measurements made within an approximately 500 by 500 meter area of Rosslyn, Virginia. Measurements were made using street level and rooftop transmitters with street level receivers. For the street level transmitters the predictions were made using a two-dimensional version of the model which assumes the buildings are vertically uniform and neglects diffraction over rooftops and terrain effects. The predictions for rooftop transmitters were made using a fully three-dimensional version.

Introduction

With high frequency portable communication systems becoming more common, the need for fast and accurate predictions of high frequency radio propagation in urban environments has rapidly increased. Until recently such predictions were usually based on empirical methods, especially if a relatively large number of predictions were required. But advances in both computational methods and computer speeds now allow for fast, site-specific predictions of radio propagation even in a complex urban area. In this paper we are primarily concerned with narrow band signal attenuation, but the methods to be discussed are also applicable to signal delay and delay spread predictions.

When applied to urban areas, a propagation model which only includes line-of-sight and multiply reflected rays can not yield accurate predictions when the receiver location is in the shadow of a large building. For these cases accurate predictions require determining the fields scattered by the building into the shadow region. The Geometrical Theory of Diffraction (GTD) has been applied for over a decade in making accurate site-specific propagation prediction over hilly terrain [1] and has more recently been applied to making predictions in urban areas [2,3]. In these papers the ray paths to a field point have been found using the generalized Fermat's principle and the method of multiple images. For the urban propagation situation considered here with hundreds or perhaps thousands of building faces and a large number of receiver locations, the method of multiple images could require large amounts of computer time.

To avoid this a hybrid model which combines GTD with the Shooting and Bouncing Ray (SBR) method has been developed. A two-dimensional (2D) "canyon" version of the model is used when transmitter and receiver antennas are at heights below the building heights and the terrain is relatively flat, otherwise a fully three-dimensional (3D) version which includes rooftop diffraction and terrain effects is used.

Shooting and Bouncing Rays

The SBR method was developed by Professor Lee of the University of Illinois and coworkers [4]. Prior to this development the GTD was the preferred ray method for calculating high frequency radar scattering from aircraft and other complicated structures. But as the amount of detailed geometry information available from Computer Aided Design data bases increased, the algorithms for finding the GTD rays were not efficient enough to find the ray trajectories. In the GTD approach, the rays traveling from the transmitter to the receiver must follow precise paths determined by the extended Fermat's principle. This prescribes that each ray path must have a length that is a local minimum, maximum, or inflection, and when thousands of flat reflecting surfaces are involved, finding these particular rays takes a large amount of computer time. Furthermore, for each receiver location the process must be repeated, since the ray paths will change.

The SBR method avoids this by "shooting" large numbers of rays from the transmitter location. These rays are shot without regard for the receiver location. They then "bounce" off the reflecting surfaces following the laws of reflection. Since no particular ray paths are being searched for, the path for each ray is found extremely quickly. Many more rays are considered than with GTD, but each SBR ray is much faster to compute since the shooting and bouncing process is very straightforward for a geometry which consists entirely of planar surfaces.

Using the SBR method, one cannot initially evaluate the field at a particular point, since one cannot be guaranteed that all of the important SBR rays will pass through that point. One must use a collection region enclosing the point, and then use the rays that pass through this collection region to determine the predicted field strength. In 2D the collection regions are circles or rectangles and in 3D spheres or rectangular boxes are used. The size of the regions should be chosen to be much smaller than the distance characterizing the slow fading along the streets. Results in this paper were made using collection regions five meters across.

All of the rays passing through the collection area are sorted and combined to determine the predicted field strength. The sorting is done to select just one SBR ray for each unique path. For example, perhaps several line-of-sight rays are intercepted by the collection region. The sorting process finds all of these, and the one line-of sight ray passing closest to the center of the collection region will be selected. The sorting process may also find several rays that were collected after bouncing from the same set of building faces. Again, from these rays the one closest to the center of the collection area is selected.

We assume that the density of the SBR rays has been adjusted for the collection area size so that at least two to three rays for each unique ray path are intercepted. In order to set the number of rays to be shot we use the following approximate rule. Let d be the longest possible distance traveled by a ray (approximately 3 times the distance across the area of buildings being considered), let L be the length of one side of the collection area in the same units as d, and let n be the desired minimum number of rays for each distinct path (usually 2 or 3) to be intercepted by the collection area. Then an estimate of the number N of rays to be shot from the source is

$$N \approx \frac{2\pi nd}{L} \qquad (1)$$

In 2D the rays are shot on a single horizontal disk. In 3D the rays are shot on many cones, and the

number of rays on a cone can be reduced as the cone angle decreases.

In addition to the relative speed for computing individual SBR rays, there is another advantage. With one "shooting" the SBR rays for all the receiver locations are found. That is, the rays are "shot" without regard to receiver location, and then the rays going through the collection region surrounding a particular receiver location are collected and combined to determine the field strength at that location. To consider another receiver location, one merely changes the collection region and repeats the process on the rays going through the new region. A computer work station typically has enough memory to store all the ray trajectories for each source, so that the computer hard disk need not be read during this process. Thus once the rays are shot and bounced, finding the signal levels for a large number of receiver locations takes relatively little computer time. While the SBR method is not particularly efficient if the field amplitude is only evaluated at a few locations, it becomes increasingly efficient as more field points are included.

Once the paths to each field point location are found from the SBR process the amplitudes are easily evaluated. If we let point 0 denote the location of the transmitter, point 1 the first reflection point, N the last reflection point, R_n the reflection coefficient for the nth reflection, r_{0F} the total distance traversed by the ray between in traveling from the source to the field point, and $E_0(\theta,\phi)$ be the amplitude of the electric field 1 meter from a unity gain transmitting antenna in the direction in which the ray initially travels. Then the complex amplitude of the field for the qth path is given by

$$E_q = E_0(\theta,\phi)\,\frac{e^{j\beta r_{0F}}}{r_{0F}} \cdot \prod_{n=1}^{N} R_n \qquad (2)$$

where in general the R_n reflection coefficients may be angle and polarization dependent. For the 3D case the electric fields are 2D vectors (one term for each polarization), the reflection coefficients are dyads, and the polarization vectors must be converted at each reflection into the ray-fixed coordinates suitable for application of the reflection coefficients.

In 2D, for each SBR ray that travels directly to the receiver location as described in equation (2), another will reach the receiver after being reflected from the ground. So if there are a total of Q paths found by the SBR, there would be an additional Q ground reflected paths. In order to calculate the length of this path the source point will be located at point 0', which is the image of point 0 in the ground surface. Using the image has the effect of removing the ground from the calculation, and extending the buildings below the former ground level. The electric field amplitude is evaluated using an equation similar to (2), but modified to include the ground reflection coefficient R_G. The equation for the amplitude of the qth ground reflected SBR ray E'_q which undergoes N reflections in addition to the ground reflection is

$$E_q' = E_0(\theta',\phi')\,R_G\,\frac{e^{j\beta r_{0'F}}}{r_{0'F}} \cdot \prod_{n=1}^{N} R_n \qquad (3)$$

In order for the direct and ground reflected SBR rays to combine properly, the phase information in (2) and (3) must be retained by combining E_q and E_q' coherently. The uncorrelated paths are then combined incoherently without including phase, and the average total field due to all the Q paths is

given by

$$E_{Tot} = \sqrt{\sum_{q=1}^{Q} |E_q + E_q'|^2} \quad . \tag{4}$$

If the field strengths at all receiver points were determined by line-of-sight and reflected energy, then the approach described above would be sufficient to determine the field levels. However, for many receiver locations diffracted fields make an important contribution. For these receiver locations the SBR method must be augmented by adding diffraction. The predictions are made by combining the SBR method with the Geometrical Theory of Diffraction (GTD).

SBR/GTD Hybrid Method

The Geometrical Theory of Diffraction (GTD) was originated by Joseph Keller [5]. As with the SBR method, it uses rays to predict electromagnetic scattering from conducting objects. But while SBR includes line-of-sight and multiple reflections, the GTD also includes edge diffracted rays. In the approach described here, the SBR is used to determine the ray paths, and GTD to evaluate the amplitudes of the diffracted rays. Within the framework of the GTD, the Uniform Theory of Diffraction wedge diffraction coefficient developed by Kouyoumjian and Pathak [6] and modified for imperfect reflection due to finite conductivity and local surface roughness [1,7] is widely used. For multiple diffraction the spreading factors given in [1] are used, although the UTD is not strictly accurate for multiple diffraction.

As outlined above, the hybrid SBR/GTD approach considered here first shoots many SBR rays. Each of these rays is then bounced through the building geometry. After the rays are determined they are sorted by building interaction. In order to find the diffracting edges (formed by building corners), this sorting process finds adjacent rays that interact differently with the building geometry. For example, let us assume that of two adjacent SBR rays one is reflected from a certain building face while the other is not. This means that a diffracting edge of a building face lies between these two rays. It is then quite simple to locate a diffraction point on this edge.

For a 2D calculation each diffracting building corner will have one disk of diffracted rays. But for 3D, different rays shot from the transmitting antenna will have diffraction points at different locations along the same diffracting edge. In GTD, each diffraction point is then the source of a cone of diffracted rays. For a 2D calculation, this cone degenerates to a disk of rays. Usually when GTD is applied only a singe ray of the cone or disk is used, since the ray trajectory from the diffraction point to the field point is known. However, applying SBR at each diffraction point involves "shooting" a partial cone (a disk in two dimensions) of diffracted rays in the region external to the building. These rays then bounce through the building geometry just as if they were "shot" from the original source location, except that their amplitude and phase are determined by the GTD wedge diffraction coefficients. For 2D there is also a companion ray that follows the same ray path except that it comes from the image of the diffraction point in the ground and is reflected once by the ground. For 3D calculations the ground reflected rays are treated separately, as for the non-diffracted rays. For double diffraction the same process is continued to locate the edges for the second diffraction and to shoot the resulting cones (2D disks) of diffracted rays.

Let us extend the equation given above in (2) to a case of single diffraction in 2D. Consider that a particular building corner has been identified as the source of a diffracted ray. Further, let this building corner be illuminated by a ray that originally came from the actual source, and that has been reflected N times, with the notation as given in conjunction with (2) above. Then assume that his ray is further reflected M times as it bounces from the diffracting building edge to the collection area near the field point. Then for the qth such ray the electric field at the field point will be given by

$$E_q = E_0(\theta,\phi)\,\frac{e^{j\beta r_{0D}}}{r_{0D}} \cdot \prod_{n=1}^{N} R_n \cdot D \cdot \sqrt{\frac{r_{DF} \cdot r_{oD}}{(r_{0D} + r_{DF})}} \cdot \frac{e^{j\beta r_{DF}}}{r_{DF}} \cdot \prod_{m=1}^{M} R_m \qquad (5)$$

For 3D calculations the electric fields are vectors and the reflection and diffraction coefficients are dyads so that the polarization information is included.

Equation (5) includes three separate aspects of propagation. First, the ray propagates from the original source with amplitude E_0 (adjusted for the antenna radiation pattern if necessary) and undergoes N reflections until it reaches the diffracting edge with r_{0D} the distance from the source to the diffracting edge. Then it is diffracted by the edge with GTD diffraction coefficient D, and with its energy spreading changed by the spreading factor given in the square root. Then it propagates from the diffracting edge to the field point F, undergoing M additional reflections along the way. For a 2D calculation (5) is modified as in (3) to give the amplitude of the corresponding ground reflected ray, and the two amplitudes are combined coherently as in (4). Equation (5) can be extended to provide a reasonable approximation to double diffraction by using the spreading factors given in [1].

Results

In this section of the paper the 2D and 3D predictions are compared to measurements made in Rosslyn, Virginia in March and July of 1995 by a group at AT&T Bell Laboratories. The measurements were made at hundreds of locations along the streets within an approximately 500 by 500 meter area of Rosslyn. All the predictions were made totally blind, that is, the predictions were made and submitted to AT&T before any path loss data were supplied. Additional information about how the measurements were made, and some other comparisons with different propagation models, is included in [8].

The approximate building plan used for the predictions is shown in Figure 1. For the 2D predictions the buildings do not vary in the vertical direction, but for the 3D calculations any vertical variation of the buildings was included in the calculations. The receiving antenna was located on a van, with the antenna approximately 2.3 m above local ground. The paths driven by the receiving van are shown in Figure 1. Measurements were made at frequencies of 900 and 1900 MHz.

All antennas were vertically polarized. For the 3D calculations the antenna pattern of the transmitting antenna was highly directional, and was included in the predictions. The 3D receiving antenna had a vertical dipole (sin θ) pattern. For the 2D calculations the vertical antenna patterns were not included, and the horizontal patterns were omnidirectional. The path loss L_p defined by

$$L_p = P_r - P_t - G_t - G_r - L_c \qquad (6)$$

where P_r is the received power, P_t is the transmitted power, G_t is the maximum transmit antenna gain, G_r the maximum receive antenna gain, L_c is the cable loss, all given in dB. Thus the path loss depends only on the building and terrain geometry and the directional gains of the antennas.

For the 2D example the transmitting antenna was located at site 2B on Figure 1, supported by a tower at a height of 10.0 m above local ground. For the 3D examples the transmitting antennas were located on buildings at sites 5 and 6 on Figure 1. These antennas were located 2 m above the building roofs and approximately 3 meters from the roof edge. Diffraction from the edge of the roof near the transmitting antenna was not included in the calculations. The antenna height at site 5 was approximately 42 m above local ground, and at site 6 approximately 43 meters above local ground. These latter two heights are above many of the nearby buildings, so that propagation over the buildings is important.

A typical 2D prediction result for the 10 m high transmitting antenna at site 2B at 900 MHz is shown in Figure 2 for the receiving van driven along the 19th Street/Nash Street path. The first 225 m of this path is a line-of-sight region, and the remainder must be reached by multiple reflection/diffraction. A 3D prediction for transmitter site 5 at 1.9 GHz is compared with measurements in Figure 3 for the Ft. Myer Dr. van path. This path also involves both line of sight and reflection/diffraction regions. Finally, a pair of predictions for transmitter site 6 at 900 MHz is shown in Figures 4 and 5 for Lynn St. and Kent St. respectively. Going from Lynn St. to Kent St. introduces an additional block of buildings between the transmitting and receiving antennas. The 3D prediction is quite accurate in showing the additional attenuation.

References

1. R. Luebbers, "Propagation prediction for hilly terrain using GTD wedge diffraction", *IEEE Trans. Antennas Propagat.*, vol 32, no 9, pp. 951-955, Sept. 1984.
2. S. Y. Tan and H. S. Tan, "A theory for propagation path-loss characteristics in a city-street grid," *IEEE Trans. on Electromagn. Compat.*, vol 37, no. 3, Aug. 1995.
3. M. C. Lawton and J. P. McGeehan, "The application of a deterministic ray launching algorithm for the prediction of radio channel characteristics in small-cell environments," *IEEE Trans. Veh. Technol.*, vol. 43, no. 4, Nov. 1994.
4. H. Ling, R. Chou, and S. Lee, "Shooting and Bouncing Rays: Calculating the RCS of an arbitrarily shaped cavity," *IEEE Trans. Antennas Propagat.*, vol. 37, no. 2, pp 194-205, Feb. 1989.
5. J. B. Keller, "Geometrical Theory of Diffraction," *J. Opt. Soc. Amer.*, vol. 52, No. 2, pp 116-130, Feb. 1962.
6. R. G. Kouyoumjian and P. H. Pathak, "A uniform geometrical theory of diffraction for an edge in a perfectly conducting surface," *Proc. IEEE*, vol. 62, no. 11, pp. 1448-1461, Nov. 1974.
7. R. Luebbers, "Finite conductivity uniform GTD versus knife edge diffraction in prediction of propagation path loss", *IEEE Trans. Antennas and Propagat.*, vol 32, no 1, pp. 70-76, Jan. 1984.
8. Willis, T. M. et al, "UHF and microwave propagation prediction in an urban environment," Paper 8, AGARD Meeting on Digital Communications Systems: Propagation Effects, Technical Solutions, Systems Design, Athens, Greece, Sept. 1995.

Figure 1: Plan view of Rosslyn VA showing the building locations, transmitter sites, and paths driven by the receiving van

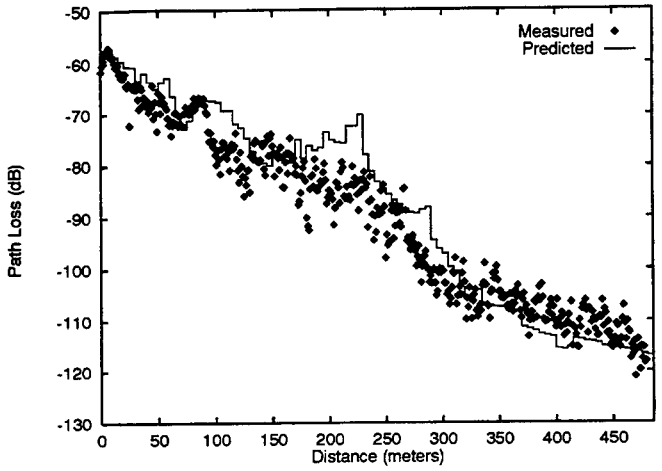

Figure 2: Prediction by 2D SBR/GTD model at 900 MHz for transmitting antenna at site 2B located at 10 m above local ground for the 19th St./Nash St. receiving van path

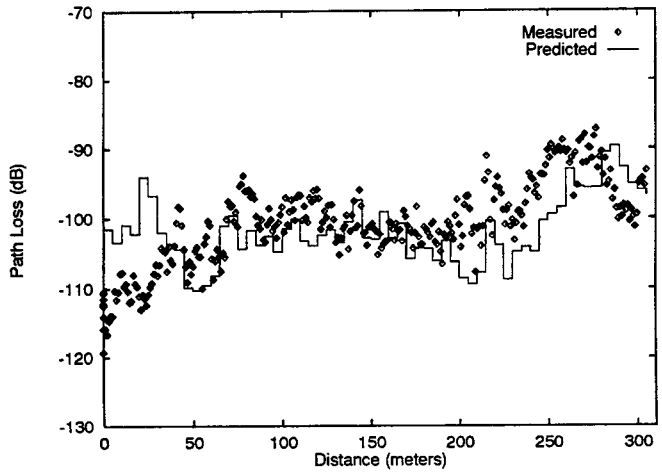

Figure 3: Prediction by 3D SBR/GTD model at 1.9 GHz for transmitting antenna at site 5 located on a roof 42 m above local ground for the Ft. Myer Dr. receiving van path

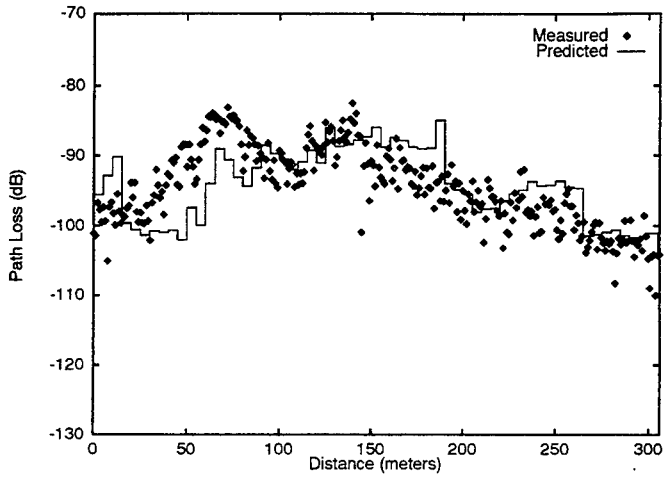

Figure 4: Prediction by 3D SBR/GTD model at 900 MHz for transmitting antenna at site 6 located on a roof 43 m above local ground for the Lynn St. receiving van path

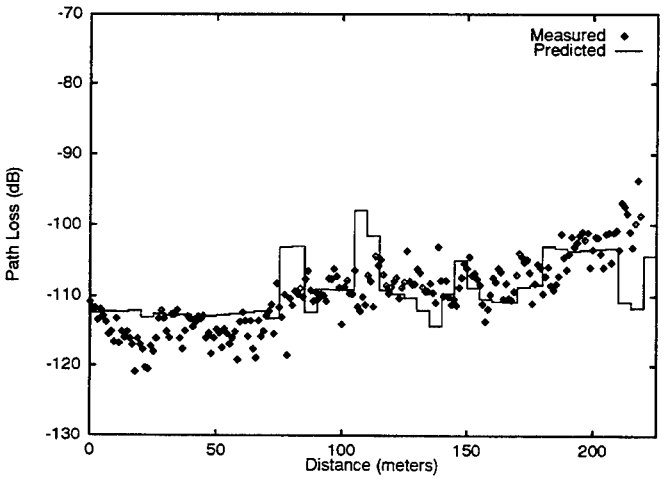

Figure 5: Prediction by 3D SBR/GTD model at 900 MHz for transmitting antenna at site 6 located on a roof 43 m above local ground for the Kent St. receiving van path

Analysis of Dielectric Structures Using the NEC-BSC

R. J. Marhefka and L. W. Henderson
The Ohio State University
ElectroScience Laboratory
1320 Kinnear Road
Columbus, OH 43212-1191
Tel: (614)292-5752
Fax: (614)292-7297
Email: rjm@tiger.eng.ohio-state.edu

I. Introduction

The NEC - Basic Scattering Code (NEC-BSC) has been used for over 20 years for the analysis of high frequency antenna performance in complicated structures such as ships, aircraft, satellites, and buildings. Because it is based on the Uniform Geometrical Theory of Diffraction (UTD), it is able to handle large structures reasonably efficiently. It has been extensively validated for perfectly conducting structures in the past. It had a limited dielectric capability, composed primarily of single multilayered dielectric plates. In order to model buildings and radomes, however, it is important to be able to model multiple plates of various compositions joined together at arbitrary angles. The user desires to know how the structure will affect the side lobe levels of the enclosed antenna, especially when the transmitted energy can be multiply bounced within the enclosure before it exits. In addition, the diffraction from the junctions needs to be modeled to ensure continuity of the predicted fields.

A new version of the NEC-BSC is being developed to handle this situation. Extensive revision to the dielectric junction diffraction coefficient has been undertaken. Now arbitrary angles between dielectric plates from 360 degrees down to 60 degrees have been implemented. This is accomplished using a heuristically derived coefficient that contains appropriate physics depending on the various reflection and transmission boundaries encountered.

A number of examples will be presented illustrating how the results from the code can help the user determine antenna performance in various dielectric enclosures. A new capability of displaying rays will be used to illustrate how the building or radome affects the patterns. The structures studied contain many plates and sources, yet volumetric patterns can be obtained in reasonable amounts of time on modern PCs or workstations.

II. Background

The NEC-BSC has had a limited dielectric/magnetic capability since Version 2 [1]. The code would allow thin slabs or coated plates to be modeled. Versions 2 can find the fields reflected and/or transmitted up to double interactions. Version 3.2 [2] added up to triple interactions. The geometrical optics reflection and transmission coefficients were obtained by a recursive method [3]. This allows for multilayered material slabs to be efficiently handled.

In both versions, the diffraction coefficient at the plate junctions is based on a paper by Burnside and Burgener [4]. In their paper, a heuristic diffraction coefficient is developed for thin "knife-edged" slabs. For the NEC-BSC, which allows for plates to be joined together at their edges, the diffraction coefficient was modified to accommodate wedge angles. The extension, however, was limited to convex wedge angles with the source and receiver on the same side of the plates. If the plates are convex and metallic backed, the results are reasonable. If the geometrical optics fields are dominant and/or the continuity of the fields are not important, this approximation is also reasonable. For the general problem, with arbitrary wedge angles, source and receiver positions, and a wide range of contrasting materials, improvements were needed for better accuracy.

Since the solution to the general material wedge or thin wedged slabs is not available, it is still necessary to base such a development on heuristic methods. The Burnside - Burgener approach is, therefore, again used to obtain a more general diffraction coefficient. A summary of the development can be found in Reference [5]. The approach entails extensively bookkeeping the physics for different situations and attaching the resulting reflection - transmission combinations to the appropriate components of the diffraction coefficient. The results [5] have been validated for simple two plate problems using the moment method [6], with good engineering agreement in most situations tried. One of the limitations present in this approximation arises from the fact that surface waves have not been included. This primarily limits the position of the antennas to be away from the surface of the material. Of course, if loss is present in the material, surface wave effects will be minimized in comparison to the optics effects.

In addition to an improved algorithm for the edge diffractions, the reflection and transmission algorithm has been generalized to include resistive and impedance boundary layers. When this is fully integrated into a new version of the NEC-BSC, a broader class of practical problems can be more accurately modeled. For example, antennas in radomes and antenna siting and coupling in an around building environments will be possible. The next section provides a hypothetical example.

III. Building Example

One of the recent topics of interest is the propagation around and through buildings. The rapid growth in personal communications technology has increased the desire to predict the performance of systems in situ. In general, real environments are very complex with wires, pipes, heating ducts, etc., buried in the walls not to mention furniture in various configurations. An analysis tool, like the NEC-BSC, can provide insight into the physical mechanisms making up the link budget between transmitter and receiver. Even a "simplified" model can, therefore, convey substantial information about the viability of a given situation. For example, purely statistical models can be difficult to validate, however, individual physical situations can be measured and/or more easily calculated by alternative means and compared.

The individual pieces can then be combined in such a way as to give ideal, typical, or worst case scenarios leading to reasonably believable bounds.

In order to better observe the capabilities of the NEC-BSC to analyze such situations, a hypothetical problem of determining the affect of a building on antenna patterns and coupling between half-wavelength dipoles is discussed. The NEC-BSC Workbench™ [7] is used to display the geometry and UTD rays. The building is a simplified model of an office room (10'x13'x9.3') with a glass window (0.125", εr=5.23, $\tan\delta$=0.013) and a open door. There are two adjoining areas and a 6' hall way. The situation is depicted in Figure 1. The building sits on a infinite ground plane with a dielectric constant of dry soil (εr=2.38, $\tan\delta$=0.048). The roof of the room is assumed to be a layer of 0.5" wood with appropriate dielectric constant (εr=3.6). The walls of the building are six inch concrete blocks. The model for the blocks is taken to be a triple layer slab. The outer layers have the thickness (0.53") and dielectric constant of the concrete (εr=3.0, $\tan\delta$=0.048). The inner layer (5.11") is an average dielectric constant between air and the concrete (εr=1.5). A paper by Honcharenko and Bertoni [8] compare the accuracy of such a model versus a more complex periodic model they developed for the inner layer. The simplified model gives good enough results for this application.

The complexity of the number of UTD interactions that can be determined is illustrated by looking at a visualization of rays. The NEC-BSC Workbench in combination with ray files produced by a new version of the NEC-BSC can be used to depicted the rays. Various numbers of bounces and/or field strength levels can be shown by using the filtering option. A half wavelength dipole is centered in the office room. A receiver is situation in the middle of the hallway. Figure 2 shows the dominant rays over a 30 dB dynamic range from the source to the receive via various wall reflections, transmissions, and diffractions. Notice that if the filter is open to a 60 dB dynamic range the number of rays greatly increases as shown in Figure 3. Notice that even thought the situation depicted is symmetric in terms of relative source and receiver position in terms of the walls, the ray picture is not symmetric. This is due to the fact that the reflection coefficient of the walls is larger than for the glass.

The next example illustrates the coupling between half wavelength dipoles. Two cases at different frequencies of 0.9 GHz and 3.0 GHz are compared. The coupling between a dipole in the center of the office to the second dipole as it proceeds down the center of the hall is shown in Figure 4. The dipoles are 4' off the floor. The coupling between the dipole in the office to a second dipole as it proceeds in the same fashion outside the building is shown in Figure 5.

The last example illustrates the affect the building has on the far zone pattern. Figure 6 shows the elevation pattern at phi=90 degrees of the dipole in the center of the office at 3.0 GHz versus the dipole over the ground plane alone. Figure 7 shows the same situation but in a conic cut at theta=86 degrees comparing 0.9 GHz case to 3.0 GHz case. Note that the no building case is a constant for the conic cut. The affect of the building is obvious in the two cases.

IV. Summary

The material plate model for the NEC-BSC is being generalized to accommodate a wider class of situations. With these improvements the code will be able to more accurately model joined plates with arbitrary wedge angles, source and receiver positions, and dielectric/magnetic constituencies. The

algorithms have been validated against simple situations using moment methods. The determination of the accuracy for more general problems, such as antennas in the present of buildings, etc., awaits further validation.

V. Acknowledgment

This work was supported in part by The Ohio State University, Research Foundation and the Naval Command, Control, and Ocean Surveillance Center, RDT&E Division (NRaD) under Contract Number N66001-93-C-0104.

VI. References

[1] R. J. Marhefka and W. D. Burnside, "Numerical Electromagnetic Code - Basic Scattering Code (Version 2), Part I: User's Manual," Technical Report 712242-14, The Ohio State University ElectroScience Laboratory, Department of Electrical Engineering, December 1982, Prepared under Contract No. N00123-79-C-1469 for Naval Regional Contracting Office.

[2] R. J. Marhefka and J. W. Silvestro, "Near Zone - Basic Scattering Code, User's Manual with Space Station Applications," Technical Report 716199-13, The Ohio State University ElectroScience Laboratory, Department of Electrical Engineering, March 1989. Prepared under Grant No. NSG 1498 for NASA - Langley Research Center.

[3] J. H. Richmond, "Efficient Recursive Solutions for Plane and Cylindrical Multilayers," Technical Report 1968-1, The Ohio State University ElectroScience Laboratory, Dept. of Elec. Engr., August 1965. Prepared under Contract No. Now 65-0329-d for Bureau of Naval Weapons.

[4] W. D. Burnside and K. W. Burgener, "High Frequency Scattering by a Thin Lossless Dielectric Slab," *IEEE Trans. Antennas Propagat.*, Vol. AP-31, No. 1, pp. 104-110, January 1983.

[5] R. J. Marhefka, "UTD Diffraction Coefficient for Dielectric Plate Junctions," in *1995 IEEE Antennas and Propagation International Symposium and URSI Meeting*, IEEE Conference Proceedings, Newport Beach, CA, pp. 2-5, June 18-23, 1995.

[6] M. Kragalott and E. H. Newman, "A User's Manual for the General Cylinder Code (GCYL)," Technical Report 722644-1, The Ohio State University ElectroScience Laboratory, Dept. of Elec. Engr., June 1990. Prepared under Contract No. PO D55951, for Rosemount, Inc.

[7] L. W. Henderson and R. J. Marhefka, "A Graphical User Interface for the NEC-BSC," in *11th Annual Review of Progress in Applied Computational Electromagnetics (ACES)*, Conference Proceedings, Monterey, CA, pp. 245-251, March 20-25, 1995.

[8] W. Honcharenko and H. L. Bertoni, "Transmission and Reflection Characteristics at Concrete Block Walls in the UHF Bands Proposed for Future PCS," *IEEE Trans. Antennas Propagat.*, Vol. 42, No. 2, pp. 232-239, February 1994.

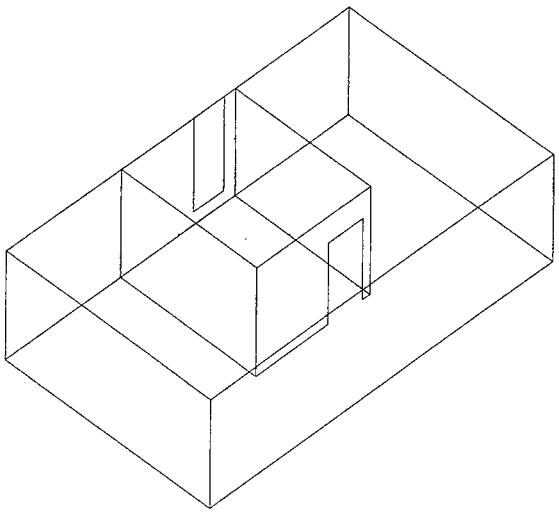

Figure 1. Geometry of building example.

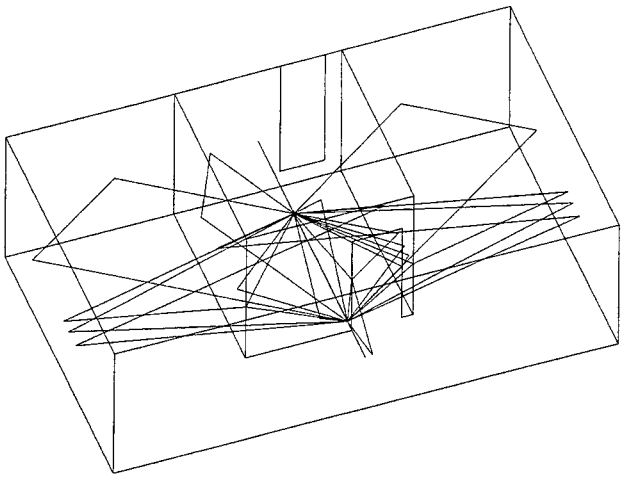

Figure 2. Coupling between dipoles showing rays over 30 dB dynamic range.

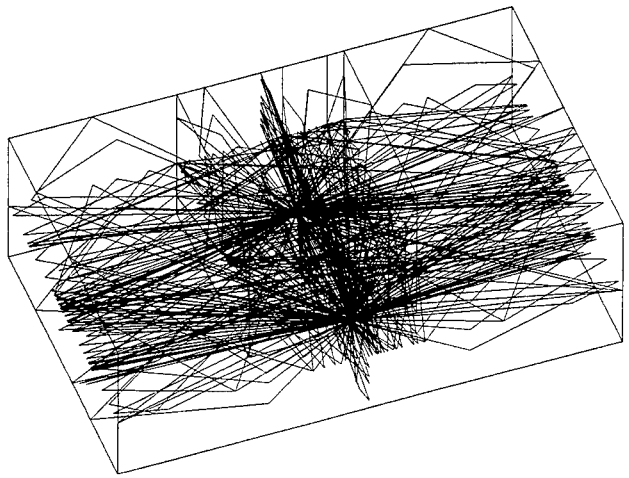

Figure 3. Coupling between dipoles showing rays over 60 dB dynamic range.

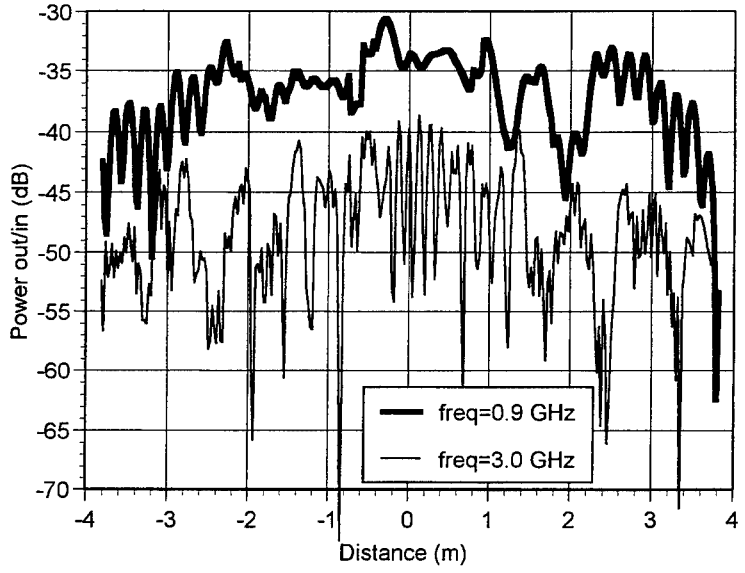

Figure 4. Coupling between dipole in room and dipole in center of hallway.

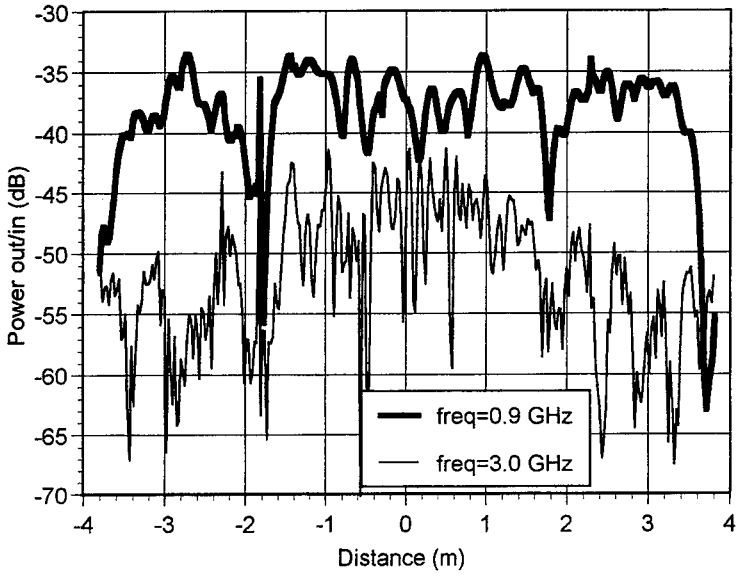

Figure 5. Coupling between dipole in room and dipole outside.

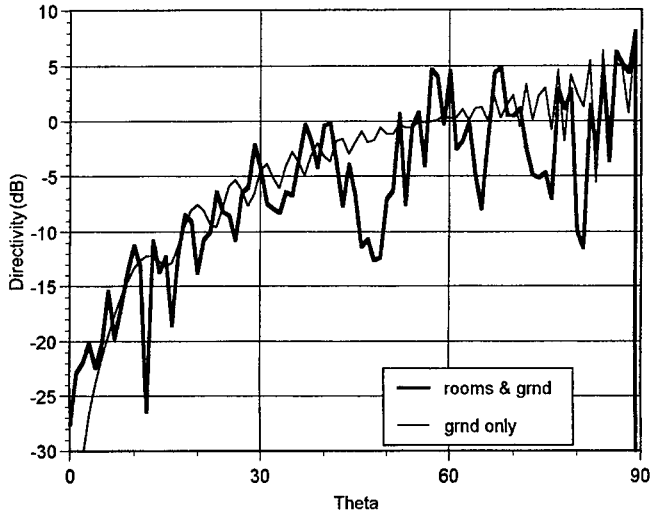

Figure 6. Pattern of dipole with Phi = 90 degrees at 3. 0 GHz.

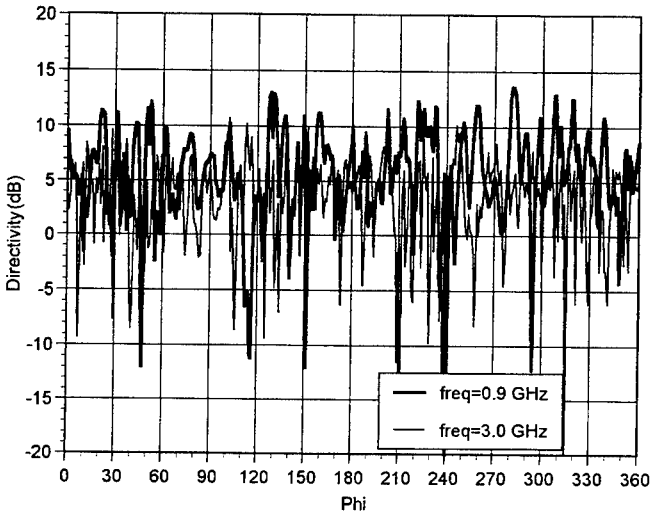

Figure 7. Pattern of dipole in room at Theta=86 degrees.

Hybrid MM–PO–Fock Analysis of Monopole Antennas Mounted on Curved Convex Bodies

U. Jakobus and F. M. Landstorfer

Institut für Hochfrequenztechnik, University of Stuttgart,
Pfaffenwaldring 47, D-70550 Stuttgart, Germany

Abstract

The present contribution deals with a hybrid method combining the method of moments (MM) with the physical optics (PO) approximation and asymptotic currents based on Fock theory. This current based hybrid approach is employed to deal with arbitrarily shaped monopole antennas located on perfectly conducting, curved convex surfaces. Some examples, e.g. an inverted–L antenna mounted on an open truncated cone, demonstrate that by the hybrid approach a drastic reduction of memory requirement and CPU–time can be achieved as compared to an application of the MM alone.

1 Introduction

Even though fast computers with large memories are available to antenna design engineers nowadays it remains a challenge to analyze a certain class of electromagnetic scattering problems. These are bodies with geometrical dimensions large as compared to the wavelength but requiring, for instance, an accurate analysis of a radiating antenna so that an application of pure asymptotic techniques such as the uniform geometrical theory of diffraction (UTD) is out of question. The MM can also not be considered because memory requirement and CPU time grow proportional to f^4 and f^6, respectively, with f being the frequency.

A remedy is found in hybrid methods combining the MM with asymptotic techniques [1, 2, 3]. In principle one has to distinguish between ray based asymptotic techniques such as UTD and current based techniques like PO or the physical theory of diffraction (PTD) [4]. Depending on the structure to be analyzed both of them offer some advantages. Hybrid MM/UTD formulations (e.g. [5, 6, 7]) are suitable for problems when e.g. an antenna is located in front of a large scattering body. On the other hand, current based techniques should be prefered when parts of one large scatterer are to be treated with MM and the remaining parts with asymptotic techniques. In this case a uniform current based formulation can be applied ensuring current continuity at the boundary between the MM– and the asymptotic region.

Current based hybrid methods are summarized in [8]. An application to three–dimensional bodies can be found in [9, 10, 11], where PO is employed in the asymptotic region. In [11, 12] the authors proposed corrections of the PO current to improve the accuracy by accounting for effects of edges in the asymptotic region. The present paper aims at demonstrating a similar improvement by replacing PO by Fock currents [13] for curved convex surfaces. As opposed to [14] our approach is not restricted to bodies of revolution but arbitrarily shaped three–dimensional perfectly conducting bodies can be investigated.

2 Hybrid method

Like the MM, the hybrid method represents a current based formulation where first an electric surface current density $\vec{J}$ is determined on the metallic surfaces including surfaces of cylindrical wires. Then the electric and magnetic fields radiated by $\vec{J}$ can be computed at an observation point $\vec{r}$ from the relations

$$\vec{E}(\vec{r}) = \vec{\mathcal{E}}\left\{\vec{J}\right\} = -\frac{j}{4\pi\varepsilon\omega}\,\vec{\nabla}\iint\limits_{A'}(\vec{\nabla}'_A\cdot\vec{J}(\vec{r}\,'))\cdot G(\vec{r},\vec{r}\,')\,dA' - j\omega\frac{\mu}{4\pi}\iint\limits_{A'}\vec{J}(\vec{r}\,')\cdot G(\vec{r},\vec{r}\,')\,dA' \quad (1)$$

$$\vec{H}(\vec{r}) = \vec{\mathcal{H}}\left\{\vec{J}\right\} = \frac{1}{4\pi}\,\vec{\nabla}\times\iint\limits_{A'}\vec{J}(\vec{r}\,')\cdot G(\vec{r},\vec{r}\,')\,dA'. \quad (2)$$

with the free space Green's function

$$G(\vec{r},\vec{r}\,') = \frac{e^{-j\beta|\vec{r}-\vec{r}\,'|}}{|\vec{r}-\vec{r}\,'|}. \quad (3)$$

Here $\vec{r}$ denotes the observation point, $\vec{r}\,'$ refers to the source point, and $\beta = \frac{2\pi}{\lambda}$ is the wavenumber.

Fig. 1 shows a monopole antenna mounted on a curved convex surface element. In general, the antenna as well as a small region of the surface around the antenna (gray shaded in Fig. 1) are modeled by MM whereas the current on the remaining part of the surface is based on asymptotic expansions.

In the MM–region the current $\vec{J}^{MM}$ is expressed as linear superposition of basis functions

$$\vec{J}^{MM} = \sum_{n=1}^{N_f}\alpha_n\cdot\vec{f}_n + \sum_{n=1}^{N_g}\beta_n\cdot\vec{g}_n + \sum_{n=1}^{N_h}\gamma_n\cdot\vec{h}_n \quad (4)$$

with $N^{MM} = N_f + N_g + N_h$ denoting the total number of basis functions in the MM–region. Metallic surfaces are subdivided into electrically small triangular patches. On these patches the rooftop basis functions $\vec{f}_n$ according to Rao et al. [15] are used. Wire antennas, e.g. the monopole antenna depicted in Fig. 1, are subdivided into small wire segments where we employ triangular basis functions $\vec{g}_n$. Furthermore special basis functions $\vec{h}_n$ are required to model the transition from segments to patches.

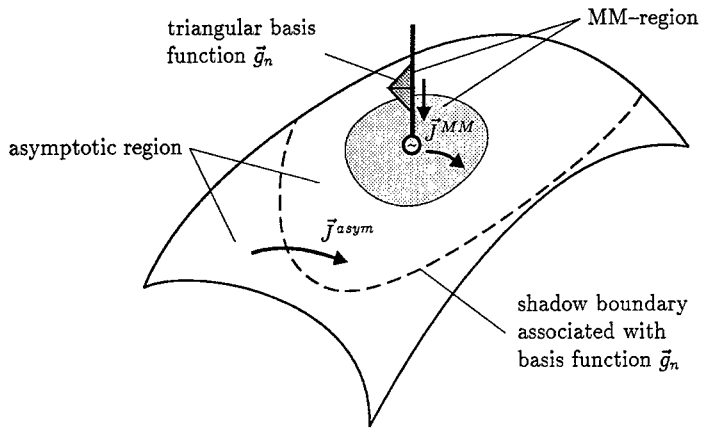

Fig. 1: General structure of a monopole antenna mounted on a curved convex surface element.

In the asymptotic region in Fig. 1 the current $\vec{J}^{asym}$ is expressed as linear superposition of rooftop basis functions on triangular patches as well:

$$\vec{J}^{asym} = \sum_{n=N_f+1}^{N_f+N^{asym}} \alpha_n \cdot \vec{f}_n \tag{5}$$

This representation as superposition of basis functions offers advantages concerning the continuity of the surface current density across the boundary between the MM– and the asymptotic region [11].

Only the N^{MM} coefficients α_n, β_n, and γ_n in eqn. (4) are obtained by solving a system of linear equations resulting from an electric field integral equation. The N^{asym} remaining coefficients α_n in eqn. (5), however, are directly based on an asymptotic current representation (PO or Fock currents), i.e. the time and memory consuming process of solving a system of linear equations is avoided.

The details of the hybrid method can be found in [11]. Here we will concentrate on some fundamental equations only.

From the boundary condition

$$\vec{E}_{tan} = 0 \tag{6}$$

valid on the whole surface of the perfectly conducting scattering body the electric field integral equation

$$\vec{\mathcal{E}}\left\{\vec{J}^{MM}\right\}_{tan} + \vec{\mathcal{E}}\left\{\vec{J}^{asym}\right\}_{tan} = -\vec{E}_{i,tan} \tag{7}$$

can be derived. Here $\vec{E}_{i,tan}$ represents the tangential component of the impressed electric field strength of the excitation. When dealing with monopole antennas $\vec{E}_i$ might be caused by a

magnetic frill current. The operator $\vec{\mathcal{E}}$ in eqn. (7) acting on $\vec{J}$ yields the scattered electric field according to eqn. (1).

In the following the asymptotic current $\vec{J}^{asym}$ can always be expressed as a function of the incident magnetic field strength $\vec{H}_{inc}$. As an example consider the PO current $\vec{J}^{PO} = 2\hat{n} \times \vec{H}_{inc}$ in the illuminated region. The more general case with Fock currents will be described in Section 3. Therefore we can introduce an operator $\vec{\mathcal{K}}$ so that the current in the asymptotic region is expressed as

$$\vec{J}^{asym} = \vec{\mathcal{K}} \left\{ \vec{H}_{inc} \right\} = \vec{\mathcal{K}} \left\{ \vec{H}_i + \vec{\mathcal{H}} \left\{ \vec{J}^{MM} \right\} \right\}. \tag{8}$$

The incident magnetic field $\vec{H}_{inc}$ is the superposition of the impressed magnetic field $\vec{H}_i$ of the excitation and the magnetic field radiated by currents $\vec{J}^{MM}$ in the MM–region. It is very important to take this radiated field into account as for example looking at the scatterer in Fig. 1 the impressed magnetic field $\vec{H}_i$ of the excitation is mainly confined to the feed zone of the monopole antenna so that the current in the asymptotic region is caused by the magnetic field radiated by the currents $\vec{J}^{MM}$ along the antenna.

By inserting eqn. (8) in (7) we arrive at

$$\left(\vec{\mathcal{E}} + \vec{\mathcal{E}} \vec{\mathcal{K}} \vec{\mathcal{H}} \right) \left\{ \vec{J}^{MM} \right\}_{tan} = -\vec{E}_{i,tan} - \vec{\mathcal{E}} \vec{\mathcal{K}} \left\{ \vec{H}_i \right\}_{tan}. \tag{9}$$

With eqn. (4) and by exploiting linearity of operators $\vec{\mathcal{E}}$, $\vec{\mathcal{H}}$, and $\vec{\mathcal{K}}$ we finally obtain

$$\begin{aligned} &\sum_{n=1}^{N_f} \alpha_n \cdot \left[\left(\vec{\mathcal{E}} + \vec{\mathcal{E}} \vec{\mathcal{K}} \vec{\mathcal{H}} \right) \left\{ \vec{f}_n \right\}_{tan} \right] \\ &+ \sum_{n=1}^{N_g} \beta_n \cdot \left[\left(\vec{\mathcal{E}} + \vec{\mathcal{E}} \vec{\mathcal{K}} \vec{\mathcal{H}} \right) \left\{ \vec{g}_n \right\}_{tan} \right] \\ &+ \sum_{n=1}^{N_h} \gamma_n \cdot \left[\left(\vec{\mathcal{E}} + \vec{\mathcal{E}} \vec{\mathcal{K}} \vec{\mathcal{H}} \right) \left\{ \vec{h}_n \right\}_{tan} \right] = -\vec{E}_{i,tan} - \vec{\mathcal{E}} \vec{\mathcal{K}} \left\{ \vec{H}_i \right\}_{tan}. \end{aligned} \tag{10}$$

By applying the scalar product with suitable weighting functions (e.g. Galerkin method) the integral equation (10) can be converted into a system of linear equations for the $N^{MM} = N_f + N_g + N_h$ unknown coefficients in the MM–region. After solving this system of linear equations the current $\vec{J}^{MM}$ is known. Then from eqn. (8) the current $\vec{J}^{asym}$ in the asymptotic region is obtained in a straightforward manner. Once this current is known the scattered electric and magnetic fields can be computed with the aid of eqns. (1) and (2).

3 Asymptotic currents

The simplest possible expression for the asymptotic current $\vec{J}^{asym}$ has already been briefly mentioned in Section 2. It is the physical optics approximation

$$\vec{J}^{PO} = \begin{cases} 2\hat{n} \times \vec{H}_{inc} & \text{illuminated region} \\ 0 & \text{shadowed region} \end{cases} \tag{11}$$

with the normal vector $\hat{n}$ on the surface pointing to the source. In this case the operator $\vec{\mathcal{K}}$ in eqn. (8) takes the form

$$\vec{\mathcal{K}}\left\{\vec{H}_{inc}\right\} = 2\delta\,\hat{n} \times \vec{H}_{inc} \tag{12}$$

with δ being zero or one depending on the location of the observation point in the illuminated or shadowed region, respectively.

The PO current is not very suitable for the analysis of monopole antennas on curved convex bodies as shown in Fig. 1 for two reasons:

- There is a discontinuity of $\vec{J}^{PO}$ at the shadow boundary[1].
- In the whole shadowed region $\vec{J}^{PO}$ is set to zero.

We employ Fock currents [13] in order to overcome these difficulties. They are continuous across the shadow boundary and account for the creeping waves in the shadowed region.

Expressions similar to those in Refs. [1, 3] are used for the Fock currents in the illuminated and in the shadowed region, but we have eliminated the dependence on the incident electric field $\vec{E}_{inc}$ so that a formulation $\vec{J}^{Fock} = \vec{\mathcal{K}}\left\{\vec{H}_{inc}\right\}$ according to eqn. (8) becomes possible. Detailed expressions for $\vec{J}^{Fock}$ can be found in [16].

4 Examples

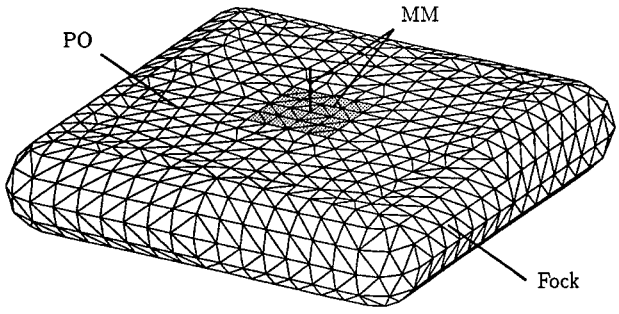

Fig. 2: $\frac{\lambda}{4}$–monopole antenna mounted on a thick rectangular body with rounded edges. The dimensions of the body are $2\lambda \times 2\lambda \times \frac{\lambda}{2}$.

The first example is shown in Fig. 2 where a $\frac{\lambda}{4}$–monopole antenna is mounted on a thick rectangular body with rounded edges. The surface of the scattering body has been divided into three regions. The MM–region consists of the monopole antenna and the small gray shaded square area around the antenna. The remaining flat part of the top surface is assigned to the PO–region, while the

[1]Please note that the location of the shadow boundary in Fig. 1 depends on the source point, i.e. on the location of the basis function under consideration in eqn. (10).

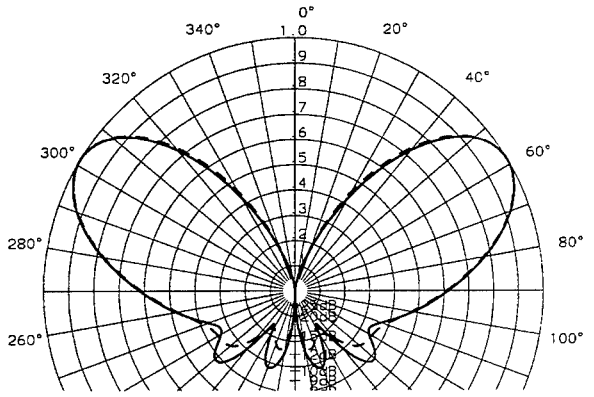

Fig. 3: Vertical radiation pattern of the monopole antenna depicted in Fig. 2.

cylindrical and spherical elements represent the Fock–region. The subdivision of all surfaces — independent from which region they are assigned to — into triangular patches, which is necessary in order to apply basis functions $\tilde{f}_n$ in eqns. (4) and (5), is also displayed in Fig. 2.

The vertical radiation pattern of the structure in Fig. 2 is shown in Fig. 3. The solid line is a reference solution based on an application of the MM to the entire structure, while the dashed curve represents the result of the hybrid method combining MM, PO and Fock theory. The results are in very good agreement, while the memory requirement for the matrix of the system of linear equations has been reduced by a factor of about 10.

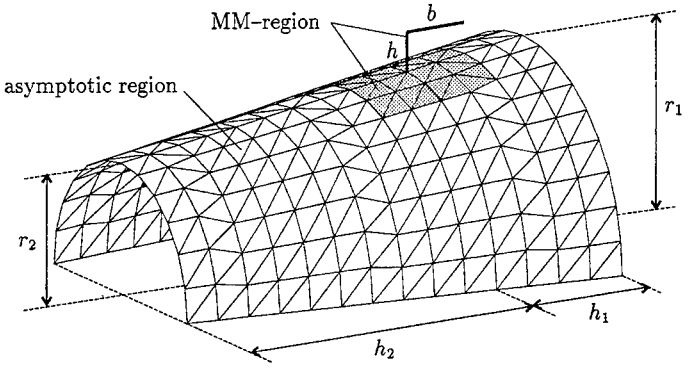

Fig. 4: Inverted–L antenna mounted on an open truncated cone.

Another example taken from [9] is shown in Fig. 4. An inverted–L antenna is located on an open truncated cone. Here two different hybrid formulations are compared: The gray shaded area in Fig. 4 is treated with MM while either PO or Fock currents are employed on the remaining conical surface.

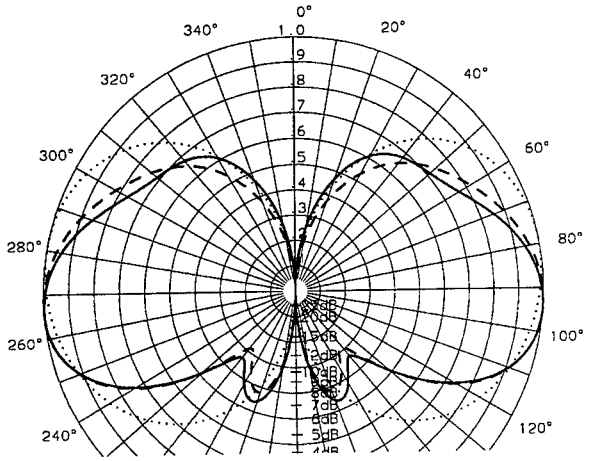

Fig. 5: Vertical radiation pattern of the inverted–L antenna on a cone depicted in Fig. 4 (vertical polarization). Frequency $f = 1\,\mathrm{GHz}$ and dimensions

$r_1 = 0.18\,\mathrm{m}$
$r_2 = 0.16\,\mathrm{m}$
$h_1 = 0.12\,\mathrm{m}$
$h_2 = 0.36\,\mathrm{m}$
$h = 0.025\,\mathrm{m}$
$b = 0.050\,\mathrm{m}$

The vertical radiation pattern in a plane perpendicular to the axis of the cone is depicted in Fig. 5. The solid line is again a reference solution obtained by applying MM to the entire structure. The hybrid methods with PO and Fock currents are represented by the dotted and dashed curves, respectively. It is obvious that the hybrid method with Fock currents is in much better agreement to the reference solution (solid line) than the hybrid method with PO. The main reason for this is that Fock theory also accounts for the currents in the shadowed region.

5 Conclusions

A current based hybrid method has been presented that combines MM with asymptotic expansions such as PO or Fock currents. Even though the approach is a very flexible one concerning shape and size of the scatterer, we have restricted the scope of application in this paper to monopole antennas mounted on curved convex bodies. This particular geometry requires special basis functions to model a continuous current flow from the surface of the curved convex body to the wire antenna. It also turned out to be advantageous to determine not only the currents along the antenna but also the currents on a small area around the antenna by MM. The asymptotic expansion (PO or Fock theory) has been employed on the remaining parts of the surface.

Two examples have been demonstrated where the results of the hybrid method compare well to those of the conventional MM.

References

[1] L. N. Medgyesi-Mitschang and D.-S. Wang, "Hybrid methods in computational electromagnetics: a review," *Computer Physics Communications*, vol. 68, pp. 76–94, 1991.

[2] G. A. Thiele, "Overview of selected hybrid methods in radiating system analysis," *Proceedings of the IEEE*, vol. 80, pp. 67–78, Jan. 1992.

[3] D. P. Bouche, F. A. Molinet, and R. Mittra, "Asymptotic and hybrid techniques for electromagnetic scattering," *Proceedings of the IEEE*, vol. 81, pp. 1658–1684, Dec. 1993.

[4] P. Y. Ufimtsev, "Elementary edge waves and the physical theory of diffraction," *Electromagnetics*, vol. 11, pp. 125–160, 1991.

[5] W. D. Burnside and P. H. Pathak, "A summary of hybrid solutions involving moment methods and GTD," in *Applications of the Method of Moments to Electromagnetic Fields*, SCEEE Press, St. Cloud, 1980.

[6] E. P. Ekelman and G. A. Thiele, "A hybrid technique for combining the moment method treatment of wire antennas with the GTD for curved surfaces," *IEEE Transactions on Antennas and Propagation*, vol. 28, pp. 831–839, Nov. 1980.

[7] J. N. Sahalos and G. A. Thiele, "On the application of the GTD–MM technique and its limitations," *IEEE Transactions on Antennas and Propagation*, vol. 29, pp. 780–786, Sept. 1981.

[8] L. N. Medgyesi-Mitschang and D.-S. Wang, "Hybrid methods for analysis of complex scatterers," *Proceedings of the IEEE*, vol. 77, pp. 770–779, May 1989.

[9] C. S. Kim and Y. Rahmat-Samii, "Low profile antenna study using the physical optics hybrid method (POHM)," in *IEEE International Symposium on Antennas and Propagation, London, Ontario*, pp. 1350–1353, June 1991.

[10] L. N. Medgyesi-Mitschang and J. M. Putnam, "Hybrid formulation for arbitrary 3-D bodies," in *10th Annual Review of Progress in Applied Computational Electromagnetics, ACES Conference, Monterey*, vol. II, pp. 267–274, Mar. 1994.

[11] U. Jakobus and F. M. Landstorfer, "Improved PO–MM hybrid formulation for scattering from three–dimensional perfectly conducting bodies of arbitrary shape," *IEEE Transactions on Antennas and Propagation*, vol. 43, pp. 162–169, Feb. 1995.

[12] U. Jakobus and F. M. Landstorfer, "Improvement of the PO–MM hybrid method by accounting for effects of perfectly conducting wedges," *IEEE Transactions on Antennas and Propagation*, vol. 43, pp. 1123–1129, Oct. 1995.

[13] V. A. Fock, *Electromagnetic Diffraction and Propagation Problems, International Series of Monographs on Electromagnetic Waves*, vol. 1. Pergamon Press, Oxford, 1965.

[14] L. Medgyesi-Mitschang and D.-S. Wang, "Hybrid solutions for large–impedance coated bodies of revolution," *IEEE Transactions on Antennas and Propagation*, vol. 34, pp. 1319–1329, Nov. 1986.

[15] S. M. Rao, D. R. Wilton, and A. W. Glisson, "Electromagnetic scattering by surfaces of arbitrary shape," *IEEE Transactions on Antennas and Propagation*, vol. 30, pp. 409–418, May 1982.

[16] U. Jakobus and F. M. Landstorfer, "Application of Fock–currents for curved convex surfaces within the framework of a current–based hybrid method," in *CEM'96, IEE 3rd International Conference on Computation in Electromagnetics, Bath*, Apr. 1996.

Numerical Diffraction Coefficient for an Impedance Wedge with a Material Body Attached to its Edge [1]

Michael F. Otero and Roberto G. Rojas

ElectroScience Laboratory
Department of Electrical Engineering
The Ohio State University
Columbus, OH 43212-1191, U.S.A.

Abstract

The analysis for the electromagnetic radiation or scattering from a material cylinder in the presence of a wedge with impedance faces is presented. The problem considered is two dimensional where the incident field is polarized TM or TE to the axis of the wedge, and the material body may be of arbitrary shape and inhomogeneous. An integral equation is formulated where the field inside the material cylinder is the unknown quantity to be determined and the Green's function for the impedance wedge is included in the kernel of the integral equation which accounts for the presence of the wedge. The integral equation is then solved using a method of moments technique, which allows us to obtain modified numerical diffraction coefficients to represent the effect of the body. The primary application for this analysis is to study methods for reducing the EM scattering from wedge shaped objects; specifically the fields which diffract from the sharp corner formed by the edge of the wedge. Attaching a lossy material body to the tip of the wedge is an effective method for reducing these diffracted fields.

1. Introduction

The diffraction of an electromagnetic wave by a wedge is a fundamental problem that has been extensively studied. The very general configuration of a wedge, whose faces can have different impedance boundary conditions, was chosen for its versatility in representing more specialized geometries; i.e., conducting half-planes, right angle corners, wedges with coated surfaces, etc. Studying the fields that diffract from the edge of the wedge can provide valuable insights into the

[1]This work was supported in part by the Joint Services Electronics Program (Contract N00014-89-J-1007) and by the Ohio State University Research Foundation.

role that sharp edges have on the scattering characteristics of structures. Obtaining the diffraction coefficient for the wedge can therefore provide a valuable tool for incorporating the effect of edge diffraction when determining the scattering from certain objects. There have been numerous asymptotic solutions for the diffraction coefficient for an impedance wedge [1, 2, 3]; most of which are closed form solutions that allow for convenient numerical implementation. However, this paper will focus on the more complex configuration of a material body attached to the vertex of a wedge; an example of which is shown in Figure 1. The problem is a two-dimensional one where the wedge

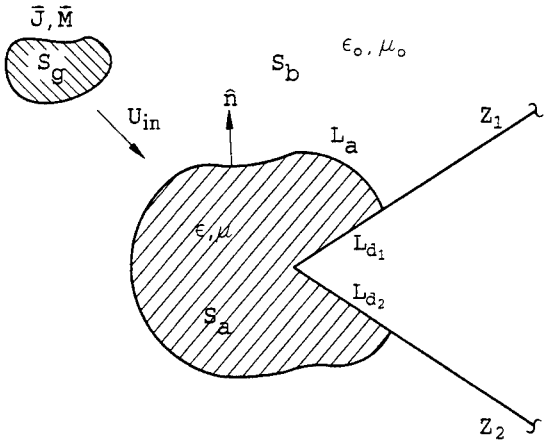

Figure 1: Configuration for a material body in the presence of an impedance wedge.

faces have different impedance values given by Z_1 and Z_2. The material body can be of arbitrary shape and its material parameters, ϵ and μ, may be inhomogeneous. The problem will then be to determine how incorporating this material body modifies the diffraction coefficient of the wedge. Solutions for these modified diffraction coefficients are, in general, too complex to obtain in closed form and therefore will be obtained numerically. This will involve formulating an integral equation to determine the scattering from the material body in the presence of the wedge and then using a numerical technique to solve it. By allowing these material bodies to be lossy, this analysis can have practical applications for studying methods for reducing the electromagnetic fields that diffract from sharp edges.

The analysis proposed here will use the MM/Green's function approach where the Green's function that is employed in the kernel of the integral equation is the specialized one for the

impedance wedge. Using the specialized Green's function, as opposed to the free-space one, reduces the number of unknowns since the boundary conditions along the wedge faces do not have to be enforced. The problem is a two-dimensional one where its edge is located along the z-axis, and the structure is infinite in the z direction. For the case when the fields have no z-dependance, it can be shown that the problem can be reduced to two scalar problems: namely, $\mathrm{TM}_z, E_z \neq 0, H_z = 0$ and $\mathrm{TE}_z, E_z = 0, H_z \neq 0$. Thus, the scalar function U will be defined as $U = E_z$ for TM_z, and $U = H_z$ for TE_z. The wedge faces have surface impedance values given by Z_1 and Z_2, and $n\pi$ is the exterior wedge angle (n need not be an integer). The faces of the wedge satisfy the impedance or Leontovich boundary condition. The expressions for this Green's function are extremely complicated and will therefore be omitted in this paper; however, the reader can refer to [4] for a thorough development of these expressions.

2. Development of the integral equation

The configuration to be analyzed is shown in Figure 1 where S_a is the region occupied by the material body, S_g is the source region, and S_b is the region in free space exterior to both the wedge and S_a. The contour which surrounds S_a has three segments: L_a is the segment which borders on S_b, and L_{d_1} and L_{d_2} are the segments which border on the wedge faces 1 and 2, respectively. Since the material body may be inhomogeneous, the permittivity and permeability are allowed to be functions of position within S_a. An integral equation is then formulated which utilizes a single field component as the unknown variable to be solved for. This method of formulating an integral equation was developed by Jin, et. al. [5]. The formulation that they developed, as applied to the two-dimensional problem used in this paper, involves a surface integral over the material region and a line integral along the contour enclosing that region where the unknown quantity to solve for is either the z-component of the electric field for the TM_z case or the z-component of the magnetic field for the TE_z case.

An outline of this method for formulating the integral equation in terms of a single field component is as follows: 1) consider the region exterior to the material body S_b and use Green's second identity to obtain the relationship between the field U_{in} and the field U_b along the contour L_a; 2) consider the region interior to the material body S_a and use the divergence theorem to obtain a relationship between the field along the contour L_a and the internal field U_a; 3) use the boundary conditions along the contour L_a to relate the exterior field to the interior field, therefore obtaining a relationship between the field U_{in} and the internal field U_a. The field U_{in} is the field

due to the impressed sources at S_g (see Figure 1) in the presence of the wedge with the material removed, U_a is the total field inside the material body S_a and U_b is the total outside S_a.

Certain terms will be introduced in order to simplify the notation. The term ν is defined as

$$\sin\nu_{1,2} \;=\; \eta/Z_{1,2};\quad \text{for } \mathrm{TM}_z: \quad \sin\nu_{1,2} = Z_{1,2}/\eta;\quad \text{for } \mathrm{TE}_z \tag{1}$$

where η is the intrinsic impedance of free space. The two-dimensional Green's function for the impedance wedge is denoted by $G_w(\vec{\rho},\vec{\rho}\,')$, which represents the field at the observation point $\vec{\rho}$ due to a line source at $\vec{\rho}\,'$. The terms τ and σ represent the distribution of the material parameters within the body.

$$\tau(\vec{\rho}) \;=\; \begin{cases} \epsilon_a(\vec{\rho})/\epsilon_o; & \mathrm{TM}_z, \\ \mu_a(\vec{\rho})/\mu_o; & \mathrm{TE}_z, \end{cases} \qquad \sigma(\vec{\rho}) = \begin{cases} \mu_o/\mu_a(\vec{\rho}); & \mathrm{TM}_z, \\ \epsilon_o/\epsilon_a(\vec{\rho}); & \mathrm{TE}_z \end{cases} \tag{2}$$

The resulting integral equation for the unknown field U_a within the material region is

$$\begin{aligned} U_{in}(\vec{\rho}) \;&+\; \int_{L_a} U_a(\vec{\rho}\,')\,\nabla_t{}'G_w(\vec{\rho},\vec{\rho}\,')(1-\sigma(\vec{\rho}\,'))\cdot\hat{n}'\;dl' \\ &+\; \sum_{n=1}^{2} ik_o\sin\nu_n \int_{L_{d_n}} G_w(\vec{\rho},\vec{\rho}\,')U_a(\vec{\rho}\,')(\sigma(\vec{\rho}\,')-1)dl' \\ &+\; \int_{S_a} U_a(\vec{\rho}\,')\left[\nabla_t{}'\sigma(\vec{\rho}\,')\cdot\nabla_t{}'G_w(\vec{\rho},\vec{\rho}\,') + k_o^2 G_w(\vec{\rho},\vec{\rho}\,')(\tau(\vec{\rho}\,')-\sigma(\vec{\rho}\,'))\right] ds' \\ &=\; \begin{cases} U_b(\vec{\rho}); & \vec{\rho}\in S_b, \\ \sigma(\vec{\rho})U_a(\vec{\rho}); & \vec{\rho}\in S_a \text{ or } \vec{\rho}\in L_{d_{1,2}}, \\ \frac{1}{2}U_a(\vec{\rho})(1+\sigma(\vec{\rho})); & \vec{\rho}\in L_a, \end{cases} \end{aligned} \tag{3}$$

where the above integrals are principle value integrals when $\vec{\rho}\in S_a$ or $L_{d_{1,2}}$ and $\nabla_t{}' = \nabla' - \hat{z}\frac{\partial}{\partial z'}$. Once U_a is found, U_b can also be computed as indicated above.

An MM technique is used to obtain a solution to the integral equation given in (3). To implement this technique, the material region S_a is subdivided into trapezoidal cells and the bordering contour (L_a, L_{d_1}, and L_{d_2}) is subdivided into linear segments. Pulse basis functions are used over each of the cells and point matching is applied at the centroid of the cell, and pulse basis functions are also used for the line segments and point matching is applied at the center of each segment.

3. Numerical results

Far field scattering patterns showing the interaction of a material body and an impedance wedge have been generated. To verify these results, the limiting case when the impedance wedge becomes a perfectly conducting semi-infinite half-plane was used so that a comparison could be made to the results obtained using a code that was developed by Newman which uses a MM/Green's function technique to solve for the scattering from a complex material body in the presence of a PEC half-plane [6]. The agreement with the reference solution was found to be excellent which provides a strong validation for the formulation of the integral equation since it is a completely different one from that which is used in the reference solution, and also verifies the numerical implementation of the MM solution.

A material body will now be attached to the edge of a wedge for the purpose of reducing its scattering characteristics. A wedge was chosen with an interior wedge angle of 72° and has impedance faces with the surface impedance values $Z_1 = Z_2 = 300 + i30\Omega/\text{sq}$. The configuration for this material body is shown in Figure 2. The general shape of this body was chosen for what

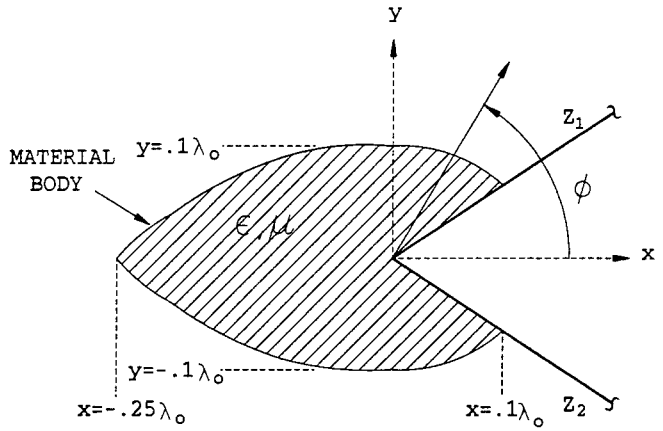

Figure 2: Configuration for an inhomogeneous, lossy material body attached to a wedge for the purpose of reducing its scattering characteristics.

would appear to be a good shape for reducing scattering and one that could easily conform to the edge of the wedge. A lossy dielectric was used where the material parameters were carefully chosen so that they would be consistent with what is physically realizable with carbon loaded microwave absorber materials. The relative permeability is $\mu_r = 1$ and two different distributions were used

for the relative permittivity: one which is homogeneous and the other which has an exponential distribution in ρ. For the homogeneous case the relative permittivity is given by $\epsilon_r = 2 + i\epsilon_r''$, and the exponential distribution is given by $\epsilon_r = 1 + (1 + ia)e^{-b\rho}$, where ρ is in wavelengths and ϵ_r'', a, and b, are real, positive parameters.

A procedure will now be introduced which will use numerical optimization to provide a means to design the distribution for the material parameters. For this procedure, the coefficients ϵ_r'', a, and b are the unknown quantities to be determined. A cost function is defined which involves determining the scattered field over a specified spatial region, and an iterative numerical optimization routine is then used to minimize the cost function. The cost function is defined as

$$F(\vec{\alpha}) = \int_{\phi_1}^{\phi_2} |U^s(\phi, \phi', \vec{\beta})|^2 d\phi, \tag{4}$$

where, in this paper, U^s is referred to as the "scattered" field (which is defined as the total field minus the incident field and the reflected fields from the wedge faces), ϕ is the observation angle, ϕ' is the incidence angle, $\vec{\beta}$ is a vector consisting of the unknown coefficients for the material profile, and the angular sector for which the cost function is minimized over is given by $\phi_1 < \phi < \phi_2$. An iterative numerical technique is then employed to minimize this cost function. For this application, it was decided to use a conjugate gradient algorithm. An initial guess for the coefficients is entered and the routine then iterates; each time incrementing the coefficients in such a way so as to minimize the gradient of the cost function. When it is felt that the routine has sufficiently converged to a minimum value for the cost function, the process is then terminated; yielding the optimum values for the coefficients of the material distribution.

For the following examples, the bistatic case was considered where the incidence angle is $\phi' = 180°$ and the specified region to minimize the scattered field is $135° < \phi < 225°$. A lossy dielectric material body, where the relative dielectric constant could be either homogeneous or have an exponential variation in ρ, was studied. The results for the TM_z case are shown in Figure 3(a). Optimization was used to obtain the material parameters ϵ_r=2+i0.676 for the homogeneous case, and a=0.669 and b=4.262 for the exponential variation. The exponential distribution provides a respectable reduction of about 25dB around endfire for the impedance wedge, as opposed to only about 6dB for the homogeneous material body. Results for the TE_z case are shown in Figure 3(b) where optimization was used to obtain the material parameters ϵ_r=2+i0.53 for the homogeneous case, and a=7.04 and b=114.6 for the exponential variation. The homogeneous material body actually increases the scattering from the wedge, which would indicate that it somehow interferes

(a)

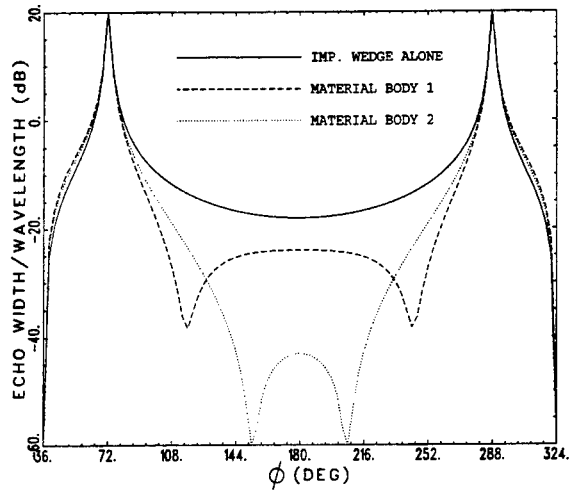

(b)

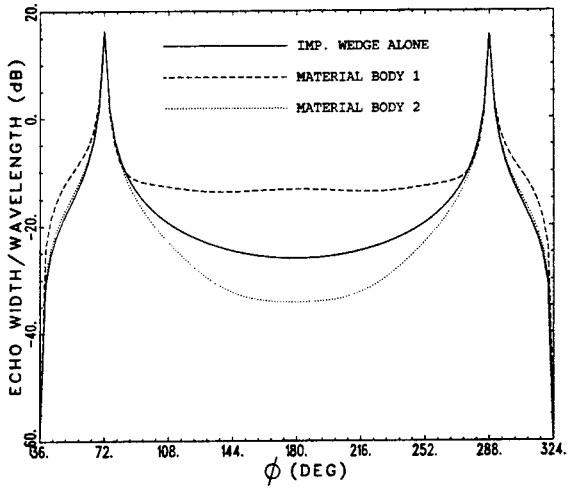

Figure 3: Bistatic echo width plots for the TM_z case (a) and the TE_z case (b) with $\phi' = 180°$ for the configuration of a lossy material body attached to an impedance wedge shown in Figure 2. For the TM_z case material body 1 is homogeneous with $\epsilon_r = 2 + i0.676$, and material body 2 has an exponential distribution in ρ with $\epsilon_r(\rho = 0) = 2 + i0.669$ (at the edge of the wedge) and $\epsilon_r(\rho = .25) = 1.34 + i0.23$ (at the tip of the material body); and for the TE_z case material body 1 is homogeneous with $\epsilon_r = 2 + i0.53$, and material body 2 has an exponential distribution in ρ with $\epsilon_r(\rho = 0) = 2 + i7.04$ (at the edge of the wedge) and $\epsilon_r(\rho = .25) = 1$ (at the tip of the material body).

with the natural scattering reduction properties of the impedance surface. As for the exponential distribution, the exceedingly large value for b causes the relative dielectric constant to decay very rapidly to 1 which would essentially concentrate the lossy material to a very small region about the edge and reducing the effectiveness of the rest of the body. This distribution only provides a slight reduction in scattering.

4. Conclusions

A method for analyzing the EM scattering from a two-dimensional complex material cylinder in the presence of an impedance wedge has been presented in this paper. A lossy dielectric material body was chosen and different profiles for the material inhomogeneities were considered. Numerical optimization was used to design the distributions for the material parameters. The results showed reasonable levels of scattering reduction are achievable with this type of configuration. The dielectric material parameters that were considered in this study were kept consistent with those that are physically realizable by typical carbon loaded microwave absorber materials. The application of a lossy material body to the edge of a wedge is an effective technique for reducing the electromagnetic diffraction from the edge.

References

[1] G.D. Maliuzhinets, "Excitation, Reflection and Emission of Surface Waves from a Wedge with Given Face Impedances," *Sov. Phys. Dokl.*, Vol. 3, pp. 752–755, 1959.

[2] R. G. Rojas, "Electromagnetic Diffraction of an Obliquely Incident Plane Wave Field by a Wedge with Impedance Faces," *IEEE Trans. Antennas Propagat.*, Vol. AP-36, No. 7, pp. 956–969, July 1988.

[3] R. Tiberio, G. Pelosi, G. Manara and P.H. Pathak, "High-Frequency Scattering from a Wedge with Impedance Faces Illuminated by a Line Source, Part I: Diffraction," *IEEE Trans. Antennas Propagat.*, Vol. AP-37, No. 2, pp. 212–218, Feb. 1989.

[4] M. F. Otero, "Radiation and Scattering from a Complex Material Cylinder in the Presence of an Impedance Wedge," Ph.D. dissertation, Dep. of Electrical Eng., Ohio State University, Columbus, 1995.

[5] J. M. Jin, V. V. Liepa, and C. T. Tai, "A Volume-Surface Integral Equation for Electromagnetic Scattering by Inhomogeneous Cylinders," *Journal of Electromagnetic Waves and Applications*, Vol 2, No. 5/6, pp. 573–588, 1988.

[6] E. H. Newman, "TM and TE Scattering by a Dielectric/Ferrite Cylinder in the Presence of a Half-Plane," *IEEE Trans. Antennas Propagat.*, Vol. AP-34, No. 6, pp. 804–813, June 1986.

REFLECTION AND DIFFRACTION OF WELL-FOCUSSED GENERAL ASTIGMATIC EM GAUSSIAN BEAMS*

G. Zogbi‡, H.T. Chou†, P.H. Pathak†, and R.J. Burkholder†

†The Ohio State University ElectroScience Laboratory
1320 Kinnear Road, Columbus, Ohio 43212

‡MIT Lincoln Laboratory, Lexington, MA 02173

I Introduction

Closed form, asymptotic high frequency expressions have been obtained for describing the reflection and diffraction of a general electromagnetic (EM) astigmatic Gaussian beam (GB) which is incident on a curved, perfectly conducting screen or reflector surface containing an edge. The incident GB can be obliquely incident on the curved edge of the reflector. In the present development, the edge of the reflector is required to lie in a plane which is oriented in a specific manner as explained below. Furthermore, it is assumed that at each point of reflection where the axis of the incident GB intersects the actual reflecting surface (or its extension if the incident GB axis misses to intersect the reflector), the actual surface can be approximated locally about that point by a second degree surface (or a paraboloid) with the same principal radii of curvature as the original surface at that point. This assumption is consistent with the usual asymptotic high frequency approximations based on the local properties of high frequency fields. Also, the surface radii of curvature are assumed to be sufficiently large and slowly varying for the high frequency assumptions to be valid. Specifically, the plane containing the edge of the reflecting surface is chosen to be parallel to the surface normal at the apex of the local paraboloidal surface. Recently, this condition has been relaxed so that the plane containing the edge can be oriented relatively arbitrarily with respect to the reflecting surface; this more recent work will be reported separately in the near future with applications of GB's to the analysis and even synthesis of large, offset fed reflector antennas. The present analysis is based on the use of the physical optics (PO) formulation which is valid for electrically large reflecting surfaces. The PO integral for the field scattered by the reflector, when it is illuminated by an incident, general astigmatic GB, is evaluated in closed form after introducing the Fresnel approximation within the integrand. For a reflecting surface with no edges, only a reflected field is predicted within this formulation; the leading term in this case can be shown within its paraxial region to behave as a reflected general astigmatic GB, whereas the additional terms include the effects of beam distortion not contained in the leading term. In practical applications, such as in the analysis/synthesis of reflector antennas, the reflecting surface contains an edge; in such cases, the incident GB can also undergo diffraction by the edge. However, since the incident GB decays exponentially transverse to the beam axis, the effects of edge diffraction become negligible if the axis of the incident GB is not

*This work reported here was supported in part by the Joint Services Electronics Program, under contract N00014-89-J-1007.

very close to the edge of the reflector. The reflection of a general, EM astigmatic GB incident on a smooth curved perfectly conducting surface is discussed first; that discussion is then subsequently followed by one on composite reflection and diffraction effects which arise when the incident beam axis is very close to an edge in the reflecting boundary. When the incident beam axis strikes the reflector such that it is not very close to the edge, then only surface reflection effects dominate and the effects of edge diffraction can be ignored.

II GB Reflection

Let a general, EM astigmatic GB be incident on a smooth perfectly-conducting surface as shown in Figure 1. Let the incident GB axis (along the $\hat{z}^i$ direction) intersect the reflecting surface at O which now constitutes the origin of the surface coordinate system (x, y, z) in which $\hat{z}$ is the unit outward normal to the surface at O. The surface at and near O can be approximated by a local paraboloid as:

$$z = -\frac{1}{2}\left[\frac{x^2}{R_1} + \frac{y^2}{R_2}\right] \tag{1}$$

Where R_1 and R_2 are the local principal surface radii of curvature of the original surface at O along the $\hat{x}$ and $\hat{y}$ directions, respectively. The magnetic field $\overline{H}^i$ associated with this incident GB is given as:

$$\overline{H}^i(x_i, y_i, z_i) = \left[\hat{x}_i H_1 + \hat{y}_i H_2\right] B(x_i, y_i, z_i) \tag{2}$$

with

$$B(x_i, y_i, z_i) = \sqrt{\frac{\rho_1^i}{z_i + \rho_1^i}}\sqrt{\frac{\rho_2^i}{z_i + \rho_2^i}} e^{-jkz_i} e^{-j\frac{k}{2}\left\{\frac{x_i^2(z_i+\rho_1^i\rho_2^i Q_{11}^i)+y_i^2(z_i+\rho_1^i\rho_2^i Q_{22}^i)+2x_iy_i\rho_1^i\rho_2^i Q_{12}^i}{(z_i+\rho_1^i)(z_i+\rho_2^i)}\right\}} \tag{3}$$

in which ρ_1^i and ρ_2^i are given by:

$$\rho_1^i = \rho_{c1}^i + jb_1^i \tag{4}$$

$$\rho_2^i = \rho_{c2}^i + jb_2^i \tag{5}$$

and also

$$\frac{1}{\rho_{1,2}^i} = \frac{1}{2}(Q_{11}^i + Q_{22}^i) \pm \frac{1}{2}\sqrt{(Q_{11}^i + Q_{22}^i)^2 - 4(Q_{11}^i Q_{22}^i - Q_{12}^i Q_{21}^i)}. \tag{6}$$

The ρ_{c1}^i and ρ_{c2}^i represent the principal radii of curvatures of the incident GB wavefront at O, and the b_1^i as well as b_2^i are related to the incident spot sizes at the waists:

$$b_1^i = \frac{k\omega_1^{i^2}}{2} \tag{7}$$

$$b_2^i = \frac{k\omega_2^{i^2}}{2}. \tag{8}$$

Finally, the c_{11}, c_{12}, c_{21} and c_{22} relate the coordinates (x^i, y^i, z^i) fixed in the incident GB to the surface coordinates (x, y, z) at O. For convenience, the origin of (x^i, y^i, z^i) is also chosen to be at O with $\hat{z}^i$ being the direction of axial propagation of the incident GB and $(\hat{x}^i, \hat{y}^i)$ being $\perp \hat{z}^i$; thus,

$$\begin{bmatrix} x_i \\ y_i \\ z_i \end{bmatrix} = \begin{bmatrix} c_{11} & c_{12} & c_{13} \\ c_{21} & c_{22} & c_{23} \\ c_{31} & c_{32} & c_{33} \end{bmatrix} \begin{bmatrix} x \\ y \\ z \end{bmatrix}. \tag{9}$$

Under the PO approximation, the reflected magnetic field, $\bar{H}^r$ can be shown to be expressed in terms of the PO integral by:

$$\overline{H}^r \cong \frac{-jk}{2\pi} \int_{-\infty}^{\infty}\int_{-\infty}^{\infty} \overline{W}(x', y') B(x', y') \frac{e^{-jkR}}{R} dx' dy' \tag{10}$$

in which (x', y', z') are the coordinates at any point on the reflecting surface (with $z' \cong -\left(\frac{x'^2}{2R_1} + \frac{y'^2}{2R_2}\right)$) and (x, y, z) are the coordinates of the observation point off the surface, and R is given as usual by:

$$R = \sqrt{(x-x')^2 + (y-y')^2 + (z-z')^2}. \tag{11}$$

Also, $\bar{W}$ in (10) is given approximately in Fresnel region by

$$\begin{aligned} \overline{W}(x', y') &= \frac{\hat{x}}{R}\left[V_z(y-y') - V_y(z-z')\right] + \frac{\hat{y}}{R}\left[V_x(z-z') - V_z(x-x')\right] \\ &\quad + \frac{\hat{z}}{R}\left[V_y(x-x') - V_x(y-y')\right] \end{aligned} \tag{12}$$

with

$$\begin{aligned} \overline{V}(x', y') &= \hat{x}\left[-W_2 + \frac{y'}{R_2}W_3\right] + \hat{y}\left[W_1 - \frac{x'}{R_1}W_3\right] + \hat{z}\left[\frac{x'}{R_1}W_2 - \frac{y'}{R_2}W_1\right] \\ &\equiv \hat{x}V_x + \hat{y}V_y + \hat{z}V_z \end{aligned} \tag{13}$$

and

$$W_1 = H_1 c_{11} + H_2 c_{21} \tag{14}$$

$$W_2 = H_1 c_{12} + H_2 c_{22} \tag{15}$$

$$W_3 = H_1 c_{13} + H_2 c_{23} \tag{16}$$

After introducing the proper Fresnel approximation in the phase terms within the integrand of (10) and replacing R by r in the amplitude terms, one obtains [1]

$$\bar{H}^r(x, y, z) \sim -\frac{jk}{2\pi}\frac{e^{-jkr}}{r}\left[\bar{W}_{00}I_{00} + \bar{W}_{10}I_{10} + \bar{W}_{01}I_{01}\right] \tag{17}$$

with

$$\overline{W}_{00} = -\hat{x}W_1\frac{z}{r} - \hat{y}W_2\frac{z}{r} + \hat{z}\left(W_1\frac{x}{r} + W_2\frac{y}{r}\right) \tag{18}$$

$$\overline{W}_{10} = \hat{x}\frac{1}{R_1}\left(W_2\frac{y}{r} + W_3\frac{z}{r}\right) - \hat{y}\frac{W_2}{R_1}\frac{x}{r} - \hat{z}\left(\frac{W_3}{R_1}\frac{x}{r} + \frac{W_1}{r}\right) \tag{19}$$

$$\overline{W}_{01} = -\hat{x}\frac{W_1}{R_2}\frac{y}{r} + \hat{y}\frac{1}{R_2}\left(W_3\frac{z}{r} + W_1\frac{x}{r}\right) - \hat{z}\left(\frac{W_3}{R_2}\frac{y}{r} + \frac{W_2}{r}\right) \tag{20}$$

$$\tag{21}$$

and

$$I_{00} = \frac{\pi}{\sqrt{a_1 a_0 - c^2}}\, e^{\frac{a_1 b_0^2 + a_0 b_1^2 - 2b_1 b_0 c}{4[a_0 a_1 - c^2]}} \tag{22}$$

$$I_{10} = \frac{\partial I_{00}}{\partial b_0} = \frac{a_1 b_0 - b_1 c}{2(a_0 a_1 - c^2)} I_{00} \tag{23}$$

$$I_{01} = \frac{\partial I_{00}}{\partial b_1} = \frac{a_0 b_1 - b_0 c}{2(a_0 a_1 - c^2)} I_{00} \tag{24}$$

where

$$a_0 = \frac{jk}{2}\left\{\frac{1}{R_1}\left(\frac{z}{r} - c_{33}\right) + \frac{1}{r}\left(1 - \frac{x^2}{r^2}\right) + c_{11}^2 Q_{11}^i + c_{21}^2 Q_{22}^i + 2c_{11}c_{21}Q_{12}^i\right\} \tag{25}$$

$$b_0 = jk\left(\frac{x}{r} - c_{31}\right) \tag{26}$$

$$a_1 = \frac{jk}{2}\left\{\frac{1}{R_2}\left(\frac{z}{r} - c_{33}\right) + \frac{1}{r}\left(1 - \frac{x^2}{r^2}\right) + c_{12}^2 Q_{11}^i + c_{22}^2 Q_{22}^i + 2c_{12}c_{22}Q_{12}^i\right\} \tag{27}$$

$$b_1 = jk\left(\frac{y}{r} - c_{32}\right) \tag{28}$$

$$c = \frac{jk}{2}\left\{c_{11}c_{12}Q_{11}^i + c_{21}c_{22}Q_{22}^i + (c_{11}c_{22} + c_{21}c_{12})\,Q_{12}^i - \frac{xy}{r^3}\right\}. \tag{29}$$

Within the paraxial approximation for (22), one obtains a reflected astigmatic GB for the first term in (17) as shown in [1]; however, the form in (22) is more accurate for this first term. The additional terms in (17) represent effects of reflected beam distortion on the reflected field; in particular,

$$I_{10} = \frac{\partial I_{00}}{\partial b_0} = \frac{a_1 b_0 - b_1 c}{2(a_0 a_1 - c^2)} I_{00} \tag{30}$$

$$I_{01} = \frac{\partial I_{00}}{\partial b_1} = \frac{a_0 b_1 - b_0 c}{2(a_0 a_1 - c^2)} I_{00} \tag{31}$$

III GB Diffraction

When the reflecting surface contains an edge, the scattered magnetic field $\bar{H}^s$ contains composite surface reflection and edge diffraction effects. Consider the special edge configuration in Figure 2 in which case the PO integral for the scattered field $\bar{H}^s$ is given by (22) but with the limits of integration on x' being from $-\infty$ to x_e instead of $-\infty$ to $+\infty$. Thus, instead of (22) one now obtains

$$\bar{H}^s(x,y,z) = -\frac{jk}{2\pi}\frac{e^{-jkr}}{r}\left[\bar{W}_{00}I^d_{00} + \bar{W}_{10}I^d_{10} + \bar{W}_{01}I^d_{01}\right] \tag{32}$$

with

$$I^d_{00} = I_{00}\frac{1}{2}\left[1 + \mathrm{erf}(z_d)\right] \tag{33}$$

in which the argument z_d of the error function is

$$z_d = \sqrt{\frac{a_0a_1 - c^2}{a_1}}\left[x_e - \frac{a_1b_0 - b_1c}{2(a_0a_1 - c^2)}\right] \tag{34}$$

and

$$I^d_{10} = \frac{\partial I^d_{00}}{\partial b_0} \tag{35}$$

$$I^d_{01} = \frac{\partial I^d_{00}}{\partial b_1} \tag{36}$$

(37)

IV Numerical Results and Discussion

In Figs. 3–5, the incident beam axis is normal to the surface at the origin and the principal beam axes line up with the principal surface directions. The edge extends past the reflection point in Figure 3 and the scattering mechanism is predominantly reflection. In Figure 4 the edge of the surface coincides exactly with the beam reflection point and the scattering is almost equally due to reflection and diffraction. The incident beam axis actually misses the surface in Figure 5; in this case the scattering is mostly due to the diffraction of the incident beam tail. Figure 6 illustrates a case where the principal beam axes are rotated 45 degrees with respect to the principal surface directions and in Figure 7 the incident beam direction makes an angle of 20 degrees with the z axis in the x–z plane. In all cases the agreement with the numerical PO integration is excellent. Figure 8 illustrates the presence of the Keller cone phenomena for beam diffraction.

This new GB technique can be employed together with an iterative algorithm to efficiently optimize the synthesis of reflector antennas for generating spot, multiple and contour beams in applications as satellite communications antennas. Such an approach would provide a useful and efficient analysis/design tool for reflector antennas [2, 3]. This GB technique is expected to be

very fast in comparison to conventional numerical PO based techniques which may take many hours of computer time when doing a reflector synthesis problem. In the proposed procedure, the feed array distribution for illuminating a parabolic reflector may be synthesized for generating multiple or contoured beams by expanding the feed radiation into a set of GB's with unknown amplitudes which then can be found by matching the resulting reflected and diffracted fields, produced by the reflector illuminated by the GB's, to the desired reflector radiation pattern. The iterative optimization algorithm may be used to find the optimal beam amplitudes, which also directly provide the corresponding fields at their launching points at the feed; i.e., they provide directly the optimal feed pattern and/or feed aperture distribution. In the case of shaped reflector synthesis for producing a contoured beam with a given feed antenna, the given feed radiation is expanded into a set of GB's with known amplitudes because the feed pattern is known in this case. The shape of the reflector can be determined by repeatedly but very efficiently bouncing (reflecting) and diffracting the GB's incident from the feed at each iteration in the optimization algorithm where the reflector shape is changed appropriately in iterative steps until the reflected/diffracted GB's produce the desired contoured beam.

References

[1] G. Zogbi, "Reflection and Diffraction of General Astigmatic Gaussian Beams from Curved Surfaces and Edges," Ph.D. dissertation, The Ohio State University, 1994.

[2] H.T. Anastassiu and P.H. Pathak, "High Frequency Analysis of Gaussian Beam Scattering by a Two-Dimensional Parabolic Contour of Finite Width," *Radio Science*, Vol. 30, No. 3, pp. 493–503, May–June 1995.

[3] R.J. Burkholder and P.H. Pathak, "Analysis of EM Penetration Into and Scattering by Electrically Large Open Waveguide Cavities Using Gaussian Beam Shooting," invited paper, *Proc. IEEE*, Vol. 79, No. 10, October 1991.

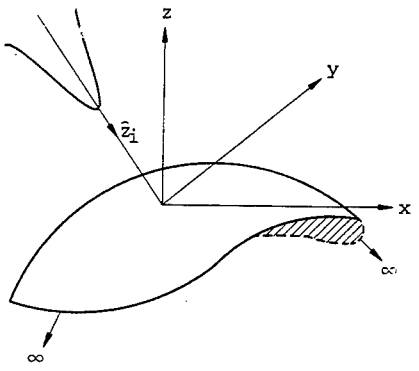

Figure 1: 3-D Gaussian beam reflection from a curved surface.

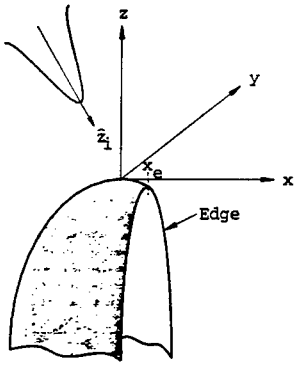

Figure 2: 3-D Gaussian beam scattering from a curved edge.

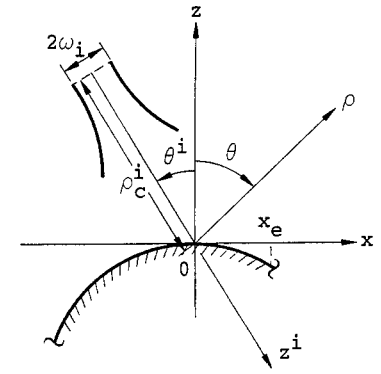

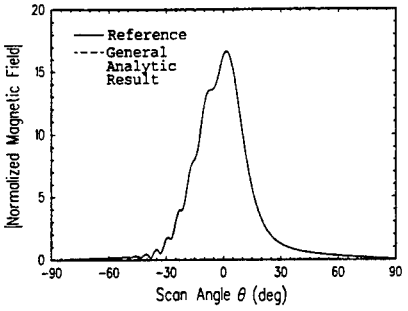

Figure 3: 3-D Gaussian beam scattering from a curved edge. Beam reflection point is on the surface. Incident beam and surface parameters: $R_1 = 50\lambda, R_2 = 60\lambda, x_e = 4\lambda, b_1^i = 15\lambda, b_2^i = 20\lambda, \omega_1^i = 2.19\lambda, \omega_2^i = 2.52\lambda, \rho_{c1}^i = 30\lambda, \rho_{c2}^i = 25\lambda, \theta_i = 0.$

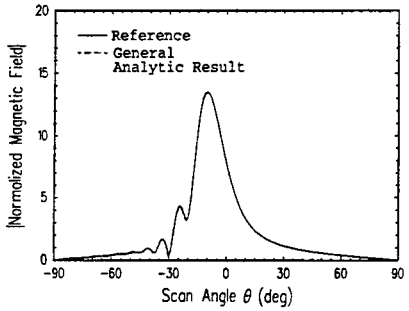

Figure 4: 3-D Gaussian beam scattering from a curved edge. Beam reflection point is on the edge. Incident beam and surface parameters: $R_1 = 50\lambda, R_2 = 60\lambda, x_e = 0, b_1^i = 15\lambda, b_2^i = 20\lambda, \omega_1^i = 2.19\lambda, \omega_2^i = 2.52\lambda, \rho_{c1}^i = 30\lambda, \rho_{c2}^i = 25\lambda, \theta_i = 0.$

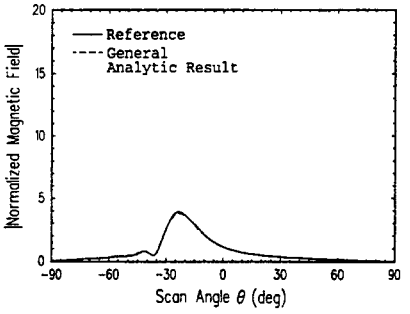

Figure 5: 3-D Gaussian beam scattering from a curved edge. Beam reflection point is off the surface. Incident beam and surface parameters: $R_1 = 50\lambda, R_2 = 60\lambda, x_e = -4\lambda, b_1^i = 15\lambda, b_2^i = 20\lambda, \omega_1^i = 2.19\lambda, \omega_2^i = 2.52\lambda, \rho_{c1}^i = 30\lambda, \rho_{c2}^i = 25\lambda, \theta_i = 0.$

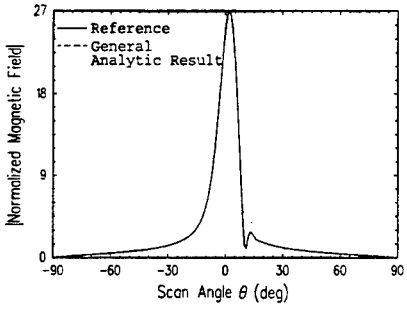

Figure 6: 3-D Gaussian beam scattering from a curved edge. Incident beam and surface parameters: $R_1 = -50\lambda, R_2 = -40\lambda, x_e = 4\lambda, b_1^i = 20\lambda, b_2^i = 40\lambda, \omega_1^i = 2.52\lambda, \omega_2^i = 3.57\lambda, \rho_{c1}^i = 25\lambda, \rho_{c2}^i = 30\lambda, \theta_i = 0$.

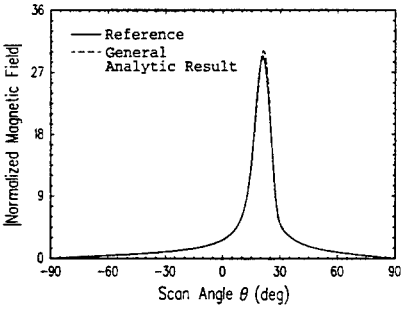

Figure 7: 3-D Gaussian beam scattering from a curved edge. Incident beam and surface parameters: $R_1 = -50\lambda, R_2 = -60\lambda, x_e = 1\lambda, b_1^i = 10\lambda, b_2^i = 40\lambda, \omega_1^i = 1.78\lambda, \omega_2^i = 3.57\lambda, \rho_{c1}^i = 25\lambda, \rho_{c2}^i = 20\lambda, \theta_i = 20°$.

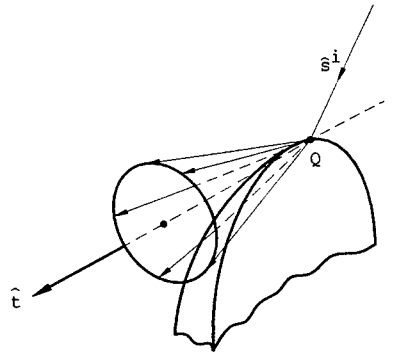

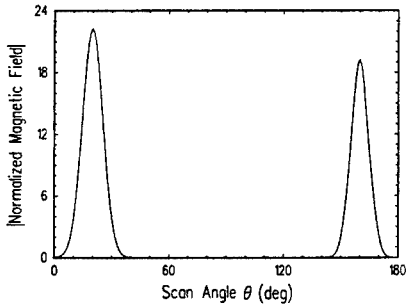

Figure 8: 3-D Gaussian beam scattering from a curved edge. Plot of total field illustrating the Keller cone. Scanning is in a plane containing the edge. Incident beam and surface parameters: $R_1 = -60\lambda, R_2 = -50\lambda, x_e = 0, b_1^i = 10\lambda, b_2^i = 30\lambda, \omega_1^i = 1.78\lambda, \omega_2^i = 3.09\lambda, \rho_{c1}^i = 25\lambda, \rho_{c2}^i = 20\lambda, \theta_i = 20°$.

POLARIZED SCATTERED LIGHT BY A SEMICYLINDRICAL BOSS ON A CONDUCTING FLAT PLANE

Hashim A. Yousif
Natural Sciences Division
University of Pittsburgh at Bradford
Bradford, Pa 16701

ABSTRACT

A brief description of the analytical solution for the scattering of electromagnetic plane waves by a semicylindrical boss of finite conductivity on a perfectly conducting flat surface is introduced. Numerical calculations for the angular distribution of the scattered intensity and the Mueller scattering matrix elements (S_{ij}) in the far field scattering region are presented. The TM and TE polarizations of the incident wave are considered. These calculations are compared with those for a lone cylinder. No similarities are noted between the scattering pattern of a boss and that of a lone cylinder with the same composition and radius.

INTRODUCTION

The analytical solution of the scattering of light by a perfectly conducting boss on a perfectly conducting surface was investigated by Lord Rayleigh[1] at the turn of this century. Since then many have extended or generalized the solution to include the general case of a boss with finite conductivity.[2] Numerical calculations for the perfectly conducting boss are limited and nonexistent for the general case. In addition, the analytical solution has not been formulated in terms of the Stokes vectors and the Mueller scattering matrix elements to the best knowledge of this author. These elements are of great theoretical and experimental importance because they measure the influence of the scatterer on the state of polarization of the incident light. There are only 8 non-zero elements for the boss problem.

This problem is important because it serves as a simplified model to study the scattering of light from a rough or imperfect surface. Clearly if the radius of the boss is zero, there will be no scattering because perfectly flat surfaces do not scatter; they only reflect. However, if the radius of the boss is not zero, the scattering of light from surface may be used as a tool to monitor and detect imperfections, roughness, or defects in that surface. This model helps achieving the previous goal by showing that light scattering signals are sensitive to the change in the radius and the material of the boss.

THE ANALYTICAL SOLUTION DESCRIPTION

A semicylindical boss of radius a on a flat perfectly conducting surface is shown in figure 1. The axis of the boss is parallel to the z axis of the cylindrical coordinate system (ρ, ϕ, z). The permittivity, conductivity, and permeability of the boss are ϵ_b, σ_b, and μ_b, respectively. The medium outside the boss is non-absorbing ($\sigma_0 = 0$) having permittivity ϵ_0 and permeability μ_0. The incident ray makes an angle

ϕ_0 with the x-axis.

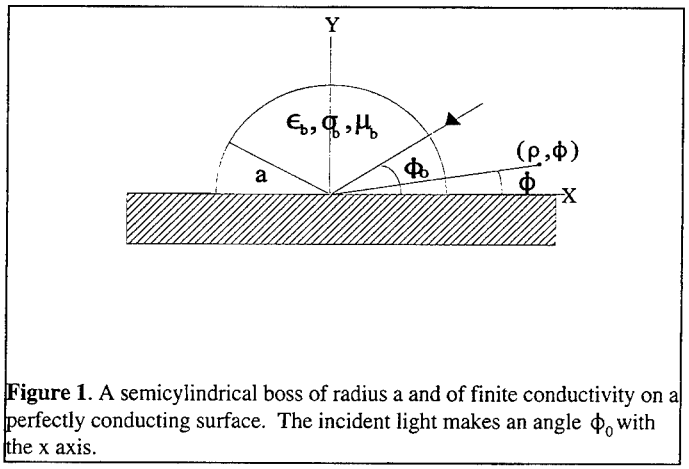

Figure 1. A semicylindrical boss of radius a and of finite conductivity on a perfectly conducting surface. The incident light makes an angle ϕ_0 with the x axis.

The analytical solution of this problem is similar to that of a lone cylinder, with the exception that the incident wave is no longer a simple plane wave but a standing wave.

A. The incident TM wave. For this case, the electric field vector of the incident plane wave is parallel to the axis of the boss. The analytical solution can be obtained by employing the image method. According to this method, the boss can be replaced by a lone cylinder and the effective incident field is composed of the actual incident field on the boss and the field reflected by the flat plane. The effective incident field for the $\exp(i\omega t)$ time dependence is:

$$E^{eff} = E_0[\exp(ik_0\rho(\phi-\phi_0)+R\exp(ik_0\rho\cos(\phi+\phi_0)], \qquad (1)$$

where E_0 is the amplitude of the incident wave, R is the reflection coefficient, whose value is -1 for this polarization, $k_0=\sqrt{\epsilon_0\mu_0}\omega$ is the wave number of the medium outside the boss.

The z component of the scattered electric field satisfies the scalar wave equation and can be written as a series solution of the Hankel functions and the scattering angle. Similarly the z component of the electric field inside the boss satisfies the wave equation and can be written as a series solution too. By applying the boundary conditions (E_z , H_ϕ are continuous at the surface of the boss), expressions for the scattering coefficients can be obtained. These coefficients are functions of the Bessel and Hankel functions and their derivatives and the electric properties of the boss and the outside medium. The wave number of the boss can be written:

$$k_b^2 = -i\mu_b\omega(\sigma_b+i\epsilon_b\omega).$$

From which the complex index of refraction of the boss can be obtained

$$N_b = \frac{k_b}{k_0}$$

B. *The TE Incident wave.* For this case the effective incident magnetic field vector is parallel to the axis of the boss. The expression for the incident magnetic field is the same as the field given by equation (1) with E_0 is replaced by the amplitude of the incident magnetic field. In addition, the value of the reflection coefficient R is one for this case.

The scattering coefficient for the TE case can be found from the TM coefficients by the use of the symmetry.

THE MUELLER SCATTERING MATRIX ELEMENTS

The expressions for the scattering amplitudes at the far field region can be obtained by replacing the Hankel functions with their asymptotic expressions. The Mueller scattering matrix elements are found from the scattering amplitudes. There are only 8 non-vanishing elements of the Mueller scattering matrix for the boss problem. In the limit $|k_0\rho| \to \infty$, these elements relate the Stokes parameters of the scattered field (I^s, Q^s, U^s, V^s) to the parameters of the incident field by [3]

$$\begin{pmatrix} I^s \\ Q^s \\ U^s \\ V^s \end{pmatrix} = \left(\frac{2}{\pi k_0 \rho}\right) \begin{pmatrix} S_{11} & S_{12} & 0 & 0 \\ S_{12} & S_{11} & 0 & 0 \\ 0 & 0 & S_{33} & S_{34} \\ 0 & 0 & -S_{34} & S_{33} \end{pmatrix} \begin{pmatrix} I^i \\ Q^i \\ U^i \\ V^i \end{pmatrix}.$$

In writing the above equation, we have used the fact that not all the Mueller scattering matrix elements are independent. The Mueller scattering matrix elements describe how the scatterer treats the various states of polarization of the incident radiation. In other words, these elements can be used to predict the state of polarization of the scattered light if the state of the incident radiation is given. These elements are measurable quantities. They can be described briefly as:

1) $S_{11}(\phi)$ represents the intensity of the scattered light if the incident intensity is unpolarized. In general, if the incident field is unpolarized, the scattered light is partially unpolarized.

2) $S_{12}(\phi)$ is the difference of the scattered intensities for the incident electric vector parallel and perpendicular to the axis of the boss. If the boss treats these two polarizations equally, this element would be zero. However, for our case, if the electric vector of the incident wave is parallel to the axis of the cylinder, the electric vector of the scattered wave is also parallel to the cylinder axis. This holds true for the other polarization. In short, the scattered and the incident beams have the same polarizations.

3) $S_{33}(\phi)$ is determined by the four combinations of illuminating the scatterer with linearly polarized beam makes an angle of $\pm 45^\circ$ with the axis of the boss and calculating the $\pm 45^\circ$ linearly polarized scattered radiation. It is important to note that if the incident light is linearly polarized at $\mp 45^\circ$ with the axis of the boss, thescattered radiation is elliptically polarized.

4) $S_{34}(\phi)$ is similar to $S_{33}(\phi)$ except the incident and the scattered beams are left or right hand circularly polarized. Also, four combinations of right and left handed circular polarizations are needed in this kind of calculation. In general, if the incident light is circularly polarized, the scattered beam is elliptically polarized.

It is important to note that the four elements are not independent. In fact they are related to each other by the following relation

$$(S_{12}(\phi)/S_{11}(\phi))^2 + (S_{33}(\phi)/S_{11}(\phi))^2 + S_{34}(\phi)/S_{11}(\phi))^2 = 1.$$

Therefore, there are only three independent elements for the boss problem. This is the same number as for a lone cylinder. The interested reader should consult the paper by Bickel.[4] That paper contains information

about determining all the sixteen elements of the Mueller scattering matrix experimentally.

COMPUTER PROGRAM

A Fortran computer program was developed to generate numerical calculations for the far field scattered intensities and the Mueller scattering matrix elements. The program first calculates Bessel functions and their various derivatives. These functions are used to compute the scattering coefficients. Once these coefficients are calculated, the Mueller scattering matrix elements and the scattered intensities are computed using a series solution. The input parameters of the program are: a) the radius of the boss; b) the refractive indices and the permeabilities of the boss and the outside medium; c) the wavelength of the incident radiation, and d) the angle of incidence. The program has been tested for wide range of the input parameters and gives accurate results.

NUMERICAL CALCULATIONS

We have generated some numerical calculations for the angular distribution of the 4 non-vanishing elements of the Mueller scattering matrix and for the far field scattered intensities. I_1 is the scattered intensity when the electric vector of the incident wave is parallel to the axis of the boss (TM) and I_2 is scattered intensity when the incident magnetic vector is parallel to that axis (the incident electric vector is perpendicular to the axis of the boss). We plotted the normalized I_1, I_2, and S_{11} as functions of the scattering angle. We have normalized the previous quantities by dividing each its maximum value. Therefore, each of these quantities is bounded between 0 and 1. The other elements (S_{12} , S_{33} , S_{34}) are normalized by dividing each of them by $S_{11}(\Phi)$ at any angle. The value of each of these elements is always between -1 and +1. The calculations were made for various values of the refractive index, the radius of the boss, and the angle of incidence (Φ_0). The medium outside the boss

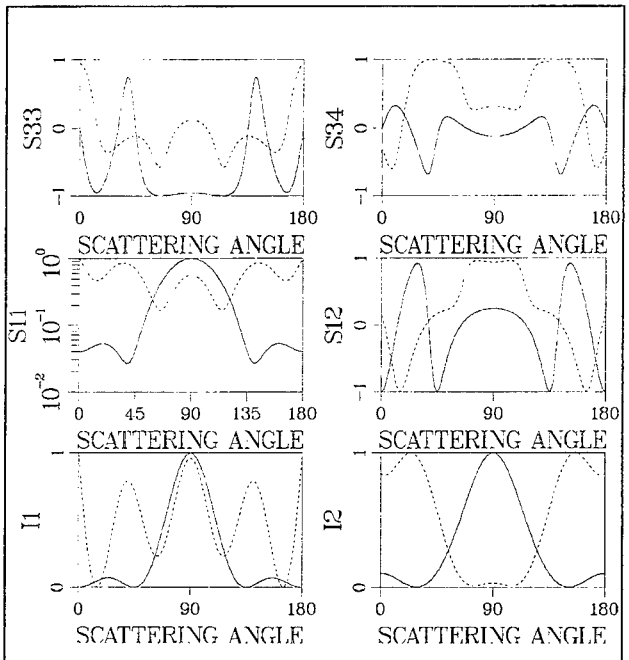

Figure. 2. S_{ij} and the normalized scattered intensities (I_1, I_2) as functions of the scattering angle (Φ). The refractive index (N_b) and size parameter ($k_0 a$) of the boss (solid line) are same as the lone cylinder (dashed line). $k_0 a$=3.14, N_b=1.6 + $i0.01$ and Φ_0=90°.

is assumed to be free space.

Figure 2 shows $S_{ij}(\phi)$ and the far field scattered intensities for a boss (solid line) and a lone cylinder (dashed line) as functions of the scattering angle. The refractive index and the radius of the boss are the same as these of a lone cylinder. The size parameter ($k_0 a$) and the refractive index are 3.14 and 1.6-i0.01, respectively, and $\phi_0 = 90°$ (the incident ray is perpendicular to the flat surface). The scatterers are assumed to be non-magnetic. As can be seen from the diagram, the scattering patterns of the boss and the lone cylinder are different. In addition, there is a noticeable difference between I_1 and I_2 of the boss; however, the difference is more pronounced for the cylinder. The scattering patterns of the boss and the cylinder are symmetric with respect to the scattering angle $\phi = 90°$ as they should be. We can draw the following important general conclusions regarding the Mueller scattering matrix elements and the scattered intensities for the boss problem:

a) $S_{12}(0) = S_{12}(180) = -1$,

b) $S_{33}(0) = S_{33}(180) = 0$,

c) $S_{34}(0) = S_{34}(180) = 0$,

d) $I_1(0) = I_1(180) = 0$.

These are not surprising results because the total electric field (incident+reflected by the flat surface+scattered by the boss) must be zero at $\phi = 0°, 180°$. We investigated this case further by varying the imaginary part of the refractive index starting with the current value of zero for this index. Initially, the diffraction pattern of the boss shows a noticeable change for a very small change in this index. However, the scattering pattern remains virtually unchanged if the index is increased beyond 20. This is again not surprising since the boss becomes totally reflecting.

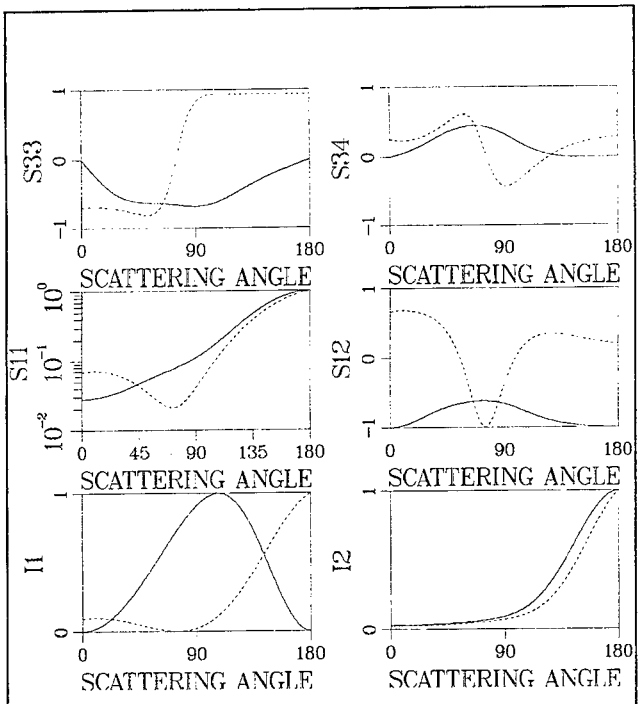

Figure 3. S_{ij} and the normalized scattered intensities for a boss (solid line) and a lone cylinder (dashed line) with the same compositions and radii. The size parameter and the refractive index of the boss are 1.5708 and 1.6, respectively. The angle of incidence $\phi_0 = 10°$

We have studied the influence of the angle of incidence on the diffraction pattern of a boss and a lone cylinder. We found that this parameter has a great effect especially for the boss. Figure 3 shows S_{ij}, I_1, I_2 as functions of the scattering angle. The size parameter and the refractive index of the boss are 1.5708 and 1.6, respectively. The angle of incidence is

$10°$. The dashed line shows the calculations for the lone. It is importrant to note that as the angle of incidence is decreased, the scattered intensity of the incident TM wave ($I_1(\phi)$) decreases and becomes smoother.

CONCLUSION

We have generated numerical data for the Mueller scattering matrix elements and the scattered intensities as functions of the scattering angle for various values of angle of incidence, refractive index, and radius of the boss. These calculations indicate that the light scattering patterns are very sensitive to small changes in the radius and the material of the boss. When the radius of the boss is small comparable to the incident wavelength, the scattering pattern is smooth. As the radius starts to grow, the pattern begins to develop structure. In addition, our calculations for the boss are compared with those of a lone cylinder. No similarities are noted between the scattered signal of a boss and that of a cylinder. This is unexpected result since the analytical solution of the boss is very similar to that of a cylinder.

REFERENCES

1. Lord Rayleigh, "On the electromagnetic theory of light, "Philos. Mag. **12**, 81-101 (1881).

2. J. R. Wait, *Introduction to Antennas and Propagation (Peregrinus, London, 1986).*

3. C. F. Bohren and D. R. Huffman, *Absorption and Scattering of Light by Small Particles* (Wiley, New York, 1983).

4. W. S. Bickel and W. M. Baily, "Stokes vectors, Mueller matrices, and polarized scattered light," Am. J. Phys. **53**, 468-478 (1985).

DIVERGENCE OF RAYS IN MODULATED ATMOSPHERIC DUCTS

I.P. Zolotarev
Institute of Terrestrial Magnetism, Ionosphere and Radio Wave Propagation (IZMIRAN), Troitsk, Moscow reg., 142092 RUSSIA.

1. Introduction.

Atmospheric ducts give an opportunity for transhorizon HF/UHF radio communication. Due to presence of atmospheric ducts the distance of radio communication can reach 2500 km. The facts of radar observation at such distances are well known. In many regions atmospheric ducts is regular phenomena. The percent incidence of ducting conditions in many regions is 40%- 80% [2], [3]. There exists a rich statistics of atmospheric ducts appearance and its parameters. To be used practically in precise radar or high quality communication systems the behavior of radio wave under different conditions in atmospheric ducts must be thoroughly investigated. The vertical structure of atmospheric ducts along distance is not stable. Many of natural processes such as different types of acoustic or gravity waves can periodically modify the vertical profile of refractive index [2]. Similar perturbations of atmospheric ducts are very essential for long distance radio wave propagation in atmospheric ducts. Even very weak perturbations can change completely the behavior of rays in duct. Space periodicity in refractive index profile along the ray path can cause fast divergence of rays in atmospheric ducts. As result the main part of rays in duct becomes mixed and the structure of receiving signal is distorted significantly. This can create a serious problems for the work of radar or wireless communication systems. From other side the weak perturbations of atmospheric parameters can lead to creation of a set of additional subducts that can trap a part of rays increasing so the total range of radio communication.

For investigation of ray propagation in modulated atmospheric ducts a special Duct Radio Wave Propagation (DRWP) program was developed. It allows to receive phase portrait of ray propagation in ducts and determine ray divergence and phase shift of radio waves.

2. Ray approximation.

In many cases the radio wave propagation in ducts can be described using approximation of geometric optics. In approach of geometric optics the optical length of path for valid ray must be minimal. This means that the variation of action S for valid path must be equal to zero

$$\delta S = 0 \qquad (2.1)$$

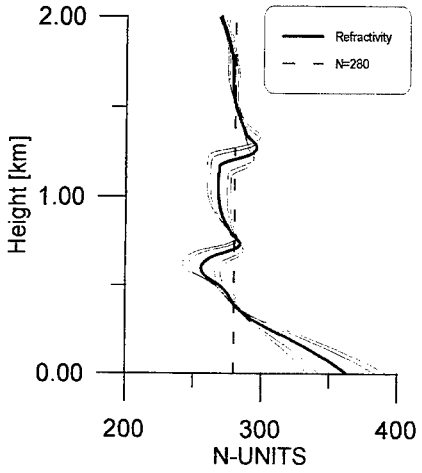

Figure 1. Refractivity profile of surface based duct.

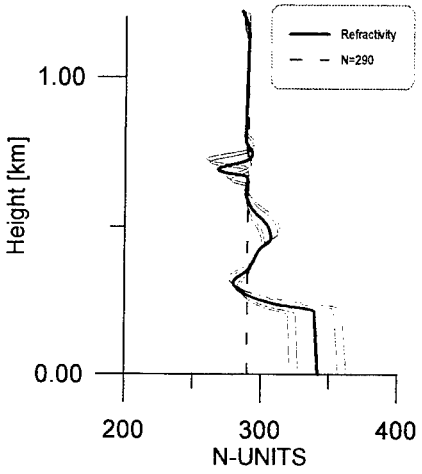

Figure 3. Refractivity profile of elevated duct.

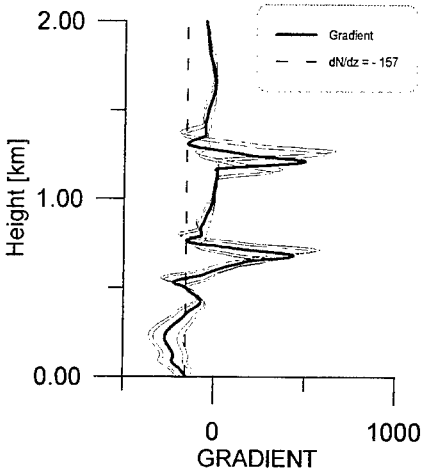

Figure 2. Refractivity gradient of surface based duct.

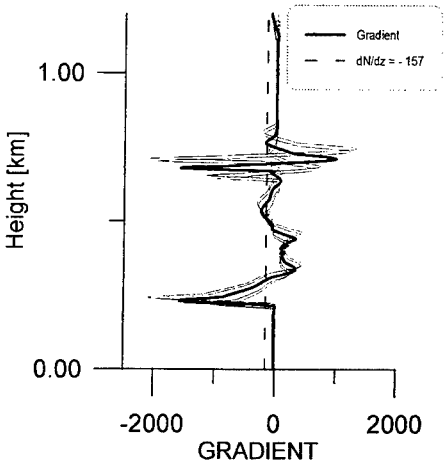

Figure 4. Refractivity gradient of elevated duct.

Action S can be expressed in the form

$$S = \int_P^Q L dt = \int_P^Q \frac{n^2\left(1+\frac{x_1}{R_E}\right)}{\sqrt{n^2-x_2^2}} dt \tag{2.2}$$

where $t = R_E\theta$ - parameter along the path (θ- angle in the plane of great circle), x_1- height above the earth, P and Q are the beginning and ending points of the ray path, R_E - radius of the Earth, n - radio refractive index, x_2 - impulse, $x_2 = n\sin\alpha$, α - angle of ray inclination to the Earth. The altitude - impulse variables (x_1, x_2) satisfy to Hamilton equations and describe completely the behavior of rays in ducts [6]. For ray propagation in duct with slowly changing along path refractive index profile there exists the ray adiabatic invariant

$$I = \oint x_2 dx_1 = const \tag{2.3}$$

DRWP program solves the Hamilton equations that define the evolution of variables (x_1, x_2), draw ray propagation phase portrait and calculate phase shift and space coordinates of rays.

3. Radio wave propagation in atmospheric ducts.

Very often ray tracing and predicting programs use different analytical or semi empirical models of refractive index. As input these models can use several (5-15) points of refractive index obtained from measurement. For short distance of 1-3 ray hops in duct this gives a good result in evaluation of field strength and ray tracing. For larger distances it is necessary to use more detailed structure. DRWP program allows to use all information about refractive index structure along the ray path without any restriction. The examples of two used for calculation refractive index profiles are presented in Figures 1,3. The refractivity profile in Figure 1 corresponds to the surface based duct and is typical for region in vicinity of Pt. Mugu, CA [4]. The height gradient of that profile is presented in Figure 2. The refractivity profile in Figure 3 corresponds to the elevated duct and is typical for San Diego region [1]. The corresponding height gradient of profile is presented in Figure 4. The numerical value of height gradient of refractive index profile determines the directions of ray propagation and zones where rays can be trapped in ducts. If the vertical gradient of radio refractive index is negative and less then -157 N units/km the rays bend downward to the earth [5]. It is the regions where ducting is possible.

During calculations the weak periodical perturbations were superimposed on background refractive index profile. The resulting variations of refractive index profile and its gradients are represented in Figures 1-4 as thin curves. Results of calculations for different conditions are represented as phase portraits in Figures 5-8.

The ray propagation phase portrait in unperturbed duct for refractivity profile shown in Figure 3 is represented in Figure 5. The height gradient of refractivity profile (thick curve in Figure 2) has two regions where the numerical value of gradient is less then -157 N units/km. In accordance with Figures 1,3 the phase portrait in Figure 5 has two regions with trapped rays. The first is surface based duct in which the rays reflect from the earth. The second is elevated subduct. The rays propagate in it not touching the earth. From Figure 2 it is seen that gradient of background refractive profile has two regions where the numerical value of gradient is near the critical value of

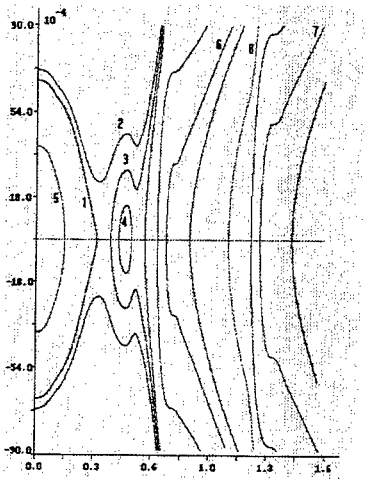

Figure 5. Phase portrait of surface based duct.

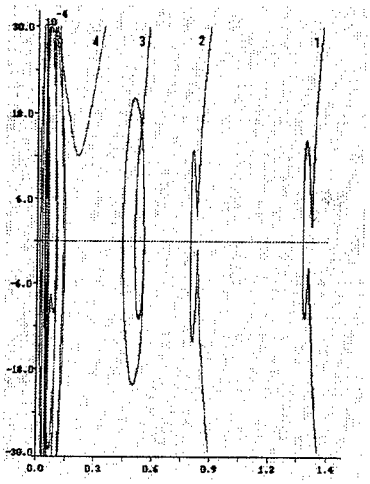

Figure 6. Subducts.

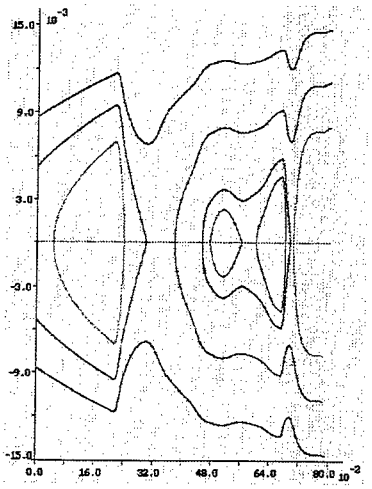

Figure 7. Phase portrait of elevated duct.

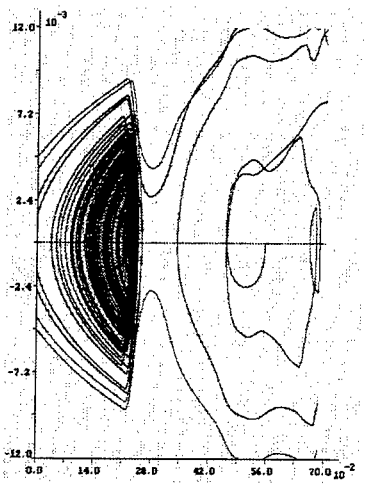

Figure 8. Phase portrait of modulated duct.

-157 N units/km. In the absence of perturbation no duct exists at these heights (Figure 5). But during modulation of refractive index the gradient can become slightly less then -157 N units/km (thin curves in Figures 1,3). This leads to arising of additional two subducts that can trap rays. The examples of rays trapped in these additional elevated subducts are shown on phase portrait in Figure 6.

The phase portrait of ray propagation for refractive index structure shown in Figure 3 is represented in Figures 7,8. Figure 7 corresponds to unperturbed duct while Figure 8 corresponds to periodically modulated duct. In the absence of disturbances the total phase space (Figure 7) consists of non intersecting separate curves. Each curve corresponds to the separate ray path. It is seen that the duct has complex thin structure. One part of rays propagate in upper system of elevated subducts. Another part of rays propagate in elevated duct near the earth and can periodically reflect from the earth.

Evolution of several rays in modulated duct is shown in Figure 8. The single ray in modulated duct can fill in the whole area in the phase portrait. These are regions with fast ray divergence. For a great part of rays it is possible only temporal trapping in duct because of fast divergence. Comparison of phase portrait in Figures 7,8 shows that the upper system of elevated subducts is destroyed due to perturbation of refractive index profile.

4. Divergence of rays in periodically modulated ducts.

The velocity of ray divergence is a very important factor to be taken into account under elaboration of different radio communication systems. To investigate the ray divergence in ducts the paths of several close rays for profile shown in Figure 3 were tracked. An example of ray trace in periodically modulated duct is represented in Figure 9. A part of the same ray trace in unperturbed duct is shown in Figure 10. In unperturbed duct the ray performs regular sine like oscillations (Figure 10) while in modulated duct the form of oscillations is rather complicated (Figure 9).

Phase shift of radio waves in duct is proportional to optical length of their ray paths. The absolute values of refractive index variations for radio waves are very small. For all rays in narrow beam the optical length of path is almost the same. Plots of optical length for ray in narrow beam as in modulated and unperturbed ducts lie almost on the same straight line (Figure 12). In unperturbed duct narrow beam remain to be narrow at all the range. In modulated duct because of the rapid divergence of rays the beam widens quickly and rays fill in all space in duct. Straight line in Figure 12 illustrates the fact that the ray adiabatic invariant (2.3) is approximately constant for close rays in duct although the ray traces can differ significantly. Radio waves propagating in modulated duct have almost the same phase shift as in unperturbed duct. In more detail scope there exists difference in optical length for rays in perturbed and unperturbed ducts. In relative units the difference in optical length for close rays is represented in Figure 11. The straight lines 4,5 in Figure 11 correspond to two initially close rays in unperturbed duct. The difference in optical path for them is very small. These rays continue to be close during all the range. Curves 1,2,3 in Figure 11 correspond to rays in narrow beam that propagate in modulated duct. They have oscillating character. This means the receiving signal will have additional oscillations too. The difference in optical length for rays in modulated duct is far more than for rays in unperturbed duct. In modulated duct the divergence of rays is almost in 50 times more than in unperturbed duct. At long distances the absolute value of optical length for rays propagating in modulated

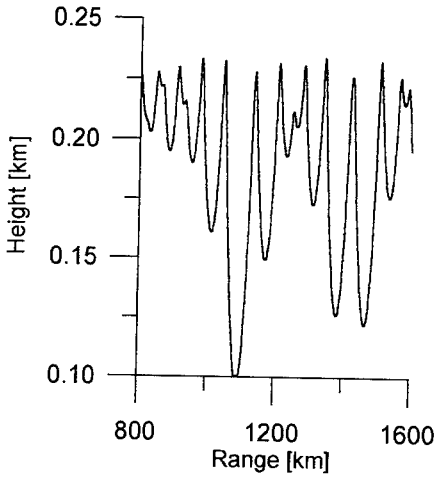

Figure 9. Ray trace in modulated duct.

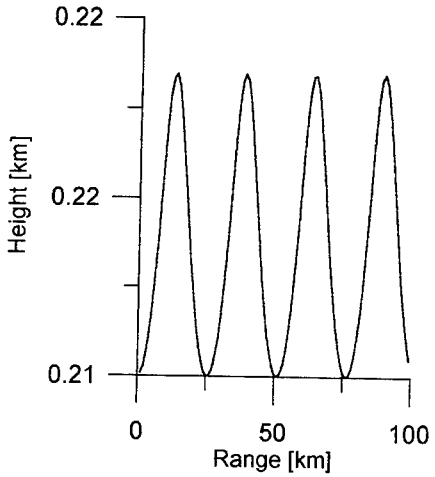

Figure 10. Ray trace in unperturbed duct.

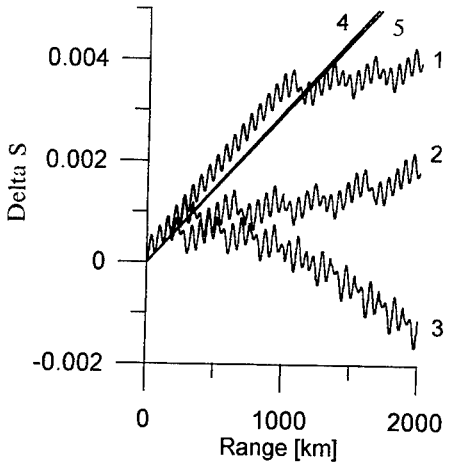

Figure 11. Diffrence in optical length for close rays.

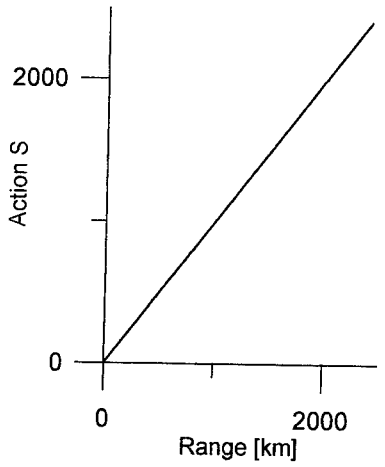

Figure 12. Optical length of rays in modulated duct.

duct is less than in unperturbed duct. It is connected with the fact that in modulated duct rays penetrate in the regions where the refractive index has less value and propagate there for a lot of time. Meantime the path length of rays in modulated duct is more than for rays in unperturbed duct.

In spite of small value of periodical perturbations of atmospheric ducts they can change significantly the propagation of radio waves. Ray divergence in periodically modulated duct can be very large. At distance of about 100 km the height difference between two initially close rays can reach full height thickness of duct. This makes difficult the restoring of images in radar observation systems. Another effect is connected with additional phase shift of radio waves in modulated ducts. For close rays propagating in modulated duct the phase shift can reach critical value at distance of 20 km for frequency 1.4GHz. After this distance the work with devices based on phase methods can faced with problems. In unperturbed ducts the critical length is about 1000 km, that is enough for many of applications.

5. Summary.

DRWP program was elaborated specially to investigate radio wave propagation in atmospheric ducts. The results of calculations are represented as ray propagation phase portraits. The phase portraits give explicit picture of regions were ducting is possible and allow to estimate and predict radio wave propagation in atmospheric ducts under different real natural conditions. DRWP program tracks rays in modulated duct and calculates ray divergence and phase shift of radio waves. It allows to to estimate the range of radio communication in modulated ducts and conditions under which the ducting is possible.

References

[1] Gossard, E.E. (1981), Clear weather meteorological effects on propagation at frequencies above 1 GHz, *Radio Sci.*, **16**, N5, 589-608.

[2] Crane, R.K. (1981), A review of transhorizon propagation phenomena, *Radio Sci.*, **16**, N5, 649-669.

[3] Helvey, R.A. (1994), Diurnal Variation in Oceanic Elevated Ducting, Beyond Line-Of-Sight Conference, session 5, 2-4 august, Austin, Texas, 1-7.

[4] Philbrick, C.R., Blood, D.W. (1994), Refractive Propagation Effects measured by Lidars, Beyond Line-Of-Sight Conference, session 4, 2-4 august, Austin, Texas, 1-21.

[5] Stephansen, E.T. (1981), Clear-air propagation on line-of-sight paths: A review, *Radio Sci.*, **16**, N5, 609-629.

[6] Zolotarev I.P. (1994), Effects of periodical modulation of atmospheric ducts on propagation of UHF/VHF waves, Beyond Line-Of-Sight Conference, session 8, 2-4 august, Austin, Texas.

DIFFRACTION BY A WEAK DIELECTRIC WEDGE

Alexei V.Popov

Institute of Terrestrial Magnetism, Ionosphere and Radiowave Propagation
Troitsk, Moscow region, Russia

Abstract

An approximate description of the plane wave diffraction by a dielectric wedge with small refractivity and absorption is found using the parabolic equation method.

Diffraction by dielectric wedge remains to be one of the most intriguing problems of the linear wave theory due to its deceiving simplicity and numerous technical applications. It serves as a key problem for any diffractive element containing grooves, strips or abrupt edges. Novel technologies (subsurface radio sounding,optical microlithography, X-ray imaging optics etc.) demand a very accurate determination of the wave field distribution near the features under investigation. It stimulates the search of new analytical and numerical solutions of this classical but still unsolved problem [1].

Here, we consider an important particular case of a rectangular dielectric wedge illuminated by a plane wave impinging its face normally, with zero angle of incidence. It is assumed that the dielectric material is characterized by weak refraction and absorption: $n = \sqrt{\varepsilon} = 1 + \alpha + i\beta$, $|\alpha, \beta| << 1$ (it depends on its structure and chemical content but it is always true for EM waves of the extreme UV and X-ray spectral band). Under these assumptions, one can separate the diffraction phenomena occurring at both wedge faces: the incident wave enters the dielectric medium trough its front side practically unperturbed, with a small reflection coefficient, and propagates along the second interface with small but noticeable absorption and with phase velocity different from the free-space light velocity. If one uses the geometric optics approximation, a gradually growing discontinuity arises between this wave and its free-space counterpart propagating outside the dielectric wedge. Diffraction matches these two waves, and this effect can be described separately from the wave phenomena occurring at the front side. This simplifies the analytical technique and allows one to obtain an exact solution of our simplified problem.

Let the dielectric material fill the quadrant $0 < \varphi < \pi/2$ of the cross-section plane $z = r\cos\varphi$, $y = r\sin\varphi$. Under the condition $|\varepsilon - 1| << 1$, we can use the paraxial Ansatz

$$E_x(z, y) = u(z, y)\exp(ikz - iwt) \tag{1}$$

for a wave packet propagating along z-axis which leads to a pair of parabolic equations

$$\begin{array}{ll} 2ik\frac{\partial u}{\partial z} + \frac{\partial^2 u}{\partial y^2} + k^2(\varepsilon - 1)u = 0, & y > 0 \\ 2ik\frac{\partial u_0}{\partial z} + \frac{\partial^2 u_0}{\partial y^2} \quad , & y < 0 \end{array} \tag{2}$$

describing the wave field on both sides of the interface $y = 0$, $z > 0$ [2]. The reflected wave for $z < 0$ is determined by the small Fresnel reflection coefficient $R = (1 - \sqrt{\varepsilon})/(1 + \sqrt{\varepsilon}) << 1$ and can be neglected. The transmission coefficient $T = 2/(1 + \sqrt{\varepsilon}) \approx 1$, consequently, to the first approximation, the initial condition can be written as

$$\begin{array}{ll} u(0, y) = 1, & y > 0 \\ u_0(0, y) = 1, & y < 0 \end{array} \tag{3}$$

The matching conditions at the interface $y = 0$ (continuity of E_x and H_z) resulting in

$$\begin{array}{l} u(z, 0) = u_0(z, 0) \\ \frac{\partial u}{\partial y}(z, 0) = \frac{\partial u_0}{\partial y}(z, 0) \end{array} \tag{4}$$

and some radiation condition excluding waves coming from $y = \pm\infty$ must be added to complete the boundary value problem formulation [3].

An exact solution of Eqs.(2)-(4) can be found in the form of Laplace transform:

$$u(z, y) = \frac{1}{2\pi i} \int\limits_{c-i\infty}^{c+i\infty} e^{pz} U(p, y) dp \tag{5}$$

Substitution into (2) yields a pair of ordinary differential equations

$$\begin{array}{ll} \frac{\partial^2 U}{\partial y^2} + [2ikp + k^2(\varepsilon - 1)]U = 2iku(0, y), & y > 0 \\ \frac{\partial^2 U_0}{\partial y^2} + 2ikpU_0 = 2iku_0(0, y) \quad , & y < 0 \end{array} \tag{6}$$

Their solutions satisfying the matching conditions (4) and bounded at infinity are

$$\begin{array}{l} U(p, y) = \frac{2ik}{q^2}\left[\left(\frac{q}{q_0} - 1\right) e^{iqy} + 1\right] \\ U_0(p, y) = \frac{2ik}{q_0^2}\left[\left(\frac{q_0}{q} - 1\right) e^{-iq_0 y} + 1\right] \end{array} \tag{7}$$

with $q = \sqrt{2ikp + k^2(\varepsilon - 1)}$, $\quad q_0 = \sqrt{2ikp}$.

Substitution into the Laplace integral (5), after deformation of the integration path and the change of variables $p = -t^2/z$, yields

$$u_0(z, y) = \frac{1}{2\pi i} \int\limits_{\Gamma} e^{pz} U_0(p, y) dp = 1 + \frac{1}{\pi i} \int\limits_{-\infty-ic}^{\infty-ic} \left(\frac{1}{\sqrt{t^2 - \gamma^2}} - \frac{1}{t}\right) \exp\left(-t^2 - 2t\eta e^{i\pi/4}\right) dt. \tag{8}$$

Here, the dimensionless parameters $\eta = |y|\sqrt{k/2z}$ and $\gamma = \sqrt{kz(\varepsilon - 1)/2i} \approx \sqrt{kz(\beta - i\alpha)}$ are introduced. This expression can be decomposed into the sum

$$u_0(z, y) = \Phi(\eta) + \Psi(\eta, \gamma) \tag{9}$$

of the Fresnel integral

$$\Phi(\eta) = 1 - \frac{1}{\pi i} \int\limits_{-\infty - ic}^{\infty - ic} \exp\left(-t^2 - 2t\eta e^{i\pi/4}\right) \frac{dt}{t} = \frac{2}{\sqrt{\pi}} e^{-i\pi/4} \int\limits_0^{\eta} e^{i\zeta^2} d\zeta \tag{10}$$

and another special function

$$\Psi(\eta, \gamma) = \frac{1}{\pi i} \int\limits_{-\infty - ic}^{\infty - ic} \exp\left(-t^2 - 2t\eta e^{i\pi/4}\right) \frac{dt}{\sqrt{t^2 - \gamma^2}} \tag{11}$$

The first term $\Phi(\eta)$ is generic for all the edge diffraction problems. The second term $\Psi(\eta, \gamma)$ depends on the material properties α and β modifying the simple Fresnel diffraction pattern in the penumbra region. At the interface $y = 0$, it can be reduced to the modified Bessel function:

$$\Psi(0, \gamma) = \frac{1}{2\pi} \int\limits_{-1}^{1} e^{-\gamma^2 s^2} \frac{ds}{\sqrt{1 - s^2}} = e^{-\gamma^2/2} I_0\left(\frac{\gamma^2}{2}\right). \tag{12}$$

Quite similarly, in the upper quadrant $z > 0, \quad y > 0$ (inside the dielectric wedge), the solution (5), (7) can be expressed in terms of the Fresnel integral and the Ψ-function:

$$u(z, y) = \frac{1}{2\pi i} \int\limits_{\Gamma} e^{pz} U(p, y) dp =$$

$$e^{-\gamma^2} \left[1 + \frac{1}{\pi i} \int\limits_{-\infty - ic}^{\infty - ic} \left(\frac{1}{\sqrt{t^2 + \gamma^2}} - \frac{1}{t}\right) \exp\left(-t^2 - 2t\eta e^{i\pi/4}\right) dt\right] =$$

$$e^{-\gamma^2} [\Phi(\eta) + \Psi(\eta, i\gamma)] \tag{13}$$

In virtue of (12), formulae (8) and (13) coincide at the interface $u = 0$. Taken together, they provide continuous matching of two plane waves propagating, accordingly, in free space and the dielectric body with different phase velocities and absorption. They describe a joint effect of transversal diffusion [3], edge diffraction and surface refraction forming a rather complicated field distribution near the interface $y = 0$.

Asymptotic evaluation of the integrals (8) and (13) yields approximate formulae consistent with geometrical theory of diffraction [4]. The off-integral terms correspond to the unperturbed plane waves $\exp(ikz)$ and $\exp(ikz - \gamma^2) = \exp[ikz(1 + \alpha + i\beta)] = \exp(iknz)$ inside in free space and the dielectric wedge.

Generally, the main contribution into the integrals (8) and (13) is given by the saddle point $t = -\eta e^{i\pi/4}$. The corresponding exponential $\exp(i\eta^2) = \exp(iky^2/2z)$ after multiplication by the rapidly oscillating factor $\exp(ikz)$, yields the edge wave with the approximate eikonal

$$S_{edge} = \begin{cases} z + y^2/2z \approx \sqrt{z^2 + y^2}, & y < 0 \\ z(1 + \alpha - i\beta) + y^2/2z \approx n\sqrt{z^2 + y^2}, & y > 0. \end{cases} \tag{14}$$

By deformation of the integration path to the steepest descent path $Imt = -\frac{\eta}{\sqrt{2}}$, one of the branch points $t = \pm\gamma$ in (8) and $t = i\gamma$ in (13) may be crossed. Integration around the cut between the branch points gives a contribution corresponding to the "head wave" propagating along the wedge side $y = 0$ in the medium with maximum phase velocity (vacuum or dielectric, depending on the sign of α) and leaving the interface at the angle of total reflection. The most pronounced effect is observed if the absorption is small: $\beta << \alpha$. In this case, the head wave exists in the sector $0 < y < z\sqrt{2\alpha}$ inside the dielectric wedge for $\alpha > 0$ (this is typical for radio- and optical frequences) and in the free-space sector $-z\sqrt{-2\alpha} < y < 0$ for $\alpha < 0$ (in the extreme UV and X-ray spectral region). The corresponding eikonals are $S^{+}_{head} \approx z + y\sqrt{2\alpha}$ and $S^{-}_{head} \approx z(1+\alpha) - y\sqrt{-2\alpha}$. Interference of the head wave, within the domain of its existence, with the unperturbed plane wave and the edge wave results in a rather complicated field distribution with maxima higher than in the case of Fresnel knife-edge diffraction. This effect has been revealed in numerical modeling of thick Fresnel zone plates [5].

This work has been supported in part by the Russian Basic Research Foundation, Grant No 95-05-14027.

REFERENCES

1. Borovikov V. and Budaev B., 1994, "Diffraction by Wedge-shaped Insertion and by Cone of Arbitrary Cross-section" (in Russion),
Proc. 10th School-seminar on Wave Diffraction and Propagation, 66-95.

2. Popov A. and Popova M., 1971, "Diffraction Losses of Dielectric Open Cavity" (in Russian), Radiotekhnika i Electronika, 16, 2175-2181. UV", J.Opt.Soc.Am., 64, 301-309.

3. Malyuzhinets G., 1959, "Progress in Understanding Diffraction Phenomena" (in Russian), Soviet Phys. (Uspekhi),

4. Borovikov V. and Kinber B, Geometrical Theory of Diffraction, IEE, London, 1994.

5. Kopylov Yu., Popov A., Vinogradov A., 1995, "Application of the Parabolic Wave Equation to X-ray Diffraction Optics", Optics Comm., 118, 619-636

FAR FIELD DIFFRACTION EFFECTS OF EUV FRESNEL ZONE PLATES

Yu.V.Kopylov, V.A.Baranov, A.V.Popov, and A.V.Vinogradov[1]

Institute of Terrestrial Magnetism, Ionosphere and Radio Wave Propagation
Russian Academy of Sciences, 142092 Troitsk, Moscow region, Russia
[1] *Lebedev Physical Institute, Russian Academy of Sciences, 117924 Moscow, Russia*

Introduction

Fresnel zone plates, being the main elements of X-ray and EUV transmission imaging optics, are very fine and expensive objects. They require accurate design and high precision manufacturing to achieve desirable performance. For testing their quality and final alignment of the optical system, special methods and experimental facilities are being developed. The straightforward measurement of the wave field near the focal plane is difficult due to microscopic size of the zone plate, small focal length (about 1 mm) and submicron spatial resolution. Instead, information about the wave front structure and aberrations is obtained from the far field ($z \sim 10cm$) measurements [1].This introduces new problems as the relation between the far and near fields is not described by simple formulae of geometric optics and requires accurate diffraction calculations.

The objective of this paper is to simulate and theoretically investigate the far-field intensity and phase distribution produced by realistic EUV Fresnel zone plates and their idealized models. Such theory is necessary for adequate interpretation of the observed diffraction patterns and helps one to distinguish between the fundamental diffraction effects and the aberrations introduced by manufacturing and alignment errors.

1.Numerical modeling of the far-field intensity distribution in EUV interferometry experiments

We used L-3 computer code developed at Moscow X-ray Optics Group to simulate the far-field EUV light intensity distribution observed in the point diffraction interferometry experiments [1]. The mathematical basis of the L-3 code is described in [2]. Here we present some results of straightforward field calculation for a realistic Fresnel zone plate (ZP) with the parameters close to [1], for an idealized thin Fresnel ZP and for a model perfect lens of the same optical parameters. Our main goal was to understand the nature of the intensity modulation of the far-field radiation patterns produced by the zone plates tested in [1]. Two hypotheses has been considered:

1. Two-scale quasiperiodic intensity modulation arises in the near field of the ZP due to resonance effects inside it [3] and is transferred into the far zone according to the laws of geometric optics;

2. This intensity modulation is caused by Fresnel diffraction of the ZP first-order spherical wave by the order sorting diaphragms.

We also had in mind that the observed effects might be caused by random manufacturing errors of zone positioning.

In order to verify these hypotheses we reproduced numerically the experimental setup: a thick

zone plate of external radius $r_N = 96\mu m$ composed of N = 640 alternative opaque zones and vacuum spacings is illuminated by EUV plane wave radiation with $\lambda = 13.5nm$. The refraction and absorption constants of the material (Ni) are $\delta = 0.138$, $\beta = 0.031$ at this wavelength. The zone plate thickness is $t = 200\,nm$, and the outer zone width is $dr_N = 75\,nm$. The diaphragms used are: central stop (CS) of radius $r_{cs} = 48\,\mu m$ and order sorting aperture (OSA) of $r_{OSA} = 24.3\,\mu m$ placed at $z_{OSA} = 0.8\,mm$ from the ZP (the focal distance at this wavelength is $f = 1.1\,mm$).

The global diffraction field distribution has been calculated via numerical integration of the parabolic wave equation [2] beginning from the front side of the zone plate up to the range $z = 1.8\,mm$ ($0.7\,mm$ behind the focus) where a steady far-field radiation pattern is already formed. In some calculations, an additional diaphragm in the focal plane was introduced in order to simulate the effect of knife-edge diffraction.

Consider the numerical results. In Fig.1a, radial amplitude and phase distribution over the back side of the zone plate is plotted (its fragment centered at the CS edge is shown in Fig.1b). After removing the sharp oscillations due to edge diffraction at the interfaces [3], it reproduces with enough accuracy the ZP transmission function calculated in Kirz's approximation [4]

$$T(r) = \begin{cases} \exp(-ik\delta - k\beta)\,t & for \quad r_{2n-2} < r < r_{2n-1}, \\ 1 & for \quad r_{2n-1} < r < r_{2n}, \quad n = N_o, \ldots, N \end{cases}$$

-see Fig.2a,b. This calculation proves that in our case there is no pronounced intensity modulation at the ZP output and the first hypothesis must be rejected.

The next pictures (see Fig.3) show the far-field amplitude distribution across the illuminated ring $r \sim 30 - 60\,\mu m$ at the distance $z = 1.8\,mm$ from the ZP. Here, two scales of radial amplitude variation are clearly seen: a very fast oscillations looking as a projection of the ZP transmission function and a broader modulation resembling classical Fresnel diffraction patterns. Their superposition produces a complex chaotic quasiperiodic pattern with up to 30% amplitude modulation consistent with the experimental results [1]. It must be stressed that no zone positioning error had been introduced into the computational model. Even the idealized infinitely thin Fresnel zone plate displays the same far-field radiation pattern (with a smaller peak amplitude due to different diffraction efficiency) - see Fig.4.

So the two-scale far field intensity modulation observed in [1] is an intrinsic feature of the ZP diffraction field though the nature of these two scales is apparently different.

In order to separate these effects we performed calculation of the wave field produced by a model perfect lens of the same diameter and focal length. The same optical scheme (CS + OSA) has been modeled. Fig.5 shows the far-field radial distribution over the illuminated region at the range $z = 1.8\,mm$.

We see that the short-period oscillations have disappeared while the slower modulation remains (some high-frequency "noise" is present in the outer part of the illuminated ring which is due to knife-edge diffraction caused by a diaphragm put in the focal plane). Generally, large-scale features of the far field amplitude distribution for the ZP and for its equivalent lens are similar (number of peaks about 20, modulation depth about 20% in amplitude or 40% in intensity) The main difference is less regular but more stochastically uniform distribution of the peak amplitudes in the former case. Nevertheless, the lens model may be quite useful for a rough prediction of the ZP far field structure. Below, in Section 2, we derive a simple analytical formula describing this effect as a result of edge diffraction by the central stop and OSA.

2. Diffraction of convergent spherical wave by annular aperture

Let $\zeta(\rho) = f - \sqrt{f^2 - \rho^2}$ be a convergent spherical wave front produced by a lens of focal length f - see Fig.6. Suppose that it is partly blocked by a diaphragm and a central stop of corresponding angular radii $\beta = B$ and $\beta = A$. We are interested in spatial distribution of light intensity in the far zone at ranges $z \geq f$.

Following Debye's classical analysis - see [5] we use the Kirchhoff diffraction integral

$$E(P) \approx \frac{E_0}{i\lambda} \iint \frac{e^{ikR}}{R}\, dS = E_0 \frac{f^2}{i\lambda} \iint \frac{e^{ikR}}{R}\, d\Omega \tag{1}$$

over the open portion of the initial wave front. Here, $R(P,Q)$ is the distance between the observation and integration points $P(z,r,\varphi)$ and $Q(\zeta,\rho,\psi)$, $\lambda = 2\pi/k$ is the wavelength.

In polar coordinates centered at the focal point $z = f$:

$$\begin{aligned} r &= h sin\theta, \quad z = f + h cos\theta \\ \rho &= f sin\beta, \quad \zeta = f(1 - cos\beta) \end{aligned}$$

the optical path R takes the form

$$\begin{aligned} R &= \sqrt{(r cos\varphi - \rho cos\psi)^2 + (r sin\varphi - \rho sin\psi)^2 + (z - \zeta)^2} = \\ &= \sqrt{h^2 + f^2 + 2hf[cos\theta cos\beta - sin\theta sin\beta cos(\varphi - \psi)]} \end{aligned} \tag{2}$$

In our case, $\lambda \sim 10\,nm$, $f \sim 10^6\,nm \gg \lambda$. Unlike [5], we do not consider the observation point P being close to the focus. On the contrary, we suppose $h \sim f$ whereas the polar angles β, θ are small due to limited numerical aperture $A, B \leq 0.1$. Neglecting the terms of the order of magnitude $O(\beta^4 + \beta^2\theta^2 + \theta^4)$ yields

$$R \approx h + f - \frac{hf}{2(h+f)}[\beta^2 + 2\theta\beta cos(\varphi - \psi) + \theta^2] \tag{3}$$

We denote:

$$\begin{aligned} H &= \tfrac{hf}{h+f} = O(f), \qquad p = kH \gg 1 \\ \psi &= \varphi + \pi + \gamma, \quad cos(\varphi - \psi) = -cos\gamma \end{aligned}$$

To this approximation,

$$E(P) = E_0 \frac{f}{h} e^{ik(h+f)}\, F(h,\theta) \tag{4}$$

where the radiation pattern

$$F(h,\theta) = \frac{H}{i\lambda} \int_A^B e^{ip\frac{\beta^2+\theta^2}{2}} \beta\, d\beta \int_{-\pi}^{\pi} e^{ip\theta\beta cos\gamma}\, d\gamma = \frac{p}{i} \int_A^B e^{-iP\frac{\beta^2+\theta^2}{2}} J_0(p\theta\beta)\beta\, d\beta \tag{5}$$

As $p = kH \sim 5 \times 10^5$, β, $\theta \sim 0.1$, the argument. $p\theta\beta \sim 10^3$ is large, and the Bessel function can be replaced by its asymptotics

$$J_0(t) \sim \sqrt{\frac{2}{\pi t}} cos\left(t - \frac{\pi}{4}\right)$$

We obtain approximately

$$F(h,\theta) \approx \frac{pe^{-i\pi/4}}{\sqrt{2\pi p\theta}} \int_A^B \left[e^{ip\frac{(\beta+\theta)^2}{2}} - ie^{-ip\frac{(\beta-\theta)^2}{2}} \right] \sqrt{\beta}\, d\beta = \tag{6}$$
$$= \frac{1}{\sqrt{\pi}} \left[e^{-i\pi/4} \int_{(A+\theta)\sqrt{\frac{p}{2}}}^{(B+\theta)\sqrt{\frac{p}{2}}} e^{-it^2} \sqrt{\frac{t}{\theta}\sqrt{\frac{2}{p}} - 1}\, dt - e^{i\pi/4} \int_{(A-\theta)\sqrt{\frac{p}{2}}}^{(B-\theta)\sqrt{\frac{p}{2}}} e^{-it^2} \sqrt{1 + \frac{t}{\theta}\sqrt{\frac{2}{p}}}\, dt \right]$$

Integration by parts shows that the first integral in the brackets is of the order $O\left(\frac{1}{\sqrt{p\theta}}\right)$, and the second one can be reduced, in the first approximation, to the ordinary Fresnel integral. So we get finally

$$F(h,\theta) \approx -\frac{e^{i\pi/4}}{\sqrt{\pi}} \int_{(A-\theta)\sqrt{\frac{p}{2}}}^{(B-\theta)\sqrt{\frac{p}{2}}} e^{-it^2} dt \tag{7}$$

Conclusion

The very good agreement between theoretical and computational experiments shows that we have a self-consistent analytical and numerical description of the diffraction-limited EUV optical systems and allows us to make a reliable statement on the nature of the interference fringes observed in the far field of the zone plates tested in [1]: they arise independently from the manufacturing accuracy as a result of the edge diffraction by the central stop and the order sorting aperture. An equivalent perfect lens placed into this environment would produce a similar far field pattern. The zone plates give more indented intensity distributions due to projection of the near-field fine structure into the far zone. The individual peculiarities are probably dependent mostly on the edge features ot the zone plate at test.

References

1. K.A.Goldberg et al. At-wavelength testing of optics for EUV, SPIE 2437-30 (1995)
2. Yu.V.Kopylov, A.V.Popov, A.V.Vinogradov. Application of the parabolic wave equation to X-ray diffraction optics, Optics Comm., v.118, 619-636 (1995)
3. Yu.V.Kopylov, A.V.Popov, A.V.Vinogradov. Diffraction phenomena inside the body of Fresnel zone plates with high aspect ratio, Proc. URSI Internat. Symposium on EM Theory, St.Petersburg, 822-824 (1995)
4. J.Kirz. Phase zone plates for X-ray and the extreme UV, J. Opt. Soc. Am., v. 64, No 3, 301-309 (1974)
5. M.Born, E.Wolf. Principles of optics, Pergamon Press, Oxford,1980

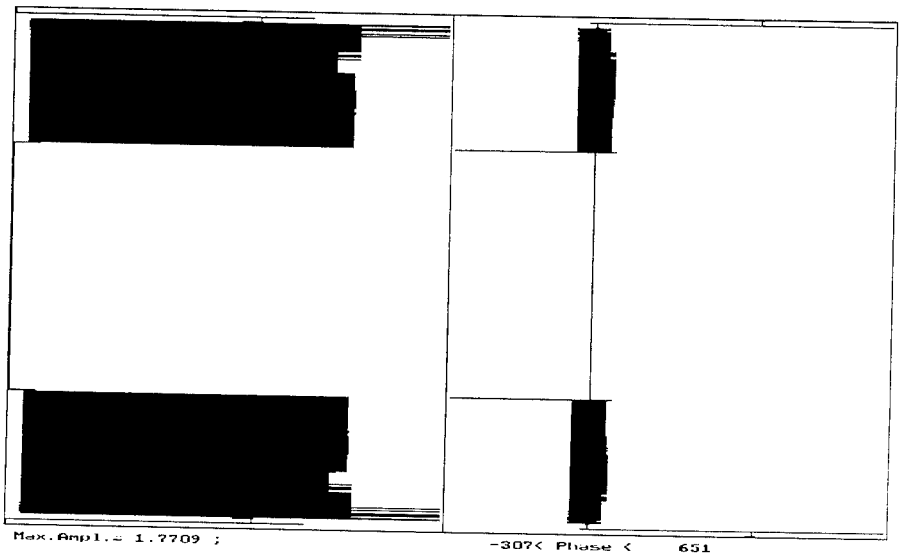

Fig.1a Output wave field of a thick Ni-vacuum ZP with central stop

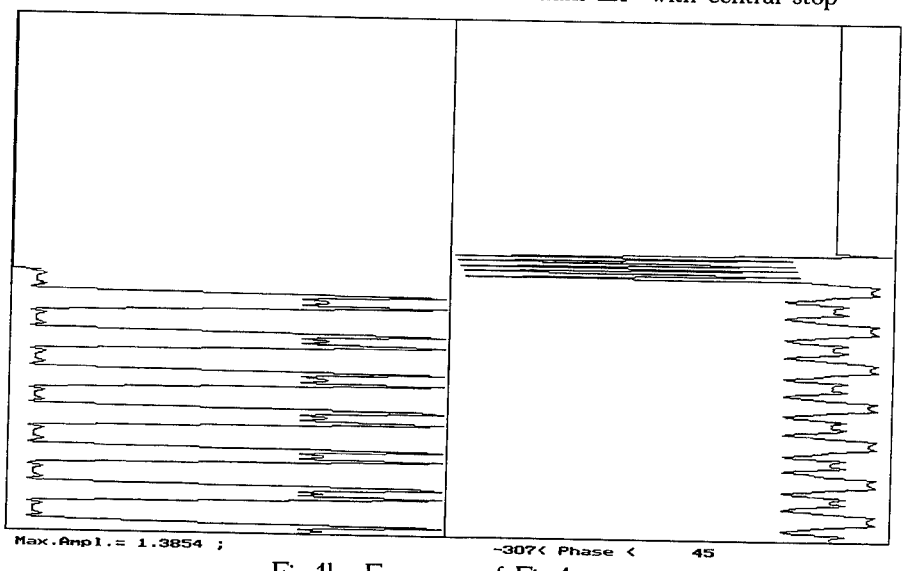

Fig.1b Fragment of Fig.1a

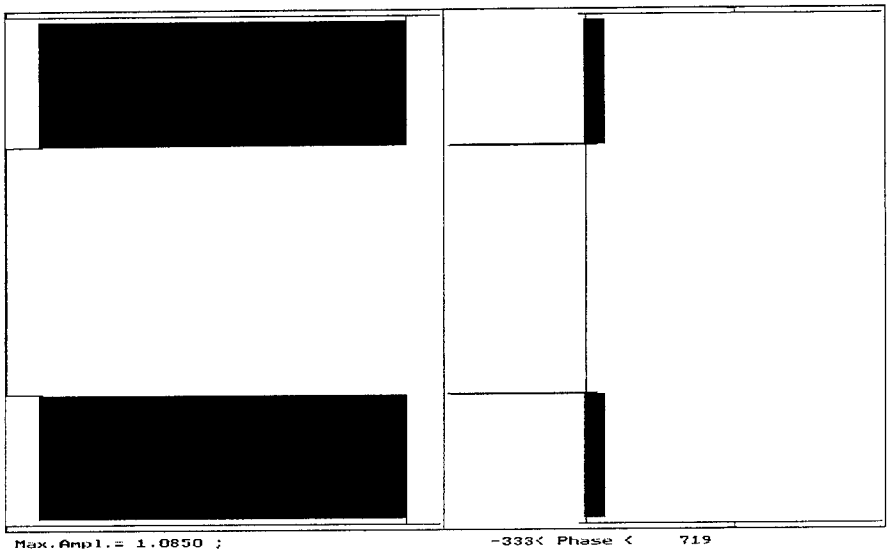

Fig.2a Kirz's transmission function of the thick ZP of Fig.1

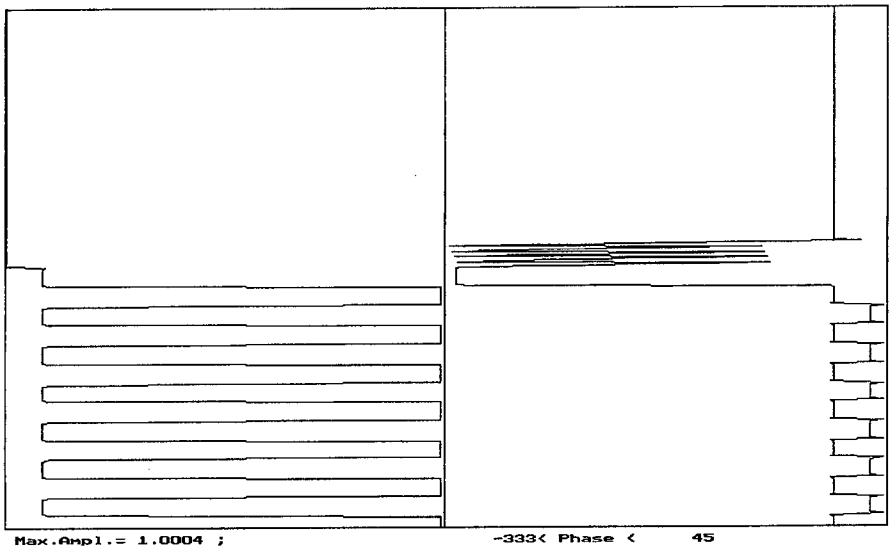

Fig.2b Fragment of Fig.2a

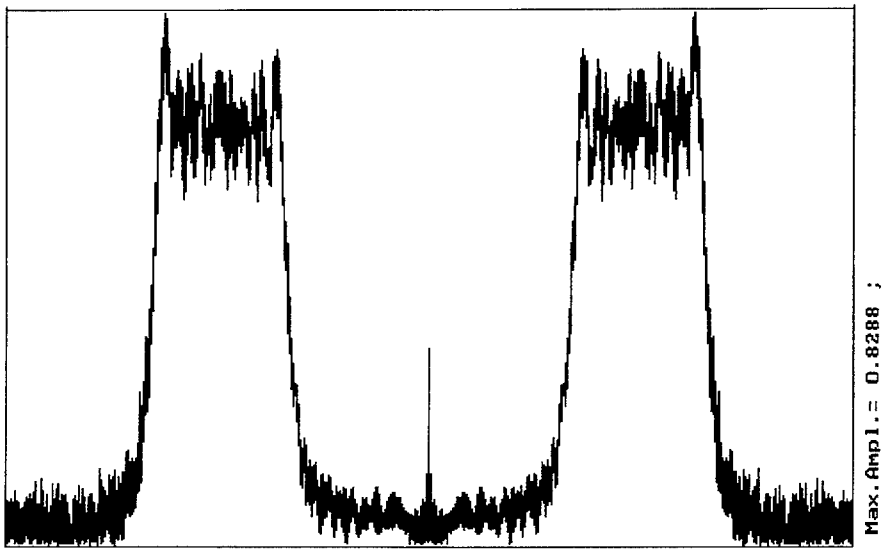

Fig.3 Far field diffraction pattern of the ZP of Fig.1

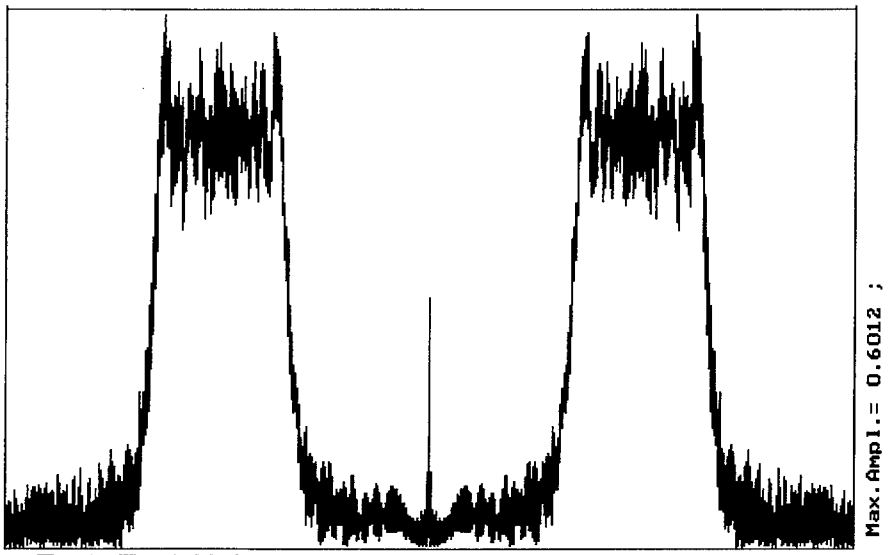

Fig.4 Far field diffraction pattern of the idealized thin Fresnel ZP

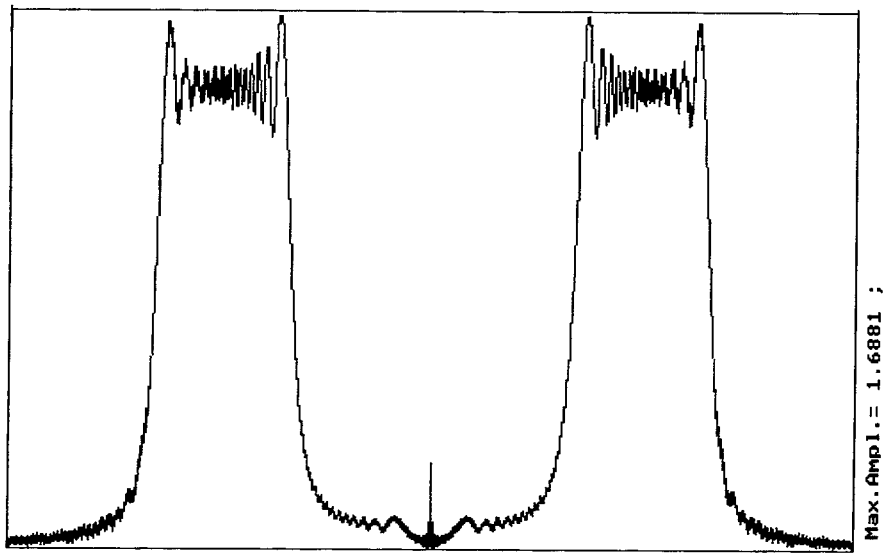

Fig.5 Far field amplitude pattern of the equivalent perfect lens

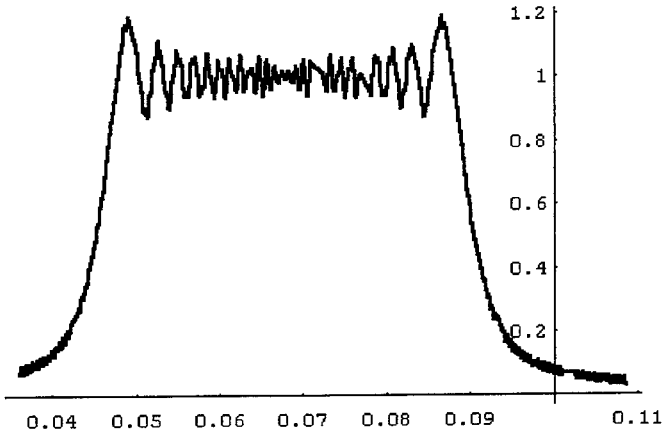

Fig.6 Far field amplitude pattern calculated via formula (7)

SESSION 2:

INVERSE SCATTERING

Chairs: P. Goggans and L. Riggs

RADAR TIME- AND FREQUENCY-DOMAIN RECEIVED SIGNALS FOR REALISTIC ANTENNAS AND SCATTERERS*

Paul M. Goggans and Jeffrey D. Pursel
University of Mississippi, Department of Electrical Engineering
University, MS 38677

All current radar target identification (RTID) methods based on high range-resolution radar require a target library. The target library stores the encoded target specific scattering behavior of each target to be identified. Because of the expense and difficulty of making radar measurements, calculated returns are almost always used to construct target libraries.

Currently, target libraries are constructed from antenna-independent radar profiles using calculated returns. The antenna-independent radar profile of a target is the time-domain radio frequency (RF) envelope of a specified component of the scattered electric field which results from a linearly polarized transmitted wave with a specified electric field direction. For the antenna-independent radar profile, the electric field components of both the transmitted and scattered electric fields are specified in the target's coordinate system. For example, for a target ID system where the radar antenna is linearly polarized with vertical polarization (with respect to the antenna's coordinate system), the antenna-independent radar profile is calculated from the vertical (with respect to the target's coordinate system) component of the scattered electric field due to a linearly polarized transmitted wave with a vertically (with respect to the target's coordinate system) directed electric field.

Use of the target's coordinate system is convenient because it avoids adding another dimension to the target library storage. Unfortunately, this results in an inadequate description of the target's scattering characteristics since, in the example above, it assumes that the vertical direction with respect to the antenna coordinates is the same as the vertical direction with respect to the target coordinates. Although the two vertical unit vectors lie in the same plane, it can be demonstrated that in general they are rotated by a constant angle which depends on the relative orientation of the antenna's coordinate system with respect to the target's coordinate system.

In this presentation, we examine the impact on radar target identification systems of using antenna-independent radar profiles to generate the target library. This examination is accomplished by comparing antenna-independent radar profiles with antenna-dependent radar profiles. The antenna-dependent radar profile of a target is the time-domain radio frequency envelope of the signal traveling out of the receiver antenna which results from a band-pass limited signal traveling into the transmitter antenna. Antenna-dependent radar profiles were developed for this work. The method used to generate the antenna-dependent radar profile precisely accounts for the frequency-dependent polarization of the antenna, the vector nature of the transmitted electromagnetic field, the vector nature of the electromagnetic field scattered from the target, as well as the exact geometrical relationship between the antenna and the target.

This presentation begins with development of the bistatic radar equation in a form which is explicitly in terms of parameters which fix the geometrical relationship between the antennas and the target, and in terms of the measured or calculated antenna and target responses. The radar equation is developed in both the time and frequency domains. The antenna-dependent radar profile and antenna-independent radar profile are then defined and discussed. The presentation ends with computed results for one and two vector-component wire antennas and for two aircraft targets. The conclusions return to a discussion of the target library and suggest several possible remedies to the current methods of determining the target library for RTID applications.

* This work was partially supported by the MICOM Research, Development, and Engineering Center (Dr. C. Ray Smith) under the auspices of the U.S. Army Research Office Scientific Services Program administered by Battelle (Task Control Number 94265, Delivery Order Number 1313, Contract Number DAAL03-91-C-0034).

THE EXTRACTION OF SCATTERING MECHANISMS FROM MEASURED DATA

by

Hirsch M. Chizever
Mission Research Corporation
Dayton, OH 45430

Krishna M. Pasala
University of Dayton
Dayton, OH 45459

1. INTRODUCTION

In this paper we consider the processing of measured scattered field data over a wideband of frequencies. The scattering from any target illuminated by a plane wave consists of contributions from several different scattering centers, each of which may represent a different scattering mechanism. These scattering mechanisms may be specular reflections, edge diffractions, creeping waves or multi-mode resonances associated with a cavity. Signals from all of these diverse mechanisms are buried in the measured composite signal. In addition, error sources such as scattering from support structures are also embedded in the measured data. It is of interest to delineate these scattering centers even when they are close together and further, to determine their frequency dispersion characteristics resulting in a one-dimensional radar range profile of the target. Such a decomposition is of great value in the context of RCS measurements in a range. It becomes possible to edit the range profile in the frequency domain to eliminate the spurious scattering centers and the mechanisms associated with the support structures. As a result, the true scattered signal may be obtained from the measured signal. Such editing in the frequency domain is superior to the more conventional editing carried out in the time domain. Editing in the time domain eliminates the skirts of the responses from adjacent scattering centers. Also, the frequency dispersion characteristics determined here may serve as distinct "signatures" facilitating the identification of the target.

The technique used here consists of two steps. In the first step, the signal model assumes the scattering from various scattering centers to be frequency invariant. This model is then used to determine the time delays associated with each of the scattering centers. The MUSIC [1] algorithm is used for this purpose. As a result, the resolution obtained is beyond that possible with Fourier based techniques. In the second step, the time delays computed in the first step are incorporated into the signal model. In addition, the frequency dispersion characteristic associated with each of the scattering centers is parameterized and is no longer considered frequency invariant. These parameters are then determined using a least squares approach. This technique is applied to a variety of synthetic and measured data sets to assess its strengths and limitations. It is shown that the method works very well and that it is possible to extract any arbitrary dispersion characteristic. Using measured scattering data from an ogive and sphere, editing of a radar range profile in the frequency domain is demonstrated.

2. THEORY

We consider here a target illuminated by a plane wave resulting in the excitation of L scattering centers on the target. Let the back scattered field be measured over a band of frequencies from f_1 to f_N at equal frequency increments denoted by Δf . The received signal at any frequency, f, may be modeled as,

$$v(f) = \sum_{k=1}^{L} a_k(f)\, e^{-j2\pi f t_k} + n(f) \qquad 2.1$$

Here, $a_k(f)$, which may be complex, represents the dispersive scattering amplitude and t_k is the round-trip time delay corresponding to the k^{th} scattering center. The measurement noise and modeling error is represented by $n(f)$. Our objective here is to estimate the time delays, t_k, k=1, 2, ... L, and the corresponding dispersion characteristics, $a_k(f), k = 1,2 \ldots L$, from the measured data, $v_i = v(f_i), i=1,2 \ldots N$. This is accomplished in two steps. In the first step, the signal model assumes the scattering from various scattering centers to be invariant with frequency. This model is then used to determine the time delays associated with each of the scattering centers. Here, we have used the MUSIC algorithm. This results in super resolution, making it possible to separate scattering centers that are very close to each other in range. It may be mentioned that any other super resolution technique could be used. In the second step, the time delays computed in the first step are incorporated into the signal model. In addition, the frequency dispersion characteristic associated with each of the scattering centers, $a_k(f)$, is parameterized and is no longer considered frequency invariant. These parameters are then determined using a least squares approach.

2.1 Step-1: Time Delay Estimation

Here we take the $a_k(f)$ to be frequency invariant, i.e., a_k. The signal model of equation 2.1 then becomes,

$$v_i = v(f_i) = \sum_{k=1}^{L} a_k e^{-j2\pi f_i t_k} + n_i, \quad i = 1,2 \ldots N \qquad 2.2$$

Equation 2.2 may be expressed more compactly as,

$$\vec{v} = \mathbf{W}\vec{a} + \vec{n}, \qquad 2.3$$

where, $\vec{v} = [v_1, v_2, \ldots v_N]^T$

$\vec{n} = [n_1, n_2, \ldots n_N]^T$

$\mathbf{W} = [\vec{W}_1, \vec{W}_2, \ldots, \vec{W}_L]$

$\vec{W}_k = [e^{-j2\pi f_1 t_k}\ e^{-j2\pi f_2 t_k} \ldots e^{-j2\pi f_n t_k}]^T, \qquad k = 1,2, \ldots N$

and $\vec{a} = [a_1, a_2, \ldots a_L]^T$.

The superscript, T, indicates transposition. Under the assumption that $\vec{n}$ is white with variance σ^2 and uncorrelated with the scattered fields, the correlation matrix, $\mathbf{R}_{\vec{v}}$ is given by,

$$\mathbf{R}_{\vec{v}} = \mathbf{E}[\vec{v}\vec{v}^H] = \mathbf{W}\,\mathbf{R}_{\vec{a}}\,\mathbf{W}^H + \sigma^2\mathbf{I}, \qquad 2.4$$

where, $\mathbf{R}_{\vec{a}} = \mathbf{E}[\vec{a}\,\vec{a}^H]$ and $\mathbf{I}$ is the identity matrix. The superscript, H, indicates conjugation and transposition. Since the vector of scattering amplitudes, $\vec{a}$, is deterministic and not random,

$$\mathbf{R}_{\vec{a}} = \mathbf{E}[\vec{a}\vec{a}^H] = \vec{a}\,\vec{a}^H \qquad 2.5$$

$\mathbf{R}_{\vec{a}}$, therefore, is a $L \times L$ matrix of rank-1 and is singular. As a result, the MUSIC algorithm cannot be applied directly without further modifications, even though, equation 2.4 has the appropriate form. Shan et. al. [2] have devised a scheme using spatial smoothing to decorrelate a coherent signal environment in the context of angle of arrival

estimation. A similar "frequency smoothing" scheme may be employed here and is discussed in [3]. This procedure consists of the following steps:

a) A subaperture of size N' is chosen. Then, from the signal vector $\vec{v}$, $M=(N-N'+1)$ different signal vectors, $\vec{v}'_k$, $k=1,2,\ldots M$, each of length N', may be chosen. The signal vector corresponding to the k^{th} subaperture is obtained from rows k to $(N'+k-1)$ of $\vec{v}$ and is defined by,

$$\begin{aligned}\vec{v}'_k &= \vec{v}\,(k:N'+k-1)\\ &= \sum_{k=1}^{L} a_k\, e^{-j2\pi(k-1)\Delta f t_k}\,\vec{W}'_k + \vec{n}'_k\\ &= \mathbf{W}'\mathbf{D}^{(k-1)}\,\vec{a}+\vec{n}'_k \end{aligned} \qquad 2.6$$

where

$$\begin{aligned}\mathbf{W}' &= [\vec{W}'_1, \vec{W}'_2, \ldots \vec{W}'_L]\\ \vec{W}'_k &= [e^{-j2\pi f_1 t_k} \quad e^{-j2\pi f_2 t_k} \ldots e^{-j2\pi f_{N'} t_k}]^T\\ \vec{n}'_k &= [n_k, n_{k+1}, \ldots n_{N'+k-1}]^T\\ \mathbf{D} &= \mathrm{diag}(e^{-j2\pi\Delta f t_1}, e^{-j2\pi\Delta f t_2}, \ldots, e^{-j2\pi\Delta f t_L}).\end{aligned}$$

The correlation matrix corresponding to each $\vec{v}'_k$ is given by,

$$\begin{aligned}\mathbf{R}_{\vec{v}'_k} &= \mathbf{E}[\vec{v}'_k(\vec{v}'_k)^H]\\ &= \mathbf{W}'\mathbf{D}^{(k-1)}\,\mathbf{R}_{\vec{a}}\left(\mathbf{D}^{(k-1)}\right)^H\mathbf{W}'^H + \sigma^2\mathbf{I}\\ &= \mathbf{W}'\mathbf{R}'_{\vec{a},k}\,\mathbf{W}'^H + \sigma^2\mathbf{I}\end{aligned} \qquad 2.7$$

b) The averaged correlation matrix of size N' x N' is defined by,

$$\begin{aligned}\mathbf{R} &= \frac{1}{M}\sum_{k=1}^{M}\mathbf{W}'\mathbf{R}'_{\vec{a},k}\,\mathbf{W}'^H + \sigma^2\mathbf{I}\\ &= \mathbf{W}'\mathbf{R}'_{\vec{a}}\,\mathbf{W}' + \sigma^2\mathbf{I}\end{aligned} \qquad 2.8$$

where,

$$\mathbf{R}'_{\vec{a}} = \frac{1}{M}\sum_{k=1}^{M}\mathbf{R}'_{\vec{a},k}$$

It has been shown in [2] and [3], that $\mathbf{R}'_{\vec{a}}$ is not singular and that the larger the number of "subapertures", M, the greater the degree of decorrelation achieved, though, attained at the expense of reduced size of the correlation matrix. Equation 2.8, now, is in a form suitable for analysis using the MUSIC [1] algorithm.

The space defined by the eigenvectors corresponding to the lowest $(N'-L)$ eigenvalues of $\mathbf{R}'_{\vec{a}}$ is the noise subspace, Q_N. That is,

$$\mathbf{Q}_N = [\vec{q}_{L+1}\ \vec{q}_{L+2}\ldots\vec{q}_{N'}] \qquad 2.9$$

where $\vec{q}_i$ are the eigenvectors of $\mathbf{R}'_{\vec{a}}$. The MUSIC spectrum, then, is defined by,

$$P_{MUSIC}(t_d) = \frac{1}{\vec{S}^H Q_N Q_N^H \vec{S}} \qquad 2.10$$

where the scanning vector $\vec{S}$ is given by,

$$\vec{S} = [e^{-j2\pi f_1 t_d}\ e^{-j2\pi f_2 t_d} \ldots e^{-j2\pi f_N t_d}] \qquad 2.11$$

The peaks of this spectrum correspond to estimates of the round trip delays associated with the L scattering centers.

2.2 Step-2: Dispersion characteristics of scattering centers

We now consider the procedure for determining the scattering amplitude response at the p^{th} frequency $a_k(f_p)$, $k = 1,2,\cdots L$. Towards this end we consider a band of frequencies of width B_r and centered at f_p. Let there be $(\overline{N}+1)$ samples of data over this band. The signal model corresponding to this band of frequencies is given by,

$$v_l = v(f_l) = \sum_{k=1}^{L} a_k(f_l)\, e^{-j2\pi f_l \hat{t}_k}, \quad l = p - \frac{\overline{N}}{2}, \cdots, p + \frac{\overline{N}}{2} \qquad 2.12$$

Note that the scattering amplitudes are not constant as in equation 2.2 and the round trip time delays of equation 2.1 are deemed to be known and replaced by their estimates, $\hat{t}_k$. We assume a functional form for the k^{th} scattering amplitude function $a_k(f)$. These functional forms may be different for different k, but here, we consider a polynomial of order q, as given by,

$$a_k(f) = a_{k0} + a_{k1} f + a_{k2} f^2 + \ldots + a_{kq} f^q. \qquad 2.13$$

The problem of obtaining the dispersion characteristics may now be formulated as the determination of the parameters a_{kl}, $k = 1,2,\cdots L$ and $l = 0,1,2\cdots q$, that results in the best match between the measured data and the signal model in equation 2.13 in the least squares sense. The measurement vector, $\vec{v} = [v_0\ v_1 \ldots v_{\overline{N}}]^T$ may now be expressed as,

$$\vec{v} = \mathbf{W}^T \vec{a} + \vec{\varepsilon} \qquad 2.14$$

where,

$$\mathbf{W} = [\vec{W}_0\ \vec{W}_1 \ldots \vec{W}_{\overline{N}}]$$

$$\vec{\varepsilon} = [\varepsilon_0, \varepsilon_1, \ldots \varepsilon_{\overline{N}}]^T$$

$$\vec{W}_k^T = [\vec{W}_{k1}^T\ \vec{W}_{k2}^T \ldots \vec{W}_{kL}^T]$$

$$\vec{W}_{kj}^T = [e^{-j2\pi f_k \hat{t}_j}\ f_k e^{-j2\pi f_k \hat{t}_j} \ldots f_k^q e^{-j2\pi f_k \hat{t}_j}], \quad j = 1,2,\ldots L$$

$$\vec{a} = [a_{10} \ldots a_{1q}, a_{20} \ldots a_{2q}, \ldots, a_{L0} \ldots a_{Lq}]^T$$

The parameter vector $\vec{a}$ may now be determined by requiring the error power $J = \|\vec{\varepsilon}\|^2$ to be the least possible. This optimum vector may be shown to be given by [4],

$$\vec{a} = (\mathbf{W}^* \mathbf{W}^T)^{-1} \mathbf{W}^* \vec{v} \qquad 2.15$$

Once this parameter vector is defined, the dispersion characteristics evaluated at $a_k(f_p), k = 1,2,\ldots,L$ are readily determined. The frequency then is incremented from f_p to $(f_p + \Delta f)$ and the procedure is repeated to determine the frequency response at this new frequency. The frequency response over the entire band may be determined in this fashion, except for small bands of width $\frac{B_r}{2}$ at the edges of the band. Consideration for proper choice of B_r and other parameters are discussed in the next section.

3. RESULTS

The theory described in Section-2 is used to process a variety of synthetic, experimentally obtained and theoretically predicted scattered fields. The results obtained depend upon the choices made for the regression bandwidth, B_r, the frequency increment, Δf, and the number of subapertures, M, used to decorrelate $\mathbf{R}_{\bar{s}}$. The condition number of $(\mathbf{W}^*\mathbf{W}^T)$ depends upon B_r. The condition number is << 1.0 if B_r is too small and equation 2.15 becomes ill-conditioned resulting in degraded estimates of scattering center frequency responses. The regression bandwidth corresponding to the first maximum in the plot of B_r vs. condition number of $(\mathbf{W}^*\mathbf{W}^T)$ is the optimal choice. The choice of Δf determines the rate of sampling of the scattered fields in the frequency domain and as such dictates the range of time delays that are not aliased. Δf must be chosen so that the expected range of time delays corresponding to the scattering centers on the target lie between $-\frac{1}{2\Delta f}$ and $\frac{1}{2\Delta f}$. Our simulations indicate that choosing M, the number of sub apertures, to be greater than 6, sufficiently decorrelates $\mathbf{R}_{\bar{s}}$.

Illustration-1: Synthetic Data:

For purposes of illustration, we generate scattered fields by prescribing three scattering centers with specified round trip delays and corresponding frequency responses (SNR=20 dB and M=16).

The first scattering center is at -1 ns and its frequency response is linearly increasing. The second scattering center is resonant with center frequency at 10 GHz and is located at 0 ns. The third scattering center is located at 1 ns and its frequency response is linearly decreasing. Figure 1 shows the MUSIC and Fourier spectra overlaid using the data in the band 7-13 GHz with a Δf =0.2 GHz. Figure 2 shows the specified and estimated frequency responses overlaid. The regression bandwidth used in obtaining these results is 1 GHz.

Illustration-2: Measured 8" Diameter Sphere

The field scattered by a sphere involves reflection from the specular point and creeping wave diffraction. In the case of measured fields, there may also be additional scattering mechanisms associated with structures used for mounting the target. We process here, for purposes of comparison, the scattered field computed using the Mie series [5], which, of course, does not have any spurious scattering mechanisms. Figure 3 shows the MUSIC spectrum obtained from both the measured and computed scattered fields. The offset between the peaks in the two spectra is due to the phase center difference between the 8" sphere and its reference target and is of no consequence. The specular and creeping wave returns are at -0.65 ns and 1.32 ns respectively. The round trip time delay between specular and creeping wave returns is given by,

$$\Delta t = \text{radius} * (2 + \pi)/c. \qquad 3.1$$

The measured results give a result of 1.97 ns and compares well with the predicted value of 1.74 ns. The spectrum due to measured data also shows, corresponding to a time delay of -.44 ns, a return due to the support structure. The frequency responses associated with these three scattering centers are shown in figure 4. The specular and creeping wave frequency responses obtained from the computed data is also included in figure 4. Having identified the scattering from the

spurious scattering center, it is possible to edit it out of the scattered field. This reconstructed scattered field from measured data and the Mie solution are shown in figure 5.

Illustration-3: Measured 9.6" Ogive

We next consider a 9.6" ogive, whose scattered field is measured for the nose-on angle of incidence. The scattered field is also computed using the body of revolution code CICERO [6]. The MUSIC spectra corresponding to both sets of data is shown in figure 6. As before, the offset in the peaks is due to an inconsequential phase offset between target and reference. In addition to the scattering centers corresponding to the front and rear tips, measured data reveals two additional scattering centers. These scattering centers are due to the foam structure used to mount the ogive. Estimated frequency responses of all the scattering centers is shown in figure 7. The edited scattered field with the contribution from the two error terms removed, and the scattered field computed by CICERO are overlaid in figure 8.

4. Conclusions

This study has presented a method for extracting arbitrary-shaped frequency dispersions of scattering mechanisms from a composite signal. The method demonstrated how spurious scattering sources could be removed from a composite signal to provide the "true" scattering of a target. Unlike Fourier methods, this technique performs its signal reconstruction in the frequency domain, thus avoiding Fourier transform induced errors from multiplicative time domain gating.

The method showed minor degradation to the reconstructed scattering of the targets under study. This can be primarily attributed to limiting the number of scattering centers found by the MUSIC algorithm. By allowing MUSIC to search for additional mechanisms, a more accurate rendering of the actual scattering may be found. In addition, by tailoring the assumed frequency dispersion functions for individual scattering mechanisms, the method will predict the response for each mechanism more accurately.

The signal model presented here assumed that the phase centers of the mechanisms under study remained constant with frequency. However, for many targets such as antennas and radar absorbing materials, this assumption is not valid. The method may readily accommodate this by applying the MUSIC algorithm to small sub-bands to account for the frequency dependent time delays, of course at the cost of resolution.

5. Acknowledgments

The authors extend their appreciation to Dr. Brian M. Kent for use of the Wright Laboratory Advanced RCS Measurement Range. Also, to Mr. Michael A. Menter of Mission Research Corporation for performing the RCS measurements presented in this study.

6. References

[1] R. Schmidt, "Multiple Emitter Location and Signal Parameter Estimation," *RADC Spectrum Estimation Workshop*, pp. 243-258, 1979.

[2] T. J. Shan, M. Wax, and T. Kailath, "On Spatial Smoothing for Direction of Arrival Estimation of Coherent Signals," *IEEE Trans. Acoust., Speech, Signal Processing*, Vol. ASSP 33, pp. 806-811, August 1985.

[3] H. P. Yamada, M. P. Ohmiya, and Y. Ogawa, "Superresolution Techniques for Time-domain Measurements with a Network Analyzer," *IEEE Trans. on Ant. and Propagat.*, Vol. AP 39, No. 2, pp. 177-183, February 1991.

[4] S. Haykin, *Adaptive Filter Theory, Second Edition*, Prentice Hall, 1991.

[5] C.A. Balanis, *Advanced Engineering Electromagnetics*, John Wiley & Sons, 1989.

[6] J.M. Putnam and L.N. Medgyeshi-Mitschang, "Combined Field Integral Equation Formulation for Axially Inhomogeneous Bodies of Revolution (Combined Field Formulation of CICERO)," Report MDCQA003, December 1987, McDonnel Douglas Research Laboratories; prepared under Contract No. 33-4257 for Sandia National Laboratory.

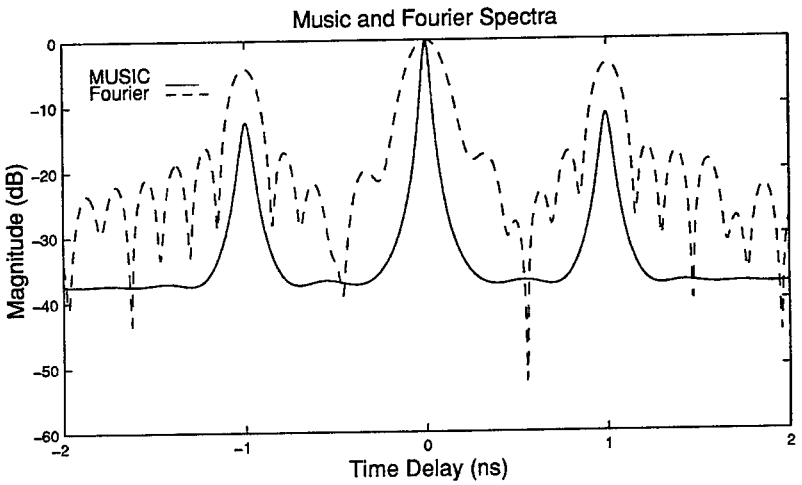

Figure 1. MUSIC and Fourier Spectra for Synthetic Data Illustration

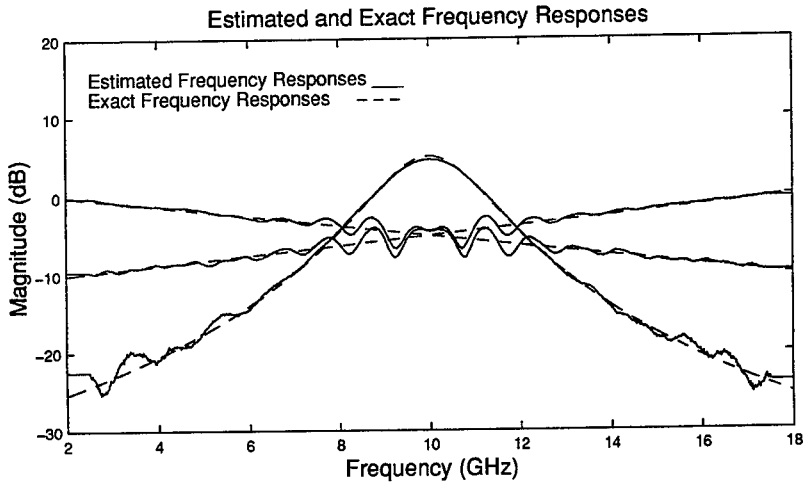

Figure 2. Exact and Estimated Frequency Responses for Synthetic Data Illustration

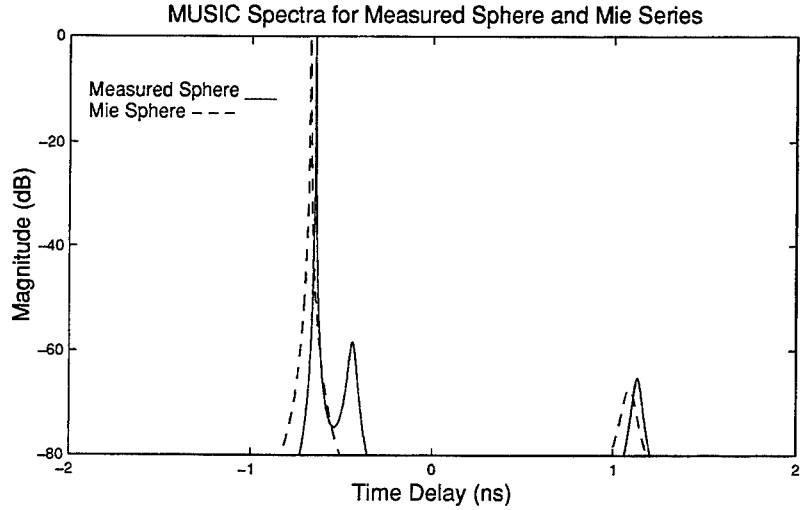

Figure 3. MUSIC and Fourier Spectra for Measured Sphere

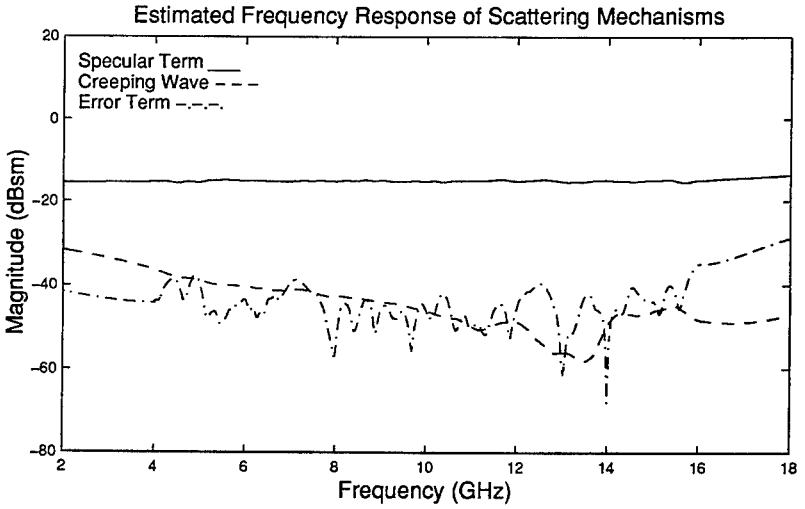

Figure 4. Estimated Frequency Response of Scattering Mechanisms for Measured Sphere

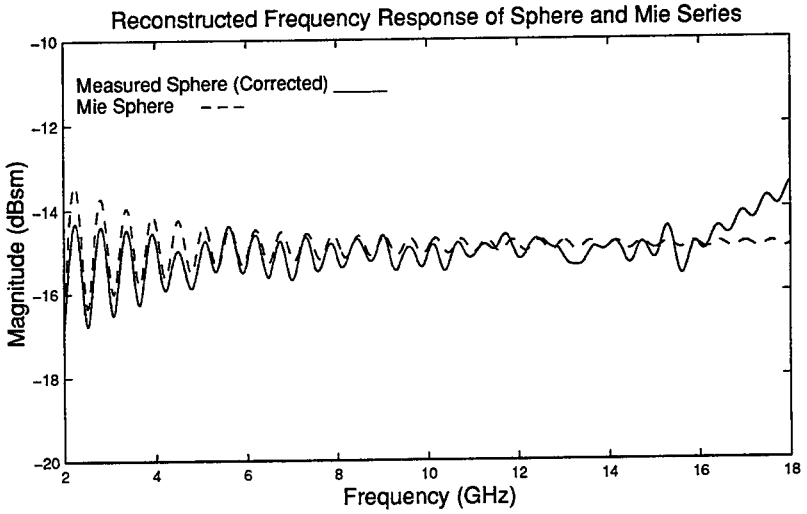

Figure 5. Mie Series and Corrected Frequency Response for Measured Sphere

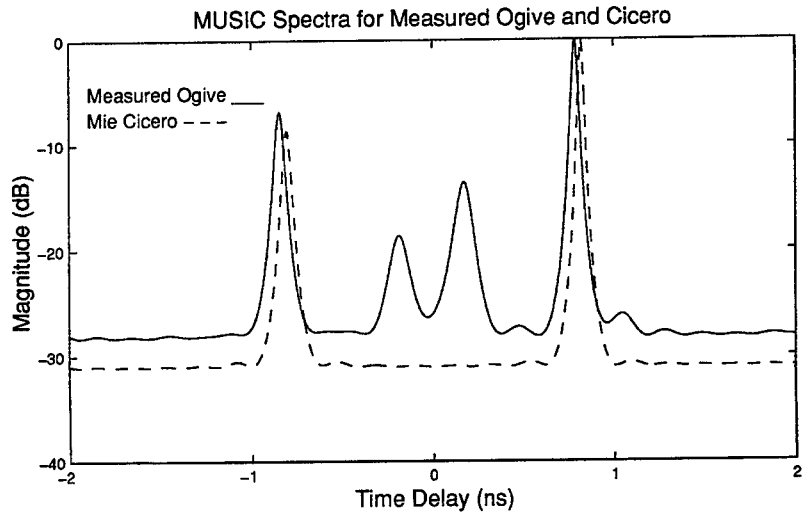

Figure 6. MUSIC and Fourier Spectra for Measured Ogive

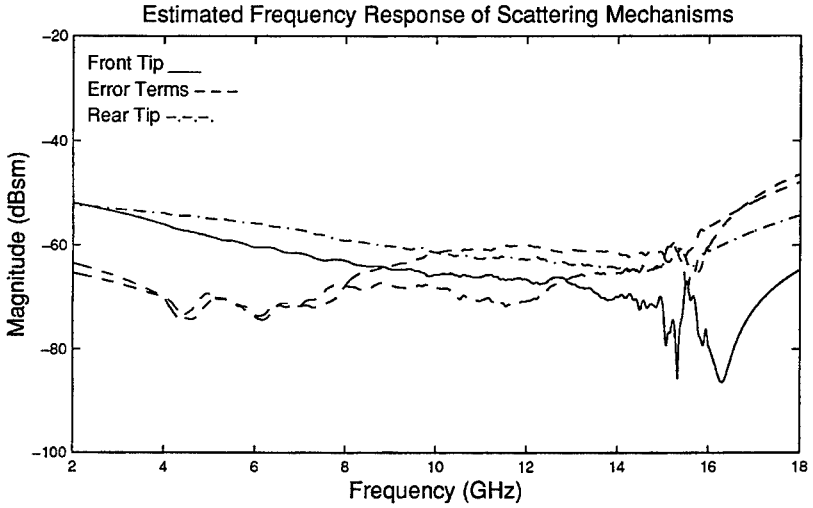

Figure 7. Estimated Frequency Response of Scattering Mechanisms for Measured Ogive

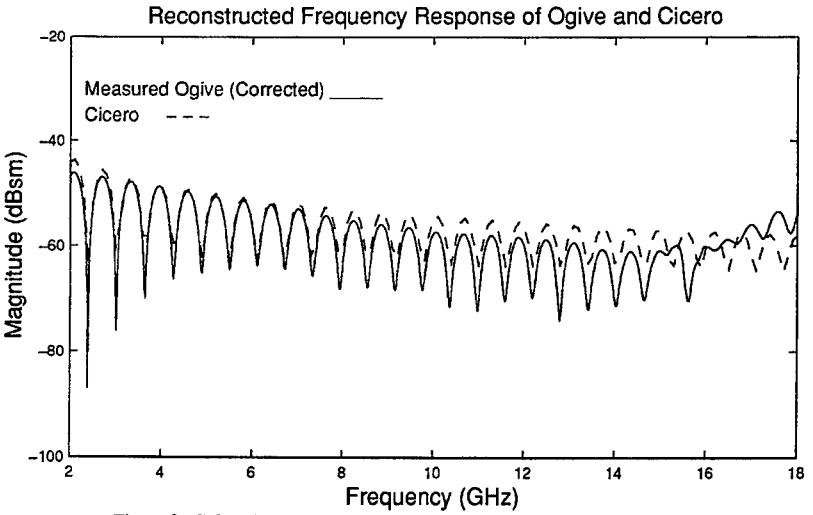

Figure 8. CICERO and Corrected Frequency Response for Measured Ogive

USING THE E-PULSE TECHNIQUE AND HYPOTHESIS TESTING TO PERFORM RADAR TARGET IDENTIFICATION

Lloyd Riggs, Jon Mooney, and C. Ray Smith
Department of Electrical Engineering
200 Broun Hall • Auburn University, Alabama 36849

Abstract

In this paper, the Extinction pulse (E-pulse) technique is combined with hypothesis testing to perform target identification. Based upon the natural resonances of a conducting body, the E-pulse is constructed to annihilate the natural modal content of the scattered field response from a specific target. Convolving the same E-pulse with the impulse response from a dissimilar target yields a *nonzero* response. Thus, the E-pulse scheme reduces the identification process to discriminating between no response and a "large" response. However, in a real environment where noise will inevitably corrupt the radar signature, the robustness of the E-pulse technique is diminished. Convolving the E-pulse with the signature from it's intended target in the presence of noise will not produce a null late-time response. Although the E-pulse scheme definitely has merit, it alone cannot completely resolve the target ID problem, especially under the influence of such nuisance parameters as noise and aspect angle. One possible method of overcoming these parameters while retaining the E-pulse approach is to conduct a binary hypothesis test at the output of the E-pulse filter. Such a test will yield a measure of belief (a probability) as to whether the output is either "noise" (correct target) or "signal plus noise" (wrong target). This paper will expound on the rationale of using the E-pulse technique and binary hypothesis testing to perform target identification.

I Introduction

The E-pulse radar target discrimination technique is based on the singularity expansion method (SEM) representation of the transient scattered field returned from a target which has been illuminated by an "impulsive" (wide bandwidth) radar pulse. The SEM, as formulated by Baum in 1971 [1], represents electromagnetic interaction or scattering in terms of simple pole terms (or singularities) in the complex frequency plane, or correspondingly, as simple damped sinusoids in time domain. For example, the SEM representation of the late-time-scattered field impulse response of a conducting object may be written as

$$r(t) = \sum_{n=1}^{N} a_n e^{\sigma_n t} \cos(\omega_n t + \phi_n), \qquad t > T_L \tag{1}$$

where the amplitude and phase of the nth mode, a_n and ϕ_n , depend on the orientation of the target with respect to the radar (aspect dependent parameters) while ω_n and σ_n (< 0) are the aspect-independent frequency and damping constant of the nth mode, respectively, and only N modes are assumed excited by the incident field waveform. Late time, denoted by $t > T_L$, is defined as the time period after the incident pulse has passed over the target, so that subsequent radiation is associated with the target's free natural resonances [2]. Equation (1) is constructed using what is referred to as a class I coupling coefficient [3]. An SEM representation for the scattered field employing a class II coupling coefficient may also be constructed and enjoys the advantage of greater accuracy than the class I form in early time, $0 < t < T_L$, albeit at the expense of greater complexity [4].

The E-pulse and related single mode extraction pulse (S-pulse), are purported to be *aspect independent* discriminatory waveforms which, when convolved with the late-time response of a matched target, produce null or single-mode responses, respectively. When an E-pulse waveform tailored to one target is convolved with the late-time response for a different target, a nonzero response results. Complete details regarding the synthesis of E- and S-pulse waveforms will not be discussed here. Instead, the interested reader is referred to a review article on the subject by Baum et. al [5]. A simple example will suffice in providing the reader with an adequate understanding of the E-pulse discrimination technique relevant to this discussion.

Figure 1 presents a block diagram of a system designed to discriminate between a pair of targets using the E-pulse technique. For simplicity, only the two target case will be considered since generalization to the N-target case is straightforward. Designate target A as the thin cylinder and target B as the swept

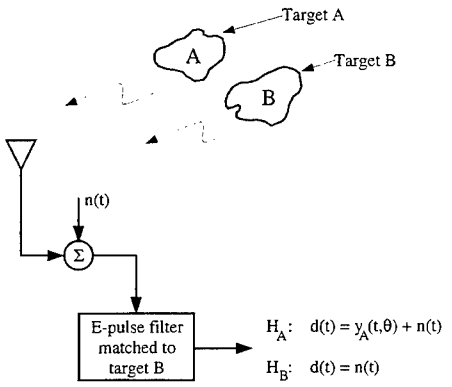

Figure 1: Block diagram of a system to discriminate between targets A and B using the E-pulse method.

wing aircraft. A suitable wide bandwidth source illuminates the unknown target (either A or B) and the scattered field from the target is received and convolved with the E-pulse matched to target B, or equivalently, as depicted in Figure 1, the return is multiplied (frequency domain) by the E-pulse filter matched to target B. (Note that an E-pulse filter matched to target A/B will have zeros at positions in the complex plane where the impulse response function of target A/B has poles. See Eq. (1) above.) Figure 2a shows that in late time a null signal results at the output of the E-pulse filter matched to target B if target B is indeed responsible for generating the return. In contrast, Figure 2b shows that if target A were the true target present an oscillatory *nonzero* return is observed. In short, a *late-time nonzero* output from the E-pulse filter matched to target B indicates, for this simple binary discrimination problem, that target A is present.

Several additional comments pertaining to the results in Figure 2 are in order before proceeding. First, referring to Figure 2a one may observe that the late-time output from the filter is zero when target B is present independent of the orientation of target B with respect to the transmitting antenna. When noise is present, *which will be the case for all practical systems*, Figure 2c indicates, as expected, that the late-time output from the filter is just noise when target B is present, and this noise is independent of the orientation of target B. On the other hand, when target A is present the output from the filter will, in

general, consist of a target-orientation-dependent signal (see Figure 2b), or when noise is also present, a target-orientation-dependent signal plus noise (see Figure 2d). In summary, binary target discrimination using an E-pulse filter matched to target B requires one to decide between two distinct conditions:

1. Only noise is observed in which case the declaration is made that target B is present.
2. A *target-orientation-dependent* signal *plus* noise is present in which case the declaration is made that target A is present.

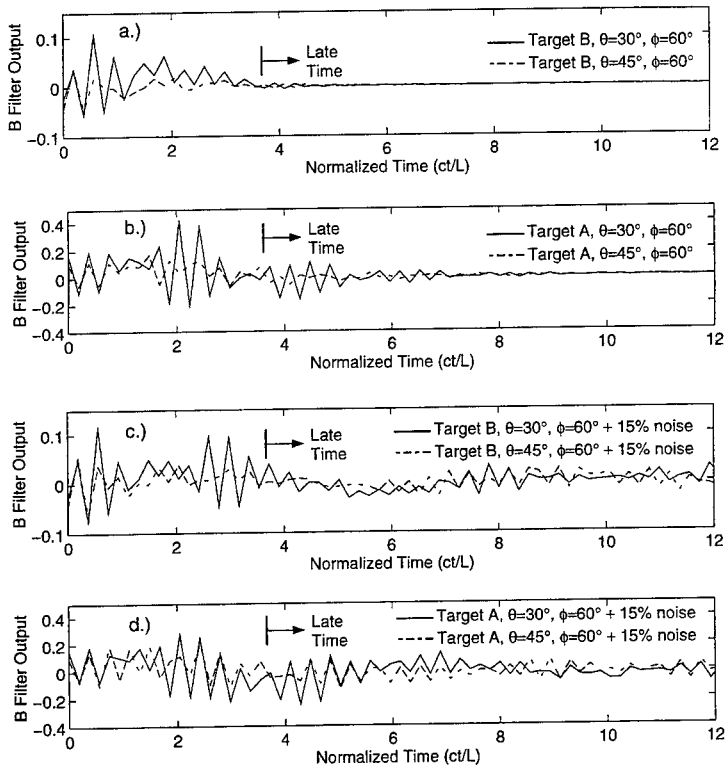

Figure 2: a.) Impulse response of target B filtered with the E-pulse for target B. b.) Impulse Response of target A filtered with the E-pulse for target B. c.) Impulse Response of target B with 15% random noise filtered with the E-pulse for target B. d.) Impulse Response of target A with 15% random noise filtered with the E-pulse for target B.

II Hypothesis Testing

In this section the hypothesis testing problem outlined in the previous paragraph will be examined in greater detail; that is, we seek to specify a decision rule based on the data stream at the output of the E-pulse filter which will enable us to "determine" which of the two possible targets is present.

According to Van Trees [6], there are four components to the hypothesis testing problem. First, we have a *source* which generates an output, the output is one of two choices, and these choices are referred to as hypotheses. The source (of data) here is the transient radar return from one of the targets and we define the mutually exclusive and exhaustive hypotheses:

H_A : target A generated the radar return.

H_B : target B generated the radar return.

In terms of the impulse response functions of targets A and B one may write:

$$H_A: \quad y_A(t,\theta) = \int r_A(t-t')f(t')\,dt' \tag{2}$$

$$H_B: \quad y_B(t,\theta) = \int r_B(t-t')f(t')\,dt' \tag{3}$$

where $y_A(t,\theta)$ and $y_B(t,\theta)$ are the aspect dependent returns from target A and B respectively expressed in terms of a convolution of the incident waveform, $f(t)$, with the impulse response function associated with the targets $r_A(t,\theta)$ and $r_B(t,\theta)$. It should be pointed out that although $r(t,\theta)$ is referred to as the impulse response function of the target (either A or B) it might just as well represent the effect of many system components in cascade:

$$r(t,\theta) = h_1(t) * h_2(t) * h_3(t) \ldots \tag{4}$$

($*$ denotes convolution) where $h_1(t)$ could be the impulse response of the transmitting antenna, $h_2(t)$ could represent the impulse response of the target, $h_3(t)$ that of the receiving antenna, etc. Of course if the impulse response of the E-pulse were included in (4), then the output in the absence of noise would be either zero or a target-aspect-dependent signal as discussed above.

The second component of the problem is a *probabilistic transition mechanism*, and the third is an *observation space*. Probability enters the problem because of an *unavoidable* noise component which is added to the radar return. When the E-pulse filter is employed one cannot say with complete confidence that the output is just noise (H_B) or signal plus noise (H_A). Each target return is mapped, via the addition of noise, to some point in an observation space. The observation space can be viewed as the set of all possible signals at the output of the E-pulse filter. The fourth and final component of the detection problem is a *decision rule*. After making an observation, a decision is made as to which hypothesis is true. Such a decision results in the assignment of each point in the observation space to one of the hypotheses.

Assuming observations are made at the output of the E-pulse filter matched to target B, in the presence of noise, the hypotheses may be rewritten as

$$H_A: \quad d(t,\theta) = y_A(t,\theta) + n(t)$$
$$H_B: \quad d(t,\theta) = n(t)$$

where $d(t,\theta)$ is the data stream, and we take the probability of a given noise function $n(t)$ to be

$$p(n(t)|\sigma) = \frac{1}{\sqrt{2\pi}\sigma} \exp\left\{-\frac{1}{2\sigma^2}\int n^2(t)\,dt\right\} \tag{5}$$

(zero mean Gaussian noise) and σ^2 is the noise power. Note that $p(n(t)|\sigma)$ is read: the probability of observing a given noise signal $n(t)$ given the noise power σ^2 . Now if target A is the true target present, then the probability of getting a given data function $d(t,\theta)$ can be found by solving for the noise $n(t)$ in terms of $y_A(t,\theta)$ and $d(t,\theta)$ and substituting into Eq. (5)

$$p(\mathrm{D}|\mathrm{A},\theta,\sigma) = \frac{1}{\sqrt{2\pi}\sigma} \exp\left\{-\frac{1}{2\sigma^2}\int [d(t,\theta) - y_A(t,\theta)]^2\, dt\right\}. \tag{6}$$

Once again, (6) is read: the probability of getting a given data function (D) given that target A is present at an orientation angle θ with respect to the transmitting antenna, and the noise power is σ^2. Equations (5) and (6) are referred to as the sampling probabilities for the problem and play a pivotal role in constructing the desired decision rule.

III Constructing a Decision Rule (Bayes Criterion)

In the binary hypothesis problem, we know that either H_A or H_B is true, and so making a decision can result in only four possible outcomes:

Target A is chosen, and target A is the true target.

Target A is chosen, and target B is the true target.

Target B is chosen, and target B is the true target.

Target B is chosen, and target A is the true target.

Obviously, the first and third alternatives are correct choices, and the second and fourth are incorrect choices. In general, one would expect that the decision rule (the method used to process the data) to depend upon the relative importance of the four possible outcomes. Costs , C_{ij} , are therefore assigned to each of the four possible outcomes with C_{ij} representing the cost of choosing hypothesis i when hypothesis j is actually true. One would assume that an incorrect decision would exact a greater toll (have a greater cost) than a correct decision so that $C_{AA} < C_{AB}$ and $C_{BB} < C_{BA}$.

A Bayesian decision rule [6] assumes that the source outputs are governed by probability assignments P_A and P_B which are referred to as prior probabilities and represent the state of knowledge about the outcome (which target is present) *before* the data is received. In the absence of prior knowledge, one would assign $P_A = P_A = \frac{1}{2}$. Our decision rule should be constructed so that on the average the cost will be as small as possible. It certainly seems intuitively correct that the risk (the average value of the *total* cost) should be proportional to: (1) the individual cost C_{ij}, (2) the probability that target j is present before getting any data (prior information) P_j, and (3) the probability that we declare that target i is present given that target i is actually present. Taking these three factors into account, an expression for the risk (total average cost) becomes

$$\begin{aligned}\Re \;=\; & C_{AA}P_A P(\text{say A}\,|\,\mathrm{A},\theta,\sigma) + C_{AB}P_B P(\text{say A}\,|\,\mathrm{B},\theta,\sigma) + \\ & C_{BB}P_B P(\text{say B}\,|\,\mathrm{B},\theta,\sigma) + C_{BA}P_A P(\text{say B}\,|\,\mathrm{A},\theta,\sigma)\end{aligned} \tag{7}$$

which can be viewed as a rule for dividing the observation space into regions Z_A (where we declare that target A is present) and Z_B (where we declare that target B is present).

Assuming that the observation space has been divided into regions Z_A and Z_B the risk can be written in terms of the previously defined transition probabilities (Eqs. (5) and (6)) as

$$\begin{aligned}\Re &= C_{AA}P_A \int_{Z_A} p(D \mid A,\theta,\sigma)dD + C_{AB}P_B \int_{Z_A} p(D \mid B,\theta,\sigma)dD + \\ &\quad C_{BB}P_B \int_{Z_B} p(D \mid B,\theta,\sigma)dD + C_{BA}P_A \int_{Z_B} p(D \mid A,\theta,\sigma)dD. \end{aligned} \tag{8}$$

Since the entire observation space is $Z = Z_A + Z_B$ the integrals over Z_B can be replaced with integrals over $Z - Z_A$, and additionally, the probability density functions must have the property that

$$\int_Z p(D \mid A,\theta,\sigma)dD = \int_Z p(D \mid B,\theta,\sigma)dD = 1. \tag{9}$$

Using Eq. (9) in Eq. (8) allows one to express the risk as

$$\begin{aligned}\Re &= P_A C_{AB} + P_B C_{BB} + \int_{Z_A} \{P_B(C_{AA} - C_{BB})p(D \mid B,\theta,\sigma) - \\ &\quad P_A(C_{BA} - C_{AA})\,p(D \mid A,\theta,\sigma)\}\,dD. \end{aligned} \tag{10}$$

The first two terms in Eq. (10) represent the fixed cost. As mentioned above, the cost of making an incorrect declaration is greater than the cost of making a correct one, or $C_{AB} > C_{BB}$ and $C_{BA} > C_{AA}$. Thus, the terms in parentheses in Eq. (10) must be positive. Furthermore, since the probability density functions in Eq. (10) are positive, minimizing the risk requires that Z_A be that portion of the observation space which satisfies

$$P_A(C_{BA} - C_{AA})\,p(D \mid A,\theta,\sigma) \geq P_B(C_{AA} - C_{BB})p(D \mid B,\theta,\sigma). \tag{11}$$

In other words, if, after receiving the data, the inequality in Eq. (11) holds, then we declare that target A is present. If the inequality is violated, then we declare that target B is present. Alternatively, Eq. (11) may be manipulated to yield

$$\frac{p(D \mid A,\theta,\sigma)}{p(D \mid B,\theta,\sigma)} \underset{H_B}{\overset{H_A}{\gtrless}} \frac{P_B(C_{AB} - C_{BB})}{P_A(C_{BA} - C_{AA})} \tag{12}$$

where the quantity on the left is called the likelihood ratio and that on the right the threshold. Equation (12) is the desired decision rule and is often called a threshold test. Our data processor evaluates the likelihood ratio, and if this likelihood ratio exceeds the threshold, then we declare that hypothesis H_A is true. Otherwise, if the likelihood ratio is less than the threshold, then hypothesis H_B is declared true.

IV Threshold Testing The Output of the E-pulse Filter

In this section the threshold test is examined for the case of uniform priors and uniform cost. In addition, the dependence of the threshold test on target aspect is considered.

The assumption of uniform priors implies that $P_A = P_B = \frac{1}{2}$ (before getting any data target A is just as likely to be present as target B), and if the cost are still assumed uniform, $C_{AA} = C_{BB} = 0$ and $C_{AB} = C_{BA}$, then the threshold becomes unity. If target A is present, then the probability of observing a given data function D is given by Eq. (6). On the other hand, if target B is present, the probability of getting a given data function becomes

$$p(D|B,\theta,\sigma) = \frac{1}{\sqrt{2\pi}\sigma} \exp\left\{-\frac{1}{2\sigma^2}\int d(t,\theta)^2\,dt\right\} \tag{13}$$

where Eq. (5) has been used with the noise replaced by the data which is true when target B is present. Substituting Eqs. (5) and (13) into Eq. (12) and taking the logarithm of both sides allows the threshold test to be written as

$$\int d(t)\, y_{\mathrm{A}}(t,\theta)\, dt \underset{H_B}{\overset{H_A}{\gtrless}} \frac{1}{2} \int y_{\mathrm{A}}^2(t,\theta)\, dt. \tag{14}$$

Note that in Eq. (14) the orientation of the target, θ, is assumed known. The new form of the decision rule in Eq. (14) is based on a comparison of energies. The right hand side of Eq. (14) is just one half the total late time energy in the signal at the output of the E-pulse filter when target A is present. If target A is actually present, the left hand side of Eq. (14) should exceed the threshold which is certainly true since

$$\int d(t)\, y_{\mathrm{A}}(t,\theta)\, dt \;=\; \int [y_{\mathrm{A}}(t,\theta)]^2\, dt \;+\; \int n(t) y_{\mathrm{A}}(t,\theta)\, dt, \tag{15}$$

and the right most integral is zero since the noise is as likely to be positive as negative. On the other hand if target B is present then the output of the E-pulse filter will just be noise, $d(t) = n(t)$, and the left hand side of Eq. (14) has an expected value of zero which is less than the threshold.

As mentioned above, Eq. (14)was derived under the assumption that the target aspect, θ, is known. When this is not the case, θ is referred to as a nuisance parameter [7] or unwanted parameter, and a technique known as marginalization must be employed. In effect, marginalization allows one to take into account all possible target orientations as demonstrated below.

According to Eq. (6), $p(\mathrm{D} \mid \mathrm{A}, \theta, \sigma)$ represents the probability of getting a data set D given that target A is present at an orientation angle θ with noise power σ^2. However, if the dependence on target aspect is to be eliminated we actually desire $p(\mathrm{D} \mid \mathrm{A}, \sigma)$, which is obviously independent of θ. The latter may be obtained from the former by applying what essentially amounts to the elementary sum and product rules of probability theory, that is

$$p(\mathrm{D} \mid \mathrm{A}, \sigma) \;=\; \int p(\mathrm{D}, \theta \mid \mathrm{A}, \sigma)\, d\theta \;=\; \int p(\mathrm{D} \mid \mathrm{A}, \theta, \sigma) p(\theta \mid \mathrm{A}, \sigma) d\theta. \tag{16}$$

As pointed out by Jaynes [7], "This is a weighted average of all possible values of $p(\mathrm{D} \mid \mathrm{A}, \theta, \sigma)$, weighted according to the prior probability $p(\theta \mid \mathrm{A}, \sigma)$." Of course Eq. (16) cannot be evaluated until the prior for the target orientation, $p(\theta \mid \mathrm{A}, \sigma)$, has been specified.

As an example, assume a uniform probability distribution for the target in the form

$$\mathrm{p}(\mathrm{D} \mid \mathrm{A}, \sigma) = \begin{cases} \frac{1}{\theta_2 - \theta_1} & \theta_1 < \theta < \theta_2 \\ 0 & \text{elsewhere.} \end{cases} \tag{17}$$

Now using Eqs (17) and (6) in Eq. (16) yields

$$\mathrm{p}(\mathrm{D} \mid \mathrm{A}, \sigma) \;=\; \frac{1}{\theta_2 - \theta_1} \frac{1}{\sqrt{2\pi}\sigma} \int_{\theta_1}^{\theta_2} \exp\left\{ -\frac{1}{2\sigma^2} \int [d(t,\theta) - y_{\mathrm{A}}(t,\theta)]^2\, dt \right\} d\theta. \tag{18}$$

The reader should be aware that other probability density functions for the target angle θ may also be appropriate. In fact, if the target orientation is known, by some other means, to be within a small angular sector about θ then Eq. (18) is evaluated by sampling the integrand at that value of θ and the previous form of the ratio test given by Eq. (15) results. If, on the other hand, very little knowledge on the target orientation is available, then the integral in Eq. (18) might extend over a wide range so that *all* the θ-dependent data would be taken into account. Using Eqs. (18) and (5) in Eq. (12) results in

the final form for the ratio test taking into account all the data for target orientations within the range $\theta_1 < \theta < \theta_2$

$$\frac{\frac{1}{\theta_2-\theta_1}\int_{\theta_1}^{\theta_2} \exp\left\{-\frac{1}{2\sigma^2}\int [d(t,\theta)-y_{\mathrm{A}}(t,\theta)]^2\,dt\right\}\,d\theta}{\exp\left\{-\frac{1}{2\sigma^2}\int d^2(t)\,dt\right\}} \underset{H_B}{\overset{H_A}{\gtrless}} 1. \tag{19}$$

V Concluding Remarks

In this paper an overview of the E-pulse target discrimination technique has been provided. To the best of our knowledge, this work represents the first time that the E-pulse identification scheme has been investigated from the point of view of probability theory. We point out that the E-pulse and related S-pulse target identification schemes have been purported not to depend upon target orientation. The reason for this assumption is based on the fact that when a target is present the output of the E-pulse filter matched to that target is indeed noise, independent of the matched target's orientation. However, when probability theory and standard hypothesis testing techniques are applied to the problem, target orientation must once again be considered. The reason is, as discussed above, the output of the E-pulse filter when the "incorrect" target is present is *aspect dependent.* One reason for the confusion may be related to the erroneous assumption that, in general, the E-pulse scheme allows one to compare a large signal (target not matched to the filter) to a small signal (noise), matched case. This condition may in fact prevail, but only in high signal-to-noise ratio scenarios. (If the signal-to-noise ratio is large enough, in may be more convenient to carry out identification visually!) When the signal-to-noise ratio begins to fall the matched response (noise) will, to the human operator, began to closely resemble the unmatched response and one must resort to more appropriate means of signal detection (e.g. probability theory).

References

[1] C.E. Baum, *Transient Electromagnetic Fields*, ch. The Singularity Expansion Method, pp. 129–179. Springer-Verlag, 1976.

[2] E.J. Rothwell and D.P. Nyquist, "Radar target discrimination using the extinction-pulse technique," *IEEE Trans. Antennas Propagation*, vol. AP-33, pp. 929–936, Sept. 1985.

[3] C.E. Baum, "Represenatation of surface current desnity and far scattering in EEM and SEM with entire functions," Interaction Note 486, Phillips Laboratory, Kirtland AFB, Feb. 1992.

[4] M. Richards, "SEM representation of the early and late time fields scattered from wire targets," *IEEE Trans. Antennas Propagation*, vol. AP-42, Apr. 1994.

[5] C.E. Baum, E.J. Rothwell, K.M. Chen, and D.P. Nyquist, "The singularity expansion method and its application to target identification," *IEEE Proceedings*, vol. 79, pp. 1481–1492, Oct. 1991.

[6] H.L. Van Trees, *Detection, Estimation, and Modulation Theory Part I.* John Wiley & Sons, 1967.

[7] E.T. Jaynes and C.R. Smith, "Theory of radar target discrimination," Technical Report RD-AS-91-6, U.S. Army Missile Command, ATTN: AMSMI-RD-AS-RA, Redstone Arsenal, AL 35898-5253, Feb. 1991. Procurement Identification number DAAl03-86-D-001, D.O.1515.

[8] G.L. Bretthorst, *Bayesian Spectrum Analysis and Parameter Estimation.* Springer-Verlag, 1988.

A BOUNDARY-INTEGRAL CODE FOR ELECTROMAGNETIC NONDESTRUCTIVE EVALUATION

Kim Murphy and Harold A. Sabbagh
Sabbagh Associates, Inc.
4635 Morningside Drive
Bloomington, IN 47408

INTRODUCTION

Volume-integral equations have proven to be very successful in the computation of eddy-current probe-flaw responses for nondestructive evaluation (NDE) problems having a number of simple geometries. This approach to NDE computations has proven superior to the finite-element approach in both accuracy and computer resources required, and is the basis of our proprietary code VIC-3D[1]. The volume-integral approach, however, is not as well adapted to accommodating the complex geometries sometimes required in practical applications. An example is the separation of edge and corner effects from the response of a flaw. We will discuss an extension of the volume-integral approach that incorporates boundary-integral equations to provide a description of complicated surface geometries.

BACKGROUND

Requirements for eddy-current probe simulation software for the aerospace industry include

1. Coil Modeling:
   - .1 conventional absolute and differential coils (side mount and end mount),
   - .2 single eddy-current array probe (ECAP) coils (air core and ferrite backed),
   - .3 ECAP arrays (air core and ferrite backed), including interactions between coils.
2. Part Geometry Modeling (aircraft engine components):
   - .1 sharp edges,
   - .2 chamfered and filleted edges,
   - .3 bolt holes,
   - .4 dovetail contours.
3. Defect Modeling:
   - .1 EDM notches,
   - .2 idealized cracks away from edges,
   - .3 idealized cracks at edges,
   - .4 pits and other geometrically defined defects.
4. Coil Surface Interaction:
   - .1 compute the complex impedance due to coil surface interaction

[1]VIC-3D is a registered trademark of Sabbagh Associates, Inc.

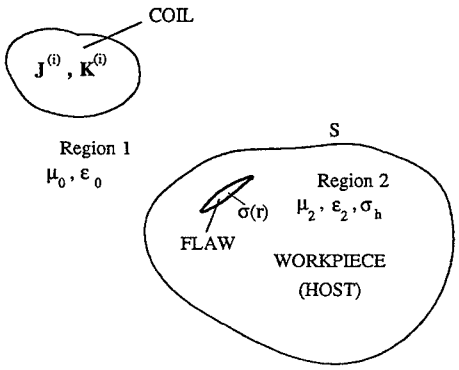

Figure 1: Electromagnetic NDE problem to be solved. Region 1 contains the probe coil, and region 2 the workpiece (or host) and flaw.

.2 compute lift-off resulting from any combination of coil and geometry models

.3 calculate complex impedance as a function of drive frequency.

VIC-3D already solves most of these problems quite efficiently using volume-integral equations [1-3]. We propose to couple boundary-integral equations to the volume-integral equations to enhance VIC's ability to solve the complex geometries of item 2, while, at the same time, distinguishing flaws at edges and corners, as described in item 3.

THE TWO SYSTEMS OF COUPLED INTEGRAL EQUATIONS

We will derive the equations for the general electromagnetic NDE problem, which consists of two regions, as in Figure 1. The first is the exterior of the workpiece, contains the probe coil, and consists of free-space, whereas the second is the finite workpiece which contains a flaw. The boundary of region 2 is labeled S. The "incident" fields established by the volume currents produce "scattered" fields at boundary S. We want to calculate the scattered fields by using boundary-integral equations.

We use the equivalence principle of Figure 2 to determine various boundary-integral equations. The electric surface current, $\mathbf{J}_e$, and magnetic surface current, $\mathbf{K}_e$, of Figure 2(b) are fictitious sources for the scattered and transmitted fields, $\mathbf{E}_1^{(s,t)}$, $\mathbf{H}_1^{(s,t)}$, and $\mathbf{J}_d$, $\mathbf{K}_d$ serve the same purpose for $\mathbf{E}_2^{(s,t)}$, $\mathbf{H}_2^{(s,t)}$ in Figure 2(c). The "transmitted" fields, those with the superscript t, are auxiliary fields, whereas the "scattered" fields, those with the superscript s, are actual. We define the surface currents by $\mathbf{J}_s = \mathbf{a}_n \times \mathbf{H}$, and $\mathbf{K}_s = -\mathbf{a}_n \times \mathbf{E}$.

One can derive a host of boundary-integral equations by choosing the auxiliary fields appropriately. For example, if we let $\mathbf{a}_n \times \mathbf{E}_1^{(t)} = 0$, $\mathbf{a}_n \times \mathbf{E}_2^{(t)} = 0$, $\mathbf{a}_n \times \mathbf{H}_1^{(t)} = 0$, $\mathbf{a}_n \times \mathbf{H}_2^{(t)} = 0$, which is Love's equivalence theorem, then it can be easily shown that $\mathbf{J}_e = -\mathbf{J}_d = \mathbf{J}_s$, $\mathbf{K}_e = -\mathbf{K}_d = \mathbf{K}_s$. Using these facts we can derive the following system:

$$j\omega(\hat{\epsilon}_2 + \epsilon_0)\mathbf{K}_s(\mathbf{r}) = 2j\omega \mathbf{a}_n \times (\epsilon_0 \mathbf{E}_1^{(i)} - \hat{\epsilon}_2 \mathbf{E}_2^{(i)})$$

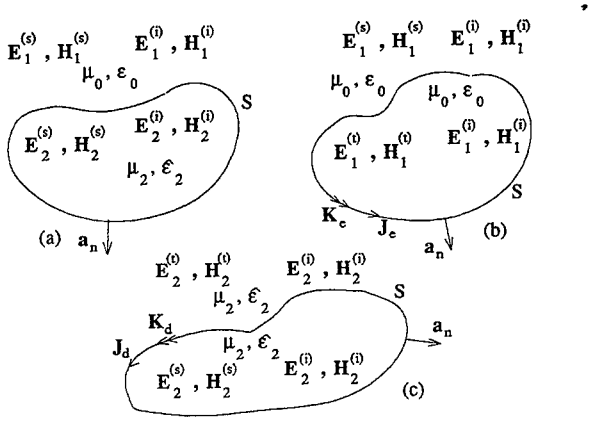

Figure 2: Equivalence principle. (a) Original problem. (b) External equivalence case. (c) Internal equivalence case.

$$-\mathbf{a}_n \times \frac{1}{2\pi}\int_{S^+}[\mathbf{J}_s(-k_2^2\phi_2 + k_0^2\phi_1) + j\omega \mathbf{K}_s \times \nabla'(\hat{\epsilon}_2\phi_2 - \epsilon_0\phi_1) + \nabla'_s \cdot \mathbf{J}_s \nabla'(\phi_2 - \phi_1)]dS' \quad (1)$$

$$j\omega(\mu_0+\mu_2)\mathbf{J}_s(\mathbf{r}) = j\omega 2\mathbf{a}_n \times (\mu_2\mathbf{H}_2^{(i)} - \mu_0\mathbf{H}_1^{(i)})$$
$$+\mathbf{a}_n \times \frac{1}{2\pi}\int_{S^+}[\mathbf{K}_s(-k_2^2\phi_2 + k_0^2\phi_1) - j\omega \mathbf{J}_s \times \nabla'(\mu_2\phi_2 - \mu_0\phi_1) + \nabla'_s \cdot \mathbf{K}_s \nabla'(\phi_2 - \phi_1)]dS' \quad (2)$$

$$\mathbf{J}_a(\mathbf{r}) - \sigma_a(\mathbf{r})\int_{\text{flaw}} \mathcal{G}_2^{ee}(\mathbf{r}|\mathbf{r}') \cdot \mathbf{J}_a(\mathbf{r}')dv' =$$
$$-\sigma_a(\mathbf{r})\frac{1}{4\pi}\int_S [j\omega\mu_2 \mathbf{J}_s\phi_2(\mathbf{r}|\mathbf{r}') + \mathbf{K}_s \times \nabla'\phi_2(\mathbf{r}|\mathbf{r}') + \frac{1}{j\omega\hat{\epsilon}_2}\nabla'_s \cdot \mathbf{J}_s\nabla'\phi_2(\mathbf{r}|\mathbf{r}')]dS' \,. \quad (3)$$

A second system of boundary-integral equations can be obtained by letting the tangential components of $\mathbf{a}_n \times \mathbf{E}_1^{(t)} = \mathbf{a}_n \times \mathbf{E}_1^{(s)}$, which implies that $\mathbf{K}_e = 0$, as can be seen from Figure 2(b). Similarly, let $\mathbf{a}_n \times \mathbf{E}_2^{(t)} = \mathbf{a}_n \times \mathbf{E}_2^{(s)}$, which means that $\mathbf{K}_d = 0$. Hence, the magnetic surface currents vanish, and we are left with only electric surface currents to be determined. The equations for these currents, $\mathbf{J}_e$, $\mathbf{J}_d$, are obtained by returning to Figure 2(a), and equating the tangential components of the total electric and magnetic fields. The result is

$$\left(\mathbf{E}_2^{(i)} - \mathbf{E}_1^{(i)}\right)_{\tan} = \left\{\frac{1}{4\pi}\int_S \left[j\omega\mu_0 \mathbf{J}_e\phi_1(\mathbf{r}|\mathbf{r}') + \frac{1}{j\omega\epsilon_0}\nabla'_s \cdot \mathbf{J}_e\nabla'\phi_1(\mathbf{r}|\mathbf{r}')\right]dS'\right.$$
$$\left. - \frac{1}{4\pi}\int_S \left[j\omega\mu_2 \mathbf{J}_d\phi_2(\mathbf{r}|\mathbf{r}') + \frac{1}{j\omega\hat{\epsilon}_2}\nabla'_s \cdot \mathbf{J}_d\nabla'\phi_2(\mathbf{r}|\mathbf{r}')\right]dS'\right\}_{\tan} \quad (4)$$

$$2\mathbf{a}_n \times \left(\mathbf{H}_2^{(i)} - \mathbf{H}_1^{(i)}\right) = \mathbf{J}_e - \frac{1}{2\pi}\int_S \mathbf{a}_n(\mathbf{r}) \times (\mathbf{J}_e \times \nabla'\phi_1(\mathbf{r}|\mathbf{r}'))dS'$$
$$+ \mathbf{J}_d + \frac{1}{2\pi}\int_S \mathbf{a}_n(\mathbf{r}) \times (\mathbf{J}_d \times \nabla'\phi_2(\mathbf{r}|\mathbf{r}'))dS' \quad (5)$$

$$\mathbf{J}_a(\mathbf{r}) - \sigma_a(\mathbf{r}) \int_{\text{flaw}} \mathcal{G}_2^{ee}(\mathbf{r}|\mathbf{r}') \cdot \mathbf{J}_a(\mathbf{r}') dv' = -\sigma_a(\mathbf{r}) \frac{1}{4\pi} \int_S \left[j\omega\mu_2 \mathbf{J}_d \phi_2(\mathbf{r}|\mathbf{r}') + \frac{1}{j\omega\hat{\epsilon}_2} \nabla_s' \cdot \mathbf{J}_d \nabla' \phi_2(\mathbf{r}|\mathbf{r}') \right] dS' \tag{6}$$

where $\mathbf{r} \in S$ in the boundary-integral operators of (1), (2), (4), and (5), $\nabla_s' \cdot$ is the surface divergence, and $\int_S$* denotes the principal value. The scalar Green's functions are

$$\phi_1(\mathbf{r}, \mathbf{r}') = \frac{e^{-jk_0|\mathbf{r}-\mathbf{r}'|}}{|\mathbf{r}-\mathbf{r}'|}, \quad \phi_2(\mathbf{r}, \mathbf{r}') = \frac{e^{-jk_2|\mathbf{r}-\mathbf{r}'|}}{|\mathbf{r}-\mathbf{r}'|}, \tag{7}$$

and $k_0^2 = \omega^2\mu_0\epsilon_0$, $k_2^2 = \omega^2\mu_2\hat{\epsilon}_2$, $\hat{\epsilon}_2 = \epsilon_2 + \sigma_h/j\omega$, and μ_2, $\hat{\epsilon}_2$ are constants. σ_h is the conductivity of the workpiece, which is taken to be homogeneous, and the anomalous conductivity is defined to be $\sigma_a(\mathbf{r}) = \sigma(\mathbf{r}) - \sigma_h$. Note that σ_a vanishes off the flaw.

System (1) and (2) is a modest extension of the system that appears in [4], in that our system contains terms corresponding to the presence of the incident fields in region 2. Poggio and Miller [5] have developed a system for $\mathbf{K}_s$ and $\mathbf{J}_s$, but their system is of the first kind, whereas (1) and (2) are of the second kind. Systems of the second kind usually result in better conditioned matrix equations, which provides significant advantages in numerical computations.

System (4) and (5), like the previous one, has four surface current components as unknowns. It consists of a first-kind integral equation, (4), and a second-kind integral equation, (5). The first equation is the electric-field integral equation (EFIE), and the second the magnetic-field integral equation (HFIE). EFIE's and HFIE's, as individual equations, are well known and understood in the computational electromagnetics community [5]. MacCamy and Stephan [6], and Wang and Ida [7] have used a similar system to solve eddy-current problems.

In both of these systems, $\mathbf{J}_a(\mathbf{r})$ is the anomalous current density that is associated with the flaw. Equations (3) and (6) are volume-integral equations for the anomalous current. These same equations (with a different right-hand side, of course) are already solved very efficiently in VIC-3D.

The incident fields in region 1 are due to the exciting coil. Hence, we have

$$\mathbf{E}_1^{(i)}(\mathbf{r}) = \int_{\text{coil}} \mathcal{G}_1^{ee}(\mathbf{r}|\mathbf{r}') \cdot \mathbf{J}_c(\mathbf{r}') dv' \tag{8}$$

$$\mathbf{H}_1^{(i)}(\mathbf{r}) = \int_{\text{coil}} \mathcal{G}_1^{me}(\mathbf{r}|\mathbf{r}') \cdot \mathbf{J}_c(\mathbf{r}') dv', \tag{9}$$

whereas those in region 2 are given by integrals over the region of the flaw:

$$\mathbf{E}_2^{(i)}(\mathbf{r}) = \int_{\text{flaw}} \mathcal{G}_2^{ee}(\mathbf{r}|\mathbf{r}') \cdot \mathbf{J}_a(\mathbf{r}') dv' \tag{10}$$

$$\mathbf{H}_2^{(i)}(\mathbf{r}) = \int_{\text{flaw}} \mathcal{G}_2^{me}(\mathbf{r}|\mathbf{r}') \cdot \mathbf{J}_a(\mathbf{r}') dv'. \tag{11}$$

$\mathcal{G}$ is a dyadic Green's function whose subscript defines its region, and whose superscripts denote its type. The first superscript denotes the nature of the field at $\mathbf{r}$, e being electric, and m magnetic, whereas the second superscript denotes the nature of the source at $\mathbf{r}'$. $\mathcal{G}_1$ is determined from ϕ_1, and $\mathcal{G}_2$ from ϕ_2.

The integral equations are discretized by means of Galerkin's variant of the method of moments. The anomalous current, $\mathbf{J}_a(\mathbf{r})$, is expanded in three-dimensional pulse functions that are defined on a regular grid, and the resulting equation is then tested with the same functions. This results in a matrix equation in which the matrix is Toeplitz in all three dimensions:

$$\mathbf{G}(jlm, JLM) = \mathbf{G}^{(0)}(l - L, m - M, j - J) \,. \tag{12}$$

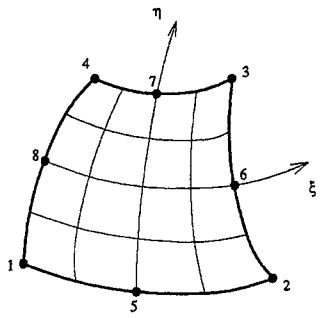

Figure 3: Eight-node serendipity element.

This feature gives VIC-3D its ability to solve very large problems efficiently on personal computers with a minimum of storage. (We have solved problems with 50,000 unknowns in a day, using less than 20MB on a personal computer.)

DISCRETIZATION OF THE BOUNDARY-INTEGRAL OPERATORS

The discretization of the boundary-integral operators also uses Galerkin's variant of the method of moments, except that the unknown surface currents are expanded in vector edge-elements that are defined on a surface mesh [12],[13]. These elements preserve continuity of normal components of the currents across edges of the mesh, thereby guaranteeing that the unknown currents belong to $H(div)$, the space of square-integrable functions, whose divergences are also square-integrable.

We have developed a theory of higher-order edge-elements (i.e., elements that interpolate to higher-order than linear), which is implemented using the eight-node serendipity element of finite-element theory [8]. The element is shown in Figure 3, and the interpolating polynomials are listed in (13).

$$\begin{aligned}
&\text{Eight}-\text{node serendipity quadrilateral}: \\
&\psi_1(\xi,\eta) = [(1-\xi)(1-\eta) - (1-\xi^2)(1-\eta) - (1-\eta^2)(1-\xi)]/4 \\
&\psi_2(\xi,\eta) = [(1+\xi)(1-\eta) - (1-\xi^2)(1-\eta) - (1-\eta^2)(1+\xi)]/4 \\
&\psi_3(\xi,\eta) = [(1+\xi)(1+\eta) - (1-\xi^2)(1+\eta) - (1-\eta^2)(1+\xi)]/4 \\
&\psi_4(\xi,\eta) = [(1-\xi)(1+\eta) - (1-\xi^2)(1+\eta) - (1-\eta^2)(1-\xi)]/4 \\
&\psi_5(\xi,\eta) = (1-\xi^2)(1-\eta)/2 \\
&\psi_6(\xi,\eta) = (1-\eta^2)(1+\xi)/2 \\
&\psi_7(\xi,\eta) = (1-\xi^2)(1+\eta)/2 \\
&\psi_8(\xi,\eta) = (1-\eta^2)(1-\xi)/2.
\end{aligned} \tag{13}$$

One can expand both the geometry of the workpiece and the surface currents using (13) for interpolation, which makes this an isoparametric element. If, however, the order of the geometric shape function is greater than the order of approximation of the fields, then the geometric elements are called *superparametric*; conversely, the geometric elements are called *subparametric* if their order is less than that of the field shape elements [9]. There are advantages to using different orders of approximation of the geometry and fields. Ingber and Ott [9] have gotten good results when approximating the geometry to second order, while approximating the currents with linear shape functions. This means that there may be fewer variables required to represent the field than

to represent the geometry, with a consequent reduction in computer resources to solve for the fields.

The interpolating vector-basis functions are given by

$$\begin{aligned} \mathbf{f}_{i1} &= \psi_i(\xi,\eta)\frac{\mathbf{a}_\xi}{\mathbf{a}_n\cdot(\mathbf{a}_\xi\times\mathbf{a}_\eta)} = \psi_i(\xi,\eta)\frac{\mathbf{a}_\xi}{\boldsymbol{\tau}_\xi\cdot\mathbf{a}_\xi} \\ \mathbf{f}_{i2} &= \psi_i(\xi,\eta)\frac{\mathbf{a}_\eta}{\mathbf{a}_n\cdot(\mathbf{a}_\xi\times\mathbf{a}_\eta)} = \psi_i(\xi,\eta)\frac{\mathbf{a}_\eta}{\boldsymbol{\tau}_\eta\cdot\mathbf{a}_\eta}\,. \end{aligned} \tag{14}$$

The vectors $\mathbf{a}_\xi$ and $\mathbf{a}_\eta$ are the unit tangent vectors to the surface along the ξ and η directions, while $\mathbf{a}_n$ is the unit normal to the surface. The vector, $\boldsymbol{\tau}_\xi$, is normal to the ξ = constant curve, and points in the direction of increasing ξ. Thus, $\boldsymbol{\tau}_\xi$ is normal to $\mathbf{a}_\eta$. $\boldsymbol{\tau}_\eta$ is normal to the η = constant curve, and points in the direction of increasing η. Thus, $\boldsymbol{\tau}_\eta$ is normal to $\mathbf{a}_\xi$. The interpolating vector-basis functions satisfy $\boldsymbol{\tau}_\xi\cdot\mathbf{f}_{i1}=1$, at the ith node, and vanish at the other nodes; $\boldsymbol{\tau}_\eta\cdot\mathbf{f}_{i2}=1$ at the ith node, and vanishes at the other nodes.

We have developed a method of handling the improper integrals that occur in computing the matrix elements of the boundary-integral operators. This algorithm, which is based on an idea of Hayami [10], requires one to locate the field point that is nearest the source region, and then translating the origin of coordinates to this point. The computation is then completed in a polar coordinate system, which has the effect of removing the singularity.

SOLUTION STRATEGIES

The discretized equations that are obtained by applying the method of moments to integral equations involve dense matrices, with no particular mathematical structure. Hence, it is important to develop efficient algorithms for solving the discretized equations. We used the Linpack [16] routine CGECO to compute the LU factorization of the system matrix, and CGESL to solve the resulting system of equations. If the problem is too large to accomodate the LU factorization, we employ the conjugate gradient algorithm that is used in **VIC-3D©**.

In order to understand the conjugate gradient algorithm, we write the system to be solved as the operator equation

$$Y = \mathcal{A}X, \tag{15}$$

where Y stands for the array of applied electric and magnetic fields, and X stands for the unknowns $J_q^{(e,d)}$. The algorithm also uses the adjoint operator, $\mathcal{A}^*$, which corresponds to the conjugate transpose of a matrix.

The conjugate gradient algorithm starts with an initial guess, X_0, from which we compute $R_0 = Y - \mathcal{A}X_0$, $P_1 = Q_0 = \mathcal{A}^*R_0$. Then for $k = 1, 2, \ldots$, we update X_k by the following steps:

$$\begin{aligned} S_k &= \mathcal{A}P_k \\ a_k &= \frac{\|Q_{k-1}\|^2}{\|S_k\|^2} \\ X_k &= X_{k-1} + a_kP_k \\ R_k &= R_{k-1} - a_kS_k \\ Q_k &= \mathcal{A}^*R_k \\ b_k &= \frac{\|Q_k\|^2}{\|Q_{k-1}\|^2} \\ P_{k+1} &= Q_k + b_kP_k\,. \end{aligned} \tag{16}$$

When $\|R_k\|/\|Y\|$ is sufficiently small, X_k is accepted as the solution of (15).

The quality of the solutions obtained from the matrix factorization and conjugate gradient are comparable and the errors in the unknown currenst J are quite small. In a typical problem, solution

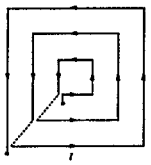

Figure 4: A printed-circuit coil.

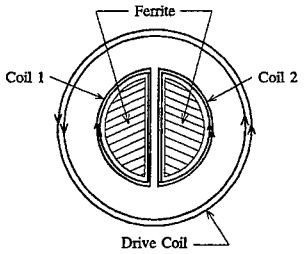

Figure 5: A split-core differential probe.

by LU decomposition required about 13 min. on the Sun workstation, while the conjugate gradient solution took about 90 min to converge. While this initially makes the conjugate gradient approach look less attractive, there is a potentially bright future.

The discretized boundary-integral equations do not possess the special Toeplitz and Hankel structure of the volume-integral equation that is solved in **VIC-3D©**, so it appears that we must compute the matrix-vector products in the usual manner when applying the conjugate gradient algorithm. Rokhlin, [14] and [15], has recently developed an algorithm, called the "fast multipole method (FMM)," to obviate this problem. The algorithm is based on the expansion of the full-space Greens's function, e^{-jkr}/r, in terms of multipoles, i.e., products of spherical Bessel functions, spherical Hankel functions, and Legendre polynomials. In its simple single-stage form, the algorithm reduces the computational complexity of a matrix-vector multiplication from $O(N^2)$ to $O(N^{3/2})$, where N is the number of unknowns. Coifman, *et al* [15] indicate how the algorithm may be applied to vector problems in electromagnetics, when the appropriate integral equation is the electric field integral equation, but not the magnetic field integral equation. During our present research we will apply the algorithm to our system, which consists of both equations.

ANALYSIS OF PRINTED-CIRCUIT AND SPLIT-CORE DIFFERENTIAL PROBES

The model will include the incident fields of (8) and (9) that are produced by the printed-circuit coil of Figure 4 and the split-core differential probe of Figure 5.

Arrays of printed-circuit coils are becoming prominent in precision measurements of complex

shapes, such as dovetail slots in aircraft turbine disks [11]. A significant advantage of such arrays is that they are fixed in space on the part, and no mechanical scanning is required.

The split-core differential probe is also used in studying complex shapes. It consists of two identical ferrite cores, around each of which is a coil. The arrangement produces a differential signal, which is the difference of the signals seen by each of the two parts when the probe is scanned over a flaw. The differential probe is sensitive to edges, and not to slowly varying background conditions.

REFERENCES

1. Sabbagh Associates, Inc. "An Eddy-Current Model For Three-Dimensional Nondestructive Evaluation of Advanced Composites," Final Report, Naval Surface Warfare Center - White Oak, Silver Spring, MD, 25 July, 1988.
2. L. D. Sabbagh, H. A. Sabbagh, "A Computer Model of Eddy-Current Probe-Crack Interaction," Review of Progress in Quantitative Nondestructive Evaluation, Brunswick, ME, July, 1989
3. L. D. Sabbagh, K. H. Hedengren, D. C. Hurley, "Interaction of Flaws with a Ferrite-Core Eddy Current Probe: Comparison between Model and Experiment," D. O. Thompson and D. E. Chimenti, editors, *Review of Progress in Quantitative Nondestructive Evaluation Vol 10A*, p 883, Plenum, New York, 1991.
4. C. Müller, *Foundations of the Mathematical Theory of Electromagnetic Waves.* New York: Springer-Verlag, 1969.
5. A. J. Poggio and E. K. Miller, "Integral Equation Solutions of Three-dimensional Scattering Problems", in R. Mittra, ed., *Computer Techniques for Electromagnetics*, Chapter 4. Oxford: Pergamon Press, 1973.
6. R. C. MacCamy and E. Stephan, "Solution Procedures for Three-Dimensional Eddy Current Problems," J. Mathematical Analysis and Applications, Vol. 101, pp. 348-379, 1984.
7. J-S. Wang and N. Ida, "Utilization of Geometric Symmetries in "Edge" Based Boundary Integral Eddy Current Solutions," IEEE Trans. Magnetics, Vol. 28, No. 2, March 1992, pp. 1704-1707.
8. T. J. R. Hughes, *The Finite Element Method: Linear Static and Dynamic Finite Element Analysis.* Englewood Cliffs: Prentice-Hall, 1987.
9. M. S. Ingber and R. H. Ott, "An Application of the Boundary Element Method to the Magnetic Field Integral Equation," IEEE Trans. Antennas and Propagation, Vol. 39, No. 5, May 1991, pp. 606-611.
10. K. Hayami, "High Precision Numerical Integration Methods for 3-D Boundary Element Analysis," IEEE Trans. Magnetics, Vol. 26, No. 2, March 1990, pp. 603-606.
11. D. C. Hurley, K. H. Hedengren, and J. D. Young, in *Review of Progress in QNDE*, vol. 11, eds. D. O. Thompson and D. E. Chimenti (Plenum, New YOrk, 1992), p. 1137.
12. Z. J. Cendes, "Vector Finite Elements for Electromagnetic Field Computation," IEEE Trans. Magnetics, Vol. 27, No. 5, September 1991, pp. 3958-3966.
13. A. Bossavit and I. Mayergoyz, "Edge-Elements for Scattering Problems," IEEE Trans. Magnetics, Vol. 25, No. 4, July 1989, pp. 2816-2821.
14. V. Rokhlin, "Rapid Solution of Integral Equations of Scattering Theory in Two Dimensions," Journal of Computational Physics, Vol. 86, pp. 414-439, 1990.
15. R. Coifman, V. Rokhlin, S. Wandzura, "The Fast Multipole Method for the Wave Equation: A Pedestrian Approach," IEEE Antennas & Propagation Magazine, Volume 35, No. 3, June 1993, pp. 7-12.
16. J. J. Dongarra, J. R. Bunch, C. B. Moler, and G. W. Stewart, LINPACK Users' Guide, SIAM, Philadelphia, 1979.

The Numerical Analysis of Planar Antennas Buried in Layered Media

J.J. van Tonder, J.H. Cloete and D.B. Davidson*

Department of Electrical and Electronic Engineering,
University of Stellenbosch, Stellenbosch 7600, South Africa.
e-mail: jhcloete@firga.sun.ac.za
tel: +27-21-808 4337

1 Introduction

The near-fields of microstrip antennas printed on a single layered substrate and radiating into free-space, have recently been computed and measured by Mosig *et al.* [1]. Their ideas have been extended [2] to deal with multi-layered dielectrics and the resulting formulation was used to develop a triangular subdomain moment method code which is based on the theory of Rao, Wilton and Glisson [3] but incorporating Mosig's [4] multi-layered Green's function. The code is efficient and suitable for use on present generation personal computers; by contrast we note that Mosig *et al.* [1] used a 4 processor CRAY-2 computer. The new code was tested by comparing numerical predictions with measurements made for a planar two-arm Archimedes spiral antenna [5, 6, 7, 8, 9], *embedded in a multi-layered medium* and fed by a Marchand balun [10, 11]. The antenna was designed for operation between 2 to 6 GHz. The self-complementary spiral pattern was etched onto a thin copper clad dielectric substrate and a multilayered microwave absorber was placed between the spiral and the conducting ground plane to suppress interference due to reflections. To stringently test the code the antenna was also covered with a multilayered superstrate. Unlike Archimedes spiral antennas for avionic applications, which are usually backed by a closed cavity with conducting side walls, the test antenna was not cavity backed. Table 1 lists some of the antenna parameters and the conductor pattern is shown in Fig. 1.

2 Computation of the Radiated Fields

Using the notation of Rao, Wilton, and Glisson [3], the electric and magnetic fields are computed at an observation point (ϕ, ρ, z) due to a source triangle T_n^+ supporting a certain known current distribution as shown in Fig. 2. The coordinates x, y, z are global coordinates, and X, Y, Z are local coordinates, with $\hat{\mathbf{X}}$ the unit vector of $\boldsymbol{\rho}_n^+$, and $\hat{\mathbf{Z}}$ parallel to $\hat{\mathbf{z}}$. The horizontal electric dipole (HED) is $\hat{\mathbf{X}}$ directed. In Section 2.9 [2, pp. 11-14] the Green's functions for the fields (electric and magnetic) of a HED buried in a multi-layered medium were computed in terms of

$$G^{XX}(\beta, \mid \mathbf{P} \mid, z_j),\ G^{YX}(\beta, \mid \mathbf{P} \mid, z_j) \text{ and } G^{ZX}(\beta, \mid \mathbf{P} \mid, z_j)$$

where $\mathbf{P} = \boldsymbol{\rho} - \mathbf{r}'$, $\alpha = \angle \boldsymbol{\rho}_n^+$, $\beta = \angle \mathbf{P} - \alpha$ and $\mathbf{r}' = \xi \mathbf{r}_1 + \eta \mathbf{r}_2 + (1 - \eta - \xi)\mathbf{r}_3$. Here $\mathbf{r}_1$, $\mathbf{r}_2$ and $\mathbf{r}_3$ are the vectors to the vertexes of triangle T_n^+ in the global coordinate system.

Transform these Green's functions from the local to the global coordinates to obtain

$$\begin{aligned} G^{xX} &= \cos\alpha\, G^{XX} - \sin\alpha G^{YX}, \\ G^{yX} &= \sin\alpha\, G^{XX} + \cos\alpha G^{YX}, \\ G^{zX} &= G^{ZX}. \end{aligned} \tag{1}$$

Now substitute the expressions of G^{XX}, G^{YX}, and G^{ZX} obtained in Section 2.9, Eq. 2.46 [2, pp. 13] to get

$$\begin{aligned} G_E^{xX} &= \cos\alpha\left[\cos^2\beta E_1 + \sin^2\beta E_2\right] - \sin\alpha\left[\sin\beta\cos\beta(E_1 - E_2)\right] \\ &= \cos\beta\cos(\beta+\alpha)E_1 + \sin\beta\sin(\beta+\alpha)E_2. \end{aligned} \tag{2}$$

Similarly, for the other components

$$\begin{aligned} G_E^{yX} &= \cos\beta\sin(\beta+\alpha)E_1 - \sin\beta\cos(\beta+\alpha)E_2, \\ G_E^{zX} &= \cos\beta I_3, \\ G_H^{xX} &= \sin\beta\cos(\beta+\alpha)H_1 - \cos\beta\sin(\beta+\alpha)H_2, \\ G_H^{yX} &= \sin\beta\sin(\beta+\alpha)H_1 + \cos\beta\cos(\beta+\alpha)H_2, \\ G_H^{zX} &= \sin\beta I_{10}. \end{aligned} \tag{3}$$

Here $E_1, E_2, I_3, H_1, H_2, I_{10}$ are Sommerfeld integrals [2, Section 2.9] which must be evaluated numerically [2, Chapter 3].

This gives the total Green's functions for an HED. The total fields due to the current distribution are found by integration over the source triangle, thus

$$\left\{ \begin{array}{c} \mathbf{E} \\ \mathbf{H} \end{array} \right\} = \int_{T_n^+} \bar{\mathbf{G}}_{E,H} \cdot \mathbf{J}\, dS = 2A_n^+ \int_0^1 \int_0^{1-\eta} \bar{\mathbf{G}}_{E,H} \cdot \mathbf{J}\, d\xi\, d\eta. \tag{4}$$

Now substitute the current in terms of the basis function given by

$$\mathbf{J} = \frac{I_n l_n}{2A_n^+} \mid \boldsymbol{\rho}_n^+ \mid \hat{\boldsymbol{\rho}}_n^+,$$

to obtain

$$\begin{aligned} \left\{ \begin{array}{c} \mathbf{E} \\ \mathbf{H} \end{array} \right\} &= I_n l_n \int_0^1 \int_0^{1-\eta} \bar{\mathbf{G}}_{E,H} \cdot \hat{\boldsymbol{\rho}}_n^+ \mid \boldsymbol{\rho}_n^+ \mid d\xi\, d\eta \\ &= I_n l_n \int_0^1 \int_0^{1-\eta} \left[\hat{\mathbf{x}} G_{E,H}^{xX} + \hat{\mathbf{y}} G_{E,H}^{yX} + \hat{\mathbf{z}} G_{E,H}^{zX}\right] \mid \boldsymbol{\rho}_n^+ \mid d\xi\, d\eta. \end{aligned} \tag{5}$$

In the last step, the Green's functions of Eqs. 2 to 3 were used, since $\hat{\mathbf{X}} = \hat{\boldsymbol{\rho}}_n^+$. Eq. 5 gives the $\mathbf{E}$ and $\mathbf{H}$ fields radiated by triangle T_n^+. Add the contribution of triangle T_n^-, which is also spanned by the nth basis function

$$\left\{ \begin{array}{c} \mathbf{E} \\ \mathbf{H} \end{array} \right\} = I_n l_n \left[\int_0^1 \int_0^{1-\eta} \bar{\mathbf{G}} \cdot \hat{\boldsymbol{\rho}}_n^+ \mid \boldsymbol{\rho}_n^+ \mid d\xi\, d\eta + \int_0^1 \int_0^{1-\eta} \bar{\mathbf{G}} \cdot \hat{\boldsymbol{\rho}}_n^- \mid \boldsymbol{\rho}_n^- \mid d\xi\, d\eta\right], \tag{6}$$

where $\boldsymbol{\rho}_n^-$ is directed towards the free vertex of triangle T_n^-.

The total fields are obtained by adding the contributions of all the basis functions

$$\left\{ \begin{array}{c} \mathbf{E} \\ \mathbf{H} \end{array} \right\} = \sum_{n=1}^{N} I_n l_n \left[\int_0^1 \int_0^{1-\eta} \bar{\mathbf{G}} \cdot \hat{\boldsymbol{\rho}}_n^+ \mid \boldsymbol{\rho}_n^+ \mid d\xi\, d\eta + \int_0^1 \int_0^{1-\eta} \bar{\mathbf{G}} \cdot \hat{\boldsymbol{\rho}}_n^- \mid \boldsymbol{\rho}_n^- \mid d\xi\, d\eta\right], \tag{7}$$

where N is the total number of basis functions.

3 Spiral Buried in Layered Media

Consider Fig. 3 where the Archimedes spiral antenna is located inside a multi-layered medium consisting of free-space, polystyrene foam spacers ($\epsilon_r = 1.1 - j0.00011$) and a three layered absorber (ECCOSORB AN 75, GRACE Electronic Materials). The AN 75 absorber consists of three layers A, B and C; the thickness of each layer is given in Fig. 3. The dielectric properties of the layers were measured in S-band waveguide, and Table 2 gives the resulting values of $\epsilon_r = \epsilon_r'(1 - j \tan\delta)$. Note that the upper layers A and B in Fig. 3 are thinner than their counterparts at the bottom. The reason is that the upper AN 75 was split into its three component layers A, B and C, when the permittivity was measured, and the machining reduced the thickness of layers A and B in the upper AN 75.

Fig. 4 gives the magnitude of E_y at 4.03 GHz, measured and computed in the radiating near-field along the y-axis, at $z = 50$ mm from the conductor surface, with and without the polystyrene and AN 75 superstrates. The measurement and computational grids were both 300 mm $\times$ 300 mm in steps of 5 mm. The dimensions of the polystyrene and AN 75 slabs were also 300 mm $\times$ 300 mm.

The measured and computed magnitude patterns compare well. The narrowing of the beam due to the superstrate is a notable feature which is of practical interest. The measured and computed attenuation, when the polystyrene and AN 75 are inserted between the spiral and the observation point, are -13.9 dB and -15.1 dB respectively which is considered to be good agreement.

Fig. 5 gives the measured and computed *phase difference* in E_y at 4.03 GHz, with and without the polystyrene and AN 75 slab in front of the spiral. Agreement is very good except near the edges of the polystyrene and AN 75 slabs where it is thought that diffraction may become significant, as suggested by the bottom graph of Fig. 5.

4 Execution Speed

It took 3 min 17 sec (on a 6 Megaflops/sec 66 MHz Pentium computer) to compute the current distribution and the far-field parameters of the spiral. When the fields were computed on a grid of 51 $\times$ 51 points, it required an additional 13 min. The spiral was discretized into 524 triangles, resulting in 523 basis functions. The code was written in Fortran, FTN77/486 version 2.73, created at Salford Software Ltd. on 27 October 1993. The subroutines used to calculate the Bessel functions with complex arguments, were written by Donald E. Amos, at Sandia National Laboratories. In the moment method code, most of the memory is used by the $\bar{\bar{Z}}$ matrix, for which only the upper triangle was stored. The set of linear equations was solved using two of LINPACK's algorithms: **zspfa.f** and **zspl.f**. The amount of memory needed to store the complex elements of the $\bar{\bar{Z}}$ matrix, is

$$16 \times (\frac{N^2 - N}{2} + N) \approx 16 \times (\frac{N^2}{2}) \text{ Bytes} ,$$

where N is the total number of basis functions. With $N = 1414$, the size of the $\bar{\bar{Z}}$ matrix is 16 Megabytes. The program requires a small amount of overhead memory, therefore (on a 16 Megabytes machine) N must be a little smaller than 1414. To confirm this, the Archimedes spiral antenna was analyzed by increasing the number of triangles to $T_N = 1254$, resulting in $N = 1322$ basis functions. The execution time (6 Megaflops/sec 66 MHz Pentium computer) to compute the current distribution and the far-field parameters for a single frequency point, was 15 min. 18 sec.

5 Conclusions

An efficient method of moments (MoM) technique has been developed to analyze arbitrarily shaped planar antennas which are buried in multi-layered media. The total fields are computed with the observation point located inside any layer, and at any arbitrary distance within that layer. The numerical predictions were verified by measuring the amplitude and the phase of the near-fields of an Archimedes spiral antenna and some of those results have been presented here. Conventional far-field pattern measurements also show good agreement with predictions [2]. Results of the code were also compared, with good agreement, to other (albeit less powerful) codes [2].

Since the new code computes the total fields, including the near-fields, of planar antennas embedded in multi-layered media it may be used to study the properties of antennas for ground penetrating radars, low profile communication systems, and microwave hyperthermia.

References

[1] J. R. Mosig, F. E. Gardiol, S. A. Bokhari, and J. F. Zurcher, "Near fields of microstrip antennas," *IEEE Trans. on Antennas and Propagation*, vol. 43, pp. 188–197, Feb. 1995.

[2] J. J. van Tonder, *Electromagnetic Radiation by Planar Antennas Buried in Layered Media.* PhD dissertation, University of Stellenbosch, 1995.

[3] S. M. Rao, D. R. Wilton, and A. W. Glisson, "Electromagnetic scattering by surfaces of arbitrary shape," *IEEE Trans. on Antennas and Propagation*, vol. 30, pp. 409–418, May 1982.

[4] J. R. Mosig, "Integral equation technique," in *Numerical Techniques for Microwave and Millimeter Wave Passive Structures* (T. Itoh, Ed.), Chapter 3, John Wiley and Sons, 1989.

[5] J. A. Kaiser, "The Archimedian two wire spiral antenna," *IRE Trans. on Antennas and Propagation*, pp. 312–322, May 1960.

[6] R. Bawer and J. J. Wolfe, "The spiral antenna," *IRE International Convention Record, Pt. 1*, pp. 84–95, 1960.

[7] H. Nakano, K. Nogami, S. Arai, H. Mimaki, and J. Yamauchi, "A spiral antenna backed by a conducting plane reflector," *IEEE Trans. on Antennas and Propagation*, vol. 34, pp. 791–796, June 1986.

[8] H. Nakano, "Research on spiral and helical antennas at Hosei university," *IEEE Antennas and Propagation Society Newsletter*, pp. 19–28, June 1988.

[9] J. J. van Tonder and J. H. Cloete, "A study of a two-arm Archimedes spiral antenna," *IEEE International Antenna and Propagation Symposium Digest*, pp. 1302–1305, Seattle, June 1994.

[10] J. H. Cloete, "Exact design of the Marchand balun," *Microwave Journal*, pp. 99–100, May 1980.

[11] J. H. Cloete, "Graphs of circuit elements for the Marchand balun," *Microwave Journal*, pp. 125–128, May 1981.

Table 1: Parameters of Archimedes Spiral Antenna

Parameter	Value
Spiral constant, a	1.1459 mm
Strip width, w	1.8 mm
Feed wire length, e_{st}	3 mm
Spiral arm length, L	519.3 mm
Range of winding angle, ϕ	2.618 rad $\leq \phi \leq$ 30.137 rad

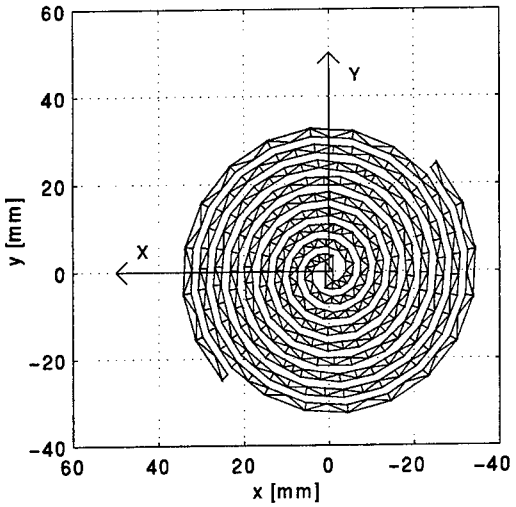

Figure 1: Archimedes spiral conductor pattern showing the segmentation used for the triangular moment method model.

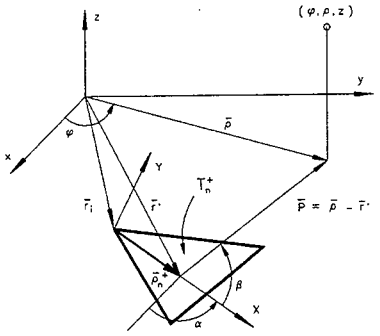

Figure 2: Coordinate system with source triangle and observation point at (ϕ, ρ, z).

Table 2: Measured ϵ_r' and $\tan\delta$ of the three layers forming AN 75

frequency [GHz]	A		B		C	
	ϵ_r'	$\tan\delta$	ϵ_r'	$\tan\delta$	ϵ_r'	$\tan\delta$
2.5000	1.5977	0.3957	1.5783	0.5318	5.4342	2.5347
2.6700	1.6333	0.4203	1.6208	0.5476	5.2044	2.5811
2.8400	1.6091	0.4391	1.6003	0.5612	5.0594	2.5515
3.0100	1.5908	0.4292	1.5870	0.5443	4.8974	2.5247
3.1800	1.5859	0.4182	1.5860	0.5264	4.6838	2.5241
3.3500	1.5618	0.4155	1.5646	0.5188	4.5146	2.5038
3.5200	1.5348	0.3999	1.5412	0.4984	4.3797	2.4796
3.6900	1.5389	0.3775	1.5492	0.4706	4.1759	2.5034
3.8600	1.5489	0.3789	1.5604	0.4678	3.9444	2.5343
4.0300	1.5213	0.3960	1.5319	0.4825	3.8150	2.4998
4.2000	1.5108	0.3777	1.5252	0.4593	3.7785	2.4306

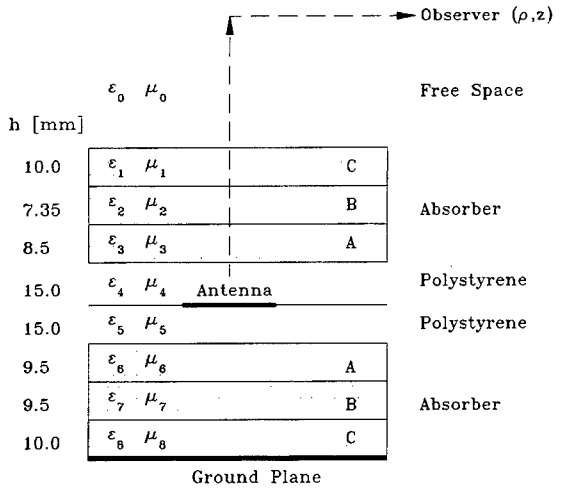

Figure 3: Archimedes spiral backed by AN 75 and radiating through AN 75.

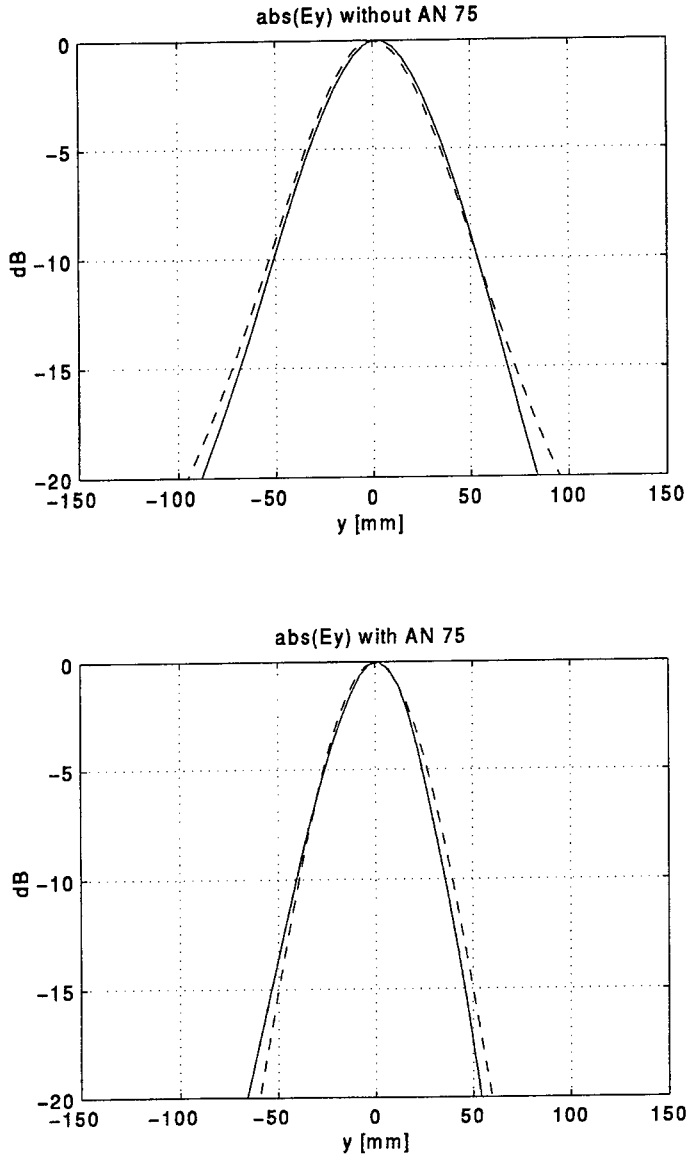

Figure 4: Measured (solid) and computed (dashed) E_y along the y-axis at 4.03 GHz without (top) and with (bottom) AN 75 absorber in front of the spiral. See the text for details.

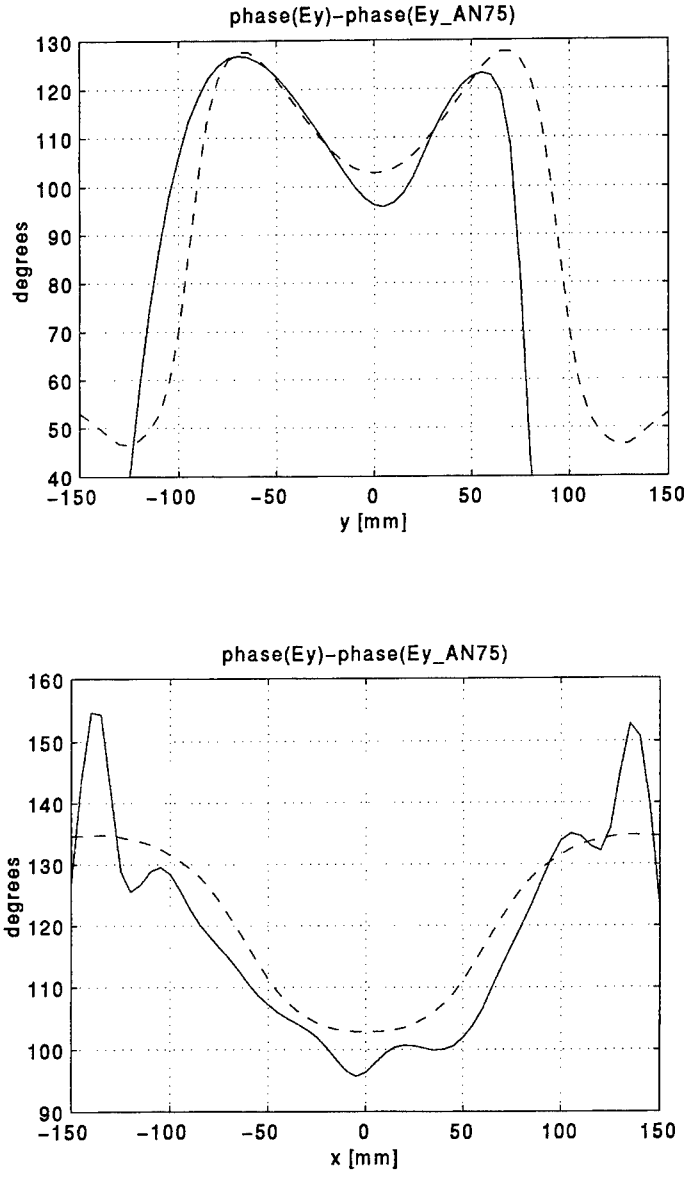

Figure 5: Measured (solid) and computed (dashed) phase difference in E_y at 4.03 GHz, along the y-axis (top) and along the x-axis (bottom). See the text for details.

SESSION 3:

RCS ANALYSIS

Chair: M. El-Shenawee

A RESPONSE SURFACE METHODOLOGY STUDY OF ELECTROMAGNETIC DATA COMPRESSION AND RECONSTRUCTION [1]

V. M. Floyd, Jr., A. J. Terzuoli, Jr., G. C. Gerace, P. F. Auclair
Air Force Institute of Technology • Dayton, Ohio 45433

INTRODUCTION

When a radar illuminates an object, the complex back scattered field will vary rapidly in both frequency and orientation angle. Consequently, high sampling rates in both frequency and angle are required. The product of this dense sampling is a large amount of data that must be stored and processed.

It is clearly of interest to reduce the vast amount of data required while still preserving adequate accuracy of images that can be produced. A reduced data set allows for compactibility and quick reconstruction, thus enabling real-time processing. A compression technique has been developed [1, 2] which analyzes the scattering centers of a return on an individual basis in the frequency domain where the return has a simple and smooth shape. Therefore, if these scattering centers are extracted and their individual responses found, each scattering center can be sampled fewer times due to its smooth shape and still be reconstructed accurately. Obviously, with fewer samples required, the data has been effectively compressed. In fact, the technique has compressed image data by a factor as large as several hundred, depending upon the specific object.

This study examines the many tradeoffs and assumptions of the compression and reconstruction algorithm through the application of Response Surface Methodology (RSM). The first goal of this work was to identify which variables, parameters, and assumptions most affect reconstruction accuracy. The second goal was to characterize how the input variables relate to reconstruction accuracy. RSM also affords the ability to predict optimum settings for the variables without the need for years of experience. Thus, RSM would provide less experienced operators with a systematic method of choosing variables and settings to attain optimal results.

BACKGROUND

In a broad sense, the compression technique identifies scattering centers, uses Fourier analysis, and is iterative in nature. The first method, explored by Tseng [1], was based on the assumption that a object's scattered field can be viewed as the superposition of various scattering centers' responses. Tseng could then transform the data to construct an image of the object and show spatial locations of the scattering centers. These scattering centers were then extracted from the data set through image gating or spectral smoothing. Tseng showed that the spectral response of these scattering centers was smooth and simple with respect to scanning frequency and angle. Thus, sampling this spectrum data could greatly reduce the required number of samples, and hence, reduce data storage.

Further work by Burnside and Chang [2] showed the assumption that a complicated object could be viewed as a superposition of isolated scattering centers was insufficient due to the fact that such objects exhibit anisotropic frequency dependent characteristics. These mechanisms may have very sophisticated phase histories due to the object's complicated structure. Consequently, the image that is created may not exhibit isolated peaks spatially, but instead may show clusters of peaks that may not be individually extractable. Therefore, they decided to treat these scattering centers as either a complex point scattering mechanism or a line segment scattering mechanism. With these definitions and the appropriate algorithms for each, one can follow the same extraction process as presented by Tseng.

The focus of this research was the application of RSM to these data compression and reconstruction algorithms. RSM is a collection of statistical tools by which an organized series of

[1]This work was supported by the U. S. Air Force Wright Laboratories.

experiments can be executed with prescribed procedures for response analysis. It seeks to mathematically represent the connection between a series of inputs and outputs. Box and Draper [3] more formally define RSM as *a group of statistical techniques for empirical model building and exploitation.* By careful design and analysis of experiments, it seeks to relate a response, or output variable to the levels of a number of predictors, or input variables. According to Khuri and Cornell [4], RSM encompasses: *(1) Designing a series of experiments that will yield adequate and reliable measurements of the response(s) of interest in a region of interest; (2) Analyzing the results of those experiments to determine a mathematical model that best fits the data collected; (3) Searching for the optimal settings of the input variables that produce a desired (often the maximum) response.*

RESULTS

A simplified object data set (line scatterer) was selected to verify the technique before considering more complicated data sets. The simulated scattering fields of the line scatterer are based upon a physical optics (PO) approximation and simulate the co- and cross- polarized measured fields as if measured in a compact range. Figure (1) shows two images, one from the original data set and one generated from the compressed data set.

Based on Design of Experiments criteria, a fractional factorial design was selected to accomplish the data runs with the parameter settings shown in Table (1) with the resulting output statistics shown in Table (2). The parameters used in the tables are explained below. All of the output statistics were based upon a normalized multi-angle correlation metric given by

$$Correlation\_Metric = \rho = \frac{\left|\sum_{i=1}^{n} x_i y_i^*\right|}{\left|\sum_{i=1}^{N} x_i x_i^*\right|} \tag{1}$$

that was calculated on a point by point basis. The original *(x)* and reconstructed *(y)* values are the complex electromagnetic fields at a given angle and frequency. This metric is thus a measure of the error between the fields computed with the original data and those computed with the compressed data. The sums are performed over N angles at a single frequency. This metric was chosen due to the wide use of correlation in other research. Due to non-normalization with respect to reconstruction energy, values of correlation may be above and below one, with one being the ideal.

The following equations were used in calculating the correlation error metrics as shown in Table (2).

$$Average\ Correlation = \bar{\rho} = \sum_{i=1}^{n} \frac{\rho_i}{n} \tag{2}$$

$$Mean\ Square\ Error = MSE = \sum_{i=1}^{n} \frac{(\rho_i - 1)^2}{n} \tag{3}$$

$$Root\ Mean\ Square\ Error = Root\_MSE = \sqrt{\sum_{i=1}^{n} \frac{(\rho_i - 1)^2}{n}} \tag{4}$$

$$Average\ Absolute\ Difference = Avg\_Abs\_Diff = \sum_{i=1}^{n} \frac{|\rho_i - 1|}{n} \tag{5}$$

$$Sample\,Variance = \sum_{i=1}^{n} \frac{(\rho_i - \overline{\rho})^2}{n-1} \qquad (6)$$

$$Standard\,Deviation = Stnd\_Dev = \sqrt{Var} = \sqrt{\sum_{i=1}^{n} \frac{(\rho_i - \overline{\rho})^2}{n-1}} \qquad (7)$$

These metrics seek to characterize the correlation shown in Figure (2) and ideally drive the correlation plot to 1.00 across the entire angle span. Equations (2), (3), (4), and (6) were examined for empirical model building appropriateness.

Looking at the Root Mean Square Error (Root MSE) as the primary response variable, a coded linear equation was produced via a least square analysis given by

$$\hat{Y}(x) = 0.2291 + 0.0109x_1 + 0.0490x_2 + 0.0442x_3 + 0.0288x_4 - 0.0311x_5 \qquad (8).$$

The analysis of variance (ANOVA) table shown in Table (3) shows a large value of 0.8880 for R^2 signaling a high accounting of the model variability and a small MSE value of 0.01. Additionally, F = 9.5156 indicates a good fitting model even though it is acting more like a signal-to-noise ratio than a true F statistic (the higher the better). Gradient points were generated and are shown in Table (4). Note that the data compression and reconstruction process is deterministic, i.e. the same results are obtained with every repeated run. Additionally, all of the model error is attributed to lack of fit since the compression and reconstruction process is deterministic. A gradient search technique was employed to reduce the Root MSE values. Integer multiples were calculated and new runs executed corresponding to Runs 13 to 17 in Table (2). Scanning down the associated Root MSE column, the numbers appear to be declining with each run as would be expected. Note, however, Run 16's value for Root MSE is greater than the two previous. This increase in response indicates curvature in the surface and is the beginning of "hill" on the response surface. Run 17, however, shows a smaller value for Root MSE, and in fact the smallest of any run made so far. Achieving this value indicates the *hill* that was previously encountered is actually just a small *bump* on the surface. The gradient technique as performed in effect passed through the bump and continued on to the next point. Considering all the gradient points, the technique appears to be tracking the surface and not being overly influenced by its *bumpy* surface. If that is indeed the case, then Root MSE does pose as a viable response predictor variable.

Average Correlation was examined next; a coded linear equation was produced via a least square analysis and given by

$$\hat{Y}(x) = 0.9017 - 0.0019x_1 - 0.0402x_2 - 0.0433x_3 - 0.0194x_4 - 0.0203x_5 \qquad (9).$$

ANOVA values are shown in Table (5). From the ANOVA table, it is seen that the R^2 value has increased from the 0.8880 value for the Root MSE measure to a value of 0.9499. It is usually meaningless to compare the MSE between data sets because MSE only has meaning in the context of the total sum of squares and degrees of freedom (accounted for in the F ratio). The F statistic is F = 22.7376 and is much larger than Root MSE. Both of these improvements signal an even better fitting model. Gradient points were generated and are shown in Table (6). These points correspond to Runs 18 to 22 of Table (2). Again, by examining the associated values for Average Correlation for these runs, the numbers decrease from the start and then increase to a fairly high value of average correlation. The same phenomena can again describe the response for Average Correlation where the gradient is encountering *bumps* along the surface but is continuing to show improved responses.

CONCLUSION

This research effort used data compression and reconstruction computer codes comprising a compression technique in which individual scattering centers are analyzed in the frequency domain through the use of Fourier techniques. In this domain, the scattering centers possess simple and smooth shapes. Their shapes allow for broader sampling in the frequency domain, and reduce the storage requirements. In the reconstruction process, the relatively smooth shapes allow for simple interpolation schemes to be employed to recreate the frequency response. Examples of reconstructed data for a simple object were shown and compared to the original data. Actual examples appear in [1] and [2]. All of the examples show a favorable comparison between the original and reconstructed data.

A set of empirical model building and exploitation techniques, known as the Response Surface Methodology (RSM), was applied to the data compression and reconstruction algorithms. By careful design and analysis of experiments, RSM seeks to relate a response (or output variable) to the levels of a number of predictors (or input variables) that affect it. A set of five variables was selected as the key input variables, and four response variables were considered as a possible means of measuring the reconstruction accuracy. First-order linear empirical models were developed for the four responses. A gradient search was conducted to identify an improved set of inputs for what was deemed the top two responses which were Average Correlation and Root MSE. Based on the gradient points, the fitted response surface appeared to exhibit a slight irregularity *(bumpiness)* for the responses considered.

The focus of this effort was to empirically model reconstruction correlation, in a fashion that allows for input and output variable characterization. One would like to be able to drive the response (reconstruction accuracy) up or down in the most efficient manner given a particular set of input variables. Four models were developed that showed, via ANOVA statistics, a good fitting empirical model. Two of the four (Average Corr and Root MSE), were exploited via a gradient search. These results showed that the models could indeed identify the trend of the response surface. Slight irregularities were present, however, the gradient points continued to improve the overall response. Therefore, based on the results attained thus far, RSM seems to provide a means of choosing the best input variables for the data compression and reconstruction algorithms examined. This technique appears to provide a systematic input variable selection procedure for both experts and non-experts to effectively utilize when compressing RCS data. Hopefully, continuing efforts with this topic will indeed produce further conclusive results.

REFERENCES

[1] N. Y. Tseng, "A very efficient RCS data compression and reconstruction technique," MS Thesis, The Ohio State University, 1992.

[2] L.C. Chang and W.D. Burnside, "A data compression technique for the scattered fields from complex objects," Technical Report, ElectroScience Laboratory, Department of Electrical Engineering, The Ohio State University, Columbus, Ohio, 1994.

[3] G.E.P. Box and N.R. Draper, Empirical Model-Building and Response Surfaces, New York: John Wiley & Sons, 1987.

[4] A.I. Khuri and J.A. Cornell, Response Surfaces: Designs and Analysis, New York: Marcel Dekker, Inc., 1987.

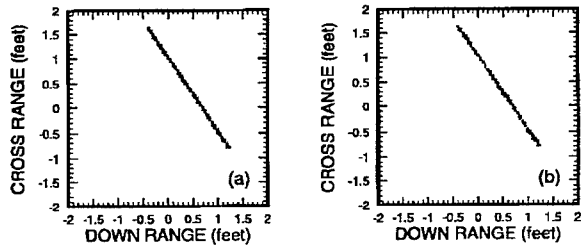

Figure (1): Simulated line scatterer (a) original (b) reconstructed

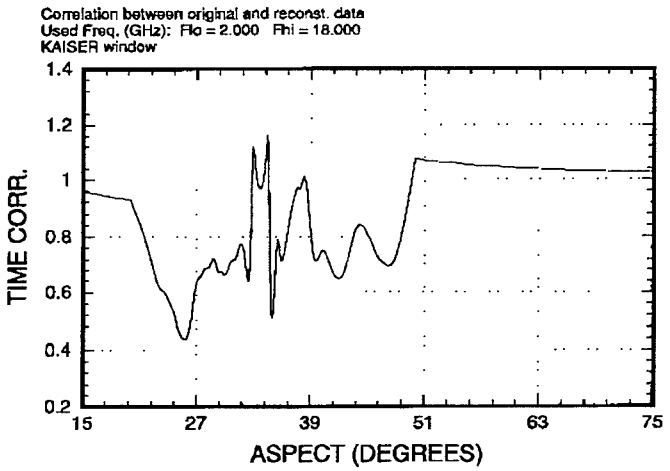

Figure (2): Sample correlation plot

Run #	xstep,ystep	# freq bands	angle span	line thresh	point thresh
1	1	-1	-1	-1	-1
2	-1	1	1	-1	-1
3	1	1	-1	1	-1
4	-1	-1	1	1	-1
5	-1	1	-1	-1	1
6	1	-1	1	-1	1
7	-1	-1	-1	1	1
8	1	1	1	1	1
9	0	0	0	0	0
10	0	0	0	0	0
11	0	0	0	0	0
12	0	0	0	0	0
Coded Value	Corresponding Actual Parameter Values				
-1	0.25 in	2	20.0°	-20.0 dB	-20.0 dB
1	0.35 in	4	24.0°	-24.0 dB	-24.0 dB
0	0.30 in	3	22.0°	-22.0 dB	-22.0 dB

Table (1): Resolution III experimental design set-up: 2^{5-2}_{III} Fractional Factorial Design

TIME DOMAIN DATA						
RUN #	AVG CORR	MSE	RT MSE	AVG ABS DIFF	VARIANCE	STND DEV
1	0.9772	0.0199	0.1412	0.0949	0.0194	0.1394
2	0.7967	0.1239	0.352	0.2154	0.0827	0.2875
3	0.8589	0.1085	0.3294	0.2122	0.0887	0.2979
4	0.8738	0.0635	0.2519	0.1538	0.0476	0.2182
5	0.9593	0.0201	0.1418	0.0935	0.0185	0.136
6	0.9319	0.04	0.2	0.0928	0.0354	0.1882
7	0.9654	0.0259	0.161	0.1073	0.0248	0.1574
8	0.812	0.1043	0.3229	0.1953	0.069	0.2628
9	0.9112	0.0451	0.2123	0.1259	0.0372	0.193
10	0.9112	0.0451	0.2123	0.1259	0.0372	0.193
11	0.9112	0.0451	0.2123	0.1259	0.0372	0.193
12	0.9112	0.0451	0.2123	0.1259	0.0372	0.193
13	0.9801	0.0602	0.2453	0.1556	0.0599	0.2447
14	0.9738	0.024	0.1549	0.1027	0.0234	0.1528
15	0.9505	0.0226	0.1504	0.0866	0.0202	0.1422
16	0.9648	0.0327	0.1809	0.1262	0.0315	0.1776
17	0.9877	0.0078	0.0886	0.0641	0.0077	0.0886
18	0.9633	0.0337	0.1836	0.1317	0.0324	0.18
19	0.938	0.0371	0.1927	0.1149	0.0334	0.1826
20	0.9266	0.0303	0.1739	0.0845	0.0249	0.1578
21	0.9765	0.0203	0.1425	0.091	0.0198	0.1407
22	0.9829	0.0092	0.0962	0.0546	0.009	0.0947

Table (2): Data runs for experimental design set-up

Source	Degrees of Freedom	Sum of Squares	Mean Squares
Regression	5	0.0501	0.0100
Error	6	0.0063	0.0011
Total	11	0.0564	

R^2	F Test Statistic	F - Lack of Fit
0.8880	9.5156	Inf

SSPE	SSLF	SSPQ	MSPE
0	0.0063	0.0017	0

Table (3): ANOVA table for Root MSE

	Coded Variable Form				
	x_1	x_2	x_3	x_4	x_5
Center Point	0	0	0	0	0
Step Size	-0.1371	-0.619	-0.5581	-0.3635	0.3929
Point 1	-0.1371	-0.619	-0.5581	-0.3635	0.3929
Point 2	-0.2741	-1.2381	-1.1162	-0.7271	0.7858
Point 3	-0.4112	-1.8571	-1.6743	-1.0906	1.1787
Point 4	-0.5483	-2.4762	-2.2324	-1.4541	1.5716
Point 5	-0.6855	-3.095	-2.7905	-1.8175	1.9645
Point 6	-0.8226	-3.714	-3.3486	-2.181	2.3574
Point 7	-0.9597	-4.333	-3.9067	-2.5445	2.7503
	Uncoded Variable Form				
	x_1	x_2	x_3	x_4	x_5
Center Point	0.3	3	22	-22	-22
Step Size	-0.0069	-0.619	-1.1162	-0.7271	0.7858
Point 1	0.2931	2	20.8838	-22.7271	-21.2142
Point 2	0.2862	2	19.7676	-23.4542	-20.4284
Point 3	0.2793	2	18.6514	-24.1813	-19.6426
Point 4	0.2724	2	17.5352	-24.9084	-18.8568
Point 5	0.2655	2	16.419	-25.6355	-18.071
Point 6	0.2586	2	15.3028	-26.3626	-17.2852
Point 7	0.2517	2	14.1866	-27.0897	-16.4994

Table (4): Gradient point runs for Root MSE

Source	Degrees of Freedom	Sum of Squares	Mean Squares
Regression	5	0.0342	0.0068
Error	6	0.0018	0.0003
Total	11	0.0360	

R^2	F Test Statistic	F - Lack of Fit
0.9499	22.7376	Inf

SSPE	SSLF	SSPQ	MSPE
0	0.0018	0.0005	0

Table (5): ANOVA table for Average Correlation

Coded Variable Form					
	x_1	x_2	x_3	x_4	x_5
Center Point	0	0	0	0	0
Step Size	-0.029	-0.6142	-0.662	-0.2962	0.3096
Point 1	-0.029	-0.6142	-0.662	-0.2962	0.3096
Point 2	-0.0581	-1.2285	-1.324	-0.5925	0.6192
Point 3	-0.0871	-1.8427	-1.986	-0.8887	0.9288
Point 4	-0.1162	-2.4569	-2.6481	-1.1849	1.2384
Point 5	-0.145	-3.071	-3.31	-1.481	1.548
Uncoded Variable Form					
	x_1	x_2	x_3	x_4	x_5
Center Point	0.3	3	22	-22	-22
Step Size	-0.0015	-0.6142	-1.324	-0.5925	0.6192
Point 1	0.02985	2	20.676	-22.5925	-21.3805
Point 2	0.297	2	19.352	-23.185	-20.761
Point 3	0.2955	2	18.028	-23.7775	-21.3805
Point 4	0.294	2	16.704	-24.37	-19.522
Point 5	0.2925	2	15.38	-24.9625	-18.9025

Table (6): Gradient point runs for Avg Corr

Curvilinear, isoparametric modelling for rcs prediction, using time domain integral equations

S P Walker, M J Bluck, M D Pocock, C Y Leung, S J Dodson

Imperial College, London

1. Introduction

The integral equation approach has well known advantages, including the need for discretisation of only the surface, and the satisfaction of boundary conditions at infinity. In the time domain, it has the additional advantage of not requiring the solution of large dense matrices, and of being able to provide results at a many frequencies from a single computation[1].

Here we describe the implementation of a time domain integral equation treatment, employing curvilinear, isoparametric elements, with implicit quadratic modelling of the temporal variation. This has the advantage of being able to represent arbitrarily curved surfaces accurately, avoiding facetting, and to provide a similarly efficient representation of the spatial variation of the fields. In sections 2 and 3 the main features of the approach are outlined, with a discussion of its successful implementation on a 256 processor Cray T3D presented in section 4. The direct coupling to industry standard CAD software, for solid modelling, meshing and post processing and display is described in section 5. Example rcs results, including the 8.4 wavelength NASA almond[2], and the 18 wavelength NASA cone-sphere with gap, are presented in section 6. Current developments are noted in section 7.

2. Numerical Treatment

The MFIE for scattering from a perfect conductor can be written

$$2\pi \mathbf{H}(\mathbf{r},t) = 4\pi \mathbf{H}_{inc}(\mathbf{r},t) + \int_{\partial\Omega} \left(\mathbf{n}'\times\mathbf{H}(\mathbf{r}',t^*)\right)\times\frac{\hat{\mathbf{R}}}{R^2} + \left(\mathbf{n}'\times\frac{\partial\mathbf{H}}{\partial t'}(\mathbf{r}',t^*)\right)\times\frac{\hat{\mathbf{R}}}{cR}\,ds' \quad (1)$$

Here Ω is the surface of the body, $\mathbf{r}$ is the point on the surface at which the field is sought, and primes denote other points on the surface, a distance R away, where the unit normal is $\mathbf{n}'$. The time is t, with an asterisk denotes retarded time.

Geometry representation

To evaluate the integral we partition the surface into M elements m, over each of which the geometry is represented in terms of intrinsic co-ordinates (see figure 1):

$$x^i = x^i(\xi,\eta) \quad (2)$$

The actual form of the geometric transformation is

$$x^i(\xi,\eta) = x^i_\alpha\, S_\alpha(\xi,\eta) \qquad \alpha = 1,..,\alpha_{\max} \quad (3)$$

where the summation is over the $\alpha_{\max}$ nodes associated with a particular element, the x^i_α are the nodal locations, and the $S_\alpha(\xi,\eta)$ are shape functions associated with each node. A Jacobian, $J(\xi,\eta)$, provides the necessary (position dependant) scaling factor between areas ds in real space and areas $d\xi\,d\eta$ in intrinsic space.

The full range of element types available in (two dimensional) finite elements can be used. We have thus far implemented 8 and 9 noded quadrilaterals and 6 noded triangles. In each of these cases the geometry is thus allowed to vary quadratically between nodal locations. The particular forms of the shape functions for these various element types are given in any good finite element text[3]. Local mesh refinement to model particular features of the geometry, or local rapid field variations, is readily performed.

Field representation

Exactly the same representation is adopted for the spatial variation of field quantities; the time dependant H field at some intrinsic location is approximated in terms of the nodal field component values:

$$\mathbf{H}(\xi,\eta;t) = \mathbf{H}_\alpha(t) S_\alpha(\xi,\eta) \qquad \alpha = 1,..,\alpha_{\max} \tag{4}$$

The time dependence itself is modelled in a similar fashion, with 3 noded quadratic elements, of length $2\Delta t$, with associated shape functions $T_\beta(\tau)$, with τ the intrinsic time. Once we have found the timesteps k corresponding to the temporal nodes β of the time element in which the retarded time falls, we have

$$\mathbf{H}_\alpha(t) = \sum_{\beta=1}^{3} T_\beta(\tau)\mathbf{H}_\alpha^\beta \tag{5}$$

Assembly of discretised equations

Inserting all the above into (1), we can write the integration for the field at a particular timestep for each of the N nodes k as the sum of integrations over M elements:

$$\begin{aligned} &2\pi\mathbf{H}_i^k = 4\pi\mathbf{H}_{inc,i}^k \\ &+\sum_{m=1}^{M}\iint_{\xi\eta}\sum_\alpha S_\alpha(\xi,\eta)\sum_\beta\left(\frac{T_\beta(\tau(R))}{R^3}+\frac{\dot{T}_\beta(\tau(R))}{c\Delta t R^2}\right)\left[\left(\mathbf{n}'\times\mathbf{H}_j^{k^*}\right)\times\mathbf{R}\right]J(\xi,\eta)d\xi d\eta \end{aligned} \tag{6}$$

where the dot denotes the time derivative. This in turn can be written as a matrix equation

$$2\pi\mathbf{H}_i^k = 4\pi\mathbf{H}_{inc,i}^k + \sum_{m=1}^{M}\sum_\alpha\sum_\beta[\mathbf{K}]\mathbf{H}_j^{k^*} \tag{7}$$

where

$$[\mathbf{K}] = \int_{\xi=-1}^{1}\int_{\eta=-1}^{1} S_\alpha(\xi,\eta)\left[\frac{T_\beta(\tau)}{R^3}+\frac{\dot{T}_\beta(\tau)}{c\Delta t R^2}\right][A'][\mathbf{J}(\xi,\eta)]d\xi d\eta \tag{8}$$

in which the matrix A' is defined

$$[A'] = \begin{bmatrix} n_2'R_2 + n_3'R_3 & -n_1'R_2 & -n_1'R_3 \\ -n_2'R_1 & n_1'R_1 + n_3'R_3 & -n_2'R_3 \\ -n_3'R_1 & -n_3'R_2 & n_1'R_1 + n_2'R_2 \end{bmatrix} \tag{9}$$

The integrations in (8) are performed using Gaussian quadrature; typically between 2x2 and 6x6 point.

Singular and Hypersingular integrands

The integrand in (7) is seen to contain both $1/R$ and $1/R^2$ terms. The need to treat these does not arise in the more usual flat-facetted treatments; the n x H term is then necessarily zero. Proper treatment is one price which must be paid for the other benefits of a curvilinear geometric model.

The $1/R$ term is of the kind which arises also in elastostatics, and we have applied essentially the treatments developed there [4]. Each element is repartitioned into triangles, with the location of the singularity at a vertex. Re-expression in polar co-ordinates removes one power of $R_{,}$ rendering the integrand well behaved.

The $1/R^2$ is more difficult. It is accommodated by construction of a local 'virtual' element; a flat parallelogram tangent to the surface at the location of the singularity[5]. The tangent element allows in effect subtraction of the hypersingular term, and its replacement by a singular contour integral. However, since this all contours meeting at the location of the singularity are traversed in both directions, this never need be evaluated. (A more detailed description, and investigation of the significance of careful treatment of such terms, is in preparation.)

Boundary Conditions

Equation (6) above represents $3N$ equations, with $3N$ terms on each right hand side. Imposing perfect conductor boundary conditions allows both the number of equations, and the right hand side terms, to be reduced to $2N$.

3. Main Solution Stages and Cost Scalings

We consider below the relative costs and costs scaling of the various portions of the analysis, initially for a single look angle. Figure 2 shows the relative times taken for the various stages, on a series of increasingly finely meshed spheres.

Matrix formation

Equation (6) shows the field at a point to be a weighted sum of the historical field values elsewhere on the surface, with the weights being essentially the results of the integrations in (8). For a non-conducting dielectric (vacuum), the Green function is a 'pure' delta function, so that only the field at exactly the retarded time ago is of relevance. With the quadratic modelling of the temporal variation, typically ~5 historical values are required to approximate this. The result is that a matrix of size N x N x ~5 has to be formed. Each member is a 2x2 submatrix, giving an overall formation and storage cost of ~20 N^2. Since N will vary with frequency squared, these costs both scale with frequency to the fourth power.

Matrix solution

The right hand side of (7) involves historical values only if the distance to the nearest integration point is larger than the distance light travels in one timestep; otherwise matrix coefficients multiply as yet still unknown field values. The result is that (7) represents an implicit matrix equation, rather than an explicit formula for the field. The matrix is very sparse, and increasingly so as larger problems are addressed. A matrix equation must be solved at each timestep. We employ an iterative (biconjugate gradient, or CGS) method. With the previous timestep's solution as the initial guess, convergence is typically obtained in a few, or at most a couple of tens of, iterations. It is found that the solution is generally a small and declining fraction of the total work. One major advantage of the implicit approach is that a stable solution is achieved. Explicit time domain integral methods have been found to suffer from instability; we can induce instability, by modifying timestep, quadrature order and mesh size to approach explicitness, but do not observe it when using the codes normally.

Right hand side formation

Equation (7) is evaluated at each timestep. It is in essence a large matrix-vector multiplication, and thus involves summing ~20 N^2 products. It is here that the dominant cost of the method lies; a (frequency)^4 cost at each step, with ~(frequency) steps required, giving an overall cost scaling of (frequency)^5.

In-core / Out-of-core

Once the matrix size exceeds the available core memory it must either be read from disk at each time step, or re-evaluated as required. We employ both approaches; for a single processor machine the former is faster by

a factor ~2 to ~5. For a parallel machine, re-evaluation would be quicker. Cost scalings are unchanged, but in both cases there is a sharp increase in the total time required. The dominant cost then becomes matrix evaluation (or reading) rather than right hand side formation.

Once multiple look angles are considered the penalty associated with matrix re-formation at each timestep is much reduced, by being shared over all angles. For example, for a single scan with 180 look angles, the total time is about a factor of two greater than if the matrix fitted in core and thus needed to be formed only once.

4. Parallelisation Issues

The issues which arise in parallelisation of time domain BIE analyses are significantly different from those for both frequency domain MoM and finite difference / element methods; they revolve around both the need for economic storage of the surface field history, and the need for repeated right hand side formation.

Matrix formation

Such work on parallelisation of integral equation methods as has been published addresses steady state or frequency domain problems. The main issue considered (albeit not actually the dominant cost for large problems) has been the parallelisation of the formation of the matrix. This is found to parallelise well, as would be expected for an aspect of the solution which exhibits such little interdependence. Matrix formation for the time domain parallelises equally well.

Right hand side formation

This, the dominant cost in the time domain, has no frequency domain counterpart. The most efficient strategy has been found to be the allocation of portions of the surface ('columns', in equation (7)) to individual processors. Integration over its portions from every node is then performed by each processor, both for matrix formation and, more significantly, for right hand side formation. This is the reverse of the usual procedure in the frequency domain, where 'nodes' are allocated to processors, and each processor integrates over the whole surface. This approach, which offers considerable gains in simplicity, requires storage of the entire history on each processor.

Achievement of optimal domain decomposition is desirable if matrix re-evaluation is required. The ideal is to allocate equal, contiguous portions of surface to each processor, shaped to minimise their total perimeter, and hence the influence of 'halo nodes'. This has not been implemented.

Matrix solution

As is seen in figure 2, matrix solution is a tiny part of the total cost, and accordingly we have not (yet) implemented it in parallel. As will be seen below, the very good parallelisation the method exhibits in the matrix formation and right hand side formation stages does increase the fraction of the time spent on solution quite markedly, and this is now an issue which need to be addressed.

5. Computational Implementation

The code was designed from the beginning to make use of the large body of high quality CAD, mesh generation and post-processing and display software available commercially. Geometry definition is performed in a solid modelling package, and surface meshes generated on this solid model using (in principle any) mesh generation software. The output from this is read into an interface routine, which generates an input file for Zeus. Currently interface routines for the packages Patran (Macneal Schwendler) and Ideas (SDRC) exist.

The main processing in Zeus is in two stages; matrix generation, and subsequent timestepping (although for the 'out of core' cases discussed below, these are actually combined). The output of this stage is a history of the surface currents. If the rcs is required, these are provided to an rcs routine which performs a Fourier transform (or equivalent). If the currents themselves are of interest, the interface process is reversed, and the currents are provided to the CAD package for graphical display. This can be either of 'snapshots', or can be an animated display of the evolution of the fields. The option also exists to display the fields in the space around the body; for example, over an equatorial plane. Figure 3 shows a diagram of the software structure.

6. Examples of performance

The following paragraphs describe a few examples of the use of the codes, both on a single processor workstation (DEC Alpha 600, 256 Mb), and on a 256 processor Cray T3D.

Cylindrical cavity

Although not strictly an rcs application, the cylindrical cavity in figure 4 demonstrates the ability to predict time dependent surface current on a body of fairly complex shape. Figure 5 shows the surface current induced on-axis, inside and outside the rear wall, when subject to an incident pulse along the axis into the open end. The pulse width was about one cavity length, and the time history shown extends to ~5 transit times.

Almond; 3 GHz (2.53 wavelengths, 1400 nodes)

The almond (4154 node mesh shown in figure 6) is one of the set of benchmark targets reported by Woo[2]. A 1202 node mesh was used to generate the monostatic rcs shown in figure 7. Also indicated are measured rcs values (Woo), and values calculated by Carlos[6]. This problem was run in core on the DEC workstation, with the 90 look angles taking a total of 9.3 cpu hours.

Almond; 7 GHz (5.89 wavelengths, 2450 nodes)

This will not run in-core on the serial DEC workstation; with matrix re-evaluation at each timestep, one look angle took ~30 hours; subsequent look angles would take ~3 hours each. Computed and measured head-on rcs were both -42dB m^2. As an illustration of the postprocessing information available, figure 8 shows the magnitude of surface currents induced on the almond (albeit here in rather less informative black and white than the colour of the workstation.)

As an illustration of the effectiveness of parallelisation, this same problem was run twice on the T3D with 32 and 64 processors. For a single look angle, the total times were 807 and 409 seconds respectively; a reduction by a factor of 1.97, indicating highly efficient processor utilisation.

Cone-sphere and gap; 9 GHz (18.15 wavelengths, 5924 nodes)

Also from Wu, this 18 wavelength body, shown in figure 9, is a severe test for the 200Mb DEC workstation, and only a single, head-on, illumination was run. Matrix re-evaluation at each timestep was required, taking one hour for each of the ~250 timesteps (~3 1/2 transits) modelled, a total time of ~10 days. Additional simultaneous look angles would take rather less than 1 day each.

Extracting a 0.869 GHz result gave a backscattered rcs result of -17.5 dB m^2, the same as the body of revolution code Cicero[2]. A frequency of 9 GHz corresponds to a nodal separation of ~1/5 wavelength, and is probably at the upper end of the frequency for which the mesh is adequate. The measured and computed rcs values were both ~-6 dB m^2.

Almond; 9.92 GHz (8.36 wavelengths, 5090 nodes)

Figure 10 shows the monostatic rcs of the almond, illuminated so as to be 8.36 wavelengths long, with some measured values. This problem was run on the T3D with 256 processors. Four minutes were required to form the matrix the once required, and 30 minutes per look angle for right hand side formation and solution.

7. Discussion and Conclusions

A curvilinear, isoparametric implementation of time domain integral equation methods has been demonstrated to be an effective tool for EM analysis. Such a treatment also permits the important practical advantage of direct coupling to industry standard, commercial CAD and pre- and post-processing software.

It is still an active research area. The principal current projects include:

-hybridisation with time domain optical methods

-the inclusion of lossy (RAM, human tissue) target materials

-developments which promise very marked reductions in both storage needs and operations.

8. Acknowledgements

The developments described here have been (and are indeed currently being) funded by a variety of sources. It is a pleasure to acknowledge the particular support of British Aerospace, the Ministry of Defence Defence Research Agency, the Engineering and Physical Sciences Research Council, the Medical Research Council, Macneal Schwendler Corporation and Thorn EMI Electronics.

Figure captions

Figure 1: Mapping of general, curved surface patches into flat squares in intrinsic space.

Figure 2: Relative times for the different solution stages as a function of problem size

Figure 4: Mesh of cylindrical cavity

Figure 3: Diagram of software structure

Figure 5: Magnitude of surface current induced on-axis of cylindrical cavity, inside and outside the rear wall, when subject to an incident pulse along the axis into the open end.:

Figure 6: Mesh of NASA almond; 4154 nodes

Figure 7: Computed monostatic (VV) rcs of almond at 3 GHz, with some measured and Carlos values shown also.

Figure 8: Magnitude of induced surface currents on the almond at 7 GHz.

Figure 9: Mesh of NASA cone-sphere with gap; 5924 nodes

Figure 10: Computed monostatic (VV) rcs of almond at 9.92 GHz, with some measured values shown also.

References

1. Miller, E.K. Time-domain modelling in electromagnetics. *Journal of Electromagnetic Waves and Applications* 8:1125-1172, 1994.

2. Woo, A.C., Wang, H.T.G. and Schuh, M.J. Benchmark radar targets for the validation of computational electromagnetics programs. *IEEE Ant.Prop.Mag* 35:84-89, 1993.

3. Zienkiewicz, O.C. *The Finite Element Method in Engineering Science*, London:McGraw-Hill, 1971.

4. Lachat, J.C. and Watson, J.O. Effective Numerical Treatment of Boundary Integral Equations: A Formulation for Three-Dimensional Elastostatics. *International Journal for Numerical Methods in Engineering* 10:991-1005, 1976.

5. Bluck, M.J. and Walker, S.P. Time Domain BIE Analysis of Large Three Dimensional Electromagnetic Scattering Problems. *IEEE Tr.Ant.& Prop.* 1995.(In Press)

6. Volakis, J.L. Carlos-3D; A general purpose three dimensional method of moments scattering code. *IEEE Ant.Prop.Mag* 35:1993.

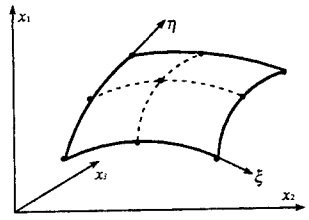
x_1
η
x_3
ξ
x_2

1.

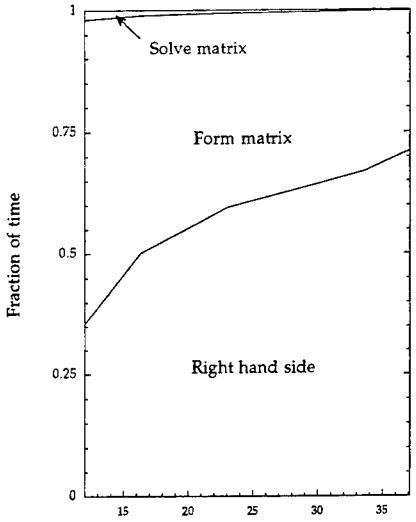
Solve matrix
Form matrix
Right hand side
Fraction of time
1
0.75
0.5
0.25
0
15
20
25
30
35
Problem size (root nodes)

2.

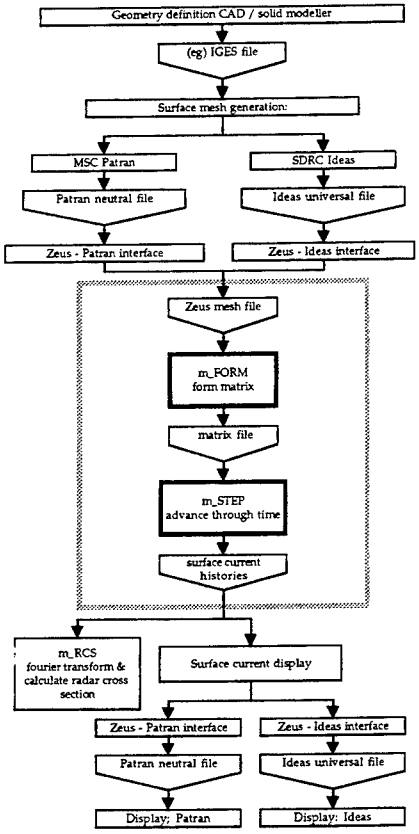
Geometry definition CAD / solid modeller
(eg) IGES file
Surface mesh generation:
MSC Patran
SDRC Ideas
Patran neutral file
Ideas universal file
Zeus - Patran interface
Zeus - Ideas interface
Zeus mesh file
m_FORM
form matrix
matrix file
m_STEP
advance through time
surface current
histories
m_RCS
fourier transform &
calculate radar cross
section
Surface current display
Zeus - Patran interface
Zeus - Ideas interface
Patran neutral file
Ideas universal file
Display: Patran
Display: Ideas

3.

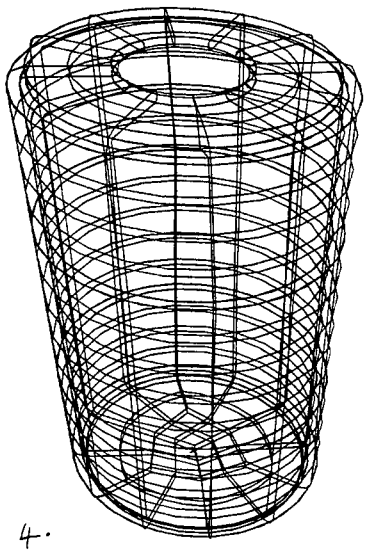

4.

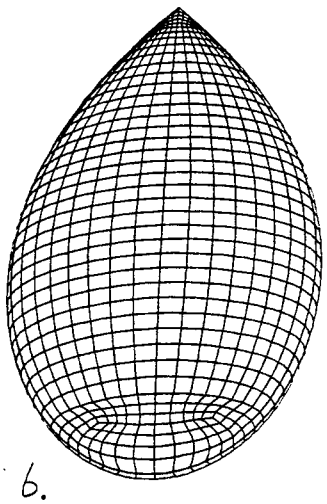

6.

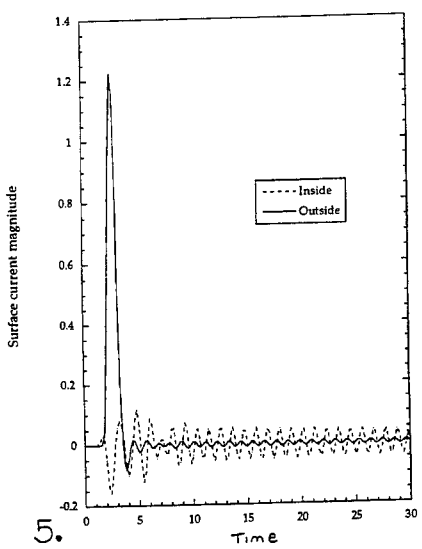
Surface current magnitude
Inside
Outside
Time

5.

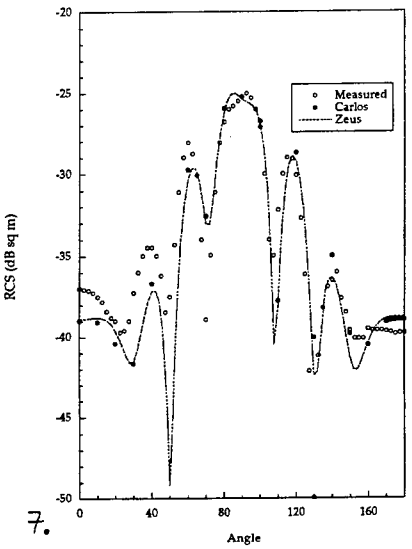
RCS (dB sq m)
Measured
Carlos
Zeus
Angle

7.

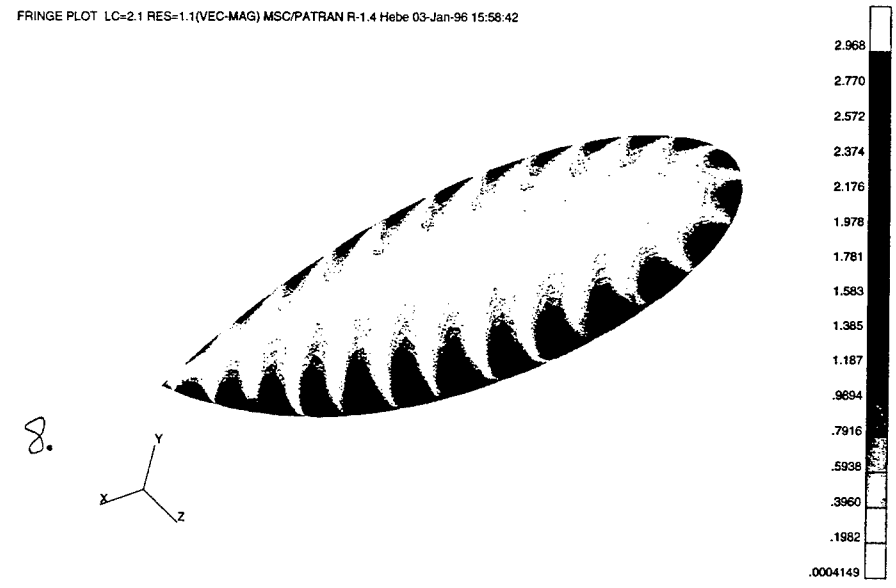
FRINGE PLOT LC=2.1 RES=1.1(VEC-MAG) MSC/PATRAN R-1.4 Hebe 03-Jan-96 15:58:42
2.968
2.770
2.572
2.374
2.176
1.978
1.781
1.583
1.385
1.187
.9894
.7916
.5938
.3960
.1982
.0004149
Y
X
Z

8.

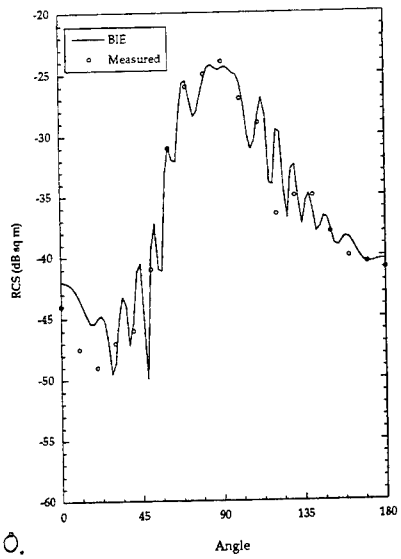
BIE
Measured
RCS (dB sq m)
-20
-25
-30
-35
-40
-45
-50
-55
-60
0
45
90
135
180
Angle

10.

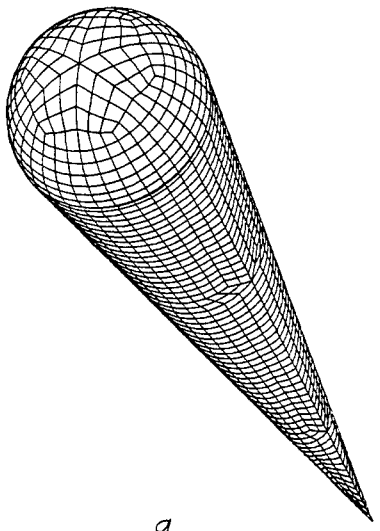

9.

DOUBLE SCATTER RADAR CROSS SECTIONS FOR TWO DIMENSIONAL RANDOM ROUGH SURFACES THAT EXHIBIT BACKSCATTER ENHANCEMENT

M. El-Shenawee* and E. Bahar
Department of Electrical Engineering
University of Nebraska-Lincoln
Lincoln, NE 68588–0511, USA
* Electronics Research Institute
El-Tahrir St., Dokki, Cairo, Egypt
e.mail: magda@sgiris.unl.edu

In this work, full wave solutions for the single and double scatter radar cross sections from two dimensional random rough surfaces are given. The solutions are expressed as multidimensional integrals. The high frequency approximations are used to reduce the double scatter integrals from twelve to four dimensional. The single scatter cross section is given in closed form. The large radius of curvature approximation is used. The incident waves are assumed to be plane waves.

Similar to scattering from one dimensional random rough surfaces, the major contributions to the double scatter cross sections come from two different pairs of paths. They are the quasi parallel double scatter paths and the quasi antiparallel double scatter paths. The total incoherent double scatter cross section is the sum of the incoherent quasi parallel and quasi antiparallel double scatter cross sections.

In the high frequency limit, the major contributions to the double and single scatter cross sections come from the neighborhood of the specular points on the rough surface. Thus the surface element scattering coefficients are evaluated at the specular points after integrating with respect to the slopes. The probability density functions of the slopes are assumed to be Gaussian. Shadow functions are included in the expressions.

The effects of changing the rough surface parameters, such as mean square height and mean square slope, on the double scatter cross sections are studied. The level and width of the peak in the backscatter direction depend on the mean square height and slope of the rough surface. The numerical results show sharp enhancement in the backscatter directions. This sharp backscatter enhancement, which is observed for all polarizations and for both normal and oblique incident angles, is associated with the quasi antiparallel double scatter paths.

I. FORMULATION OF THE PROBLEM

The full wave solution for the double scatter far fields $G_d^f(\bar{r})$ from two dimensional rough surfaces $(y = h(x_s, z_s))$ is given by [1]

$$G_d^f(\bar{r}) = \left(\frac{k_0}{2\pi j}\right)^3 \frac{\exp(-jk_0 r)}{r} \int \frac{D_{2'}(\bar{n}^f, \bar{n}')}{\left(n_y^f - n_y'\right)} \exp\left(jk_0 \bar{n}^f \cdot \bar{r}_{s2'}\right) \exp\left(jk_0 \bar{n}' \cdot (\bar{r}_{s2'} - \bar{r}_{s1'})\right)$$

$$\times \frac{D_{1'}(\bar{n}', \bar{n}^i)}{\left(-n^i + n_y'\right)} \exp\left(-jk_0 \bar{n}^i \cdot \bar{r}_{s1'}\right) \frac{dn_y' dn_z'}{\sqrt{1 - n_y'^2 n_z'^2}} U(\bar{r}_{s1'}) U(\bar{r}_{s2'}) dx_{s1'} dz_{s1'} dx_{s2'} dz_{s2'} G^i(0) \tag{1}$$

in which the time harmonic excitations $\exp(j\omega t)$ are assumed and the free space wave number is $k_0 = \omega\sqrt{\varepsilon_0 \mu_0}$. The incident waves are in the direction $\bar{n}^i$ and the scattered waves are in the direction $\bar{n}^f$ to receive at $\bar{r}$, where

$$\bar{n}^i = n_x^i \bar{e}_x + n_y^i \bar{e}_y + n_z^i \bar{e}_z \tag{2a}$$

$$\bar{n}^f = n_x^f \bar{e}_x + n_y^f \bar{e}_y + n_z^f \bar{e}_z \tag{2b}$$

$$\bar{r} = x\bar{e}_x + y\bar{e}_y + z\bar{e}_z \tag{2c}$$

The scattering matrices at points $1'$ and $2'$ on the rough surface are $D_{1'}(\bar{n}', \bar{n}^i)$ and $D_{2'}(\bar{n}^f, \bar{n}')$. The elements of the scattering matrices depend on the local slope of the rough surface [1]. Moreover, they depend on the polarization of the incident and scattered waves and the media on both sides of the rough interface. The incident fields are assumed to be plane waves and the receiver is located in the far field. The wavevectors of the scattered waves at the point on the surface at $\bar{r}_{s1'}$ are in the direction $\bar{n}' = n'_x\bar{e}_x + n'_y\bar{e}_y + n'_z\bar{e}_z$ (see Fig. 1). The position vectors to points $1'$ and $2'$ on the rough surface (see Fig. 1) are given by

$$\bar{r}_{s1'} = x_{s1'}\bar{e}_x + h(x_{s1'}, z_{s1'})\bar{e}_y + z_{s1'}\bar{e}_z \tag{3a}$$

$$\bar{r}_{s2'} = x_{s2'}\bar{e}_x + h(x_{s2'}, z_{s2'})\bar{e}_y + z_{s2'}\bar{e}_z \tag{3b}$$

At high frequencies, the shadow functions $U(\bar{r}_{s1'})$ and $U(\bar{r}_{s2'})$ are equal to one if the point at $\bar{r}_{s1'}$ is illuminated by the incident waves and visible at point $2'$ on the surface and if the point at $\bar{r}_{s2'}$ is illuminated by a point source at $1'$ and visible at the receiver [2]. The double scatter average cross section is obtained by multiplying (1) by its complex conjugate. The radar cross section for the two dimensional rough surface is defined as

$$\sigma T = \frac{4\pi^2}{A}\left|\frac{G^f}{G^i}\right|^2 \tag{4}$$

in which A is the radar footprint, thus

$$\begin{aligned}
\sigma T = \frac{k_0^6}{16A\pi^5} \int & \frac{D_{2'}(\bar{n}^f, \bar{n}')D^*_{2''}(\bar{n}^f, \bar{n}'')D_{1'}(\bar{n}', \bar{n}^i)D^*_{1''}(\bar{n}'', \bar{n}^i)}{\left(n_y^f - n'_y\right)\left(n_y^f - n''_y\right)\left(-n_y^i + n'_y\right)\left(-n_y^i + n''_y\right)} \\
& \times \exp\left\{jk_0\left[n_x^f(x'_{s2} - x''_{s2}) + n_y^f(h_{2'} - h_{2''}) + n_z^f(z_{s2'} - z_{s2''})\right]\right\} \\
& \times \exp\left\{-jk_0\left[n'_x(x_{s2'} - x_{s1'}) + n'_y(h_{2'} - h_{1'}) + n'_z(z_{s2'} - z_{s1'})\right]\right\} \\
& \times \exp\left\{jk_0\left[n''_x(x_{s2''} - x_{s1''}) + n''_y(h_{2''} - h_{1''}) + n''_z(z_{s2''} - z_{s1''})\right]\right\} \\
& \times \exp\left\{-jk_0\left[n'_x(x_{s1'} - x_{s1''}) + n^i_y(h_{1'} - h_{1''}) + n^i_z(z_{s1'} - z_{s1''})\right]\right\} \\
& \times \frac{dn'_y dn'_z}{\sqrt{1 - {n'_y}^2 - {n'_z}^2}} \frac{dn''_y dn''_z}{\sqrt{1 - {n''_y}^2 - {n''_z}^2}} dx_{s1'}dz_{s1'}dx_{s2'}dz_{s2'}dx_{s1''}dz_{s1''}dx_{s2''}dz_{s2''}
\end{aligned} \tag{5}$$

For the quasi parallel double scatter paths ($n'_\alpha, n''_\alpha < 0$ and $n'_\alpha, n''_\alpha > 0$; $\alpha = x, z$), the following transformations of variables are used:

$$x_{d1} = x_{s1'} - x_{s1''}, \quad x_{d2} = x_{s2'} - x_{s2''}, \tag{6a}$$

$$z_{d1} = z_{s1'} - z_{s1''}, \quad z_{d2} = z_{s2'} - z_{s2''} \tag{6b}$$

and

$$x_{a1} = (x_{s1'} + x_{s1''})/2, \qquad x_{a2} = (x_{s2'} + x_{s2''})/2 \tag{7a}$$

$$z_{a1} = (z_{s1'} + z_{s1''})/2, \qquad z_{a2} = (z_{s2'} + z_{s2''})/2 \tag{7b}$$

Thus from (5), (6) and (7), one gets for the quasi parallel case

$$\sigma T = \frac{k_0^6}{16A\pi^5}\int \frac{D_{2'}(\bar{n}^f,\bar{n}')D^*_{2''}(\bar{n}^f,\bar{n}'')D_{1'}(\bar{n}',\bar{n}^i)D^*_{1''}(\bar{n}'',\bar{n}^i)}{\left(n_y^f-n_y'\right)\left(n_y^f-n_y''\right)\left(-n_y^i+n_y'\right)\left(-n_y^i+n_y''\right)}$$

$$\times \exp\left\{jk_0\left[n_x^f x_{d2}-n_x'(0.5x_{d2}-0.5x_{d1}+x_{a2}-x_{a1})+n_x''(-0.5x_{d2}+0.5x_{d1}+x_{a2}-x_{a1})-n_x^i x_{d1}\right]\right\}$$

$$\times \exp\left\{jk_0\left[n_z^f z_{d2}-n_z'(0.5z_{d2}-0.5z_{d1}+z_{a2}-z_{a1})+n_z''(-0.5z_{d2}+0.5z_{d1}+z_{a2}-z_{a1})-n_z^i z_{d1}\right]\right\}$$

$$\times \exp\left\{jk_0\left[n_y^f(h_{2'}-h_{2''})-n_y'(h_{2'}-h_{1'})+n_y''(h_{2''}-h_{1''})-n_y^i(h_{1'}-h_{1''})\right]\right\}$$

$$\times \frac{dn_y'dn_z'}{\sqrt{1-{n_y'}^2-{n_z'}^2}}\frac{dn_y''dn_z''}{\sqrt{1-{n_y''}^2-{n_z''}^2}}dx_{d1}dz_{d1}dx_{d2}dz_{d2}dx_{a1}dz_{a1}dx_{a2}dz_{a2} \tag{8}$$

The major contributions to the double and single scatter cross sections, in the high frequency limit, come from the neighborhood of the specular points of the rough surface. The heights at any two neighbor points on the two dimensional rough surface are expanded and written as functions of the heights and slopes at the midpoint between them. The heights at points $1'$ and $1''$ on the rough surface are expanded about the heights at the midpoint between them. The statistical average of the radar cross section (8) with respect to the random heights and slopes of the surface is taken. Upon changing the integration variables n_y', n_y'', n_z', and n_z'' to the spherical coordinate variables ϑ' and ϕ' one gets

$$\left\langle \sigma_{dp}^{PQ}\right\rangle = \frac{(2k_0Lm)^2}{\pi}P_2(\bar{n}^i)P_2(\bar{n}^f)\sum_{R,S=V,H}\left\{\int \frac{\left[D_{2'}^{PS}(\bar{n}^f,\bar{n}')D_{1'}^{SQ}(\bar{n}',\bar{n}^i)D^{*PR}_{2''}(\bar{n}^f,\bar{n}'')D^{*RQ}_{1''}(\bar{n}'',\bar{n}^i)\right]}{\left(n_y^f-n_y'\right)\left(n_y^f-n_y''\right)\left(-n_y^i+n_y'\right)\left(-n_y^i+n_y''\right)}\right.$$

$$\times \frac{p(h_{xc1s},h_{xc2s},h_{zc1s},h_{zc2s})}{\left(n_y^f-(n_y'+n_y'')/2\right)^2\left(-n_y^i+(n_y'+n_y'')/2\right)^2}$$

$$[1-P_2(|n_y'|)][1-P_2(|n_y''|)]\,\mathrm{sinc}\,[k_0L_m(n_x'-n_x'')]\,\mathrm{sinc}\,[k_0L_m(n_z'-n_z'')]$$

$$\left.\times \exp\left(-\langle h^2\rangle k_0^2(n_y''-n_y')^2\right)\sin\vartheta'\sin\vartheta''d\vartheta'd\vartheta''d\varphi'd\varphi''\right\} \tag{9}$$

The integrations with respect to x_{d1}, x_{d2}, z_{d1}, and z_{d2}, yield Dirac delta functions in the high frequency limit. In (9) the surface element scattering coefficients D^{PQ} are evaluated at the slopes at the specular points h_{xc1s}, h_{xc2s}, h_{zc1s} and h_{zc2s}, as a result of integrating the Dirac Delta functions $\delta(.)$ with respect to the random slopes. The probability density functions of the (large scale) slopes $p(h_{xc1}, h_{xc2}, h_{zc1}, h_{zc2})$ are assumed to be Gaussian. The slopes at the specular points are given by

$$h_{xc1s} = -\left[-n_x^i+\frac{n_x'+n_x''}{2}\right]\Big/\left[-n_y^i+\frac{n_y'+n_y''}{2}\right] \tag{10a}$$

$$h_{xc2s} = -\left[-n_x^f+\frac{n_x'+n_x''}{2}\right]\Big/\left[-n_y^f+\frac{n_y'+n_y''}{2}\right] \tag{10b}$$

$$h_{zc1s} = -\left[-n_z^i+\frac{n_z'+n_z''}{2}\right]\Big/\left[-n_y^i+\frac{n_y'+n_y''}{2}\right] \tag{10c}$$

$$h_{zc2s} = -\left[-n_z^f + \frac{n_z' + n_z''}{2}\right] / \left[-n_y^f + \frac{n_y' + n_y''}{2}\right] \tag{10d}$$

The integrations over x_{a1}, x_{a2}, z_{a1} and z_{a2} yield the footprint area A and the sinc functions. Furthermore, L_m is the mean width of a typical depression on the rough surface [1], [3], [4]. The probabilities that the surface does not shadow the incident and scattered waves are given by $P_2(\bar{n}^i)$ and $P_2(\bar{n}^f)$, respectively [2], and $[1 - P_2]$ is associated with the probability of a double scatter event. The symbols V and H are for vertical and horizontal polarizations. For the quasi antiparallel double scatter paths, the following transformations of variables are used in (5):

$$x_{d1} = x_{s1'} - x_{s2''}, \qquad x_{d2} = x_{s2'} - x_{s1''}, \tag{11a}$$

$$z_{d1} = z_{s1'} - z_{s2''}, \qquad z_{d2} = z_{s2'} - z_{s1''} \tag{11b}$$

Thus, one gets the following expression for the high frequency quasi antiparallel ($n_\alpha' < 0$, $n_\alpha'' > 0$ and $n_\alpha' > 0$, $n_\alpha'' < 0$; $\alpha = x, z$) double scatter cross section

$$\left\langle \sigma_{dp}^{PQ} \right\rangle = \frac{(2k_0 Lm)^2}{\pi} P_2(\bar{n}^i) P_2(\bar{n}^f) \sum_{R,S=V,H} \left\{ \int \frac{\left[D_{2'}^{PS}(\bar{n}^f, \bar{n}') D_{1'}^{SQ}(\bar{n}', \bar{n}^i) D_{2''}^{*PR}(\bar{n}^f, \bar{n}'') D_{1''}^{*RQ}(\bar{n}'', \bar{n}^i)\right]}{\left(n_y^f - n_y'\right)\left(n_y^f - n_y''\right)\left(-n_y^i + n_y'\right)\left(-n_y^i + n_y''\right)} \right.$$

$$\times \frac{p(h_{xc1s}, h_{xc2s}, h_{zc1s}, h_{zc2s})}{\left(\left(n_y^f + n_y' - n_y'' - n_y^i\right)/2\right)^2 \left(\left(n_y^f - n_y' + n_y'' - n_y^i\right)/2\right)^2}$$

$$\left[1 - P_2(|n_y'|)\right]\left[1 - P_2(|n_y''|)\right] \operatorname{sinc}\left[k_0 L_m (n_x^f + n_x^i - n_x' - n_x'')\right] \operatorname{sinc}\left[k_0 L_m (n_z^f + n_z^i - n_z' - n_z'')\right]$$

$$\left. \times \exp\left(-\langle h^2 \rangle k_0^2 (n_y^f - n_y' - n_y'' + n_y^i)^2\right) \sin\vartheta' \sin\vartheta'' d\vartheta' d\vartheta'' d\varphi' d\varphi'' \right\} \tag{12}$$

The slopes at the specular points for the quasi antiparallel case are given by

$$h_{xc1s} = -\left[-n_x^i + n_x' - n_x'' + n_x^f\right] / \left[n_y^f - n_y^i + n_y' - n_y''\right] \tag{13a}$$

$$h_{xc2s} = -\left[n_x^f - n_x' + n_x'' - n_x^i\right] / \left[n_y^f - n_y' + n_y'' - n_y^i\right] \tag{13b}$$

$$h_{zc1s} = -\left[n_z^f - n_z^i + n_z' - n_z''\right] / \left[n_y^f - n_y^i + n_y' - n_y''\right] \tag{13c}$$

$$h_{zc2s} = -\left[n_z^f - n_z' + n_z'' - n_z^i\right] / \left[n_y^f - n_y' + n_y'' - n_y^i\right] \tag{13d}$$

The sharp enhancement in the backscatter direction $(-\bar{n}^i = \bar{n}^f)$ is associated with the quasi antiparallel ($\bar{n}' \approx -\bar{n}''$) double scatter cross section (12). Note the difference in the expressions for the slopes at the specular points for the quasi parallel and the quasi antiparallel cases (10) and (13). For backscatter at normal incidence the major contributions to the double scatter cross sections come from quasi horizontal paths between points 1 and 2 (see Fig. 1) and the slopes at the stationary points are approximately $\pm 45^\circ$.

II. NUMERICAL EXAMPLES

The incoherent double scatter cross sections (quasi parallel + quasi antiparallel) for two dimensional rough surfaces are plotted in Figs. 2, 3 and 4 as functions of the scatter angle $\vartheta^f \cos\varphi^f$ (where $\varphi^i = 0$, $\varphi^f = 0, \pi$). The two dimensional rough surface is assumed to be coated with gold of permittivity $\varepsilon_r = -9.888312 - j1.051766$ at $\lambda = 0.633\mu m$. The incident angle is equal to 10^o. The Rayleigh roughness parameter $\beta = 4k_0^2\langle h^2\rangle$ is assumed to equal 394.105 in Figs. 2 and 4. In Figs. 2 and 3, the VV polarized double scatter cross sections are shown. The effect of changing the mean square slope (m.s.s.) is shown in Fig. 2 where it is assumed to be 0.25, 0.4, 0.5, 0.65, 0.75, 0.85 and 1.0. The level of the peak enhanced backscatter cross section is highest for mean square slope equal to 1.0 and it decreases as the mean square slope decreases to 0.25. In Fig. 3, the mean square slope is assumed to be 0.5 and the Rayleigh roughness parameter is assumed to be 10, 50, 100, 200, 300, and 394.105. The level of the peak enhanced backscatter increases as the Rayleigh roughness parameter increases. The width of the enhanced backscatter peak increases as both the Rayleigh roughness parameter and the mean square slope decrease. The cross sections for different polarizations (VV, HH, VH, HV) are shown in Fig. 4 in which the mean square slope is assumed to be 0.5 and β is assumed to be 394.105. Enhanced backscatter is observed for the four polarizations considered. The levels of the peak double scatter cross sections (in the backward direction) are approximately the same for both the like and cross polarized cases. The sharp backscatter enhancement observed for all polarizations, is associated with the quasi antiparallel double scatter paths.

CONCLUSIONS

The results for the double scatter radar cross sections exhibit sharp enhancement in the backscatter direction at normal and oblique incident angles. This sharp enhancement is associated with the quasi antiparallel double scatter path. The height and width of the peak in the backscatter direction depends on the mean square height and slope of the two dimensional random rough surface. The high frequency approximations make the computations more tractable; however, the polarization dependence is less obvious [3].

ACKNOWLEDGMENT

This work is supported partially by the Department of Electrical Engineering and the Center for Electro-Optics at the University of Nebraska-Lincoln and the Supercomputer facility at Cornell University.

REFERENCES

[1] Bahar and M. El-Shenawee, "Enhanced Backscatter from One Dimensional Random Rough Surfaces — Stationary Phase Approximations to Full Wave Solutions," The Journal of the Optical Society of America A, Vol. 12, No. 1, pp. 151–161, January 1995.

[2] M. I. Sancer, "Shadow-Corrected Electromagnetics Scattering from a Randomly Rough Surface," IEEE Trans. Antennas Propagat., Vol. AP-17, No. 5, pp. 577–585, September 1969.

[3] E. Bahar and M. El-Shenawee, "Vertically and Horizontally Polarized Diffuse Double Scatter Cross Sections of One Dimensional Random Rough Surfaces that Exhibit Enhanced Backscatter — Full Wave Solutions," Journal of the Optical Society of America A, pp. 2271–2285, August 1994.

[4] M. El-Shenawee and E. Bahar, "Double Scatter Radar Cross Sections for Two Dimensional Random Rough Surfaces — High Frequency Approximation," proceedings of the 1995 IEEE AP-S International Symposium and USNC/URSI Radio Meeting, Newport Beach, CA, June 18–23, 1995.

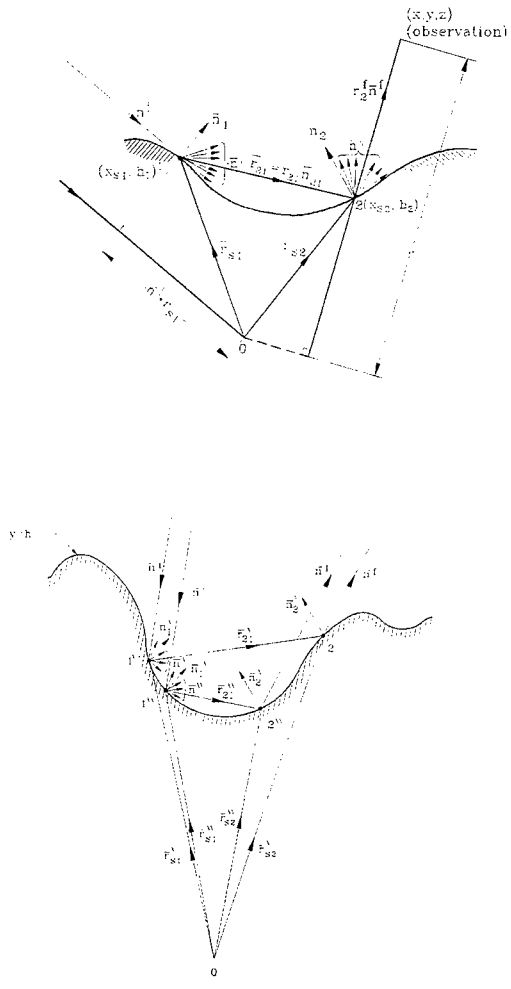

Fig. 1 Double scattered electromagnetic waves

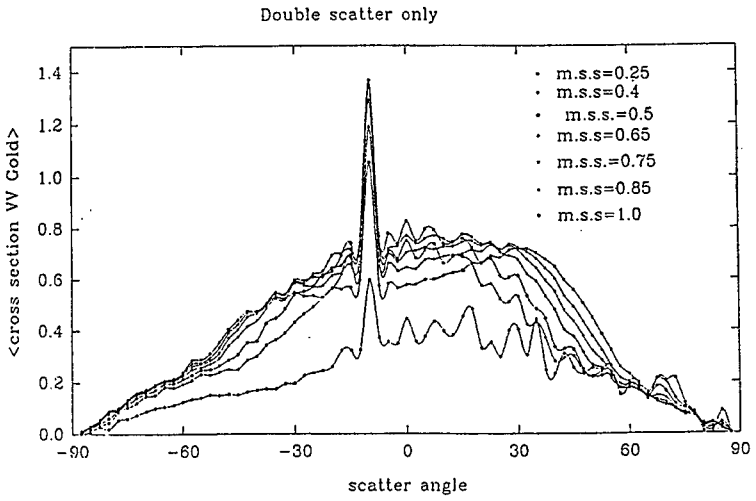

Fig. 2, ϑ^i=10°, ε_r=-9.888312-j1.051766, λ=0.633 μ.m., β=394.105.

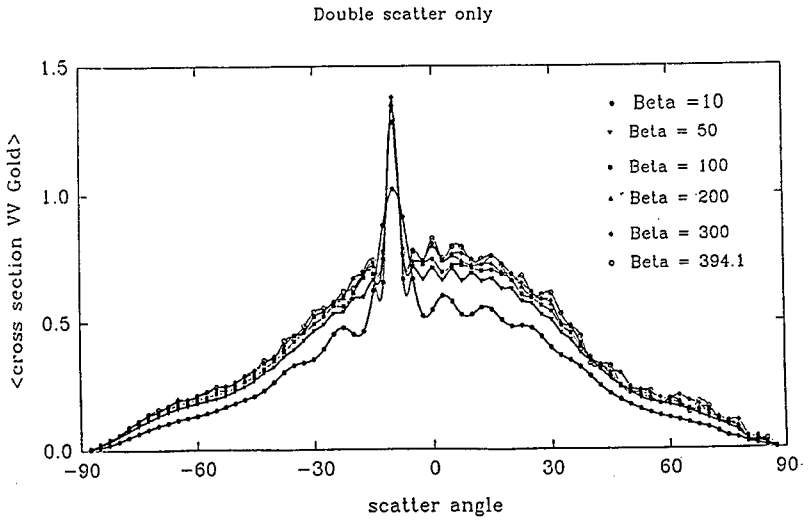

Fig. 3, ϑ^i=10°, ε_r=-9.888312-j1.051766, λ=0.633 μ.m., mean square slope=0.5.

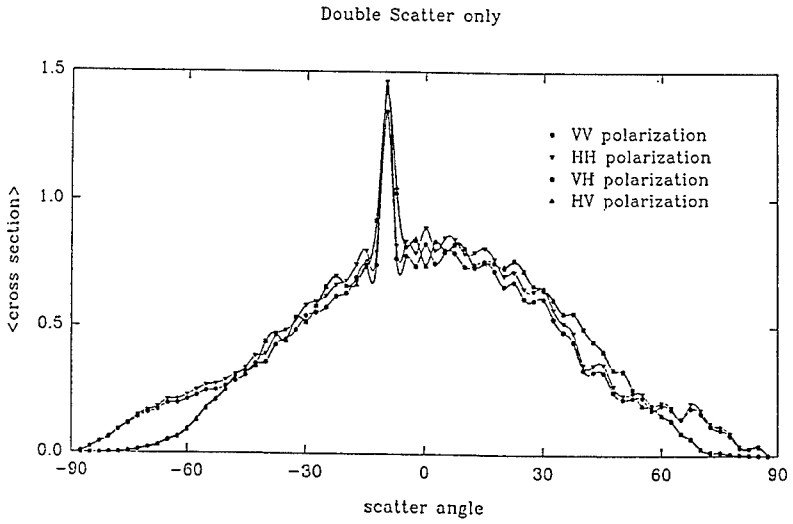

Fig. 4, ϑ^i=10°, ε_r=-9.888312-j1.051766, λ=0.633 μ.m., mean square slope=0.5, β=394.105.

SESSION 4:

APPLICATIONS OF PARALLEL COMPUTING

Chairs: L. Epp and K. Naishadham

SOLUTION OF ELECTROMAGNETIC EIGENPROBLEMS ON MULTIPROCESSOR SUPERSCALAR COMPUTERS

M. P. Dębicki, P. Jędrzejewski, J. Mielewski, P. Przybyszewski, M. Mrozowski
Department of Electronics,
The Technical University of Gdańsk
80-952 Gdańsk, POLAND.
e-mail: mim@pg.gda.pl

Abstract

The paper compares performance of two public domain procedures based on the QR and Arnoldi methods for the solution of dense matrix eigenvalue problems on a medium cost multiprocessor suuperscalar SGI PowerChallenge architecture. The propagation of waves in a rectangular image guide is used as an illustration. It is found that not only is the Arnoldi method better suited for the solution of typical computational electromagnetics eigenproblems, but also can exploit the computer hardware features more efficiently than the QR method.

I. Introduction

One of the current trends in computer hardware are the new medium cost multi processor architectures built around superscalar RISC processors. It has been observed [4] that computer hardware trends will have significant implications on how the the computational electromagnetics (CEM) codes are developed. It is important then to reconsider the basic CEM problems in order to find algorithms which may take the advantage of the available software and hardware resources. The most important issue which have to be addressed is memory bandwidth. All modern medium cost workstations and multiprocessor systems rely on the hierarchical memory structure with the data and instruction caches integrated on the chip and the a larger secondary cache capable of fetching data in one cycle. This hierarchical memory structure can be used to obtain significant speedup on electromagnetic simulations in a multiprocessor system.

II. Numerical algorithms

Many engineering problems require the solution of an eigenvalue equation. For instance, in electromagnetics, finding modes in waveguides or resonators is equivalent to finding eigenvalues and eigenfunctions of a differential or integral operator derived from Maxwell's equations. The most popular way to solve these problems is to approximate the operator through a matrix via some sort of a projection. Different projection methods generate various matrix formats. For instance the method of moments with entire domain basis functions yields dense matrices, while

the finite difference frequency domain method (FDFD) or the finite element method both generate sparse matrices.

In the simplest case the matrix eigenvalue problem to be solved has the following form

$$\underline{\underline{A}}\,\underline{u} = \lambda \underline{u} \tag{1}$$

where $\underline{\underline{A}}$ is a matrix of the size n and λ and $\underline{u}$ is the eigenvalue and eigenvector, respectively. Usually only the eigenvalues (and the corresponding eigenvectors) located near the upper or lower limit of the operator spectrum are of the practical interest.

Solving eigenproblems requires the use of appropriate numerical algorithms, which differ one from another with respect to the numerical complexity and the memory access pattern. In the solution of a specific problem, the operator matrix might be symmetric or non-symmetric, dense or sparse. The non-symmetric problems, arising in the investigation of modes in inhomogeneously loaded waveguides waveguides, are more difficult to solve. In the case of a dense non-symmetric matrix the traditional approach it to apply the numerical algorithm known as the *QR* method [1]. The method consists in reducing the matrix to the Hessenberg form via Householder transformations and finding the Schur form in a series of QR steps [1]. Diagonal elements of the Schur matrix are equal to the eigenvalues λ of $\underline{\underline{A}}$.

This method has a few disadvantages and the most important of them are:

- The high numerical cost of the computation of the order $O(N^3)$. This is due to the fact that the QR calculates of **all** the eigenvalues of the operator. (Note that in electromagnetic problems usually only the eigenvalues located near the upper or lower limit of the operator spectrum are to be found).
- Operation on **dense** matrices, which makes this method impractical for the sparse non-symmetrical problems.

The *QR* method is implemented in several libraries. One of the most efficient implementation is the `DGEEV` routine from *LAPACK* public-domain library [6]. The *LAPACK* procedures rely on the *BLAS2* operations optimized for memory access pattern. Hand tuned *BLAS* routines are also often provided with the system thereby ensuring the most optimal performance of LAPACK routines on a given computer architecture. The QR method is easy to use and straightforward in parameter selection.

Recently an alternate approach based on the *Arnoldi* [2][1] method has attracted the attention of numerical algebra experts. The particular feature of the *Armoldi* method is that it enables calculation of selected eigenvalues (and the corresponding eigenvectors), and does not require the information of the layout of individual matrix entries. The *Arnoldi* method is based on the concept of Krylov subspaces K_m

$$K_m \equiv \mathrm{span}\{\underline{v}, \underline{\underline{A}}\,\underline{v}, \underline{\underline{A}}^2\underline{v}, \ldots, \underline{\underline{A}}^{m-1}\underline{v}\} \tag{2}$$

where $\underline{v}$ is an vector. The *Arnoldi* method constructs a non square $\underline{\underline{V}}_m$ matrix with the columns forming an orthonormal basis $\{\underline{v}_i\}_{i=1,\ldots,m}$ of the subspace K_m. The construction of the $\underline{\underline{V}}_m$ does not require the knowledge of $\underline{\underline{A}}$ and relies only on the data obtained from the multiplication of suitably selected vectors with $\underline{\underline{A}}$. This operation can be done very fast using the user specified routines (for instance with the GEMV form BLAS2). The desired eigenvalues and eigenvectors of matrix $\underline{\underline{A}}$ are then recovered based on the information obtained in the construction of $\underline{\underline{V}}_m$.

The size of $\underline{\underline{V}}_m$ is $n \times m$ where n is the size of the eigenvalue problem. In the Arnoldi method, m, the size of the Krylov space, is usually only a few times larger than the number of desired eigenvalues. This implies that a relatively small additional memory space and a modest number of $\underline{\underline{A}}\,\underline{v}$ operations is required for the problems in which only a few eigenvalues are of interest.

The *Arnoldi* method can be implemented in many ways. In our work we used version 1.1 of the DNAUPD subroutine, taken from the one of the *NETLIB* packages *ARPACK* [5]. This procedure is an implementation of the implicit restarted k-step Arnoldi update algorithm [3]. It is a particularly versatile routine due to *reverse communication* scheme - an iterative process which consists in performing certain operations outside the subroutine. In case of the *Arnoldi* method, every iteration of the DNAUPD requires the product of the matrix $\underline{\underline{A}}$ and the vector $\underline{v}$ provided by the procedure. Matrix $\underline{\underline{A}}$ is not passed to the routine. In this case format of the matrix is not important for the procedure, it can be dense, sparse or produced "on-line". It allows the application of fast and efficiently optimized mathematical subroutines intended for a particular format of the matrix.

III. Results

We compared the numerical efficiency of the *Arnoldi* and *QR* methods on a multiprocessor architecture for a problem of finding a few low order modes in a rectangular waveguide loaded with a dielectric slab. The problem is converted into a matrix eigenvalue equation using the method of moments. The resultant matrix is dense and nonsymmetric. The eigenvalues of the matrix are then solved using both algorithms on a multiprocessor SGI POWER Challenge system.

Fig. 1 shows the total computation time versus the problems size using the QR algorithm for the increasing number of processors. Fig. 2 shows the speedup due to the multiprocessor execution. The speedup is defined as the ratio of computation time for $n > 1$ processors to the execution time for a single processor system. It is seen that the QR algorithm does not scale well. The speedup for 4 processor does not exceed 1.5. and the speedup does not change much with the problem size. The situation is drastically different for the *Arnoldi* method (Fig. 3). For this method we limited the number of eigenvalues to four, corresponding to four lowest order modes. As might be expected the computation time is much shorter than for the QR method. However, the most interesting properties of the *Arnoldi* method show up when one considers the speedup curves (Figs 4,5). For some problem sizes the speedup exceeds the number of processors. This super linear speedup is related to the efficient use of the memory bandwidth. For the system used in testing the secondary cache size per CPU was 1MB which corresponds to the dense matrix of the size $N = 370$. Increasing the number of processors increases the fast access memory available to the algorithm. The QR algorithm operates on individual matrix elements and has to hold in the memory the matrix, its Hessenberg decomposition and then its reduced form. The procedure runs out of cache when $N > 370$ and increasing the cache by adding processors has little effect since data has to be moved between processors. On the other hand the *Arnoldi* requires little memory in addition the memory required for storing the matrix $\underline{\underline{A}}$ itself. When the number of processors is increased the matrix is distributed over caches and what is even more important the only operation on the matrix elements is a simple matrix times vector product. This operation, when optimized for a specific multiprocessor architecture, does not generate significant amount of data traffic between processors. As a result the *Arnoldi* method can make an efficient use of the increased amount of secondary level cache available with multiprocessor execution. Obviously,

when the matrix data becomes too large or can be held within a single processor cache the super linear speedup disappears since the access time is comparable for single and multiprocessor execution. This effect is clearly seen in Fig. 5 for $N = 338$ and $N = 1682$.

It is now interesting to compare the relative performance performance of the two algorithms. The results are shown in Fig. 6 where the ratio of the execution times of the Arnoldi code to the QR code for single and multiprocessor case is plotted versus the problem size. It is seen that due to the more efficient use of cache, the Arnoldi method parallelizes much better than the QR method. While for a single processor case the Arnoldi method offers up to 24 fold reduction in the CPU time, the parallelization of both algorithm results in the Arnoldi code giving up to 70 times shorter execution times than the parallelized version of the QR method.

IV. Conclusions

The *Arnoldi* method combined with the *reverse communication* technique is a very powerful new technique much more suitable to the solution of electromagnetic eigenproblems with dense matrices than a very popular *QR* method. It enables calculation of only selected eigenvalues and inherently preserves the locality of data reference which implies good performance on the multiprocessor super scalar architectures

VI. Acknowledgments

This work was supported by the Polish Committee of Scientific Research. The numerical results reported in this contribution were obtained using the facilities of the TASK Computing Center.

References

[1] G. H. Golub, Ch. F. van Loan, "Matrix Computations", (2nd ed.), The Johns Hopkins University Press, 1989 (1991).

[2] Y. Saad, "Numerical methods for large eigenvalue problems", Manchester University Press Series in Algorithms and Architectures for Advanced Scientific Computing, 1992.

[3] D. C. Sorensen, "Implicit application of polynomial filters in k-step Arnoldi method", *Technical Report TR90-27*, Rice University, Department of Math. Sci., Houston, TX, 1990.

[4] W. R. Stone, "Practical implications of computer architecture for CEM code developers", *Proc. Intnl. Conf. on Electromagnetics in Advanced Applications*, pp. 297–300, Torino 1995.

[5] `http://www.netlib.org` in *ScaLAPACK*.

[6] `http://www.netlib.org` in *LAPACK*.

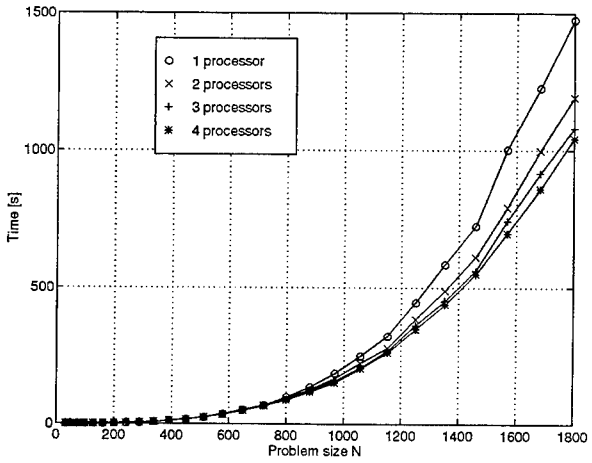

Figure 1: *Total time spent in the computation of the eigenvalues using the QR method for various problem sizes and various number of processors. The parallel version of the* `DGEEV` *(LAPACK) routine from* `complib.sgimath_mp` *has been used.*

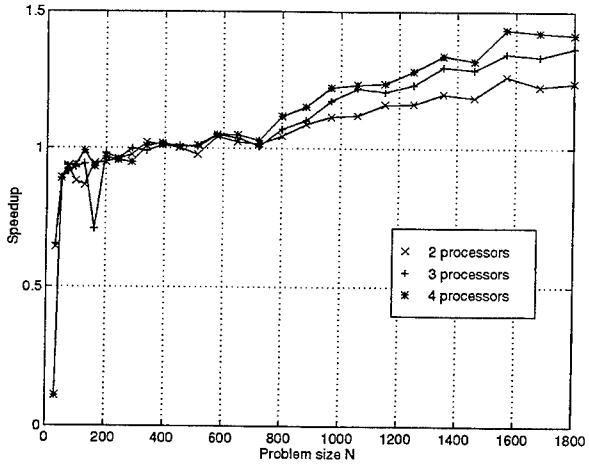

Figure 2: *Speedup of the computation of the eigenvalues using the QR method for various problem sizes and various number of processors. The parallel version of the* `DGEEV` *(LAPACK) routine from* `complib.sgimath_mp` *has been used.*

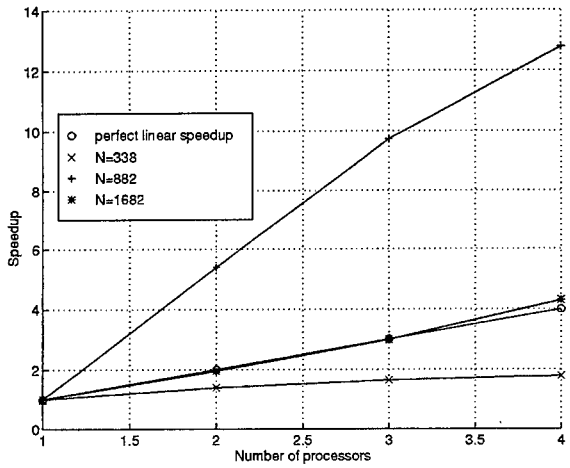

Figure 5: *Speedup of the Arnoldi algorithm for various problem sizes and various number of processors. The super linear speedup is seen for N=882.*

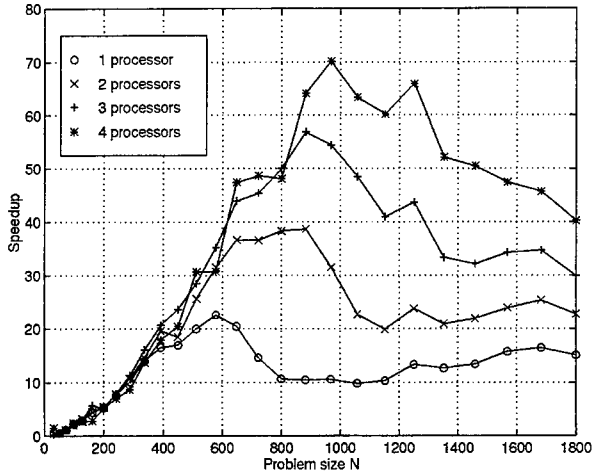

Figure 6: *Speedup of the Arnoldi method over the QR method for various problem sizes and various number of processors.*

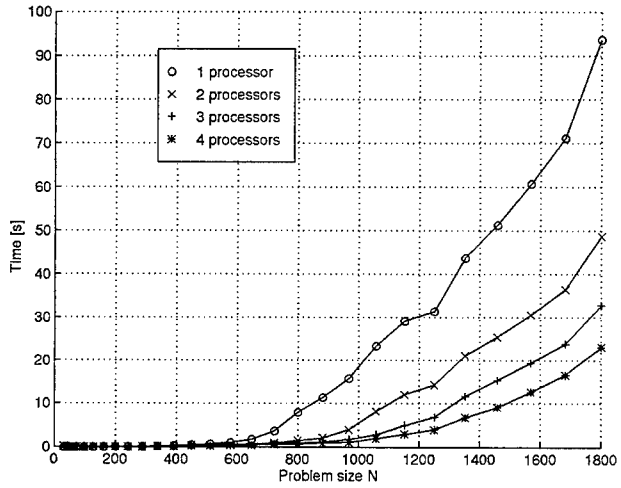

Figure 3: *Time required for finding 4 lowest order modes with the Arnoldi algorithm for various problem sizes and various number of processors. The parallel version of* DGEMV *(BLAS2) routine from* `complib.sgimath_mp` *has been used for matrix* $\times$ *vector operation.*

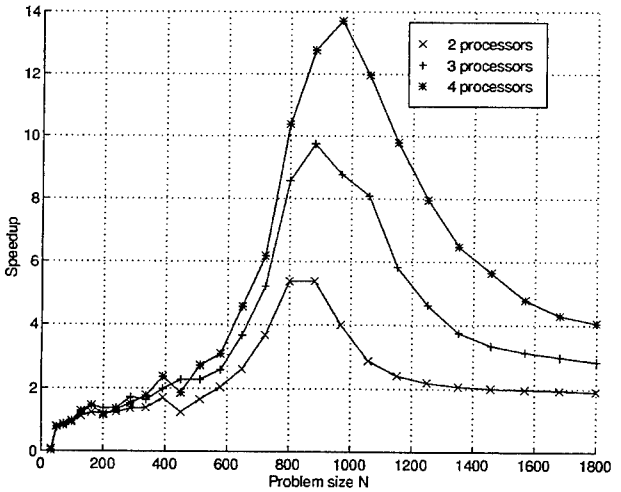

Figure 4: *Speedup of the Arnoldi algorithm for various problem sizes and various number of processors. The parallel version of* DGEMV *(BLAS2) routine from* `complib.sgimath_mp` *has been used. Note the strong super linear speedup.*

IMPLEMENTATION OF HYBRID FDTD/FVTD CONFORMAL ALGORITHM ON A MASSIVELY PARALLEL COMPUTER

Jei S. Chen and Andrew A. Seidl
Lockheed Palo Alto Research laboratory
Palo Alto, California

ABSTRACT

The hybrid FDTD/FVTD conformal algorithm is implemented on a massively parallel computer for calculating electromagnetic scattering of smooth surfaces with unstructured triangles. Necessary modifications from the serial code to the parallel code to improve computing speed and reduce memory space are discussed. The parallel FDTD/FVTD code run on the MASPAR 1104 is ten times faster than the serial code run on the Sparc 10. Numerical simulation of the parallel code is validated through the RCS of a PEC sphere by comparing with the Mie series.

INTRODUCTION

The hybrid finite difference and finite volume time domain (FDTD/FVTD) algorithm have been implemented on both serial and parallel computers. The serial code have been tested intensively on both SUN and IBM (RS6000) workstations. The development of hybrid FDTD/FVTD techniques can be found in papers[1-3]. In this paper, we discuss the implementation of the conformal FDTD/FVTD code on a massively parallel machines . The parallel code accepts unstructured triangles for smooth objects the same as the serial code. Due to different computer architectures, some subroutines in the serial code need to be modified to fit to the parallel computation. Our effort is to improve the computing speed and reduce the memory space.

The parallel computer MASPAR 1104 has 4K processors. The computer consists of a front end machine , the scalar unit and a single instruction multiple data (SIMD) parallel units . Scalars are stored on the front end and the parallel arrays are stored on the parallel unit. The code is written in FORTRAN and the variables used in parallel FORTRAN 90 constructs are stored on the parallel unit and mapped across the processors. Communication between the front end and the parallel unit is very time consuming and

must be minimized. We also need to maximize the number of processors computing at any one time and minimize router communication between the processors.

The massively parallel FDTD/FVTD code contains two parts; A) preprocessing routines which are executed only once before the FVTD/FDTD calculation for inputting the grid point data, and generating the tables of dependency graph, interpolation coefficients and parameters. B) time domain FDTD/FVTD computing routines for the recursive loops of updating E and H fields and calculating the far field time domain electric field and RCS. Due to the complicated relations between the nodes and elements in the unstructured grid, all the calculations which involve the dependency graph between nodes and elements must be done in the preprocessing routines as much as possible. The preprocessing routines also have advantages for solving scattering problems with very large objects, since the same pre-calculated data can be routinely used for different analysis cases.

A brief discussion of the hybrid FDTD/FVTD algorithm is given as well as the interpolations between two overlapping grids, the far field extrapolation and the boundary simulations. Software structure of the parallel FDTD/FVTD code and the necessary modifications in the subroutines so that it can take advantage of parallelism and avoid the computational bottleneck caused by the communication between front end and parallel unit are discussed. The performance of the parallel code is evaluated by comparing with the computing time of the serial code. Numerical results of the RCS from a PEC sphere obtained by the parallel code are compared with the Mie series.

The OVERLAPPING FDTD/FVTD HYBRID Method

The development of the hybrid FDTD/FVTD method is given in [2]. The integral forms of Maxwell's equations that are used in the time domain numerical solutions are given by:

$$-\int_A \dot{\vec{B}} \bullet d\vec{a} = \int_{\partial A} \vec{E} \bullet d\vec{l} \quad \text{Faraday's Law (line-surface form)} \qquad (1a)$$

$$\int_A \dot{\vec{D}} \bullet d\vec{a} = \int_{\partial A} \vec{H} \bullet d\vec{l} \quad \text{Ampere's Law (line-surface form)} \qquad (1b)$$

$$-\int_V \dot{\vec{B}}\, dv = \int_{\partial V} \hat{n} \times \vec{E}\, da \quad \text{Faraday's Law (surface-volume form)} \qquad (2a)$$

$$\int_v \dot{\vec{D}}\, dv = \int_{\partial v} \hat{n} \times \vec{H}\, da \quad \text{Ampere's Law (surface-volume form)} \quad (2b)$$

The FDTD (generalized) algorithm is developed from the discretization of Eqs. 1 and the FVTD algorithm is based on the discretization of Eqs. 2. For more details on these relations and the derivations of their discretized forms, please see the references [2]. Similar to the original [5], the/ hybrid is also time-domain leap-frog and spatially staggered. The overlapping grid consists of a rectangular grid and a body conferral grid. In the rectangular grid, we assign the field components as in the original FDTD. The conformal grid consists of several layers of triangular prisms constructed from the surface triangles. The electric vectors are assigned at the vertices and the magnetic vectors at the centroids of these triangular prisms. The outer boundary electric vectors on the FVTD primary grids are obtained through interpolation of the calculated rectangular FDTD electric fields; the inner boundary of the rectangular electric fields are obtained through interpolation of the calculated FVTD electric vectors. For the electric vertices at the boundary, we make use of the physical boundary condition; for the outer boundary of the rectangular grid we apply the absorbing boundary condition. The near-to-far field extrapolation can be obtained either from the calculated fields on the rectangular box of the FDTD grid or from the fields on the unstructured triangles of the FVTD conformal grid.

SOFTWARE STRUCTURE OF THE PARALLEL FDTD/FVTD CODE

A) Pre-Processing program

In developing the parallel FDTD/FVTD code, the algorithm must be mapped to the machine to take advantages of any parallelism. Unfortunately, for the unstructured grid, the dependency graph between the nodes and elements for primary grid and dual grids are too complicated to fit to the massively parallel architecture. To overcome this difficulty, we separate the program into two phases; the pre-processing phase and the routinely FDTD/FVTD calculating phase. The pre-processing program generates tables of dependency graph for both triangular elements and the vertices, calculates the area normal (area vectors) and volumes of primary and dual grids and generates the table of interpolate coefficients. The preprocessing program can be run either on the serial computer or the parallel computer. The data files generated from the preprocessing program are then read by the FVTD/FDTD calculating program to do the routine computation. Due to the complicated relations in the unstructured dependency graph, the

difficulty in obtaining the interpolation coefficients, and since these routines are called only once, the parallelization of the preprocessing subroutines was deemphasized, and therefore, the computational speed of the parallel version of preprocessing program is slower than the serial code. In solving a large problem, we can run the pre-processing program on a serial machine and then dump the precalculated data files to the well parallelized FDTD/FVTD code to do the routine calculations. The precalculated data files can also be reused for analyzing different cases with the same scattering geometry.

B) The parallel FDTD/FVTD calculating program

The parallel hybrid FDTD/FVTD is based on the serial code with necessary modifications to improve the computational speed and reduce the memory space. We first eliminate computational bottlenecks in some subroutines to improve the speed and limit the array dimensions to avoid massive memory requirements so that the code is able to solve a very large problem. The subroutines of the parallel FDTD/FVTD code and major differences from the serial code are in the following:

1) In subroutine EXTRAP, we replace the near-to-far field extrapolation from the rectangular box in FDTD grid by the extrapolation from the triangles of the conformal FVTD grid. The far field extrapolation subroutine obtains far fields from the calculated field components on an enclosed surface using the Stratton-Chu formula. For a rectangular box, the orientation of field components on six faces are all different, the bookkeeping is complicated and is difficult for parallel computing. Instead of calculating the far field from the rectangular box, we obtain the extrapolated far field from the triangles. Since all triangular elements are on the same zone and oriented in the same direction, the bookkeeping is simple and can be easily put on the parallel computer. The other important modification in this subroutine for the parallel version is that a "Collisions directive" is used to accumulate arrays with duplicate index values. This new parallel array assignment statement allow the MASPAR to execute the vector-subscribed value A(IEV(:N))=A(IEV(:N))+B(:N) the same as the serial DO loop even when duplicate index values are in array IEV(:N). With this new "Collisions" parallel array assignment, the speed can be improved. Because we avoid the storage of the tremendously whole time history of FDTD field components, memory space can be reduced.

2) In absorbing boundary, we replace the second order Mur absorbing boundary by our new artificial tapered damping radiation condition[4] in subroutines ABSORBE and ABSORBH. The advantage of the tapered damping absorbing condition is that it is very

simple and more suitable to massively parallel computing and more flexible for non-rectangular grids.

3) In subroutines FVTDE and FVTDH, we vectorize the summation of H-vorticity (FVTDE) and E-vorticity (FVTDH) to speed up the computation. Since the computation time in FVTDE depends on the maximum number of triangles around a vertex, we also use our newly developed unstructured mesh generator to create more uniform surface grids. The speed improves as the maximum number of triangles around a vertex decreases. In Subroutine FVTDINCB, the boundary condition simulation is performed. There are different approximations for the boundary condition as discussed in [3], here we use PEC1 because it is more suitable for parallel computing. Due to the complicated dependency graph of the unstructured grid, the calculations of area normal of the facet of dual or primary cells are very time consuming. In order to improve the computing speed, the area normal vectors are pre-calculated in the initial step of each subroutine and are stored into the memory.

4) Subroutines INTPCTR, INTPRTCE and INTPRTCH calculate the interpolated data from curvilinear to rectangular grids or from rectangular to curvilinear grids. Since all the coefficients are pre-calculated in the preprocessing program, the parallelization of these subroutines is easy.

EVALUATION OF THE PARALLEL CODE AND NUMERICAL RESULTS

The numerical simulation is carried out with PEC spheres of different sizes. Comparisons of the computing time between the parallel code on the MASPAR 1104 and the serial code on the SUN workstation Sparc 10 and Sparc IPX are based on the same condition. The radius of the sphere ranged from 0.5 meters to 4 meters. The grid size is delx=0.1m. The outer boundary of the FDTD box is 20 zones from the surface of the sphere. The taper damping absorbing boundary is 10 zones from the outer FDTD box. The number of triangles for the 1 meter sphere is 2400, for the 2 meter sphere is 9600, etc. Figure 1 shows comparisons of computing time for each iteration on serial and parallel machines. Table 1 is the distribution of timing of each subroutine in the parallel code on the MASPAR 1104 for a sphere with radius 1m and 2m. Table 2 is the distribution of timing of each subroutine for a sphere with radius 1m and 4m run on MASPAR 1104 and Sparc 10. Figure 2 is the RCS of a 1 meter sphere comparing with the Mie series. Note the improved accuracy over classical "staircasing" FDTD techniques.

ACKNOWLEDGMENT

This work was supported in part by the Electromagnetic Code Consortium and ARPA under contract F33615-93-2373 with Wright Laboratory, Wright-Patterson AFB, Ohio..

REFERENCES

1. Kane S. Yee, J. S. Chen, and A. H. Chang, "Conformal Finite Difference Time Domain (FDTD) with Overlapping Grids", IEEE Trans on Ant. and Propagation, Vol. 40, No. 9, pp,1068-1075, Sept. 1992.

2. Kane S. Yee, J. S. Chen "Conformal Hybrid Finite Difference Time Domain and Finite Volume Time Domain", IEEE Trans on Ant. and Propagation, Vol. 42, No. 10, Oct. 1994

3. J. S. Chen and Kane S. Yee, "Numerical Experiments on Late Time Growth Involving the FDTD/FVTD Hybrid", to be submitted to IEEE Trans. on Ant. and Propagation.

4. J. S. Chen and Kane S. Yee, "Artificial Tapered Damping near the Outer Computational Boundary", to be submitted to IEEE Trans. on Ant. and Propagation.

5. Kane S. Yee, "Numerical Solution of Initial Boundary Value Problems in Isotropic Media", IEEE Trans. Ant. and Propagation, Vol. 14, No.3, pp. 302-307, May 1966.

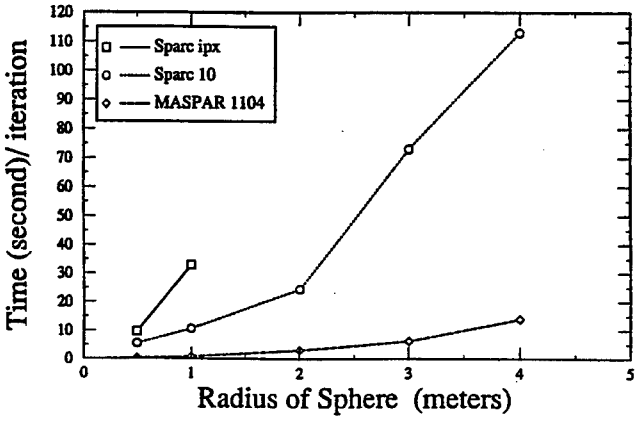

Figure 1. Computing time pre iteration vs. sphere radius.

Name of Subroutines	time(ms) /iter. (%) radius=1m, MASPAR		time(ms)/iter. (%) radius=2m, MASPAR	
FVTDE	281 ms	35 %	934 ms	42 %
FVTDINCB	19	2	42	1
RECFDTDE	19	3	175	6
INTPRTCE	27	3	85	3
INTPCTR	78	10	231	7
ABSORBE	13	2	78	3
EXTRAP	132	17	554	18
RECFDTDH	23	3	164	5
FVTDH	70	9	200	6
INTPRTCH	110	14	562	18
ABSORBH	17	2	74	2
total time	789 ms		3099 ms	

Table 1. Distribution of timing for FDTD/FVTD subroutine for spheres with radius 1m and 2m on MASPAR 1104 .

Name of Subroutine	time(ms)/iter. (%) radius=1m, Sparc ipx		time(ms)/iter. (%) radius=1m, Sparc 10	
FVTDE	4645 ms	33 %	29688 ms	24 %
FVTDINCB	156	1	7618	6
RECFDTDE	270	2	14290	11
INTPRTCE	667	4	482	4
INTPCTR	285	2	320	3
ABSORBE	121	1	16585	13
EXTRAP	2657	2	256	2
RECFDTDH	249	2	14590	12
FVTDH	844	6	18917	15
INTPRTCH	3950	28	3759	3
ABSORBH	121	1	16622	13
total time	13965 ms		123127 ms	

Table 2. Distribution of timing for FDTD/FVTD subroutine for spheres with radius 1m on MASPAR 1104 and Sparc 10.

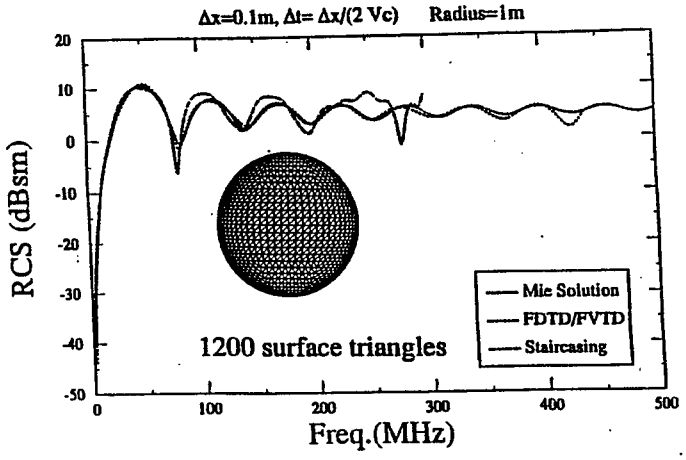

Figure 2. RCS of a 1 meter sphere comparing with Mie series.

Parallel CARLOS-3D Code Development

J. M. Putnam
McDonnell Douglas Corporation
J. D. Kotulski
Sandia National Laboratories

Abstract
CARLOS-3D is a three-dimensional scattering code which was developed under the sponsorship of the Electromagnetic Code Consortium (EMCC), and is currently used by over 80 aerospace companies and government agencies. The code has been extensively validated and runs on both serial workstations and parallel super computers such as the Intel Paragon. CARLOS-3D is a three-dimensional surface integral equation scattering code based on a Galerkin method of moments formulation employing Rao-Wilton-Glisson roof-top basis for triangular faceted surfaces. Fully arbitrary 3D geometries composed of multiple conducting and homogeneous bulk dielectric materials can be modeled. Thin materials can be modeled as either bulk regions or using various approximate boundary conditions such as impedance surfaces or resistive and magnetically conducting sheets. Matrix symmetry and geometric symmetry are used extensively in the code in order to reduce the computational and memory requirements for large scatterers. A unique feature of the code is the Galerkin operator structure of the code which is based on an indexing scheme which relates basis functions to unknown numbers in the matrix equation. All of the integral equation formulations are implemented using this structure, and are based on six Galerkin matrix operators. This operator based structure is independent of the geometry representation and basis functions used.

In this presentation, we will describe some of the extensions to the CARLOS-3D code, and how the operator structure of the code facilitated these improvements. Body of revolution (BOR) and two-dimensional geometries were incorporated by simply including new input routines, and the appropriate Galerkin matrix operator routines. Some additional modifications were required in the combined field integral equation (CFIE) matrix generation routine due to the symmetric nature of the BOR and 2D operators. Quadrilateral patched surfaces with linear roof-top basis functions were also implemented in the same manner. Quadrilateral facets and triangular facets can be used in combination to more efficiently model geometries with both large smooth surfaces and surfaces with fine detail such as gaps and cracks. Since the parallel implementation in CARLOS-3D is at high level, these changes were independent of the computer platform being used. This approach minimizes code maintenance, while providing capabilities with little additional effort.

Results will be presented showing the performance and accuracy of the code for some large scattering problems. Comparisons between triangular faceted and quadrilateral faceted geometry representations will be shown for some complex scatterers.

Introduction

CARLOS-3D is a general-purpose method of moments (MM) code [1] for computing the scattering from complex three-dimensional scatterers. It is based on a McDonnell Douglas Aerospace proprietary code CARLOS, which models antenna and scattering problems for 2D and 3D geometries. CARLOS-3D was developed under the sponsorship of the Electromagnetics Code Consortium (EMCC), and is available to qualified organizations through them, subject to US export control laws. The code uses the MM technique, with Galerkin testing to solve the Stratton-Chu surface integral equations for a user specified geometry. All of the surfaces describing the scatterer, consisting of conducting surfaces and boundaries between different dielectric regions are replaced with equivalent electric (J) and magnetic (M) currents. The code solves for these induced equivalent currents, which are then used to compute the scattered far-fields.

Code Description

Arbitrary 3D surfaces are modeled using flat triangular facets, with the electric and magnetic currents expanded in terms of the Rao, Wilton, Glisson roof-top functions [2]. A roof-top function spans the two facets forming each interior edge of a surface. At junction edges, which are formed by the intersection of two or more surfaces, half roof-top expansion functions are used to expand the currents. Current continuity across a junction is enforced by equating the unknowns associated with each of the half roof-top functions for the edge. Junction edges are determined automatically for surfaces which have common node points along a line of intersection between surfaces.

Complex geometries, which are composed of multiple conducting and bulk dielectric regions can be modeled. Various boundary conditions can be imposed separately on each of the surfaces comprising the target. For a given geometry, each dielectric region is given a number, and every surface which forms a boundary between different regions must be entered as a faceted surface. Infinitesimally-thin conducting, resistive, and impedance sheets must also be defined. The user must specify both the interior and exterior regions for each surface, along with the boundary condition to impose. Resistive and magnetically-conducting boundaries can either be embedded in a region, or be defined on the interface between different regions. Tapered resistive and impedance surfaces are modeled by specifying values for each facet forming the surface. Impedance (Leontovich) boundary conditions are modeled as an equivalent combination resistive/magnetically-conducting boundary.

The Stratton-Chu integral equations can be solved using several different formulations. For conducting surfaces, either the electric field integral equation (EFIE), the magnetic field integral equation (MFIE), or the combined field integral equation (CFIE) can be used. The coupling parameter in the CFIE formulation is specified separately on each surface, allowing the formulation to be used for geometries with both open and closed surfaces. For dielectric boundaries, the PMCHW formulation (after Poggio, Miller, Chu, Harrington, and Wu) is used. Galerkin testing, in conjunction with the form of the current expansions, results in a symmetric system of equations whenever the PMCHW/EFIE formulation is used. In addition, the formulations implemented for treated surfaces also

result in symmetric matrices which require only half of the matrix elements to be computed and stored.

Scattering from apertures, cavities, and gaps in a conducting surface can be modeled using an infinite ground plane option. Image theory is used to model both the source and the induced currents on all of the surfaces which are either conducting, dielectric or treated. The resulting system of equations is again symmetric.

Code Structure

The CARLOS-3D code has a flexible and modular structure which facilitates the incorporation of new features. The major components of the code are independent of the surface representation (i.e., flat facets, quadrilaterals, curved surfaces, etc.), and of the basis functions which are used to approximate the surface currents, permitting the code to be easily adapted to advanced basis functions. The section of code which generates the system matrix for an arbitrary geometry is written in terms of a generalized Galerkin matrix operator notation [3]. These operators result from testing either the integral operators in the Stratton-Chu equations, the equivalent currents directly, or the incident fields. The subroutines which assemble the system matrix and right-hand-side vector refer to these generic operators. The generic operators then reference routines which are specifically written for a given basis function type. Only the geometry input routine, and these specialized Galerkin operator routines depend upon the surface representation and basis functions used. Symmetry relations, which can be established for the Galerkin matrix operators, are used to efficiently fill the system matrix by eliminating redundant calculations.

A systematic approach [4] is used to generate the matrix equation, $\mathbf{ZI=V}$, for an arbitrary geometry with various boundary conditions imposed on the surfaces. This approach is based on a simple indexing scheme, which assigns an index number to each edge (roof-top or half roof-top function) defining the entire geometry. The index number for a particular edge specifies the location within the column vector, **I**, of either the **J** or **M** current coefficient associated with that edge. This indexing is performed in the geometry input routine, and is based on the boundary condition which is imposed on each surface. The boundary condition is used to define the equivalent currents which reside on the surface, and the relationship between the interior and the exterior current coefficients. Current continuity across junction edges connecting separate surfaces is enforced by equating the indices associated with the half roof-top functions for the edge. The matrix assembly routine is based on the index associated with each basis function (edge), and not on the explicit form of the basis function or the surface representation.

Quadrilateral Patch Implementation

A quadrilateral patch formulation [5] was incorporated into the parallel version of the code. In the quad-patch formulation, the currents on each patch are represented in terms of local parametric coordinates. For large smooth surfaces, the parametric coordinate directions are nearly orthogonal and the formulation has been shown to require fewer unknowns. This formulation employs a quadrilateral patched mesh to represent the

surface geometry and uses linear roof-top basis functions which span the pair of quad patches which form each interior edge of the grid. These basis function are edge based, and are implemented in manner similar to the Rao-Wilton-Glisson (RWG) roof-top functions. In this implementation, each quad patch is represented by four points on the surface of the scatterer, and a bi-linear surface description over the quad is assumed. The matrix elements can be computed in a manner analogous to the RWG basis functions using a combination of analytic and numerical procedures to compute the self and near-self terms.

The modifications to the parallel code were straightforward. The input routine was modified to accept either triangular or quad patches, and perform the unknown counting and indexing. Galerkin operator routines were written for the linear basis functions on quad patches using the triangular facet routines as templates. The high level operator routines were then modified to call the new operator routines for the quad patched surfaces.

Hybrid Combinations

Hybrid combinations of triangular and quad meshed surfaces have also been implemented into the code. The half roof-top functions for triangular and quadrilateral patches can be combined for edges which are formed by adjacent triangles and quads. Current continuity normal to a hybrid edge is maintained, and the representation is free of line charges. Note that the RWG half roof-top function is different than the half roof-top function which occurs for a degenerate quad patch where two points are identical. The RWG basis functions appear to be superior for this degenerate situation. A combination of triangular meshed and quad meshed surfaces is an efficient way to model geometries which have both surfaces with fine detail and large smooth surfaces. Galerkin operator routines were written to compute the interactions between triangular and quad surfaces.

BOR and 2D Implementation

The subroutines contained in the CICERO code [6] for both body of revolution (BOR) and two-dimensional (2D) geometries were incorporated into the parallel CARLOS-3D code. This was a straightforward way of implementing a parallel version of a BOR code by taking advantage of the operator structure and unknown indexing of CARLOS-3D. This permitted the modeling of some large missile shapes using an efficient formulation for BORs. In addition, some of the formulations and features of CARLOS-3D which were not contained in the CICERO code were available with little additional effort.

The input routines for BOR and 2D geometries were incorporated into the code with only minor modifications. The Galerkin operator routines were then integrated into the code with some additions added relating to the block matrix fill used in CARLOS-3D for the parallel implementation. The generic matrix assembly routines were then modified to call these new routines for BOR of 2D surfaces. Some additional changes were made to take advantage of the matrix symmetry which results from the BOR and 2D formulations due to the orthogonal components of the basis functions.

Results

The results for a number of selected problems will now be shown. All of the results were generated on the Intel Paragon at Sandia National Laboratories. The first problem to be shown is the scattering of the upper stages of a STRYPI missile at 1 GHz using the triangular patch representation and the BOR representation of the missile. The upper stages of this missile is 5.7m long with a circular cross section of radius 0.39m. The triangular patch model was generated using two symmetry planes resulting in a total of 62172(15798,15543,15543,15288) unknowns. The spatial resolution of this model was 309 facets/λ^2. The BOR representation of this scatterer consisted of 54.6 segments/λ which resulted in 1124 unknowns per Fourier mode. Thirty Fourier modes were used along with a 61 point Gaussian quadrature. The results of these two calculations are shown in Figure 1. and it is pointed out that the combined field formulation was used for both calculations.

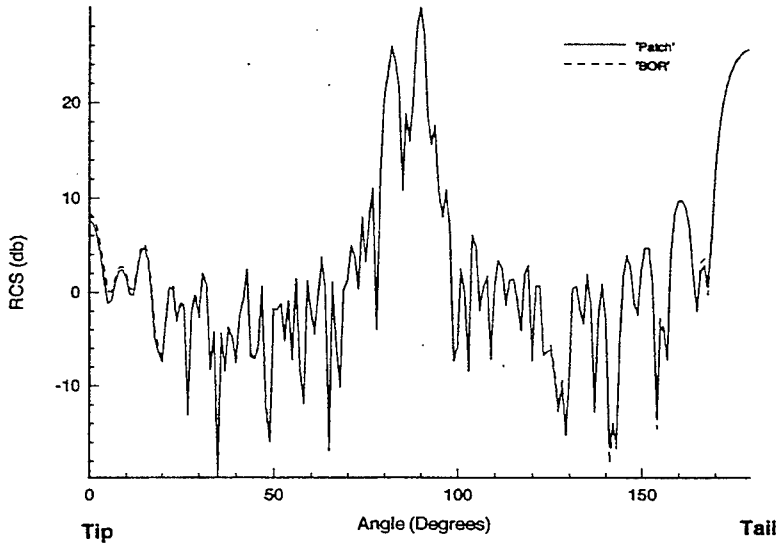

Figure 1. BOR and Triangular Patch monostatic RCS for STRYPI at 1GHz, Theta polarization.

The results clearly show excellent comparison between the two methods with a slight discrepancy at nose on (or tip aspect). The solution times for the two methods are presented in Table 1.

Formulation	# of Nodes	Matrix Fill	Matrix Solve	Total Time
BOR	512	4.8e-02	2.7e-02	.1
Triangular Patch	768	1.0	.26	2.16

Table 1. Solution Times for BOR and Patch formulations(all times are in hours).

The second problem addresses the triangular versus the quad-patch formulation of the scatterer. The test scatterer for this case is the 1 meter almond at 2 GHz. The geometry and unknown information for this model is shown in Table 2.

Formulation	Nodes	Facets	Total Number of Unknowns
Quad	1980	1872	14976
Triangle	1787	3359	20154

Table 2. Geometry and unknown information for quad and triangular patch formulation.

Note that the geometry information is actually for the quarter model of the almond so two planes of symmetry are used and the resulting total number of unknowns is approximately four times the quarter model unknowns. The monostatic rcs is shown in Figure 2 for theta polarization calculated using the EFIE.

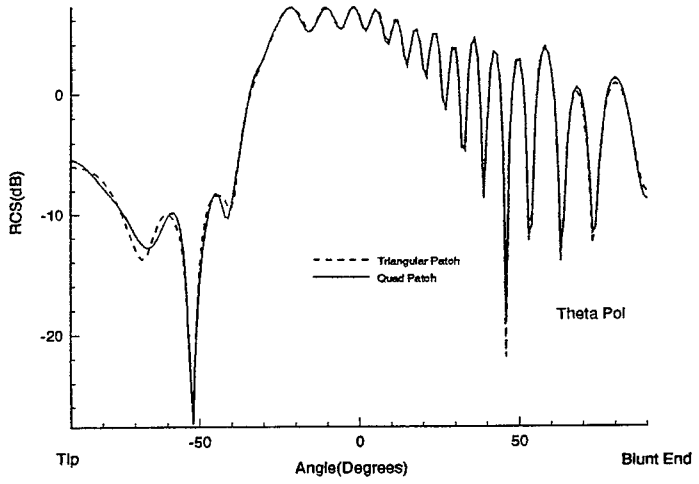

Figure 2. RCS of the 1 meter almond at 2 GHz for the two formulations using the EFIE.

The above results clearly show excellent agreement between the two formulations. The solution times for these runs are collected in Table 3. Note that the problems were run on 64 nodes of the Intel Paragon.

Formulation	Matrix Fill	Matrix Solve
Quad	.16	.16
Triangle	.14	.29

Table 3. Solution times for the quad and triangular patch models(time in hr.).

Conclusions

The previous parallelization effort on CARLOS-3D resulted in a code that permitted new features to be added independent of the parallel implementation[7]. Two new features have been added namely the BOR formulation and the quad-patch version of the code. These features were easily added due to the original structure of the code. These features have been validated for a number of large test cases a few of which have been presented here.

References

[1] J.M. Putnam and M.B. Gedera, "CARLOS-3D: A General-Purpose Three-Dimensional Method-of-Moments Scattering Code," IEEE Antennas & Propagation Magazine April, 1993.

[2] S.M. Rao, D.R. Wilton, and A.W. Glisson, "Electromagnetic Scattering by Surfaces of Arbitrary Shape", IEEE Trans. Ant. Prop., AP-30, 3, pp. 409-418, 1982.

[3] J.M. Putnam and L.N. Medgyesi-Mitschang, "Combined Field Integral Equation Formulation for Inhomogeneous Two- and Three-Dimensional Bodies: The Junction Problem", IEEE Trans. Ant. Prop. AP-39, 5, PP. 667-672, 1991.

[4] J.M. Putnam, "General Approach for Treating Boundary Conditions on Multi-Region Scatterers Using the Method of Moments", Proceedings of the 7th Annual Review of Progress in Applied Computational Electromagnetics, Monterey, CA, March 1991, pp. 304-319.

[5] R. Agarwal, D.S. Wang, and M.R. Axe, *A Hybrid Method of Moments and Computational Fluid Dynamics Method for Computational Electromagnetics,* Theory Report, NAS2-13891, NASA-Ames, Moffett Field, CA, 1994.

[6] J.M. Putnam and L.N. Medgyesi-Mitschang, "Combined Field Integral Equation Formulation for Inhomogeneous Bodies of Revolution (Combined Field Formulation of CICERO)", MDC Report No. QA003 for Sandia National Laboratories Contract No. 33-4257, December 1987.

[7] J.M. Putnam, D.D. Car, and J.D. Kotulski, "Parallelization of the CARLOS-3D Method of Moments Code", Proceedings of the 11th Annual Review of Progress in Applied Computational Electromagnetics, Monterey, CA, March 1995, pp. 848-855.

SESSION 5:

NEW DEVELOPMENTS IN TLM MODELING

Chair: W.J.R. Hoefer

On the Advantages of ATLM over Conventional TLM

Michael Krumpholz[1], Peter Russer[2]

[1] Radiation Laboratory, EECS Department, University of Michigan, Ann Arbor, MI 48109-2122
[2] Technische Universität München, Lehrstuhl für Hochfrequenztechnik, Arcisstraße 21
D-80333 München, Germany

Abstract

In contrast to the TLM scheme for the symmetrical condensed node (SCN), the field variables of the alternating transmission line matrix scheme (ATLM) are sampled at the center of the three-dimensional TLM cell. Considering the spatial derivatives of the electric and magnetic field components yields a bijective one-to-one mapping between the six field components, six spatial derivatives of the field components and the twelve wave amplitudes. ATLM does not support any nonphysical or spurious solutions and it represents the only TLM scheme with the same number of linearly independent field variables per cell as Yee's FDTD scheme.

I Introduction

The close relationship between the TLM and FDTD method has been shown recently by deriving both methods directly from Maxwell's equations [1, 2, 3]. Applying the method of moments to Maxwell's equations yields a finite difference scheme depending on the choice of the subdomain basis functions. While for FDTD, the field variables are the electric and magnetic field components, TLM uses incident and scattered wave amplitudes instead. The wave amplitudes represent a linear combination of the field components allowing to rewrite the finite difference scheme in a form in which the scattered wave amplitudes at the time $(k+1)\Delta t$ are only dependent on the incident wave amplitudes at $k\Delta t$. This relationship between the incident and reflected wave amplitudes defines a scattering matrix which describes the properties of a multiport and thus determines an equivalent network for the TLM cell.

The network model of TLM has become useful in many applications, however it also results in nonphysical solutions which do not satisfy Maxwell's equations [1]. The presence of nonphysical or spurious solutions limits the applicability of the TLM method and indicates the use of unnecessary field variables. In fact, it has been shown that for the conventional three-dimensional TLM schemes, half of the field variables do not contribute to the calculation of physical solutions indicating the unnecessary use of half of the field variables [3]. In this paper, the foundations of the novel alterning transmission line matrix scheme (ATLM) [4] are presented. ATLM does not support any spurious solutions and therefore, it does not exhibit a redundancy factor of two as conventional three-dimensional TLM.

Since ATLM is based on the TLM scheme for the symmetrical condensed node (SCN) [5], its field theoretical derivation is similar to the field theoretical derivation of the SCN [2].

However, the sampling of the field components is different for the two TLM schemes: While for TLM with SCN, every three–dimensional cell with the spatial coordinates l, m, n is sampled at every time sampling point $k\Delta t$ in the cell boundaries [2], for ATLM, either the odd cells with odd $l+m+n+k$ or the even cells with even $l+m+n+k$ are sampled in the center of the three–dimensional cell [4]. This sampling leads to a bijective one–to–one mapping between the six field components, six spatial derivatives of the field components and the twelve wave amplitudes. Each one of the six spatial derivatives represents the sum of the derivatives in the two directions perpendicular to a field component. This sum of the derivatives is called the tangential derivatives of a field component.

II Derivation of ATLM

We proceed in the same way as demonstrated for the SCN [2] and expand the electric and magnetic field components in the same series of basis functions. Inserting the field expansions in Maxwell's equations and sampling the equations in the odd and even cells yields two coupled finite differences schemes for the electric and magnetic field components. Applying the cell boundary mapping [2], we obtain two finite difference schemes for the wave amplitudes describing the scattering of the wave amplitudes at the even and at the odd nodes.

Using the state–space representation of the electromagnetic field [2, 6], we have

$$|b_v\rangle \;=\; \boldsymbol{T}\,\boldsymbol{S}\;|a_v\rangle \tag{1}$$

with $v = e, o$. For the index e, eq. (1) describes the scattering at the nodes for which the sum of the spatial coordinates l, m, n of the cell is even, for the index o, eq. (1) describes the scattering at the nodes for which the sum of the spatial coordinates l, m, n of the cell is odd. The vectors $|a_v\rangle$ summarize all incident wave amplitudes, the vectors $|b_v\rangle$ all scattered wave amplitudes of the TLM mesh at all time sampling points $k\Delta t$. $\boldsymbol{S}$ represents the scattering matrix of the SCN and $\boldsymbol{T}$ the time shift operator indicating that the scattering at a node is connected with the time delay Δt. For each cell boundary surface, the wave amplitudes incident into one TLM cell are identical with the wave amplitudes scattered from the neighboring TLM cells. This relation is expressed by the connection operator $\boldsymbol{\Gamma}$ [2, 3] via

$$|a_v\rangle \;=\; \boldsymbol{\Gamma}\;|b_v\rangle \qquad . \tag{2}$$

The connection operator $\boldsymbol{\Gamma}$ is a matrix of space shift operators [6].

As explained in [4], for homogeneous regions, the scattering and propagation of the wave amplitudes at the even cells and at the cells for which the sum of the spatial coordinates l, m, n and the time index k is even, respectively, is independent of the scattering and propagation of the wave amplitudes at the odd cells. We combine both independent processes by defining the vectors of the incident and scattered wave amplitudes at the even and odd nodes,

$$|\tilde{a}_v\rangle \;=\; 1/2\;(1+\boldsymbol{T})\;|a_v\rangle \tag{3}$$

and

$$|\tilde{b}_v\rangle \;=\; 1/2\;(1+\boldsymbol{T})\;|b_v\rangle \qquad . \tag{4}$$

Eq. (1) yields

$$|\tilde{b}_v\rangle \;=\; \boldsymbol{T}\,\boldsymbol{S}\;|\tilde{a}_v\rangle \tag{5}$$

for the scattering at the even and odd nodes. For the propagation of the wave amplitudes from the even nodes to the odd nodes and vice versa, we obtain

$$|\tilde{a}_o\rangle \;=\; \boldsymbol{\Gamma}\,|\tilde{b}_e\rangle \tag{6}$$

and

$$|\tilde{a}_e\rangle \;=\; \boldsymbol{\Gamma}\,|\tilde{b}_o\rangle \quad . \tag{7}$$

Eliminating the wave amplitudes at the odd nodes as well as the scattered wave amplitudes at the even nodes yields

$$|\tilde{a}_e\rangle \;=\; \boldsymbol{T}^2\,(\boldsymbol{\Gamma}\,\boldsymbol{S})^2\,|\tilde{a}_e\rangle \quad . \tag{8}$$

The latter equation represents ATLM: the twelve linearly independent wave amplitudes are defined only at the even nodes. Thus there are twelve linearly independent field variables for two TLM cells and for one ATLM cell, respectively, or six linearly independent field variables per TLM cell. This is the same ratio as for FDTD and therefore ATLM does not exhibit any redundancy as it is the case for conventional three–dimensional TLM [3].

Fig. 1(a) illustrates the elemenatary cell for ATLM. While for conventional three–dimensional TLM, the elementary cell is a cube with a side length of Δl and a volume of $(\Delta l)^3$, the ATLM elementary cell is a rhomboedron with a volume of $2(\Delta l)^3$ and with a volume of two TLM cells, respectively.

III Mapping between the field components and the wave amplitudes

The cell boundary mapping introduced for the TLM scheme for the SCN [2] is not applicable for ATLM, since it relates the electric and magnetic field components to the wave amplitudes of both odd and even nodes. In order to obtain a mapping which relates the field components to the wave amplitudes of either the even or the odd cells, the field components have to be sampled at the center of the even or odd cells. In this section, we derive a bijective one–to–one mapping between the field components and their spatial derivatives at the center of the even cells and the wave amplitudes incident into the even nodes. This is done by sampling the expansions of the electric and magnetic field components in the same way as sampling Maxwell's equations for the derivation of ATLM and the TLM scheme for the SCN, respectively. As shown in [2], Maxwell's equations have to be sampled with delta functions as well as with the sum of their spatial derivatives in order to determine the scattering matrix of the SCN uniquely. A detailed discussion of sampling Maxwell's equations with the sum of the spatial derivatives of the delta functions can be found in [7].

We define the electric and magnetic field components at the center of the even ATLM cells by

$${}_{k+1/2}F^{xe}_{l,m,n} \;=\; \iiint F_x(\vec{x},t)\;\delta(t-(k+1/2)\Delta t)$$

$$\times\ \delta(x - l\Delta l)\ \delta(y - m\Delta l)\ \delta(z - n\Delta l)\ dx\ dy\ dz\ dt$$

$$_{k+1/2}F^{ye}_{l,m,n} = \iiiint F_y(\vec{x},t)\ \delta(t-(k+1/2)\Delta t) \times \delta(x - l\Delta l)\ \delta(y - m\Delta l)\ \delta(z - n\Delta l)\ dx\ dy\ dz\ dt$$

$$_{k+1/2}F^{ze}_{l,m,n} = \iiiint F_z(\vec{x},t)\ \delta(t-(k+1/2)\Delta t) \times \delta(x - l\Delta l)\ \delta(y - m\Delta l)\ \delta(z - n\Delta l)\ dx\ dy\ dz\ dt \qquad (9)$$

with $F = E, H$. Each of the four integrations extends from $-\infty$ to $+\infty$ and $l+m+n+k$ is an even number. Inserting the field expansions given in [2] yields

$$|F_e\rangle = \boldsymbol{P}_1\ |\tilde{a}_e\rangle \qquad (10)$$

with the operator

$$\boldsymbol{P}_1 = \frac{1}{2}\begin{bmatrix} 0 & 0 & 0 & 0 & 0 & 0 & 1 & 1 & 1 & 1 & 0 & 0 \\ 1 & 1 & 0 & 0 & 0 & 0 & 0 & 0 & 0 & 0 & 1 & 1 \\ 0 & 0 & 1 & 1 & 1 & 1 & 0 & 0 & 0 & 0 & 0 & 0 \\ 0 & 0 & 0 & 0 & 1 & -1 & 0 & 0 & 0 & 0 & -1 & 1 \\ 0 & 0 & -1 & 1 & 0 & 0 & 0 & 0 & 1 & -1 & 0 & 0 \\ 1 & -1 & 0 & 0 & 0 & 0 & -1 & 1 & 0 & 0 & 0 & 0 \end{bmatrix} . \qquad (11)$$

The vector

$$|F_e\rangle = \sum_{k,l,m,n=-\infty}^{+\infty} \begin{bmatrix} {}_kE^{xe}_{l,m,n} \\ {}_kE^{ye}_{l,m,n} \\ {}_kE^{ze}_{l,m,n} \\ Z\ {}_kH^{xe}_{l,m,n} \\ Z\ {}_kH^{ye}_{l,m,n} \\ Z\ {}_kH^{ze}_{l,m,n} \end{bmatrix} |k;l,m,n\rangle \qquad (12)$$

is a vector in the field state space $\mathcal{H}_F$ [2, 3]. It summarizes the field components at the even ATLM nodes of the complete mesh at all time sampling points $k\Delta t$. The impedance Z represents the wave impedance of the free space. Eq. (10) describes the mapping of the wave amplitudes incident into the even nodes onto the six electric and magnetic field components at the center of the even ATLM cells. This mapping is identical to the traditional mapping between the incident wave amplitudes and the field components [5], however, as discussed in [2], it is not bijective.

In order to obtain a bijective one–to–one mapping, the spatial derivatives of the field components at the center of the ATLM cells have to be considered. We sample the expansions of the electric and magnetic field components with the sum of the spatial derivatives of the delta functions in the directions perpendicular to the field components. Thus we define the tangential derivatives of the electric and magnetic field components at the center of the even ATLM cells by

$$_{k+1/2}\partial F^{xe}_{l,m,n} = \frac{\Delta l}{4}\iiiint \left(\frac{\partial}{\partial y}+\frac{\partial}{\partial z}\right) F_x(\vec{x},t)\ \delta(t-(k+1/2)\Delta t)$$

$$\times\ \delta(x - l\Delta l)\ \delta(y - m\Delta l)\ \delta(z - n\Delta l)\ dx\ dy\ dz\ dt$$

$$_{k+1/2}\partial F^{ye}_{l,m,n} = \frac{\Delta l}{4}\iiiint\left(\frac{\partial}{\partial x}+\frac{\partial}{\partial z}\right)F_y(\vec{x},t)\ \delta(t-(k+1/2)\Delta t)$$
$$\times\ \delta(x - l\Delta l)\ \delta(y - m\Delta l)\ \delta(z - n\Delta l)\ dx\ dy\ dz\ dt$$

$$_{k+1/2}\partial F^{ze}_{l,m,n} = \frac{\Delta l}{4}\iiiint\left(\frac{\partial}{\partial x}+\frac{\partial}{\partial y}\right)F_z(\vec{x},t)\ \delta(t-(k+1/2)\Delta t)$$
$$\times\ \delta(x - l\Delta l)\ \delta(y - m\Delta l)\ \delta(z - n\Delta l)\ dx\ dy\ dz\ dt \qquad (13)$$

with $F = E, H$. Again, each of the four integrations extends from $-\infty$ to $+\infty$ and $l+m+n+k$ is an even number. Introducing the vector

$$|\partial F_e\rangle = \sum_{k,l,m,n=-\infty}^{+\infty}\begin{bmatrix} {}_k\partial E^{xe}_{l,m,n} \\ {}_k\partial E^{ye}_{l,m,n} \\ {}_k\partial E^{ze}_{l,m,n} \\ Z\ {}_k\partial H^{xe}_{l,m,n} \\ Z\ {}_k\partial H^{ye}_{l,m,n} \\ Z\ {}_k\partial H^{ze}_{l,m,n}\end{bmatrix}|k;l,m,n\rangle \qquad (14)$$

as a vector in the field state space $\mathcal{H}_F$ and proceeding in the same way as demonstrated for the field components, we obtain

$$|\partial F_e\rangle = \boldsymbol{P}_2\ |\tilde{a}_e\rangle \qquad (15)$$

with the operator

$$\boldsymbol{P}_2 = \frac{1}{2}\begin{bmatrix} 0 & 0 & 0 & 0 & 0 & 0 & 1 & 1 & -1 & -1 & 0 & 0 \\ -1 & -1 & 0 & 0 & 0 & 0 & 0 & 0 & 0 & 0 & 1 & 1 \\ 0 & 0 & 1 & 1 & -1 & -1 & 0 & 0 & 0 & 0 & 0 & 0 \\ 0 & 0 & 0 & 0 & -1 & 1 & 0 & 0 & 0 & 0 & -1 & 1 \\ 0 & 0 & -1 & 1 & 0 & 0 & 0 & 0 & -1 & 1 & 0 & 0 \\ -1 & -1 & 0 & 0 & 0 & 0 & -1 & 1 & 0 & 0 & 0 & 0 \end{bmatrix} . \qquad (16)$$

Combining eqs. (10) and (16) yields a bijective one–to–one mapping between the six field components, their six tangential derivatives and the twelve wave amplitudes given by

$$\begin{bmatrix} |F_e\rangle \\ |\partial F_e\rangle \end{bmatrix} = \begin{bmatrix} \boldsymbol{P}_1 \\ \boldsymbol{P}_2 \end{bmatrix}|\tilde{a}_e\rangle \qquad (17)$$

with the inverse mapping

$$|\tilde{a}_e\rangle = [\boldsymbol{Q}_1, \boldsymbol{Q}_2]\begin{bmatrix} |F_e\rangle \\ |\partial F_e\rangle \end{bmatrix} , \qquad (18)$$

where

$$\boldsymbol{Q}_1 = \boldsymbol{P}_1^T \quad \text{and} \quad \boldsymbol{Q}_2 = \boldsymbol{P}_2^T . \qquad (19)$$

IV Dispersion analysis for ATLM

As described in [3], eq. (8) requires

$$\det\left[\left(\overline{\boldsymbol{\Gamma}}\,\boldsymbol{S}\right)^2 - e^{\jmath 2\Omega}\right] = 0 \tag{20}$$

in both frequency and wave vector domains for any non–trivial solution of TLM. The normalized frequency Ω is given by $\Omega = 2\pi\Delta t f$ and the connection operator in wave vector domain, $\overline{\boldsymbol{\Gamma}}$, represents a twelve–dimensional matrix with the elements $e^{\jmath\chi}$, $e^{\jmath\eta}$ and $e^{\jmath\xi}$, where $\chi = \Delta l\, k_x$, $\eta = \Delta l\, k_y$ and $\xi = \Delta l\, k_z$ are the normalized wave vector components of the wave vector $\vec{k} = [k_x, k_y, k_z]^T$. From eq. (20), we obtain twelve eigenvalues $\lambda_i = e^{\jmath 2\Omega_i}$ given by

$$\lambda_{1,2} = C_1 + \sqrt{(C_1)^2 - 1} \qquad \lambda_{3,4} = C_1 - \sqrt{(C_1)^2 - 1} \qquad \lambda_{5,6} = 1 \tag{21}$$

with

$$C_1 = \frac{1}{2}\Big(\cos(\chi)\cos(\eta) + \cos(\chi)\cos(\xi) + \cos(\eta)\cos(\xi) - 1\Big) \quad . \tag{22}$$

The eigenvalues $\lambda_7, \ldots, \lambda_{12}$ are identical with $\lambda_1, \ldots, \lambda_6$. All the eigenvectors of these twelve eigenvalues describe physical solutions and solutions converging to solutions of Maxwell's equations for frequencies approaching zero, respectively. Thus there are no more nonphysical solutions that means no artifacts introduced by the discretization of Maxwell's equations as in conventional three–dimensional TLM [3]. Note that if we calculate the eigenvalues of FDTD, we obtain six physical eigenvalues [3]. Four eigenvalues describe the propagating solutions and two eigenvalues describe the electro– and magnetostatic case. If we consider the eigenvalues for FDTD for two subsequent time steps, we obtain twelve eigenvalues, where eight eigenvalues describe the propagating solutions and four eigenvalues the electro– and magnetostatic case. This corresponds to the situation in ATLM, where we also have eight eigenvalues describing the propagating solutions and four eigenvalues describing the electro– and magnetostatic case. This confirms the results of the second section: Both ATLM and FDTD exhibit six linearly independent field variables per cell.

The eigenvectors corresponding to the eigenvalues $\lambda_1, \ldots, \lambda_4$ describe solutions propagating in a mesh of ATLM nodes. For these solutions, we obtain the dispersion relation

$$\cos^2(\Omega) = \frac{1}{4}\Big(\cos(\chi)\cos(\eta) + \cos(\chi)\cos(\xi) + \cos(\eta)\cos(\xi) + 1\Big) \tag{23}$$

which is the same as for the SCN [3]. Therefore, the dispersion relation exhibits the same ambiguity for solutions approaching zero for modes with $\vec{k} \approx [0,0,0]^T$ and with $\vec{k} \approx [\pi/\Delta l, \pi/\Delta l, \pi/\Delta l]^T$. For the SCN, this ambiguity leads to the appearance of spurious modes [8]. For ATLM however, spurious modes cannot be excited, since the range of the wave numbers for ATLM is smaller than the range of the wave numbers for conventional TLM. This is obvious from the first Brillouin zone corresponding to the ATLM elementary cell depicted in Fig. 1(b). While the first Brillouin zone corresponding to the TLM elementary cell is again a cube with a side length of $2\pi/\Delta l$ and a volume of $(2\pi/\Delta l)^3$, the first Brillouin zone corresponding to the ATLM elementary cell is a polyhedron with a side length of $2\pi/\Delta l$ with only half of the volume of the first TLM Brillouin zone. Thus for wave propagation in $(1,1,1)$ direction,

we have $\vec{k} < [\pi/\Delta l, \pi/\Delta l, \pi/\Delta l]^T$ for TLM, but only $\vec{k} < [\pi/(2\Delta l), \pi/(2\Delta l), \pi/(2\Delta l)]^T$ for ATLM. The latter condition excludes the appearance of spurious modes in ATLM. Fig 2 illustrates the effect of the smaller volume of the ATLM Brillouin zone on the dispersion diagrams for wave propagation in $(1, 1, 1)$ direction with $\chi = \eta = \xi$.

V Conclusions

While the field theoretical derivation of ATLM is very similar to the field theoretical derivation of TLM with SCN, the mapping relating the field components to the wave amplitudes is different. Sampling the expansions of the electric and magnetic field components in the center of the ATLM cells yields a bijective one–to–one mapping between the six field components, six spatial derivatives of the field components and the twelve wave amplitudes. One part of this mapping, the mapping of the twelve wave amplitudes onto the six electric and magnetic field components is identical to the traditional mapping proposed for TLM with SCN [5]. The other, new part of the mapping is necessary in order to obtain a bijective mapping for the twelve field variables.

As shown by a dispersion analysis, ATLM does not support any nonphysical or spurious solutions and therefore, it does not exhibit a redundancy factor of two as conventional three–dimensional TLM. From a field theoretical point of view, ATLM represents the only TLM scheme which does not exhibit any disadvantages in comparison to Yee's FDTD scheme.

Acknowledgments

This work was supported by the Deutsche Forschungsgemeinschaft and by a scholarship of the NATO science committee through the German Academic Exchange Service.

References

[1] M. Krumpholz, P. Russer, "Two–dimensional FDTD and TLM", International Journal of Numerical Modelling : Electronic Networks, Devices and Fields, vol. 7, no. 2, pp. 141-153, February 1993.

[2] M. Krumpholz, P. Russer, "A Field Theoretical Derivation of TLM", IEEE Transactions on Microwave Theory and Techniques, vol. 42, no. 9, pp. 1660-1668, September 1994.

[3] M. Krumpholz, C. Huber, P. Russer, "A Field Theoretical Comparison of FDTD and TLM", IEEE Transactions on Microwave Theory and Techniques, vol. 43, no. 8, pp. 1935-1950, August 1995.

[4] P. Russer, B. Bader, "The Alternating Transmission Line Matrix (ATLM) Scheme", IEEE MTT–S International Microwave Symposium Digest, Orlando, pp. 19-22, May 1995.

[5] P.B. Johns, "A Symmetrical Condensed Node for the TLM–Method", IEEE Trans. Microwave Theory Tech., vol. MTT-35, no.4, pp. 370-377, April 1987.

[6] P. Russer, M. Krumpholz, "The Hilbert Space Formulation of the TLM Method", International Journal of Numerical Modelling : Electronic Networks, Devices and Fields, vol. 6, no. 1, pp. 29-45, February 1993.

[7] M. Aidam, "Grundlagen der TLM–Methode zur Berechnung Elektromagnetischer Felder", Diplomarbeit at the Lehrstuhl für Hochfrequenztechnik, Technische Universität München, July 1995.

[8] J.S. Nielsen, W.J.R. Hoefer, "A Complete Dispersion Analysis of the Condensed Node TLM Mesh", IEEE Trans. Magnetics, vol. 27, no. 5, pp. 3982-3985, September 1991.

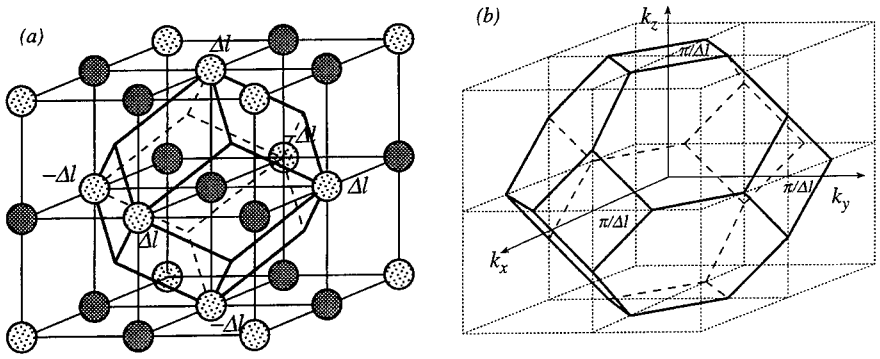

Figure 1: (a) The ATLM elementary cell and (b) the first ATLM Brillouin zone.

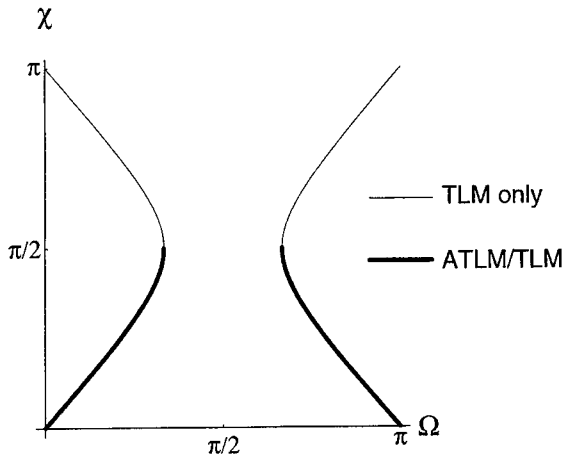

Figure 2: Dispersion diagram for propagation in $(1, 1, 1)$ direction.

Advanced Node Formulations in TLM – The Matched Symmetrical Condensed Node (MSCN)

V. Trenkic, C. Christopoulos and T. M. Benson
Numerical Modelling Group
Department of Electrical and Electronic Engineering
University of Nottingham
University Park, Nottingham NG7 2RD, United Kingdom
Tel: (44) 1159 515557, Fax: -616, E-mail: vmt@eee.nott.ac.uk

Abstract

A novel node for TLM symmetrical condensed schemes is presented, which unlike existing nodes, contains link lines with the characteristic impedance equal to the intrinsic impedance of modelled medium. Open and short-circuit stubs are loaded into this node in equal proportions, thus ensuring dispersion solutions independent of the wave polarization. Another advantage of such a node is that the scattering at material interfaces is described more accurately due to the matching impedance condition. The development and characterization of this node gives more insight into the influence of stub-loading on the dispersion behaviour of a TLM condensed scheme and provides a theoretical basis for the combination of stub-loading and alteration of link line impedances to develop in the future a more accurate, adaptable node.

Introduction

In recent years, the conventional TLM based on the stub-loaded symmetrical condensed node (SCN) [1] has been enhanced by a wider choice of nodes offering computational savings and/or improved accuracy. Notable among these nodes are hybrid symmetrical condensed nodes (HSCN) [2, 3] and the symmetrical super-condensed node (SSCN) [4]. In the stub-loaded SCN all deviations from material properties and a regular cubic mesh are accounted for by stubs, with link lines representing free space properties. In the case of the HSCN the same deviations are partly modelled by stubs and partly by link lines. Finally, in the SSCN all deviations are modelled by the link lines as there are no stubs present.

Our main objective in the derivation of the SSCN [4] was to reduce storage requirements by eliminating the need for stubs. An additional benefit of this, as explained in [5], was a higher efficiency in terms of CPU run-time, compared to the stub-loaded and hybrid nodes. Also, the time step allowed in a graded mesh was found to be substantially higher in the SSCN than in the previous nodes [4]. The dispersion analysis of TLM schemes with different condensed node schemes [6, 7, 8] showed that the alterations made to the basic 12-port SCN, in terms of adding stubs and varying the characteristic impedance of link lines, caused different effects in the dispersion characteristics, depending on how these alterations were done. The most notable effect in the stubless SSCN was that error due to dispersion increases with an increase in the material properties (or equivalently, by decrease in the time step) [6, 7, 9]. Otherwise, dispersion behaviour of the SSCN is similar to that of the basic 12-port SCN: the solution is independent on the field polarization, the solution is identical for $\varepsilon_r \mu_r = const$ and all errors in the magnitude of propagation vector extend in the same (positive) direction.

The most notable effect of the stub-loading in the SCN and the HSCN was the existence of two dispersion solutions corresponding to the two orthogonal wave polarizations. This ambiguity, called also *mesh anisotropy* [8], arises from the fact that open and short-circuit stubs are added to the node in unequal proportions, and because of this, the overall coupling of stub and link lines with the electric and magnetic field is asymmetrical. The mesh anisotropy has an effect that two different orthogonal wave polarizations of the electric field propagate in a TLM mesh based on the HSCN and the stub-loaded SCN with different dispersion characteristics. The only exception from this behaviour is the TLM mesh with stubbed SCN modelling materials with $\varepsilon_r = \mu_r$. From the dispersion analysis of the stub-loaded SCN [7] it also follows that the dispersion characteristics are dependent on the wave impedance, i.e. on the ratio μ_r/ε_r for the $\varepsilon_r\mu_r = const$ which is in contrast to physical conditions. For all these reasons, it is difficult to interpret error trends due to stub-loading.

In order to eliminate these undesirable features of the stub-loaded SCN, we develop here a new stub-loaded node, maintaining a constant link line impedance, but equal to the intrinsic impedance of modelled medium rather than to the impedance of the background medium. This node will be referred to as the matched SCN (MSCN). Another benefit of constructing such a node is that reflections at material interfaces are modelled more accurately. In the previous nodes, the impedance of the link lines does not in general coincide with the impedance of the medium being modelled. The consequence of this is that waves pass through the interface without experiencing immediately the correct amount of reflection and transmission. Intuitively, it can be expected that the new MSCN models more accurately the physical conditions at the material interfaces in inhomogeneous problems.

The complete derivation of the matched SCN from the unified formulation of TLM parameters [10] will be described in the next section, followed by implementation issues and the dispersion analysis. A comparison of errors in the MSCN with those found in other nodes, particularly in the SSCN, will be made and an emphasis will be placed on assessing errors due to reflections at interface between different materials.

Derivation of the MSCN

From the dispersion analysis of the stub-loaded SCN [7] it can be seen that the two physical solutions of the dispersion relation become identical only in the case when $\varepsilon_r = \mu_r$ (Case 2 in [7]). The intrinsic impedance of the medium Z equals in this case the characteristic impedance of the link lines Z_0, since it follows that:

$$Z = \sqrt{\frac{\mu}{\varepsilon}} = \sqrt{\frac{\mu_r\mu_0}{\varepsilon_r\varepsilon_0}} = \sqrt{\frac{\mu_0}{\varepsilon_0}} = Z_0$$

This observation suggests that one may expect that the dispersion characteristics of a node having link lines whose characteristic impedance is equal to the intrinsic impedance of the modelled medium will be similar to those of the stub-loaded SCN when $\varepsilon_r = \mu_r$. The parameters of such a node can be derived from the general TLM constitutive relations, formulated as [10]:

$$C_{ik}\Delta i + C_{jk}\Delta j + C_o^k = \varepsilon_k \frac{\Delta i \Delta j}{\Delta k} \quad (1)$$

$$L_{ij}\Delta i + L_{ji}\Delta j + L_s^k = \mu_k \frac{\Delta i \Delta j}{\Delta k} \quad (2)$$

where $i, j, k \in \{x, y, z\}$ and $i \neq j, k$. In the above equations, distributed characteristic capacitance and inductance of an i-directed, j-polarized link line is denoted by C_{ij} and L_{ij}, respectively, whilst

total capacitance and inductance of open and short circuit stubs, respectively, modelling fields in the k-direction are denoted by C_o^k and L_s^k.

In time domain schemes, synchronism must be maintained, which is described by six equation in the form:

$$\Delta t = \Delta i \sqrt{C_{ij} L_{ij}} \tag{3}$$

where $i, j \in \{x, y, z\}$ and $i \neq j$. The system of twelve equations determined by the generic formulae (1)–(3) is referred to as the general system of equations describing the parameters of a TLM time-domain scheme.

The characteristic impedance and admittance of an i-directed j-polarized line are defined as $Z_{ij} = 1/Y_{ij} = \sqrt{L_{ij}/C_{ij}}$. Taking into account the time synchronism condition (3), the characteristic impedance and admittance of link lines can be written as function of the time step:

$$Z_{ij} = \frac{L_{ij}\Delta i}{\Delta t} \qquad Y_{ij} = \frac{C_{ij}\Delta i}{\Delta t} \tag{4}$$

In stubs, pulses have to make a round trip during the time step Δt, thus requiring the effective transit time along the length of a stub to be equal to $\Delta t/2$. Therefore, the characteristic impedance of short-circuit stubs and the characteristic admittance of open-circuit stubs are defined, respectively as [11]:

$$Z_{sk} = \frac{2L_s^k}{\Delta t} \qquad Y_{ok} = \frac{2C_o^k}{\Delta t} \tag{5}$$

where $k \in \{x, y, z\}$.

Dividing the system of equations (1)–(2) by Δt and using formulae (4)–(5), we obtain:

$$Y_{ik} + Y_{jk} + \frac{Y_{ok}}{2} = \varepsilon_k \frac{\Delta i \Delta j}{\Delta k \Delta t} \tag{6}$$

$$Z_{ij} + Z_{ji} + \frac{Z_{sk}}{2} = \mu_k \frac{\Delta i \Delta j}{\Delta k \Delta t} \tag{7}$$

In the MSCN, all characteristic impedance of link lines are equal to the intrinsic impedance of the medium and the system of equations (6)–(7) with the condition $Z_{ij} = Z$ (or equivalently $Y_{ij} = Y = 1/Z$) reduces in the case of an isotropic medium to:

$$2Y + \frac{Y_{ok}}{2} = \varepsilon \frac{\Delta i \Delta j}{\Delta k \Delta t} \tag{8}$$

$$2Z + \frac{Z_{sk}}{2} = \mu \frac{\Delta i \Delta j}{\Delta k \Delta t} \tag{9}$$

The characteristic admittance of open-circuit stubs and the impedance of short-circuit stubs in the k-direction, Y_{ok} and Z_{sk} respectively, are obtained from (8) and (9) as:

$$Y_{ok} = 4Y \left(\frac{\Delta i \Delta j}{2c\Delta t \Delta k} \sqrt{\varepsilon_r \mu_r} - 1 \right) \tag{10}$$

$$Z_{sk} = 4Z \left(\frac{\Delta i \Delta j}{2c\Delta t \Delta k} \sqrt{\varepsilon_r \mu_r} - 1 \right) \tag{11}$$

Normalizing the values of Y_{ok} and Z_{sk} to those of the link lines (Y, Z) we obtain:

$$\hat{Y}_{ok} = \hat{Z}_{sk} = 4\left(\frac{\Delta i \Delta j}{2c\Delta t \Delta k}\sqrt{\varepsilon_r \mu_r} - 1\right) \tag{12}$$

The scattering matrix for the MSCN can be easily derived from the original stub-loaded SCN scattering matrix [1] by taking into account the definitions of stub parameters given by (12). For the case of a uniform mesh, with $\Delta i = \Delta j = \Delta k = \Delta l$ and $\Delta t = \Delta l/(2c)$, the stub parameters simplify to:

$$\hat{Y}_o = \hat{Z}_s = 4(\sqrt{\varepsilon_r \mu_r} - 1) \tag{13}$$

Since the MSCN is identical to the stub-loaded SCN when $\varepsilon_r = \mu_r$, they will have identical dispersion characteristics in this case. And since the parameters of the MSCN are independent of the ratio μ_r/ε_r for $\mu_r\varepsilon_r = const$ the dispersion characteristics of the MSCN, in contrast to those of the stub-loaded SCN, will be independent of the ratio ε_r/μ_r for $\varepsilon_r\mu_r = const$. Furthermore, the dispersion relation of the MSCN will have the identical functional form as the dispersion relation of the stub-loaded SCN in Case 2, derived in [7], yielding the same physical solution for the two orthogonal wave polarizations. The dispersion characteristics of the MSCN are therefore advantageous compared to the stub-loaded SCN because of: a) the independence on the wave impedance (i.e. the factor μ_r/ε_r) for $\varepsilon_r\mu_r = const$ and b) the existence of a unique propagating solution for any ratio μ_r/ε_r. A disadvantage of the MSCN dispersion characteristics is a high error range. Namely, since the error range in the stub-loaded SCN is the highest in Case 2 [7] and following the equivalence between the dispersion relations of the MSCN and the Case 2 stub-loaded SCN, it follows that the total error range in the MSCN will never be smaller than for the stub-loaded SCN, especially when a dielectric ($\mu_r = 1$) or magnetic ($\varepsilon_r = 1$) material is modelled (Case 1 SCN [7]).

However, when modelling inhomogeneous media, the errors due to dispersion are found to be smaller in the MSCN than predicted from the dispersion analysis for homogeneous problems, as it will be shown later. This behaviour can be attributed to the fact that the impedance of link lines always matches the impedance of the modelled medium in the MSCN. Accordingly, the scattering of voltage pulses occurring at the interface between two materials is directly equivalent to the scattering of waves on the boundaries between different media. In the conventional stub-loaded SCN, the voltage pulses pass the interface without immediately 'seeing' the boundary, while in the HSCN and the SSCN, a reflection/transmission process occurs due to different values of the link line characteristic impedances which do not generally match the intrinsic impedances of the modelled media.

From the computational point of view, the MSCN is clearly as demanding as the stub-loaded SCN. In cases when only dielectric or only magnetic materials are modelled, where the stub-loaded SCN normally uses only one type of stub, the MSCN is more demanding since it always uses both types of stubs. It appears that a symmetrical use of both types of stubs in the MSCN, expressed through equation (12), is a price which must be paid in order to retain identical dispersion characteristics for the two wave polarizations. Due to the impedance matching condition, the connection between neighbouring nodes on different sides of a material interface must be modelled as for the HSCN and the SSCN, as explained in [5]. The extra amount of calculations needed in this case can be justified, however, since the reflections on the interface are in accordance with problem requirements. Finally, the matching impedance condition simplifies the implementation of external boundaries in TLM based on the MSCN, since the line reflection coefficients will always be equal to the medium reflection coefficients [12].

Comparison of error trends in the MSCN and the SSCN

Having eliminated the presence of the two orthogonal solutions of the dispersion relation and their dependence on the wave impedance in the conventional stub-loaded SCN, by developing a new stub-loaded node with the matching impedance condition (MSCN), it is now possible to investigate more closely the effects of stub-loading and link line impedance changing on the numerical accuracy of a general condensed node TLM scheme. It appears most useful to compare the dispersion characteristics of the SSCN and the MSCN, since the former uses exclusively the altering of link lines to model local changes in the material properties, while the later always uses stubs.

Figure 1 shows, in the same manner as in [7], the percentage propagation errors in the SSCN and the MSCN for propagation in a coordinate and a diagonal plane, for the discretization of $\Delta l/\lambda = 0.1$. The angle φ represent the angle between the propagation vector an the z-axis. It can be clearly seen from the plots in Figure 1 that, with an increase in $\varepsilon_r\mu_r$ the propagation error is shifted in the positive direction for the SSCN but in the negative direction for the MSCN. The error trends observed from Figure 1 suggest that if a part of the excess material properties is modelled through stubs, as in the MSCN, and a part through varying the characteristic impedances of link lines, as in the SSCN, one may expect that the propagation error in such a combined node might average out, i.e. the error may be small and fluctuate around zero. This possibility is currently being explored by the authors in order to formulate more accurate TLM condensed nodes.

Influence of material interfaces

The traditional dispersion analysis for the TLM nodes applies for an infinite space with a homogeneous medium [13]. However, in real problems, nodes with stubs and varied link line impedance are used in order to model local increases in the medium parameters, i.e. for modelling inhomogeneous problems. A full investigation into the effect of interface discontinuities in the TLM method has not yet been described in the literature. However, these effects have been investigated empirically [14] by studying frequency errors in inhomogeneous resonators. A similar approach is used here in order to test the performance of different nodes and to estimate the influence of spurious reflections on propagation behaviour. The two square resonators depicted in Figure 2, partly filled with a medium with materials parameters: Case 1) $\varepsilon_r = 4$, $\mu_r = 1$ and Case 2) $\varepsilon_r = \mu_r = 2$ are studied in the simulations. Note that the stub-loaded SCN and the HSCN are identical in Case 1, while the stub-loaded SCN and the MSCN are identical in Case 2. The resonant frequencies of TE modes **10, 20, 30, 11, 21** and **31** are calculated for each case using TLM simulations with different nodes on a mesh with node spacing $\Delta l = 1$cm. The relative propagation error normalized to the benchmark discretization of $\Delta l/\lambda = 0.1$ is calculated as [14]:

$$\overline{\delta k} = \frac{(f_0 - f)}{f}\left(\frac{0.1}{\Delta l/\lambda}\right)^2 = \frac{(f_0 - f)}{f}\left(\frac{0.1c}{\Delta l f_0\sqrt{\varepsilon_r\mu_r}}\right)^2 \tag{14}$$

where f is the modelled frequency, c is speed of light and f_0 is the reference frequency obtained by performing calculations on a very fine mesh. Note that the normalization is done with respect to the wavelength in the material. The results for the two resonators are presented in Tables 1 and 2.

The spurious reflections can be studied by comparing the results for resonator b (with two interfaces medium-air) with the results for resonator a. In all nodes the accuracy in modelling the two resonators differs greatly, expect in the MSCN where accuracy is generally the same (most noticeable in Case 2). This indicates that in problems with multiple interfaces the MSCN might provide greater accuracy. In the

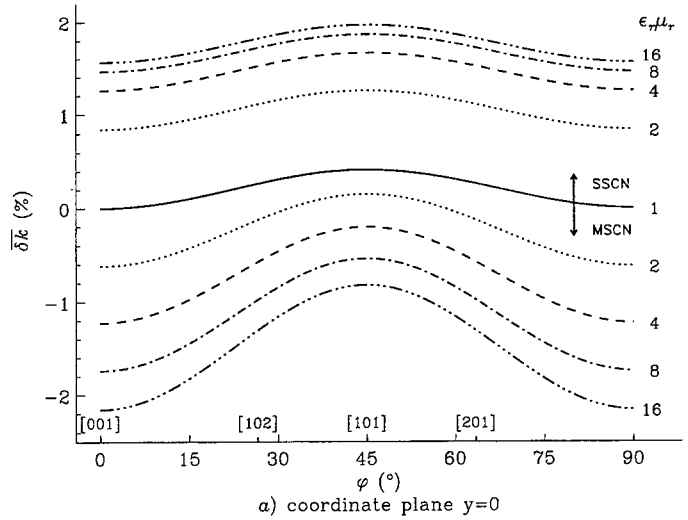

a) coordinate plane y=0

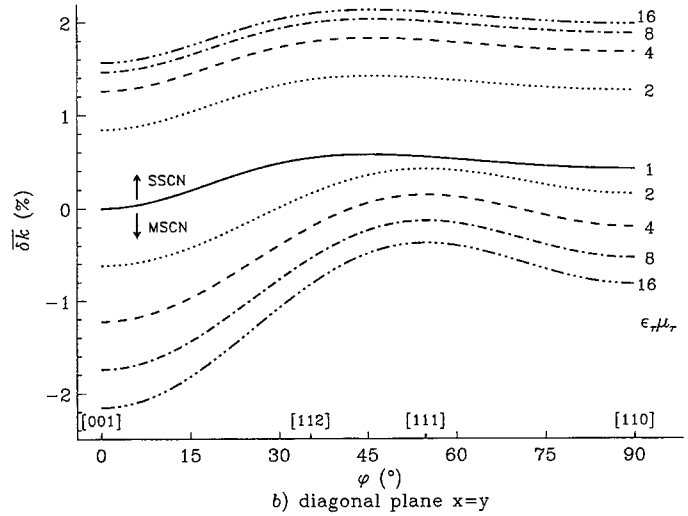

b) diagonal plane x=y

Figure 1: Comparison of the percentage propagation error in the MSCN and the SSCN in different propagation planes for $\varepsilon_r\mu_r \in \{1, 2, 4, 8, 16\}$ and $\Delta l/\lambda = 0.1$

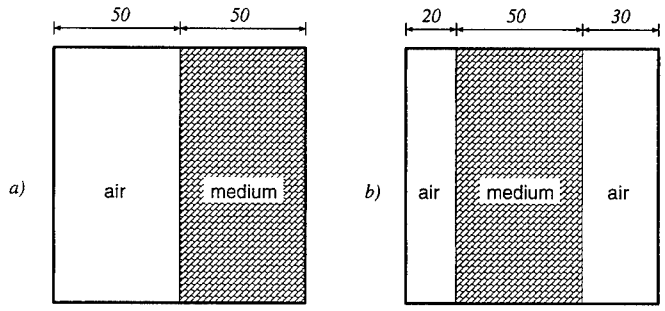

Figure 2: Schematic of inhomogeneous resonators (dimensions are in mm)

TE mode →		10	20	30	11	21	31
Case 1: $\varepsilon_r = 4$, $\mu_r = 1$							
f_0 [GHz] →		0.9116	2.0863	2.9980	1.2523	2.3176	3.2314
SCN & HSCN		-0.22	-0.55	-0.25	+0.03	-0.35	-0.20
MSCN	$\overline{\delta k}$	-0.90	-0.90	-0.58	-0.15	-0.63	-0.40
SSCN	[%]	+1.48	+0.75	+0.64	+1.77	+1.11	+0.62
Case 2: $\varepsilon_r = 2$, $\mu_r = 2$							
f_0 [GHz] →		0.9993	1.9987	2.9980	1.3476	2.2845	3.1883
SCN & MSCN		-0.82	-0.80	-0.78	-0.19	-0.50	-0.57
HSCN	$\overline{\delta k}$	-0.11	-0.53	-0.35	+0.03	-0.29	-0.28
SSCN	[%]	+1.46	+0.57	+0.86	+1.73	+0.92	+0.80

Table 1: Normalized percentage propagation error in resonator (a)

SSCN, the propagation error for resonator b is always shifted in the positive direction compared to that for resonator a. It is also interesting to note that for different propagation modes in the axial direction (**10, 20, 30**) all nodes, except perhaps the MSCN, exhibit significant variations in errors. Clearly, this requires further investigation but it would appear from these preliminary results that the lower order modes are influenced more by the spurious reflections at interfaces.

Conclusion

A new nodal structure for the TLM method with condensed nodes was presented. The ambiguity of two dispersion solutions dependent on the wave polarization found in the traditional stub-loaded SCN was eliminated in the new matched SCN (MSCN), enabling better insight into the error trends caused by the stub-loading. It was shown that the numerical errors caused by spurious reflections at material interfaces when modelling inhomogeneous problems were minimized in the MSCN due to the matched impedance condition.

TE mode →		10	20	30	11	21	31
Case 1: $\varepsilon_r = 4$, $\mu_r = 1$							
f_0 [GHz] →		0.8066	1.8316	2.9980	1.1346	2.0305	3.1452
SCN & HSCN		+0.28	-0.21	-0.43	+0.25	-0.05	-0.33
MSCN	$\overline{\delta k}$	-0.74	-0.91	-0.93	+0.02	-0.50	-0.75
SSCN	[%]	+2.22	+1.49	+1.11	+2.14	+1.68	+1.27
Case 2: $\varepsilon_r = 2$, $\mu_r = 2$							
f_0 [GHz] →		0.9993	1.9987	2.9980	1.2868	2.2094	3.1778
SCN & MSCN		-0.83	-0.80	-0.78	-0.09	-0.48	-0.61
HSCN	$\overline{\delta k}$	+0.07	-0.14	-0.36	+0.18	-0.01	-0.25
SSCN	[%]	+2.00	+1.42	+0.97	+2.04	+1.62	+1.14

Table 2: Normalized percentage propagation error in resonator (b)

References

[1] P. B. Johns, "A symmetrical condensed node for the TLM method", *IEEE Trans.*, vol. MTT-35, no. 4, pp. 370–377, April 1987.

[2] R. A. Scaramuzza and A. J. Lowery, "Hybrid symmetrical condensed node for TLM method", *Electronics Letters*, vol. 26, no. 23, pp. 1947–1949, Nov. 1990.

[3] P. Berrini and K. Wu, "A pair of hybrid symmetrical condensed TLM nodes", *IEEE Microwave and Guided Wave Letters*, vol. 4, no. 7, pp. 244–246, July 1994.

[4] V. Trenkic, C. Christopoulos, and T. M. Benson, "Theory of the symmetrical super-condensed node for the TLM method", *IEEE Trans. Microwave Theory Tech.*, vol. 43, no. 6, pp. 1342–1348, June 1995.

[5] V. Trenkic, C. Christopoulos, and T. M. Benson, "Efficient computational algorithms for TLM", in *First International Workshop on TLM*, Victoria, Canada, Aug. 1995, pp. 77–80.

[6] V. Trenkic, C. Christopoulos, and T. M. Benson, "Dispersion analysis of TLM symmetrical super-condensed node", *Electronics Letters*, vol. 30, no. 25, pp. 2151–2153, Dec. 1994.

[7] V. Trenkic, C. Christopoulos, and T. M. Benson, "Dispersion of TLM condensed nodes in media with arbitrary electromagnetic properties", in *IEEE Microwave Symp.*, Orlando, Florida, May 1995, vol. 2, pp. 373–376.

[8] P. Berini and K. Wu, "A comprehensive study of numerical anisotropy and dispersion in 3-D TLM meshes", *IEEE Trans. Microwave Theory Tech.*, vol. 43, no. 5, pp. 1173–1181, May 1995.

[9] V. Trenkic, C. Christopoulos, and T. M. Benson, "Minimization and elimination of dispersion in electromagnetic simulations by selection of node aspect ratio and time step in the TLM super-condensed node", in *PIERS*, Seattle, Wa, USA, July 1995.

[10] V. Trenkic, C. Christopoulos, and T. M. Benson, "A unified approach to the derivation of TLM node parameters", in *First International Workshop on TLM*, Victoria, Canada, Aug. 1995, pp. 23–26.

[11] C. Christopoulos, *The Transmission-Line Modelling (TLM) Method*, Series on Electromagnetic Wave Theory. IEEE/OUP Press, 1995.

[12] J. L. Herring, *Developments in the Transmission-Line Modelling Method for Electromagnetic Compatibility Studies*, PhD thesis, University of Nottingham, UK, 1993.

[13] J. S. Nielsen and W. J. R. Hoefer, "A complete dispersion analysis of the condensed node TLM mesh", *IEEE Trans. Magnetics*, vol. 27, no. 5, pp. 3982–3985, Sept. 1991.

[14] M. Celuch-Marcysiak and W. K. Gwarek, "On the effect of bilateral dispersion in inhomogeneous symmetrical condensed node modelling", *IEEE Trans. Microwave Theory Tech.*, vol. 42, no. 6, pp. 1069–1073, June 1994.

A GENERAL AND COMPLETE TWO-DIMENSIONAL TLM HYBRID NODE FORMULATION BASED ON MAXWELL'S INTEGRAL EQUATIONS

Nestor Peña and Michel M. Ney

Laboratory for Electronics and Communication Systems (LEST)
Telecom Bretagne, BP 832, 29285 Brest Cédex, FRANCE

INTRODUCTION

In order to make the TLM algorithm more flexible for the electromagnetic analysis of general structures, it is essential that a variable mesh procedure is applied. Indeed, a fine mesh is required in regions where fields are rapidly varying in space (e.g., conducting edges, corners, narrow strips). This allows one to reduce computer requirement as a coarse mesh can be used in other locations where fields do not have high gradients. However, there are some constraints about how the TLM grid can be varied [1]. In order to reduce the number of constraints, a more general TLM node must be constructed. Recently, Hoefer and Sautier [2] presented a 2D-TLM rectangular node with arbitrary aspect ratio without stubs. Homogeneous sub regions can use different aspect ratio but not arbitrarily. In this paper, Maxwell's equations in integral form are used to construct a general 2D-TLM cell with variable time step by using a stub. The hybrid nature of the node allows an arbitrary aspect ratio for all regions and arbitrary mesh size variation. When used with maximum time-step, the stub can be removed and the proposed node coincides with the one proposed by Hoefer and Sautier.

The formulation starts with a definition of incident and reflected voltages in terms of fields. Maxwell-Ampère and Maxwell-Faraday equations are then used to establish independent relationships between incident and reflected voltages. As a result, a scattering matrix is obtained which also accounts for electric and magnetic losses. In addition, the formulation allows the presence of magnetic and electric source current densities. This demonstrates the general nature of the proposed node which allows rigorous two-dimensional field modeling for both TM and TE cases [3]. Finally, dispersion characteristics of the proposed node is investigated. The equivalence with the FDTD cell for arbitrary time-step is demonstrated.

APPROXIMATED INTEGRAL FORM OF MAXWELL'S EQUATIONS

Consider an anisotropic medium for which permittivity, permeability and conductivity tensor are diagonal. Maxwell-Faraday and Maxwell-Ampère's equations can be written as

$$\oint_{\Gamma} \vec{H} \circ d\vec{l} = \iint_{S} \hat{\varepsilon} \frac{\partial \vec{E}}{dt} \circ d\vec{s} + \iint_{S} \hat{\sigma}_e \vec{E} \circ d\vec{s} + \iint_{S} \vec{J}_e \circ d\vec{s} \tag{1}$$

$$\oint_{\Gamma} \vec{E} \circ d\vec{l} = -\iint_{S} \hat{\mu} \frac{\partial \vec{H}}{\partial t} \circ d\vec{s} - \iint_{S} \hat{\sigma}_m \vec{H} \circ d\vec{s} - \iint_{S} \vec{J}_m \circ d\vec{s} \tag{2}$$

where $\vec{J}_e$ and $\vec{J}_m$ are electric and magnetic source current densities, respectively and, $\hat{\varepsilon} = \varepsilon_0 \mathrm{diag}(\varepsilon_{xx}, \varepsilon_{yy}, \varepsilon_{zz})$, $\hat{\mu} = \mu_0 \mathrm{diag}(\mu_{xx}, \mu_{yy}, \mu_{zz})$, $\hat{\sigma}_e = \mathrm{diag}(\sigma_{ex}, \sigma_{ey}, \sigma_{ez})$, $\hat{\sigma}_m = \mathrm{diag}(\sigma_{mx}, \sigma_{my}, \sigma_{mz})$ are permittivity, permeability, electric conductivity, magnetic conductivity tensors, respectively. In order to approximate (1) and (2), consider the rectangular cell with dimensions Δx and Δy ($\alpha = \Delta y / \Delta x$). Without loss of generality, let us investigate the TM case (Transverse Magnetic) for which electric and magnetic fields are sampled as shown in figure 1. Samples are taken every Δt at time $(k \pm 1/2)\Delta t$ and $(k+1/2)\Delta t$ if no time reference is mentioned. Taking the path Γ in the plan ZOY (figure 2), an approximation of (2) can be written. Hence, averaging between time $(k-1/2)\Delta t$ and $(k+1/2)\Delta t$, one obtains

$$\oint_{\Gamma} \vec{E} \circ d\vec{l} \cong \frac{(1+T)}{2} \Delta l (E_3^z - E_1^z) \tag{3}$$

for which the field was supposed constant along the sides of the cell, where T is the retardation operator given by $Tu^{(k)} = u^{(k-1)}$ and Δl an arbitrary spatial step. The right-hand side of (2) can also be approximated, which with (3) gives:

$$\frac{(1+T)}{2}\Delta l\cdot(E_3^z - E_1^z) = \frac{(T-1)}{2}Z_0\left(\frac{\mu_{xx}\Delta_y\Delta l}{c\Delta t\Delta_x}\right)\cdot\Delta_x\cdot(H_1^x + H_3^x) - Z_0\hat{R}_{mx}\Delta_x\cdot H_x^{(k)} - V_{mx}^{(k)} \tag{4}$$

where $\hat{R}_{mx} = \frac{1}{Z_0}\frac{\sigma_{mx}\Delta l\cdot\Delta_y}{\Delta_x}$ and $V_{mx}^{(k)} = J_{mx}^{(k)}\Delta l\cdot\Delta_y$ (see appendix A)..

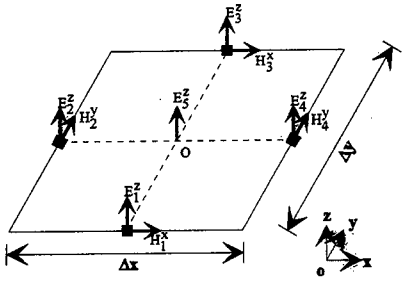

Figure 1: Generic cell for field sample definition (TM case)

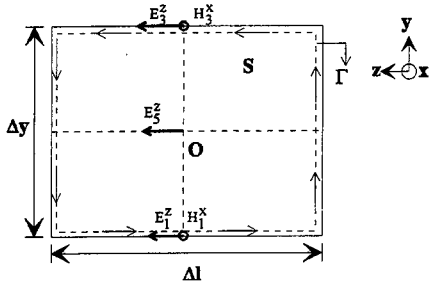

Figure 2: Path for approximation of (2)

At this stage, one has the elements to define the incident voltage vector $\vec{a}$ (at time [k-1/2]Δt) and the reflected voltage vector $\vec{b}$ (at time [k+1/2]Δt) which can be written as

$$\begin{aligned}\vec{a} &= \frac{1}{2}\left[\Delta l\cdot E_1^z + Z_y\Delta_x\cdot H_1^x,\ \Delta l\cdot E_2^z - Z_x\Delta_y\cdot H_2^y,\ \Delta l\cdot E_3^z - Z_y\Delta_x\cdot H_3^x,\ \Delta l\cdot E_4^z + Z_x\Delta_y\cdot H_4^y,\ \Delta l E_5^z\right]^t \\ \vec{b} &= \frac{1}{2}\left[\Delta l\cdot E_1^z - Z_y\Delta_x\cdot H_1^x,\ \Delta l\cdot E_2^z + Z_x\Delta_y\cdot H_2^y,\ \Delta l\cdot E_3^z + Z_y\Delta_x\cdot H_3^x,\ \Delta l\cdot E_4^z - Z_x\Delta_y\cdot H_4^y,\ \Delta l E_5^z\right]^t\end{aligned} \tag{5}$$

where $Z_i = Z_0/\hat{Y}_i$, with normalized admittance $\hat{Y}_i$ is defined in [4]:

$$\hat{Y}_y = \frac{c\Delta t\cdot\Delta_x}{\mu_{xx}\Delta_y\cdot\Delta l} = \frac{c\Delta t}{\mu_{xx}\Delta l}\frac{1}{\alpha} \quad \text{and} \quad \hat{Y}_x = \frac{c\Delta t\cdot\Delta_y}{\mu_{yy}\Delta_x\cdot\Delta l} = \frac{c\Delta t}{\mu_{yy}\Delta l}\alpha \tag{6}$$

Finally, using (4) and (5) yields:

$$b_3^{(k+0.5)} - b_1^{(k+0.5)} = -a_3^{(k-0.5)} + a_1^{(k-0.5)} - Z_0\hat{R}_{mx}\Delta_x H_x^{(k)} - V_{mx}^{(k)} \tag{7}$$

Using the same procedure in the ZOX-plane yields:

$$b_2^{(k+0.5)} - b_4^{(k+0.5)} = -a_2^{(k-0.5)} + a_4^{(k-0.5)} - Z_0\hat{R}_{my}\Delta_y H_y^{(k)} - V_{my}^{(k)} \tag{8}$$

Similarly, approximating (1) on the XOY-plane (see figure 1) gives a third relation. This time, five samples are used to approximate $\overline{E}_z$ (appendix A):

$$\overline{E}_z \equiv \frac{\hat{Y}_x(E_2^z + E_4^z) + \hat{Y}_y(E_1^z + E_3^z) + \hat{Y}_s E_5^z}{2\hat{Y}_x + 2\hat{Y}_y + \hat{Y}_s} \tag{9}$$

where $\hat{Y}_s$ is the stub normalized admittance defined by E_5^z (see figure 2) and which is calculated by setting:

$$\varepsilon_{zz}\frac{\Delta_x\Delta_y}{c\Delta t\Delta l} = \hat{Y}_x + \hat{Y}_y + \hat{Y}_s/2 \tag{10}$$

Finally,

$$\begin{aligned}&\hat{Y}_y(b_1+b_3)^{(k+0.5)} + \hat{Y}_x(b_2+b_4)^{(k+0.5)} + (\hat{Y}_s + \hat{G}_{ez})b_5^{(k+0.5)} \\ &= \hat{Y}_y(a_1+a_3)^{(k-0.5)} + \hat{Y}_x(a_2+a_4)^{(k-0.5)} + (\hat{Y}_s - \hat{G}_{ez})a_5^{(k-0.5)} - V_{ez}^{(k)}\end{aligned} \tag{11}$$

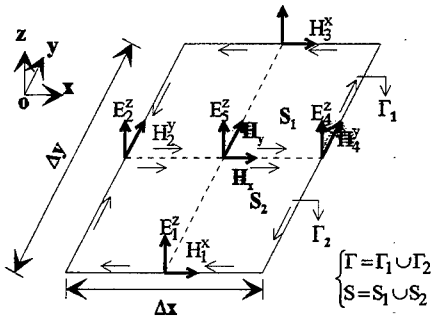

Figure 3: Path for evaluating $H_x^{(k)}$

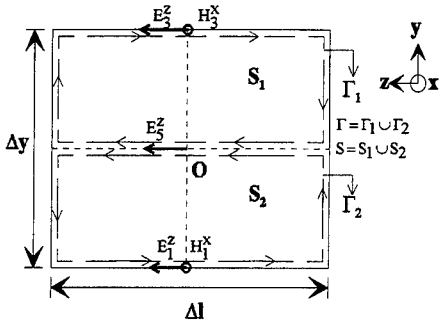

Figure 4: Evaluation of $E_z^{(k)}$ in the YOZ-plane

Before determining the two remaining relationships, one has to establish expressions for $H_x^{(k)}$ and $H_y^{(k)}$. For this purpose, two paths Γ_1 and Γ_2 are considered in the XOY-plane (figure 3). Thus:

$$\oint_\Gamma \vec{H}.d\vec{l} \equiv 2\Delta_x H_x^{(k)} - \frac{(1+T)}{2}\Delta_x(H_1^x + H_3^x)$$

Taking into account that S_1 and S_2 have opposite normal vector, the only non-zero integral contribution through S (within the assumed approximation) is the one due to the displacement current. Indeed, others are approximated by values at the center of the rectangle. Hence,

$$\varepsilon_0\varepsilon_{zz}\iint_S \frac{\partial\vec{E}}{\partial t}.d\vec{s} \equiv \frac{(1-T)}{2}\frac{\hat{Y}_y}{Z_0}\Delta l\cdot(E_3^z - E_1^z)$$

and

$$\Delta_x H_x^{(k)} = \frac{1}{2}\frac{\hat{Y}_y}{Z_0}\left[(b_3-b_1)^{(k+0.5)} - (a_3-a_1)^{(k-0.5)}\right] \tag{12}$$

$$\Delta_y H_y^{(k)} = \frac{1}{2}\frac{\hat{Y}_x}{Z_0}\left[(b_2-b_4)^{(k+0.5)} - (a_2-a_4)^{(k-0.5)}\right] \tag{13}$$

Now, one can calculate $E_z^{(k)} = (1+T)E_5^z/2$ along two paths, each one contained in mutually perpendicular planes. For instance, applying the procedure pertaining to figure 4 allows one to obtain:

$$2(b_5^{(k+0.5)} + a_5^{(k-0.5)}) = (b_1 + b_3)^{(k+0.5)} + (a_1 + a_3)^{(k-0.5)} \tag{14}$$

Similar reasoning yields the last relation:

$$2(b_5^{(k+0.5)} + a_5^{(k-0.5)}) = (b_2 + b_4)^{(k+0.5)} + (a_2 + a_4)^{(k-0.5)} \tag{15}$$

Equations (7), (8), (11), (14) and (15) can be written in matrix form:

$$[P_1] \circ \vec{b}^{(k+0.5)} = [P_2] \circ \vec{a}^{(k-0.5)} - [P_3] \circ \vec{u}^{(k)} \tag{16}$$

Introducing $[S]$ and $[S_s]$ the scattering voltage and source matrices, respectively (see appendix B):

$$\vec{b}^{(k+0.5)} = [S] \circ \vec{a}^{(k-0.5)} - [S_s] \circ \vec{u}^{(k)} \tag{17}$$

where $\vec{u} = \left[V_{ez}^{(k)}, V_{mx}^{(k)}, V_{my}^{(k)}\right]^t$,

$$[P_1] = \begin{bmatrix} \hat{Y}_y & \hat{Y}_x & \hat{Y}_y & \hat{Y}_x & \hat{Y}_s + \hat{G}_{ez} \\ -1 - \frac{1}{2}\hat{R}_{mx}\hat{Y}_y & 0 & 1 + \frac{1}{2}\hat{R}_{mx}\hat{Y}_y & 0 & 0 \\ 0 & 1 + \frac{1}{2}\hat{R}_{my}\hat{Y}_x & 0 & -1 - \frac{1}{2}\hat{R}_{my}\hat{Y}_x & 0 \\ -1 & 0 & -1 & 0 & 2 \\ 0 & -1 & 0 & -1 & 2 \end{bmatrix} \quad [P_2] = \begin{bmatrix} \hat{Y}_y & \hat{Y}_x & \hat{Y}_y & \hat{Y}_x & \hat{Y}_s - \hat{G}_{ez} \\ 1 - \frac{1}{2}\hat{R}_{mx}\hat{Y}_y & 0 & -1 + \frac{1}{2}\hat{R}_{mx}\hat{Y}_y & 0 & 0 \\ 0 & -1 + \frac{1}{2}\hat{R}_{my}\hat{Y}_x & 0 & 1 - \frac{1}{2}\hat{R}_{my}\hat{Y}_x & 0 \\ 1 & 0 & 1 & 0 & -2 \\ 0 & 1 & 0 & 1 & -2 \end{bmatrix}$$

and $[P_3] = \begin{bmatrix} 10000 \\ 01000 \\ 00100 \end{bmatrix}^t$. In the above, $\hat{G}_{ez} = Z_0 \frac{\sigma_{ez}\Delta_x \cdot \Delta_y}{\Delta l}$ and $\hat{R}_{mk} = \frac{1}{Z_0}\frac{\sigma_{mk}\Delta l \cdot \Delta_j}{\Delta_k}$

NODE MAIN FEATURES

For the sake of simplicity, consider first $\mu_{xx} = \mu_{yy} = \mu_r$, and $\varepsilon_{zz} = \varepsilon_r$. In this case, using (6) and (10) yields:

$$\hat{Y}_s = \frac{1}{\Delta l}\left[\frac{2\varepsilon_r \Delta_x \Delta_y}{c\Delta t} - \frac{2c\Delta t}{\mu_r}\left(\frac{\alpha^2+1}{\alpha}\right)\right] \tag{18}$$

In order to eliminate the stub ($\hat{Y}_s = 0$), Δt is maximum and, according to (18), is given by

$$\Delta t_{max} = \frac{\sqrt{\mu_r \varepsilon_r}}{c}\Delta_x \frac{\alpha}{\sqrt{\alpha^2+1}} = \frac{\sqrt{\mu_r \varepsilon_r}}{c}\Delta_y \frac{1}{\sqrt{\alpha^2+1}} \tag{19}$$

It is easy to see that

$$[S] = \frac{1}{\alpha^2+1}\begin{bmatrix} -\alpha^2 & \alpha^2 & 1 & \alpha^2 \\ 1 & -1 & 1 & \alpha^2 \\ 1 & \alpha^2 & -\alpha^2 & \alpha^2 \\ 1 & \alpha^2 & 1 & -1 \end{bmatrix}$$

which is indeed the scattering matrix of the node without stub proposed by previous authors [2,3]. Hence, the general nature of the proposed node is demonstrated.

The next step is to consider the TLM algorithm and investigate whether a reduction of the number of operations is possible. By manipulating (12)-(15) one can establish the following relation:

$$\vec{b}^{(k+1/2)} = \begin{bmatrix} \Delta l E_z^{(k)} - Z_y \Delta_x H_x^{(k)} \\ \Delta l E_z^{(k)} + Z_x \Delta_y H_y^{(k)} \\ \Delta l E_z^{(k)} + Z_y \Delta_x H_x^{(k)} \\ \Delta l E_z^{(k)} - Z_x \Delta_y H_y^{(k)} \\ \Delta l E_z^{(k)} \end{bmatrix} - \begin{bmatrix} a_3 \\ a_4 \\ a_1 \\ a_2 \\ a_5 \end{bmatrix}^{(k-1/2)}$$

As a result, only field values at the center of the cells are needed and can be calculated from incident voltages [4] and adding source contributions if any. For instance, by using (14) and (16):

$$\Delta l E_z^{(k)} = 2\left[\frac{\hat{Y}_y}{\hat{Y}_{eq}}(a_1 + a_3) + \frac{\hat{Y}_x}{\hat{Y}_{eq}}(a_2 + a_4)\right]^{(k-1/2)} - \frac{V_{ez}^{(k)}}{\hat{Y}_{eq}}, \quad Z_y \Delta_x H_x^{(k)} = \frac{2}{2 + \hat{R}_{mx}\hat{Y}_y}\left[(a_1 - a_3)^{(k-1/2)} - 0.5V_{mx}^{(k)}\right] \text{ and}$$

$$Z_x \Delta_y H_y^{(k)} = \frac{2}{2 + \hat{R}_{my}\hat{Y}_x}\left[(a_2 - a_4)^{(k-1/2)} - 0.5V_{my}^{(k)}\right] \text{ where } \hat{Y}_{eq} = \hat{Y}_s + \hat{G}_{ez} + 2\hat{Y}_x + 2\hat{Y}_y .$$

To achieve the construction of the hybrid node, one has to consider the TE case. The above relations remain valid if one makes the following permutations:

$$\vec{E} \to \vec{H} \to -\vec{E},\ \mu \to \varepsilon \to \mu,\ \vec{J}_e \to \vec{J}_m \to -\vec{J}_e,\ \sigma_e \to \sigma_m \to \sigma_e \text{ and } (Z,R) \leftrightarrow (Y,G).$$

VARIABLE MESH

As mentioned before, the advantage of the hybrid node is that arbitrary variation of the mesh size within the same region can be performed. The only constraint is that it has to remain structured, i.e., every cell has always exactly four neighbors (see figure 5). This requires the use of the same time step Δt throughout the network. The selection is such that numerical stability is guaranteed, i.e., $\hat{Y}_s \geq 0$ for all nodes.

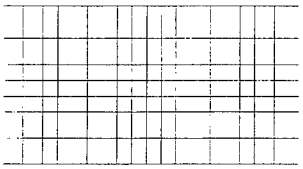

Figure 5 : Irregular structured mesh

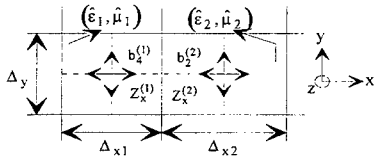

Figure 6: Transfer of impulses between cells with different size.

In addition, appropriate transfer of impulse voltages towards neighboring nodes is applied to insure that continuity of tangential components of both magnetic and electric fields is enforced. For instance, voltages at interface (figure 6) are given by

$$b_4^{(1)} = \Delta l \cdot E_z - Z_x^{(1)} \Delta_y \cdot H_y \quad \text{and} \quad b_2^{(2)} = \Delta l \cdot E_z + Z_x^{(2)} \Delta_y \cdot H_y \tag{20}$$

$$a_4^{(1)} = \Delta l \cdot E_z + Z_x^{(1)} \Delta_y \cdot H_y \quad \text{and} \quad a_2^{(2)} = \Delta l \cdot E_z - Z_x^{(2)} \Delta_y \cdot H_y . \tag{21}$$

where E_z and H_y are the tangential components at the interface between cell 1 and 2. Hence, transfer in x-direction is made as follows [5]:

$$\begin{bmatrix} a_4^{(1)} \\ a_2^{(2)} \end{bmatrix} = \begin{bmatrix} \rho & 1-\rho \\ 1+\rho & -\rho \end{bmatrix} \circ \begin{bmatrix} b_4^{(1)} \\ b_2^{(2)} \end{bmatrix} \qquad (22), \qquad \text{where the reflection coefficient is } \rho = \frac{Z_x^{(2)} - Z_x^{(1)}}{Z_x^{(2)} + Z_x^{(1)}}.$$

NUMERICAL DISPERSION

Consider a homogeneous and lossless medium for which $\varepsilon = \varepsilon_0 \varepsilon_r$ and $\mu = \mu_0 \mu_r$. From Maxwell's equations in local form, the wave equation for the TE case can be easily derived. A decomposition in a plane wave spectrum gives a dispersion relation [6]:

$$\omega\mu\,(k_x^2 + k_y^2 - \omega^2 \varepsilon\mu) = 0 \qquad (23)$$

where $\omega = 2\pi f$ and $\vec{k} = [k_x, k_y]^t$ is the wave vector. The case $\omega = 0$ is the electrostatic case and $\omega^2\mu\varepsilon = k_x^2 + k_y^2$ corresponds to traveling waves. Reflected voltages can also be written as:

$$\vec{b}_{m,n}^{(t)} = \vec{b}_0 \cdot e^{-j\omega t} e^{-j(mx+ny)} \qquad (24)$$

where $x = k_x \Delta_x$, $y = k_y \Delta_y$ and (m,n) are the node central discrete coordinates. For neighboring nodes, voltage transfer is written as:

$$\vec{a}_{m,n}^{(k-1/2)\Delta t} = [T] \circ \vec{b}_{m,n}^{(k-1/2)\Delta t} \qquad (25)$$

where the transfer or connection matrix [T]. Elements are zeros except $T_{13} = Y$, $T_{24} = X$, $T_{31} = Y^{-1}$, $T_{42} = X^{-1}$; $T_{55} = 1$, with $X = e^{jx}$ and $Y = e^{jy}$. Finally, (16) becomes:

$$\left(\lambda \cdot [P_1] - [P_2] \circ [T]\right) \circ \vec{b}_0 = [M(\lambda)] \circ \vec{b}_0 = 0 \qquad (26)$$

where $\lambda = e^{-j\theta}$ and $\theta = \omega\Delta t$. Dispersion equation is obtained by setting det([M(λ)])=0. One can show (see appendix C) that $\lambda = \pm 1$ are eigenvalues of first and second order, respectively. The eigensolution associated to $\lambda = 1$ is the electrostatic solution of (23) and $\lambda = -1$ corresponds to a high-frequency spurious mode ($f = 1/2\Delta t$) [3]. The traveling-wave equation can be written as:

$$\sin^2\left(\frac{\omega\Delta t}{2}\right) = \left(\frac{c_m \Delta t}{\Delta_x}\right)^2 \sin^2\left(\frac{x}{2}\right) + \left(\frac{c_m \Delta t}{\Delta_y}\right)^2 \sin^2\left(\frac{y}{2}\right) \qquad (27)$$

where $0 \le \Delta t \le \Delta t_{max}$, Δt_{max} given by (19) and c_m is the medium velocity. Setting $\theta = \omega \frac{\Delta_x}{c_m} = 2\pi \frac{\Delta_x}{\lambda}$, $s = \frac{c_m \Delta t}{\Delta x}$, $\bar{x} = k_x \Delta_x$ and $\bar{y} = k_y \Delta_x$, dispersion relation becomes:

$$\sin^2\left(\frac{1}{2}\theta \cdot s\right) = \left(\frac{s}{\alpha}\right)^2 \left[\alpha^2 \sin^2\left(\frac{\bar{x}}{2}\right) + \sin^2\left(\frac{\alpha \cdot \bar{y}}{2}\right)\right] \qquad (28)$$

It turns out that (28) has the same form as for the FDTD cell [7]. Thus, there is a complete equivalence in terms of dispersion performance and, also, the stability limit is the same [8]. However, the algorithm for field computation is different.

CONCLUSIONS

In this paper, a new two-dimensional TLM node is presented. It is constructed from the approximation of Maxwell-Ampère and Maxwell-Faraday laws in integral form. The final node is hybrid as a stub is connected to vary the time-step. This feature makes it flexible as non regular (but structured) mesh can be used with arbitrary variation. In addition, the formulation is complete which gives to the node a general form as constant magnetic and dielectric losses are

accounted for and magnetic and electric source current densities can be introduced. Also media represented by (non-dispersive) diagonal tensors can be modeled. Finally, it is found that at maximum time-step value the proposed node corresponds to the rectangular cell with arbitrary aspect ration proposed by previous papers.

In terms of dispersion, theoretical investigation for homogeneous and sourceless medium and uniform rectangular mesh shows that the 2D-TLM hybrid node has the same dispersion relation as in the case of the 2D-FDTD node. This equivalence is valid for arbitrary time-step value within the stability interval. However, if performances in terms of dispersion are identical, the corresponding computational algorithms are different as fields are not directly computed with TLM and it needs more variables than FDTD. Finally, optimization techniques are implemented to accelerate the TLM algorithm. For instance, computing time for reflected voltages can be reduced substantially by first evaluating field components at the center of the cell. Then, reflected voltages are computed by a reduced number of operations without using the scattering matrix as it is usually done in TLM.

REFERENCES

[1] P. Saguet and E. Pic, "Le maillage rectangulaire et le changement de maille dans la méthode TLM en deux dimensions", Electronics Letters, vol. 17, April 1981, pp 277-278.

[2] W. J. R. Hoefer and P. Sautier, "Characteristics of the general rectangular 2D-TLM network", Int. J. Numer. Modelling (Electron. Networks, Devices and Fields), vol. 7, pp. 127-139, 1994.

[3] M. Krumpholz et al., "Field-Theoretic Foundation of Two-Dimensional TLM Based on A Rectangular Mesh", proc. IEEE MTT-S Digest, 1994.

[4] V. Trenkic, C. Christopoulos and T. M. Benson, "Simple and elegant formulation of scattering in TLM nodes", Electronics Letters, vol. 29, no. 18, pp. 1651-1652, Sep. 1993.

[5] D. A. Al-Mukhtar, M. Tech, and J. E. Sitch, "Transmission-line matrix method with irregularly graded space", IEE Proc., vol. 128, pt. H, no.6, pp. 299-305, Dec. 1981.

[6] D. R. Lynch and K. D. Paulsen, "Origin of Vector Parasites in Numerical Maxwell Solutions", IEEE Trans. Microwave Theory Tech., vol. 39, no. 3, pp. 383-394, March 1991.

[7] K. S. Kunz and R. J. Luebbers, "The Finite Difference Time Domain Method for Electromagnetics", CRC Press, Inc., 1993.

[8] M. Krumpholtz and P. Russer, "On the Dispersion in TLM and FDTD", IEEE Trans. Microwave Theory Tech., vol. 42, no. 7, pp. 1275-1279, July 1994.

APPENDIX A :

Evaluation of current density fluxes (see (1) and (2)) can be achieved by taking an average value of fields ($\overline{E}_k$ and $\overline{H}_k$) at the center of S (see figure A.1) and an approximation in time. Hence,

$$\iint_S \hat{\varepsilon}\frac{\partial \vec{E}}{\partial t}.\hat{k}ds \cong \frac{1}{Z_0}\frac{(1-T)}{c\Delta t}\frac{\varepsilon_{kk}\Delta_i\Delta_j}{\Delta_k}\Delta_k\overline{E}_k \qquad (A.1)$$

$$-\iint_S \hat{\mu}\frac{\partial \vec{H}}{\partial t}.d\vec{s} \cong Z_0\frac{(T-1)}{c\Delta t}\frac{\mu_{kk}\Delta_i\Delta_j}{\Delta_k}\Delta_k\overline{H}_k \qquad (A.2)$$

in which $\overline{F}_k = \frac{1}{\Delta_i\Delta_j}\iint_S \vec{F}.\hat{k}ds$ with $\vec{F} = \vec{E}$ or $\vec{H}$. Now, one has to evaluate an average value of the normal component of $\vec{F}$ by using known values on the surface.

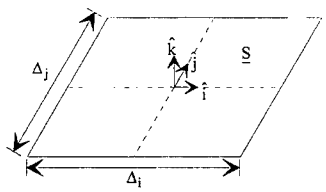

Figure A.1 - Surface integral approximation

Concerning loss modeling, surface integral approximation is done by taking the value of the field at the center of the cell at time $r\Delta t$. Thus,

$$\iint_S \hat{\sigma}_e \vec{E}.\hat{k}ds \cong \frac{1}{Z_0}\hat{G}_{ek}\Delta_k E_k^{(r)} \qquad (A.3)$$

$$\iint_S \hat{\sigma}_m \vec{H}.\hat{k}ds \cong Z_0\hat{R}_{mk}\Delta_k H_k^{(r)} \qquad (A.4)$$

in which: $\hat{G}_{ek} = Z_0\frac{\sigma_{ek}\Delta_i\Delta_j}{\Delta_k}$ and $\hat{R}_{mk} = \frac{1}{Z_0}\frac{\sigma_{mk}\Delta_i\Delta_j}{\Delta_k}$. The approximated value is then expressed in terms of incident and reflected voltages.

Finally, for evaluating surface integrals due to sources, ones takes the value at the center of the cell. Hence,

$$\iint_S \vec{J}_e.\hat{k}ds \cong \frac{1}{Z_0}V_{ek}^{(r)} \qquad (A.5)$$

$$\iint_S \vec{J}_m.\hat{k}ds \cong V_{mk}^{(r)} \qquad (A.6)$$

where $V_{ek}^{(r)} = Z_0 J_{ek}^{(r)}\Delta_i\Delta_j$ and $V_{mk}^{(r)} = J_{mk}^{(r)}\Delta_i\Delta_j$.

APPENDIX B

Expression of scattering matrices are found by comparing (16) and (17):

$$[S] = [P_1]^{-1}\circ[P_2] = \begin{bmatrix} \alpha_y-\beta_y & \alpha_x & \alpha_y+\beta_y-1 & \alpha_x & \alpha_s \\ \alpha_y & \alpha_x-\beta_x & \alpha_y & \alpha_x+\beta_x-1 & \alpha_s \\ \alpha_y+\beta_y-1 & \alpha_x & \alpha_y-\beta_y & \alpha_x & \alpha_s \\ \alpha_y & \alpha_x+\beta_x-1 & \alpha_y & \alpha_x-\beta_x & \alpha_s \\ \alpha_y & \alpha_x & \alpha_y & \alpha_x & \alpha_s-1 \end{bmatrix}$$

in which $\alpha_n = \frac{2\hat{Y}_n}{\hat{Y}_{eq}}$ et $n \in \{x, y, s\}$ and $\beta_n = \frac{2}{2+\hat{R}_{mk}\hat{Y}_n}$, $n, k \in \{x, y\}$ and $n \neq k$.

Finally,

$$[S_s] = [P_1]^{-1}\circ[P_3] = \begin{bmatrix} \hat{Z}_{eq} & -\frac{\beta_y}{2} & 0 \\ \hat{Z}_{eq} & 0 & \frac{\beta_x}{2} \\ \hat{Z}_{eq} & \frac{\beta_y}{2} & 0 \\ \hat{Z}_{eq} & 0 & -\frac{\beta_x}{2} \\ \hat{Z}_{eq} & 0 & 0 \end{bmatrix} \quad \text{with } \hat{Z}_{eq} = \frac{1}{\hat{Y}_{eq}}$$

APPENDIX C

For the derivation of the dispersion relation (27), one has to express the determinant of the matrix $[M(\lambda)]$. It is given by the polynomial expression:

$$P(\lambda) = (\lambda-1)(\lambda+1)^2(\lambda^2 - A\lambda + 1) \qquad (C.1)$$

where $A = 2\alpha_x\cos(x) + 2\alpha_y\cos(y) + \frac{\alpha_s}{2}$. In addition, by using admittance definition (6) and (10) one obtains:

$$\frac{\alpha_s}{2} + \alpha_x + \alpha_y = 1 \qquad (C.2)$$

$$\alpha_n = \left(\frac{c_m\Delta t}{\Delta_n}\right)^2 \text{ for n = x or y} \qquad (C.3)$$

A GENERAL FORMULATION OF A THREE - DIMENSIONAL TLM CONDENSED NODE WITH THE MODELING OF ELECTRIC AND MAGNETIC LOSSES AND CURRENT SOURCES

Nestor Peña and Michel M. Ney

Laboratory for Electronics and Communication Systems (LEST)
Telecom Bretagne, BP 832, 29285 Brest Cédex, FRANCE

INTRODUCTION

TLM is known as a numerical model of propagation based on Huygens principle. The formulation is based on the analogy between electromagnetic wave propagation and electrical signal propagating in a network of interconnected lines or guides. However, a deduction of the TLM algorithm directly from Maxwell' equations seems more appropriate. Indeed, this provides to a better understanding of the method. As a result, the possibility to combine the TLM with other numerical techniques based on field formulation is enhanced. For instance, efficient boundary conditions have to be implemented for open problems. These conditions are generally formulated in terms of fields which cannot be directly transformed in electrical quantities for TLM. Recently, Krumpholz and Russer [1] derived the TLM scattering matrix for both two and three-dimensional cases by using an approach based on moment method. Jin and Vahldieck [2] made a similar derivation for the 3D basic (SCN) and hybrid (HSCN) symmetrical condensed node. Their approach is based on a finite-difference approximation of Maxwell's equations.

In this paper, a general 3D condensed node is formulated based on the approximation of Maxwell-Ampère and Maxwell-Faraday equations in global form. This new contribution consists in a systematic procedure which allows a general formulation which includes all types of condensed TLM nodes namely, the super condensed symmetrical node (SSCN) [3], the HSCN and the basic SCN proposed by Johns [4]. Integral form of Maxwell-Ampère and Maxwell-Faraday's laws produce a sufficient number of independent relations in terms of incident and reflected voltages at nodes. Then, a general scattering matrix describing all types of nodes is derived as well as expressions for fields at the center of a parallelepiped TLM cell. In addition, the general formulation includes electric and magnetic losses [9] and anisotropic media as long as these cans be modeled by diagonal (real) tensors. Finally, the node accounts for insertion of magnetic or electric source current densities.

MAXWELL'S LAW INTEGRAL FORM APPROXIMATION

Let us start with the two first Maxwell's laws in integral form in the case of media which can be lossy, anisotropic (diagonal real tensor) and in which electric or magnetic sources can exist.

$$\oint_{\Gamma} \vec{H} \circ d\vec{l} = \iint_{S} \hat{\varepsilon} \frac{\partial \vec{E}}{\partial t} \circ d\vec{s} + \iint_{S} \hat{\sigma}_e \vec{E} \circ d\vec{s} + \iint_{S} \vec{J}_e \circ d\vec{s} \tag{1}$$

$$\oint_{\Gamma} \vec{E} \circ d\vec{l} = -\iint_{S} \hat{\mu} \frac{\partial \vec{H}}{\partial t} \circ d\vec{s} - \iint_{S} \hat{\sigma}_m \vec{H} \circ d\vec{s} - \iint_{S} \vec{J}_m \circ d\vec{s} \tag{2}$$

where $\vec{J}_e$ and $\vec{J}_m$ are the electric and magnetic source densities, respectively and $\hat{\varepsilon} = \varepsilon_0 \mathrm{diag}(\varepsilon_{xx}, \varepsilon_{yy}, \varepsilon_{zz})$, $\hat{\mu} = \mu_0 \mathrm{diag}(\mu_{xx}, \mu_{yy}, \mu_{zz})$, $\hat{\sigma}_e = \mathrm{diag}(\sigma_{ex}, \sigma_{ey}, \sigma_{ez})$, $\hat{\sigma}_m = \mathrm{diag}(\sigma_{mx}, \sigma_{my}, \sigma_{mz})$ are isotropic medium constitutive parameter tensors. In order to approximate (1) and (2), consider the parallelepiped cell of dimensions Δ_x, Δ_y and Δ_z illustrated by figure 1. As defined in [1], tangential field components are sampled at the center of the faces of the cell. Thus, there is a total of twelve samples for both fields to account for all cases of polarization. Electrical samples are numbered according to the SCN model presented by Johns [4] (see figure 1). Conveniently, magnetic field samples with corresponding number are located at the same point on the face but oriented perpendicularly with respect to their

electrical corespondent (e.g., E_1^x and H_1^z). In addition, either electric or magnetic field samples at the center of the cell are required for both SCN and HSCN [2].

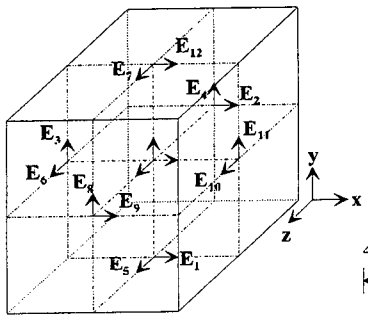

Figure1:-Basic cell for 3D TLM

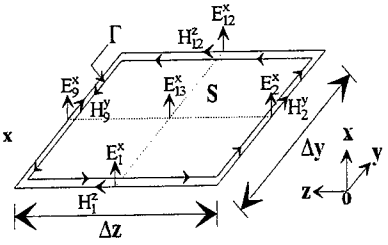

Figure 2: Maxwell-Ampère's law in the YOZ-plane

First of all, let us define $\vec{a}$ and $\vec{b}$ the local incident and reflected voltage vector , respectively, according to the definition used in [1]:

$$\vec{a}_{SCN}^{(k-1/2)} = \begin{Vmatrix} \begin{bmatrix} \vec{a}_{SSCN}^{(k-1/2)} \\ \vec{V}_E^{(k-1/2)} \end{bmatrix} \\ \begin{bmatrix} \vec{V}_H^{(k-1/2)} \end{bmatrix} \end{Vmatrix} \vec{a}_{HSCN}^{(k-1/2)} \quad \text{and} \quad \vec{b}_{SCN}^{(k+1/2)} = \begin{Vmatrix} \begin{bmatrix} \vec{b}_{SSCN}^{(k+1/2)} \\ \vec{V}_E^{(k+1/2)} \end{bmatrix} \\ \begin{bmatrix} \vec{V}_H^{(k+1/2)} \end{bmatrix} \end{Vmatrix} \vec{b}_{HSCN}^{(k+1/2)} \tag{3}$$

where components for the various case are defined in appendix A. Then, (1) is evaluated in the YOZ according to the path detailed in figure 2. For evaluation of (2), the plane XOZ is used (see figure 1). Without loss of generality, losses and sources are not considered for the moment. Line integrals are evaluated by averaging field values between time (k-1/2)Δt and (k+1/2)Δt and assuming them constant on each side of the paths:

$$\oint_\Gamma \vec{H} \circ d\vec{l} \cong \frac{1}{2}(1+T)\left[\Delta_z(H_{12}^z - H_1^z) + \Delta_y(H_2^y - H_9^y)\right] \tag{4}$$

$$\oint_\Gamma \vec{E} \circ d\vec{l} \cong \frac{1}{2}(1+T)\left[\Delta_z(E_7^z - E_5^z) + \Delta_y(E_4^y - E_8^y)\right] \tag{5}$$

where T is the delay operator: $T\,u^{(k)} = u^{(k-1)}$ and fields are supposed evaluated at time (k+1/2)Δt.

Approximation of the right-hand side of (1) and (2) is done as in [6]: The flux is computed by an average value of the fields at the center of the surface. Hence, for the SCN $\overline{E}_x$ and $\overline{H}_x$, need five field values:

$$\overline{E}_x \cong \frac{E_1^x + E_{12}^x + E_2^x + E_9^x + \hat{Y}_{sx}E_{13}^x}{4 + \hat{Y}_{sx}} \tag{6}$$

$$\overline{H}_x \cong \frac{H_4^x + H_8^x + H_5^x + H_7^x + \hat{Z}_{sx}H_{16}^x}{4 + \hat{Z}_{sx}} \tag{7}$$

where the stub normalized admittance and impedance are defined by E_{13}^x and H_{16}^x , respectively:

$$\frac{4\varepsilon_{kk}\Delta_i\Delta_j}{2c\Delta t\Delta_k} = 4 + \hat{Y}_{sk} \text{ et } \frac{4\mu_{kk}\Delta_i\Delta_j}{2c\Delta t\Delta_k} = 4 + \hat{Z}_{sk} \tag{8}$$

In the case of the HSCN (type I) [7], approximation of $\overline{H}_x$ is done using four field values:

$$\overline{H}_x \cong \frac{H_4^x + H_8^x + H_5^x + H_7^x}{4} \tag{9}$$

and for $\overline{E}_x$, the approximation become:

$$\overline{E}_x \cong \frac{\hat{Y}_z\left(E_1^x + E_{12}^x\right) + \hat{Y}_y\left(E_2^x + E_9^x\right) + \hat{Y}_{sx}E_{13}^x}{2\hat{Y}_z + 2\hat{Y}_y + \hat{Y}_{sx}} \tag{10}$$

and $\hat{Y}_{sx}$ is evaluated from:

$$\frac{4\varepsilon_{kk}\Delta_i\Delta_j}{2c\Delta t\Delta_k} = 2\hat{Y}_i + 2\hat{Y}_j + \hat{Y}_{sk} \tag{11}$$

where $\hat{Y}_k = \frac{2c\Delta t\Delta_i}{\mu_{ii}\Delta_j\Delta_k}$ [7].

Finally for the SSCN [3]:

$$\overline{E}_x \cong \frac{\left\{C_{yx}\Delta_y(E_1^x + E_{12}^x) + C_{zx}\Delta_z(E_2^x + E_9^x)\right\}}{2\left(C_{yx}\Delta_y + C_{zx}\Delta_z\right)} \tag{12}$$

$$\overline{H}_x \cong \frac{\left\{L_{yz}\Delta_y(H_3^x + H_7^x) + L_{zy}\Delta_z(H_4^x + H_8^x)\right\}}{2\left(L_{yz}\Delta_y + L_{zy}\Delta_z\right)} \tag{13}$$

where C_{ij} and L_{ij} are calculated from [3]:

$\varepsilon_0\frac{\varepsilon_{kk}\Delta_i\Delta_j}{\Delta_k} = C_{ik}\Delta_i + C_{jk}\Delta_j$ and $\mu_0\frac{\mu_{kk}\Delta_i\Delta_j}{\Lambda_k} = L_{ij}\Delta_i + L_{ji}\Delta_j$. Line impedance Z_{ij} (see appendix A) are given by [3]:

$Z_{ij} = \frac{\Delta t}{C_{ij}\Delta_i}$ and $\Delta t = \Delta_i\sqrt{L_{ij}C_{ij}}$ with $i \neq j$ and $i,j \in \{x,y,z\}$.

The above relations allow one to write (1) and (2) in the YOZ-plane [5]:

	Maxwell-Ampère	Maxwell-Faraday
(SCN):	$b_1 + b_{12} + b_2 + b_9 + \hat{Y}_{sx}b_{13} = a_1 + a_{12} + a_2 + a_9 + \hat{Y}_{sx}a_{13}$	$b_4 - b_8 + b_7 - b_5 + \hat{Z}_{sx}b_{16} = -a_4 + a_8 - a_7 + a_5 + \hat{Z}_{sx}a_{16}$
(HSCN):	$\hat{Y}_z(b_1 + b_{12}) + \hat{Y}_y(b_2 + b_9) + \hat{Y}_{sx}b_{13} = \hat{Y}_z(a_1 + a_{12}) + \hat{Y}_y(a_2 + a_9) + \hat{Y}_{sx}a_{13}$	$b_4 - b_8 + b_7 - b_5 = -a_4 + a_8 - a_7 + a_5$
(SSCN):	$Y_{yx}(b_1 + b_{12}) + Y_{zx}(b_2 + b_9) = Y_{yx}(a_1 + a_{12}) + Y_{zx}(a_2 + a_9)$	$b_4 - b_8 + b_7 - b_5 = -a_4 + a_8 - a_7 + a_5$

Hence, we obtained six relations for the SCN, HSCN and SSCN. Thus, 18, 15 and 12 more relations are needed for these nodes, respectively. Evaluating fields in two perpendicular planes and at the center of the cells allow one to obtain more relations between incident and reflected voltages. For instance, path Γ_1 and Γ_2 illustrated in figure 3 are considered and field y-component at the center of the cell at time $k\Delta t$ evaluated.

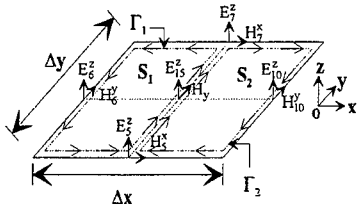

Figure 3: Evaluation of $H_y^{(k)}$ at the cell center.

The line integral of $\vec{H}$ along $\Gamma = \Gamma_1 \cup \Gamma_2$, assuming $H_y^{(k)}$ is the average value between time (k-1/2) and (k+1/2), yields:

$$\oint_{\Gamma} \vec{H}.d\vec{l} \cong \Delta_y \left[2H_y^{(k)} - \frac{1}{2}(1+T)(H_6^y + H_{10}^y) \right] \tag{14}$$

Using the same assumptions:

$$\varepsilon_0 \varepsilon_{zz} \iint_{S_1 \cup S_2} \frac{\partial \vec{E}}{\partial t}.d\vec{s} \cong \frac{1}{2}(1-T)\left[Y_{xz}(E_6^z - E_{10}^z \right] \tag{15}$$

for SSCN. For the SCN and the HSCN, one has to change Y_0 into $Y_0 \hat{Y}y$. Hence, Maxwell-Ampère's law yields:

$$2\Delta_y H_y^{(k)} = Y_{xz}\left[(b_6^{(k+1/2)} - b_{10}^{(k+1/2)}) + (a_{10}^{(k-1/2)} - a_6^{(k-1/2)}) \right] \tag{16}$$

Similarly, Maxwell-Faraday's law yields:

$$2\Delta_y E_y^{(k)} = b_3^{(k+1/2)} + b_{11}^{(k+1/2)} + a_3^{(k-1/2)} + a_{11}^{(k-1/2)} \tag{17}$$

Using both laws in the YOZ-plane (figure 1) yields:

$$2\Delta_y H_y^{(k)} = Y_{zx}\left[(b_9^{(k+1/2)} - b_2^{(k+1/2)}) + (a_2^{(k-1/2)} - a_9^{(k-1/2)}) \right] \tag{18}$$

$$2\Delta_y E_y^{(k)} = b_4^{(k+1/2)} + b_8^{(k+1/2)} + a_4^{(k-1/2)} + a_8^{(k-1/2)} \tag{19}$$

Equations (16), (18) and (17), (19) ; allows one to write two more relations:

$$Y_{xz}(b_{10} - b_6) + Y_{zx}(b_9 - b_2) = Y_{xz}(a_{10} - a_6) + Y_{zx}(a_9 - a_2) \tag{20}$$

$$b_3 - b_4 - b_8 + b_{11} = -a_3 + a_4 + a_8 - a_{11} \tag{21}$$

In [5], equation (20) and (21) are presented as continuity equations for magnetic and electric field components, respectively. At this stage we have twelve independent relations relating incident and reflected voltages. This is sufficient for the SSCN, while the HSCN and the SCN need three and six others relations, respectively. This can be done by evaluating field components at the center of the cell. Consider for instance $E_y^{(k)} = a_{14}^{(k-1/2)} + b_{14}^{(k+1/2)}$, one can use (17) or (19) to establish an other relation.

To summarize, from integral form of Maxwell's laws, relations between incident and reflected voltages for all condensed type of TLM nodes are found. They can be written under the matrix form:

$$[P_1]\vec{b}^{(k+1/2)} = [P_2]\vec{a}^{(k-1/2)} \tag{22}$$

in which matrices $[P_1]$ and $[P_2]$ are presented in appendix B for the lossy case. The scattering matrix is readily found from (22):

$$[S] = [P_1]^{-1}[P_2].$$

Finally, it is worth to mention that the formulation presented by Herring and Cristopoulos [8] is based on the magnetic flux and electric charge conservation and field continuity from transmission-line theory.

LOSSES AND SOURCE MODELING

Loss modeling in TLM consists of accounting for the surface integral contribution due to current densities in terms of incident and reflected voltages. This can be approximated by considering field values at the cell center. For instance, the integrals on S illustrated in figure 2 can be approximated as follows:

$$\iint_S \hat{\sigma}_e \vec{E} \circ d\vec{s} \cong G_{ex}\left(\Delta_x E_x^{(k)}\right) \text{ (electric losses)} \tag{24}$$

$$-\iint_S \hat{\sigma}_m \vec{H} \circ d\vec{s} \cong R_{mx}\left(\Delta_x H_x^{(k)}\right) \text{(magnetic losses)} \tag{25}$$

where, in general form:

$$G_{ek} = \sigma_{ek}\frac{\Delta_i \Delta_j}{\Delta_k} \text{ and } R_{mk} = \sigma_{mk}\frac{\Delta_i \Delta_j}{\Delta_k} \quad k = x, y, z \tag{26}$$

For the SCN and the HSCN, normalized conductance $\hat{G}_{ek}$ and resistance $\hat{R}_{mk}$ are used [2]. Terms due to losses are introduced in $[P_1]$ et $[P_2]$ (see appendix B) by using for instance $E_x^{(k)} = a_{13}^{(k-1/2)} + b_{13}^{(k+1/2)}$. Hence, (24) becomes:

$$\iint_S \hat{\sigma}_e \vec{E}.d\vec{s} \cong \frac{1}{Z_0}\hat{G}_{ex}\left(a_{13}^{(k-1/2)} + b_{13}^{(k+1/2)}\right) \text{ with } \hat{G}_{ek} = Z_0 G_{ek}$$

Finally, a similar approach is taken for contributions due to source integrals which transforms (22) as follows:

$$[P_1]\vec{b}^{(k+0.5)} = [P_2]\vec{a}^{(k-0.5)} - [P_3]\vec{u}^{(k)} \tag{27}$$

where $\vec{u}^{(k)}$ in the source vector.

SIMULATION RESULTS

In order to validate TLM source modeling, a waveguide is excited by an electrical current sheet with sinusoidal spatial distribution. The current source is a gaussian pulse amplitude modulated by a carrier at frequency f_0. Parameters are adjusted such that the excitation frequency spectrum is above waveguide cutoff. Constitutive parameters are $\varepsilon_r = 1$, $\mu_r = 4$ and $\Delta l / \lambda_{max} = 0.067$. A comparison between the different nodes in terms of time response in shown in figure 4. Dispersion introduced by the TLM model can be observed when compared with the theory. No significant difference is observed between the different node modeling. One can also observe the physical dispersion introduced by the guide. Finally, figure 5 shows the dispersion characteristics of a microstrip cavity on anisotropic substrate. Comparison is made between the distributed TLM node (ND) and FDTD [14], SCN and SSCN. It is observed that differences are increasing with frequency. The various nodes behave differently when numerical dispersion becomes significant ($\Delta l/\lambda \cong 0.1$ à 10 GHz). Finally, this application shows the applicability of the SSCN [3] for anisotropic media.

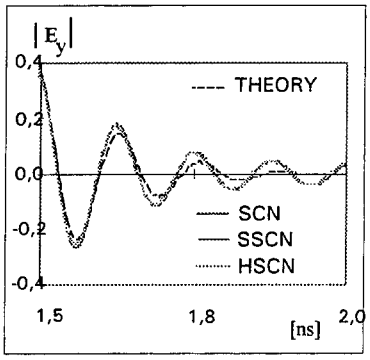

Figure 4: Numerical dispersion (waveguide above cutoff)

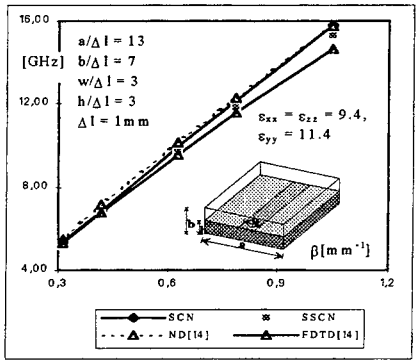

Figure 5: Dispersion for shielded microstrip line -

CONCLUSION

In this paper, a general 3D-TLM formulation including all condensed nodes SCN, HSCN and SSCN) and derived directly from field Maxwell's law in integral form was presented. The general scattering matrices relating incident and reflected voltages at every node account for electric and magnetic losses and allows the insertion of electrical and magnetic source current densities.

The presented algorithms have been validated through electromagnetic modeling of homogenous and inhomogenous structures. In addition, current source modeling capability of the proposed node is demonstrated. Also, structure including anisotropic media was analyzed and satisfactory results were found. In addition, comparisons between all three types of condensed nodes namely, the SCN, HSCN and SSCN seem to confirm a slightly better performance in terms of dispersion for the SCN. However, other criteria must be accounted for, in order to issue any conclusion about the overall performance of the nodes. In particular, number of operations required per iteration and the computer storage.

REFERENCES

[1] M. Krumpholz and P. Russer, "A Field Theoretical Derivation of TLM", IEEE Trans. Microwave Theory Tech., vol. 42, no. 9, pp. 1660-1668, Sept. 1994.

[2] H. Jin and R. Vahldieck, "Direct Derivations of TLM Symmetrical Condensed Node and Hybrid Symmetrical Condensed Node from Maxwell's Equations Using Centered Differencing and Averaging", IEEE Trans. Microwave Theory Tech., vol. 42, no. 12, pp. 2554-2561, Dec. 1994.

[3] V. Trenkic, C. Christopoulos and T. M. Benson, "Theory of the Symmetrical Super-Condensed Node for the TLM Method", IEEE Trans. Microwave Theory Tech., vol. 43, no. 6, pp. 1342-1348, June 1995.

[4] P. B. Johns, "A Symmetrical Condensed Node for the TLM Method", IEEE Trans. Microwave Theory Tech., vol. MTT-35, no. 4, pp. 370-377, April 1987.

[5] V. Trenkic, C. Christopoulos and T. M. Benson, "Simple and elegant formulation of scattering in TLM nodes", Electronics Letters, vol. 29, no. 18, pp. 1651-1652, Sep. 1993.

[6] N. Peña and M. Ney, "A General and complete Two - Dimensional TLM Hybrid Node formulation based on Maxwell's integral equations", Proc. ACES, Monterey CA., March 1996.

[7] P. Berrini and K. Wu, "A pair of hybrid symmetrical condensed TLM nodes", IEEE Microwave and Guided Wave Letters, vol. 4, no. 7, pp. 244-246, July 1994.

[8] J. L. Herring and C. Christopoulos, "The application of different meshing techniques to EMC problems", Pro. 9th Annual Review of Prog. in Appl. Com. Electromagnetics, Montrrey, CA., pp. 755-762, Mar 1993.

[9] R. Scaramuzza and A. J. Lowery, "Hybrid symmetrical condensed node for the TLM method", Electronics Letters, vol. 26, no. 23, pp. 1947-1948, Nov. 1990.

[14] D. H. Choi and W. J. R. Hoefer, "The Finite - Difference - Time Domain Method and its Application to Eingenvalue Problems", IEEE Trans. Microwave Theory Tech., vol. MTT-34, no. 12, Dec. 1986.

APPENDIX A

Incident and reflected voltages (see eq. (3)) for the SSCN are defined as follows:

$$\bar{a}_{SSCN}=\frac{1}{2}\begin{bmatrix}\Delta_x E_1^x - Z_{yx}\Delta_z H_1^z\\ \Delta_x E_2^x + Z_{zx}\Delta_y H_2^y\\ \Delta_y E_3^y + Z_{xy}\Delta_z H_3^z\\ \Delta_y E_4^y - Z_{zy}\Delta_x H_4^x\\ \Delta_z E_5^z + Z_{yz}\Delta_x H_5^x\\ \Delta_z E_6^z - Z_{xz}\Delta_y H_6^y\\ \Delta_z E_7^z - Z_{yz}\Delta_x H_7^x\\ \Delta_y E_8^y + Z_{zy}\Delta_x H_8^x\\ \Delta_x E_9^x - Z_{zx}\Delta_y H_9^y\\ \Delta_z E_{10}^z + Z_{xz}\Delta_y H_{10}^y\\ \Delta_y E_{11}^y - Z_{xy}\Delta_z H_{11}^z\\ \Delta_x E_{12}^x + Z_{yx}\Delta_z H_{12}^z\end{bmatrix}\quad \bar{b}_{SSCN}=\frac{1}{2}\begin{bmatrix}\Delta_x E_1^x + Z_{yx}\Delta_z H_1^z\\ \Delta_x E_2^x - Z_{zx}\Delta_y H_2^y\\ \Delta_y E_3^y - Z_{xy}\Delta_z H_3^z\\ \Delta_y E_4^y + Z_{zy}\Delta_x H_4^x\\ \Delta_z E_5^z - Z_{yz}\Delta_x H_5^x\\ \Delta_z E_6^z + Z_{xz}\Delta_y H_6^y\\ \Delta_z E_7^z + Z_{yz}\Delta_x H_7^x\\ \Delta_y E_8^y - Z_{zy}\Delta_x H_8^x\\ \Delta_x E_9^x + Z_{zx}\Delta_y H_9^y\\ \Delta_z E_{10}^z - Z_{xz}\Delta_y H_{10}^y\\ \Delta_y E_{11}^y + Z_{xy}\Delta_z H_{11}^z\\ \Delta_x E_{12}^x - Z_{yx}\Delta_z H_{12}^z\end{bmatrix}$$

where Z_{ij} with $i,j\in\{x,y,z\}$ and $i\neq j$ are the line impedance along the axis i and polarized in the direction j.[3]. Furthermore, the same above definition applies for the SCN by setting all impedances to Z_0. For the HSCN $Z_x=\frac{Z_0}{\hat{Y}_x}=Z_{zy}=Z_{yz}$, $Z_y=\frac{Z_0}{\hat{Y}_y}=Z_{zx}=Z_{xz}$ and $Z_z=\frac{Z_0}{\hat{Y}_z}=Z_{xy}=Z_{yx}$. Finally, field samples at the center of the cell are accounted by vectors: $\bar{V}_E=\frac{1}{2}\left[\Delta_x E_{13}^x \quad \Delta_y E_{14}^y \quad \Delta_z E_{15}^z\right]^t$ and $\bar{V}_H=\frac{1}{2}Z_0\left[\Delta_x H_{16}^x \quad \Delta_y H_{17}^y \quad \Delta_z H_{18}^z\right]^t$.

APPENDIX B

The structure of $[P_1]$ and $[P_2]$ (see eq. (22)) is:

$$[P_i]=\begin{array}{c|cc} & 12 & 15 \quad 18\\ \hline 12 & [A_{El}] & 0\\ & 0 & [A_{Hl}]\\ [P_i]^0 & 0 & 0\\ \hline 15 & [B_{rl}] & [C_{rl}] \quad 0\\ 18 & [B_{ml}] & 0 \quad [C_{ml}]\end{array}$$

where $[P_i]^0=[P_i]$ for the SSCN are given below:

$$[P_i]^0=\begin{bmatrix}
Y_{yx} & Y_{zx}^{(+)} & 0 & 0 & 0 & 0 & 0 & 0 & Y_{zx}^{(+)} & 0 & 0 & Y_{yx}\\
0 & 0 & Y_{xy} & Y_{zy}^{(+)} & 0 & 0 & 0 & Y_{zy}^{(+)} & 0 & 0 & Y_{xy} & 0\\
0 & 0 & 0 & 0 & Y_{yz} & Y_{xz}^{(+)} & Y_{yz} & 0 & 0 & Y_{xz}^{(+)} & 0 & 0\\
0 & 0 & 0 & A_x^{(+)} & -1 & 0 & 1 & B_x^{(-)} & 0 & 0 & 0 & 0\\
0 & -1 & 0 & 0 & 0 & A_y^{(+)} & 0 & 0 & 1 & B_y^{(-)} & 0 & 0\\
A_z^{(+)} & 0 & -1 & 0 & 0 & 0 & 0 & 0 & 0 & 0 & 1 & B_z^{(-)}\\
0 & -Y_{zx} & 0 & 0 & 0 & -Y_{xz} & 0 & 0 & Y_{zx} & Y_{xz} & 0 & 0\\
0 & 0 & 0 & Y_{zy} & Y_{yz} & 0 & -Y_{yz} & -Y_{zy} & 0 & 0 & 0 & 0\\
Y_{yx} & 0 & Y_{xy} & 0 & 0 & 0 & 0 & 0 & 0 & 0 & -Y_{xy} & -Y_{yx}\\
0 & 0 & 1 & -1 & 0 & 0 & 0 & -1 & 0 & 0 & 1 & 0\\
1 & -1 & 0 & 0 & 0 & 0 & 0 & 0 & -1 & 0 & 0 & 1\\
0 & 0 & 0 & 0 & -1 & 1 & -1 & 0 & 0 & 1 & 0 & 0
\end{bmatrix}$$

where $Y_{uv}^{(\pm)}=Y_{uv}\pm\frac{1}{2}G_{ev}$,

$A_k^{(\pm)}=\pm 1+\frac{1}{2}R_{mk}Y_{ij}$,

$B_k^{(\pm)}=\pm 1-\frac{1}{2}R_{mk}Y_{ij}$

with $i,j,k\in\{x,y,z\}, i\neq j\neq k$ and $(k,j)\in\{(x,y),(y,z),(z,x)\}$.

For the SCN same matrices apply, but with:

$$Y_{ij}=1 \text{ and } G_{ek}=0=R_{mk}.$$

$$[P_2]=\begin{bmatrix}
Y_{yx} & Y_{zx}^{(-)} & 0 & 0 & 0 & 0 & 0 & 0 & Y_{zx}^{(-)} & 0 & 0 & Y_{yx} \\
0 & 0 & Y_{xy} & Y_{zy}^{(-)} & 0 & 0 & 0 & Y_{zy}^{(-)} & 0 & 0 & Y_{xy} & 0 \\
0 & 0 & 0 & 0 & Y_{yz} & Y_{xz}^{(-)} & Y_{yz} & 0 & 0 & Y_{xz}^{(-)} & 0 & 0 \\
0 & 0 & 0 & A_x^{(-)} & 1 & 0 & -1 & B_x^{(+)} & 0 & 0 & 0 & 0 \\
0 & 1 & 0 & 0 & 0 & A_y^{(-)} & 0 & 0 & -1 & B_y^{(+)} & 0 & 0 \\
A_z^{(-)} & 0 & 1 & 0 & 0 & 0 & 0 & 0 & 0 & -1 & B_z^{(+)} & \\
0 & -Y_{zx} & 0 & 0 & 0 & -Y_{xz} & 0 & 0 & Y_{zx} & Y_{xz} & 0 & 0 \\
0 & 0 & 0 & Y_{zy} & Y_{yz} & 0 & -Y_{yz} & -Y_{zy} & 0 & 0 & 0 & 0 \\
Y_{yx} & 0 & Y_{xy} & 0 & 0 & 0 & 0 & 0 & 0 & -Y_{xy} & -Y_{yx} & \\
0 & 0 & -1 & 1 & 0 & 0 & 0 & 1 & 0 & 0 & -1 & 0 \\
-1 & 1 & 0 & 0 & 0 & 0 & 0 & 0 & 1 & 0 & 0 & -1 \\
0 & 0 & 0 & 0 & 1 & -1 & 1 & 0 & 0 & -1 & 0 & 0
\end{bmatrix}$$

Likewise , for the HSCN one has

$G_{ek}=0$,

$R_{mk}\rightarrow\hat{R}_{mk}$,

$(Y_{zy},Y_{yz})\rightarrow\hat{Y}_x$,

$(Y_{zx},Y_{xz})\rightarrow\hat{Y}_y$,

$(Y_{xy},Y_{yx})\rightarrow\hat{Y}_z$.

Other sub matrices account for the presence of stubs. Hence, for the SCN and by including losses, these sub matrices are:

$$|A_{E1}|=\begin{bmatrix}\hat{Y}_{sx}+\hat{G}_{ex} & 0 & 0\\ 0 & \hat{Y}_{sy}+\hat{G}_{ey} & 0\\ 0 & 0 & \hat{Y}_{sz}+\hat{G}_{ez}\end{bmatrix},\qquad |A_{E2}|=\begin{bmatrix}\hat{Y}_{sx}-\hat{G}_{ex} & 0 & 0\\ 0 & \hat{Y}_{sy}-\hat{G}_{ey} & 0\\ 0 & 0 & \hat{Y}_{sz}-\hat{G}_{ez}\end{bmatrix}$$

$$|A_{H1}|=\begin{bmatrix}\hat{Z}_{sx}+\hat{R}_{mx} & 0 & 0\\ 0 & \hat{Z}_{sy}+\hat{R}_{my} & 0\\ 0 & 0 & \hat{Z}_{sz}+\hat{R}_{mz}\end{bmatrix},\qquad |A_{H2}|=\begin{bmatrix}\hat{Z}_{sx}-\hat{R}_{mx} & 0 & 0\\ 0 & \hat{Z}_{sy}-\hat{R}_{my} & 0\\ 0 & 0 & \hat{Z}_{sz}-\hat{R}_{mz}\end{bmatrix}$$

$$|B_{E1}|=\begin{bmatrix}0&-1&0&0&0&0&0&0&-1&0&0&0\\0&0&0&-1&0&0&0&-1&0&0&0&0\\0&0&0&0&0&-1&0&0&0&-1&0&0\end{bmatrix},\qquad |B_{E2}|=-|B_{E1}|$$

$$|B_{H1}|=\begin{bmatrix}0&0&0&-1&0&0&0&1&0&0&0&0\\0&1&0&0&0&0&0&0&-1&0&0&0\\0&0&1&0&0&0&0&0&0&0&-1&0\end{bmatrix},\qquad |B_{H2}|=-|B_{H1}|$$

$$|C_{E1}|=|C_{H1}|=\begin{bmatrix}2&0&0\\0&2&0\\0&0&2\end{bmatrix}\quad\text{and}\quad |C_{E2}|=|C_{H2}|=-|C_{E1}|$$

For the HSCN, stubs electric losses are included in elements of $|A_{Ei}|$, $|B_{Ei}|$ and $|C_{Ei}|$.

Finally, source vector is

$\vec{u}^{(k)}=\begin{bmatrix}I_{ex}^{(k)} & I_{ey}^{(k)} & I_{ez}^{(k)} & V_{mx}^{(k)} & V_{my}^{(k)} & V_{mz}^{(k)}\end{bmatrix}^t$ for the SSCN, and $\vec{u}^{(k)}=\begin{bmatrix}V_{ex}^{(k)} & V_{ey}^{(k)} & V_{ez}^{(k)} & V_{mx}^{(k)} & V_{my}^{(k)} & V_{mz}^{(k)}\end{bmatrix}^t$,for the HSCN and the SCN where $I_{ek}^{(r)}=J_{ek}^{(r)}\Delta_i\Delta_j$, $V_{ek}^{(r)}=Z_0I_{ek}^{(r)}$ and $V_{mk}^{(r)}=J_{mk}^{(r)}\Delta_i\Delta_j$.

A Numerical Comparison Of Dispersion In Irregularly Graded TLM and FDTD Meshes

Fred J. German*, John A. Svigelj* and Raj Mittra**
*Texas Instruments, Inc.
2501 W. University, MS 8019
McKinney, Texas 75070
Tel: (214)952-3723
FAX: (214)952-3773
german@hertz.dseg.ti.com
**Electromagnetic Communication Laboratory
University of Illinois at Urbana-Champaign
Urbana, Illinois 61801

INTRODUCTION

Time domain numerical solutions have enjoyed an increase in popularity over the past decade as more powerful and affordable computational platforms have made their application in practical engineering design work feasible. The ability to model arbitrary geometric detail and homogenous regions with ease enables the design engineer to use a single time domain code to solve a very wide variety of electromagnetic interaction problems. Two techniques which have become quite prominent in time domain electromagnetic analysis are the finite difference time domain (FDTD) method and the transmission line matrix (TLM) method. Both of the methods are differential equation based time domain field solvers and their similarity has invited numerous comparison between the two. Most of these studies have been of a theoretical nature comparing the mathematical equivalence and differences between the various formulations of the two algorithms [1,2,3,4]. Advantages and disadvantages to each of the two methods have been touted by various authors. Some of these studies claim that FDTD is superior because it requires fewer computer operations per nodal update and less memory storage per cell. In addition, FDTD does not suffer from spurious solutions that, theoretically at least, can corrupt TLM results. On the other hand, TLM practitioners tend to cite the superiority of TLM due to less numerical dispersion and denser spatial field sampling leading to finer boundary resolution for a given mesh size. To date, however, no thorough study comparing the accuracy and efficiency of the numerical results obtained from TLM and FDTD when applied to problems in identical settings has been published.

In this paper we compare the performance of FDTD and TLM in terms of numerical dispersion for meshes that use non-uniform variable grading. Specifically, we examine the error in the propagation constant calculated with the two methods. In addition we will comment briefly on the impact that the existence of spurious field solutions in condensed node TLM algorithms has in practical applications. While the computational resources are a very important part in the comparison of any numerical techniques, a thorough study is beyond the scope of this paper and consequently will be addressed only briefly.

NUMERICAL METHODS

We will assume a familiarity with the basic workings of both the FDTD and condensed node TLM algorithms. Only the basic features unique to the particular analysis codes used in this study will be discussed.

The TLM program used here is based on the hybrid symmetrical condensed node (HSCN) formulation [5]. This node is formulated to easily permit a non-uniformly graded cartesian mesh to be implemented. As with all condensed node TLM algorithms, all six vector field components are located at cell centers. In addition, tangential electric and magnetic field components are available on the cell faces. In practical engineering problems it is usually advantageous to operate the algorithm at the largest time step permissible. This practice has been followed here where the maximum time step is chosen based on the requirement that all impedances in the condensed node mesh remain positive. For the purposes of terminating the numerical simulation space, a second order Higdon absorbing boundary condition (ABC) is used.

The FDTD program used in this study was derived based on a curvilinear algorithm to achieve variable mesh grading. The nonuniform orthogonal implementation [6] maintains the accuracy of the curvilinear algorithm while keeping the same form for the staggered grid leap-frog update equations as used in the standard Yee algorithm. The time step is chosen to satisfy the Courant stability condition and second order Higdon ABCs are used to truncate the computational domain.

RESULTS

In this section we compute the error in the propagation constant for the FDTD and TLM algorithms in waveguide structures which are discretized using both uniformly and non-uniformly graded meshes. The error in propagation constant for waves propagating in the numerical meshes arises from the numerical dispersion that the waves experience as they travel through the discretized problem space. The problem of dispersion has been studied analytically quite thoroughly for both the FDTD [7] and TLM [8] algorithms. Many analytic investigations are limited for the most part to the study of uniformly graded meshes. (By uniform grading we refer to a mesh in which the spatial discretizations in the x-, y- and z-axis directions (Δx, Δy, Δz) can differ, but do not change throughout the problem space resulting in non-cubic cells of equal dimensions. On the other hand, non-uniform grading refers to those case where Δx, Δy and Δz may change from cell to cell throughout the mesh).

Two types of waveguides are studied here: a parallel plate waveguide and a standard WR-90 waveguide. These examples are by no means intended to provide a thorough investigation of dispersion. Rather, our intent is to provide some insight into the effects of dispersion in meshes used for modeling a very limited number of practical waveguiding structures.

In order to compute the numerical propagation constant in the mesh the temporal signature of the fields is saved at two points a distance of L apart in the direction of propagation (the z-direction for the examples presented here). Fourier transform of these time domain fields yields the phase shift between the points as a function of frequency. Knowledge of the phase shift and distance between the points allows the calculation of the numerical phase constant, β_n. The percent error in the propagation constant is defined as

$$\% \text{ Error In Propagation Constant} = \frac{|\beta_n - \beta_t|}{\beta_t} x100$$

where β_t is the theoretical propagation constant. A Gaussian pulse was used as the excitation waveform in all cases.

The first structure examined is the parallel plate waveguide shown in Figure 1. While very simple, this structure is useful for simulating normal incidence on a periodic grid of scatterers or antennas for array analysis [10]. It also provides a very convenient way of numerically determining mesh dispersion along a coordinate axis (in this case the z-axis) for various mesh grading schemes.

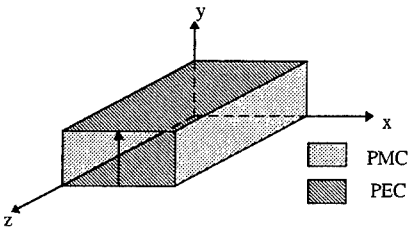

Figure 1. Geometry of parallel plate waveguide.

The parallel plate guide is meshed with two cells in the x-direction and one cell in the y-direction. Note that the number of cells is irrelevant in these directions since there is no field variation. The scheme used was chosen only for ease of boundary definition in the FDTD code. For the first example the guide was meshed uniformly. Figure 2 shows the propagation constant error for six different graded meshes obtained from the two algorithms. Note that the x axis is plotted in terms of the *minimum* cell size in the mesh divided by the wavelength where the minimum cell size is 1 in all cases. In the axial direction it is well known that a uniformly graded condensed node TLM mesh has no dispersion and this is readily seen in Figure 2. As the cell size in the z-direction is increased the error also increases. It is interesting to note that for TLM the error is a function only of the grading in the direction of propagation, while for FDTD grading the cells in the transverse directions has a slight effect on the error for a constant cell size in the propagation direction. In all cases the TLM results display a smaller error than the corresponding FDTD results. It must be realized that this conclusion is only valid for waves traveling in the axial direction. The error is also a function of propagation direction which is not evident here. However, when using a parallel plate waveguide for simulating periodic structures propagation is in the axial direction only.

In order to reduce the total number of cells required for a practical waveguiding problem it is often the practice to mesh finely in areas of large field gradients and to grade the mesh to larger cell sizes as one moves away from the discontinuity region(s). The next example is designed to investigate various techniques for increasing the cell size in the direction of propagation as the waves propagate away from a fine mesh region to a coarse mesh region. Propagation is initiated in a parallel plate waveguide in a region of the mesh where $\Delta z = 1$ and propagates away from the source for a distance of 14 cells. At this point the cell size in the propagation direction is slowly increased by a constant multiplying factor for a distance of approximately $15\Delta_{min}$ where Δ_{min} is the minimum cell size used in the mesh. Four different growth rates were considered resulting in a total of 15 (no grading), 12, 10 and 8 cells in the $15\Delta_{min}$ growth region. Once the cells reached their maximum size that cell size was maintained to the end of the mesh. The discretization in the propagation direction for the growth region in each case is displayed in graphical form in Figure 3 and is detailed in tabular form in Table 1. The results of the simulations are shown in Figure 4. As expected the propagation error increases for fewer cells in the growth region. It is

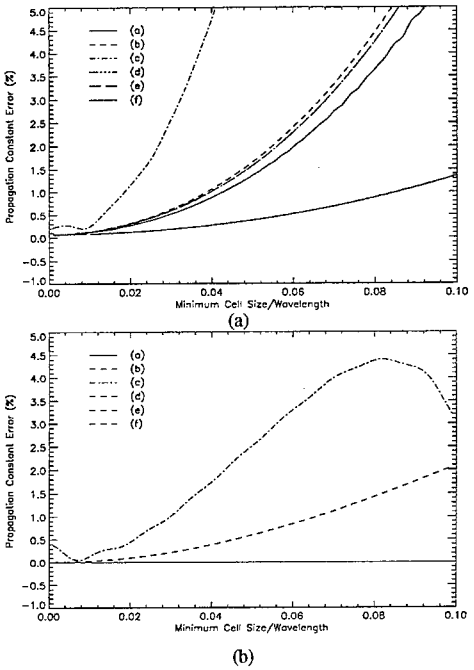

Figure 2. Propagation error for (a) FDTD and (b) TLM for uniformly graded parallel plate waveguide. The different curves are defined by: (a) $\Delta_x=\Delta_y=\Delta_z=1$, (b) $\Delta_x=\Delta_y=1,\Delta_z=2$, (c) $\Delta_x=\Delta_y=1,\Delta_z=4$, (d) $\Delta_x=1, \Delta_y=2, \Delta_z=2$, (e) $\Delta_x=2, \Delta_y=1, \Delta_z=2$, and (f) $\Delta_x=2, \Delta_y=2, \Delta_z=2$.

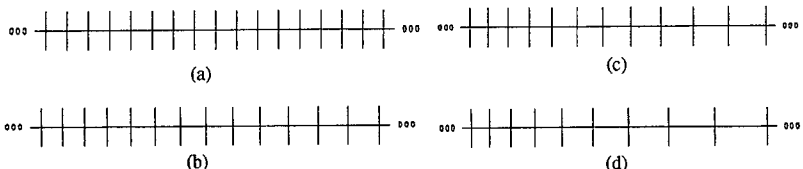

Figure 3. Mesh discretization in propagation direction for (a) 15 cells, (b) 12 cells, (c) 10 cells and (d) 8 cells used in the growth region.

TABLE 1

Z-Cell Number	Δz/Δmin			
	Case A	Case B	Case C	Case D
1-14	1.000	1.000	1.000	1.000
15	1.000	1.034	1.073	1.139
16	1.000	1.069	1.150	1.297
17	1.000	1.105	1.234	1.477
18	1.000	1.143	1.323	1.682
19	1.000	1.181	1.419	1.915
20	1.000	1.221	1.522	2.181
21	1.000	1.263	1.633	2.483
22	1.000	1.305	1.751	2.828
23	1.000	1.350	1.879	2.828
24	1.000	1.395	2.015	2.828
25	1.000	1.443	2.015	2.828
26-200	1.000	1.491	2.015	2.828

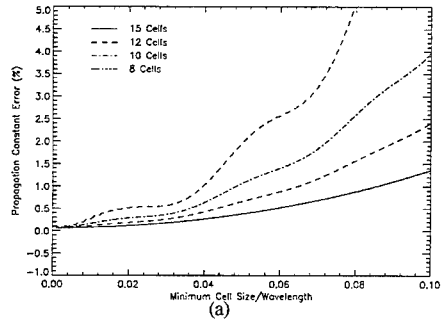

(a)

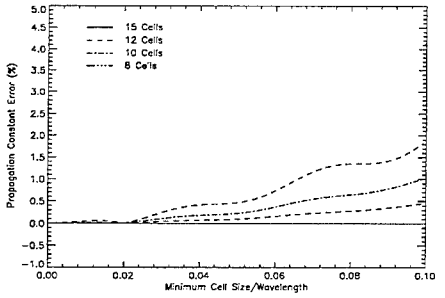

(b)

Figure 4. Propagation error for (a) FDTD and (b) TLM algorithms for the case of constant growth rates in cell size over a fixed mesh region.

very interesting to note, however, that the propagation error for the TLM algorithm is substantially less than for the FDTD algorithm. In fact, the maximum error for the 8 cell case with TLM is less than the maximum error for the all but the 15 cell FDTD case. For the 8 cell case the maximum "electrical cell size" defined as Δ_{max}/λ_o is 0.2828 which is well over the usually cited maximum electrical cell size of 0.10. The undulations in the curves are due to numerical reflections from the absorbing boundaries and could be eliminated by the use of a better ABC.

For the final example involving the parallel plate waveguide, the effect of an abrupt change in cell size in the propagation direction is investigated. Consider Case C in Table 1 where the maximum cell size is 2.015. This maximum cell size is attained by gradually increasing the cell size by a constant growth ration. To see the effects of an abrupt change in cell size, we have run the case where the cell

size changes from 1 to 2.015 at the beginning of the growth region and is maintained to the far end of the mesh. The results obtained from the FDTD and TLM algorithms for the propagation error are shown in Figure 5. It is observed that an abrupt change results in larger errors than when the maximum cell size is reached gradually. Once again it is interesting to note that the TLM error is significantly less than the FDTD error in both cases. In fact, the TLM error for the abrupt change in cell size is less than the FDTD error for a gradual change in cell size.

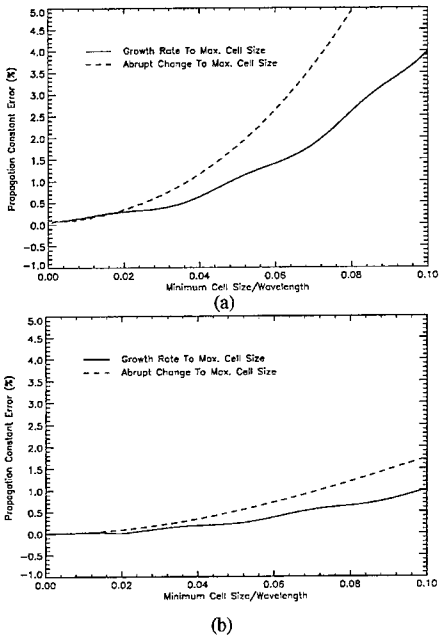

Figure 5. Propagation error for (a) FDTD and (b) TLM algorithms for gradual and abrupt changes in cell size.

All of the results thus far have been for waves propagating in a direction parallel to a mesh coordinate axis in a parallel plate waveguide. Now, consider propagation in a rectangular waveguide operating in the TE_{10} mode. In this situation the waves propagate at an angle to the mesh coordinate axis and this angle depends on the frequency of operation. For the following results a standard WR-90 waveguide has been used.

First a section of WR-90 with a uniform mesh grading will be considered. Figure 6 shows the propagation error for two uniformly graded meshes. The trends are the same as those for the parallel plate guide, i.e., "stretching" the mesh in the direction of propagation results in a larger propagation error and the TLM error is less than the FDTD error. An interesting point to note is that for the stretched TLM mesh there is actually less propagation error below 10 GHz than for the ungraded mesh. This is likely due to the dependence of numerical dispersion on the propagation angle (measured away from the propagation direction) which varies from 61° at 7.5 GHz to 26° at 15 GHz.

As a final example we consider the propagation error associated with a numerical mesh constructed to solve a "real" problem. The problem is a resonant waveguide iris in WR-90 waveguide and is shown in Figure 7. The details for the non-uniformly graded mesh used in the simulation are given in Table 2. The mesh was constructed such that fine cells were used in the vacinity of the infinitesimally thin iris edges and increased in size away

from these regions of large field gradients. The maximum cell size occurs in the direction of propagation and is six times larger than the smallest cell dimension.

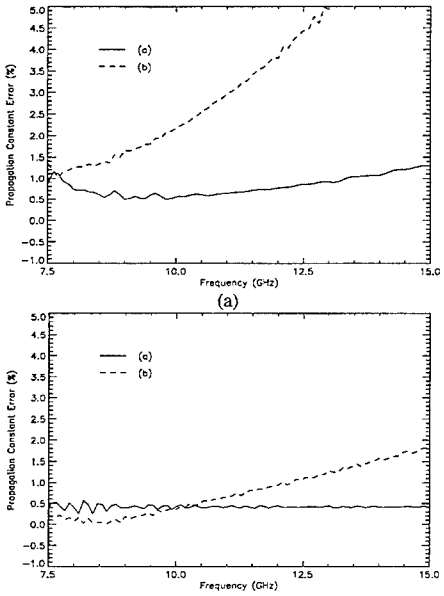

Figure 6. Propagation error for (a) FDTD and (b) TLM algorithms for WR-90 waveguide with uniformly graded meshes. The curves are defined as (a) $\Delta z=\Delta x=\Delta y$ and (b) $\Delta z=2\Delta x=2\Delta y$.

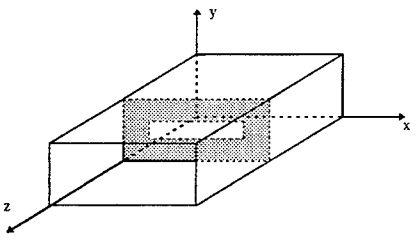

Figure 7. WR-90 waveguide with resonant iris. Iris aperture dimensions are 0.65x0.14 inches.

The sample field points chosen for the calculation of the propagation error were located at the input and output ports of the device. These were the same points that would have been chosen for the calculation of the S-parameters of the iris. The simulations were run without the iris present in the numerical models in order to quantify the propagation error associated with waves traveling through the highly non-uniform graded mesh. The resulting propagation error is shown in Figure 8. The "noise" present in the data is due to the sensitivity of the propagation error to the ABCs used. The ABC parameters were adjusted to optimize absorption at various angles of incidence and these changes also changed the ripple pattern in the data. The overall trend of the error levels remained consistent however. Use of a higher order ABC is likely to improve the appearance of this data. For the present simulations identical ABC parameters were used for the FDTD and TLM simulations. This result is actually quite interesting in the sense that the propagation error has been calculated on a realistic mesh that is used to solve a practical waveguide discontinuity problem. By computing the propagation error accumulated by the waves propagating in the mesh from the input to the output point, it may be possible to determine an accuracy bound on the results. Alternatively, for a required phase accuracy, it may be possible to determine the maximum permissible cell size that the mesh can be expanded to. The data for propagation error computed here would seem to indicate that a larger cell size can be

used for a given accuracy using the TLM method. However, there are many other factors to be considered before any such conclusions can be drawn from any of the data presented here. These and other key considerations are discussed in the following section.

TABLE 2

x-axis		y-axis		z-axis	
cell #	$\Delta x/\Delta$	cell #	$\Delta y/\Delta$	cell #	$\Delta z/\Delta$
1	3.0	1	3.0	1-36	6.0
2-3	2.0	2-4	2.0	37-40	4.0
4	1.5	5-12	1.0	41-44	3.0
5-12	1.0	13-15	2.0	45-48	2.0
13	1.5	16-23	1.0	49-56	1.0
14-16	2.0	24-26	2.0	57-60	2.0
17-33	3.0	27	3.0	61-64	3.0
34	1.5			65-68	4.0
35-42	1.0			69-104	6.0
43	1.5				
44-45	2.0				
46	3.0				

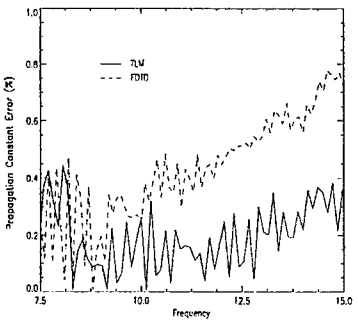

Figure 8. Propagation error for waveguide iris mesh.

CONCLUSIONS

In this paper we have presented a comparison of the propagation error associated with the FDTD and TLM methods when applied to practical waveguiding problems. While many studies have been performed to analytically characterize numerical dispersion in both techniques, very little work has been done to quantify the error in non-uniform graded meshes. While the results seen here are very interesting, one must exercise extreme caution before drawing conclusions from this very limited data set.

For all cases considered here the TLM method has displayed smaller propagation errors than the FDTD method. This would seem to indicate that when applying TLM a coarser mesh could be used for a given level of accuracy. However, there are many other factors that must be considered before drawing such rash conclusions. It is well recognized that condensed node TLM schemes require more storage per node than Yee's FDTD scheme. Further, the number of operations to update each node is greater for TLM. Whether or not this larger requirement of computational resources can be offset by the use of a coarser non-uniform mesh requires further investigation. Another area that hasn't been considered here concerns the description of boundaries and fine features within the mesh. Any advantages gained via the ability to use a coarse mesh to obtain a given level of propagation error is rendered useless if that mesh is too coarse to model the fine features of the structure under investigation. The development of "smart cells" which allow fine features to be modeled in a relatively coarse mesh is crucial in order to be able to exploit non-uniform meshing to its fullest potential in both methods.

Finally, there has been quite a bit of discussion recently concerning the existence of spurious modes in condensed node TLM schemes [8]. These are non-physical solutions that have the potential to corrupt the actual solution. While there is little doubt from a theoretical standpoint that these spurious modes modes can exist, their impact on solutions to practical problems is questionable.

REFERENCES

[1] P.B. Johns, "On the relationship between TLM and finite-difference methods for Maxwell's equations," IEEE Trans. Microwave Theory Tech., vol. MTT-35, no. 1, pp.60-61, 1987.

[2] D.H. Choi, "A comparison of dispersion characteristics associated with the TLM and FD-TD Methods," Int. J. of Numerical Modelling, vol. 2, pp. 203-214, 1989.

[3] M. Krumpholz, C. Huber and P. Russer, "A field theoretical comparison of FDTD and TLM," IEEE Trans. Microwave Theory Tech., vol. 43, no. 8, pp. 1935-1950, 1995.

[4] N.R.S. Simons and A.A. Sebak, "Spatially weighted numerical models for two dimensional wave equation: FD algorithm and synthesis of the equivalent TLM model," Int. J. Numerical Modelling, vol. 6, no. 1, pp. 47-65, 1993.

[5] R. Scaramuzza and A.J. Lowery, "Hybrid symmetrical condensed node for the TLM method," Electronics Letters, vol 26, no. 23, pp. 1947-1949, 1990.

[6] J.A. Svigelj, "Efficient solution of Maxwell's equations using nonuniform orthogonal finite difference time domain method," Ph.D. Dissertation, University of Illinois at Urbana-Champaign, 1995.

[7] P. Monk and E. Suli, "Error estimates for Yee's method on non-uniform grids," IEEE Trans. Magnetics, vol. 30, no. 5, pp.3200-3203, 1994.

[8] J.S. Neilsen and W.J.R. Hoefer, "Generalized dispersion analysis and spurious modes of 2-D and 3-D TLM formulations," IEEE Trans. Microwave Theory Tech., vol. 11, no. 8, pp.1375-1384, 1993.

[10] F.J. German, "Analysis and design of phased array antenna systems using the TLM method," Proceedings First Int. Workshop On TLM, pp. 155-164, 1995.

Accuracy Considerations of a Class of Frequency-Domain TLM Nodes

Shuoqi Chen and Ruediger Vahldieck

Laboratory for Lightwave Electronics, Microwaves and Communications (LLiMiC)
Dept. of Electrical & Computer Engineering
University of Victoria, Victoria, B.C., Canada, V8W 3P6
Tel: (604) 721-8679, Fax: (604) 721-6052
E-mail: sqchen@ece.uvic.ca

Abstract

The accuracy of the frequency-domain TLM (FDTLM) simulation is directly related to the dispersion error produced by the FDTLM nodes. This paper presents a direct comparison between the various FDTLM nodes and their dispersion characteristics. A class of FDTLM symmetrical condensed nodes (SCNs) have been characterized in terms of rearranging the order of the node ports and determining both the characteristic admittance and the propagation constants of the link transmission lines. The dispersion characteristics of these FDTLM SCNs are analyzed by the numerical solution of an eigenvalue equation.

Introduction

The frequency-domain TLM (FDTLM) method has been developed recently as a frequency-domain counterpart to the time-domain TLM (TDTLM) method [1~2]. In contrast to the TDTLM, the FDTLM works entirely in the frequency domain, that is no time iterations are involved and thus no Fourier transform is required to determine the frequency response of the simulated circuits. The "workhorse" for the FDTLM discretization of a circuit is the symmetrical condensed node (SCN), which was first introduced by Jin, Vahldieck and Huang (i.e. [1~3]) and the formulation was based on P. B. Johns' SCN [4]. The FDTLM SCN is essentially an intersection of six transmission lines with certain propagation constants and characteristic impedances illustrated in Fig. 1. First, the 12-port symbolic scattering matrix is found at the center if the node from the power conservation law. Then, the scattering matrix at the ports of the node is obtained by shifting the reference planes from the center to the ports of the nodes. To do so, the propagation characteristics of the link lines must be determined. There are several approaches to accomplish this and each of the approaches lead to a different port scattering matrix. Huang has investigated the following possibilities [5]: The propagation constant is the same on all link lines and the characteristic admittances are calculated accordingly (*Propagation Constant Node*); the characteristic impedance is the same on all link lines and the propagation constant is calculated accordingly (*Characteristic Admittance Node*); the SCN was considered a hybrid node represented by three series and shunt nodes coupled at the center of the nodal point, whereby the link lines may be considered as either series or shunt lines. In [5] the link lines were only

considered as series lines. By defining the characteristic impedances on the three sets of series link lines, the propagation constants can be calculated (*Hybrid Node with Series Decomposition).* To complete this investigation, the hybrid SCN with shunt link lines was considered in [6] (*Hybrid Node with Shunt Decomposition).* In the present paper a brief review of the different node representations will be provided. Since the accuracy of the FDTLM simulation is directly related to the dispersion error produced by the FDTLM nodes a direct comparison will be given between the various FDTLM nodes and their dispersion characteristic, in particular for the graded mesh and high permittivity materials. Before we begin it should be noted that both hybrid frequency domain nodes (*Hybrid Node with Series Decomposition and Hybrid Node with Shunt Decomposition)* are different from the hybrid nodes in the time-domain. In the latter the characteristic impedances or admittances of the link lines are real quantities and are varied to account for a graded mesh as well as to model the property of the medium. To maintain time-synchronism, shunt-circuited open stubs are needed throughout the mesh if an inhomogeneous propagation medium is modelled or if losses need to be accounted for. The resulting symbolic scattering matrix in the time-domain hybrid node contains only real elements and its size can vary from 12x12 (lossless homogeneous case) to 18x18 (lossy electric and magnetic material). In the frequency-domain hybrid node (as in all FDTLM nodes), time synchronism need not be preserved and thus stubs are eliminated.The electric and magnetic losses are included in the various characteristic impedances and propagation constants of the link lines which become now complex quantities. However, the size of the scattering matrix is always 12 x 12.

Theory

The equivalent symmetrical condensed FDTLM node is sketched in Fig.1. In the frequency-domain TLM, time-harmonic variations are assumed and hence only the discretization of space is required. Incident voltage waves on each port are scattered to couple into other ports. By following the equivalences of the voltage and current to the electric and magnetic fields, the differential equations that described the behavior of voltages and currents at a symmetrical condensed FDTLM node are given in the form as shown below.

$$\begin{aligned} v\frac{\partial I_z}{\partial y} - w\frac{\partial I_y}{\partial z} &= j\omega C_x V_x \quad ; \quad v\frac{\partial V_z}{\partial y} - w\frac{\partial V_y}{\partial z} = -j\omega L_x I_x \\ w\frac{\partial I_x}{\partial z} - u\frac{\partial I_z}{\partial x} &= j\omega C_y V_y \quad ; \quad w\frac{\partial V_x}{\partial z} - u\frac{\partial V_z}{\partial x} = -j\omega L_y I_y \\ u\frac{\partial I_y}{\partial x} - v\frac{\partial I_x}{\partial y} &= j\omega C_z V_z \quad ; \quad u\frac{\partial V_y}{\partial x} - v\frac{\partial V_x}{\partial y} = -j\omega L_z I_z \end{aligned} \tag{1}$$

where u, v and w are the dimensions of the node in x, y, and z directions, respectively. The difference to reference [1~2][5] and this paper is that here we have implemented the node's notation proposed by Krumpholz and Russer [7] and a symmetric scattering matrix is obtained, which lead to a Hermitian matrix in the case of lossless media. The nodal inductances and capacitances of the TLM branches are calculated from the relationship for the distributed inductances and capacitances of the link lines in all six polarized directions as follows:

$$C_x = \varepsilon\frac{vw}{u} = C_{ji}v + C_{ki}w \quad ; \quad L_x = \mu\frac{vw}{u} = L_{jk}v + L_{kj}w$$

$$C_y = \varepsilon\frac{uw}{v} = C_{ij}u + C_{jk}w \quad ; \quad L_y = \mu\frac{uw}{v} = L_{ik}u + L_{ki}w \qquad (2)$$

$$C_z = \varepsilon\frac{uv}{w} = C_{ik}u + C_{jk}v \quad ; \quad L_z = \mu\frac{uv}{w} = L_{ij}u + L_{ji}v$$

where $i, j, k \in \{x, y, z\}$ and $i \neq j \neq k$.

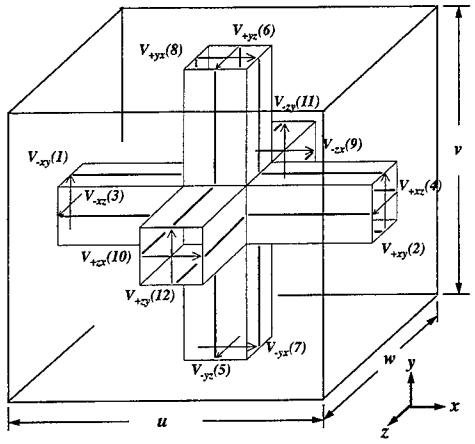

Fig. 1 The equivalent symmetrical condensed FDTLM node.

The scattering matrix of the frequency-domain symmetrical condensed node can be presented in the following form with compact blocks and symmetry on the main diagonal [6]:

$$S = \begin{bmatrix}
a_{ij} & d_{ij} & 0 & 0 & 0 & 0 & c_{ij} & -c_{ij} & 0 & 0 & b_{ij} & b_{ij} \\
d_{ij} & a_{ij} & 0 & 0 & 0 & 0 & -c_{ij} & c_{ij} & 0 & 0 & b_{ij} & b_{ij} \\
0 & 0 & a_{ik} & d_{ik} & b_{ik} & b_{ik} & 0 & 0 & c_{ik} & -c_{ik} & 0 & 0 \\
0 & 0 & d_{ik} & a_{ik} & b_{ik} & b_{ik} & 0 & 0 & -c_{ik} & c_{ik} & 0 & 0 \\
0 & 0 & b_{jk} & b_{jk} & a_{jk} & d_{jk} & 0 & 0 & 0 & 0 & c_{jk} & -c_{jk} \\
0 & 0 & b_{jk} & b_{jk} & d_{jk} & a_{jk} & 0 & 0 & 0 & 0 & -c_{jk} & c_{jk} \\
c_{ji} & -c_{ji} & 0 & 0 & 0 & 0 & a_{ji} & d_{ji} & b_{ji} & b_{ji} & 0 & 0 \\
-c_{ji} & c_{ji} & 0 & 0 & 0 & 0 & d_{ji} & a_{ji} & b_{ji} & b_{ji} & 0 & 0 \\
0 & 0 & c_{ki} & -c_{ki} & 0 & 0 & b_{ki} & b_{ki} & a_{ki} & d_{ki} & 0 & 0 \\
0 & 0 & -c_{ki} & c_{ki} & 0 & 0 & b_{ki} & b_{ki} & d_{ki} & a_{ki} & 0 & 0 \\
b_{kj} & b_{kj} & 0 & 0 & c_{kj} & -c_{kj} & 0 & 0 & 0 & 0 & a_{kj} & d_{kj} \\
b_{kj} & b_{kj} & 0 & 0 & -c_{kj} & c_{kj} & 0 & 0 & 0 & 0 & d_{kj} & a_{kj}
\end{bmatrix} \qquad (3)$$

where

$$a_{ij} = \frac{Y_{ij}-Y_{kj}}{2(Y_{ij}+Y_{kj})} + \frac{Y_{ij}-Y_{ji}}{2(Y_{ij}+Y_{ji})} \;;\quad b_{ij} = \frac{Y_{kj}}{Y_{ij}+Y_{kj}} \;;\quad c_{ij} = \frac{Y_{ji}}{Y_{ij}+Y_{ji}} \;;\quad d_{ij} = \frac{Y_{ij}-Y_{kj}}{2(Y_{ij}+Y_{kj})} - \frac{Y_{ij}-Y_{ji}}{2(Y_{ij}+Y_{ji})} \;;$$

$i, j, k \in \{x, y, z\}$ and $i \neq j \neq k$.

The normalized characteristic impedances of the link transmission lines are associated with the field polarization and defined as follows:

$$Y_{\pm xy} = Y_{ij} \;;\; Y_{\pm yx} = Y_{ji} \;;\; Y_{\pm xz} = Y_{ik} \;;\; Y_{\pm yz} = Y_{jk} \;;\; Y_{\pm zx} = Y_{ki} \;;\; Y_{\pm zy} = Y_{kj} \tag{4}$$

Matrix (3) is symmetric and, generally, the elements are complex. In case of a lossless medium, the matrix becomes Hermitian.

The next step in the development is to shift the symbolic scattering matrix from the center of the node to the ports. This is possible only after the characteristic impedances and the propagation constants of the link lines are determined [5~6]:

1. *The Characteristic Admittance Node*: In this FDTLM node the characteristic admittance of each link transmission line is assumed to be the same and equal to the intrinsic admittance of the medium. The normalized propagation constants on each branch can then be computed from the node's dimensions as

$$\begin{aligned}
\tilde{\gamma}_x &= \frac{\gamma_x}{k_0} = \frac{1}{2}\left(\frac{v^2+w^2}{vw} - \frac{vw}{u^2}\right) \\
\tilde{\gamma}_y &= \frac{\gamma_y}{k_0} = \frac{1}{2}\left(\frac{u^2+w^2}{uw} - \frac{uw}{v^2}\right) \\
\tilde{\gamma}_z &= \frac{\gamma_x}{k_0} = \frac{1}{2}\left(\frac{u^2+v^2}{uv} - \frac{uv}{w^2}\right)
\end{aligned} \tag{5}$$

In general, these propagation constants are complex when modelling the permittivity and permeability in lossy media.

2. *The Propagation Constant Node*: In contrast to the previous approach, the characteristic admittances of the link lines are different and have been selected as follows:

$$Y_{\pm xy} = \frac{w}{v}Y_0 \;;\; Y_{\pm yx} = \frac{w}{u}Y_0 \;;\; Y_{\pm xz} = \frac{v}{w}Y_0 \;;\; Y_{\pm yz} = \frac{u}{w}Y_0 \;;\; Y_{\pm zx} = \frac{v}{u}Y_0 \;;\; Y_{\pm zy} = \frac{u}{v}Y_0 \tag{6}$$

If the characteristic admittances are so selected, the propagation constants along all 12 link lines are the same and equal to 1/2 of the intrinsic propagation constant k_0 of the media. The disadvantage of this node is that due to the same propagation constant a graded mesh cannot be utilized.

3. *The Hybrid Node*: In this case the SCN is considered as three shunt nodes and three series nodes coupled at the center of the node. In the hybrid node with *series decomposition* three characteristic admittances are chosen which are related to the inductances of the series link lines, *i.e.*,

$$Y_{ij} = Y_{ji} = \frac{sw}{uv}\sqrt{\frac{\varepsilon}{\mu}} \quad ; \quad Y_{ik} = Y_{ki} = \frac{sv}{uw}\sqrt{\frac{\varepsilon}{\mu}} \quad ; \quad Y_{ji} = Y_{kj} = \frac{su}{vw}\sqrt{\frac{\varepsilon}{\mu}} \quad ; \tag{7}$$

The normalized propagation constants of all link lines are then given as

$$\begin{aligned} \tilde{\gamma}_{xy} &= \frac{\gamma_{xy}}{k_0} = \frac{su}{u^2+v^2} \; ; & \tilde{\gamma}_{yx} &= \frac{\gamma_{yx}}{k_0} = \frac{sv}{u^2+v^2} \\ \tilde{\gamma}_{xz} &= \frac{\gamma_{xz}}{k_0} = \frac{uv^2}{s(u^2+v^2)} \; ; & \tilde{\gamma}_{yz} &= \frac{\gamma_{yz}}{k_0} = \frac{vu^2}{s(u^2+v^2)} \\ \tilde{\gamma}_{zx} &= \frac{\gamma_{zx}}{k_0} = \frac{w(u^2+v^2-s^2)}{s(u^2+v^2)} \; ; & \tilde{\gamma}_{zy} &= \frac{\gamma_{zy}}{k_0} = \tilde{\gamma}_{zx} \end{aligned} \tag{8}$$

On the other hand, in the hybrid node with *shunt decomposition* three characteristic admittances of the corresponding shunt transmission lines are chosen, which are related to the capacitance of the link lines, *i.e.*,

$$Y_{ij} = Y_{kj} = \frac{uw}{sv}\sqrt{\frac{\varepsilon}{\mu}} \quad ; \quad Y_{ik} = Y_{jk} = \frac{uv}{sw}\sqrt{\frac{\varepsilon}{\mu}} \quad ; \quad Y_{ji} = Y_{ki} = \frac{vw}{su}\sqrt{\frac{\varepsilon}{\mu}} \quad ; \tag{9}$$

where $s = \sqrt{(u^2w^2+u^2v^2+v^2w^2)/(u^2+v^2+w^2)}$; u, v and w are the dimensions of the node in x, y, and z directions, respectively. The normalized propagation constants of the corresponding link transmission lines can be derived as:

$$\begin{aligned} \tilde{\gamma}_{xy} &= \frac{\gamma_{xy}}{k_0} = \frac{uv^2}{s(u^2+v^2)} \; ; & \tilde{\gamma}_{yx} &= \frac{\gamma_{yx}}{k_0} = \frac{u^2v}{s(u^2+v^2)} \\ \tilde{\gamma}_{xz} &= \frac{\gamma_{xz}}{k_0} = \frac{su}{u^2+v^2} \; ; & \tilde{\gamma}_{yz} &= \frac{\gamma_{yz}}{k_0} = \frac{sv}{u^2+v^2} \\ \tilde{\gamma}_{zx} &= \frac{\gamma_{zx}}{k_0} = \frac{w(u^2+v^2-s^2)}{s(u^2+v^2)} \; ; & \tilde{\gamma}_{zy} &= \frac{\gamma_{zy}}{k_0} = \tilde{\gamma}_{zx} \end{aligned} \tag{10}$$

According to Floquet's theorem applied to a three-dimensional TLM mesh, the dispersion characteristics for the frequency-domain TLM nodes are based on the numerical solution of an eigenvalue equation which is an implicit function of the propagation constant k_m of the wave travelling in the medium and the mesh propagation constants k_x, k_y and k_z along the x, y, and z directions. The eigenvalue equation can be expressed in the form [8~10]:

$$det(PS_p - I) = 0 \tag{11}$$

where I is a 12 x 12 unit matrix, P is a matrix containing the mesh propagation constants, and S_p is the scattering matrix of the frequency-domain TLM nodes which are related to the ports of the twelve link transmission lines. It should be noted that in contrast to [8~9,] matrix T no longer exists in equ. (11) because the matrix elements are incorporated into *Sp*, the scattering matrix at the ports of the node.

Results and Discussions

To verify the validity and accuracy of the class of FDTLM nodes, the dispersion characteristics of a suspended stripline is investigated and the results are shown in Fig. 2. The number of nodes

along the x-axis is chosen as 8 and along the y-axis as 7. A graded mesh arrangement is used. Compared with other FDTLM nodes, it can be seen that the results from the frequency-domain hybrid node converges better to the results of the spectral domain approach (SDA) [5]. The error can be further reduced by refining the mesh discretization. The flexibility of the frequency-domain hybrid node is further demonstrated by calculating the S-parameters of some microstrip discontinuities [6].

The dispersion relations of the FDTLM nodes can be obtained from the general equation (11). Fig. 3 illustrates the relative dispersion errors of the propagation constant node and characteristic admittance node [5] compared with those of the hybrid node [6] for a plane wave propagation in the y-z plane. The x-axis represents the angle between the propagation vector and the y-direction is given as $\phi=arctan(k_y/k_z)$. The y-axis represents the relative propagation error given as $(|k| - k_m)/k_m$, where $|k|$ is written as $|k| = (k_y^2 + k_z^2)^{1/2}$ and k_m is the propagation constant of the medium. The results are given for a graded mesh where $k_m u = k_m v = 0.1\pi$, $k_m w = 0.2\pi$ and $\varepsilon_r = \mu_r = 1$. The factor $k_0 d$ is directly proportional to the node's spacing, because the FDTLM mesh usually corresponds to frequencies whose wavelength corresponds to 1/10 of a FDTLM cell. It can be seen from Fig. 3 that the relative dispersion error for the frequency-domain hybrid node is always positive and much less than those of the other nodes.

In the next example, we investigate the dispersion effect in a dielectric medium with a graded mesh. Fig. 4. illustrates a family of curves representing plane wave propagating in a graded mesh in the y-z propagation plane. The permittivity of the dielectric medium is $\varepsilon_r = 12$. The normalized propagation vector is plotted in a polar representation for the propagation constant node and the characteristic admittance node. The shunt and series decomposition nodes are not shown, because their dispersion is too close to the unit circle. The vector k_m describes the unit circle for the infinitesimal mesh case, indicating no dispersion occurs for the FDTLM nodes at low frequencies, even for a graded mesh. When a coarse discretization is selected, for example $k_m u = k_m v = 0.05\pi$, $k_m w = 0.1\pi$, the wavelength can not be considered very large compared to the graded cell, and the phase velocity becomes frequency dispersive and depends on the propagation direction. The maximum dispersion occurs in the axial direction for the characteristic admittance node. In this example the parameter w is larger than v; and the dispersion depends on the node's dimension along the propagation directions. Thus, the dispersion is higher in z-direction. A comparison of the relative dispersion errors in the different graded FDTLM nodes in the y-z propagation plane is shown in Fig. 5. The highest dispersion occurs in the characteristic admittance node. The dispersion error is smaller for the hybrid node than for both the propagation constant node and the characteristic admittance node solutions, for all angles of propagation in the y-z plane. This better accuracy and lower dielectric propagation error for the hybrid node compared to other nodes may be due to the fact that the link lines take into account the line capacitance rather than the link line inductances as in the series decomposition [5]. The dispersion analysis is also consistent with the results shown in Fig. 2.

Conclusion

In this paper, a class of FDTLM SCNs has been reviewed and compared in terms of their accuracy. Numerical results show that the hybrid FDTLM node shows much less dispersion than other FDTLM nodes and that the shunt decomposition scheme is the most accurate of all..

Acknowledgments

The authors would like to thank Dr. H. Jin and Dr. J. Huang for their many helpful discussions and comments.

References

[1] H. Jin and R. Vahldieck, 'The frequency-domain TLM method', 1992 IEEE Int. Microwave Symp. Dig., pp. 775-778, June, 1992.

[2] H. Jin and R. Vahldieck, 'The frequency-domain transmission line matrix method -- A new concept', IEEE Trans. Microwave Theory Tech., vol. MTT-40, pp. 2207-2218, Dec., 1992.

[3] J. Huang, R. Vahldieck, and H. Jin, 'Fast frequency-domain TLM analysis of 3-D circuit discontinuities', Proc. 9th Annual Review of Progress in Applied Computional Electromagnetics Symp., pp. 475-481, March, 1993.

[4] P.B. Johns, 'A symmetrical condensed node for the TLM method,' IEEE Trans. Microwave Theory Tech., vol. MTT-35, pp. 370-377, Apr., 1987.

[5] J. Huang, 'Frequency domain transmission line matrix method and its applications to electromagnetic analysis', Ph. D. dissertation, Chapter 2, Univ. of Victoria, Canada, 1995.

[6] S. Chen and R. Vahldieck, 'A new hybrid symmetrical condensed node for the frequency-domain TLM method', submitted to 1996 IEEE Int. Microwave Symp., San Fransisco, Califoria, USA.

[7] M. Krumpholz and P. Russer, 'A field theoretical derivation of TLM', IEEE Trans. Microwave Theory Tech., vol. MTT-42, pp. 1660-1668, Sept., 1994.

[8] J. Nielsen and W. Hoeffer, 'Generalized dispersion analysis and spurious modes of 2D and 3D TLM formulations', IEEE Trans. Microwave Theory Tech., vol. MTT-41, pp. 1375-1384, Aug., 1993.

[9] D. Johns and C. Christopulos, 'Dispersion characteristics of 3-D frequency-domain TLM node', Electron. Lett. vol. 29, (no.17), pp. 1536-1537, Aug., 1993.

[10] H. Jin and R. Vahldieck, 'A new frequency-domain TLM symmetrical condensed node derived directly from Maxwell's equations', to be published in IEEE Trans. Microwave Theory Tech., vol. MTT-43, Dec., 1995.

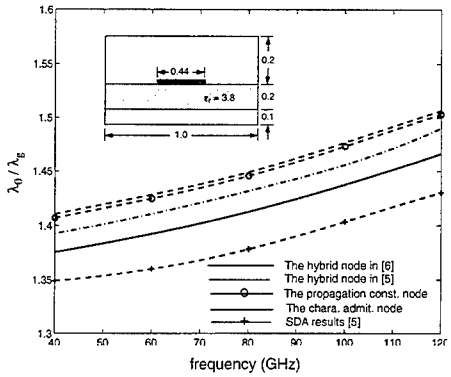

Fig. 2 The dispersion characteristics of a suspended stripline obtained with the different frequency-

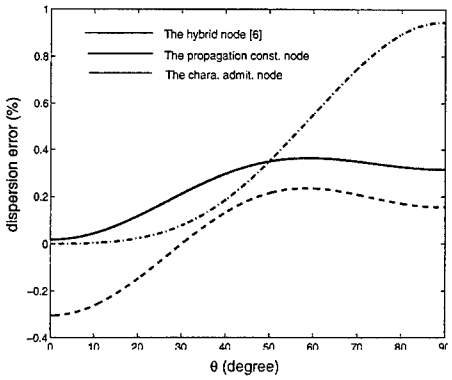

Fig. 3 Comparison of the relative dispersion errors of the different graded FD-TLM nodes in the y-z propagation plane (free space). $k_m u = k_m v = 0.1\pi$, $k_m w = 0.2\pi$ and $\varepsilon_r = \mu_r = 1$, where k_m is the free space propagation constant.

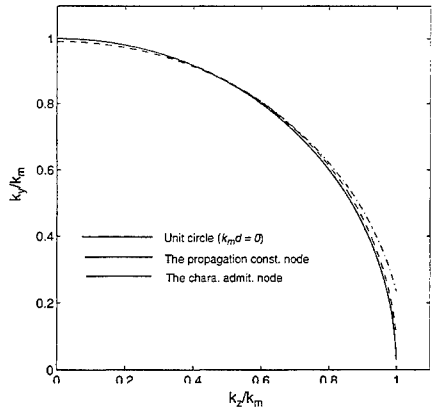

Fig. 4 Dispersion characteristics of a graded mesh of different FD-TLM nodes in the y-z propagation plane (dielectric). $k_m u = k_m v = 0.05\pi$, $k_m w = 0.1\pi$, $\varepsilon_r = 12$, and $\mu_r = 1$, where k_m is the medium propagation constant.

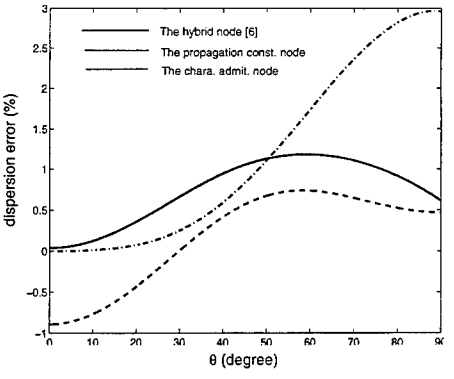

Fig. 5 Comparison of the relative dispersion errors of the different graded FD-TLM nodes in the y-z propagation plane (dielectric). $k_m u = k_m v = 0.05\pi$, $k_m w = 0.1\pi$, $\varepsilon_r = 12$, and $\mu_r = 1$, where k_m is the medium propagation constant.

Distributed Simulation of Planar Circuits by TLM Method in a Parallel Computing Environment

B. Isele, J. Schmöller, P. Russer

Lehrstuhl für Hochfrequenztechnik, Technische Universität München, Arcisstr. 21, D-80333 München 2, Germany, phone +49(0)89/21058390, fax +49(0)89/21053365

Abstract

The time-domain simulation of coplanar waveguide (CPW) elements for picosecond pulse applications is described. The circuit characteristics of the CPW elements were simulated in time domain using the 3D transmission-line-matrix (TLM) method. We present a cost–effective approach for the time–domain simulation of coplanar circuit structures utilizing distributed computing within a parallel software environment. The application of TLM method and distributed computing to the efficient analysis of several coplanar structures is presented.

Introduction

The present work arose from the requirement of an accurate analysis of planar circuits for monolithic microwave integrated circuits (MMICs). Time-domain modeling enables a direct broadband simulation utilizing arbitrary excitation signals, which may be useful in the investigation of circuits processing digital signals. In recent years, the transmission line matrix (TLM) method has emerged as a powerful tool to solve electromagnetic field problems in the time domain [1, 2]. Recently, efforts have been made to improve the accuracy and efficiency of the TLM schemes based on symmetrical condensed nodes [3]. The occurence of spurious modes caused by unphysical excitations of TLM meshes can be minimized using methods given in [4]. In particular, the modeling of planar circuits with several interfering discontinuities requires a TLM mesh with a large number of nodes. Thus the simulation of complex microwave circuits is limited by the accessible computer memory and computer performance. Parallel and distributed computing provides a cost effective way to overcome these limitations. Since the TLM algorithm is based on local operations at neighbouring mesh nodes only, the TLM method is predestinated for parallel computing. Distributed computing makes best use of the available resources and features the re-use of existing software modules if high-level parallel programming interfaces are provided. As a parallel computing environment for distributed computing we use the Parallel Virtual Maschine (PVM) V3.x, which became a standard environment for parallel computation [5, 6, 7] and which is largely compatible to the up-coming (MPI-)Message-Passing-Standard for parallel computation. PVM supplies a platform for portable parallel programming and provides a reliable communication interface also in heterogeneous computing environments. Load

balancing is achieved by an optimum segmentation of the mesh based on an initial guess of the available computer power at the particular maschines before starting the simulation task. The segmentation is optimized also for minimum communication traffic between the computing nodes. We are employing clusters of interconnected HP-7xx Workstations as well as an IBM-SP2 supercomputer with up to 56 computing nodes.

Simulation in a parallel computing enironment

In general, solvers for partial differental equations (PDEs) are candidates for parallel computing. In particular, methods yielding decoupled systems of equations, are suited well for parallelization. This implies that the simulation task can be divided into smaller subtasks, without introducing much communication effort between these subtasks. Since the TLM algorithm is based on local operations at neighbouring mesh nodes only, the TLM method is predestinated for parallel computing.

Distributed computing makes best use of the available resources and features the re-use of existing software modules if high-level parallel programming interfaces are provided. As a parallel computing environment for distributed computing we use the Parallel Virtual Machine (PVM), which became a standard environment for parallel computation [5, 6, 7] and is largely compatible to the up-coming (MPI-)Message-Passing-Standard for parallel computation. PVM supplies a platform for portable parallel programming and provides a reliable communication interface also in heterogeneous computing environments. Within PVM the processing units interchange their information by message passing techniques, which can be implemented easily into TLM. Some focus lies upon the granularity of the parallelization problem. Fine granularity involves considerable communication overhead, decreasing the computational power, whereas a coarse granularity requests computing nodes of higher computational power. In TLM a strict synchronization pattern is given by the TLM timestep, since each client has to wait for its adjacent neighbors for completion of one TLM iteration. The time needed for the communication between all adjacent clients is considerably larger than the accumulated communication time between each two clients operating on adjacent submeshes. The speedup for parallel computation is usually defined as ratio between the execution time on a standalone computer and the execution time in a parallel or distributed environment

$$S = \frac{T_s}{T_d}. \tag{1}$$

In multi-user-environments with computing nodes doing many other jobs concurrently, it is senseful to measure the execution time by means of cpu and user time required by the simulation tasks rather than the staying time of the simulation tasks. The speedup defined by cpu and user time increases nearly linear, whereas the performance measured by staying time of the simulation processes saturates due to communication bottlenecks and idle times. Fig. 2 shows the performance within a workstation cluster measured by accumulation of cpu- and user-time as well as by the staying time of the simulation tasks. The overall performance is dependent to the utilization of all available computing nodes. On networks with a bus topology, all computing nodes have to share the available communication bandwidth. The connection-less access mode in commonly used Ethernet based networks, which accepts even collisions of data packets, leads to a further descent of the throughput and limits also the number of computing nodes working on the same network segment within the computing environment. Therefor we admit only a sequential communication scheme,

allowing only one pair of clients to communicate with each other concurrently during the communication phase between the TLM timesteps. This guarantees that only one client submits messages at one time and thus additional collisions are avoided. Enhanced networking technologies like switched ethernet or FDDI networks will also reduce the communication bottlenecks. Using specialized hardware, such as IBM's SP2 computer, consisting of high-speed-interconnected processing nodes, these problems became unprimed, and the communication phase can be shortened by concurrent communication between pairs of clients. PVM supports the message-passing paradigm and preserves compatibility to the now up-coming MPI-(Message-Passing-Standard) for portable distributed computing.

An important feature is the re-usability of existing software components. Since our approach uses existing sequential code, which was extended for communication and controlling tasks, re-use is introduced at a high-level and the effort for the maintainance of the software package is kept small. The decision starting a simulation task standalone or distributed depends on the mesh size and the actual available computing resources. The parallelization model is given in Fig. 1. We use a hybrid model for the embedding of the existing computer codes, leaving most of communication between the working clients and introduce only a small overhead for controlling tasks managed by a master program.

PVM yields a very reliable communication interface also in heterogeneous environments, hiding all details of a specific platform. Also the embedding of machines with very different architecture like MIMD-and/or SIMD-computers is straightforward whereby only minor changes in the computer code are necessary. The approach yields a transparent simulation tool hiding all details of the specific computing node. Automatic space partitioning is performed by a off-line preprocessing, according to minimize the number of variables, which have to be exchanged and due to the available computational power of the specific computing nodes and network links.

Simulation of planar circuits

Planar circuits are designed for the application in microwave circuits of high package density and are optimized for minimum square dimensions and minimum aspect ratio. For such problems the three–dimensional TLM method is inherently suitable, especially if also multilayer structures or/and three-dimensional discontinuities such as via-holes, air-bridges are included into the planar circuit. The investigation of structures with metallic boundaries requires also a correct modeling of the skin effect surface impedance of thin metallic boundaries, taking also into account its $f^{\frac{1}{2}}$ dependence. In such cases a conventional TLM scheme is not applicable for the discretization. We have introduced a surface impedance model, which allows the consideration of thin conducting sheets enclosed in a TLM mesh [10]. Therein the skin effect surface impedance is modeled with arbitrary accuracy by lumped element ladder networks consisting of cascaded L-R - sections. For the extraction of S-Parameters high-quality absorbing boundery conditions are necessary especially in the port regions. One-way absorbing boundery conditions lack from their stability, often limiting the length of the observable time response, whereas global boundery conditions like the radiating boundery condition based on discrete green's function given in [11], requires a lot of nonlocal communication between several nodes. This will decrease the computational performance considerablely and will not be advantagous for distributed computing. The use of absorbing materials for modeling accurate boundery conditions found growing interest in the finite-difference community and may by-pass this problems. Berenger [12] found

that non-physical materials comply with the relation

$$\frac{\sigma_m}{\sigma_e} = \frac{\mu}{\epsilon} \tag{2}$$

yields absorbing material for incident waves at arbitrary angles. Utilizing several layers with quadratically increasing conductivity σ_e and magnetic conductivity σ_m, a perfect matching layer (PML) is constructed. The PML technique can be implemented easily into the TLM method preserving the locality of the TLM algorithm.

Simulation examples

We demonstrate the application of distributed TLM simulator for the modeling the electromagnetic field in complex planar circuits. In the current work we investigate CPW elements for MMICs. Planar circuits are designed for the application in microwave circuits of high package density and are optimized for minimum square dimensions and minimum aspect ratio. For such problems the three–dimensional TLM method is inherently suitable, especially if also multi-layer structures or/and three-dimensional discontinuities such as via-holes, air-bridges are included into the planar circuit.

We have investigated several coplanar structures including discontinuities, meander lines and spirals as well as self–similar structures such as the 3/2–line and Hilbert curves, in which the structures are distributed evenly over the dedicated area. The Hilbert curves represent optimum space-filling curves with appropriate aspect ratios. Fig. 3 shows the schematic of a modified hilbert curve and its time response. In Fig. 4 the field distribution is shown at different instants of time.

In Fig. 5 the schematic of a coplanar 35-to-50Ω-transition is given, which has been investigated previously by [13]. The geometrical parameters at the 35 Ω line are given by the width of the center conductor $w = 20\mu$m and the gap width $s = 5\mu$m, the parameters at the 50 Ω line are given by $w = 15\mu$m and the gap width $s = 10\mu$m. The simulation was performed for an GaAs substrate with an dielectric constant $\epsilon = 12.9$. The input reflection coefficient is shown by Fig. 6 in magnitude and phase. Currently we are working on simulation of interconneting structures and multilayer structures.

Conclusion

We have presented an extremely cost–effective approach for the time–domain simulation of coplanar circuit structures with the TLM method utilizing a parallel software environment. The use of matched layers, skin effect model and performance aspects are discussed. The feasibility of the approach is demonstrated by the analysis of several complex coplanar structures.

Reference

[1] P.B. Johns, "A Symmetrical Condensed Node for the TLM Method", *IEEE Trans. Microwave Theory Tech.*, vol. 35, pp. 370–377, April 1987.

[2] W.J.R. Hoefer, "The Transmission Line Matrix (TLM) Method", Chapter 8 in "Numerical Techniques for Microwave and Millimeter Wave Passive Structures", ed. by T. Itoh, J. Wiley, New York, 1989, pp. 496-591.

[3] P. Russer, "On the Field Theoretical Foundation of the Transmission Line Matrix Method", 1st International Workshop on Transmission Line Matrix (TLM) Modeling Theory and Applications, Victoria, British Columbia, Canada, August 1-3, 1995, pp. 3–12.

[4] S. Lindenmeier, B. Isele, R. Weigel, P. Russer, "Improved initial conditions for the symmetrical condensed TLM-node with respect to physical propagation characteristics, Progress in Electromagnetics Research Symposium PIERS, Noordwijk, Netherlands, July 1994, CD-ROM (4 Pages).

[5] A. Geist, A. Beguelin, J. Dongarra, W. Jiang, R. Manchek, V. Sunderam; "PVM 3.3 User's Guide and Reference Manual", Oak Ridge National Laboratory, May 1994.

[6] V. Varadarajan, R. Mittra, "Finite–Difference Time Domain (FDTD) Analysis Using Distributed Computing", *IEEE Microwave and Guided Wave Lett.* Vol. 4, No. 5, May 1994.

[7] B. Isele, J. Schmöller, P. Russer, "Simulation of Coplanar Resonators with TLM Method in a Parallel Computing Environment", Proceedings of the *PIERS 1995*, Seattle, July 1995, p. 733.

[8] W. Thomann, B. Isele, F. Stöckeler, R. Weigel, P. Russer "Characterization and Simulation of Bi-Quadratic Coplanar Waveguide Tapers for Time-Domain Applications", *IEEE-MTT-S International Microwave Symposium 1993*, (Atlanta, USA)), 14–18. Juni, 1993, S. 835–838.

[9] B. Isele, W. Thomann, F. Stöckeler, R. Weigel, P. Russer "Time-Domain Simulation of Low-Reflection Broadband Coplanar Waveguide Tapers and Circular Bends" *PIERS 1993, Pasadena*, S. 372.

[10] Isele, B., P. Russer: "Improved Skin Effect Model in TLM", In *Proc. COMPUMAG 1993*, (Miami, Florida)), 31. Oktober–4. November, 1993, pp. 450-451.

[11] M. Krumpholz, P. Russer, "Discrete Time-Domain Greens Functions for Three-Dimensional TLM Modelling of the Radiating Boundery Conditions", Proc. ACES, March 1993, pp. 458–466.

[12] J. P. Berenger, "A perfect matched layer for the Absorbtion of Electromagnetic Waves", J. Comp. Phys., Vol. 114., pp. 185–200, 1994.

[13] R. Schmidt, P. Russer "Modelling of Cascaded Coplanar Waveguide Discontinuities by the Mode-Matching Approach", *IEEE-MTT-S International Microwave Symposium 1995*, (Orlando, USA)), May 1995, S. 281–284.

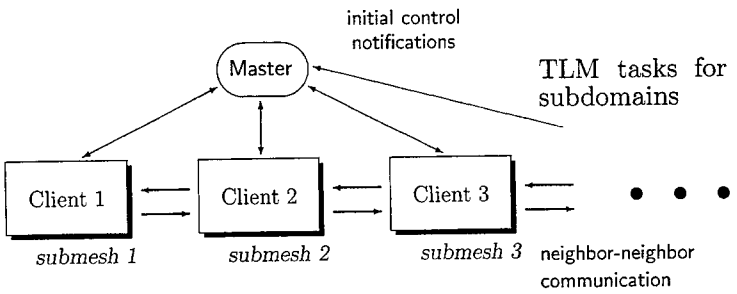

Figure 1: Parallel Programming Model using the Parallel Virtual Machine (PVM)

Problem size 320x32x12

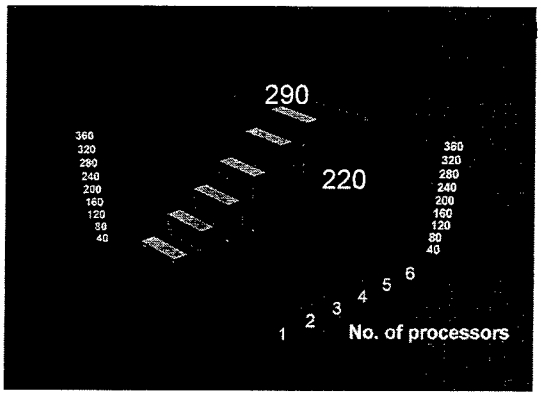

Dependance from number of computing nodes

Figure 2: Performance of distributed TLM simulation

length l	8.2 mm
gap width	36.8 μm
conductor width	70.0 μm
substrate height	635 μm
ϵ	9.8

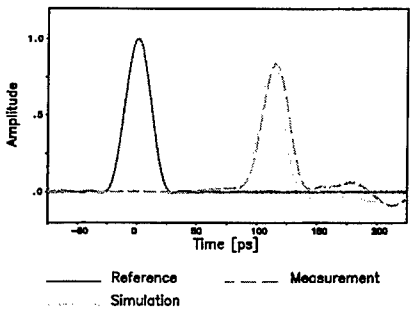

Figure 3: Time Response of the Modified Hilbert Curve

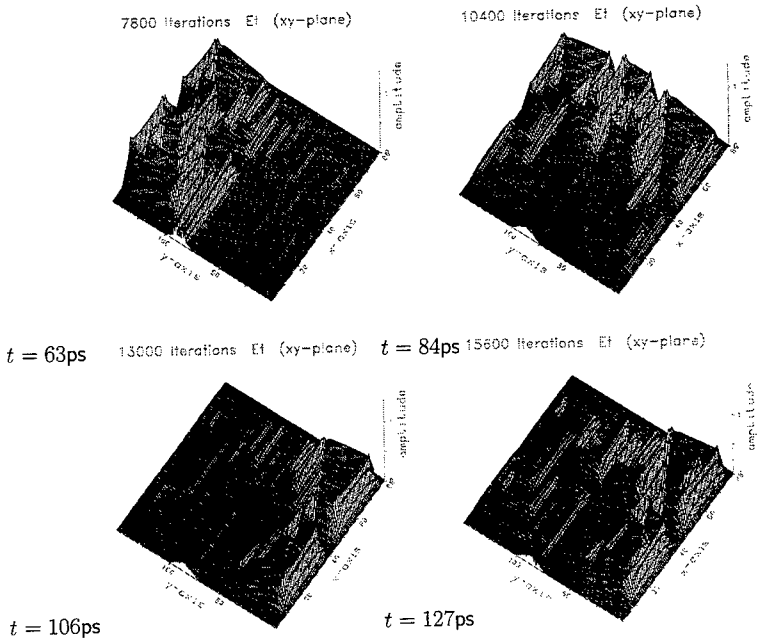

Figure 4: TLM Field Simulation of the Modified Hilbert Curve

Figure 5: Schematic of 35-to-50Ω-transition

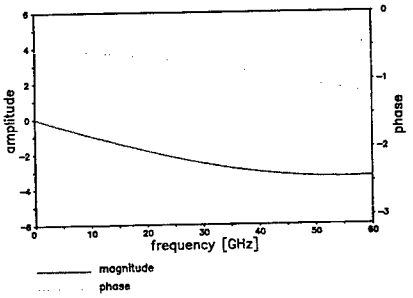

Figure 6: Input reflection coefficient

Modeling gyromagnetic media in symmetrical condensed node TLM

L. de Menezes, W.J.R.Hoefer

NSERC/MPR Teltech Research Chair in RF Engineering, Department of Electrical and Computer Engineering, University of Victoria, Victoria B.C., CANADA

Abstract

In this paper the symmetrical condensed node (SCN) TLM model of gyromagnetic materials is described. The constitutive relations of the medium are represented by equivalent sources connected to the node. The resulting TLM scattering matrix is independent of the material behavior. The equivalent sources are calculated at each timestep and included in the scattering procedure of TLM. This approach is robust, general, and capable of modeling the frequency dependent characteristics of the gyromagnetic medium in time domain. The technique has been implemented and used in the simulation of a resonance ferrite isolator.

Introduction

The TLM method yields the numerical solution of Maxwell's equations using the discretized Huygens principle [1]. The technique is efficient, general, and useful for solving complex electromagnetic problems. In TLM the medium constants are usually represented by open and short circuited stubs connected to the node, [2]. This works well for frequency independent permittivity and pemeability; however, in more complex relationships, other approaches must be used.

A major research effort in TLM is devoted to modeling of electromagnetic constitutive relationships ([3]-[5]), which describe the interaction of electric and magnetic fields with the medium. This work shows a simple procedure to represent the behavior of gyromagnetic media in the TLM algorithm.

The medium behavior is represented by equivalent sources connected to the node. The sources are determined by the constitutive equations and the total voltages and currents at the node. The differential equations describing these relationships are solved using state-variable techniques with suitable discretization schemes [6]. The resulting system of difference equations is solved at each TLM timestep.

This technique has several advantages over conventional dielectric and magnetic models used in TLM. While the use of the stub-loaded approach is more efficient for frequency independent media, the proposed technique can model several kinds of constitutive equations with few modifications to the TLM algorithm. The technique is robust, can be used with several discretization schemes, results in a

scattering matrix independent of the medium behavior, [5], and can be integrated with conventional circuit analysis programs, if the equivalent circuit of the medium behavior is available.

Theory

The general constitutive relationships are modeled in the symmetrical condensed node (SCN) TLM by decoupling the scattering matrix from the dielectric and magnetic behavior of the medium. The medium is represented by sources connected to the node.

Equivalent source approach

The SCN formulation is obtained by combining 2D shunt and series nodes, [7], decoupled from the medium. The resulting TLM procedure is:

$$[v]^r = \frac{1}{4}\begin{bmatrix} 0 & 1 & 1 & 0 & 0 & 0 & 0 & 0 & 1 & 0 & -1 & -2 \\ 1 & 0 & 0 & 0 & 0 & 1 & 0 & 0 & -2 & -1 & 0 & 1 \\ 1 & 0 & 0 & 1 & 0 & 0 & 0 & 1 & 0 & 0 & -2 & -1 \\ 0 & 0 & 1 & 0 & 1 & 0 & -1 & -2 & 0 & 0 & 1 & 0 \\ 0 & 0 & 0 & 1 & 0 & 1 & -2 & -1 & 0 & 1 & 0 & 0 \\ 0 & 1 & 0 & 0 & 1 & 0 & 1 & 0 & -1 & -2 & 0 & 0 \\ 0 & 0 & 0 & -1 & -2 & 1 & 0 & 1 & 0 & 1 & 0 & 0 \\ 0 & 0 & 1 & -2 & -1 & 0 & 1 & 0 & 0 & 0 & 1 & 0 \\ 1 & -2 & 0 & 0 & 0 & -1 & 0 & 0 & 0 & 1 & 0 & 1 \\ 0 & -1 & 0 & 0 & 1 & -2 & 1 & 0 & 1 & 0 & 0 & 0 \\ -1 & 0 & -2 & 1 & 0 & 0 & 0 & 1 & 0 & 0 & 0 & 1 \\ -2 & 1 & -1 & 0 & 0 & 0 & 0 & 0 & 1 & 0 & 1 & 0 \end{bmatrix} [v]^i + \frac{1}{4}\begin{bmatrix} 1 & 0 & 0 & 0 & 0 & 4 \\ 1 & 0 & 0 & 0 & -4 & 0 \\ 0 & 4 & 0 & 0 & 0 & -1 \\ 0 & 4 & 0 & 1 & 0 & 0 \\ 0 & 0 & 4 & -1 & 0 & 0 \\ 0 & 0 & 4 & 0 & 1 & 0 \\ 0 & 0 & 4 & 1 & 0 & 0 \\ 0 & 4 & 0 & -1 & 0 & 0 \\ 4 & 0 & 0 & 0 & 1 & 0 \\ 0 & 0 & 4 & 0 & -1 & 0 \\ 0 & 4 & 0 & 0 & 0 & 1 \\ 4 & 0 & 0 & 0 & 0 & -1 \end{bmatrix} [v_s]^i \tag{1}$$

$$[v_s]^r = \frac{1}{4}\begin{bmatrix} 1 & 1 & 0 & 0 & 0 & 0 & 0 & 0 & 1 & 0 & 0 & 1 \\ 0 & 0 & 1 & 1 & 0 & 0 & 0 & 1 & 0 & 0 & 1 & 0 \\ 0 & 0 & 0 & 0 & 1 & 1 & 1 & 0 & 0 & 1 & 0 & 0 \\ 0 & 0 & 0 & 4 & -4 & 0 & 4 & -4 & 0 & 0 & 0 & 0 \\ 0 & -4 & 0 & 0 & 0 & 4 & 0 & 0 & 4 & -4 & 0 & 0 \\ 4 & 0 & -4 & 0 & 0 & 0 & 0 & 0 & 0 & 0 & 4 & -4 \end{bmatrix} [v]^i$$

$$[v] = \begin{bmatrix} v_1 & v_2 & v_3 & v_4 & v_5 & v_6 & v_7 & v_8 & v_9 & v_{10} & v_{11} & v_{12} \end{bmatrix}^t$$

$$[v_s] = \begin{bmatrix} v_{ax} & v_{ay} & v_{az} & v_{nx} & v_{ny} & v_{nz} \end{bmatrix}^t$$

where the [v] are vectors of the branch voltages, $[v_s]$ is the source vector, and the index t indicates the transpose vector. The propagation part of the TLM method remains unchanged. The calculation of the source incident voltages $[v_s]^i$ in terms of the branch incident voltages, via the constitutive relationship of the medium and the source reflected voltages $[v_s]^r$, completes the algorithm.

Since the node sources represent the magnetizability and polarizability of the material, the source incident voltages are calculated by:

$$
\begin{aligned}
i_{polx} &= Y_r(v^r_{ax} - v^i_{ax}) = 2Y_0\Delta t\frac{dp_x}{dt} & v_{magx} &= v^r_{nx} + v^i_{nx} = 2Z_0\Delta t\frac{dm_x}{dt} \\
i_{poly} &= Y_r(v^r_{ay} - v^i_{ay}) = 2Y_0\Delta t\frac{dp_y}{dt} & v_{magy} &= v^r_{ny} + v^i_{ny} = 2Z_0\Delta t\frac{dm_y}{dt} \\
i_{polz} &= Y_r(v^r_{az} - v^i_{az}) = 2Y_0\Delta t\frac{dp_z}{dt} & v_{magz} &= v^r_{nz} + v^i_{nz} = 2Z_0\Delta t\frac{dm_z}{dt}
\end{aligned}
\tag{2}
$$

in combination with:

$$
\begin{aligned}
v_x &= v^r_{ax} + v^i_{ax} = E_x\Delta l/2 & p_x &= p_x(E_x, E_y, E_z, H_x, H_y, H_z) \\
v_y &= v^r_{ay} + v^i_{ay} = E_y\Delta l/2 & p_y &= p_x(E_x, E_y, E_z, H_x, H_y, H_z) \\
v_z &= v^r_{az} + v^i_{az} = E_z\Delta l/2 & p_z &= p_x(E_x, E_y, E_z, H_x, H_y, H_z) \\
i_x &= (v^r_{nx} - v^i_{nx})/Z_r = H_x\Delta l/2 & m_x &= m_x(E_x, E_y, E_z, H_x, H_y, H_z) \\
i_y &= (v^r_{ny} - v^i_{ny})/Z_r = H_y\Delta l/2 & m_y &= m_y(E_x, E_y, E_z, H_x, H_y, H_z) \\
i_z &= (v^r_{nz} - v^i_{nz})/Z_r = H_z\Delta l/2 & m_z &= m_z(E_x, E_y, E_z, H_x, H_y, H_z)
\end{aligned}
\tag{3}
$$

The set of equations (1)-(3) allows the modeling of arbitrary constitutive relationships in the SCN. The medium equations (2)-(3) are solved at each timestep by solving the discretized constitutive relationship differential equations.

Equations (1)-(3) can be solved using the Thevenin/Norton circuit equivalents of the node in the calculation. The node is replaced by equivalent Norton circuits (used in the calculation of the electric field), and Thevenin circuits (used in the calculation of the magnetic fields), Fig. 1.

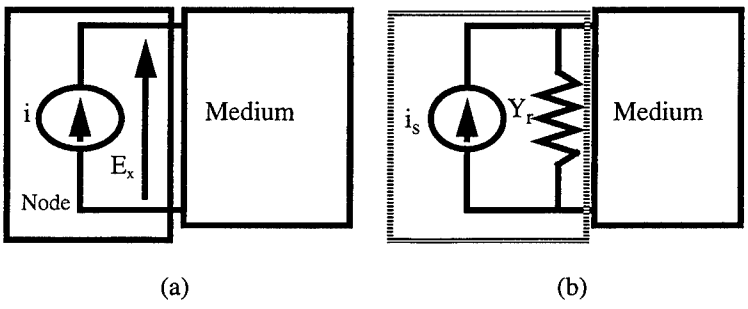

Fig. 1 Norton equivalent circuit of the node for the electric field in the x direction.

The voltage and current at the input port of each equivalent circuit can be expressed as:
a) Norton network (represents the electric field):

$$i(t) = 2Y_r v_a^r(t) - Y_r v(t) \qquad v_a^i(t) = v(t) - v_a^r(t) \tag{4}$$

b) Thevenin network (represents the magnetic field):

$$v(t) = 2Z_r v_n^r(t) - Z_r i(t) \qquad v_n^i(t) = -(4i(t) - v_n^r(t)) \tag{5}$$

These equations can be rearranged and substituted into (2), resulting in:

$$\begin{aligned} i_s(t) &= 2Y_r v_a^r(t) = Y_0 2\Delta t \frac{d}{dt} p(t) + Y_r v(t) \\ v_s(t) &= 2Z_r v_n^r(t) = Z_0 2\Delta t \frac{d}{dt} m(t) + Z_r i(t) \\ Y_r/Y_0 &= 4 \qquad Z_r/Z_0 = 4 \end{aligned} \tag{6}$$

The equivalent current sources in the three coordinate directions (Norton) are obtained from the polarization currents i_{pol} and the total voltages - representing the electric field components - across the node, similarly the equivalent voltage sources (Thevenin) are obtained from the magnetization voltages v_{mag} and total currents - representing the magnetic field components - across the node:

$$\begin{aligned} 8v_{ax}^r(t) &= 2\Delta t \frac{d}{dt} p_x(t) + 4v_x(t) & 8v_{nx}^r(t) &= 2\Delta t \frac{d}{dt} m_x(t) + 4i_x(t) \\ 8v_{ay}^r(t) &= 2\Delta t \frac{d}{dt} p_y(t) + 4v_y(t) & 8v_{ny}^r(t) &= 2\Delta t \frac{d}{dt} m_y(t) + 4i_y(t) \\ 8v_{az}^r(t) &= 2\Delta t \frac{d}{dt} p_z(t) + 4v_z(t) & 8v_{nz}^r(t) &= 2\Delta t \frac{d}{dt} m_z(t) + 4i_z(t) \end{aligned} \tag{7}$$

Since the total voltages and currents across the node are obtained in the solution of (7), an efficient way to execute the TLM algorithm is to calculate the sources $[v_s]^r$ at each timestep using, and then solve (7) using $[v_s]^r$ for the voltages (v_x, v_y, v_z) and currents (i_x, i_y, i_z). The reflected branch voltages can be obtained by [7]:

$$\begin{aligned} v_1^r &= v_x(t) - Z_r i_z(t) - v_{12}^i & v_5^r &= v_z(t) + Z_r i_x(t) - v_7^i(t) & v_9^r &= v_x(t) - Z_r i_y(t) - v_2^i \\ v_2^r &= v_x(t) + Z_r i_y(t) - v_9^i & v_6^r &= v_z(t) - Z_r i_y(t) - v_{10}^i & v_{10}^r &= v_z(t) + Z_r i_y(t) - v_6^i \\ v_3^r &= v_y(t) + Z_r i_z(t) - v_{11}^i & v_7^r &= v_z(t) - Z_r i_x(t) - v_5^i & v_{11}^r &= v_y(t) - Z_r i_z(t) - v_3^i \\ v_4^r &= v_y(t) - Z_r i_x(t) - v_8^i & v_8^r &= v_y(t) + Z_r i_x(t) - v_4^i & v_{12}^r &= v_x(t) + Z_r i_z(t) - v_1^i \end{aligned} \tag{8}$$

This procedure is applicable to all kinds of constitutive relationships. It is adapted to usual TLM programs [2] by setting $Y_x=Y_y=Y_z=Z_x=Z_y=Z_z=4$. The reflected voltages for the stubs are obtained, then (1) and (7) are used to obtain the incident voltages from the stubs, and then the reflected voltages in branches 1-12 are calculated with the scattering matrix (1).

Solving of the constitutive equations in the equivalent source approach

The equivalent node sources allow the solution of the network using nodal or Tableau analysis, [8]. Therefore, a SPICE circuit simulator could be used to solve the network at all nodes at each timestep. The problem of this approach is the need for an equivalent circuit of the medium. While this may be easy for most linear dispersive isotropic materials, it is more difficult for an arbitrary constitutive relationship.

However, the use of state-variable formulation of the constitutive relationship equations avoids this problem. In this approach, equivalent circuits for the constitutive relationships are not necessary, since the state-equations can be obtained directly from nonlinear differential equations. The state-variable technique is easily incorporated into the TLM simulator without loss of generality. A general procedure for linear differential equations shown in [6] is outlined for a medium described by a fourth order linear differential equation:

$$a\frac{d^4f}{dt} + b\frac{d^3f}{dt} + c\frac{d^2f}{dt} + d\frac{df}{dt} + ef = g \tag{9}$$

resulting in:

$$\frac{d}{dt}\begin{bmatrix} x_1(t) \\ x_2(t) \\ x_3(t) \\ x_4(t) \end{bmatrix} = \frac{1}{a}\begin{bmatrix} -b & 1 & 0 & 0 \\ -c & 0 & 1 & 0 \\ -d & 0 & 0 & 1 \\ -e & 0 & 0 & 0 \end{bmatrix}\begin{bmatrix} x_1(t) \\ x_2(t) \\ x_3(t) \\ x_4(t) \end{bmatrix} + \begin{bmatrix} 0 & 0 & 0 & 0 \\ 0 & 0 & 0 & 0 \\ 0 & 0 & 0 & 0 \\ 0 & 0 & 0 & \frac{1}{a} \end{bmatrix}\begin{bmatrix} 0 \\ 0 \\ 0 \\ g(t) \end{bmatrix} \tag{10}$$

where: $x_1(t)=f(t)$

The resulting equations can be incorporated into TLM either by discretizing the solution or the differential operator. The discrete solution of (10) would result in a convolution procedure, restricting the use of the formulation to linear materials. If the discretized operator approach is used, several discretization schemes may be chosen. However, there are two major schemes that are very attractive, for reasons of efficiency:

- Backwards Euler, [6]
- Trapezoidal (or bilinear mapping), [6]

The first scheme introduces losses in the final result, it is first-order accurate, but it is very simple to implement. The second scheme is accurate to the second order, conserves energy and uses the same kind of discretization as in TLM. Therefore, for linear isotropic non-dispersive materials, the results given by this approach and usual TLM are virtually indistinguishable.

However, the use of trapezoidal schemes for the solution of gyromagnetic materials can cause instabilities in the result due to the nature of the constitutive equation.

The discretization schemes transform the continuous state equations:

$$\begin{aligned} \frac{d}{dt}[x(t)] &= [A][x(t)] + [B][u(t)] \\ [y(t)] &= [C][x(t)] + [D][u(t)] \end{aligned} \tag{11}$$

into the discretized form:

$$[x(t+\Delta t)] = [P][x(t)] + [Q][u(t)] + [R][x(t-\Delta t)]$$
$$[y(t+\Delta t)] = [C][x(t+\Delta t)] + [D][u(t+\Delta t)] \tag{12}$$

The matrices [P], [Q] and [R] will depend on the discretization scheme. In the backwards Euler approach:

$$[P] = ([U] - \Delta t[A])^{-1} \qquad ([Q] = ([U] - \Delta t[A])^{-1}\Delta t[B] \qquad [R] = [0]) \tag{13}$$

where [U] is the nxn identity matrix, and [0] is the null matrix.

Representation of the constitutive relationships in the state-variable form

This section describes the implementation of the state-variable equations for gyromagnetic media. Considering a gyromagnetic material subject to a magnetization field H_0 in the z-direction with magnetization M_0 in the same direction, the linearized constitutive equations for the permeability are:

$$\frac{dm_x}{dt} = \omega_0 m_y - \omega_m m_y \qquad \frac{dm_y}{dt} = -\omega_0 m_x + \omega_m m_x \tag{14}$$

where ω_0 and ω_m are obtained from the bias magnetic field and the saturation magnetization:

$$\omega_0 = \Upsilon H_0 \qquad \omega_m = \Upsilon M_0$$
$$\Upsilon = 2\pi \times 2.8 \times 10^6 \, (Hz/Oe) \tag{15}$$

The constitutive equations (14) can be expressed in the state variable form:

$$\frac{d}{dt}\begin{bmatrix} m_x \\ m_y \end{bmatrix} = \frac{2\omega_0 Z_r}{Z_r^2 + (2\Delta t\omega_m)^2}\begin{bmatrix} 2\Delta t\omega_m & -Z_r \\ Z_r & 2\Delta t\omega_m \end{bmatrix}\begin{bmatrix} m_x \\ m_y \end{bmatrix} + \frac{2\omega_m Z_r}{Z_r^2 + (2\Delta t\omega_m)^2}\begin{bmatrix} -2\Delta t\omega_m & Z_r \\ -Z_r & 2\Delta t\omega_m \end{bmatrix}\begin{bmatrix} v_{nx} \\ v_{ny} \end{bmatrix}^r \tag{16}$$

where the total magnetic fields in the x- and y-directions are calculated using (3) and (7).

Results

The technique presented in this work has been used to simulate an E-plane resonance isolator in a WR90 waveguide, [9]. The device was designed to have a 30 dB reverse attenuation at 10 GHz. The ferrite slab was 0.5 mm wide, 24 mm long, and placed at 2.54 mm from one of the inner waveguide walls, with a saturation magnetization of 1700 Gauss and a bias magnetic field of 2840 Oersteds, (Fig. 2). The scheme used to solve (16) was the backwards Euler scheme, because of stability problems encountered with the trapezoidal discretization approach.

Since the backwards Euler scheme introduces numerical losses, it avoided the instability problems obtained using energy conservative schemes. The results, presented in Fig. 3, are the transmission coefficients for the forward and backward propagation (S21 and S12).

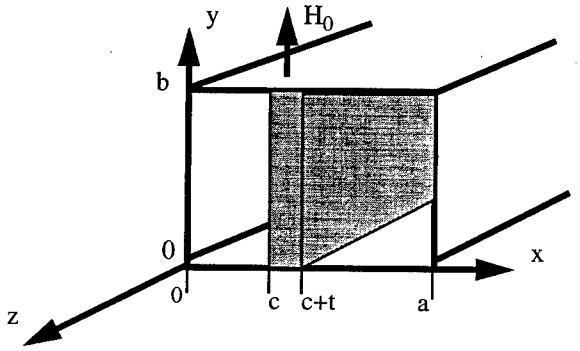

Fig. 2 Geometry of the resonance ferrite isolator.

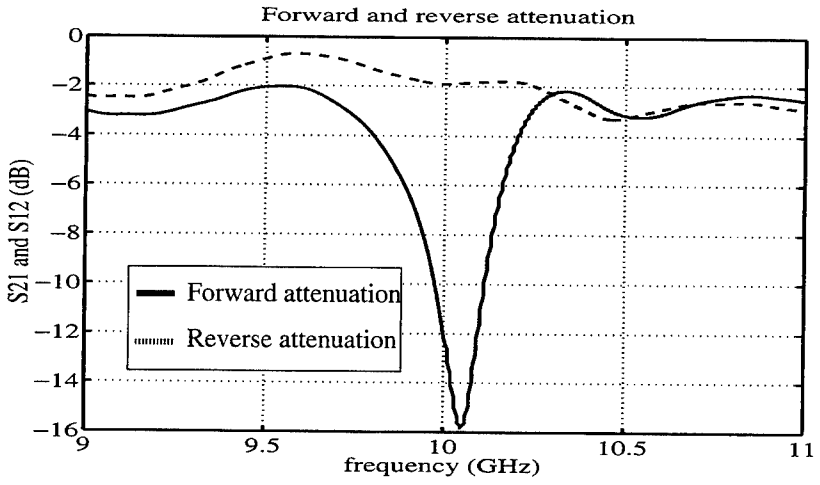

Fig. 3 Forward and reverse transmission coefficients of the resonance isolator.

The results shown in Fig. 3 show less reverse attenuation than expected. This was caused by the sensitivity of the results to the placement of boundaries, and the difficulty to simultaneously position the slab and to discretize its thickness. However, there was very good agreement of the forward attenuation (- 2.0 dB at 10 GHz), and of the bandwidth of the isolator (4%).

Conclusions

This work presented the symmetrical condensed node (SCN) TLM model of gyromagnetic materials. The constitutive relationships were represented by equivalent sources connected to the node. The resulting TLM scattering matrix was independent of the material behavior. The equivalent source was calculated at each timestep using state-variable techniques and included in the scattering procedure of TLM. The approach was presented for general medium equations, and used in the calculation of the forward and reverse attenuation of a resonance ferrite isolator. The main difficulties encountered in the simulation of this structure were stability and sensitivity problems. The resulting state-variable equations showed instability problems for lossless discretization schemes, which were solved by using backwards Euler discretization procedure. The energy loss associated with the scheme caused an increase in the forward and reverse attenuation of the isolator. The forward and reverse attenuations of the isolator were highly sensitivity to the positioning and width of the ferrite slab. Since its was not possible to model accurately both position and width of the slab, the computed s reverse attenuation was less than the design specification. The results can be improved by using special TLM cells with arbitrary boundary positioning. This technique is now being extended to gyromagnetic materials with losses and to other kinds of TLM nodes.

References

[1] W.J.R. Hoefer, "The transmission line matrix method - theory and applications", *IEEE Trans. Microwave Theory and Tech.*, vol. 33, Oct. 1985.

[2] P.B. Johns, "A Symmetrical Condensed Node for the TLM Method", *IEEE Trans. Microwave Theory and Tech.*, vol. 35, n. 4, pp. 370-377, Apr. 1987

[3] L. de Menezes, W.J.R. Hoefer, "Modelling frequency dependent dielectrics in TLM", *IEEE AP-S Symposium Digest*, pp. 1140-1143, Jun. 1994

[4] L. de Menezes, W.J.R. Hoefer, "Modelling nonlinear dispersive media in 2D-TLM", *24th European Microwave Conference Proceedings*, pp.1739-1744, Sept. 1994

[5] L. de Menezes, W.J.R. Hoefer, "Modelling of general constitutive relationships in SCN TLM", *IEEE MTT-S Symposium Digest*, pp. 365-368, Jun. 1995

[6] R. DeCarlo *Linear Systems - A State-Variable Approach with Numerical Implementation,* Prentice-Hall, 1989.

[7] P. Naylor and R. Ait-Sadi, "Simple method for determining 3-D TLM nodal scattering in non-scalar problems," *Electronic Letters*, vol. 28, pp. 2353-2354, Dec. 3, 1992.

[8] L. Chua, C, Desoer and E. Kuh - *Linear and nonlinear circuits*, McGraw-Hill, 1987

[9] D. M. Pozar, *Microwave Engineering, Addison* Wesley, 1990

A Comparative Performance Study of Absorbing Boundary Conditions in TLM and FDTD

Channabasappa Eswarappa and Wolfgang J. R. Hoefer

NSERC/MPR Teltech Research Chair in RF Engineering, Department of Electrical and Computer Engineering, University of Victoria, Victoria, B.C., CANADA V8W 3P6

Abstract

In this paper, a comparative performance study of Higdon's absorbing boundary conditions (ABCs) in TLM and FDTD under identical conditions (such as same time step, excitation, etc.) is described. It has been observed that an ABC applied directly to the TLM voltage impulses absorbs better than the same ABC applied to the TLM total node voltages or FDTD field values. It has also been found that in a FDTD analysis, the damping factors have a greater influence on the stability than the way in which the absorbing boundary operators are discretized, while in a TLM analysis the opposite is true. Also, in a TLM analysis, the absorbing boundaries can be placed closer to a scatterer than in a FDTD analysis without affecting the accuracy. These observations have been demonstrated by applying them to examples such as waveguides and high permittivity dielectric cubes.

Introduction

The Transmission Line Matrix (TLM) [1] and Finite-Difference Time-Domain (FDTD) [2] methods are suitable for time-domain simulation of complex guiding and radiating structures. The TLM method is a physical discretization model whereas FDTD is a mathematical discretization model. The TLM method has advantages in boundary description, while the FDTD method requires less computer memory. Recently, we have developed real-time interfaces between TLM and FDTD modules [3-4], and Marcysiak and Gwarek [5] have given the equivalent excitation schemes that produce identical field values at all time steps in the expanded-TLM and FDTD meshes.

Good quality ABCs are very important for time-domain simulations of electromagnetic structures. Even though a number of ABCs have been reported in the literature, Higdon's ABCs [6-8] have been found to perform better than others [9]. The advantages of Higdon's ABCs are that prior information about the incident angles can be used to optimize the absorption in the required frequency bandwidth, and long term stability can be achieved by using proper discretization of the boundary operators (derivatives) and/or by providing damping factors. Very low reflections can be obtained by concatenating two or more first-order boundary operators.

In TLM, the absorbing boundary conditions can be applied directly to the TLM voltage impulses reflected by the ABC or to the total node voltages, while in FDTD they are normally applied to the electric fields. We have studied the absorption properties of Higdon's absorbing boundaries in TLM and FDTD by applying them to a rectangular waveguide, while the stability aspect has been studied by computing the RCS of a high permittivity dielectric cube. As this cube rings for a very long time, it is a very good test case to check the stability aspect of the absorbing boundaries.

Absorbing Boundary Conditions

To obtain good absorption over a wide range of incident angles, we have concatenated two first-order Higdon's boundary operators to obtain a second-order absorbing boundary condition [8]. In FDTD, a field value at the absorbing boundary can be computed from the knowledge of field values at the cells in front of the boundary using the following equation:

$$\begin{aligned} E^n(m,j,k) &= (\alpha_1+\alpha_2)E^{n-1}(m,j,k) - \alpha_1\alpha_2 E^{n-2}(m,j,k) + (\beta_1+\beta_2)E^n(m-1,j,k) \\ &+ (\gamma_1+\gamma_2-\alpha_1\beta_2-\beta_1\alpha_2)E^{n-1}(m-1,j,k) - (\alpha_1\gamma_2+\gamma_1\alpha_2)E^{n-2}(m-1,j,k) \\ &-\beta_1\beta_2 E^n(m-2,j,k) - (\beta_1\gamma_2+\gamma_1\beta_2)E^{n-1}(m-2,j,k) - \gamma_1\gamma_2 E^{n-2}(m-2,j,k) \end{aligned} \quad (1)$$

The interpolation coefficients are:

$$\alpha_i = \frac{(a-g_i(1-b))}{(a-1-g_i(1-b)-\varepsilon_i\Delta l)}, \beta_i = \frac{(a-1+g_i b)}{(a-1-g_i(1-b)-\varepsilon_i\Delta l)}, \gamma_i = \frac{(-a-bg_i)}{(a-1-g_i(1-b)-\varepsilon_i\Delta l)} \quad (2)$$

where coefficients a and b are weighted time and space averages of the space and time differences, respectively. ε_1 and ε_2 are damping factors. The parameter g_i is

$$g_i = \frac{\cos\theta_i}{c}\,\frac{\Delta l}{\Delta t} \quad (3)$$

where Δl and Δt are the space resolution and time step, respectively. θ_i are the incidence angles which can be chosen to optimize the absorption bandwidth. The values of coefficients a and b can be chosen to control the stability of the absorbing boundaries. According to Higdon [6], a must be less than or equal to 0.5 (for $a=b$) to get stable absorbing boundary conditions.

In TLM, the above ABC can be applied in the following two ways:

a) Application of ABC to the total node voltages, V_z:

The interpolation equation (1) is applied to the total voltages at the nodes on the absorbing boundary. Then the impulses incident at the nodes from the absorbing boundary can be obtained by subtracting the other three voltage impulses from the total node voltages (see Fig. 1):

$${}_{inc}V_4^{n-\frac{1}{2}}(i,JR) = 2V_z^n(i,JR) - {}_{inc}[V_1(i,JR)+V_2(i,JR)+V_3(i,JR)]^{n-\frac{1}{2}} \quad (4)$$

b) Application of ABC directly to the TLM voltage impulses:

The interpolation equation (1) is applied directly to the TLM voltage impulses to obtain the voltage impulses incident at the absorbing boundary nodes. For example, in Fig. 2, the absorbing boundary conditions are applied directly to the incident voltage impulses ${}_{inc}V_4$. Since, these incident voltage impulses contain both E_z and H_y, it is equivalent to applying ABC to both electric and magnetic fields simultaneously.

Numerical Results

First, we have applied the above ABCs at the two ends of a WR 28 rectangular waveguide section. We have employed a 2D shunt TLM mesh and a 2D FDTD mesh. The mesh size was (100x42). The space resolution and time step were 0.169 mm and 0.399 ps, respectively. The dominant TE_{10} mode in the waveguide was excited by injecting the total voltages (E_z values in FDTD) in a line

whose magnitudes distributed according to the sine function. Cosine modulated Gaussian temporal variation was used to make sure that only the frequencies of interest were excited. The electric field values were sampled along the propagation direction and Fourier transformed to obtain the minimum and maximum field values at each frequency. The magnitude of reflections obtained as (VSWR-1)/(VSWR+1) are plotted in Figs. 3a and 3b for two sets of incident angles. We can see that the plot of the reflections of the ABC applied to the TLM total node voltages is overlapping with that of the reflections of the ABC applied to FDTD. But, the reflections obtained for the ABC applied to the incident TLM impulse voltages are lower by about 20 dB. It should be noted here that the superior performance of the absorbing boundaries in the TLM environment has also been independently observed by Giannopoulos and Tealby [10]. They have observed that even the first-order ABC applied to the TLM voltage impulses performs better than the second-order ABC applied to the FDTD/TLM (total node voltage).

As mentioned before, we have considered a high permittivity dielectric cube to study the stability aspect. The size of the cube was 7.72 mm and its permittivity was 79.46. This cube rings for a very long time [11-12]. We have employed a 3D symmetrical condensed node TLM [13] mesh and a 3D FDTD mesh for the analysis of the cube. It was discretized with 15 cells on each side. The space resolution and time step were 0.5147 mm and 0.8578 ps, respectively. A plane wave with a electric field component E_y and magnetic field component H_z was incident on one face of the cube normally (shown in Fig. 4). This was achieved in the symmetrical condensed node by launching the impulses on branch 3. We have used a cosine modulated Gaussian pulse as the excitation to make sure that only the frequencies of interest were excited. This also ensured that the D.C. and very low frequencies were not excited, otherwise, the absorbing boundaries could not be placed close to the cube surface. The excitation Gaussian pulse width (corresponding to -34 dB) was 148 Δt. The values of the incidence angles used in the design of the absorbing boundaries were 30^0 and 80^0.

The absorbing boundaries were placed 20 cells away from the cube surfaces. This distance is often referred to as white space [11]. The mesh size was (55x55x55). In case of the TLM analysis, we observed growing oscillations beyond 2000 time steps for positive values of coefficients $a=b=0.25$. However, for negative values of the coefficients $a=b=-0.25$ there is no stability problem (see Figs. 5a and 5b). Stability beyond 60,000 time steps has been obtained with a white space of just 20 Δl. The RCS computed with 60,000 TLM time steps is plotted in Fig. 8 for a bistatic angle of 8 degrees. The computation compares well with the measurements.

Next, we have used the FDTD method to analyze the same structure. The same space resolution, time step, white space (20 Δl) and absorbing boundary parameters were used. We observed growing time responses for both positive and negative values of the coefficients a and b (see Figs. 6a and 6b). Growing oscillations beyond 32,768 time steps have also been reported in the FDTD analysis of the cube using Mur's absorbing boundaries in spite of a larger white space of 40 Δl [11]). However, introduction of the damping factors controlled the growth, but the time response (see Figs. 7a) has a slight oscillatory behaviour around D.C. The RCS plot computed with this time response is not smooth (see Fig. 9), and the results are machine dependent. This shows how the computer round off errors can affect a time-domain analysis when the absorbing boundaries are placed close to a scatterer. We tried with different values of the damping factors, but the results were only slightly better. This may be due to the interaction of near fields with the absorbing boundaries. To ascertain this, we increased the white space from 20 Δl to 30 Δl. This increases the

computational space from 166,375 cells to 274,625 cells, i.e. by a factor of 1.65 times. The FDTD time response is plotted in Fig. 7b It does not have any oscillatory behavior around D.C. RCS data computed with this time response are plotted in Fig. 8. Both FDTD and TLM results compare well with measurements at lower frequencies. At higher frequencies, the FDTD and TLM results are shifted towards the lower end with respect to the measurement. However, this shift is larger for the FDTD results than the TLM results.

Conclusions

The performance of Higdon's ABCs in TLM and FDTD under identical conditions has been studied. ABCs applied directly to the TLM voltage impulses absorb better than those applied to the TLM total node voltages or FDTD fields. Our study shows that in a FDTD analysis the damping factors have a greater influence on the stability, while in a TLM analysis the discretization coefficients such as the weighted space average of the time difference and the weighted time average of the space difference have a greater effect than the damping factors. Also, in a TLM analysis, the absorbing boundaries can be placed closer to the scatterer than in a FDTD analysis. These features of TLM outweigh the computational efficiency of the FDTD method in the examples presented above.

References

[1] W. J. R. Hoefer, "The Transmission Line Matrix (TLM) Method", in T. Itoh: *Numerical Techniques for Microwave and Millimeter Wave Passive Structures*, John Wiley & Sons, New York.

[2] K.S. Yee, "Numerical Solution of Initial Boundary Value Problems Involving Maxwell's Equations", *IEEE Trans. Antennas and Propagation,* vol. 14, no.3, pp. 302-307, May 1966.

[3] C. Eswarappa and W.J.R. Hoefer, "Bridging the gap between TLM and FDTD", *IEEE Microwave and Guided Wave Letters*, vol. 6, no. 1, pp. 1-3, January 1996.

[4] C. Eswarappa and W.J.R. Hoefer, "Implementation of Berenger Absorbing Boundary Conditions in TLM by interfacing FDTD Perfectly Matched Layers", *Electronics Letters,* vol. 31, no. 15, pp. 1264-1266, 20th July 1995.

[5] M. Celuch-Marcysiak and W.K. Gwarek, "Generalized TLM Algorithms with Controlled Stability Margin and Their Equivalence with Finite-Difference Formulations for Modified Grids", *IEEE Trans. Microwave Theory and Techniques*, vol. 43, no. 9, pp. 2081-2089, Sept. 1995.

[6] R. L. Higdon, "Numerical absorbing boundary condition for the wave equation," *Mathematics of Computation*, vol. 49, no. 179, pp. 65-91, July 1987.

[7] Z. Chen, M.M. Ney, and W.J.R. Hoefer, "Absorbing and Connecting Boundary Conditions for the TLM Method", *EEE Trans. Microwave Theory Tech.*, vol. MTT-41, no. 11, pp. 2016-2024, 1993.

[8] C. Eswarappa and W.J.R. Hoefer, "One-Way Equation Absorbing Boundary Conditions for 3-D TLM Analysis of Planar and Quasi-planar Structures", *IEEE Trans. Microwave Theory Techniques*, vol. 42, no. 9, pp. 1669-1677, Sep. 1994.

[9] D. Steich and R. Luebbers, "Comparison and Generation of Higher Order FDTD Absorbing Boundaries", *10th Annual Review of Progress in Applied Computational Electromagnetics* Digest, pp. 212-233, March 21-26, 1994, Monterey, CA.

[10] A. Giannopoulos and J.M. Tealby, "Comparison of performance of absorbing boundary conditions in TLM and FDTD", *Electronics Letters*, 14th Sept. 1995, vol. 31, no. 9, pp. 1639-1640.

[11] C.W. Trueman, S.J. Kubina, R.J. Luebbers, S.R. Mishra, and C. Larose, "RCS of High Permittivity Cubes by FDTD and by Measurement", *9th Annual Review of Progress in Applied Computational Electromagnetics* Digest, pp. 2-10, March 22-26, 1993, Monterey, CA.

[12] C. Eswarappa and W.J.R. Hoefer, "RCS of high permittivity cubes computed with the TLM method" *11th Annual Review of Progress in Applied Computational Electromagnetics* Digest, pp. 13-20, March 20-25, 1995, Monterey, CA.
[13] P. B. Johns, "Symmetrical Condensed Node for the TLM method", *IEEE Trans. Microwave Theory Tech.*, vol. MTT-35, no. 4, pp. 370-377, April 1987.

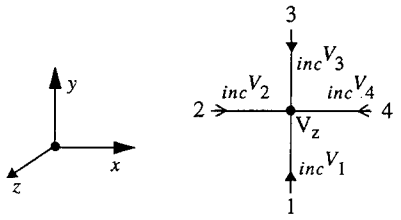

Fig. 1a: 2-D Shunt TLM Node

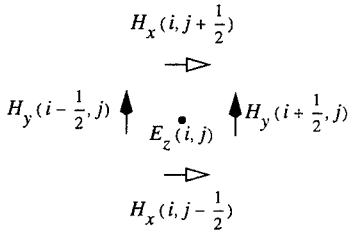

Fig. 1b: 2-D FDTD Node

$$E_z^n(i,j) \equiv V_z^n(i,j) = \frac{1}{2}\,{}_{inc}[V_1(i,j) + V_2(i,j) + V_3(i,j) + V_4(i,j)]^{n-\frac{1}{2}}$$

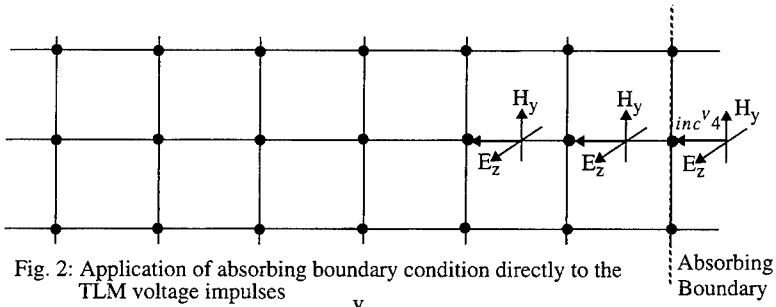

Fig. 2: Application of absorbing boundary condition directly to the TLM voltage impulses

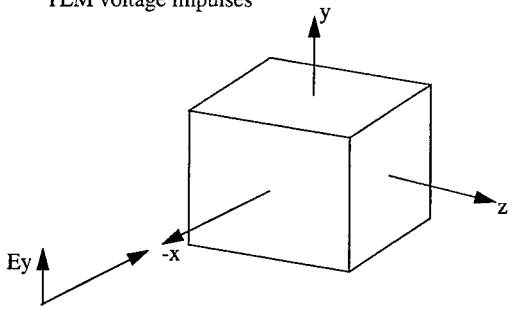

Fig. 4: The high permittivity cube with incident electric field E_y (cube side length = 7.72 mm, $\varepsilon_r = 79.46$, bistatic angle = 8 degrees)

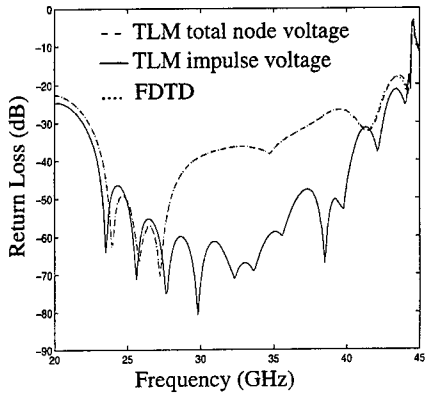

Fig. 3a: Return loss of Higdon's second-order absorbing boundary condition in a WR28 waveguide (a = 0.5, b = 0.5, $\theta_1 = 30^0$, $\theta_2 = 45^0$, $\varepsilon_1 = 0.0$, $\varepsilon_2 = 0.0$)

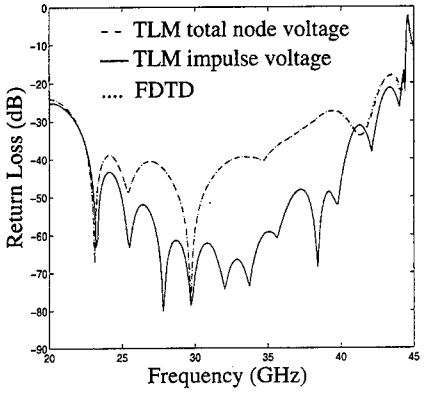

Fig. 3b: Return loss of Higdon's second-order absorbing boundary condition in a WR28 waveguide (a = 0.5, b = 0.5, $\theta_1 = 5^0$, $\theta_2 = 60^0$, $\varepsilon_1 = 0.0$, $\varepsilon_2 = 0.0$)

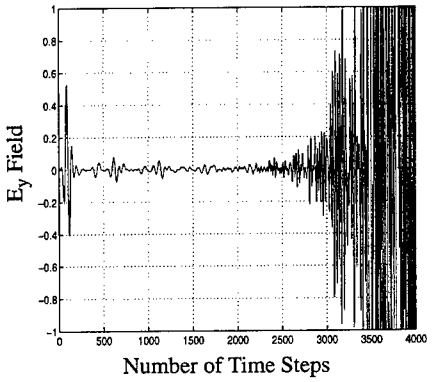

Fig. 5a: TLM time response of the high permittivity cube with positive coefficients *a* and *b* (*a*=0.25, *b*=0.25, $\theta_1=30^0$, $\theta_2=80^0$, $\varepsilon_1 = 0.0$, $\varepsilon_2 = 0.0$, white space = 20 Δl)

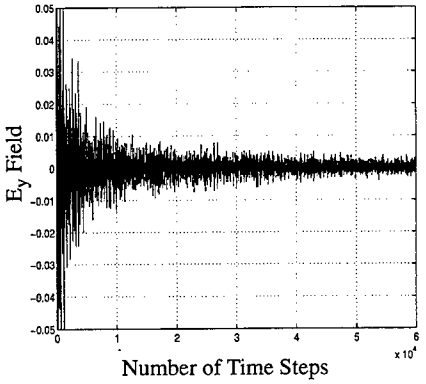

Fig. 5b: TLM time response of the high permittivity cube with negative coefficients *a* and *b* (*a*=-0.25, *b*=-0.25, $\theta_1=30^0$, $\theta_2=80^0$, $\varepsilon_1 = 0.0$, $\varepsilon_2 = 0.0$, white space = 20 Δl)

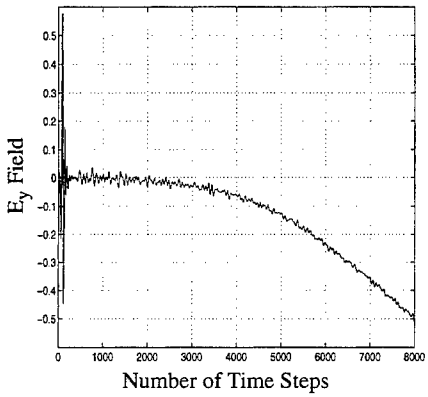

Fig. 6a: FDTD time response of the high permittivity cube with positive coefficients a and b (a = 0.5, b = 0.5, θ_1 = 30^0, θ_2 = 80^0, ε_1 = 0.0, ε_2 = 0.0, white space = 20 Δl)

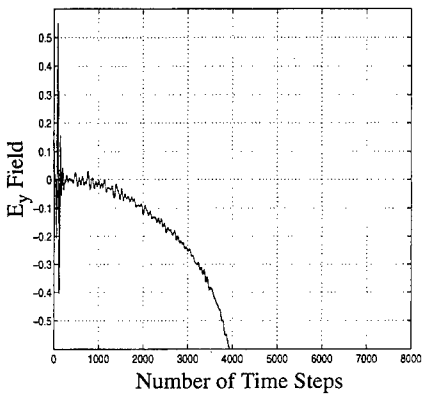

Fig. 6b: FDTD time response of the high permittivity cube with negative coefficients a and b (a = - 0.25, b = - 0.25, θ_1 = 30^0, θ_2 = 80^0, ε_1 = 0.0, ε_2 = 0.0, white space = 20 Δl)

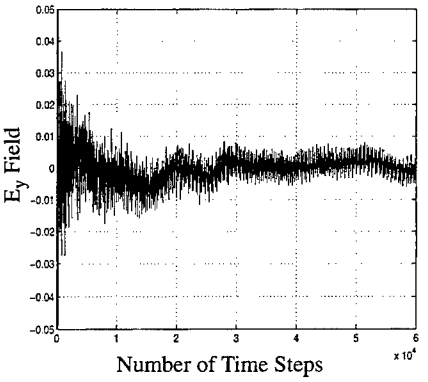

Fig. 7a: FDTD time response of the high permittivity cube with white space = 20 Δl (a = 0.5, b = 0.5, θ_1= 30^0, θ_2= 80^0, ε_1 = 0.001, ε_2 = 0.001)

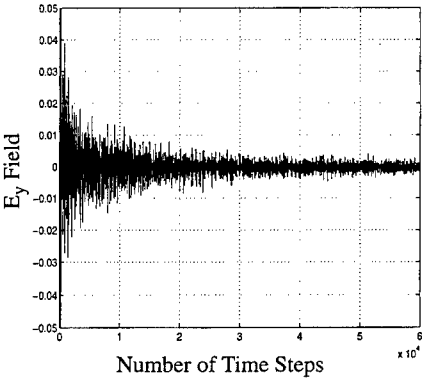

Fig. 7b: FDTD time response of the high permittivity cube with white space = 30 Δl (a = 0.5, b = 0.5, θ_1= 30^0, θ_2= 80^0, ε_1 = 0.01, ε_2 = 0.0)

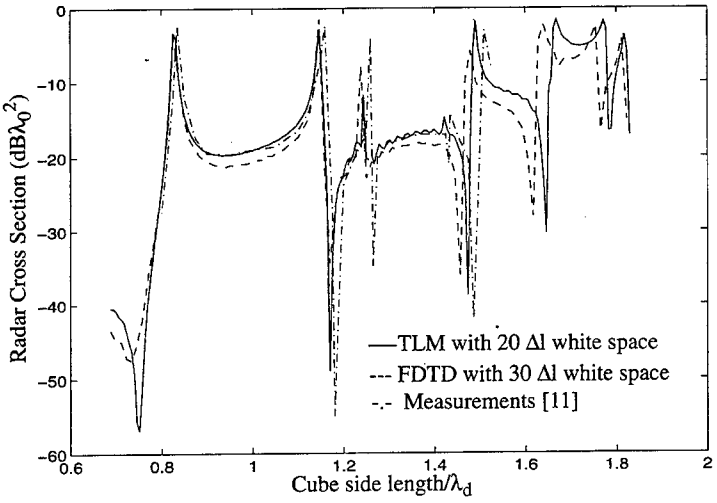

Fig. 8: RCS computed with TLM, FDTD and comparison with measurements

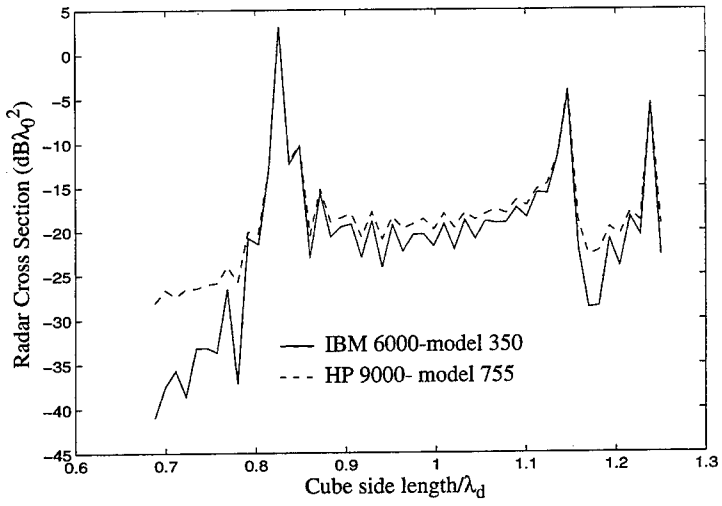

Fig. 9: RCS computed with FDTD for white space = 20 Δl

Modelling of Coplanar Waveguide Discontinuities using the Alternating Transmission Line Matrix (ATLM) Method

B. Bader[1], P. Russer[2]

[1] Ferdinand-Braun-Institut für Höchstfrequenztechnik, Berlin, Germany, Rudower Chaussee 5, D-12489 Berlin, Germany, phone +49 30 63922628, fax +49 30 63922602

[2] Lehrstuhl für Hochfrequenztechnik, Technische Universität München, Arcisstr. 21, D-80333 München, Germany, phone +49 89 21058390, fax +49 89 21053365

Abstract

The three-dimensional alternating transmission line matrix scheme (ATLM) is applied to the modelling of coplanar waveguide discontinuities. In the ATLM scheme the TLM cells are subdivided into two subsets of mutually neighbouring cells. Within each time step the state of one subset of cells is computed from the states of the neighbouring cells at the previous time step. Compared with existing TLM schemes the numerical effort as well as the storage requirements are reduced by up to 50% without loss of accuracy. Furthermore, spurious solutions occuring in existing TLM schemes can be avoided by ATLM.

1 Introduction

The modelling of coplanar waveguide structures requires three-dimensional electromagnetic full-wave simulation [1]. For modelling coplanar discontinuities the TLM method exhibits the advantage, that a great variety of structures may be analyzed without a high effort of adapting the method to the specific problem. The three-dimensional TLM method with symmetrical condensed node (SCN) introduced by Johns [2] has proven to be a very powerful method of electromagnetic field computation [3]. In the alternating transmission line matrix (ATLM) scheme the TLM cells are subdivided into two subsets of mutually neighbouring cells. Within each time step the state of one subset of cells is computed from the states of the neighbouring cells at the previous time step. Compared with existing TLM schemes the numerical effort as well as the storage requirements are reduced by up to 50% without loss of accuracy. Furthermore, spurious solutions occuring in existing TLM schemes can be avoided by ATLM [4, 5].

In homogeneous regions modelled by TLM without stubs there is no mutual dependence of the states of neighbouring cells. This can be seen clearly if we define a so-called parity p assigned to TLM wave pulses discrete space coordinates l, m, n and the discrete time coordinate k by

$$p = \text{sign}\,(k + l + m + n)\,. \tag{1}$$

If the sum $k + l + m + n$ is even then $p = +1$ and if $k + l + m + n$ is odd then $p = -1$. Now it is easy to check that in any TLM mesh without stubs and boundaries the TLM pulses

depend only on previous pulses with the same parity. If in the complete TLM mesh including stubs only transmission line elements of length Δl are used, the parity of all transmitted and reflected pulses is conserved. Regions with different permittivites can be modeled using a TLM mesh with constant Δl if stubs are introduced. In order to maintain synchronism, in ATLM stubs of length Δl instead of stubs with length $\Delta l/2$ have to be used.

2 Modelling of Dielectric Media in SCN-ATLM

In ATLM with symmetrical condensed node (SCN) dielectric and resistive media are modelled via stubs. The permittivity and the permeability of the material determine the characteristic admittance and impedance of the stubs. If regions with different permittivities are modelled the region with the lowest permittivity may be modelled without stub. Modelling of losses is also possible. Therefore resistive stubs are introduced, which do not reflect incident pulses.

In contrast to ordinary SCN-TLM with stubs the stub length has to be increased from $\Delta l/2$ to Δl. If a stub length of Δl is chosen, the pulses reflected from the end of the stub are synchronous with the pulses propagating in the mesh. This is achieved by storing the pulses for two time steps in the stubs. Therefore, we have to change the stub admittances and impedances for compensating the double length, i. e. one half of y_s and z_s of the $\Delta l/2$ stubs are assigned to the corresponding parameters of the Δl stubs.

The three-dimensional condensed node scheme will be extended in the following way. The scattering matrix $\boldsymbol{S}$ in the symmetrical notation corresponding to fig. 1 is given by

$$\boldsymbol{S} = \begin{bmatrix} \boldsymbol{S}_0 & \boldsymbol{K} \\ \boldsymbol{K}^\top & \boldsymbol{L} \end{bmatrix} , \tag{2}$$

$$\boldsymbol{S}_0 = \begin{bmatrix} \boldsymbol{A} & \boldsymbol{B} & \boldsymbol{B}^\top \\ \boldsymbol{B}^\top & \boldsymbol{A} & \boldsymbol{B} \\ \boldsymbol{B} & \boldsymbol{B}^\top & \boldsymbol{A} \end{bmatrix}, \quad \boldsymbol{A} = \begin{bmatrix} \alpha & \beta & 0 & 0 \\ \beta & \alpha & 0 & 0 \\ 0 & 0 & \alpha & \beta \\ 0 & 0 & \beta & \alpha \end{bmatrix}, \quad \boldsymbol{B} = \begin{bmatrix} 0 & 0 & \delta & -\delta \\ 0 & 0 & -\delta & \delta \\ \gamma & \gamma & 0 & 0 \\ \gamma & \gamma & 0 & 0 \end{bmatrix}, \tag{3}$$

and

$$\boldsymbol{K} = \begin{bmatrix} \boldsymbol{K}_{11} & \boldsymbol{K}_{12} \\ \boldsymbol{K}_{21} & \boldsymbol{K}_{22} \\ \boldsymbol{K}_{31} & \boldsymbol{K}_{32} \end{bmatrix}, \quad \boldsymbol{L} = \begin{bmatrix} \boldsymbol{L}_{11} & 0 \\ 0 & \boldsymbol{L}_{22} \end{bmatrix}, \tag{4}$$

$$\boldsymbol{K}_{11} = \begin{bmatrix} 0 & \chi_1 & 0 \\ 0 & \chi_1 & 0 \\ 0 & 0 & \chi_1 \\ 0 & 0 & \chi_1 \end{bmatrix}, \quad \boldsymbol{K}_{21} = \begin{bmatrix} 0 & 0 & \chi_1 \\ 0 & 0 & \chi_1 \\ \chi_1 & 0 & 0 \\ \chi_1 & 0 & 0 \end{bmatrix}, \quad \boldsymbol{K}_{31} = \begin{bmatrix} \chi_1 & 0 & 0 \\ \chi_1 & 0 & 0 \\ 0 & \chi_1 & 0 \\ 0 & \chi_1 & 0 \end{bmatrix},$$

$$\boldsymbol{K}_{12} = \begin{bmatrix} 0 & 0 & -\chi_2 \\ 0 & 0 & \chi_2 \\ 0 & \chi_2 & 0 \\ 0 & -\chi_2 & 0 \end{bmatrix}, \quad \boldsymbol{K}_{22} = \begin{bmatrix} -\chi_2 & 0 & 0 \\ \chi_2 & 0 & 0 \\ 0 & 0 & \chi_2 \\ 0 & 0 & -\chi_2 \end{bmatrix}, \quad \boldsymbol{K}_{32} = \begin{bmatrix} 0 & -\chi_2 & 0 \\ 0 & \chi_2 & 0 \\ \chi_2 & 0 & 0 \\ -\chi_2 & 0 & 0 \end{bmatrix}, \tag{5}$$

and

$$\boldsymbol{L}_{11} = \begin{bmatrix} \chi_3 & 0 & 0 \\ 0 & \chi_3 & 0 \\ 0 & 0 & \chi_3 \end{bmatrix}, \quad \boldsymbol{L}_{22} = \begin{bmatrix} \chi_4 & 0 & 0 \\ 0 & \chi_4 & 0 \\ 0 & 0 & \chi_4 \end{bmatrix}. \tag{6}$$

The parameters α, β, γ, δ and χ_i are given by

$$\alpha = -\frac{y_s + g_s}{8 + 2y_s + 2g_s} + \frac{z_s + r_s}{8 + 2z_s + 2r_s}, \quad \beta = -\frac{y_s + g_s}{8 + 2y_s + 2g_s} - \frac{z_s + r_s}{8 + 2z_s + 2r_s}, \tag{7}$$

$$\gamma = \frac{2}{4 + y_s + g_s}, \quad \delta = \frac{2}{4 + z_s + r_s}, \tag{8}$$

$$\chi_1 = \sqrt{y_s}\gamma, \quad \chi_2 = \sqrt{z_s}\delta, \quad \chi_3 = \frac{y_s - g_s - 4}{y_s + g_s + 4}, \quad \chi_4 = \frac{4 - z_s + r_s}{4 + z_s + r_s}, \tag{9}$$

with the stub admittance and impedance

$$y_s = 2(\varepsilon_r - 1) \quad , \qquad z_s = 2(\mu_r - 1)\,. \tag{10}$$

The electric losses σ_e and the magnetic losses σ_m are introduced by

$$g_s = \frac{1}{2}\sigma_e \Delta l Z_0\,, \quad r_s = \frac{1}{2}\sigma_m \Delta l Y_0\,. \tag{11}$$

We use the mapping introduced by Johns [2,6], which relates all six field components at the center of the node to the wave amplitudes of its twelve ports.

3 Modelling of the Walls in SCN-ATLM

In order to conserve the parity of the TLM pulses in ATLM transmission lines of length $\Delta l/2$ are not allowed. Walls may only be located therefore in planes spanned by the centers of the TLM cells. This requires the introduction of boundary and wall nodes for plane surfaces, corners, and edges. The scattering matrices describing the boundary- and wall nodes of SCN-ATLM may be derived from the scattering matrix the SCN with stubs of length Δl. Scattering matrices for boundary nodes are computed in the following way:

1. Elimination of ports:
   - Ports in the plane of an electric wall with polarization parallel to the wall are short-circuited.
   - Ports in the plane of a magnetic wall with polarization normal to the wall are open-circuited.
   - Ports behind an electric wall are open-circuited.
   - Ports behind a magnetic wall are short-circuited.
2. Change of the characteristic impedances:
   - The characteristic impedance of a line in the plane of an electric wall with polarization normal to the wall is divided by 2.
   - The characteristic impedance of a line in the plane of a magnetic wall with polarization parallel to the wall is multiplied by 2.

As an example we present the scattering matrix for the electric wall bounding a dielectric medium with relative permittivity ε_r. We obtain the scattering matrix for the electric wall using the SCN with stubs

$$\boldsymbol{S}_{ew} = \begin{bmatrix} 0 & 0 & -\frac{1}{\sqrt{2}} & \frac{1}{\sqrt{2}} & 0 & 0 & 0 \\ 0 & 0 & 0 & 0 & -\frac{1}{\sqrt{2}} & \frac{1}{\sqrt{2}} & 0 \\ -\frac{1}{\sqrt{2}} & 0 & \xi_1 & \xi_1 & \xi_2 & \xi_2 & \xi_4 \\ \frac{1}{\sqrt{2}} & 0 & \xi_1 & \xi_1 & \xi_2 & \xi_2 & \xi_4 \\ 0 & -\frac{1}{\sqrt{2}} & \xi_2 & \xi_2 & \xi_1 & \xi_1 & \xi_4 \\ 0 & \frac{1}{\sqrt{2}} & \xi_2 & \xi_2 & \xi_1 & \xi_1 & \xi_4 \\ 0 & 0 & \xi_4 & \xi_4 & \xi_4 & \xi_4 & \xi_3 \end{bmatrix}, \tag{12}$$

with the parameters

$$\xi_1 = \frac{1-\varepsilon_r}{2\,\varepsilon_r - 1}, \quad \xi_2 = \frac{1}{4\,\varepsilon_r - 2}, \quad \xi_3 = \frac{2\,\varepsilon_r - 3}{2\,\varepsilon_r - 1}, \quad \xi_4 = \frac{\sqrt{2\,\varepsilon_r - 2}}{2\,\varepsilon_r - 1}. \tag{13}$$

Since boundaries and walls are intersecting the ATLM cells the scattering matrices of the boundary and wall cells and have to be calculated numerically prior to the start of the field simulation. However this requires only a minor part of the computational effort.

4 Numerical Simulations with ATLM

We have applied the ATLM scheme to the modelling of coplanar lines and coplanar line discontinuities on GaAs substrate. The reduction of the computational effort and the memory requirements does not affect the accuracy of the computation. In the case of the stubless SCN a reduction of factor 2 is achieved. When using SCN with stubs, memory requirement reduces by a factor of 2/3.

Tab. 1: Memory requirements of ATLM and traditional TLM

SCN with stubs	ATLM	trad. TLM
mesh size	$71 \times 71 \times 174$	$71 \times 71 \times 174$
number of cells	877134	877134
actual numer of cells in memory	438567	877134
data per cell	TLM amplitudes: 12 stub amplitudes: 6 media pointer: 1	TLM amplitudes: 12 stub amplitudes: 6 media pointer: 1
effective data per cell	TLM amplitudes: $\frac{1}{2} \times 12$ stub amplitudes: 6 media pointer: 1	TLM amplitudes: 12 stub amplitudes: 6 media pointer: 1
total memory	46.8 Mb	66.9 Mb

The ATLM scheme is used to determine the reflection coefficient of the CPW discontinuity located in a hollow waveguide. Fig. 2 shows the dimensions of the structure's geometry. For comparison, reference values of the same structure are calculated by mode matching [1].

For performing the ATLM-simulation equidistant meshing is applied. In order to reduce computational effort a symmetry plane is introduced, which cuts the CPW in longitudinal direction. With $\Delta l = 0.05$mm, the mesh is discretized by $71 \times 71 \times 174$ TLM nodes in cubic cells. An electric field with gaussian time dependance is excited at the front end of the line. As a result of the simulation, we obtain the time response $E_{\mathrm{cpw}}(n\Delta t)$ at the observation point, which includes both, injected and reflected signals. Of particular interest is the reflection coefficient $S_{11}(n\Delta f)$. Therefore, one has to separate incoming and outgoing signals. This requires the simulation of a reference structure which does not contain the discontinuity, but only the CPW-line. With this reference signal $E_{\mathrm{ref}}(n\Delta t)$, one obtains for the reflection coefficient

$$S_{11}(n\Delta f) = \frac{\tilde{E}_{\mathrm{cpw}}(n\Delta f) - \tilde{E}_{\mathrm{ref}}(n\Delta f)}{\tilde{E}_{\mathrm{ref}}(n\Delta f)} \quad , \tag{14}$$

where $\tilde{E}(n\Delta f)$ is the discrete Fourier transformation of $E(n'\Delta t)$.

In our simulation, absorbing boundary conditions are necessary at both ends of the waveguide. It is important to suppress the artificial reflection signals caused by the mesh boundaries. For that purpose we insert layers of lossy media, as shown in fig. 3. The absorbing layers are terminated by electric walls. To prevent the problem of reflections at transitions between layers with different characteristic impedances, we have to choose the properties of the media of the layers in a suitable way. We not only introduce an electric conductivity σ, but also a magnetic conductivity σ_{m}. If the impedance matching condition

$$\frac{\varepsilon}{\mu} = \frac{\sigma}{\sigma_{\mathrm{m}}} \quad , \tag{15}$$

is fulfilled, the characteristic impedances of the absorbing layers are equal. In our example, we use ten layers of matched lossy media with increasing conductivity towards the outside. For quasi TEM-waves, the absorbing capabilities are very good. The magnitude $|S_{11}|$ of the reflection coefficient of the double step discontinuity after fig. 2 is depicted in fig. 4. The result of the ATLM simulation is compared with the result of the mode matching simulation according to [1].

5 Acknowledgement

This work has been supported by the Deutsche Forschungsgemeinschaft.

References

[1] R. Schmidt, P. Russer, "Modelling of Cascaded Coplanar Waveguide Discontinuities by the Mode-Matching Approach", MTT-Symposium, Orlando, May 16-20, 1995, pp. 281-284

[2] P. B. Johns, "A Symmetrical Condensed Node for the TLM-Method", IEEE Trans. Microwave Theory Tech., vol. MTT-35, no. 4, Apr. 1987, pp. 370-377

[3] W. J. R. Hoefer, "The Transmission Line Matrix (TLM) Method", Chapter 8 in "Numerical Techniques for Microwave and Millimeter Wave Passive Structures", edited by T. Itoh, J. Wiley, New York, 1989, pp. 496-591

[4] P. Russer, B. Bader, "The Alternating Transmission Line Matrix Scheme", Proc. IEEE MTT-Symposium, May 16-20, 1995, Orlando, Florida, pp. 19-22

[5] P. Russer, "On the Field Theoretical Foundation of the Transmission Line Matrix Method", 1^{st} International Workshop on Transmission Line Matrix (TLM) Modelling Theory and Applications, Victoria, British Columbia, Canada, August 1-3, 1995, pp. 3-12

[6] M. Krumpholz, P. Russer, "A Field Theoretical Derivation of TLM", IEEE Trans. Microwave Theory Tech., vol. MTT-42, no. 9, Sep. 1994, pp. 1660-1668

[7] P. P. M. So, W. J. R. Hoefer, "A New Look at the 3D Condensed Node TLM Scattering", IEEE MTT-S Digest, vol. 3, June 1993, pp. 1443-1446

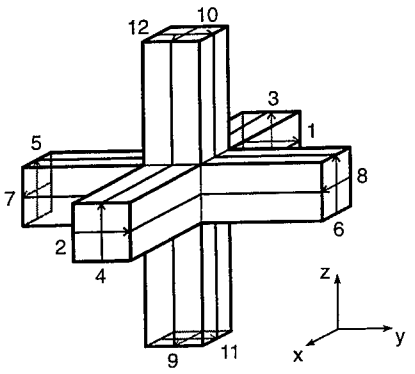

Fig. 1: Numbering schemes for the TLM ports.

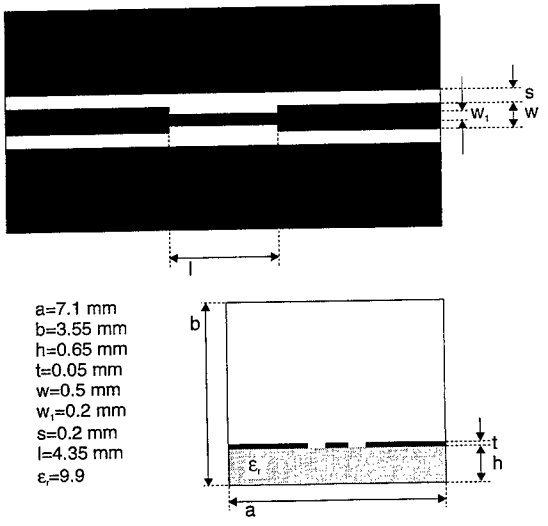

Fig. 2: CPW with discontinuity.

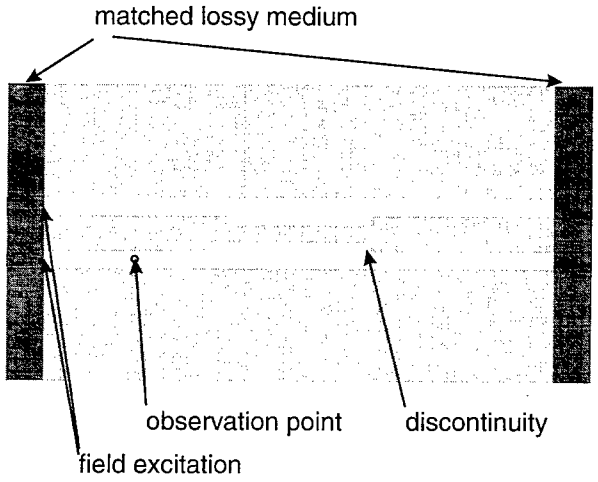

Fig. 3: Location of the mached absorbing layers.

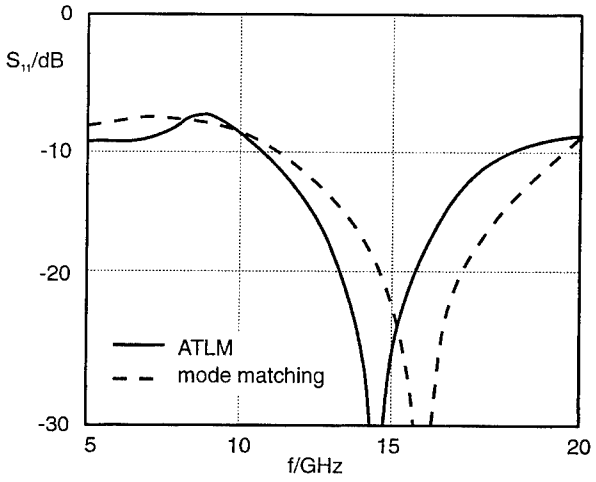

Fig. 4: Reflection coefficient S_{11} calculated with ATLM and mode matching.

Quasi-Static Correction of a Knife Edge Corner in 2D TLM Algorithm

Lucia Cascio°, Giampaolo Tardioli°, Tullio Rozzi*, and Wolfgang J.R. Hoefer°

°NSERC/MPR Teltech Research Chair in RF Engineering.
Department of Electrical and Computer Engineering, University of Victoria,
Victoria, B.C. V8W3P6, CANADA

*Dipartimento di Elettronica ed Automatica, Universita' di Ancona
Ancona, I-60131, ITALY

Abstract

Numerical techniques such as TLM and FDTD are used presently to solve a large class of electromagnetic problems. However, a common drawback of these techniques resides in the difficulty toaccurately describe structures in the presence of fine features such as sharp edges, where a singularity of the electromagnetic fields is encountered.

In this paper a local modification of the 2D-TLM algorithm for the nodes surrounding a knife edge is proposed. The Green's function for a semi-infinite knife edge is evaluated under a quasi-static approximation and used to derive an equivalent circuit of the corner, characterized as a three-port device.

The method is tested by evaluating the resonant frequencies of a 2D septum-coupled cavity. An accurate value for the resonant frequencies of the cavity is extracted by Richardson extrapolation of TLM results for increasingly fine discretization.

The resonant frequencies obtained with the corner correction algorithm for different discretizations are finally compared with the extrapolated results.

Introduction

The transmission line matrix (TLM) method [1] is widely regarded as an efficient and flexible technique for the analysis of a large class of electromagnetic problems. One of the main limitations of this and other numerical techniques is that the spatial discretization fails to accurately describe the singularities of the electromagnetic field, which occur, for example, close to sharp edges.

Unless a very fine discretization mesh is used, the singular behavior around the corner is poorly represented, and the frequency domain characteristics of the structure will typically be shifted. This error is very often unacceptable when we are dealing with narrow-band structures such as filters.

The accuracy of the discretized model can be improved by introducing a better description of the field singularity, through local modification of the algorithm.

An approach based on the local modification of the standard TLM method to account for the energy stored around the edge has been proposed in [2]. The nodes surrounding the corner are loaded with stubs with optimized characteristics.

In this paper a new approach based on the quasi-static approximation of the Green's function for an infi-

nite conductive wedge is proposed. The field distribution around a corner is represented in terms of an equivalent three-port circuit; its implementation in the TLM algorithm is straightforward and particularly efficient.

Theory

Consider a current filament adjacent to a conducting wedge, as shown in Fig. 1, where (ρ',ϕ') indicate the source position and (ρ,ϕ) the field point. The excitation is an impulsive current of strength I.

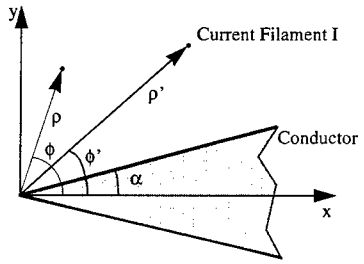

Fig. 1 Perfectly conducting wedge

In this two-dimensional problem the electric field component E_z can be expressed as a series of trigonometric and Bessel functions given in [3] as:

$$E_z(\rho,\phi) = G(\rho,\phi;\rho',\phi')\, I$$

$$G(\rho,\phi;\rho',\phi') = -\frac{\omega\mu\pi}{2(\pi-\alpha)} \cdot \begin{cases} \sum_{\nu=1}^{\infty} H_\nu^{(2)}(k\rho')\, J_\nu(k\rho) \sin(\nu(\phi-\alpha)) \sin(\nu(\phi'-\alpha)) & \rho<\rho' \\ \sum_{\nu=1}^{\infty} H_\nu^{(2)}(k\rho)\, J_\nu(k\rho') \sin(\nu(\phi-\alpha)) \sin(\nu(\phi'-\alpha)) & \rho>\rho' \end{cases} \quad (1)$$

$$\nu = \frac{n\pi}{2(\pi-\alpha)}$$

In the special case when the angle α is equal to zero we have a so-called knife edge. In this case the expression for the Green's function G(ρ,ϕ;ρ',ϕ') is given by:

$$G(\rho,\phi;\rho',\phi') = -\frac{\omega\mu}{2} \begin{cases} \sum_{n=1}^{\infty} H_{n/2}^{(2)}(k\rho')\, J_{n/2}(k\rho) \sin(\frac{n}{2}\phi) \sin(\frac{n}{2}\phi') & \rho<\rho' \\ \sum_{n=1}^{\infty} H_{n/2}^{(2)}(k\rho)\, J_{n/2}(k\rho') \sin(\frac{n}{2}\phi) \sin(\frac{n}{2}\phi') & \rho>\rho' \end{cases} \quad (2)$$

The expression (2) presents a complex frequency dependance, the variable k being a function of ω.
Using the approximation for the Bessel and Hankel functions for small values of the argument [4], (2) can be considerably simplified, leading to a quasi-static solution. Since

$$H_{n/2}^{(2)}(k\rho')\,J_{n/2}^{(2)}(k\rho) \rightarrow j\frac{2}{n\pi}\left(\frac{\rho}{\rho'}\right)^{\frac{n}{2}} \qquad if \quad (k \rightarrow 0) \tag{3}$$

the quasi-static approximation for E_z is [5]:

$$E_z(\rho,\phi) = G(\rho,\phi;\rho',\phi')\,I$$

$$G(\rho,\phi;\rho',\phi') = -j\frac{\omega\mu}{\pi}\begin{cases}\displaystyle\sum_{n=1}^{\infty}\frac{1}{n}\left(\frac{\rho}{\rho'}\right)^{\frac{n}{2}}\sin\left(\frac{n}{2}\phi\right)\sin\left(\frac{n}{2}\phi'\right) & \rho<\rho' \\ \displaystyle\sum_{n=1}^{\infty}\frac{1}{n}\left(\frac{\rho'}{\rho}\right)^{\frac{n}{2}}\sin\left(\frac{n}{2}\phi\right)\sin\left(\frac{n}{2}\phi'\right) & \rho>\rho'\end{cases} \tag{4}$$

Application to the TLM mesh

The quasi-static expression for the electric field described in (4) represents the basis for the determination of an equivalent circuit describing the field around the edge. In the TLM method the boundary conditions can be placed either between two nodes or on the nodes. In the second case the basic scattering process must be modified for the boundary node.
In order to keep the number of ports of the equivalent circuit for the edge as small as possible, the latter approach has been chosen (Fig. 2). In this way only three TLM nodes are directly connected to the edge, and a three-port equivalent circuit is sufficient to characterize its behavior.

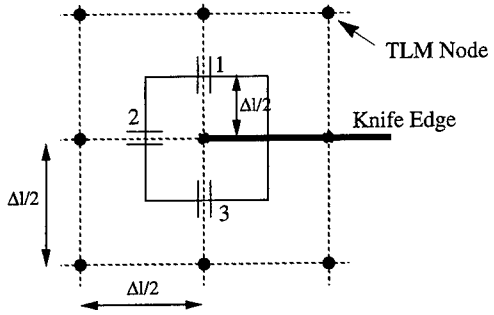

Fig. 2 TLM mesh and knife edge location

The expression (4) leads to a Z-matrix representation of the equivalent circuit. Since the voltages and currents at the three ports are related to the electric field E_z and to the current density J_z (5), the imped-

ance elements depend on the Green's function as given in (6).

$$V_i \rightarrow E_z(\rho_i, \phi_i)$$

$$I_i \rightarrow -J_z(\rho_i, \phi_i) = -\frac{I(\rho_i, \phi_i)}{2\pi\rho_i} = -\frac{I(\rho_i, \phi_i)}{\pi\Delta l}\ ; \qquad \rho_i = \frac{\Delta l}{2}\ ; \quad \phi_i = i\frac{\pi}{2} \tag{5}$$

$$Z_{ij} = \left.\frac{V_i}{I_j}\right|_{I_{k\neq j}=0} = -\pi\Delta l G(\rho_i, \phi_i; \rho'_j, \phi'_j) = \overline{G}(\rho_i, \phi_i; \rho'_j, \phi'_j); \qquad i, j = 1, 2, 3 \tag{6}$$

Due to the reciprocity of the Green's function and to the geometrical symmetry of the problem there are only four distinct elements Z_{ij}. The general form of the impedance matrix is:

$$[Z] = j\frac{\omega\mu}{\pi}\begin{bmatrix} z_{11} & z_{12} & z_{13} \\ z_{12} & z_{22} & z_{12} \\ z_{13} & z_{12} & z_{11} \end{bmatrix} = j\omega[\overline{Z}] \tag{7}$$

where the elements z_{ij} are frequency independent.
A more general definition for the impedances is given by:

$$Z_{ij} = \frac{1}{W_i W_j}\int_{W_i}\int_{W_j} \overline{G}(s; s_0)\, ds ds_0 \tag{8}$$

where $\overline{G}(s;s_0)$ represents the Green's function determined in (6), and W_i, W_j are the domains of integration for the source variables and for the field variables. Three different domains of integration have been taken into account (Fig. 3), leading to different formulations for the impedance elements.

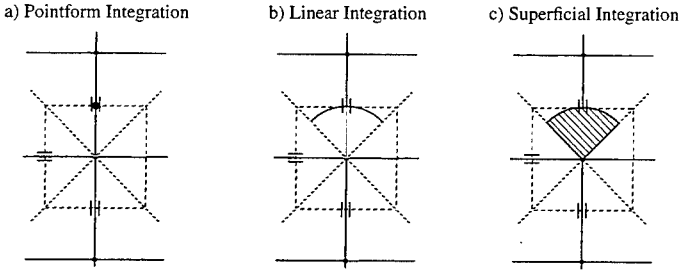

Fig. 3 Possible domains of integration for Z_{ij}

In the case of pointform integration, expression (8) presents a singular behavior for the main diagonal impedances Z_{ii}, corresponding to coincident source and field points. To determine a finite value for these impedances, it is therefore necessary to consider the source point and the field point in slightly different positions; in particular, we can assume that the radii ρ and ρ' are not equal. Introducing this

approximation into expression (8) we obtain:

$$z_{11} = \frac{1}{4}\log\left[\frac{1+x^2}{(1-x)^2}\right] \qquad z_{12} = \frac{1}{2}\log\left[\frac{\sin\frac{3\pi}{8}}{\sin\frac{\pi}{8}}\right] \tag{9}$$

$$z_{13} = \frac{1}{4}\log(2) \qquad z_{22} = \frac{1}{2}\log\left[\frac{1+x}{1-x}\right]$$

where the term x represents the ratio between ρ' and ρ, and is assumed to be less than unity.

On the other hand, the pulses traveling along the TLM lines represent the field distribution over the entire cell; we can therefore assume either a linear or superficial distribution of field and of the sources (Fig. 3) around the edge. In particular, we expect that the superficial integration will yield the best results, since it better accounts for the energy stored around the corner.

Expression (8) has been evaluated for both the linear and superficial integrations and has given rapidly convergent results for all the elements of the matrix; the expressions for the two cases are shown in (10) and (11), respectively.

$$z_{ij} = \frac{64}{\pi^2}\sum_{n=1}^{\infty}\frac{1}{n^3}\sin\left(\frac{n}{2}\varphi_i\right)\sin\left(\frac{n}{2}\varphi_j\right)\left[\sin\left(\frac{n\pi}{8}\right)\right]^2 \tag{10}$$

$$z_{ij} = \left(\frac{16}{\pi}\right)^2\sum_{n=1}^{\infty}\frac{1}{n^3(4+n)}\sin\left(\frac{n}{2}\varphi_i\right)\sin\left(\frac{n}{2}\varphi_j\right)\left[\sin\left(\frac{n\pi}{8}\right)\right]^2 \tag{11}$$

Once the Z-matrix has been obtained, it is also possible to extract a lumped element representation of the equivalent circuit (Fig. 4).

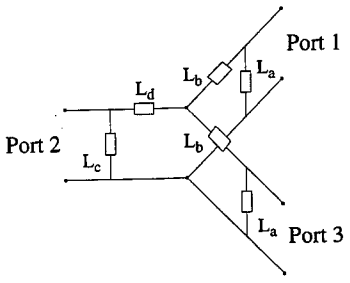

Fig. 4 Equivalent circuit for the knife edge

Discretization process

In order to realize the equivalent circuit in the TLM mesh, we need to determine the relation between

the incident and reflected voltages at the ports as a function of the Z-matrix elements (7). So far, we have obtained a complete description of the three port circuit by means of its impedance matrix Z:

$$\bar{V} = j\omega\,[\bar{Z}]\,\bar{I}\;; \qquad \bar{V} = \begin{bmatrix} V_1 \\ V_2 \\ V_3 \end{bmatrix};\; \bar{I} = \begin{bmatrix} I_1 \\ I_2 \\ I_3 \end{bmatrix} \tag{12}$$

The vectors $\overline{V}$ and $\overline{I}$ can be expressed in terms of the incident and reflected TLM voltages at the edge, $\overline{V}^{\,i}$ and $\overline{V}^{\,r}$, according to the relation:

$$\bar{V} = \bar{V}^r + \bar{V}^i \qquad \bar{I} = Y_0\,(\bar{V}^r - \bar{V}^i) \tag{13}$$

where Y_0 is the TLM link line admittance.

The frequency dependance jω is discretized using a bilinear transformation [6]; this scheme guarantees the stability of the discretized model. The frequency distortion introduced is irrelevant for frequencies propagating with low dispersion error in the TLM mesh ($\lambda \geq 10 \cdot \Delta l$). Hence:

$$j\omega \approx j\frac{2}{\Delta t}\tan\left(\frac{\omega\Delta t}{2}\right) = \frac{2}{\Delta t}\left(\frac{1 - e^{-j\omega\Delta t}}{1 + e^{-j\omega\Delta t}}\right); \qquad A_k e^{-j\omega\Delta t} = A_{k-1} \tag{14}$$

Substituting relations (13) and (14) in equation (12), we obtain a recursive formulation (15) characterizing the corner condition in the TLM process.

$$\bar{V}_k^r = \left(\frac{2}{\Delta t}Y_0\,[\bar{Z}] - [I]\right)\left(\frac{2}{\Delta t}Y_0\,[\bar{Z}] + [I]\right)^{-1}(\bar{V}_k^i + \bar{V}_{k-1}^r) - \bar{V}_{k-1}^i \tag{15}$$

In this expression $\overline{V}_k{}^r$ and $\overline{V}_k{}^i$ are the vectors of the reflected and incident voltages at the discrete time step k.

Expression (15) states that the reflected voltages at the edge depend simply on the incoming voltages and on the incident and reflected voltages at the previous time step. The implementation of the equivalent circuit in the TLM algorithm is extremely effective and requires that only a few extra values be stored.

Results

The method has been tested by evaluating the first resonant frequency of a 2D septum-coupled cavity (Fig. 5). An accurate value (reference line) for the resonant frequency of the cavity has been extracted by Richardson extrapolation of TLM data for increasingly fine discretization (Fig. 6).

We have obtained different results for the different Z-matrices given by equations (9), (10) and (11). As expected, the best results have been obtained with the superficial integration (11); they lead to a much faster convergence to the accurate values than those obtained with the basic 2D-TLM algorithm.

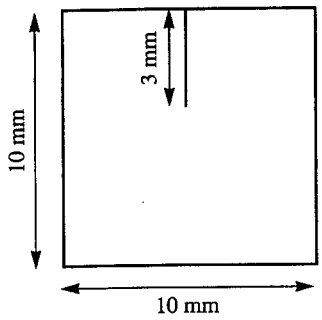

Fig. 5 Septum-coupled cavity

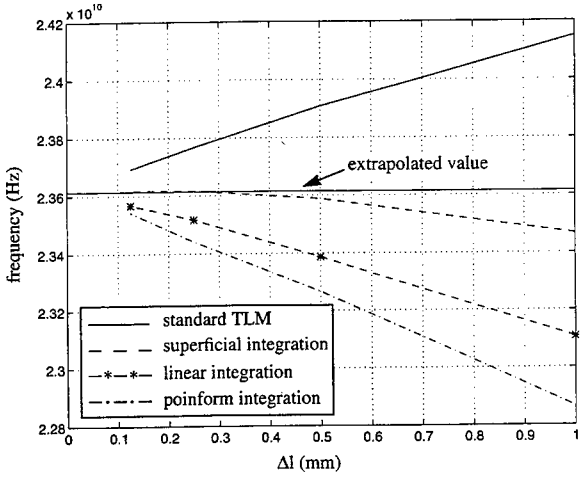

Fig. 6 Comparison between the first resonant frequencies obtained with the standard TLM and different corner corrections

Even with a very coarse mesh (Δl=1 mm) the superficial corner correction yields an improvement in the accuracy, reducing the percentage error from more than 2% to 0.6%.

If an accuracy of 0.1% is required, the corner correction allows to use a cell size at least four times larger than that necessary with the standard TLM. Therefore, when high accuracy is desired, the corner correction reduces considerably the computational effort.

Conclusion

In this paper a local modification of the 2D-TLM algorithm for the nodes surrounding a knife edge has

been proposed. The Green's function for a semi-infinite knife edge has been evaluated under a quasi-static approximation and used to derive an equivalent circuit of the corner, in the form of a three-port device.Three possible definitions for the Z-matrix of the circuit have been considered, corresponding to different domains of integration for the source and field coordinates.

The method has been tested by determining the first resonant frequency of a septum-coupled cavity and, as expected, has yielded rapidly convergent results in the case of superficial integration.

The improved description of the singular behavior of the field around the edge allows considerable savings in computer time and memory requirements, since the desired accuracy can be achieved by using a coarser discretization.

References

[1] W.J.R. Hoefer, "The transmission line matrix method - theory and applications", *IEEE Trans. Microwave Theory and Tech.*, vol. 33, Oct. 1985.

[2] J. L. Herring, W. J. R. Hoefer, "Compensation of Coarseness Error in TLM Modeling of Microwave Structures with the Symmetrical Condensed Node", *IEEE MTTS Symposium Digest*, 1995, Paper TU1B-2, pp. 23-26.

[3] R.F. Harrington, *Time-Harmonic Electromagnetic Fields*, New York: McGraw Hill.

[4] R. E. Collin, *Field Theory of Guided Waves*, 2nd ed., New York: IEEE Press.

[5] P. M. Morse, H. Feshbach, *Methods of Theoretical Physics*, , New York: McGraw Hill, 1953.

[6] A.V. Oppenheim, R.W. Schafer, *Digital Signal Processing*, Englewood Cliffs: Prentice-Hall.

SESSION 6:

INTERACTIVE TECHNICAL SESSION

ELECTROMAGNETIC VISUALISATION USING COMMERIAL SOFTWARE.

H.A. Nott BEE, MIEE,
Army Technical and Engineering Agency,
Department of Defence, Australia.
E-mail nott@brolga.atea.mat.army.defence.gov.au

ABSTRACT

The Australian Army Technical and Engineering Agency (ATEA) developed its AutoNEC capability as a convenient means of creating and editing models to be run in the Numerical Electromagnetics Code (NEC), and for examining the results. It comprises a number of procedures which interface the drafting package AutoCAD to NEC. During the last year, AutoNEC has been extended to interface to 3D Studio, a rendering and animation program. This has resulted in a considerably enhanced electromagnetic visualisation capability. This paper describes some of the aspects of AutoNEC, its continuing development and the use of 3D Studio.

BACKGROUND

Computing power and speed have increased considerably over the last decade. So to have the capabilities of computer programs to model the complexities of electromagnetic phenomena associated with radiating and radiated structures. The electromagnetics worker can now choose from a wider variety of more readily available and sophisticated tools, and work in greater detail than ever before. An inevitable consequence of such advancements is the difficulty in interpreting, in a global sense, the vast amounts of data which can be generated. The extension of ATEA's AutoNEC capability to interface to the rendering and animation package 3D Studio, was undertaken to address this problem, and has demonstrated considerable potential in the art of electromagnetic visualisation.

Antenna radiation patterns have traditionally been displayed as graphs showing cross sections of what is essentially a three dimensional structure - theta, phi and antenna gain.

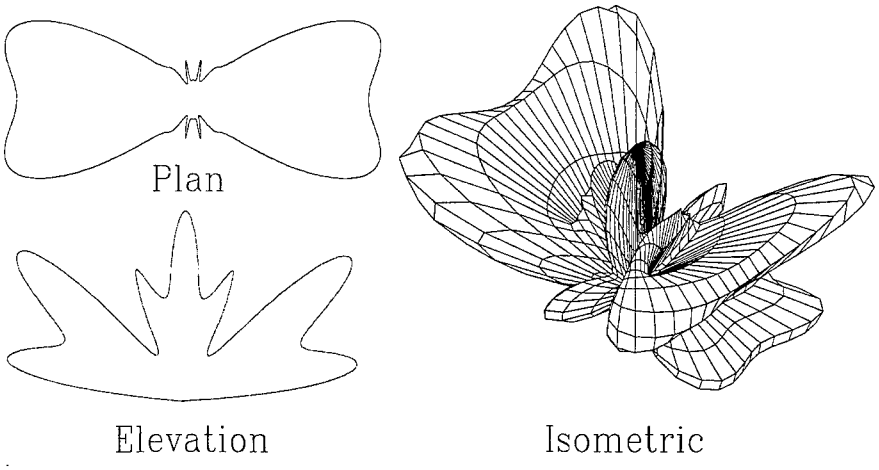

Figure 1: Plan, elevation and isometric views of antenna gain (far field) pattern.

The preceding images show antenna radiation patterns for an Army field antenna for HF communications. The patterns are for one frequency and were drawn in AutoCAD, using AutoNEC. The plan view gives some idea of the directional performance of the antenna, in this case at a takeoff angle of five degrees. The elevation shows the variation of gain with takeoff angle, an important factor for skywave communications. The isometric view gives a more global impression of the pattern. Understanding the overall pattern, particularly where its shape is complex, usually requires generation and comprehension of a multitude of such graphs. Consideration of polarisation and phase add further complexity as additional data dimensions become involved.

Near field data is of importance to radiation hazard (RADHAZ) studies. In its simplest case this data is a four dimensional structure (x,y,z and field magnitude) and the difficulties of meaningful display are correspondingly greater.

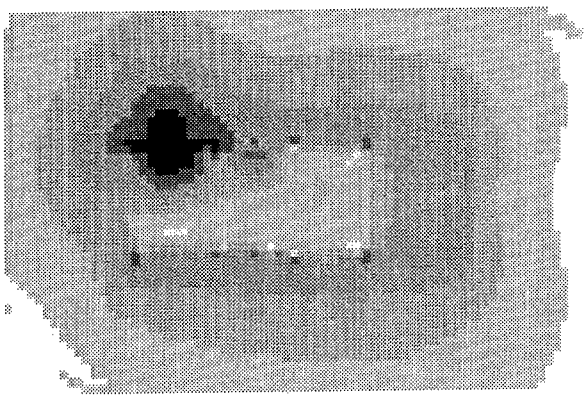

Figure 2: Cross-section of near field data. This horizontal cross section shows RADHAZ profiles for personnel and explosives. The subject is an Army vehicle (Land Rover) fitted with a high frequency (HF) transmitter, with its whip antenna in the upper left location (dark area). Even with this crude resolution, each cross section contains some 4500 separate data points. Examination of up to thirty cross sections taken at different heights is necessary to adequately investigate hazardous areas in three dimensions. With 28 steps across the HF band (2 to 30 MHZ), the total data amounts to some 4,000,000 points. The NEC output files for this investigation before processing amounted to over 150 Mbyte.

There will always be a need for tabular representation of field data to obtain values at specific points. The masochist may still be prepared to wade through many pages of printout in an attempt to gain an overall appreciation of the results. A number of approaches to displaying this data in a meaningful graphical form have already been developed, and met with varying degrees of success. However, recent advances in rendering and animation software have opened the door to another dimension in electromagnetic visualisation. This paper deals predominantly with AutoNEC and the application of rendering and animation capabilities of 3D Studio to the visualisation of far field radiation patterns.

AutoNEC

For several years, ATEA has been developing and enhancing its AutoNEC capability. Running on a personal computer, it uses a customised AutoCAD Version 12 to generate three dimensional models for analysis, perform model integrity checks, and to examine the results. Although AutoNEC uses NEC-2D as the electromagnetics engine, there is no reason why the techniques developed could not be adapted to later versions of NEC as well as other modelling tools. The customising software developed runs both within and outside AutoCAD and is constantly evolving as new and different types of analysis problems are encountered. A paper on AutoNEC, as it stood in 1994, was presented at the ACES Tenth Annual Review of Progress of that year.

Commercial rendering and animation packages such as 3D Studio have little inherent capability that might be exploited to directly investigate electromagnetic phenomena, and although AutoCAD has some rendering capability, the exporting of data to 3D Studio provides a vastly improved capability. The rendered and animated images so produced provide dramatically realistic images and sequences of electromagnetic phenomena.

AutoCAD ENHANCEMENTS

AutoCAD is a drafting package with an uncommitted architecture. User-written menus, dialogue boxes, drafting and other processes and even special drawing entities can be developed to provide user-specific capabilities. User processes embedded in AutoCAD can be written in the languages of AutoLISP, as well as C, and can easily be incorporated as extensions of AutoCAD's already extensive capability.

AutoCAD's Extended Entity Data is a means of attaching non-drafting parameters to drawing entities. Wire diameters, excitations and loading are attached as extended data to the lines representing the wires of the model, thus creating drawing entities that closely mimic the corresponding entries in the NEC input file. Taking this capability further, special drawing entities have been developed to define networks, transmission lines and run time parameters. Observation points for near and far field runs are input as special drawing entities which geometrically represent the observation point sets, ground parameters are stored as extended entity data on a 3D face physically representing the ground location, and frequency data is similarly input as a 'drawing' entity. Thus the drawing can contain not only the geometry of the model, but also its electrical and run-time parameters.

In order to accurately represent structures close to a finite ground, NEC uses the Sommerfeld/Norton method for ground modelling. Although NEC can model using surfaces patches, the Sommerfeld/Norton method is only available for wire models. Since the Australian Army is predominantly concerned with equipment near the ground, AutoNEC development has concerned itself primarily with wire models

Once the model is drawn in AutoCAD, and the electrical and run-time parameters are added, these are output as a text file essentially in the form of a NEC input file. Because of the limitations in AutoLISP's formatting capabilities, file formatting and NEC pre-processing is done outside AutoCAD using procedures written in Pascal. In addition to the problem definition, the output file also contains the first entries in an audit trail which is extended as processing proceeds.

NEC PRE-PROCESSING

The NEC pre-processor creates the NEC input files from the AutoCAD output files. As well as format adjustment, model integrity checks are performed. Duplicated or zero length wires resulting from inaccurate drafting are removed, and wire ends within a specified window size can be merged. Some dubious modelling strategies can be flagged and the resulting files read back into AutoCAD for further examination. As the files are in a text format, they can also be edited with a text editor - at the user's risk.

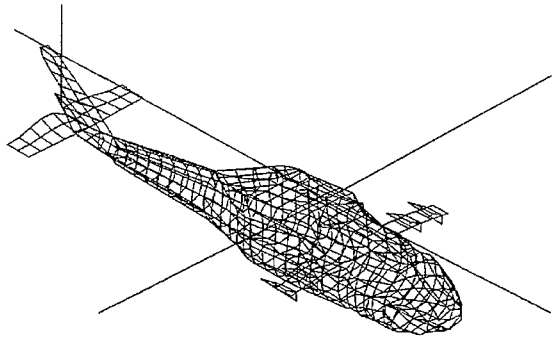

Figure 3: Wire mode of Helicopter

This 1500-wire model was received as 25 pages of 10 columns of data. It contained some 800 geometric errors and not surprisingly, it would not run. Software was written to check model integrity, to locate the errors and correct them. These procedures are being extended so as to automatically generate a critique of the model, flag dubious model structures, suggest possible improvements, as well as to note violations of the NEC modelling guidelines.

The NEC capability to perform multiple passes with frequency stepping is not used in AutoNEC. If multiple frequencies are required, a separate input file is created for each frequency, together with batch file to run the whole job. Because the files for each frequency are separate, wire segmentation can be optimised as a function of frequency, and this is performed automatically when the files are created. This results in a faster turn-around of jobs covering a wide frequency range, and saves the user from determining the segmentation himself. Similarly, the diameters of wires representing the edges of surfaces are automatically computed at this point in accordance with NEC guidelines. Another advantage of the multi-file approach is that it minimises the havoc resulting from NEC hanging or a power failure, particularly where jobs run for extended periods.

NEC PROCESSING

Before the batch file passes an input file to NEC, it calls a timer program which provides the user with an estimation of the completion time of the current NEC run. This is based on the time history of previous NEC runs within the current batch file.

The program SOMNEC (provided as part of the NEC codes) is used to create the interpolation tables used by NEC-2 for Sommerfeld/Norton ground modelling (not required in NEC-4). If the Sommerfeld/Norton method is requested, before running NEC the batch file calls a program which extracts the ground parameters from the NEC input file, creates a SOMNEC input file, and runs SOMNEC to generate the interpolation table. This saves the user from having to create his own SOMNEC input file for each run.

NEC POST-PROCESSING

NEC output files contain a significant amount of data other than direct results. This data should be examined as it can reveal an ill conditioned model, and checking for negative radiated power and antenna efficiency are performed by AutoNEC. To reduce file size, a significant amount of filtering is applied. Data extraction filters have been developed to cover far field (radiation patterns) as well as near field runs. The resultant files contain the essence of the results over the whole of the frequency range investigated, as well as the audit trail, and is in a form that can be printed for detailed examination. Although there is no geometry data in this file, it can be recovered if necessary by reference to the audit trail, which points to the AutoCAD drawing file where the model was created.

RADIATION PATTERN GENERATION

AutoNEC reads the radiation pattern data files into AutoCAD to create a series of three dimensional antenna gain surfaces, each surface being automatically assigned to a separate drawing layer. The initial wire model can also be imported to show pattern alignment. While near field data correlates exactly in orientation and scale with the wire model, radiation pattern data is represented as a surface of antenna gain, specified over a range of spatial angles, and although there is correlation with orientation, there is no **scale** relationship between the model and the antenna gain surface. Thus when the drawing of the model is overlaid on a series of antenna gain surfaces, its scale can be adjusted with impunity to assist visualisation of pattern orientation. As the patterns are created on different layers, these can be displayed or hidden by the user to show images of single radiation patterns. Using standard AutoCAD techniques, these images can be stored as slides and a simple animation created and run within AutoCAD. Rendered views as well as mesh representations of the surfaces can be created.

RENDERING AND ANIMATION WITH 3D STUDIO

3D Studio is one of several commercial programs used to create rendered images and animations of geometries. Used extensively in the architectural and advertising industries, it interfaces with AutoCAD using DXF (Drawing eXchange Format) files to both import and export geometries and paths. 3D Studio cannot create a renderable object using the wire drawing defining the model for NEC as it treats lines as paths rather than surface edges. Thus, if the model is to be imported into 3D Studio, a 3D FACE version of it must be created in AutoCAD. This generally means overlaying the existing wire model with a series of 3D FACES. Code is being developed that will generate this automatically from the wire model.

3D Studio EDITORS

3D Studio contains five different editors which are of interest in the production of animations of radiation patterns:

2D Editor - This is used for creation of two dimensional objects, and is used in AutoNEC for generation of text for annotation of images.

Lofter - This editor takes a two dimensional shape and lofts (extrudes) it along a path. Thus text can be given depth to enhance its appearance.

3D editor - This editor reads the AutoCAD-generated DXF files containing the radiation pattern data. It is also where scene (the view of the objects) is created. Lights, cameras, backgrounds and other scenic parameters are initially defined here, and materials (colours and textures) are assigned to the various objects in the scene. If the model geometry is simple, it can often be drawn directly in this editor. Alternatively, if a suitable 3D FACE model has been created in AutoCAD, it can be imported from a DXF file. Textual data created in the 2D Editor or Lofter is transferred to annotate the scene. This editor can create still image files in a variety of standard formats including GIF, TIG, TARGA, JPEG. These are suitable for printing, and for inclusion into presentation packages such as Powerpoint, as well as word processors.

Materials Editor - This editor provides a means of creation and modification of materials to be assigned to objects in the scene. 3D Studio Version 4 comes with some 183 materials in its standard library and any of these can be modified in the materials editor. Alternatively the user can create his own materials. A wide range of material parameters can be adjusted including texture, transparency, bump and reflection maps, shininess, ambient, diffuse and specular colour, and shading methods. Of the standard materials provided, Blue Marble has been found to be the most useful for radiation pattern depiction. When properly attached to a radiation pattern geometry, the rendered image has a series of lines radiating from the centre of the pattern which enhance its visual interpretation. Alternatively the user may decide to create a library of materials more suited to his needs, and a material specifically for radiation pattern display is being developed at ATEA.

Keyframer - This editor allows the various steps in an animation sequence to be set up. Of particular interest is the morphing capability. Having imported (say) twenty eight radiation pattern geometries covering the HF band, the lowest frequency pattern is morphed in subsequent image frames so that it adopts the shape of the patterns at other frequencies. If morphing is done between other than successive frames, 3D Studio performs a spline interpolation between successive shapes to generate intermediate images. As well as creating animation files, the keyframer can create series of still images in any of the formats available in the 3D editor, file names being derived from the source file name and the frame number.

GENERATING ANIMATIONS

The generation of good quality animations requires a considerable amount of effort, patience and experience. Unless the user is familiar with both AutoCAD and 3D Studio, a great variety of errors and frustrations await the unwary. Drawing in three dimensions is an art in itself. Unlike AutoCAD, 3D Studio does not yet support a language that will allow the user to create his own procedures. Many similar and repetitive steps are taken during the creation of each animation. Performing these under program control rather than manually would considerably reduce the effort required, as well as the number of mistakes that occur along the way. It is hoped that some programmability will be built into future versions of 3D Studio.

One of the prime requirements for animation creation is a fast computer, with significant amounts of RAM and file storage. ATEA is currently using a 90 Mhz Pentium machine, with 64 Mbyte of RAM, 2 Gbyte of disk and DAT tape backup. Even with this speed, some animations have required over ten minutes per frame, and a week to create a 60 Mbyte animation file. With this sort of investment in processing time, rework must be avoided by careful checks made at strategic points during the creation process.

In broad terms, the following steps are typical of those performed in creating a simple animation of radiation patterns:

1. Create model in AutoNEC and generate NEC input files.
2. Run NEC and extract the data from the NEC output files.
3. Create a series of 3D Surfaces in AutoCAD, representing the radiation patterns.
4. Transfer the surfaces to 3D Studio using a DXF file.
5. In the 3D Editor, create the scene for the pattern (lights, cameras, background, materials, text etc)
6. In the Keyframer hide all but one (the first) radiation pattern surface.
7 Morph this pattern to the other patterns at successive frames.
8. Run the renderer to create the animation.

The process is basically simple. Familiarity with the multitude of scenic variables that can be used in scene creation is essential to creating good quality animations and images. A sense of the theatrical, and a knowledge of lighting and camera techniques is also of considerable use, particularly when preparing training material where the most dramatic images tend to leave the long-lasting impressions.

PLANNED ACTIVITIES

The Australian Army's current single channel radio system (RAVEN) includes a variety of field antennas. The user presently relies on limited radiation pattern data in the printed documentation, as well as his basic communications training. ATEA is preparing training aids to remedy this deficiency. With appropriate image compression techniques, almost 50,000 images of antenna patterns can be stored on a single compact disk (CD). Using a mouse to adjust frequency, viewing angle and other parameters, the aids will provide an interactive visualisation of radiation patterns.

Because of the large distances involved, the Australian Army makes extensive use of HF radio for both voice and data in its operations in the north west of the continent. The ionospheric prediction program ASAPS (Advanced Stand Alone Prediction System), is similar to the US IRONCAP, and is used to predict the best HF frequency allocations under the prevailing ionospheric conditions. Antennas characterised in the standard ASAPS do not well match those in service, and preparation of more appropriate antenna data files is under way. Initial issues of these files have already demonstrated improvements in HF communications availability.

Other work includes a study of the design and performance of aircraft HF antennas, particularly those mounted on helicopters - one of the worst possible platforms for an HF antenna. This work will not only cover investigations into different and hopefully improved antenna configurations, but will provide pattern visualisation to assist pilots to a better understanding of their HF communications anomalies.

Some work has been done on visualising near field data. Early attempts to display this four dimensional data used a series of cross-sections, (see figure 2) and were of some use. However a significant number of such cross-sections were needed for visualisation of the whole field structure in three dimensions. Work with 3D Studio using semi-transparent materials (glasses) to create three dimensional images of near fields has shown some promise. The materials represent three dimensional contour surfaces, like the layers of an onion. Being transparent and of different colours, the internal structure can be seen. A method of transforming near field data to the form needed by 3D Studio is yet to be devised.

VALIDATION

There is a continuing need to improve methods of integrity and robustness checking of models. Assessment of results against actual measurements are an essential part of this process. Validation data are scrutinised to find weaknesses in apparently good models and extend modelling guidelines above those specified in the NEC documentation. Validation of near field data against actual measurement has been part of the Land Rover RADHAZ investigation, and some modifications were made to the initial model. Good (i.e. within a few db) correlation is now being obtained. Checks against antenna impedance and coupling also show promise of a robust model. Validation of far field data is a different proposition as measurements require large physical

separation in three dimensions between the source and the measurement points and present considerable logistic problems. Scale models are a possible alternative and 1/10 scale model of Black Hawk fuselage has been constructed for this purpose. Results from this work should not only enhance confidence in the computer modelling, but also lead to improvements in the NEC pre-processor in flagging dubious model constructions. Thus a continuous improvement in models will be achieved, without imposing any significant overhead on the modeller.

The data used to create the images in this paper and in the projected images accompanying the presentation, although not specifically validated, is generated from robust models of antennas, and are thus believed to be accurate. Such accuracy, however, is not fundamental to the thrust of this paper, which is to demonstrate the potential of animation packages such as 3D Studio in the field of electromagnetic visualisation.

QUIRKS

One initially puzzling aspect of morphing in 3D Studio was that the radiation pattern moved during the morphing, even though all the patterns from which the sequence was created had their origins fixed at 0,0,0. It was eventually found that the 3D Studio morphing algorithm maintains the **geometric centre** of the morphed object at the geometric centre of the initial object. Thus morphing from a initial pattern with little vertical development to one with significant vertical development would cause the origin of the resultant patterns to move downwards. Initially, the positions of the patterns were hand corrected in the keyframer to maintain a fixed origin, requiring successive frame by frame adjustments in three directions - a tedious and exacting process. Once the reason for this behaviour had been identified, the radiation pattern creation procedure in AutoCAD was modified to generate a path derived from the geometric centres of the pattern shapes. This path was then used in the keyframer to adjust the geometric centres of the morphed objects and maintain the origin fixed.

Another curious behaviour was found when using the entity selection process in AutoCAD. When the selection process is invoked during DXF file creation, AutoCAD Version 12 apparently modifies the order of faces. When 3D Studio morphs between objects across multiple frames, it creates intermediate objects by geometric interpolation, thus the face order is important. Objects (field patterns) which appeared quite normal when imported into 3D Studio, showed gross distortions during interpolation as a result of face order inconsistencies. The solution was not to use entity selection, even though this results in larger DXF files.

IMAGES

The following images are necessarily printed in grey scales. When reproduced in full colour by 3D Studio, the visualisation of the images is dramatically enhanced. Animation further adds to the realism.

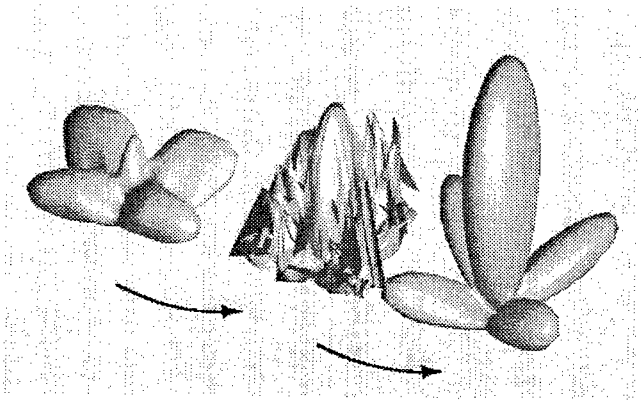

Figure 4: Result of AutoCAD entity selection process.

3D Studio has created the centre shape by interpolation between the left and right radiation patterns. The selection process within AutoCAD has not preserved the order of faces between the left and right patterns, resulting in the gross distortions during morphing, as shown in the centre shape.

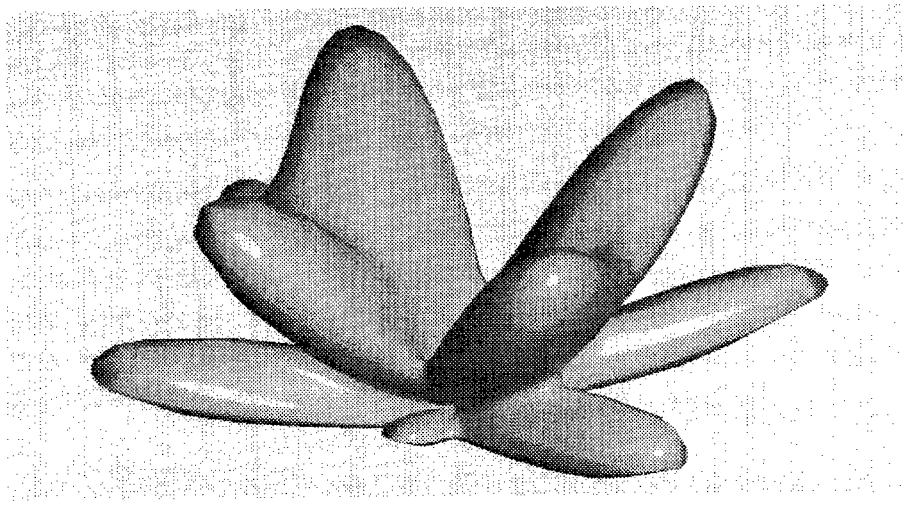

Figure 5: Rendered image of far field data. This image is one of many thousands produced for the bidirectional delta antenna used in the field by the Australian Army. The suite of images will be stored on a compact disk for display (in colour) as a training aid for signals personnel.

CONCLUSIONS

The development of the techniques described in this paper have already demonstrated significant potential in visualisation of electromagnetic phenomena. The pilot training aid as well as computer-based and video-tape animation displays have aroused considerable interest within Army and other areas within the Australian Department of Defence as well as overseas. The visualisation techniques are not limited to electromagnetics, but could be used to display virtually any static or varying phenomena, provided that an adequate mathematical description is available which will allow the shape(s) of the phenomena to be created within AutoCAD.

It is expected that the electromagnetic visualisation provided by the antenna training aids will significantly contribute to better field communications. Their use stimulates an 'antenna intuition' previously resulting only from long years of field experience and generally found only amongst long retired communications personnel.

Performance of Multiple, Thin Layers of Lossy Dielectrics as Broadband Attenuators

George W. Jarriel Jr., Michael E. Baginski, Lloyd Riggs
Department of Electrical Engineering
200 Broun Hall • Auburn University, Alabama 36849

January 9, 1996

Abstract

In the past, single layers of radar absorbers have been used to attenuate unwanted reflections due to an incident electromagnetic wave on a conductor over a narrow range of frequencies. However, recent advances in materials sciences have made the use of multiple, thin layers of lossy materials, each with different electrical constituitive paramters, to create broad-band radar absorbers feasible. Properly applied, this would ideally lead to a significant increase in performance over single layer absorbers.

This paper focuses on a numerical model for determining the attenuation of unwanted reflections due to multiple layers of radar absorbers coated on a perfectly electric conductor.

I Introduction

The suppression of unwanted reflections off metal structures is often an important consideration when introducing a transmitter/reciever set into a system. Reflections from other antennas, metal buildings, and nearby structures can impair the performance, and even damage a radar system. Possible methods for reducing reflections include altering the geometry of the system, distancing the transmitter/reciever from the reflecting surface, and coating the reflector with a radar absorbing materials.

In order to effectively implement a RAM solution to reflection problems, care must be taken in order to determine the proper material for the job. Unfortunately, the performance of many RAM are dependent on the geometry of the structure they are applied to, as well as the frequency of the incident energy, material constituitive parameters (ϵ,μ), and RAM depth. Complex geometry is difficult to simulate alone, and extremely computationally intensive when a lossy coating is applied.

A simpler geometry, the flat plate coated with RAM is simple to calculate, requires minimal computational resources, but only gives the investigator raw RAM performance under ideal circumstances. This says very little about the materials performance on more complex geometries.

A infinitely long, right circular cylinder could be considered a compromise geometry. Using a numerically exact infinite series method to calculate the fields due to a coated cylinder requires a negligible amount of CPU time, and at the same time gives a greater sense of scale to the investigator, allowing for inferences to possible behavior on more complex geometries.

This paper is concerned with presenting a method for the prediction of absorber performance for materials with graded constituitive parameters. This model will then be used to calculate the radar cross section, RCS, of three different material parameter profiles. First as a single homogeneous layer, secondly as multiple thin layers where the constituitive parameters are graded linearly as shown in Figure 1, and finally multiple thin layers where the constituitive parameters are graded exponentially. These thin layers can be taylored with a specific set of desired constituitive parameters by methods such as suspending an lossy material in powder form in a matrix (such as a polymer) [1].

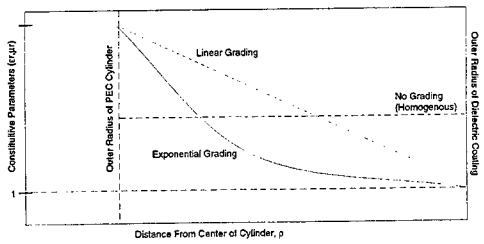

Figure 1: Profile of constituitive parameters for linearly graded, exponentially graded, and homogeneous dielectrics analyzed.

While more difficult to fabricate, materials with continuously graded constituitive parameters can be used, if properly designed, to attenuate a greater range of frequencies than a single layer of homogeneous RAM.

Due to the large number of variables involved, this paper will focus on concentric coatings where the grading of the constituitive parameters is dependent only on the distance from the center of the PEC cylinder, ρ. Oblique incidence, non-circular, symetric cylinders, and non-concentric coatings can be investigated using the same methods described here, but are beyond the scope of this paper.

II Analytic Formulation

Shown in Figure 2 is a TM_z electric field incident on an infinitely long (no z-variation) wire with N concentric, dielectic coatings (regions 1 to N) where each region has constituitive parameters (ε_r,μ_r, and k_m). From Harrington [2] we know that the total electric field for the N+1th region (free space) is defined as

$$\mathbf{E}^t_{z,N+1} = \mathbf{E}^i_{z,N+1} + \mathbf{E}^s_{z,N+1} = \mathbf{E}_0 \sum_{n=-\infty}^{+\infty} j^{-n}(J_n(k_{N+1}\rho) + a_n H^{(2)}_n(k_{N+1}\rho))e^{jn\phi} \tag{1}$$

and for regions m$\leq$N, the total electric field is defined as

$$\mathbf{E}^t_{z,m} = \mathbf{E}^i_{z,m} + \mathbf{E}^s_{z,m} = \mathbf{E}_0 \sum_{n=-\infty}^{+\infty} j^{-n}(b_{n,m}J_n(k_m\rho) + c_{n,m}N^{(2)}_n(k_m\rho))e^{jn\phi} \tag{2}$$

where the subscript m denotes the region, $\mathbf{E}^t_{z,m}$ is the z-component of the total electric field, $\mathbf{E}^i_{z,m}$ and $\mathbf{E}^s_{z,m}$ are the incident and scattered z-directed fields respectively, and E_0 is the magnitude of the incident field. J_n is the bessel function of the first kind, N_n is the Neuman function, and $H^{(2)}_n$ represents the hankel function of the second kind. A_n, $b_{n,m}$, and $c_{n,m}$ are scattering coefficients modifying the bessel functions. Solving for the coefficients The boundary conditions at each interface scattering coefficients are determined by applying.

$$\mathbf{E}^t_{z,Region\ m}(\rho = \rho_1) = 0.0 \tag{3}$$

$$\mathbf{E}^t_{z,Region\ m}(\rho = \rho_{m+1}) = \mathbf{E}^t_{z,Region\ m+1}(\rho = \rho_{m+1}) \text{ for all } \rho_m\ 2\leq m\leq N+1 \tag{4}$$

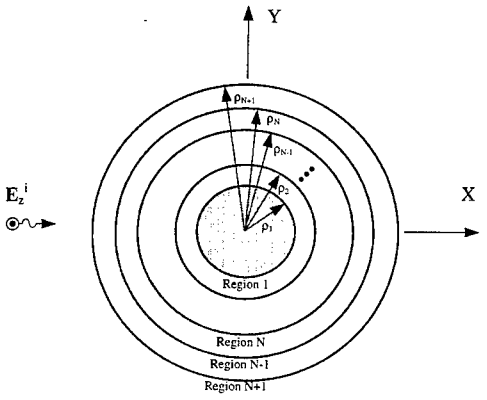

Figure 2: Geometry of Problem. Circular PEC cylinder coated with N layers of dielectic material.

$$\mathbf{H}^t_{\phi,Region\ m}(\rho = \rho_{m+1}) = \mathbf{H}^t_{\phi,Region\ m+1}(\rho = \rho_{m+1}) \text{ for all } \rho_m \ 2 \leq m \leq N+1 \tag{5}$$

Application of Maxwell's equations and these boundry conditions to 1 and 2 yield

$$a_n = -\left(\frac{J_n(k_{N+1}\rho_{N+1}) - J_n'(k_{N+1}\rho_{N+1})D_{n,N+1}}{H_n^{(2)}(k_{N+1}\rho_{N+1}) - H_n'^{(2)}(k_{N+1}\rho_{N+1})D_{n,N+1}}\right) \tag{6}$$

where

$$D_{n,m} = \begin{cases} 0 & \text{if m=1} \\ \frac{\eta_{m-1}}{\eta_m}\frac{J_n(k_{m-1}\rho_m)+F_{n,m-1}N_n(k_{m-1}\rho_m)}{J_n'(k_{m-1}\rho_m)+F_{n,m-1}N_n'(k_{m-1}\rho_m)} & \text{otherwise} \end{cases} \tag{7}$$

and

$$F_{n,m} = -\left(\frac{J_n(k_m\rho_m) - J_n'(k_m\rho_m)D_{n,m}}{N_n(k_m\rho_m) - N_n'(k_m\rho_m)D_{n,m}}\right) \tag{8}$$

In order to determine a_n, $F_{n,1}$ must be determined. Once found, can then be used to solve for $D_{n,2}$ which is used to solve for $F_{n,2}$. This process is repeated until $D_{n,N+1}$ is determined, at which point a_n can be calculated. Once the coefficient a_n has been determined, the scattered field, $\mathbf{E}_z^s$, is known, and so the RCS can be calculated.

A similar method to that outlined above may be employed to determine scattered fields when the RAM coated wire is illuminated by a TE plane wave.

The formula for the RCS is defined as

$$\mathbf{RCS} = \lim_{\rho\to\infty} 2\pi\rho\frac{|E_z^s|^2}{|E_z^i|^2} \tag{9}$$

$\mathbf{E}_z^i$ is usually to be unity, and furthermore, in the rar field asymptotic formula for the hankle function of the second kind reduces the formula to a readily calculable form.

For initial code verification, the formulas presented here were used to calculate the RCS for various cases with a lossless coating. Results for the lossless coating were in excellent agreement with RCS predictions computed using other methods [5] [6].

To test possible errors introduced due to the large number of layers surrounding the cylinder necessary to simulate continuous media, the RCS of a cylinder was calculated when coated with sixty thin layers of free space ($\mu_r = 1, \varepsilon_r = 1$). The results, shown in figure 3, were compared with a known solution [4], and showed excellent agreement. This simulation confirms that the series of bessel functions is an adequate approximation, provided that orders up to 10 are included.

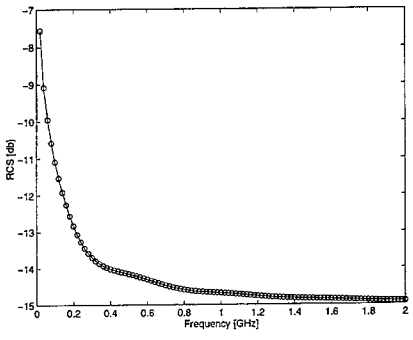

Figure 3: Comparison of RCS of bare cylinder for known solution (-) and RCS of cylinder surrounded by 60 thin layers of free-space (o-o).

The number of shells required to adequately simulate a continuously graded media is dependent on two factors, maximum frequency simulated and peak constituitive parameters of the absorber. Shown in figure 4 is the RCS for a coated cylinder, where a continuous, exponentially graded absorber is simulated using N layers. As the number of layers increase, the solution converges. However, it can be seen from figure 4 the solutions agree initially at lower frequecies for a smaller number thin layers. Therefore, if the frequency range of interest were to be expanded, the number of layers required to effectively simulate the continuous material would also have to be increased. Increasing the peak values for the constituitive parameters would also require an increase in the number of layers in the model.

III Numerical Results

Shown in figure 5 is an example of typical performance due to exponentially and linearly graded absorbers. The PEC cylinder is 2 cm in diameter with a 2 mm layer of material. The RAM has a complex permitivity of 9.511-i0.8679 and a complex permeability of 0.9511-i0.09. Both graded materials were simulated using 60 thin layers of equal radius. The geometry is illuminated by a normally incident TM field.

Both graded materials give attenuation over a broad range, but the linearly graded material has better overall performance. It is important to note at this point that data studied to date shows greater performance from a single homogeneous layer with the contituitive paramters equal to the peak values of

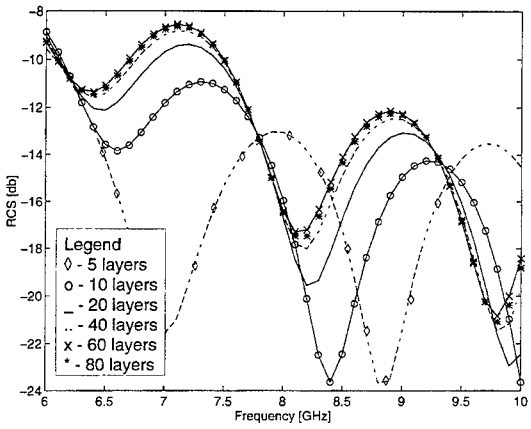

Figure 4: RCS of a 0.1m cylinder coated with an exponentially graded absorber simulated with N layers of homogeneous material.

the graded materials for some geometries. This is heavily dependent on system geometry and material parameters.

IV Summary

A model was presented for the determination of the fields and RCS of a right circular cylinder surrounded by a layer of lossy material where the constituitive parameters vary continuously with the radius, ρ. By separating the material in multiple thin layers of homogeneous material to approximate the continuous material, an accurate, computationally efficient model was developed.

Data was shown suggesting that a model for using graded materials can be useful in the determination of constituitive parameter profiles for enhanced attenuation of reflections..

Areas if future research include determining the bistatic RCS of graded RAM.

V Acknowlegements

Matlab routines for calculating bessel functions with complex arguments were written by D.E. Amos.

References

[1] K. C. Pitman, M. W. Lindley, D. Simkin, and J. F. Cooper, "Radar absorbers: Better by design," in *Radar and Signal Processing*, 1991.

[2] R. F. Harrington, *Time-Harmonic Electromagnetic Fields*. McGraw-Hill, Inc., 1961.

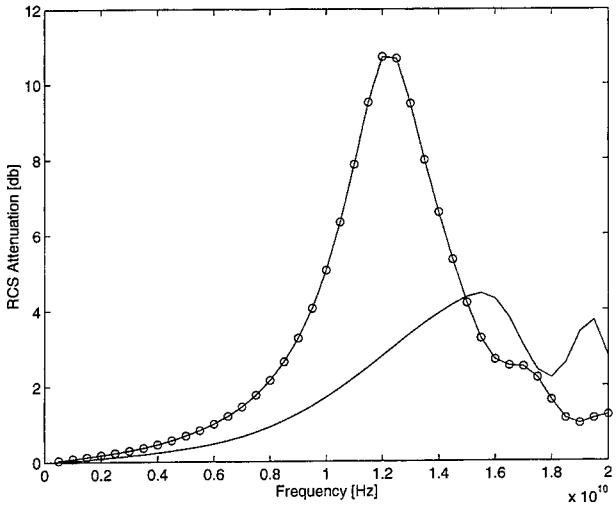

Figure 5: RCS of a 0.1m cylinder coated with an exponentially graded absorber (--) and a linearly graded absorber (-o-).

[3] M. Abramowitz and I. A. Stegun, eds., *Handbook of Mathematical Functoins with Formulas, Graphs, and Mathematical Tables.* U. S. Government Printing Office, 1964.

[4] G. W. J. Jr., L. S. Riggs, and M. E. Baginski, "Analytic solution for calculating the radar cross section and related parameters of a conducting right circular cylinder surrounding by multiple layers of lossy dielectrics," in *Conference Proceedings, 10th Anual Review of Progress in Applied Computational Electromagnetics* (A. Terzuoli, ed.), Applied Computational Electromagnetics Society, 1995.

[5] C. Lin and M. T. Yaquoob, "Electromagnetic scattering from a conducting cylinder covered with a multilayered dielectric," *Journal of Applied Physics*, vol. 72, no. 15, 1992.

[6] N. Wang, "Electromagnetic scattering from a dielectric coated circular cylinder," *IEEE Transactions on Antennas and Propagation*, vol. 33, no. 9, 1985.

[7] J. J. Pesque, D. P. Bouche, and R. Mittra, "Optimization of multilayer antireflection coatings using an optimal control method," *IEEE Transactions on Microwave Thoery and Techniques*, vol. 40, no. 9, 1992.

Research & Engineering Framework (REF) Data Dictionary Specification for Computational Electromagnetics [1]

Mr. Jeffrey A. Evans
Decision-Science Applications, Inc.
1300 Floyd Ave, Bldg B
Rome, NY 13440

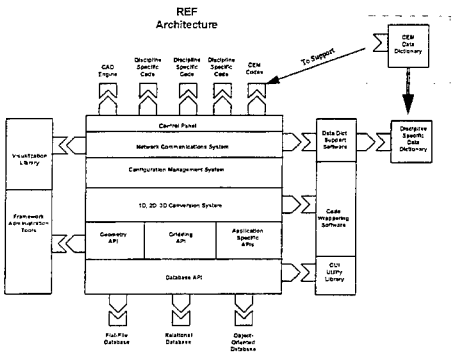

Figure 1. REF CEM Data Dictionary

dictionary for the REF as shown in Figure 1. Types of data covered by this dictionary will include: CEM analysis techniques; geometry elements; material properties; excitation information; and observables Information. The CEM data dictionary is being developed as a baseline data dictionary for the wide variety of CEM codes available. A developer need only tie his/her application-specific code into the REF directly or through wrappering to access this data dictionary.

Figure 2 shows a fundamental structure of the type of CEM data base we have developed. This data base layout has as its "leaves", or lowest nodes, a CEM description of a physical object for analysis.

The Data Dictionary design is being developed to be used as a template to enable existing, or legacy, CEM tools to be interfaced with the REF as shown in Figure 3. These codes as well

BACKGROUND

The Research and Engineering Framework (REF) manages data for a variety of design and analysis codes. Each of these different design and analysis codes has its own data requirements (data model) for input and output. The method that the REF uses to handle these different data models is through the use of a data dictionary. By utilizing the data dictionary REF users will have the ability to switch between data models thereby transforming the generic REF into a discipline-specific design system.

This paper discusses the ongoing effort to design and develop a Computational Electromagnetic (CEM) specific data

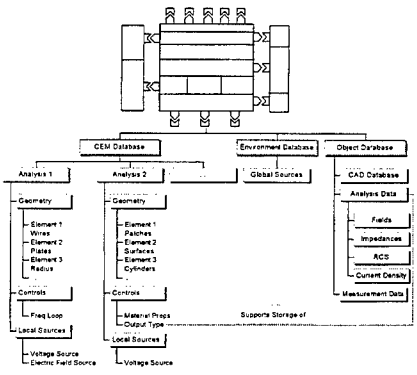

Figure 2. CEM Database for the REF

[1]This work was sponsored by Rome Laboratory under the Expert Science and Engineering Program (BAA 93-07), Contract # F30602-95-C-0049.

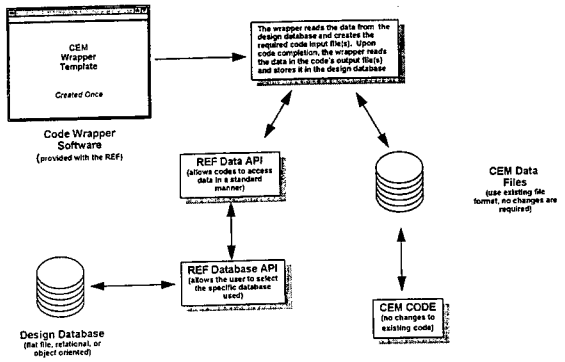

Figure 3. CEM Code Interface with the REF

as new CEM tools will be able to be fully integrated into the REF. This is possible because of the supporting set of development APIs (Application Programmer Interfaces) in the REF. These APIs allow other existing codes to be modified to access the databases in the REF. There are also APIs that provide the developer with a robust set of code that allows programs to perform graphics, gridding, etc. These APIs allow the developer to concentrate on the EM development rather than worrying how he/she is going to store and visualize the data. Figure 4 shows how the codes will be integrated with the REF.

DATA DICTIONARY DESCRIPTION

A data dictionary is a description of all the databases composing a data base system. The content of the data dictionary may best be thought of as "data about the data"—that is, descriptions of all of the other objects (e.g., files, programs, and so on) in the system. In particular, a data dictionary stores all the various schemas and file specifications and their locations. The dictionary is consulted before actual data is read or modified in the data base system. A complete data dictionary also includes information about which programs use which data and which users are interested in which reports. The data dictionary is frequently integrated into the system it describes.

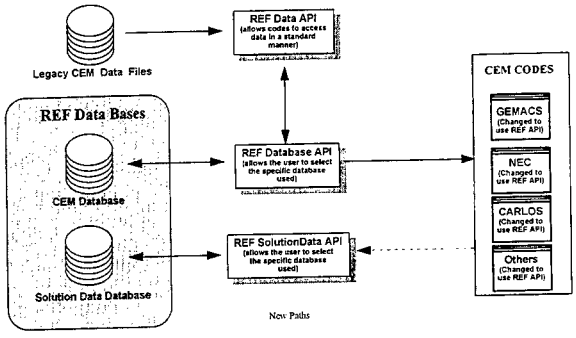

Figure 4. CEM Code Integration with the REF

A relational data base system needs to maintain data about the relations among the data. Among the types of information the data dictionary stores on the system are:

- Names of the relations
- Names of the attributes of each relation
- Domains of attributes
- Names of views defined on the data base, and the definition of those views
- Integrity constraints for each relation (e.g., key constraints)

CEM DATA DICTIONARY DESIGN CONSIDERATIONS

When developing a data base for tools that exist and for codes that haven't been written yet there are a number of considerations to examine. For this effort there are three general considerations:

1. Do we design a data base that incorporates all of the specific data types that are used by CEM codes today which may limit our expansion capability?
2. Do we design a data base that uses only generic entities that answer the need of a wide variety CEM codes and will allow future codes to be incorporated easily? But current codes will require additional coding to incorporate them into this framework.
3. Do we approach the design of the data base as a combination of the best of both of the first two options?

The first option above at the outset appears to be the most logical step when designing the data base. All one needs to do is to survey the CEM community and get a complete inventory on the types of data that are required for each code and then build an appropriate description (table) to hold the data. However, this approach brings with it two major concerns. The first is that the volume of data types will soon become unmanageable, and the second is that many of the data elements will be found to have common areas covered by other data elements causing redundancy in the data base which is undesireable.

The second of the two approaches provides the most flexibility in designing the data base. The CEM data entities can be modeled such that the layout of the data base is extremely flexible. For example, instead of separate entities for patches, plates, and facets a new *surface area* element could be designed such that any of the other entities could be generated from it. Also an element like the surface area could be used along with the gridding interface in the REF to generate a MoM wire mesh. Therefore, with this approach the amount of data that would need to be stored would be greatly reduced.

There are two concerns with this approach however, the first being that any existing code would have to either be modified extensively or a very robust wrapper would need to be generated to translate these new generic entities into the more traditional CEM entities. The second concern with the general approach is that the contents of the data base may be less intuitive to a user who is browsing through a group of models. The surface area means little unless the user knows *a priori* that this is a MoM wire grid model and the surface will be subdivided by a wire gridding algorithm.

The last approach would utilize the best of both the specific cases of CEM data types and the more general approach. By designing a data base that incorporates existing data types we have a very intuitive data base that can be used by today's codes. Also having the general data types like the surface area entity future codes can be written to take advantage of this data abstraction and utilize the power of the utilities and libraries in the REF.

CEM DATA DICTIONARY

The CEM data dictionary is being developed such that the data is logically grouped into functional areas. The specific areas that were addressed are Input Commands, Input Geometry, and Output Commands. Each of these areas was broken down further into more manageble subareas that were then used to create the tables and data elements in the tables. Figures 5 through 10 show the tables that were constructed for the CEM data dictionary and their relationships with each other.

The trouble with creating a CEM data base is ensuring that it is generic for any of the existing codes and flexible enough to be easily expanded to incorporate new advances in CEM. In creating a generic CEM data base some CEM code specific constructs are not available. This is because these constructs would have little or no meaning to another code. An example of one of these constructs is a geometry reflection command that is allowed by codes like NEC MoM and GEMACS. Other codes like CARLOS 3D don't recognize a reflection command and therefore an analysis would potentially produce invalid results. Two possible solutions to this problem include storing the complete geometry after the reflection command has been executed or by making a note in a comments section that the geometry that is stored will need to be reflected in some manner prior to its use. Both of these solutions are possible

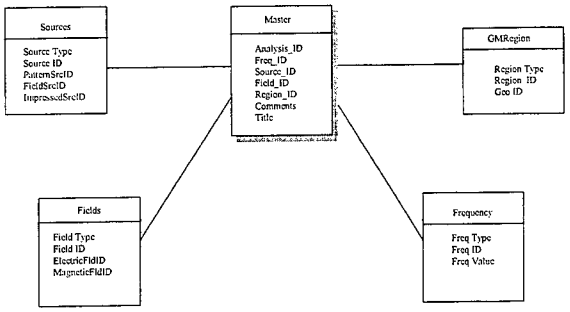

Figure 5. CEM Data Dictionary Master Table and Relations

with the data dictionary of this effort. The former would be handled by a preprocessor that would create the correct geometry, whereas the latter solution is handled by a comments entry in the geometry table described later.

Figure 5 shows the Master Table and how it provides access to the other tables in the data base. In the data base the individual analyses are uniquely identified by their Analysis_ID in the Master Table. There are other columns in the table where an analysis title can be added, and comments about the analysis can be added. The other columns in the table are IDs that point to other tables in the data base where the remainder of the analysis information is stored. These other tables include the Sources Table, the Fields Table, the Geometry Region Table and the Frequency Table. Each of these tables are described in the following paragraphs and figures.

The Sources Table and its related tables, shown in Figure 6, are used to store the information necessary to create an excitation command for the CEM analysis. There are three source types defined in the data base. The Pattern Source table stores information to be able to use previously generated field data (measured or simulated) as the excitation source. The Electric Field table is used to store information to create a fixed or stiff source at a given location and orientation. The Impressed Source Table stores information to create an excitation that can be applied to some portion of the structure such as a voltage on a wire or patch. In all three of these tables there are coordinate system parameters that allow for placement, polarization and, if necessary, orientation of the source.

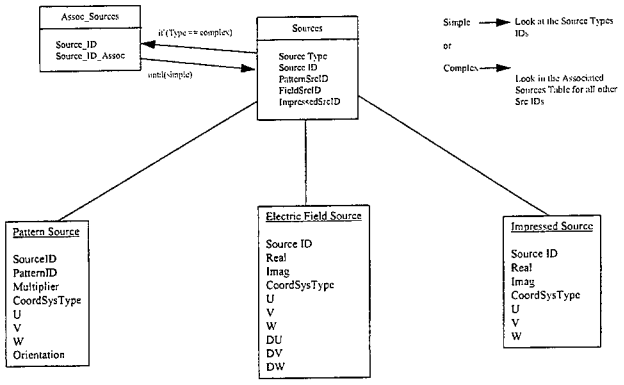

Figure 6. CEM Data Dictionary Sources Table and Relations

The Assoc_Sources Table provides the capability of storing more than one source per analysis. An example of an analysis requiring multiple sources would be the simulation of an array antenna where each of the individual elements in the array is represented by an Electric Field source.

Similar to the set of tables for source is the Fields Table, Figure 7, and its related tables. These

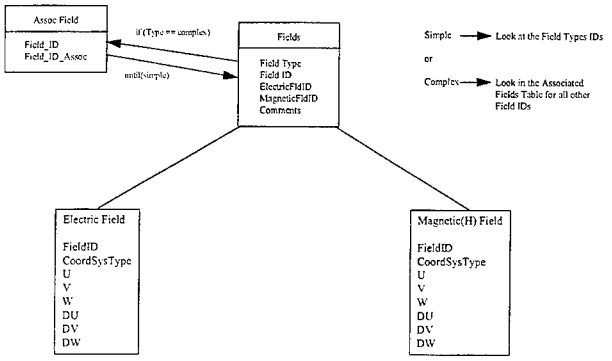

Figure 7. CEM Data Dictionary Fields Table and Relations

tables store the information necessary to create the command to identify where field data are to be generated in the analysis. The results of the field command, the solution data, would be stored in another data base.

Two types of field command information can be stored in the data base, Electric Field and Magnetic Field. As with the sources the field tables store information on the location and coverage of the requested fields. Also multiple field commands can be stored via the Assoc_Fields Table.

Scalar frequencies or frequency ranges are stored in the Frequency Table, Figure 8. The Assoc_Frequency Table allows multiple scalar frequencies or ranges to be stored with a single analysis. Nonuniformly spaced scalar frequency values could be stored in this manner.

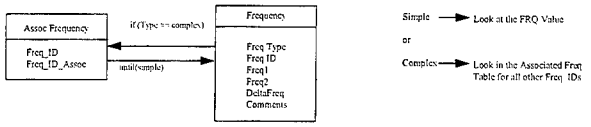

Figure 8. CEM Data Dictionary Frequency Setting Table and Relations

The Geometry Region tables, Figure 9, and relations provide storage for the structure under analysis. The storage of multiple regions allows the user to build the model in reusable sections such as wings, fuselage, stabilizers, etc. It also allows for multi-region (i.e., external vs. internal) analyses to be stored for analysis by one code or a set of codes.

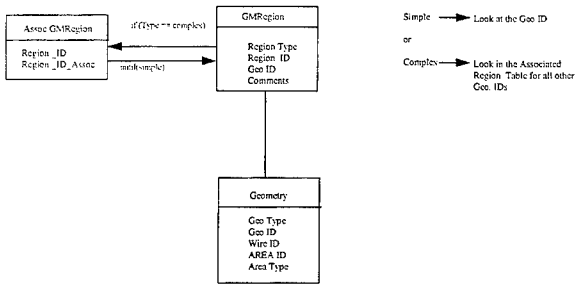

Figure 9. CEM Data Dictionary Geometry Region Table and Relations

The Geometry Table and its related tables, shown in Figure 10, stores the low level geometric description of the structure. This description is in CEM model terms, i.e., wires, plates, patches, cylinders, etc, to facilitate the

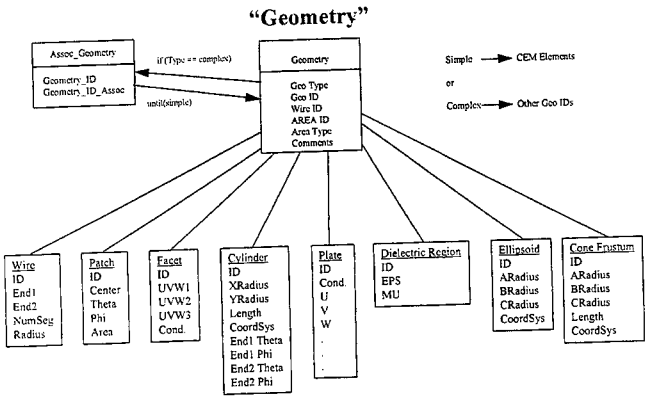

Figure 10. CEM Data Dictionary Geometry Table and Relations

ease of interfacing existing CEM codes with the REF. As these codes are integrated into the REF to utilize more of the REF APIs, it is envisioned that the geometry tables will progress toward one of the standard CAD data formats like IGES.

SAMPLE DATABASE

A sample CEM data base was constructed using the Microsoft Access Relational Database Management System. Support software routines to load and subsequently extract the analyses from the data base were developed for the GEMACS analysis code. Figure 11 shows the flow of loading existing analysis input files into the data base and then extracting the data from the data base for use in an analysis.

SUMMARY

Common areas of CEM, Computation Fluid Dynamics, and Finite Element Analysis for Structural and Thermal investigations are also being considered to facilitate transfer of information and the future development of discipline-specific REF data dictionaries. These areas are of immediate interest due to their interaction with electromagnetics.

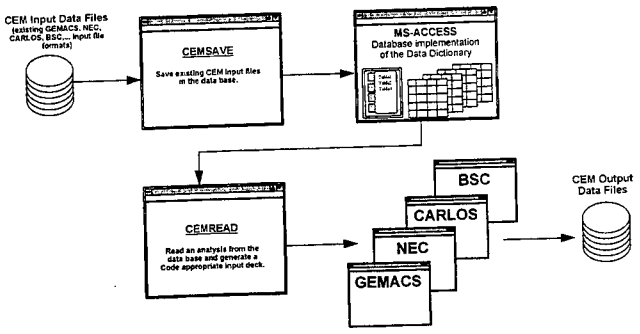

Figure 11. CEM Data Dictionary Support Code

The REF data dictionary and its support software were developed to provide a means for validating application data input and facilitate extending the data model and dictionary to a wide variety of engineering disciplines. It is the authors desire to have the members of ACES provide feedback on this data base of CEM requirements such that the product will incorporate as diverse an information base as possible.

REFERENCES

Burke, G. J., Poggio, A. J., "Numerical Electromagnetic Code (NEC) - Method of Moments," Part III: User's Guide, Lawrence Livermore National Laboratory, prepared under contract N-7405-Eng-48, January 1981.

Coffey, E.L., D.L. Kadlec, "General Electromagnetic Model for the Analysis of Complex Systems (GEMACS), Version 5.0", Advanced Electromagnetics, RADC-TR-90-360, Volumes I, II and III, Dec 1990.

Coffey, E.L., D.L. Kadlec, "GEMACS Source Book, Advanced Electromagnetics", RADC-TR-87-102, February 1988.

Date, C.J., "An Introduction to Database Systems Volume 1, Fourth Edition", Addison-Wesley Publishing Company, Reading MA, 1986.

Evans, J. A., "Research and Engineering Framework Data Dictionary Specification for Computational Electromagnetics", Applied Computational Electromagnetics Society 11th Annual Review of Progress in Applied Electromagnetics, p 126, Mar 1995.

Korth, H.F. and A. Silberschatz, Database Systems Concepts, McGraw Hill Book Company, New York, 1986.

Lee. S. W., D. J. Andersh, "Users Manual for XPATCH", DEMACO, Inc. Sep, 1993.

Marhefka, R. J., Burnside, W. D., "Numerical Electromagnetic Code (NEC) - Basic Scattering Code (Version 2)," Part I: User's Manual, Technical Report 712242-14, The Ohio State University ElectroScience Laboratory, Columbus; prepared under Contract N00123-79-C-1469 for Naval Regional Contracting Office, December 1982.

DEVELOPMENT OF AN ELECTROMAGNETIC AND MECHANICAL SIMULATION TOOL FOR THE COMPUTER MODELING OF THE TACAMO LF/VLF COMMUNICATION SYSTEM*

Mary C. Longtin, Richard W. Sutton, Kenneth J. Laskey and Philip J. Morrison
Science Applications International Corporation
1710 Goodridge Dr.
McLean, Virginia 22102

ABSTRACT

Over the past several years, the Naval Air Systems Command has sponsored the development, at SAIC, of a computer simulation tool for the dynamic electromagnetic and mechanical modeling of the TACAMO LF/VLF communications system. This paper will discuss the development of that simulation tool, especially the use of the code NEC (Numerical Electromagnetics Code) in that tool, along with numerical and parameter issues that arose as a part of the development.

INTRODUCTION

The TACAMO LF/VLF communications system includes two wires trailing from an aircraft. The longer wire of the two can vary in length from about 15,000 feet to 26,000 feet, and the shorter wire can vary in length from about 1,600 feet to 4,000 feet. The wires are driven by a power amplifier on the aircraft at frequencies from about 17 to 60 KHz.

Over the past several years, the Naval Air Systems Command (NAVAIR) has sponsored the development at SAIC of the TACAMO Electromagnetic Simulation System (TESS), a computer simulation tool for the dynamic electromagnetic and mechanical modeling of the TACAMO system. The TESS system enables a user to predict the signal strength and signal-to-noise ratio of the TACAMO transmission at locations distant from the TACAMO transmitter.

The TACAMO Electromagnetic Simulation System contains three parts or separate codes. The first part is a dynamic mechanical model of the long and short trailing wire antennas (LTWA and STWA). This part calculates the wire shape and position as a function of the flight path of the aircraft, wind conditions, wire length and other variables. The second part consists of a NEC calculation of the current distribution on the LTWA and the STWA and the electric field radiated from the antennas based on the wire shapes that are output from the mechanical model. The third part consists of a calculation of the signal propagating from the transmitter, based on the result of the NEC calculation. In the current phase of this project, the NEC output is used to develop an

*This work was performed for the Naval Air Systems Command under contract number N00421-91-D0206.

equivalent dipole to the TACAMO system, that is, an elemental dipole whose radiated electric fields would best fit the calculated electric fields radiated by the TACAMO transmitter. This equivalent dipole is an input for the propagation segment. Another input for the propagation segment of TESS is the total power emitted by the TACAMO antennas. This total power is also obtained from the NEC output file. All three segments of TESS are controlled by a user-friendly GUI interface. The sequence of calculations in TESS is shown in Figure 1.

Currently, we are using either SIMBAL (Simulation for Multiple Bursts And Links) or WEDCOM (Weapon Effects on D-region COMmunications) as the part of TESS that describes the propagation of the TACAMO signal to the receiver site. Both codes describe the propagation of a signal over long distances, taking into account the earth's curvature, the ionosphere, signal sources due to storms, etc. The choice between these two codes is based on factors such as accuracy and run-time requirements. For example, SIMBAL runs much faster for a given problem than WEDCOM does, since SIMBAL uses look-up tables while WEDCOM performs the electromagnetic calculation. Therefore, a user that requires a faster calculation will opt for using SIMBAL for the propagation part of TESS. The version of NEC that we are currently using is NEC4.

The GUI interface automatically generates the NEC input file from the output of the dynamic mechanical model, and the SIMBAL input file from the NEC output file. For example, the user chooses a simulation time and some flight parameters and conditions, the mechanical model calculates the TACAMO wire shape at that simulation time, and the user interface generates an approximation to that wire shape using straight wires and converts that approximation into the correct format for a NEC input file. Likewise, the GUI interface calculates the total power emitted from the TACAMO antenna and the equivalent dipole to the antenna, as discussed earlier, and converts those results to the correct format for a SIMBAL or WEDCOM input file.

DETAILS OF THE NEC MODEL

Figure 2 shows a schematic of the NEC model of the TACAMO system. The TACAMO long and short wires are modeled by connected series of straight wire sections. The aircraft is simulated in the model by a "wire" with a diameter such that the capacitance of the resulting cylinder to ground is approximately equal to the capacitance of the aircraft to ground. The wire series representing the long and short TACAMO wires meet at a point on the aircraft. A voltage is driven between two segments at that point.

The accuracy of the end result of a TESS calculation, the electric field some distance from the transmitter, depends greatly on how accurately TESS can calculate the total emitted power and the equivalent dipole. The total power emitted from the TACAMO antenna is calculated by integrating the Poynting vector over a surface containing the antenna. The emitted power and the equivalent dipole, then, depend in turn on how accurately NEC can calculate the current on the TACAMO wires and the electric fields radiated from the wires. Therefore, the NEC model of the TACAMO antenna is important for the accuracy of the TESS calculation. The focus of this paper will be on the work that has been done to refine the NEC model with respect to the parameters that define the model.

Note that since the NEC portion of TESS only needs to calculate the electric fields near the antenna in order to enable TESS to calculate the power emitted from the antenna, and the propagation code calculation deals with propagation of the fields over long distances, the results of the NEC calculation only need to be considered in the near field of the antenna. Therefore, the effects of parameter variations only need to be considered on the near field, not the far field, results. For example, one can include a model of ionospheric reflections in the NEC model and study the

variations in the NEC results with variations in the ionosphere height, but it turns out that including the ionosphere is only important for results in the far field of the antenna, and so is not considered as a factor in the NEC portion of TESS.

The following parameters define the TACAMO NEC model: the number of wires to simulate the long and short TACAMO antennas, the number of segments per wire, the frequency of the transmission, the wire resistivity and the ground plane dielectric constant and conductivity. Some of these parameters are very accurately known or can be very accurately measured by the TACAMO system, and so we do not need to consider the effects on the accuracy of the TESS calculation of variations in these parameters. The transmitter frequency and the wire resistivity are two such parameters. The TACAMO transmitter controls the transmitting frequency to a high degree of accuracy, and the physical characteristics of the TACAMO wires are very well known. On the other hand, the ground plane characteristics may not be precisely known in advance, so we needed to determine if a variation in these characteristics had a significant effect on the results of the NEC calculation. The best number of wires per TACAMO antenna and number of segments per wire in the NEC model also needed to be explored. The rule of thumb is that the segment length must be less than a tenth of a wavelength for the frequencies of interest[1], but we have found further constraints on the segment length for this problem.

PHYSICAL WIRE LENGTHS VS EM WIRE LENGTHS AND SEGMENTATION

In this paper, we use the following terminology in order to be consistent with the NEC manual: The actual TACAMO trailing wire antennas are referred to as "antennas", the largest subdivisions of the antennas are referred to as "wires" or "straight wires", and the smallest subdivisions of the antennas are referred to as "segments".

Both the physical model and the NEC model of the TACAMO system are based on approximating the TACAMO antennas by connected series of shorter, straight wires, and in both calculations, the accuracy of the calculation and the run times increase with the number of divisions into which the TACAMO antennas are divided. Due to the way the GUI interface handles the division of the antennas, there must be at least as many straight wires in the NEC model as there are in the mechanical model.

Figure 3 shows the relative accuracy when the number of wires in the mechanical and NEC models of the TACAMO antenna are varied. Each data point refers to a mechanical calculation and a NEC calculation in series, where the NEC calculation is based on the output wire shape from the mechanical calculation. The point labeled "Baseline model" represents the mechanical and electromagnetic segmentation chosen for TESS, based on the run time/accuracy trade-offs. For the mechanical calculation, this baseline model entails dividing the LTWA into 50 straight wires. For the NEC calculations, this baseline model entails dividing the LTWA into 10 straight wires and the STWA into 5 wires. Dividing the antennas more finely for the mechanical or NEC calculation causes an increase in run-time without greatly increasing the accuracy.

This leaves the question of how to divide the straight wires of the NEC model into segments for the NEC calculation. As has been mentioned, the rule of thumb is that the segment lengths must be less than a tenth of a wavelength at the frequencies of interest for an accurate NEC calculation. A typical transmission frequency for the TACAMO system is 25 KHz, which gives a wavelength

---

[1]"Numerical Electromagnetics Code -- NEC-4 User's Manual", Gerald J. Burke, LLNL Report Number UCRL-MA-109338, page 3, January, 1992.

of 12 km. By comparison, the long TACAMO wire is typically about 5.9 km. Dividing the long TACAMO wire into ten straight wires gives a wire length of about .05 wavelengths, so by the previously mentioned "rule of thumb" we would not expect to need more than one segment per straight wire.

However, Figure 4 shows results from a representative calculation that indicates the sensitivity of the NEC model to the number of segments near the drive point. This figure shows the polar component of the electric field from the TACAMO system as a function of the polar angle. The numbers of straight wires and segments in the models are indicated in the legend. For example, the curve labeled "16 Away, 18 Near" refers to the case where the NEC model has 16 segments per wire on wires away from the drive point and 18 segments per wire on wires near the drive point. As expected, reducing the number of segments per wire from six to one does not change the results of the calculation except when the number of segments on the wire closest to the drive point is changed. When the segments away from the drive point remains at one, but the segments on the wire nearest the drive point are reduced from 18 to 10, we begin to see a change in the accuracy of the NEC calculation. Based on a series of similar runs and on run-time considerations, we have chosen the NEC model to use in TESS to contain ten straight wires for the long wire and five for the short wire, with ten segments per wire for the wires nearest the drive point and one segment per wire for all the other wires.

GROUND PLANE CHARACTERISTICS

The other parameters that were mentioned above as possibly having some effect on the NEC model results are the dielectric constant and conductivity of the ground plane under the TACAMO system. We performed a trade study to determine the importance of changing these parameters. The results of the trade studies show that the current distributions and the wires and electric fields from the wires are almost independent of the ground plane characteristics, where the parameters characterizing the ground plane were varied from those typical of ocean water to those typical of dry earth. The impedance of the TACAMO wires were also basically independent of these changes. Therefore, the power emitted from the TACAMO antenna is essentially independent of the ground plane characteristics, for a physically reasonable range of those characteristics, and the ground plane dielectric constant and conductivity are found to be unimportant for the NEC part of TESS. The physical reason for this is that the conductivity of the ground plane gives the effective position at which the boundary conditions would be applied, i.e. a skin depth. This skin depth, however, is negligible compared to the antenna height or wavelength. The NEC model does, however, require a ground plane beneath the TACAMO system, in the location of the ground.

This does not mean that the characteristics of the ground over which the radiation from the TACAMO antenna is propagating are unimportant to the end result of the TESS calculation. The ground plane characteristics have a large effect on the propagation part of the calculation. However, that information is already contained accurately in SIMBAL and WEDCOM. Those characteristics do not affect the near field results of the NEC part of TESS.

Figure 5 shows an example of results from a full TESS calculation. This curve shows the vertical component of the electric field as a function of distance from the TACAMO antenna, near the ground plane, as calculated by the full TESS code, with SIMBAL as the propagation section of the code. Within 500 km of the TACAMO antenna, the vertical electric field falls off as $1/r$, as would be expected. Farther from the TACAMO antenna, the vertical electric field falls off more sharply, approximately as $r^{-1.55}$, due to the increased effects of ionosphere and ground plane losses at larger distances. At the distance of the "knee", the TACAMO antenna and reception location are

out of line-of-sight of each other, resulting in the increased importance of ionospheric losses. This full TESS calculation is in very good agreement with data.

CONCLUSION

The current version of the TESS system is a useful tool for calculating the expected electric fields long distances from the TACAMO transmitter. This paper has shown results of trade studies which have determined the NEC model used in TESS. Future versions of TESS will include detailed, automated graphical output and a refined version of the NEC-SIMBAL interface. In the future versions of this interface, SIMBAL will be modified to accept as input from NEC the actual near-field electric fields that NEC calculates based on the model of the TACAMO transmitter, rather than the dipole approximation that the NEC-SIMBAL interface now uses. This should improve the accuracy of the final results of the TESS calculation even further.

Figure 1. Sequence of Calculations in the TACAMO Electromagnetic Simulation System

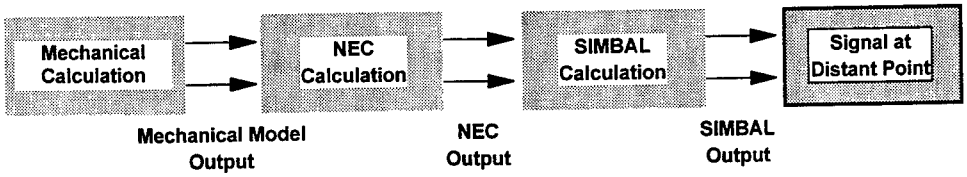

Figure 2. NEC Model of the TACAMO Antennas

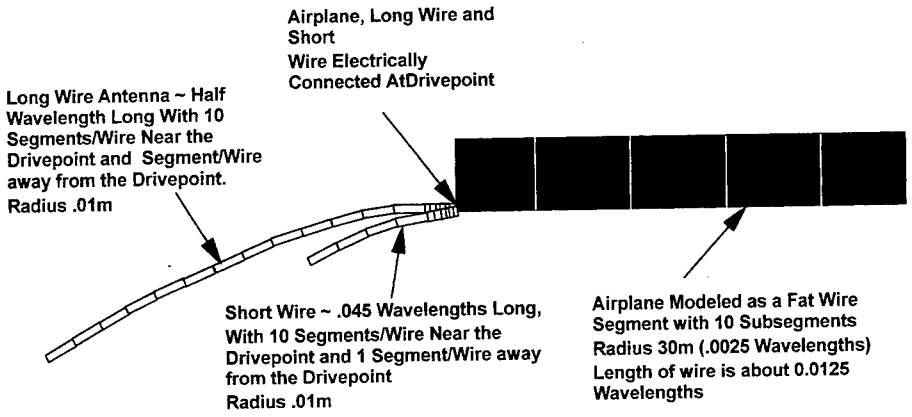

Figure 3. Dependence of Accuracy and Run-Time on Segmentation Methods

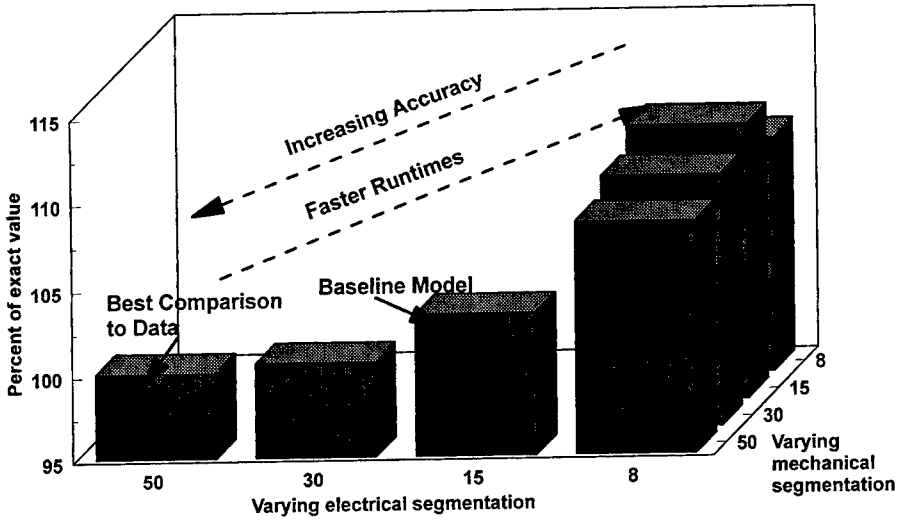

Figure 4. Sensitivity of the NEC Model Results to Number of Segments/Wire

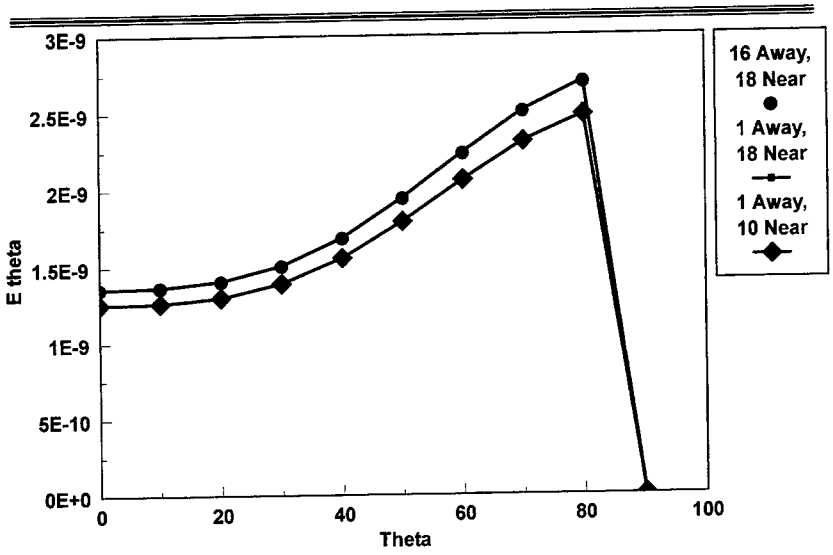

Figure 5. Sample Results from a TESS Calculation

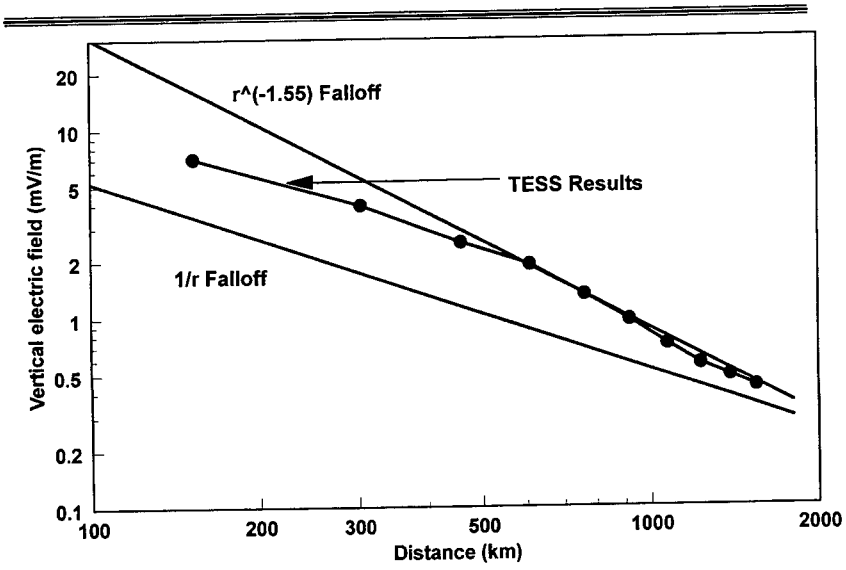

A New Look at Antenna Traps

Paul W. Leonard, P. E. (W7LMX)

Hatfield & Dawson Consulting Engineers
4226 Sixth Avenue N. W.
Seattle, WA 98107

Abstract: A trap monopole is described which gives gain at the high-band frequency in trade for a poor matching impedance.

Introduction: Trap antennas have been used for a long time, and are very convenient for multiband antennas since they give a good impedance on each frequency band. However, the antenna is effectively one-quarter wavelength long (assuming a monopole) at each frequency. At the higher frequencies the structure is long enough to support a gain antenna. There is plenty of precedence for this. One example is known as the "Franklin Antenna," Reference 1. These antennas depend upon a phase reversal at the current node in order the keep the current in phase along the length of the antenna. Another example (Reference 2) is call a controlled current antenna. These designs are single band antennas. At the low frequency, say 40-meters (7.24 MHz), a short monopole with inductive loading will give a good impedance and the antenna gain is comparable to a short dipole. I propose to put a resonant circuit approximately in the center of a 25-foot monopole which at 40-meters (7.24 MHz) provides inductive loading and at 10-meters (29.0 MHz) provides capacitive reactance for gain.

Test calculations: A twenty-five foot monopole was modeled using our MININEC program, MBPRO, Reference 3. A capacitive reactance was modeled at the middle of the antenna. Several values of capacitance were tried to determine the value for maximum gain at 29 MHz. Figure 1 shows the monopole gain over a short monopole versus the center reactance. This shows that a value between -700 and -900 ohms gives more than 2.8 dB gain. Now let's look at the base impedance, Figure 2. This is a poor impedance match to 50-ohms. However, the new transceivers frequently have an antenna tuner placed at the base of the monopole that is capable of matching the impedances to 50-ohms. Therefore, by use of a capacitive reactance in the center of the antenna we can have nearly 3-dB gain.

At 40-meters wavelength the 25-foot antenna is only 66 electrical degrees high. The radiation pattern is almost the same as that of a very short monopole. This was verified with the computer model and is true even if the current along the monopole is uniform, the case for maximum gain. Therefore, all the loading coil can do at the 40-meter wavelength is improve the base impedance. Figure 3 shows the base impedance versus loading coil reactance. An inductive reactance of 290 ohms gives a base impedance that can be matched easily.

The trap impedance is defined as follows:

7.24 MHz	+290 ohms
29.0 MHz	-700 ohms

Implementation: A shunt resonant circuit consisting of a 5.42-microhenry inductance in parallel with a 13.39- picofarad capacitor will provide the above impedance. Note that this circuit has a resonant frequency of 18.68 MHz. There are many ways to construct this circuit. The coil can be about 10 turns, one inch in diameter and one inch long. The capacitor can be made from telescoping the upper mast tube about one-half inch into the lower tube with one-eighth inch thick insulation. Another way to construct a trap is given in Reference 4.

Conclusion: This antenna has a reasonable impedance at 7.24 MHz, but will need an antenna tuner at the base for 29 MHz. You will get better than 2.8 dB gain over a short monopole at the 29 MHz frequency. The above frequencies were for demonstration purposes. Many other pairs of frequencies can be used.

REFERENCES

1. Edmund A Laport, "Radio Antenna Engineering," McGraw-Hill Book Co. Inc. p. 82
2. Stanly Kaplan & E. Joseph Bower, "The controlled Current Distribution (CCD) Antenna," The ARRL Antenna Compendium Volume 2 p. 132
3. J. W. Rockway and J. C. Logan, "MININEC Professional for Windows," EM Scientific, Inc.
4. Albert C. Buxton, W8NX, "An 80/40/17-Meter Super-Trap Dipole," The ARRL Antenna Compendium, Volume 3.

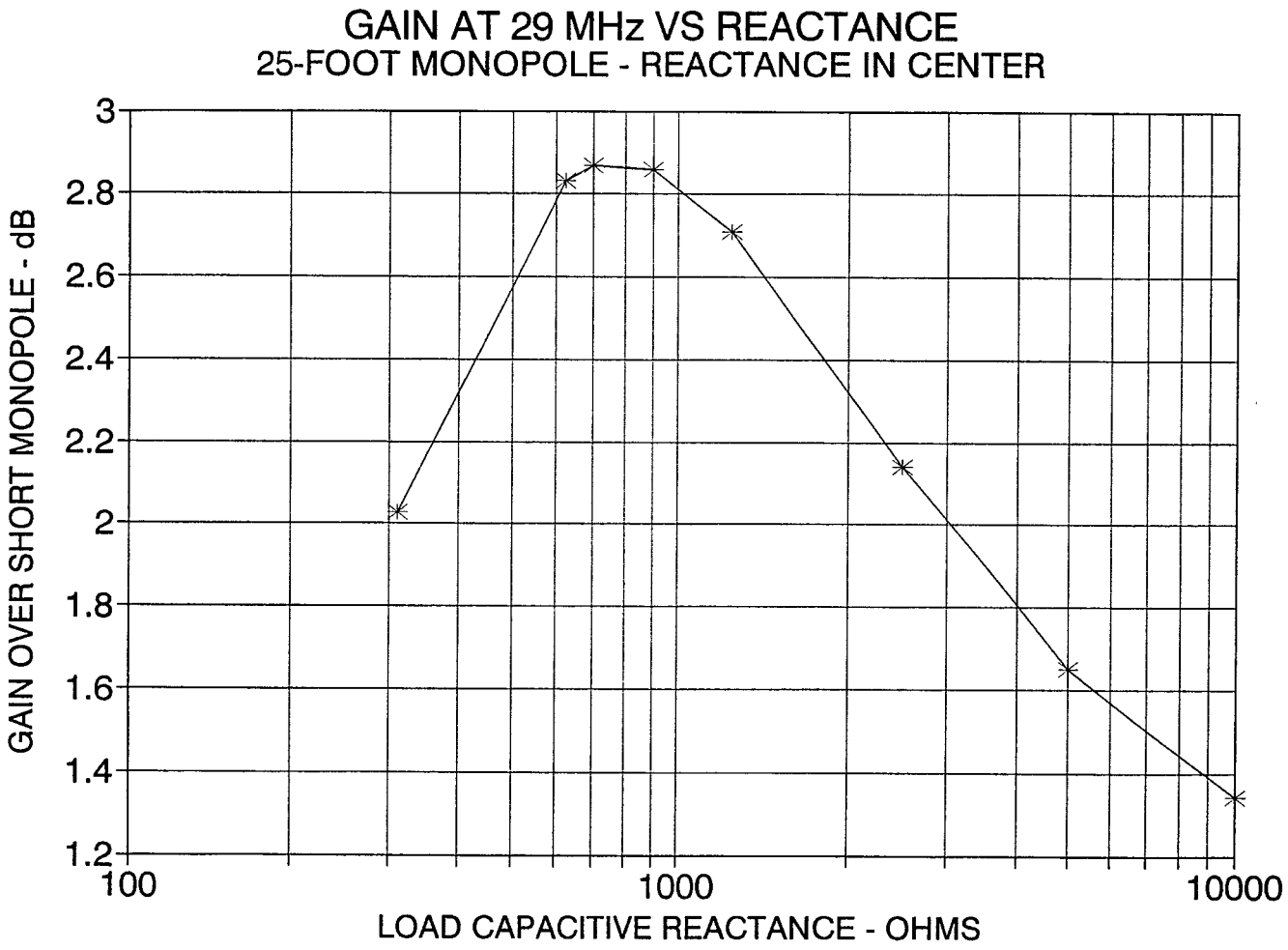
GAIN AT 29 MHz VS REACTANCE
25-FOOT MONOPOLE - REACTANCE IN CENTER
GAIN OVER SHORT MONOPOLE - dB
3
2.8
2.6
2.4
2.2
2
1.8
1.6
1.4
1.2
100
1000
10000
LOAD CAPACITIVE REACTANCE - OHMS

FIGURE 1

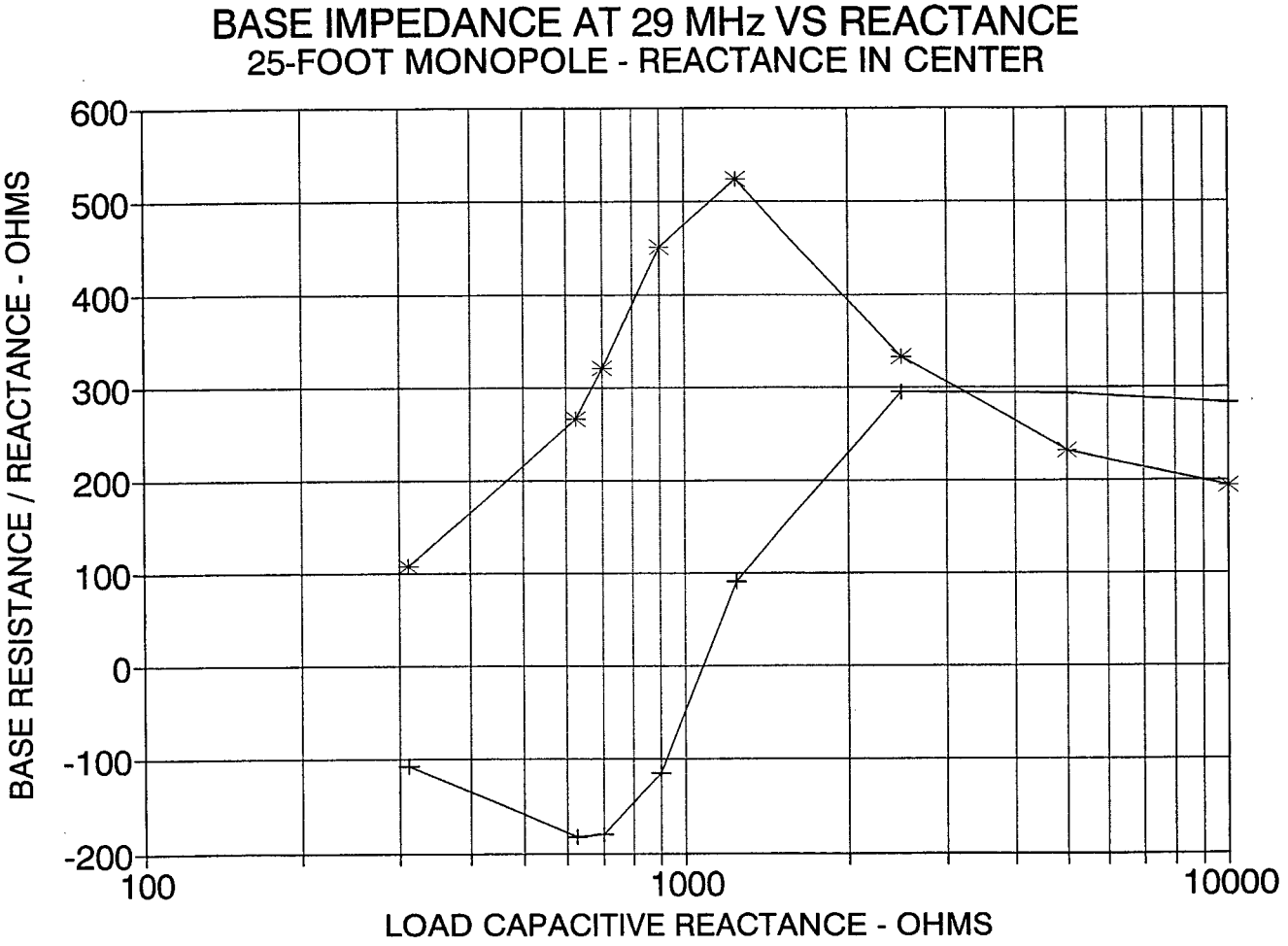
BASE IMPEDANCE AT 29 MHz VS REACTANCE
25-FOOT MONOPOLE - REACTANCE IN CENTER
BASE RESISTANCE / REACTANCE - OHMS
600
500
400
300
200
100
0
-100
-200
100
1000
10000
LOAD CAPACITIVE REACTANCE - OHMS

FIGURE 2

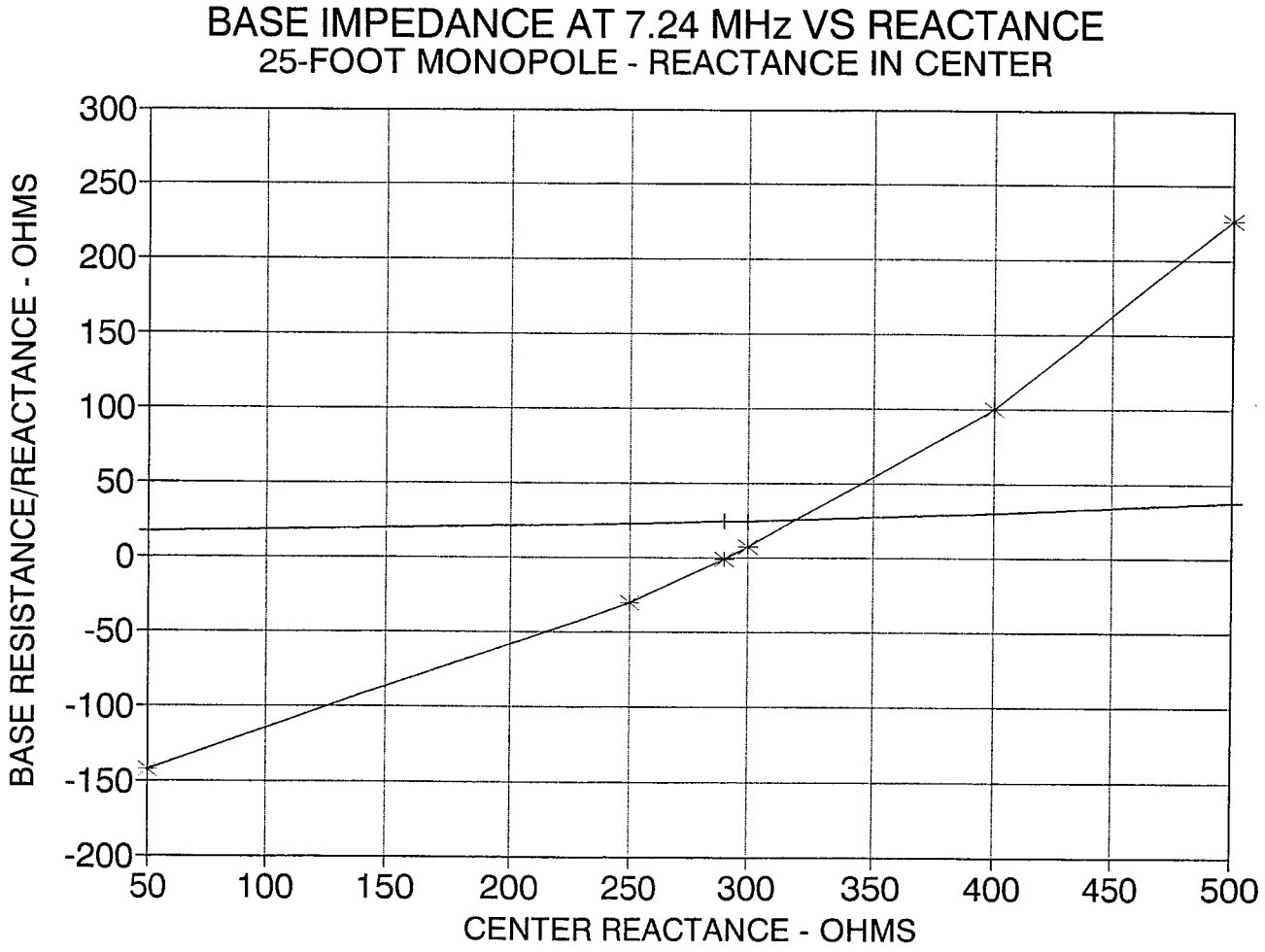
BASE IMPEDANCE AT 7.24 MHz VS REACTANCE
25-FOOT MONOPOLE - REACTANCE IN CENTER
BASE RESISTANCE/REACTANCE - OHMS
300
250
200
150
100
50
0
-50
-100
-150
-200
50
100
150
200
250
300
350
400
450
500
CENTER REACTANCE - OHMS

FIGURE 3

Imaging of Conductive and Ferromagnetic Materials Using a Magnetic Induction Technique

J. Ferreira, F. Linhares, J. Velez, J. E. de Oliveira, A. R. Borges

INESC Aveiro
Departamento de Electrónica e Telecomunicações
Universidade de Aveiro, 3810 Aveiro, Portugal
Fax: +351 34 370545 email: jjf@vlsina.inesca.pt

Abstract

This paper describes a tomographic system which images conductive and ferromagnetic materials using a magnetic induction technique. The region of interest has a circular shape and is surrounded by 16 excitation/detection coils, equally spaced and radially oriented. Data acquisition implies that each coil in turn is energised with a 100 kHz sinusoidal current while all others are sensing the generated magnetic flux. A total of 240 independent measurements (16 projections times 15 measurements each) are then taken in about 10 ms. The sensor design has been validated by simulation and a close agreement was found between simulated and real data. Two different algorithms were used for imaging of objects. The first is a heuristic algorithm based on a priori *knowledge and enables the detection of both the location and the diameter of a rod of different materials (highly conductive, highly conductive and ferromagnetic, non-conductive and ferromagnetic) with a small error. This algorithm is very efficient and works at almost real time. The second is a ART-type algorithm which uses the experimentally acquired sensitivity maps to build the projection matrix. Presently, qualitative images of different combinations of highly conductive and ferromagnetic objects placed within the region of interest, are obtained. In a 66 MHz 486 PC, 5 iterations of this algorithm take about 3 seconds.*

1 Introduction

Interest on the use of electrical tomographic methods for process applications, specially on-line monitoring and control, has been growing in the past few years.

Electrical Impedance Tomography (EIT), originally introduced for medical imaging [Barber 84, Seager 87], and Electrical Capacitance Tomography (ECT) [Huang 92, Xie 92] are techniques relatively well developed today. Systems based on them and targeted for specific applications are under evaluation [Gutierrez 95, Reinecke 95].

Electromagnetic Tomography (EMT) or Magnetic Inductance Tomography, on the other hand, is not so well understood. A few scanners based on its principles have been built [Zeibak 93, Yu 93, Yu 94] and the potential of this imaging technique for processing applications is currently being assessed. General overviews may be found in [Peyton 95, Peyton 94].

In this paper, a system to image conductive and ferromagnetic materials is described. It is shown how scanner design has been validated through simulation, and results produced by two different imaging algorithms are presented.

2 Physical Principle

Figure 1 describes in a schematic way the physical principle of EMT.

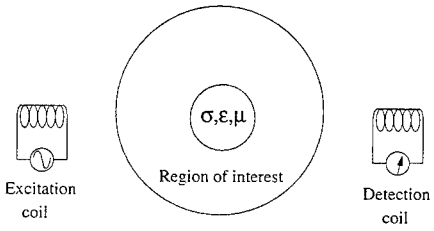

Figure 1: Physical principle of an EMT system.

The region of interest is energised by an AC sinusoidal magnetic field created by one or more excitations coils placed at its border. Magnetic field distribution is, in general, affected by its angular frequency (w) and by the electrical conductivity (σ), the electrical permittivity (ϵ) and the magnetic permeability (μ) of the medium.

For media having linear and isotropic electrical and magnetic properties, and further assuming that σ, ϵ and μ are constant throughout the different materials in the region of interest, and that the displacement currents may be neglected, the Maxwell equations in phasor notation yield [Kraus 92]:

$$\nabla \times \nabla \times \mathbf{B} = -jw\sigma\mu \cdot \mathbf{B} \tag{1}$$

$$\nabla \cdot \mathbf{B} = 0 \quad . \tag{2}$$

The tomographic reconstruction problem can then be stated in the following way: knowing for different excitation patterns the values of the radial component of the magnetic flux density vector $\mathbf{B}$ along the border of the region of interest (which can be deduced from the induced voltage in the detection coils), estimate the spatial distributions of the electrical conductivity σ and the magnetic permeability μ of the materials that lay inside.

3 Description of the Imaging System

Figure 2 presents a general view of the EMT system that was built. Its block diagram is illustrated in figure 3 and, as it can be seen, consists of three main sub-systems: the scanner, the coils interface, signal conditioning and data acquisition circuitry and the host computer.

The scanner is made of three concentric plastic pipes. The region of interest is defined inside the innermost (or third) one and has a diameter of 150 mm. Sixteen coils, consisting of a small winding on a core mounted ferrite rod, are positioned between the second and the third pipe, equally spaced and radially oriented. Between the first and the second pipe, a ring shaped shield, made of compressed ferrite powder, surrounds the region of interest in order to confine the magnetic flux and, thus, increases sensitivity and acts as a screen against external interference.

The sixteen coils are wired in such a way that each can operate as an emitting or receiving coil. The coils interface electronics, through computer control, defines the excitation pattern. The main function of the signal conditioning unit is to convert each induced voltage into two basic measurements (amplitude and phase shift) which are then transferred to the host computer by the data acquisition circuitry.

The adopted excitation pattern implies that each coil in turn will be energised with a 100 kHz sinusoidal electrical current while all the others will be sensing the generated magnetic flux at the border of the region of interest. This constitutes a projection. At the end of a complete scan, 16 projections with 15 measurements each are obtained, yielding a total of 240 independent measurements. This is carried out in about 10 ms.

The host computer, a PC, besides acting as a front-end to the user, controls the sensing set up, runs the tomographic algorithms and displays the reconstructed images.

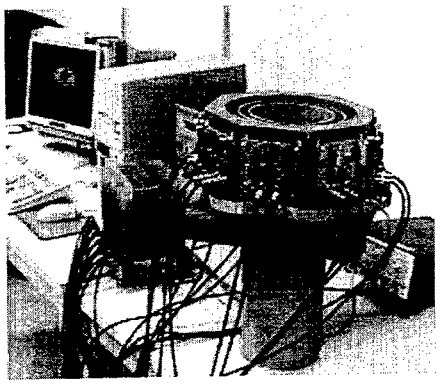

Figure 2: EMT system's general perspective.

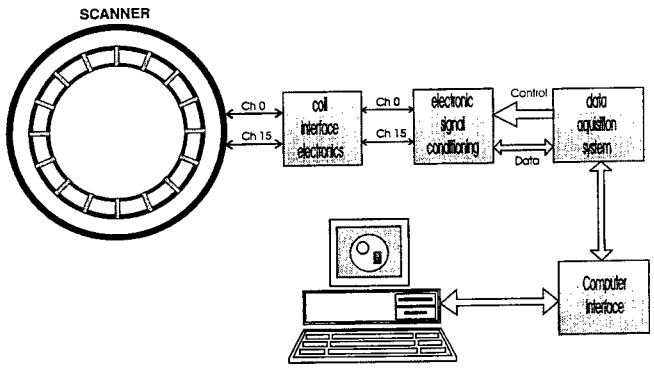

Figure 3: Block diagram of the EMT system.

4 Design Validation

A computer simulation of the scanner was carried out to check its performance and to provide data to help the design of future enhanced EMT scanners.

The analytic solution of field equations for the scanner geometry with and without the presence of a sample object was not yet developed due to its complexity, although some results for a related geometry (parallel excitation field) have already been reported [Albrechtsen 95, Xiong 95].

The simulation model was input into an electromagnetic simulator, the Ansoft Maxwell 2D Simulator, version 1.3. The simulation output was the flux linkage computed by the Eddy Current Field Solver [Ansoft 94] at the location of each detection coil.

The region of interest was sampled at 97 different locations, as shown in figure 4. Sensitivity maps were obtained by successively placing a 10 mm sample rod at those locations. For the simulation, only 55 positions are needed due to the symmetrical properties of the geometry used. Three different materials were considered (aluminium,

ferrite and soft iron).

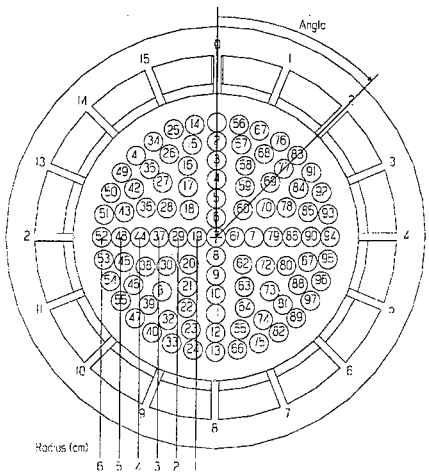

Figure 4: Locations at which the region of interest was sampled.

Figure 5 shows the sensitivity maps of the scanner at coil number 7 for both simulated and real data. As it can be seen, the two maps are rather close even though one results from a 2D simulation of a 3D structure. The reason for that stems from the fact that the diameter of the coils is 0.4 cm, while the sample rods used were cylinders 3 cm height placed half way through the plane that contains the axis of the coils. The noise present in the simulation data sensitivity maps results from the re-meshing which takes place every time a new position is computed.

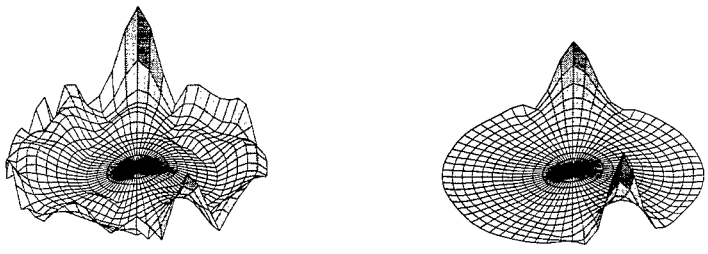

Figure 5: Sensitivity maps with simulated data (left) and experimental data (right).

5 Imaging Algorithms

5.1 Heuristic Procedure

Simple image reconstruction algorithms can be devised for EMT systems in certain situations by assuming *a priori* knowledge of the object being imaged. This type of algorithms solve very simplified problems, for example, locating the position of a single target object of known geometry and material in the region of interest which is otherwise non-magnetic and non-conductive.

The heuristic algorithm being applied can be subdivided into four steps:

1. Measurements are evaluated to decide in which coarse category the target material falls in:
   - non-conductive and ferromagnetic.
   - highly conductive and ferromagnetic.
   - highly conductive.

   This information is used in the following steps for the selection of proper internal parameters.
2. The angular coordinate of the target object centre in a polar system is determined by selecting the projection with the highest variation for the detection coil just opposite to the excitation one. A correction is then introduced by fitting the measurements to a gaussian curve.
3. The radial coordinate of the target object centre in a polar system is determined next by selecting one of the orthogonal projections to the one found in step 2 and performing linear interpolation.
4. Having found the target centre location and having an idea about the target material, the target diameter is finally determined also by linear interpolation.

Experiments have shown that it is possible to determine the (x,y) position, the diameter and the type of material of a sample rod with good results. Figure 6 shows the plots of the estimated error for different situations.

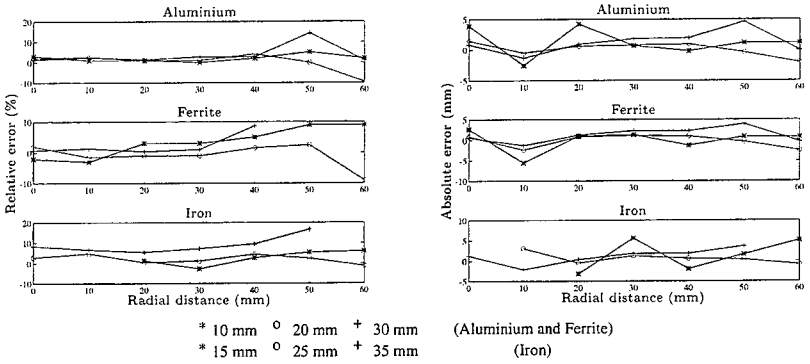

Figure 6: Estimated error on the evaluation of the diameter of a sample rod (left) and estimated error on the evaluation of the distance from the sample rod centre to the middle of the region of interest (right). Different materials are considered.

5.2 ART

Inverting equations (1-2) represents a strongly ill-posed problem. Only the radial component of the magnetic flux density vector **B** is known and even that, at only a finite set of points at the boundary of the region of interest. Thus, even if noise is not taken into account, the problem will be underdetermined for the general case. So the best approach is to proceed in an iterative way.

ART-type (Algebraic Reconstruction Techniques) form a class of iterative algorithms for solving large systems of equations, based on a quadratic optimisation criterion, which were introduced into image reconstruction by Gordon, Bender and Herman in 1970 [Gordon 70]. A good overview is found in [Herman 80].

In matrix notation, the system of equations may be represented in the following way:

$$\mathbf{p} = \mathbf{A}.\mathbf{f} \quad . \tag{3}$$

$\mathbf{p} = (p_i) \in \Re^M$ represents the measurement vector, $\mathbf{f} = (f_i) \in \Re^N$ the image vector and $\mathbf{A} = (a_{ij}) \in \Re^M \times \Re^N$ the projection matrix, which accounts for the physical model of data collection.

The algorithm that has been used is a straightforward implementation of Kaczmarz projection method based on a least squares minimum norm criterion, which can be summarised as follows:

Initialisation:

$$\mathbf{f}^{(0)} \text{ is arbitrary}$$

Each step:

$$\mathbf{f}^{(k+1)} = \mathbf{f}^{(k)} + \lambda \cdot \frac{p_i - < \mathbf{a}_i . \mathbf{f}^{(k)} >}{\|\mathbf{a}_i\|^2} \cdot \mathbf{a}_i \quad . \tag{4}$$

The projection matrix was computed from the sensitivity map data and was stored in memory which makes the algorithm rather efficient. In a 66 MHz 486 PC, five iterations take about 3 seconds.

However, the convergence towards a reasonable solution is not assured. The projection matrix **A** was built assuming linearity which is not true since the field interactions are quite non-linear. So it does not pay to proceed iterating after a certain point, since the noise in the image will rise. The rate of convergence can be increased with the proper ordering of the equations, the choice of a good value for the relaxation factor and the use of *tricks* [Herman 80].

Figure 7 shows an example of what has currently been achieved. Spatial resolution is not very good and the images are only qualitative, although one can already distinguish between highly conductive non-ferromagnetic objects and non-conductive ferromagnetic objects.

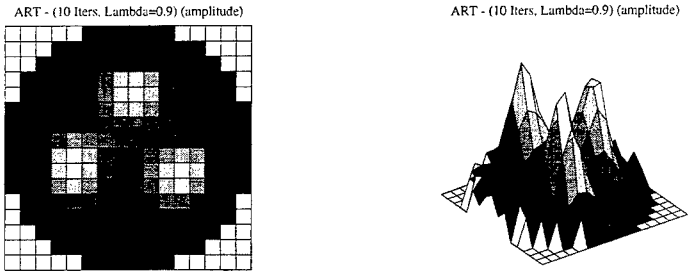

Figure 7: ART reconstruction of three 2.5 cm diameter aluminium rods placed at the corners of a 2.5 cm equilateral triangle located at the centre of the region of interest.

6 Conclusions

This paper has described a EMT tomographic system able to image conductive and ferromagnetic materials. At present, this system is only laboratory based and was developed primarily to assess the technique. However, the results so far obtained show promise at its application to process monitoring and control.

An inherent limitation of the technique has to do with the signal to noise ratio. Magnetic field distortions due to the presence of objects in the region of interest are usually very small when compared with the applied magnetic field. This means that signal conditioning electronics has to be designed very carefully to minimise this effect.

On the other hand, reconstruction algorithms produce presently only qualitative images. Further investigation is needed to develop more sophisticated algorithms which will separate the images of the spatial distributions of the electrical conductivity and the magnetic permeability. Thus, turning EMT into a true dual modality imaging technique.

Acknowledgements

The authors would like to thank the CEU (Brite EuRam contract no. BRE2-CT94-0604) for their support.

References

[Albrechtsen 95] R. Albrechtsen, Z. Yu, and A. Peyton, "Towards an analytical approach for determining the sensitivity limits and sensitivity maps of mutual inductance tomography", *ECAPT-European Concerted Action on Process Tomography, Bergen-Norway*, 288–299, 1995.

[Ansoft 94] *Maxwell 2D Field Simulator Users's Reference.* Ansoft Corporation, June 1994.

[Barber 84] D. Barber and B. Brown, "Applied potential tomography", *J. Phys. E., Sci. Instrum.*, 17:723–733, 1984.

[Gordon 70] R. Gordon, R. Bender, and G. Herman, "Algebraic reconstruction techniques (ART) for three-dimentional electron microscopy and X-ray photography", *J. Theor. Biol.*, 29:471–481, 1970.

[Gutierrez 95] J. Gutiérrez, E. Etuke, T. Dyakowski, and M. Beck, "Use of electrical impedance tomography for multiphase flow imaging in hydrocyclones", *ECAPT-European Concerted Action on Process Tomography, Bergen-Norway*, 29–40, 1995.

[Herman 80] G. Herman, *Image Reconstruction from Projections: The Fundamentals of Computerized Tomography.* Academic Press, 1980.

[Huang 92] S. Huang, C. Xie, R. Thorn, D. Snowden, and M. Beck, "Design of sensor electronics for electrical capacitance tomography", *IEE Proc. G*, 139:83–88, 1992.

[Kraus 92] J. D. Kraus, *Electromagnetics.* McGraw-Hill, fourth edition, 1992.

[Peyton 94] A. Peyton, Z. Yu, S. Al-Zeibak, N. Saunders, and A. Borges, "Electromagnetic imaging using mutual inductance tomography: Potential for process applications", *ECAPT-European Concerted Action on Process Tomography, Porto-Portugal*, 439–450, March 1994.

[Peyton 95] A. Peyton and A. Borges, "Principles of mutual inductance tomography", *Frontiers in Industrial Process Tomography, S. Luis Obispo-California, USA*, October 1995.

[Reinecke 95] N. Reinecke, C. Xie, D. Mewes, and M. Beck, "Application of capacitance tomography for the two-dimensional imaging of pulse flow in trickle-bed reactors", *ECAPT-European Concerted Action on Process Tomography, Bergen-Norway*, 71–83, 1995.

[Seager 87] A. Seager, D. Barber, and B. Brown, "Electrical impedance imaging", *IEE Proc. A*, 201–210, 1987.

[Xie 92] C. Xie, S. Huang, B. Boyle, R. Thorn, C. Lenn, D. Snowden, and M. Beck, "Electrical capacitance tomography for flow imaging: System model for development of image reconstruction algorithms & design of primary sensors", *IEE Proc. G*, 139:89–98, 1992.

[Xiong 95] H. Xiong, "Electromagnetic tomographic imaging for process measurement and control: Theoretical analysis and mathematical formulation". 1995. Submitted for publication.

[Yu 93] Z. Yu, A. Peyton, W. Conway, L. Xu, and M. Beck, "Imaging system based on electromagnetic tomography (EMT)", *Electronics Lett.*, vol. 29(7):625–626, 1993.

[Yu 94] Z. Z. Yu, *Non-Intrusive Inductance Based Electromagnetic Tomography (EMT) Techniques for Process Imaging.* PhD thesis, UMIST, September 1994.

[Zeibak 93] S. Al-Zeibak and N. Saunders, "A feasibility study of *in vivo* electromagnetic imaging", *Phys. Med. Biol.*, 38:151–160, 1993.

Investigation of the Properties of Wavelet-like Basis Functions in the Finite Element Analysis of Elliptic Problems

Lee A. Harrison and Richard K. Gordon
Department of Electrical Engineering
University of Mississippi
University, MS 38677

Abstract

In this paper, the use of wavelet-like basis functions in the finite element analysis of elliptic problems in which the mesh has a fine discretization in one region, and a coarse discretization over the remainder of the region, will be presented. Construction of the wavelet-like basis functions for this type of discretization will be discussed. The condition numbers of the resulting matrices, along with the number of steps required for convergence of the conjugate gradient solution will be presented. Comparisons will be made with results obtained from a finite element algorithm employing traditional basis functions.

Introduction

A wavelet is a function that is localized in both the spatial and frequency domains, and is such that any square integrable function can be expressed in terms of translations and dilations of the wavelet. The properties of wavelets give them numerous applications in such areas as sampling, time-frequency analysis, and signal compression. Only recently have wavelet methods been applied in areas of computational electromagnetics. The use of wavelet methods in integral equation techniques, in which the unknown response is represented in terms of shifted and dilated forms of the wavelet, has been examined [1]; and more recently wavelets have been used in the finite element solution of partial differential equations [2]. Gordon has discussed the use of wavelet-like basis functions in the finite element analysis of elliptic problems over highly heterogeneous domains [3].

One problem of the finite element method lies in the solution of a large matrix equation. As the number of basis functions is increased, the dimension of the system matrix increases; and as this occurs, the condition number of the system matrix increases as well. With the use of the usual preconditioning methods, the condition number of the system matrix will increase as $\frac{C}{h}$ (where h is the subsection length). If simple diagonal preconditioning is used, the condition number will go to infinity as $\frac{C}{h|\log(h)|}$, as the number of points of discretization is increased. This increase in condition number can create solution problems such as numerical instabilities, slow convergence, or even lack of convergence. With the use of wavelet-like basis functions and simple diagonal preconditioning, it has been shown that the finite element method yields a system matrix that is bounded by a constant as the number of basis functions is increased [4]. Thus, the

use of wavelet-like basis functions appears to have significant potential in the solution of large matrix equations arising from the finite element method.

Construction of the Wavelet-like Basis Functions

To construct the wavelet-like basis functions to be used in the finite element algorithm, the technique described in [4] is employed. This is a multiresolution analysis and proceeds as follows. An appropriate initial discretization of the problem domain is chosen. This initial discretization is chosen such that it contains only a few nodes. The traditional basis functions corresponding to the nodes in this initial discretization are orthonormalized with respect to each other. These orthonormalized functions are the first of the wavelet-like basis functions. New nodes are then added to the mesh at locations that divide the subsections between the previous nodes. The traditional basis functions corresponding to these new nodes are then orthogonalized against the existing wavelet-like basis functions. Then, the resulting functions are orthonormalized with respect to each other. The functions that follow from this procedure are then added to the basis of wavelet-like functions. To further refine the mesh in a given region, new nodes are added between the existing nodes only in the region of interest. The traditional basis functions associated with these new nodes are orthogonalized against the existing wavelet-like functions, and the resulting functions are then orthonormalized with respect to each other. The number of points of discretization may be increased by repeating this procedure. Once the desired discretization is obtained, the standard finite element method is then employed using the wavelet-like functions which have been constructed.

Consider the elliptic problem:

$$-\nabla \cdot (a\nabla u) + bu = g \text{ on } \Omega$$

$$u = h \text{ on } \partial\Omega$$

where Ω is the problem domain, $\partial\Omega$ is the boundary of Ω, $a \geq C > 0$, and $b \geq 0$.

As an illustration of these ideas consider the following one dimensional problems:

Case A: Ω is the line segment from x=0 to x=1 and:

$$a(x) = \begin{cases} 1.0 \text{ for } 0.25 < x < 0.5 \\ 25.0 \quad \text{otherwise} \end{cases}$$

$$b(x) = 0.0$$

$$u(0) = 10.0$$

$$u(1) = 25.0$$

$$g(x) = 0.0$$

Case B: Ω is the line segment from x=0 to x=1 and:

$$a(x) = 1.0$$

$$b(x) = 3.0$$

$$u(0) = 5.0$$

$$u(1) = 15.0$$

$$g(x) = x\exp(x)$$

With the above conditions, it is desired to have more basis functions in the region $.25<x<.5$, and fewer basis functions outside this region. The first few basis functions are shown in figures 1-5. The initial discretization contains a single node located at the midpoint of the interval. Figure 1 shows the first function added to the basis corresponding to this node. Figures 2 and 3 show the basis functions which result from new nodes being added to the mesh. At this point, new nodes are only added in the region $.25<x<.5$, and the resulting basis functions are shown in figures 4 and 5.

Numerical Results

Case A: The problem above was solved using 7, 9, 13, 21, 37, 69, 133, 261, 517, and 1029 wavelet-like and traditional basis functions. Figure 6 shows the condition number versus number of basis functions when wavelet-like basis functions are used. The corresponding plot for the traditional basis functions can not be shown on the same graph because it would be far off scale, thus Figure 7 is presented to show these results. From these figures, it can be seen that the condition number is 576,513 when 1029 traditional basis functions are used, and that when wavelet-like basis functions are used the condition number reaches a value of 37.64 and then decreases as the number of basis functions is increased. Clearly, the preconditioned global matrix arising from the use of wavelet-like functions is much better conditioned than that arising from the use of traditional basis functions. The importance of this is demonstrated in figures 8 and 9. In these figures we see plots of the number of steps required for the convergence of the conjugate gradient algorithm for each of the cases presented in figures 6 and 7. (The conjugate gradient algorithm was applied using the preconditioned global matrix for which the condition number is plotted in figures 6 and 7.) From these figures, it is seen that when wavelet-like basis functions are used, the number of steps remains less than 21 even when 1029 basis functions are used. For the same number of traditional basis functions, the number of steps required is 1029. From Figure 8 it can bee seen that when wavelet-like basis functions are used, the number of steps required for a matrix of order 1029 is only 5.26% greater than the number of steps required for a matrix of order 69, and only 25% greater than that required for a matrix of order 21.

Case B: This problem was also solved using 7, 9, 13, 21, 37, 69, 133, 261, 517, and 1029 wavelet-like and traditional basis functions. Figures 10 and 11 show the condition number versus

number of basis functions, when wavelet-like and traditional basis functions are used. In this case, the effect on the condition number is more dramatic. When traditional basis functions are used, the condition number climbs to more than 2.8 million for 1029 basis functions. For the same number of wavelet-like basis functions, the condition number remains less than 17. Figures 12 and 13 show the number of steps required for convergence of the conjugate gradient algorithm for the preconditioned matrices arising from the use of wavelet-like and traditional basis functions. Again, these figures show that the performance obtained using the wavelet-like basis functions is much better than that of the traditional basis functions. From Figure 12, we can see that the number of steps required for a matrix of order 1029 is 7.69% greater than that for a matrix of order 69, and only 27.2% greater than the number of steps required for a matrix of order 21.

Conclusions

In this paper, the use of wavelet-like basis functions in the solution of elliptic problems over one-dimensional domains is discussed. In this case, the use of such basis functions yields matrices that, with simple diagonal preconditioning, are much better conditioned than are those resulting from the use of traditional finite element basis functions. This leads to much more rapid convergence of the conjugate gradient algorithm when these wavelet-like basis functions are employed.

REFERENCES

[1] Ben Zion Steinberg and Yehuda Leviatan, "On the use of wavelet expansions in the method of moments," *IEEE Transactions on Antennas and Propagation*, vol. 41, num. 5, pp. 610-619, May 1993.

[2] T. K. Sarkar, L. E. Garcia-Castillo, and M. S. Salazar-Palma, "Utilization of wavelet concepts in finite elements for efficient solution of Maxwell's equation," *1994 Digest of the IEEE Antennas and Propagation Society International Symposium*, vol. 1, p. 7, June 1994.

[3] Richard K. Gordon, "On the use of wavelet-like basis functions in the finite element analysis of elliptic problems", Proceedings of The Eleventh Annual Review of Progress in Applied Computational Electromagnetics, pp. 559-567, Monterey, CA, March, 1995.

[4] Stephane Jaffard, "Wavelet methods for fast resolution of elliptic problems," *SIAM Journal on Numerical Analysis*, vol. 29, num. 4, pp. 965-986, August 1992.

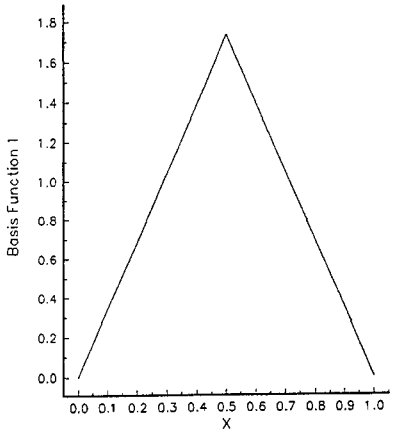

Figure 1. Wavelet–like basis function 1

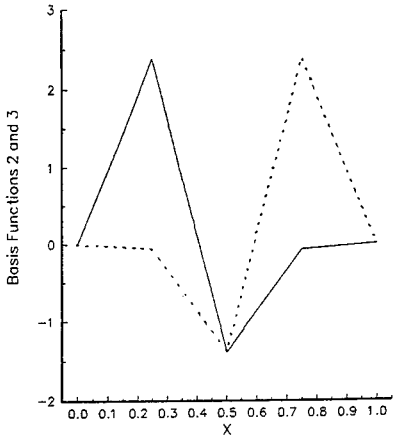

Figure 2. Wavelet–like basis functions 2 and 3

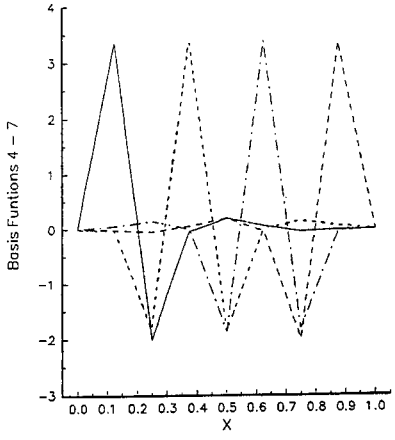

Figure 3. Wavelet–like basis functions 4 – 7

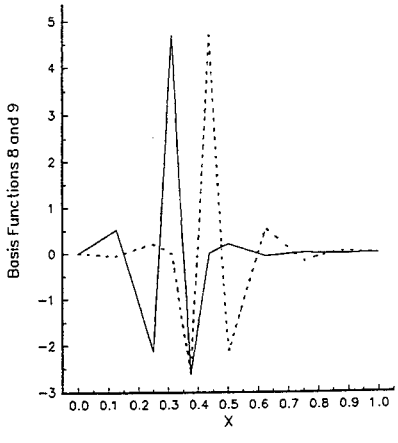

Figure 4. Wavelet–like basis functions 8 and 9

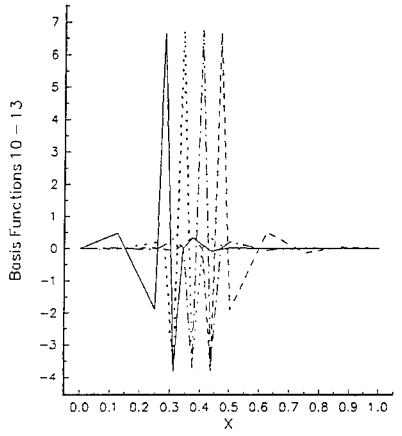

Figure 5. Wavelet–like basis functions 10 – 13

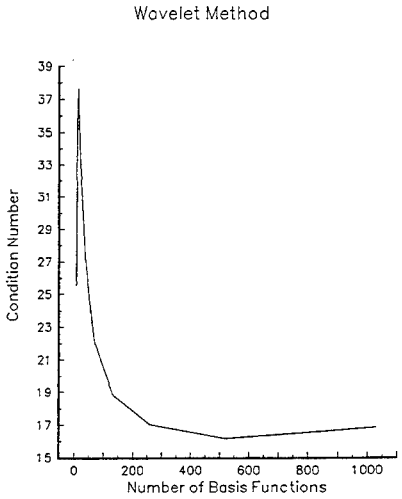

Figure 6. Condition number for Case A

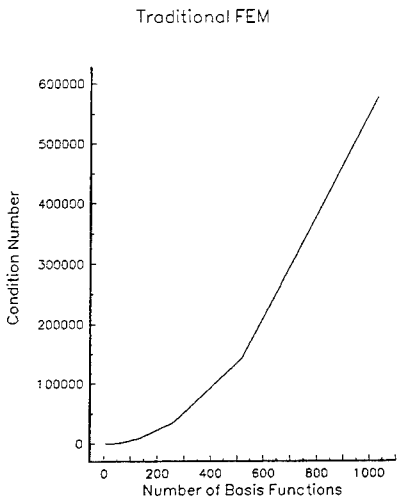

Figure 7. Condition number for Case A

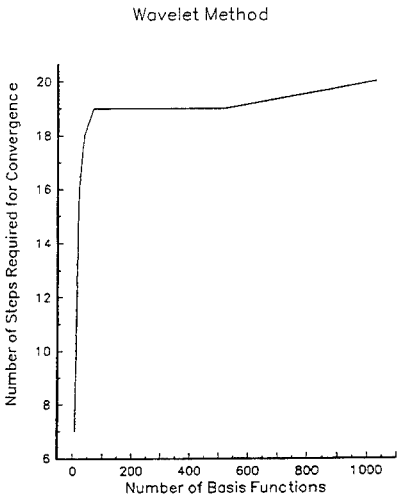

Figure 8. Number of steps for Case A

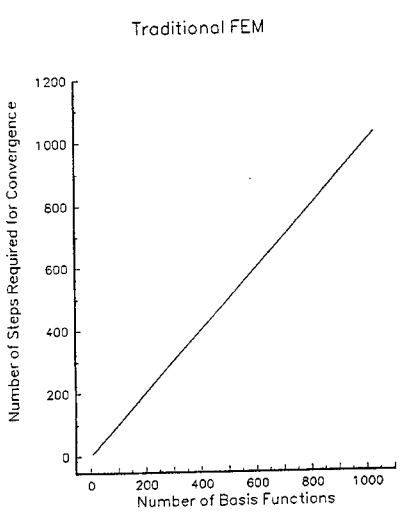

Figure 9. Number of steps for Case A

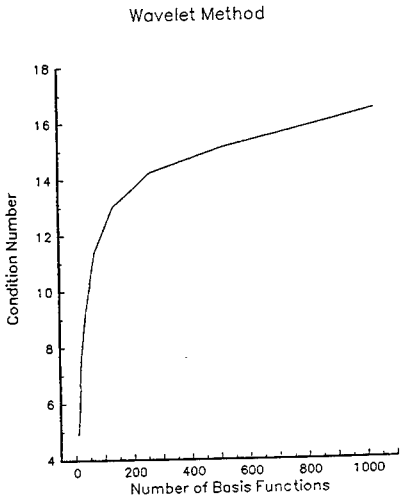

Figure 10. Condition number for Case B

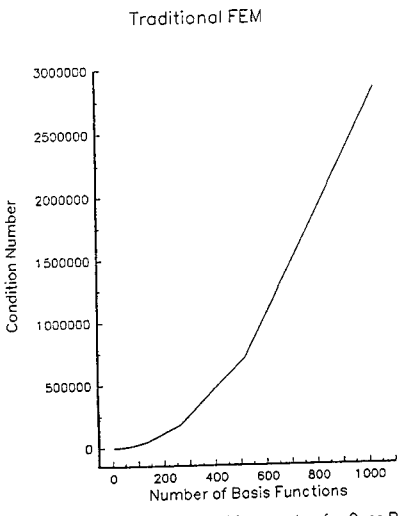

Figure 11. Condition number for Case B

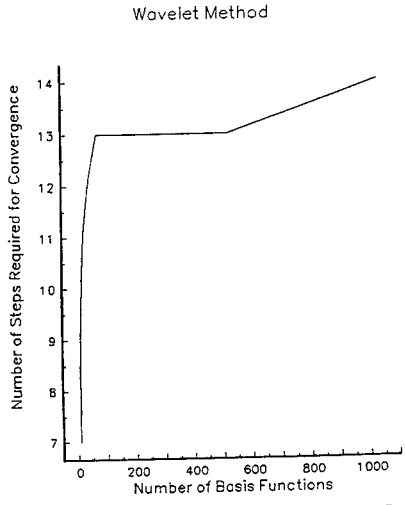

Figure 12. Number of steps for Case B

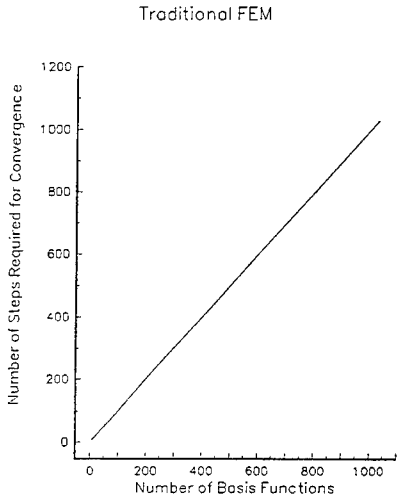

Figure 13. Number of steps for Case B

CONTINUING DEVELOPMENT OF THE RESEARCH AND ENGINEERING FRAMEWORK (REF) FOR COMPUTATIONAL ELECTROMAGNETICS*

L. W. Woo[ψ], B. Hantman[§], K. Siarkiewicz[◊], J. LaBelle[§], R. Abrams[‡]

Correspondence to:
Barry Hantman
Raytheon Company, Mailstop T3MR8
Tewksbury, MA 01876
Phone: (508) 858-5778
FAX: (508) 858-5976
Email: hantman@msmg02.msd.ray.com

ABSTRACT

Scientific and engineering research and design codes are typically FORTRAN-based, having vastly different data structures and I/O, and unique and inconsistent user interfaces resulting in long learning curves and difficulties in usage. This is true of the codes implementing the various computational electromagnetics (CEM) and thermomechanics (TM) formulations. Manual manipulation of data from code to code is required to ensure validity of the input. Coupled with the difficulty of graphically viewing the geometry and translating it to an analysis model, the result is numerous opportunities for the introduction of human errors into the design process. This situation also adversely affects the cost (human and software/hardware) of maintaining and extending design capabilities as the theoretical foundation and design needs advance. The Research and Engineering Framework (REF) provides a coherent, heterogeneous design environment which is the first step toward addressing the above problems. Although the REF was initially developed to address the problems of the U.S. power tube industry, the underlying framework is open; it can accommodate a broad range of scientific and engineering disciplines, including CEM modeling and simulation. The REF focuses on providing enabling technology in several critical areas including: ease of use and consistency; support for a "master" geometry; data sharing; integration of codes at different dimensionalities; heterogeneous networking; numerical grid generation; visual connection of tools and data flows; and configuration management of design data for project teams.

During the past year, the REF Development Team has made several enhancements to the framework including a new control panel, a visualization suite, a programmatic interface for sharing solution data, standards for the exchange of mesh data, enhanced code wrappering techniques, a configuration management system, and data dictionary management software allowing REF users to more readily insert discipline specific dictionaries (such as that required for CEM) into the environment.

This paper expands on those given at earlier ACES conferences[1-4] and on an article in the ACES Newsletter[6] to provide an updated view of the capabilities of the Research and Engineering Framework.

* Work supported by the Naval Research Laboratory, Contract #N00014-94-C-2064
ψ Permanent Address: Sabbagh Associates, 4635 Morningside Dr., Bloomington, IN 47408
§ Permanent Address: Raytheon Co., 50 Apple Hill Dr. T3MR8, Tewksbury, MA 01876
◊ Permanent Address: Rome Lab./ERST, 525 Brooks Rd. Rome, NY 13441-4505
‡ Permanent Address: Naval Research Lab., Code 6840, Washington, DC 20375-5347

BACKGROUND

The MMACE program has been underway for over four years and is now in its second phase. The first phase, which began in 1992, was an investigation phase. Four teams were put in place to study the problems of the Microwave Power Tube industry and develop roadmaps for the implementation of a framework to address those problems. The teams found an existing design environment that: was based largely on in-house developed software; was largely unsupported by commercial vendors; did not take advantage of the latest advances in CAD, visualization, database technology, and networking; was addressing technically difficult problems; contained a collection of tools that were not well integrated with each other; and was crucial to projects deemed important to the US government. While these items were true of the power tube industry, the same can be said of many niche scientific disciplines including CEM. Once the investigation was complete, the four MMACE teams began constructing a prototype system to experiment with some of the proposed solutions. This prototype was released in early 1994.

Phase II of the MMACE program, scheduled to last three years, began in March of 1994. Raytheon Company and Compact Software, along with several subcontractors[1], are under contract to jointly develop the complete framework. However, it became obvious that the problem should be split into two parts. The first part of the problem addresses those areas specific to power tube design. The second part of the problem addresses areas that are common to multiple design disciplines and therefore have far greater applicability. The portion of the system common to multiple disciplines, including CEM, is referred to as REF, the Research and Engineering Framework. Version 2.0 of the REF was shipped in January of 1996 and is now available for both the Hewlett-Packard and Sun platforms. Source code is available for those wishing to port the system to additional platforms.

OVERVIEW

The REF contains programming interfaces, standards, and tools to aid in the integration of codes. In addition, it provides the data management, networking, visualization, and "Master" geometry needed to drive analysis codes. The REF also provides the utilities needed to construct graphical user interfaces including the top level control panel. The REF portion of the system can be compared to a computer operating system: generic, powerful, and providing much functionality but of little interest to the end user who requires software that is written to operate on top of it. Figure 1 shows the structure and major components of the REF.

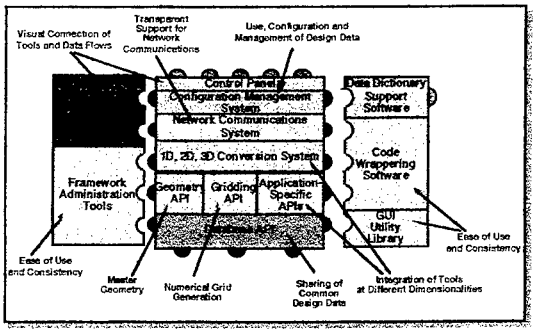

Figure 1 - REF Architecture

[1] The Compact/Raytheon Team includes Sabbagh Associates, Hughes, Litton, Triton Services, Teledyne, CPI and Northrop Grumman as subcontractors.

On top of the REF, one can layer design tools specific to a given design discipline, such as CEM. For the MMACE program, we have tested the REF by integrating a collection of design tools used in the design and analysis of power tubes and the data dictionary describing the data elements needed for that design and analysis. These design and analysis codes can be compared to off the shelf software that can be loaded on a system and accessed by the end users to perform specific functions. However, like off the shelf software, without the underlying operating system (in this case the REF) the software would be useless. Figure 2 shows the REF with discipline specific tools, databases, and data dictionaries connected to provide the user with a complete environment. Although the specific codes that would be integrated for CEM would be different from those that have been integrated to date, the concept is the same.

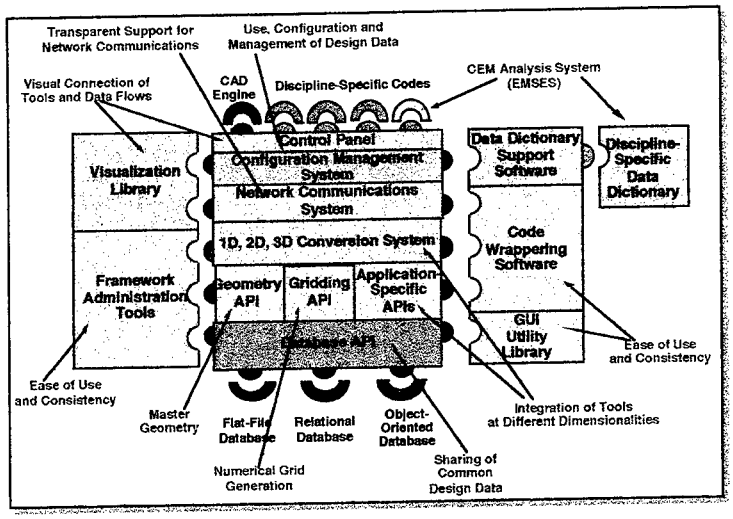

Figure 2 - REF Environment Customized for a Specific Design Discipline

RESEARCH AND ENGINEERING FRAMEWORK (REF) DETAIL

While Phase I of the MMACE program concentrated on developing design requirements and implementation of a prototype framework, Phase II focuses on enhancing, extending, and developing framework technology in eight key areas:

- Ease of use and consistency
- Sharing of common design data
- "Master" geometry driven analysis
- Standard foundation for numerical grid generation
- Integration of tools at different dimensionalities
- Visual connection of tools and data flows
- Use, configuration & management of design data
- Transparent support for network communications & distributed processing

During the year that has past since the last ACES conference, the MMACE program has made great progress in several of these key areas.

ENHANCED CONTROL PANEL

During the past year, the control panel for the system, shown in figure 3, has been completely redesigned. The MMACE Control Panel is the first thing the user sees when accessing the Framework. While the REF provided the underlying tools for creating the control panel, the specific button layout and dependencies that are shown are specific to power tube design. Obviously, the buttons and layout would be different for CEM. The control panel contains buttons for each of the codes available to the user. These buttons are laid out in the process flow appropriate to a given project. Each design could have a different process. These tool flows can be saved for use on other projects and can also be shared between users on the same project. The user simply executes codes by pushing buttons available on the OSF/Motif compliant interface. The control panel has been designed in such a way to make it possible to "plug" in new codes as needed. It automatically checks to make sure that a code has the data necessary to execute and triggers the code's wrapper, if necessary, to create all needed input files. The new control panel also includes logic to automatically run parametric studies. The control panel will execute the code over a range of database values saving the results for later analysis.

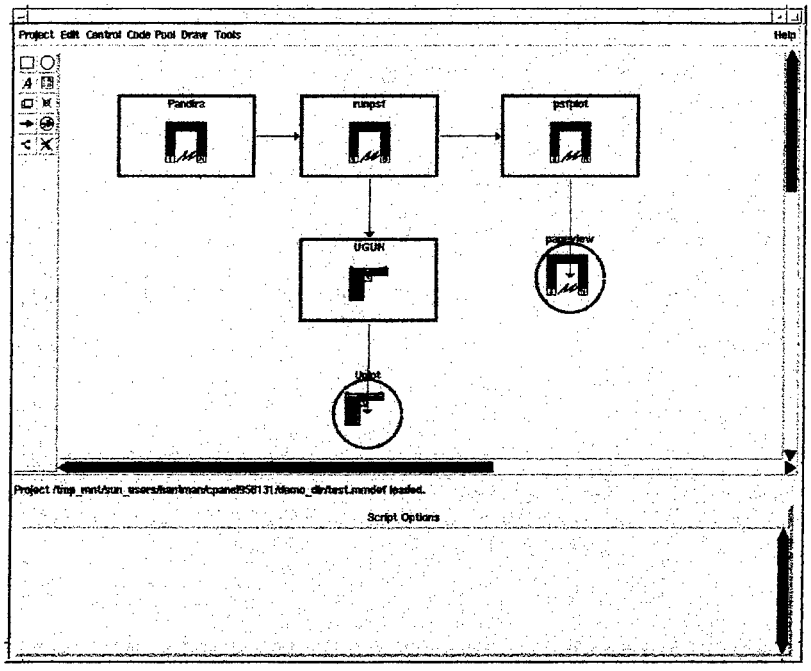

Figure 3 - Enhanced Control Panel

The control panel can be configured to run through a series of analysis codes without user intervention. This is especially useful for codes that require several hours to complete. The user can simply start the first code and go home. The control panel will continue executing down stream codes until the sequence is completed or an error occurs.

CEM design and analysis tools can easily be integrated into the system using the wrappering tools included with the REF. Once wrappered, the user can interactively add a button on the control panel to access that code.

DATA DICTIONARY SUPPORT

Another major enhancement made to the system over the past year is the inclusion of software to allow users to easily view and modify the data dictionary. The data dictionary can be thought of as the index to the data entities known by the framework. Each design discipline, and possibly each company, might have its own data dictionary. This software, shown in figure 4, provides an easy way to search and edit the dictionary. Code developers can use the system to find the database name of the parameter needed for their code's input. Likewise, the code's end user can use the system to find the description, default value, and constraints of a given field needed by the code. The Data Dictionary software also allows the code developer to extend the dictionary as needed to allow for additional data entities to be included in an analysis. The software automatically keeps track of changes to the dictionary so that the user can easily distinguish "approved" dictionary information from later modifications to the dictionary.

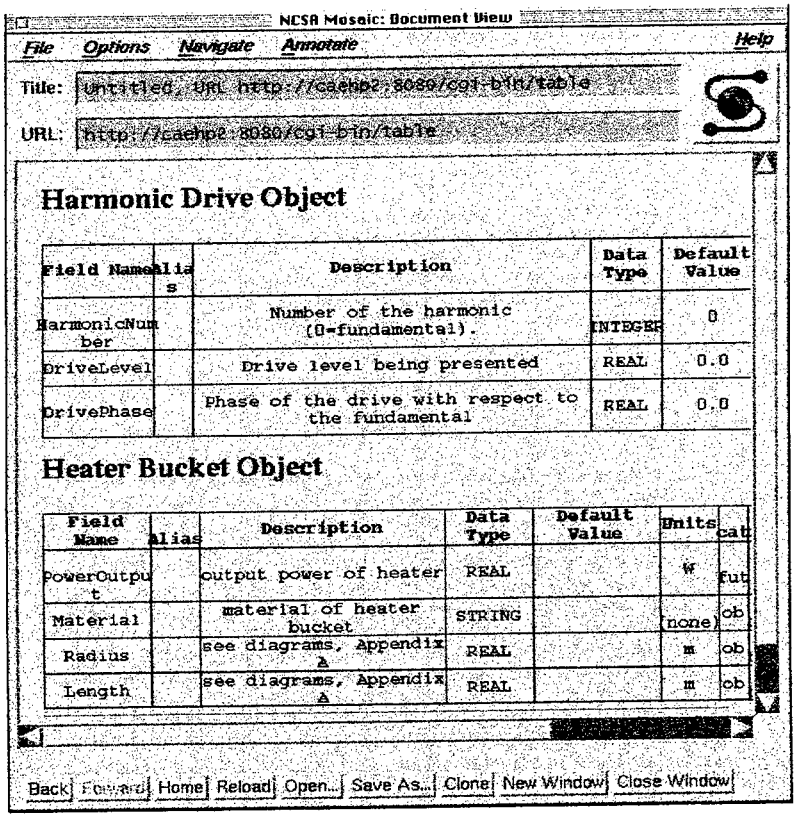

Figure 4 - Data Dictionary Support Software

NUMERICAL GRID GENERATION

A key feature of the REF environment is the support for numerical grid generation. In the current design environment, gridding software is often tied to a particular code and is sometimes embedded within that code. The objective of the MMACE program is to develop standards for the exchange of grid information and, in doing so, allow multiple codes to share grid information. In addition, by creating this standard layer, users are able to plug-in the latest gridding software as it becomes available. To test this, an existing grid generator, Ingrid, has been adapted to use the REF gridding standard. The grids can then be saved and later accessed by both electromagnetic and thermomechanical codes. An example of the type of grids supported is shown in figure 5.

The REF grid generation requirements for both thermomechanical (TM) and computational electromagnetic (CEM) analysis can be briefly summarized as follows:

- Mixture of line, surface and solid elements - node-based geometric entities in TM, and both node and edge-based in CEM.
- Steep gradient of grid density to accurately model localized phenomena.
- P-type and H-type grid refinements in adaptive gridding
- Specification of boundary codes, loadings, initial conditions and material properties (e.g., density, thermal and electrical conductivities, Young's modulus, Poisson's ratio, permeability, dielectric permitivity, etc.)
- Sliding interfaces and joints in TM, and surfaces of discontinuities in CEM.
- Symmetry (or anti-symmetry) planes
- Computed quantities for post processing - for TM: temperature, displacements, velocities, accelerations, stresses, bending moments, material-dependent variables, etc.; for CEM: electric and magnetic fields, current density, scalar and vector potentials, etc. These may involve complex numbers.
- Rectangular grids used in the finite-difference and volume-integral methods in CEM.

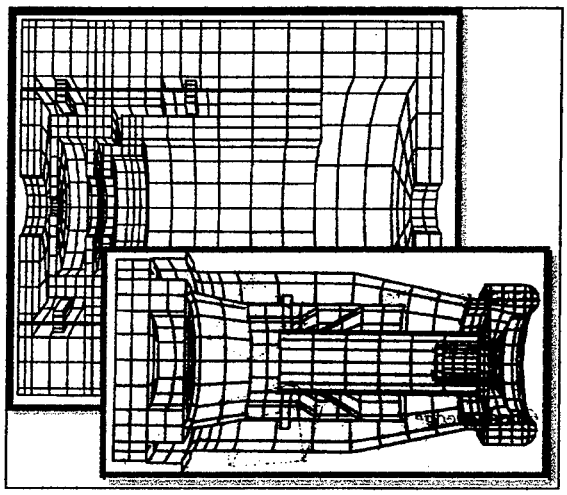

Figure 5 - Gridding

These requirements were used as input for the design and development of the REF gridding interface, a FORTRAN library for the storage and retrieval of grid information.

Configuration and Management of Design Data

Proper management of design data is critical to producing a quality product. Typically, design data has been maintained by the design engineer in hardcopy format. Data is often stored in several filing cabinets and in other places throughout the organization. It is often difficult to find the latest version of the data, especially if people involved in the original design are no longer around.

A configuration and management system was developed during the past year so that the REF can automatically track design data. The system, shown in figure 6, keeps electronic copies of different versions of the data, both for designs under development and for products that have shipped. Users are able to instantly retrieve data from any version of the product. In addition, by automatically keeping track of the data, users are able to explore different design variations without having to worry about overwriting information from alternate design options.

Once a design is complete, data for alternate design options can be deleted to conserve space and the final database can be archived in an electronic vault for future reference. Often, this archived version will be used as the starting point for upgrades or even for new designs that are similar to the one archived. A browser, included with the CM system, makes it easy to locate archived designs.

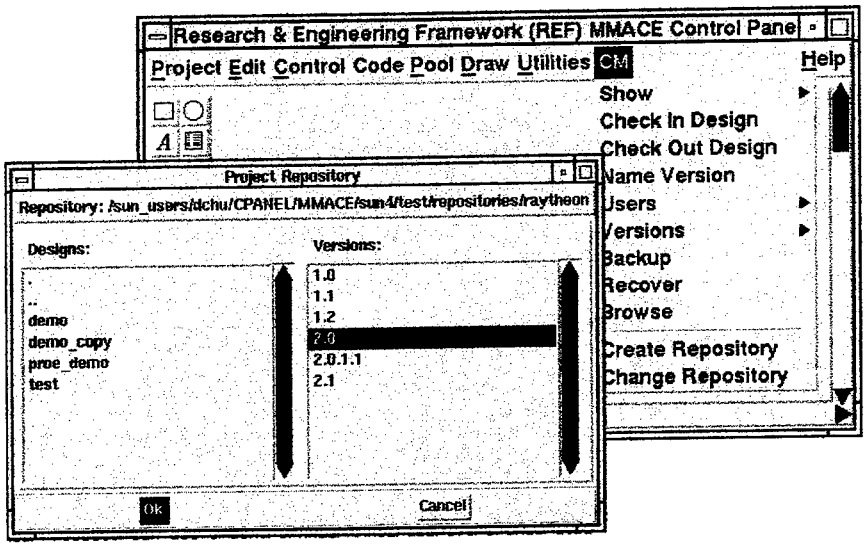

Figure 6 - Configuration Management

The REF design data management system is intended to be an adjunct to, not a replacement for, more capable and full-featured corporate data management systems. The focus of REF data administration capabilities is to provide for the support of small R&D groups in the configuration and management of their technical data.

ADDITIONAL ENHANCED FUNCTIONALITY

In addition to the portions of the framework described above, the MMACE program has also made significant advances during the past year in the areas of data visualization, code wrappering, and the exchange of solution data.

In the area of visualization, a suite of visualization tools has been integrated which provide a wide range of visualization capabilities including animation[2]. By utilizing these tools, code developers can focus their time on developing the physics portions of the code rather than on data presentation.

In the area of code wrappering, the existing utilities were extended to allow a much wider range of codes to be easily inserted into the framework. The wrappering software has also been extended to allow users to perform unit conversions and data formulations within the code wrapper.

For solution data, a standard interface was developed to allow codes to store and exchange finite element and finite difference solution data. This is extremely useful, especially when used in conjunction with the gridding interface.

SUMMARY

Phase II of the MMACE program is providing a full research and engineering framework for specialized technical communities which will approach the functionality, quality, and robustness found in commercial products. The REF core development is focusing on some of the problems not addressed adequately by commercial vendors because of the typically small market size of engineering and scientific communities. Specifically, MMACE and its underlying REF core will provide a low-cost environment that is easy to use, has a consistent interface, promotes data sharing, provides a unified source of geometry, supplies standards for numerical grid generation, integrates 1D, 2D, and 3D codes, provides a visual means for the user to view data and data flows, performs configuration management of the design data, and supports the use of heterogeneous networks of computers. The program has made significant progress toward meeting these objectives.

The REF is providing the foundation for design environments that are applicable to a wide variety of technical design disciplines including, power tube design, antenna design, and computational electromagnetics among others. The REF software is distributed at no charge[3] and the developers are eager to work with anyone who desires to make use of the software.

REFERENCES

1. Siarkiewicz, K. "The Electromagnetic Modeling and Simulation Environment for Systems (EMSES)." *9th Annual Review of Progress in Applied Computational Electromagnetics Conference Proceedings*, March 1993, pages 114-121.

2. Siarkiewicz, K. "Further Considerations Regarding the Electromagnetic Modeling and Simulation Environment for Systems (EMSES)." *10th Annual Review of Progress in Applied Computational Electromagnetics Conference Proceedings*, Volume II, March 1994, pages 86-93.

3. Hantman, B et. al. "Research and Engineering Framework (REF) for Computational Electromagnetics." *11th Annual Review of Progress in Applied Computational Electromagnetics Conference Proceedings*, Volume I, March 1995, pages 118-125.

4. Woo, L. W. et. al. "Standardized Grid Generation for the Research and Engineering Framework." *11th Annual Review of Progress in Applied Computational Electromagnetics Conference Proceedings*, Volume I, March 1995, pages 135-142.

5. Siarkiewicz, K. et. al. "Computational Electromagnetics Using the Research & Engineering Framework as a Backbone." *Applied Computational Electromagnetics Society Newsletter, Volume 10, Number 3*, November 1995.

---

2 The FERRET software developed by NOAA and the Collage software developed by NCSA have been integrated.

3 Software is available to US defense contractors and universities. Requests for software should be sent to the Naval Research Laboratory.

Numerical and Experimental Modelling of Liquid Dielectrics using a Coaxial Cavity

M. Bingle, D.B. Davidson and J.H. Cloete
Department of Electrical and Electronic Engineering
University of Stellenbosch, Stellenbosch
7600 South Africa

email: davidson@firga.sun.ac.za

Abstract

A body of revolution finite difference time domain formulation has been developed for obtaining the broadband (30MHz to 6GHz) reflection coefficient of dispersive liquids in a short-circuited coaxial cavity fed by a coaxial transmission line. The dispersive behavior is described by a convolution integral. The code solves the discretised convolution integral by recursion. The predictions of the code for the reflection coefficient of a transition from Teflon to distilled water are compared, in the frequency domain, both to data measured by an HP 8753C network analyzer and to the numerical predictions of a transmission line equivalent circuit model. A second feature of the code handles a step discontinuity in a coaxial system with a non-dispersive dielectric material. It is shown how this feature was used to optimize the stepped transition in the coaxial measuring system. The results of the FDTD code show good agreement with the experimentally determined optimum design.

1 Introduction

Knowledge of the dielectric properties of materials and their frequency dependent behaviour at radio and microwave frequencies is important both in fundamental and applied research. The measurement of reflections from samples placed in coaxial lines is a well-known technique for determining the dielectric properties of materials.

This paper describes a body of revolution finite difference time domain (BOR-FDTD) formulation, based on the work of Davidson and Ziolkowski [1], which has been developed for obtaining the broadband (30MHz to 6GHz) reflection coefficient of dispersive liquids in a short-circuited coaxial cavity fed by a coaxial transmission line.

The resultant code solves for the time evolution of all six field components inside a coaxial system. The code has two features. The first simulates the time evolution of the field components in a coaxial line with a non-dispersive dielectric material and allows for step discontinuities in both the inner and outer coaxial conductors. It is shown how this feature was used to optimize the design of a sample holder for liquid dielectrics.

The second feature simulates the time evolution of the field components in a coaxial line which contains a transition from a non-dispersive to a dispersive material. The predictions of the code for the reflection coefficient of a transition from Teflon to distilled water are compared, in the frequency domain, both to data measured by an HP 8753C network analyzer and to the numerical predictions of a transmission line equivalent circuit model.

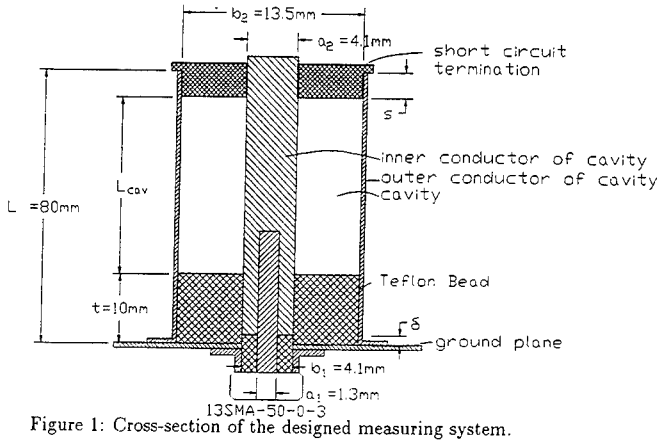

Figure 1: Cross-section of the designed measuring system.

2 Body of revolution finite difference time domain formulation

The measurement system for measuring the reflections from a dispersive liquid sample in a short-circuited coaxial cavity with a network analyser is shown in Figure 1. The cavity is fed by a coaxial connector and terminated in a removable short circuit. The dimensions of the cavity result in a 50Ω system in Teflon. The transition from the connector to the cavity occurs in a region filled with Teflon.

A body of revolution finite difference time domain (BOR-FDTD) formulation was developed to model the measuring system. The BOR-FDTD formulation solves the time-dependent Maxwell curl equations numerically. The rotational symmetry in the geometry is exploited using a Fourier modal expansion. Expanding the azimuthal field dependence as a Fourier series, the problem space is effectively reduced to two dimensions, but the solution is three dimensional; the code solves for the full-wave vector Maxwell equations. The code was developed to simulate the TEM wave propagation inside a coaxial transmission line system.

The code handles two specific discontinuities in a coaxial transmission line. The first application simulates the time evolution of the field components in a non-dispersive dielectric material and includes step discontinuities in the coaxial geometry. This feature was developed in order to investigate the transition from coaxial connector to coaxial cavity. The code is based on tabulated formulae in [1, 2].

The second application simulates the time evolution of the field components in a coaxial line with a discontinuity in the dielectric. The dielectric change may involve a dispersive dielectric material. The finite difference equations of Maxwell's equations for dispersive materials were derived for the body of revolution formulation [3]. The dispersive materials are handled by the discretised convolution integral with recursion, as suggested by [4]. The dispersive dielectric is modelled by a time-dependent susceptibility function with constant parameters. Only the Debye model for the permittivity was implemented in the code (Appendix A). The Lorentz and Drude models for permittivity can easily be added to the code, using the same recursion formulae.

The excitation pulse has the $1/\rho$ spatial distribution of the TEM (k=0) mode. The time-history is Gaussian. The source treatment is a total field/scattered field treatment at the source plane. The details may be found in [1, §3.2]. It simulates a plane wave with $1/\rho$ spatial weighting in a homogeneous non-dispersive dielectric space. The fields on and above this plane are assumed to be total fields (i.e. incident and reflected fields); the fields below this plane are reflected (scattered) fields.

The $z = 0$ plane is treated using a one-dimensional absorbing boundary condition for the $\mathbf{E}_{tan}$ field compo-

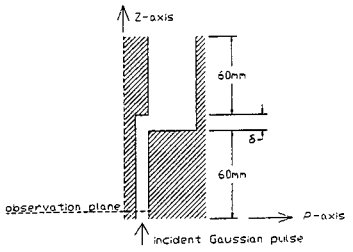

Figure 2: Geometry of the coaxial cavity system with a stepped discontinuity.

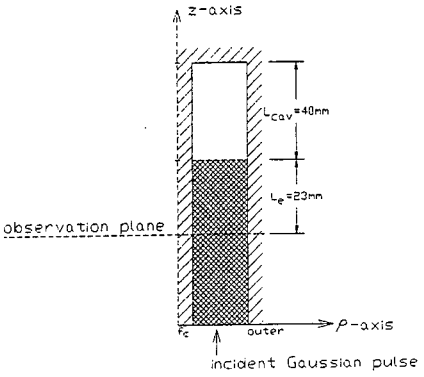

Figure 3: Equivalent geometry of the coaxial cavity system with a dielectric discontinuity.

nents; the $z = z_{max}$ plane can either similarly be treated as an absorbing boundary condition or as a perfect electric conductor, depending on the load. The constant ρ boundary planes (the inner and outer conductors of the coaxial transmission line) are treated as perfect electric conductors.

3 Modelling of a stepped disontinuity in a coaxial transmission line

The transition from the feeding connector to the coaxial cavity involves a stepped discontinuity in the coaxial geometry (Figure 1). Changing the value of δ, changes the amount of reflection that will occur from the transition. The discontinuity was investigated numerically and experimentally to optimize the design of the sample holder.

The geometry for the BOR-FDTD analysis is shown in Figure 2. It consists of the perfectly conducting areas of the inner and outer conductors surrounding a region filled with a dielectric. The physical dimensions shown in Figure 1 for the coaxial cross-sections are used. The coaxial line is filled with Teflon with $\varepsilon_r = 2.0$.

The time-history of the field components at a z-plane before the step discontinuity is stored for output. This plane is selected far enough from the discontinuity so that only the TEM (to z) field components need to be considered. The reflection coefficient at this plane is calculated by taking the Fourier transform of the reflected wave and dividing it by the Fourier transform of the incident wave.

Simulations were run for several lengths of δ and the Fourier transform of the solution was computed to obtain the frequency dependent reflection coefficient caused by the transition (Figure 4). The reflections from the transition between the coaxial line and the coaxial cavity were measured with an HP 8753C network analyser. The offset δ was changed systematically to find the optimum value for the least reflection.

The BOR-FDTD analysis of the coaxial transmission line system with a stepped discontinuity was found to be consistent with measurements. The BOR-FDTD analysis predicted an optimum value of $\delta = 1.7$mm with a reflection coefficient between -35dB and -34dB over the 6GHz frequency band. This corresponds well

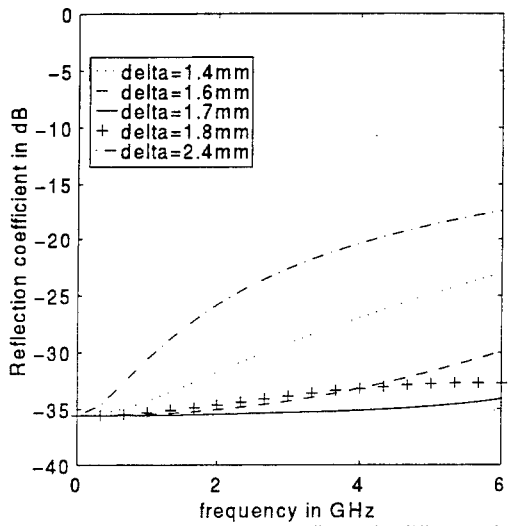

Figure 4: BOR-FDTD simulation: reflection coefficient for different values of δ.

with the experimentally determined value of $\delta \approx 1.6$mm which yielded a reflection coefficient between -40dB and -33dB over the 30MHz to 6GHz band.

4 Modelling of a dispersive material in a coaxial transmission line

The BOR-FDTD formulation for the analysis of the measurement system, consisting of a short-circuited coaxial cavity filled with a dispersive material and driven by a coaxial transmission line, uses an equivalent geometry. The measuring system is modelled as a 50Ω transmission line (with Teflon dielectric) feeding a transmission line containing the liquid dielectric (Figure 3). Due to the low reflections from the stepped discontinuity, the transition is simply modelled as a 50Ω transmission line. The distance from the calibration (observation) plane to the Teflon bead/cavity interface was determined experimentally from a time domain measurement on the network analyser.

The predictions of the code for the reflection coefficient of a transition from Teflon to distilled water are compared, in the frequency domain, both to data measured by an HP 8753C network analyzer and to the numerical predictions of a transmission line equivalent circuit model.

The water is modelled as a Debye dispersive medium, with typical parameters (dependent on pressure and temperature) $\varepsilon_s = 81$, $\varepsilon_\infty = 1.8$ and $\tau_e = 9.4$ps [4]. The parameters are supplied to the code and the BOR-FDTD equations are updated at each time step using the discretised convolution integral equation and recursion (Appendix A). The same parameters were used in the BOR-FDTD analysis and the transmission line analysis.

Although the Teflon bead that shields the connector and transition region from the liquid in the cavity fits tightly into the cavity, water leaked down the sides of the conductor surfaces into the transition region. This had a significant influence on the measured reflection coefficient. Silicon gel was applied to the surfaces of the

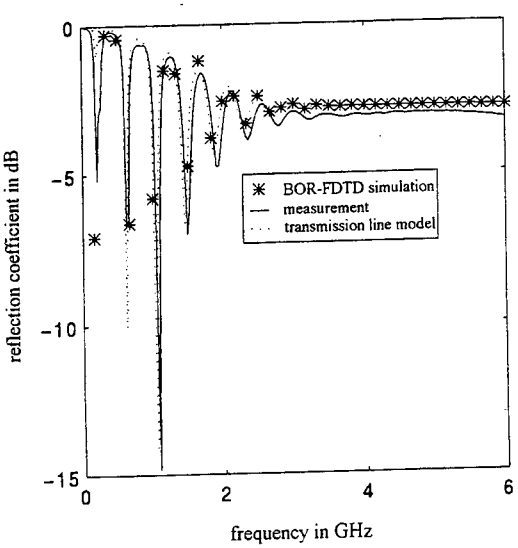

Figure 5: Magnitude of the reflection coefficient with purified water inside the cavity. A comparison between the results of the BOR-FDTD analysis, transmission line analysis and measurement. Parameters used for water: $\varepsilon_s = 81$, $\varepsilon_\infty = 1.8$ and $\tau_e = 9.4$ps.

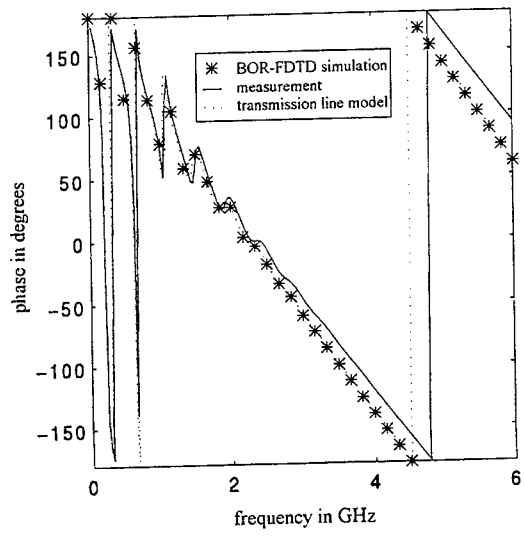

Figure 6: Phase of the reflection coefficient with purified water inside the cavity. A comparison between the results of the BOR-FDTD analysis, transmission line analysis and measurement. Parameters used for water: $\varepsilon_s = 81$, $\varepsilon_\infty = 1.8$ and $\tau_e = 9.4$ps.

Teflon bead to prevent water from entering the transition region.

After the experimental difficulties were eliminated, very good results were obtained over the entire band from 30MHz to 6GHz. The results for the reflection coefficient are shown in Figure 5 for the magnitude and in Figure 6 for the phase. The comparison between the BOR-FDTD analysis, the measured magnitude of the reflection coefficient and the transmission line analysis is good. The results of the analyses are in exact agreement for frequencies above 2GHz. Below 2GHz the agreement is good, although not exact. The BOR-FDTD and transmission line results for the phase of the reflection coefficient are in excellent agreement over the frequency range. The phase shift in the high frequency (2.5 to 6GHz) result of the measured phase can be attributed to the effect of the silicon gel.

The rapid changes in the reflection coefficient require a high resolution in the frequency data of the analyses. A stability and phase error analysis should be conducted to determine the stability restriction for this system of partial differential equations and discretised convolution integral. For accuracy the discretization has to adequately sample the shortest timescale in the problem [5]. The relaxation timescale for water was taken as 9.4ps while the timestep size was 0.37ps (i.e. $\Delta t = \frac{1}{25}\tau_e$). Finer timestepping should improve the results of the BOR-FDTD analysis.

5 Conclusion

A common discontinuity in a coaxial system occurs when the dimensions of the line are scaled up, while characteristic impedance is maintained. The line will no longer be reflectionless, in general. It was shown how a BOR-FDTD formulation of a coaxial system with a stepped coaxial discontinuity was used to optimize the transition in the system. The predicted optimum value of the analysis (δ = 1.7mm), as well as the predicted optimum reflection coefficient (between -35dB and -32dB over the 6GHz frequency band) was found to be consistent with measurements, which yielded an optimum value of $\delta \approx$ 1.6mm and a reflection coefficient between -40dB and -33dB over the 30MHz to 6GHz band.

A BOR-FDTD formulation for wave propagation inside a coaxial system containing a dispersive dielectric material was discussed. The Debye model for a dispersive dielectric material was sucessfully incorporated in the BOR-FDTD formulation, using the discretised convolution integral. The predictions of the code for distilled water compare well in the frequency domain to measured data and the numerical predictions of a transmission line equivalent circuit.

Appendix A

Dispersive dielectric materials can be modelled by use of the convolution integral constitutive relationship between the displacement flux and the electric field,

$$\mathbf{D}(\mathbf{x},t) = \varepsilon_0\varepsilon_\infty \mathbf{E}(\mathbf{x},t) + \int_0^\infty \varepsilon_0 \chi(\tau)\mathbf{E}(\mathbf{x},t-\tau)d\tau \tag{1}$$

$$\varepsilon_r(\omega) = \varepsilon_r(\infty) + \chi(\omega) \tag{2}$$

$\chi(\tau)$ is determined as the Fourier transform of the frequency dependent susceptibility function $\chi(\omega)$. Kunz and Luebbers [4] discretise this integral to use in the finite difference Maxwell equations,

$$D^{n+1}(i,j) - D^n(i,j) = \varepsilon_0(\varepsilon_\infty + \chi^0)E^{n+1}(i,j) - \varepsilon_0\varepsilon_\infty E^n(i,j) - \varepsilon_0\Psi^n(i,j) \tag{3}$$

where

$$\Delta\chi^m \equiv \chi^m - \chi^{m+1} \tag{4}$$

$$\Psi^n(i,j) = \sum_{m=0}^{n-1} E^{n-m}(i,j)\Delta\chi^m \tag{5}$$

i, j and n are the indexes for the ρ, z and time dimensions respectively.

The convolution sum in Equation (3) is dependent on the time domain susceptibility function. If the susceptibility function has an exponential time dependence, the convolution sum can be written as a recursive formula. Recursive formulas are derived by Kunz and Luebbers for Debye and Lorentz dispersive media [4, pp. 127-145]. The formulas for a Debye medium are repeated here for reference.

Debye model for permittivity

$$\varepsilon_r(\omega) = \varepsilon_\infty + \frac{\varepsilon_s - \varepsilon_\infty}{1 + j\omega\tau_e} \tag{6}$$

Discretised time domain susceptibility function

$$\chi(n\Delta\tau) = \frac{\varepsilon_s - \varepsilon_\infty}{\tau_e} e^{-\frac{n\Delta\tau}{\tau_e}} u(n\Delta\tau) \tag{7}$$

Recursive property

$$\Delta\chi^{m+1} = \Delta\chi^m e^{-\frac{\Delta\tau}{\tau_e}} \tag{8}$$

Recursion formula

$$\Psi^n(i,j) = \Delta\chi^0 E^n(i,j) + e^{-\frac{\Delta\tau}{\tau_e}} \Psi^{n-1}(i,j) \tag{9}$$

$$\chi^0 = (\varepsilon_s - \varepsilon_\infty)(1 - e^{-\frac{\Delta\tau}{\tau_e}}) \tag{10}$$

$$\Delta\chi^0 = (\varepsilon_s - \varepsilon_\infty)(1 - e^{-\frac{\Delta\tau}{\tau_e}})^2 \tag{11}$$

References

[1] D.B. Davidson and R.W. Ziolkowski, "Body-of-revolution finite-difference time-domain modelling of space-time focusing by a three-dimensional lens," Journal Optical Society of America, A, vol. 11, pp. 1471–1490, April 1994.

[2] D.E. Merewether and R. Fisher, "Finite difference solution of Maxwell's equation for EMP applications," Defense Nuclear Agency, Washington D.C. 20305, Report no. EMA-79-R-4, April 1980.

[3] M. Bingle, "The Finite Difference Time Domain Modelling of Liquids with Dispersive Dielectric Properties," *M. Eng. Thesis*, University of Stellenbosch, 1995.

[4] K.S. Kunz and R.J. Luebbers, *The Finite Difference Time Domain Method for Electromagnetics*. Boca Raton: CRC Press, 1993.

[5] P.G. Petropoulos, "Stability and Phase Error Analysis of FD-TD in Dispersive Dielectrics," IEEE Trans. Antennas Prop., vol. AP-42, pp. 62–69, January 1994.

HARDWARE/SOFTWARE CODESIGN MODEL FOR XPATCHF OPTIMIZATION[1]

B. A. Kadrovach, T .S. Wailes, A. J. Terzuoli, Jr., D. S. Gelosh
Air Force Institute of Technology

1. Introduction

1.1 Background

The Xpatch [1] software package generates very accurate field scattering predictions. At present, Xpatch has over 350 users worldwide with that number growing every day. In addition, extensive research has been conducted to validate the accuracy of the Xpatch software package [2]-[4]. Thus, given a detailed description of an object and a specific viewing angle, Xpatch can accurately predict the object's scattered field.

The Xpatch software package consists of two programs, Xpatchf and Xpatcht. These programs are for frequency domain analysis and time domain analysis respectively. The research presented in this paper focuses on the frequency domain version and produces a functional codesign model of the Xpatch software. Therefore, the products of this research are the behavioral description of the hardware and the specification of the interface between the software platform and the hardware elements. The ultimate goal is an overall speed-up of prediction time.

1.2 Assumptions

Since extensive validation of the Xpatch system has already been conducted, this research does not validate Xpatch as a scattered field prediction program. However, the codesign system was tested to ensure operation is consistent with the existing Xpatchf. Further, the software platform is assumed to be a single, general purpose microprocessor communicating with the hardware components through shared memory. In order to exercise Xpatchf in a realistic fashion, three separate objects were selected. These objects; a boxfin, a turkey, and an aircraft [1], provided a realistic exercise of the Xpatchf run-time.

1.3 Approach

This research consists of two parts. First, the existing Xpatchf software was analyzed and profiled to reveal areas of optimization. Then, based on the results of the profiling analysis, the existing software system was partitioned between hardware and software.

1.3.1 Profiling

The Xpatchf software was profiled in several ways. All methods entailed the scattered field prediction of a variety of objects. These objects were sufficiently complex so as to vigorously exercise the Xpatchf computation engine.

Extensive run-time analysis was used to determine which subroutines and functions were used most often and to identify periodicity in Xpatchf execution. Periodicity or cyclic operation would be used to optimize the execution of the system by allowing individual cycles to operate concurrently. Each subroutine and function was assigned a unique identification number. This number was used to track the sequence of subroutine and function calls during run-time.

Figure 1 shows a possible Xpatchf profile. The horizontal axis represents time, and the vertical axis represents different functions or subroutines that are called during Xpatchf operation. If the cycle shown in Figure 1 can be executed concurrently, the time for the 3 cycles can be collapsed down to the time for only one cycle. Profiling also identified data interdependencies. In order to take advantage of the periodic nature of the software, the data being manipulated in each

[1]This work was supported by the U. S. Air Force Wright Laboratories.

cycle must be independent. Several areas of the Xpatchf software were identified as periodic. Further analysis was conducted to determine which area would benefit the most from implementation in hardware.

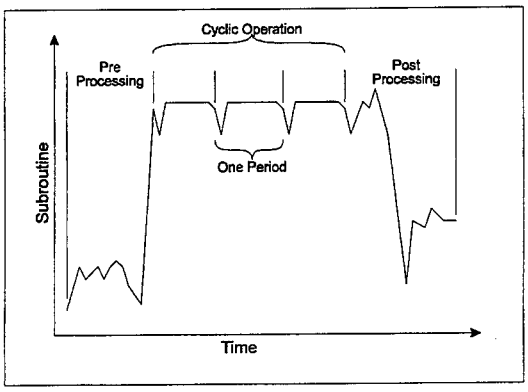

Figure 1. Periodic Nature of a Program

1.3.2 Behavioral Description

Once an area of the Xpatchf software was identified as a candidate for hardware implementation, the functionality of that area was described using the Very High Speed Integrated Circuit (VHSIC) Hardware Description Language (VHDL). VHDL was used to obtain a structural decomposition of the source code functionality. The structural decomposition was made in the context of possible hardware implementation strategies. Attention was given to obtain the greatest advantage of concurrency. Additionally, the interface between the VHDL components and the revised Xpatchf software was specified. Once the VHDL model was obtained, the model was verified for correct operation using real xpatchf inputs.

2. Software Profiling

As explained in another paper in this volume, the Xpatchf program flow was determined by profiling the software in the run-time environment. This was done by tracking function and subroutine calls in both the FORTRAN code and the C code. Since most of the C code functions exist as library functions, the melding of FORTRAN subroutine calls with the C code function calls presented a major difficulty. There was no easy way to determine the temporal relationship between the FORTRAN and C source code. The only alternative was a line-by-line analysis of the source code to determine the subroutine/function hierarchy. These temporal relationships were used to identify the Xpatchf functionality that would achieve the most benefit from a hardware implementation. The results of that analysis are summarized in Table 1 and shown pictorially in Figure 2.

Table 1. Run-time Percentages

Object	BSP Generation	1st Bounce	Multi-Bounce
Boxfin	0.10%	11.16%	87.97%
Turkey	0.63%	2.94%	95.56%
V1 Aircraft	12.85%	42.37%	42.17%

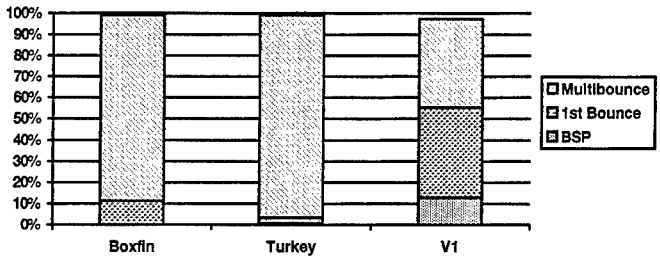

Figure 2. Run-time Summary

The times of execution are shown as percentages of the total time of execution. This provides a normalized view of the relative time spent in each phase. It should be noted that not all of the run-time is accounted for in the above table. The pre- and post-processing are not shown and therefore, the percentages of each row do not add up to 100%. Since the SBR portion of the code required the largest portion of the run-time, it was decided that this area would most benefit from a hardware/software codesign implementation.

3. VHDL Model

Since the calculations involved in determining a ray/facet intersection are independent of other intersection calculations, the processing of many intersections may proceed simultaneously. This fact is used to provide a significant speed-up in the Xpatchf processing of the multi-bounce calculations. As a result, the existing Xpatchf program will be modified to operate with the codesign model hardware developed during this research.

The method used to implement the xpatchf calculations is known as Single Program, Multiple Data or SPMD. The same program operates concurrently on several sets of input data in order to produce several sets of results all simultaneously (or very nearly so). Figure 3 illustrates the concept. The input data is *flowed* across the top of the array of processing units. Once the data is properly positioned, each processing unit performs its computations. The results are flowed out in the same manner as the data was flowed in. With the abstract functionality described, the particulars of the implementation may be discussed.

At the top level there is a model that includes a general purpose microprocessor and associated RAM/ROM. This microprocessor is responsible for providing overall control of the processing units to include data flow control. This takes care of the input data flow plane and the output data flow plane. The processing units, called Voxel Units (VU), consist of three modules each. The first module, called the Global Memory Module (GMM), is used to store "global" object data. The second module, called the Local Memory Module (LMM), provides the processing necessary to traverse the BSP tree as it is stored in the GMM and to retrieve facet data once a leaf voxel is found. The third and last module, called the Computation Module (CM), provides the floating point processing necessary to implement the intersection calculations identified for the codesign.

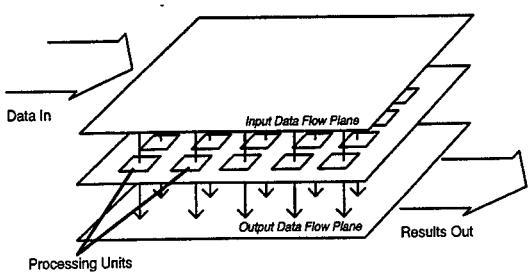

Figure 3. SPMD Operation

3.1 Microprocessor Controller

The microprocessor controller is responsible for overall control to include data flow control. The microprocessor can be any general purpose processor such as one of the PowerPC 60X series. While it is easy to talk about simply flowing data across the processing units, the actual implementation must be made in the context of finite data bus sizes and finite time required for data transfers. Immediately after the object facet data is loaded by the modified Xpatchf program, the pertinent object data is *broadcast* to each VU, specifically to each GMM. The object data is maintained in the Xpatchf program in an abstract data type (ADT) called `data`. Only the data relevant to the object need be copied to the VUs. Since the data is maintained and managed by the C library functions, pointers are used for arrays while discrete values are contained in memory allocated at run-time. In addition to the dynamic arrays and discrete memory elements, the ADT data contains a pointer to the head of the Binary Space Partition (BSP) tree.

3.2 Global Memory Module (GMM)

The GMM will consist of dynamic RAM and cache memory. Both of these items are available from industry and are extremely reliable, therefore no model is provided for this unit except for that which is necessary to demonstrate the function of the other modules. Once the appropriate global data is in place in the LMM and the CM, the Voxel Unit (VU) array remains in an idle state until the modified Xpatchf program makes a call for ray/object intersections.

When intersection calculations are required, the modified Xpatchf program signals the VU array (by writing to a predetermined address). The signal is followed by the transfer of ray data to the VU array. The ray data consists of the ray start point and the ray direction vector (a unit vector). One ray is assigned to each VU along with the ID of the last facet hit by the ray (meaningless for initial rays). The ID of the last facet hit ensures that this facet is not processed for the next intersection.

A possible method of flowing the ray data to all of the VUs is shown in Figure 4. Assuming that there are four separate data channels to the VU array, a set of 4 ray data elements may be transferred to the VU array at a time. For brevity's sake, assume the array is 4 wide and only 4 deep. With every memory cycle, 4 ray data elements are transferred to the VU array. The horizontal lines in the Data Flow portion of Figure 4 represent computational processing and are shown to last longer than 4 memory cycles. It will be shown later that this is indeed the case. In fact, the computational processing will last much longer than 4 memory cycles. The first results (a set of 4 result elements) will be available after the first row of VUs finish their computations. Let this time be t_c memory cycles. Then, for the next 4 memory cycles, 4 result elements will be available to the main program. In general, for n blocks of 16 rays each, the processing time in memory cycles is given by $t_{total} = n(t_c + 1) + 2$.

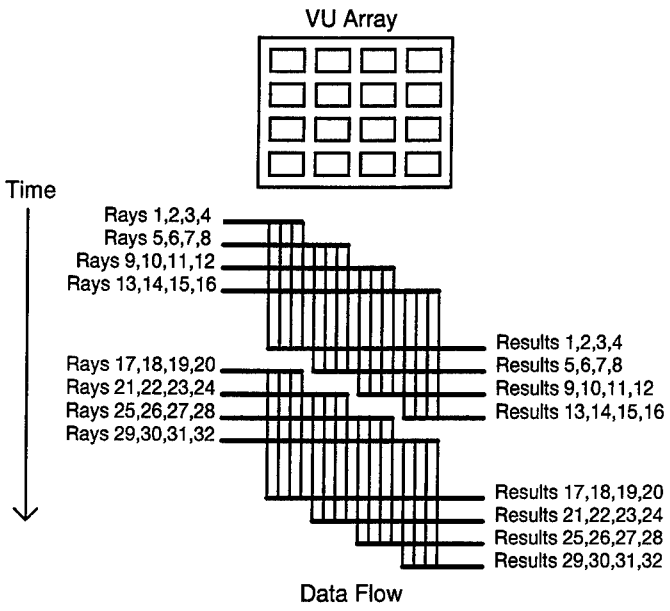

Figure 4. Data Flow Relationships

The number of blocks can be specified in terms of the total number of rays. If the number of rays is k, then n satisfies $n = \left\lceil \frac{k}{16} \right\rceil$ and therefore $t_{total} = \left(\frac{k}{16} + 1\right)(t_c + 1) + 2$. This is an upper bound on the total computation time for the VU array. It is evident from this equation that for $k >> 16$ and $t_c >> 1$, the total time can be approximated by $t_{total} \cong \frac{kt_c}{16}$. However, the total time to compute k rays sequentially is simply kt_c (assuming the sequential computation time and concurrent computation time for one ray are about equal). From this analysis, the speed-up obtained is approximately equal to the number of VUs in the VU array. The above equation represents an upper bound on the computation time that can never be achieved, but for a first order approximation, it is useful to show the relationship between speed-up and number of VUs.

3.3 Local Memory Module

The Local Memory Module (LMM) provides memory management for the VU. When data is required by the Computation Module (CM), the LMM generates the addresses for that data. The controller for the LMM is implemented using microcode. Another feature of the LMM is the implementation of a hardware stack. This is included in order to allow traversal of the BSP tree when looking for leaf voxels.

3.4 Computational Module

The CM performs the calculations necessary to determine the path throught the BSP tree and whether a ray intersects the object. Once a leaf voxel is reached, the CM performs the ray/facet intersection calculations for each facet in the leaf voxel. When all facets have been processed, the CM outputs the results of those calculations. Those results include whether a hit was made, the coordinates of the closest hit point, the distance from the ray origin to the hit point, and the ID of the facet involved in the intersection.

3.5 Voxel Unit

The Voxel Unit (VU) combines the Global Memory Module, Local Memory Module and Computational Module together and provides the data and address routing necessary for proper operation. Figure 5 shows a block diagram of the VU.

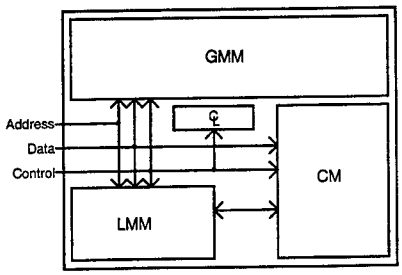

Figure 5. Voxel Unit

The combinational logic manages the routing of data and address signals within the VU. Addresses are provided to the GMM by the microprocessor controller when loading global data. When traversing the BSP tree or computing a ray/facet intersection, the addresses to the GMM are provided by the LMM. Data is written to the GMM by the microprocessor controller when loading global data, otherwise data is read by the LMM when traversing the BSP tree or data is read by the CM when a ray/facet intersection is to be calculated. Data is provided to the CM by the microprocessor when a ray is assigned else data is provided by the GMM in response to LMM addresses when a leaf voxel is found.

4. Validation/Verification

Testing was accomplished using test address data and actual Xpatchf data generated from a run on the boxfin object. This data was used to verify the proper operation of the Local Memory Module (LMM) and the Computation Module (CM). The LMM was tested by verifying address outputs against expected values of data addresses. The CM was tested by applying known data and checking results against known good data from the Xpatchf run. The data used for verification included the bounding box for the boxfin object, data for two rays, and data for four facets with results of two hits and six misses. The Voxel Unit (VU) was created by integrating the LMM and CM with a GMM simulation. The VU was then tested by performing a simulated run with the available data. Again, the results obtained were verified against known good data.

5. Results and Conclusion

5.1 Performance

Performance for the VHDL model is measured relative to the source code being implemented, using floating point (FP) operations as the metric. The number of FP operations in the source code implemented in the VU model is dependent on the depth of the BSP tree, the number of leaf voxels processed, and the number of facets in a leaf voxel.

The function of processing a ray can be divided into 4 parts. These parts and the associated number of FP operations are summarized in Table 2.

Table 2. FP Operations for Ray Processing

Compute:	Xpatchf	VU
Preprocessing	27	28
BSP Traversal (per level)	6	9
Intersection Processing (per facet)	33	30
Post Processing	7	7

In general, the number of FP operations for the Xpatchf source code is given by $x_{Xpatchf} = 34 + 6i + (33k)j$, and the number of FP operations for the VU model is given by $x_{VU} = 35 + 9i + (30k)j$ where i is the number of levels traversed, j is the number LVs processed, and k is the number of facets in each of the LVs.

The MFLOPS (millions of FP operations per second) of the CM is assumed to be approximately equal to that for a general purpose workstation. This assumption is based on the fact that the CM is, in reality, a specialized floating point processor and is expected to have FP processing capabilities on par with commercially available FP processors. The features which set the CM apart from general purpose FP processors are the hardware stack and the special looping capability. The advantage of the VU architecture is the ability to array the units to take advantage of concurrent operation. If it is assumed that the MFLOPS rating for the VU model is the same as that for a general purpose workstation, then the execution time of the Xpatchf source code can be compared to the execution time of the VU model for one ray.

This discussion has shown that the performance of the VU model for one ray is approximately equal to that of a general purpose microprocessor executing the Xpatchf source code. However, the advantage of the VU model is that it may be arrayed and many VUs operated concurrently. If arrayed, the MFLOPS is multiplied by a factor approximately equal to the number of VUs included in the array. The result would be a "card" with all the components necessary to implement one array of VUs. The components would include the microprocessor controller and its associated memory and the array of VUs (such as the 4 x 4 array as shown in Figure 4). From this arrangement, the approximate speed-up would be 16 from $t_{total} \cong \frac{kt_c}{16}$. In general, if an n x m array is used, the speed-up would be approximately nm. The n dimension is limited to the number of separate memory channels between the workstation main memory and the VU array. The m dimension is limited by the processing time of a VU element and the time required to transfer ray data from the workstation and the VU array.

A set of VU array "cards" could more efficiently use the available memory bandwidth and increase speed-up. This is possible since the a VU spends a majority of its time doing computations and not memory accesses. If 8 cards were included in one workstation, the speed-up would be approximately 128 or 2 orders of magnitude improvement in processing time.

Additional speed up could be obtained by networking these workstations. If N "Xpatchf" workstations were connected in a network, the speed-up would be $128N$. This figure is obtained for a system where communication costs are zero. However, in reality there would be a time penalty associated with every message passed between workstations. When considering performance of a system that incorporates message passing, the metric used must be execution time. Speed-up is related to execution time given by $t_{new} = \frac{t_{old}}{speed-up}$ where t_{old} is the time for the original system. When considering the delays associated with message passing, the execution time will increase by an amount proportional to the number of messages passed. In the case of an Xpatchf "network," message passing would only be necessary to assign ray data elements and signal completion of ray/object computations. Other message passing would be necessary to initialize each workstation with common data (associated with the object). However, this should not be considered as part of the ray/object computation time since the system could be initialized once with object data and reused for multiple incident angles; i.e., calculating multiple predictions. Messages would be necessary to pass new angles to each workstation. Delays associated with these messages are negligible compared to the number of messages associated with assigning ray data elements.

Consider a star network topology with one controlling workstation and $N - 1$ other nodes. Rays are fired from a virtual screen similar to that used for the Z-buffer. Therefore, the natural choice is to divide the screen into N blocks and assign each node a single block. This approach will be used for the remainder of this discussion, but it should be evident that this is not the most optimum choice. There is a high probability that entire blocks of rays would miss the object

completely. This would result in some nodes setting idle for long periods of time while others continued processing computations. A method of load balancing would alleviate this problem. Since this is outside the scope of this research, no further discussion will be given. The simplistic network model will be used to demonstrate the communication costs of a network implementation.

The number of messages associated with assigning rays is N - 1 since the control workstation does not need a message. If workstations only pass results when all rays assigned have been processed, there will be an additional N - 1 completion messages. It is also assumed that multiple bounces of a ray are processed on the workstation to which the original ray assignment was made. The total number of messages is 2(N - 1). The new processing time is give by $t_{new} = \frac{t_{old}}{sN} + 2\alpha(N-1)$. The equation is generalized for a speed-up of s.

The parameter α is a constant of proportionality that allows the message delay contribution to be incorporated into the equation for the new time of execution. The value for α is unknown but could be obtained. It represents the magnitude of the effect of message passing on the networked system performance. Since the desire is to minimize execution time, the optimum number of nodes can be found by setting the first derivative of the above equation to zero and solving for N. This solution is $N = \sqrt{\frac{t_{old}}{2s\alpha}}$. It can be observed from this solution that, as the processing time increases, the number of nodes must be increased to maintain optimum performance. However, as α increases, the number of nodes must be reduced to maintain optimum performance.

5.2 Conclusion

The research described in this paper resulted in an architectural model for improving Xpatchf processing. The optimization was accomplished by implementing highly repetitive computations in a VHDL model. Because of the nature of the computations being implemented in VHDL, the research product has applications outside of scattered field predictions. The implementation is the foundation for a ray tracing algorithm. Therefore, the area of possible use is expanded to the graphics processing arena and may prove to be very useful for speeding up graphics processing applications.

Bibliography

1. S. W. Lee and D. J. Andersh, User Manual for xpatch, DEMACO, Inc., Sep. 1993

2. E. M. Miller, D. J. Andersh, A. J. Terzuoli, Jr., "Facetization Level and the Effect on XPATCH Predictions," *Proceedings of the Ninth Annual Review of Progress in Applied Computational Electromagnetics*, Naval Postgraduate School, Monterey, CA, March 22-26, 1993, pp. 610-617.

3. R. O. Jernejcic, A. J. Terzuoli, Jr., R. Schindel, "Evaluation of Full Radar Signature Predictions Using XPATCH," *Proceedings of the Tenth Annual Review of Progress in Applied Computational Electromagnetics*, Monterey, CA, March 21-25, 1994, pp. 343-351.

4. J. P. Meyers, A. J. Terzuoli, Jr., G. C. Gerace, P. F. Auclair, "Quantitative Methods for Measuring and Improving the Performance of Electromagnetic Scattering Prediction Codes," *Proceedings of the Eleventh Annual Review of Progress in Applied Computational Electromagnetics*, Monterey, CA, March 20-25, 1995, pp. 49-56.

3D FDTD Simulation of EM Detection of Buried Waste

Dennis Sullivan
University of Idaho
Idaho Falls, Idaho 83402

Byron Hansen and Neil Skousen
Scientech, Inc.
Idaho Falls, Idaho 83402

I. Introduction

The location of buried waste by some sort of ground penetrating EM method would be a valuable tool in locating hazardous materials that would be both difficult and dangerous to find by invasive methods. One approach under consideration is the use of RF applicators to launch EM pulses whose echoes can be analyzed to determine if a foreign object lay beneath the ground.

Such an approach is plagued by numerous practical and theoretical difficulties: unknown terrain under the surface, lossy materials in the terrain which attenuate the signal, the fact that the buried objects can be of unknown size and composition, etc. Because of the complexity of the problem, it is believed that computer simulation can play an invaluable role in finding the best solution to overcome these difficulties.

Using the finite-difference time-domain (FDTD) method [1, 2, 3], programs have been developed to simulate a plane EM wave penetrating into the earth and reflecting off various objects. Although any practical applicator will ultimately generate a signal other than a plane wave, it is believed that this is a valid approach in gaining insight into the problems. The program can simulate any material over a wide frequency range, and scattered objects can consist of canonical shapes or arbitrary shapes determined at run time. Furthermore, analytic programs using Bessel function expansions have been developed to verify the accuracy of these models. This Bessel function method has been enhanced to be able to verify simulations of objects in lossy materials.

II. Problem Description

The basic simulation is described in figure 1. The problem space is divided up into a scattered field and total field. An incident plane wave is generated at one end and subtracted out the other end. Therefore, anything that goes outside the boundary must be the result of a scattered wave. Note that two or more different background media may be used. Figure 1 illustrates the case where the incident wave originates in free space, and penetrates into the ground. The boundary of the problem space is surrounded by a perfectly matched layer (PML). It is a slight modification to the Berenger PML which is completely impervious to the background medium. It will be described in the following section.

The object in the total field is the target object which is being sought. The model for this object is loaded from an external file, which is specified at run time. These models can be generated 'off-line,' and can be modified or even created just using a text editor. (This borrows from previous experience in hyperthermia treatment planning where a model of a patient is created and stored, and then read in by the program at run time [4].)

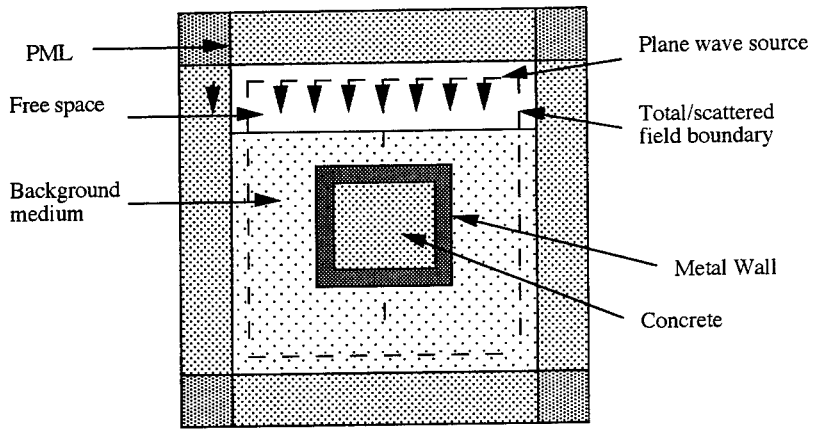

Figure 1. Problem space with a rectangular scatterer.

The incident field can also be generated at any angle between zero and ninety degrees, as illustrated in figure 2. However, this is only valid for a single background The incident field can also be generated at any angle between zero and ninety degrees, as illustrated in figure 2.

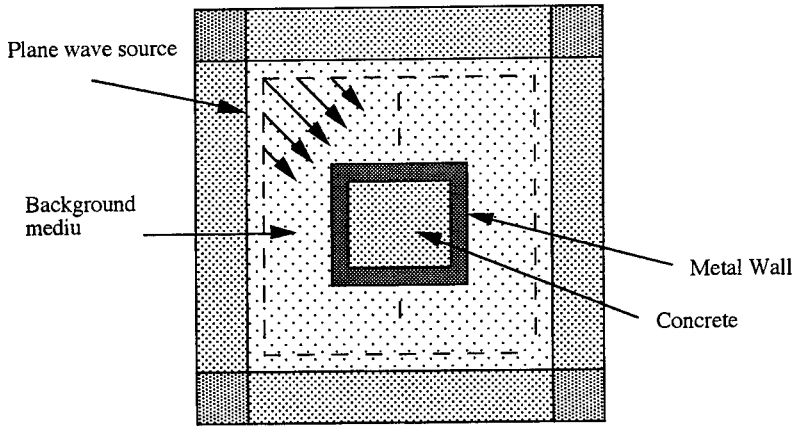

Figure 2. Plane wave source from an arbitrary direction.

III. PML

The absorbing boundary conditions for this FDTD approach is handed by a perfectly matched layer (PML) which is a slight modification of the original developed by Berenger [5]. The details have been given elsewhere [6], and will only briefly by described here.

For the purpose of the FDTD formulation, the Maxwell's equations are take in the form

$$\frac{\partial \tilde{\boldsymbol{D}}}{\partial t} = \frac{1}{\sqrt{\varepsilon_0 \mu_0}} \cdot \nabla \times \boldsymbol{H} \tag{1.a}$$

$$\tilde{\boldsymbol{D}}(\omega) = \varepsilon_r^*(\omega) \cdot \tilde{\boldsymbol{E}}(\omega) \tag{1.b}$$

$$\frac{\partial \boldsymbol{H}}{\partial t} = -\frac{1}{\sqrt{\varepsilon_0 \mu_0}} \nabla \times \tilde{\boldsymbol{E}} \tag{1.c}$$

The type of formulation in equations 1 is used because dispersive, or even nonlinear, properties of the material are all contained in equation 1.b. (Assuming a non magnetic material). Numerous approaches have been taken to solve E from D in 1.b , however, that is not germane to the present discussion. What is important is that the dielectric properties of the material being simulated are expressed in equation 1.b. Regardless of how complex the material is, it will not impact the implementation of the PML in equations 1.a and 1.c.

Of the six differential equations represented within equations 1.a and 1.c, the method will be illustrated by using only the D and H components in the z direction

$$\frac{\tilde{D}_z}{\partial t} = \frac{1}{\sqrt{\varepsilon_0 \mu_0}} \left(\frac{H_y}{\partial x} - \frac{H_x}{\partial y} \right) \tag{2.a}$$

$$D_z = \varepsilon_r^*(\omega) \cdot E_z \tag{2.b}$$

$$\frac{H_z}{\partial t} = -\frac{1}{\sqrt{\varepsilon_0 \mu_0}} \left(\frac{\partial \tilde{E}_y}{\partial x} - \frac{\partial \tilde{E}_x}{\partial y} \right) \tag{2.c}$$

Berenger's approach was to introduce fictitious electric and magnetic directional conductivites, and to split the E and H fields in each direction into sub components depending on the direction of the spatial derivative used to calculate it. We will deviate from this only slightly by introducing fictitious conductivites associated with H and D, instead of H and E

$$\frac{\tilde{D}_{zi}}{\partial t} + \frac{\sigma_{Di}}{\varepsilon_0} \tilde{D}_{zi} = \frac{1}{\sqrt{\varepsilon_0 \mu_0}} \left(\frac{H_{yi}}{\partial x} + \frac{H_{yk}}{\partial x} \right) \tag{3.a}$$

$$\frac{\tilde{D}_{zj}}{\partial t} + \frac{\sigma_{Dj}}{\varepsilon_0} \tilde{D}_{zj} = -\frac{1}{\sqrt{\varepsilon_0 \mu_0}} \left(\frac{H_{xj}}{\partial y} + \frac{H_{xk}}{\partial y} \right) \tag{3.b}$$

$$\tilde{D}_{zx} + \tilde{D}_{zx} = \varepsilon_r^*(\omega) \cdot \tilde{E}_z \tag{3.c}$$

$$\frac{H_{zi}}{\partial t} + \frac{\sigma_{Hi}}{\mu_0} H_x = -\frac{1}{\sqrt{\varepsilon_0 \mu_0}} \frac{\partial \tilde{E}_y}{\partial x} \tag{3.d}$$

$$\frac{H_{zj}}{\partial t} + \frac{\sigma_{Hj}}{\mu_0} H_y = \frac{1}{\sqrt{\varepsilon_0 \mu_0}} \frac{\partial \tilde{E}_x}{\partial y} \tag{3.e}$$

These fictitious conductivities are in addition to any "real" conductivity associated with the complex portion of $\varepsilon_r^*(\omega)$. Putting equations 3.a and 3.d in an FDTD formulation (3.b and 3.e would have the same form):

$$\begin{aligned}\tilde{D}_{zj}^{\,n+1}(i,j,k+1/2) &= gj(j)\cdot\tilde{D}_{zj}^{\,n}(i,j,k+1/2)\\ &+ 0.5\cdot(H_{xj}^{\,n+1/2}(i,j+1/2,k+1/2) - H_{xj}^{\,n+1/2}(i,j-1/2,k+1/2)\\ &+ H_{xk}^{\,n+1/2}(i,j+1/2,k+1/2) - H_{xk}^{\,n+1/2}(i,j-1/2,k+1/2))\end{aligned} \tag{4.a}$$

$$\begin{aligned}H_{zi}^{\,n+1/2}(i+1/2,j+1/2,k) &= fi(i)\cdot H_{zi}^{\,n-1/2}(i+1/2,j+1/2,k)\\ &- 0.5\cdot(\tilde{E}_y^{\,n}(i+1,j+1/2,k) - \tilde{E}_y^{\,n}(i,j+1/2,k))\end{aligned} \tag{4.b}$$

The PML is formed from the parameters

$$gi(i) = \left(1 - \frac{T\cdot\sigma_{Di}(i)}{\varepsilon_0}\right) \tag{5.a}$$

$$fi(i+1/2) = \left(1 - \frac{T\cdot\sigma_{Hi}(i+1/2)}{\mu_0}\right) \tag{5.b}$$

In the Berenger formulation, values of σ_D and σ_H are increased as one goes further into the PML to give greater absorption. Therefore, the terms $(1 - T\cdot\sigma_{Di}/\varepsilon_0)$ and $(1 - T\cdot\sigma_{Hi}/\mu_0)$ will become increasingly smaller, so *gj, and fi* go from 1 at the edge of the PML, to a smaller number at the outer boundary of the FDTD space. (Using .5 as the smallest value has been found to be the most effective without leading to instabilities.) For instance, if a PML of n layers were being developed for the X direction at the lower end, the values of *gi* and *fi* would be computed as

$$gi(i) = 1 - 0.5\cdot\left(\frac{n-i}{n}\right)^3 \qquad \text{i=0,1,..,n} \tag{6.a}$$

$$fi(i+1/2) = 1 - 0.5\cdot\left(\frac{n-i-.5}{n}\right)^3 \qquad \text{i=0,1,..,n-1} \tag{6.b}$$

The values at the high end would be

$$gi(i_{max} - i) = 1 - 0.5\cdot\left(\frac{n-i}{n}\right)^3 \qquad \text{i=0,1,..,n} \tag{7.a}$$

$$fi(i_{max} - i + 1/2) = 1 - 0.5\cdot\left(\frac{n-i-.5}{n}\right)^3 \qquad \text{i=0,1,..,n-1} \tag{7.b}$$

This PML has been found to be extremely effective, usually requiring no more than four cells. Because it is implemented throughout the problem space, it has slightly higher computer memory requirements. However, it because it is completely impervious to the medium of the problem space, it presents a substantial advantage in simulations where the background medium is often changed.

IV. Comparison with Bessel Function Expansion

The configuration illustrated in figure 3 is used to evaluate the accuracy of the method by comparison with Bessel function expansion. The Bessel program is capable of operation in lossy media. The background medium has a dielectric constant of 10 and a conductivity of .02. The sphere is 2 meters in diameter. The inner core is metal with a 40 cm diameter. The next layer is 2 cm thick and has a dielectric constant of 50 and conductivity of .2. The outer layer has a dielectric constant of 20 and a conductivity of .02. (Values were chosen to test the method and do not necessarily correspond to likely physical materials.) The results along the incident axis are shown in figure 4 for 1, 10 and 30 MHz. The plane wave is in impulse and the results are evaluated by a running Fourier transform, so information for multiple frequencies is available for one run [7]. Clearly, there is good agreement for all frequencies.

A similar test is made by evaluating the scattering from a sphere at various levels through or in front of the sphere, as illustrated in figure 5. This is potentially of more significance, because the purpose of the program is to evaluate reflected waves. Results are shown in figure 6 for scattering off a metal sphere, where the comparison is made through the plane of the sphere and 10 cm in front of the sphere.

V. Discussion

A three dimensional simulation program has been described which is being used towards the development of an electromagnetic method of locating buried waste. Emphasis, thus far, has been on developing the flexibility of the programs and verifying their accuracy. It has been shown that these programs can operate with arbitrary background media, and that objects of any size and shape can be developed outside the program, and then read in at run time. Similarly, analytic programs using Bessel function expansions have been developed which can determine the scattering from layered spheres in any background medium.

References

1. K. S. Yee, "Numerical solution of initial boundary value problems involving Maxwell's equations in isotropic media," *IEEE Trans. on Antennas and Propagation,* AP-17, pp. 585-589, 1966.
2. A. Taflove, "Review of the formulation and applications of the finite-difference time-domain method for numerical modeling of electromagnetic wave interactions with arbitrary structures," *Wave Motion,* vol. 10, pp. 547-582, Dec. 1988.
3. K. Kunz, R. Luebbers, *The Finite Difference Time Domain Method for Electromagnetics,* Boca Raton, CRC Press, 1993.
4. B. J. James and D. M. Sullivan, "Creation of three-dimensional patient models for hyperthermia treatment planning," *IEEE Trans. on Biomedical Engineering,* BME-39, pp. 204-211, Feb., 1990.
5. J. Berenger, "A perfectly matched layer for the absorption of electromagnetic waves," *J. Computational Physics,* vol. 114, pp. 185-200, 1994.
6. D. M Sullivan, "A simplified PML for use with the FDTD method," *IEEE Microwave and Guided Wave Letters,* Vol. 6, Feb., 1996.
7. D. M. Sullivan, "Mathematical methods for treatment planning in deep regional hyperthermia" *IEEE Trans. on Microwave Theory and Tech.,* MTT-39, pp. 864-872, May, 1991.

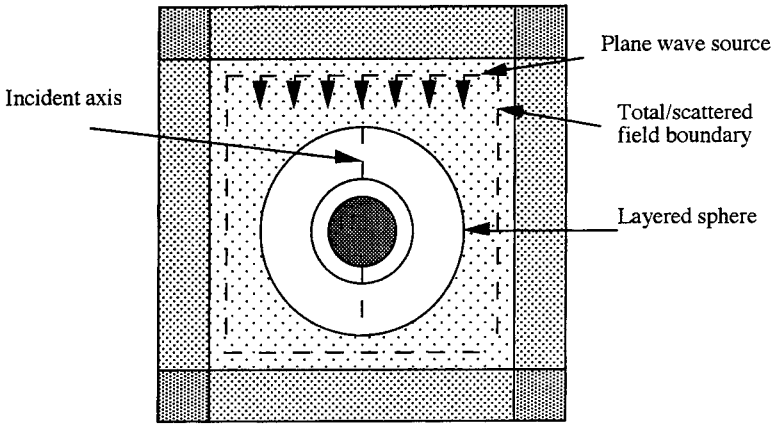

Figure 3. Configuration used to test the FDTD program against analytic programs using Bessel function expansions.

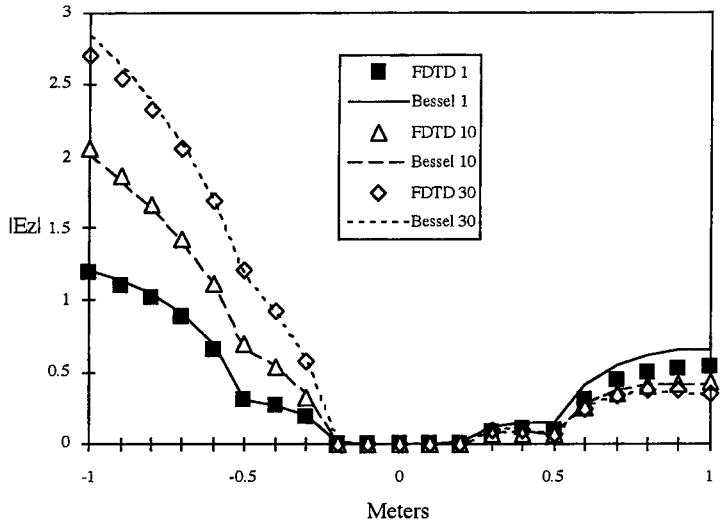

Figure 4. Results of FDTD vs. Bessel function for a sphere in a lossy background of eps = 10, sigma = .02. The sphere has a metal core and two dielectric layers. Results are shown at 1, 10, and 30 MHz. The FDTD program was in a 40^3 problem space and required 500 time steps . The cells were 10 cm^3.

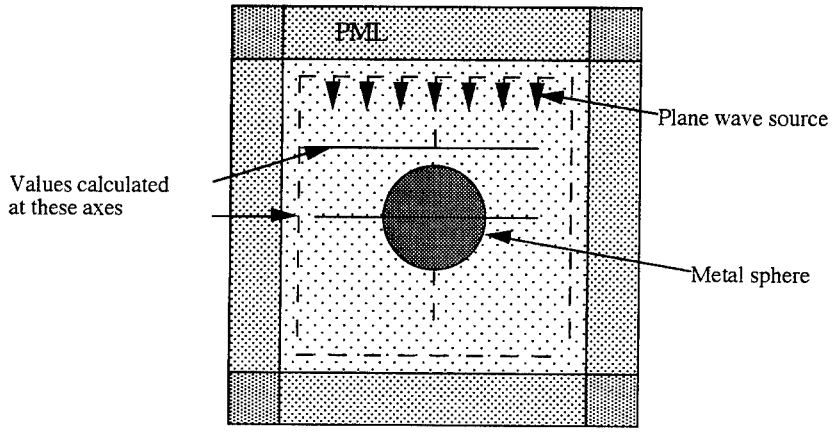

Figure 5. Diagram of sample problem

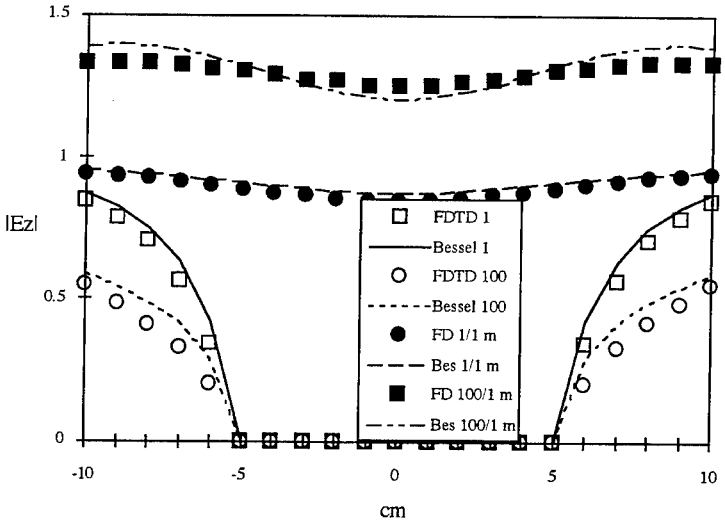

Figure 6. FDTD vs. Bessel Function for a metal sphere, 10 cm in diameter at 1 and 100 MHz. Comparison made at the axis perpendicular to the incident field 10 cm in front of the sphere.

APPLICATION OF DIGITAL FILTERS TO THE CONSTRUCTION OF WIDEBAND DISPERSIVE BOUNDARY CONDITIONS

Michał Mrozowski, Maciej Niedźwiecki, Piotr Suchomski
Technical University of Gdańsk,
Department of Electronics,
80-952 Gdańsk, POLAND.
e-mail: mim@pg.gda.pl

ABSTRACT

The paper presents there different fast implementations of a time domain diakoptics technique applied to the modeling of the highly dispersive ABC. The algorithms discussed are based on the digital filters using low order zero-pole, Laguerre and Kautz models. The performance of the most successful designs is compared with the Berenger's perfectly matched layer.

I. INTRODUCTION

Time domain numerical methods using finite differencing scheme in the modeling of uniform infinite structures require the proper termination of computational space in the plane where no physical boundary exists. Recently a significant breakthrough in this area has been achieved by Berenger [1] who proposed termination of the computational space with a non-physical lossy medium called the perfectly matched layer (PML). It has been found [2], however, that although the Berenger's perfectly matched layer performance is excellent for propagating waves, it deteriorates drastically for evanescent waves. This limits the applicability of the PML to the analysis of scattering phenomena in cylindrical waveguides, where nonpropagating modes can be excited at discontinuities.

In the contribution we will discuss the application of various structures of digital filters to modeling the termination condition in cylindrical waveguides. We found that for the propagating waves the digital filters offer the performance equal or for some filter configurations even better than PML, and yet remain effective in absorbing cutoff modes.

The digital filters use an idea known as the time domain diakoptics [3, 4, 6]. Time domain diakoptics consists in finding the impulse response of a section of the waveguide and using the convolution integral to predict value of the field at the ABC from the value of the field at the input of this section. This relation is written in the form

$$r(t) = f(t) * h(t) \tag{1}$$

where $*$ is the symbol for the convolution integral and $h(t)$ is the impulse response of the system, $f(t)$ is the field value at the input of the waveguide section and $r(t)$ is the required field value at the ABC. The numerical cost of calculating the convolution is high (at least a few hundreds of floating point operations per iteration step). The synthesis of the ABC in the form of a digital filters is in fact is a fast implementation of the time domain diakoptics method. In a digital filter the convolution is replaced by fast recursive formulae so that the overall computing time of the time domain analysis can be greatly reduced.

II. DIGITAL FILTER ALGORITHMS FOR TIME DOMAIN DIAKOPTICS

Digital filters can be realized in many forms. In this contribution we discuss several implementations of digital filters which stem from

1. non orthogonal filters such as zero-pole (ARX)
2. orthogonal filters using Laguerre and Kautz-Laguerre basis

1. Zero-pole filters

The zero-pole filter the simplest model in which the transfer function is represented as a rational function. The output signal in time domain is given by

$$r(k) = \sum_{i=0}^{n} b_i f(k-i) - \sum_{i=1}^{p} a_i r(k-i) \tag{2}$$

where b_i and a_i are the coefficients of the polynomials in numerator and denominator of the transfer function. The unknown coefficients can be found from samples of input and output signals of a "tuning" sequence in time domain by means of least squares method. Note that this procedure does not require the explicit specification of the impulse response. One disadvantage of the zero-pole model is that it does not guarantee the stability of the digital filter (i.e. some poles may fall outside the unit circle).

2. Orthogonal filters

In an orthogonal filter the impulse response is expressed as a linear combination of basis functions $\phi_i(t)$, orthonormal in L_2

$$h(t) = \sum_{i=1}^{\infty} c_i \phi_i(t) \tag{3}$$

For a known impulse response the value of the expansion coefficients c_i can be found by taking the inner product of $h(t)$ with each expansion function. If the impulse response is not know a least squares fit in time domain, analogous to the one discussed for zero-pole filter, can provide the expansion coefficients.

The z-transfer function of the filter having the impulse response $h(t)$ expressed in the form (3) is

$$H(z) = \sum_{i=1}^{\infty} c_i \Phi_i(z) \tag{4}$$

where $\Phi_i(z)$ denotes the z-domain operator corresponding to the basis function $\phi_i(t)$. In practical computations the expansion (3) is truncated at $i = I_{max}$ and one obtains a I_{max}-th order approximation of $H(z)$.

The only problem which should be now examined concerns the "optimal" choice of basis functions. It has recently been shown there is an infinite number of possible orthogonal bases. The two most frequently used are the bases involving Laguerre and Kautz polynomials. They have been suggested [10], to reduce the number of estimated parameters without increasing the computational complexity of the filter. In general, it was observed that Laguerre models yield good approximations of filters with real poles while Kautz models work better for filters with complex poles.

2.1 Laguerre basis

The z-transform of the Laguerre polynomial $\mathcal{L}_i(z;\xi)$ of the i-th order is given by

$$\mathcal{L}_i(z;\xi) = \sqrt{1-\xi^2}\frac{z}{z-\xi}\left[\frac{1-\xi z}{z-\xi}\right]^{i-1} \tag{5}$$

The parameter ξ can take any value from the interval $(-1,1)$ and has be selected through a optimization process so as to design a best fitted filter for a given model order.

Since the Laguerre polynomials are orthogonal then, using representation (3), the convolution (1) becomes

$$r(t) = \sum_{i=1}^{\infty} c_i f(t) * L_i(t;\xi) \tag{6}$$

The convolution terms are computed computed recursively. Denoting $y_i(t) = f(t) * L_i(t;\xi)$ $y_i(t)$ at the time instant $t = m\Delta t$ is given by

$$y_1(m) = \xi y_1(m-1) + \sqrt{1-\xi^2} f(m) \tag{7}$$

$$y_i(m) = x_i(m) - \xi x_i(m+1) \quad i = 2, 3 \ldots \tag{8}$$

with

$$x_i(m+1) = \xi x_i(m) + y_{i-1}(m) \quad i = 2, 3 \ldots \tag{9}$$

2.2 Kautz basis

In this model the Kautz functions are used as expansion functions. The z-transform of Kautz functions $\mathcal{K}_i(z;\alpha,\beta)$ of the i-th order is given by

$$\mathcal{K}_i(z;\alpha,\beta) = \frac{z(z-\beta)\sqrt{1-\alpha^2}}{z^2+\beta(\alpha-1)z-\alpha}\left[\frac{-\alpha z^2+\beta(\alpha-1)z+1}{z^2+\beta(\alpha-1)z-\alpha}\right]^{(i-1)/2} \quad i \text{ odd} \tag{10}$$

or

$$\mathcal{K}_i(z;\alpha,\beta) = \frac{z\sqrt{(1-\alpha^2)(1-\beta^2)}}{z^2+\beta(\alpha-1)z-\alpha}\left[\frac{-\alpha z^2+\beta(\alpha-1)z+1}{z^2+\beta(\alpha-1)z-\alpha}\right]^{(i-2)/2} \quad i \text{ even} \tag{11}$$

for parameters $\alpha, \beta \in (-1, 1)$. Like in the previous model, the parameters α and β provide additional degrees of freedom which allows one to find a best approximation for a given filter order.

The response of the Kautz filter is given by:

$$r(t) = \sum_{i=1}^{\infty} c_i f(t) * K_i(t;\alpha,\beta) \tag{12}$$

Again, the convolution terms can be computed recursively. Denoting $y_i(t) = f(t) * K_i(t;\alpha,\beta)$, we have the following formulae for $y_i(t)$ at the time instant $t = m\Delta t$

$$y_1(m) = x_1^{(2)}(m+1) - \beta x_1^{(1)}(m+1) \tag{13}$$

$$y_2(m) = x_2^{(2)}(m) \tag{14}$$

$$y_i(m) = x_i^{(1)}(m) + (\alpha-1)\beta x_i^{(2)}(m) - \alpha x_i^{(2)}(m+1) \quad i = 3, 4 \ldots \tag{15}$$

The auxiliary state variables $x_i^{(1)}, x_i^{(2)}$ are defined as

$$x_1^{(1)}(m+1) = x_1^{(2)}(m) \tag{16}$$

$$x_1^{(2)}(m+1) = \alpha x_1^{(1)}(m) - (\alpha-1)\beta x_1^{(2)}(m) + \sqrt{1-\alpha^2} f(m) \tag{17}$$

$$x_2^{(1)}(m+1) = x_2^{(2)}(m) \tag{18}$$

$$x_2^{(2)}(m+1) = \alpha x_2^{(1)}(m) - (\alpha-1)\beta x_2^{(2)}(m) + \sqrt{(1-\alpha^2)(1-\beta^2)} f(m) \tag{19}$$

$$x_i^{(1)}(m+1) = x_i^{(2)}(m) \quad i = 3, 4 \ldots \tag{20}$$

$$x_i^{(2)}(m+1) = \alpha x_i^{(1)}(m) - (\alpha-1)\beta x_i^{(2)}(m) + y_{i-2}(m) \quad i = 3, 4 \ldots \tag{21}$$

III. IMPLEMENTATION OF THE MODELS

The application of the digital filters to the modeling of dispersive phenomena involves two steps:

1. finding the model parameters, usually off line, prior to simulation
2. calculation of the convolution in the actual time domain simulations using the digital filter model of the dispersive problem

The first step may be regarded as a form of tuning of the model. As indicated in the previous sections, the model parameters, for the investigated class of filters, can either be found directly from a known impulse response or using the least squares approach. We found that the latter strategy is very efficient for the modeling of dispersive ABC in waveguides. Prior to simulation we have recorded short time sequences at two points along waveguide separated by a discretization step Δd. These sequences were used for "tuning" the filters. We used the least squares method to find filter coefficients. Once the filter coefficients have been found the quality of the model was tested by exciting the filter with the input "tuning" sequence and comparing the filter output with the recorded output tuning sequence.

Parameters ξ for the Laguerre and (α, β) for Kautz structures were found by means of optimization procedure using the L_2 error of the tuning process as a goal function. The model parameters were saved and subsequently used for modeling ABC using the excitation signal which was **totally different** from the "tuning" signal.

The numerical cost of implementing the convolution using the digital filters depends on the filter structure and order. The costs of the three models discussed in this paper are compared in Table 1.

Table 1: Numerical cost and memory requirements for computation of convolution integrals using digital filter models of order I_{max}

Model	Zero-pole	Laguerre	Kautz
Number of multiplications	$2I_{max}+1$	$3I_{max}-1$	$4I_{max}$
Number of additions	I_{max}	$3I_{max}-2$	$5I_{max}-3$
Number of memory cells	$2I_{max}+2$	$2I_{max}+4$	$3I_{max}+7$

It is assumed that the filters have the same order I_{max}, where I_{max} is the number of expansion terms for Laguerre and Kautz models or the number of zeroes and poles for the zero-pole model. It is seen that the lowest cost in terms of memory and computing time is associated with a zero-pole filter. The advantage of orthogonal filters is, however, the ability to optimize their performance by means of the free parameters and the unconditional stability of their impulse response.

IV. RESULTS

As an example of the application of the fast diakoptics algorithms we shall present the numerical results obtained for for modeling the ABC in TE_{10} mode in a 10.16 by 22.86mm rectangular waveguide. First, a wideband behavior of the models was examined. The filters were tuned using a signal bandwidth of 30 GHz and a center frequency 15 GHz. Table 2 shows the lowest values of the squared filter error which were obtained during the tuning phase.

Table 2: Square of the final prediction error relative to output tuning sequence obtained at the end of the tuning stage for filters tuned for wide band (0–30GHz) operation

Model order	Model		
	zero-pole	Laguerre	Kautz
2	$2.8 \cdot 10^{-5}$	$8.6 \cdot 10^{-6}$	$1.4 \cdot 10^{-6}$
4	$7.2 \cdot 10^{-6}$	$1 \cdot 10^{-6}$	$1.2 \cdot 10^{-7}$
8	$3 \cdot 10^{-6}$	$3 \cdot 10^{-7}$	$8.6 \cdot 10^{-8}$
16	$3.2 \cdot 10^{-7}$	$3.6 \cdot 10^{-8}$	$2.6 \cdot 10^{-8}$
32	$4 \cdot 10^{-8}$	$1 \cdot 10^{-8}$	$8.7 \cdot 10^{-9}$

It is seen that for the low order filters the lowest errors are obtained for Kautz filters but differences between the models are not very significant. The tuning phase can not provide the answer how the model behaves for other signals. To examine the performance of the digital filters as an ABC, the model parameters corresponding to the optima found at the tuning stage were used for time domain simulations of a infinitely long waveguide. The guide was excited with a wideband Gaussian pulse (0-60GHz). Note that this signal was entirely **different** from tuning sequence. In order to measure of the model performance we have calculated the return loss based at 8196 time samples taken a few cells from the ABC. Figs.1-2 show the return loss for the zero-pole, Laguerre and Kautz filters for the filter order $I_{max} = 4$ and $I_{max} = 16$ respectively. It is seen that even for the low approximation order the results are good as the return loss is lower than -50, -60 dB over a very wide frequency band, with the best results obtained for the Kautz filters. The worst performance is seen near the cutoff frequency, especially for a low order zero-pole filter. Increasing the approximation order the quality of the ABC improves quickly, and the differences between models disappear. It has to be noted that in practical simulations the most interesting is the behaviour of the ABC in the single mode band. For this reason we created a new set of models optimizing the filters for the

narrow band operation. To this end we used a tuning signal with the bandwidth form 6.9 to 13.1GHz. The error norms obtained in this process are given in Table 3. The results for Kautz and Laguerre filters are quite remarkable.

Table 3: Square of the final prediction error relative to output tuning sequence obtained at the end of the tuning stage for filters tuned for narrow band (6.9–13.1 GHz) operation

Model order	Model		
	zero-pole	Laguerre	Kautz
2	$8.4 \cdot 10^{-5}$	$1.1 \cdot 10^{-6}$	$9.1 \cdot 10^{-8}$
4	$2.9 \cdot 10^{-5}$	$1.3 \cdot 10^{-7}$	$1.1 \cdot 10^{-8}$
6	$1 \cdot 10^{-7}$	$2.2 \cdot 10^{-8}$	$4.4 \cdot 10^{-9}$
8	$9 \cdot 10^{-8}$	$1.1 \cdot 10^{-8}$	$2.5 \cdot 10^{-9}$

For the filter orders as low as 4 or even 2, for the Kautz model, the prediction errors are by two or even three orders of magnitude lower than for the zero-pole model. The quality of this tuning was again verified by calculating the return loss of the ABC in the single mode operation band of the waveguide. The results are shown in figs 3 and 4. The Kautz filter clearly provides the best results. For the filter order 4 it provides on average more than 15 dB improvement over zero-pole and Laguerre filters especially for the lower frequencies. Also, for this filter, increasing the filter order form 2 to 4 results in approximately 20 dB improvement in the performance.

Fig 5 shows the comparison of the performance of the PML and two orthogonal digital filters based on Laguerre and Kautz polynomials. This time the digital filters were tuned for the 2-20GHz operation. The Berenger's perfectly matched layer was assumed to consist of 16 layers and have parabolic profile of the conductivity and normal incidence reflection factor of 10^{-4}. For the digital filters the model order was 16. For these parameters the Berenger's ABC performs very poorly below cutoff because of the short length of the PML It is seen that below cutoff, both types of digital filters give a significant improvement over the PML, while giving a similar level of reflection coefficient for higher frequencies. The Kautz model also outperforms PML in the high dispersion region.

V. CONCLUSIONS

Fast algorithms for time domain diakoptics were presented. There different implementations using low order zero-pole, Laguerre and Kautz digital filters were described and compared. A highly dispersive absorbing boundary condition is used as an example of application. It was found that very good results can be obtained at a marginal numerical cost. Generally, the orthogonal filters seem to be superior for low order models with the Kautz filter providing particularly encouraging results for single mode applications. The Kautz filters also clearly outperform the PML.

VI. ACKNOWLEDGMENTS

This work was supported by the Polish Committee of Scientific Research under contract 8 T11D 001 08. The numerical results reported in this contribution were obtained using the facilities of the TASK Computing Center. The authors are grateful to Dr M.A.Stuchly and Dr J.De Moerloose for providing the results for PML.

References

[1] J.-P. Berenger,"A perfectly matched layer for absorption of electromagnetic waves," *J. Computational Physics*, vol.114, No.1, pp.185-200, 1994.

[2] Z.Wu and J.Fang, "Performance of the perfectly matched layer in modeling wave propagation in microwave and digital circuit interconnects", *Proc. 11th Annual Review of Progress in ACES*, Monterey, USA, pp.504-511.

[3] P.B. Johns, A. Akhtarzad, "The use of time domain diakoptics in time domain discrete models of fields," *Int. J. Numer. Methods Eng.*,vol.18, pp. 1361-1373, 1982.

[4] W.J.R. Hoefer, "The discrete time domain Green's function of Johns Matrix - A powerful concept in transmission line modeling," *Int. J. of Numerical Modeling*, vol.2, no4, pp.215–225, 1990.

[5] Moglie F., T. Rozzi ,P. Marcozzi and A. Schiavoni. "A new termination condition for the application of FDTD techniques to discontinuity problems in close homogeneous waveguide," *IEEE Microwave and Guided Wave Letters*, vol.2, pp.475–477. Dec.1992.

[6] M. Righi, M. Mongiardo, R. Sorrentino and W.J. Hoefer, "Efficient TLM diakoptics for separable structures" *IEEE MTT-S Int. Microwave Symp. Dig.* , pp.425–428., 1993

[7] K.S. Kunz and J.R. Luebbers, *The Finite Difference Time Domain Methods for Electromagnetics.* CRC Press, Boca Raton, 1993.

[8] T.W.Huang, B.Housmand and T.Itoh, "Fast sequential diakoptics method using the system identification technique," *IEEE Microwave and Guided Wave Letters*, vol.3, pp.337–380. Oct.1993.

[9] R.E.King and P.N. Paraskevopoulos, "Digital Laguerre Filters," *Circuit Theory and Applics.* vol.5, pp.81-91, 1977.

[10] B.Wahlberg, E.J. Hannan,"Estimation of noise models by means of discrete Laguerre/Kautz filters," Identification and System Parameters Estimation, 9th IFAC/IFORS Symposium, Budapest, Hungary, vol.2, pp.1236–1241, July 1991.

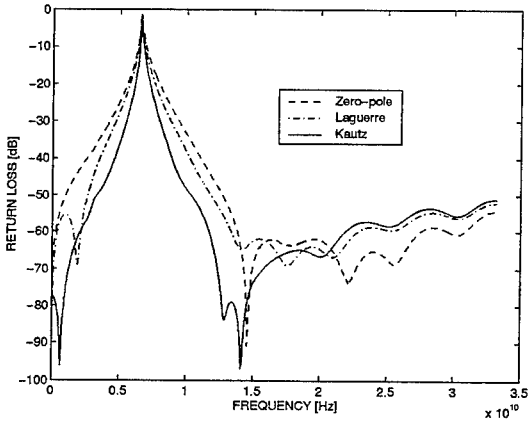

Figure 1: The return loss of the ABC for a TE_{10} mode in a 10.16 by 22.86mm rectangular waveguide and the filter order $I_{max} = 4$. Models optimized for wideband operation

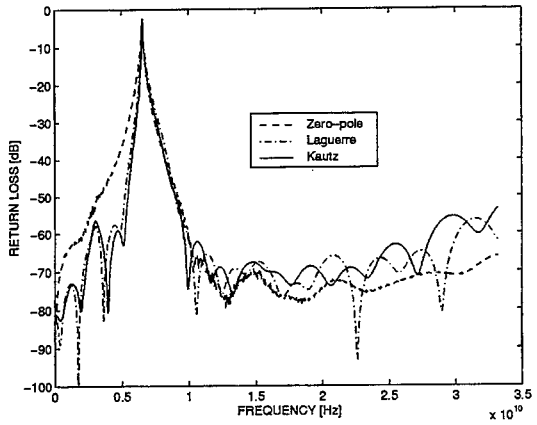

Figure 2: The return loss of the ABC for a TE_{10} mode in a 10.16 by 22.86mm rectangular waveguide and the filter order $I_{max} = 16$. Models optimized for wideband operation

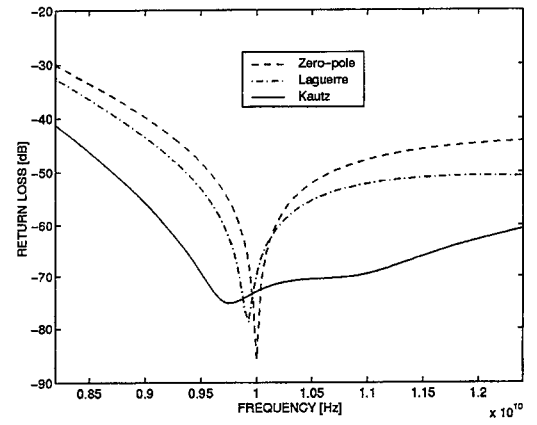

Figure 3: The return loss of the ABC for a TE_{10} mode in a 10.16 by 22.86mm rectangular waveguide and the filter order $I_{max} = 2$. Models optimized for operation within the single mode operation

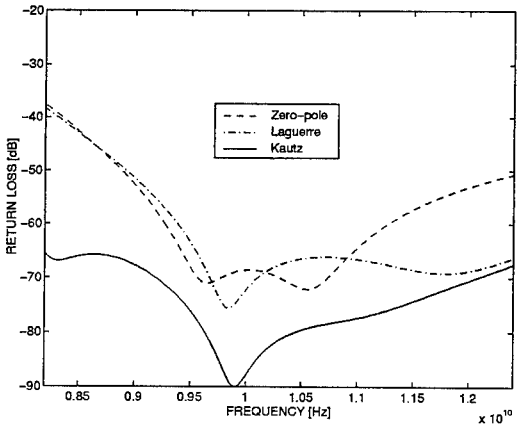

Figure 4: The return loss of the ABC for a TE_{10} mode in a 10.16 by 22.86mm rectangular waveguide and the filter order $I_{max} = 4$. Models optimized for operation within the single mode operation

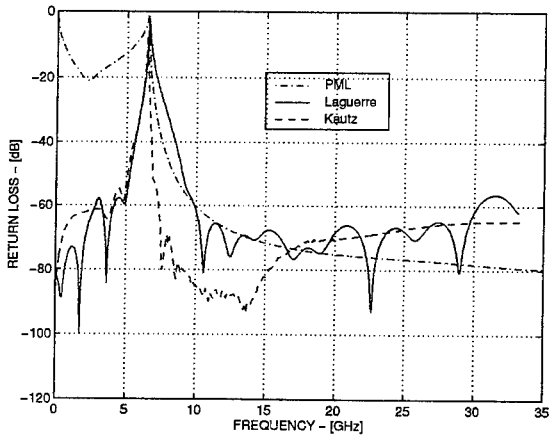

Figure 5: Comparison of the performance of the 16-cell PML having R(0)=10^{-4} and a parabolic conductivity profile with the the orthogonal digital filters for a TE_{10} mode in a 10.16 by 22.86mm rectangular waveguide. The filters order was assumed to be $I_{max} = 16$

Note on Large Crane Coupling to Nearby AM Radio Station

Paul W. Leonard & J. B. Hatfield
Hatfield & Dawson Consulting Engineers
2226 Sixth Avenue N. W.
Seattle, WA 98107

ABSTRACT: The measured hook current of a large cargo crane near a 50-kilowatt medium wave antenna system is compared to the predicted current by the MININEC PROFESSIONAL. Good correlation was obtained.

INTRODUCTION: Large cargo container cranes (Figure 1) are frequently located near AM radio stations. Longshoremen and other crane workers can be exposed to RF shocks or burns when they come into contact with a crane hook as shown In Fig. 2. This office was recently involved in the measurement of crane hook human contact current at a port terminal located adjacent to a standard broadcast AM station that operates with 50 KW antenna input power. The effectiveness of crane hook insulators at reducing the human exposure to RF crane hook currents was also measured and computations of crane hook insulator effectiveness were made using a beta test version of the MININEC Broadcast Professional program.

RF CRANE HOOK CURRENT MEASUREMENTS: The hook current was measured using an ANSI average human equivalent impedance (360 -j30 ohms at 1000 kHz). The ANSI average human impedance is the impedance of the current path to ground that is created when a person contacts the crane hook. The average human impedance is shown as a function of frequency in the appendix to **IEEE/ANSI C95.1-1992**, ***"Standard for Safety Levels with Respect to Human Exposure to Radio Frequency Electromagnetic Fields, 3 kHz to 300 Ghz"***. The contact current measurement device is called the "ANSI MAN". The "ANSI MAN" simulates the electrical characteristics of a human in the circuit. It consists of a plastic tube, 5-feet tall with an impedance of 360 -j30 ohms and a radio frequency ammeter. The "ANSI MAN" was connected between the crane hook and ground. The current was measured as shown in Fig. 3.

THE MININEC CRANE MODEL: The cargo crane dimensions as estimated from a photograph have a base that is about 18 meters in height and 12 meters square. On top of that is an arm about 46 meters long protruding upward at an angle of about 60 degrees. The crane was modeled as two cylinders and a wire to the hook at ground level as shown on Figure 4.

The current measured through the "ANSI MAN" was 0.9 amperes. Since the original MININEC model dimensions were estimated from a photograph of the crane and the computed current was 1.3 amperes, the height of the crane was adjusted from 57-meters to 50-meters so that the computed contact current, at 0.96 amperes, was close to the measured current. The MININEC model ignored stacks of containers, light poles and other nearby equipment associated with an active port. Also, the crane was modeled as two straight cylinders since the detailed structural components are small compared to *a* wavelength.

COMPUTATIONS OF CRANE HOOK INSULATOR EFFECTIVENESS: The MININEC Broadcast Professional computer program was used to predict the effectiveness of a crane hook insulator that was installed to reduce the human contact currents caused by the nearby AM radio station. Contact current is inversely proportional to the total impedance seen by the crane Thevenin equivalent circuit voltage source. The total impedance seen by the crane voltage source when the hook is insulated is the sum of the crane internal impedance, the impedance of the hook insulator and the ANSI average human equivalent impedance (360 -j30 ohms at 1000 kHz).

The total impedance is strongly affected by the summation of the reactive component of the crane internal impedance and the hook insulator reactance. If the hook insulator reactance is opposite in sign to the reactance of the crane internal impedance it is possible for the crane insulator to have the effect of increasing the crane hook contact current. The crane hook contact current will be increased if the hook insulator capacitive reactance is less than twice the magnitude of the inductive reactance of the crane internal impedance. Hook insulators designed for use at 60 Hz power line frequencies have low capacitive reactance at higher frequencies and may exacerbate crane hook RF contact current problems.

To determine the effectiveness of the hook insulator it is necessary to compute the Thevenin equivalent circuit impedance of the crane as a receiving antenna, Figure 5. The open circuit

voltage and short circuit current can be easily computed from the radio station tower and crane model. The open circuit voltage is computed from the current through a 1 megohm resistance load from the hook to ground. The short circuit current is just the current in the grounded hook. Since the program provides the current as a polar number the ratio of the open circuit voltage to the short circuit current yields the complex internal impedance of the crane. If the crane source voltage is independent of the load on the hook the reduction in crane hook contact current is given by the ratio of the total impedance seen by the crane source voltage without the hook insulator to the impedance seen by the crane source voltage with the hook insulator.

The short circuit current at the hook of the crane model was 1.06 amps at an angle of -160 degrees while the open circuit current through 1 megohm was 3.3 milliamps at an angle of -132 degrees. The resulting internal impedance is 3090 ohms at 28 degrees. The total impedance with the human equivalent impedance added is 3402 ohms. When a 22 pF insulator reactance and the ANSI equivalent human impedance are added to the internal impedance, the total load impedance seen by the source voltage is 6938 ohms. The ratio of these two impedances gives the expected reduction in contact current provided by the hook insulator to 49 % of the uninsulated value. The uninsulated contact current was measured Jan 1996 on the crane for which a MININEC model was constructed. The uninsulated crane hook current to ground was 600 mA. When the hook insulator was installed the measured contact current was 300 mA. The measured value of contact current with the crane hook insulator installed is 50% of the uninsulated value.

CONCLUSION: Very useful current and voltage predictions can be made using a relatively simple model in MININEC. At higher frequencies more crane detail will be required. The impedance of both the hook insulator and the crane must be known before an insulator is used. It is possible for a hook insulator to have the effect of increasing the crane hook RF contact current when a crane has a high inductive reactance.

The authors thank Steven S. Lockwood for assistance in providing the test data for this paper

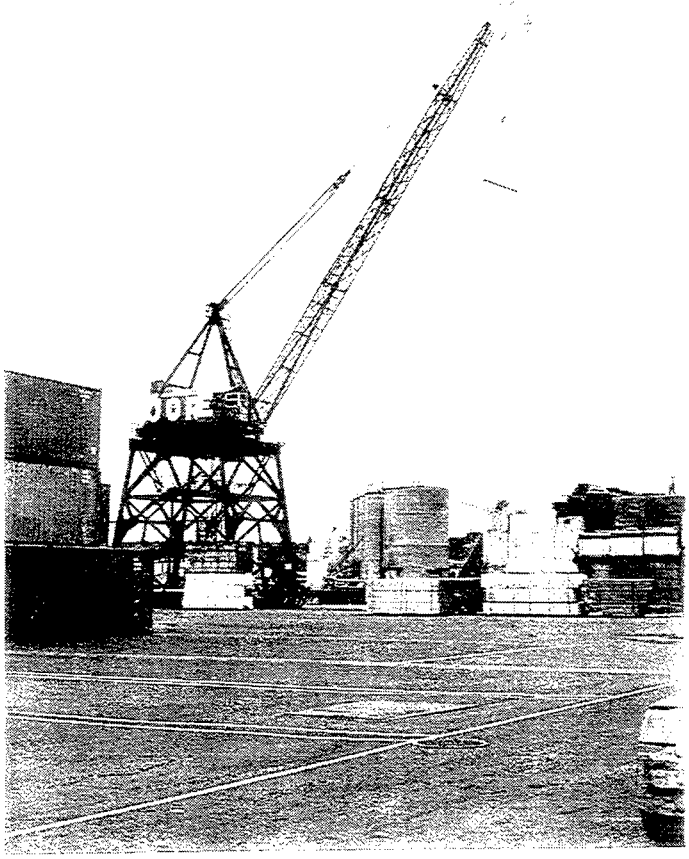

FIGURE 1

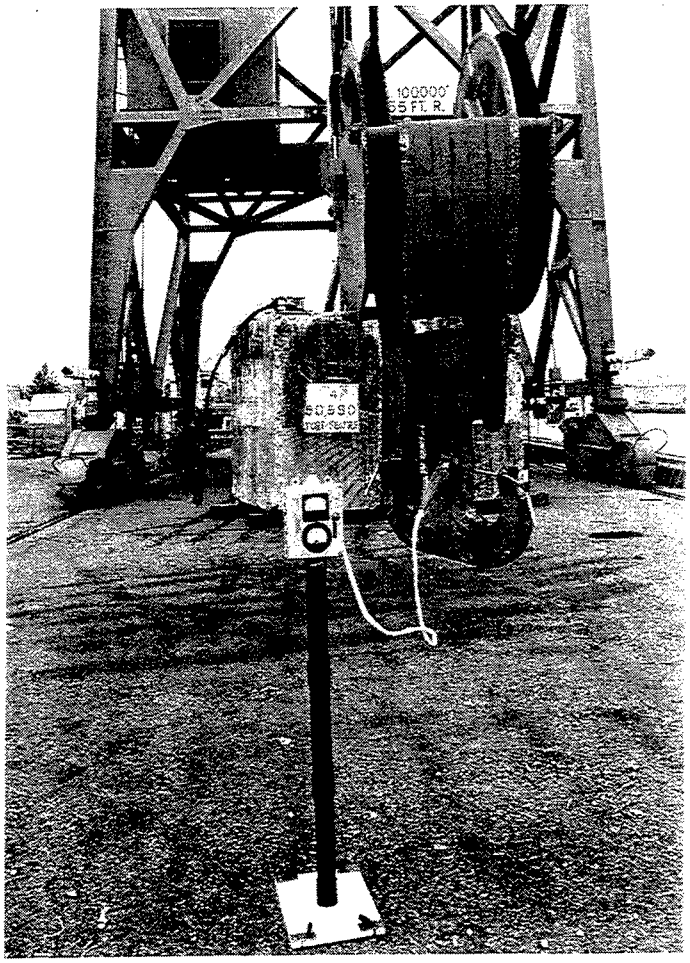

FIGURE 3

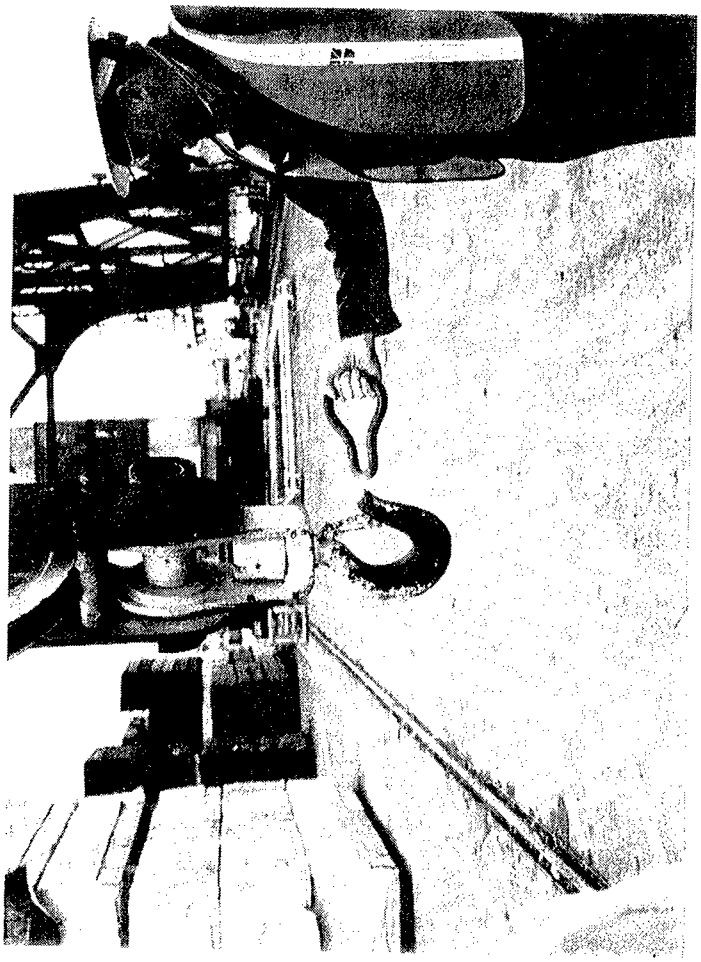

FIGURE 2

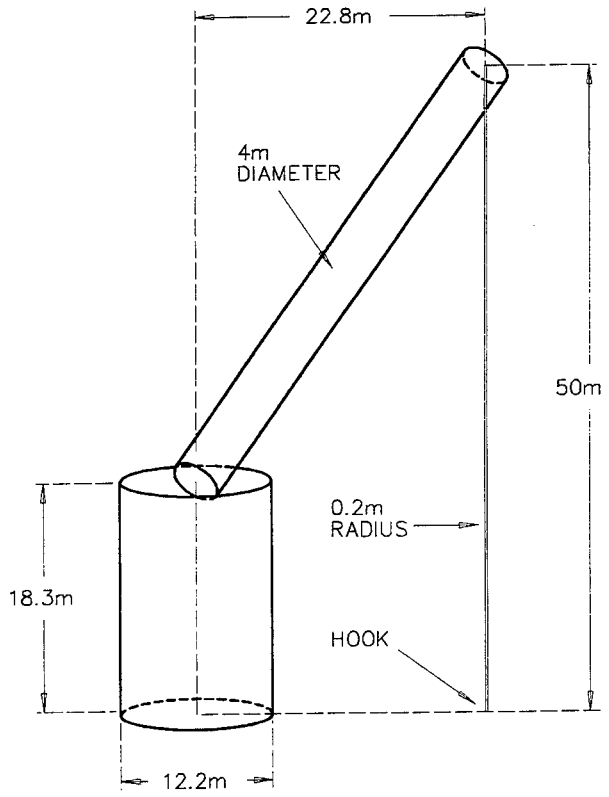

FIGURE 4

MININEC CRANE MODEL

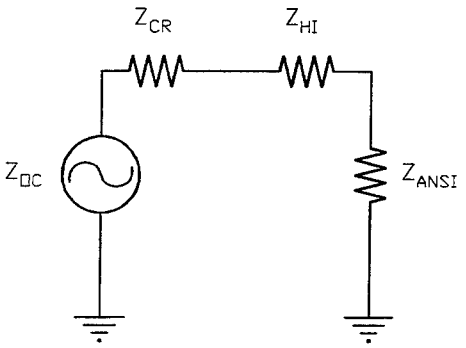

$$Z_{TI} = Z_{CR} + Z_{HI} + Z_{ANSI}$$

$$Z_{TU} = Z_{CR} + Z_{ANSI}$$

$$= $$

$$I_I = \frac{E_{DC}}{Z_{TI}}$$

$$I_U = \frac{E_{DC}}{Z_{TU}}$$

$$\frac{I_I}{I_U} = \frac{Z_{TU}}{Z_{TI}}$$

E_{DC}	= CRANE THEVENIN EQUIVALENT CIRCUIT SOURCE VOLTAGE
Z_{CR}	= CRANE INTERNAL IMPEDANCE
Z_{HI}	= IMPEDANCE OF HOOK INSULATOR
Z_{ANSI}	= EQIVALENT IMPEDANCE ANSI AVERAGE PERSON
Z_{TI}	= TOTAL IMPEDANCE SEEN BY CRANE SOURCE VOLTAGE WITH HOOK INSULATED
Z_{TU}	= TOTAL IMPEDANCE SEEN BY CRANE SOURCE VOLTGAGE WITH HOOK UNINSULATED
I_I	= INSULATED CRANE HOOK CONTACT CURRENT
I_U	= UNINSULATED CRANE HOOK CONTACT CURRENT

FIGURE 5

CRANE EQUIVALENT CIRCUIT
AND DEFINITION OF TERMS

XPATCHF SOFTWARE SYSTEM ANALYSIS AND PROFILING[1]

B. A. Kadrovach, T .S. Wailes, A. J. Terzuoli, Jr., D. S. Gelosh
Air Force Institute of Technology

1. Introduction

Xpatchf is a powerful radar scattering prediction software package with proven accuracy [1]. However, Xpatchf requires a significant amount of time to generate a single prediction for an object of moderate size. Therefore, studies are being conducted to improve the performance of Xpatchf through hardware/software codesigns or implementations on parallel computers. This paper details the functionality of Xpatchf and describes the methods used to identify and isolate the portions of Xpatchf that are best suited for implementation in a parallel environment.

2. Xpatchf Functionality

The source code of Xpatchf consists of a mixture of FORTRAN and C. The main functionality of Xpatchf, as it pertains to the calculation of the scattered field, is written in FORTRAN. C is used to provide dynamic memory management and ray tracing capabilities.

The only abstract data type used by the Xpatchf FORTRAN code is the array --specifically, a fixed-length array. Previous versions of Xpatch required the user to specify the sizes of the various arrays used before compilation. However, the incorporation of key C language routines allows the combined C and FORTRAN program to make use of dynamic length arrays.

Object input data, such as the geometry, are initially read from an input file. Data of similar nature are then stored in contiguous memory blocks. For instance, the x, y, and z nodes of the facet geometry are stored as 3-tuples in an array. The length is given in the input file and is used to specify a sufficiently large contiguous block of memory in which to store the node data. These arrays are managed and maintained by the C functions. FORTRAN subroutines that require access to these data elements as input parameters are called by other FORTRAN subroutines through a C function call. Figure 1 shows the relationship between the FORTRAN subroutines and the C function *wrapper*.

[1]This work was supported by the U. S. Air Force Wright Laboratories.

In calling Fortran subroutine:

```
c_foo(a, b, c)
```

In C function:

```
void c_foo(AType a, BType b, CType c)
{
 foo(a, b, c, a_array, b_array);
};
```

In called Fortran subroutine:

```
foo(a, b, c, a_array, b_array)
dimension a_array(a), b_array(b)
```

Figure 1. FORTRAN/C Interface

The dimension of each array may be passed as a parameter or may exist as a global variable. Global variables are used extensively through-out the FORTRAN code of Xpatchf.

The execution of Xpatchf occurs in three phases. The preprocessing phase establishes initial configuration parameters and reads the geometry file into memory. The second phase consists of the single bounce calculation, and the final phase consists of the multiple bounce calculations. Each of these phases are described in more detail in the following sections.

2.1 Preprocessing

In the preprocessing phase, the configuration parameters are read in from the input file. Since a facet model is assumed for the object, there are two possible methods for calculating the single bounce.[2] The Physical Optics (PO) method is used for smooth objects with little blockage while the Z-buffer method is used for complicated objects. Since realistic objects are unlikely to be simple and smooth, it was decided to assume that the Z-buffer method would be used to calculate the single bounce. This method will be discussed in greater detail in the next section.

Preprocessing continues with the building of the Binary Space Partition (BSP) Tree. The BSP Tree greatly speeds the ray-tracing process for the multiple bounce calculations. For complicated objects, the amount of run-time devoted to building the BSP Tree can be significant. In the case of the V1 aircraft test object [2], the time required to build the BSP Tree was approximately 13% of the total run-time.

The BSP Tree is used to sort the facets of an object. This is accomplished first by calculating a *bounding box* for the object in three dimensions. Then, the bounding box is evenly divided along the x-axis to form two *child* boxes also known as *voxels* (volume elements). In general, any voxel that is evenly divided becomes a *parent* to the two children. At the topmost level, the facets of the object are sorted into the child voxel that either contains all or part of the facet. Each child voxel becomes a parent to two more child voxels. At the second level, the voxels are divided along the y-axis. The facets of the parent voxels are then sorted into their respective children voxels. At the third level, the process is repeated except that the division of the parent voxels is made along the z-axis. This divide and conquer process is continued by repeating the voxel division along the successive axes (x then y then z) until a stopping condition is met. The user specifies the maximum number of facets in the leaf voxels. This is the stopping condition. Only the leaf voxels contain the list of facets. All non-leaf voxels contain

a null lists of facets. This is critical to the traversal of the BSP Tree when searching for a facet. The use of the BSP Tree is a trade-off between speed and memory requirements. If the maximum number of facets allowed in a leaf voxel is small, the ray-tracing (to be described in detail later) will proceed at a much faster rate. However, the memory necessary to store the BSP Tree increases significantly.

2.2 Single Bounce Calculations

The single bounce calculation may be accomplished using either the Physical Optics (PO) or Z-buffer methods. The Z-buffer technique was chosen because of its ability to handle complicated objects. The Z-buffer method is a computer graphics algorithm that finds all the visible surfaces from a particular viewing angle. In the case of Xpatchf, the viewing angle is the angle of the incident wave.

Figure 2 shows the way in which the Z-buffer technique is used. A *viewing screen* is created and divided into pixels. For each pixel, the object is searched for the facet closest to the *screen.*

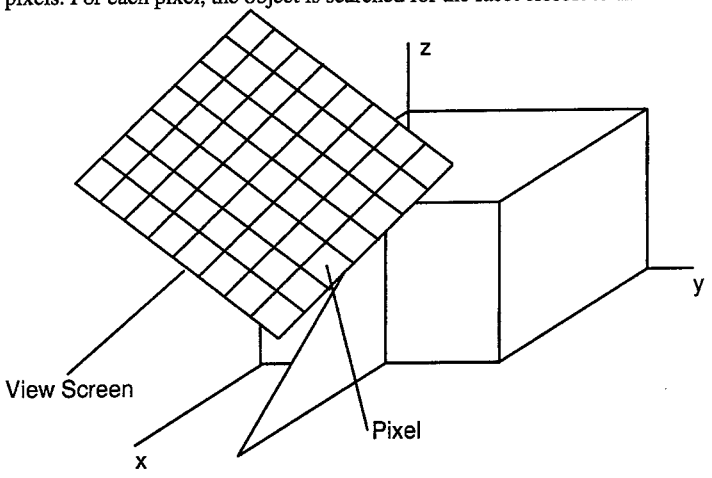

Figure 2. Z-buffer

The buffer is filled with the facet information of the closest facet. Once the buffer is built, the facet information is used to calculate the single bounce.

2.3 Multiple Bounce Calculations

The second and higher bounces of the incident wave are calculated using the Shooting-Bouncing Ray (SBR) technique. The SBR method is used for all of the object geometries available to the Xpatchf user.

The SBR method is a ray-tracing technique usually used in computer graphics applications. Rays are fired at the object from a virtual screen somewhat similar to the Z-buffer *screen.* But rather than building a buffer, each ray is followed as it bounces within the object until it either exits the object or bounces a maximum number of times (specified by the user). In normal operation of Xpatchf, only

the 1st and last bounces of the incident wave are used. Since the single bounce is found by other means, only the last bounce of the SBR is of interest. When a ray is detected as leaving the object, its contribution is calculated and the next ray is then followed. The number of rays fired at an object depend on its size and the frequencies being simulated. As an example, if the boxfin [2] is to be calculated for a frequency of 11GHz, approximately 1 million rays will be fired.

Of the three main phases of Xpatchf operation, the last phase offers the greatest potential for optimization in some form of a concurrent architecture. However, all three phases could benefit from the advantages offered by concurrent operation. This will be discussed in the next section.

3. Identified Potential Concurrencies

Each of the three phases (preprocessing, single bounce, and SBR) have potential for implementation in a concurrent architecture since each phase consists of one or more loops. The largest percentage of computational effort in the preprocessing phase is devoted to building the BSP Tree. Since the tree is a dynamic memory structure, it does not lend itself well to optimization in a parallel execution. The remaining two phases deserve a closer look. First, an analysis of the Z-buffer implementation will be described. Then, an in-depth investigation of the SBR method will be presented.

3.1 Z-Buffer

The program flow of the Z-buffer source code is best described with an illustration. Figure 3 shows a graphical representation of the Z-buffer method as implemented in Xpatchf.

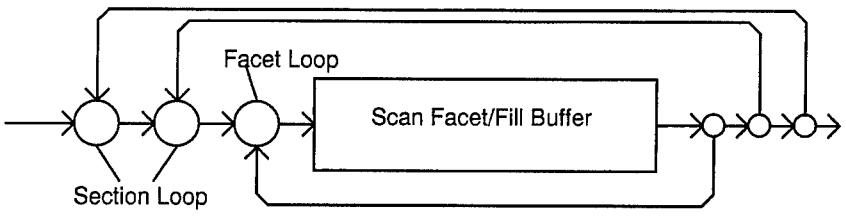

Figure 3. Fill-Buffer Loop

The *screen* is divided into sections with each section no larger than 600 x 600 pixels. The size of a pixel is specified by the user and is relative to the wavelength being simulated. The relationship between the number of total pixels, *ipixxtot*, and the size of the object is given by $ipixxtot = \frac{\Delta x}{pixsize \cdot \lambda}$. This equation is shown for the x axis but the same applies for the y axis. In the above equation, *pixsize* is specified by the user and is relative to the wavelength. The wavelength, λ, is the smallest wavelength being considered in the calculations. The size of the object, Δx, is the size of the projection of the object onto the Z-buffer *screen*. For instance, if the largest frequency being considered is 12.0GHz (λ = 0.025m) and the user specifies the pixel size to be 0.1λ, the resulting total number of x pixels is 2,000 for an object with a size of 5 meters.

Once the number of pixels is determined and the number of zones necessary to ensure that the size does not exceed the 600 x 600 pixel requirement, the Z-buffer is filled with object data. Specifically, for each zone, all facets of the object are examined to find their place in the Z-buffer. If facets overlap, the closest facet is used to fill the Z-buffer with the appropriate data. This data includes the facet identification (a unique integer is assigned to each facet), the facet material, and the facet normal. Finally, with the Z-buffer filled, Xpatchf calculates the far field.

3.2 SBR

The Shooting Bouncing Ray (SBR) method, used to calculate the multiple bounce contributions, is somewhat similar to the Z-buffer manipulation with the exception of the multiple bounces of the ray. As before, a virtual *screen* is used to fire rays at the object. The dimensions of this screen are specified by size of the object projection onto the virtual screen. The axes of the screen are elevation and azimuth (rather than x and y). Once the extents of the screen are calculated, a grid is established to fire the rays at the object. The number of rays to be fired are determined from a combination of object dependent parameters and user specified parameters [2].

In order to speed the ray tracing, the virtual screen can be divided into user defined zones. A typical zone size is a square of 20 x 20 rays. A test ray is fired into the center of the zone. If the ray intersects the object, all the rays in the zone are fired, otherwise the zone is skipped saving 400 ray computations.

When a ray is found that intersects the object, it is followed for a specified maximum number of bounces. The default maximum is 50, however the user may specify any value between 1 and 50. If the ray does not exit the object before this maximum value is reached, the ray is discarded and the next ray is traced. It is important to note that even though the first bounce is calculated using a different method, the SBR ray tracing routines must still fire each ray and calculate the first bounce information. Figure 4 illustrates the program flow for the SBR source code.

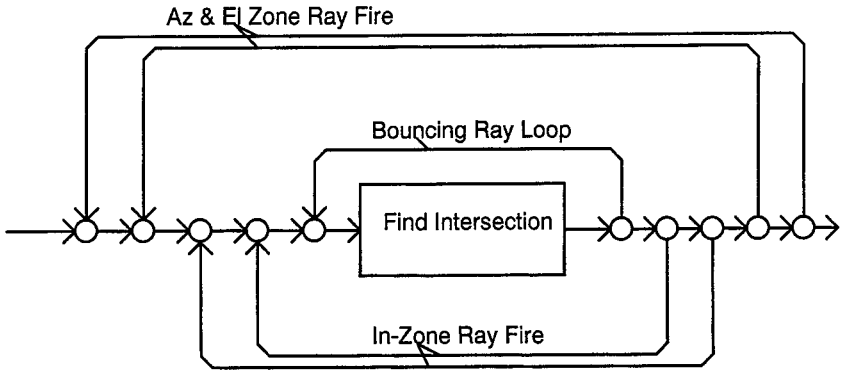

Figure 4. SBR Program Flow

The SBR routine contains numerous conditional exits from each of the loops. This complicates the implementation of this code into a VHDL model since application specific hardware does not easily

handle conditional data flow. These conditional branches require a flexible model able to manage the changes in data flow.

The functionality of Xpatchf was determined by profiling the software in the run-time environment. This was done by tracking function and subroutine calls in both the FORTRAN and C code. Since most of the C code functions exist as library functions, the blending of FORTRAN subroutine calls with the C code function calls presented a major difficulty. There was no easy way to determine the temporal relationship between the FORTRAN and C source code. The only alternative was a line-by-line analysis of the source code to determine the subroutine/function calling hierarchy.

In order to profile the FORTRAN source code, each of its subroutines was changed so that a unique flag was written to a file every time that the subroutine was called. Then, special support programs were written to manage and analyze the vast amounts of information produced. A table was generated to show the statistics for each subroutine. This data was used to focus the analysis effort toward those subroutines used most frequently. Next, a time plot was generated to show the temporal relationship of each subroutine. These plots showed the periodicity of the Xpatchf run-time environment. Since these plots consist of several thousand lines of text data, none are included with this paper.

The same method was applied to the C functions. Some of the C functions simply provided the necessary dynamic memory management as explained earlier. The C functions of interest performed the management of the BSP Tree and the actual ray tracing. Once the source code was analyzed and the hierarchy was understood, the temporal relationship between the FORTRAN and C functions could be determined. These temporal relationships were used to identify the Xpatchf functionality that would achieve the most benefit from a hardware implementation. The results of that analysis are shown in Table 1.

Table 1. Run-time Percentages

Object	BSP Generation	Single Bounce	Multi-Bounce
Boxfin	0.10%	11.16%	87.97%
Turkey	0.63%	2.94%	95.56%
V1 Aircraft	12.85%	42.37%	42.17%

The times of execution are shown as percentages of the total time of execution. This provides a normalized view of the relative time spent in each phase. It should be noted that not all of the run-time is accounted for in the above table. The pre- and post-processing is not shown and therefore, the percentages of each row do not add up to 100%. The first phase (BSP generation) was small for the first two objects but became significant for the V1 aircraft due to its complexity. The other two phases (single bounce and multi-bounce calculations) showed wide variations. The run-time for boxfin and turkey indicated that most of the time was spent in the multi-bounce portion of the code while the run-time for the V1 aircraft showed about equal proportions of time spent in the single bounce and multi-bounce calculations. It is hypothesized that the processing of the V1 aircraft could be improved by eliminating the single bounce calculation by Z-buffer (or PO) and stay strictly with SBR. The Single Bounce and Multi-Bounce calculations would most benefit from a parallel implementation since they require the greatest portion of the run-time.

4. Conclusion

This paper presented a method to analyze and profile the Xpatchf software system for a parallel implementation. The approach was to identify, through run-time analysis, the portions of the program that repeat. Data interdependencies between repeated cycles of code must be identified to ensure that one cycle may be executed independently of another. In Xpatchf those cycles exist in both the Single Bounce and Multi-Bounce calculations.

Bibliography

1. E. M. Miller, D. J. Andersh, A. J. Terzuoli, Jr., "Facetization Level and the Effect on XPATCH Predictions," *Proceedings of the Ninth Annual Review of Progress in Applied Computational Electromagnetics*, Naval Postgraduate School, Monterey, CA, March 22-26, 1993, pp. 610-617.

2. S. W. Lee and D. J. Andersh, User Manual for xpatchf, DEMACO, Inc., Sep. 1993.

THEORETICAL STUDIES OF PHOTONIC BAND GAP MATERIALS

M. M. Sigalas, R. Biswas, C. T. Chan, K. M. Ho, and C. M. Soukoulis

Ames Laboratory and Department of Physics and Astronomy, Iowa State University, Ames IA 50011

1. INTRODUCTION

Photonic band gap (PBG) materials are periodic dielectric structures exhibiting a frequency gap in which all modes are forbidden, analogous to the electronic band gap in the case of semiconductors.[1-3] In such materials, spontaneous emission is suppressed for photons with frequencies in the forbidden region. Already, there have been a number of proposals for photonic band gap based devices with operating frequencies ranging from microwave to optical, including zero-threshold lasers, novel resonators and cavities, and efficient microwave antennas.[2,3] Most of these applications rely on the availability of structures with full three-dimensional photonic band gaps.

In the present paper, we are using the transfer matrix method[4] in order to calculate the transmission and reflection properties of PBG materials. In particular, we study defects in periodic PBG materials which can be used as filters and high Q cavities. We also study PBG materials as a substrate for planar dipole antennas. Since PBG materials are perfectly reflecting materials for frequencies inside the photonic band gap, one expects that they will impove the performance of antennas.

According to the transfer-matrix method (TMM), the space is divided in small cells and the fields in each cell are coupled with those in the neighboring cells; then the transfer matrix can be defined by relating the fields on one side of the material's slab with those on the other side. So, the transmission and reflection coefficients for EM waves of various frequencies incident on a finite thickness material can be obtained; the system assumed periodic in the directions parallel to the interfaces. The method has been used in two-dimensional[5] and three-dimensional[6] structures as well as in cases where the dielectric constant is complex and frequency dependent.[7,8] In all the cases, the agreement between theory and experiment is very good.

2. FILTERS

We use a layer-by-layer PBG crystal which has been designed and fabricated by the Iowa State group.[9-11] The structure is assembled by stacking layers consisting of parallel rods with a center-to-center separation of a. The rods are rotated by 90° in each successive layer. Starting at any reference layer, the rods of every second neighboring layer are parallel to the reference layer, but shifted by a distance 0.5a perpendicular to the rod axes. This results in a stacking sequence that repeats every four layers. This lattice has face-centered-tetragonal (fct) lattice symmetry with a basis of two rods. The photonic band gap is not sensitive to the cross-section shape of

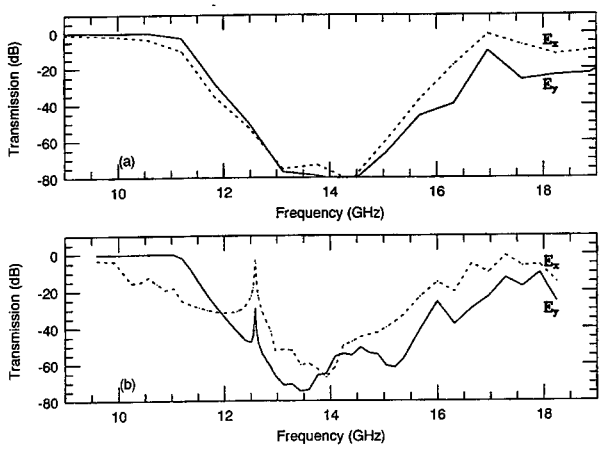

Figure 1: The transmission characteristics of EM waves propagating in a perfect (a) and a periodic with defect (b) layer-by-layer structure with k perpendicular to the plane of the rods (x-y plane). The systems consists of 16 layers of rods. The defect is created by removing every other rod from the 8th layer.

the rods. This structure has a photonic band gap when both the filling ratio and the dielectric contrast meet certain requirements.[9–11]

In the present case, we use circular rods with dielectric constant 9.61 and 0.318 cm in diameter; a=1.123 cm and the filling ratio of around 0.26. We define the plane of each layer as the x-y plane. Using the TMM, we calculate the transmission (Fig. 1a) of a structure with four conventional unit cells along the z-axis (16 stacked layers). We use one unit cell along the x- and y-axis with periodic boundary conditions (the system is infinite along the x- and y-axes). Each conventional unit cell is divided into 7×7×8 cells in order to ensure good convergence. For both polarizations, there is a gap between 11.2 and 16.9 GHz. This is in very good agreement with the experimental measurments as well as with the results of the plane wave (PW) method[6,10] There are differences between the two polarizations, especially at high frequencies. It is worth noting that the difference between the two polarizations is due to the surface of the system (the rods on the surface are parallel to the z-axis). Band structure calculations of a corresponding infinite system do not show any difference between the two polarizations. The transmission at the middle of the gap is around -80 dB. Calculations for thinner structures show the drop of the transmission is about -19 dB per unit cell; by using just two unit cells (8 layers of rods), we can have a PBG with a transmission of about -38 dB which is enough for most of the possible applications.

Defects are created by removing or adding rods into the structure. We first investigate the properties of defect structure made by removing every other rod from the 8th layer. The system is otherwise similar with the one described previously. A peak in the transmission appears at 12.58 GHz. The peak is sharper for the polarization where E is parallel to the axes of the removed rods (E_x in Fig. 1b); in particular, Q=800 and the transmission at the peak is -4 dB for the

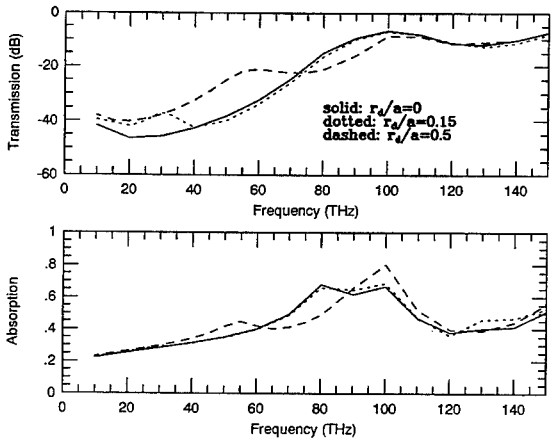

Figure 2: Transmission and absorption for EM waves propagating in a 3D s.c. lattice consisting of metallic tetragonal rods connecting nearest neighbors with f=0.03, L= 3a and θ= 0°. A supercell of width 2a has been used with periodic boundary conditions at the edges of the supercell. Part of the metal, which is included in a sphere with a center in one of the crossing points of the rods at the second layer and radius r_d- has been removed. Solid, dotted, and dashed lines correspond to r_d/a= 0, 0.15 and 0.5, respectively.

wave with E//x while Q=900 and the transmission at the peak is -29.7 dB for the wave with E//y. The defect frequency and Q-factor are not very sensitive to separation between the defects. In particular, the defect frequency changes from 12.58 to 12.68 to 12.39 GHz as the separation between the removed rods increases from 2a to 3a to 4a. Also, the Q-factor increases rapidly by increasing the thickness of the PBG crystal. For a defect structure with 8 unit cells (32 layers) made by removing every other rod from the 16th layer, calculations predict a defect frequency at 12.61 GHz with a Q-factor more than 1.4×10^6. This suggests the possibility of building cavity structures with very high Q-factors from this geometry. We can also adjust the defect frequency by changing the radius of the rods. In a 4-unit cell system (16 layers), we assume that every other rod in the 8th layer has radius r_d instead of r. A defect peak inside the gap appears when r_d/r is around 0.65. By decreasing r_d/r, the defects frequency increases and for r_d/r=0 (this is the case where every other rod has been removed; see Fig. 1b) the defect frequency is 12.58 GHz as discussed previously.

We have also studied photonic band gap materials constructed by metallic components. We use a s.c. lattice consisting of metallic tetragonal rods connecting nearest neighbors (network topology) with filling ratio, f= 0.03, lattice constant, a=1.27 μm, and the surrounding medium is air. The periodic system (solid lines in Fig. 2) has a band gap from zero up to a cut-off frequency of 100 THz. This band gap appears for any angle and polarization. We also study the effect of the introduction of defects in a periodic lattice. A supercell has been used with width 2a along the x- and y-axis and periodic boundary conditions are imposed at the edges of the supercell; the

system is finite along the z-axis with thickness L= 3a. A defect is introduced by removing part of the metal, which is included in a sphere of radius r_d centered at one of the crossing points of the rods in the second layer. Figure 2 shows the transmission and absorption for such a defect structure and incident waves with $\vec{k}$ parallel to the z-axis and a= 1.27 μm. Once again the results are identical for both polarizations due to the symmetry of the structure. For r_d/a=0.15, a small peak in the transmission appears at around 31 THz; the quality factor is very small (Q= 3) and the transmission at the top of the peak is also small (-37.2 dB). Apart from the frequency region around the defect, the transmissions of the defect and the periodic structures are almost the same (compare dotted and solid lines in Fig. 2). For r_d/a=0.5 (dashed line in Fig. 2), there is a peak in the transmission at higher frequency (60 THz) which is even wider and with higher transmission at the top of the peak. Thus, one can adjust the frequency of the defect inside the gap by just changing the volume of the removed metal; the higher the amount of the removed metal, the higher the frequency where the defect peak appears. Studies in dielectric PBG materials[12] have shown that a defect band emerges from the lower edge of the gap and approaches the upper edge of the gap as the volume of the removed dielectric material increases. The behavior of the defect band is similar in the present case, despite the fact that the lower edge of the gap is actually at zero frequency. The absorption for r_d/a=0.15 is almost identical with the absorption of the periodic case except for a small maximum at the frequency where the defect peak appears (hardly noticed by comparing dotted and solid lines in Fig. 2). However, the differences in the absorption between the r_d/a=0.5 and the periodic cases (compare dashed and solid lines in Fig. 2) are more obvious with a more prominent peak of the absorption in the r_d/a=0.5 case at the frequency where defect appears (60 THz). Since the light is trapped around the defect region, one actually expects the absorption will be higher in this case.

In conclusion, dielectric and metallic PBG materials can be used as high Q cavities and filters by creating defects in those structures. The frequency where the transmission peak appears can be controlled by the size of the defect. Dielectric PBG materials exhibit much higher values of Q (of the order of 10^3 or more) than the metallic PBG materials. The reason for that difference lies in the absorption of the metals and it becomes more prominent as the frequency increases.[13] However, metallic PBG materials may be more attractive in microwave and millimeter wave aplications and for cases where the size and weight of the material is an important factor. One can make the metallic PBG filters very small in size by using high dielectric material as a background material and by decreasing the volume of the removed metal (r_d in Fig. 2).[13]

3. PBG AS SUBSTRATES FOR ANTENNAS

Conventional integrated circuit antennas on a semi-infinite semiconductor substrate (with dielectric constant ϵ) have the drawback that the power radiated into the substrate is a factor $\epsilon^{3/2}$ larger than the power into the free space.[14] Hence, antennas on GaAs or Si, radiate only 2% of their power into free space. Of the power radiated into the substrate, a large fraction is in the form of trapped waves propagating at angles larger than the critical angle.[14] By fabricating the antenna on a PBG material with a driving frequency in the stop band, no power should be transmitted into the PBG material and all power should be radiated in the free space assuming that there are no evanescent surface modes. Brown et al.[15] demonstrated this concept by fabricating a bow-tie antenna on their 3-cylinder PBG material and found a complex radiation pattern confined to free

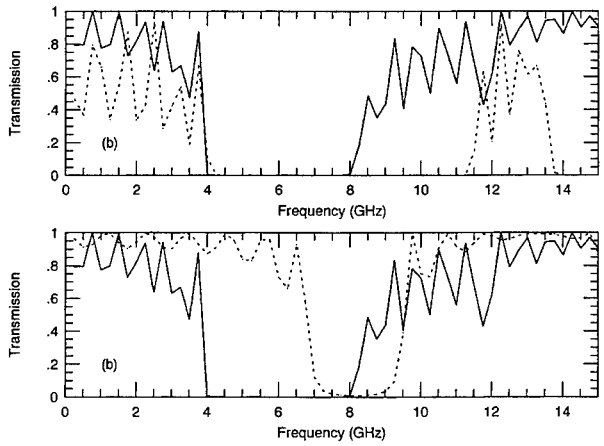

Figure .3: The transmission for s- and p-polarized waves (a and b panels, respectively) for EM waves propagating in a multilayer described in the text. Solid and dotted lines correspond to incident angles of 0 and 60 degrees.

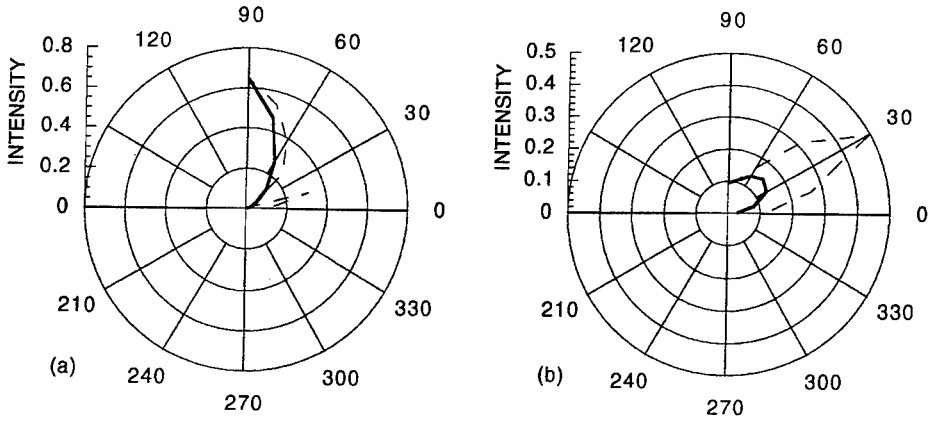

Figure 4: The radiation pattern of a dipole placed on top of a multilayer with driving frequency of 8 and 6 GHz (a and b panels, respectively). Solid and dashed lines corespond to H- and E-planes.

space. Subsequently, they improved the directionality of a dipole antenna by placing it on high- and low-dielectric surfaces of their PBG materials.[16] More recently, Cheng et al.[17] have measured the radiation pattern of planar dipole antennas in the 12-15 GHz regime placed on a layer-by-layer PBG material.

Theoretical studies of radiation patterns of antennas with PBG substrates are needed in order to compare and probably improve the existing antennas. We can solve this problem by using the reciprocity relation for radiation patterns. According to reciprocity, the problem where a transmitting antenna is placed on top of a PBG material and a receiving antenna at infinity, is actually equivalent to the problem where a transmitting antenna is placed at infinity and the receiving antenna on top of the PBG substrate. The second problem problem can be easily solved using the transfer matrix method. Since the transmitting antenna is at infinity, we can approximate the radiated waves in the vicinity of the surface of the PBG material by plane waves. Using the TMM, we can find the pattern of the electric field on the surface of the PBG materials which is actually the radiation pattern. We tested this method for a uniform dielectric substrate and the results are in very good agreement with numerical results reported by Cheng et al.[17] For the results of Ref. 17, the far-field radiation of the dipole placed above a finite dielectric slab was calculated by expanding the spherical dipole fields in plane waves, and utilizing Fresnel reflection and transmission coefficients.

As a next step, we calculate the radiation pattern of a dipole placed on top of a periodic multilayer. The multilayer is constructed by two different layers placing them one after the other. We call the high and the low dielectric constants layers by H and L, respectively. The dielectric constants of the layers are $\epsilon_H = 9.61$ and $\epsilon_L = 1$ while the ratio of their thicknesses is $d_H/d_L = 0.314$. The multilayer consists of 13 layers with total thickness of 0.104 m. Fig. 3 shows the transmission for s- and p-polarized waves. The width of the gap increases as the incident angle increases for s-polarized waves, while it tends to disappear as the incident angle increases for p-polarized waves.

Fig. 4 shows the radiation pattern of an electric dipole placed on top of the multilayer with driving frequencies 8 and 6 GHz. The calculated pattern have been found using the method described previously. The patterns are symmetrical relative to the vertical axis. For 8 GHz, the patterns in the E- and H-plane (dashed and solid lines in Fig. 4a) are similar for almost all the angles except for small angles where a peak appears in the E-plane pattern. For 6 GHz (dashed and solid lines in Fig. 4b), there are important differences for the E- and H-plane patterns. In particular, the E-plane pattern has a peak at 30° with intensity 0.49 while the H-plane pattern has a peak at 45° with intensity 0.15.

Preliminary results as well the measurment reported in Ref. 17 show that in the case of the layer-by-layer PBG the pattern is strongly depended on the driving frequency as well as the position and orientation of the antenna. Virtually no power is lost to the PBG material resulting in gains and radiation efficiencies larger than antennas on other conventional substrates.

Acknowledgment - Ames Laboratory is operated by the U.S. Department of Energy by Iowa State University under Contract No. W-7405-Eng-82.

REFERENCES

1. See the proceedings of the NATO ARW, *Photonic Band Gaps and Localization,* ed. C. M.

Soukoulis, (Plenum, New York, 1993).
2. See the special issue of the J. Opt. Soc. Amer. **B 10**, 208-408 (1993) on *Development and Applications of Materials Exhibiting Photonic Band Gaps.*
3. Special issue of J. Mod. Opt. **41**, 171-294, (1994) on *Photonic Band Structures.*
4. J. B. Pendry and A. MacKinnon, Phys. Rev. Lett. **69**, 2722 (1992); J. B. Pendry, J. Modern Optics **41**, 209 (1994).
5. M. M. Sigalas, C. M. Soukoulis, E. N. Economou, C. T. Chan and K. M. Ho, Phys. Rev. **B48**, 14121 (1993).
6. E. Ozbay, E. Michel, G. Tuttle, M. Sigalas, R. Biswas, and K. M. Ho, Appl. Phys. Lett. **64**, 2059 (1994).
7. M. M. Sigalas, C. M. Soukoulis, C. T. Chan and K. M. Ho, Phys. Rev. **B49**, 11080 (1994).
8. D. R. Smith, S. Shultz, N. Kroll, M. Sigalas, K. M. Ho and C. M. Soukoulis, Appl. Phys. Lett. **65**, 645 (1994).
9. K. M. Ho, C. T. Chan, C. M. Soukoulis, R. Biswas, and M. Sigalas, Solid State Commun. **89**, 413 (1994).
10. E. Ozbay, E. Michel, G. Tuttle, M. Sigalas, R. Biswas, and K. M. Ho, Appl. Phys. Lett. **64**, 2059 (1994).
11. E. Ozbay, A. Abeyta, G. Tuttle, M. Tringides, R. Biswas, C. M. Soukoulis, C. T. Chan, and K. M. Ho, Phys. Rev. **B50**, 1945 (1994).
12. E. Yablonovitch, T. J. Gmitter, R. D. Meade, A. M. Rappe, K. D. Brommer, and J. D. Joannopoulos, Phys. Rev. Lett. **67**, 3380 (1991).
13. M. M. Sigalas, C. T. Chan, K. M. Ho, and C. M. Soukoulis, Phys. Rev. **B52**, 11744 (1995).
14. D. B. Rutledge, D. P. Neikirk, and D. P. Kasilingam, in *Infrared and Millimeter Waves* (Academic, Orlando, 1983), Vol. 10, p. 1.
15. E. R. Brown, C. D. Parker, and E. J. Yablonovitch, J. Opt. Soc. Am. B**10**, 404 (1993).
16. E. R. Brown, C. D. Parker, and O. B. McMahon, Appl. Phys. Lett. **64**, 3345 (1994).
17. S. D. Cheng, R. Biswas, E. Ozbay, S. McCalmont, G. Tuttle, and K.-M. Ho, Appl. Phys. Lett. **67** 3399 (1995).

On the Use of Richardson Extrapolation in the Finite Element Analysis of Two-Dimensional Electrostatics Problems

W. Elliott Hutchcraft and Richard K. Gordon
Department of Electrical Engineering
University of Mississippi
University, MS 38677

Abstract

Richardson extrapolation can be used to obtain an accurate solution to a problem while being efficient with both computer time and memory. In this paper, Richardson extrapolation is used in conjunction with the finite element method to solve two-dimensional electrostatics problems. Numerical results are presented, and it is seen that high accuracy can be achieved when Richardson Extrapolation is used..

Introduction

Error analysis has become increasingly important in the computational sciences, and has recently received abundant attention in the scientific literature. A posteriori error estimation in conjunction with the first order finite element method was discussed in [1] by Babuska, Duran, and Rodriguez.. Also, in [2], adaptive finite element methods have been employed by Eriksson and Johnson to solve parabolic partial differential equations. In [3], Drago, Molfino, Nervi, and Repetto discuss error estimation in the finite element determination of the magnetic field in a two-dimensional region using node-based elements. And, in [4], Hutchraft and Gordon discuss the use of Richardson extrapolation in one- and two-dimensional finite difference problems.

One distinct advantage of the use of error analysis is that it makes possible the calculation of an accurate solution without extremely long compute time or substantial computer memory capacity. In this paper, Richardson extrapolation is used to obtain accurate solutions for two-dimensional electrostatics problems using the finite element method.

In the following, the implementation of Richardson extrapolation to solve electrostatics problems will be discussed.

Technique

Consider the finite element analysis of electrostatics problems. When linear basis and testing functions are used in the finite element method, it can be shown that the error in the finite element solution will vary as h^2, where h is the mesh spacing [5]. With Richardson extrapolation, the solution is calculated with two different values of mesh spacing, and then a more accurate solution is obtained by forming a linear combination of the two results. With the correct combination, some of the truncation error that is introduced into the solution from the choice of basis and testing functions can be eliminated.

The solution is obtained with an original mesh spacing, h, and then the spacing between nodes is halved to $(h/2)$, and the numerical solution is calculated again. From these solutions, an extrapolate at each node in the original mesh is obtained. For example, consider the use of the one-dimensional meshes shown in Figures 1 and 2.

Figure 1. Original Mesh

Figure 2. Refined Mesh with Halved Spacing

The problem is solved using the original mesh and solved again using the refined mesh. Then, the Richardson extrapolate solution is calculated using the equation:

$$u_{ext}(x,y) = u_{ref}(x,y) + \frac{u_{ref}(x,y) - u(x,y)}{3.0}$$

where $u_{ext}(x,y)$ is the extrapolated solution, $u(x,y)$ is the original numerical solution obtained using the mesh spacing h, and $u_{ref}(x,y)$ is the numerical solution calculated using the refined mesh with mesh spacing $\frac{h}{2}$.

Numerical Results

As an illustration of these ideas in the two-dimensional case, consider the finite element solution to the problem:

$$-\nabla \bullet (a\nabla u) + bu = 0 \text{ on } \Omega$$

$$u = h \text{ on } \partial\Omega$$

For simplicity, we will consider the problem in which Ω is the square region from x=0.0 to x=2.0 and y=0.0 to 2.0 and:

$$a(x,y) = 1.0$$

$$b(x,y) = 0.0$$

$$u(0.0,y) = 0.0$$
$$u(2.0,y) = 0.0$$
$$u(x,0.0) = 0.0$$
$$u(x,2.0) = \sin(\pi x / 2.0)$$

The problem was solved with meshes having 3, 6, 9, 12, and 15 nodes in both the x and y directions. In each case, the distance between nodes was then halved and the problem was solved again. The Richardson extrapolate solution was then calculated using the equation shown above.

In order to quantify the accuracy of the solutions, a nodal error defined by the equation

$$nodal\ error = \sqrt{\frac{\sum_{i=1}^{n}(V_{i_{numerical}} - V_{i_{analytic}})^2}{n}}$$

was used. In this equation, the summation is over all nodes at which the solution must be calculated, i.e., the interior nodes. We refer to this as the nodal error because it is a measure of the error of the solution at the mesh node locations. The improved accuracy of the Richardson extrapolate solution can be seen when the natural logarithm of the nodal error is plotted against the logarithm of the spacing distance, h. This is shown for the two-dimensional case in Figure 3. Because the truncation error due to the use of linear basis functions is second order, the error in the original finite element solution of the problem varies as h^2. This can be seen from Figure 3, as the slope of the line for the error in the original solution (solid line) is approximately two. However, the linear combination that is used to calculate the Richardson extrapolate is such that that part of the error that varies as h^2 is canceled out. This is seen from the fact that the slope of the line representing the error in the extrapolated solution (dotted line) is greater than two.

In order to determine the efficiency of using this technique, we investigated the question of what mesh density would be needed, without using extrapolation, to obtain the same accuracy as was obtained using a 6 x 6 mesh and Richardson extrapolation. Note that a rough idea of the answer can be predicted from the top graph in Figure 3. It was found that if extrapolation were not used, it would be necessary to use a 30 x 30 mesh to obtain as much accuracy as was obtained using Richardson extrapolation on a 6 x 6 mesh. Of course, to calculate the Richardson extrapolate on a 6 x 6 mesh, it is necessary to also calculate the refined solution on a 11 x 11 mesh. But this requires only the use of a 121 x 121 finite element matrix while the analysis of the problem defined on the 30 x 30 mesh

without extrapolation requires the use of a 900 x 900 finite element matrix. So, clearly, the use of Richardson extrapolation is very efficient in terms of the use of computer memory. But it is also beneficial in terms of the computational time required. The total time to compute the Richardson extrapolate solution (time to compute solution for original spacing + time to compute solution for halved spacing + time for extrapolation) was 6.37 seconds, which is much less than the 17.306 seconds it took to compute the solution using the 30 x 30 mesh and no extrapolation.

In order to get a better idea of the kind of improvement that the use of Richardson extrapolation makes, we consider the same problem as was discussed above but with the boundary condition along the top of the square changed to $u(x,2.0) = \sin(\pi x)$. Figure 4 presents a comparison of the original solution obtained using a 9 x 9 mesh (dotted line) and the analytic solution (solid line) along the line y=1.0 while Figure 5 shows a comparison of the Richardson extrapolate (dotted line) and the analytic solution (solid line) along the same line. Clearly, the Richardson extrapolate is considerably more accurate. In fact, at the node locations, there is very nearly perfect agreement between the Richardson extrapolate solution and the analytic solution.

Conclusion

In this paper, the use of Richardson extrapolation to reduce the truncation errors in the finite element analysis of two-dimensional domains is discussed. It is observed that use of Richardson extrapolation yields highly accurate results with quite modest requirements in terms of computation time and computer memory.

REFERENCES

[1] I. Babuska, R. Duran, and R. Rodriguez, "Analysis of the efficiency of an a posteriori error estimator for linear triangular finite elements", *SIAM J. Numer. Anal.*, vol. 29, no. 4, pp. 947-964, August, 1992.

[2] K. Eriksson, C. Johnson, "Adaptive finite element methods for parabolic problems II: optimal error estimates in $L_\infty L_2$ and $L_\infty L_\infty$", *SIAM J. Numer. Anal.*, vol. 22, no. 3, pp. 706-740, June, 1995.

[3] G. Drago, P. Molfino, M. Nervi, M. Repetto, "A 'local field error problem' approach for error estimation in finite element analysis", *IEEE Transactions on Magnetics*, vol. 28, no. 2, pp. 1743-1746, March, 1992.

[4] W. Elliott Hutchcraft, Richard K. Gordon, "The Use of Richardson Extrapolation to Reduce the Truncation Error in the Finite Difference Solution of One and Two Dimensional Electrostatics Problems", to appear in the Proceedings of the 28th IEEE Southeastern Symposium on System Theory, Baton Rouge, LA, April, 1996.

[5] Gilbert Strang, George J. Fix, "An Analysis of the Finite Element Method", Prentice-Hall Inc., Englewood Cliffs, N.J., 1973.

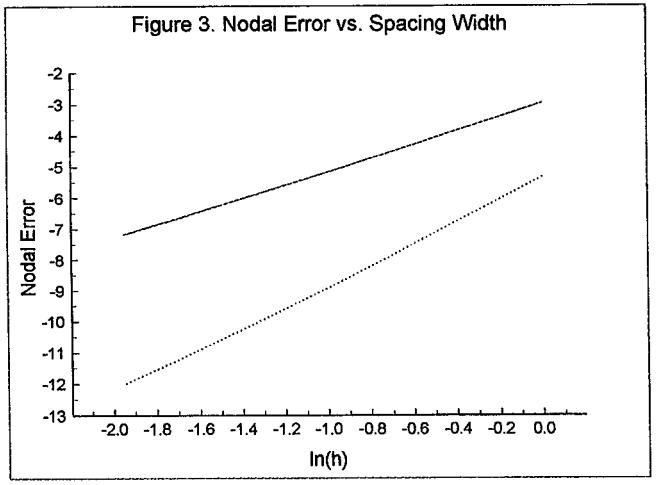
Figure 3. Nodal Error vs. Spacing Width
Nodal Error
-2
-3
-4
-5
-6
-7
-8
-9
-10
-11
-12
-13
-2.0 -1.8 -1.6 -1.4 -1.2 -1.0 -0.8 -0.6 -0.4 -0.2 0.0
ln(h)

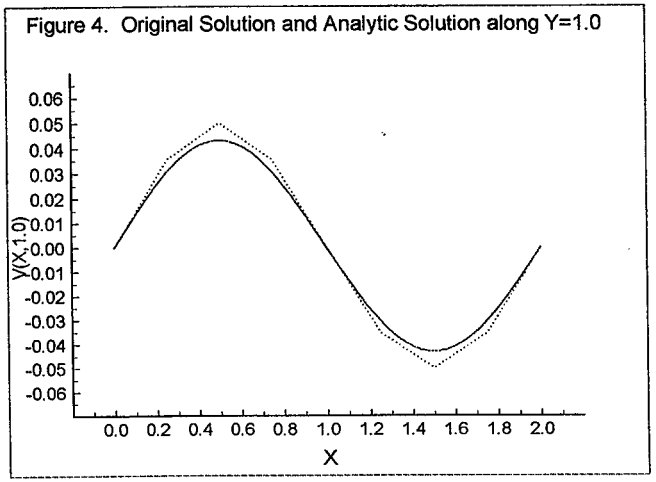
Figure 4. Original Solution and Analytic Solution along Y=1.0
V(X,1.0)
0.06
0.05
0.04
0.03
0.02
0.01
0.00
-0.01
-0.02
-0.03
-0.04
-0.05
-0.06
0.0 0.2 0.4 0.6 0.8 1.0 1.2 1.4 1.6 1.8 2.0
X

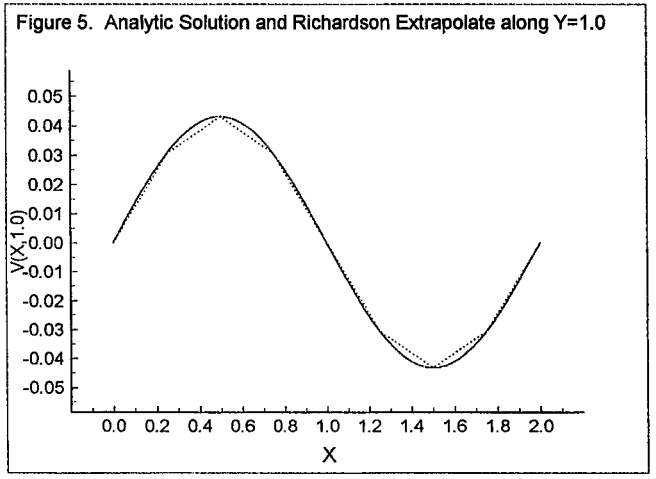
Figure 5. Analytic Solution and Richardson Extrapolate along Y=1.0
V(X,1.0)
0.05
0.04
0.03
0.02
0.01
0.00
-0.01
-0.02
-0.03
-0.04
-0.05
0.0 0.2 0.4 0.6 0.8 1.0 1.2 1.4 1.6 1.8 2.0
X

Scattering from Chirally Coated Bodies

Reena Sharma [1] and N. Balakrishnan [2]
Department of Aerospace Engineering
Indian Institute of Sciences, Bangalore, 56 0012.
INDIA

Abstract

Chiral coatings have been advocated in the past for management and reduction of radar cross-section of a variety of scattering objects. The theoretical analysis of the scattering from chirally coated bodies is complicated due to the fact that the left and right circularly polarised waves propogate in the chiral layer with different propagation constants. In this paper, the T-matrix method has been used to analyse the scattering from chirally coated scatterers. The scattering characteristics. *viz*, absorption, extinction, radar and the scattering cross sections have been computed for realistic chiral materials. The results have been presented for various volume concenterations of embedded metal helices, angles of incidence, frequency and coating thickness. From the results it can be seen the normalised Radar Cross Section of chirally coated spheroid is 8-10 dB lower than the conducting spheroid in the range of 8-12 GHz. This performance, is also superior in comparison with the conventinal RAMs. This reduction in the RCS has been shown to be due to increased absorption and reduced scattering cross section.

1 Introduction

The objective of this paper is to evaluate the scattering characteristics of axisymmetric bodies coated by a chiral material, when a plane electromagnetic wave is incident on it. By chirality we

[1]Research Scholar
[2]Professor, also affiliated to Jawaharlal Nehru Centre for Advanced Scientific Research

mean *lack of symmetry* or in other words, an object which cannot be brought into congruence with its mirror image either by rotation or by translation is said to be chiral object/material. A lot of work in the past has been done on chiral/chirally coated spheres and spheroids [1], [2], [3], [4], *etc.* Often the permeability of the chiral materials has been ignored by assuming it to be equal to that of free space as seen in [1], [5], and [6]. Such a treatment is not correct while dealing with chiral materials. Even though the chiral inclusions may be non-magnetic to begin, the composite chiral material will have magnetic properties [7]. The properties of such chiral materials can be controlled by altering the size and concentration of the embedded chiral particles to yield prespecified chirality.

The principle of operation of realistic chiral materials is based on the judicious combination of front surface matching and absorption. The role of chirality is in providing an additional degree of freedom for this match which cannot be achieved by using conventional Radar Absorbing Materials (RAMs). Regardless of the incident polarisation, back scattered incident waves travel half the time with propagation constant k_L, the propagation wave vector for the left circularly polarised wave, and half the time with k_R, the propagation wave vector for the right circularly polarised wave, so that the skin depth for the two propagating waves plays an equal role in absorption. Chirality increases the average absorption.

Mie solution has been modified to compute the scattering cross sections of chirally coated cylinders and spheres of small size [8]. Lakhtakia, Varadan and Varadan [1] have used the T-Matrix method to analyse single layered chiral spheroids. In this paper, the scattering from multilayered chiral objects has been cast into a form amenable for the application of T-Matrix method. The constitutive parameters of realistic chiral materials made by Varadan, Varadan and Rho [9] are used to gauge the extent of RCS reduction possible with chiral coatings.

2 Formulation of the Problem

The Extended Boundary Condition Method (EBCM) or the Transition Matrix (T – Matrix) technique was originally developed by [10] for conducting sphere. In this method the fields in the various regions are expanded in terms of vector spherical harmonics and the principle of surface field equivalence has been used to evaluate the unknown fields. The EBCM relates the unknown scattered field coefficients to the known incident field coefficients through a matrix called the T–matrix. The T–matrix method is known to work well for scatterers of arbitrary shape and of sizes beyond the resonance region. Further the polarisation is inherent in the formulation. For the mutilayered case, the formulation is done by expanding the fields in each region in terms of vector spherical harmonics with unknown (known coefficients for the incident fields) coefficients. The problem is divided into three subproblems as given in [11], using the surface field equivalence principle. Each subproblem is such that the fields in the region of interest are radiating in space, with the constitutive parameters to be the same as that of the region of interest. The subproblems can be reduced to a set of simultaneous equations and then can be cast into a matrix equation. The unknown scattered field coefficients can be computed from the known incident field

coefficients, from the T-Matrix.

3 Results and Discussion

Ro, Varadan and Varadan [9] have made left handed, right handed and the racemic samples of chiral composites with 0.8%, 1.6% and 3.2% volume concenterations [9]. The matrix material used by [9] is eccogel 1365-90 from Emerson and Cuming. The left handed (right handed) sample consists of only left handed (right handed) springs, while for the racemic samples the same amount of left and right handed spring have been mixed. The sample consists of four layers. One layer has pure eccogel and the remaining three layers have chiral inclusions inside. The spherical inclusion is made up of metal because of easy availability and relatively low cost. It could also be made of polymers.The data presented in [9] are the measurements made at discrete frequencies and are used in this work.

The real and the imaginary parts of the permittivity, permeability and the chirality parameter are plotted as a function of frequency in Figs. 1 for a 1.6 % and 3.2 % concentration of right handed helices. The variation for the left handed helices are similar and hence not shown. From Fig. 1 it can be seen that the permeability of realistic chiral material may not be set to unity. This has also been emphasised in [7].

Chirally coated oblate spheroids are considered for illustrative purposes. The axial ratio has been chosen to be 0.8. The equivalent diameter of the conducting sphere has been chosen to be 6 cm. The coating thickness has been chosen to be 5 mm. The results for the scattering characteristics are presented for right handed helices only. The results in Fig. 2 are for two different concentrations of the right handed helices, 1.6 % and 3.2 % for vertical polarisation. The results for the other polarisation and for left handed and racemic type of helices are the same and hence not plotted here. The results are actually for discrete set of frequencies and thus the graph is as shown. The results for the absorption cross section, extinction cross section, radar cross section and the scattering cross section are shown. The normalised RCS reduces by more than 12 dB for a 3.2% conc. and below 6 dB for a 1.6% conc. of right handed helices. From Fig. 2 (b) the normalised scattering cross section is seen to reduce with the increase in the volume concentration of the helices which is as expected. The normalised absorption cross section increases as the volume concentration of the right handed helices increases, leading to a higher reduction in RCS. As seen from Fig. 2 (d) the normalised extinction cross section is almost the same for both the volume concentrations.

For the purpose of comparison a practical RAM was chosen from [12] of $\epsilon_r = 1.3 + i0.29$. An oblate conducting spheroid, was coated by such a RAM and the coating thickness was kept fixed as 5 mm as that of chiral coating. The inner aspect ratio was chosen to be 0.8. The outer equivolume diameter was chosen to be 6 cm. The RCS of the conducting oblate spheroid coated by a conventional RAM is compared with the chirally coated spheroid. The response is shown for the frequency range of 8-12 GHz. The RCS comparison between the two coatings has been shown for both the horizontal and the vertical polarisations in Figs. 3. It can be seen from the plots that

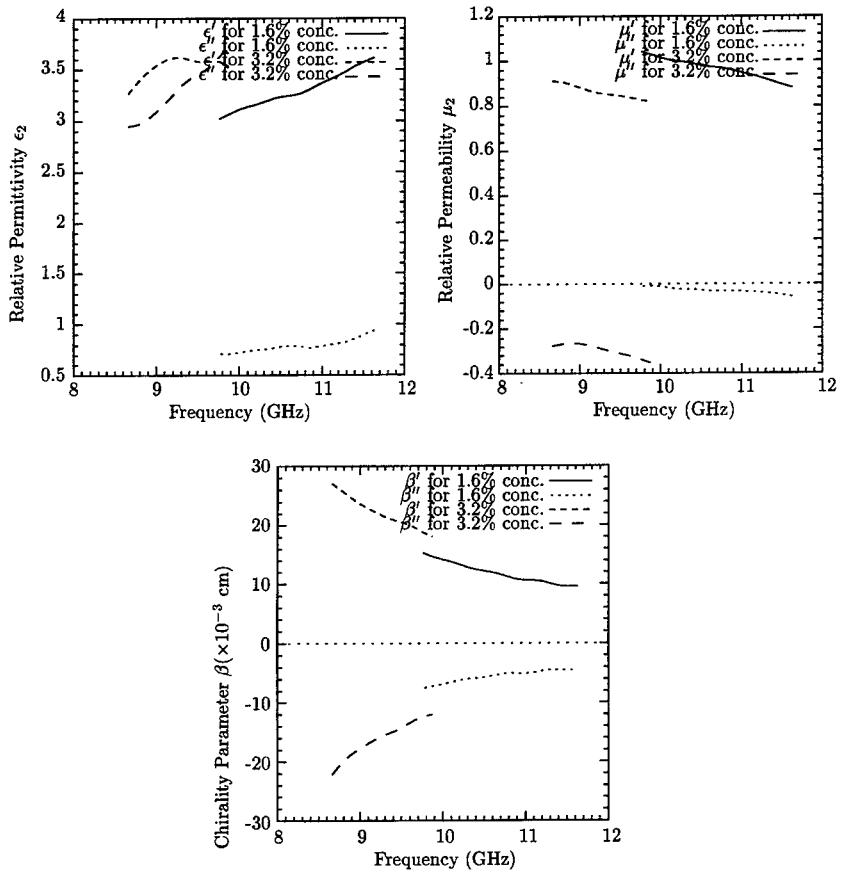

Figure 1: Variation of the complex permittivity, permeability and the chirality parameter as a function of frequency

for the same coating thickness, the RCS for a RAM coating gets reduced by 5 dB, as compared to a reduction of more than 15-20 dB when coated by a realistic chiral material of concentration 3.2%. The reduction in the RCS is only 5-6 dB for a volume concentration of 1.6%. This was seen for both the horizontal and vertical polarisations.

The variation in the scattering characteristics as a function of the angle of incidence is shown

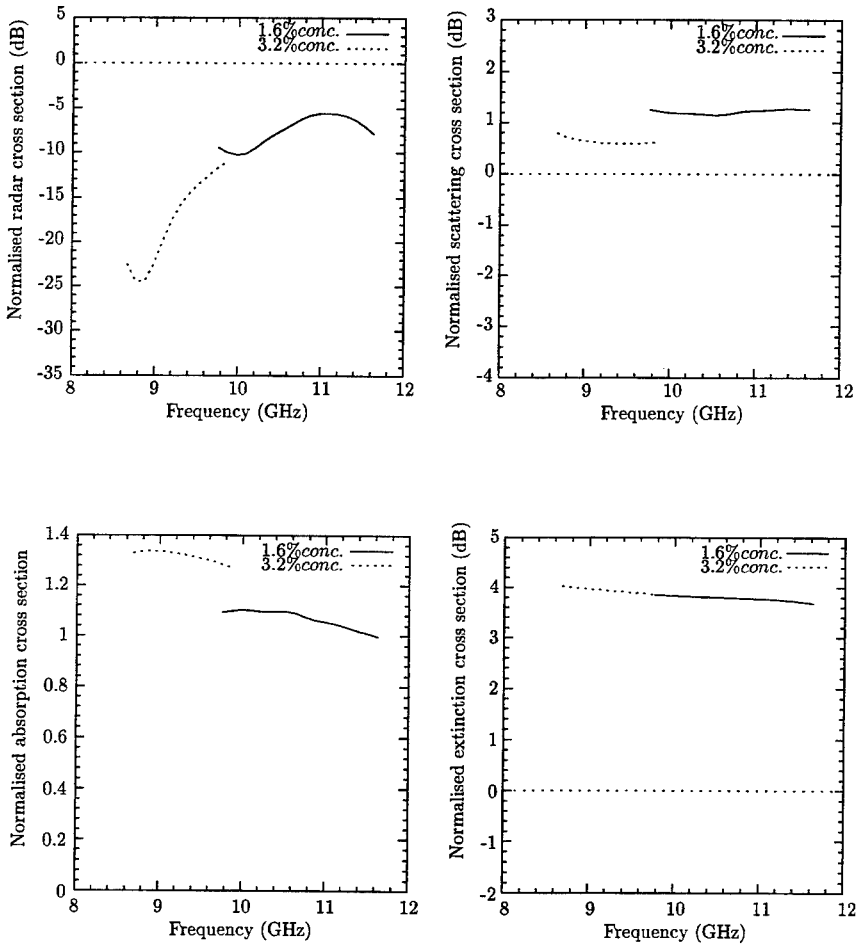

Figure 2: Variation of normalised (a)radar cross section, (b)scattering (c)absorption and (d)extinction cross section for an chirally coated spheroid of aspect ratio 0.8, equivalent outer diameter = 6 cm, as a function of frequency

in Fig. 4 . The frequency has been fixed at 9.87 GHz. The values for the complex permittivity, complex permeability and the complex chirality as taken from [9], are $\epsilon_r = 3.529 + i3.731$, $\mu_r =$

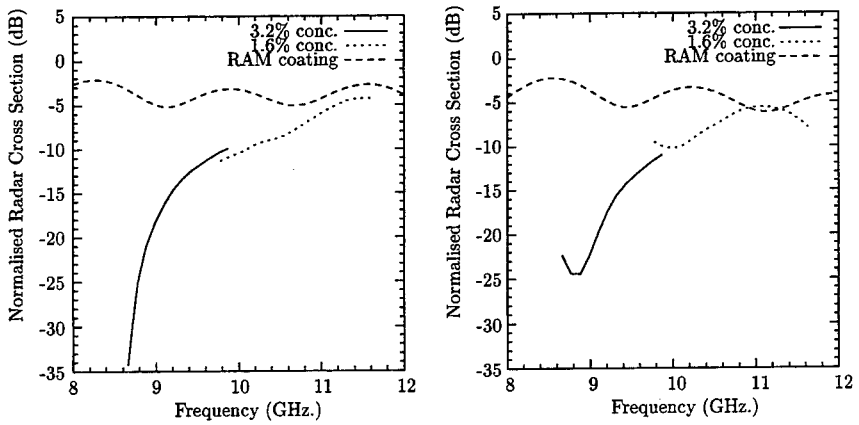

Figure 3: Variation of normalised radar cross section for a RAM and a chiral coated oblate spheroid for an aspect ratio of 0.8, (a)horizontal (b)vertical polarisation as a function of frequency

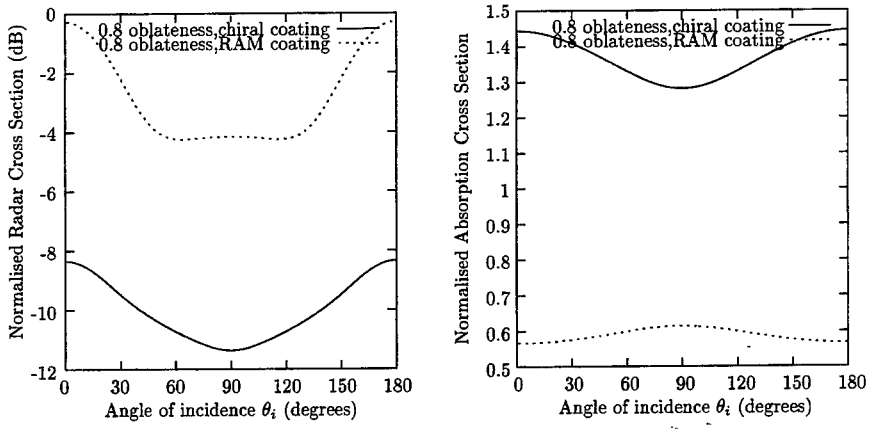

Figure 4: Variation of (a)normalised radar cross section (b)absorption cross section for a RAM and a chiral coated oblate spheroid for an aspect ratio of 0.8, as a function of angle of incidence

$0.820 - i0.353$ and $\beta = (18.091 - i12.01) \times 10^{-3}$ cm. These are for RCP helices embedded in the host medium with a 3.2% volume concenteration. The results have been plotted for only vertical polarisation even though the results are the same for horizontal polarisation.. These results are

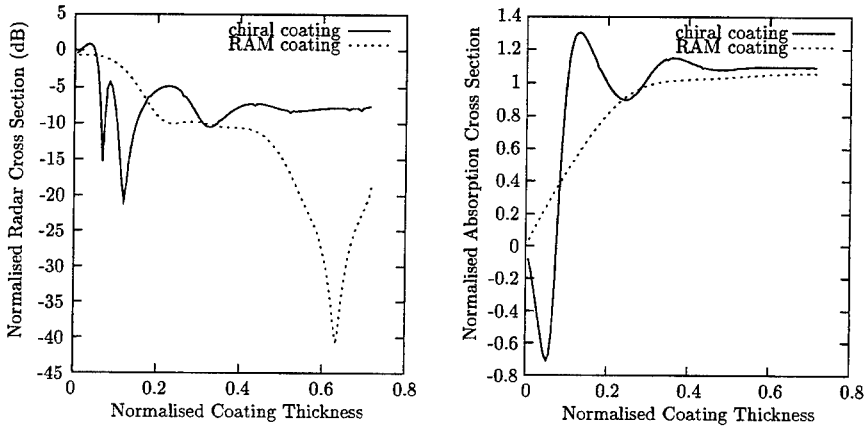

Figure 5: Variation of (a)normalised radar cross section (b)absorption cross section for a RAM and a chiral coated oblate spheroid for an aspect ratio of 0.8, as a function of normalised coating thickness

compared with an conventional RAM coating of $\epsilon_r = 1.3 + i0.29$ at 9.87 GHz. The coating thickness is kept the same as that for the chiral coating. The aspect ratio of 0.8 has been chosen for the RAM. As seen from the graphs, the normalised RCS for RAM coated oblate spheroid for this particular frequency is less than that for the chirally coated spheroid. The absorption cross section for the RAM is almost half of that seen for a chirally coated conducting spheroid.

Fig. 5 shows the variation of the scattering characteristics of RAM and chirally coated oblate spheroid as a function of normalised coating thickness for vertical polarisation. The outer oblateness has been chosen to 0.8 and the equivalent diameter has been fixed to be 7 cm. The frequency has been chosen to be 9.87 GHz and the constitutive parameters are same as that chosen earlier in the case of angle of incidence variation. The results are shown once again for a right handed helices embedded in a epoxy host medium. As seen from the figure the reduction in the RCS for a chirally coated spheroid is more than for a RAM coating for small coating thicknesses. The reduction in RCS for a normalised coating thickness of 0.12 is about 21 dB for chiral coating and about 3 dB for a RAM coating. The sharp null in the RCS that is seen around the normalised coating thickness of 0.62 (coating thickness of 2.2 cm) is due to the resonance occuring when the coating thickness is nearly a multiple of λ and is of low bandwidth. However the RCS reduction seen in chiral coating is devoid of such oscillations, and would offer wider bandwidth. The absorption cross section is about 1.2 for the chiral coating and 0.5 for RAM coating for the same coating thickness. As the coating thickness increases the conducting spheroid reduces to a fully chiral/dielectric spheroid of oblateness (outer) 0.8.

References

[1] A. Lakhtakia, V. K. Varadan, and V. V. Varadan, "Scattering and absorption characteristics of lossy, dielectric, chiral, non-spherical objects," *Applied Optics*, vol. 24, pp. 4146–4154, December 1985.

[2] A. Lakhtakia, V. K. Varadan, and V. V. Varadan, *Time Harmonic Electromagnetic Fields in Chiral Media*. Springer-Verlag, 1985.

[3] I. V. Lindell, A. H. Sihvola, S. A. Tretyakov, and A. J. Viitanen, *Electromagnetic waves in chiral and Bi-isotropic media*. Artech House,Boston, London, 1994.

[4] D. L. Jaggard and N. Engheta, "$CHIROSORB^{TM}$ as an invisible medium," *Electronics Letters*, vol. 25, pp. 172–173, February 1989.

[5] A. K. Bhattacharyya, "Control of radar cross-section and crosspolarisation characteristics of an isotropic chiral sphere," *Electronic Letters*, vol. 26, pp. 1066–1067, July 1990.

[6] H. Cory and I. Rosenhouse *IEE Proceedings - H*, vol. 138, no. 51-54, pp. 51–54, 1991.

[7] A. Lakhtakia, "On the maxwell -garnett model of chiral composites," *Journal of Material Research*, vol. 8, pp. 917–922, April 1993.

[8] D. L. Jaggard and J. C. Liu, "Chiral layers on curved surfaces," *Journal of Electromagnetic Waves and Applications*, vol. 6, no. 5/6, pp. 669–694, 1992.

[9] R. Ro, *Determination of the Electromagnetic Properties of Chiral Composites Using Normal Incidence Measurements*. PhD thesis, The Pennsylvania State University, University Park, Pennsylvania, 1991.

[10] P. C. Waterman, "Matrix formulation of electromagnetic scattering," *Proc. of the IEEE.*, pp. 805–812, August 1965.

[11] V. N. Bringi and T. A. Seliga, "Scattering from axisymmetric dielectrics or perfect conductors imbedded in an axisymmetric dielectric," *IEEE Transactions on Antennas and Propagation*, vol. 25, pp. 575–580, July 1977.

[12] A. K. Bhattacharya and D. L. Sengupta, *Radar Cross Section Analysis and Control*. Artech House, 1991.

A mixed formulation to compute the source current density in inductors of any shape

F. Robert, P. Dular, J.F. Remacle, M. Umé, W. Legros*

University of Liège - Dept of Electrical Engineering
Institut Montefiore - Sart Tilman Bât. B28 - B-4000 Liège (Belgium)
tel: +32-41_663710
fax: +32-41-662910
robert@montefiore.ulg.ac.be

* This author is a Senior Research Assistant with the Belgian National Fund for Scientific Research.
This text presents research results of the Belgian program on Interuniversity Poles of Attraction initiated by the Belgian State, Prime Minister's Office, Science Policy Programming. The Scientific responsibility is assumed by its authors.

Abstract – This paper presents a general method, based on the electrokinetic problem, to compute the source current density in inductors of any shape. The so-computed current density has the same continuity property as the physical one because the zero divergence condition is strongly satisfied. Moreover, using a tensorial form of the electrical conductivity, coil inductors can be modelized in addition to massive inductors. The computed current density can be directly introduced in a magnetic vector potential formulation or in some kind of mixed **h-a** formulation or used to compute a source magnetic field which is needed in a **h** formulation using a magnetic scalar potential.

I. Introduction

Solving magnetostatic or eddy current problems using a magnetic vector potential formulation or some kind of mixed formulation requires the computation of a source current density $\mathbf{j}_s$ associated with the inductors. Moreover, a formulation using a magnetic scalar potential, i.e. a **h** formulation, necessitates the computation of a source magnetic field $\mathbf{h}_s$ associated with inductors. Several methods have been proposed by many authors [1,2,3,4] to compute such source fields, but are not general in the sense that they are either dependent on the shape of the inductor [1,2] or usually need a high CPU time [3,4]. In the following is presented a method entirely general to compute the source current density in inductors of any shape and, eventually thereafter, a source magnetic field. This method enables to take into consideration different kinds of inductors, i.e. massive or coil inductors.

II. A mixed formulation based on the electrokinetic problem

The electrokinetic problem consists in finding two vector fields, the electric field **e** and the current density **j**, in an inductor Ω (Fig. 1). These fields have to satisfy the equations obtained from Maxwell's equations where time dependent terms are omitted, i.e.

$$\operatorname{div} \mathbf{j} = 0 \qquad \text{in } \Omega \,, \tag{1}$$

$$\operatorname{curl} \mathbf{e} = 0 \qquad \text{in } \Omega \,, \tag{2}$$

associated with the boundary conditions, on the complementary parts Γ_j and Γ_e of $\partial\Omega$,

$$\mathbf{n} \cdot \mathbf{j} = 0 \qquad \text{on } \Gamma_j \,, \tag{3}$$

$$\mathbf{n} \times \mathbf{e} = 0 \qquad \text{on } \Gamma_e \,, \tag{4}$$

where $\mathbf{n}$ is the external unitary normal of the corresponding surface. To these equations is added the electrical constitutive law, i.e. the local Ohm law

$$\mathbf{j} = \sigma \, \mathbf{e} \,, \tag{5}$$

where σ is the electrical conductivity of the inductor Ω. As it will be explained further, the conductivity can be either scalar or tensorial to be able to take into consideration different kinds of inductors.

Since the electric field $\mathbf{e}$ is a zero curl field (2), it can derive from a scalar potential v, i.e.

$$\mathbf{e} = - \operatorname{grad} v \,. \tag{6}$$

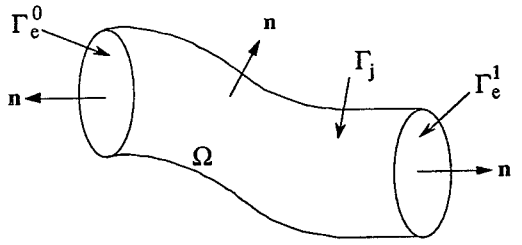

Fig.1. Inductor Ω and its complementary boundaries Γ_j and Γ_e ($\Gamma_e = \Gamma_e^0 \cup \Gamma_e^1$).

The Withney sequence [6] and its generalized form [7] defining some mixed finite elements, appear to be well suited to the approximation of fields in mixed formulations [5,8]. Such finite elements can be defined on tetrahedra, hexahedra and prisms. The so-defined finite element spaces are associated with nodes, edges, facets and volumes of the discretized domain, i.e. the mesh, and are respectively denoted S^0, S^1, S^2 and S^3 [7]. The sets of nodes, edges, facets and volumes of the mesh are denoted by N, E, F and V, respectively. Their sizes are #N, #E, #F and #V. A subscript associated with a function space ($-_j$ or $-_e$) denotes the associated boundary condition (on Γ_j or Γ_e).

The following notations are used for integrations of products of scalar or vector fields over a volume Ω, where L^2 and $\mathbf{L}^2$ are the spaces of square-summable scalar and vector functions :

$$(u,v) = \int_\Omega u(\mathbf{x})\, v(\mathbf{x})\, d\mathbf{x} \,, \quad u, v \in L^2(\Omega) \,, \qquad (\mathbf{u},\mathbf{v}) = \int_\Omega \mathbf{u}(\mathbf{x}) \cdot \mathbf{v}(\mathbf{x})\, d\mathbf{x} \,, \quad \mathbf{u}, \mathbf{v} \in \mathbf{L}^2(\Omega) \,.$$

From the equations of the electrokinetic problem (1-6), a mixed formulation can be written where two fields, $\mathbf{j}$ and v, are approximated simultaneously. The problem is to find $\mathbf{j}$ in S^2 and v in S^3, S^2 and S^3 being the function spaces of facet and volume finite elements defined on the discretized domain [7], such that

$$(\sigma^{-1} \mathbf{j} , \mathbf{j}') - (v , \operatorname{div} \mathbf{j}') = 0 \,, \qquad \forall \, \mathbf{j}' \in H(\operatorname{div}_j) \,, \tag{7}$$

$$(\operatorname{div} \mathbf{j} , v') = 0 \,, \qquad \forall \, v' \in L^2(\Omega) \,, \tag{8}$$

$H(div_j)$ and $L^2(\Omega)$ being approximated by S^2 and S^3; $\mathbf{j}'$ and v' are test functions of these spaces. Equation (7) is actually a weak form of the definition of an electric scalar potential v, given by (6), and is obtained by its integration by parts while equation (8) expresses a strong form of the charge conservative equation (1). These equations can also be obtained using Lagrangian multipliers [12], these being interpreted as associated with a weak electric potential v.

Facet and volume finite elements are used to approximate respectively the unknown current density $\mathbf{j}$ and the scalar potential v, i.e.

$$\mathbf{j} = \sum_{j \in F} j_j^F \, \mathbf{s}_j^F \quad \text{and} \quad v = \sum_{k \in V} v_k^V \, s_k^V \ , \tag{9-10}$$

where $\mathbf{s}_j^F$ and s_k^V are respectively the shape functions associated with the j-th facet in set F and the k-th volume in set V of the mesh and where j_j^F and v_k^V are the associated degrees of freedom, respectively the flux of the current density across the j-th facet and the volume integral of the potential v in the k-th volume. Then, the discretization of equations (7) and (8) leads to the following finite element equations:

$$\sum_{j \in F} \left(\sigma^{-1} \mathbf{s}_j^F \, , \mathbf{s}_i^F \right) j_j^F - \sum_{k \in V} \left(s_k^V \, , \mathrm{div} \mathbf{s}_i^F \right) v_k^V = 0 \quad , \ i = 1, \ \ldots, \ \#F \, , \tag{11}$$

$$\sum_{j \in F} \left(\mathrm{div} \mathbf{s}_j^F \, , s_i^V \right) j_j^F = 0 \quad , \ i = 1, \ \ldots, \ \#V \, . \tag{12}$$

Therefore, by imposing the current density on a cross section of an inductor of any shape and by setting to zero its normal component on the lateral faces (which define essential boundary conditions), the source current density $\mathbf{j}_s$ and the potential v can be calculated everywhere in the inductor by using the proposed mixed formulation. This source field has the same continuity property as the physical one, i.e. the continuity of its normal component, because the zero divergence condition is strongly satisfied by (8). This method presents the advantage of being entirely general for inductors of any shape and requires no more CPU time than usual finite element computations.

III. Massive and coil inductors

The electrical conductivity σ introduced in the local Ohm law (5) can take different mathematical forms: it can be either scalar or tensorial.

First, if the conductivity is chosen as being scalar, equal to the conductivity of the material, the inductor is therefore considered as an isotropic material with identical electrical properties in any direction. In consequence, only massive inductors can be modelized with this kind of conductivity. The obtained current density will be higher in the vicinity of the interior bends than in the vicinity of the exterior bends.

This kind of current distribution, characteristic of massive inductors, cannot be accepted if one wants to modelize coil inductors, in which the current is not affected by the bends and remains uniformly distributed on any cross sections. An accurate determination of the current distribution in coil inductors is necessary for an accurate evaluation of force or torque quantities [10]. This can be done by introducing a tensorial form of the conductivity instead of a scalar one. In this way, coil inductors can be taken into account thanks to an anisotropic tensor σ having a principal conductivity along the wires of the

inductor equal to the conductivity of the material, and two weak principal conductivities in the perpendicular directions to the wires, resulting from the residual insulator conductivity.

In each finite element of the discretized conductor, one principal direction of anisotropy is chosen along the fiber of the inductor, the two others being perpendicular to this direction (Fig. 2). Fig. 3 illustrates the alignment, in each finite element, of the principal axis along the fiber of a circular inductor.

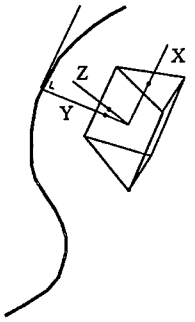

Fig. 2. The three principal axis in a finite element.

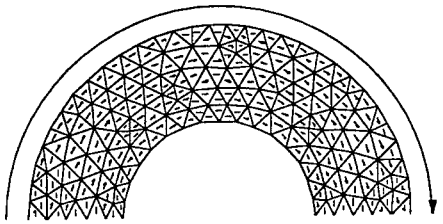

Fig. 3. Alignment of one principal axis along the fibers of an inductor.

IV. Magnetic vector potential formulation

The equations of the magnetostatic problem are

$$\text{curl } \mathbf{h} = \mathbf{j}_s \quad , \quad \text{div } \mathbf{b} = 0 \quad , \quad \mathbf{b} = \mu \, \mathbf{h} \, , \tag{13-14-15}$$

where $\mathbf{h}$ is the magnetic field, $\mathbf{b}$ is the magnetic flux density, $\mathbf{j}_s$ is the source current density associated with the inductors and μ is the magnetic permeability. A magnetic vector potential $\mathbf{a}$ can be defined by

$$\mathbf{b} = \text{curl } \mathbf{a} \, , \tag{16}$$

so that (14) is implicitly satisfied. Then, by expressing (13) in a weak form and introducing (15) and (16), one gets

$$(\mu^{-1} \text{ curl } \mathbf{a} \, , \text{curl } \mathbf{a}') = (\mathbf{j}_s \, , \mathbf{a}') , \quad \forall \, \mathbf{a}' \in H(\text{curl}_e) \, , \tag{17}$$

$H(\text{curl}_e)$ being approximated by S^1; $\mathbf{a}'$ is a test function of this space. If edge elements are used for the dicretization of $\mathbf{a}$, this equation takes the following form

$$\sum_{j \in E} \left(\mu^{-1} \text{curl} s_j^E \, , \text{curl} s_i^E \right) a_j^E - \sum_{k \in F} \left(s_k^F \, , s_i^E \right) j_k^F = 0 \quad , \, i = 1, \, \ldots, \, \#E_{ct} \, , \tag{18}$$

where s_j^E is the shape function associated with the j-th edge of the mesh and a_j^E is the circulation of the vector potential along this edge [7,11]. A gauge condition on $\mathbf{a}$ can be defined in the space of edge finite elements thanks to a tree built in the mesh [11]; $\#E_{ct}$ is the number of edges of the associated co-tree and the equations (16) are only associated with these edges.

One way to deal with this problem is first to solve (11) and (12), and afterwards to solve (18), which is more efficient for transient or nonlinear problems. Another possibility is to solve (11), (12) and (18) simultaneously, which leads to a matrix associated with the system given by

$$\begin{pmatrix} S_1 & C & 0 \\ C^T & S_2 & D \\ 0 & D^T & 0 \end{pmatrix} . \tag{19}$$

The number of edges, facets and volumes being respectively denoted #E, #F and #V, matrix S_1, S_2, C and D are of size (#E×#E), (#F×#F), (#E×#F) and (#F×#V) respectively, the number of equations being equal to #E+#F+#V. The global matrices are indefinite so that classical iterative techniques such as conjugate gradients are not suitable. So, the large number of equations and the very small bandwidth have led to use the following sequence of algorithm to solve the entire system: RCMK reordering of the matrix, ILUTP preconditioner and GMRES solver [9]. This sequence takes no more computational time and is even more efficient than ordinary gradient methods.

Other kinds of formulations, such as mixed **h**-**a** formulations for instance [13], which require the knowledge of the source current density, can be coupled with the proposed mixed formulation for the computation of that source field. Furthermore, the source current density $\mathbf{j}_s$ can also be used to calculate a source magnetic field $\mathbf{h}_s$ which is needed by formulations using a magnetic scalar potential, i.e. **h** formulations. Indeed, the curl of a source field $\mathbf{h}_s$ has to be equal to $\mathbf{j}_s$, which can be satisfied exactly using edge finite elements to interpolate $\mathbf{h}_s$ [3].

V. Applications

In order to illustrate the effectiveness of the method mentioned above, the source current density in practical inductors surrounded by air has been computed. The same mesh is used for both massive and coil inductors (Fig. 4).

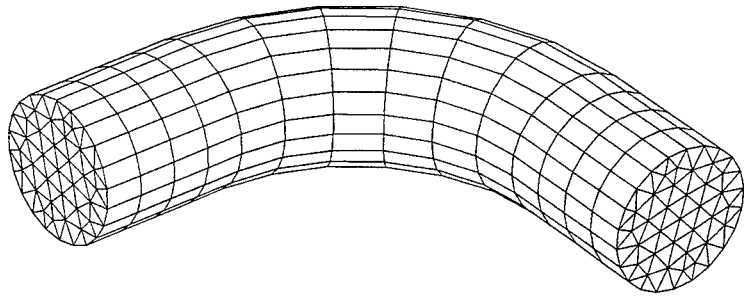

Fig. 4. Mesh of a part (1/4th) of the studied inductors.

Fig. 5 and 6 show the current density distribution on two cut planes in a copper massive inductor whose conductivity is equal to $5.9\ 10^7$ S/m. As mentioned above, those figures show that the current density is higher in the vicinity of the interior bend of the inductor.

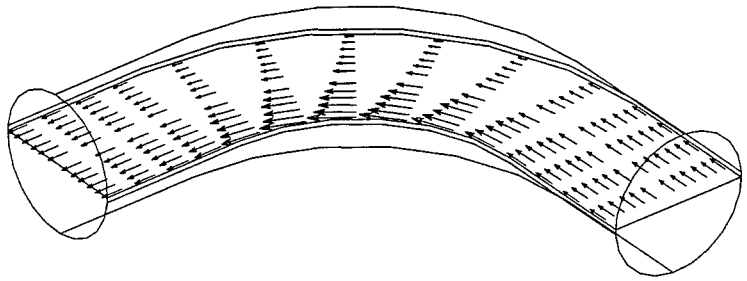

Fig. 5. Current density distribution in the massive inductor.

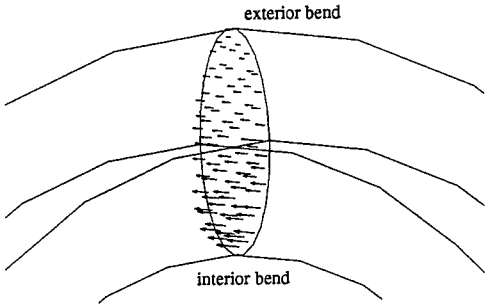

Fig. 6. Current density distribution in the massive inductor (cut plane in the bend).

On the other hand, a copper coil inductor is also considered, with a principal conductivity along the direction of the wires equal to the copper conductivity and two principal conductivities along the perpendicular directions equal to 10^{-6} S/m. Fig. 7 shows the computed current density distribution. In that case, the current density distribution is not affected by the bend and is the same as in the initial cross section of the inductor; it remains uniform all along the inductor.

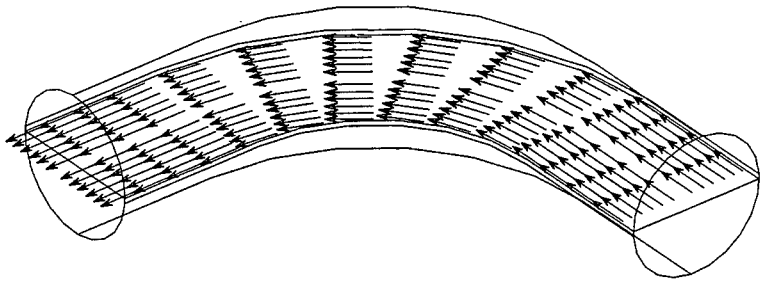

Fig. 7. Current density distribution in the coil inductor.

The computed source current density can then be used in the **a**-formulation. As an example, Fig. 8 shows the magnetic flux density distribution in the air around a coil inductor of another shape. This figure also shows the computed source current density in the inductor.

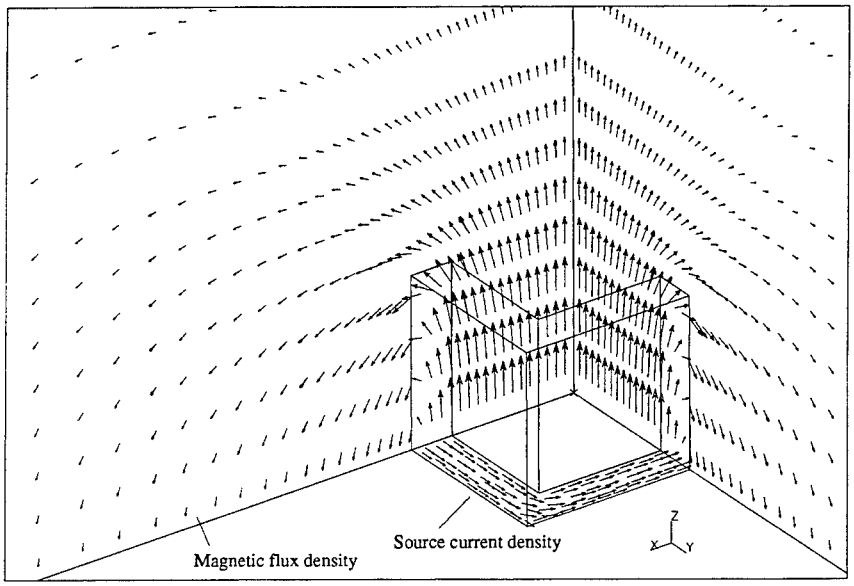

Fig. 8. Source current density (on plane z = 0) in a coil inductor and associated magnetic flux density (on planes x = 0 and y = 0) computed with a **a**-formulation.

VI. Conclusions

A mixed formulation for the computation of the source current density appears to be a simple and accurate method and is always applicable to inductors of any shape. Moreover, the method of defining an anisotropic conductivity to take into account coil inductors appears to be reliable and can be applied in any coil inductor to compute the associated source fields. Finally, the method can be coupled with any formulation needing the computation of a source field, i.e. a source current density or a source magnetic field. In each case, the interpolation of the source current density in the space of facet finite elements is well adapted to each formulation, which requires the continuity of this density.

VII. References

[1] T. Nakata, N. Takahashi, K. Fujiwara & Y. Okada, "Improvements of the T-Ω method for 3-D eddy current analysis", IEEE Trans. Magn., Vol. 24, No. 1, pp. 94-97, January 1988.

[2] A.G. Kladas & J.A. Tegopoulos, "A new scalar potential formulation for 3-D magnetostatics necessitating no source field calculation", *IEEE Trans. Magn.*, Vol. 28, pp. 1103-1106, March 1992.

[3] J.P. Webb & B. Forghani, "A single scalar potential method for 3D magnetostatics using edge elements", *IEEE Trans. Magn.*, Vol. 25, No. 5, pp. 4126-4128, September 1989.

[4] K. Preis, I. Bardi, O. Biro, C. Magele, G. Vrisk & K.R. Richter, "Different finite element formulations of 3D magnetostatic fields", *IEEE Trans. Magn.*, Vol. 28, No. 2, pp. 1056-1059, March 1992.

[5] F. Brezzi, "A survey of mixed finite element methods", D.L. Dwoyer et al. eds., *Finite Elements, Theory and Application*, Springer-Verlag, pp. 34-49, 1988.

[6] A. Bossavit, "A rationale for "edge-elements" in 3-D fields computations", *IEEE Transactions on Magnetics*, Vol. 24, No. 1, pp. 74-79, January 1988.

[7] P. Dular, A. Nicolet, A. Genon & W. Legros, "Mixed finite elements associated with a collection of tetrahedra, hexahedra and prisms", *IEEE Trans. Magn.*, Vol. 30, No. 5, pp. 2980-2983, September 1994.

[8] J.-C. Nedelec, *Notions sur les techniques d'éléments finis*, Mathématiques & Applications, Ellipses, 1991.

[9] Y. Saad, "Preconditioning techniques for nonsymmetric and indefinite linear systems", Journal of Computational Applied Mathematics 24, pp. 89-105, 1988.

[10] K. Fujiwara, T. Nakata, N. Takahashi & H. Ohashi, "On the Continuity of the Magnetizing Current Density in 3-D Magnetic Field Analysis with Edge Element", *IEEE Transactions on Magnetics*, Vol. 31, No. 3, pp. 1364-1367, May 1995.

[11] P. Dular, A. Nicolet, A Genon, W. Legros, "A discrete sequence associated with mixed finite elements and its gauge condition for vector potentials", *IEEE Trans. Magn.*, Vol. 31, No. 3, pp. 1356-1359, May 1995.

[12] A. Bossavit, "Un nouveau point de vue sur les éléments mixtes", Bulletin de la Société de Mathématiques Appliquées et Industrielles, No. 20, pp. 23-35.

[13] P. Dular, J.-F. Remacle, F. Henrotte, W. Legros, "*Magnetostatic and magnetodynamic mixed formulations compared with conventional formulations*", to be presented at CEFC'96, Okayama, Japan, March 18-20, 1996.

HIGH POWER MICROWAVE AMPLIFICATION BY HIGH-INTENSITY RELATIVISTIC ELECTRON-BEAM STORAGE-RINGS

Ross A. Speciale

Redondo Beach, California

A very interesting and challenging set of rather fundamental computational electromagnetics problems is posed by the development of a recently conceived new type of high power microwave amplifier, that is capable of generating gigawatt-level output peak-pulse powers, anywhere in the 1 to 40 GHz frequency range, with high power gain, efficiency, duty cycles, phase coherence, and spectral purity.

The new type of high power microwave amplifier combines the basic concepts of the relativistic klystron amplifier (RKA) with the well-known technology of electron-beam storage-rings (EBSR), by using a high-intensity, relativistic electron-beam (HIREB), circulating along re-entrant, multi-turn, toroidal-helical orbits. The nominal, toroidal-helical equilibrium orbits wrap many times around a virtual toroidal surface, with large radius R , and small radius r , exactly closing after a integral number of turns.

A nine-turn set of re-entrant, toroidal-helical orbits is shown in figures 1-3 , as an example.

Unlike the Gyrotron and the Relativistic Magnetron, the new electron-beam device operates as a low phase-noise, high power-gain amplifier, rather than a self-oscillator. A sharply bunched, high-intensity relativistic electron beam, typically carrying a 10^4 Amp average current at a 1 Mev electron energy, interacts along the re-entrant, multi-turn, toroidal-helical orbits, with two azimuthally-periodic, electrically-large, and mutually-interleaved microwave wave-guiding structures, each comprising widely-separated, multiple clusters of mutually-coupled beam-bunching, and power-extraction cavity resonators.

The two microwave wave-guiding structures perform the functions of input, and respectively output microwave circuits of the amplifier, and can operate on harmonically-related input, and output frequencies, if the input beam-bunching cavities are coupled to a single turn of the re-entrant, multi-turn, toroidal-helical orbit, while the output power-extraction cavities are coupled to all the turns. In this case the high power microwave amplifier also performs an additional frequency-multiplication function.

High efficiency, and high duty cycles are attained by re-circulating the high-intensity relativistic electron beam, rather than wasting most of its stored power in a beam-dump, as in the still largely experimental relativistic klystron amplifiers described to date. Further, no high-power bank of large storage capacitors is required, as very large total circulating beam current can be attained in the re-entrant, multi-turn, toroidal-helical electron orbit, with each turn carrying only a fraction of the total circulating current, and by gradually building up the circulating beam current by synchronous, multi-turn beam-injection (*beam-stacking*).

A very large number of high-space-charge-density electron-bunches circulates, within azimuthally-periodic, *alternating-gradient* (AG) guiding magnetic fields, along the re-entrant, multi-turn, toroidal-helical orbits of the new type of high power microwave amplifier, at an essentially constant orbital frequency. A total of 120 electron bunches are shown as small circles in the figure 1-3 examples, where the electron bunches are shown azimuthally spaced by 27° along each of the nine orbit turns.

The bunching cavity resonators of the input microwave structure, and the power-extracting cavity resonator of the output structure are interleaved to the azimuthally-periodic set of storage-ring magnets, that generate the *'strong focusing, alternating-gradient'* , guiding magnetic field. The use of strong-focusing, alternating-gradient guiding fields (apparently never before applied to the high-intensity, relativistic RKA electron beams) vastly reduces the required beam-aperture.

Further, a large number of electrostatic beam-deflection channels, periodically distributed around

the electron-beam storage-ring, introduce a radially-oriented DC electric deflection-field, pointing outward of the virtual toroidal surface of the equilibrium orbits, along the direction of the torus small radius r. The radially-oriented electric field provides the input DC power to the amplifier, by forcing the path of partially energy-depleted electron-bunches that exit the power-extraction cavity resonators, on a constant, nominal small radius r. The described electrostatic beam-deflection channels deliver all the required input DC current, and power required for operation, performing a function similar to that of the radially-oriented electrostatic deflection field is similar to that of the *'crossed'* radial electric field between the cathode and the anode of a conventional magnetron.

The new high-power microwave amplifier concepts provides a number of substantial, rather obvious technical advantages. First, high efficiency is attained by re-circulating the high-intensity electron-beam, thus totally recovering its residual kinetic energy. This eliminates the need for a beam-dump, and for a multi-joule pulse-generator. The continuous supply of DC power by the electrostatic beam-deflection channels makes higher duty-cycles possible, as no large bank of capacitors needs re-charging between output pulses. The large number of orbit turns reduces the average current each carries, and the very large total number of electron bunches reduces the required local space-charge density. The large number of power-extracting cavity resonators reduces the power each of the cavities is required to extract from the beam, a most remarkable advantage with the smaller, higher frequencies cavities. The use of strong-focusing, alternating-gradient guiding fields largely reduces the required beam aperture in both the input bunching cavities, and the output power-extracting cavities. Finally, the capability of combining frequency-multiplication with power amplification, eliminates feedback-induced instability.

These technical advantages may be attained by solving a number of new, challenging problems.

First, the well-established theory of betatron, and synchrotron oscillations in strong-focusing, alternating-gradient guiding fields [1,2] must be reformulated in the context of high space-charge densities, that induce high-intensity self-generated fields around the electron bunches. These fields may provide beam self-focusing, under appropriate conditions. Further, the electro-dynamic beam-loading on the input and output cavity resonators must be evaluated, as a basis for the design of the input, power-splitting microwave structure, and of the high-power, power-combining output structure. The impedance matching to both sets of cavity resonators is obviously rather critical at the indicated power levels, as is the amplitude and phase stability of the resonator internal fields.

The input, and output microwave wave-guiding structures must therefore meet stringent phase-coherence, and phase-stability requirements, in performing the input power-splitting, and respectively the output power-combining functions, under conditions of high peak-pulse power, and the high-energy electrodynamic loading, and cavity cross-coupling, due to the circulating electron-beam bunches. These requirements are somewhat similar to those that must be met by the beam-forming networks of large, high-directivity phased arrays, where the electromagnetic proximity coupling between radiating elements can not be neglected, without incurring in the notorious array-blindness effect.

REFERENCES.

[1] E. T. Whittaker," Analytical Dynamics," 4th ed. , Chapter XII , Cambridge University Press, London and New York, 1937.

[2] E. D. Courant and H. S. Snyder," Theory of the Alternating-Gradient Synchrotron," Annals of Physics, Vol. 3 , 1-48 , 1958.

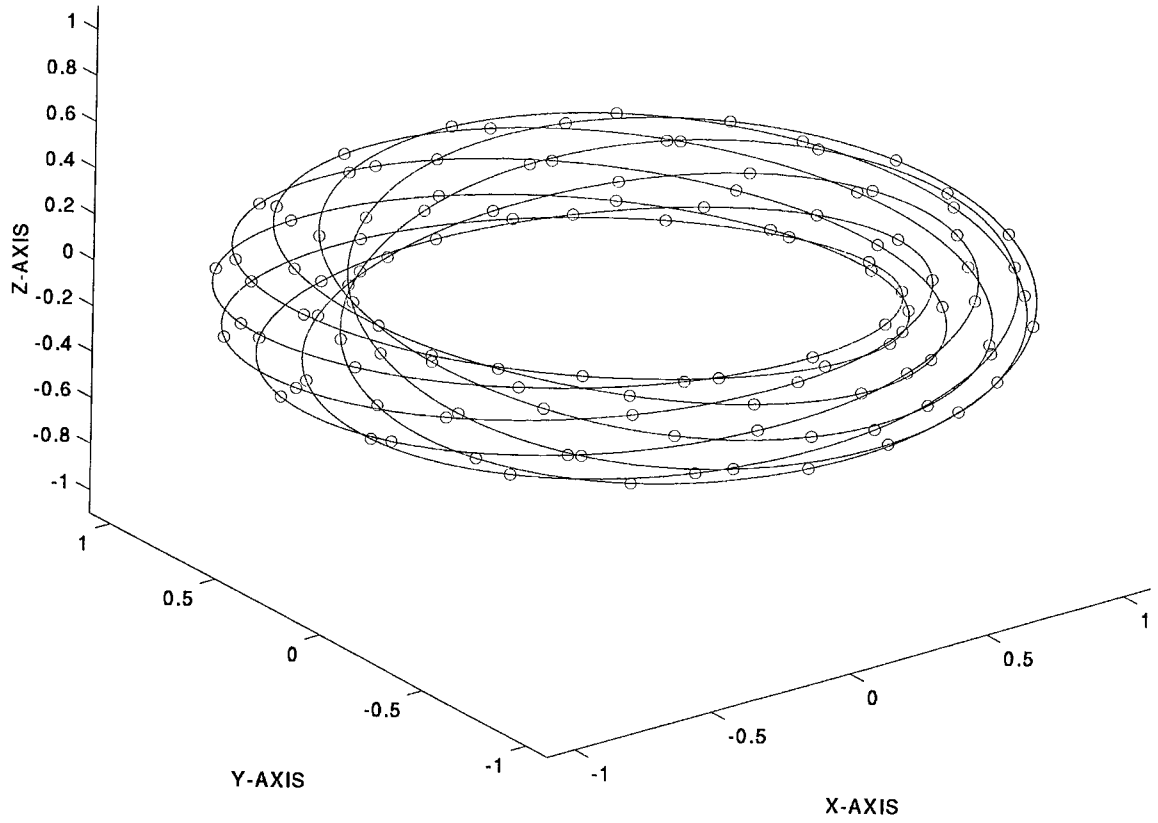

Figure 1 - 3 D Plot of the Nine Toroidal-Helical Electron Orbits : The 120 electron bunches are shown as small circles.

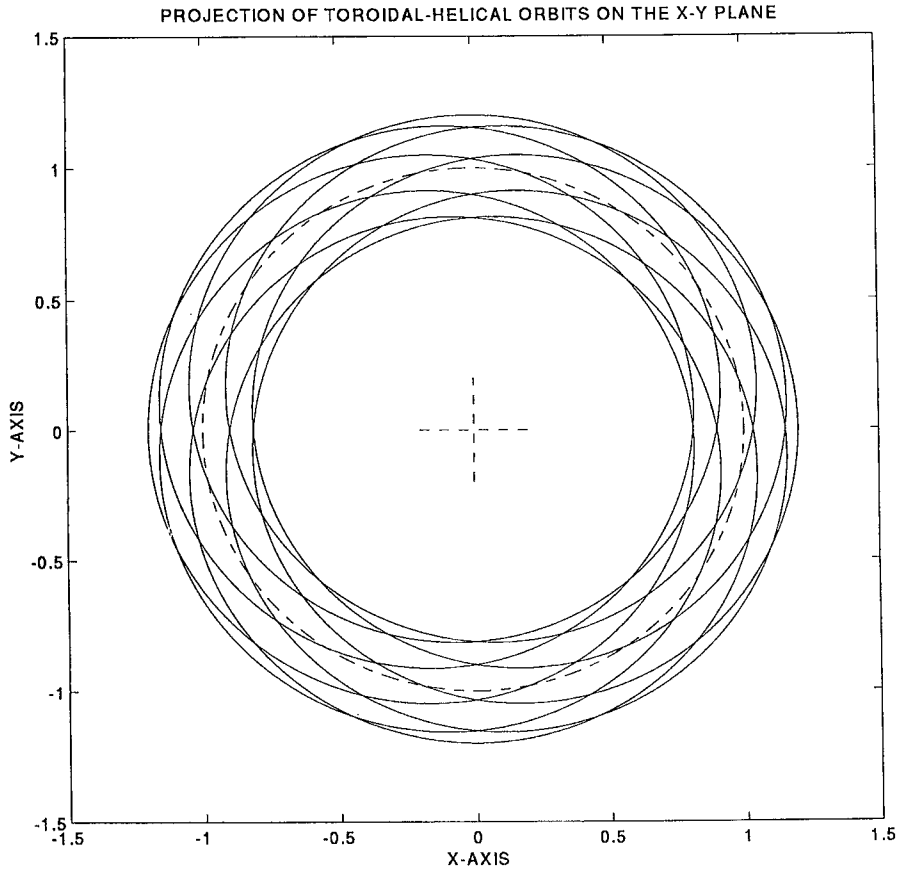

Figure 2 - Projection of the Nine Toroidal-Helical Electron Orbits on the X - Y Plane (the dashed line is the torus central circle).

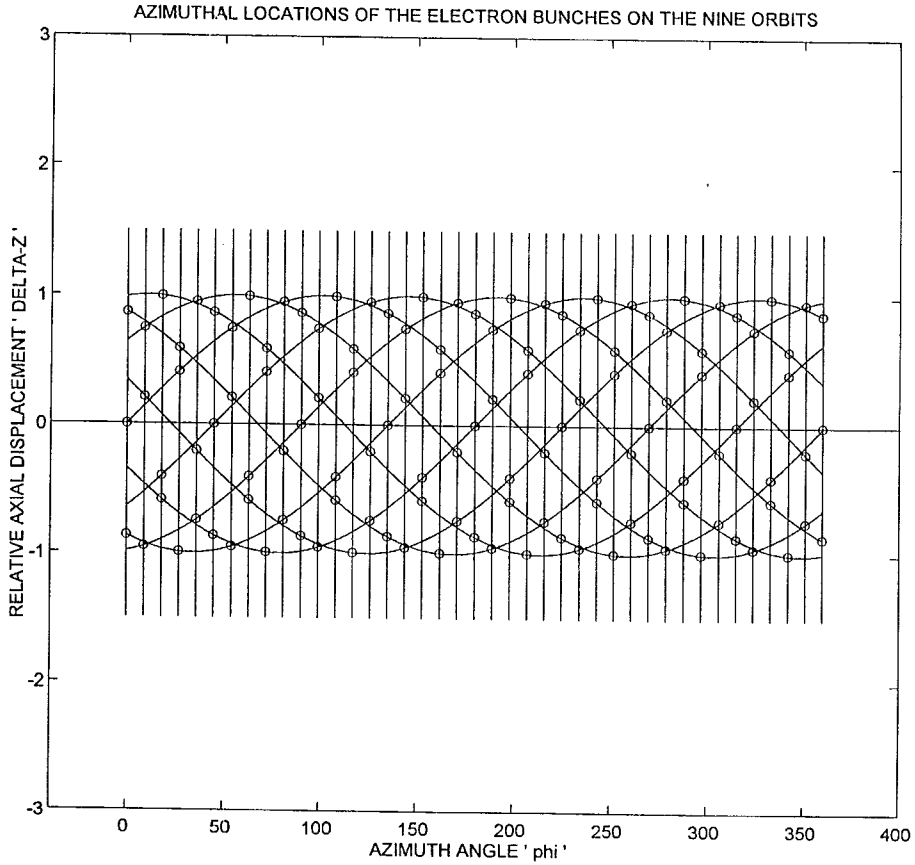

Figure 3 - Azimuthal Locations of the 120 Electron Bunches on the Nine Unwrapped Toroidal-Helical Electron Orbits.

REAL-TIME DIGITAL SIGNAL PROCESSOR IN IONOSPHERE MEASUREMENTS.

A.L.Karpenko*, V.V.Koltsov

Institute of Terrestrial Magnetism, Ionosphere and Radio Wave Propagation.
IZMIRAN, Troitsk, Moscow Region, 142092, Russia
PHONE: [+7]-095-334-02-94; FAX: [+7]-095-334-09-08
E-MAIL: karpenko@charley.izmiran.rssi.ru

1. INTRODUCTION

Ionosphere sounding consists of transmitting of short HF radio pulses on a set of frequencies and registration of characteristics of reflected of ionosphere signals. Registered parameters of signals may be: time delay, that is called virtual height of reflection region, amplitude, phase, polarization of the received signal. Now for acquisition of these data are used digital ionosonde. The block diagram of our ionosonde "Parus" is presented on fig. 1. The sounding pulses are formed by digital Receiver-synthesizer. High frequency transmitting signal Fe enters to wideband Power amplifier and further through Antenna switch is excited by transmitting antenna. The signal Fr, reflected of ionosphere, enters from receiver to A/D converter. Signal processor performs all necessary actions with digitized data Ud according to regime given by personal computer (PC). The total control of all processes of different modules of ionosonde is managed by PC and modulus of Synchronization and control.

In our report we describe the results of using DSP TMS320C25 in order to provide the process of sounding data treatment.

The feature of DSP work is its periodic repeatability, synchronized the process of radio pulses excitation. The speed of processing of arriving data should be sufficient for maintenance in rate of sounding pulses. Though the volume of data, received in each cycle of sounding is comparably small (2 Kwords in our case), it is required to perform the sufficiently large calculations to the utmost fast.

After getting of 2*1024 samples from ADC on a set of distances, DSP starts the processing of received digital data: calculations values of quadrature components, phases and amplitudes, and, in dependence on given regime, proceeds the detection of signals, estimation of current receiver attenuation or characteristics of accepted signal.

The main operations, executed by DSP processor are:

- -reception of realizations of signals and their buffering;
- -quadrature processing of realizations;
- -amplitude/phase detecting of signals from quadratures;
- -separation of O/X components;
- -calculation of threshold of signal separately in both channels;
- -estimation of amplification factor using calculated amplitudes;
- -average filter (16 points);
- -"triangular" filter (3 points);
- -accumulation of realizations;
- -search of useful signal;
- -search of amplitude maxima;
- -correlation processing of signals in case of use of Pseudo-noise coding.

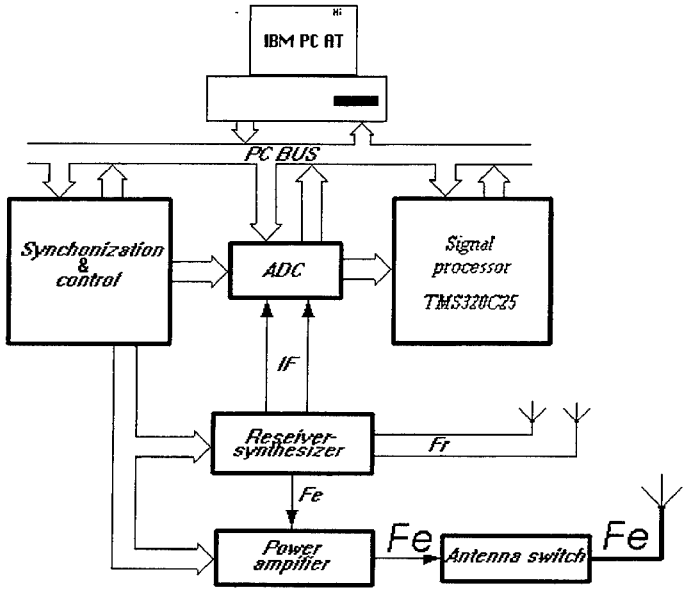

Fig. 1

All operations are proceeded simultaneously in two channels (we use two-channel radio receiver to get the opportunity of separation Ordinary/Extraordinary components of received signals. The DSP software allows to treat data from two types receiver: the first with final intermediate frequency (IF) 128 KHz, the second with zero IF and quadrature output. Almost all program components in both cases are common, despite the fact, that in the system with IF 128 KHz first operation is the calculation of quadratures.

2. DESCRIPTION OF MOST COMPLICATED COMPONENTS OF SOFTWARE DSP25

2.1 THE QUADRATURE PROCESSING OF REALIZATIONS.

We use two realizations of procedure of quadrature restoration from digitized IF data. First is based on the less-square method. Let U_k , k=1,..., n realization of signal on IF. We designate:

$x=2\pi F0/Fd$,

$A=\sin(nx)\cos((n+1)x)/\sin(x)$,

$B=\sin(nx)\sin((n+1)x)/\sin(x)$,

Where: F0 - average frequency of signal IF, Fd - sampling frequency.

Then the following estimation of the quadrature components As and Ac takes place:

$$Ac = 2\sin^2(x)\frac{(n-A)\{U_1\cos(x)+...+U_n\cos(nx)\}-B\{U_1\sin(x)+...+U_n\sin(nx)\}}{(n\sin(x))^2-\sin^2(nx)}$$

$$As = 2\sin^2(x)\frac{(n+A)\{U_1\sin(x)+...+U_n\sin(nx)\}-B\{U_1\cos(x)+...+U_n\cos(nx)\}}{(n\sin(x))^2-\sin^2(nx)}$$

Here n - number of data, on which are evaluated "quadratures" Ac and As. We used n=16, at which the received estimation of signal of constant level has the error not more than 0.5 %.

Second variant of procedure uses only two samples of ADC for estimation of quadratures. Except really measured data the special precalculated array of reference frequency IF is used. The defect of such algorithm is the loss of absolute value of phase of received signal, but the amount of calculations is approximately in five times reduced.

2.2 AMPLITUDE/PHASE DETECTION OF SIGNAL.

The detection of amplitudes and phases of signals is proceeded similarly to the procedure, accepted in signal processor "MOST" [1].

First we determine the maximal element from As and Ac. The binary value of fraction Amin / Amax is the argument of table function:

$$S1 = \sqrt{1+\left(\frac{A_{min}}{A_{max}}\right)^2}$$

After tabulated Log transformation of Amax general resulting value of signal amplitude can be received with use of inverse tabulated exponential transformation.

The fraction Amin/Amax also in aggregate with complex of logic conditions is used for tabulated determination of signal phase.

2.3 CALCULATION OF SIGNAL THRESHOLD.

The procedure is based on calculation of average amplitude of signal Am, average deviation Dm, received threshold is equal Am+kDm, where k is given by PC processor.

2.4 THE ESTIMATION OF FACTOR OF AMPLIFICATION ON CALCULATED AMPLITUDES

The realized procedure is similar to one used in [2], except for other levels of thresholds of overflow counters. This levels are: 8, 16,...,1024, 1984. The coefficient of receiver amplification is calculated with the step 6 dB.

2.5 THE FILTERING OF SIGNAL.

Given realization has the opportunity to make the operation " Sliding average " on 16 points of amplitude of signal as before accumulation, as afterwards. The "triangular FILTER" is realized on 3 points. It is used recursive procedure:

$$U_k = \{U_{k-1} + 2U_k + U_{k+1}\}$$

so here it does not arise signal time shift.

2.6 SEARCH OF USEFUL SIGNALS.

The selection of useful signals in realization is proceeded using calculated threshold. In target files only the elements, which amplitude exceeds the threshold level, remain. All other are filled in by zero.

3 RESULTS

As the results we show the times of completion of operations of TMS320C25 in milliseconds. The table is adduced for the case of two channels with 1024 elements in realization.

Operation	Time
Quadratures	**18.5**
Amplitudes + phases	**29.75**
Amplitudes only	**25.25**
Separation of the O/X components	**2.25**
Calculation of threshold of signal	**2.25**
Estimation of amplification	**7.5**
Sliding average (16 elements)	**2.75**
'Triangular' filter	**2.25**
Amplitude + phase + sliding average filter	**32.5**
Amplitude + phase + 'triangular' filter	**32.5**

4. CONCLUSIONS

Our experience of construction of system of signal processing on the basis of fixed-point processor TMS320C25 has shown opportunities and restrictions of such systems. The performance of processor permits to process the signals of ionosphere sounding in real time, with pulses repetition rate up to 25 Hz. At the same time the standard is the frequency of pulses 50 and even 100 Hz. The resolving in such situation can be the use more fast signal processors (for example TMS320C50) or processors with total system of arithmetical operations. The most limiting factor of use of processor TMS320C2* is the absence of command of integer division.

5. REFERENCES

1. Ariste A.P., Arro I.O., Germ E.I. Signal microprocessor "MOST". Digital ionosondes and applications (in Russian), IZMIRAN, Acad.Sci. USSR, 1986, pp. 38-42.
2. Arro I.O. The automatic correction of output signal level of receiver with ADC dynamic range (in Russian), Proc. of Tallinn polit. inst., N 540, 1982, pp. 11-15.

High Frequency Electromagnetic Safety Analysis by Numerical and Empirical Methods on Mobile Platforms

Malcolm J. Packer **Richard C. Ferguson**
Harris Corporation, RF Communications Division
1680 University Avenue, Rochester, NY 14610

Abstract

Positioning high frequency antennas on mobile platforms is usually a trade-off between adaptability and antenna performance. Harris is presently analyzing another factor, electromagnetic safety of personnel within or near the platform. The goal is to compare measured empirical data to data predictions from different numerical models to determine the models' validity. Then use the numerical models to determine the ideal antenna mounting position. The initial effort that this paper documents details a militarized M-998 HMMWV platform with a 10.7 meter whip antenna mounted on the left rear fender using a typical military mount.

Our results indicate that in localized areas the IEEE established thresholds for electromagnetic field strengths are just exceeded for the M-998 HMMWV with 125 watt transmitter using a fender mounted whip antenna. These localized areas around the HMMWV exterior are small compared to the size of an average person. Therefore, the average person's body is not totally immersed in electromagnetic fields that exceed the IEEE established thresholds. The personnel within the HMMWV are not exposed to levels of electromagnetic energy above the IEEE established threshold. All the results are for transmission of continuous wave (CW) power; therefore, all results can be relaxed depending on modulation and duty cycle.

Introduction

Military and personal communications use a variety of wireless equipment to send messages and data from 1 km to half way around the world. The use of high frequency (HF) communication equipment is ideal for communication beyond line-of-sight via ionosphere reflection. HF communications from mobile platforms require tactical equipment using an omni-directional antenna to provide continuous communication while the platform is moving. Under certain conditions it is possible that the electromagnetic fields radiated from the antenna could be potentially harmful to the radio operator as well as other personnel in the vicinity. This paper discusses numerical predictions and empirical validation to determine the electromagnetic field strengths about the platform's exterior and within the platform. The field strength levels are compared to preset thresholds to determine if a personnel safety hazard exists.

Maximum Permissible Exposure of Electromagnetic Fields

According to IEEE standards, safety to personnel from electromagnetic fields and contact with conductive objects exposed to such fields is a function of body resistance and capacitance to ground. Our work was confined to determine the electromagnetic fields associated with platform mounted HF systems and not to set thresholds on health hazards. More specifically, we were attempting to determine whether the empirical electromagnetic field data agreed with our numerical models for specific platform and antenna configurations.

The current IEEE guideline[1] provides the Maximum Permissible Exposure (MPE) in terms of rms electric (E) and magnetic (H) field strengths, power density (S), and the induced currents (I) in the human body. The MPE to electric and magnetic fields shown in Figure 1 are for the equivalent vertical cross-sectional area of the

human body. These MPE field levels are set to limit the maximum inducted current over the body to 100 ma through each foot to ground. Over a six minute time frame, this results in about 144 J/kg in the average 68 kg person. This is equivalent to a specific absorption ratio (SAR) of about 0.4 W/kg averaged over the entire body mass.

All thresholds are set based on normal healthy people. People with cardiac pacemakers and other medical devices can be in danger with electromagnetic levels below the IEEE thresholds. Munitions and other electronically detonated explosives should be adequately shielded from all electromagnetic sources.

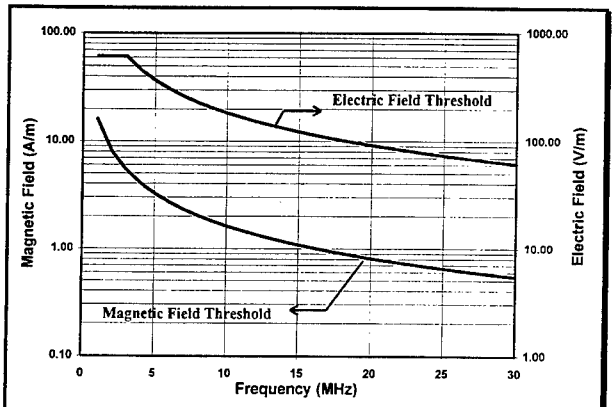

Figure 1. Threshold Maximum Permissible Exposure for 6 minutes of RMS Electric and Magnetic Field Strength from 1 to 30 MHz.

When field strengths are above these levels current induced on the platform can cause an RF shock or burn hazard. The relationship between the electric field in V/m and the current is a function of metallic surface exposed. Two levels are defined for humans: perception- feel a tingling sensation and let-go- maximum current that the a muscle can be stimulated and still voluntarily release[2]. Perception current is 50 ma at 1 MHz is and 100 ma at 30 MHz. The let-go current is 150 ma at 1 MHz and 220 ma at 30 MHz. These current levels can be induced on a compact car immersed in approximately 50 V/m and 100 V/m for perception and let-go at 10 MHz. As the size of vehicle increases the field values are reduced to, for example, 15 V/m and 35 V/m for a truck. Of course, perception and let-go currents are dependent on the size of person and type of touch. Conductive contact measurements with rod electrodes and humans determined that the RF burn threshold from 2 to 20 MHz is approximately 200 ma[3].

Platform and HF Equipment

The M-998 High Mobility Multi-purpose Wheeled Vehicle (HMMWV) is the typical military vehicle used for mobile platforms. This platform can be delivered in many different forms, this paper discusses measurements made on an open platform with a soft-top. Harris is presently performing measurements on a closed platform as well as a number of different antennas.

Harris designed a tactical HF radio system for the HMMWV and other highly mobile vehicles. The HF radio system (AN/GRC-231) has the following equipment cascaded together: receiver/transmitter (RF-5022), power amplifier (RF-5032) and an antenna coupler (RF-382) connected to a narrowband antenna. On our test HMMWV, the radio equipment was mounted in the typical location, between the vehicle's rear seats. The antenna coupler was located above and inside the left rear fender close to the base of the AT-1011 (10.7 m. whip) antenna. The radio configuration is specific, but any generic 125 watt radio system with the identical antenna and mounted should produce identical electromagnetic fields.

The equipment was configured to transmit 125 watts of unmodulated continuous wave (CW) power into the antenna coupler. Continuous wave mode represents the worst case electromagnetic field exposure. Modulation or reduction in duty cycle will reduce the electromagnetic field levels.

Theoretical Attenuation with Distance

Theoretical derivation of the near and intermediate electromagnetic fields generated from a whip antenna attached to a complex metallic structure is difficult without significant simplifications. The electromagnetic fields were evaluated using numerical methods as discussed later. It is useful to examine the rate of attenuation from a simple infinitesimal element. In free space, an infinitesimal current element with zero thickness oriented along the z-axis will give rise to the following field vector components[4].

$$E_r = \eta \frac{I_0 l \cos\theta}{2\pi r^2}\left[1+\frac{1}{jkr}\right]e^{-jkr}$$

$$E_\theta = j\eta \frac{kI_0 l \sin\theta}{4\pi r}\left[1+\frac{1}{jkr}-\frac{1}{k^2r^2}\right]e^{-jkr}$$

$$H_\phi = j\frac{kI_0 l \sin\theta}{4\pi r}\left[1+\frac{1}{jkr}\right]e^{-jkr}$$

$$E_\phi = H_r = H_\theta = 0$$

where:
$k = 2\pi/\lambda$ - wave number
$\eta = \sqrt{\mu_o/\varepsilon_o}$ - intrinsic impedance of free space
I_o - uniform current distribution magnitude
l - infinitesimal current element length
r - distance to observation point in meters
λ - wavelength in meters

The two orthogonal electric field vector components attenuate at different rates. Initially when distance from the antenna is small, $kr<<1$, E_θ and E_r are both inversely proportional to r^3, when the distance is increased to $kr>1$, E_r is inversely proportional to r^2 whereas E_θ is inversely proportional to r. At large distance, $kr>>1$, only the remaining E_θ and H_ϕ components make up the propagating wave.

$$E_r \cong -j\eta \frac{I_0 l e^{-jkr}}{2\pi k r^3}\cos\theta \qquad kr<<1$$

$$E_\theta \cong -j\eta \frac{I_0 l e^{-jkr}}{4\pi k r^3}\sin\theta$$

$$H_\phi \cong j\frac{I_0 l e^{-jkr}}{4\pi r^2}\sin\theta \qquad kr<<1$$

$$E_r \cong -\eta \frac{I_0 l e^{-jkr}}{2\pi r^2}\cos\theta \qquad kr>1$$

$$E_\theta \cong j\eta \frac{kI_0 l e^{-jkr}}{4\pi r}\sin\theta$$

$$H_\phi \cong j\frac{kI_0 l e^{-jkr}}{4\pi r}\sin\theta \qquad kr>1$$

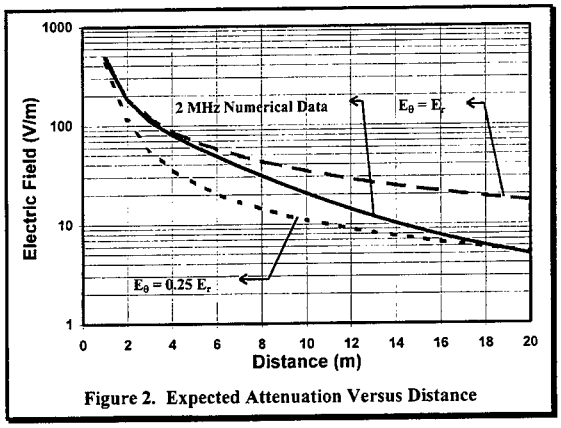

Figure 2. Expected Attenuation Versus Distance

Our analysis is concerned with near and intermediate electromagnetic field. Based on the simple dipole attenuation, our data should fall-off at $1/r^3$ close to the antenna then at a mixture of $1/r^2$ and $1/r$ depending on the magnitudes of the individual components. Figure 2 shows theoretical curves of the expected attenuation versus distance. The two dashed curves show attenuation rates for different initial E_θ and E_r. The solid curve is numerical data from modeling the whip and platform over real earth at 2 MHz. In a real environment, the magnitude of E_θ and E_r and even E_ϕ are combinations of reflections from nearby objects.

Numerical Predictions

The Numerical Electromagnetic Code Version 4[5] (NEC-4) is a well-known implementation of the moment method[6] algorithm. NEC-4 is considered the "gold-standard" electromagnetic modeling tool, having achieved this status through constant improvement and extensive validation performed by many independent users. NEC-4 computes the current distribution on a segmented wire-grid model of the HMMWV platform with the 10.7 m whip antenna. The current distribution in each wire-grid segment is then used to compute near electric and magnetic field strengths. The platform is electrically close to the ground and therefore requires the use of the Sommerfeld-Norton formulation to correctly model the interaction at the earth-air interface.

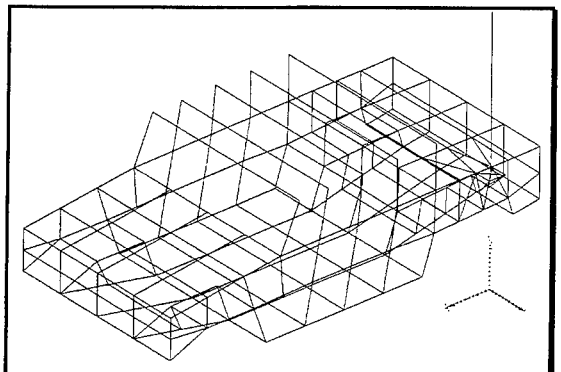

Figure 3. Wire-Grid Model of HMMWV with 10.7 m Whip Antenna

The antenna and conductive vehicle surface have intense interaction, requiring accurate numerical modeling. The HMMWV wire-grid model was created using an interactive graphical user interface, EAM:NEC[7]. Figure 3 displays the resulting numerical model used to compute the electromagnetic fields. A soft-top HMMWV was used for testing which represents the worst case exposure to the passengers. The wire-grid model contains 386 wire segments to model the entire outer conductive surface including the undercarriage[8]. The wire-grid radius and spacing were adjusted to correctly model a solid surface as defined by Ludwig's "twice surface area" criteria[9]. The entire model is situated such that the 10.7 meter whip is aligned with the z-axis in the Cartesian coordinate system.

Measurements

To approximate realistic conditions, the HMMWV was situated in a large open paved parking lot free of metallic obstacles. Measurements were performed in linear paths away from the platform centered on the antenna. Frequencies were measured at selected allocated frequencies that are close to even integers throughout the HF band. To correctly represent the true operational scenario, the HMMWV battery powered the radio system. A watt meter insured that 125 Watts of power was delivered to the antenna coupler.

The electromagnetic field strengths were measured using several small probes. A number of probes were used: a 3.6 cm. ball probe, a calibrated 1 meter long probe and a Holaday 3-axis probe. The magnetic field was measured with an 3.0 cm. loop, a 10 cm. loop and Holaday 3-axis probes. The majority of the tests were measured with the 3.6 cm. ball and 3.0 cm. loop probes.

Electromagnetic fields vary along the body length. The human body has different specific absorption rates (SAR) along its surface. The highest SAR levels are shown to be on the neck[10]. Measurements were performed with each probe on a non-metallic tripod at 165 cm. height. The signal received on these probes were connected to a spectrum analyzer via a short length of coaxial cable. The tripod was moved along a linear path away from the antenna at 0.5, 1, 2, 4, 8, and 16 meters.

HMMWV interior electromagnetic fields were measured at the location of the four seats. Two points were measured at each seat location; waist level and neck level in the seated position.

Numerical and Empirical Results

The time involved with gathering empirical data limits the amount of data that was obtained. The empirical data was used to validate and verify the numerical predictions. All results displayed compare both measured and modeled electric and magnetic field strengths.

Exterior Electric Fields

The curves in Figure 4 show the measured and modeled electric field strength versus distance from the antenna. The 2 MHz data has excellent agreement in magnitude and attenuation rate versus distance. At 4 MHz, the agreement is good overall, but the $1/r^3$ reduction rate is not seen in the measured data. At 8 MHz, the measured data has the $1/r^3$ reduction rate while the numerical doesn't, but overall the data compares well. At 16 MHz, the data has excellent agreement in magnitude and attenuation rate. The numerical data at 24 MHz disagrees with the theoretical attenuation rate, where the measured data agrees with the theoretical curve. At 30 MHz, the measured and modeled data attenuates at different rates. Overall there is good agreement between the measured data and modeled data, particularly at 2 and 16 MHz. The numerical model data tracks the measured data well close to the HMMWV at the lower frequencies, but above 24 MHz the attenuation rate diverges. All the field strength curves in Figure 4 are below the IEEE thresholds (Figure 1). These curves represent attenuation in one linear path away from the antenna and not all around the HMMWV.

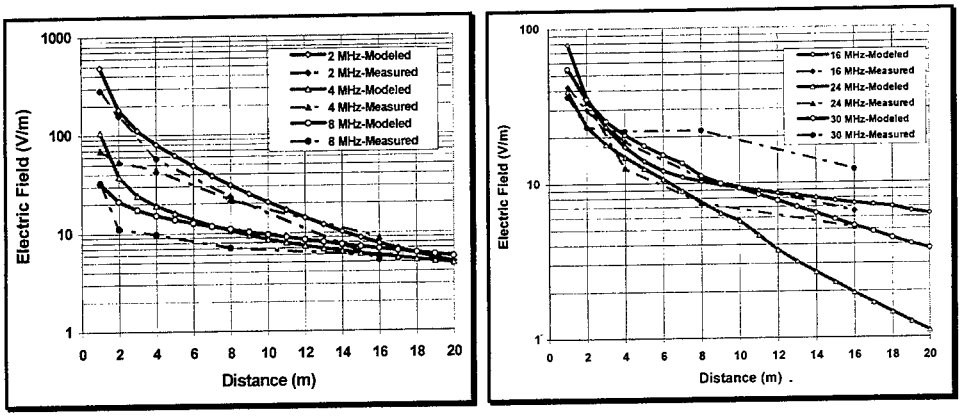

Figure 4. Measured and Modeled Electric Field Strength Versus Distance

The platform and the antenna mounting lack symmetry resulting in asymmetric electromagnetic fields. Figure 5 shows a contour plot looking down on the platform with the antenna located at x = 0 and y = 0. The plot shows the magnitude of the electric field out to 5 meters at a 1.65 meter height for 2 MHz. This figure has a contour line every 100 V/m starting with levels above the IEEE threshold of 614 V/m. The rectangular HMMWV influence on field strength is clearly evident. Threshold levels are exceeded around the rear of the platform and up the driver's side. If the driver has his arm out the window the arm would be exposed to levels that exceed the IEEE threshold. The electric field levels attenuate outwardly at different rate due the off center antenna mounting. This figure reveals that an electric field null exists within the passenger space.

The strongest electromagnetic fields are at the HMMWV rear surface edges, they exceed the IEEE thresholds shown in Figure 1. The size of the exceeded volume is not large enough for a person to be confined within. Therefore, at 2 MHz the worst case condition does not constitute an electromagnetic danger. The driver is not

homogeneously exposed to this level so at most only a body portion is exposed. Localized SAR of 8 W/kg averaged over one gram of body mass is deemed the localized threshold. This level is 20 times the level for homogenous exposure, or approximately 4.5 times the electric field. These localized levels only just exceeded MPE levels and are below 4.5 times the 614 V/m level.

Similar testing was performed using the AN/GRC-193 radio with a 4.6 meter vehicular whip antenna. This system can produce power density levels in excess of 1.0 mW/cm^2 to a distance of 1.1 m from the antenna with 100 w of power[11].

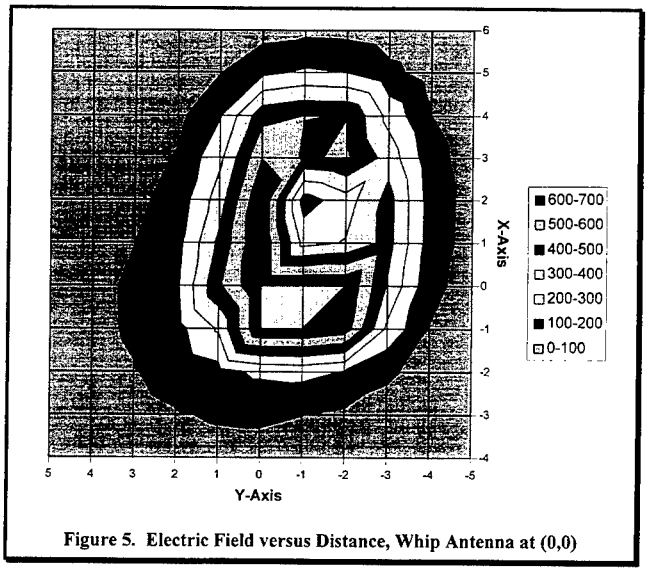

Figure 5. Electric Field versus Distance, Whip Antenna at (0,0)

Exterior Magnetic Fields

Figure 6 shows the measured and modeled magnetic field strength levels. The agreement between measured and model magnetic field strengths are exceptionally good. The 16 MHz data shows a dip a 2 meters that is seen in both the measured and modeled data. At 30 MHz, the initial rise in field strength is seen with both the measured and modeled data. Both 24 and 30 MHz curves have an abrupt oscillation in the modeled data at 10 meters from the antenna. Our measured data is at 8 and 16 meters, so the oscillation at 10 meters can not be validated. Overall the data has exceptional agreement; therefore we feel that these oscillations are correct. All these curves are far below the IEEE thresholds shown in Figure 1.

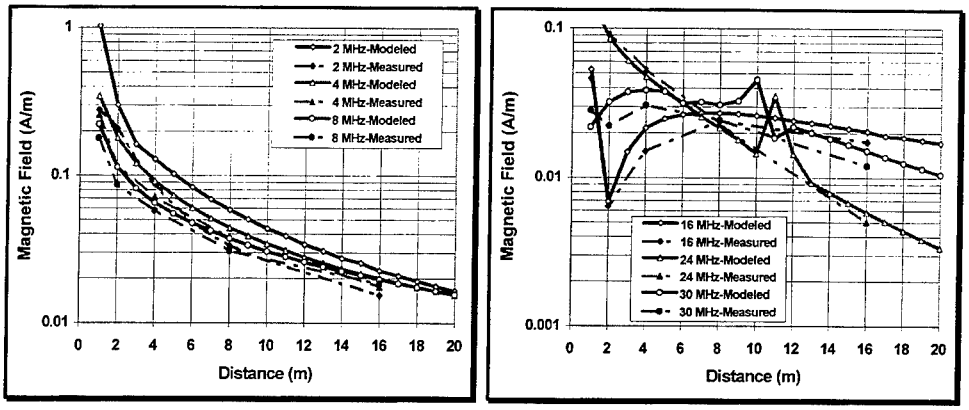

Figure 6. Measured and Modeled Magnetic Field Strength Versus Distance

Interior Electric Fields

Measurements were taken within the HMMWV at each of the four seats. In each seat, two data points were taken; one at 0.1 meters above the seat and 0.2 m below the roof. It was found that there is a difference in driver's side and passenger's side, but only a small difference in height and front or back seats. Shown in Figure 7 are two dashed curves that represent the measured data on the driver's side and passenger's side across the frequency band. The numerical data shows driver's side front and back seat and passenger's side front and back seat. The IEEE threshold is also shown as the solid line. At 2 MHz, the data is on the fringe of exceeding MPE. As the frequency is increased, the measured and modeled data drops well below threshold levels up to 16 MHz. Above 16 MHz, the electric field levels increase to the threshold level at 24 MHz, then decrease.

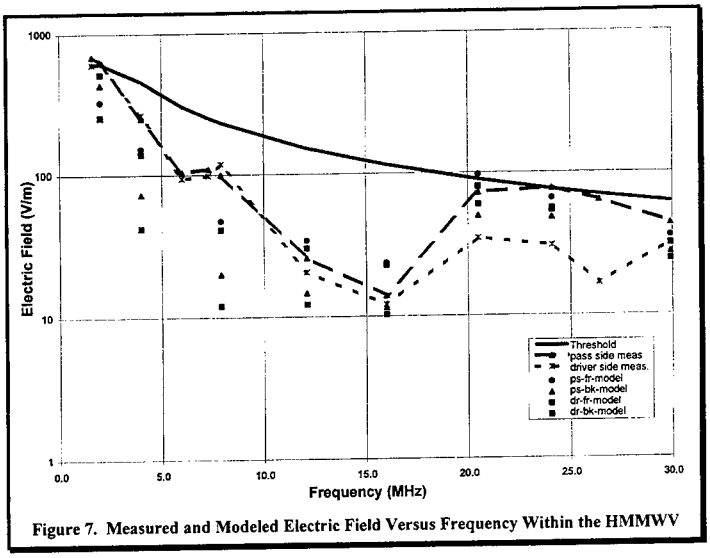

Figure 7. Measured and Modeled Electric Field Versus Frequency Within the HMMWV

RF Shock

The limited ability to ground a mobile platform results in circulating currents. These currents often are high enough to cause RF burns depending on the antenna's input impedance. When a narrow-band antenna is excited with a frequency so that the antenna appears electrically short, high voltages in the order of thousands of volts are developed at the coupler's output port. A safety hazard exists from the RF current present on the coupler's output port, interconnecting wire, and antenna base anytime the HF communications system is in the transmit mode. During transmit the coupler's output port, interconnecting coupler wire, or the antenna base should not be touched.

Conclusions

Harris has recently analyzed and is continuing to analyze electromagnetic safety of personnel within or in proximity of mobile platforms with tactical HF radios. Our goal is to determine if IEEE maximum permissible exposure thresholds are exceeded around different antennas on different platforms versus frequency. The effort involves numerical predictions with validation and verification by empirical methods. The results documented in this paper are for a militarized M-998 HMMWV platform with a 10.7 meter whip antenna mounted on the left rear fender using a typical military mount. Any change of platform, radio, antenna, or mounting may not produce the same results.

Overall, there is good agreement between the measured data and modeled data, both external and internal to the platform. The numerical model tracks the measured data well close to the HMMWV at the lower frequencies. Our results conclude that IEEE MPE thresholds are exceeded for localized areas around the external surface of the M-998 HMMWV with 125 watt transmitter using a fender mounted whip antenna. These localized areas around the HMMWV are small compared to the size of an average person. Therefore, the average person's body is not totally immersed in electromagnetic fields that exceed the IEEE MPE thresholds. The IEEE localized thresholds are invoked which are well above our measured field strengths. The personnel within the HMMWV are not exposed to levels of electromagnetic energy above the IEEE MPE threshold. All the results are for CW mode; therefore, even the small localized hot areas can disappear depending on modulation and duty cycle.

To remain outside any localized area that exceeds the IEEE MPE thresholds of electromagnetic field strengths in CW mode a safety zone contour is recommended. The safety contour for a 10.7 meter rear fender mounted whip antenna on a M-998 HMMWV operating at 125 watts is as follows:

> A distance of 0.5 meters away from the HMMWV conductive surface starting at the front of the driver's side door proceeding towards the antenna to the HMMWV left rear corner, along the back to the right rear corner, and back up to the rear of the passenger's side door. At distances greater than 0.5 meters, all electromagnetic field levels are below the IEEE MPE thresholds.

During HF transmission, as with any radio, an RF shock hazard exists if physical contact is made with the antenna coupler's output port, coupler's interconnect cable, or antenna base.

References

[1] IEEE Standard for Safety Levels with Respect to Human Exposure to Radio Frequency Electromagnetic Fields, 3 kHz to 300 GHz, IEEE C95.1-1991.

[2] O. P. Gandhi, and I Chatterjee, "Radio-Frequency Hazards in the VLF to MF Band," *Proceedings of the IEEE*, vol. 70, no. 12, December 1982.

[3] R.J. Rogers, "Radio-frequency burn hazards in the MF/HF band," *Aromedical Review-Proc. Workshop in the Protection of personnel Against RF Electromagnetic Radiation*, Review 3-81, J.C. Mitchell, Ed.

[4] Balanis, C.A. Antenna Theory - Analysis and Design, Harper & Row, NY, 1982, pp. 100-103

[5] G. J. Burke, "Numerical Electromagnetics Code - NEC-4, Method of Moments," Part I: User's Manual, Lawrence Livermore National Laboratory, Jan. 1992.

[6] R.F. Harrington, *Field Computation by Moment Methods*, Krieger Publishing Company, 1968.

[7] M.J. Packer, "Graphical Shell for Numerical Electromagnetic Code," *Applied Computational Electromagnetic Society Symposium*, March 1993.

[8] B.A. Austin, R.K. Najm, "Wire-Grid Modeling of Vehicles with Flush-Mounted Window Antennas," *IEE 7th International Conference on Antenna and Propagation*, vol. 2,1992.

[9] A.C. Ludwig, "Wire Grid Modeling of Surfaces," *IEEE Trans. On Antennas and Propagation*, vol. AP-35, no. 9, Sept. 1987.

[10] M.A. Stuchly, R. J. Spiegel, S.S. Stuchly, and A. Kraszewski, "Exposure of Man in the Near-Field of a Resonant Dipole: Comparison Between Theory and Measurements," *IEEE Trans on MTT*, vol. MTT-34, no. 1, January 1986.

[11] Technical Bulletin-Hazard Criteria for CECOM radio Frequency and Optical Radiation Producing Equipment, TB-43-0133, Department of the Army, 1 April 1991.

COMPUTATIONAL MODELING OF WAVE PLASMA INTERACTION

V.A.Eremenko and Yu.N.Cherkashin

Institute of Terrestrial Magnetism, Ionosphere and Radio Wave Propagation
Russian Academy of Sciences, 142092 Troitsk, Moscow region, Russia

Abstract

The wave-plasma interaction is considered with taken into account the thermal conductivity. It is proposed the computational algorithm to solve the nonlinear problem. It is shown that, the thermal nonlinearity creates additional duct. This interaction makes the wave beam trajectory less steep.

1.Introduction

The problem of nonlinear wave plasma interaction appears when a powerful EM wave propagates in plasma medium. Usually such interaction is described by means of the nonlinear wave equation [1] or some approximation such as parabolic equation of diffraction theory [2]. However, such description is possible only in the case of negligible thermal conductivity. To take into account the thermal losses, it is necessary to include another equation describing the electron density disturbance initiated by the powerful electric field.

2. Analysis

We analyze a problem of intensive wave beam propagation in the ionosphere. The small region is considered near the reflection point where the interaction of the beam with the ionospheric plasma is the most effective. We represent the wave electric field in the form of $E(x,y) = U(x,y) \cdot \exp(iKx)$, where x, y are Cartesian coordinates, K is the wave number. For the wave amplitude U we can write down the parabolic equation [3]

$$2iK\frac{\partial U}{\partial x} + \frac{\partial^2 U}{\partial y^2} + K^2(\varepsilon - 1)U = 0,$$

$\varepsilon-$ being the dielectric permittivity. The electric field heats the plasma causing a disturbance of the electron temperature. The distribution of the electron temperature is described by the heat equation across the wave propagation direction.

$$L^2\frac{d^2\Delta T}{dy^2} - \Delta T - \left(\frac{|U|}{E_p}\right)^2 \cdot T_0 = 0.$$

Here, ΔT is the disturbance of the electron temperature, T_0 is the background electron temperature, L is the characteristic scale of the thermal conduction, E_p is the characteristic plasma field ($E_p = 3T_0\frac{m}{e^2}\omega^2\delta$), m, e are the charge and the mass of the electron, ω is the radiation frequency, δ is the average part of the energy which the electron losses

at one collision. Following [4], we can write down the equation for the electron density diffusion

$$T_0 \frac{d^2 \Delta N}{dy^2} + k_T N_0 \frac{d^2 \Delta T}{dy^2} = 0$$

Here, k_T is the coefficient of thermal diffusion, ΔN is the disturbance of the electron density, N_0 is the not perturbed electron density. Dielectric permittivity ε is connected with the electron density $N = N_0 + \Delta N$ by the relation

$$\varepsilon = 1 - \frac{4\pi e^2}{m\omega^2} N$$

Thus, we can easily obtain the equation of diffusion across the direction of the wave propagation for the dielectric permittivity perturbation $\Delta\varepsilon$

$$\frac{d^2 \Delta\varepsilon}{dy^2} - \alpha \cdot \Delta\varepsilon - \beta \cdot |U|^2 = 0$$

Where $\alpha = k_T / L^2$ is the coefficient of thermal losses, $\beta = \alpha \frac{4\pi e^2}{m\omega^2} N_0$ is the coefficients of nonlinearity. Thus we have a set of two equations for describing nonlinear interaction of the wave field with the ionospheric environment. We can assume that the coefficients of the second equation do not vary in the considered region because this region is sufficiently small. In this case, we can obtain the solution of this equation in terms of an integral representation

$$\Delta\varepsilon = b \int_{-\infty}^{\infty} |U(x,z)|^2 \exp\left(-a\,|y - z|\right) dz$$

where $a = \sqrt{\alpha}, b = \beta/(2\alpha)$. Thus we can reduce our problem to one integral - differential equation.

$$2iK \frac{\partial U}{\partial x} + \frac{\partial^2 U}{\partial y^2} + K^2 \left[\varepsilon_0 - 1 + b \int_{-\infty}^{\infty} |U(x,z)|^2 \exp\left(-a\,|y - z|\right) dz \right] U = 0,$$

where $\varepsilon_0 = \varepsilon_0(x,y)$ - is the background dielectric permittivity.

This representation is useful for analytical investigation but for numerical procedure maybe, it is more convenient to use the system of two equation.

3. Numerical method

Now, we can replace the differential operator by their difference analogue and using the sweep method we can obtain the numerical solution of the nonlinear problem. However, the variance relation of the difference equation is significantly distinguished from variance relation of the differential equation for higher harmonics [5]. This fact is not terrible for linear problems, because we can put sufficient number of points of the difference

network for the initial date approximation. But in the nonlinear problem, new harmonics can appear in the process of the propagation and we can not anticipate a priory the spectrum limits of the solution. Therefore we have modified the well known decomposition method to solve the our problem. The construction of the numerical solution on the step $x_j, x_{j+1} = x_j + \Delta x$ is decomposed into two stage-diffraction step

$$2iK\frac{\partial U_1}{\partial x} + \frac{\partial^2 U_1}{\partial y^2} = 0$$

and refraction step

$$2iK\frac{\partial U_2}{\partial x} + K^2(\varepsilon - 1)U_2 = 0$$

where $U_1(x_j, y) = U(x_j, y), U_2(x_j, y) = U_1(x_{j+1}, y), U(x_{j+1}, y) = U_2(x_{j+1}, y)$ To avoid the difference derivative across the wave propagation, we construct some difference analogue of the generalized solution of the diffraction equation. For this aim, we designate $V_j(y) = U_1(x_j, y)$, and rewrite the first step equation in the form

$$2iK\frac{V_{j+1} - V_j}{\Delta x} + \frac{1}{2}\left(\frac{d^2V_{j+1}}{dy^2} + \frac{d^2V_j}{dy^2}\right) = 0 \tag{1}$$

Now, we consider the scalar product of this equation on a sufficiently smooth function φ which is satisfied the boundary conditions. Then we can transfer the differentiation from the function V to the function φ and thus, we can get the relation

$$\left(V_{j+1}, \frac{d^2\varphi}{dy^2} + \gamma \cdot \varphi\right) + \left(V_j, \frac{d^2\varphi}{dy^2} - \gamma \cdot \varphi\right) = 0$$

were $\gamma = \frac{4iK}{\Delta x}$ is the complex-valued constant. Next, we approximate the functions $\varphi(y)$ and $V_j(y)$ by its difference analogues at N points of across coordinate. We construct N scalar product using N linearly independent functions φ_n. Thus, we obtain the set of N equation for the definition of the vector $\overrightarrow{v}_{j+1}$ which is the difference analogue of the function $V_{j+1}(y)$ .Introducing matrixes A and B. with elements $a_{n,m} = \frac{d^2\varphi_n}{dy^2} + \gamma \cdot \varphi_n$. and $b_{n,m} = \frac{d^2\varphi_n}{dy^2} - \gamma \cdot \varphi_n$ at the points of the network y_m, we can write down the relation

$$\overrightarrow{v}_{j+1} = \left(A^{-1} \cdot B\right) \cdot \overrightarrow{v}_j$$

Thus, it is enough to calculate one time the transition matrix $(A^{-1} \cdot B)$ and then to use this matrix every time passing from layer to layer. It is most easily to calculate the transition matrix if the eigenfunctions of the differential operator are used as the base functions φ_n

4. Conclusion

In the case of the characteristic scale of thermal conduction L being very small, the problem can be reduced to the well-known nonlinear parabolic equation. However, if this

scale is not negligible, a numerical procedure is to be used. The numerical solution of this problem allows us to investigate the deformation of the wave form solution by thermal diffusion. For the ionosphere the nonlinearity is very small ($\beta << 1$) and, therefore, we can use the perturbation method. At the reflection point the wave field is sufficiently well described by the oscillating Airy function (fig.1). But the disturbance of dielectric permittivity is described by a smooth function (fig.2). Thus the thermal nonlinearity creates some additional duct for the wave propagation which makes the trajectory of the beam more slanting. As result, the exit angle of wave from the ionosphere is not equal to the entrance angle (fig.3). This conclusion is in a very good agreement with the experimental results [2].

References

1. I.A.Molotkov, Yu.N.Cherkashin. Some nonlinear effects of wave beams propagation in the ionosphere. Journal of Atmos. and Terr.Phys. 1994, v.56, N11, 1477-1481.

2. G.S.Bochkarev, V.A.Eremenko, L.A.Lobachevsky at al. Nonlinear Interaction of Decameter Radio waves at close Frequencies on oblique propagation. Journal of Atmos. and Terr.Phys. 1982, v.44, N 12.

3. V.A.Fock. Electromagnetic Diffraction and Propagation Problems. Pergamon Press, Oxford, 1965.

4. A.V.Gurevich, A.B.Shvarcburg. Nonlinear Theory of Radiowave Propagation in the Ionosphere. Moscow, Nauka, 1973. (in russian)

5. D.Potter. Computational Physics. John Wiley and sons, London, 1973

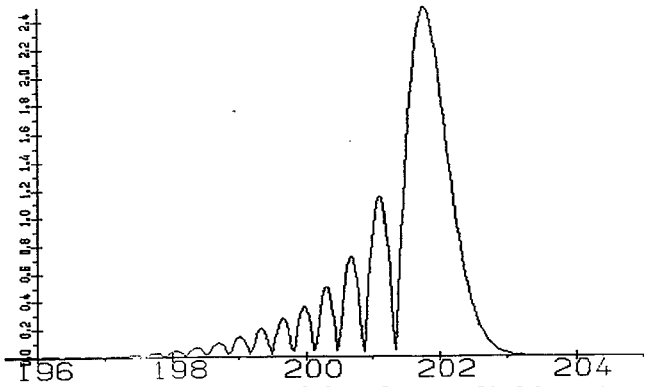

Fig.1. The dependence of module of wave field amplitude U versus across coordinate.

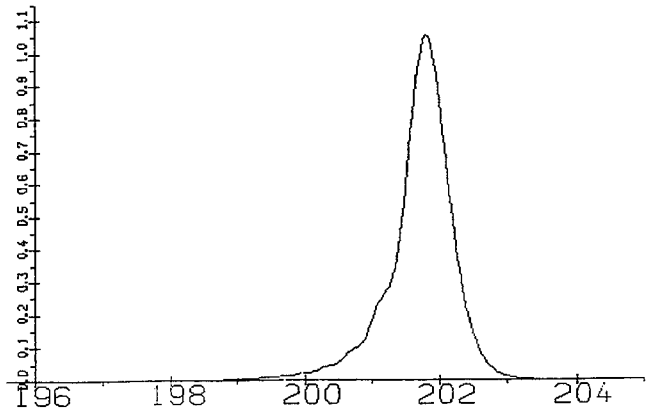

Fig.2. The perturbation of dielectric permittvity versus across coordinate.

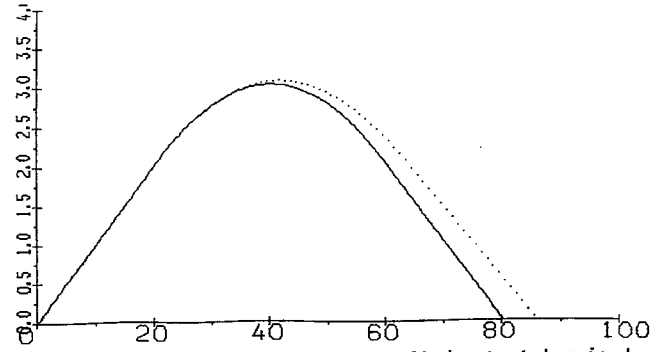

Fig.3. The ray trajectories: the undisturbed trajectory (solid line); the trajectory is disturbed by thermal nonlinearity (dotted line).

ATTENUATION OF HF RADIO WAVES IN A FOREST: RESULTS FROM EXPERIMENT.

I.P. Zolotarev, V.A. Popov, V.P. Romanuk.
Institute of Terrestrial Magnetism, Ionosphere and Radio Wave Propagation (IZMIRAN), Troitsk, Moscow reg., 142092 RUSSIA.

1. Introduction.

Radio frequency (RF) propagation path loss through trees and foliage determines mainly the distance of radio communication in forest. Usually path loss of radio waves in forests is far more than in clear air and depends strongly on different conditions (moisture, density of trees, foliage, kind of wood). By estimations the attenuation of radio waves due to foliage can vary at 400MHz from 100 dB/km for sparse forest to 1000 dB/km for very dense forest [1]. Extremely high path loss of radio waves in dense forest makes radio communication there almost impossible. Under certain conditions the radio waves can propagate in forest at far more distances than it could be expected from estimations. For such conditions the attenuation of radio waves due to foliage can be 40÷50 dB/km [1]. This effect can be explained by formation of lateral radio waves in the model where forest is described as dielectric slab. For prediction of path loss for different conditions several mathematical models can be used [4], [1].

In present paper results of measurements of radio wave attenuation in the forest and outside of forest are presented. Features of radio wave propagation in clear air outside forest and in forest are compared and discussed. Spectra of received signals are presented. The results of measurements of radio wave attenuation are compared with the theoretical estimations.

2. Experiment.

Measurements of radio wave attenuation were performed in 1995 in Troitsk forest near Moscow, Russia. For experiment a special acquisition system was elaborated. Hardware included portable transmitter, super sensitive receiver and a personal computer with 16 bit resolution DAC/ADC digital board inside it. Available software allowed to select one of four discrete gain amplifier ranges of DAC/ADC digital board and change the gain of digital board amplifier within each range continuously. Additionally there was an opportunity to change the gain of receiver amplifier from 2 to 10000 manually. This gave very wide total dynamical range of acquisition system. During experiment the receiver was located at the same point near the forest while the transmitter was moving in forest in transverse direction to the border of forest and then in opposite direction outside of forest. For controlling purposes an independent voice channel in different frequency range was additionally used. The positions of transmitter were exactly determined. Transmitter

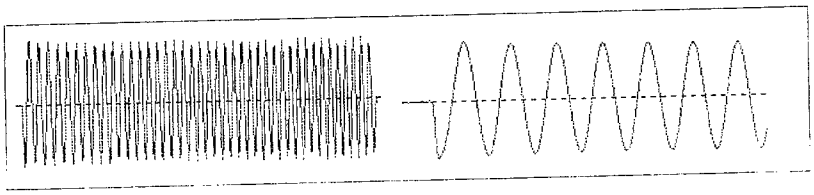

(a) short distance signal from forest transmitter

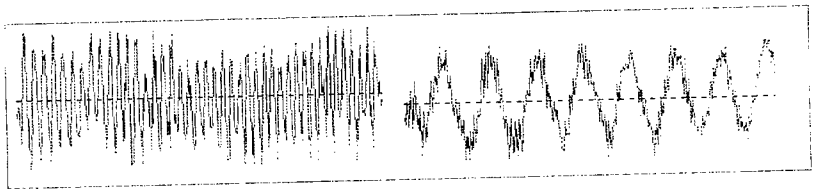

(b) middle distance signal from forest transmitter

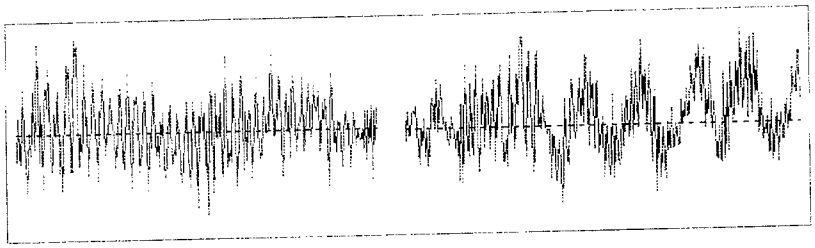

(c) long distance signal from forest transmitter

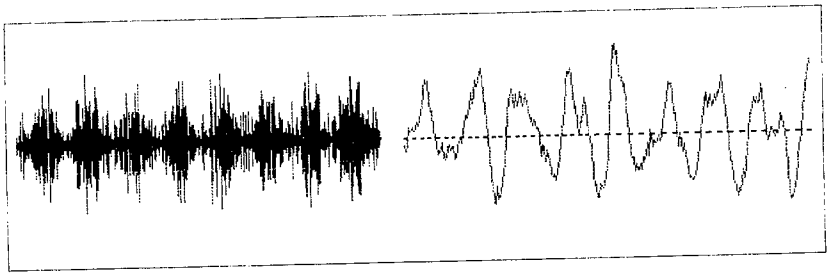

(d) clear air long distance signal from outside of forest transmitter

Figure 1. Waveforms of received signals.

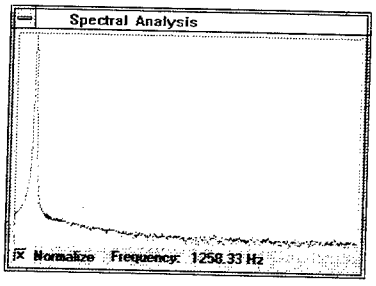

(a) spectrum of signal from short distance forest transmitter

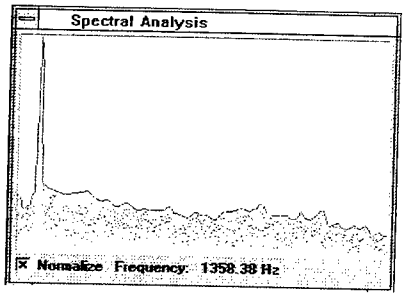

b) spectrum of signal from long distance outside of forest transmitter

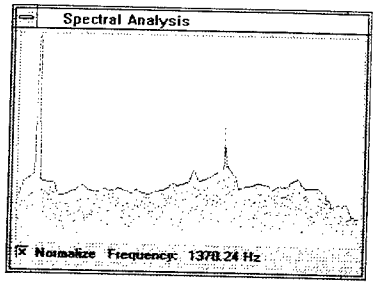

(c) spectrum of signal from middle distance forest transmitter

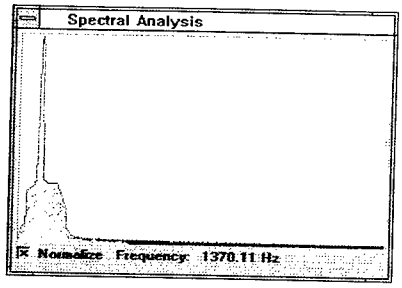

(d) spectrum of filtered signal from middle distance forest transmitter

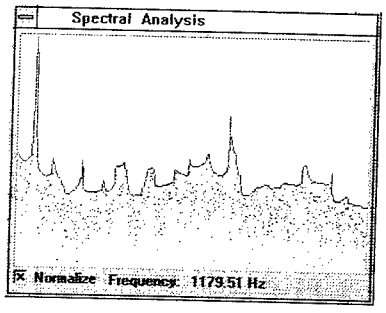

(e) spectrum of signal from long distance forest transmitter

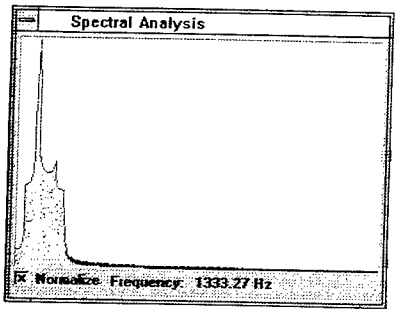

(f) spectrum of filtered signal from long distance forest transmitter

Figure 2. Spectra of received signals.

worked in pulse mode. The data were acquired into personal computer, digitized and saved in binary format. For each record the information about gain of amplifiers and position of transmitter were kept.

3. Characteristics of received signals.

Waveform of signal from transmitter located in forest at short distance is shown in Figure 1 (a). On the left and right sides is the same signal. Both pictures represent the beginning of transmitter pulse. On the right side the signal is shown in magnified scope to reveal the detail structure of registered signal. The transmitter was at a short distance and the level of signal is far more than the level of noise. So the signal has the pure sine form. The spectrum of this signal is shown in Figure 2(a). The width of spectral pick in Figure 2(a) is determined mainly by the length of emitted transmitter pulses. The pulse structure of emitted/received signals can be seen in Figure 1(d). Here the signal from transmitter located outside of forest at large distance is represented. In Figure 1(d) several pulses are shown. Because of the large distance the level of noise is compared with the level of useful signal. So the form of pulses in Figure 1(d) is masked by noise.

Signal from transmitter located in forest at middle distance is shown in Figure 1(c). As earlier on the left and right side is the same signal in different scales. In right side picture it is seen that signal contains small component of high frequency noise. This component grows with increasing of distance between transmitter and receiver. The larger distance the more the volume of noise component. The signal from transmitter located in forest at large distance is shown in Figure 1(e). High frequency noise component increases and becomes compared with the amplitude of useful signal. The spectra of signals from transmitter located in forest at middle and long distance are shown in Figures 2(c), 2(e). It is seen from comparison of right sides of Figures 1(a)÷1(d) that noise component can significantly distort the form of received signal.

Analysis of signals shows that noise component of signals differs for transmitter located in forest and outside of forest. The difference is understandable from comparison of right sides of Figures 1(c) and 1(d), where in the same scope the signals from transmitter located in forest and outside of forest are shown. The form of signal received from outside of forest transmitter is more pure than the form of signals received from the forest.

Although the spectrum of received signal with noise component can be very wide the spectral intensity of useful signal is more than the noise component in frequency range of useful signal. This allows to extract useful signal from total signal using narrow frequency band flittering. The spectra of filtered signals from transmitter located in forest at middle and large distances are shown in Figures 2(d), 2(f). It is seen that filtering removes from signal low and high frequency noise component. To reduce the influence of noise component on final results all signals were passed through narrow frequency band filter. Obtained data were statistically processed and average amplitude of useful signal was calculated.

4. Attenuation of radio waves in forest.

The results of measurements of attenuation of radio waves are shown in Figures 3,4, where are represented the plots of decreasing with distance of average amplitude of received signals for clear air propagation (Figure 3) and for propagation through the forest (Figure 4). The amplitude

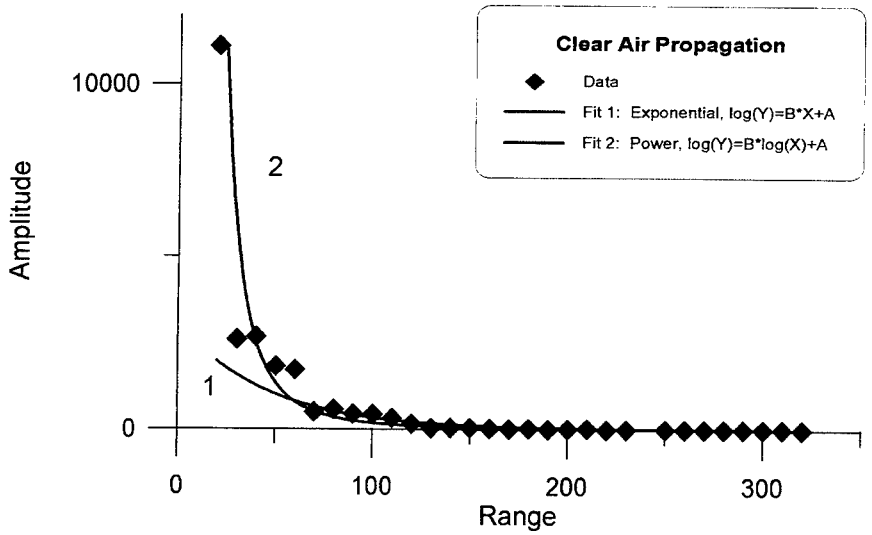

Figure 3. Attenuation of Radio Waves in Clear Air.

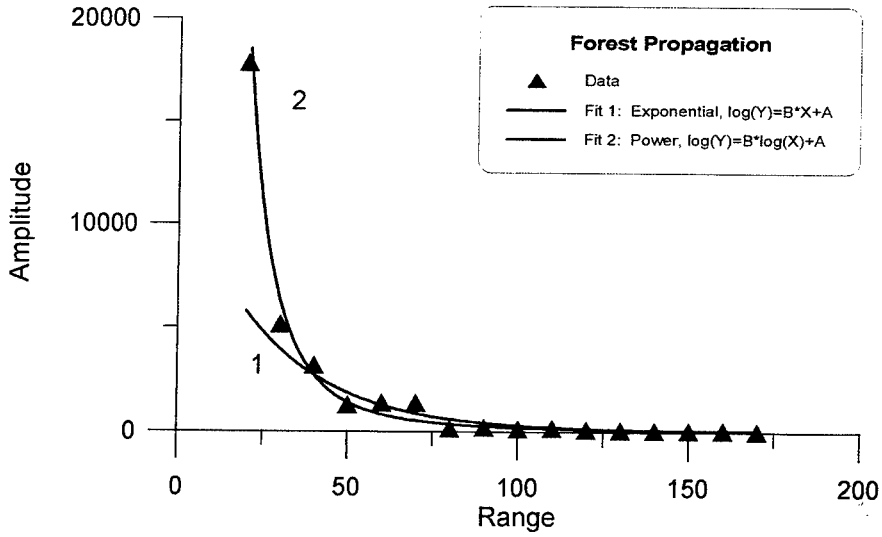

Figure 4. Attenuation of Radio Waves in Forest.

in figures is proportional to the strength of electrical field of received radio waves. In figure 3 the plot of attenuation of radio waves in clear air with exponential and power fits is represented. Similar plots for the case when transmitter was in forest are shown in Figure 4. The behavior of curves in both pictures is similar. The amplitude of signal reduces sharply with distance. Numerical analysis of experimental data gives extra 134 dB/km attenuation of radio waves in forest in comparison with clear air propagation.

The theoretical rate of attenuation of radio waves passing through trees can be evaluated from the expression [1], [2], [3]

$$L_p = -20 \log e^{-2\sqrt{\sigma} f} \tag{4.1}$$

where L_p - loss rate in dB/m, $e = 2.71828$, σ - conductivity in siemens, f - frequency in MHz. The family of curves representing path loss for various conductivities is available in [1]. Reversing (4.1) gives a convenient method of evaluation of conductivity σ using path loss data [1]. Under conditions of experiment the evaluation of L_p using (4.1) gives value $L_p = 152$ dB/km. This is enough good agreement with the value obtained from the experiment because conductivity σ of forest can be determined rather approximately.

5. Discussion.

Experimental data show strong attenuation of radio waves in forest. The distance of radio communication in forest for condition of experiment was almost in 2 times less than for clear air propagation. The numerical value of path loss obtained from experimental data is slightly less than evaluated for propagation through forest. From other side this value is far more than for the situation when the lateral wave could arise. Numerical analysis of asymptotes of curves of radio wave attenuation indicates faster than for lateral wave decreasing of wave amplitude with distance. Formation of lateral wave in forest is an attractive opportunity to increase the distance of radio communication. Conditions when lateral waves could arise should be investigated more thoroughly.

References

[1] Welch, C., Lemark, C., Corrington, L. (1995), A model for estimating electromagnetic wave attenuation in a forest (EWAF) environment. 11th Annual Review of Progress in Applied Computational Electromagnetics at Naval Postgraduate School, Monterey,CA, March 20-25, 1995. Conference Proceedings, 801-808.

[2] Losee, F.A., "The Influence of Trees on PLRS Communication Capability", Huges Aircraft Company, July 1978.

[3] Kivett, J.A., Diederichs, P.J., "PLRS Ground-to-Ground Propagation Test Technical Report (Draft)", Huges Aircraft Company, January 1980.

[4] Whitteker, J.H. (1994), The CRC VHF/UHF Propagation Prediction Program. Beyond Line-Of-Sight Conference, session 9, 2-4 august, Austin, Texas.

Statistical Reflection Properties of Electromagnetic Monopulse by Buried Objects in Subsurface Random Ground Using FD-TD

Yasumitsu MIYAZAKI and Yuki JYONORI

Toyohashi University of Technology
1-1,Hibarigaoka,Tempaku-cho,Toyohashi-shi,441 Japan
Phone 0532-47-0111 ext.576, Fax 0532-48-3422

1. Introduction

Recently microwave techniques incorporating advances in signal processing have been developing rapidly. In particular mapping of sub-surface random ground and detection of underground objects are important applications. As a consequence, underground radar systems which display the scattering field patterns of electromagnetic waves have become practical [1]-[4]. However due to randomness and inhomogeneous nature of the underground media, it is very difficult to analyse their characteristics accurately. In principle, it is necessary to study electromagnetic wave reflection and scattering under various conditions of underground media.

One of the most powerful methods of computational analysis applicable to such problems is the Finite Difference Time Domain (FDTD) method. In this paper we apply FDTD method to simulate the scattering characteristics of an underground media consisting of an air gap target region in the presence of randomly located obstacles. Numerical results are given for various cases of the medium properties like the medium electric permittivity and the number, size and location of obstacles.

2. Analysis Model

The two dimensional analysis model is schematically displayed in Fig.1 and a general FDTD modelling in Fig.2. We consider a rectangular region consisting of a target air-gap and obstacles located randomly relative to it. The figure shows that the origin is located at the ground level, implying that the mapping is conducted at a short distance above the ground. The shapes of air-gap as well as obstacles are rectangles. Typical numerical values considered are: 2.56m along x-axis, 0.44m above the ground, 2.56m below ground for the analysis region. The size of the air-gap is 1m x 0.5m and is located 0.5m below the ground.

The analysis corresponds to illuminating the region by an electromagnetic monopulse having spatio-temporal distribution, and analysing the reflected fields. This can be practically done by placing a planar antenna along the x-axis above the ground. The length of the antenna is typically 0.3m and is placed 0.1m above the ground. Except for the target air-gap and the obstacles which are random, the medium is considered non-dispersive and homogeneous with a relative permittivity ε_g=4.0.

3. Source Modelling

Source modelling essentially consists of choosing an appropriate current distribution function corresponding to illumination of the analysis region by a pulse wave from a planar antenna. This current distribution is the source term in the Maxwell's equations which determine the reflected and scattered fields along with the boundary conditions on the region. In order to illuminate a wide subsurface region of 0.3m long, the current source distribution is characterized by sinusoidal function in the spatial domain (x-direction) (Fig.3), and by a Gaussian function in the time domain (Fig.4).

$$J_y(x,t)=\begin{cases} A\sin\left(\frac{\pi}{L}x\right)\exp\left\{-a\left(\frac{t-3}{t_w}\right)^2\right\} & 0\le t\le t_w, 0\le x\le L \\ 0 & \text{otherwise} \end{cases} \qquad (1)$$

where A, a , t_w and L are 100, 30, 5nsec, 0.3m respectively.

4. FD-TD Method

Characteristics of electromagnetic waves are expressed by Maxwell's curl-equations. FD-TD method proposed by K.S.Yee[5] is used, in which these partial differential equations are approximated by difference equations first, and then the electric and magnetic fields are calculated mutually from initial

values at every incremental time Δt. For the two-dimensional model shown Fig.1, and Maxwell's curl-equations are transformed to the following difference equations.

$$H_x^{n+\frac{1}{2}}\left(p,q+\frac{1}{2}\right)=H_x^{n-\frac{1}{2}}\left(p,q+\frac{1}{2}\right)+C_1\left\{E_y^n(p,q+1)-E_y^n(p,q)\right\} \tag{2}$$

$$H_z^{n+\frac{1}{2}}\left(p+\frac{1}{2},q\right)=H_z^{n-\frac{1}{2}}\left(p+\frac{1}{2},q\right)+C_1\left\{E_x^n(p+1,q)-E_x^n(p,q)\right\} \tag{3}$$

$$E_y^n(p,q)=C_2E_y^{n-1}(p,q)-C_3J^{n-\frac{1}{2}}(p,q)+C_4\left\{H_x^{n-\frac{1}{2}}\left(p,q+\frac{1}{2}\right)-H_x^{n-\frac{1}{2}}\left(p,q-\frac{1}{2}\right)-H_z^{n-\frac{1}{2}}\left(p+\frac{1}{2},q\right)+H_z^{n-\frac{1}{2}}\left(p-\frac{1}{2},q\right)\right\} \tag{4}$$

$$C_1=\frac{\Delta t}{\Delta s\,\mu(p,q)} \tag{5}$$

$$C_2=\frac{1-\dfrac{\Delta t\,\sigma(p,q)}{2\,\varepsilon(p,q)}}{1+\dfrac{\Delta t\,\sigma(p,q)}{2\,\varepsilon(p,q)}} \tag{6}$$

$$C_3=\frac{\dfrac{\Delta t}{\varepsilon(p,q)}}{1+\dfrac{\Delta t\,\sigma(p,q)}{2\,\varepsilon(p,q)}} \tag{7}$$

$$C_4=\frac{\dfrac{\Delta t}{\Delta s\,\varepsilon(p,q)}}{1+\dfrac{\Delta t\,\sigma(p,q)}{2\,\varepsilon(p,q)}} \tag{8}$$

Where p and q are space coordinates, n is a time step number. And $\Delta x=\Delta z=\Delta s$ and Δt denote the spacial increment and temporal increment, respectively. These increments have to satisfy computational stability condition. So in this study, we set $\Delta s=0.01$m, $\Delta t=0.02$nsec.

We adopt the following absorbing boundary conditions due to G.Mur's[6], in order to replace the actual situation of infinite underground region by a finite sized rectangular region.

$$\left(\frac{\partial}{\partial \mathbf{n}}+\frac{1}{v}\frac{\partial}{\partial t}\right)E_y=0 \tag{9}$$

where **n** is out ward pointing normal on the boundary. And v is propagation velocity.

So, electric field Ey on the boundary X=0 is

$$E_y^n(0,q)=E_y^{n-1}(1,q)+C_5\left\{E_y^n(1,q)-E_y^{n-1}(0,q)\right\} \tag{10}$$

where

$$C_5=\frac{v\Delta t-\Delta s}{v\Delta t+\Delta s} \tag{11}$$

5. Statistical Representation of Random Medium

Statistically a random medium is represented by a multivariable random function with parameters representing the constants and variables of the medium including the obstacles and the target bodies within the region. In the present study the parameters are the electric permittivity, size and location of the obstacles which are random variables. Fourier analysis can be applied to this statistical representation by considering the complexity of random medium as an input data. If the input data is considered as a two dimensional random function $\varepsilon(p,q)$, where the integer variables p and q correspond to spatial and temporal coordinates in physical space, the Fourier spectrum that formally represents the complexity of random medium is given by

$$F(k,l)=\sum_{p=0}^{M-1}\sum_{q=0}^{N-1}\varepsilon(p,q)\exp\left(\frac{-2\pi jkp}{M}\right)\exp\left(\frac{-2\pi jlq}{N}\right) \tag{12}$$

Here $j=\sqrt{-1}$ and M and N denote the matrix size of the random data. k and l correspond to the two dimensional spatio-temporal frequency domain.

This spectrum can be normalized as follows:

$$F_n(k,l)=\frac{F(k,l)}{\sum_{r=0}^{M-1}\sum_{s=0}^{N-1}F(r,s)} \tag{13}$$

A limiting value of normalization can be obtained by considering an appropriate standard random medium. Thus a Gaussian distribution for the function $\varepsilon(p, q)$ is chosen as a suitable standard. Then

$$F_g(k,l) = \frac{1}{MN} \qquad (k = 0 \cdots M-1, l = 0 \cdots N-1) \tag{14}$$

For an arbitrary random function $\varepsilon(p, q)$, a formal estimation of the randomness can be given by the variance σ_f given as a deviation from the Gaussian case

$$\sigma_f = \sqrt{\sum_{k=0}^{M-1}\sum_{l=0}^{N-1}\{F_n(k,l) - E\}^2} \qquad \text{where} \quad E = \frac{1}{MN} \tag{15}$$

Another equivalent statistical representation is given by the two dimensional auto-correlation function defined by

$$g(m,n) = \sum_{x=0}^{M-1}\sum_{y=0}^{N-1}\varepsilon(x,y)\varepsilon(x+m, y+n)$$
$$= \mathrm{F}^{-1}\left\{|F(k,l)|^2\right\} \tag{16}$$

where F^{-1} indicates the inverse Fourier transform.

In this case an estimation of the medium randomness can be obtained from the Fourier transform of the auto-correlation function, by defining 1/e value of spectral intensity distribution as the indicative auto-correlation value.

Thus using Fourier analysis it is convenient to represent statistically various important features of the random medium such as the electrical permittivity of the obstacles, their size, spacing and so on.

6. Analysis Results

As specific examples of analysis, we consider a ground medium of relative electric permittivity ε_g=4, conductivity $\sigma_g = 10^{-7}$[s/m], permeability $\mu_g = \mu_o$ and

case 1: N = 400 obstacles each of size d < 10cm and $\varepsilon_r < 8$.

case 2: N = 400 obstacles each of size d < 10cm and $\varepsilon_r < 32$.

case 3: N = 200 obstacles each of size d < 10cm and $\varepsilon_r < 8$.

The models considered are shown in Figs.5-7 with their corresponding parameters displayed in Tables 1-3. The results of FDTD analysis are shown in Figs.8-10. Fourier power spectrum, auto-correlation function, spatial and temporal distribution of received signals are shown. We can understand various features from these figures.

As with the Fourier Power spectrum of the input data, observing Fig.8(a) and Fig.9(a), we see that the variance σ_f drops to very low value (σ_f:0.028→0.0078) as the relative electric permittivity ε_r increases four times (ε_r:8→32). This is when other parameters remain same i.e., for N = 400 obstacles each of size less than d < 10cm. Observing Fig.8(a) and Fig.10(a), where the number of obstacles alone is halved (N:400→200), σ_f increases (σ_f:0.028→0.040) showing a reduced randomness.

Observing the auto-correlation contour plots we do not find a change in the characteristics when there is change only in ε_r (Fig.8(b), Fig.9(b)), showing its independence with the number and size of the obstacles. As the number of obstacles reduces (Fig.8(b) and Fig.10(b)) we observe a spread showing again a reduced randomness.

Observing the time response of the received signal (Figs.8(f),9(f),10(f)) we confirm that detection of air-gap is easy when the randomness is not significant. For instance we can see the peak due to air-gap clearly in Fig.10(f) where σ_f=0.040 is high. As the medium becomes more random, a reduction in σ_f, it is difficult to identify the air-gap (Fig.8(f)). In Fig.8(c-d),9(c-d),10(c-d), we display three dimensional plots of electromagnetic fields showing the phenomena of reflection from air-gap. The time instants are chosen closer to be around the reflection phenomena. We are unable to identify the air-gap clearly when the medium is complicated.

From this analysis we conclude that it is possible to understand the underground conditions statistically using the Fourier analysis of the medium conditions and estimating the auto-correlation of the medium.

7. Conclusion

Statistical representation of a random medium is done, and the relationship between the received signal and the medium is established. The analysis may be further developed in many ways like increasing the accuracy and speed of the FDTD algorithm, extending to three dimensional cases, incorporating more randomness and parameters and considering the cases much closer to practical conditions. Improvements can also be accomplished through more sophisticated signal processing of the received signal patterns.

Reference

[1] T.Suzuki:J.IEICE,vol.37,No.3,pp308-311,(1984-3)
[2] Y.Nagashima et al:IEICE of Japan,Trans.vol.J74-C-II,No.5,pp317-324,(1984-3)
[3] H.Dobashi et al:T.IEE Japan,vol.109-D,No.12,pp937-943,(1989-12)
[4] Y.Michiguchi et al:IEEE Trans on GRS,vol.26,No.6,pp733-740,(1988-11)
[5] K.S.Yee:IEEE Trans on AP,vol.14,No.3,pp302-307,(1966-5)
[6] G.Mur:IEEE Trans on EMC,vol.23,No.4,pp1073-1077,(1981-11)
[7] Y.He et al:IEICE of Japan,Trans.vol.J76-B-II,No.4,pp245-252,(1993-4)
[8] K.Taketomi and Y.Miyazaki:Proc.ISAP,Sapporo,Japan,PP1249-1252
[9] J.Sonoda and Y.Miyazaki:Int.Symp.EMC,Sendai,Japan,PP382-385(1994-5)
[10] J.Sonoda and Y.Miyazaki:Optical Fiber Science and Electromagnetic Theory.(1995-10)

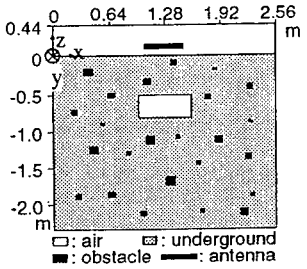

Fig.1 Analysis Model

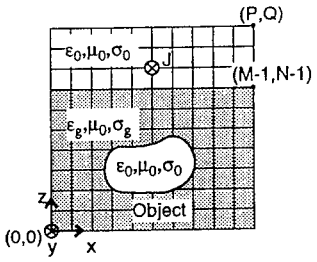

Fig.2 Divide of Feild

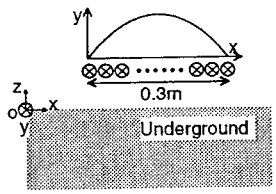

Fig.3 Source Model

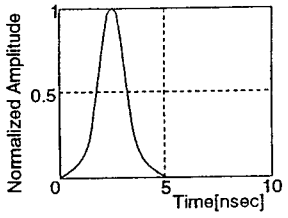

Fig.4 Incident Pulse

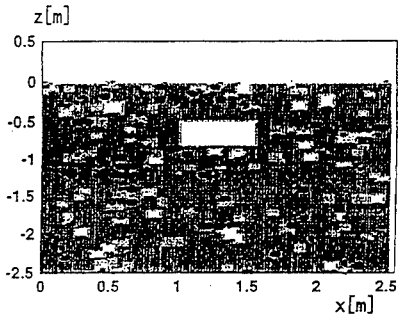

Fig.5 Underground random model: case 1

Table1 Position of Obstacles(Case 1)

	X axis	Z axis	Size	εr
1	2.13	-1.81	0.060	1.68
2	1.41	-1.07	0.070	7.15
⋮	⋮	⋮	⋮	⋮
400	0.54	-1.13	0.070	7.95
Max	2.45	-0.01	0.090	8.97
Min	0.00	-2.56	0.010	1.02
Mean	——	——	0.051	5.06

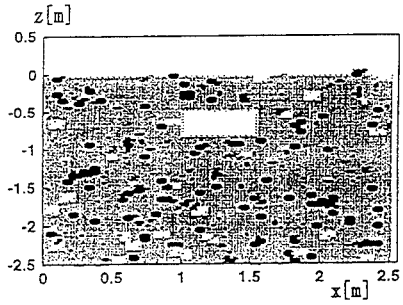

Fig.6 Underground random model: case 2

Table2 Position of Obstacles(Case 2)

	X axis	Z axis	Size	εr
1	1.62	-2.28	0.060	5.19
2	2.06	-1.02	0.010	28.6
⋮	⋮	⋮	⋮	⋮
400	0.34	-1.32	0.090	29.5
Max	2.45	-0.02	0.090	32.9
Min	0.01	-2.56	0.010	1.03
Mean	——	——	0.049	16.6

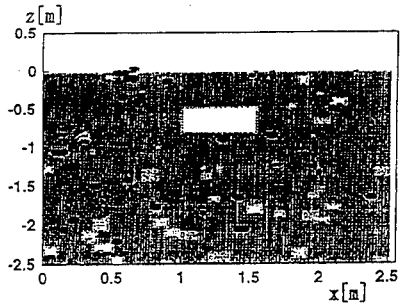

Fig.7 Underground random model: case 3

Table3 Position of Obstacles(Case 3)

	X axis	Z axis	Size	εr
1	2.33	-1.71	0.080	8.39
2	0.99	-1.15	0.070	6.88
⋮	⋮	⋮	⋮	⋮
200	0.33	-1.10	0.070	3.63
Max	2.44	-0.02	0.090	8.93
Min	0.01	-2.56	0.010	1.04
Mean	——	——	0.047	5.03

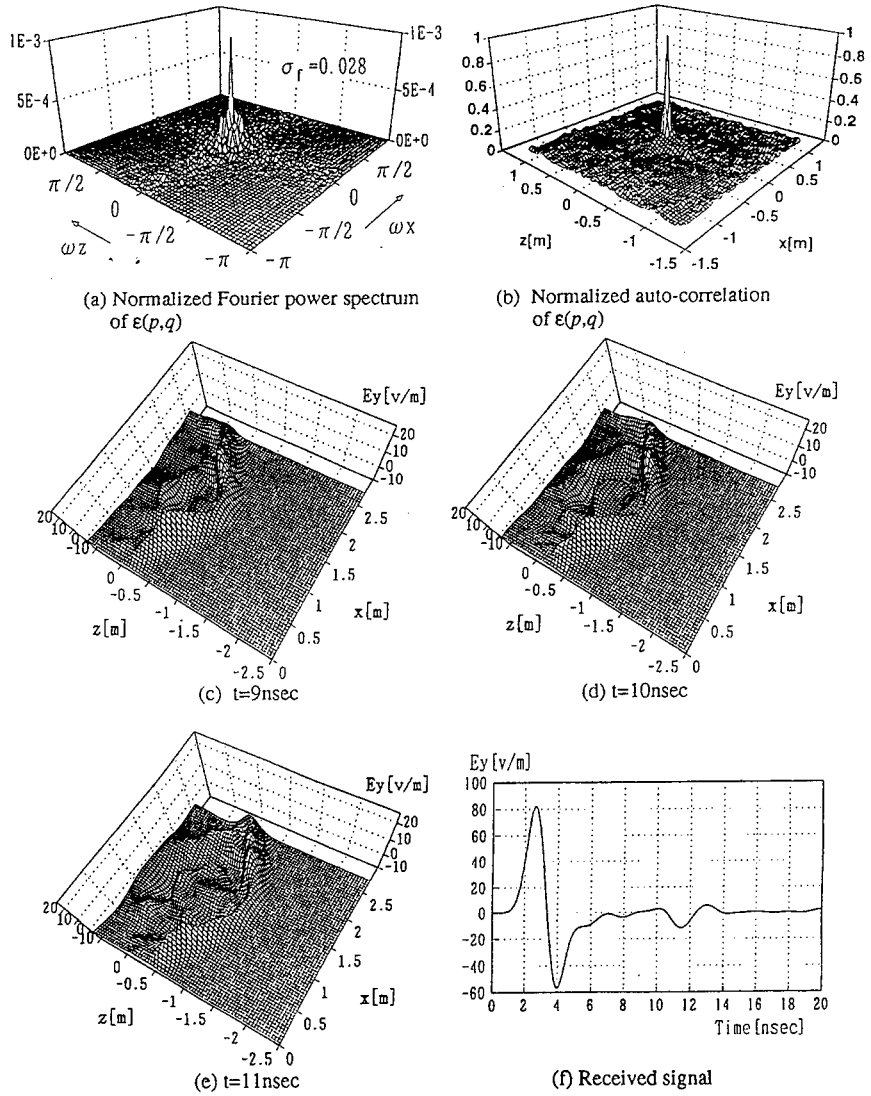

(a) Normalized Fourier power spectrum of $\varepsilon(p,q)$

(b) Normalized auto-correlation of $\varepsilon(p,q)$

(c) t=9nsec

(d) t=10nsec

(e) t=11nsec

(f) Received signal

Fig. 8 Analysis results of underground random model in the case 1. $\varepsilon(p,q)$ is the relative electric permittivity in the underground. (c)~(e) show time response of Ey in the analysis region, and (f) time response of Ey at the observation point(1.28,0.1).

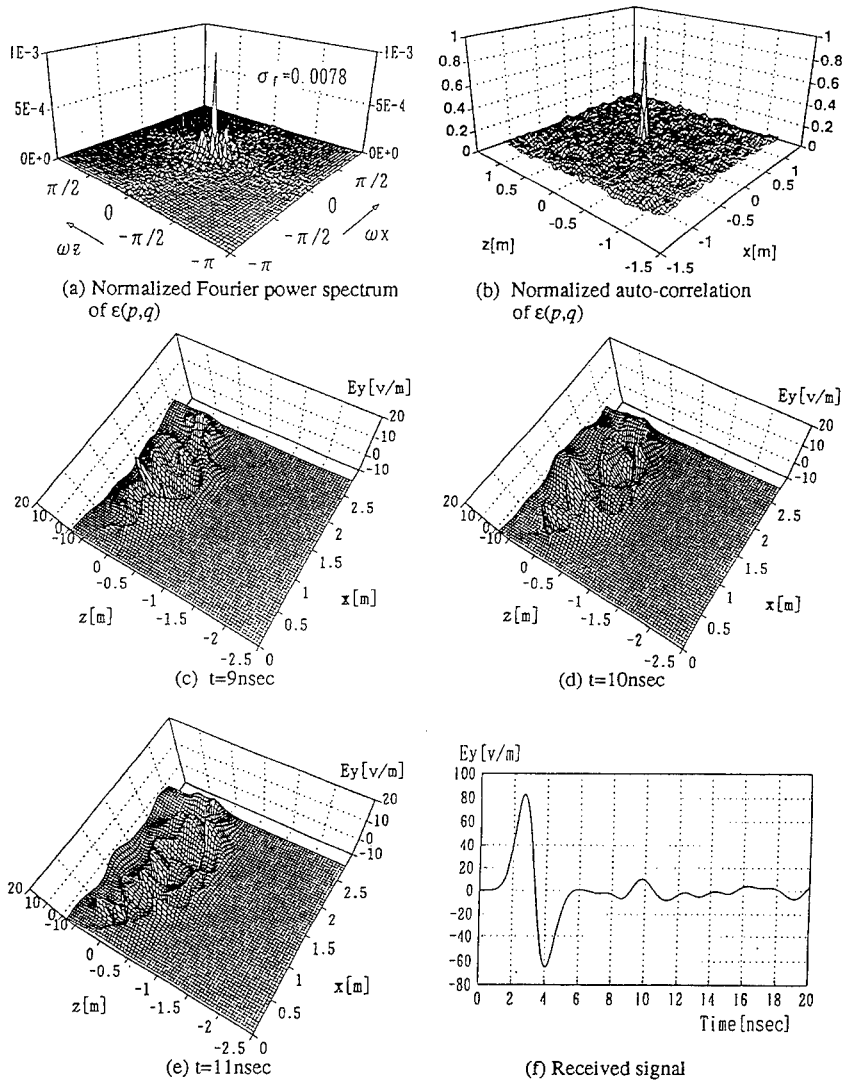

(a) Normalized Fourier power spectrum of $\varepsilon(p,q)$

(b) Normalized auto-correlation of $\varepsilon(p,q)$

(c) t=9nsec

(d) t=10nsec

(e) t=11nsec

(f) Received signal

Fig. 9 Analysis results of underground random model in the case 2. $\varepsilon(p,q)$ is the relative electric permittivity in the underground. (c)~(e) show time response of Ey in the analysis region, and (f) time response of Ey at the observation point(1.28,0.1).

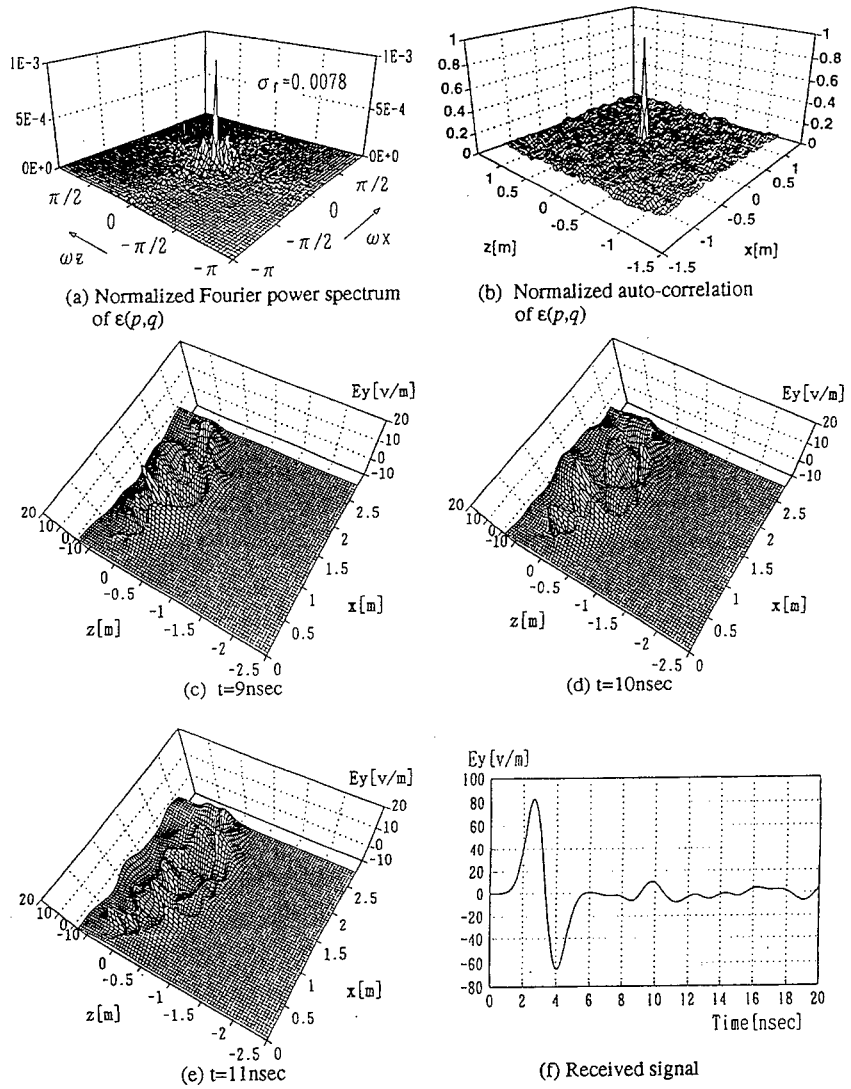

(a) Normalized Fourier power spectrum of $\varepsilon(p,q)$

(b) Normalized auto-correlation of $\varepsilon(p,q)$

(c) t=9nsec

(d) t=10nsec

(e) t=11nsec

(f) Received signal

Fig. 9 Analysis results of underground random model in the case 2. $\varepsilon(p,q)$ is the relative electric permittivity in the underground. (c)~(e) show time response of Ey in the analysis region, and (f) time response of Ey at the observation point(1.28,0.1).

SESSION 7:

FDTD APPLICATIONS AND ENHANCEMENTS

Chair: J. Beggs

UHF/VHF Propagation Model Characterization over Irregular Terrain using MoM/FDTD

Keith A. Lysiak*
The Applied Research Laboratory
The Pennsylvania State University
P.O. Box 30
State College, PA 16804

James K. Breakall
The Electrical Engineering
Department
The Pennsylvania State University
University Park, PA 16802

James Zmyslo
Kaman Sciences Corp.
2560 Huntington Ave.
Alexandria, VA 22303

Abstract

A hybrid Method of Moments/Finite Difference Time Domain (MoM/FDTD) approach is used to characterize UHF/VHF propagation over irregular terrain. The effect of terrain on path loss is examined. Of particular interest is the shadow region behind the hills. The standard NEC-4 MoM code is used to determine the fields propagated by the antenna over flat earth. A two dimensional FDTD code is used to calculate the fields in the area of the terrain feature. The vertical field calculated by FDTD is converted to path loss for display.

I. Introduction

The military community has a strong interest in UHF/VHF propagation. To enable military planners to position communication resources, a knowledge of path loss over irregular terrain must be obtained. With recent improvements to propagation models and computers, the military planners have been overwhelmed with solutions to this problem. These improvements have made it possible for communication officers to quickly calculate the path loss from several models to use as inputs to planning. Trade-offs must be made in the selection of the model used such as calculation time versus accuracy. With limited theoretical knowledge in the area of electromagnetics, and the significant differences in the answers given by various models, reliable planning becomes very difficult.

When considering the complexity of a real earth environment, it is apparent that even the experienced propagation specialist would have difficulty based only on the information supplied by the models. After considerable research into the theory used in each model, one can begin to conjecture on the various mechanisms that each model can predict accurately. For example, a particular model may only calculate reflections and not diffraction. Though it is commonly known that this is not the correct solution, it may be accurate enough for a particular use. The problem is complicated by the interactions between individual mechanisms.

II. Specific Problem

In support of the Radio Frequency Mission Planner (RFMP), the Naval Information Warfare Activity (NIWA) has implemented the RFMP Model Characterization Program. The RFMP includes several UHF/VHF propagation models that predict terrain effects. These models are based on different theories such as Geometric Theory of Diffraction (GTD) [1], knife-edge diffraction [2] and Parabolic Equation (PE) [3]. This program was implemented to characterize how well these models perform. A generalized measurement campaign would be costly and include many uncontrollable variables. Given the computer resources on hand, Finite Difference Time Domain (FDTD) was a viable option for a first look at simple scenarios.

The purpose of this project is to establish a rule set for the UHF/VHF propagation models and to assist in developing a measurement system. The path loss predicted by the propagation models will be compared to those predicted by the Method of Moments / Finite Difference Time Domain (MoM/FDTD) approach and color contour plots showing the differences will be presented. In other words, this research provides a "yard stick" with which to compare the propagation models to determine their characteristics. That yardstick is the MoM/FDTD approach.

III. The MoM/FDTD Approach

The hybrid MoM/FDTD approach was developed to characterize UHF/VHF propagation models. FDTD is a complete solution to Maxwell's curl equations [4]. When properly implemented, FDTD includes the effects of diffraction, reflections, surface waves, and all others. FDTD has been shown to be extremely accurate for scattering calculations [5]. The unusual application in this case involves calculations over an infinite half-plane of lossy dielectric. FDTD by itself can provide very good results for small propagation problems. Two of the main limitations of FDTD are speed and memory requirements. For this application, the only reasonable solution is to calculate only small portions of the area with FDTD. The fields produced by MoM, which take into account both the antenna pattern and the effects of the ground plane, are used to excite the FDTD space. The FDTD portion of the code then calculates the electric fields in the area of the terrain feature.

IV. Typical Real Scenario

A basic set of scenarios was chosen that could provide good terrain characterization. The models are compared on the basis of path loss in the area of a two-dimensional cross section of terrain. The scenarios consist of 10 kilometer flat paths between the transmitter and a terrain feature (i.e. hill). The transmitter is a vertical dipole placed at the origin. The hill is 150 meters wide and 100 meters high (approximately 30 wavelengths). The hill is modeled as a simple wedge or gaussian curve. Double hills are also examined. The ground constants are those of average earth: relative dielectric constant of 13 and conductivity of 0.005 Siemens/meter. The ground is homogeneous. The skin depth is approximately 3.8 meters and the loss tangent is approximately 0.07 [6].

The coordinate system is defined as follows. The radial distance from the antenna will be along the x-axis. The elevation is along the y-axis. The non-varying coordinate of the 2-D system is the z-axis. The ground is in the x-z plane.

V. MoM Implementation

The standard Numerical Electromagnetics Code (NEC)-4 is a widely accepted MoM antenna modeling code [7,8]. It is used here to calculate the fields produced by a vertical antenna over an infinite ground plane. A half-wavelength vertical dipole is modeled at a frequency of 100 Megahertz and located one wavelength (3 meters) above ground. The ground parameters are relative dielectric constant of 13.0 and conductivity of 0.005 Siemens/meter. The Sommerfeld/Asymptotic method is used for the ground to include the surface wave. An excitation of 1 watt is used. The Near Electric Field (NE) option is used to calculate the electric fields along a vertical line 10 kilometers from the transmit antenna. The vertical spacing of 2000 samples is 40 per wavelength or 0.075 meters.

The magnitude and phase of the incident electrical field is used to excite the FDTD space. The NEC samples are located at the center of each vertical FDTD cell. For simple antennas near the ground and far from the FDTD space, a single vertical slice is sufficient since the horizontal magnitude variation of the incident field over the FDTD area is small (about 1/2 dB). This is a very important point. If the

radiation from the antenna is not propagating primarily along the ground plane this method may not work well. The assumption that the magnitude of the incident field has very little variation along the horizontal direction, leads to this simple excitation. If the fields were propagating diagonally across the FDTD calculation space, a more complex incident field would have to be developed. The radial variation of the phase is calculated analytically by the FDTD code.

The NEC code is also used to calculate the free-space fields in the area of interest. This is an area 250 meters horizontally and 150 meters vertically. It is sampled on a 1 meter by 1 meter grid. This information is used later along with the FDTD calculated fields to produce path loss [3].

VI. FDTD Implementation

The two-dimensional FDTD space includes a terrain feature such as a gaussian hill. The source input from the NEC MoM code is used to excite the FDTD space. This will require a steady-state FDTD code since NEC will only provide fields for one frequency.

A two-dimensional FDTD code is used based on a scattered field formulation and uses a Liao second order outer radiation boundary condition [4]. Several areas of the original 2-D FDTD code have been modified. The major modification involves the source field. The FDTD calculation space must be excited by an incident field. This will be derived from MoM calculations over flat earth. The code originally used an exponentially ramped steady-state plane wave with an specified angle of incidence. This was modified to read in an input file of magnitude and phase along the y-axis and propagated in the x direction. This input is linearly ramped in magnitude and propagated from outside the FDTD space in a similar manner as the original source. This method of introducing the source reduces transient fields, but significantly increases calculation speed. The code was also hard-coded for propagation along the ground plane or x-axis. Subroutines have been added to sample the x and y components of the electric field. All FDTD calculations are transverse electric (TE). The field components included are Ex, Ey and Hz. Square cells are used.

A ten cell layer of real earth cells are placed along the lower edge of the FDTD space. This basically nullifies the lower free space boundary condition. Due to the fact that propagation is primarily in the x direction and upward from the hill, this provides an adequate lower boundary. This method worked very well and was simple to do. An alternate method of redefining the lower and corner boundary conditions was not found to be necessary at this time.

The terrain feature or hill is built of real earth cells on top of this ground plane. A secondary hill is built inside the first hill. This hill is built of Perfect Electric Conductor (PEC) material and is kept at least two skin depths inside the first hill. Since the fields at this point inside the real earth hill have dropped by about 20 dB, the PEC hill has little effect on the fields in free space but greatly reduces calculation time. This reduction in time is due to the simplicity of the PEC update equation. This also reduces possible error fields, caused by grid dispersion, from passing through the hill. The overall effect of this is similar to the use of a Surface Impedance Boundary Condition (SIBC) which has not yet been implemented. But due to the size of the calculation space, grid dispersion errors are significant [9]. It has been found that 30-40 cells per wavelength are required to reduce this error sufficiently and obtain good results in the shadow region. Although calculation times could be reduced, little memory savings would be gained by implementing a SIBC, since 40 cells per wavelength are required for these ground parameters.

Current computer resources consist of an HP 9000/755 UNIX workstation with 128 megabytes of memory. Trial FDTD runs indicate a 40 MFLOP calculation rate. The maximum terrain feature size is determined by the frequency and computer memory. Calculations are conducted at 100 megahertz. Using typical ground constants of 13 for relative dielectric constant and 0.005 Siemens/meter for conductivity,

requires a cell size of 0.075 meters (40 cells per wavelength). This allows approximately seven million cells in memory. Initial calculations show that good results can be obtained by running the FDTD code for three times the number of time steps as there are horizontal cells. This will allow a calculation space of 45,000 square meters (150 meters by 250 meters) and require approximately 33 hours to run. The original code required 78 hours for this calculation.

Due to the size and number of cells used, 3000 horizontally by 2000 vertically, sampling of all cells was not required for good resolution plots. Therefore the fields are sampled on a 1 meter by 1 meter grid. The samples are taken at two time intervals near the end of the FDTD run and one-quarter time cycle apart. This data is written to an external file. These fields are then processed to determine the magnitude and phase of the steady-state field and the path loss. This provides a plot of 250 by 150 points. Since the objects are very large, stair casing is negligible. The staircasing of the terrain appears coarser in the plots than the actual FDTD calculation space.

VII. Results

The FDTD code was tested against the exact solution [6] for a 2-D cylinder. The cylinder had a diameter of 30 meters (10 wavelengths at 100 megahertz). These results were excellent. It was also shown that a half cylinder over an "infinite" plane will also give correct results. This shows that some special problems can be run with FDTD using a half-space.

The FDTD code was also tested against the Numerical Electromagnetic Code - Basic Scattering Code (NECBSC), Version 3 [10]. A flat plate 30 meters (10 wavelengths at 100 megahertz) high was illuminated with a plane wave. Extremely good results were obtained. Once again, half the plate was placed above an "infinite" plate with very good results.

The next test case involved a half-wave vertical dipole placed one wavelength above a ground plane. The antenna was placed inside the FDTD space. The space was 60 meters by 30 meters. The space included a 15 meter by 15 meter PEC wedge. The x and y components of the electric field were compared on an interval of one tenth of a wavelength. This case was run with NECBSC and FDTD. The results were very similar, but NECBSC showed very distinct shadow and reflection boundaries as expected from UTD theory.

Finally, the NEC input was used. The same half-wave vertical dipole was modeled one wavelength above the ground and 10 kilometers from the FDTD calculation space. A large problem space of 250 meters by 150 meters was run with good results. The first hill was a simple wedge. This hill was run with NECBSC and MoM/FDTD. Both PEC and real earth materials were used and only subtle differences appeared with different materials. The comparisons between models were very good. The major difference was in the shadow region where MoM/FDTD shows an interference pattern of +/- 3dB. See Figure 1.

A single real earth gaussian hill was also modeled. This hill showed very similar effects from the MoM/FDTD result for wedge. See Figure 2. This was expected due to the similarity in the shapes. This case could not be modeled using NECBSC because the hill was made up of multiple plates and Version 3 of NECBSC does not include multiple diffractions. Double gaussian hills were also modeled with expected results.

VIII. Conclusions

Several sample objects have been modeled using the 2-D FDTD code and the MoM/FDTD hybrid approach. These objects include scatter type objects (i.e. cylinders and plates) and terrain objects (i.e. wedges and gaussian hills). The FDTD results were compared against NECBSC and exact results. These

results show extremely good comparisons. It has been shown that a MoM/FDTD hybrid approach can be applied to UHF/VHF terrain propagation problems and provide extremely detailed and accurate results. This is definitely not the end of this area of work but just the beginning. More efficient and elegant ways of applying these methods can be applied. There are also other areas of applications such as rough surfaces and inhomogeneous materials.

IX. Acknowledgments

Special thanks go to NIWA, specifically CDR John O'Dwyer, for sponsoring this research. Also, thanks go to my advisor at Penn State, Dr. James Breakall, and my supervisor at ARL, Allan Sonsteby. I would also like to thank Dr. Raymond Luebbers of Penn State for his assistance and supplying the original 2-D FDTD code.

James Zmyslo was formerly at the Naval Information Warfare Activity, 3801 Nebraska Avenue, NW, Washington, DC 20393.

X. References

[1] J. Keller, "Geometric theory of diffraction," J. Opt. Soc. of Amer., 52 ,116, 1962
[2] J. Deygout, "Multiple Knife-Edge Diffraction of Microwaves," IEEE Trans. Ant. Prop., 14, 480, 1966
[3] F. Ryan, "User's Guide for the VTRPE (Variable Terrain Radio Parabolic Equation) Computer Model," Naval Ocean Systems Center (NOSC), 1991
[4] K. Kunz, R. Luebbers, *Finite Difference Time Domain Method for Electromagnetics*, CRC Press, Boca Raton, 1993
[5] R. Luebbers, K. Lysiak, M. Husar, S. McClure, "Validation of FDTD Scattering from Realistic Targets: Generic Missile," 1994
[6] C. Balanis, *Advanced Engineering Electromagnetics*, Wiley, New York, 1989
[7] G. Burke, "Numerical Electromagnetics Code - NEC-4, Method of Moments, Part I: User's Manual," Lawrence Livermore National Laboratory, 1992
[8] G. Burke, "Numerical Electromagnetics Code - NEC-4, Method of Moments, Part II: Program Description - Theory," Lawrence Livermore National Laboratory, 1992
[9] A. Taflove, *Computaional Electrodynamics - The Finite-Difference Time-Domain Method*, Artech House, 1995
[10] R. Marhefka, J, Silvestro, "Near Zone - Basic Scattering Code User's Manual with Space Station Applications," ElectroScience Laboratory, 1989

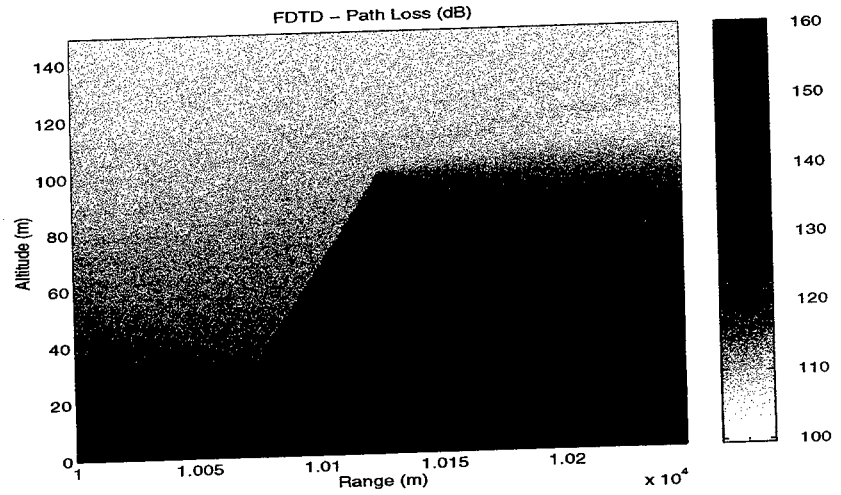

Figure 1. MoM/FDTD results for simple wedge.

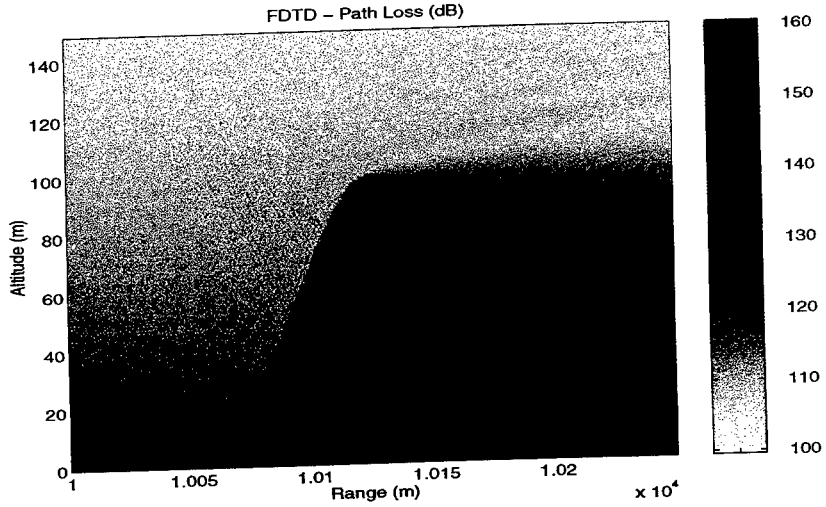

Figure 2. MoM/FDTD results for gaussian hill.

Validation of FDTD Modeling of Ground-Penetrating Radar Antennas

Brian J. Zook
Southwest Research Institute
P.O. Drawer 28510
San Antonio, TX 78228-0510
bzook@swri.edu

Introduction

Ground-penetrating radar (GPR) is commonly used for detecting buried objects. Antenna design, soil parameters, and target characteristics all strongly influence the effectiveness of any GPR system. Until recently, optimal GPR designs required extensive measurements and design iterations. Modeling offers the promise of finding quality designs before the expensive construction of prototypes.

We are using the finite-difference time-domain (FDTD) method to model GPR antennas. There are several advantages to using FDTD modeling for this applications. First, FDTD can model the fields inside the soil, which is a dispersive (and dissipative) dielectric. Second, the general and flexible nature of FDTD allows us to model complex antennas, targets (conducting and non-conducting), and possible soil inhomogeneities in a single model [1]. A third advantage is that we can find the broadband response of a system by using pulsed excitation, that is, with a single FDTD calculation. Thus we can model pulsed GPR systems directly, as well as stepped-frequency and swept-frequency systems using post-processing. We are using the damped Higdon's outer radiation boundary condition, which can model dispersive media, including the air/soil interface [2].

In this paper we present some validation results of FDTD models of GPR antennas, comparing 3D FDTD models with NEC results and analytic results. We show comparisons of the actual fields (magnitude and phase) in both the ground and the air over a broad frequency range. Field plots are our primary means of comparison, although a few quantitative measures are used.

Vertical Infinitesimal Antenna Over the Earth

Few GPR antennas have an analytic field solution. An exception is a vertical infinitesimal antenna over a lossy dielectric earth. King derived formulas for the (near-field and far-field) fields, both in the earth and above it, produced by an infinitesimal dipole located over the earth [3,4]. Simply stated, the fields are the sum of three contributions: a direct wave, an image wave, and a lateral (surface) wave. The lateral wave contribution uses a numerical integral.† The fields are proportional to I*dl, the product of the impressed driving current and the antenna length. We calculate the fields at the frequencies of interest, using the currents found in the NEC model.

†The lateral wave can be approximated using Fresnel integrals in the far-field, but we are looking at near-field effects in this paper.

The FDTD model of the infinitesimal dipole uses a single FDTD component (E_z) driven by a pulsed source. The frequency-domain view of the excitation voltage is shown in Figure 1. There is reasonable energy over the range 50-650 MHz; we can perhaps use up to 800 MHz. The cell size in all three dimensions was 1 cm. We are using a scattered-field formulation code derived from the Penn. State code [5]. We are not using the thin-wire enhancement, however, since we do not use it in our modeling of larger GPR antennas. The results shown in this paper use a 47x89x80 cell space running for 3000 timesteps, which took a little over 7 hours to run on a Sun SPARC2-class machine.† The lower 30 layers of the FDTD volume was filled with a dielectric earth having the properties ϵ=9 and σ=0.1 S/m. The center of the dipole was 4.5 cm above the earth, coordinates (0,0,4.5).

We are using NEC4D, the double-precision version of NEC-4, since we are modeling very short dipoles. The NEC model of the infinitesimal dipole uses a single unloaded segment, excited using the applied-field excitation, sitting over the lossy earth, which is modeled using the Sommerfeld/Asymptotic approach. The radius was 3.2 mm, which we found empirically to yield the same impedance as the FDTD model.

We compared the fields at 24 locations, 12 in the air and 12 in the ground. In general, there was similar agreement at all the locations, although space does not allow us to show all the results here. The magnitude and phase comparisons for the z-component of the electric field in the air at (20,0,4.5) are shown in Figures 2 and 3. The magnitude and phase comparisons for the z-component of the electric field in the air at (20,0,-14.5) are shown in Figures 4 and 5.†† The basic shapes of the magnitude plots are the same for the different methods, although the actual magnitudes are slightly different. We believe this is due to the different approximations being used. For example, the analytic solution considers the current to be constant along the dipole while NEC uses a sinusoidal current. For the two locations shown, the FDTD and analytic solutions agree to within 3.8 dB and 11° over 25-700 MHz.

Vertical Finite Dipole Over the Earth

We are really interested in using FDTD to model finite antennas. So as a validation test, we examined the fields from an 11-cm long vertical center-driven dipole. The center of the dipole was located 9.5 cm above the earth. This was modeled as 11 cells in FDTD and 11 segments in NEC (again with 3.2 mm radius). For the analytic formulation, we found the fields as the superposition of 11 infinitesimal dipoles, with the currents being supplied by the results of the FDTD model. We could have used the currents from the NEC model, but the radius we used in the NEC model resulted in a slightly (10-15%) higher antenna susceptance in the NEC model than in the FDTD model.

Again, we compared the fields in several locations, only a few of which we show here. Figures 6 and 7 show the magnitude and phase comparisons for the z-component of the electric field at (20,0,9.5). The FDTD and analytic methods show remarkable agreement, particularly considering we are using the analytic

†We probably could have ended the runs after only 2000 timesteps

††The field locations are the locations of the sampled FDTD fields, which are offset by one-half cell in the staggered-grid formulation we are using.

method in a somewhat questionable fashion. The NEC result is vastly different, however. Figures 8 and 9 show the magnitude and phase comparisons for the z-component of the electric field at (20,0,-14.5). Again the same observations apply. The NEC formulation apparently does not include the lateral wave when calculating the electric field. Indeed, the NEC-4 User's Guide contains figures showing the error at grazing incidence, which is where the lateral wave contribution is more important. The NEC result for the x-component at (20.5,0,-15), shown in Figure 10, is much closer to the other two methods. We believe this is due to the lateral wave contribution being less important for the x-component at that position. Furthermore, it appears that NEC is properly calculating the dipole currents, just not the resultant electric fields. For these cases, the FDTD and analytic solutions agree to within 1.4 dB and 23° over 25-700 MHz.

Conclusions

We have compared results from FDTD, NEC, and an analytic solution for two vertical dipole cases. The results show the FDTD method is modeling the fields produced by the antennas near and in the ground with reasonable accuracy, certainly sufficient for the insight we need as we design GPR systems. One lesson learned in this study was that NEC will not be as helpful as we had hoped in studying and validating more complex antenna models for GPR applications due to the approximations made in calculating the fields, although these approximations are accurate for most applications of NEC.

References

1. Brian J. Zook, "FDTD Modeling of Ground-Penetrating Radar Antennas," *Proc. Eleventh Annual Review of Progress in Applied Computational Electromagnetics*, March 21-24, 1995, Monterey, CA, Volume II, pp. 740-747.

2. Brian J. Zook, "A Dispersive Outer Radiation Boundary Condition for FDTD Calculations," *Proc. Tenth Annual Review of Progress in Applied Computational Electromagnetics*, March 22-25, 1994, Monterey, CA, Volume I, pp. 240-247.

3. Ronold W.P. King, "The Electromagnetic Field of a Vertical Dipole over the Earth or Sea," *IEEE Trans. Antennas Propag.*, vol. 42, no. 3, 382-389, March 1994.

4. Ronold W.P. King, Margaret Owens, and Tai Tsun Wu, *Lateral Electromagnetic Waves*, Springer-Verlag, 1992.

5. Karl S. Kunz and Raymond J. Luebbers, *The Finite Difference Time Domain Method for Electromagnetics*, CRC Press, 1993.

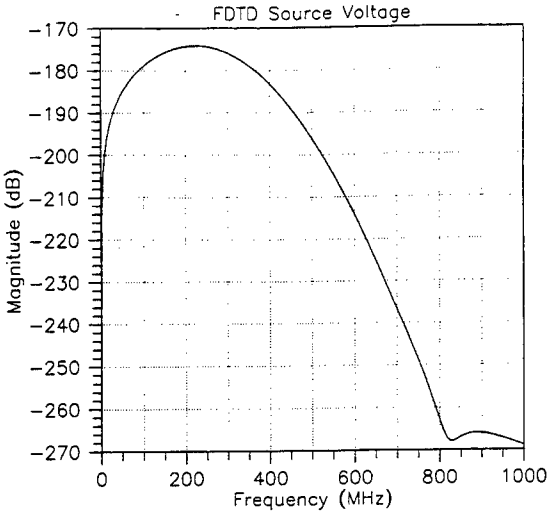

Figure 1. The amplitude spectrum of the excitation pulse used in the FDTD runs. FDTD results were divided by this spectrum to get the frequency response shown in the figures, as if the antennas were driven by 1 V/m at each frequency.

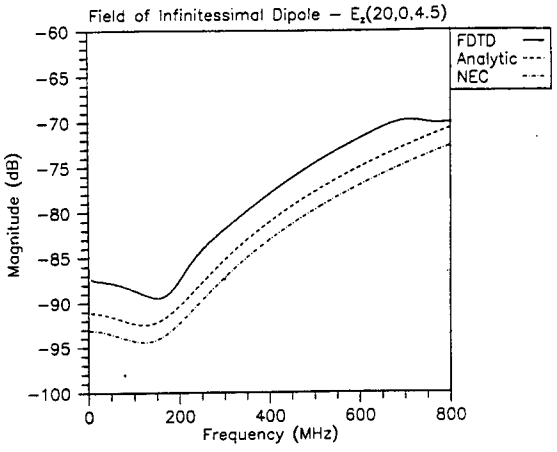

Figure 2. The magnitude of the Z-component (vertical) of the electric field 20 cm away from the infinitesimal dipole and 4.5 cm above the ground (same height as the center of the dipole)

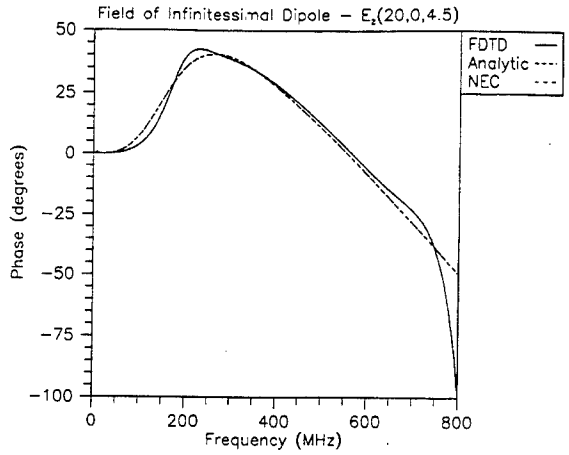

Figure 3. The phase of the Z-component of the electric field 20 cm away from the infinitesimal dipole and 4.5 cm above the ground (same height as the center of the dipole). The NEC and Analytic phase curves are too close to distinguish.

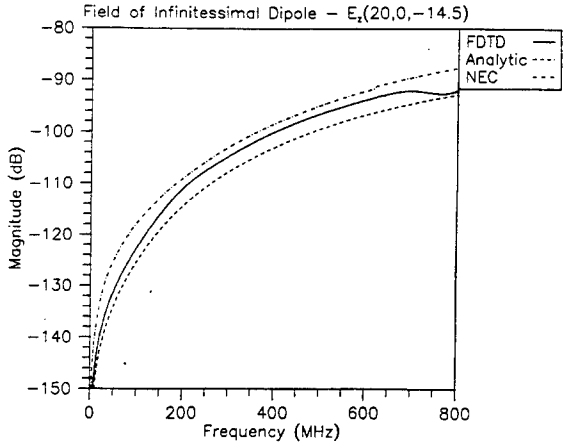

Figure 4. The magnitude of the Z-component of the electric field 20 cm away from the infinitesimal dipole and 14.5 cm below the ground surface.

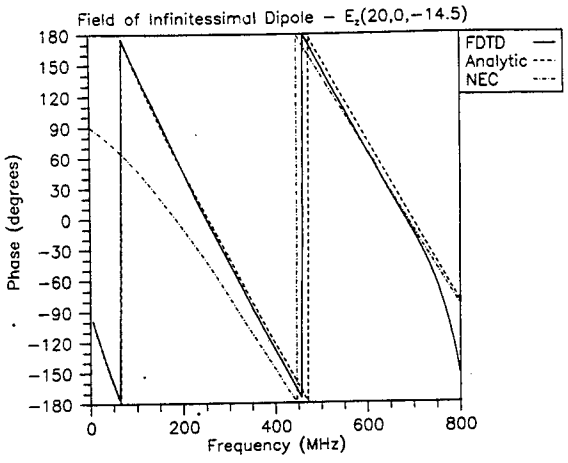

Figure 5. The phase of the Z-component of the electric field 20 cm away from the infinitesimal dipole and 14.5 cm below the ground surface.

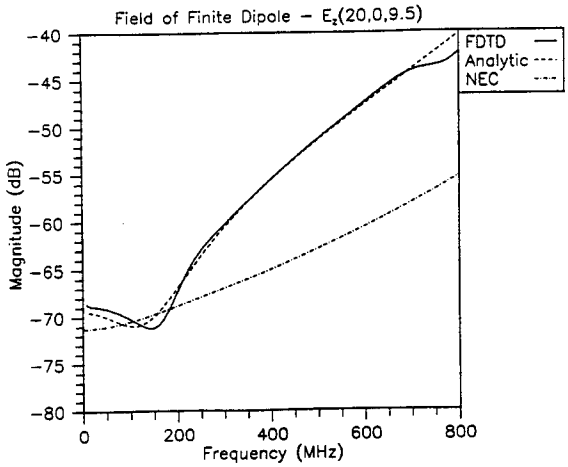

Figure 6. The magnitude of the Z-component of the electric field 20 cm away from the infinite dipole and 9.5 cm above the ground (same height as the center of the dipole). Notice the NEC result is vastly different from the other two methods.

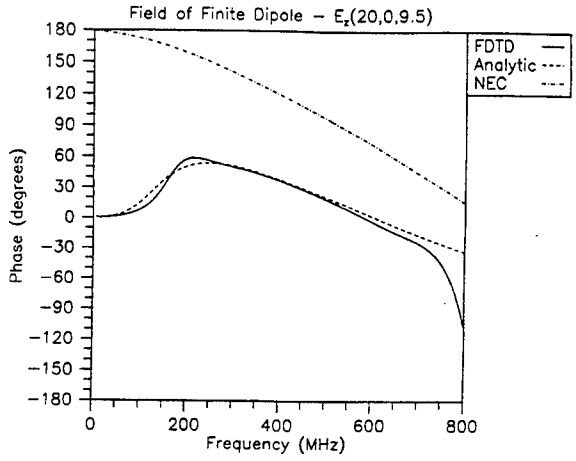

Figure 7. The phase of the Z-component of the electric field 20 cm away from the finite dipole and 9.5 cm above the ground (same height as the center of the dipole). Notice the NEC result is vastly different from the other two methods

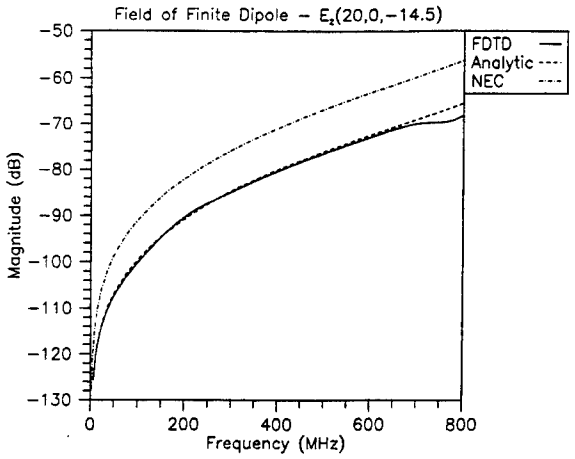

Figure 8. The magnitude of the Z-component of the electric field 20 cm away from the finite dipole and 14.5 cm below the ground surface. Notice the NEC result is significantly different from the other two methods.

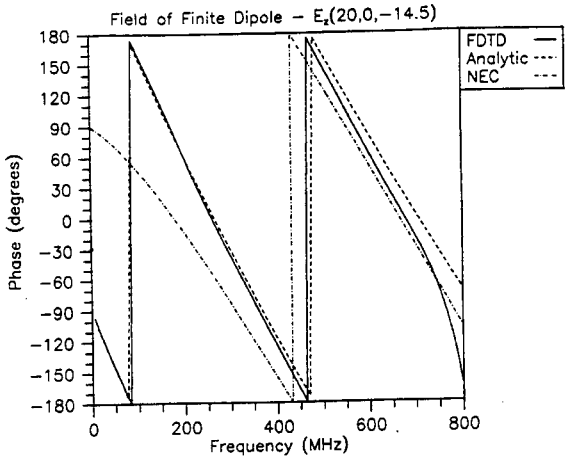

Figure 9. The phase of the Z-component of the electric field 20 cm away from the finite dipole and 14.5 cm below the ground surface. Notice the NEC result is significantly different from the other two methods.

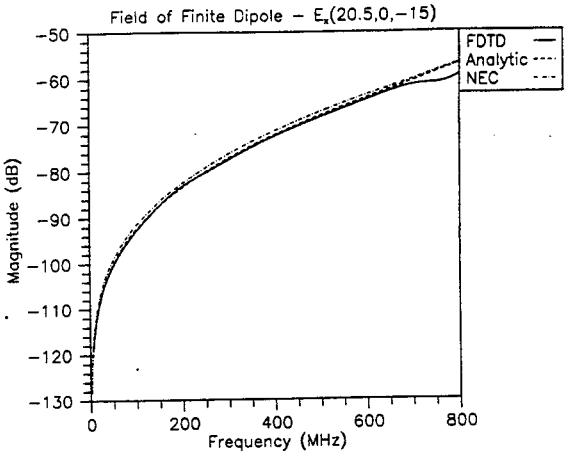

Figure 10. The magnitude of the X-component (horizontal) of the electric field 20.5 cm away from the finite dipole and 15 cm below the ground surface. Here the NEC result is in reasonable agreement with the other two methods.

FDTD Analysis of Radiation from a Lens Terminated Conical TEM Antenna

S. A. Blocher, E. A. Baca, T. S. Bowen
Phillips Laboratory Electromagnetic Effects Division
Kirtland AFB, NM 87117-5776

Abstract

The Finite Difference Time Domain (FDTD) method has been used extensively to model the radiation characteristics from a variety of antenna structures. In this paper the method is applied to a novel conical transverse electromagnetic (TEM) antenna which has a dielectric lens at the aperture opening. The TEM structure is chosen due to its ability to radiate fast transient pulses and is constrained by a lens to collimate and thus increase the boresight electric field strength in the far zone. This paper describes the application of the FDTD method to this structure and compares the numerically computed results to those obtained via experimental investigations for the same radiating structure. It will be shown that excellent agreement is obtained.

1 Introduction

In recent years, wideband antennas have gained in popularity due to their ability to radiate a broadband of energy with a single input pulse. In an effort to increase the frequency response of such antennas, researchers have been utilizing transient driving functions with faster rise-times [1]. However, since experimental investigations for antenna research are often expensive and time-consuming, computational studies are used to aide the antenna designers. The FDTD method is an ideal choice for wideband antenna simulations since all field quantities are calculated in the time-domain. In addition, the input driving function is analytically expressed as a time-domain parameter which allows maximum control over the simulations. Finally, by modeling a transient antenna response in the time-domain, the numerical investigations themselves are ideally efficient when compared to traditional frequency domain techniques.

With the preceding in mind, the FDTD technique has been applied to a novel transient antenna configuration consisting of a conical TEM with a lens termination. Initially, this research sought a determination of the suitability of FDTD for modeling fast (sub hundred picosecond) transient phenomena. To that end, the FDTD method was utilized to simulate the far zone radiated response from the conical TEM antenna (on boresight) and comparisons were made to existing experimental data for the same structure. As the following sections show, these comparisons demonstrated excellent agreement proving FDTD to be a useful tool for wideband antenna research.

2 Conical TEM Antenna

The design of the lens constrained conical TEM antenna is based on an in-house Phillips Laboratory investigation [2], and is comprised of a half-conical TEM structure over a large ground plane with a lens termination at the aperture (Figure 1).

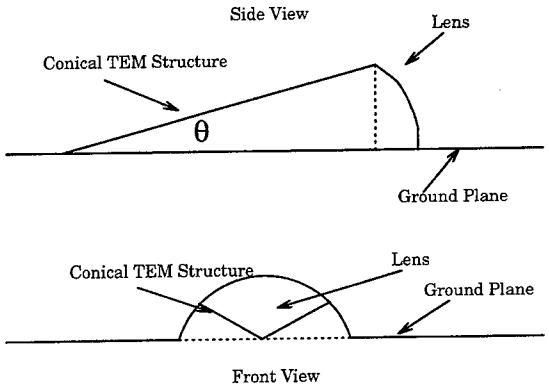

Figure 1: Schematic of conical TEM antenna with lens at aperture.

The lens is positioned on the antenna to focus the far zone electromagnetic fields on boresight thereby increasing the peak radiated field strength. This focusing allows the antenna to minimize the leaky characteristics typically found with "open" radiation structures. Made from a polyethylene material, the lens has a relative index of refraction of $n_r = 1.517$. Physically, the antenna is 33.15 inches long by 24 inches wide (at the aperture opening) with a height of 12.116 inches with respect to the feed region. The half conical angle is $\theta = 23.14°$. The large conducting ground plane is used in the antenna's configuration to allow simulation of a full conical structure via imaging techniques.

3 FDTD Simulation of the Conical TEM Antenna

The FDTD method utilizes a second order accurate finite difference approximation to the Maxwell curl equations in the time domain [3]. All vector field quantities are calculated on a uniform

spatial grid which closely approximates the physical scatterer. Therefore to maintain accuracy in the simulations, it is very important to construct an accurate mesh so that the simulations represent as closely as possible the real antenna.

The operation of the conical TEM antenna relies on the use of imaging techniques due to the large ground plane present. Unfortunately, this ground plane is a computationally prohibitively large since it requires the discretization of a large volume of free space. Thus, when modeling an antenna of this type, it is better to construct a mesh which approximates a full conical description. The electrical characteristics of these models are identical.

The mesh created for the conical TEM antenna utilized a uniform spatial increment of $\delta \equiv \delta_x = \delta_y = \delta_z = 3.815$ mm. This allowed accurate frequency resolution to approximately 7.87 GHz according to the modified Nyquist condition,

$$\delta = \frac{\lambda_{min}}{10} \tag{1}$$

where λ_{min} corresponded to the wavelength of the *highest* frequency of interest in the simulation. Additionally, this cell size also accommodated all physical characteristics of the antenna including the feed region. A mesh was generated according to this spatial increment by utilizing a Phillips Laboratory automated mesh generation tool. The resulting mesh contained approximately 7 million cubic cells requiring significant computer memory and disk space for the simulations. The time increment was determined to be 7.33 picoseconds as calculated by the Courant stability condition for cubic cells and each simulation was run for a total of 1024 time-steps.

To simulate the antenna's broadband behavior, a unit step function was analytically imposed on the grid at the feed region. The function was calculated at each time-step and had the form

$$E^n_{i,j,k} = 1 - \exp\left[-\left(\frac{t}{\tau_0}\right)^2\right] \tag{2}$$

where τ_0 was a constant to relate the numerical driving function to the actual pulse rise time. Adequate numerical simulation of the antenna's driving function was particularly important in this investigation since the conical TEM was driven with a step function whose rise-time was 80 picoseconds. In order to accurately model the antenna's transient response, there had to be a sufficient number of time-steps in the rising edge of the analytic driving function. At the spatial and temporal discretization utilized, the initial ramp of Eq. (2) was comprised of over ten time-steps, which allowed sufficient temporal resolution of the driving function.

Figure 2 is a plot of the antenna's source function, at the feed region, sampled each time-step for the duration of the simulation. The plot shows the electric field to rise to unity over 80 picoseconds and then maintain unit amplitude for the duration of the simulation. Additionally,

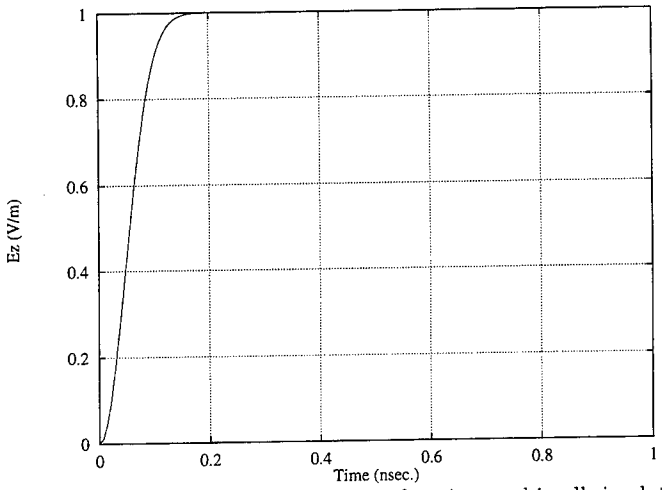

Figure 2: Plot of FDTD time-domain driving function used in all simulations.

the figure clearly indicates that the driving function has no numerical aberrations such as flutter or late time noise.

In the FDTD simulations, Liao second order boundary conditions enclosed the computational domain at a distance of five white space cells from the edges of the mesh. This allowed all spurious fields to be absorbed at the boundary truncations preventing corruption of the computed antenna response.

To test the antenna's far zone radiation characteristics, a near to far zone transformation was utilized to determine the boresight radiated field strength [4]. The FDTD code first calculated all the electric and magnetic fields on a fictitious "integration surface" surrounding the antenna. These fields then determined the surface electric and magnetic current distributions, thereby allowing numerical calculation of the far field radiation integrals. The far zone transformation was normalized with respect to distance from the scatterer so the computed far field results did not these include distance terms.

Two sets of simulations were performed on the conical TEM antenna. Initially, the antenna response of an identical conical TEM without the lens was calculated. Secondly, the lens was added and the simulations were run again so the effects of the dielectric lens could be compared to the case with no lens.

Due to the large volume of the computational domain, all simulations were run on Sun Microsystems SPARC class workstations. Each simulation required approximately 20 hours of compute time to calculate both the field quantities and the far zone transformations. All data was post-processed and analyzed utilizing in-house developed Phillips Laboratory FDTD data analysis tools.

4 Results

Since one of the primary goals of this research was to determine the suitability of the FDTD method to simulate fast transient phenomena, all calculated results were compared to experimental data for the conical TEM antenna. The experiments previously performed on the antenna involved sampling the far zone radiated electric field on boresight at the edge of the ground plane. Thus, comparisons were made between the FDTD simulated and experimentally measured antenna responses for both the lens and no lens cases previously mentioned.

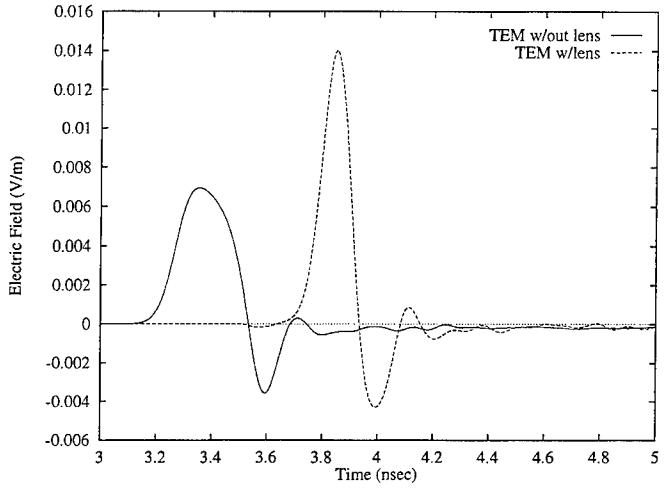

Figure 3: Computed far zone response for conical TEM antenna with and without lens.

Figure 3 is an overlay plot of the computed far zone antenna responses on boresight for the conical TEM antenna with and without the lens. The data indicates that with the lens present, the field amplitude is increased by approximately a factor of two showing that the lens acts to focus the electric field. Additionally, there is an obvious time delay for the case with the lens present due to a decrease in the field's phase velocity through the dielectric media. Figure 4 is

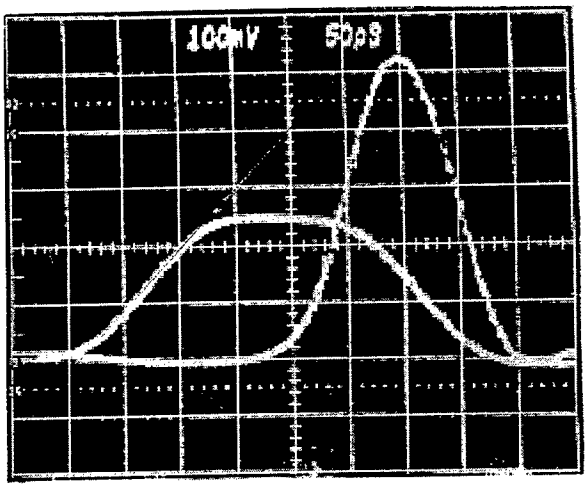

Figure 4: Measured far zone response for conical TEM antenna with and without lens.

a similar overlay for the antenna's experimental data. It shows the same features as the computational results and the agreement between the two sets of data is excellent. From Figure 3, the approximate pulse-widths with and without the lens are 113 and 230 picoseconds, respectively. This compares favorably with the experimental values of 120 and 260 picoseconds for the lens and no lens cases shown in Figure 4. The resulting average error between the computed and measured values is approximately eight percent.

5 Conclusions

This paper has shown the application of the FDTD method to a conical TEM antenna with a lens termination. The computed data demonstrated excellent agreement with experimental

investigations. Importantly, this work has also shown the applicability of the FDTD method to simulate wideband phenomena. Provided sufficient temporal resolution existed in the initial ramp of the driving function, the FDTD method accurately computed the far zone antenna response for a driving function with an 80 picosecond rise-time.

Computational simulations of antenna phenomena, as these results show, provide traditional wideband antenna designers an efficient way to augment their analysis "tool-kits." By performing numerical investigations in conjunction with experimental studies, it is possible to reduce the overall time and monetary costs associated with the antenna design and test processes.

References

[1] D. Herskovitz, "Wide, Wider, Widest," *J. Elec. Defense*, pgs. 51-58, July 1995.

[2] C. J. Buchenauer, "Lens-horn configuration and equations," unpublished technical notes, Phillips Laboratory, May 1992.

[3] K. S. Kunz, R. J. Leubbers, *The Finite Difference Time Domain Method for Electromagnetics*. CRC Press, Boca Raton, 1993.

[4] R. J. Leubbers, K. S. Kunz, M. Schneider, and F. Hunsberger, "A finite-difference time-domain near zone to far zone transformation," *IEEE Trans. Antennas Propagat.*, vol. AP-39, pgs. 429-433, April 1991.

FDTD ANALYSIS OF A DIPOLE ANTENNA DRIVEN FROM VARIOUS EXCITATION SOURCES

M.R. Zunoubi, N.H. Younan, C.D. Taylor, and J.H. Beggs

Department of Electrical and Computer Engineering
Mississippi State University
Mississippi State, MS 39762

ABSTRACT

A center-fed radiating electric dipole antenna driven from various excitation sources is analyzed using the Finite-Difference Time-Domain technique (FDTD). The sources that are considered are a Gaussian pulse, a modulated Gaussian pulse, and an impulse. The antenna is modeled with a source resistance. Results in terms of the magnitude of the radiation impedance of the dipole are obtained for various sources and a comparison with the Numerical Electromagnetic Code (NEC) results is made to investigate their accuracy. In addition, due to the great effect of the antenna radius on the NEC results, a study is done to yield a close approximation of the wire radius based on the FDTD cell dimensions.

I. INTRODUCTION

The Finite-Difference Time-Domain technique, first introduced by Yee [1], has been proven to be an effective and convenient tool for time-domain analysis of various electromagnetic problems. Although it has been applied to numerous scattering and penetration problems, its application to problems involving antenna radiation has been limited [2-4]. In addition, its effectiveness is somewhat limited by the choice of the excitation source used to drive the radiating object.

A Gaussian pulse or a modulated Gaussian pulse is commonly used to drive a radiating system. This type of excitation limits the frequency domain analysis to a specific frequency range provided by the source. Moreover, excessive computer time and memory are required if a broad frequency range is desired.

In this paper, a center-fed electric dipole antenna is analyzed using the FDTD technique [5]. The antenna is driven by various sources of excitation namely, a Gaussian pulse, a modulated Gaussian pulse, and an impulse. The radiation impedance of the antenna is computed and compared with the results obtained the Method of Moments (MoM) via NEC [6]. In addition, In order to compare the FDTD results with those obtained by MoM, a study is done to determine the radius of the dipole required for NEC computations based on the FDTD cell dimensions. The analysis of the antenna is carried out with a source resistance of 50Ω. The source resistance is incorporated in the original FDTD formulations employing the technique described in [7].

II. ANALYSIS

In order to model and analyze the electric dipole antenna, the technique presented in [8] is employed. A wire dipole of 0.41 cm length is considered. The problem space is 41x41x80 cells with the cell dimensions being $\Delta x = \Delta y = 0.5$ cm and $\Delta z = 1.0$ cm. This results in a time step of $\Delta t = 11.11$ ps set at the current limit. The FDTD problem space is shown in Figure 1.

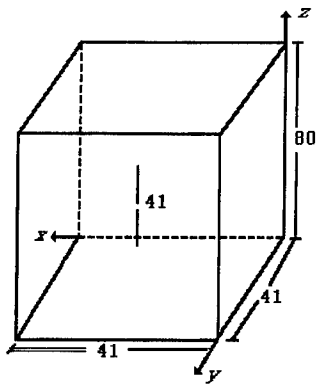

Figure 1. FDTD problem space of a dipole antenna for calculating the radiation impedance. Dimensions are given in FDTD cells, where the cell size is 0.5 x 0.5 x 1.0 cm.

To model the dipole antenna, the z-component of the electric field is set to zero along the wire except for the component at the wire center. This field component is used to represent the excitation source for the FDTD calculations. This is illustrated in Figure 2. In addition, the electric field given by equation (1) is modified to take into consideration the source impedance. This leads to adding the contribution of the current flowing through the excitation source resistance to equation (1). The technique is clearly outlined in [7].

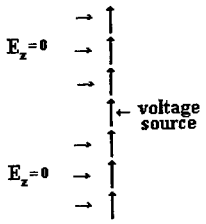

Figure 2. Excitation of the dipole antenna using the electric field component on the wire axis at the center of the wire.

If the electric field at the center of the antenna is defined as $E_z(I,J,K)$, then

$$E_z(I,J,K) = \frac{-V(n\Delta t)}{\Delta z} \quad , n=1, 2, ..., nstop \tag{1}$$

where $V(n\Delta t)$ is the amplitude of the excitation source and nstop is the maximum number of time steps. The current, I(t), flowing through the wire center can be sampled by taking the discrete approximation of the line integral of the x and y components of the magnetic field, H_x and H_y, encircling the electric field. Accordingly,

$$I(n\Delta t) = [H_x^{n+1/2}(I,J-1,K) - H_x^{n+1/2}(I,J,K)]\Delta x + [H_y^{n+1/2}(I,J,K) - H_y^{n+1/2}(I-1,J,K)]\Delta y \tag{2}$$

with the values of indices I, J, and K correspond to the location of the $E_z(I,J,K)$ electric field along the wire axis at the center of the antenna.

In order to perform the radiation impedance computations, the discrete time-domain currents and voltages at the antenna center are Fourier transformed except for the case of the impulse excitation which requires only the discrete frequency results of the current values.

III. RESULTS

First, the dipole antenna is fed at the center with a Gaussian pulse of 1.0V maximum amplitude of the form:

$$V(t) = 1.0\, e^{-\alpha(t - \beta\Delta t)^2} \qquad (3)$$

with $\beta = 64$, $\alpha = (4/(\beta\Delta t))^2$, and the pulse truncated for $t < 0$ and $t > 2\beta\Delta t$. Second, the Gaussian pulse of equation (3) is modified and used as the excitation source so that a modulated Gaussian pulse is obtained, i.e.,

$$V(t) = 1.0\, e^{-\alpha(t - \beta\Delta t)^2} \cos(2\pi f_0 t) \qquad (4)$$

where the center frequency f_0 is chosen to be 800 MHZ. Finally, an impulse is applied at time $t = 3\Delta t$ to the dipole's center to drive the radiating antenna. The radiation impedance of the antenna is then computed by performing a Fourier transform analysis to the time-domain values of both currents and voltages, obtained from the FDTD, at the feeding point of the dipole. This analysis excludes the case where the antenna is driven by an impulse, where the frequency-domain analysis of the currents is only required to study the antenna characteristics. The FDTD computations are carried out for nstop = 8192 time steps to make sure that all transients are dissipated.

For comparison purposes, the NEC computer code is employed to evaluate the antenna radiation impedance. However, an intensive study is performed to determine the wire radius for the NEC computations based on the FDTD cell dimensions. It is concluded that the best approximation of the radius is 25% of the FDTD cell dimensions. The FDTD results for various excitation sources along with the NEC results are shown in Figure 3. While the FDTD calculations are valid up to approximately 1.5 GHz based on having 20 FDTD cells per wavelength, the thin wire approximation for the MoM code becomes questionable at approximately 2.0 GHz. As seen from Figure 3, the FDTD response to all three sources of excitation is identical and in fairly close agreement with the NEC results even up to 2.0 GHz which is beyond the limitation set by the FDTD technique.

IV. CONCLUSION

It is shown that the electric dipole antenna can be effectively analyzed by the FDTD technique when driven from different sources of excitation. When the source impedance is incorporated in the original FDTD formulations, the analysis of the antenna becomes more practical. When an impulse excitation is used to drive the wire dipole, the antenna characteristics can be studied over a wide frequency range in a single FDTD code execution. Comparable results are obtained from the different excitation sources. However, no frequency-domain analysis of the voltage source is required to obtain the

impedance and/or admittance of the antenna. This makes the antenna analysis more efficient and simple.

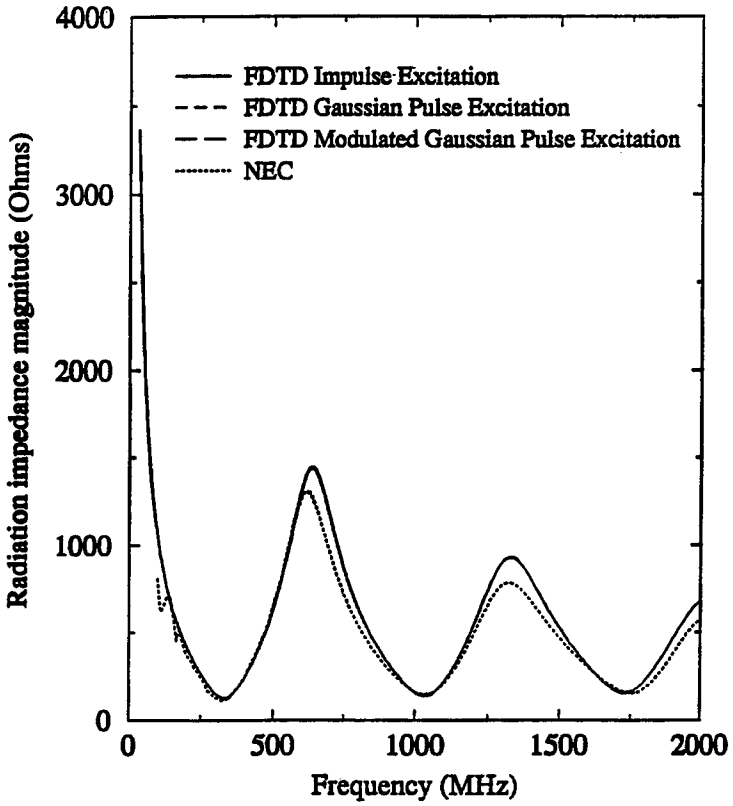

Figure 3. Radiation impedance due to different excitation sources

REFERENCES

[1] K.S. Yee, "Numerical solution of initial boundary value problems involving Maxwell's equations in isotropic media," *IEEE Trans. Antennas Propagat.*, Vol. AP-14, pp. 302-307, May 1966.

[2] J.G. Maloney, G.S. Smith, and W.R. Scott, Jr., "Accurate computation of the radiation from simple antenna using the Finite-Difference Time-Domain method," *IEEE Trans. Antennas Propagat.*, AP-38, 7, pp. 1059-1068, 1990.

[3] P.A. Tirkas and C.A. Balanis, "Finite-Difference Time-Domain method for antenna radiation," *IEEE Trans. Antennas Propagat.*, AP-40, 3, pp. 334-340, 1992.

[4] J.J. Boonzaaier and C.W.I. Pistorius, "Thin-wire dipoles: A finite-difference time-domain approach," *Electronic letters*, 26, 22, pp. 1891-1892, 1990.

[5] J.H. Beggs, R.J. Luebbers, H.S. Langdon, K.S. Kunz, and D. Steich, "User's manual for three dimensional FDTD version C code for scattering from frequency-independent dielectric and magnetic materials," PSU Rep., Dec. 1992.

[6] G.J. Burke and A.J. Poggio, "Numerical Electromagnetics Code (NEC) - Method of Moments," Vol. 2, Naval Ocean Systems Center, Technical Report NOSC TD 116, January 1981.

[7] R.J. Luebbers and H.S. Langdon, "Reducing the Number of Time Steps Needed for FDTD Antennas and Microstrip Calculations," 11th annual review of progress in Applied Computational Electromagnetics at Naval postgraduate school, Monterey, CA, March 20-25, 1995.

[8] K.S. Kunz, and R.J. Luebbers, *The Finite Difference Time Domain Method for Electromagnetics*, Boca Raton, Florida: CRC Press, 1993.

An Efficient Hybrid PEE-FDTD Field Modeling Technique in Cylindrical Co-ordinates

M. Mrozowski[2], M. Okoniewski[1] and M. A. Stuchly[1]
[1]Dept. of Electrical & Computer Engineering
University of Victoria, Victoria, BC, Canada, V8W 3P6
[2]Dept. of Electronics,
The Technical University of Gdansk, Gdansk, Poland

Indexing terms: numerical methods, elecromagnetics, FDTD.

Abstract: Two algorithms are combined in the cylindrical coordinates for accelerated computations of electromagnetic fields in the time domain. The partial eigenfunction expansion (PEE) algorithm is used close to the coordinate system origin and the FDTD algorithm in the remaining region. This eliminates the use of a prohibitively short time step if high circumferential resolution is required away from the origin. A significant acceleration of computations is obtained, due to the superior stability and higher efficiency of the PEE method.

Introduction: As time domain techniques, particularly the finite difference time domain (FDTD), are increasingly used to simulate electromagnetic fields in more complex and larger structures, there is a need for new algorithms that require fewer computer resources and are stable. Recently, an efficient hybrid PEE (partial eigenfunction expansion) - FDTD method was developed for shielded structures in the Cartesian coordinates [1]. For some structures, e.g. a corrugated waveguide, antenna arrays on a cylinder etc., it is advantageous to formulate FDTD in cylindrical coordinates. But, exceedingly large computer resources are required when a high circumferential resolution imposes a small time step. The problems associated with a short time step are particularly pronounced at low frequencies, where time cycles are long. The solution described interfaces two methods: the PEE and the classical FDTD in cylindrical coordinates, which results in a new efficient modeling tool.

Analysis: The geometry of the structure is shown in Figure 1. The PEE algorithm described in [1] is used inside the radius R_i where the field components are expanded in a Fourier series with respect to ϕ. A typical component has a form:

$$E_r(r,\phi,z) = \sum_{n=1}^{N} e_{rn}(r,z)e^{jn\phi} \qquad (1)$$

Between R_i and R_{max} an FDTD algorithm in cylindrical coordinates is used. The transition between the two algorithms (interior PEE and exterior FDTD) is done as follows. Fields calculated from the PEE on the surface $r = R_i$ are directly imported to the FDTD algorithm. In the opposite direction, the fields given by the FDTD at $R_i + \Delta r$ are used to obtain the expansion coefficients of the PEE by taking the inner product of each function [1]. In cylindrical coordinates and media independent of ϕ this algorithm resembles the PEE - FDTD [2]. However, there are two important differences between the two algorithms. The PEE computations are carried with several expansion terms simultaneously, while the BOR-FDTD considers separately each mode. Only axi-symmetric structures can be analyzed with BOR-FDTD method, while the hybrid PEE-FDTD method can be applied to any inhomogeneuity in the FDTD region of the computational space.

A relative stability criterion of the hybrid method compared to the FDTD can be derived following the method given in [3] as:

$$\frac{\Delta t_{PEE}}{\Delta t_{FDTD}} = \left[\frac{A + (\Delta\phi)^{-2}}{A + N^2/4} \right]^{1/2} \qquad (2)$$

where A is a constant dependent on Δr and R_i, and N is the number of terms in the expansion series. Thus, the smaller the $\Delta\phi$ and the lower the number of terms in the expansion required, the greater the increase in the time step. Additionally, the dispersion of the PEE algorithm is inherently lower, because of a lack of discretization in ϕ direction, so more accurate results are to be expected.

The increase in speed of the hybrid method as compared with the FDTD is due to two factors: (i) as the required number of terms in the expansion is usually small, a larger time step can be used resulting in fewer computations, and (ii) fewer unknowns are used to evaluate the fields close to the origin. The gain in speed due to the latter factor is proportional to $R_i/(R_{max} - R_i)$ for a large number of discretization points along r and small N. The overall acceleration is a product of both factors, and large gains in speed are expected for large R_i/R_{max}. The gain in speed is also accompanied by savings in the computer memory.

Numerical Example: To test the hybrid method and to estimate improvements in the computation speed and accuracy, the cut-off frequency for the TM modes was computed with $\Delta r = R_{max}/23$ and 12,000 iterations. The interface between the two algorithms was at $R = 12/23\ R_i$. The accuracy of the hybrid and FDTD methods is compared in Table 1 for different number of discretization points in ϕ direction. For the sake of brevity only the results for the TM_{21} mode are given, but other modes with different ϕ dependence were computed simultaneously. Figure 2 illustrates the effect of the number of terms in the series expansion. As the number of expansion terms increases, the time ratio becomes

smaller, however it remains significantly greater than 1 for all cases considered. The overall speed gain of the hybrid method with both factors contributing to the acceleration considered is shown in Figure 3. Higher gains are achieved as the area covered by the PEE increases.

Conclusions: The hybrid PEE-FDTD method in the cylindrical coordinates provides significant improvements in speed, and gains in memory required and accuracy in analysis of quasi-symmetrical structures with high radial resolution for large radii. This method is particularly attractive for structures that are homogeneous close to the z-axis, but have subregions that need to be modeled with high resolution close to the periphery.

Acknowledgments . This work was supported by the NSERC/BC Hydro/TransAlta research chair (Canada) and the KBN (contract 8T 11D00108) and CPU time grant at the TASK supercomputing center in Gdansk (Poland).

References :

[1] M. Mrozowski, "Stability condition for the explicit algorithms of the Time Domain analysis of Maxwell's equations", *IEEE Microwave & Guided Wave Letters,* vol. 4, pp. 279-281, 1994.

[2] C. L. Britt, "Solution of electromagnetic scattering problems using Time Domain techniques", *IEEE Trans. on Antennas & Propagation,* vol. 37, pp. 1181-1191, 1989.

[3] M. Mrozowski, "A hybrid PEE-FDTD algorithm for accelerated Time Domain analysis of electromagnetic waves in shielded structures", *IEEE Microwave & Guided Wave Letters,* vol. 4, pp. 323-325, 1994.

Table 1. Error in the cut-off frequency for the TM_{21} mode.

Number of points in ϕ direction	10	20	40	80
FDTD error (%)	-3.91	-0.92	-0.28	-0.15
Hybrid error (%)	-1.78	-0.41	-0.08	-0.02

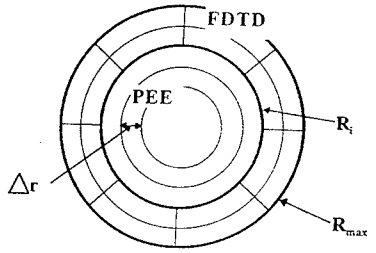

Fig. 1 Schematic diagram of the method of analysis

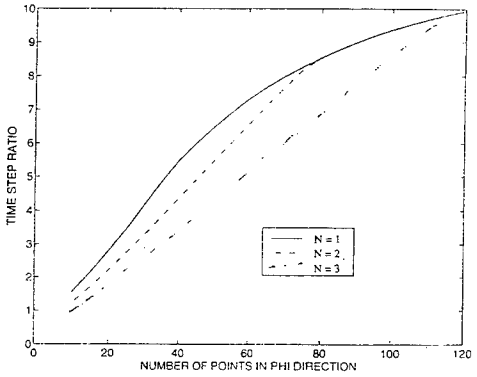

Fig. 2 The ratio of the time steps of the hybrid and the FDTD method with the number of terms in the series expansion as a parameter for the TM_{21} mode (R_i=0.5R_{max}).

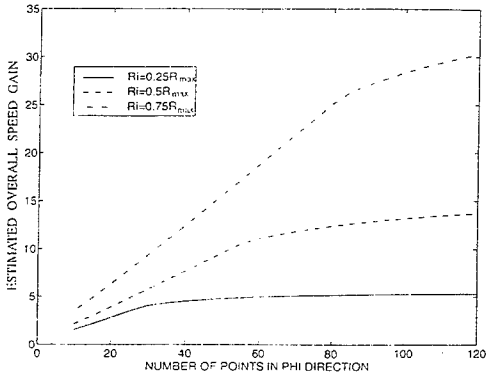

Fig. 3 Overall speed gain for various areas in which PEE algorithm is applied (N-2).

ABSORBING BOUNDARY CONDITIONS FOR OPTICAL PULSES IN DISPERSIVE, NONLINEAR MATERIALS

Peter M. Goorjian
NASA Ames Research Center
Mail Stop T27B-1
Moffett Field, California 94035-1000

Abstract

This paper will present results in computational nonlinear optics. An algorithm will be described that provides absorbing boundary conditions for optical pulses in dispersive, nonlinear materials. A new numerical absorber at the boundaries has been developed that is responsive to the spectral content of the pulse. Currently, no absorbing boundary conditions exist for dispersive materials; rather an outer region of vacuum must be added and then absorbing boundary conditions applied to the vacuum region. This procedure produces reflections at the boundary between regions. Absorbing boundary conditions are needed for dispersive materials in applications to both linear and nonlinear optical device simulations, for such devices as wave guides and optical fibers.

Also, results will be shown of calculations of 2-D electromagnetic nonlinear waves computed by directly integrating in time the nonlinear vector Maxwell's equations. The results will include simulations of "light bullet" like pulses. Here diffraction and dispersion will be counteracted by nonlinear effects. Comparisons will be shown of calculations that use the standard boundary conditions and the new ones.

References:

1. Goorjian, P. M., and Silberberg, Y., "Numerical Simulations of Light Bullets, Using the Full Vector, Time Dependent, Nonlinear Maxwell Equations." 1995 Applied Computational Electromagnetics Symposium, (ACES'95), Naval Postgraduate School, Monterey, CA, March 20-25, 1995.

2. Goorjian, P. M., Taflove, A., and Joseph, R. M., "FD-TD Algorithm for the Nonlinear Maxwell's Equations with Applications to Femtosecond Soliton Propagation," 1994 ACES Symposium, Applied Computational Electromagnetics Society, Monterey, CA, March 21-26, 1994.

3. Goorjian, P. M., Taflove, A., Joseph, R. M., and Hagness, S. C., "Computational Modeling of Femtosecond Optical Solitons from Maxwell's Equations," IEEE Journal of Quantum Electronics, special issue on "Ultrafast Optics and Electronics," vol. 28, No. 10, pp. 2416-2422, Oct., 1992.

SESSION 8:

FINITE ELEMENT AND FINITE VOLUME METHODS FOR ELECTROMAGNETIC FIELD SIMULATION

Chairs: R. D.-Edlinger and R. Lee

Local Tetrahedron Modeling of Microelectronics Using the Finite-Volume Hybrid-Grid Technique

Douglas J. Riley and C. David Turner
Radiation and Electromagnetic Analysis Dept.
Sandia National Laboratories
Albuquerque, New Mexico 87185-1166
Internet: djriley@sandia.gov

1. Introduction

Transient finite-difference, finite-element, and finite-volume methods represent powerful tools for the analysis of complex geometries. The finite-difference time-domain (FDTD) method introduced by Yee nearly 30 years ago [1] has been extensively applied to a wide variety of problems that range from microelectronics to biomedical applications. An extensive collection of references can be found in [2]. The standard FDTD method is mature, conceptually simple, and computationally efficient but possesses the well-known topological limitation of staircasing [3]. Finite-element and finite-volume methods provide increased geometrical flexibility by conforming elements to complex features, but often at a prohibitively high computational cost. Finite-element methods (FEM) have traditionally been applied in the frequency domain to electrostatics, magnetostatics, and interior dynamic problems [4], but more general application is becoming possible through the use of edge elements and accurate absorbing boundary conditions [5]. Finite-element formulations based on explicit and implicit time-differencing methods are also under development [6,7]. Published work on transient finite-volume techniques has been based on the application of computational fluid-dynamics (CFD) methods to Maxwell's equations [8] and on a direct generalization of rectilinear FDTD to arbitrary convex polyhedrons [9-15]. Both techniques use explicit time differencing, but the CFD-based methods define the vector electric and magnetic fields on a single grid, whereas the generalized-Yee formulations use two interleaved grids referred to as primary and dual grids. It is noted that some finite-element formulations using Whitney elements applied to Maxwell's two curl equations also use a dual-type, secondary grid to evaluate the electric field along edges [6].

Much of the previous work involving time-domain volumetric solvers applied to open-region problems used mapped-meshing techniques. Primary grids of this type consist of skewed hexahedral and/or wedge elements. The grids are generally block structured but can, of course, be referenced in an unstructured manner. An example of mapped-meshing applied to microstrip problems consists of forming a surface grid on a planar geometry, and then extruding the surface, or shell, elements into solid elements. The resulting grid is considered to be 2-1/2 dimensional because the grid can not accommodate geometry variations along the extrusion direction (although different materials can be incorporated along this direction). The technique has been successfully applied by Gedney and Lansing [15]. For general geometries, mapped-meshing requires mapping, or projecting, one surface onto another. Geometries must be zoned using this approach, generality is limited, and user intervention is often high. Free-meshing, on the other

hand, provides increased geometrical flexibility and generally lower user intervention. The resulting grids typically consist of tetrahedral elements, although fully free-meshed hexahedral grids are possible in some situations [16,17]. Tetrahedral grids are computationally expensive because cell count can become exceedingly high for practical problems. Compared to cubical hexahedral grids (FDTD), filling the same volume with free-meshed tetrahedra that possess an average edge length close to that of the hexahedral cells will lead to approximately eight times the number of cells. Consequently, it is desirable to minimize the number of tetrahedra in the problem space. The present paper addresses using local tetrahedron grids interfaced with FDTD grids and applied to microelectronics.

The software package VOLMAX (Volumetric Maxwell solver) is based on the finite-volume hybrid-grid (FVHG) technique. This technique permits non-orthogonal, unstructured grids to be embedded in traditional rectangular-cell, structured-grid, FDTD [13,14]. The FVHG method enables high complexity regions to be modeled and gridded using commercial solid-modeling software. The resulting complex unstructured grid is interfaced to simple FDTD cells without spatial interpolation across the grid interface. This is accomplished by forcing the unstructured grid to terminate on a closed rectangular surface [14]. The FVHG technique is particularly useful for open-region problems and/or geometries with local regions of high complexity. The method has been shown to provide high accuracy in scattering applications.

Microelectronics applications are well suited to an FVHG formulation. This is because uniform microstrips are often used at the input and output ports of the device under study. To obtain accurate *S*-parameter data, these microstrips usually extend a long distance and require accurate absorbing boundary conditions at the line terminations. This portion of the problem can be modeled accurately and efficiently using FDTD. However, the device under study may be of high complexity and require a conforming grid. This complex region can be designed using solid-modeling software and then gridded with free-meshed, tetrahedral elements.

The finite-volume portion of the FVHG solver [13] is based on a generalization/simplification of the modified finite-volume technique introduced in [9]. A (variably dissipative) time-averaging scheme is used to obtain long-term stability. Achieving stability for tens-of-thousands of time steps on *arbitrary* grids with explicit, time-domain, finite volume and finite element schemes without using dissipation remains an open research issue across many disciplines. It is noted that the non-dissipative discrete surface integration (DSI) method [10] has been found to delay, but not eliminate, late-time growth on complex grids [13]. The technique used by the FVHG method permits either no dissipation, or a moderate amount of dissipation, depending on the grid complexity. Unfortunately, the "right amount" of dissipation is generally not known *a priori*, but guidelines are provided here that have been found to be successful for complex tetrahedron grids.

This paper provides an overview of the finite-volume algorithm, the time-averaging scheme, boundary condition implementation, grid generation, and time-step definition. Three simple microstrip applications with well-known FDTD solutions are examined. The examples demonstrate the accuracy that can be obtained by launching microstrip-guided waves on cubical hexahedron (FDTD) grids and through a dense, linear tetrahedra region. More complex geometries that fully exploit the power of the FVHG approach to microelectronics will be topics of future papers.

2. Analysis

The finite-volume method can accommodate arbitrary convex polyhedron-element primary grids. The vector magnetic fields are defined at the centroids of the primary cells, whereas the vector electric fields are defined at their vertices. Dual cells contain the vertices. The dual cells can be extremely complex and typically possess many faces, edges and nodes. A preprocessor builds the dual grid from the primary grid. The primary grid is equivalently labeled an **H**-grid, whereas the dual grid is equivalently labeled an **E**-grid. A typical **H**-grid tetrahedral element, referenced as $\mathbf{H}_i^{\mathbf{t}}$, is shown in Fig. 2.1 (superscript **t** denotes total field). Dual cells (not shown) surround the four vertices and are referred to as $\mathbf{E}_j^{\mathbf{t}}, j$ = 1-4. The dual edge, $\mathbf{s}_l^e$, connects the centroids of primary-cell, *i*, with a neighboring cell, *k*. The primary edge, $\mathbf{s}_p^h$, connects $\mathbf{E}_1^{\mathbf{t}}$ and $\mathbf{E}_2^{\mathbf{t}}$. The volume of primary cell, *i*, is denoted V_i^h, while the volume of dual cell, *j*, is denoted V_j^e. The area of face, *l*, on primary cell, *i*, is denoted by $A_{i,l}^h$, while the area of face, *p*, on dual cell, *j*, is denoted $A_{j,p}^e$. $\mathbf{n}_{i,l}^h$ and $\mathbf{n}_{j,p}^e$ denote outward normals for each face of the primary and dual cells, respectively.

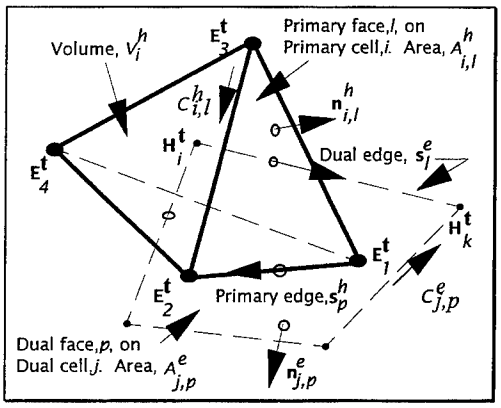

Fig. 2.1. Cell definitions.

Maxwell's equations are given by

$$\varepsilon \frac{\partial}{\partial t}\mathbf{E}^{\mathbf{t}} + \sigma_e \mathbf{E}^{\mathbf{t}} = \nabla \times \mathbf{H}^{\mathbf{t}}$$

$$\mu \frac{\partial}{\partial t}\mathbf{H}^{\mathbf{t}} + \sigma_m \mathbf{H}^{\mathbf{t}} = -\nabla \times \mathbf{E}^{\mathbf{t}}$$

where, ε, σ_e, μ, and σ_m denote electric permittivity, electric conductivity, magnetic permeability, and magnetic conductivity, respectively. By integrating over each cell on the primary and dual grids, the finite-volume time-domain (FVTD) form of Maxwell's equations is

$$\tilde{\varepsilon}_j \frac{\partial}{\partial t}\iiint_{V_j^e}\mathbf{E}^{\mathbf{t}}\,dV_j^e + \tilde{\sigma}_{ej}\iiint_{V_j^e}\mathbf{E}^{\mathbf{t}}\,dV_j^e = \sum_p \iint_{A_{j,p}^e}\mathbf{n}_{j,p}^e \times \mathbf{H}^{\mathbf{t}}\,dA_{j,p}^e \tag{2.1}$$

$$\mu_i \frac{\partial}{\partial t}\iiint_{V_i^h}\mathbf{H}^{\mathbf{t}}\,dV_i^h + \sigma_{mi}\iiint_{V_i^h}\mathbf{H}^{\mathbf{t}}\,dV_i^h = -\sum_l \iint_{A_{i,l}^h}\mathbf{n}_{i,l}^h \times \mathbf{E}^{\mathbf{t}}\,dA_{i,l}^h \tag{2.2}$$

All materials are defined relative to primary cells. For magnetic materials this is the natural definition. However, electric materials are associated with the spatially staggered dual cells and therefore the permittivity and electric conductivity require averaging. The average values are denoted by $\tilde{\varepsilon}_j$ and $\tilde{\sigma}_{e_j}$, respectively. These are defined as follows. The average permittivity on dual *face*, p, is defined by

$$\tilde{\varepsilon}_p^f = \frac{\sum_n \varepsilon_n V_n^h}{\sum_n V_n^h} \tag{2.3}$$

where the sums are taken over the primary cells associated with the dual face. The average permittivity for the dual *cell*, j, is constructed by forming

$$\tilde{\varepsilon}_j = \frac{\sum_p \tilde{\varepsilon}_p^f}{N_j^f} \tag{2.4}$$

where the sum is taken over all dual faces on dual cell, j, and N_j^f denotes the number of faces on the cell. The electric conductivity is similarly defined.

Volume-Integral Approximation

The volume integrals are easily evaluated by assuming the vector field remains constant throughout the cell volume. This leads to the following equations

$$\tilde{\varepsilon}_j \frac{\partial}{\partial t}\mathbf{E}^{\mathbf{t}} + \tilde{\sigma}_{e_j}\mathbf{E}^{\mathbf{t}} = \frac{1}{V_j^e}\sum_p \iint_{A_{j,p}^e} \mathbf{n}_{j,p}^e \times \mathbf{H}^{\mathbf{t}}\, dA_{j,p}^e \tag{2.5}$$

$$\mu_i \frac{\partial}{\partial t}\mathbf{H}^{\mathbf{t}} + \sigma_{m_i}\mathbf{H}^{\mathbf{t}} = -\frac{1}{V_i^h}\sum_l \iint_{A_{i,l}^h} \mathbf{n}_{i,l}^h \times \mathbf{E}^{\mathbf{t}}\, dA_{i,l}^h \tag{2.6}$$

A first-order approximation to the vector fields within cells can be constructed by expanding the fields in a first-order Taylor series and applying the relationship $\iiint \nabla\Psi\, dV = \iint \Psi\, \mathbf{n}\, dA$, where Ψ denotes a scalar field and $\mathbf{n}$ denotes an outward normal. This relationship enables the field derivatives to be easily evaluated. The results in this paper are based on constant fields throughout the cell volume. The effect of higher-order representations will be examined in a future paper.

Area-Integral Approximation

Similar to Madsen and Ziolkowski [9], the cross product in the area integral is expanded as a vector triple product at each vertex and an average value for the integral is constructed by summing over all vertices of the face, dividing by the number of vertices, and multiplying by the face area (which is not unique for non-planar faces). Note that for tetrahedral elements the faces are triangles, which leads to the following simplification (cf. Fig. 2.2):

$$\iint_{A^h_{i,l}} \mathbf{n}^h_{i,l} \times \mathbf{E}^{\mathbf{t}}\, dA_l \approx -\frac{1}{3} \sum_p \mathbf{E}^{\mathbf{t}}_p \times \left(\frac{\mathbf{s}^h_{p1} \times \mathbf{s}^h_{p2}}{\left| \mathbf{s}^h_{p1} \times \mathbf{s}^h_{p2} \right|} \right) \frac{1}{2} \left| \mathbf{s}^h_{p1} \times \mathbf{s}^h_{p2} \right| =$$

$$-\frac{1}{6} \sum_p \mathbf{E}^{\mathbf{t}}_p \times \mathbf{s}^h_{p1} \times \mathbf{s}^h_{p2} \approx \frac{1}{6} \sum_p \left(\left(\tilde{\mathbf{E}}^{\mathbf{t}} \cdot \mathbf{s}^h_{p1} \right) \mathbf{s}^h_{p2} - \left(\tilde{\mathbf{E}}^{\mathbf{t}} \cdot \mathbf{s}^h_{p2} \right) \mathbf{s}^h_{p1} \right) \tag{2.7}$$

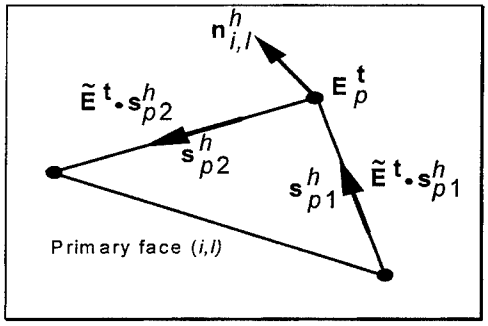

Fig. 2.2. Evaluation of surface integral around boundary.

The summation is taken over all vertices of primary face, (*i, l*) (cf. Figs. 2.1, 2.2). The symbol, ~, represents an average field along the edge (defined below). An expression similar to (2.7) applies to quadrilateral faces, with the overall face normal often becoming an average direction. For faces with an arbitrary number of vertices, as is generally the case on the dual grid, the faces are subdivided into triangles from which the overall area is computed. For these faces, the face-normal generally becomes an average direction.

Time-Advancement Scheme

The application of explicit time-domain methods to complex cell shapes often leads to a well known, late-time, weak instability in the simulation [13,18]. This occurs in both finite-element and finite-volume formulations across many disciplines. The true nature of the instability is not fully understood but is believed to be due to a shifting of the eigenvalues of the discrete formulation relative to the continuous equations [18]. CFD-based methods rely on a dissipative term in the discrete equations to suppress problematic high-frequency modes [8]. The impact of this term as applied to Maxwell's equations has not been thoroughly addressed in the literature. For generalized-Yee formulations, the use of time-averaging to create a variably dissipative time-integration scheme has been found to be effective [13]. However, dissipative time-integration can lead to "over-damping" of the simulation. This is particularly true when applied to lossless,

closed, cavities. Problems that possess natural dissipation, such as radiation, can exhibit slightly enhanced attenuation in the higher frequencies due to the artificial dissipation, particularly as the grid resolution becomes less than approximately 20 cells per wavelength.

Traditional FDTD uses a second-order, centered time difference for the time derivatives. Second-order accuracy requires that the differences are offset in time between the electric and magnetic fields which gives rise to the well-known "leap-frog" time-differencing scheme. Applied to the magnetic field (with the electric field similar), the usual centered time difference is written as

$$\frac{\partial}{\partial t}\mathbf{H}^{\mathbf{t}}\Big|_{t=(n+1)\Delta t} \rightarrow \frac{\left(\mathbf{H}^{\mathbf{t}}\right)^{n+3/2} - \left(\mathbf{H}^{\mathbf{t}}\right)^{n+1/2}}{\Delta t} \tag{2.8}$$

where Δt denotes the time step. A (first-order) time average for $\left(\mathbf{H}^{\mathbf{t}}\right)^{n+1/2}$ is the following

$$\left(\mathbf{H}^{\mathbf{t}}\right)^{n+1/2} = \frac{1}{\alpha+2}\left(\left(\mathbf{H}^{\mathbf{t}}\right)^{n+3/2} + \alpha\left(\mathbf{H}^{\mathbf{t}}\right)^{n+1/2} + \left(\mathbf{H}^{\mathbf{t}}\right)^{n-1/2}\right) \tag{2.9}$$

where $\alpha \geq 0$, but practical values are dependent on Δt. The average corresponds to discrete time samples of the magnetic field. The magnitude of the Fourier Transform of the sampling function

$$\frac{1}{\alpha+2}\left[\delta\left(t-(n+\frac{3}{2})\,\Delta t\right)+\alpha\,\delta\left(t-(n+\frac{1}{2})\,\Delta t\right)+\delta\left(t-(n-\frac{1}{2})\,\Delta t\right)\right] \tag{2.10}$$

where $\delta(\cdot)$ represents the Dirac delta function, is given by

$$\left|\frac{1}{1+\frac{2}{\alpha}}+\frac{1}{1+\frac{\alpha}{2}}\cos(\omega\,\Delta t)\right| \tag{2.11}$$

Here, ω corresponds to radian frequency. For values of α less than infinity, the time average provides increasing attenuation with increasing frequency (with practical upper frequencies selected considerably below the Nyquist sampling requirement). Consider a uniform grid in free space. Define $\Delta t = \Delta/(c\,N)$, where c denotes the speed of light in vacuum, Δ denotes the spatial step throughout the grid, and N represents a positive real constant required for stability. $\omega\,\Delta t$ can now be written as $(2\pi/N)(\Delta/\lambda)$, where λ denotes free-space wavelength.

Writing the grid resolution as $\Delta = \lambda / M$, where M is a positive constant, leads to the result, $\omega \Delta t = 2\pi / (N \cdot M)$. A graph of Eq. 2.11 as a function of $N \cdot M$ is shown in Fig. 2.3.

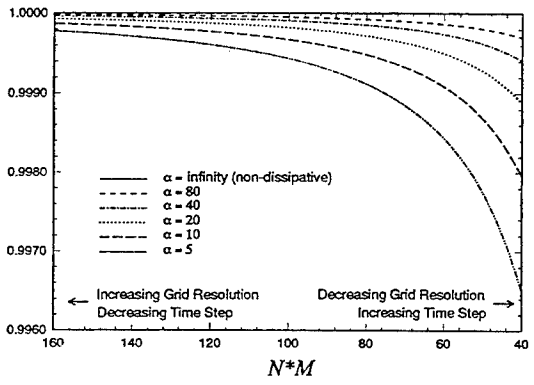

Fig. 2.3. Filter spectrum.

As an example of using Fig. 2.3, consider a grid resolution of 20 cells per wavelength (M = 20) and N = 2 (which is typical for three-dimensional FDTD on a uniform grid); thus, $N \cdot M$ = 40. Choosing $\alpha = 40$ leads to an attenuation value of 0.999400. At 80 cells per wavelength with the same N and α, the attenuation factor is 0.999963. Although these values may seem insignificant, they become cumulative in a time-advancement scheme. Just as the standard Yee algorithm is dispersive, leading to increased phase error over propagation distance [19], the presented time-averaging scheme gives rise to frequency-dependent attenuation. Consider pulse propagation in one dimension over a distance of 100 cells with N = 2; thus, 200 time steps are required to travel the line. Using $\alpha = 40$, the frequency content of the signal at the end of the line is attenuated by approximately 12% (1 dB) at 20 cells per wavelength and 0.8% (0.06 dB) at 80 cells per wavelength compared to lossless propagation. These results were obtained by raising the appropriate value from Fig. 2.3 to the required number of time steps.

For fixed values of α and M, increasing N (corresponding to decreasing Δt) leads to decreasing dissipation. Although this may appear desirable, the resulting dissipation may be insufficient to damp the growth of problematic high-frequency modes, and consequently, a smaller value of α may be required. For embedded, free-meshed, tetrahedron grids, numerical experiments have lead to the required relationship, $N \cdot \alpha \leq 80$, for long-term stability over tens-of-thousands of time steps. Taking $N \cdot \alpha$ in the range 60-80 has generally been found to be successful.

The advancement equations based on time-averaging are the following:

$$\left(\mathbf{E}_j^{\mathbf{t}} \right)^{n+1} \left[A_e - \frac{B_e}{\alpha + 2} \right] =$$

$$\frac{B_e}{\alpha + 2} \left[\alpha \left(\mathbf{E}_j^{\mathbf{t}} \right)^{n} + \left(\mathbf{E}_j^{\mathbf{t}} \right)^{n-1} \right] + \frac{1}{V_j^e} \sum_p \iint_{A_{j,p}^e} \mathbf{n}_{j,p}^e \times \mathbf{H}^{\mathbf{t}} \, dA_{j,p}^e - \tilde{\sigma}_{e_j} \mathbf{E}^{\mathbf{t}} \qquad (2.12)$$

$$\left(\mathbf{H}_i^{\mathbf{t}}\right)^{n+3/2}\left[A_h-\frac{B_h}{\alpha+2}\right]=$$

$$\frac{B_h}{\alpha+2}\left[\alpha\left(\mathbf{H}_i^{\mathbf{t}}\right)^{n+1/2}+\left(\mathbf{H}_i^{\mathbf{t}}\right)^{n-1/2}\right]-\frac{1}{V_i^h}\sum_l \iint_{A_{i,l}^h}\mathbf{n}_{i,l}^h\times\mathbf{E}^{\mathbf{t}}\,dA_{i,l}^h-\sigma_{m_i}\mathbf{H}^{\mathbf{t}} \qquad (2.13)$$

where

$$A_e=\left(\frac{\tilde{\varepsilon}_j}{\Delta t}+\frac{\tilde{\sigma}_{e_j}}{2}\right),\quad B_e=\left(\frac{\tilde{\varepsilon}_j}{\Delta t}-\frac{\tilde{\sigma}_{e_j}}{2}\right),\quad A_h=\left(\frac{\mu_i}{\Delta t}+\frac{\sigma_{m_i}}{2}\right),\quad B_h=\left(\frac{\mu_i}{\Delta t}-\frac{\sigma_{m_i}}{2}\right)$$

The effect of the time average on the usual Courant condition for a uniform, free-space, three-dimensional FDTD grid is easily established by performing a Fourier (von Neumann) stability analysis [20] of the advancement equations. The analysis is straightforward to implement and only the final result is presented here. In terms of the filter parameter, α, the resulting equation for determining the relationship between the time and spatial steps is given by

$$\beta^4(\alpha+1)^2+2\beta^3[2(\alpha+2)^2\eta-\alpha(\alpha+1)]+\beta^2[\alpha^2-2(\alpha+1)]+2\alpha\beta+1=0 \qquad (2.14)$$

where $|\beta|\le 1$ for stability, and $c\Delta t=\sqrt{\frac{\eta}{3}}\Delta$. Sample calculations are shown in Table 2.1.

α	$\sqrt{\eta}$
∞	1
80	0.975
40	0.952
10	0.833
5	0.714

Table 2.1
Effect of Time Average on Uniform-Grid Courant Condition

It is seen that the Courant condition slightly tightens with decreasing α. Although it is not possible to derive a similar rigorous relationship for arbitrary unstructured grids, a similar conclusion has been observed numerically.

FDTD Contribution and Edge-Projected Field

Knowledge of the vector fields at cell vertices enables the calculation of an average field projected along connecting edges. Arithmetic or volumetric averaging can be used. However, the approach does not guarantee that the fields are divergence free on a single cell level, and the algorithm does not reduce identically to an FDTD form when cells become orthogonal. These issues are rectified by incorporating an FDTD correction to the edge-projected vector field. With reference to Fig. 2.1, Ampere's and Faraday's laws specialized to the field components normal to primary-face (*i, I*), and dual-face, (*j, p*), are

$$\tilde{\varepsilon}_p^f \frac{\partial}{\partial t} \iint\limits_{A_{j,p}^e} E_p \, dA_{j,p}^e + \tilde{\sigma}_{e_p}^f \iint\limits_{A_{j,p}^e} E_p \, dA_{j,p}^e = \oint\limits_{C_{j,p}^e} \tilde{\mathbf{H}}^{\mathbf{t}} \cdot \mathbf{dl} \tag{2.15}$$

$$\tilde{\mu}_l^f \frac{\partial}{\partial t} \iint\limits_{A_{i,l}^h} H_l \, dA_{i,l}^h + \tilde{\sigma}_{m_l}^f \iint\limits_{A_{i,l}^h} H_l \, dA_{i,l}^h = - \oint\limits_{C_{i,l}^h} \tilde{\mathbf{E}}^{\mathbf{t}} \cdot \mathbf{dl} \tag{2.16}$$

Where H_l and E_p denote the (face) normal components of the magnetic and electric fields (traditional FDTD). The fields are assumed to remain constant over the area integrals. The time-averaging scheme discussed in the previous section is used for the time derivatives. The "face average" permittivity and electric conductivity discussed above have been used (cf. Eq. (2.3)). In addition, a face average for the permeability ($\tilde{\mu}_l^f$) and magnetic conductivity ($\tilde{\sigma}_{m_l}^f$) has been introduced. This is because the evaluation face is located at the interface of two cells. The average permeability is defined by $\tilde{\mu}_l^f = (V_i^h \, \mu_i + V_k^h \, \mu_k)/(V_i^h + V_k^h)$, with $\tilde{\sigma}_{m_l}^f$ similar.

The magnetic field projected along dual-edge, $\mathbf{s}_l^e$, is finally constructed by forming

$$\tilde{\mathbf{H}}^{\mathbf{t}} \cdot \mathbf{s}_l^e = \frac{1}{2}\left(\mathbf{H}_i^{\mathbf{t}} + \mathbf{H}_k^{\mathbf{t}}\right) \cdot \mathbf{s}_l^e + \left[H_l - \frac{1}{2}\left(\mathbf{H}_i^{\mathbf{t}} + \mathbf{H}_k^{\mathbf{t}}\right) \cdot \mathbf{n}_{i,l}^h\right]\left(\mathbf{n}_{i,l}^h \cdot \mathbf{s}_l^e\right) \tag{2.17}$$

This expression directly incorporates the FDTD term into the average vector field. Note that when $\left|\mathbf{n}_{i,l}^h \cdot \mathbf{s}_l^e\right| = 1$, the expression returns only the FDTD result. Arithmetic averaging of the vector fields at the edge endpoints has been used. The average electric field, $\tilde{\mathbf{E}}^{\mathbf{t}}$, projected along primary-edge, $\mathbf{s}_p^h$, is similar. Note the use of edge-projected fields in Eqs. (2.7, 2.15, 2.16).

Boundary-Condition Implementation for Open Conductors

When a primary grid is generated for an inhomogeneous region, nodes lie along the material interfaces (cf. Fig. 2.4). Dual cells associated with these nodes extend across the interface which is why material averaging is used. In the case of a conducting sheet, the boundary dual cells become split, either completely or partially, depending on the location of the primary-cell node. Direct computation for the vector electric field is no longer possible in the usual sense for these cells. Of course, the tangential component of the vector field is zero, but the normal component generally is not. A similar situation occurs with traditional FDTD, but due to its rectilinear nature, no complication occurs. However, a complication does occur with non-orthogonal cells whenever the computation of $\tilde{\mathbf{E}}^{\mathbf{t}} \cdot \mathbf{s}_p^h$, where $\mathbf{s}_p^h$ denotes a primary edge with one node on the

conductor, doesn't simplify to the FDTD term, E_p. In this case, the following alternative expression for $\tilde{\mathbf{E}}^{\mathbf{t}} \cdot \mathbf{s}_p^h$ is used (noting $\tilde{\mathbf{n}}_{s_p} \times \mathbf{E}_j^{\mathbf{t}} = 0$)

$$\tilde{\mathbf{E}}^{\mathbf{t}} \cdot \mathbf{s}_p^h = \frac{1}{2}\left(\mathbf{E}_i^{\mathbf{t}} + \left(\tilde{\mathbf{n}}_{s_p} \cdot \mathbf{E}_i^{\mathbf{t}} \right) \tilde{\mathbf{n}}_{s_p} \right) \cdot \mathbf{s}_p^h + \left[E_p - \frac{1}{2}\left(\mathbf{E}_i^{\mathbf{t}} + \left(\tilde{\mathbf{n}}_{s_p} \cdot \mathbf{E}_i^{\mathbf{t}} \right) \tilde{\mathbf{n}}_{s_p} \right) \cdot \mathbf{n}_{j,p}^e \right] \left(\mathbf{n}_{j,p}^e \cdot \mathbf{s}_p^h \right) \tag{2.18}$$

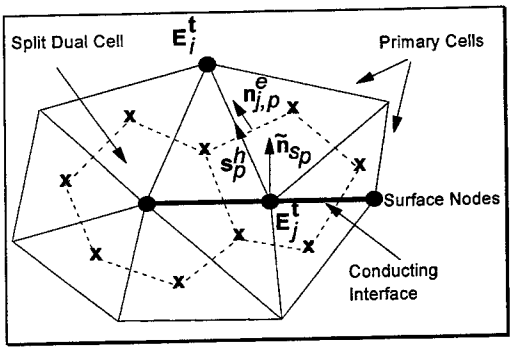

Fig. 2.4. Dual cells along a conducting interface.

where $\tilde{\mathbf{n}}_{s_p}$ denotes an average surface normal at the boundary node and $\mathbf{E}_i^{\mathbf{t}}$ denotes the *known* vector field associated with edge, $\mathbf{s}_p^h$. The average surface normal is constructed by forming a weighted average of neighboring face normals using only those faces residing on the conductor. Note that expression (2.18) incorporates the known zero tangential field at the boundary node, but relies upon the vector field off the surface to provide the estimate for the (surface) normal component. As before, the FDTD contribution is used to correct the (face) normal component (which has been found to be a critical contribution). Improved representations remain an active area of research.

Grid Generation and Selection of Time Steps

The FVHG algorithm implemented here uses the CAD package I-DEAS [21] to generate solid models, free-meshed linear tetrahedron grids, and/or mapped-mesh hexahedral/wedge grids. The method to terminate the tetrahedron grid and connect a structured FDTD grid can be found in Ref. [14]. The method is based on embedding the geometry of interest in a series of rectangular boxes that are partitioned with quadrilateral sub-surfaces. These surface partitions force the tetrahedron grid to terminate such that the surface nodes will spatially align with the nodes of the structured FDTD grid that will be connected. The creation of the proper surface partitions is easily automated within I-DEAS. The direct interface to hexahedral cells is realized through the use of seven-faced, six-sided elements called "wrapper cells." These cells are generated through the pre-processor as a consequence of the topology of a hexahedral element being interfaced to the bases of two tetrahedra. The wrapper completely encloses the unstructured region. The resulting grid (including the wrapper) represents the unstructured primary grid. The corresponding dual grid is constructed during the pre-processing phase. It is noted that because the use of wrapper cells enables the connection of mapped-mesh hexahedral elements to free-meshed tetrahedra, these two gridding methods can be logically combined within I-DEAS.

The primary and dual grids are scanned to determine their maximum, minimum, and average edge lengths. The time step to be used in the unstructured region is related to the minimum edge length, but it can generally be chosen considerable larger than what the absolute smallest edge length would dictate. The following provides *guidelines* for the choice of the unstructured-grid time step obtained through numerical experiments.

Define the ratio of the maximum to minimum edge lengths on the primary and dual grids to be R_p and R_d, respectively, and let $N_u = [[\xi \max([[R_p]],[[R_d]])]]$, with $[[\cdot]]$ denoting the closest integer greater than the argument, and $\frac{1}{2} \le \xi \le \frac{2}{3}$. Define $\Delta t_u = \Delta t_s / N_u$, where Δt_u denotes the time step in the unstructured grid and Δt_s denotes the time step in the structured (FDTD) grid. The unstructured-grid time step becomes an integral sub-division of the FDTD time step which enables this region to be advanced several sub-time steps for each time step in the FDTD grid. Second-order time-interpolation has been found to be an effective means to time-couple the two regions [13]. Assuming a uniform, free-space FDTD grid with spatial step, Δ, $\Delta t_s = \Delta / (c\, N_s)$. For this type of grid, N_s is typically defined to be equal to 2 (but could be taken as small as $\sqrt{3}$). In a free-space unstructured region, $\Delta t_u = \Delta / (c\, N_s\, N_u)$. It is assumed that time averaging is only used in the unstructured region, and as previously shown, time averaging slightly tightens the Courant condition. This is why the parameter ξ can not be uniquely defined. As the filtering effect increases (corresponding to decreasing α), ξ generally needs to be chosen toward the upper end of the defined range. Having defined the time step, the dissipation effect is easily estimated from Fig. 2.3 by setting $N = N_u \cdot N_s$.

3. Microstrip Applications

Three well known rectangular microstrip geometries have been selected to study the effect of local embedded tetrahedron grids on accuracy. Issues involving grid reflection at the hexahedron-tetrahedron interfaces, propagation through dense tetrahedron regions, sub-time stepping, and the effect of dissipation in the unstructured grid, are examined through these examples.

Uniform Microstripline

As a first example, the simple microstrip shown in Fig. 3.1 was investigated. The substrate relative permittivity was 2.2. The geometry was modeled by a uniform collection of hexahedral elements with an edge length of 0.1985 mm, along with an embedded tetrahedron region with an average edge length of 0.1985 mm. The location and form of the tetrahedron region are shown in Figs. 3.1 and 3.2. The microstrip was locally terminated with a simple first-order Mur absorbing boundary condition (ABC). Both the hexahedron and tetrahedron grids shown in Fig. 3.2 were created within I-DEAS and jointly define the unstructured grid (excluding the wrapper). Upon adding the wrapper during the preprocessing phase, the unstructured grid was embedded in a uniform FDTD mesh that measured 202 x 68 x 88 cells in the x, y, and z directions, respectively. The FDTD cell size was also 0.1985 mm. The FDTD mesh was terminated with second-order Mur boundaries. In the FDTD mesh, N_s was set to 2, and $\alpha = \infty$. In the unstructured region, $N_u = 3$ (3 sub-time steps), and $\alpha = 12$ (based on the previous guideline, $N_s \cdot N_u \cdot \alpha \le 80$).

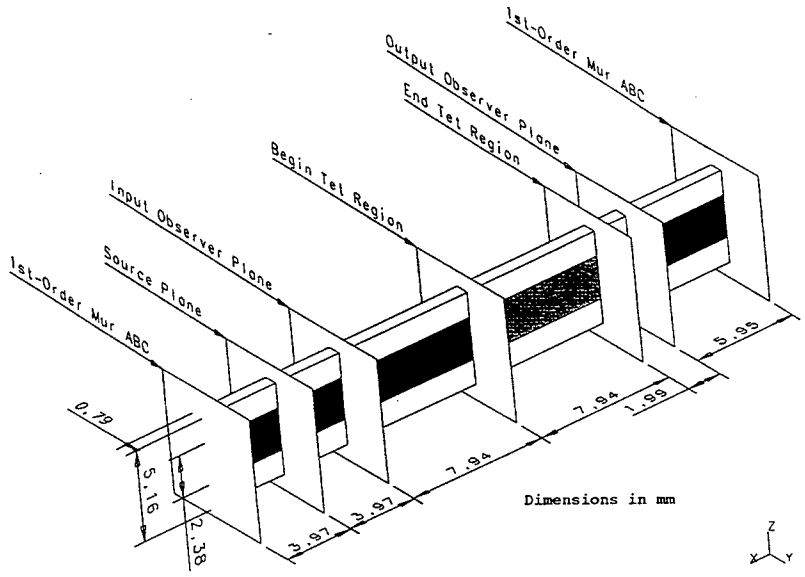

Fig. 3.1. Uniform microstrip test geometry. (Dimensions in mm.)

The microstrip was driven by adding a gaussian source between the power and ground planes at the location shown in Fig. 3.1. Fig. 3.3 shows the voltage under the midpoint of the power trace at the input and output observer planes. A comparison is made by replacing the FVHG tetrahedron region with cubical hexahedral cells so that the finite-volume algorithm resorts exclusively to the FDTD term. Although this comparison mesh is now exclusively FDTD, the microstrip remains unstructured with the same values for N_u and α; this permits a careful examination of guided-wave propagation through tetrahedrons and across hex-tet interfaces. As shown in Fig. 3.3, the results at the two observers are nearly identical for the two grid types. The only noticeable difference is a slight delay at the output observer when the tetrahedrons are present (FVHG results). This is most likely due to the increased cell density associated with the tetrahedrons.

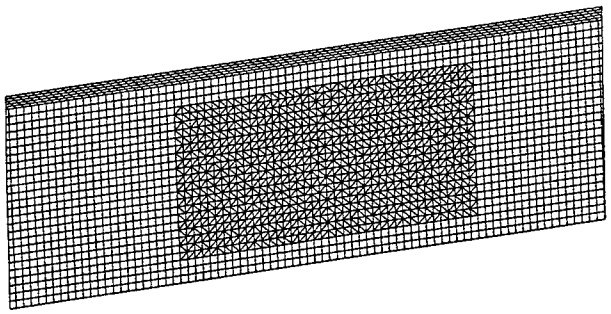

Fig. 3.2. Portion of unstructured grid for Fig. 3.1 showing tetrahedra region, which extends from one hexahedral cell-width above the power trace to the ground plane.

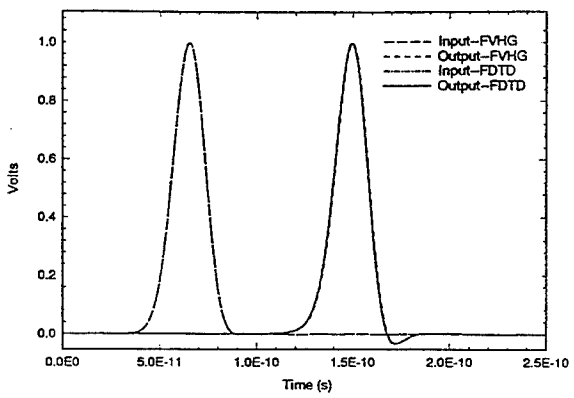

Fig. 3.3. Results at input and output planes based on all hexahedral (FDTD) and embedded tetrahedral (FVHG) cells.

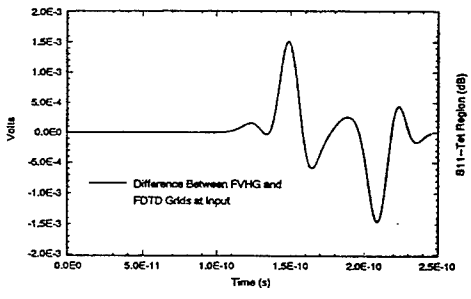

Fig. 3.4a. Difference of Fig. 3.3 results at input observer.

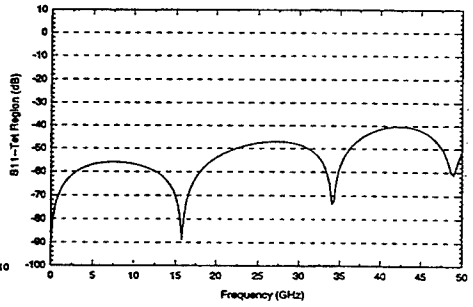

Fig. 3.4b. Normalized spectrum.

The difference between the FDTD and FVHG results at the input observer is shown in Fig. 3.4a. This reveals the subtle propagation differences between the grid types. The (peak) voltage difference is seen to be nearly three orders of magnitude below the peak voltage in Fig. 3.3. It is believed that this can be further reduced with improved boundary conditions for open conductors (cf. Section 2). The spectrum of the difference field, normalized to the incident-field spectrum, is shown in Fig. 3.4b. This result can be considered the return loss ($S11$) of the tetrahedra region. In the substrate, the FVHG grid resolution is approximately 20 "cells" per wavelength at 50 GHz based on the maximum of the average edge lengths of the primary and dual grids.

Low-Pass Filter

The second example is the well known low-pass filter originally studied by Sheen, *et al.*, [22]. A portion of the filter modeled in the current paper is shown in Fig. 3.5a. Linear microstrip lines connect to the input and output ports. The geometry shown in Fig. 3.5a was modeled with tetrahedral elements with an average edge length of 0.264667 mm. This portion of the overall grid contained approximately 50,000 tetrahedra and is shown in Fig. 3.5b. Uniform hexahedral elements with an edge length of 0.264667 mm were used to model the microstrips that connect to the input and output ports depicted in Fig. 3.5a; these element were created using mapped-mesh techniques within I-DEAS. It is noted that some modeling flexibility has been lost by forcing the tetrahedra to interface with these hexahedral elements; this accounts for the slight shifting of the port locations and the reduced trace widths relative to the actual geometry shown by Sheen, *et al.*, [22]. The complete unstructured grid, including the wrapper, is shown in Fig. 3.6. This grid was embedded in a large, uniform FDTD grid that measured 180 x 66 x 148 cells. Second-order Mur boundaries terminated the FDTD grid. The FDTD cell size was 0.264667 mm. The microstrip was driven and terminated similar to the previous example. The source plane was located 16 cells from the left side of the unstructured grid shown in Fig. 3.6. The number of subtime steps in the unstructured grid was 4, and the stabilization parameter was set to 10.

The location of the observer on the input microstrip was under the midpoint of the power trace and placed three cells from the edge of the left side of the unstructured grid shown in Fig. 3.6. The observer on the output microstrip was located 16 cells from the right side of this grid. The operating range for this circuit is less than 10 GHz. The time response at the input observer is shown in Fig. 3.7a. The corresponding result for $S11$ is shown in Fig. 3.7b. Results at the output observer are shown in Figs. 3.8a,b. The simulation ran for 20,000 time steps in the unstructured grid (5,000 in the FDTD grid) and required approximately 8 hours using 8 processors of a Sun Sparcserver 1000 (with 50 MHz Sparc-51 chips, which are not vector processors).

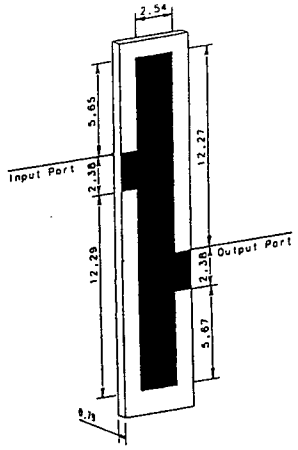

Fig. 3.5a. Low-pass filter model. Substrate relative permittivity was 2.2. (Dimensions in mm.)

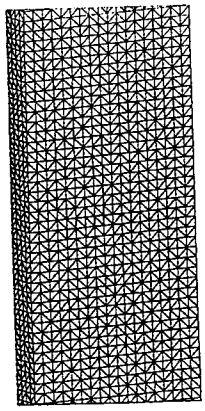

Fig. 3.5b. A section of the tetrahedron grid that encloses the low-pass filter.

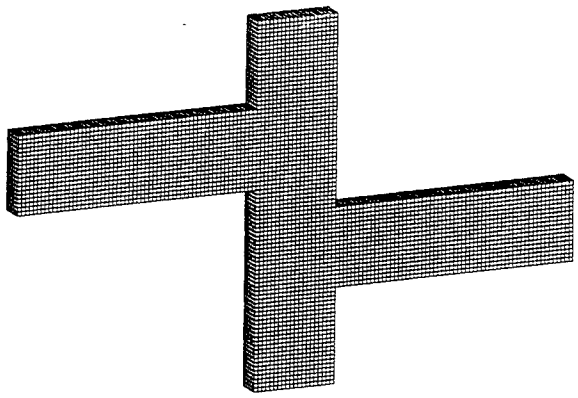

Fig. 3.6. Full unstructured grid for low-pass filter including connecting traces at input and output ports. Tetrahedra region shown in Fig. 3.5b is enclosed in the mid-section.

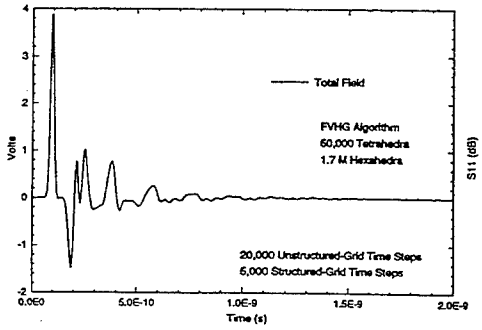

Fig. 3.7a. Time response at input observer for low-pass filter.

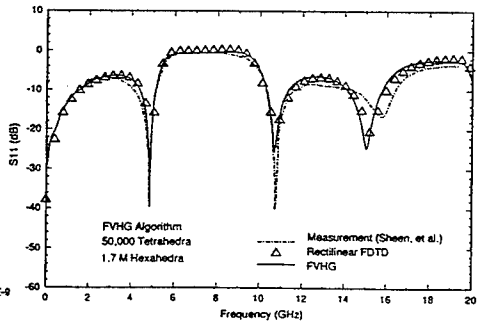

Fig. 3.7b. Return loss.

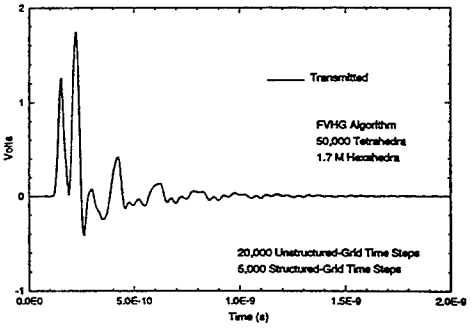

Fig. 3.7a. Time response at output observer for low-pass filter.

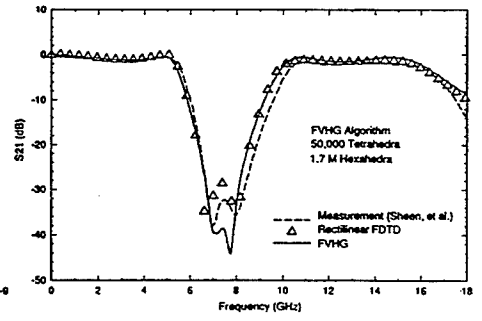

Fig. 3.8b. Insertion loss.

Microstrip Patch Antenna

The final example is the well-known patch antenna originally studied by Sheen, *et al.*, [22]. A portion of the antenna modeled here is shown in Fig. 3.9. For this problem, a low-density hexahedron grid, with an edge length equal to the substrate width (0.794 mm), was used with a high-density tetrahedron grid of the geometry shown in Fig. 3.9. A surface grid with an average edge length of 0.3 mm was placed on the patch antenna. A portion of the unstructured grid showing the grid transition is shown in Fig. 3.10. The driving microstrip, including the source, observer, and termination planes, was in the low-density hexahedron region. The observer was located under the midpoint of the power trace and positioned 2 cells from the left edge of the grid shown in Fig. 3.10. A local first-order Mur boundary condition was applied at the left edge of this grid, and the source plane was located 15 cells from the left edge. Upon adding the wrapper, the un-

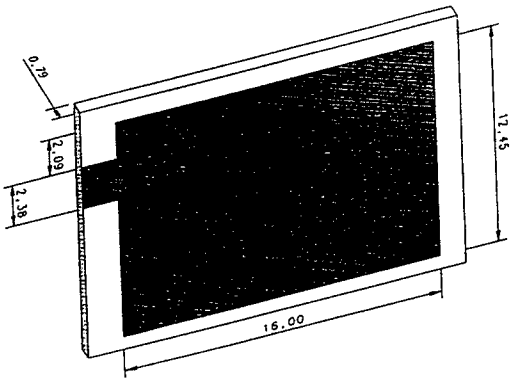

Fig. 3.9. Model of patch antenna. Substrate relative permittivity is 2.2. The input port is at the trace "stub" on the left side of the figure. (Dimensions in mm.)

structured grid was placed in a uniform FDTD grid that measured 96 x 44 x 60. The FDTD grid used a uniform cell size of 0.794 mm and was terminated with second-order Mur boundaries. Note that the hexahedral grid only provides about 13 cells per wavelength in the substrate at 20 GHz.

Using the high-density surface grid gave rise to a maximum to minimum edge length ratio on the primary grid of 11.4 (R_p), while on the dual grid this ratio was 17.25 (R_d). Twelve sub-time steps were required in the unstructured grid ($N_u = 12$), $N_s = 2$, and the stabilization parameter, α, was set to 3 (based on the guideline, $N_s \cdot N_u \cdot \alpha \leq 80$). The unstructured grid contained approximately 36,000 tetrahedra and 520 hexahedra (excluding the wrapper). Results at the input observer are shown in Figs. 3.11a,b. The simulation ran for 36,000 time steps in the

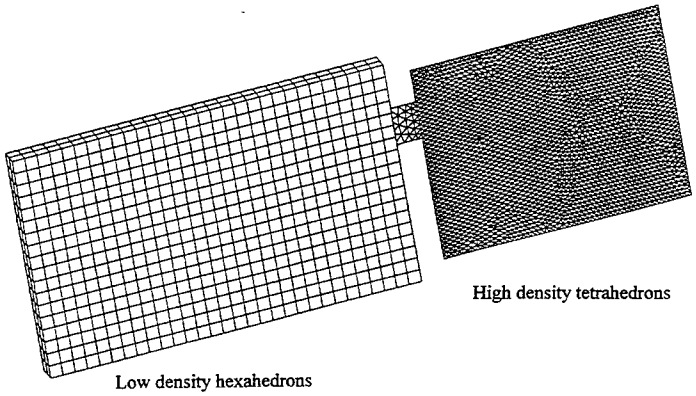

Fig. 3.10. Partial grid of patch antenna. The feeding trace, modeled with uniform quadrilateral shell elements, resides in the low-density hexahedron mesh and connects to the input port of the patch antenna. At this point, the grid transitions to a dense triangular-element surface mesh surrounded by tetrahedral elements.

unstructured grid (3,000 in the structured grid) and required approximately 6 hours using 6 processors of the Sun Sparcserver 1000. It is noted that the patch antenna required approximately 1 hour to generate the solid model, tetrahedra grid, and mapped-mesh hexahedra grid for the input trace extension using I-DEAS (cf. Fig. 3.10), as well as all primary and dual grid information from the preprocessor.

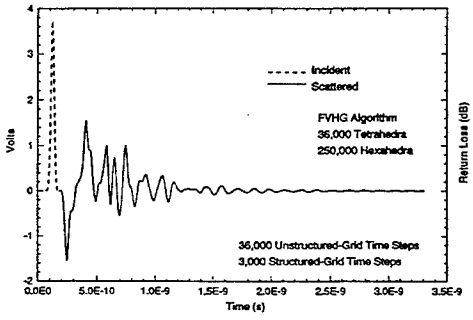

Fig. 3.11a. Time response at input observer for patch antenna.

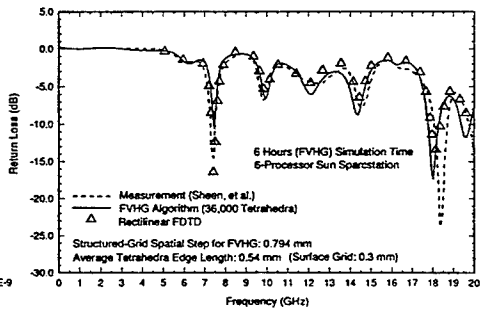

Fig. 3.11b. Return loss.

4. Conclusions

This paper has examined the effect of local, free-meshed tetrahedron grids in uniform-grid FDTD as applied to microstrip geometries. By comparing with well known FDTD solutions, the FVHG approach was shown to provide very accurate results when specialized to rectangular geometries. Numerical reflections at the hexahedron-tetrahedron interfaces have typically been found to be suppressed by at least 40 dB. Much of the reflection is believed to be due to current boundary condition approximations in the finite-volume formulation as applied to open conductors. Improved approximations remain an active topic of research. Abrupt changes in grid density and different dispersion characteristics between hexahedrons and tetrahedrons also contribute. However, the dynamic range that is currently obtainable is sufficient for most practical microstrip applications. Extensive numerical experimentation has revealed that a good indicator for the grid resolution of a tetrahedron primary grid is based on the maximum of the *average* edge lengths of the primary and dual grids. The upper frequency resolution is then obtained by equating this distance to the wavelength divided by twenty. Because the FVHG approach uses commercial solid-modeling and local free-meshed grids, the efficient modeling of high complexity devices is possible. Examples will be discussed in future papers.

The development and application of unstructured finite volume and finite element methods to transient computational electromagnetics is only beginning to evolve. Important research areas in FDTD such as radiation boundary conditions and sub-grid models will undoubtedly be revisited in this context. Additional research into the late-time stability of explicit difference schemes on complex grids is also needed. This paper has utilized an effective, variably dissipative time-averaging scheme to obtain stability in the unstructured grid, but non-dissipative time-differencing is ultimately desired.

Acknowledgment

The authors thank Dr. Mike Pasik for supplying comparison data for the microstrip low-pass filter and patch antenna obtained from the rectilinear FDTD code, QUICKSILVER [23].

References

[1] K.S. Yee, "Numerical solution of initial boundary value problems involving Maxwell's equations in isotropic media," *IEEE Trans. Antennas Propagat.*, **14**, 4, pp. 302-307, 1966.

[2] K.L. Shlager and J.B. Schneider, "A selective survey of the finite-difference time-domain literature," *IEEE Antennas Propagat. Mag.*, **37**, 4, pp.39-57, 1995.

[3] R. Holland, "Pitfalls of staircase meshing," *IEEE Trans. EMC*, **35**, 4, pp.434-439, 1993.

[4] M.N.O. Sadiku, *Numerical Techniques in Electromagnetics*, pp. 407-500, CRC Press, FL, 1992.

[5] A. Chatterjee and J.L. Volakis, "Conformal absorbing boundary conditions for 3-D problems: derivation and applications," *IEEE Trans. Antennas Propagat.*, **43**, 8, pp. 860-866, 1994.

[6] C.H. Chan, J.T. Elson, and H. Sangani, "An explicit finite-difference time-domain method using Whitney elements," *IEEE Antennas Propagat. Symp. Dig.*, **3**, pp. 1768-1771, Seattle, WA, 1994.

[7] J.-F. Lee, "Whitney elements time domain (WETD) methods for solving three-dimensional waveguide discontinuities," *11th Annual Review of Progress in Applied Computational Electromagnetics (ACES) Symp. Dig.*, pp. 1258-1265, 1995.

[8] V. Shankar, A.H. Mohammadian, and W.F. Hall, "A time-domain, finite-volume treatment for the Maxwell equations," *Electromagnetics*, **10**, 1-2, pp. 127-145, 1990.

[9] N.K. Madsen and R.W. Ziolkowski, "A three-dimensional modified finite volume technique for Maxwell's equations," *Electromagnetics*, **10**, 1-2, pp. 147-161, 1990.

[10] N.K. Madsen, "Divergence preserving discrete surface integral methods for Maxwell's curl equations using nonorthogonal unstructured grids," RIACS Tech. Rep. 92.04, NASA Ames Research Center, CA, 1992.

[11] K.S. Yee and J.S. Chen, "Conformal hybrid finite-difference time-domain (FDTD) with finite-volume time domain," *IEEE Trans. Antennas Propagat.*, **42**, 10, pp. 1450-1455, 1994.

[12] T.G. Jurgens and A. Taflove, "Three-dimensional contour FDTD modeling form single and multiple bodies," *IEEE Trans. Antennas Propagat.*, **41**, 12, pp. 1703-1708, 1993.

[13] D.J. Riley and C.D. Turner, "Unstructured finite-volume modeling in computational electromagnetics," *11th Annual Review of Progress in Applied Computational Electromagnetics (ACES) Symp. Dig.*, pp. 435-444, 1995.

[14] D.J. Riley and C.D. Turner, "Interfacing unstructured tetrahedron grids to structured-grid FDTD," *IEEE Microwave and Guided Wave Letters*, **5**, 9, pp. 284-286, 1995.

[15] S.D. Gedney and F. Lansing, "A parallel discrete surface integral equation method for the analysis of three-dimensional microwave circuit devices with planar symmetry," *IEEE Antennas Propagat. Symp. Dig.*, **3**, pp. 1778-1781, Seattle, WA, 1994.

[16] CUBIT, Sandia National Laboratories, Albuquerque, NM, Dept. 1425, private communication, 1994.

[17] Hexagen, Algor, Inc., Pittsburgh, PA, 15238.

[18] T.J.R. Hughes, *The Finite Element Method*, pp. 490-569, Prentice-Hall, Englewood Cliffs, NJ, 1987.

[19] K.L. Shlager, J.G. Maloney, S.L. Ray, and A.F. Peterson, "Relative accuracy of several finite-difference time-domain methods in two and three dimensions," *IEEE Trans. Antennas Propagat.*, **41**, 12, pp. 1732-1737, 1993.

[20] W.F. Ames, *Numerical Methods for Partial Differential Equations*, pp.47-49, Academic Press, NY, NY, 1977.

[21] I-DEAS Master Series, Structural Dynamics Research Corporation, Milford, OH, 45150-2789.

[22] D.M. Sheen, S.M. Ali, M.D. Abouzahra, and J.A. Kong, "Application of the three-dimensional finite-difference time-domain method to the analysis of planar microstrip circuits," *IEEE Trans. Microwave Theory and Tech.*, **38**, 7, pp. 849-857, 1990.

[23] D.B. Seidel, M.L. Kiefer, R.S. Coats, T.D. Pointon, J.P. Quintenz, and W.A. Johnson, "The 3-D electromagnetic, particle-in-cell code, QUICKSILVER," *Proceedings of the CP90 Europhysics Conference on Computational Physics*, pp. 475-482, 1991.

Full Wave Vector Maxwell Equation Modeling of Self-Limiting Effects and Optical Nonlinear Vortices

Sergey V. Polstyanko and Jin-Fa Lee
Department of Electrical and Computer Engineering, Worcester Polytechnic Institute,
Worcester, MA 01609 USA

Abstract

We have developed a new nonlinear hybrid vector finite element method to model wave propagation in nonlinear media. This method is based on the vectorial wave equation and can adequately describe the vectorial properties of fields in nonlinear structures. With this approach we have studied such effects as optical soliton formations, self-focusing effects.

1 Introduction

The properties of nonlinear optical waves guided by dielectric nonlinear waveguides are of great interest because of their unique features, such as soliton formation and subsequent propagation and self-focusing effects [1, 2, 3]. These effects and their potential use in all optical signal processing devices have stimulated the theoretical investigation of the behavior of the nonlinear guided waves [3, 4]. Under the assumption of negligible transverse effects, analytical solution can be obtained for many cases by employing plane-wave approximation. This approximation can be used when one is interested only in the evolutional variation along the propagation axis z. However, the introduction of transverse effects, which are unavoidable in practical situations because of the finite cross section of the optical beam, complicates the problem and in many cases numerical methods are needed to study the transverse effects of optical beams. Consequently, the growing attention has been paid to numerical methods for studying electromagnetic wave propagation in nonlinear optical media [5, 6, 7, 8]. Among the available methods, three techniques are most widely used and provide practical information for various nonlinear phenomena. They are: beam propagation method (BPM) [9, 10, 11], nonlinear time domain finite difference (NL-FDTD) method [12, 13] and split-step finite element method (SSFEM) [7]. In our effort to meet an increasing demand for more accurate and realistic nonlinear optics simulations, we have developed a three-dimensional nonlinear hybrid vector finite element method (NL-HVFEM) to study different phenomena due to wave propagation in nonlinear Kerr-type media. Contrary to the most of the existing one-dimensional, scalar models, the NL-HVFEM approach is based upon the vector Helmholtz equation and thus can predict the vectorial properties of fields in nonlinear media without any assumptions. In the following chapters, we describe the NL-HVFEM approach and its application to the modeling of nonlinear wave propagation in three-space dimensions. Numerical results for different nonlinear effects are given and comparisons with previously reported results are made.

2 Basic Equations

We consider nonlinear electromagnetic wave propagation in an isotropic medium, which is uniform in z with an arbitrary shape in the transverse (xy) plane, having intensity-dependent relative permittivity ϵ_r, such that

$$\epsilon_r = \epsilon_L + \alpha f(|E|^2) \tag{1}$$

where $\epsilon_L = n_0^2$ denotes the linear relative permittivity, α is the nonlinear coefficient and f can be an arbitrary function of the intensity $|E|^2$ such that $f(0) = 0$. When $f(|E|^2) = |E|^2$, Eq. (1) corresponds to the Kerr-type

nonlinearity. Assuming $\exp(j\omega t)$ dependence of EM fields, the time-harmonic form of Maxwell's equations is given by

$$\begin{aligned} \nabla \times \vec{H} &= j\omega\epsilon_0\epsilon_r\vec{E} \\ \nabla \times \vec{E} &= -j\omega\mu_0\vec{H} \end{aligned} \tag{2}$$

The assumption, concerning time variation, is valid as long as the pulse duration of the optical beam is longer than a subnanosecond. To study the spaciotemporal behavior of short pulses, which are obtainable with modern mode-locked laser technology, the present approach is not valid and a nonlinear time domain method, such as the NL-FDTD [12], has to be adopted. Equations (2) can be reduced to a single vector equation in term of $\vec{E}$. The resulting Helmholtz vector wave equation is

$$\nabla \times \nabla \times \vec{E} = k_0^2\epsilon_r\vec{E} \tag{3}$$

where k_0 is the wavenumber in free-space. Using the conventional approximation of a slowly varying envelope and assuming also that the axis of the propagation is z, we can rewrite $\vec{E}$ as

$$\vec{E} = \vec{\mathcal{E}}(x,y,z)\exp j(\omega t - \beta z) \tag{4}$$

where $\vec{\mathcal{E}}$ represents slowly varying amplitude of the original field $\vec{E}$. Furthermore, we define the transverse operator ∇_τ as

$$\nabla_\tau = \hat{x}\partial_x + \hat{y}\partial_y$$

and

$$\vec{E} = \vec{\mathcal{E}}_\tau + \hat{z}\mathcal{E}_z \qquad \nabla = \nabla_\tau + \hat{z}\partial_z \tag{5}$$

where $\vec{\mathcal{E}}_\tau, \mathcal{E}_z$ are the transverse and the z components of $\vec{E}$, respectively. Finally, based on Eqs. (3)-(5), the vector Helmholtz wave equation becomes

$$\left\{ \begin{array}{c} \nabla_\tau \times \nabla_\tau \times \vec{\mathcal{E}}_\tau - \hat{z}\nabla_\tau^2\mathcal{E}_z + \hat{z}\nabla_\tau \cdot \partial_z\vec{\mathcal{E}}_\tau - j\beta\hat{z}\nabla_\tau \cdot \vec{\mathcal{E}}_\tau \\ +\partial_z\nabla_\tau\mathcal{E}_z - \partial_z^2\vec{\mathcal{E}}_\tau - j\beta\nabla_\tau\mathcal{E}_z + \beta^2\vec{\mathcal{E}}_\tau \end{array} \right\} - k_0^2\epsilon_r\vec{\mathcal{E}} = 0 \tag{6}$$

Furthermore, in derivation of Eq. (6) we have considered all terms and no approximations were made.

3 NL-HVFEM Formulation

First we subdivide the entire cross-sectional domain (xy plane) of the system into a number of small subdomains, using finite elements. In the two-dimensional case one way of achieving this is by Delaunay triangulation. Galerkin's weighted residual approach has been used to construct our finite element formulation [14], and its application to Eq. (6) leads to the following bilinear form

$$\begin{aligned} B(\vec{W},\vec{E}) = &\int_\Omega \left(\nabla_\tau W_z \cdot \partial_z\vec{\mathcal{E}}_\tau - \vec{W}_\tau \cdot \partial_z\nabla_\tau\mathcal{E}_z - 2j\beta\vec{W}_\tau \cdot \partial_z\vec{\mathcal{E}}_\tau + \vec{W}_\tau \cdot \partial_z^2\vec{\mathcal{E}}_\tau \right) d\Omega \\ &- \int_\Omega \left(\begin{array}{c} (\nabla_\tau \times \vec{W}_\tau) \cdot (\nabla_\tau \times \vec{\mathcal{E}}_\tau) + \nabla_\tau W_z \cdot \nabla_\tau\mathcal{E}_z + j\beta\nabla_\tau W_z \cdot \vec{\mathcal{E}}_\tau \\ -j\beta\vec{W}_\tau \cdot \nabla_\tau\mathcal{E}_z + \beta^2\vec{W}_\tau \cdot \vec{\mathcal{E}}_\tau - k_0^2\vec{W} \cdot \epsilon_r\vec{\mathcal{E}} \end{array} \right) d\Omega \end{aligned} \tag{7}$$

where Ω is the cross section of the waveguide and $\vec{W}, \vec{E}$ are the testing and trial fields, respectively. In the current formulation the hybrid finite element approach, namely edge-elements for the transverse component and nodal FEM for z component of electric field, is applied to the waveguide cross section [15]. It has been shown that this method is free of spurious modes and results in a reliable numerical solution. By setting

$B(\vec{W},\vec{E})=0$ for every $\vec{W}$ in the testing function space, one comes up with the following differential matrix equation.

$$[M]\frac{\partial}{\partial z}\underline{e}=[F]\underline{e} \tag{8}$$

and the matrices are defined as

$$[M]=\begin{bmatrix}[M_{\tau\tau}] & [M_{\tau z}] & [N_{\tau\tau}]\\ [M_{z\tau}] & 0 & 0\\ [N_{\tau\tau}] & 0 & 0\end{bmatrix};\quad [F]=\begin{bmatrix}[F_{\tau\tau}] & [F_{\tau z}] & 0\\ [F_{z\tau}] & [F_{zz}] & 0\\ 0 & 0 & [N_{\tau\tau}]\end{bmatrix};\quad \underline{e}=\begin{bmatrix}\underline{e}_\tau\\ \underline{e}_z\\ \underline{g}_\tau\end{bmatrix} \tag{9}$$

where $\underline{e}_\tau, \underline{e}_z$ are column vectors of coefficients for the transverse and z components, respectively, and $\underline{g}_\tau$ denotes

$$\underline{g}_\tau=\frac{\partial \underline{e}_\tau}{\partial z} \tag{10}$$

Moreover, the element matrices in Eq. (8) are given by

$$\begin{aligned}
[M_{\tau\tau}] &: -2j\beta\int_\Omega\{\vec{W}_\tau\cdot\vec{\mathcal{E}}_\tau\}d\Omega\\
[M_{\tau z}] &: -\int_\Omega\{\vec{W}_\tau\cdot\nabla_\tau\mathcal{E}_z\}d\Omega\\
[M_{z\tau}] &: \int_\Omega\{\vec{\mathcal{E}}_\tau\cdot\nabla_\tau W_z\}d\Omega\\
[N_{\tau\tau}] &: \int_\Omega\{\vec{W}_\tau\cdot\vec{\mathcal{E}}_\tau\}d\Omega\\
[F_{\tau\tau}] &: \int_\Omega\{(\nabla_\tau\times\vec{W}_\tau)\cdot(\nabla_\tau\times\vec{\mathcal{E}}_\tau)+\beta^2\vec{W}_\tau\cdot\vec{\mathcal{E}}_\tau-k_0^2\vec{W}_\tau\cdot\epsilon_r\vec{\mathcal{E}}_\tau\}d\Omega\\
[F_{\tau z}] &: -j\beta\int_\Omega\{\vec{W}_\tau\cdot\nabla_\tau\mathcal{E}_z\}d\Omega\\
[F_{z\tau}] &: j\beta\int_\Omega\{\nabla_\tau W_z\cdot\vec{\mathcal{E}}_\tau\}d\Omega\\
[F_{zz}] &: \int_\Omega\{\nabla_\tau W_z\cdot\nabla_\tau\mathcal{E}_z-k_0^2W_z\cdot\epsilon_r\mathcal{E}_z\}d\Omega
\end{aligned} \tag{11}$$

Finally, application of the finite difference method, based on the backward difference scheme, to Eq. (8) yields

$$([M]-[F]\Delta z)\underline{e}^{i+1}=[M]\underline{e}^i \quad for \quad i=0,1,2... \tag{12}$$

where $\underline{e}^i$ corresponds to e at $z=i\Delta z$, e_0 is the initial state and Δz is the difference step along the z axis. Furthermore, we would like to emphasize to in our iterative process for each step i after we find a solution vector $\underline{e_i}$ we have to update not only relative permittivity ϵ_r from Eq. (1), but also propagation constant β based on Eq. (8). Consequently we end up with the following iterative scheme

(i) Specify $\beta,\epsilon_L,\alpha,k_0,e^0$ as an input data.

(ii) Calculate the coefficient matrices [M],[F] and solver Eq. (12) for a new solution e^{i+1}.

(iii) Update ϵ_r form Eq.(1) and β from Eq. (8).

(iv) Iterate the above procedure (*ii*) and (*iii*) until we reach the desired number of iterations in z direction.

Finally, in the iterative procedure the following stability condition should be observed to ensure numerical stability of computed results

$$\beta\Delta z\geq 1. \tag{13}$$

Step-by-step calculation of Eq. (12) results in the variation of the field profile that is initially fired at the entrance (z = 0) of the waveguide.

4 Numerical Results

The following section is devoted to the problem of the behavior of light beam in a nonlinear medium. In the first example, a planar nonlinear waveguide has been analyzed and numerical results are shown. In the second example, a so-called *self-focusing* effect of an axially symmetrical optical beam has been studied.

Nonlinear Slab Waveguide

In our first example we apply NL-HVFEM to a planar nonlinear waveguide (NLWG) and compared our results with previously published ones. Shown in Fig.1 is a three-layered slab-type dielectric optical waveguide that consists of a linear substrate, a linear film and a Kerr-type cladding, with a nonlinear permittivity given by Eq. (1). Waveguide parameters are chosen from Ref.(5), i.e., linear refractive indices of the substrate ($x < -d$), film ($|x| \leq d$) and cladding ($x > d$) are $n_s = 1.55$, $n_f = 1.57$ and $n_c = 1.55$, respectively, and nonlinear coefficients are $\alpha_s = \alpha_f = 0.0$, $\alpha_c = 1.5 \times 10^{-2}$, where the subscripts s, f, c refer to the substrate, film and cladding, respectively.

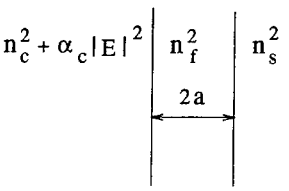

Figure 1: The geometry of the nonlinear slab waveguide.

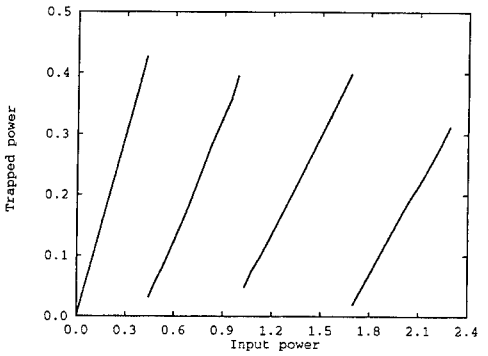

Figure 2: Power trapped in the NLWG P_t versus the input power P_{in} for the beam initially shaped as TE_0 linear mode.

The numerical experiment consisted of launching an input beam of a fixed profile but variable power into the waveguide. The input profile was chosen to be the linear TE_0 mode of the linear planar waveguide. The point of interest is the way in which the nonlinear system sheds the excess energy: a single self-channeled wave, or soliton, is emitted through the film-cladding interface into the nonlinear medium and propagates away. Figure 2 plots the power trapped in the waveguide P_t versus the input power P_{in}, where the power is defined by

$$P = \int_X \vec{E} \times \vec{H}^* \cdot \hat{z}\, dx \tag{14}$$

and x is the transverse coordinate in unit of ω/c. The figure clearly shows the sequence of thresholds.

For the low input power the beam is confined in the linear film and has only a small displacement in the nonlinear region and no soliton is emitted. Only with the input power is greater than a certain threshold, one reaches a situation when a single soliton is emitted in the nonlinear cladding (Fig. 3). The single soliton emission continues with the power of the soliton staying almost constant as we increase the input power even more (this can be deduced from the almost linear slope of the corresponding portion of the P_t vs. P_{in} curve). Furthermore, if the input power is further increased we should expect a second threshold leading to the emission of the second soliton and so on. Indeed the transmission of the multi-solitons through a nonlinear interface was observed up to the third threshold (Fig.3). Moreover, it turns out that:

(i) The distance required for the formation of the solitons from the initial TE_0 excitation decays when the input power increases

(ii) The angle of the emission of the solitons is a function of the input power

(iii) The higher thresholds do not simply occur at multiples of the input critical power P_c (for the parameter values used here, $P_c \cong 0.449$)

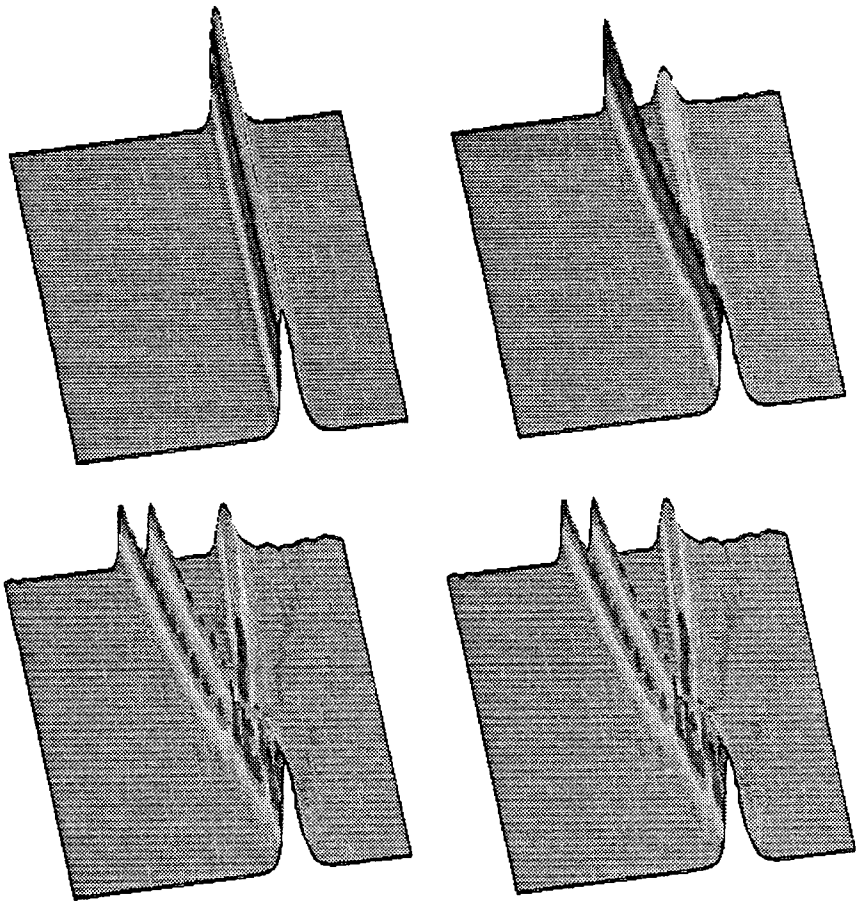

Figure 3: Evolution for $k_0 a = 2\pi$ of the input fields initially shaped as TE_0 mode for different values of the input power.

Nonlinear optical fiber

In our second example the NL-HVFEM was applied to study self-focusing effect in a nonlinear optical fiber. A number of theoretical and experimental papers have been devoted to self focusing of wave beams in nonlinear media [1, 2, 3]. For the simulation runs we fixed the initial intensity profile to be a Gaussian distribution and the initial phase front was assumed to be plane. Consequently,

$$E(r,0) = E_0 \exp(-\frac{r^2}{2a^2}) \tag{15}$$

where a, the initial waist, has been taken $a = 0.4m$. We note that all dimensions and parameters of nonlinear medium were chosen simply as a representative case. It would be easy to tailor the problem to some specific dimensions and materials. Chosen parameters will rather simplify our simulations and will ensure the the self-focusing will occurs near the center of our computational grid. In our study we have tried several grid sizes to perform numerical simulations. Most of them were run for approximately 6000 triangular elements per optical fiber cross section with spatial resolution $\delta z = \lambda_0/8$. Our calculations were limited simply by the amount of available computer memory. We would like to study here conditions under which an initial Gaussian beam can produce its own dielectric waveguide and propagate without spreading. Such self-trapping appears to be possible only for the hight intensity of an input beam when an input power is greater then a critical one. To come up with an expression for a critical power we ran our simulations for different parameters characterizing nonlinear medium , such as ϵ_L and α as well as for different frequency points. Based on our numerical results, the critical power can be approximated fairly well by

$$P_{cr} = \frac{(1.22\lambda_0)^2 \pi (\epsilon_0 \epsilon_r)^{1/2}}{16\alpha \mu_0^{1/2}} \tag{16}$$

where λ_0 is the wavelength in vacuum. To obtained the corresponding result in cgs unit we divide by $4\pi\epsilon_0$ and result in the formula numerically found by previous researchers

$$P_{cr} = \frac{(1.22\lambda_0)^2 c}{64\alpha} \tag{17}$$

where c denotes speed of light in vacuum. Only when the input power is greater them P_{cr} the light beam

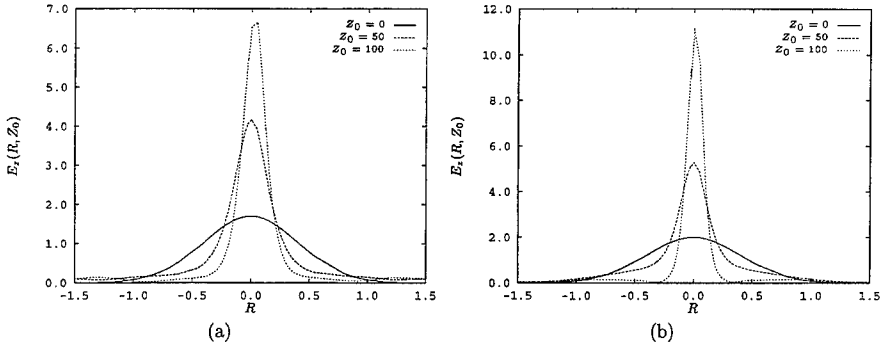

Figure 4: Radial distribution of the total electric field for nonlinear medium with $\alpha = 0.01$ and $\epsilon_L = 2$ for $f = 1.5GHz$. Curves are parameterized by z/λ_0 for a) $P_{in}/P_{cr} = 1.243$ and b) $P_{in}/P_{cr} = 1.720$.

transforms into the self-trapped regime. If we define the self-focusing length as the distance in which the intensity of an optical beam reaches the maximum then from Fig.4 we conclude that the growth of the input

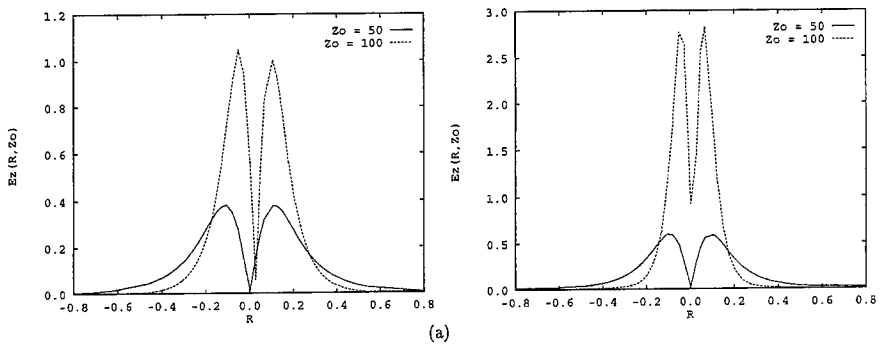

Figure 5: Numerical simulations for nonlinear medium with $\alpha = 0.01$ and $\epsilon_L = 2$ for $f = 1.5GHz$. Curves are parameterized by z/λ_0 for $P_{in}/P_{cr} = 1.243$ (left column) and $P_{in}/P_{cr} = 1.720$ (right column). a) Radial distribution of the E_z component b) Fringe plot corresponding to the E_z component.

power decreases the self-focusing length. The characteristic profiles of the amplitude $E(r, z)$ for different z are also shown in Fig. 4 for a nonlinear medium with $\epsilon_r = 2$ and $\alpha = 0.01$.

In addition to the self-trapping behavior of an optical beam, we also can observe a new effect that may occur only when the full vector nature of Maxwell's equations is taken into account. As an input beam propagates in the z direction, the self-focusing effect seems to be limited by the generation of the longitudinal field component E_z. The growth of the longitudinal electric field component of an initial TE optical beam is addressed specifically in Fig.5 and its behavior is similar to that of the transverse component. This effect of E_z component is unavailable from scalar modes and can be explained only as a complete solution of vector Maxwell's equations and exhibits the nonlinear energy transfer phenomena associated with the longitudinal electric field component. Fig.5 presents sequences of plots that illustrate this effect in the self-focusing process.

5 Conclusion

The NL-HVFEM approach described in this paper solves directly the vector Helmholtz wave equation and is applicable to optical structures of arbitrary geometry and reflection index distribution. The vectorial

properties of the fields are fully considered. Using this method we have studied such effects as soliton formation and subsequent propagation in a nonlinear slab waveguide and self-focusing effects in a nonlinear optical fiber. For these cases the conventional analytical approach is of little use. However, full-wave numerical solution techniques, such as the NL-HVFEM developed herein, can be used to study general nonlinear optical systems.

References

[1] R. Y. Chiao, E. Garmire, and C. H. Townes. "Self-Trapping of Optical Beams". *Phys. Rev. Lett.*, **13**(15):pp. 479–482, 1964.

[2] P. L. Kelley. "Self-Focusing of Optical Beams". *Phys. Rev. Lett.*, **15**(26):1005–1008, 1965. Erratum **16**, pp. 384 (1966).

[3] Y. R. Shen. *The principles of nonlinear optics.* John Wiley & Sons, Inc., 1984.

[4] V. I. Talanov. "Self Focusing of Wave Beams in Nonlinear Media". *JETP Lett.*, **2**:pp. 138–141, 1965.

[5] C. Angelis, and G. F. Nalesso. "Spatial Soliton Switching Modes of Nonlinear Optical Slab Waveguides". *J. Opt. Soc. Am. B*, **10**:pp. 55–59, 1993.

[6] E. M. Wright, G. I. Stegeman, C. T. Seaton, J. V. Moloney, and A. D. Boardman. "Multisoliton Emission from a Nonlinear Waveguide". *Phys. Rev. A*, **34**:pp. 4442–4444, 1986.

[7] K. Hayata, A. Misawa, and M. Koshiba. "Spatial Polarization Instabilities due to Transverse Effects in Nonlinear Guided-Wave Systems". *J. Opt. Soc. Am. B*, **7**:pp. 1268–1280, 1990.

[8] E. L. Dawes and J. H. Marburger. "Computer Studies in Self-Focusing". *Phys. Rev.*, **179**(3):pp. 862–869, 1969.

[9] M. D. Feit and J. A. Fleck. "Light Propagation in Graded-Index Optical Fibers". *Appl. Opt.*, **17**:pp. 3990–3998, 1978.

[10] N. Finlayson, E. M. Wright, C. T. Seaton, G. I. Stegeman, and Y. Silberberg. "Beam Propagation Study of Nonlinear Coupling between Transverse Electric Modes of a Slab Waveguide". *Appl. Phys. Lett.*, **50**:pp. 1562–1564, 1987.

[11] K. Hayata, A. Misawa, and M. Koshiba. "Nonlinear Beam Propagation in Tapered Waveguide". *Electron. Lett.*, **25**:pp. 661–662, 1989.

[12] R. W. Ziolkowski and J. B. Judkins. "Full-Wave Vector Maxwell Equation Modeling of the Self-Focusing of Ultrashort Optical Pulses in a Nonlinear Kerr Medium Exhibiting a Finite Response Time". *J. Opt. Soc. Am. B*, **10**(2):pp. 186–198, 1993.

[13] R. W. Ziolkowski and J. B. Judkins. "Applications of the Nonlinear Finite Difference Time Domain (NL-FDTD) Method to Pulse Propagation in Nonlinear Media: Self-Focusing and Linear-Nonlinear Interfaces". *Radio Science*, **28**:pp. 901–911, 1993.

[14] J. Jin. *The Finite Element Method in Electromagnetics.* John Wiley & Sons, Inc, 1993.

[15] Jin-Fa Lee. Finite Element Analysis of Lossy Dielectric Waveguide. *IEEE Trans. Microwave Theory Tech.*, **42**(6):pp. 1025–1031, 1994.

A hybrid FEM-FMM technique for electromagnetic scattering

Sunil S. Bindiganavale and John L. Volakis

Radiation Laboratory
Department of Electrical Engineering and Computer Science
The University of Michigan
Ann Arbor, MI 48109-2122

Abstract

In this paper, we apply a version of the Fast Multipole Method (FMM) to reduce the storage and computational requirement of the boundary integral in the finite element-boundary integral method. By virtue of its $0(N^{1.5})$ operation count, the application of the single-stage FMM, results in substantial speed-up of the boundary integral portion of the code, independent of the shape of the BI contour. We will discuss the efficiency of the method and present the application of this technique to the computation of electromagnetic scattering from large grooves recessed in a ground plane.

1 Introduction

Over the past few years different hybrid versions of the finite element method have been explored for application to scattering by composite structures. Among them, the finite element-boundary integral equation (FE-BI) and the finite element-absorber boundary condition (FE-ABC) methods have been quite popular and extensively applied to many applications. The FE-BI method [1],[2] employs the exact boundary integral equation which provides an independent relation between the tangential E and H fields on the mesh outer boundary and is therefore an exact method. This is in contrast to the FE-ABC method [3] which employs an approximate truncation operator but leads to fully sparse systems. On the other hand, the FE-BI method, although "exact", leads to a partly full and partly sparse system (see figure 1) and is thus more computationally intensive. For special cases, where the boundary is rectangular or circular, the FFT can be used [4] to reduce the memory and CPU requirements to $N \log N$. However, in general, the boundary integral is not convolutional and in that case the CPU requirements will be of $O(N_b^2)$ where N_b denotes the unknowns on the boundary.

In this paper, we apply a version of the Fast Multipole Method (FMM) to reduce the storage and computational requirement of the boundary integral when the size of the contour is large. By virtue of its $0(N^{1.5})$ operation count, the application of the FMM, results in substantial speed-up of the boundary integral portion of the code, independent of the shape of the BI contour. We consider the application of this technique (referred to hereon as the FEM-FMM method) to scattering from a material-filled groove in a conducting plane. The FEM is employed to formulate the fields within the cavity and establish a relationship with those at the aperture. The fields external to the groove are expressed as an integral over the aperture and a system of integral equations is then obtained

by enforcing field continuity across the aperture. To reduce the storage requirement and speed up the computation of the boundary integral, an approximate version of the fast multipole method [5] is employed.

2 Formulation

Consider a filled PEC groove of width w and depth d in an otherwise uniform ground plane as shown in figure 2(a). The material filling the groove has a permittivity ϵ_r and permeability μ_r. The free space region exterior to the groove is denoted as region I while the groove itself is denoted as region II (see figure 2). The fields in the two regions are decoupled by closing the aperture with a perfect conductor and introducing an equivalent magnetic current based on the equivalence principle

$$\mathbf{M}_1 = \mathbf{E}_1 \times \hat{y} \tag{1}$$

where $\mathbf{E}_1$ is the electric field at the aperture. The ground plane can be removed by application of image theory and hence the field in region I can be expressed as the radiation caused by $\mathbf{M}_1$ and the external sources $(\mathbf{J}^i, \mathbf{M}^i)$. The coupling of the fields in each region is achieved by requiring continuity of the tangential magnetic field across the aperture

$$\mathbf{H}^I_{tan}|_{y=0} = \mathbf{H}^{II}_{tan}|_{y=0} \tag{2}$$

The magnetic field, $\mathbf{H}^{II}$, inside the groove is formulated via the finite element method which has the inherent geometrical and material adaptability and low $O(N)$ storage requirement. This procedure and the coupling in (2) is described in detail in [1]. $\mathbf{H}^I$ is expressed as an integral of $\mathbf{M}_1$ using the free space Green's function. To this integral equation we apply a version of the fast multipole method [5] to reduce the operation count from $O(N_b^2)$ to $O(N_b^{1.5})$ where N_b is the number of unknowns on the boundary; the next section describes this procedure for TE incidence.

2.1 Boundary integral for TE case

The groove is illuminated by the plane wave

$$\mathbf{H}^i = \hat{z} e^{jk_0(x\sin\phi_0 + y\cos\phi_0)} \tag{3}$$

where $k_0 = 2\pi/\lambda_0$ is the free space wavenumber and ϕ_0 is the angle of incidence. With a z-directed impressed magnetic field $\mathbf{H}^i$, the scattered magnetic field will also be z-directed, and consequently the equivalent magnetic current $\mathbf{M}_1$ may be written as

$$\mathbf{M}_1 = \hat{z} M_1(x) \tag{4}$$

From figure 2(b), the magnetic field in region I due to M_1 is given by

$$\begin{aligned} H^I_z(\mathbf{r}) &= H^{inc}_z(x,y) + H^{refl}_z(x,y) \\ &- jk_0 Y_0 \int_{C_1} M_1(x') G_0(\rho,\rho') dx' \end{aligned} \tag{5}$$

where

$$G_0(\rho,\rho') = \frac{-j}{2}\left\{ H_0^{(2)}\left(k_0\sqrt{(x-x')^2+(y-y')^2} \right) \right\} \tag{6}$$

is the free space Green's function. Applying Galerkin's technique to (5) yields the matrix equation

$$[C]\{\phi\} \;=\; \{\phi^{inc}\} - [P]\{\psi\} \tag{7}$$

where $\{\phi\}$ is the column vector with $N_b + 1$ elements representing the nodal magnetic field on C_1, and N_b is the number of segments employed for the discretization of C_1. $\{\psi\}$ is the column vector with N_b elements representing the magnetic current on the boundary. The column vector $\{\phi^{inc}\}$ has N_b elements given by

$$\phi_m^{inc} = \left(H_z^{inc}(x_m, 0) + H_z^{refl}(x_m, 0)\right) \Delta x_m, \quad m = 1, 2, \ldots, N_b \tag{8}$$

with Δx_m being the segment length of the mth segment on C_1 and x_m being its midpoint. The product $[C]\{\phi\}$ in (7) is of not much concern since $[C]$ is a sparse matrix assembled from the interaction of the magnetic field and current on the boundary segments. The product $[P]\{\psi\}$ is of concern because of the $0(N_b^2)$ storage required by the full matrix $[P]$ whose elements are given by

$$P_{mn} \;=\; \frac{-j}{2}\left\{H_0^{(2)}(k_0\,|x_m - x_n|)\,\Delta x_m \Delta x_n\right\} \quad m \neq n \tag{9}$$

To employ the approximate version of the FMM in solving (7), the unknowns on the boundary are divided into groups with M_b unknowns in each group and thus the number of groups will then be $\frac{N_b}{M_b}$. For large source to observation distances, the kernel in (9) is approximated by using the large argument expansion as [5]

$$H_0^{(2)}(k_0\,|x_m - x_n|) \sim e^{-\mathrm{j}k_0 x_{lm}} \sqrt{\frac{2\mathrm{j}}{\pi}} \frac{e^{-\mathrm{j}k_0 x_{l'l}}}{\sqrt{k_0 x_{l'l}}} e^{-\mathrm{j}k_0 x_{nl'}} \tag{10}$$

where $x_{l'l}$ is the distance between the center of the test group l and the center of the source group l'; $x_{nl'}$ is the distance between the nth source element and its group center and x_{lm} is the distance between the mth test element and its group center. The decoupling of test-source element interactions in the kernel as in (10) enables the computation of the matrix-vector product for far-field groups with a reduced operation count as detailed in the following sequence.

1. For each test group, the aggregation of source elements in a single source group involves M_b operations, corresponding to the number of elements in the source group. The aggregation operation corresponds to

$$b_{l'l} = \sum_{j=1}^{M_b} M_j e^{-\mathrm{j}k_0 x_{nl'}} \tag{11}$$

2. Since the above aggregation operation needs to be done for all source groups the operation count becomes $O(\frac{N_b}{M_b} M_b) \sim O(N_b)$, where $\frac{N_b}{M_b}$ represents the total number of groups. Also this operation, being dependent only on the test *group* rather than the test *element*, needs to be repeated for $\frac{N_b}{M_b}$ test groups leading to a total operation count of $O(\frac{N_b^2}{M_b})$ for aggregation.

3. The next step would be a translation operation corresponding to

$$c_{l'l} = \sqrt{\frac{2\mathrm{j}}{\pi}} \frac{e^{-\mathrm{j}k_0 x_{l'l}}}{\sqrt{k_0 x_{l'l}}} b_{l'l} \tag{12}$$

Since this needs to be done only at the group level, it involves $O(\frac{N_b^2}{M_b^2})$ operations for all possible test and source group combinations and is the least computationally intensive step.

4. The final step in the sequence would be the process of disaggregation corresponding to the operation

$$I_{lm} = \sum_{l'=1}^{N_b/M_b} c_{l'l} e^{-\mathrm{j}k_0 x_{lm}} \tag{13}$$

Conceptually, this process is the converse of aggregation. Since this operation involves only the source *group* instead of the source *element* it needs to be done for each source group thus implying an $O(\frac{N_b}{M_b})$ operation to generate a single row of the matrix-vector product. To generate M_b rows corresponding to a test group the operation count would be $O(N_b)$. With $\frac{N_b}{M_b}$ test groups, the operation count would be of $O(\frac{N_b^2}{M_b})$.

5. The near field operation count being of $O(N_b M_b)$ and the far field being $O(\frac{N_b^2}{M_b})$ gives a total operation count of

$$Op.count \sim C_1 N_b M_b + C_2 \frac{N_b^2}{M_b} \tag{14}$$

Typically, we can set the elements in each group, $M_b = \sqrt{N_b}$ and as a result the total operation count is $O\sim N_b^{1.5}$.

Once the currents are computed in this manner, the far-fields are computed in th usual manner. Thus the maximum computational requirement in this hybrid algorithm is $O(N^{1.5})$ unlike the usual FE-BI which results in $O(N^2)$ if the boundary has N unknowns.

3 Results

A computer code based on the above formulation was implemented and executed on a HP 9000/750 workstation with a peak flop rate of 23.7 MFLOPS. The geometry considered was the rectangular groove shown in figure 1. Figure 3 shows the bistatic RCS at normal incidence for a groove 20λ wide and 0.25λ deep with a material filling of $\epsilon_r = 4$ and $\mu_r = 1$. The discretization of this geometry results in 2106 unknowns with a boundary integral of 300 unknowns. To obtain a measure of the speed-up realized by the application of the FEM-FMM to this problem, we refer to the CPU time comparisons also shown in figure 3. The compiled data on the FE-BI and FEM-FMM methods include the CPU time, storage requirement and average error. Data are also give for the FE-BI implementation using the special CG-FFT solver but it should be noted that the application of the CG-FFT is only suited for planar apertures. Clearly, the compiled run data show that the FEM-FMM is about three times faster than the traditional FE-BI implementation and requires only one sixth of the memory. However, the FEM-FMM has some deterioration in accuracy (average error of 2 dB for this example [6]) and this should be considered depending on the application and usage of the results. Similar data shown in figure 4 for plane wave incidence at an off-normal incidence angle (45^0) seem to verify the previous conclusions. The groove analyzed in figure 4 is 30λ wide and is 0.15λ deep with a material filling of $\epsilon_r = 6$ and $\mu_r = 1$. The discretization of this geometry results in 1803 unknowns with a boundary integral of 450 unknowns. The error in the FEM-FMM solution is lower but this could be attributed to the use of a larger near-group window (4.3λ instead of 2.45λ) which results in an increase in storage and execution time of the boundary integral. Clearly the CG-FFT solver is substantially faster and arguably uncontested by the FEM-FMM method. This simply gives credence to modifications of the boundary integral surface so that the CG-FFT can be applied whenever possible even though the boundary surface may not be completely planar.

References

[1] J.M. Jin and J.L. Volakis, "TE scattering by an inhomogeneously filled aperture in a thick conducting plane," *IEEE Trans. Antennas Propagat.*, vol.38, pp.1280-1286, Aug. 1990.

[2] J.M. Jin and J.L. Volakis, "TM scattering by an inhomogeneously filled aperture in a thick conducting plane," *IEE Proc.*, pt. H, vol.137, pp. 153-159, June 1990.

[3] A. Chatterjee, J.M. Jin, and J.L. Volakis, "Edge-based finite elements and vector ABCs applied to 3D scattering," *IEEE Trans. Antennas Propagat.*, vol. 41, pp.221-226, Feb 1993.

[4] J.D. Collins, J.L. Volakis, and J.M. Jin, "A combined finite element-boundary element formulation for solution of two-dimensional scattering problems via CGFFT," *IEEE Trans. Antennas Propagat.*, vol. 38, pp. 1852-1858, 1990.

[5] C.C. Lu and W.C. Chew, Fast far field approximation for calculating the RCS of large objects, *Micro. Opt. Tech. Lett.*, 8(5):238-241, April 1995.

[6] S.S. Bindiganavale and J.L. Volakis, Guidelines for using the fast multipole method to calculate the RCS of large objects, *Micro. Opt. Tech. Lett.*, March 1996.

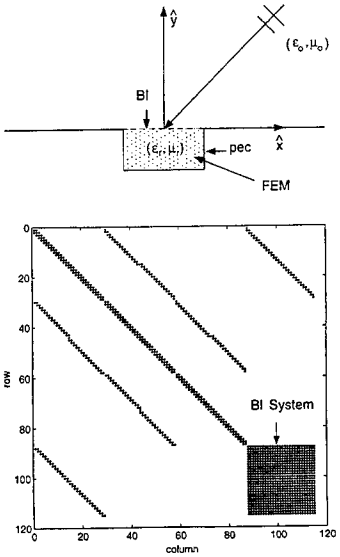

Figure 1: The FE-BI system matrix arising from the scattering/radiation problem of a groove ina ground plane. Unknowns 88-105 are the boundary integral unknowns.

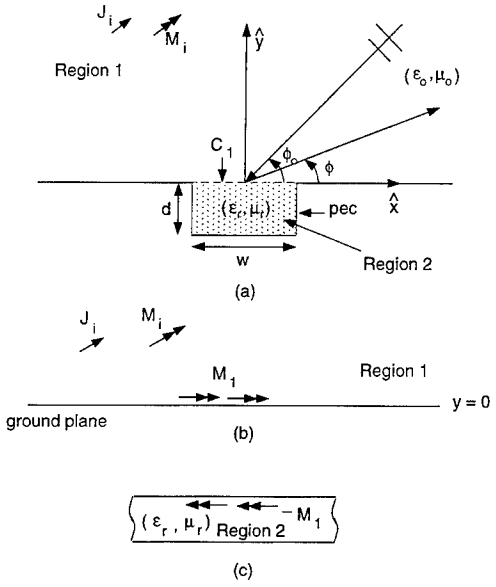

Figure 2: (a) Geometry of the groove recessed in a ground plane (b) Equivalent problem for region 1, and (c) region 2

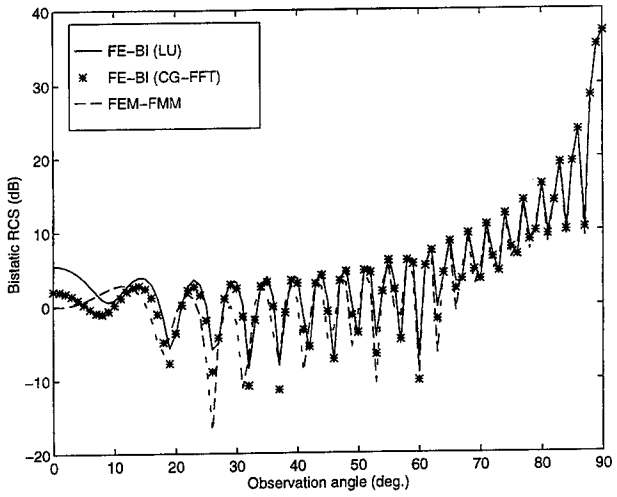

Time (for BI only)	FEM-BI (CG)	FEM-FMM	FEM-BI (CGFFT)
(Minutes,seconds)	15 mins 14 secs	4 mins 48 secs	1 min 40 secs

Memory (for BI only)	LU	FEM-FMM
(KB)	680	116

Average error	FEM-FMM	FEM-BI (CGFFT)
(dB)	2.016	0.98

Figure 3: Bistatic scattering from a rectangular groove 20λ wide and 0.35λ deep at normal incidence

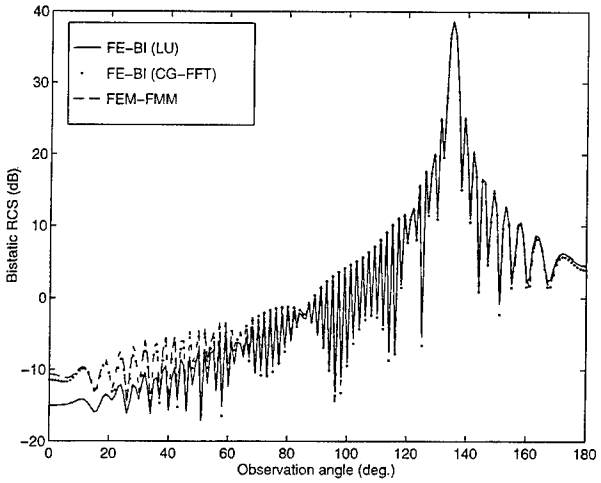

Time (for BI only)	FEM-BI (CG)	FEM-FMM	FEM-BI (CGFFT)
(Minutes,seconds)	30 mins 36 secs	9 mins 1 sec	2 min 15 secs

Memory (for BI only)	LU	FEM-FMM
(KB)	1544	436

Average error	FEM-FMM	FEM-BI (CGFFT)
(dB)	1.553	1.0267

Figure 4: Bistatic scattering from a rectangular groove 30λ wide and 0.15λ deep at 45^0 incidence

Finite Element Method Analysis of the Celestron-8 Telescope

R. R. DeLyser
University of Denver
Denver, Colorado

H. Pohle
Phillips Laboratory/WSWM
Kirtland AFB, New Mexico

Introduction

The Celestron-8 cassegranian telescope (Figure 1) is representative of typical sensors that could be vulnerable to high power microwave (HPM) energy. It was therefore analyzed using the Hewlett Packard High Frequency Structure Simulator (HFSS).

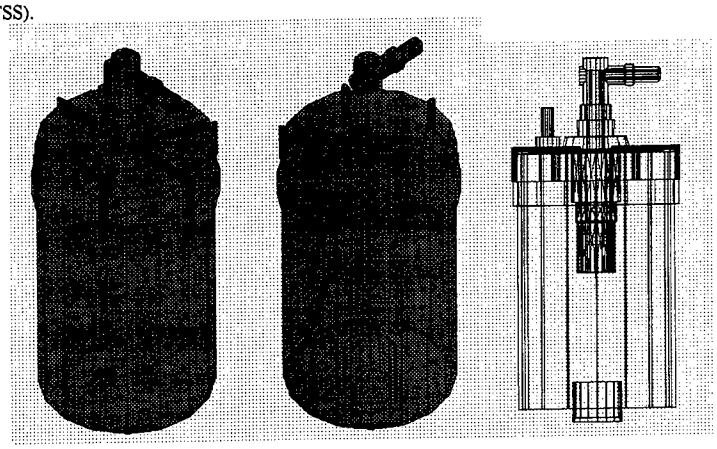

Figure 1. The Celestron-8 telescope.

HFSS is a three dimensional finite element simulator. In the simulator, the geometric model is automatically divided into a large number of tetrahedra, the finite element mesh. Within each tetrahedron, the vector field components perpendicular to the edges and tangential to the edges are mathematically modeled using polynomials. The finer the mesh, the more accurate the solution. Of course, the finer the mesh, the greater the demands on computational resources in terms of memory, disk space and solution time. In order to find a good solution to the problem and minimize computer resources, HFSS uses "an iterative process in which the mesh is automatically refined in critical regions." The simulator first solves the problem using a course initial mesh, refines the mesh in areas of high error density, generates a new solution, etc., until selected S-parameters converge to within a desired limit, or until all computer resources have been exhausted.

The computer that we use to run HFSS is an IBM RS6000 model 570 PowerServer with 128 MBytes of random access memory (RAM) and two 1 GByte hard drives. We have access to all of the RAM, about 200 MBytes of paging space, and 340 MBytes of disk space for user files. During the solution process, a convergence menu can be monitored containing memory and file size values. Two matrices are written to disk (user files); the A matrix is the "full matrix" and the U matrix is the "upper triangular matrix". All other memory size values indicated on the convergence menu are RAM

usage. As stated above, the iterative process of mesh refinement is continued until convergence, or until the computer resources are exhausted. If the disk space, paging space or RAM is exhausted, the solution did not converge.

A total of eight projects were created for HFSS. They were:
1. cyltest.pjt - A cylindrical waveguide port excited cylinder which is the same size as the outer cylinder of the Celestron Telescope (see Figure 2.) The radiation boundary was positioned 150 mm from the cylinder boundary. This was done so that the radiation boundary would be 1/4 λ (at the lowest frequency of interest - 0.5 GHz) from the radiating surface as suggested by HP.

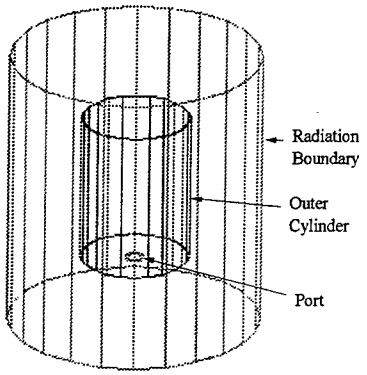

Figure 2. The cylindrical waveguide port excited cylinder.

2. cylinder.pjt - A coaxial probe excited cylinder which is the same as shown in Figure 24 with the exception that the port is replaced by a coaxial probe which has its center conductor inserted along the z axis into the cylinder a distance of 3 cm. The probe is 1 mm in radius. The outer conductor of the coaxial port is 2.3 mm in radius.
3. telescop.pjt - A full model of the telescope with the exception that the large mirror is flat. We could not get the 2-D cross-section to close using the true radius of curvature. Since the 2D cross-section would not close, the 3D mirror could not be created. Thus, a flat mirror with approximate tilt was created. The center of the mirror is at z = 72 mm and the outside is at z = 73.8 mm. This model is excited by a cylindrical waveguide port located at the eye piece.
4. teletest.pjt - A full model of the telescope (Figure 3) as detailed above in telescop.pjt with the exception that the eye piece is open and a coaxial probe and port as described in cylinder.pjt is located at z = 167.5 mm.
5. telehf.pjt - A model of the telescope excluding the volume behind the large mirror and with the radiation boundary located 17 mm from the large cylinder boundary. This model was specifically created at a frequency of 4.5 GHz in an attempt to have a model at a frequency higher than the cutoff frequency of the inner cylinder (4.4 GHz).
6. cyltest2.pjt - An open cylinder excited by a square coaxial probe at the center of the cylindrical shell with the probe oriented along the x axis. The square cross-section probe was used to alleviate the problem of a high mesh density at the small cylindrical probe. The inner conductor (probe) of the coaxial feed is 4 mm wide, the outer conductor has a 9.2 mm inside width. The radiation boundary was chosen to accommodate a 0.75 GHz - 1.5 GHz frequency range.
7. cyltest3.pjt - This project is the same as cyltest2.pjt with the exception that the radiation boundary is closer to accommodate a 1.5 GHz - 2 GHz frequency range.
8. telerad.pjt - This model was like that for telescop.pjt except that the radiation boundary condition was enforced at the aperture of the telescope. This in effect eliminates any fields due to currents on the outside of the telescope. This has some effect on the fields inside the telescope but should provide minimal error. The goal was to get a model that would work at a frequency above the cutoff frequency of the small inner cylinder. HFSS failed to refine the mesh on the second pass. We think that this is an indication that we ran out of RAM (>128 MBytes.)

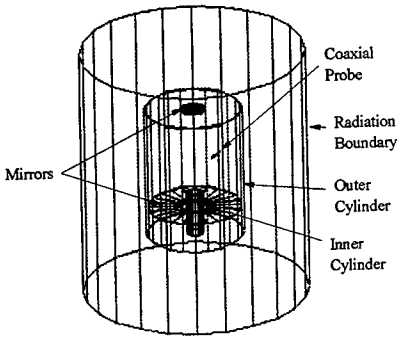

Figure 3. The coaxial probe excited telescope.

Table 1 shows the details of the various projects and models at the given frequencies along with the memory requirements (disk space and RAM) of each. We were unable to converge to a 2 GHz model for the telescop.pjt or to even a 1 GHz model for the teletest.pjt. An attempt at a 870 MHz model was made because a resonance at that frequency has been measured. The model did not converge. Also, the telehf.pjt model did not converge.

Table 1. Summary of HFSS projects and resource requirements.

Name of Project	Frequency	A matrix Disk Space (K)	U matrix Disk Space (K)	csolve RAM (K)	Total Time
cyltest.pjt	1 GHz	16,302	65,965	37,340	31:39
	2 GHz	25,717	134,732	67,996	1:25:54
cylinder.pjt	500 MHz	23,588	123,220	65,820	1:22:42
telescop.pjt	1 GHz	14,130	77,376	66,332	17:13
	1.5 GHz	23,122	164,935	103,132	41:48
	2 GHz	---	>340,000	---	---
teletest.pjt	1 GHz	---	>340,000	---	---
	870 MHz	---	>340,000	---	---
telehf.pjt	4.5 GHz	---	>340,000	---	---
cyltest2.pjt	1.5 GHz	34,083	211,128	107,996	2:40:00
cyltest3.pjt	2 GHz	39,834	243,013	114,396	3:03:00
telerad.pjt	4.5 GHz	---	---	---	---

Figures 4 - 7 show results for telescop.pjt at 1.18 GHz. Even though a good model was not generated at 4.5 GHz for this project, we looked at the radiation results (Figure 8) for the best model generated. When compared to the radiation plot of Figure 7, it is clear that once we get above the cutoff frequency of the inner cylinder, the radiation increases substantially. It is interesting to note that even though the frequency of excitation (1.18 GHz) is below the cutoff frequency of the inner cylinder waveguide, there are calculable fields at the end of the inner cylinder and at the aperture of the large cylinder (see Figure 4.) The magnetic field intensity magnitude plots of Figures 5 and 6 also show significant fields behind the large mirror.

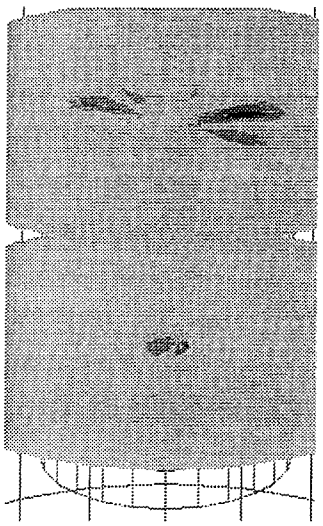

Figure 4. Electric field - cylinder openings.

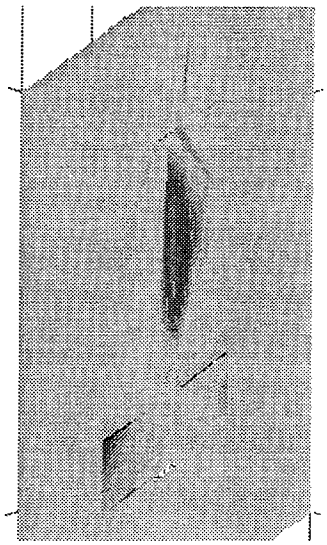

Figure 5. Magnetic field - x axis.

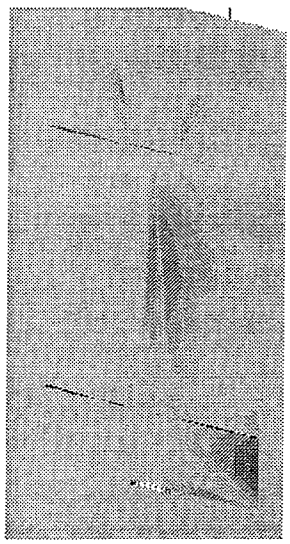

Figure 6. Magnetic field - y axis.

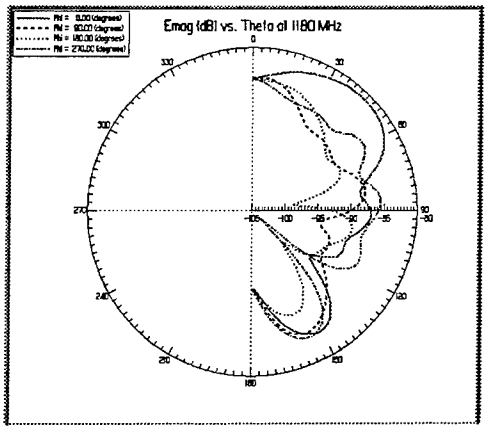

Figure 7. Radiation at 1.18 GHz.

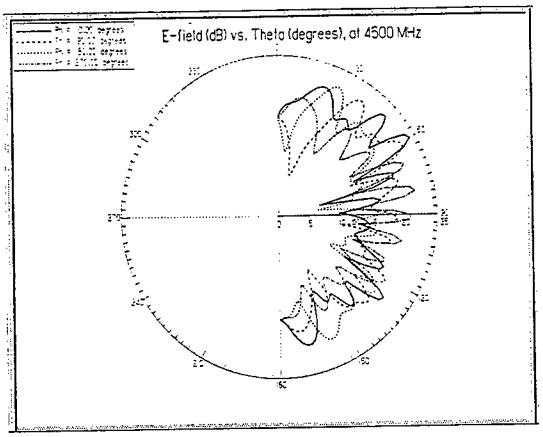

Figure 8. Radiation at 4.5 GHz.

HFSS Results vs. Physical Testing

The most successful models were cyltest2.pjt and cyltest3.pjt. Results for the fields and radiation plots at the two major resonances are shown in Figures 9 - 14. As a reference, the TE_{211} and TE_{311} modes for a closed cylindrical cavity of the dimensions of our open cavity resonate at 1.36 GHz and 1.822 GHz. The electric field plots at 1.35 GHz and 1.8 GHz clearly indicate that the transverse modes are TE_{21} and TE_{31} respectively.

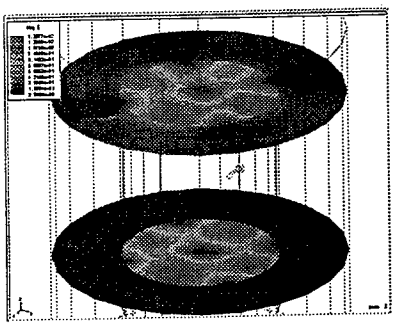

Figure 9 Electric field - 1.35 GHz.

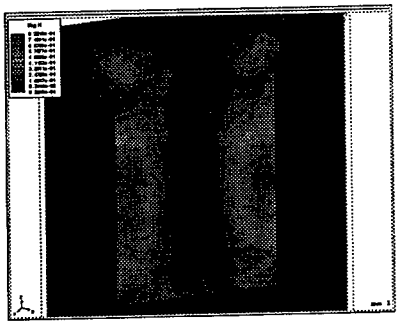

Figure 10. Magnetic field - 1.35 GHz, ϕ=45°.

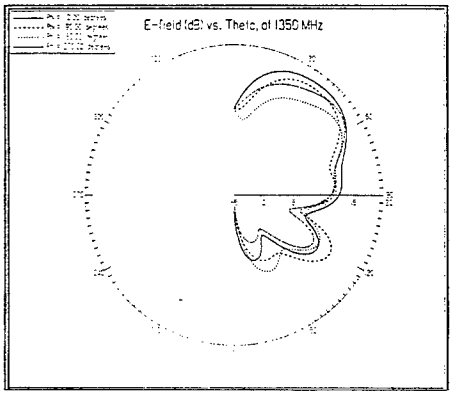

Figure 11. Radiation at 1.35 GHz.

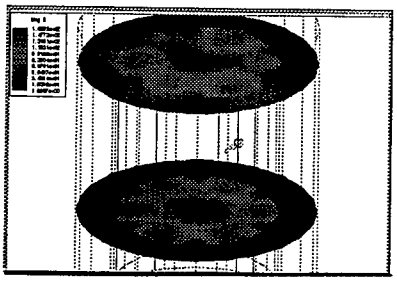

Figure 12. Electric field - 1.80 GHz.

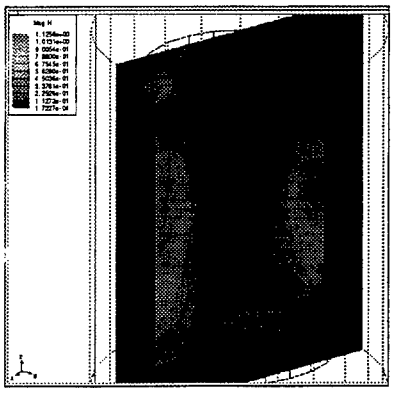

Figure 13. Magnetic field - 1.80 GHz, $\phi = 30°$ plane.

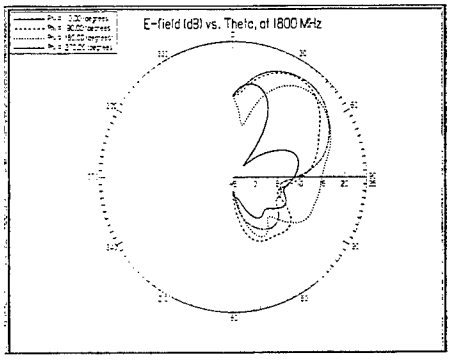

Figure 14. Radiation at 1.80 GHz.

Figures 15 - 17 show results for S_{11} from HFSS and two tests of the telescope with a coaxial probe positioned as for cyltest2.pjt and cyltest3.pjt. These measurements were done once having a conducting plate at the aperture of the telescope and then same measurements were done having no cover plate at the aperture. Figures 16 and 17 show that the resonances are at the same location but of different depths. It appears that our simple model of an open cylinder accurately models the telescope for these low frequency resonances.

Finally, the quality factors for the two resonances at 1.8 GHz and 1.35 GHz are calculated by the HFSS post processor. These values are 55.5 at 1.8 GHz and 25.20 at 1.35 GHz.

Conclusions

The concept of determining energy at a particular point or area in a system by doing the inverse (antenna) problem is an attractive one. The vast amount of information contained in the HFSS solution can be used to determine optimum incidence angles to couple the energy into the system, field quantities anywhere in the system, system resonances, quality factor for the system, etc. HFSS was used in this study to demonstrate the concept; perhaps other types of codes such as TEMAC-3D (Temporal Electromagnetic Analysis Code, a finite difference time domain (FDTD) code), FERM (Finite Element Radiation Model, a MOM code) and CARLOS-3D (Code for Analysis of Radiators on Lossy Surfaces) could also be used to solve the antenna problem. All of these codes are available to DOD authorized personnel and are designed (with the exception of CARLOS-3D) to do the radiation problem. FERM and TEMAC-3D will be installed on the University of Denver computer to explore the radiation problem. CARLOS-3D would also be a good candidate to do the radiation problem because of its ability to handle dielectrics as well as conductors. However, modifications to CARLOS-3D would have to be made to do the radiation problem.

Acknowledgments

This work was funded by Phillips Laboratory/WSTS and the Air Force Office of Scientific Research.

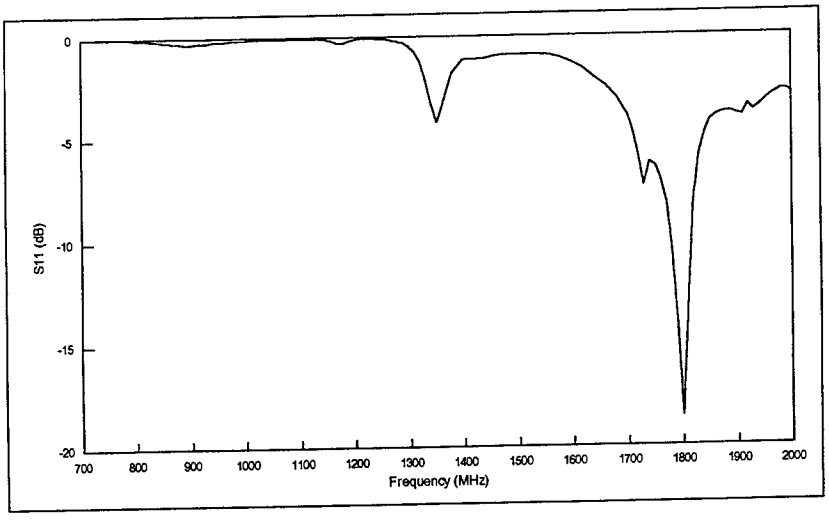

Figure 15. HFSS results for the probe excited open cylinder (10 MHz resolution.)

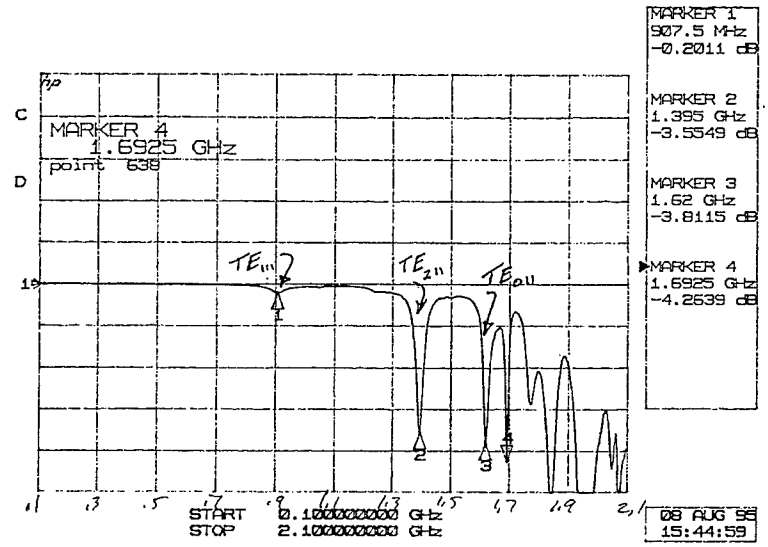

Figure 16. Measured S_{11} results for the open telescope.

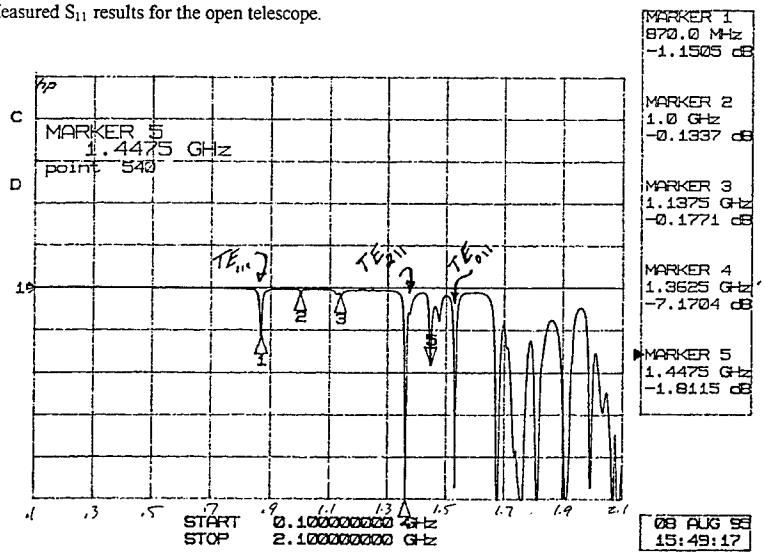

Figure 17. Measured S_{11} results for the covered telescope.

SESSION 9:

NUMERICAL ERROR ANALYSIS AND CONTROL I

Chair: J. Volakis

Error Analysis in the Adaptive Integral Method (AIM)

E. Bleszynski[+], M. Bleszynski[++] and T. Jaroszewicz[+++]

[+]North American Aircraft Division, Rockwell International Corporation

P.O. Box 3644, Seal Beach, CA 90740-7644

[++] Science Center, Rockwell International Corporation

P.O. Box 1085, Thousand Oaks, CA 91360

[+++] Monopole Research, 2725 Glendon Ave, Los Angeles, Ca 90064

Abstract

Some results of the analysis of errors for the Adaptive Integral Method (AIM) are presented. The errors are introduced by the use of auxiliary basis functions in computing far field impedance matrix elements. The error dependence on the multipole expansion order, the size of the Cartesian grid spacing and the geometry of the problem, i.e. the size and the shape of the basis functions' supports and their relative location, are discussed.

1. Description of the AIM algorithm

The Adaptive Integral Method (AIM) [1] belongs to the class of "fast" iterative solvers of Maxwell's equations in their integral form. These methods significantly improve upon the conventional Method of Moments (MoM) order $O(N^2)$ impedance-matrix storage and matrix-vector multiplication complexity, where N is the number of unknowns. The improvement is achieved by effectively "compressing" the impedance matrix by means of either purely algebraic or physically motivated algorithms.

In the AIM algorithm, the impedance matrix is decomposed into "near-" and "far-field" components. The near-field component is, by construction, a *sparse* matrix, whose elements are computed as in the conventional MoM, using the Galerkin method with arbitrary localized basis functions, representing volume, surface, or line current elements.

In the far-field component the original current elements are approximated by appropriately specified equivalent distributions of pointlike sources located at nodes of a regular three-dimensional Cartesian grid. Since the transformation between the original and the equivalent current distributions is given by a sparse matrix, and the Green's function discretized on the grid is a (three level) Toeplitz matrix, the storage is, asymptotically, $O(N_C)$, where N_C is the required total number of Cartesian grid nodes, proportional to $N^{3/2}$ in surface problems, and to N in volumetric problems. Similarly, the serial matrix-vector multiplication complexity is $O(N^{3/2} \log N)$ and $O(N \log N)$ for surface and volumetric problems, respectively.

One of teh methods of determining the equivalent Cartesian grid sources is to require that they reproduce the multipole moments of the original current element, up to a desired multipole order M. The AIM solver based on this approximation criterion has been fully implemented in both serial and massively parallel versions, and successfully applied to large-scale three-dimensional scattering problems involving perfectly and imperfectly conducting bodies. Here we present some implications of the error analysis for the multipole-based approximation, including issues such as the choices of the Cartesian grid and the expansion order.

The far-field approximation of the AIM algorith is applicable to any Galerkin matrix elements of the form

$$A_{\alpha\beta} = \int \mathrm{d}x_1 \, \mathrm{d}x_2 \, \psi_\alpha(\mathbf{x}_1) \, g(\mathbf{x}_1 - \mathbf{x}_2) \, \psi_\beta(\mathbf{x}_2) \equiv (\psi_\alpha, \, g \, \psi_\beta) \; , \tag{1.1}$$

where

$$g(\mathbf{x}) = \frac{\mathrm{e}^{\mathrm{i}\, k\, |\mathbf{x}|}}{4\pi |\mathbf{x}|} \tag{1.2}$$

is the homogeneous-space Helmholtz equation Green's function with $k = 2\pi/\lambda$ being the wave number in the medium. The form (1.1) includes all the matrix elements arising in the discretization of Maxwell's equations, in which case the functions ψ_α and ψ_β are components of vector-valued basis functions representing electric and magnetic current elements, as well as derivatives (divergences and curls) of these basis functions.

In the far-field matrix elements the basis functions are approximated by linear combinations of Dirac delta-functions,

$$\psi_\alpha(\mathbf{x}) \simeq \widehat{\psi}_\alpha(\mathbf{x}) \equiv \sum_{\mathbf{u} \in C_\alpha} \Lambda_{\alpha \mathbf{u}} \, \delta^3(\mathbf{x} - \mathbf{u}) \; , \tag{1.3}$$

localized at some set C_α of grid nodes $\mathbf{u}$, depending on the basis function ψ_α. In the present implementation C_α is a cubic *expansion box* of $(M+1)^3$ nodes, whose center is nearest to the center of the support of ψ_α.

According to the multipole-expansion criterion, the coefficients Λ are determined by the set of $(M+1)^3$ equations expressing equality of the multipole moments

$$Q_{\alpha,(m_1\,m_2\,m_3)} = \int \mathrm{d}^3x\, x_1^{m_1}\, x_2^{m_2}\, x_3^{m_3}\, \psi_\alpha(\mathbf{x}) \tag{1.4}$$

and the corresponding moments $\widehat{Q}_{\alpha,(m_1\,m_2\,m_3)}$ of the function $\widehat{\psi}_\alpha$ for all orders $0 \le m_1, m_2, m_3 \le M$. This set of condition leads to a Vandermonde-type linear system of equations for Λ.

With Eq.(1.3), we define the approximate far-field matrix elements as

$$\begin{aligned} A^{\mathrm{Far}}_{\alpha\beta} \equiv (\widehat{\psi}_\alpha,\, g\,\widehat{\psi}_\beta) &= \int \mathrm{d}x_1\, \mathrm{d}x_2\, \widehat{\psi}_\alpha(\mathbf{x}_1)\, g(\mathbf{x}_1-\mathbf{x}_2)\, \widehat{\psi}_\beta(\mathbf{x}_2) \\ &= \sum_{\mathbf{u}\in C_\alpha} \sum_{\mathbf{v}\in C_\beta} \Lambda_{\alpha\mathbf{u}}\, g(\mathbf{u}-\mathbf{v})\, \Lambda_{\beta\mathbf{v}}\ . \end{aligned} \tag{1.5}$$

The AIM approximation A^{AIM} to the impedance matrix A is then constructed as

$$A^{\mathrm{AIM}} = A^{\mathrm{Near}} + A^{\mathrm{Far}}\ , \tag{1.6}$$

where

$$A^{\mathrm{Near}}_{\alpha\beta} = \begin{cases} A_{\alpha\beta} - A^{\mathrm{Far}}_{\alpha\beta} & \text{if } \mathrm{dist}(C_\alpha, C_\beta) \le d_{\mathrm{Near}} \ \text{ and } |A_{\alpha\beta} - A^{\mathrm{Far}}_{\alpha\beta}| \ge \varepsilon_{\mathrm{Near}}\, |A_{\alpha\beta}|, \\ 0 & \text{otherwise,} \end{cases} \tag{1.7}$$

and $\mathrm{dist}(C_\alpha, C_\beta)$ is the distance between the expansion boxes defined in terms of the $\|\cdot\|_\infty$ norm in grid-spacing units.

The accuracy of the approximation $A \simeq A^{\mathrm{AIM}}$ is controlled, in addition to the expansion order M, by the *near-field range* d_{Near}, and the *near-field tolerance* $\varepsilon_{\mathrm{Near}}$: if the distance between the expansion boxes exceeds d_{Near}, the near-field component of the matrix is set to zero; for smaller distances, $A^{\mathrm{Near}}_{\alpha\beta}$ is defined as the *difference* of the MoM and far-field matrix elements, or as zero, if that difference is small (in terms of the required tolerance $\varepsilon_{\mathrm{Near}}$).

Eqs. (1.6) and (1.7) exhibit the structure of A^{AIM} as a compressed approximate A: A^{AIM} is a sum of the *sparse* matrix A^{Near}, and a product of sparse and Toeplitz matrices,

$$A^{\mathrm{Far}} = \Lambda\, g\, \Lambda^{\mathrm{T}} \tag{1.8}$$

(cf. Eq.(1.5)).

2. Results of the Error Analysis for the $A \simeq A^{\mathrm{AIM}}$ Approximation

We present below the main results of the analysis of errors associated with the approximation $A \simeq A^{\mathrm{AIM}}$. Since this approximation is, typically, used in the framework of iterative solution methods, we base our error analysis on the estimates of residuals in the equation $A\,x = b$. If y is an approximate solution to the equation $A^{\mathrm{AIM}}\,x = b$, then the residual of the original equation satisfies the bound

$$\begin{aligned} \|b - A\,y\|_2 &\le \|b - A^{\mathrm{AIM}}\,y\|_2 + \|A - A^{\mathrm{AIM}}\|_2\ \|y\|_2 \\ &\le \|b - A^{\mathrm{AIM}}\,y\|_2 + \|A - A^{\mathrm{AIM}}\|_{\mathrm{F}}\ \|y\|_2\ , \end{aligned} \tag{2.1}$$

with the Frobenius norm defined by

$$\|A - A^{\mathrm{AIM}}\|_{\mathrm{F}}^2 = \sum_{\alpha\beta} |A_{\alpha\beta} - A^{\mathrm{AIM}}_{\alpha\beta}|^2\ . \tag{2.2}$$

Therefore, in order to control the accuracy of the solution, we have to estimate the norm (spectral, or at least Frobenius) of the difference $A - A^{\mathrm{AIM}}$. As the measure of the relative error we take thus the ratio

$$\Delta_{\mathrm{AIM}} \equiv \frac{\|A - A^{\mathrm{AIM}}\|_{\mathrm{F}}^2}{\|A\|_{\mathrm{F}}^2}\ . \tag{2.3}$$

According to Eq.(1.7), equivalent to

$$A_{\alpha\beta} - A^{\mathrm{AIM}}_{\alpha\beta}$$

$$\equiv \delta A_{\alpha\beta} = \begin{cases} 0 & \text{if } d_{\alpha\beta} \le d_{\mathrm{Near}} \quad \text{and} \quad |A_{\alpha\beta} - A^{\mathrm{Far}}_{\alpha\beta}| \ge \varepsilon_{\mathrm{Near}}\,|A_{\alpha\beta}| & \text{(2.4a)} \\ A_{\alpha\beta} - A^{\mathrm{Far}}_{\alpha\beta} & \text{if } d_{\alpha\beta} \le d_{\mathrm{Near}} \quad \text{and} \quad |A_{\alpha\beta} - A^{\mathrm{Far}}_{\alpha\beta}| < \varepsilon_{\mathrm{Near}}\,|A_{\alpha\beta}| & \text{(2.4b)} \\ A_{\alpha\beta} - A^{\mathrm{Far}}_{\alpha\beta} & \text{if } d_{\alpha\beta} > d_{\mathrm{Near}} & \text{(2.4c)} \end{cases}$$

(with $d_{\alpha\beta} \equiv \mathrm{dist}(C_\alpha, C_\beta)$), the norm $\|A - A^{\mathrm{AIM}}\|_{\mathrm{F}}$ receives near- and far-field contributions, resulting from Eqs. (2.4b) and (2.4c), respectively. An upper bound on the near-field contribution is

$$\|A - A^{\mathrm{AIM}}\|_{\mathrm{F\,(Near)}} \le \varepsilon_{\mathrm{Near}}\,\|A\|_{\mathrm{F\,(Near)}} \le \varepsilon_{\mathrm{Near}}\,\|A\|_{\mathrm{F}}\ , \tag{2.5}$$

where the norm $\|\cdot\|_{\mathrm{F\,(Near)}}$ is defined as in Eq.(2.2), but with the sum restricted to $d_{\alpha\beta} \le d_{\mathrm{Near}}$. We have thus

$$\Delta_{\mathrm{AIM(Near)}} \le \varepsilon_{\mathrm{Near}}\ . \tag{2.6}$$

In practice, however, we find that the near-field error is typically much smaller, because only a relatively small fraction of matrix elements satisfies the conditions of Eq.(2.4b). We concentrate, therefore, on the far-field contribution to the error; with a fixed near-field range d_{Near}, this contribution always becomes dominant for sufficiently large problem sizes.

At large distances, the accuracy of the approximation (1.5) is controlled by the oscillatory behavior of the Green's function (1.2). Eq.(1.5) can be interpreted as an $(M+1)^3$-point quadrature of the integral of Eq.(1.1), with quadrature points $\mathbf{u}$, $\mathbf{v}$. By construction of the coefficients Λ, the weights are such that the quadrature is *exact* if g is a polynomial of order up to M in any of the components of $\mathbf{x}_1$ and $\mathbf{x}_2$. This interpretation suggests that the expansion order M should be sufficiently high for the oscillatory Green's function, $\sim \exp(\mathrm{i}\,\mathbf{k}\cdot\mathbf{x})$, to be well approximated by an M-th order polynomial within the support of the basis function and within the expansion box. Thus, if the support size is b, and the grid spacing is a, the relative error is expected to be of the order of the Taylor series remainder,

$$\frac{(\max\{b, Ma\}\, k)^{M+1}}{(M+1)!} \,. \tag{2.7a}$$

A more precise estimate of the far-field error is obtained from the large distance expansion of the Green's function; if $\mathbf{R} = \mathbf{c}_1 - \mathbf{c}_2$ is the distance between the centers $\mathbf{c}_1$ and $\mathbf{c}_2$ of the basis functions' supports, we have

$$A_{\alpha\beta} = g(R)\; \widetilde{\psi}_\alpha(k\hat{\mathbf{R}})\, \widetilde{\psi}_\beta(-k\hat{\mathbf{R}}) \left[1 + O\Big(\frac{b}{R}\Big) + O\Big(\frac{kb^2}{R}\Big)\right] , \tag{2.8}$$

where $b \equiv (b_1 + b_2)/2$, and the Fourier transforms $\widetilde{\psi}$ of the basis functions are defined relative to the centers $\mathbf{c}_1$ and $\mathbf{c}_2$. The asymptotic error is thus expressible in terms of the error in the Fourier transforms,

$$\delta\widetilde{\psi}(\mathbf{k}) \equiv \widetilde{\psi}(\mathbf{k}) - \widetilde{\widetilde{\psi}}(\mathbf{k}) = \int\limits_{|\mathbf{x}|\le b/2} \mathrm{d}x\; \mathrm{e}^{\mathrm{i}\,\mathbf{k}\cdot\mathbf{x}}\, \psi(\mathbf{c}+\mathbf{x}) - \sum_{\mathbf{u}\in C} \Lambda_{\mathbf{u}}\, \mathrm{e}^{\mathrm{i}\,\mathbf{k}\cdot(\mathbf{u}-\mathbf{c})} \,. \tag{2.9}$$

In particular, the relative error becomes independent of the distance,

$$\Delta_{\alpha\beta} \equiv \frac{|\, A_{\alpha\beta} - A^{\mathrm{AIM}}_{\alpha\beta}\,|}{|\, A_{\alpha\beta}\,|} \simeq \frac{|\delta\widetilde{\psi}_\alpha(\mathbf{k})|}{|\widetilde{\psi}_\alpha(\mathbf{k})|} + \frac{|\delta\widetilde{\psi}_\beta(\mathbf{k})|}{|\widetilde{\psi}_\beta(\mathbf{k})|} \equiv \Delta\widetilde{\psi}_\alpha(\mathbf{k}) + \Delta\widetilde{\psi}_\beta(-\mathbf{k}) \tag{2.10}$$

$\mathbf{k} = k\hat{\mathbf{R}}$), and provides a simple estimate for the far-field contribution to the error (2.3),

$$\Delta_{\mathrm{AIM(Far)}} \leq 2 \max_{\alpha,\hat{\mathbf{k}}} \Delta\widetilde{\psi}_\alpha(\mathbf{k}) \ . \tag{2.11}$$

By construction, the basis functions $\psi(\mathbf{x})$ and $\widehat{\psi}(\mathbf{x})$ have identical power-series expansions in components of $\mathbf{k}$ up to the order M. Therefore, the error (2.9) is of order k^{M+1}, with the coefficient proportional to the difference between the multipole moments, $Q - \widehat{Q}$, of order $(M+1)$. Although the moments $\widehat{Q}$ depend in a complicated way on the original moments Q of orders up to M, and on the grid parameters, we have obtained a rigorous bound

$$|\delta\widetilde{\psi}(\mathbf{k})| \leq \frac{2}{(M+1)!}\left(\frac{bk}{2}\right)^{M+1} \int \mathrm{d}x\, |\psi(\mathbf{x})|\, [1 + O(bk)]$$
$$\text{for } M \geq 1\,,\ 0 \leq a \leq 2b/\max\{5, M\}\ . \tag{2.12}$$

The restriction on the grid spacing a is crucial here: As long as a is small compared to the size b, the moments $\widehat{Q}$ of order higher than M remain comparable to the corresponding moments Q (in particular, they vanish when $a \to 0$). For larger grid spacings, however, the moments $\widehat{Q}$ typically grow uncontrollably large, especially for higher expansion orders M. For large a and M the error may become as large as

$$|\delta\widetilde{\psi}(\mathbf{k})| \simeq \sqrt{\frac{2}{\pi M}}\left(\frac{ak}{2}\right)^{M+1} \int \mathrm{d}x\, |\psi(\mathbf{x})|\ . \tag{2.13}$$

Physically, the constraint $aM \leq 2b$ implies that the size of the expansion box should not significantly exceed the size of the basis function support. On the other hand, memory requirements and complexity of the algorithm grow rapidly with the decreasing grid spacing (proportionally to $(\lambda/a)^3$); therefore, the optimal choice is the largest grid spacing providing an acceptably small error.

We carried out an extensive numerical analysis of the errors in matrix elements for the Maxwell's equation case, using the conventional vectorial Rao-Wilton-Glisson basis functions. As an example, we show in Fig. 1 the magnetic-field operator error (which is larger than the electric-field one) $\Delta_{\alpha\beta}$ (Eq.(2.10)) as a function of the distance $R = R_{\alpha\beta}$ between the current elements. We used typical values of parameters: $a = \lambda/8$, $b = 2a$, and $M = 2, 3, 4$.

The curves in Fig. 1 exhibit characteristic periodic oscillations due to the error dependence on the location of the basis functions relative to the grid nodes. They clearly show the convergence of the expansion, and the fact that the asymptotic, R-independent accuracy level sets in already at relatively small distances, well within the wavelength $\lambda = 8a$. Since the AIM multipole expansion can be interpreted as a specific quadrature applied to matrix-element computation, we also compared the matrix element errors in the AIM algorithm with the typical quadrature errors of the "exact" MoM. Fig. 1 shows (marked as "MoM") the difference in the MoM matrix elements calculated using 12-point and 3-point two-dimensional Gaussian quadratures on triangles; the latter is the customary choice for the non-self terms, especially for large problems, where the matrix fill is one of the most computationally intensive parts of the algorithm. The comparison indicates that the typical Gaussian quadrature errors in the MoM matrix elements are of order 0.1%; it would be thus pointless to attempt to reduce the multipole expansion errors below the $\sim 10^{-3}$ level.

Since, ultimately, we expect the accuracy of the solution to be controlled by the relative Frobenius norm (2.3), we also analyzed that quantity numerically for a number of representative scattering problems. As expected, Δ_{AIM} for larger problems is dominated by the far-field contributions, and becomes independent of the problem size. We give here some results for the perfectly conducting NASA almond of lenghts $2.5\,\lambda$ and $5\,\lambda$, corresponding to $N \simeq 2,500$ and $N \simeq 10,000$ unknowns. The surface triangulation in both cases corresponds to $b \simeq \lambda/8$. We found, in particular, that the accuracy $\Delta_{\mathrm{AIM}} \lesssim 10^{-4}$ results in the back-scattering cross-section deviating from its MoM value by less than about 0.1 dB for all polarizations and in the full angular range. Such an accuracy can be attained with $\varepsilon_{\mathrm{Near}} \sim 10^{-2}$, $d_{\mathrm{Near}} \leq 2$, and, e.g., with $M = 2$ and $a \simeq b/2$ or $M = 3$ and $a \simeq b$; computationally, the latter choice (a higher expansion order and a larger grid spacing) is much more economical than the first one. We also found that for larger grid spacings ($a > 2b$) the accuracy is relatively poor, and does not improve markedly with the increasing expansion order.

Acknowledgments

This work was partially supported by the Electromagnetic Code Consortium under contract F33615-93-C-1350.

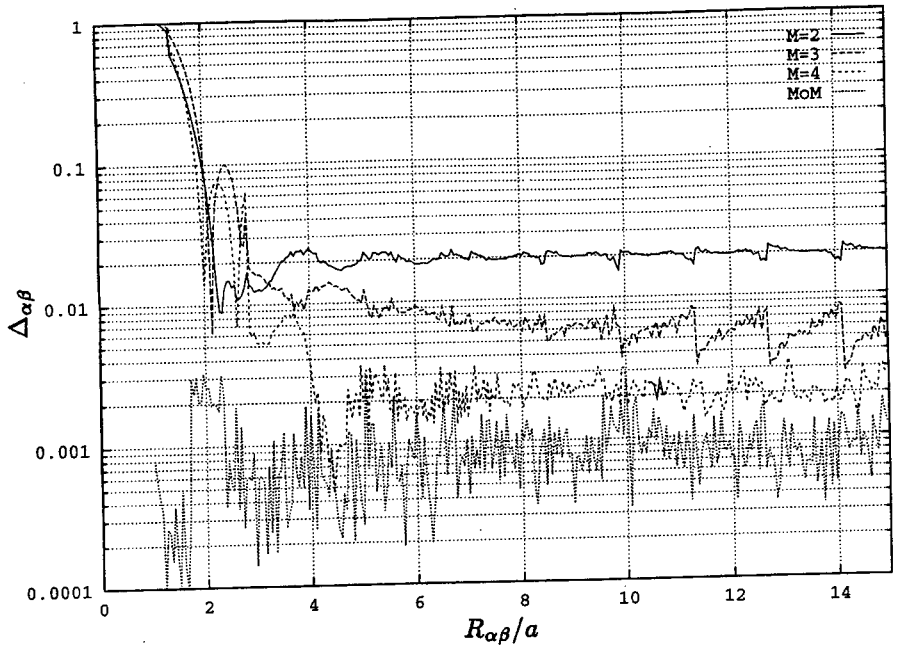

Fig.1. Relative errors $\Delta_{\alpha\beta}$ in the matrix elements for the Maxwell equation, for expansion orders $M = 2, 3, 4$, together with the quadrature error in the MoM matrix elements (marked "MoM'). Details are desribed in the text.

References

1. E. Bleszynski, M. Bleszynski, and T. Jaroszewicz, "A Fast Integral Equation Solver for Electromagnetic Scattering Problems", in *Proceedings of the 1994 IEEE APS International Symposium, Seattle, Washington*, pp. 417-420.

USING MODEL-BASED PARAMETER ESTIMATION TO ESTIMATE THE ACCURACY OF NUMERICAL MODELS

E. K. Miller
3225 Calle Celestial, Santa Fe, NM 87501-9613
505-820-7371, emiller@esa.lanl.gov

ABSTRACT

Determining the accuracy of the results produced by a numerical model remains an ongoing and important problem in computational electromagnetics, one to which there are relatively few options. Perhaps the most desirable and convincing approach is to perform a quantitative comparison between experimental data and the model output. Such a comparison, though undeniably useful, has the disadvantage that it embodies two different kinds of errors, these being the physical modeling error (PME) and the numerical modeling error (NME). The former arises from any differences that exist between the actual physical problem and its numerical representation, and the latter occurs because the numerical results actually obtained represent only an approximate solution to that numerical representation. Although the PME can normally be expected to be the larger of the two and also the more difficult to evaluate, quantitative knowledge of the NME itself is essential, estimation of which is the topic of this paper.

There are two approaches now used to estimate the NME, one being the internal checks that can be done within a specific model or code (e.g., convergence tests, boundary conditions, power conservation, etc.), and the other the external checks that involve comparing the results of two or more different models. The approach discussed here is another kind of internal check, but different from the others in the sense that it seeks a "noise" level in the model output as a measure of the model accuracy.

The basic idea is to apply a low-order, physically motivated, fitting model (FM) to a sampled, generating model (GM, based on a first-principles formulation) to be tested. Were these GM samples known exactly, then some minimum number would in principle permit the continuous transfer function (TF) to be exactly reconstructed across the frequency range that they span if the FM exactly represents the GM behavior. In fact, however, the GM samples and the FM are only approximations, and were no more samples available the FM-based TF could possess no better accuracy either. However, by using more samples from the GM, the additional information they provide can be used to estimate the accuracy of the TF derived from the FM and of the GM samples themselves. Furthermore, these extra GM samples might also be used to improve the accuracy of the FM estimate.

INTRODUCTION

However obtained, determining the quantitative accuracy of the numerical results developed for a particular electromagnetic problem is essential if such results are to be reliable. This is a problem of data validation. Another related, but broader, problem is that of establishing the accuracy that may be expected to be obtained from a given computer model when it is employed following accepted guidelines for its use. This is a problem of code validation. The latter problem is intrinsically open-ended and one in which one or just a few code developers might be involved while the former is more specific and can involve relatively many more users of that code. Attention in the following is addressed to the problem of data validation.

The basic question that confronts anyone who has to deal with numerical results is how accurate they are relative to the requirements of the problem for which they have been obtained. This issue can be expressed in various ways, but ultimately reduces to a problem of associating error bars, or uncertainty bounds, with numerical data. Traditionally, the purpose of error bars is to indicate that the results are

thought to have some numerical probability of lying within the band they span at some level of confidence. The question of accuracy, in other words, has a probabilistic, or statistical, context. While that degree of analytical formality and rigor could be useful in computational electromagnetics (CEM), it goes well beyond current practice and is not necessary as a first step towards satisfying some minimally acceptable accuracy statement for computed results. In the discussion here, attention is limited instead to deriving a quantitative estimate of numerical solution, or data, accuracy. Systematic extension of the idea presented here, or some alternative, could lead to a more rigorous methodology for error assessment. In the following sections we discuss in turn the kinds of data validation that can be used, how to model EM observables or data using reduced-order models, how such models can provide an estimate of the error in the transfer function that data represents, and then demonstrate application of this procedure to a pole spectrum and the current induced on an infinite, circular cylinder.

KINDS OF DATA VALIDATION

There are two fundamental ways by which data validation, or estimating the accuracy of electromagnetic observables, can be attempted. One is the compare the results in question with independent data, the expectation being that the true values are probably as close to these data as they are to each other, something that can be described as an external validation or check. This is a more convincing test when the independent data are experimental and come from the actual problem of interest, as the close agreement of two numerical results doesn't necessarily prove that they are correct and also doesn't shed any light on the physical modeling error (PME).

The other is to perform some test on the numerical results themselves, either to evaluate the conformity of the results relative to Maxwell's equations or their numerical consistency, as an internal validation or check. In the context of CEM an internal check that derives from Maxwell's equations is most satisfactory, of which some examples are reciprocity, energy conservation and boundary-field checks. An example of perhaps the most commonly used internal numerical check is a convergence test whereby the behavior of the numerical solution is examined as the number of unknowns is progressively increased. Unfortunately, the convergence of a numerical model is not always assured to occur, nor is convergence to a correct answer guaranteed either. Furthermore, a convergence test can be very expensive and even impractical for large problems.

A different kind of internal check using Maxwell's equations is discussed here. It is based on the observation that the various field quantities derived from a defining microscopic description, i.e., Maxwell's equations, must subsequently exhibit a known, reduced-order, macroscopic behavior. The specific behavior of interest for our purposes is the resonance-like structure of an electromagnetic frequency response, which is well-described by a rational function [Miller and Burke (1991)]. As is shown in the next section, knowledge that the transfer function (TF) has a simple analytical description can be exploited to test the numerical accuracy of the macroscopic field variables, and hence, of the model that produced them.

The approach taken here to estimate the accuracy of a numerical model is thus based on modeling the solution as a function of frequency. An alternative model-based, approach might also be employed, where the error in the solution is the quantity being modeled rather than the value of the solution itself. This approach requires knowledge of how the error varies with the number of unknowns, X or equivalently with the spatial sample interval, h, since this permits combining solutions using different values of X, to obtain a solution estimate better than that for the largest X used. When the error varies as Ah^n with n an integer, a behavior true of many numerical operations, a procedure known as Richardson extrapolation results [Ralston (1966)]. Using the observation that an EM numerical modeling error (NME) for an integral-equation formulation varies as $Ae^{(-BX)}$ [Miller et al. (1971), Miller (1996)], a similar approach can be used to improve the best result from a convergence test. The approach described in Miller (1996) extends Richardson extrapolation to this case.

MODELING GENERATING-MODEL SAMPLES

It has been demonstrated [Miller and Burke (1991)] that a sequence of numerical TF samples, $S_i = S(f_i)$, computed from a CEM model [the generating model (GM)] as a function of frequency f at sample frequencies f_i can be well-approximated using a rational function [a fitting model (FM)] as a generalization of the pole series that alone describes the resonance behavior of the former. A P-term poles series can be expressed as the rational function $r(P-1,P,f) = n(P-1,f)/d(P,f)$, where $n(P-1,f) = n_0 + n_1 f + n_2 f^2 + \ldots + n_{P-1} f^{P-1}$, and $d(P,f) = d_0 + d_1 f + d_2 f^2 + \ldots + d_P f^P$, i.e. as a ratio of two polynomials of degrees P - 1 and P, respectively. However, as P increases, this model becomes less robust numerically. Furthermore, an electromagnetic TF is not completely described by a pole series, having in addition a non-pole contribution. For these reasons it was found that a series of overlapping, windowed, low-order rational functions having the form r(N,D,f), where N = D or D + 1 is used, is a better choice to model a wideband TF. This increase in the order of n(N,f) relative to d(D,f) evidently helps to model the effects of poles that lie outside the frequency window modeled by r(N,D,f) as well as the unknown, non-pole contribution.

Each windowed, FM is quantified by fitting it to M = N + D + 1 computed GM samples over the frequency range that it spans, from which its polynomial coefficients are then obtained as a solution to an M'th-order data matrix, assuming a square data matrix is used. The number of GM samples required is one less than the number of coefficients in r(N,D,f) because one of the coefficients is set to unity, typically d_P. The minimum number of GM samples needed, were its TF to be a purely pole series, would be two per pole or resonance; otherwise a non-unique FM will result. However, because of the factors just discussed, at least 3 samples per resonance are typically required. Thus, if a FM is to span P poles, M ~ 3P GM samples will be needed at a minimum. If the FM order is to be kept below a "reasonable" number, say 20, then the number of resonances spanned by a FM should be no more than 6, with numerator and denominator polynomial orders of at most 9 or 10.

Because the condition number (CN) of the data matrix grows with increasing M for a FM spanning a fixed frequency band, the numerical match or data fit (DF) achieved between that FM and the GM samples used for quantifying it will decrease commensurately. On the other hand, the model fit (MF) obtained between the FM and additional GM samples not originally used for its quantification will increase with increasing M until some maximum, M', is reached, beyond which MF will also decrease because of the increasing CN. The opportunity for estimating the accuracy, or error, of the GM samples lies in the range between some minimum value of M and M' > M. Some results obtained using a computer precision (CP), of 24 digits for a 15-pole spectrum having $s_i = \sqrt{i}/20 + j*i$ ($j = \sqrt{-1}$) are included in Fig. 1 to illustrate these points, where the M = N + D + 1 GM samples are evenly spaced between frequency endpoints of 5.5 and 8.5.

The CN and DF as a function of N with D a parameter are shown in Fig. 1a with all results displayed in digits, i.e., where a CN of 10^X has the numerical value of X, etc. It can be seen that increasing N and/or D increases CN and decreases DF, the sum of which is furthermore about equal to CP. Thus, were a better fit to be sought between the original data and the FM, this might be accomplished by increasing CP. This possibility is not pursued further here but is an option to be considered.

The corresponding average match between the FM and additional GM samples, MF, is shown in digits in Fig. 1b. It can been seen that MF increases with both N and D, until the growing CN causes a downturn for the larger values of these parameters. By varying its parameters, it is possible to develop a FM from the original GM samples that produces an approximate 6-digit match to additional samples within the frequency range spanned by the FM. The significance of this result is further considered below.

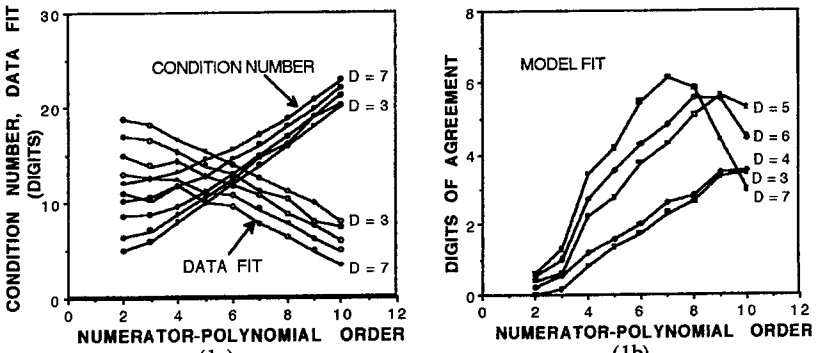

Figure 1. The condition number and data fit between the fitting model and the pole-series generating-model samples used to quantify it are presented in part (a), while in (b) is presented the agreement between the fitting model and additional generating-model samples, all results being shown in digits and as a function of the fitting-model numerator-polynomial order with the denominator-polynomial order, D, a parameter. The maximum model fit shown in (b) indicates that the smallest error detectable for this particular example would be about 10^{-6}. These calculations were performed in 24-digit computer precision.

ESTIMATING THE ERROR IN A TRANSFER FUNCTION

The accuracy of the GM samples can be expressed relative to an exact answer for the numerical representation of the physical problem being modeled, $E_i = E(f_i)$, as

$$A_i = [|(S_i - E_i)/E_i|] \tag{1}$$

or in a somewhat more convenient measure, digits of agreement using

$$B_i \equiv \log_{10}[|(S_i - E_i)/E_i|]. \tag{2}$$

For example, a 1% agreement would yield $B_i = 2.0$, while for 2×10^{-3} agreement, B_i would be 2.7, etc. The *a priori* accuracy of the numerical samples is usually unknown as is E_i, so B_i (and A_i) is also not available. It is the purpose of this discussion to develop a procedure for estimating B_i without knowledge of E_i.

First observe that when S_i is expressed in floating-point form, e.g. using an x-digit mantissa where x = 8 is often-used, these samples normally contain more digits than can be justified since a relative accuracy of 10^{-8} is usually not expected. These excess digits can be regarded as numerical "noise" that represents an accuracy floor for a given sample. Assuming no systematic error source affects the computed samples, the numerical noise should be random and the S_i samples should be randomly distributed around the unknown E_i values. The possibility of estimating B_i is based on this assumed random variation of S_i relative to E_i by comparing GM and FM samples.

The idea is to oversample across the frequency range of interest, F_{GM}, the GM whose output is to be tested, using a subset of these data samples, S_{DF}, to develop a FM that spans part or all of that bandwidth, F_{FM}. This FM is then used to compute an average DF of $\underline{B}_{DF}$ digits to the S_{DF} samples and an average MF of $\underline{B}_{MF}$ to the remaining S_{MF} samples over F_{FM}. The value of $\underline{B}_{MF}$ relative to $\underline{B}_{DF}$ provides a consistency measure between the two data sets and the FM. This is so because all of the data comes from the same GM and so S_{DF} and S_{MF} must be internally consistent to an amount determined by the average GM accuracy, $\underline{B}_{GM}$. The value of $\underline{B}_{DF}$ for the data set S_{DF} will be only as accurate as permitted by the CN of the data matrix and CP used as illustrated in Fig. 1a. It is, however, relatively independent of $\underline{B}_{GM}$ and can actually exceed it since $\underline{B}_{DF}$ provides only a measure of well the FM can match a set of numbers whose data matrix has a condition number CN when the computations are performed to a specified computer precision CP. However, the value of $\underline{B}_{MF}$ for the data set S_{MF} will be limited in accuracy to the lesser of $\underline{B}_{GM}$ and $\underline{B}_{DF}$ because the FM can match the data set S_{MF} no better than it matches the data set S_{DF} on which it is based, the accuracy of which is $\underline{B}_{GM}$. Two outcomes are thus possible: 1) $\underline{B}_{DF} \sim \underline{B}_{MF}$; and 2) $\underline{B}_{DF} > \underline{B}_{MF}$. The third possibility, $\underline{B}_{DF} < \underline{B}_{MF}$, has already been excluded. In either case, $\underline{B}_{MF}$ provides the valid, lower-bound estimate sought for $\underline{B}_{GM}$, a point to be demonstrated in the following.

It's worthwhile to observe that the procedure just outlined is similar to the use of linear regression. For that particular problem, the goal is to obtain the best fit between available data and a straight line which serves as a model for the data. Uncertainty or errors in the data can be estimated by the mismatch that is found between that data and the best-fit line. In our case, the model is a rational function rather than a pole series, but the concept is the same. Both of these problems are examples of the more general one of finding the model that best represents the data of interest, a problem also known as system identification. A general discussion of modeling data is given in Press et al. (1992).

For illustrative purposes, consider the pole-spectrum example just presented. Based on the results of Fig. 1b, it appears reasonable to select a candidate FM with D = 7 and an N varying from 6 to 9 in order to achieve a relative maximum in $\underline{B}_{MF}$, using the requisite data set S_{DF} needed to quantify the F_M parameters. Using the new data set S_{MF}, $\underline{B}_{MF}$ can then be computed over F_{FM}. In order to illustrate the effect of GM uncertainty, uniformly distributed random noise is added to all GM samples in order to determine the degree of correlation between the noise level and $\underline{B}_{MF}$. The results of this experiment are plotted in Fig. 2.

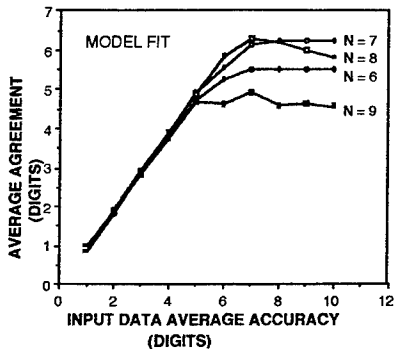

Figure 2. Shown here is the average agreement achieved between a fitting model and additional samples of the generating model for the example of Fig. 1, as a function of the generating-model sample accuracy. The fitting-model denominator-polynomial order is 7 and its numerator-polynomial order is a parameter. This result indicates the feasibility of estimating the accuracy of the generating-model samples from the agreement they exhibit with the fitting model.

The quantity $\underline{B}_{GM}$, controlled by the dynamic range of the additive noise, is plotted on the horizontal axis with $\underline{B}_{MF}$ plotted on the vertical axis. There is essentially a one-to-one correlation between $\underline{B}_{GM}$ and $\underline{B}_{MF}$ up to values between 5 and 6, beyond which variations are seen that can be deduced from Fig. 1b as being due to differences in the FM numerator-polynomial order. Note that this computation involves no *a priori* knowledge of $\underline{B}_{GM}$, its value rather being inferred from $\underline{B}_{MF}$. Thus, when using simulated frequency-response data, it appears that the MBPE procedure does provide a quantitatively valid way for estimating the noise level, or equivalently the accuracy, of the data being modeled. In the next section, we apply the technique to an electromagnetic problem.

APPLICATION TO AN ELECTROMAGNETIC TRANSFER FUNCTION

The problem to be considered is the frequency-dependent current excited on the illuminated side of an infinite, circular cylinder for a normally incident, TE plane wave. This problem has an analytical solution, which is used here, but has also become a benchmark solution for various CEM models. Using the analytical solution permits performing a computation whose accuracy can be modified in a controlled fashion by adding noise to, or otherwise affecting, the solution. Here, we use a parameter that controls the number of terms summed in the infinite series and which thereby limits it convergence and accuracy. All other calculations are otherwise done in 24-digit computer precision. The frequency range covered by the results which follow are for ka = 3 to 6 where ka is the cylinder circumference in wavelengths.

Shown in Fig. 3a are results for the CN and DF, and in Fig. 3b the MF, as a function of FM numerator-polynomial order with the FM denominator-polynomial order a parameter. As found for the pole spectrum above, the CN increases and the DF decreases with N, with their sum approximately equal to the CP. Similarly, the MF is found to increase with N until, as is seen for D = 7, the effect of the increasing CN causes it to decrease after reaching a peak value of about 8.5 digits.

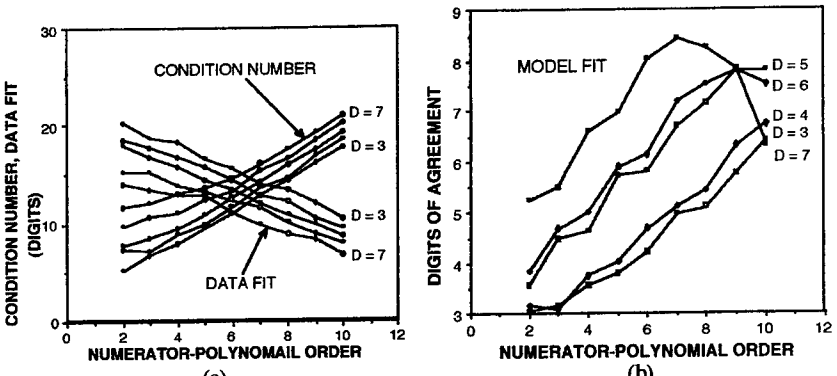

Figure 3. The results here are similar to those of Fig. 1 except that the generating model is the analytical, series solution for the current induced on the illuminated side of an infinite, circular cylinder by a normally incident plane wave and sampled between ka = 3 and 6. The lower condition numbers for this problem compared with the pole-series example of Figs. 1 and 2 results in more accurate agreement between the fitting and generating models in (b). A computer precision of 24 digits was used.

For the parameters used to model this particular response, it appears that using D = 7 and letting N vary from 3 to 7 will yield the best MF as the GM accuracy is varied, which leads to the result shown in Fig.

4. The dependence of the $\underline{B}_{MF}$ on the input-data accuracy is similar to that already seen in Fig. 2. Of most significance is that there is again a nearly one-to-one correspondence between $\underline{B}_{MF}$ and $\underline{B}_{GM}$, indicating the potential utility of the procedure for estimating the accuracy of that data, and hence, of the GM that produced it in the case of CEM. The effect of decreasing the input-data accuracy to 4 digits for the infinite-cylinder generating model, as shown in Fig. 5, further demonstrates the feasibility of determining the generating-model accuracy from its agreement with the fitting model.

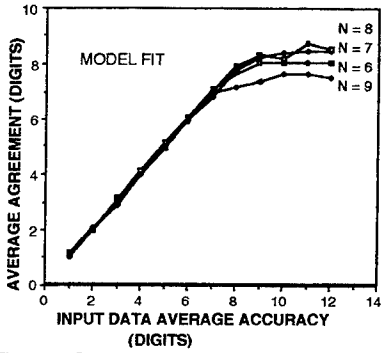

Figure 4. Shown here is the average agreement achieved between a fitting model and additional samples of the EM generating model for the example of Fig. 3, as a function of the generating-model sample accuracy. The fitting-model denominator-polynomial order is 7 and the numerator-polynomial order is a parameter. This result indicates the feasibility of estimating the accuracy of CEM samples from the agreement they exhibit with the fitting model.

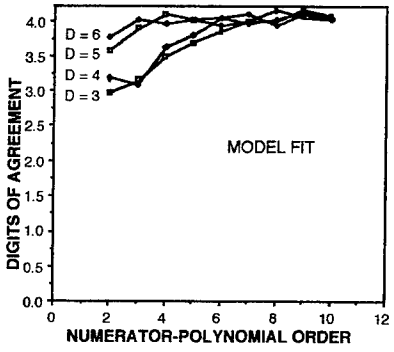

Figure 5. The results here repeat those of Fig. 3 for the infinite-cylinder generating model, but the input-data accuracy was reduced to 4 digits. It can be seen that if the fitting-model, denominator-polynomial order is 5 or 6, the fitting-model agreement to the input data is within 3×10^{-4} of the input-data accuracy, for numerator-polynomial orders of 4 or greater.

A more-detailed demonstration of this possibility is illustrated in Fig. 6 where the frequency dependence of the MF is shown with the input-data accuracy a parameter. The parameter L is the digit specification for the convergence of the series used in computing the infinite-cylinder test current, i.e., the series is computed until $|T_i/\text{Sum}(i)| < 10^{-L}$, where T_i is the i'th term in the series and Sum(i) is the series sum up through that term. The individual B_{iMF} for each L are seen to cluster randomly about that value of digits thus yielding a $\underline{B}_{MF}$ value being nearly equal to L as shown in Fig. 4.

CONCLUDING COMMENTS

A major deficiency in computational electromagnetics (CEM) is the almost-universal absence of any cost-effective way to estimate the accuracy of the solutions provided by numerical models. The rationale for the procedure described in this paper is to exploit knowledge of the macroscopic behavior of electromagnetic observables as a means of measuring the uncertainty of results computed from CEM models and thereby to estimate their accuracy. The procedure is based on the known, resonance-like frequency dependence of EM observables, a behavior well-approximated by a rational function that can thus serve as a fitting model (FM) for such observables. By quantifying the FM using a set of frequency samples from the first-principles or generating model (GM), the computed match, or fit, between this FM and additional GM samples provides an accuracy estimate of the data produced by the GM. This possibility has been demonstrated here for two problems, one a pole spectrum and the other the current excited on

an infinite circular cylinder by an incident plane wave.

It should be appreciated that quantifying the FM requires solution of a "data" matrix whose size is determined by the orders of the numerator and denominator polynomials that comprise it, and which, even though generally involving fewer than 20 equations, can have a condition number exceeding 10^{10}. Because the error estimate derived from the FM procedure can be no better than the fit achieved between the FM and the original GM data, the computer precision required will generally exceed 16 digits to overcome the effects of data-matrix ill-conditioning. The results presented here were obtained using 24-digit computer precision. It should also be appreciated that the FM is not unique and furthermore, that some experimentation is required concerning the bandwidth covered by GM samples and the parameters used for the FM. Finally, it's worth noting that the procedure outlined here can not only provide an error estimate for the data obtained from a GM, but it may be possible to improve the accuracy of the GM samples themselves by averaging the parameters of overlapping, windowed FMs. Both of these procedures, of course, derive from the fact the oversampled GM data is available whose redundancy provides the additional information that makes such operations possible.

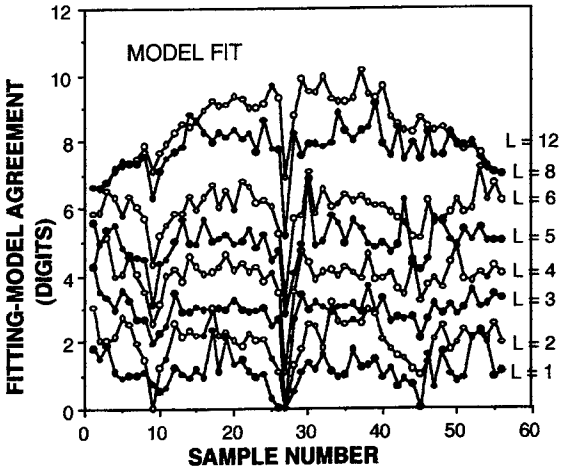

Figure 6. The fitting-model agreement for each additional data sample for the cylinder generating model, with the input-data accuracy a parameter ranging from 10^{-1} to 10^{-12} (i.e., 10^{-L}) is presented here. These results show that "noise" in the input data is accurately estimated by the fitting model. The sample numbers are roughly proportional to frequency over a range of cylinder circumference from 3 to 6 in wavelengths.

REFERENCES

Miller,E. K., G. J. Burke, and E. S. Selden (1971), "Accuracy-Modeling Guidelines for Integral-Equation Evaluation of Thin-Wire Scattering Structures", IEEE Transactions on Antennas and Propagation, AP-19, pp. 534-536.

Miller, E. K. and G. J. Burke (1991), "Using Model-Based Parameter Estimation to Increase the Physical Interpretability and Numerical Efficiency of Computational Electromagnetics," Computer Physics Communications, 68, 43-75.

Miller, E. K. (1996)], "Modeling the Convergence of Numerical Models to Achieve Increased Accuracy," to be submitted for publication.

Press, W. H., S. A. Teukolsky, W. T. Vetterling and B. P. Flannery (1992), *Numerical Recipes*, Cambridge University Press.

Ralston, A. (1966), *A First Course in Numerical Analysis*, McGraw-Hill Book Co., New York.

Guidelines for using the fast multipole method to calculate the RCS of large objects

Sunil S. Bindiganavale and John L. Volakis

Radiation Laboratory
Department of Electrical Engineering and Computer Science
The University of Michigan
Ann Arbor, MI 48109-2122

Abstract

In this paper, we consider with particular emphasis to error and execution time, the implementation of a version of the fast multipole method for scattering by large objects. In contrast to the traditional moment method, the fast multipole method (FMM) has $O(N^{1.5})$ CPU requirement per incidence angle. This substantially reduced CPU time is achieved by subdividing the far zone elements into groups whose weighted contribution is then interacted with the test element. The size of the groups and the various approximations used in the interaction of the groups play an important role on the solution accuracy, but so far the effect of these parameters on the solution accuracy has not been considered. Guidelines are given for choosing the various parameters affecting the speed and solution accuracy of the method such as the near-group distance and sampling rate based on an error criterion. Our study is carried out with reference to a version of the FMM referred to as the Fast Far Field Approximation.

1 Introduction

Integral equation methods and in particular the moment method were introduced first in the 1960s [1]. In the ensuing years the moment method achieved spectacular success and was applied to model a wide variety of complicated electromagnetic phenomena. Among its chief attractions were the exactness of the solution technique and the ability to model complicated geometries with ease. However, these advantages come at a price. The price to be paid for the exactness of the solution was the full matrix systems, a necessary part of the technique. Since full matrices need $O(N^2)$ storage, the MoM suffers severe problems of scalability, especially for 3D applications and large 2D problems. Recently, researchers have been trying to develop IE techniques which make the matrix system sparse by using special basis functions [2] or by making use of filtering techniques to isolate the dominant elements of the moment-method matrix [3]. Another technique relies on clumping the matrix elements in the far-field [4],[5],[6]. The technique which we have adopted is based on the latter principle and was introduced in [7]. This technique reduces the operation count in the iterative solution of moment method problems from $O(N^2)$ to $O(N^{1.5})$ for large N and is based on computing the interactions between different elements using different schemes depending on the electrical distance between the elements. For small interaction distances, the exact kernel is employed while for large distances an approximate kernel is used. The memory requirement,

with the preclusion of matrix factorization, is reduced to $O(N)$, thus enabling the solution of larger problems.

2 Study Objectives

Although it has already been demonstrated that the fast multipole method has $O(N^{1.5})$ or even lower computational complexity [5], there are several parameters which play a role in the CPU requirements and accuracy of the solution. More specifically, the grouping scheme, the sampling rate and the group size, all have an effect on the performance of the FMM. In this paper we examine the role of these parameters on the accuracy and computational efficiency of the FMM on the basis of some error-criterion. Specifically, we considered the scattering by two dimensional metallic structures using a solution of the EFIE and the MFIE with pulse basis and point matching [8]. In our study, the Fast Far Field Algorithm (FAFFA) [7], a variation of the FMM [6] was used for carrying out the matrix-vector products. Referring to Figure 1, the following parameters were

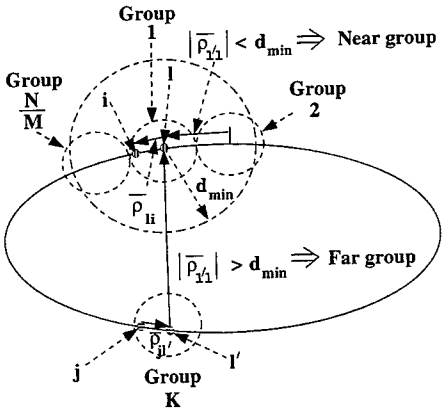

Figure 1: The process of grouping unknowns - two groups are in the near field of each other if the distance between their centers $\rho_{l'l}$ is less than d_{min}

examined with respect to the accuracy and efficiency of the FAFFA:

- the near-group radius,d_{min}
- the sampling rate
- group size, and
- memory requirements

Our benchmark for accuracy was the RMS error given by

$$ERROR_{RMS} = \sqrt{\frac{1}{M}\sum_{i=1}^{M}[RCS_{REF}(i) - RCS_{FF}(i)]^2} \qquad (1)$$

where RCS_{REF} denotes the reference radar cross sections as computed by the standard moment method approach without grouping, RCS_{FF} is the RCS calculated using FAFFA and M being the number of points at which the RCS is computed. We note that this error formula is among several that have been considered, but has been found to represent a reasonable measure of the accuracy. It has been employed by Schuh and Woo [9] for a study on the accuracy of RCS computations by various codes. In the following we will show error curves as a function of the aforementioned parameters for two cylinders. One is a PEC isosceles triangle having a base 2.5λ in length and a height of 17.95λ. The other is a rectangular PEC cylinder $25\lambda \times 4\lambda$ in size. These geometries (see Figure 2) are analyzed at grazing (0 degrees) incidence since this excitation is most stressing

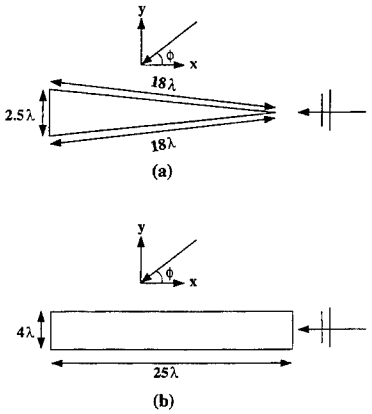

Figure 2: (a) An isosceles triangular metallic cylinder - 17.95λ high with a 2.5λ base (b) A rectangular metallic cylinder - $25\lambda \times 4\lambda$

for RCS calculations, particularly so for the triangular cylinder. In fact, the two geometries were selected to have different characteristics in the backscatter region.

2.1 RMS Error as a function of near-group separation distance and sampling rate

First we look at the RMS error of the bistatic RCS pattern as a function of the near-group radius, d_{min}. Such error curves are shown in Figures 3 and 4 for the isosceles and rectangular cylinders, respectively. These figures depicts several curves, each corresponding to a different sampling rate ($\lambda/10$, $\lambda/15$, $\lambda/20$, $\lambda/30$ or $\lambda/40$ as designated in the figure). Surprisingly, the error curves for each geometry give rise to the same conclusion. Basically, Figures 3 and 4 demonstrate that the sampling rate has a profound effect on the accuracy of the solution and the value of the error is strongly dependent on the near-group radius. For example, if d_{min} is set to 1.7λ, a tessellation rate of 10 segments per wavelength yields an RMS error of 4.79 dB whereas a tessellation rate of 30 segments per wavelength leads to an RMS error down to 1.19 dB. As expected, a higher sampling rate leads to smaller errors. However, these errors are different and much larger than those resulting from a standard moment method implementation. Specifically, a tessellation rate of 10 segments per wavelength yields an RMS error of 0.1615 dB when employing the standard unreduced moment

method solution but increases to 4.79 dB when FAFFA is employed with $d_{min} = 1.7\lambda$. As depicted in Figures 3 and 4, the values of d_{min} plays an equally important role in achieving a given RMS error. For example, when the segment length is $\lambda/10$, the error is over 4 dB when $d_{min} = 2\lambda$ but the error decreases to less than 2 dB when d_{min} reaches 3λ for the triangular cylinder and 5λ for the rectangular cylinder. This trend is, of course, logical since for larger values of d_{min} the FAFFA implementation resembles more and more the unreduced moment method.

Having found such a strong dependence of the RMS error on the tessellation rate and the near-group distance, to proceed further with our study, it is essential to look at what may be an acceptable RMS error. This error value can then be used to determine acceptable relationships between sampling rates and d_{min} on the basis of a certain RMS error. We therefore refer to Figure 5 which shows the bistatic RCS pattern of the isosceles triangle as computed using FAFFA for different sampling rates. The shown (exact) pattern has a dynamic range of 30 dB and we observe that an RMS error over 4 dB is associated with large and unacceptable RCS deviations (over 10 dB) from the reference RCS values. However, when the RMS error is about 1 dB or so, it is clear that the FAFFA results have only small deviations from the exact curve which is actually tracked very well by the FAFFA results even in low RCS regions. Consequently, we may select the RMS error value of 1 dB as the threshold level in determining whether a given choice of FAFFA parameters lead to acceptable accuracy or not.

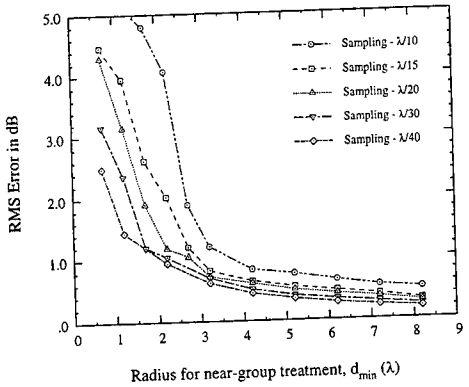

Figure 3: Error curves for the FAFFA for a isosceles triangular metallic cylinder - 17.95λ high with a 2.5λ base

2.2 CPU requirements

Returning now to Figures 3 and 4, we observe that an RMS error of 1 dB or less is obtained for the triangular cylinder if $d_{min} > 4\lambda$ when the sampling rate is 10 segments per wavelength, but d_{min} must be at least 7λ for the rectangular cylinder with the same sampling rate. Unfortunately, these values for d_{min} are much larger than 1λ which is the value often suggested by other users of the fast multipole method and its variations. It is of course important to keep the near-group radius as small as possible for CPU and memory reduction. However, the sampling rate must be increased to 30 segments per wavelength (for the isosceles triangle) if we are to reduce d_{min} to 2λ,

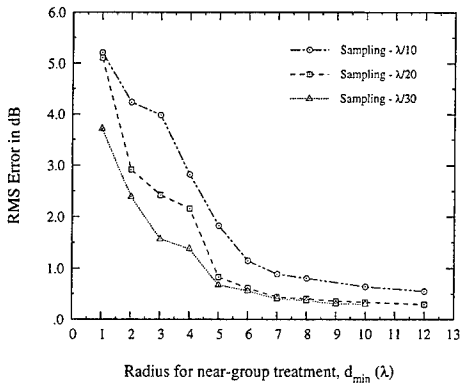

Figure 4: Error curves for the FAFFA for a rectangular pec cylinder - $25\lambda \times 4\lambda$

but clearly the increased sampling is counter to the benefits from a smaller near-group distance. Thus in Figures 6 and 7, we show curves of the CPU time as a function of the near-group distance for different sampling rates. Figure 6 refers to the triangular cylinder whereas Figure 7 corresponds to the rectangular cylinder, and both show a similar dependence on d_{min} and the sampling rate. For both cylinders the CPU time increases almost linearly with d_{min} and is, of course, higher for denser tessellations. These curves can be used in conjunction with those in Figures 3 and 4 to obtain the CPU time to determine d_{min} for a given RMS error and sampling rate. Alternatively, Figures 3 and 4 can be consolidated with the data in Figures 6 and 7 to obtain a new set of curves which explicitly give the CPU time as a function of a desired/given RMS error for the selected sampling rate. These CPU curves as a function of a specified RMS error are shown in Figures 8 and 9, corresponding to the triangular and rectangular cylinders, respectively. The trends in each of these Figures are identical, demonstrating that the dependence between CPU time, sampling, near group-distance and RMS error are likely the same regardless of geometry considerations.

Basically, Figures 8 and 9 show that the CPU time increases quadratically with sampling rate. Clearly, a lower sampling rate is more attractive in terms of CPU time since it leads to smaller systems and therefore faster convergence rate. That is, it is better to use a larger d_{min} with lower sampling rates rather than a higher sampling rate with a lower near-group window radius. For example, to achieve an RMS error of 1 dB for the triangular cylinder, the CPU time is about 10 sec when using a tessellation rate of 10 segments per wavelength and from Figure 3 the corresponding d_{min} is 3.75λ. However, to achieve the same error using a tessellation rate of 30 segments per wavelength, the corresponding CPU time is more than five times higher but the required near-group window radius is less than 2.5 wavelengths. It may seem that the higher number of degrees of freedom associated with higher segmentation rates leads to unequivocally higher memory requirements as well. However, this is not always the case with the FAFFA implementation because the value of d_{min} plays a major role on the bandwidth of the dense section of the matrix. For example, in the case of the rectangular cylinder, sampling at $\lambda/10$ would imply 580 unknowns while sampling at $\lambda/30$ would imply 1740 unknowns. To achieve a RMS error of 3.75 dB, it would require a near group window of 3.5λ for sampling at $\lambda/10$ and a window of 1λ for sampling at $\lambda/30$. Execution time considerations are of the order of 20 seconds for the first case and 75 seconds for

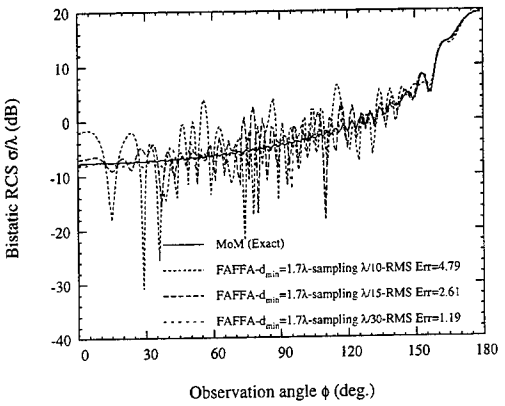

Figure 5: Comparison of bistatic patterns of an isosceles triangular pec cylinder - 17.95λ high with a 2.5λ base computed using the FAFFA at different sampling rates

the latter case. An examination of the grouping of the unknowns would reveal that the memory requirement for the latter case is smaller. Sampling at $\lambda/30$ and employing a near group radius of 1λ would mean a storage requirement of ~ 42 elements per row. Sampling at $\lambda/10$ and employing a near group radius of 3.5λ would mean a storage requirement of ~ 72 elements per row, which is higher than the previous case. Consequently, although Figures 8 and 9 suggest that a lower sampling rate has the least CPU requirements in satisfying a given error criterion, the memory requirements will be higher when compared to those associated with a higher sampling error and the same error criterion. Memory considerations will of course be an issue for very large simulations and the choice of using a high sampling or not will depend on the available computing resources.

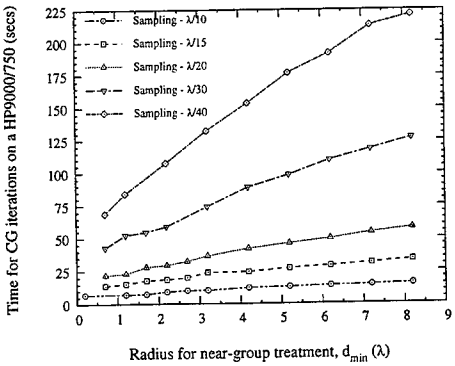

Figure 6: Time curves for the FAFFA for a isosceles triangular pec cylinder - 17.95λ high with a 2.5λ base

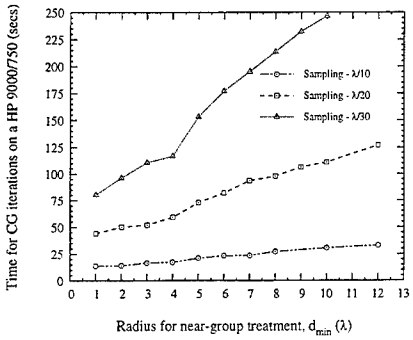

Figure 7: Time curves for the FAFFA for a rectangular pec cylinder - $25\lambda \times 4\lambda$

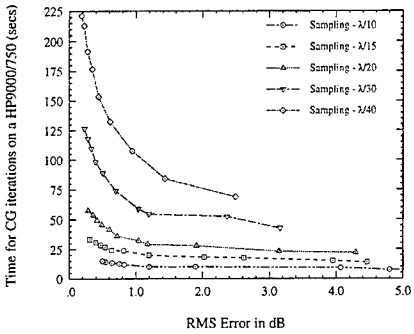

Figure 8: Time - error curves for the FAFFA for a isosceles triangular pec cylinder - 17.95λ high with a 2.5λ base

3 Conclusion

In this paper we looked at the CPU requirements of the FAFFA as a function of the different parameters affecting its performance, including the near-group window radius, sampling rate and error. We presented curves which show the required sampling rates, near-group window radius and CPU time as a function of a given error criterion. Based on these curves, one concludes that

- The error is strongly dependent on d_{min} and the sampling rate. This error dependence on the sampling is particularly inherent to the FAFFA solution method and should not be confused with similar errors associated with the unreduced moment method implementations. With higher sampling, the spatial extent of each group is reduced and thus the process of aggregation and disaggregation of group elements into group centers induces less error.
- In lieu of CPU time efficiency, it is best to employ lower sampling and larger near-group window radius.

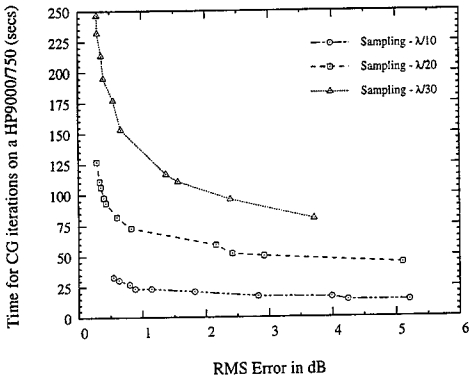

Figure 9: Time - error curves for the FAFFA for a rectangular pec cylinder - $25\lambda \times 4\lambda$

- Stringent memory requirements behooves the adoption of high sampling and small near group radius but at the expense of high execution time.

References

[1] R.F. Harrington, *Field Computation by moment methods*, IEEE press, New York, 1993.

[2] F.X. Canning, Fast integral equation solutions using GTD-like matrices, *Radio Sc.*, 29(4):993-1008, Jul-Aug 1994.

[3] J.L. Volakis and S.V. Krestianinov, ISOMOM: A new method for reducing storage and execution time of moment-method solutions in electromagnetics, *Microwave and Optical Techn. Letters*, 8(4)184-186, March 1995.

[4] N. Engheta, W.D. Murphy, V.Rokhlin and M.S. Vassiliou, The fast multipole method for electromagnetic scattering problems, *IEEE Trans. Antennas Propagat.*, 40(4):634-641, June 1992.

[5] J.M. Song and W.C. Chew, Fast multipole method solution of three dimensional integral equation, *IEEE Antennas Propagat. Soc. International Symposium 1995 Digest* , pp 1528-1531, June 1995.

[6] R. Coifman, V. Rokhlin and S. Wandzura, The fast multipole method for the wave equation: A pedestrian prescription, *IEEE Antennas and Propagat. Magazine*, June 1993.

[7] C.C Lu and W.C. Chew, Fast far field approximation for calculating the RCS of large objects, *Micro. Opt. Tech. Lett.*, 8(5):238-241, April 1995.

[8] J.J.H. Wang, *Generalized moment methods in electromagnetics*, Wiley-Interscience, 1991.

[9] M.J. Schuh and A.C. Woo, Code Scaling, *IEEE Antennas and Propagat. Magazine*, August 1995.

Developments in Error Estimation for Covolume and Staggered Mesh Approximations to Maxwell's Equations

R.A. Nicolaides and D-Q. WANG

Department of Mathematics
Carnegie Mellon University
Pittsburgh, PA 15213

Abstract

The covolume approach for solving Maxwell's equations is the most natural generalization to tetrahedral meshes of the FDTD method for rectangular meshes. In this paper a summary of the available error estimates is given. These estimates show first order accuracy for three dimensional tetrahedral meshes. For rectangular graded meshes the estimates show second order accuracy.

1 Introduction

Staggered mesh schemes for the numerical solution of Maxwell's equations go back as far as [19]. Over the years this scheme has seen a number of generalizations intended to enhance its usefulness. Mostly, these generalizations are aimed at increasing the geometric complexity that can be handled. Thus, in [3] a tensor formulation was given. This permits the method to be extended from rectangular meshes to meshes defined by curvilinear coordinates. Two dimensional generalizations using quadrilateral meshes are given in [6] and [8].

For three dimensions, hexahedral mesh formulations were proposed in [7] and [9]. These formulations use interpolation to obtain values for nonbasic field components–those which, in the rectangular situation, lie along the primal or dual mesh edges. Another approach is the "control path" method of [4], [5]. The control path method uses the classical finite difference approach of modifying the finite difference stencil near the boundary of the domain.

A natural generalization of the standard staggered mesh scheme to tetrahedral meshes was given in [10]. A similar technique was used independently in [14] to solve the Navier-Stokes equations. This "covolume" approach does not use any interpolations and is a very natural way to generalize the original rectangular staggered mesh approach. A characteristic feature of covolume schemes is the use of Voronoi-Delaunay mesh pairs to replace the rectangular staggered mesh arrangement.

Very little rigorous analysis of staggered mesh schemes for electromagnetics is available. We know only of the rectangular mesh analysis of [11] and [12]. (For the incompressible Navier–Stokes equations results may be found in [14], [15] and [17].) In this note we will survey some recent results we have obtained about the convergence of the covolume algorithm, and discuss the corresponding results for the rectangular mesh (Yee) scheme.

We begin with a section on Voronoi-Delaunay meshes. Then we cover the general error estimate for the semidiscrete (i.e. continuous time, discrete space) approximation. This is followed by results for the classical "leapfrog" time discretization. Finally, we show that for graded rectangular meshes the accuracy is one higher order than for the general tetrahedral case. Proofs of the results are given in our paper [16].

2 Mesh Notations and Discrete Vector Fields

Assume that the polyhedral domain Ω has a primal family of finite element style tetrahedral partitions, parameterized by the maximum side length which is generically denoted by h. We will assume that the ratio of radii

[1]This work was supported by the US Air Force Office of Scientific Research under Grant F-49620-94-0311.

of circumscribing spheres and inscribed spheres of all the individual tetrahedra are uniformly bounded above and below as h approaches 0. A dual mesh is formed by connecting adjacent tetrahedral circumcenters and, in the case of tetrahedron with a face on a boundary, by connecting their circumcenters with those of their boundary faces. By elementary geometry these dual edges are perpendicular to the associated tetrahedral faces. These connections also form the edges of a set of polyhedra. It follows from elementary geometry that the edges of tetrahedra are perpendicular to and in one-to-one correspondence with the faces of dual polyhedra or "covolumes". The reciprocal orthogonality between edges and faces is the key to the results which follow.

The N nodes of the tetrahedral mesh are assumed to be numbered sequentially in some convenient way, and likewise the T nodes of dual mesh. Similarly the F faces (edges) and M edges (faces) of the primal (dual) mesh are sequentially numbered. The individual tetrahedra, faces, edges and nodes of the primal mesh are denoted by τ_i, κ_j, σ_k and ν_l respectively. Those of the dual mesh are denoted by primed quantities such as σ'_j. A direction is assigned to each primal edge by the rule that the positive direction is from low to high node number. The dual edges are directed by the corresponding rule. We also denote by F_1 the number of tetrahedral interior faces (or dual edges) and by M_1 the number of tetrahedral interior edges (or dual faces).

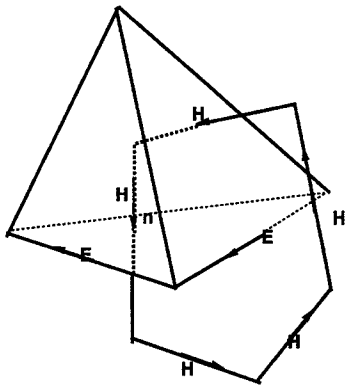

Figure 1

Let s_j denote the area of κ_j and h'_j the length of σ'_j. In R^{F_1}, where F_1 denotes the number of interior primal faces, we will introduce the inner product $(\cdot,\cdot)_W$ defined by

$$(u,v)_W := \sum_{\kappa_j \in \Omega} u_j v_j s_j h'_j = (Su, D'v) = (D'u, Sv) \tag{2.1}$$

and denote the resulting inner product space by $\mathcal{U}$ and the associated norm by

$$||u||_W := (u,u)_W^{\frac{1}{2}}. \tag{2.2}$$

In (2.1), $(\cdot,\cdot)$ denotes the standard Euclidean inner product, $S := \mathrm{diag}(s_j)$, $D' := \mathrm{diag}(h'_j)$ and $W := SD'$ are $F_1 \times F_1$ invertible diagonal matrices. The norm defined by (2.2) is clearly three times a discrete L^2 norm. Similarly, we will introduce an inner product in R^M, where M denotes the number of primal edges :

$$(u,v)_{W'} := \sum_{\kappa'_j \in \Omega} u_j v_j s'_j h_j = (S'u, Dv) = (Du, S'v) \tag{2.3}$$

and denote the inner product space by $\mathcal{U}'$. The associated norm is

$$||u||_{W'} := (u,u)_{W'}^{\frac{1}{2}}. \tag{2.4}$$

The notations in(2.3) and (2.4) correspond to those of (2.1) and (2.2). For example, s'_j denotes the area of dual face κ'_j.

For each primal face κ_i a discrete circulation is defined by

$$(Cu)_{\kappa_i} := \sum_{\sigma_j \in \partial \kappa_i} u_j \tilde{h}_j. \tag{2.5}$$

Similarly, for each interior covolume face κ'_i the discrete circulation is

$$(C'u)_{\kappa'_i} := \sum_{\sigma'_j \in \partial \kappa'_i} u_j \tilde{h}'_j. \tag{2.6}$$

A tilde on h_j or h'_j means that the quantity is to be taken with a negative sign if the dual edge is directed against the positive sense of description of $\partial\kappa_i$ or $\partial\kappa'_i$ respectively, and with a positive sign otherwise.

For each tetrahedron τ_i a discrete flux is defined by

$$(\mathcal{D}u)_i := \sum_{\mu_j \in \partial \tau_i} u_j \tilde{s_j}, \qquad \forall u \in R^{F_1}.$$

By $\tilde{s_j}$ we mean s_j negatively signed if the corresponding velocity component is directed towards the inside of τ_i and positively signed otherwise.

Using these definitions we are able to prove discrete analogs of formulas

$$\int_\Omega \operatorname{curl} \mathbf{E} \cdot \mathbf{H}\, dx = \int_\Omega \operatorname{curl} \mathbf{H} \cdot \mathbf{E}\, dx$$

which holds when $\mathbf{E} \times \mathbf{n} = \mathbf{0}$ on Γ, and $\int_\Omega \mathbf{u} \cdot \operatorname{grad} \phi\, dx = \int_\Omega (\operatorname{div} \mathbf{u})\, \phi\, dx$ for $\phi \in H_0^1(\Omega), \mathbf{u} \in H(\operatorname{div}; \Omega)$, respectively, and also of the identity $\operatorname{div}(\operatorname{curl} \mathbf{u}) = 0$.

See [13] and [18] for more details on this aspect of covolume discretizations.

3 Semi-Discrete Maxwell's Equations

We introduce, for general field $\mathbf{A}$, its "face averages" $A_f \in R^F$ and its "edge averages " $A_e \in R^M$ as follows (refer to Figure 1):

$$A_f := \frac{1}{s_i} \int_{\kappa_i} \mathbf{A} \cdot \mathbf{n}\, ds,$$

$$A'_f := \frac{1}{s_i'} \int_{\kappa'_i} \mathbf{A} \cdot \mathbf{n}\, ds,$$

$$A_e := \frac{1}{h_j} \int_{\sigma_j} \mathbf{A} \cdot \mathbf{t}\, d\sigma,$$

$$A'_e := \frac{1}{h'_j} \int_{\sigma'_j} \mathbf{A} \cdot \mathbf{t}\, d\sigma,$$

where $\mathbf{n}$ and $\mathbf{t}$ denote the unit normal vector to the face κ_i (or κ'_i) and the unit tangent vector to the edge σ_j (or σ'_j), respectively. Error functions for primal edges and faces will be denoted by

$$\epsilon_{\mathbf{A}} := A - A_f,$$

$$\eta_{\mathbf{A}} := A - A_e,$$

$$\delta_{\mathbf{A}} := A_f - A_e.$$

Error functions for dual edges and faces are defined similarly.

As shown in Figure 1, for each tetrahedron τ_i we will use the normal components of the magnetic field $\mathbf{H}$ to its faces and the tangential components of the electric field $\mathbf{E}$ in the directions of its edges.

Throughout this paper we will consider the solution of Maxwell's curl equations in a bounded domain Ω with the boundary condition $\mathbf{E} \times \mathbf{n}|_\Gamma = 0$.

Now integrate both sides of Ampere's law,

$$\epsilon \frac{d\mathbf{E}}{dt} - \text{curl}\,\mathbf{H} = \mathbf{J},$$

over the co-face κ_j' to obtain

$$\epsilon s_j' \frac{d(E_f)_j}{dt} - (C'H_e)_{\kappa_j'} = \int_{\kappa_j'} \mathbf{J}(x,t)\,dx. \tag{3.1}$$

Here, $(E_f)_j$ denotes the average of $\mathbf{E} \cdot \mathbf{n}_j$ over the face κ_j' where the $\mathbf{n}_j$ is the unit vector in the direction of σ_j, and $(C'H_e)_{\kappa_j'}$ is the discrete circulation around the face κ_j'. Similarly, from Faraday's law

$$\mu \frac{d\mathbf{H}}{dt} + \text{curl}\,\mathbf{E} = 0,$$

$$\mu s_i \frac{d(H_f)_i}{dt} + (CE_e)_{\kappa_i} = 0 \tag{3.2}$$

where $(H_f)_i$ denotes the average of $\mathbf{H} \cdot \mathbf{n}_i$ where $\mathbf{n}_i$ is the unit normal to the face κ_i and $(CE_e)_{\kappa_i}$ is the discrete circulation around the face κ_i.

Let E and H denote vectors of components in R^{M_1} and R^{F_1} respectively. Then (3.1) and (3.2) (which are exact) suggest the approximations (where it is implied that components of E associated with boundary edges are zero, i.e. $E|_\Gamma = 0$)

$$\epsilon S' \frac{dE}{dt} - C'H = \tilde{J}, \tag{3.3}$$

$$\mu S \frac{dH}{dt} + CE = 0 \tag{3.4}$$

where $\tilde{J} \in R^{M_1}$. Since μS and $\epsilon S'$ are invertible, (3.3)-(3.4) is a system of linear ordinary differential equations, and the existence and uniqueness of a solutions follow from well known results.

Using (3.4) we can show that

$$\frac{d}{dt}(\mathcal{D}H) = 0.$$

This shows the sense in which $\frac{d}{dt}\text{div}H = 0$ is satisfied at the discrete level in the covolume scheme.

The basic estimate for (3.3)-(3.4) is then:

Theorem 1 *Denote by (E,H) the solution of (3.3) and (3.4) and by*

$$(\mathbf{E},\mathbf{H}) \in W^{1,1}(0,T;(W^{1,p}(\Omega))^3)^2$$

the solution of Maxwell's equations with $p > 2$. Then we have the estimate

$$\max_{0\le t\le T}(\epsilon||(E-E_e)(t)||_{W'} + \mu||(H-H_e)(t)||_W) \le Kh(||\dot{\mathbf{E}}||_{L^1(0,T;(W^{1,p}(\Omega))^3)} + ||\dot{\mathbf{H}}||_{L^1(0,T;(W^{1,p}(\Omega))^3)}).$$

Thus, the basic scheme is first order accuracy.

4 The Fully Discrete problem

There are many possible time stepping methods that can be applied to (3.3) and (3.4). We will discuss a leapfrog scheme which is very popular in computational electromagnetics (see [19]). In this scheme we approximate $\mathbf{E}(t)$ at times $t_n = n\triangle t$, $0 \le n < \infty$ with a vector $\{\mathcal{E}^n\}_{n=0}^\infty$, and $\mathbf{H}(t)$ at time $t_{n+\frac{1}{2}}$ with a vector $\{\mathcal{H}^{n+\frac{1}{2}}\}_{n=0}^\infty$. The initial

value $\mathcal{H}^{\frac{1}{2}}$ can be computed using, for example, a Taylor expansion. Given $(\mathcal{E}^n, \mathcal{H}^{n+\frac{1}{2}})_{n\geq 0}$, the next approximation $(\mathcal{E}^{n+1}, \mathcal{H}^{n+\frac{3}{2}})$ is obtained by solving the equations

$$\epsilon S'(\mathcal{E}^{n+1} - \mathcal{E}^n) - \Delta t C' \mathcal{H}^{n+\frac{1}{2}} = \tilde{J}^{n+\frac{1}{2}} \tag{4.1}$$

$$\mu S(\mathcal{H}^{n+\frac{3}{2}} - \mathcal{H}^{n+\frac{1}{2}}) + \Delta t C \mathcal{E}^{n+1} = 0 \tag{4.2}$$

where

$$\tilde{J}^{n+\frac{1}{2}} = \int_{n\Delta t}^{(n+1)\Delta t} \tilde{J}\, dt.$$

(4.1), (4.2) is an explicit scheme, so the existence and uniqueness of a solution are apparent. Using the error functions defined last section, we can rewrite (4.1)-(4.2) as

$$\epsilon S'(\epsilon_{\mathbf{E}}^{n+1} - \epsilon_{\mathbf{E}}^n) = (\Delta t) C' \eta_{\mathbf{H}}^{n+\frac{1}{2}} + G^n, \tag{4.3}$$

$$\mu S(\epsilon_{\mathbf{H}}^{n+\frac{3}{2}} - \epsilon_{\mathbf{H}}^{n+\frac{1}{2}}) = -(\Delta t) C \eta_{\mathbf{E}}^{n+1} + \bar{G}_n. \tag{4.4}$$

By a direct computation, G^n and $\bar{G}^n$ are given by

$$G^n = \tilde{J}^{n+\frac{1}{2}} - \epsilon S'(E_f^{n+1} - E_f^n) + \Delta t C' H_e^{n+\frac{1}{2}}, \tag{4.5}$$

$$\bar{G}^n = \mu S(H_f^{n+\frac{3}{2}} - H_f^{n+\frac{1}{2}}) - \Delta t C E_e^{n+1}. \tag{4.6}$$

For the fully discrete scheme we expect a stability condition to appear in the error estimate and it does so.

Theorem 2 *Let $(\mathcal{E}^n, \mathcal{H}^{n+\frac{1}{2}})_{n\geq 0}^{N-1}$ denote the solution of (4.1)-(4.2), and let*

$$(\mathbf{E}, \mathbf{H}) \in (H^1(0,T;(W^{1,p}(\Omega))^3))^2$$

denote the solution of Maxwell's equations with $p > 2$. Under the stability condition

$$c\,\Delta t < \frac{\min(h_{ij})}{\sqrt{M_3} M_2^{\frac{3}{2}}} \tag{4.7}$$

where $c = (\epsilon\mu)^{-\frac{1}{2}}$ is the speed of the light in the medium, M_2 is the maximum of the ratios of the maximum to minimum side-lengths over the union of adjacent tetrahedra and M_3 is the maximum number of edges over all co-faces, we have the following error estimate for the fully discrete scheme (4.1)-(4.2)

$$\max_{0\leq i\leq N-1} (\epsilon ||\mathcal{E}^i - E_e^i||_{W'} + \mu ||\mathcal{H}^{i+\frac{1}{2}} - H_e^{i+\frac{1}{2}}||_W) \leq Kh(||\mathbf{E}||_{H^1(0,T;(W^{1,p}(\Omega))^3)} + ||\mathbf{H}||_{H^1(0,T;(W^{1,p}(\Omega))^3)}). \tag{4.8}$$

Once again the error is first order in h on tetrahedral mesh.

5 On Rectangular Meshes

An example of a rectangular mesh in three dimensions is one obtained by subdividing a rectangular parallelepiped by planes parallel to its faces. If the planes are equally spaced along each of the directions the mesh is "uniform". If the spacings vary from point to point the mesh is "graded". For the graded meshes both the primal and dual mesh faces are rectangular and are mutually perpendicular. The duality relations discussed in section 2 are preserved. The resulting discretization of Maxwell's equations is the standard Yee scheme [19].

For the semidiscrete equations there is the following estimate

Theorem 3 *Suppose that $(\mathbf{E}, \mathbf{H}) \in L^1(0,T;(H^3(\Omega))^3)^2$ satisfies Maxwell's equations, and denote by (E, H) the solution of (3.3)-(3.4) on graded meshes with maximum grid size h. Then*

$$\max_{0\leq t\leq T} (\epsilon ||(E - E_e)(t)||_{W'} + \mu ||(H - H_f)(t)||_W) \leq Kh^2 ||(\mathbf{E}, \mathbf{H})||_{(L^1(0,T;(H^3(\Omega))^3))^2}. \tag{5.1}$$

Here K depends on the maximum of the ratios of the maximum to minimum side-lengths in each graded cell.

A similar estimate holds for the fully discrete scheme under a stability condition.

The rectangular scheme is therefore second order accurate in h. This result implies that the rectangular approximation is inherently more accurate than the tetrahedral approximation. the reasoning behind this statement is that second order accuracy for tetrahedral meshes can be obtained only for very slowly varying meshes. (See [14] for the two dimensional case) For the rectangular case, however, there is no requirement slow variation in the mesh grading. We do not know at present how to reconcile these situations although presumably, local symmetry considerations are important.

References

[1] PHILIPPE G. CIARLET, The Finite Element Method For Elliptic Problems, North-Holland Publishing Company, 1978 .

[2] G.DUVAUT and J. LIONS, Inequalities in Mechanics and Physics, Springer-Verlag, New York, 1976.

[3] R. HOLLAND, Finite-difference solution of Maxwell's equations in generalized nonorthogonal coordinates, IEEE Trans. Nuclear Science, Vol. NS-30, 1983, pp. 4589-4591.

[4] T.G. JURGENS, A. TAFLOVE, K.UMASHANKAR and T.G. MOORE, Finite-difference time-domain modeling of curved surfaces, IEEE Trans. Antennas and Propagation, Vol. 40, 1992, pp. 1703-1708.

[5] T.G. JURGENS and A. TAFLOVE, Three-dimensional contour FDTD modeling of scattering from single and multiple bodies, IEEE Trans. Antennas and Propagation, Vol. 41, 1993, pp. 1429-1438.

[6] J.-F. LEE, Numerical solutions of TM scattering using obliquely Cartesian finite difference time domain algorithm, IEE Proc. H (Microwaves, Antennas and Propagation), Vol. 140, 1992, pp. 23-28.

[7] N. MADSEN, Divergence preserving discrete surface integral methods for Maxwell's equations using nonorthogonal unstructured grids, J. of Computational Physics, 119, 1995, pp. 34-45.

[8] N. MADSEN and R.W. ZIOLKOWSKI, Numerical solution of maxwell's equations in the time domain using irregular nonorthogonal grids, Wave Motion 10, 1988, pp. 583-596.

[9] N. MADSEN and R.W. ZIOLKOWSKI, A three dimensional modified finite volume technique for Maxwell's equations, Electromagnetics, Vol. 10, 1990, pp. 147-161.

[10] B.J. MCCARTIN and J.F. DICELLO, Three dimensional finite difference frequency domain scattering computation using the Control Region Approximation, IEEE Trans. Magnetics, Vol. 25, No. 4, 1989, pp. 3092-3094.

[11] PETER MONK and ENDRE SULI, A Convergence Analysis of Yee's Scheme on Nonuniform Grids, SIAM J. of Numerical Anal. Vol 31, 1994, pp. 393-412 .

[12] PETER MONK and ENDRE SULI, Error estimates for Yee's method on nonuniform grids, IEEE Trans. Magnetics, Vol 30, 1994, pp. 3200-3203.

[13] R.A. NICOLAIDES, Direct Discretization of Planar Div-Curl Problems, SIAM J. Numerical Anal. Vol 29, pp. 32-56 (1992) .

[14] R.A. NICOLAIDES, Flow discretization by complementary volume techniques, AIAA paper 89-1978, Proceedings of 9th AIAA CFD Meeting, Buffalo, NY, June 1989.

[15] R.A. NICOLAIDES, Analysis and convergence of the MAC scheme. 1. The linear Problem , SIAM J. Numerical Anal., Vol 29, No. 6, pp. 1579-1591, 1992.

[16] R.A. NICOLAIDES and D-Q WANG, Convergence Analysis of a Covolume Scheme for Maxwell's Equations in Three Dimensions, submitted to Mathematics of Computation.

[17] R.A. NICOLAIDES and X.WU, Analysis and convergence of the MAC scheme. 2. The nonlinear problem in the uniqueness case. To appear in Mathematics of Computation.

[18] R.A. NICOLAIDES and X.WU, Covolume Solutions of Three Dimensional Div-Curl Equations, submitted to SIAM J. of Numerical Anal.

[19] K. YEE, Numerical Solution of Initial Boundary Value Problems Involving Maxwell's Equations in Isotropic Media, IEEE Trans. Antennas and propagation, AP-16 (1966) pp. 302-307 .

Adaptive Methods for the Numerical Solution of Reaction-Diffusion Problems

Donald J. Estep
School of Mathematics,
Georgia Institute of Technology,
Atlanta, GA 30332
estep@math.gatech.edu

Mat G. Larsson
Department of Mathematics,
Chalmers University of Technology,
S41296 Göteborg, Sweden
mgl@math.chalmers.se

Roy D. Williams
Center for Advanced Computing Research,
California Institute of Technology,
Pasadena, CA 91125
roy@caltech.edu

Abstract

We describe recent work in the development of adaptive finite element methods for systems of reaction-diffusion equations. We illustrate the need for error estimation and adaptive methods using the classic bistable problem that has metastable solutions featuring rapid transients coupled to long time evolution of sharp layers. We describe the mathematical theory underlying adaptive finite element methods in the context of a scalar reaction-diffusion equation and then some of the issues in implementation. Finally, we present some computational experiments illustrating the theory as implemented in the finite element code *CARDS*.

1 Introduction

In this paper, we describe recent progress on the development of adaptive finite element methods for systems of reaction-diffusion equations. We concentrate mainly on describing and testing the underlying mathematical theory, but also describe some issues in implementation. The goal of our project is the development of a general parallel adaptive code called *CARDS* (Concurrent Adaptive Reaction-Diffusion Solver) for the numerical solution of reaction-diffusion equations

$$u_t - \nabla \cdot (D\nabla u) = F(u), \tag{1}$$

posed on a domain that is a product of a time domain $t > 0$ with a spatial domain $\Omega \in \mathbb{R}^d$ of dimension $d = 1$, 2, or 3. Here, u represents a vector of m unknown functions, so $u : \mathbb{R}^d \to \mathbb{R}^m$; F is the *reaction* term; and D is the *diffusion* term. F is a vector-valued function of u and ∇u as well as space and time and D is a semi-positive definite $m \times m$ matrix-valued function of u and space and time. The value of u is specified at the beginning of the time interval, and by Dirichlet or Neumann boundary conditions on subsets of the boundary of Ω as required.

Many physical phenomena are described by systems of reaction-diffusion equations; well-known applications occur for example in chemistry, materials science, fluid flow, and population dynamics. The interaction between

the nonlinear reaction and the diffusion gives rise to interesting behavior such as finite time blowup, long time behavior such as metastability, and localized behavior such as fast transients, steep fronts, and pattern formation. The variety of applications and interesting solutions have excited much interest, but the nonlinear nature of these problems makes the mathematical analysis of solutions exceedingly difficult. For this reason, we turn to numerical analysis to get information about the solutions. Yet, this poses a new set of difficulties because the nonlinear nature of the problems has also deterred precise mathematical analysis of numerical methods for reaction-diffusion problems. In fact, most of the numerical results in the literature are missing even a rough quantitative estimate of the size of the error. This is particularly troublesome considering that so little is known about the solutions themselves, increasing the reliance on numerical methods "working" as desired. Moreover, the fact that solutions typically exhibit several scales in their space and time behavior make accurate representation difficult.

We attempt to deal with these problems by using adaptive finite element methods with error control based on feedback from the computation. The error control rests on a recently developed theory of *a posteriori* error analysis in which the error is bounded by computable or approximatible quantities that depend on the numerical solution rather than the unknown true solution. The error estimators indicate the proper choice of resolution to achieve the required accuracy, while the use of adaptive meshing enables the computational resources to be used where needed in order to be efficient. The theory has been worked out completely for linear parabolic problems [3]; there has been much progress on systems of nonlinear ordinary differential equations of fixed dimension [5]; and also some work on nonlinear parabolic problems [4]. We have recently developed the theory further in [8] and we describe some of the work in this paper. There is much remaining to be understood, and we describe some of these issues as well.

The main deterrence to the widespread use of adaptive methods in differential equations is the computational complexity required to code them. We believe that it is possible to reduce the implementation advantage of simple explicit methods over adaptive methods for the general user because many ingredients of adaptive codes for differential equations are common to all sorts of problems. Making these ingredients accessible in a general way reduces the overhead of implementation. We describe the issues of implementation of adaptive codes on parallel computers in detail in [13], [12], [11], and [10].

2 The Bistable Equation

To simplify the presentation of the theory, we concentrate on the *bistable problem*,

$$u_t - \epsilon^2 u_{xx} = u - u^3, \quad 0 < x < 1, 0 < t, \tag{2}$$

with $\epsilon > 0$ small and Neumann or Dirichlet boundary conditions, which models for example the motion of domain walls in ferromagnetic materials. The bistable equation is one of the simplest problems that produce nonlinear relaxation to equilibrium in the presence of competing stable steady states. The stable steady states are $u \equiv 1$ and $u \equiv -1$, which are minimizers of the energy. For generic initial data, $u(x,t)$ approaches one of these steady states in the limit of large time. But, this convergence can be extremely slow because solutions of (2) can exhibit dynamic *metastability*. In general, u forms a pattern of transition layers between the values 1 and -1, where the layer thickness is of order ϵ. The subsequent time scale for substantial horizontal motion of the layers is $\exp(Cd/\epsilon)$, where $C = O(1)$ and d is the minimum distance between layers or between the layers and the boundaries. Metastable solutions are not local minimizers of the energy, and thus are always dynamic. After a metastable period, one or more of the layers disappear in a relatively quick transient and the system forms a new metastable pattern. This repeats until the eventual convergence to a steady state. We illustrate this behavior in Fig. 1a, where we plot the evolution from an nearly metastable initial condition consisting of two "wells" of different thicknesses with $\epsilon = 0.03$ In Fig. 1a, we plot the evolution of the approximation from this initial condition. The left well is slightly thinner than the right and collapses around time 41, while the well on the right collapses at time 141. The solution exhibits metastability during the time before 41 and between the two times. In [6], it was shown that the time scale for the evolution of a numerical approximation of a metastable solution depends critically on the accuracy of the space discretization, as well as the time discretization. In particular, inaccurate discretization causes the approximate metastable pattern to become stable, whereas a sufficiently accurate approximation evolves on the same time scale as the true solution. In a similar vein in [9], we report on computations made on a system of reaction-diffusion equations modelling shear flow in a Newtonian fluid with temperature dependent viscosity that illustrate the bad effect on the long time evolution of approximations

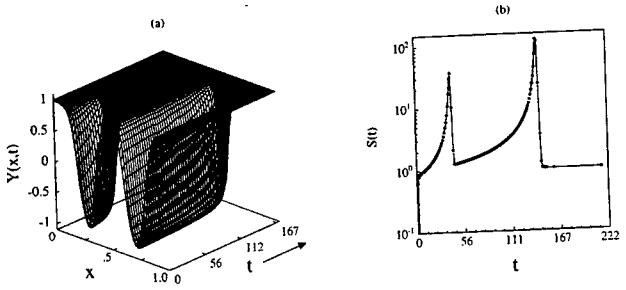

Figure 1: (a) Evolution of metastable solution computed with a relative accuracy of 2%. (b) The associated stability factor.

resulting from too coarse uniform space discretization. Those results also illustrate the effectiveness of adaptive mesh computations in such situations.

3 Classic Error Analysis

In terms of computational modelling using (2), the issue therefore is to compute the solution with sufficient accuracy. It is no terrible difficulty to construct a finite element method for a general scalar reaction-diffusion problem (1), see [7] and [4]. Nor is it very difficult to prove a standard *a priori* convergence analysis of such a method for a scalar problem of the form

$$u_t - u_{xx} = f(u,x,t), \tag{3}$$

that yields a bound on the error $e(x,t) = u(x,t) - U(x,t)$ of the form

$$\|u(\cdot,t) - U(\cdot,t)\| \leq e^{C_f t}\left(k^p + h^r\right) C(u), \tag{4}$$

where C_f is a constant depending principally on f, k is a measure of the time discretization like the largest time step while p is an integer and similarly h is a measure of the space discretization like the largest mesh size and r is another integer, $C(u)$ is a constant depending principally on the size of derivatives of the solution u up to an order determined by p and r over $[0,t]$, and $\|\cdot\|$ is a space norm like the maximum or root mean square norms. See [7].

The exponential factor $\exp(C_f t)$ is called the *stability factor* and it arises from the fact that the approximation is computed from a differential equation. By way of contrast, if the solution u were known, and U was simply a piecewise polynomial interpolant of u, then Taylor's theorem could be used to prove an error bound of the form

$$\|u(\cdot,t) - U(\cdot,t)\| \leq \left(k^p + h^r\right) C(u),$$

in other words without a factor that increases with time (other than possibly the maximum value of u and its derivatives). Unfortunately, unlike an interpolant of a known function, the error of an approximation of a solution of a differential equation suffers from the accumulation of errors that occurs during the integration of the differential equation.

Is a result like (4) useful for determining a discretization sufficiently fine that the approximation evolves on the correct time scale? Actually, not very. First of all, the derivatives of u in $C(u)$ are unknown. Second of all, the stability factor grows very rapidly. In the case of the bistable equation, the stability factor is $\exp(Ct/\epsilon^2)$ for $C \sim 1$. For the computation shown in Fig. 1, this is approximately $\exp(1000t)$. This effectively rules out any accuracy after a very short initial transient. Results like (4) are generally based on answering the question: *How well does the solution satisfy the discrete equations?*. The answer is given in terms of the truncation or local error and the error is bounded by assuming that all the local errors add constructively, rather than with some cancellation, and this produces the exponential growth in the bound.

4 An Overview of A Posteriori Error Analysis

Developing a theory of computational error estimation is a main goal of our research. The theory is based on an a posteriori error analysis that answers the question: *"How well does the approximation satisfy the differential equation?"*. The answer is given by the residual $\mathcal{R}$, defined roughly speaking as:

$$\mathcal{R}(t) = \|U_t - U_{xx} - f(U)\|.$$

This quantity is computable, since it is written in terms of derivatives of the approximation. For the methods we use, $\mathcal{R} = \mathcal{R}_x + \mathcal{R}_t$ decomposes into space and time residual errors naturally. The residual error is not the error, instead the relation between the two errors can be written generically as

$$\|u(\cdot,t) - U(\cdot,t)\| \leq S(t) \max_{s \leq t} \mathcal{R}(s).$$

where $S(t)$ is a stability factor for the a posteriori error bound and the maximum is over the space-time domain up to time t. $S(t)$ is determined by the solution of the *dual* problem to the differential equation:

$$\begin{cases} -z_t(s) - z_{xx}(s) = f'(u)z, & t > s \geq 0, \\ z(t) = e(t)/|e(t)|. \end{cases} \tag{5}$$

with $e(t) = u(t) - U(t)$. This is a linear problem integrated backwards in time from t to zero obtained by linearizing (3) around the solution. $S(t)$ is given as

$$S(t) = \int_0^t \|z_t(\cdot,s)\|\, ds.$$

The dual problem arises naturally when considering the effect of perturbations on the solution of a differential equation once it has been written in variational form, just by integrating by parts. Of course, the variational form of the differential equation is the starting point for a Galerkin finite element method as well.

There is a close parallel between these error bounds and the classic error bounds on the numerical solution of a system of linear equations $Ax = b$, where A is a matrix and x and b are vectors. The direct approach – estimating the error $\|X - x\|$ – is of course not possible. Instead, the residual error $\|AX - b\|$, which is computable, is introduced. The relationship between the error and the residual is determined by the *condition number* of the matrix: the error is bounded by condition number times residual. The stability factor plays exactly this role for differential equations: it is the "condition number" of the solution of the differential equation that we approximate.

The stability factor is not explicitly computable, because (5) involves information about the solution in the initial data and in the linearized coefficient. However, the dependence appears to be much less critical than in the a priori error bound where detailed information about the solution and its derivatives is involved. In the codes, we compute approximate stability factors using the numerical approximation. The complete mathematical justification of this step is not finished. It can be shown that a good value of $S(t)$ can be obtained by choosing a small number of random initial values for (5), while experimentally it appears that on many problems, trajectories near u, including the approximation, give approximately the same value for $S(t)$. In other words, the sensitivity of all solutions near u to perturbations is roughly the same. This kind of results are also used in the definition of Lyapunov characteristic numbers for a time dependent differential equation. In [10], we report on a set of experiments testing the effect of using different initial data and linearizing around different functions on the computed stability factor $S(t)$ for the bistable equation. While there are variations in the values of $S(t)$ for the different computations, in every case, the $S(t)$ measures the same sensitivity of u to numerical error during the critical transient periods.

We plot the approximation to the stability factor for the computation on the bistable equation shown in Fig. 1 next to the approximation. $S(t)$ clearly reflects the alternation of metastable periods, where $S(t)$ is of order 1 and slowly increasing, with the transient periods, which are marked by the very rapid increase in S. After the transient, the stability factor drops precipitously, indicating that the subsequent solution is essentially independent of accumulation of previous errors. When the solution finally converges to the uniform equilibrium state, the stability factor is one, and all previous error due to accumulation is removed. Contrary to the conclusions suggested by the classic a priori error analysis, the bistable equation is in fact computable.

5 Details in the Case of the Bistable Equation

§5.1 The discretization

We use the *discontinuous Galerkin finite element method* to discretize (3). We partition the time axis $0 = t_0 < t_1 < t_2 < \cdots < t_n$ and to the n'th interval $I_n = (t_{n-1}, t_n]$ with step $k_n = t_n - t_{n-1}$, we associate a partition of the domain $\Omega = [0,1]$ denoted $\mathcal{T}_n = \{x_{n,0} = 0 < x_{n,1} < \cdots < x_{n,M_n} = 1\}$. On $\mathcal{T}_n$, we let $h_{n,i} = x_{n,i} - x_{n,i-1}$ denote the i'th mesh length and h_n denote the mesh function with $h_n(x) = h_{n,i}$ for x in $(x_{n,i-1}, x_{n,i})$. To $\mathcal{T}_n$, we also associate the space of continuous, piecewise linear functions $\mathcal{V}_n$ in x. The approximation space $\mathcal{D}(q)$ consists of functions that are piecewise polynomials in time with coefficients in V_n on I_n,

$$W(x,t)|_{I_n} = \sum_{j=0}^{q} W_j(x)t^j, \quad W_j \in \mathcal{V}_n.$$

Because $V \in \mathcal{D}(q)$ is generally discontinuous across a time node, we use the notation V_n^- and V_n^+ to denote the value of V at t_n from below and above respectively, and $[V]_n$ to denote the change in value $V_n^+ - V_n^-$. The discontinuous Galerkin method reads: Compute U in $\mathcal{D}$ such that for $n = 1, 2, \ldots$

$$\int_{I_n} (U_t, v)\,dt + \int_{I_n} (U_x, v_x)\,dt + (U_{n-1}^+, v_{n-1}^+) = (U_{n-1}^-, v_{n-1}^+) + \int_{I_n} (f, v)\,dt. \tag{6}$$

for all polynomials v in t of degree q or less with coefficients in V_n, where $(v, w) = \int_0^1 vw\,dx$. In the case $q = 0$ for example, this yields: compute U_n^- in V_n satisfying

$$(U_n^-, v) + ((U_n^-)_x, v_x)k_n - (f(U_n^-), v)k_n = (U_{n-1}^-, v) \quad \text{for all } v \text{ in } V_n.$$

This is simply the well-known implicit Euler approximation.

§5.2 The a posteriori error bound

With $\|\cdot\|$ denoting the root mean square norm on Ω and

$$\|v\|_{I_n} = \max_{t \in I_n} \|v(\cdot, t)\|,$$

the a posteriori error bound for the piecewise constant approximation $q = 0$ reads

$$\|e_n^-\| \le S(t_n) \max_{m \le n} \mathcal{R}(U, m), \tag{7}$$

where

$$\mathcal{R}(U,m) = C_1\|h_m^2 f(U)\|_{I_m} + C_2\|h_m^2 D_2(U)\|_{I_m} + C_2\|k_m f(U)\|_{I_m} + C_4\|k_m D_1(U)\|_{I_m} + C_5\|[U]_m\| + C_6\Big\|\frac{h_n^2}{k_n}[U]_n\Big\|^*, \tag{8}$$

for some constants $C_i \sim 1$, where $D_1(U)|_{[x_{i-1},x_i]} = U_x|_{[x_{i-1},x_i]}$,

$$D_2(U)|_{[x_{i-1},x_i]} = \frac{1}{h_i}\max\Big\{\big|U_x|_{[x_i,x_{i-1}]} - U_x|_{[x_{i-1},x_{i-2}]}\big|, \big|U_x|_{[x_i,x_{i+1}]} - U_x|_{[x_{i-1},x_i]}\big|\Big\}$$

is a discrete "second" derivative of U, and the starred term is present only if the mesh is changed across t_{n-1}. The first two terms in $\mathcal{R}$ come from the residual error of the space discretization, the next three terms come from the residual error of the time discretization, and the last term arises from the effects of mesh changes. The a posteriori bound for higher order elements has a similar form but with correspondingly higher order terms arising in the residuals coming from time discretization. The derivation of (7) uses the variational formulation and Galerkin orthogonality. See [2] for an extensive discussion of the technique of a posteriori error analysis.

§5.3 Approximation of the stability factors

We compute approximate stability factors $S_p(t_n, Y)$ by applying the finite element method to the linear problem (5) obtained by linearizing around the approximation U and using a guess for the initial condition $e(t)/|e(t)|$. We use an appropriate order quadrature formula to compute $S(t)$ from this. Since (5) is linear and moreover since we are not interested in obtaining a very accurate approximation of the solution of (5), but only in obtaining $S(t)$ within in an order of magnitude, this backward integration is generally much cheaper than the forward integration.

§5.4 Adaptive error control

The algorithm for adaptive error control is essentially an iterative method for computing the solution of a constrained minimization problem: Given a tolerance TOL, compute an approximation U satisfying $\|u(\cdot,t) - U(\cdot,t)\| \leq$ TOL , for $t \geq 0$ using as little computational work as possible. TOL is the *global error tolerance*. We replace the ideal goal of this problem by the practical goal of computing U satisfying

$$S(t_n) \max_{m \leq n} \|\mathcal{R}(U,m)\| \leq \text{TOL} \quad \text{for } n \geq 0, \tag{9}$$

while using as little work as possible. We begin with an initial coarse discretization, compute the approximation, compute an approximation to $S(t)$, then refine or coarsen the mesh as appropriate in order to achieve (9). The actual refinement decisions are based on the sizes of the individual terms in $\mathcal{R}$. In practice, the error control generally achieves (9) with a couple of iterations.

§5.5 The linear solver

The discrete linear equations that are solved at each time step to get U are in general non-symmetric, non-positive-definite, and not diagonally dominant. To solve such systems efficiently, we use the QMR (Quasi-Minimal Residual) method. QMR is a Krylov-subspace technique which requires only the operations of multiplication by the matrix and its transpose, and a scalar product. This allows the code to be constructed using a matrix-free approach in which the matrix for the discrete systems are never assembled, making both the memory management and efficient implementation on parallel computers easier. See [10].

§5.6 Numerical example

We show the details of the computation presented in Fig. 1 using *CARDS*. In Fig. 2(a), we plot the finite element approximation U at times $t = 11.11$ and $t = 55.56$. The second time is during the metastable period after the first well has collapsed. We can see that there has hardly been any motion in the second well. In Fig. 2(b), we plot the mesh function $h(x)$ versus x for the same two times. The computation was started with a uniform mesh with 40 elements, and we can see how the error control refined the mesh to accurately represent the wells from the beginning. We can also see the mesh has been coarsened after the first well collapses. A convenient measure of the "amount of collapse" at time t is $\|1 - U(\cdot,t)\|$. We plot this function in Fig. 3(a). In Fig. 3(b), we plot the number of elements versus time where we can clearly see the effects of coarsening after each transient. In Fig. 3(c), we plot the time steps versus time. Again, the transient regions are marked by a substantial decrease in the time step.

6 Conclusion

Reaction-diffusion problems present an interesting challenge to engineers and mathematicians. The nonlinear nature of the problems and the generic tendency towards multiple scales in the space-time behavior of solutions makes the precise mathematical analysis difficult and numerical analysis is one of the main tools for exploration of the solutions. For this reason, it is important to provide the means to estimate the error of numerical results. Accurate estimates are difficult to obtain a priori, so we pursue the development of an a posterior error analysis that measures the error in terms of computable quantities that require only the approximation. This analysis measures the local production of error in terms of the residual error, i.e. the remainder left from substituting the approximation into the differential equation, and measures the accumulation of errors by a computational stability factor. We described this theory as applied to the bistable equation, which is a simple reaction-diffusion equation that has solutions with multiple scales in their space and time behavior.

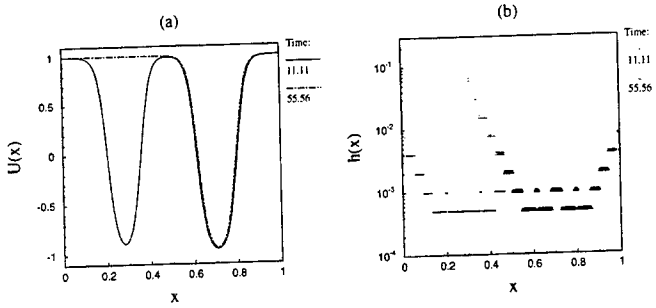

Figure 2: (a) The finite element approximation U at times $t = 11.11$ and $t = 55.56$. At the second time, the well on the left has collapsed and the solution is in a metatable state. (b) Plots of the mesh function $h(x_i)$ versus the mesh nodes x_i at the same times. Note that the mesh has coarsened in the region around the well on the left after it has collapsed.

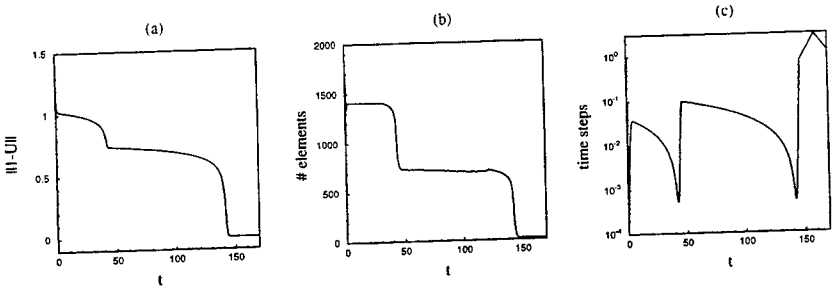

Figure 3: (a) A plot of $\|1 - U(\cdot, t)\|$, which measures the degree of "collapse" of the wells, versus t. (b) The number of elements versus t, showing how the mesh changes each time the solution becomes simpler. (c) The time steps versus t, showing the substantial decrease in the time steps as transient periods are approached.

Acknowledgments

The work of D. Estep is supported by the National Science Foundation, contract number DMS-9506519. The work of R. D. Williams is supported by Caltech, the Concurrent Supercomputing Consortium, and the Center for Research on Parallel Computation (a National Science Foundation Science and Technology Center, Grant 292-3-51393 under NSF CCR-8809615).

References

[1] Bronsard, L. and Kohn, R. V., *Motion by mean-curvature as the singular limit of Ginzburg-Landau dynamics.* J. Diff. Eq. 90 (1991), 211-237.

[2] Eriksson, K., Estep, D., Hansbo, P., and Johnson, C., *Computational Differential Equations.* Cambridge University Press, to appear.

[3] Eriksson, K. and Johnson, C., *Adaptive finite-element methods for parabolic problems 1. A linear model problem.* SIAM J. Num. Anal., 28 (1991), 43-77.

[4] Eriksson, K. and Johnson, C., *Adaptive finite element methods for parabolic problems IV: nonlinear problems* preprint #1992-44, Chalmers University of Technology, 1992.

[5] Estep, D., *A posteriori error bounds and global error control for approximations of ordinary differential equations.* SIAM J. Numer. Anal. 32 (1995), 1–48.

[6] Estep, D., *An analysis of numerical approximations of metastable solutions of the bistable equation.* Nonlinearity 7 (1994), 1445–1662 .

[7] Estep, D. and Larsson, S., *The discontinuous Galerkin method for semilinear parabolic problems.* RAIRO Mod. Math. Anal. Num. 27 (1993), 35–54

[8] Estep, D., Larsson, M., and Williams, R., *A theory for adaptive finite element methods for reaction-diffusion equations.* in preparation.

[9] Estep, D., Verduyn Lunel, S. M., and Williams, R., *Error estimation for numerical differential equations.* I.E.E.E Antennas and Propagation Magazine, to appear.

[10] Estep, D. and Williams, R., *Accurate parallel integration of large sparse systems of differential equations.* Math. Models Meth. Appl. Sci., to appear.

[11] Fox, G. C., Williams, R. D., and Messina, P. C., *Parallel Computing Works!.* Morgan-Kaufman, Los Altos, California, 1994.

[12] Williams, R. D., *Voxel databases: A paradigm for parallel computing with meshes*, Concurrency, 4 (1992), p. 619.

[13] Williams, R. D., *DIME: Distributed Irregular Mesh Environment*, Source code and documentation available from `ftp://ftp.ccsf.caltech.edu/dime/`.

Error estimates for subgridded FDTD schemes

PETER MONK (monk@math.udel.edu)
Department of Mathematical Sciences
University of Delaware
Newark, DE 19716

Local meshing or sub-gridding has been advocated by a number of authors as a way of increasing the spatial resolution of the finite difference time domain method (FDTD), see for example [1,2,3,4]. The concept is also used in other areas, for example in wave propagation [5,6], and some analysis has already been performed [5,6,7].

In this talk (which reports on work in to appear in *Journal of the ACES*), we start by giving a standard analysis of the spurious reflection that occurs at an interface between two grids for the usual FDTD scheme. This serves as a baseline to compare our analysis of subgridding schemes. We next show how to use supraconvergence techniques (see [8]) to analyze the error in a simple sub-gridding strategy in two dimensions. This strategy is based on constant interpolation (or one sided integration if the method is viewed as a finite volume scheme). Surprisingly the method is found to converge at least at order 3/2. Experimentally, the rate is second order which is the same as for the standard Yee scheme.

To give a more detailed picture of the error induced by the step change in the grid, we also analyze the spurious reflection that occurs at an interface between two grids of different size for the simple subgridding method and for another subgridding scheme employing linear interpolation (like [2]). The overall order of convergence of the reflection coefficients is the same for all the methods, but the linear scheme has a lower amplitude spurious transmitted mode compared to the simple subgridding scheme.

We expect our analysis to carry over to the FDTD discretization of the full three dimensional Maxwell system, and an effort to carry out this analysis is under way. The inclusion of time stepping error in the analysis is also necessary (in this context see [8]).

References:

[1] K. Kunz and L. Simpson, *IEEE Trans. Electromagn. Compat.*, vol. EMC-23, pp. 419–422, 1981.

[2] I. Kim and W. Hoefer, *IEEE Trans. Microwave Theory Tech.*, vol. 38, pp. 812–185, 1990.

[3] S. Zivanovic, K. Yee, and K. Mei, *IEEE Trans. Microwave Theory Tech.*, vol. 39, pp. 471–479, 1991.

[4] D. Prescott and N. Shuley, *IEEE Microwave Guided Wave Lett.*, vol. 2, pp. 434–436, 1992.

[5] R. Ewing, R. Lazarov, and P. Vassilevski, *Math. Comp.*, vol. 56, pp. 437–461, 1991.

[6] R. Ewing et al., *Math. Comp.*, vol. 56, pp. 61–86, 1991.

[7] M. Berger and J. Oliger, *J. Comp. Phys.*, vol. 53, pp. 484–512, 1984.

[8] P. Monk and E. Süli, *SIAM J. on Numer. Anal.*, vol. 31, pp. 393–412, 1994.

SESSION 10:

NUMERICAL LINEAR ALGEBRA IN COMPUTATIONAL ELECTROMAGNETICS

Chair: A. S. Hodel

Applications of Numerical Linear Algebra in Electromagnetics[1]

Griffin K. Gothard John H. Henderson A. Scottedward Hodel

Abstract

Numerical solution of electromagnetics (EM) problems is typically accomplished through (1) differential equation methods or (2) integral equation methods. The first two of these methods generally require the solution of a linear system of n equations in n unknowns $Ax = b$ in order to obtain an approximate solution to the underlying EM problem. We first present a discussion of these methods, followed by a survey of some common numerical techniques used in the solution of the linear system of equations $Ax = b$.

1 Introduction

Practical solution methods for typical problems in electromagnetics (EM) require numerical solution techniques. Many of these numerical schemes require the solution of a linear system of n equations in n unknowns

$$Ax = b \quad A \in \mathbf{C}^{n \times n}, \quad b \in \mathbf{C}^n \tag{1.1}$$

in order to obtain an approximate solution to the original EM problem. We present first a survey of numerical techniques used in electromagnetic applications to generate linear systems of equations, and second common numerical techniques used in the solution of equation (1.1).

2 Numerical Methods in Electromagnetics

EM problems are stated in terms of Maxwell's equations (partial differential equations) whose solution space is inherently infinite dimensional. In order to permit numerical solution, it is necessary to reduce the problem to one of finite dimension through direct discretization of the solution space or by discretizing the partial differential operators in Maxwell's equations. This procedure is implemented as either (1) differential equation (DE) methods, or (2) integral equation (IE) methods

Several popular algorithms are available to generate solutions to EM problems. Except for some of the high frequency techniques, they all solve either differential or integral equations in one form or another. Since only differential or integral equations are involved in the final solution, the methods described here should be of considerable interest to other areas of science. The underlying constants describing the physics of the system may differ, but the mathematical equations are similar. In fact, other branches of engineering, such as acoustics, heat transfer, and fluid dynamics have developed similar methods [1].

2.1 Differential Equation Methods

In the differential equation solution approach, we formulate a set of differential equations to describe the scattering mechanism. We divide the problem space into regular or prismatic zones and apply discretized forms of the differential equations at each zone to generate a linear system of equations. An approximate solution to the original EM problem is obtained through application of the appropriate boundary conditions followed by the solution of the corresponding equation (1.1).

In open-region DE type problems, a further reduction in problem dimension is required, since the solution space is unbounded. The problem space must be artificially terminated using some type of truncation condition. Since the fields generally are not zero beyond the truncated boundary, we must introduce a set of artificial boundary conditions, such as absorbing boundary conditions (ABC), boundary integral formulation (BIF), or the measure equation of invariance (MEI). This termination of the space grid at a finite distance introduces further inaccuracies in the problem solution.

Three examples of DE methods are the finite difference (FD) method, the finite element (FE) method, and, when using the integral form of Maxwell's equations, the finite integral technique (FIT).

[1]The authors are with the department of Electrical Engineering, Auburn University, Alabama, 36849.

Finite differences The finite difference method was first developed by A. Thom [2] in the 1920s to solve nonlinear hydrodynamic equations. Since then, the FD method has found applications in many different fields for a wide range of problems, including computational electromagnetics. The method is based upon approximations of the partial differential equations (PDE) with finite difference equations.

In the FD method, the finite difference equations relate a given unknown with neighboring unknowns. This is accomplished by dividing the problem space into discrete points, or nodes, and allowing each node to represent an unknown field quantity. Each unknown field quantity is surrounded by neighboring unknowns, *or* known boundary conditions which define individual problems within a given class of problems. Then, the particular PDE is estimated numerically with standard finite difference equations, e.g.,

$$f'(a_0) \cong \frac{f(a_0 + \Delta a) - f(a_0 - \Delta a)}{(2\Delta a)} \tag{2.1}$$

and

$$f''(a_0) \cong \frac{f(a_0 + \Delta a) - 2f(a_0) + f(a_0 - \Delta a)}{(\Delta a)^2}. \tag{2.2}$$

Equations (2.1) and (2.2) are readily derived through a truncated Taylor series expansion; see, e.g., [3].

In frequency domain computational electromagnetics, equation (2.2) is used to approximate the second spatial derivative in Laplace's or Poisson's equation. This results in the numerical analysis tool called the finite difference (FD) method. Since equation (2.2) is a discrete approximation to the second derivative, problems with no easily obtained analytical solution can be broken down and analyzed on a discrete grid. Thus an approximate solution can be found, which may closely resemble the unique solution.

Finite elements The finite element method was initially developed by Courant [4] in 1943, and in the 1950's began to see use in aircraft design. However, the method was not applied to electromagnetics until 1968. A discussion of numerical issues in the finite element method is presented in [5].

The finite element method divides the domain of the problem space into subdomains, or *elements*. (For the two-dimensional case these elements are generally rectangular or triangular in shape; three dimensional problems typically use tetrahedrons or 3-D rectangular grids.) An interpolation, or basis, function is defined on each element to provide an approximation to the unknown solution within each subdomain. This interpolation function is usually defined as a first or higher order polynomial. Third, a system of equations must be assembled, and the Rayleigh-Ritz variational or Galerkin's methods may be used for this step. Finally, the resulting system of sparse equations must be solved.

As a simple example, assuming we have discretized a static two-dimensional problem domain utilizing triangular elements, or subdomains, the interpolation function may be defined as a first order polynomial over each subdomain as

$$\mathrm{V}_n(x, y) = \mathrm{A}_n x + \mathrm{B}_n y + \mathrm{C}_n \tag{2.3}$$

where A_n, B_n and C_n are constants, and $\mathrm{V}_n(x, y)$ is the unknown potential at the n^{th} triangular subdomain. Next, we must generate the system of equations, and for this we will use Galerkin's method.

Galerkin's method is a weighted residual method that attempts to reduce the residual to the least value at all points in the problem region. Also, the weighting function is chosen to be the same as the interpolation function, which in our case is defined in equation (2.3). Following this procedure, and implementing the appropriate boundary conditions, a system of n sparse equations with n unknowns will be obtained, which then may be solved to determine the FE method generated solution.

Finite integrals The finite integral technique was originally applied by Rienen [6] in 1985 and Lebaric [7] in 1989. This method directly applies the Maxwell's equations in integral form to a discrete grid.

As in the FE method, the FIT first divides the domain of the problem space into subdomains, or *elements*. The FIT applies the integral form of Maxwell's equations integral form to each element, utilizing basis functions that explicitly define the field quantities. The result is a single equation that may be used to relate each unknown quantity in the subdomain to the neighboring unknowns. The resulting system of equations is assembled by applying the equation obtained for each element to each unknown in the problem domain.

This procedure, along with the incorporation of the appropriate boundary conditions, is used to generate a system of n equations with n unknowns (1.1), which is solved to obtain the FIT problem solution.

A matrix structure The matrix A in linear systems of equations (1.1) that arise from FD, FE, and FIT approaches have the same properties (and, in fact, may be identical for certain geometries). They are very sparse, with each row of the matrix relating each node or edge only to its immediate neighbors. Further, the off diagonal entries a_{ij}, $i \neq j$ on each row typically satisfy $|a_{ii}| > |a_{ij}|$, $i \neq j$; that is, the magnitude of the diagonal entries is larger than that of the off-diagonal entries on the same row. We call this property *diagonally strong*; this is a weaker condition than diagonal dominance, but is a useful property for some iterative solution methods for equation (1.1). The matrices usually exhibit a banded nature, and, for comparable problems, there are more unknowns than for the integral equations solutions since the differential equation techniques require discretization of the space surrounding the object of interest.

A key observation in open-region problems is that, since some kind of mesh-truncation scheme is required for solution by differential equation methods, these truncation techniques often destroy some desirable characteristic of the matrix A in equation (1.1). For example, boundary integral methods destroy sparsity, absorbing boundary conditions (ABC) and perfectly matched layer (PML) techniques require a large number of unknowns since, for good results, the truncated boundary must be removed far from the scatterer. Our experience with the measured equation of invariance (MEI) technique applied to arbitrarily shaped three-dimensional objects indicates that it also destroys properties of the matrix A such that solution by iterative methods becomes much more difficult.

2.2 Integral Equation Methods

In the integral equation solution approach, we derive integral or integro-differential equations which describe the problem. The most popular IE method is the method of moments (MoM) introduced by Harrington in 1967 [8].

In the method of moments, unlike in the DE techniques, only the body of the object in question is discretized. For a perfectly electrically conducting, or homogeneous penetrable, scatterer, only the surface is discretized, usually into rectangular or triangular patches [9,10]. An inhomogeneous penetrable body requires the discretization of its volume into rectangular prisms or tetrahedrons [11]. The currents, either actual or an equivalent, are expressed over the discretized region as a linear combination of subdomain basis, or expansion, functions such as pulse or triangular functions. For example, the currents on an arbitrarily-shaped PEC scatterer whose surface is discretized into triangular patches may be expressed as $\boldsymbol{J}(\boldsymbol{r}) = \sum_{i=1}^{n} x_i \boldsymbol{f}_i(\boldsymbol{r})$ where n is the number of edges of the discretization of the surface that are bordered by two surface triangles, x_i is the weight of each basis function, and $\boldsymbol{f}_i(\boldsymbol{r})$ is the basis function at edge i given by

$$\boldsymbol{f}_i(\boldsymbol{r}) = \begin{cases} \frac{l_i}{2A_{i+}}\boldsymbol{\rho}_{i+}, & \boldsymbol{r} \in T_{i+} \\ -\frac{l_i}{2A_{i-}}\boldsymbol{\rho}_{i-}, & \boldsymbol{r} \in T_{i-} \\ 0, & \text{otherwise} \end{cases}$$

where l_i is the length of edge i, T_{i+} and T_{i-} are the two triangles bordering edge i, A_{i+} and A_{i-} are the areas of the two triangles and $\boldsymbol{\rho}_{i+}$ and $\boldsymbol{\rho}_{i-}$ are vectors pointing from the vertex of each triangle opposite edge i to the point $\boldsymbol{r}$ [12]. The unknowns are x_i, the magnitude of the current crossing each edge. We thus require a method of constructing an $n \times n$ impedance matrix A and a right-hand-side data vector b in (1.1). We may then use a linear system solver to solve for the unknown vector x.

The method of moments (MoM) expresses the problem to be solved in the form

$$L(f) = g \tag{2.4}$$

where L represents an integro-differential operator applied to function f, and g is a forcing function. It is required to define an inner product $< f, g >$ and choose a set of testing functions, $w_i, i = 1 \ldots n$. If the expansion functions are subdomain functions, then typically the testing functions are also subdomain

functions, and may be identical to the basis functions. Note that a set of entire domain basis and/or testing functions may be applied in MoM. However, when solving three-dimensional problems, defining such functions becomes difficult.

We substitute the linear combination of expansion functions into equation (2.4) and

$$\sum_{i=1}^{n} x_i L(\boldsymbol{f}_i) = g \tag{2.5}$$

results. We take the inner product of both sides of equation (2.5) with each weighting function w_l, generating n equations of the form $\sum_{i=1}^{n} x_i < w_l, L(\boldsymbol{f}_i) > = < w_l, g >$. It follows that the entries of the matrix A and data vector b satisfy $a_{li} = < w_l, L\boldsymbol{f}_i >$, and $b_l = < w_l, g >$, $1 \leq l, i \leq n$.

For our example, we derive an integro-differential equation to find the operator L by enforcing the boundary condition $\hat{n} \times (\boldsymbol{E}_i + \boldsymbol{E}_s) = 0$ on the surface of the scatterer, resulting in

$$(-j\omega \boldsymbol{A} - \nabla\Phi)_{tan} = -\boldsymbol{E}_{i,tan}$$

where

$$\boldsymbol{A}(\boldsymbol{r}) = \frac{\mu}{4\pi} \int_S \boldsymbol{J} \frac{e^{-jkR}}{R} dS \quad \text{and} \quad \Phi(\boldsymbol{r}) = \frac{1}{4\pi\epsilon} \int_S \sigma \frac{e^{-jkR}}{R} dS \tag{2.6}$$

and σ may be determined from

$$\nabla \cdot \boldsymbol{J} = -j\omega\sigma \tag{2.7}$$

where S is the surface of the scatterer and R is the distance from the point of integration to the observation point $\boldsymbol{r}$ [10].

When the testing is applied, we obtain $a_{li} = < w_l, \boldsymbol{A}_i > + < w_l, \nabla\Phi_i >$ and $b_l = < w_l, \boldsymbol{E}_i >$ where $\boldsymbol{A}_i$ and Φ_i are determined from equations (2.6) and (2.7) by substituting the basis function $\boldsymbol{f}_i$ for $\boldsymbol{J}$.

In the method of moments, one may view the resulting matrix equation as relating the current at every basis function to the currents due to every other basis function. Although a comparable problem solved by method of moments typically would have fewer unknowns than a differential equation solution, one of the main disadvantages of the technique is that it results in a full matrix.

The system matrix from MoM has other properties that may be exploited. For one, most MoM formulations result in a matrix that is diagonally strong (see the previous subsection). This generally results in a numerically stable solution x to equation (1.1). If the testing functions are selected to be identical to the expansion functions ($w_i = \mathbf{f}_i$), the the resulting complex matrix A in equation (1.1) will be symmetric (but not hermitian). Under some very simple special cases, other matrix properties may result, such as being Toeplitz. However, these typically are not evident in most problems of a practical nature.

3 Numerical Solution Techniques

Numerical methods for the solution of linear systems of equations (1.1) that arise in EM problems continue to be an active area of research. Solution methods for both classes of problems may be loosely classified as (1) *Direct methods*, e.g., the LU decomposition, where the inverse operator of the matrix A is applied (to within machine precision) to the data vector b in order to obtain the solution x of equation (1.1), (2) *General iterative* methods, e.g., Gauss-Seidel iteration [13], GMRES [14], QMR [15], or (bi-)conjugate gradients [16], [17], [18], which require no knowledge of the spectrum (eigenvalues) of the matrix A, or (3) *Spectral iterative* methods, such as alternating direction implicit iteration (ADI) [19], [20], or successive over-relaxation techniques, which require some knowledge of the spectrum of A or of its diagonal dominance, if any. All of these numerical methods can be aided by appropriate preconditioning of the original problem. Useful references for additional reading are [13] (an essential reference for anyone doing numerical computations), [21], and [22].

3.1 Issues in numerical solution of linear systems of equations

The primary issues of import in the numerical solution of equation (1.1) are those of *problem condition*, solution accuracy, or *algorithm condition*, *algorithm reliability*, and *computational cost*. We discuss each of these below.

Problem condition refers to the change Δx induced in the solution x of equation (1.1) by small changes ΔA and Δb made in the original problem, i.e., $(A + \Delta A)(x + \Delta x) = (b + \Delta b)$, where $\|\Delta A\| \ll \|A\|$ and $\|\Delta b\| \ll \|b\|$. If small perturbations ΔA and Δb yield relatively large changes Δx in the perturbed solution vector, then the problem (1.1) is called *ill-conditioned*. Ill-conditioned problems are inherently difficult to solve accurately on a digital computer. The condition of a numerical problem is quantitatively measured by the condition number $\kappa(A) = \|A\| / \|A^{-1}\|$ of the coefficient matrix A; a large condition number relative to machine precision indicates that inaccurate results may be expected from any numerical solution procedures.

Algorithm condition refers to the error Δx induced by a computational procedure that is used to solve equation (1.1). Algorithm condition is bounded below by the problem condition; a poorly designed algorithm (e.g., Gaussian elimination without partial pivoting) may have an algorithm condition that is arbitrarily worse than the problem condition of equation (1.1). $x(\epsilon)$ to the desired nominal problem. That is, Gaussian elimination

Algorithm reliability refers to the ability of an algorithm to detect ill-conditioned problems or potentially inaccurate solutions. A condition estimator such as that proposed in [23] provides a convenient heuristic to improve the reliability of an LU-decomposition based solver, although it can greatly underestimate the condition number of a matrix [24].

The *computational cost* of an algorithm refers the the required computational resources, typically measured in terms of storage requirements or floating-point operations (flops). A well designed iterative sparse matrix solver may require relatively little storage and relatively few (say, $O(n)$) flops per iteration by taking advantage of available structure in the matrix A. Conversely, by ignoring matrix structure, an otherwise useful dense matrix solution algorithm will require $O(n^2)$ storage and $O(n^3)$ flops for solution of equation (1.1). Since the dimension n of a typical EM problem is roughly of the magnitude of 10^3–10^4, it is clearly in the best interest of the investigator to carefully exploit what structure is available in a given problem.

3.2 Direct methods

Direct methods (LU decomposition, QR decomposition) are typically applied in cases where the coefficient matrix A is large and dense, since these techniques typically do not respect sparsity or other available structure. Most methods make use of the LU decomposition, since this allows the algorithm to make use of banded structure that may be available in a given problem. Due to the high dimension n of problems (1.1) involved in EM, multiprocessor (parallel) supercomputers may be used. An early survey of parallel solution methods is in [25]; see also [26], [27], [28]. The architecture of the machine used (SIMD vs. MIMD, global memory vs. local memory) have a profound impact on the efficacy of a given algorithm choice. Numerical software packages such as LAPACK [29], the successor to LINPACK and EISPACK, have been optimized for some specific architectures and are available on many supercomputers.

3.3 General iterative methods

When the matrix A in equation (1.1) is sparse, computational costs render the application of a direct solver impractical. *Iterative* solution procedures compute a sequence of solutions $x_0, x_1, \ldots$ that, in the absence of round-off, converge to the exact solution x of equation (1.1). Iterative solution methods are typically based on either a recurrence, e.g., conjugate gradients (CG) [17], generalized conjugate gradients [16], or biconjugate gradients (BCG) [18], or on projection of the problem (1.1) into a reduced dimensional subspace, e.g., GMRES [14] or QMR [15]. A common factor in each of these methods is that they only require that it is possible to efficiently form the matrix-vector product $y = Av$ for arbitrary vectors $v \in \mathbb{C}^n$. In particular, these methods do *not* require knowledge of the spectrum (eigenvalues) of the matrix A.

The CG method [17] is an effective method for the solution of equation (1.1) when the matrix A is hermitian positive definite. In the absence of numerical roundoff, the CG method is known to converge to the solution x of equation (1.1) in at most n iterations. If A is not hermitian, one may premultiply equation (1.1) by the complex conjugate transpose A^H of the matrix A to obtain the *normal equations* $A^H Ax = A^H b$,

that may then be solved by the CG method. Such an approach is inadvisable: (1) due to numerical roundoff, convergence to the solution x of equation (1.1) rarely occurs within n iterations. Second, the two-norm induced condition $\kappa_2(A^H A) = \kappa_2(A)^2$, and so solution via the normal equations is inherently numerically less stable than solution via equation (1.1). Thus, the CG method has typically come to be regarded as an *iterative* method.

3.4 Spectral iterative methods

Spectral iterative methods, like general iterative methods, compute a sequence of solutions $x_0, x_1, ...$ that converge to the desired solution x of equation (1.1). However, spectral iterative methods require some knowledge of the eigenvalues of the matrix A or of the splitting $A = M + N$ used in the spectral method. A survey of spectral iterative methods is in [21], [22].

The principles of spectral iterative methods may be illustrated in the Jacobi method (or the related Gauss-Seidel method). Given a splitting $A = M + N$ we may write $Mx = -Nx + b$, which naturally suggests the recursion

$$Mx_{k+1} = -Nx_k + b \tag{3.1}$$

that forms the basis of the Gauss-Seidel iteration. The sequence x_k generated by equation (3.1) converges to the solution x of (1.1) if and only if the eigenvalues $\lambda 1, ..., \lambda_n$ of the matrix $M^{-1}N$ lie inside the unit circle; the speed of convergence is limited by the spectral radius $\rho(M^{-1}N) = \max_i |\lambda_i|$. The Successive Over Relaxation (SOR) method employs a free parameter ω in a modified splitting $M_\omega = D + \omega L$, $N_\omega = (\omega - 1)D + \omega U$ such that the spectral radius $\rho({M_\omega}^{-1}N_\omega) < \rho(M^{-1}N)$. The alternating direction implicit (ADI) iteration [19], [20], [30] requires a splitting $A = M + N$ such that $MN = NM$ (M and N commute) and that the eigenvalues of the matrix A be in a known region in the closed left half of the complex plane. In this case, a sequence of parameters $\rho_1, ..., \rho_k$ are computed to provide a solution x_k that is within an *a priori* known bound from the exact solution x of (1.1).

Other recurrences are discussed in [31].

3.5 Preconditioning

The numerical performance of linear system solvers may be greatly improved by *preconditioning*. Numerical preconditioning takes two forms: (1) *balancing*, or scaling, in which a diagonal transformation is applied to equation (1.1) in order to improve problem condition without introducing further roundoff error, and (2) preconditioning for iterative methods, which is used to accelerate convergence of iterative algorithms.

Balancing When the condition number $\kappa(A)$ of the matrix A in equation (1.1) is large, then it is often useful to perform some form of scaling of equation (1.1) in order to compute an equivalent problem $\hat{A}\hat{x} = \hat{b}$ in which $\kappa(\hat{A}) < \kappa(A)$ and from which the solution x to equation (1.1) may be readily obtained from the vector $\hat{x}$. For example, Parlett and Reinsch [32] present an algorithm that computes a diagonal similarity transform D to obtain $\hat{A}x = \hat{b}$ where $\hat{A} = D^{-1}AD$, $\hat{b} = D^{-1}b$ and D is selected to minimize the dynamic range of the nonzero entries of the matrix A. Curtis and Reid [33] present a similar algorithm that selects two matrices D_1, D_2 that are used to obtain $\tilde{A}\tilde{x} = \tilde{b}$ where $\tilde{A} = D_1 A D_2$, $\tilde{b} = D_1 b$. In this case, the solution x of equation (1.1) is obtained as $x = {D_2}^{-1}\tilde{x}$. Numerical balancing is appropriate only when the nonzero entries a_{ij} of the matrix A are known to roughly the same relative accuracy, regardless of their magnitudes.

Algorithm preconditioners All iterative methods can benefit from *algorithm preconditioning*. Algorithm preconditioning differs from the problem scaling discussed above §3.5 in that algorithm preconditioning is applied for the purpose of reducing the number of iterations required in order to obtain a prescribed degree of accuracy in the compute solution x. Most preconditioning techniques involve a *splitting* of the matrix $A = M + N$ where the matrix M is "easy" to invert and the pair M and N yield some desirable properties for the given algorithm, e.g., computational cost relative to a direct solver, in addition to accelerating the convergence of the underlying iterative method.

4 Conclusions

We have presented a brief survey of applications of numerical linear algebra in the solution of problems in electromagnetics (EM). A number of methods are available to reduce the *infinite-dimensional* EM problems into *finite dimensional* linear systems of equations (1.1). Care must be exercised to recognize the structure and properties of these linear systems of equations prior to selecting a solution procedure for numerical computation of the solution vector x.

References

[1] G. K. Gothard, D. A. Vechinski, and S. M. Rao, "Computational methods in transient electromagnetics: A selective survey," *IEEE Computational Science and Engineering*, pp. 50–59, 1994.

[2] A. Thom and C. J. Apelt, *Field Computations in Engineering and Physics.* London: D. Van Nostrand, 1961.

[3] G. H. Golub and J. M. Ortega, *Scientific Computing and Differential Equations: An Introduction to Numerical Analysis.* Academic Press, 1992.

[4] R. Courant, "Variational methods for the solution of problems of equilibrium and vibrations," *Bull. Am. Math. Soc.*, vol. 49, pp. 1–23, 1943.

[5] G. Strang and G. J. Fix, *An Analysis of the Finite Element Method.* Englewood Cliffs, NJ: Prentice Hall, 1973.

[6] U. van Rienen and T. Weiland, "Triangular discretization method for the evaluation of rf-fields in cylindrically symmetric cavities," *IEEE Transactions on Magnetics*, vol. 21, pp. 2317–2320, 1985.

[7] J. E. Lebaric and D. Kajfez, "Analysis of dielectric resonator cavities using the finite integration technique," *IEEE Transactions on Microwave Theory and Techniques*, vol. 37, pp. 1740—1748, November 1989.

[8] R. F. Harrington, "Matrix methods for field problems," *Proceedings of the IEEE*, vol. 55, pp. 136–149, February 1967.

[9] S. M. Rao, A. W. Glisson, D. R. Wilton, and B. S. Vidula, "A simple numerical solution procedure for statics problems involving arbitrarily-shaped surfaces," *IEEE Transactions on Antennas and Propagation*, vol. AP-27, pp. 604–607, September 1979.

[10] S. M. Rao, D. R. Wilton, and A. W. Glisson, "Electromagnetic scattering by surfaces of arbitrary shape," *IEEE Transactions on Antennas and Propagation*, vol. AP-30, pp. 409–418, May 1982.

[11] D. H. Schaubert, D. R. Wilton, and A. W. Glisson, "A tetrahedral modeling method for electromagnetic scattering by arbitrarily shaped inhomogeneous dielectric bodies," *IEEE Transactions on Antennas and Propagation*, vol. AP-32, no. 1, pp. 77–85, 1984.

[12] A. W. Glisson, *On the Development of Numerical Techniques for Treating Arbitrarily-shaped Surfaces.* PhD thesis, University of Mississippi, 1978.

[13] G. H. Golub and C. Van Loan, *Matrix Computations.* Baltimore, MD: Johns Hopkins University Press, 2nd ed., 1989.

[14] Y. Saad and M. H. Schultz, "GMRES: A generalized minimal residual algorithm for solving nonsymmetric linear systems," *SIAM J. Sci. Stat. Comput.*, vol. 7, pp. 856–869, July 1986.

[15] R. W. Freund and N. M. Nachtigal, "QMR: A quasi-minimal residual method for non-hermitian linear systems," *Numer. Math.*, vol. 60, pp. 315–339, 1991.

[16] P. Concus, G. H. Golub, and D. P. O'Leary, "A generalized conjugate gradient method for the numerical solution of elliptic partial differential equations," in *Sparse Matrix Computations* (J. R. Bunch and D. J. Rose, eds.), pp. 309–332, Academic Press, 1976.

[17] M. R. Hestenes and E. Stiefel, "Methods of conjugate gradients for solving linear systems," *Journal of Research fo the National Bureau of Standards*, vol. 49, no. 6, pp. 409–436, 1952.

[18] C. Lanczos, "Solution of systems of linear equations by minimized iterations," *J. Res. Nat. Bur. Standards*, vol. 49, pp. 33–53, 1952.

[19] E. L. Wachspress, *Iterative Solution of Elliptic Systems.* Prentice Hall, 1966.

[20] N. S. Elsner and E. L. Wachspress, "Alternating direction implicit iteration for systems with complex spectra," *SIAM J. Numerical Anal.*, vol. 28, pp. 859–870, June 1991.

[21] R. Beauwens and P. de Groen, eds., *Iterative Methods In Linear Algebra*, (Brussels, Belgium), International Association for Mathematics and Computers in Simulation, North-Holland, 1991.

[22] R. W. Freund, G. H. Golub, and N. M. Nactigal, "Iterative solution of linear systems," *Acta Numerica*, pp. 57–100, 1991.

[23] A. K. Cline, C. B. Moler, G. W. Stewart, and J. H. Wilkinson, "An estimate for the condition number of a matrix," *SIAM J. Numer. Anal*, vol. 16, pp. 368–375, April 1979.

[24] D. P. O'Leary, "Estimating matrix condition numbers," *SIAM J. Sci. Stat. Comput.*, vol. 1, pp. 205–209, June 1980.

[25] D. Heller, "A survey of parallel algorithms in numerical linear algebra," *SIAM Review*, vol. 20, pp. 740–777, October 1978.

[26] G. A. Geist and M. T. Heath, "Matrix factorization on a hypercube multiprocessor," in *Hypercube Multiprocessors 1986, Proceedings of the First Conference on Hypercube Multiprocessors*, (Knoxville, TN), pp. 161–180, SIAM, August 26-27, 1985.

[27] A. George, M. T. Heath, J. Liu, and E. Ng, "Sparse Cholesky factorization on a local-memory multiprocessor," *SIAM J. Sci. Stat. Computer*, vol. 9, pp. 327–340, March 1988.

[28] M. T. Heath and C. H. Romine, "Parallel solution of triangular systems on distributed memory multiprocessors," *SIAM J. Sci. Stat. Comput.*, vol. 9, pp. 558–588, May 1988.

[29] E. Anderson, Z. Bai, C. Bischof, J. Demmel, J. Dongarra, J. D. Croz, A. Greenbaum, S. Hammarling, A. McKenney, S. Ostrouchov, and D. Sorenson, *LAPACK User's Guide, 2nd ed.* SIAM, 1995.

[30] N. Levenberg and L. Reichel, "A generalized ADI iterative method," *Numer. Math.*, vol. 66, pp. 215–223, 1993.

[31] D. R. Kincaid and D. M. Young, "Stationary second-degree iterative methods and recurrences," in *Iterative Methods in Linear Algebra* (R. Beauwens and P. de Groen, eds.), (Brussels, Belgium), International Association for Mathematics and Computers in Simulation, North-Holland, 1991.

[32] B. N. Parlett and C. Reinsch, "Balancing a matrix for calculation of eigenvalues and eigenvectors," *Numer. Math.*, vol. 13, pp. 293–304, 1969.

[33] A. R. Curtis and J. K. Reid, "On the automatic scaling of matrices for Gaussian elimination," *J. Inst. Maths. Applics.*, vol. 10, pp. 118–124, 1972.

MULTILEVEL PRECONDITIONING FOR THE TIME-HARMONIC MAXWELL EQUATIONS

GERHARD STARKE,

INSTITUT FÜR PRAKTISCHE MATHEMATIK, UNIVERSITÄT KARLSRUHE,
76128 KARLSRUHE, GERMANY. STARKE@MATH.UNI-KARLSRUHE.DE

Abstract. The numerical approximation of the solution of the time-harmonic Maxwell equations by a least-squares finite element discretization is discussed in this paper. Our emphasis lies in the efficient solution of the system of linear algebraic equations arising from the discretization. Additive multilevel preconditioning is analyzed theoretically and by computational experiments for a simple two-dimensional model problem.

1. Introduction. The Maxwell equations for a time-harmonic electromagnetic field

$$\mathcal{E}(\mathbf{x},t) = e^{-i\omega t}\mathbf{E}(\mathbf{x})\,,\ \mathcal{H}(\mathbf{x},t) = e^{-i\omega t}\mathbf{H}(\mathbf{x})$$

in a domain $\Omega \subset \mathbb{R}^3$ are given by

$$\begin{aligned}(-i\omega\varepsilon + \sigma)\mathbf{E} - \nabla\times\mathbf{H} &= \mathbf{J}\,,\\ -i\omega\mu\mathbf{H} + \nabla\times\mathbf{E} &= \mathbf{0}\,.\end{aligned} \tag{1.1}$$

Here ε denotes the dielectric constant, μ the permeability, and σ the electric conductivity. With appropriate boundary conditions and under certain assumptions on ε, μ and σ, the corresponding boundary value problem has a unique solution (cf. e.g. [7] or [4, Section 6]). In this paper, we assume that Ω is a bounded polygonal domain and perfectly conducting boundary conditions, $\mathbf{n}\times\mathbf{E} = \mathbf{0}$ on $\partial\Omega$.

One approach to the numerical solution of this problem is to substitute the first equation into the second, leading to the second-order equation

$$\nabla\times(\mu^{-1}\nabla\times\mathbf{E}) - (\omega^2\varepsilon + i\omega\sigma)\mathbf{E} = -i\omega\mathbf{J} \tag{1.2}$$

for the electric field $\mathbf{E}$. The finite element approximation of this formulation is described in [10]. If one is interested in the approximation of the magnetic field $\mathbf{H}$ as well, mixed finite element approaches are appropriate (cf. [9]). An alternative approach which is particularly easy to implement and analyze consists in the first-order system least-squares strategy which was studied for second-order elliptic equations in [2], [3]. Since the Maxwell equations constitute a first-order system, it is natural to use the least-squares approach here. Closely related is the approach taken in [6] where the Helmholtz equation is rewritten as a first-order system, and the least-squares finite element method is applied.

Our primary aim in this paper is to show that additive multilevel preconditioning is feasible for the least-squares formulation of Maxwell's equations. This will be explained theoretically in the following three sections and illustrated by computational experiments in Section 5.

2. The Least-Squares Functional. In the sequel, we will need the space

$$\mathbf{V}_0 = \{\mathbf{v} \in H(\mathbf{curl};\Omega) : \mathbf{n} \times \mathbf{v} = \mathbf{0} \text{ on } \partial\Omega\}$$

(see [5, Theorem 2.11] for a proper definition of the trace operator associated with these boundary values). A solution of (1.1) subject to perfectly conducting boundary conditions obviously minimizes the least-squares functional

$$G_0(\mathbf{E},\mathbf{H};\mathbf{J}) = \|(-i\omega\varepsilon+\sigma)\mathbf{E} - \nabla\times\mathbf{H} - \mathbf{J}\|^2_{0,\Omega} + \|-i\omega\mu\mathbf{H} + \nabla\times\mathbf{E}\|^2_{0,\Omega} \tag{2.1}$$

among all $(\mathbf{E},\mathbf{H}) \in \mathbf{V}_0 \times H(\mathbf{curl};\Omega)$. Vice versa, a unique solution of (1.1) is also characterized by the unique minimum of (2.1). By applying the divergence operator to (1.1), we obtain (using the fact that $\nabla\cdot(\nabla\times\mathbf{v}) = 0$)

$$\nabla\cdot((-i\omega\varepsilon+\sigma)\mathbf{E}) = \nabla\cdot\mathbf{J} \text{ and } \nabla\cdot\mathbf{H} = 0$$

(assuming that $\mathbf{J} \in H(\mathrm{div};\Omega)$). Since these two equations are also satisfied by the solution of (1.1), we may use them to augment the least-squares functional (2.1). From here on, for notational convenience, we assume that $\sigma \equiv 0$ in Ω. Note that this is usually the most difficult case since (1.1) may be singular for certain values of ω (the interior Maxwell eigenvalues; cf. [7], [10]). The augmented least-squares functional is given by

$$\begin{aligned} G(\mathbf{E},\mathbf{H};\mathbf{J}) &= \|-i\omega\varepsilon\mathbf{E} - \nabla\times\mathbf{H} - \mathbf{J}\|^2_{0,\Omega} + \|-i\omega\mu\mathbf{H} + \nabla\times\mathbf{E}\|^2_{0,\Omega} \\ &+ \|\nabla\cdot(\varepsilon\mathbf{E})\|^2_{0,\Omega} + \|\nabla\cdot(\mu\mathbf{H})\|^2_{0,\Omega}\,. \end{aligned} \tag{2.2}$$

Clearly, this augmented least-squares functional requires in addition to $\mathbf{E},\mathbf{H} \in H(\mathbf{curl};\Omega)$ that $\varepsilon\mathbf{E}, \mu\mathbf{H} \subset H(\mathrm{div};\Omega)$. Moreover, the boundary conditions $\mathbf{n}\times\mathbf{E} = 0$ together with the first equation in (1.1) implies $\mathbf{n}\cdot\mathbf{H} = 0$ on $\partial\Omega$ which we might impose as boundary conditions for $\mathbf{H}$.

For the purpose of exposition, let us further simplify the problem and set $\varepsilon = \mu \equiv 1$. The least-squares functional is then given by

$$\begin{aligned} G(\mathbf{E},\mathbf{H};\mathbf{J}) &= \|-i\omega\mathbf{E} - \nabla\times\mathbf{H} - \mathbf{J}\|^2_{0,\Omega} + \|-i\omega\mathbf{H} + \nabla\times\mathbf{E}\|^2_{0,\Omega} \\ &+ \|\nabla\cdot\mathbf{E}\|^2_{0,\Omega} + \|\nabla\cdot\mathbf{H}\|^2_{0,\Omega}\,. \end{aligned}$$

Adopting the notation from [5, Chapter I], we define the spaces

$$\mathbf{V} = (H(\mathrm{div};\Omega)\cap H_0(\mathbf{curl};\Omega))\,,\mathbf{W} = (H_0(\mathrm{div};\Omega)\cap H(\mathbf{curl};\Omega))\,.$$

and seek to find $(\mathbf{E},\mathbf{H}) \in \mathbf{V}\times\mathbf{W}$ such that

$$G(\mathbf{E},\mathbf{H};\mathbf{J}) = \min_{(\hat{\mathbf{E}},\hat{\mathbf{H}})\in\mathbf{V}\times\mathbf{W}} G(\hat{\mathbf{E}},\hat{\mathbf{H}};\mathbf{J}) \tag{2.3}$$

holds. With the associated bilinear form

$$\begin{aligned} &\mathcal{F}(\mathbf{E},\mathbf{H};\hat{\mathbf{E}},\hat{\mathbf{H}}) \\ &= (-i\omega\mathbf{E} - \nabla\times\mathbf{H}, -i\omega\hat{\mathbf{E}} - \nabla\times\hat{\mathbf{H}})_{0,\Omega} + (-i\omega\mathbf{H} + \nabla\times\mathbf{E}, -i\omega\hat{\mathbf{H}} + \nabla\times\hat{\mathbf{E}})_{0,\Omega} \\ &+ (\nabla\cdot\mathbf{E},\nabla\cdot\hat{\mathbf{E}})_{0,\Omega} + (\nabla\cdot\mathbf{H},\nabla\cdot\hat{\mathbf{H}})_{0,\Omega} \end{aligned} \tag{2.4}$$

(note that the complex $L^2(\Omega)$ inner product has to be used here), the minimization problem (2.3) is equivalent to the variational problem

$$\mathcal{F}(\mathbf{E},\mathbf{H};\hat{\mathbf{E}},\hat{\mathbf{H}}) = (\mathbf{J}, -i\omega\hat{\mathbf{E}} - \nabla\times\hat{\mathbf{H}})_{0,\Omega} \text{ for all } (\hat{\mathbf{E}},\hat{\mathbf{H}}) \in \mathbf{V}\times\mathbf{W}\,. \tag{2.5}$$

Under certain assumptions on Ω (cf. [5, Section 3.4]), the above spaces are continuously embedded in $(H^1(\Omega))^3$ and we may pose the minimization problem in $(H^1(\Omega))^3 \times (H^1(\Omega))^3$ (with suitable boundary conditions) instead.

In order to obtain straightforward finite element approximation and multilevel convergence results, boundedness and ellipticity of the bilinear form (2.4) with respect to the $H^1(\Omega)$-norm in all variables is desirable. Unfortunately, this is not possible to achieve here. In fact, the ellipticity of the least-squares bilinear form would be very surprising since the bilinear form associated with (1.2) may become indefinite, in general. This indefiniteness is due to the nature of the problem which couples the achievable finite element approximation with the wave number ω. After all, the singular nature of the problem if ω is one of the interior Maxwell eigenvalues has to show up somewhere in this formulation. The variational formulation via the least-squares approach avoids the problems caused by indefiniteness (for instance, the conjugate gradient method can be used safely) but it certainly does not (and cannot) avoid the problems caused by loss of ellipticity. Similarly to the situation for indefinite problems like (1.2), a weaker form of ellipticity, a so-called Gårding's inequality, holds and ensures finite element approximation results for sufficiently fine triangulations depending on ω.

For what is to follow, it is convenient to introduce the norm $\|\cdot\|_{\omega;1,\Omega}$ defined by

$$\|\mathbf{v}\|_{\omega;1,\Omega} = \left(|\mathbf{v}|^2_{1,\Omega} + \omega^2\|\mathbf{v}\|^2_{0,\Omega}\right)^{1/2} \text{ for } \mathbf{v}\in(H^1(\Omega))^3\,. \tag{2.6}$$

where $|\cdot|_{1,\Omega}$ denotes the standard $(H^1(\Omega))^3$-seminorm. Note first that the boundedness of the least-squares bilinear form (2.4) with respect to the norm (2.6), i.e.,

$$\mathcal{F}(\mathbf{E},\mathbf{H};\hat{\mathbf{E}},\hat{\mathbf{H}}) \le \gamma_1 \left(\|\mathbf{E}\|^2_{\omega;1,\Omega} + \|\mathbf{H}\|^2_{\omega;1,\Omega}\right)^{1/2} \left(\|\hat{\mathbf{E}}\|^2_{\omega;1,\Omega} + \|\hat{\mathbf{H}}\|^2_{\omega;1,\Omega}\right)^{1/2} \tag{2.7}$$

(with γ_1 not depending on ω) follows easily from

$$\mathcal{F}(\mathbf{E},\mathbf{H};\hat{\mathbf{E}},\hat{\mathbf{H}}) \le (\mathcal{F}(\mathbf{E},\mathbf{H};\mathbf{E},\mathbf{H})^{1/2} (\mathcal{F}(\hat{\mathbf{E}},\hat{\mathbf{H}};\hat{\mathbf{E}},\hat{\mathbf{H}})^{1/2}$$

and

$$\begin{aligned}&\mathcal{F}(\mathbf{E},\mathbf{H};\mathbf{E},\mathbf{H})\\ &= \|-i\omega\mathbf{E} - \nabla\times\mathbf{H}\|^2_{0,\Omega} + \|-i\omega\mathbf{H} + \nabla\times\mathbf{E}\|^2_{0,\Omega} + \|\nabla\cdot\mathbf{E}\|^2_{0,\Omega} + \|\nabla\cdot\mathbf{H}\|^2_{0,\Omega}\\ &\le 2\left(|\mathbf{E}|^2_{1,\Omega} + |\mathbf{H}|^2_{1,\Omega} + \omega^2\|\mathbf{E}\|^2_{0,\Omega} + \omega^2\|\mathbf{H}\|^2_{0,\Omega}\right)\,.\end{aligned}$$

The Gårding-type inequality

$$\begin{aligned}&\mathcal{F}(\mathbf{E},\mathbf{H};\mathbf{E},\mathbf{H})\\ &\ge \gamma_2\left(\|\mathbf{E}\|^2_{\omega;1,\Omega} + \|\mathbf{H}\|^2_{\omega;1,\Omega}\right) - \gamma_3\omega^2\left(\|\mathbf{E}\|^2_{0,\Omega} + \|\mathbf{H}\|^2_{0,\Omega}\right)\end{aligned} \tag{2.8}$$

(with γ_2, γ_3 not depending on ω) follows from

$$\begin{aligned}&\mathcal{F}(\mathbf{E},\mathbf{H};\mathbf{E},\mathbf{H})\\ &\geq \|\nabla\times\mathbf{E}\|^2_{0,\Omega}+\|\nabla\cdot\mathbf{E}\|^2_{0,\Omega}+\omega^2\|\mathbf{E}\|^2_{0,\Omega}+\|\nabla\times\mathbf{H}\|^2_{0,\Omega}+\|\nabla\cdot\mathbf{H}\|^2_{0,\Omega}+\omega^2\|\mathbf{H}\|^2_{0,\Omega}\\ &-2\omega\left(\|\mathbf{E}\|_{0,\Omega}\|\nabla\times\mathbf{H}\|_{0,\Omega}+\|\mathbf{H}\|_{0,\Omega}\|\nabla\times\mathbf{E}\|_{0,\Omega}\right)\end{aligned}$$

using

$$\begin{aligned}2\omega\|\mathbf{E}\|_{0,\Omega}\|\nabla\times\mathbf{H}\|_{0,\Omega}&\leq\|\nabla\times\mathbf{H}\|^2_{0,\Omega}+\omega^2\|\mathbf{E}\|^2_{0,\Omega}\,,\\ 2\omega\|\mathbf{H}\|_{0,\Omega}\|\nabla\times\mathbf{E}\|_{0,\Omega}&\leq\|\nabla\times\mathbf{E}\|^2_{0,\Omega}+\omega^2\|\mathbf{H}\|^2_{0,\Omega}\end{aligned}$$

and the continuous imbedding of $\mathbf{V}$ and $\mathbf{W}$ in $H^1(\Omega)^3$.

3. Finite Element Approximation. For the numerical approximation of the solution of the Maxwell equations (1.1) by the least-squares finite element method, we choose appropriate finite-dimensional subspaces $\mathbf{V}^h \subset \mathbf{V}$ and $\mathbf{W}^h \subset \mathbf{W}$. The minimization problem (2.3) is then solved in these subspaces, i.e., $(\mathbf{E}^h, \mathbf{H}^h) \in \mathbf{V}^h \times \mathbf{W}^h$ are constructed such that

$$G(\mathbf{E}^h,\mathbf{H}^h;\mathbf{J}) = \min_{(\hat{\mathbf{E}}^h,\hat{\mathbf{H}}^h)\in\mathbf{V}^h\times\mathbf{W}^h} G(\hat{\mathbf{E}}^h,\hat{\mathbf{H}}^h;\mathbf{J}) \tag{3.1}$$

holds. With the associated bilinear form (2.4) this is equivalent to solving the variational problem of finding $(\mathbf{E}^h, \mathbf{H}^h) \in \mathbf{V}^h \times \mathbf{W}^h$ such that

$$\mathcal{F}(\mathbf{E}^h,\mathbf{H}^h;\hat{\mathbf{E}}^h,\hat{\mathbf{H}}^h) = (\mathbf{J}, -i\omega\hat{\mathbf{E}}^h - \nabla\times\hat{\mathbf{H}}^h)_{0,\Omega} \text{ for all } (\hat{\mathbf{E}},\hat{\mathbf{H}}) \in \mathbf{V}^h\times\mathbf{W}^h\,. \tag{3.2}$$

Note that, under the assumptions on Ω from [5, Section 3.4] which led us to the definition of the bilinear form in $(H^1(\Omega))^3 \times (H^1(\Omega))^3$, we are free to use standard continuous linear or bilinear finite elements with the appropriate boundary conditions.

Finite element approximation results for this least-squares approach follow along similar lines as for weakly indefinite (Helmholtz-type) problems using an observation by Schatz [11] (see also Yserentant [13]). Let $\{\mathcal{T}^h\}$ be a quasi-uniform family of triangulations of Ω, and let $\mathbf{V}^h, \mathbf{W}^h$ be corresponding finite element spaces. Denoting by $(\mathbf{E},\mathbf{H}) \in \mathbf{V}\times\mathbf{W}$ the minimum of (2.1) (which coincides with the solution of (1.1)), we may choose the mesh-size H such that there exists $(\hat{\mathbf{E}}^H, \hat{\mathbf{H}}^H) \in \mathbf{V}^H \times \mathbf{W}^H$ with

$$\|\mathbf{E}-\hat{\mathbf{E}}^H\|^2_{\omega;1,\Omega}+\|\mathbf{H}-\hat{\mathbf{H}}^H\|^2_{\omega;1,\Omega} \leq \frac{\gamma_2}{2\gamma_1^2\gamma_3\omega^2}\|\mathbf{J}\|^2_{0,\Omega}\,.$$

Following the reasoning in [11] and [13] we then obtain that, for $(\bar{\mathbf{E}},\bar{\mathbf{H}}) \in \mathbf{V}\times\mathbf{W}$ satisfying

$$\mathcal{F}(\bar{\mathbf{E}},\bar{\mathbf{H}};\hat{\mathbf{E}}^H,\hat{\mathbf{H}}^H) = 0 \text{ for all } (\hat{\mathbf{E}}^H,\hat{\mathbf{H}}^H) \in \mathbf{V}^H\times\mathbf{W}^H\,,$$

we have

$$\mathcal{F}(\bar{\mathbf{E}},\bar{\mathbf{H}};\bar{\mathbf{E}},\bar{\mathbf{H}}) \geq \frac{\gamma_2}{2}\left(\|\bar{\mathbf{E}}\|^2_{\omega;1,\Omega}+\|\bar{\mathbf{H}}\|^2_{\omega;1,\Omega}\right)\,. \tag{3.3}$$

This implies that, on all sufficiently fine triangulations $\mathcal{T}^h$ with $h \leq H$ where $H \sim 1/\omega$.

$$\mathcal{F}(\mathbf{E}-\mathbf{E}^h, \mathbf{H}-\mathbf{H}^h; \mathbf{E}-\mathbf{E}^h, \mathbf{H}-\mathbf{H}^h) \geq \frac{\gamma_2}{2}\left(\|\mathbf{E}-\mathbf{E}^h\|^2_{\omega;1,\Omega} + \|\mathbf{H}-\mathbf{H}^h\|^2_{\omega;1,\Omega}\right)$$

holds, i.e., the least-squares bilinear form of the error is an upper bound for the $(H^1(\Omega))^3 \times (H^1(\Omega))^3$-norm of the error.

We finally mention an observation in connection to the least-squares finite element approach which is of practical importance (see also [8]). Since the least-squares functional is zero at the solution $(\mathbf{E}, \mathbf{H})$ of (1.1), the functional evaluated at an approximation $(\mathbf{E}^h, \mathbf{H}^h) \in \mathbf{V}^h \times \mathbf{W}^h$ serves as an a posteriori error measure. This follows from

$$\begin{aligned} & G(\mathbf{E}^h, \mathbf{H}^h; \mathbf{J}) \\ = \; & G(\mathbf{E}^h, \mathbf{H}^h; \mathbf{J}) - G(\mathbf{E}^h, \mathbf{H}^h; \mathbf{J}) \\ = \; & \mathcal{F}(\mathbf{E}-\mathbf{E}^h, \mathbf{H}-\mathbf{H}^h; \mathbf{E}-\mathbf{E}^h, \mathbf{H}-\mathbf{H}^h) \end{aligned}$$

which is a straightforward consequence of the usual relation between a quadratic functional and its associated bilinear form. However, the functional measures the error in the norm defined by the bilinear form and this is equivalent to the $H^1(\Omega)$-norm only under the restrictions discussed above.

4. Multilevel Preconditioning. One of the advantages of this least-squares approach is that the discrete system is always positive definite and the (suitably preconditioned) conjugate gradient method can be used. The least-squares finite element method leads to a sequence of systems of linear equations associated with a nested sequence of finite element spaces. For such problems, multilevel methods have shown to be extremely efficient. This efficiency comes from the fact that the entire hierarchy of operators associated with all levels of the discretization is used. As an attempt to get an efficient solution method, we combine the multilevel approach with Krylov subspace methods. The basic idea of the additive multilevel preconditioner by Bramble, Pasciak, and Xu [1] (see also Yserentant [14]) is to use a specific scaling of the residuals associated with different discretization levels. Consider a sequence of triangulations $\{\mathcal{T}^{h_l}, l = 0, \ldots, L\}$ (with $h_0 = H, h_L = h$). Associated with each triangulation $\{\mathcal{T}^{h_l}\}$ is the finite element space $\mathbf{V}^{h_l} \times \mathbf{W}^{h_l}$. This leads to a nested sequence of spaces

$$\mathbf{V}^{h_0} \times \mathbf{W}^{h_0} \subset \mathbf{V}^{h_1} \times \mathbf{W}^{h_1} \subset \cdots \subset \mathbf{V}^{h_L} \times \mathbf{W}^{h_L}\,.$$

On each level l, $0 \leq l \leq L$, an operator $\mathcal{F}_l : \mathbf{V}^{h_l} \times \mathbf{W}^{h_l} \to \mathbf{V}^{h_l} \times \mathbf{W}^{h_l}$ is defined by

$$\langle\langle \mathcal{F}_l(\mathbf{E}, \mathbf{H}); (\hat{\mathbf{E}}, \hat{\mathbf{H}})\rangle\rangle = \mathcal{F}(\mathbf{E}, \mathbf{H}; \hat{\mathbf{E}}, \hat{\mathbf{H}}) \text{ for all } (\hat{\mathbf{E}}, \hat{\mathbf{H}}) \in \mathbf{V}^{h_l} \times \mathbf{W}^{h_l}\,,$$

where the inner product $\langle\langle \cdot; \cdot \rangle\rangle$ is given by

$$\langle\langle (\mathbf{E}, \mathbf{H}); (\hat{\mathbf{E}}, \hat{\mathbf{H}})\rangle\rangle = (\mathbf{E}, \mathbf{H})_{0,\Omega} + (\hat{\mathbf{E}}, \hat{\mathbf{H}})_{0,\Omega}\,.$$

In terms of the operator $\mathcal{F}_l$, the discrete problem (3.1) can be written as

$$\mathcal{F}_l(\mathbf{E}_l, \mathbf{H}_l) = \mathbf{J}_l \tag{4.1}$$

where the right-hand side is defined by $\langle\langle \mathbf{J}_l, (\hat{\mathbf{E}}, \hat{\mathbf{H}})\rangle\rangle = -(\mathbf{J}, -i\omega\hat{\mathbf{E}} - \nabla \times \hat{\mathbf{H}})_{0,\Omega}$ for all $(\hat{\mathbf{E}}, \hat{\mathbf{H}}) \in \mathbf{V}^{h_l} \times \mathbf{W}^{h_l}$.

The basic ingredients for multilevel preconditioning are the projection operators $\mathcal{P}_l, \mathcal{Q}_l : \mathbf{V}^h \times \mathbf{W}^h \to \mathbf{V}^{h_l} \times \mathbf{W}^{h_l}$ which are given by

$$\mathcal{F}(\mathcal{P}_l(\mathbf{E}, \mathbf{H}); (\hat{\mathbf{E}}, \hat{\mathbf{H}})) = \mathcal{F}((\mathbf{E}, \mathbf{H}); (\hat{\mathbf{E}}, \hat{\mathbf{H}})) \text{ for all } (\hat{\mathbf{E}}, \hat{\mathbf{H}}) \in \mathbf{V}^{h_l} \times \mathbf{W}^{h_l}$$

and

$$\langle\langle \mathcal{Q}_l(\mathbf{E}, \mathbf{H}); (\hat{\mathbf{E}}, \hat{\mathbf{H}})\rangle\rangle = \langle\langle (\mathbf{E}, \mathbf{H}); (\hat{\mathbf{E}}, \hat{\mathbf{H}})\rangle\rangle \text{ for all } (\hat{\mathbf{E}}, \hat{\mathbf{H}}) \in \mathbf{V}^{h_l} \times \mathbf{W}^{h_l}.$$

In this abstract setting, the additive multilevel preconditioner is equivalent to

$$\mathcal{C}_L^{-1} = \sum_{l=0}^{L} h_l^2 \mathcal{Q}_l,$$

and this leads to a condition number for the preconditioned system $\kappa(\mathcal{C}_L^{-1/2} \mathcal{F}_L \mathcal{C}^{-1/2})$ which is bounded independently of L. For details on the implementation see [1] and [11]. The framework of multilevel minimal residual methods developed in [12] allows extra flexibility in the scaling of the components associated with different levels. Experiments with different weighting strategies in order to optimize the convergence depending on ω are currently under way and will be reported elsewhere.

5. Computational Experiments. This section contains computational experiments for a simple two-dimensional model problem to illustrate the performance of the multilevel preconditioner for different values of the wave number ω and mesh-size h. We consider the Maxwell equations (1.1) with $\varepsilon = \mu \equiv 1$ on the unit square $\Omega = (0,1) \times (0,1) \subset \mathbb{R}^2$. This two-dimensional setting implies that our unknown functions are $E_1(x_1, x_2), E_2(x_1, x_2)$ and $H_3(x_1, x_2)$ and the corresponding Maxwell equations are

$$\begin{aligned} \partial_1 E_2 - \partial_2 E_1 - i\omega H_3 &= 0 \\ -\partial_2 H_3 - i\omega E_1 &= J_1 \\ \partial_1 H_3 - i\omega E_2 &= J_2 \\ \partial_1 E_1 + \partial_2 E_2 &= 0. \end{aligned} \tag{5.1}$$

The perfectly conducting boundary conditions imply that $E_1 = 0$ on that part of the boundary with $x_2 = 0$ or $x_2 = 1$ while $E_2 = 0$ for $x_1 = 0$ or $x_1 = 1$. The numerical results reported here were performed with the choice $J_1 = J_2 \equiv 1/\sqrt{2}$ in Ω. We minimize the least-squares functional

$$\begin{aligned} G(E_1, E_2, H_3; J_1, J_2) &= \|\partial_1 E_2 - \partial_2 E_1 - i\omega H_3\|_{0,\Omega}^2 + \| - \partial_2 H_3 - i\omega E_1 - J_1\|_{0,\Omega}^2 \\ &+ \|\partial_1 H_3 - i\omega E_2 - J_2\|_{0,\Omega}^2 + \|\partial_1 E_1 + \partial_2 E_2\|_{0,\Omega}^2 \end{aligned} \tag{5.2}$$

among all $(E_1^h, E_2^h, H_3^h) \in V_1^h \times V_2^h \times V_3^h$ consisting of piecewise bilinear finite elements on a triangulation of Ω into squares of side length h. The boundary conditions for E_1 and E_2 are built into the spaces V_1^h and V_2^h.

Table 5.1 shows the minimum value of the least-squares functional in dependence of h and ω. Note that these numbers serve as a measure of the discretization error as explained in Section 3. Due to our choice of $J_1 = J_2 \equiv 1/\sqrt{2}$ we have $G(0,0,0;J_1,J_2) = 1$ which means that we can interpret the numbers in Table 5.1 also as a measure for the relative discretization error. The minimum values of the functional seem to behave like $O(h^2)$ for sufficiently small h.

TABLE 5.1
Minimum value of the least-squares functional

h / ω	1/16	1/32	1/64	1/128	1/256
10	$5.43 \cdot 10^{-2}$	$3.62 \cdot 10^{-2}$	$1.73 \cdot 10^{-2}$	$5.66 \cdot 10^{-3}$	$1.54 \cdot 10^{-3}$
20	$3.64 \cdot 10^{-2}$	$1.66 \cdot 10^{-2}$	$6.92 \cdot 10^{-3}$	$2.41 \cdot 10^{-3}$	$6.86 \cdot 10^{-4}$
30	$3.61 \cdot 10^{-2}$	$1.80 \cdot 10^{-2}$	$9.33 \cdot 10^{-3}$	$4.48 \cdot 10^{-3}$	$1.64 \cdot 10^{-3}$
40	$3.61 \cdot 10^{-2}$	$1.80 \cdot 10^{-2}$	$8.99 \cdot 10^{-3}$	$4.53 \cdot 10^{-3}$	$2.59 \cdot 10^{-3}$
50	$3.61 \cdot 10^{-2}$	$1.80 \cdot 10^{-2}$	$9.02 \cdot 10^{-3}$	$4.51 \cdot 10^{-3}$	$2.03 \cdot 10^{-3}$
60	$3.61 \cdot 10^{-2}$	$1.80 \cdot 10^{-2}$	$9.02 \cdot 10^{-3}$	$4.51 \cdot 10^{-3}$	$2.34 \cdot 10^{-3}$

Listed in Table 5.2 is the number of iterations of the multilevel preconditioned CG method required to reduce the initial residual by a factor of 10^{-4}. The multilevel preconditioner uses the exact solution of the corresponding problem A_0 on a 7×7 mesh ($h_0 = 1/8$). Note that the value of the least-squares functional remains almost unchanged, indicating that discretization accuracy is reached after much fewer iterations.

TABLE 5.2
Number of iterations

h / ω	1/16	1/32	1/64	1/128	1/256
10	17	25	33	36	37
20	19	36	51	59	61
30	17	31	51	82	100
40	16	29	48	65	101
50	14	26	42	70	91
60	14	25	40	57	83

These limited numerical experiments indicate that multilevel preconditioning leads to an efficient solution method for the time-harmonic Maxwell equations. More computational experience involving three-dimensional domains and complicated geometries are needed to get a better judgment of this approach. These experiments are currently under way and will be reported elsewhere.

REFERENCES

[1] J. H. Bramble, J. E. Pasciak, and J. Xu, *Parallel multilevel preconditioners*, Math. Comp., 55 (1990), pp. 1–22.

[2] Z. Cai, R. Lazarov, T. A. Manteuffel, and S. F. McCormick, *First-order system least squares for second-order partial differential equations: Part I*, SIAM J. Numer. Anal., 31 (1994), pp. 1785–1799.

[3] Z. Cai, T. A. Manteuffel, and S. F. McCormick, *First-order system least squares for second-order partial differential equations: Part II*, SIAM J. Numer. Anal., (1995). To Appear.

[4] D. Colton and R. Kress, *Inverse Acoustic and Electromagnetic Scattering Theory*, Springer, Berlin, 1992.

[5] V. Girault and P.-A. Raviart, *Finite Element Methods for Navier-Stokes Equations*, Springer, New York, 1986.

[6] B. Lee, T. Manteuffel, S. McCormick, and J. Ruge, *Multilevel first-order system least-squares for helmholtz equations*, in Seventh Copper Mountain Conference on Multigrid Methods, N. D. Melson, T. A. Manteuffel, and S. F. McCormick, eds., Hampton, Virginia, 1995, NASA.

[7] R. Leis, *Exterior boundary-value problems in mathematical physics*, in Trends in Applications of Pure Mathematics in Mechanics 2, H. Zorski, ed., London, 1979, Pitman, pp. 187–203.

[8] T. A. Manteuffel, S. F. McCormick, and G. Starke, *First-order system least-squares for second-order elliptic problems with discontinuous coefficients*, in Seventh Copper Mountain Conference on Multigrid Methods, N. D. Melson, T. A. Manteuffel, and S. F. McCormick, eds., Hampton, Virginia, 1995, NASA.

[9] P. B. Monk, *A comparison of three mixed methods for the time-dependent Maxwell's equations*, SIAM J. Sci. Stat. Comput., 13 (1992), pp. 1097–1122.

[10] ——, *A finite element method for approximating the time-harmonic Maxwell equation*, Numer. Math., 63 (1992), pp. 243–261.

[11] A. H. Schatz, *An observation concerning Ritz-Galerkin methods with indefinite bilinear forms*, Math. Comp., 28 (1974), pp. 959–962.

[12] G. Starke, *Multilevel minimal residual methods for nonsymmetric elliptic problems*, J. Numer. Linear Algebra Appl., (1996). To Appear.

[13] H. Yserentant, *On the multi-level splitting of finite element spaces for indefinite elliptic boundary value problems*, SIAM J. Numer. Anal., 23 (1986), pp. 581–595.

[14] ——, *Two preconditioners based on the multi-level splitting of finite element spaces*, Numer. Math., 58 (1990), pp. 163–184.

Iterative Solution Methods for Ill-Posed Problems

D. Calvetti * L. Reichel † Q. Zhang ‡

Abstract

The discretization of ill-posed prolems often gives rise to large ill-conditioned linear systems of equations whose solution requires some form of regularization. We describe new solution method in which the filter function, that determines the regularization of the problem, is approximated by linear combinations of Chebyshev polynomials.

1 Introduction

The numerical solution of ill-posed problems is a challenging task that arises frequently in the context of inverse problems. Many inverse problems in physics and engineering can be formulated as Fredholm integral equations of the first kind.

The discretization of Fredholm integral equations of the first kind typically yields very ill-conditioned linear systems of algebraic equations. When the dimensions of the linear system of algebraic equations are small enough to allow factorization of the matrix, an approximate solution of the system of equations can be computed by algorithms that use a truncated singular value decomposition or other orthogonal transformations of the matrix. However, many inverse problems that are of interest in applications give rise to linear systems of algebraic equations so large that solution methods requiring the factorization of the matrix are unfeasible or undesirable. Such problems have to be solved by iterative methods.

We describe new iterative methods for the solution of discretized ill-posed problems. The new methods are particularly appealing when the discretized ill-posed problem is very large and the resulting matrix is sparse or structured. The proposed algorithms do not require that the matrix be explicitly stored, only a subroutine for the computation matrix-vector products has to be supplied by the user. Generalizations of the methods in this paper to linear systems with a nonsymmetric, and possibly nonsquare, matrix are described by Calvetti et al. [2].

Let

$$Ax = g, \qquad A \in R^{n\times n}, \qquad x, g \in R^n, \tag{1}$$

be a linear system of algebraic equations that stems from the discretization of an ill-posed problems. Throughout this paper we assume that the matrix A be symmetric. Typically, the eigenvalues of

*Department of Pure and Applied Mathematics, Stevens Institute of Technology, Hoboken, NJ 07030. E-mail: calvetti@mathrsl.stevens-tech.edu

†Department of Mathematics and Computer Science, Kent State University, Kent, OH 44242. E-mail: reichel@mcs.kent.edu

‡Department of Mathematics and Computer Science, Kent State University, Kent, OH 44242. E-mail: qzhang@mcs.kent.edu

symmetric matrices arising from discretizing ill-posed problems cluster at the origin. This causes the solution vector of the linear systems (1) to be very sensitive to perturbations in the right-hand side vector, e.g., due to measurement errors. Surveys on the treatment and solution of ill-posed problems can be found in the work by Engl [3], Groetsch [4], Hanke and Hansen [5].

A regularization method replaces the linear system (1) with a nearby system whose solution is less sensitive to the presence of noise in the right-hand side vector. The most well-known regularization method is Tikhonov regularization. Instead of computing the solution of (1), Tikhonov regularization solves the minimization problem

$$\min_{x\in R^n}\{\|g-Ax\|^2+\frac{1}{\beta}\|Lx\|^2\}, \tag{2}$$

where $\beta > 0$ is a regularization parameter and L is a linear functional which defines a seminorn. For simplicity we assume that $L = I$. Here and throughout this paper $\|\cdot\|$ denotes the Euclidean vector norm or the corresponding induced matrix norm. Introduce the spectral decomposition

$$A = U\Lambda U^T,$$

where

$$U = [u_1, u_2, \ldots, u_n], \qquad U^TU = I,$$

$$\Lambda = \mathrm{diag}\{\lambda_1, \lambda_2, \ldots, \lambda_n\}, \qquad \lambda_1 \leq \lambda_2 \leq \ldots \leq \lambda_n$$

The solution x_β of (2) satisfies

$$(A^2+\frac{1}{\beta}I)x_\beta = Ag,$$

hence

$$x_\beta = \sum_{j=1}^{n}(1-\phi_\beta(\lambda_j))\frac{u_j^Tg}{\lambda_j}u_j, \tag{3}$$

where

$$1-\phi_\beta(t) = 1-\frac{1}{\beta t^2+1}. \tag{4}$$

The function $\Phi(t) = 1-\frac{1}{\beta t^2+1}$ "filters out" from the solution vector contributions along eigenvectors corresponding to eigenvalues of small magnitude. For this reason Φ is usually referred to as the Tikhonov filter function.

The selection of a different filter function determines a different regularization method. Since the purpose of a filter function is to exclude components along eigendirections associated with the eigenvalues closest to the origin, the filter function usually vanishes at, and is small in a neighborhood of, the origin. In this paper we consider regularization methods defined by the Tikhonov filter function and by the exponential filter function $\Phi(t) = 1-\phi_\beta(t)$, defined by

$$\phi_\beta(t) = e^{-\beta t^2}. \tag{5}$$

The function (5) is analytic in the whole complex plane and therefore can be well approximated by polynomials on a finite interval. When $|\beta t^2|$ is small the exponential filter function approximates

closely the Tikhonov filter function. Notice that the Tikhonov filter function has singularities at $t = \pm i\beta^{-1/2}$, where $i = \sqrt{-1}$.

This paper is organized as follows. In section 2 we define new iterative methods based on the approximation of the filter function by a linear combination of Chebyshev polynomials of the first kind. The degree of the approximating polynomial increases by one at each iteration. Since the derivative of the residual polynomials of the iterative methods vanishes at the origin, the methods converge to the minimum norm solution when the matrix A is singular and the linear system (1) is inconsistent. Section 3 describes how to compute a regularization parameter that satisfies Morozov discrepancy principle in combination with the iterative methods. Section 4 describes how to efficiently compute a correction to the solution corresponding to a previously selected value of the regularization in order to obtain the solution corresponding to a new value of the regularization parameter.

2 Iterative methods

Assume for simplicity that $x_\beta^{(0)} = 0$. The solution of (1) by an iterative methods proceeds by computing a sequence of iterates of the form

$$x_\beta^{(k)} = q_{k-1}(A)g, \qquad k = 1, 2, \dots , \tag{6}$$

where q_{k-1} is a polynomial of degree $k-1$. The residual vectors $r_\beta^{(k)} = g - Ax_\beta^{(k)}$ satisfy

$$r_\beta^{(k)} = p_k(A)g, \qquad k = 1, 2, \dots , \tag{7}$$

where the polynomials

$$p_k(t) = 1 - tq_{k-1}(t) \tag{8}$$

are generally referred to as residual polynomials. It follows from (3) and (7) that the polynomials q_{k-1} should be chosen so that the residual polynomials p_k yield a good approximation of $\phi_\beta(x)$ over the spectrum of the matrix A. Furthermore, since the eigenvalues of A are very close to the origin, it is desirable that the derivative of the residual polynomials vanish at the origin, i.e.,

$$p_k'(0) = 0. \tag{9}$$

We remark that an iterative method must satisfy (9) to converge to the solution of minimum norm when the matrix A is singular: see [1, 5]. Assume that an interval $[a, b]$ containing the spectrum of A is known. The Chebyshev polynomials of the first kind for the interval $[a, b]$ satisfy the three-term recurrence relations

$$T_0(z(t)) = 1 \qquad T_1(z(t)) = z(t) \tag{10}$$

$$T_k(z(t)) = 2z(t)T_{k-1}(z(t)) \qquad k = 2, \dots, \qquad z(t) = \frac{2t - b - a}{b - a}, \qquad -1 \leq t \leq 1. \tag{11}$$

Let

$$w(t) = (b - t)^{-1/2}(t - a)^{-1/2}$$

be the weight for the interval $[a, b]$.

We begin with describing the iterative method for the exponential filter function. Introduce the expansion of $\tilde{\phi}_\beta(t) = e^{-\beta t^2}$ in the $T_j(z(t))$,

$$e^{-\beta t^2} = \sum_{j=0}^{\infty} a_j T_j(z(t)), \tag{12}$$

where

$$\begin{aligned} a_0 &= \frac{1}{\pi}\int_a^b \tilde{\phi}_\beta(t) w(t) dt, \\ a_j &= \frac{2}{\pi}\int_a^b \tilde{\phi}_\beta(t) T_j(z(t)) w(t) dt, \quad j = 1, 2, \dots . \end{aligned}$$

and denote its k-th partial sum by $s_k(t)$. Observe that

$$-2\beta t \tilde{\phi}_\beta(x) = \frac{d}{dt}\phi_\beta(t). \tag{13}$$

Multiply $s_k(t)$ by $-2\beta t$ and integrate in t. This yields a polynomial $q_{k+2}(t)$ of degree $k+2$, which can be written in the form

$$q_{k+2}(t) = \sum_{i=1}^{k+2} b_i T(z(t)) + C \tag{14}$$

where the constant C is chosen so that $q_{k+2}(0) = 1$. Furthermore

$$q_j'(0) = 0.$$

It can be shown, see [2], that the polynomials q_j satisfy a five-term recurrence relation of the form,

$$q_{n+1}(t) = q_n(t) - \sum_{i=n-3}^{n+1} \alpha_i^{(n+1)} (T_i(z(0)) - T_i(z(t))), \qquad n \geq 4. \tag{15}$$

The coefficients $\alpha_i^{(n+1)}, n \geq 4$, can be computed from the $(n-1)$-st Fourier coefficient of the expansion of $e^{-\beta t^2}$ in the T_j according to the following formulas

$$\begin{aligned} \alpha_{n-3}^{(n+1)} &= \Delta\beta a_{n-1}\tfrac{(b-a)^2}{8(n-3)}, \quad & \alpha_{n-2}^{(n+1)} &= \Delta\beta a_{n-1}\tfrac{b^2-a^2}{4(n-2)}, \\ \alpha_n^{(n+1)} &= -\Delta\beta a_{n-1}\tfrac{b^2-a^2}{4n} \quad & \alpha_{n+1}^{(n+1)} &= -\Delta\beta a_{n-1}\tfrac{(b-a)^2}{8(n+1)} \end{aligned}$$

The following Lemma shows that the Fourier coefficients a_k satisfy also a five-term recurrence relation.

Lemma 2.1 *The coefficients of the expansion of $e^{-\beta t^2}$ in Chebyshev polynomials for the interval $[a, b]$ satisfy the following five-term recurrence relations*

$-2a_0 - 2\frac{b+a}{b-a}a_1 - \frac{16}{\beta(b-a)^2}a_2 + 2\frac{b+a}{b-a}a_3 + a_4 = 0$

and for $i > 2$,

$-a_{i-2} - 2\frac{b+a}{b-a}a_{i-1} - \frac{8i}{\beta(b-a)^2}a_i + 2\frac{b+a}{b-a}a_{i+1} + a_{i+2} = 0$

It follows from Lemma 2.1 that, for fixed m, after computing a_0, a_1, a_{m-1}, a_m to high accuracy, the remaining $m-3$ Fourier coefficients can be obtained by solving a pentadiagonal linear system of equations. Therefore the $(n+1)$-th approximate solution for the iterative method determined by the residual polynomials q_k is of the form

$$x_\beta^{n+1} = x_\beta^n + \sum_{i=n-3}^{n+1} \alpha_i^{(n+1)} y^{(i)}, \qquad n \geq 4,$$

where

$$\begin{aligned} y^{(1)} &= -\tfrac{2}{b-a} r_{\beta_1} \\ y^{(i)} &= -\tfrac{2(b+a)}{b-a} y^{(i-1)} - y^{(i-2)} - \tfrac{4}{b-a}(T_{i-1}(z(0)) r_{\beta_1} - A y^{(i-1)}). \end{aligned}$$

Each iteration requires one matrix-vector multiplication with the matrix A. We would like to terminate the iterations when the error in the approximation of the filter function by the polynomials q_k is sufficiently small. Since the coefficients of these polynomials are related to the Fourier coefficients a_k in a fairly straightforward manner, iterations are terminated when $|a_k|$ is sufficiently small.

We remark similar iterative schemes can be defined for different choices of the filter function. The iterative method for Tikhonov filter function, for example, can be defined simply by setting $\phi_\beta(t) = \frac{1}{\beta t^2+1}$ and $\tilde{\phi}_\beta(t) = \frac{1}{(\beta t^2+1)^2}$. The following lemma gives analytic formulas for the computation of the Fourier coefficients of the expansion of $\frac{1}{(\beta t^2+1)^2}$ in Chebyshev polyomials for the interval $[a,b]$.

Lemma 2.2 *If*

$$\frac{1}{(\beta t^2+1)^2} = \sum_{j=0}^{\infty} a_j T_j(z(t)), \qquad t \in [a,b]$$

then

$$\begin{aligned} a_0 &= \frac{2}{\beta_2 (b-a)^2} Re \frac{1}{(z^2-1)} \left(i \frac{\sqrt{\beta_2}(b-a)}{2} \sqrt{z^2-1} + \frac{z}{\sqrt{z^2-1}} \right) \\ a_n &= \frac{4}{\beta_2 (b-a)^2} Re \frac{1}{(z^2-1)(z-\sqrt{z^2-1})^n} \left(-n + i \frac{\sqrt{\beta_2}(b-a)}{2} \sqrt{z^2-1} + \frac{z}{\sqrt{z^2-1}} \right), \qquad n = 1, \ldots, \end{aligned}$$

where $z = -\frac{b+a}{b-a} - i \frac{2}{\sqrt{\beta_2}(b-a)}$, $i = \sqrt{-1}$ *and Re(z) denotes the real part of a complex number* z.

3 Selection of Regularization Parameter

Often in applications the right-hand side vector g in (1) is contaminated by errors. Separate the right-hand side into two components,

$$g = g^{exact} + \eta,$$

where g^{exact} is the unperturbed and unknown right-hand side vector and η is the error. Assume that the norm of the error satisfies

$$\|\eta\| \leq \delta$$

with the bound δ explicitly known.

We want to determine the value of the regularization parameter β^* which satisfies

$$f(\beta^*) = \|g - Ax_\beta^*\| - \delta = 0. \tag{16}$$

This method for determining the regularization parameter is often referred to as the Morozov discrepancy principle and is discussed, e.g., by Engl [3] and Groetsch [4]. Introduce the function

$$g(\beta) = \|g - Ax_\beta\|^2 - \delta^2. \tag{17}$$

Then a solution to the equation $g(\beta) = 0$ is also a solution of $f(\beta) = 0$. Since $g(\beta)$ is a decreasing and convex function of β, Newton's method is globally and monotonically convergent when starting with a value $\beta_0 < \beta^*$.

The iterates computed by Newton's methods can be expressed in a particularly convenient form in the case of the exponential filter function

$$\beta_{n+1} = \beta_n + \frac{\|r_{\beta_n}\|^2 - \delta^2}{2\|Ar_{\beta_n}\|^2}$$

where $r_{\beta_n} = g - Ax_{\beta_n}$. Therefore the computation of a new value of the regularization parameter, say β_{n+1} does not require any additional work in addition to the computation of x_{β_n} by the iterative method described in section 2.

Unfortunately the iterates for Newton's methods cannot be simplified to such efficient formulation when the regularization is determined by Tikhonov filter function. In fact, in view of the additional computations which would be required to apply Newton's method, it is more convenient to determine the value of β which satisfies Morozov discrepancy principle by the secant method, whose global convergence when starting with two values, say β_{-1} and β_0, less than β^*. The iterates for the secant method can be written in the form

$$\beta_{n+1} = \beta_n + \frac{(\|r_{\beta_n}\|^2 - \delta^2)(\beta_n - \beta_{n-1})}{\|r_{\beta_n}\|^2 - \|r_{\beta_{n-1}}\|^2}$$

4 Efficient update of the solution vector

We now describe how to computed a correction of the vector x_{β_n} which yields the solution $x_{\beta_{n+1}}$ corresponding to a a new value of the regularization parameter β_{n+1}.

Let $\phi_{\beta_n}(t) = e^{-\beta_n t^2}$ and introduce

$$\Delta\beta = \beta_{n+1} - \beta_n.$$

Then

$$x_{\beta_{n+1}} = (I - e^{-\beta_{n+1}A^2}A^\dagger g \tag{18}$$

where $A^\dagger$ is the Moore-Penrose generalized inverse of A. Since

$$
\begin{aligned}
x_{\beta_{n+1}} &= (I - e^{-(\beta_n+\Delta\beta)A^2})A^\dagger g \\
&= (I - e^{-\beta_n A^2})A^\dagger g + (I - e^{-\Delta\beta A^2})A^\dagger e^{-\beta_n A^2} g \\
&= x_{\beta_n} + (I - e^{-\Delta\beta A^2})A^\dagger r_{\beta_n}
\end{aligned}
$$

where $r_{\beta_n} = g - Ax_{\beta_n}$, to compute $x_{\beta_{n+1}}$ it suffices to compute the quantity $(I - e^{-\Delta\beta A^2})A^\dagger r_{\beta_n}$, for example by the technique described in section 2. We remark that, when β_{n+1} is close to a zero of $g(\beta)$, the approximation of $e^{-\Delta\beta t^2}$ requires a polynomial $q_k(t)$ of lower degree than when approximating $e^{-\beta_{n+1}t^2}$.

The updating scheme for the solution vector when a new regularization parameter has been determined in the case were the regularization is determined by Tikhonov filter function is based on the following observation. Since

$$
\begin{aligned}
x_{\beta_{n+1}} &= (I - (\beta_{n+1}A^2 + I)^{-1})A^\dagger g \\
&= x_{\beta_{n+1}} + (I - (\beta_n A^2 + I)(\beta_{n+1}A^2 + I)^{-1})A^\dagger r_{\beta_n},
\end{aligned}
$$

we can compute the correction term to x_{β_n} in the previous formula by defining an iterative method whose residual polynomials $q_k(t)$ approximate the function $\frac{\beta_n t^2+1}{\beta_{n+1}t^2+1}$. It can be shown that, as the distance between β_n and β_{n+1} becomes smaller, this updating procedure become faster that computing $x_{\beta_{n+1}}$ by approximating $\frac{1}{\beta_{n+1}t^2+1}$.

References

[1] D. Calvetti, L. Reichel and Q. Zhang, An adaptive semiiterative method for symmetric semidefinite linear systems, in Approximation and Computation, ed. R.V.M.Zahar, Int'l Series Numer. Math. # 119 Birkhäuser, Basel, 1994, pp. 77-96.

[2] D. Calvetti, L. Reichel and Q. Zhang, A new class of iterative methods for the solution of large ill-posed problems, in preparation.

[3] H. W. Engl, Regularization methods for the stable solution of inverse problems, Surv. Math. Ind., Vol. 3, pp. 71-143, 1993.

[4] C. W. Groetsch, The theory of Tikhonov regularization for Fredholm equations of the first kind, Pitman, London, 1984.

[5] M. Hanke and P. C. Hansen, Regularization methods for large-scale problems, Surv. Math. Ind., Vol. 3, pp. 253-315, 1993.

[6] P. C. Hansen and D. P. O'Leary, The use of the L-curve in the regularization of discrete ill-posed problems, SIAM J. Sci. Comput., Vol. 14, pp. 1487-1503, 1993.

[7] W. K. Pratt, Digital image processing, John Wiley & Sons, New York, pp. 329, 1991.

[8] H. J. Trussell, Convergence criteria for iterative restoration methods, IEEE Transaction on Acoustics, Speech and Signal Processing, Vol. ASSP-31, No. 1, pp. 129-136, 1983.

[9] J. M. Varah, The prolate matrix, Linear Algebra Appl., Vol. 187, pp. 269-278, 1993.

Methods for Large Sparse Eigenvalue Problems from Waveguide Analysis*

Chang Peng and Daniel Boley
Department of Computer Science
University of Minnesota
Minneapolis, MN 55455

Abstract

We discuss several techniques for finding leading eigenvalues and eigenvectors for large sparse matrices. The techniques are demonstrated on a scalar Helmholtz equation derived from a model semiconductor rib waveguide problem. We compare the simple inverse iteration approach with more sophisticated methods, including minimum degree reordering, Arnoldi and Lanczos methods. We then propose a new Arnoldi method designed particularly for the constrained generalized eigenvalue problem, a formulation arising naturally from the scalar waveguide problem.

1 Problem Formulation

In the waveguide analysis (see e.g. [9]), the analysis of the propagation of the electric and magnetic fields in waveguides, based on the use of Maxwell's equations, often lead to scalar Helmholtz equations of the general form $\nabla_T^2 E_x + k^2 E_x = \beta^2 E_x$, where E_x denotes the x component of the electric field, k is the dielectric constant, β is the unknown propagation constant, and ∇_T^2 denotes the Laplacian operator in the transverse (x, y) coordinates (z being the longitudinal coordinate). When this Helmholtz equation is solved for the x coordinate only, one must impose internal continuity conditions across the boundaries between materials of different dielectric constants. The combined equations are then discretized by finite differences yielding a large sparse ordinary matrix eigenvalue problem $A\mathbf{x} = \lambda\mathbf{x}$ [9]. Discretizing the vector fields equations using finite element formulations leads to a large sparse generalized eigenvalue problem [2]:

$$A\mathbf{x} = \lambda B\mathbf{x} \tag{1}$$

where the matrix $A^{n\times n}$ is real and non-singular, $B^{n\times n}$ is real, symmetric, and positive definite.

Solving problem (1) constitutes the largest part of the computational effort. In this paper we are discussing several iterative algorithms that can efficiently deal with problem (1) of several thousands in size on workstations. When B is banded, as is the case in many problem formulations from waveguide analysis, the Cholesky decomposition $B = LL^T$ problem (1) can be used to reduce (1) to an ordinary eigenvalue problem:

$$L^{-1}AL^{-T}\mathbf{y} = \lambda\mathbf{y} \tag{2}$$

where L is lower triangular and $\mathbf{y} = L^T\mathbf{x}$. In an iterative method, $L^{-1}AL^{-T}$ dose not need to be explicitly formed. This is possible because most iterative methods only need to form matrix-vector products. When B is not banded but its Cholesky decomposition gives a sparse L, the reduction is still useful. But if L is not sparse, then solving problems such as (1) becomes significantly more difficult and expensive. Since waveguide analysis leads to generally banded matrices, in this paper, we will mainly concentrate on the ordinary eigenvalue problem (2), assuming that the multiplication by A^{-1} is feasible, and considering the matrix $L^{-1}AL^{-T}$ as A, if appropriate.

As a model test case, we derived the matrix A from the scalar Helmholtz equation, combined with suitable internal continuity conditions, applied to a typical semiconductor rib waveguide. See [9] for the details. In our examples, we used a matrix of modest size (1800×1800) with a zero structure shown in Figure 1. Computations were carried out in MATLAB.

*This work was funded in part by NSF grant CCR-9405380.

2 Inverse Iteration, Minimum Degree Reordering and Deflation

Inverse iteration is a simple, powerful and effective method to compute the smallest modulus eigenvalue. Since in the waveguide analysis the dominant mode (in the sense of largest real part), which is desired, generally does not correspond to the largest or smallest eigenvalue in modulus, it is often necessary to combine a shift σ into the iteration. Iterating with matrix $(A - \sigma I)^{-1}$ will yield the eigenvalue closest to the given σ. The convergence factor is:

$$\rho = \frac{|\lambda_1 - \sigma|}{|\lambda_2 - \sigma|} \tag{3}$$

where λ_1 is the closet eigenvalue to σ and λ_2 is the second close one. We can see that if σ is much closer to λ_1 than to λ_2, the convergence can be very fast. Each iteration requires that a system of linear equations of the form $(A - \sigma I)\mathbf{x}_{\text{new}} = \mathbf{x}_{\text{old}}$ be solved, often by a variant of LU Factorization [4]. If σ is updated using Rayleigh quotients during the iteration, then the iteration converges quadratically in general, and cubically if the matrix is symmetric [4], but changing σ requires that $(A - \sigma I)$ be re-factored from scratch in each iteration at great expense. So often the shift is fixed, allowing the factoring to be done just once, where the shift is estimated in advance by physical considerations. On the other hand, when only the largest eigenvalue in magnitude is needed, the more straightforward power iteration may be used, but this method may suffer from slow convergence when the first and second eigenvalues in magnitude are close to each other. The Inverse Iteration is summarized in the following.

Algorithm 2.1 Basic Inverse Iteration:
1. Choose a random unit vector $\mathbf{x}_0$ and a shift σ;
2. Compute the LU decomposition of $A - \sigma I$;
3. Iterate: for $i = 1, 2, \ldots$ until convergence do
4. Solve $Ly = \mathbf{x}_0$ and $U\mathbf{x} = \mathbf{y}$;
5. $norm = \|\mathbf{x}\|_2$, $\mathbf{x} = \mathbf{x}/norm$;
6. Compute $\lambda = \mathbf{x}^T A\mathbf{x} = (\mathbf{x}^T\mathbf{x}_0)/norm$;
7. Compute residual $r = \|Ax - \lambda\mathbf{x}\|_\infty$;
8. If r is satisfied, then stop; Otherwise $\mathbf{x}_0 = \mathbf{x}$;
9. *Optional* If $i = 0$ (mod 8 or 10), then set $\sigma = \lambda$,
and compute the LU decomposition of $(A - \sigma I)$.
(optional: for Rayleigh quotient iteration adaptive algorithm)
10. end

Line 9 is an adaptive shift step for faster convergence which can yield quadratic convergence (cubic if A is symmetric). However, it requires that the LU decomposition be repreated, which is very expensive, and especially when A is not symmetric, the converged eigenvalue may not be the one that is closest to the original shift. Thus often line 9 is skipped, or performed only once during several passes through the main loop.

If the matrix A is banded, we can reorder A using the minimum degree ordering before we do the LU decomposition [3]. This is a heuristic algorithm that reorders the equations so that (hopefully) the resulting L and U factors are more sparse, i.e. have fewer non-zero elements. Then the total number of flops needed by the algorithm will be considerably reduced. For the details of minimum degree reordering, please refer to [3]. For these experiments, we have taken advantage of MATLAB's built-in functions for various reordering algorithms including the minimum degree reordering.

Algorithm 2.2 Inverse Iteration with Minimum Degree Reordering:
1. Choose a random unit vector $\mathbf{x}_0$ and a shift σ;
2. Find the minimum degree reordering permutation P, replace A with PAP;
3. Compute the LU decomposition of $A - \sigma I$;
4. The rest is the same as the Basic Inverse Iteration (Algorithm 2.1, steps 3–8).

With MATLAB we carried out a series of numerical experiments on a 1800×1800 matrix described in Section 1. Algorithm 2.1 and 2.2 were used respectively to find the dominant mode which corresponds to the eigenvalue

Inverse Iteration	*# Eigenvalues Sought*	*Iters*	*Flop Count*	*Residual Norm*
Basic	1	4	8,255,268	6.4E-5
Reordering	1	4	5,225,559	7.4E-5
Reordering	2	18	8.485,461	3.9E-5

Table 1: Comparison of Basic and Reordering Inverse Iteration

$\lambda = 3.4404$, fixing the shift at $\sigma = 3.4$. From Table 1 we can see that reordered inverse iteration can save over 1/3 of computation needed by the basic inverse iteration. We should point out that in MATLAB the LU decomposition process may involve pivoting and this pivoting may reduce some of the advantage gained from reordering. To see the potential advantage that could be gained just from minimum degree ordering if pivoting is turned off, we computed the flop count for the Cholesky factorization on a shifted matrix A (like LU Decomposition without pivoting for symmetric positive definite matrices [4]). The resulting Flop Counts with and without minimum degree reordering are $2,013,624$ and $3,685,377$, respectively, representing a savings of 45% over the unreordered version!

If we have already obtained the leading eigenvalue and need to find the next one closest to the known eigenvalue, we can use the so called *deflation* technique, described as follows [8]. Suppose λ and $\mathbf{u}$ are the known eigenpair of A, and $\mathbf{v}$ is a vector such that $\mathbf{v}^T\mathbf{u} = 1$. Then it is easy to see that the matrix $A' = A - \gamma uv^T$ has the same spectrum as A except that the one eigenvalue λ has been shifted to $\lambda - \gamma$. For the power iteration A' can be used directly in the iteration. But we cannot do so in the case of the inverse iteration, because forming A' explicitly is too expensive and will destroy the sparsity. We here propose an efficient process that avoids forming A'. Since what the inverse iteration needs is the matrix-vector product $\mathbf{x} = A'^{-1}\mathbf{x}_0$. We express A'^{-1} in terms of A^{-1}, whose LU decomposition is already available. By the Sherman-Morrison formula [4] and using $A^{-1}\mathbf{u} = \lambda^{-1}\mathbf{u}$, we have

$$\begin{aligned} A'^{-1} &= A^{-1} + \gamma A^{-1}\mathbf{u}(1 - \gamma \mathbf{v}^T A^{-1}\mathbf{u})^{-1}\mathbf{v}^T A^{-1} \\ &= A^{-1} + \frac{\gamma}{\lambda - \gamma} uv^T A^{-1} \\ &= (I + \beta uv^T)A^{-1} \end{aligned} \tag{4}$$

where $\beta = \frac{\gamma}{\lambda - \gamma}$. Since we already have LU decomposition of A, we can first compute $\mathbf{y} = A^{-1}\mathbf{x}_0$, and then compute the product $\mathbf{x} = A'^{-1}\mathbf{x}_0 = \mathbf{y} + \beta(\mathbf{v}^T\mathbf{y})\mathbf{u}$. Combining this into Algorithm 2.1 and 2.2 is the inverse iteration with deflation. We would like to point out here that this deflation technique can be cascaded multiple time, or generalized to the block version, e.g. deflation of multiple eigenvalues at the same time, by using the Sherman-Morrison-Woodbury formula [4].

There are various choices for the vector $\mathbf{v}$. The Hotelling's deflation chooses $\mathbf{v}$ as the left eigenvector $\mathbf{w}$, e.g. $\mathbf{w}^T A = \lambda \mathbf{w}^T$ or $A^T\mathbf{w} = \lambda\mathbf{w}$. The advantage of this choice is that A' will have the same eigenvectors as A. So when A is symmetric, the right and left eigenvectors are the same, we can more easily compute the product:

$$\begin{aligned} \mathbf{x} &= A'^{-1}\mathbf{x}_0 \\ &= (I + \beta uv^T)A^{-1}\mathbf{x}_0 \\ &= \mathbf{y} + (\lambda - \gamma)^{-1}(\mathbf{u}^T\mathbf{x}_0)\mathbf{u} \end{aligned} \tag{5}$$

where $\mathbf{y} = A^{-1}\mathbf{x}_0$. The other common choice just takes $\mathbf{v} = \mathbf{u}$. But this choice will not preserve the eigenvectors. So after the eigenvalue is found, we need another iteration to determine the eigenvector.

The other strategy to compute more than one eigenpair is block inverse iteration (also known as inverse simultaneous iteration). In this iteration, we choose a shift σ and several random vectors at the start, say $X_0 = [\mathbf{x}_1, \mathbf{x}_2, ..., \mathbf{x}_m]$, and then for $i = 1, 2, ...$ until convergence, iteratively compute:

$$\begin{aligned} X_i &= (A - \sigma I)^{-1} X_{i-1} \\ X_i &= Q_i R_i \\ X_{i+1} &= Q_i \end{aligned} \tag{6}$$

Equation (6) is the result of the QR decomposition in the previous line which orthogonalizes the columns of X_i. If the iteration converges, then the upper triangular matrix R_k will tend to be the leading $k \times k$ part of the Schur canonical form of $(A - \sigma I)^{-1}$ [8], that is the diagonal elements of R_k will be close to the first k eigenvalues of $(A - \sigma I)^{-1}$ in order of magnitude. So the eigenvalues nearest to σ are obtained. The matrix Q_k will be close to the corresponding Schur vectors. If $\mathbf{y}$ is a eigenvector of R_k, then the Ritz vector $\mathbf{x} = Q_k\mathbf{y}$ is an approximate eigenvector of A.

Algorithm 2.3 Block Inverse Iteration:
1. Choose a set of random vectors $X_0 = [\mathbf{x}_1, \mathbf{x}_2, ..., \mathbf{x}_m]$ and a shift σ;
2. Compute the LU decomposition of $A - \sigma I$;
3. Iterate: for $i = 1, 2, ...$ until convergent do
4. Solve $LY = X_0$ and $UX = X_0$;
5. Compute QR decomposition $X = QR$;
6. If $i = 0$ mod k,
7. Compute the residual norm $\|AQ - QR\| = \|AQ - X\|$.
8. To compute AQ, solve $LZ = Q$ and $UY = Z$.
9. If satisfied, then stop. Otherwise, $X_0 = Q$ and go on iteration;
7. end
8. Compute the eigenvector $\mathbf{y}$ of R, and the eigenvector of A is $\mathbf{x} = Q\mathbf{y}$.

Note that the number m of iterated vectors should be larger than the number k of eigenvalues needed. Depending on the spectrum distribution, normally we could take $m = k + 2$ if k is two or three.

3 Arnoldi and Lanczos Method

Arnoldi method for the algebraic eigenvalue problem is very much like Galerkin method for the approximation of eigenfunctions. Here we just give a brief derivation of the method. The Galerkin method uses a subspace to form the approximate eigenfunctions. In a similar way, the Arnoldi method takes a subspace $\mathcal{K} \subseteq R^n$ to extract approximate eigenvectors. The subspace is chosen to be the Krylov space of the form $\mathcal{K} = \{\mathbf{v}_0, A\mathbf{v}_0, ..., A^{m-1}\mathbf{v}_0\}$, where $\mathbf{v}_0$ is an arbitrary vector and m is typically much smaller than n. Suppose we have a set of orthonormal vectors $\mathbf{v}_i$ that form the basis of $\mathcal{K}$, and denote matrix $V_m = [\mathbf{v}_1, \mathbf{v}_2, ..., \mathbf{v}_m]$. Take $\mathbf{x} = V_m\mathbf{y} \in \mathcal{K}$, and impose the Galerkin condition to the residual $r(\lambda, \mathbf{x})$:

$$r(\lambda, \mathbf{x}) = A\mathbf{x} - \lambda\mathbf{x} \perp \mathcal{K} \tag{7}$$

which is equivalent to:

$$(AV_m\mathbf{y} - \lambda V_m\mathbf{y}, \mathbf{v}_i) = 0, \mathrm{i} = 1,2, ..., \mathrm{m} \tag{8}$$

Write (8) in the matrix form and denote $H_m = V^TAV$, we then obtain a reduced approximation problem of smaller size:

$$H_m\mathbf{y} = \lambda\mathbf{y} \tag{9}$$

Now the question is how to form the orthonormal basis $\mathbf{v}_i$ of $\mathcal{K}$. Here, the modified Gram-Schmidt orthogonalization process can be used. Each $A\mathbf{v}_j$ is generated, it is orthogonalized against all $\mathbf{v}_i$ with $i < j$. It is now known that this reduced problem can indeed give good approximation to large modulus eigenvalues [7]. Below is the algorithm.

Algorithm 3.1 Arnoldi Algorithm:
1. Choose an random unit vector $\mathbf{v}_1$;
2. Iterate: for $j = 1, 2, ..., m$ do
3. Compute $\mathbf{w}_j = A\mathbf{v}_j$;
4. For $i = 1, 2, ..., j$ do
5. $h_{ij} = (\mathbf{v}_i, \mathbf{w}_j)$;

6. $\mathbf{w}_j = \mathbf{w}_j - h_{ij}\mathbf{v}_i$;
7. end
8. $h_{j+1,j} = \|\mathbf{w}_j\|$. If $h_{j+1,j} = 0$, then go to line 11;
9. $\mathbf{v}_{j+1} = \mathbf{w}_j / h_{j+1,j}$;
10. end
11. Compute all the eigenpairs $\lambda, \mathbf{y}$ of H_m;
12. Select the first k λ's in order of magnitude, and compute the eigenvectors $\mathbf{x}_i = V\mathbf{y}_i (i = 1, 2, ...k)$;
13. Compute the residual $\|A\mathbf{x}_i - \lambda_i \mathbf{x}_i\|_\infty = (\mathbf{e}_m^T \mathbf{y}_i) h_{m+1,m}$. If satisfied, then stop;
    Otherwise increase m by 5 or 10, set $\mathbf{v}_0 = \mathbf{x}_1$ and restart iteration from line 2 again.

In line 13 the residual expression is obtained by multiplying $\mathbf{y}_i$, the eigenvector of H_m, to the following equation, which comes straight from line 2 to 9.

$$AV_m = V_m H_m + h_{m+1,m}\mathbf{v}_{m+1}\mathbf{e}_m^T \tag{10}$$

In line 8, if $h_{j+1,j} = 0$, then equation (10) will becomes

$$AV_j = V_j H_j \tag{11}$$

The above equation indicates the exact invariant subspace V_j of A is obtained, and therefore the eigenvalues from line 11 will be the exact eigenvalues of A. In practice, this is a rare case. The choice of m depends on the problem size, spectrum distribution and the number of eigenvalues wanted. For a matrix of several thousands in size, choosing $m = 20 \sim 200$ may be good enough if about first $4 \sim 10$ top modulus eigenvalues are wanted.

The shift and inverse strategy as previously described for the inverse iteration can also be naturally combine into Algorithm 2.1. In case the eigenvalues near a given point are wanted, this can be the winning strategy, as the numerical experiment shows.

Algorithm 3.2 Shift and Inverse Arnoldi Algorithm:
1. Choose an random unit vector $\mathbf{v}_1$ and shift σ;
2. Compute the LU decomposition of $(A - \sigma I)$;
3. Iterate: for $j = 1, 2, ..., m$ do
4. Solve $L\mathbf{y} = \mathbf{v}_j$ and $U\mathbf{w} = \mathbf{y}$, $\mathbf{w}_j = \mathbf{w}$;
5. Continue as in Algorithm 3.1, steps 4–9.
6. Compute eigenvalues and vectors of $(A - \sigma I)^{-1}$ as in Algorithm 3.1, steps 11–12, mapping the eigenvalues back to those of A.

While the Arnoldi method reduces the large matrix A into a small upper Hessenberg matrix H_m, the Lanczos method, however, reduces the matrix into a small tridiagonal matrix, and solve the tridiagonal matrix for eigenvalues as the approximation [1]. In the Lanczos method the matrix V_m will not be orthonormal. Instead, another $n \times m$ matrix W_m will be formed such that $W_m^T V_m = I_m$ and $W_m^T A V_m = T_m$, where T_m is the tridiagonal matrix. The shift and inverse strategy can be incorporated into the Lanczos as Algorithm 3.2.

Algorithm 3.3 Lanczos Algorithm
1. Choose two vectors $\mathbf{v}_1$ and $\mathbf{w}_1$ such that $(\mathbf{v}_1, \mathbf{w}_1) = 1$ Set $\beta_1 = 0, \mathbf{v}_0 = \mathbf{w}_0 = 0$
2. Iterate: for $i = 1, 2, ..., m$ do
3. $\alpha_i = (A\mathbf{v}_i, \mathbf{w}_i)$;
4. $\mathbf{v} = A\mathbf{v}_i - \alpha_i \mathbf{v}_i - \beta_i \mathbf{v}_{i-1}$;
5. $\mathbf{w} = A^T \mathbf{w}_i - \alpha_i \mathbf{w}_i - \delta_i \mathbf{w}_{i-1}$;
6. $\delta_{i+1} = |(\mathbf{v}, \mathbf{w})|^{1/2}$;
7. $\beta_{i+1} = (\mathbf{v}, \mathbf{w}) / \delta_{i+1}$;
8. $\mathbf{v}_{i+1} = v / \beta_{i+1}$;
9. $\mathbf{w}_{i+1} = w / \delta_{i+1}$;
10. end
11. Compute the eigen pairs of $T_m = [\delta_i, \alpha_i, \beta_i]$;
12. Select the first k eigenvalues λ_i in order of their magnitude;

Iterative Method	k	m	*Flop Count*	*Residual Norm*
Arnoldi	4	15	9,308,634	4.1E-4
Lanczos	4	17	12,365,568	1.5E-5
Block Inverse itr.	3	*n.a.*	53,560,729	4.4E-5

Table 2: Comparison of FLOPS by Arnoldi and Lanczos. k is the number of eigenvalues sought, and m is the number of vectors generated.

13. Compute the corresponding eigenvectors $\mathbf{x}_i = V_m \mathbf{y}_i$;
14. Compute the residual norm $\|A\mathbf{x}_i - \lambda_i \mathbf{x}_i\|_\infty$;
15. If satisfied, then stop. Otherwise, increase m and start over again.

We used Arnoldi, Lanczos and block inverse iteration to solve the same problem as in Section 2. Shift and inverse scheme and the minimum degree ordering were all combined in each algorithm. And five eigenvalues closest to the shift $\sigma = 3.4$ were computed. The results are $\lambda : 3.4408, 3.5665, 3.1464, 3.7539, 2.8379$. Table 2 gives the comparison of flops. It is apparent that the Arnoldi and Lanczos methods are capable of computing more eigenvalues with less cost than block inverse iteration, but inverse iteration may suffice if just one eigenvalue is desired, depending on the distribution of the spectrum. When the matrix is symmetric, the the Arnoldi and Lanczos methods reduce to the same algorithm, and the resulting algorithm is known by the Kaniel-Paige theory to have very nice convergence properties, at least for the extreme eigenvalues [4]. When the matrix is nonsymmetric, the Arnoldi method is more straightforward to implement and has somewhat better convergence properties, but requires more space and cost per iteration than the Lanczos method. In addition, it is not entirely a simple matter to compute the eigenvalues of the nonsymmetric tridiagonal matrix resulting from the Lanczos method. Deflation can be incorporated into both Arnoldi and Lanczos methods.

4 Constrained Raleigh Quotient Maximization Problems

In the transverse magnetic field formulation using finite element method [5], the following problem is encountered:

$$\text{Find } (\lambda, \mathbf{x}) \text{ s.t.} \quad \lambda = \max_{\substack{C^T\mathbf{x}=0, \\ \mathbf{x}\neq 0}} \frac{(A\mathbf{x}, \mathbf{x})}{(B\mathbf{x}, \mathbf{x})} \tag{12}$$

where A is symmetric, B is symmetric positive definite, and C has full column rank. This problem would be the usual generalized eigenvalue problem if there were no constraint $C^T x = 0$. We call (12) Constrained Raleigh Quotient Maximization Problem(CRQM). Mathematically, (12) is equivalent to the following regular eigenvalue problem:

$$V^T A V \mathbf{y} = V^T B V \mathbf{y} \tag{13}$$

where the matrix V consists of an orthonormal basis spanning the constraint space $\{\mathbf{x} : C^T\mathbf{x} = 0\}$. In case that the matrix size is small, we can determine the matrix V by the Singular Value Decomposition and solve the dense problem (13). However, if the matrix size is as large as several thousands, this approach becomes computationally intractable on workstations. Here, we propose an algorithm that can efficiently deal with large sparse case of CRQM.

The algorithm is based on the Arnoldi. The regular Arnoldi forms an orthonormal basis of the Krylov space $\mathcal{K}$. As each new basis vector $A\mathbf{v}_j$ is generated, it is orthogonalized against all $\mathbf{v}_i, 1 \leq i \leq j-1$. Now we modify this process by making $A\mathbf{v}_j$ orthogonal not only to all previous $\mathbf{v}_i$'s but also orthogonal to all the column vectors of C. The column vectors of the resulting matrix V_m will be the basis of a "projected Krylov space" and will be very good components to form approximate solution vectors for CRQM.

Algorithm 4.1 Arnoldi Algorithm for CRQM:

1. Choose a unit vector $\mathbf{v}_1$ such that $C^T\mathbf{v}_1 = 0$;
2. For $j = 1, 2, ..., m$ do
3. Compute $\mathbf{w}_j = A\mathbf{v}_j$;
4. For $i = 1, 2, ..., k$ do
5. $t_{ij} = (\mathbf{c}_i, \mathbf{w}_j)$;
6. $\mathbf{w}_j = \mathbf{w}_j - t_{ij}\mathbf{c}_i$;
7. end
8. For $i = 1, 2, ..., j$ do
9. $h_{ij} = (\mathbf{v}_i, \mathbf{w}_j)$;
10. $\mathbf{w}_j = \mathbf{w}_j - h_{ij}\mathbf{v}_i$;
11. end
12. $h_{j+1,j} = \|\mathbf{w}_j\|_2$. If $h_{j+1,j} = 0$, then go to 14;
13. $\mathbf{v}_{j+1} = \mathbf{w}_j / h_{j+1,j}$.
14. Compute the eigenvalues of H_m and choose the k largest λ_is, where $k \leq m$.
15. Compute eigenvectors $\mathbf{y}_i$ of H_m associated with λ_i, and the CRQM solution vector $\mathbf{x}_i = V_m\mathbf{y}_i$, $i = 1, \ldots, k$.

We have the following relations for the above algorithm.

$$AV_m = V_m H_m + CT_m + h_{m+1,m}\mathbf{v}_{m+1}\mathbf{e}_m^T \quad (14)$$

$$V_m^T A V_m = H_m \quad (15)$$

$$C^T V_m = 0 \quad (16)$$

Notice that equation (15) lays the groundwork for the algorithm that the Ritz vector $\mathbf{x} = V_m\mathbf{y}$ is an approximation solution of CRQM.

It is seen that the Arnoldi method is easily adapted to incorporate the constraints. However, this method is still under investigation, and though we expect the behavior to be very similar to the unconstrained Arnoldi method, further numerical experiments are needed. In addition, the convergence theory has not yet been developed for this specific algorithm. This work is in progress and will be reported soon.

5 Conclusions

Arnoldi and Lanczos methods are promising for the large sparse eigenvalue problems in waveguide analysis. The computation cost of these two methods is far less than that of inverse iteration, especially when several eigenvalues are sought. Strategies such as reordering, or "shift and inverse," can be easily combined in these methods. And either of them can be modified to fit new formulations of finite element method. Reordering technique can significantly save computation, and should be explored whenever possible. We have also found MATLAB to be a convenient and efficient tool for problems with size reaching of several thousands.

References

[1] D. L. Boley. Krylov space methods on state-space control models. *Circ., Syst. & Signal Proc.*, 1992. to appear.

[2] Bernice M. Dillon and Jon P. Webb, "A comparison of Formulations for the Vector Finite Element Analysis of Waveguides", *IEEE Trans. Microwave Theory Tech.*, vol. 42, pp. 308-316, Feb. 1994.

[3] Alan George and Joseph W. Liu, *Computer Solution of Large Sparse Positive Definite Systems.* Prentice Hall, Englewood Cliffs, 1981.

[4] Gene H. Golub and Charles F. Van Loan, *Matrix Computations*, John Hopkins University Press, 1989.

[5] Zine-Eddine Abid, Klein L. Johnson, and Anand Gopinath, "Analysis of Dielectric Guides by Vector Transverse Magnetic Field Finite Elements", *J. of Lightwave Tech.*, vol. 11, pp. 1545-1549.

[6] B. N. Parlett, *The Symmetric Eigenvalue Problem*. Prentice Hall, Englewood Cliffs, 1980.

[7] Y. Saad, "Variations on Arnoldi's method for computing eigenelments of large unsymmetric matrices", *Linear Algebra Appl.*, 34:269-295, 1980.

[8] Y. Saad, *Numerical Methods for Large Eigenvalue Problems*, pp. 153-156. Manchester University Press, 1992.

[9] M.S. Stern, "Semivectorial Polarised finite difference method for Optical Waveguides with Arbitrary Index Profiles", *IEE PROCEEDINGS*, vol .135, Pt.J, No.1, pp. 56-63, Feb.

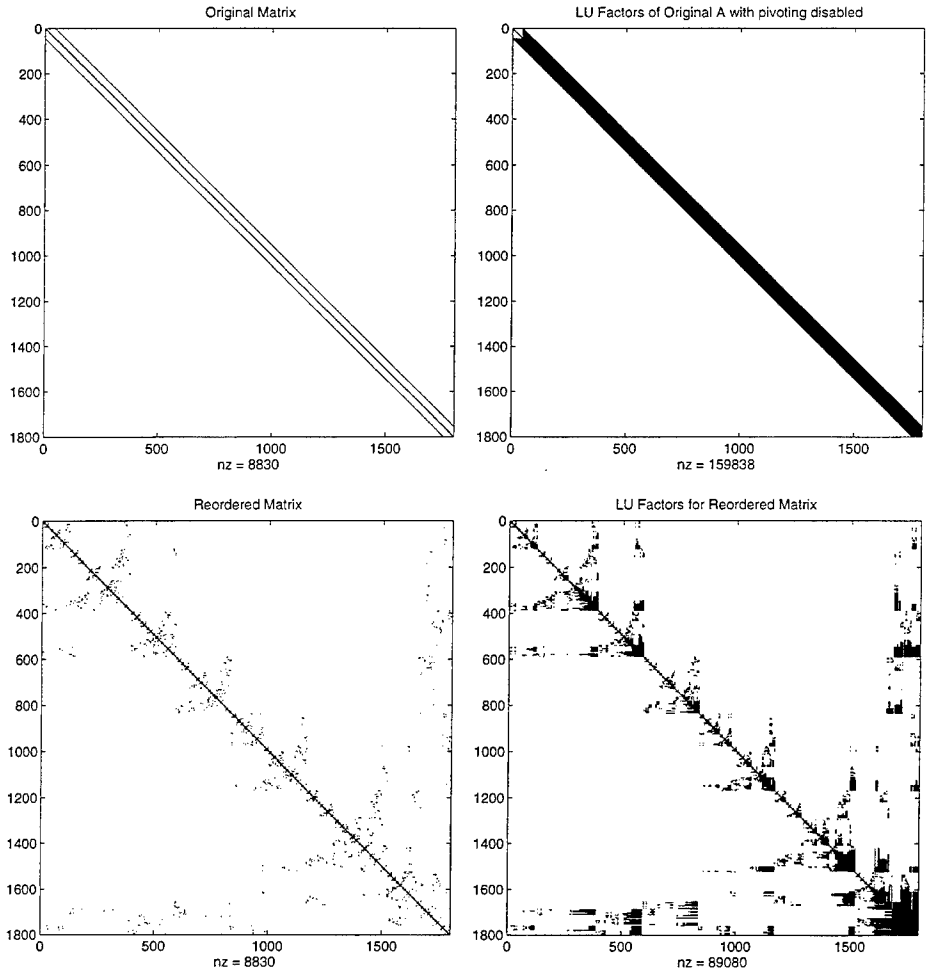

Figure1. Matrix Non-Zeroes showing original matrix and LU factors combined. Upper figures show original order, lower figures show minimum degree ordering. nz is the total number of nonzeroes.

Iterative Solution of Field Problems in Space–Decoupled Configurations

G. Bürger and H. Singer
Technical University Hamburg–Harburg
Department of Theoretical Electrical Engineering
Hamburg, Germany

Abstract

The method of moments leads to a linear equation system that is usually solved by an LU decomposition. Iterative methods are an alternative, but need an efficient preconditioner in general. We will show that there is a preconditioner for special configurations, which comes up from the interpretation of the system matrix in a simple manner. Together with a powerful iterative method (GMRES), this approach is clearly superior to the direct method.

1 Introduction

The method of moments is an efficient system for treating scattering and radiation problems in configurations of complex geometry. The method leads to the solution of a linear equation system that may contain a high number n of unknowns. Solving this equation system by the classical direct methods requires a computational effort of order n^3. Looking closer to the structure of the system matrix, one observes that dependent on the geometry of the scattering problem the system matrix has a pronounced block structure and is not necessarily completely filled. This behaviour becomes very evident if a double–current approach for dielectric or magnetic boundaries is used where each part of the current determines the field in one part of the space (left or right hand side of the boundary). Considering geometries that consist of several galvanically not coupled substructures, one gets e.g. a system matrix Z with diagonal blocks Z_{ii}, which correspond to the interactions of the equivalent currents on the substructures, and non–diagonal blocks $Z_{ij}, i \neq j$, which correspond to the mutual interactions of the substructures. The question occurs, whether this structure could be used to reduce the numerical effort in solving the equation system.

Particular versions of direct methods, which make use of this matrix structure, have the disadvantage that they only reduce the computation time of a very limited class of problems. Concerning the geometry, an appropriate solver has to be chosen that may also need a multitude of information on the matrix structure that have to be qualified in advance. By this procedure

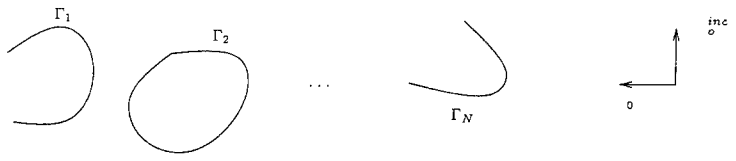

Figure 1: N scatterers in free space

the methods lose their "black-box character". There are a lot of reasons to look for more flexible and simple solvers.

Iterative methods are an alternative. The choice of the iterative method is determined by the mathematical characteristics of the system matrix. A suitable method for non-hermitian matrices is GMRES(m). Past experience has shown that a preconditioning of the system matrix will be necessary, especially if the system matrix is very ill-conditioned.

In the above-mentioned case of galvanically not coupled substructures a block Jacobi method presents itself as a preconditioner, where the blocks of the preconditioner correspond to the diagonal blocks Z_{ii} of the system matrix. This means that the mutual interaction of the substructures is neglected. This interaction is later considered by using the iterative method. Moreover, the advantages of Jacobi methods are that they need only little storage and few additional information, and that they are easily to be implemented and to parallelized.

In the following section it is briefly dealt with the underlying treatment of the scattering problem by equivalent surface currents and with the solution of the electric field integral equation EFIE by means of the method of moments. Afterwards the iterative method GMRES is introduced and it is illustrated, how the preconditioner is resulting from the interpretation of the single blocks of the impendance matrix. Finally some examples will be demonstrated and the computing times of the iterative methode will be compared to those of the LU decomposition.

2 Integral Equations, Method of Moments

Let there be a number N of scatterers in free space. Each of these scatterers is described by its surface Γ_i, which may either be open or closed. In the case of a closed surface, the encircled volume can be filled with a dielectric material, which is characterized by the material constants ϵ, μ, σ of the dielectric. Therefore such a surface represents an interface between the open space and the dielectric. In the following the surfaces are supposed to be boundaries made from an ideally conducting material, then there is no field inside the closed areas. An incoming plane wave $(\boldsymbol{E}_0^{inc}, \boldsymbol{H}_0^{inc})$ is exciting these objects (Fig. 1). We are looking for the scattered field.

The fields have to satisfy some boundary conditions on the surfaces. As the surfaces are

marginal faces made from ideally conducting material, there is

$$\boldsymbol{n}_i \times \boldsymbol{E}_0(\boldsymbol{r}) = 0 \quad \forall \boldsymbol{r} \in \Gamma_i. \tag{1}$$

Here $\boldsymbol{n}_i$ represents the normal vector on the surface Γ_i, and $\boldsymbol{E}_0$ is the sum of incoming field and scattered field in free space:

$$\boldsymbol{E}_0 = \boldsymbol{E}_0^{inc} + \boldsymbol{E}_0^{s}.$$

In order to calculate the scattered field an unknown distribution of the current on the surface $\boldsymbol{J}_j$ is assumed. The electromagnetic field of the (electric) surface currents is simulating the demanded scattered field. The electric field of the current $\boldsymbol{J}_j$ on the surface Γ_j results from the integral operator $\mathcal{E}_j$ as follows

$$\mathcal{E}_j \boldsymbol{J}_j = j\omega\mu_0 \int_{\Gamma_j} \left[\boldsymbol{J}_j + \frac{1}{k_0^2} (\boldsymbol{\nabla} \cdot \boldsymbol{J}_j) \boldsymbol{\nabla} \right] G(R)\, ds, \tag{1}$$

with

$$G(R) = \frac{1}{4\pi} \frac{e^{-jk_0 R}}{R}$$

being the Greens function and k_0 being the wave number of the incoming wave in free space. With these (equivalent) surface currents the demanded scattered field is

$$\boldsymbol{E}_0^s = \sum_{j=1}^{N} \mathcal{E}_j \boldsymbol{J}_j. \tag{2}$$

Combined with the boundary conditions of N scatterers there follows the linear operator equation system

$$\boldsymbol{n}_1 \times (\mathcal{E}_1 \boldsymbol{J}_1 + \cdots + \mathcal{E}_N \boldsymbol{J}_N) = -\boldsymbol{n}_1 \times E_0^{inc}, \quad \forall \boldsymbol{r} \in \Gamma_1,$$

$$\vdots \tag{3}$$

$$\boldsymbol{n}_N \times (\mathcal{E}_1 \boldsymbol{J}_1 + \cdots + \mathcal{E}_N \boldsymbol{J}_N) = -\boldsymbol{n}_N \times E_0^{inc}, \quad \forall \boldsymbol{r} \in \Gamma_N. \tag{4}$$

To solve the operator system the method of moments is employed. For that purpose the surface Γ_j is divided into n_j patches. For every two patches with a common edge a basis function $\boldsymbol{J}_j^{(\nu)}$ (roof top function) is defined and the particular surface currents $\boldsymbol{J}_j$ are expanded to these basis functions

$$\boldsymbol{J}_j = \sum_{\nu=1}^{n_j} I_j^{(\nu)} \boldsymbol{J}_j^{(\nu)}. \tag{5}$$

Note that there are $n = \sum_{j=1}^{N} n_j$ basis functions. Furthermore, a suitable scalar product on the surfaces is defined. The integration along certain matching paths $\boldsymbol{\eta}_j^{(\mu)}$, $\mu = 1, \ldots, n_j$ on the surfaces is e.g. such a scalar product:

$$\langle \boldsymbol{A}, \boldsymbol{\eta}_i^{(\nu)} \rangle = \int_{\eta_i^{(\nu)}} \boldsymbol{A} \cdot d\boldsymbol{s},$$

with $\boldsymbol{A}$ being any vector defined on Γ_i. Using the notation

$$Z_{ij}^{\nu\mu} = \langle \mathcal{E}_j \boldsymbol{J}_j^{(\mu)}, \boldsymbol{\eta}_i^{(\nu)} \rangle, \quad U_i^{\nu} = \langle \boldsymbol{E}_0^{inc}, \boldsymbol{\eta}_i^{(\nu)} \rangle$$

and

$$Z_{ij} = (Z_{ij}^{\nu\mu}), \quad U_i = \left[U_i^{(1)}, \ldots, U_i^{(n_i)}\right]^T, \quad I_j = \left[I_j^{(1)}, \ldots, I_j^{(n_j)}\right]^T,$$

the following linear equation system comes up

$$Z\boldsymbol{i} = \begin{pmatrix} Z_{11} & Z_{12} & \ldots & Z_{1N} \\ Z_{21} & Z_{22} & \ldots & Z_{2N} \\ \vdots & \vdots & & \vdots \\ Z_{N1} & Z_{N2} & \ldots & Z_{NN} \end{pmatrix} \begin{pmatrix} I_1 \\ I_2 \\ \vdots \\ I_N \end{pmatrix} = - \begin{pmatrix} U_1 \\ U_2 \\ \vdots \\ U_N \end{pmatrix} = -\boldsymbol{u}, \tag{6}$$

with $Z_{ij} \in \mathbb{C}^{n_i \times n_j}, I_i, U_i \in \mathbb{C}^{n_i}, i, j = 1, \ldots, N$. The diagonal blocks Z_{ii} describe the interaction of object i with itself and Z_{ij} the interaction of the object i with object j. According to the arbitrary choice of the domain of the basis functions and the matching paths these matrices are generally non–hermitian. It follows that the $n \times n$ system matrix Z is also generally non–hermitian.

3 Short Description of GMRES(m)

Here we give a very short description of GMRES and GMRES(m); for more detailed description, see Saad and Schultz [3]. GMRES is an iterative method for solving linear systems

$$A\boldsymbol{x} = \boldsymbol{b}, \tag{7}$$

with A being a non–hermitian $n \times n$ matrix, $\boldsymbol{b} \in \mathbb{C}^n$ being the given right hand side, and we are looking for a solution vector $\boldsymbol{x} \in \mathbb{C}^n$. The method belongs to the class of Krylov subspace methods: it produces approximations $\boldsymbol{x}_k$ to $A^{-1}\boldsymbol{b}$ of the form

$$\boldsymbol{x}_k \in \boldsymbol{x}_0 + \mathcal{K}_k(\boldsymbol{r}_0, A), \quad k = 1, 2, \ldots. \tag{8}$$

Here, $\boldsymbol{x}_0 \in \mathbb{C}^n$ is any initial guess for the solution of (7), $\boldsymbol{r}_0 = \boldsymbol{B} - A\boldsymbol{x}_0$ is the corresponding residual vector, and $\mathcal{K}_k(\boldsymbol{r}_0, A)$ its the k–th Krylov subspace generated by $\boldsymbol{r}_0$ and A:

$$\mathcal{K}_k(\boldsymbol{r}_0, A) = span(\boldsymbol{r}_0, A\boldsymbol{r}_0, \ldots, A^{k-1}\boldsymbol{r}_0).$$

At the k–th iteration, GMRES computes a correction $\boldsymbol{z}_k$, which minimizes the residual $\boldsymbol{r}_k$ over $\mathcal{K}_k(\boldsymbol{r}_0, A)$:

$$||\boldsymbol{b} - A\boldsymbol{x}_k||_2 = \min_{x \in \mathcal{K}_k(r_0, A)} ||\boldsymbol{b} - A\boldsymbol{x}||_2. \tag{9}$$

Therefore, the Arnoldi process is to be used to generate an orthonormal basis of the Krylov subspace:

Chose $\boldsymbol{v}_1 \in \mathbb{C}^n$, with $||\boldsymbol{v}_1||_2 = 1$.
For $j = 1$ to k
(1) $h_{ij} = (A\boldsymbol{v}_i, \boldsymbol{v}_j), \quad i = 1, \ldots, j$
(2) $\hat{\boldsymbol{v}}_{j+1} = A\boldsymbol{v}_j - \sum_{i=1}^{j} h_{ij}\boldsymbol{v}_j$
(3) $h_{j+1,j} = ||\hat{\boldsymbol{v}}_{j+1}||_2$
(4) $\boldsymbol{v}_{j+1} = \hat{\boldsymbol{v}}_{j+1}/h_{j+1,j}$

The vector recurrences in step (2) of the Arnoldi process can be rewritten compactly in matrix form as follows:

$$AV_k = V_{k+1}\bar{H}_k, \tag{10}$$

where

$$V_k = [\boldsymbol{v}_1, \boldsymbol{v}_2, \cdots, \boldsymbol{v}_k] \tag{11}$$

has orthonormal columns, and

$$\bar{H}_k = \begin{pmatrix} h_{11} & h_{12} & \ldots & h_{1k} \\ h_{21} & \ddots & & \vdots \\ 0 & \ddots & & \vdots \\ \vdots & \ddots & h_{n,n-1} & h_{nn} \\ 0 & \ldots & 0 & h_{n+1,n} \end{pmatrix} \tag{12}$$

is an $(k+1) \times k$ upper Hessenberg matrix of rank k.

If one chooses the starting vector $\boldsymbol{v}_1 = \boldsymbol{r}_0/||\boldsymbol{r}_0||$ of the Arnoldi process, then all possible iterations can be written as

$$x_k = x_0 + V_k z_n, \quad z_n \in \mathbb{C}^k. \tag{13}$$

Moreover, with (10) and (13), the minimal residual property (9) reduces to the $(k+1) \times k$ least squares problem

$$||\beta e_k - \bar{H}_k z_k||_2 = \min_{z \in \mathbb{C}^k} ||\beta e_k - \hat{H}_k z||_2, \tag{14}$$

where $e_k = [1, 0, \ldots, 0]^T \in \mathbb{R}^{k+1}$ and $\beta = ||\boldsymbol{r}_0||_2$. GMRES is an implementation of the minimal residual approach (9) that obtains the k–th iterative solution $\boldsymbol{x}_k$ by first running k steps of the Arnoldi process and then solving the $(k+1) \times k$ least squares problem (14), which can be solved by a QR factorization.

Since storage and arithmetic cost increase as the GMRES iterations proceed, the algorithm usually implemented in practice is GMRES(m), where m is any maximum allowable number of iterations, typically $m \ll n$. In one cycle of GMRES(m), beginning with a current approximate solution $\boldsymbol{x}_0$, up to m GMRES iterations are performed; the iterations are terminated when either the residual norm has been reduced sufficiently or the full m iterations have been carried out. It should be mentioned that the residual norm can be monitored during the iterations without actually computing the correction or the residual. After the iterations have been performed, the cycle is concluded with the computation of the correction $\boldsymbol{z}_m$. If $||\boldsymbol{r}_m||$ is not small enough, then $\boldsymbol{x}_m = \boldsymbol{x}_0 + \boldsymbol{z}_m$ is used as the new initial guess vector of a new cycle of iterations as needed.

4 Block Jacobi Preconditioning

We are using GMRES(m) for solving the linear system eq. (6). Past experience has shown that for a convergence of the method an efficient preconditioning technique is required. Let M be a nonsingular $n \times n$ matrix, which approximates in some sense the impedance matrix Z of the original linear system (6). GMRES(m) is then used to solve the preconditioned system

$$Z'\boldsymbol{i} = -\boldsymbol{u}', \tag{15}$$

where

$$Z' = M^{-1}Z, \quad \boldsymbol{u}' = M^{-1}\boldsymbol{u}.$$

Instead of solving (6), the equivalent system (15) is being solved. In this way GMRES(m) generates approximate solutions of the form

$$\boldsymbol{i}_k = \boldsymbol{i}_0 + \mathcal{K}_k(\boldsymbol{r}'_0, Z').$$

The interpretation of the impedance matrix recommends a block Jacobi method: On the surfaces of the bodies sources (basis functions) are placed. Every row of the impendance matrix then describes the interaction of these sources with the single reference points (test functions) on the surfaces. The interaction with a source is strong, as long as the reference points lay on the same surface, it is weak, if the reference points lay on different surfaces. That means that the diagonal blocks Z_{ii} are equivalent to the interactions of the sources with the bodies themselves, all other blocks $Z_{ij}, i \neq j$ describe the interactions of sources on body i with reference points on body j. If one neglects in a first step the mutual interactions of the bodies, then

$$M = \begin{pmatrix} Z_{11} & & & \\ & Z_{22} & & \\ & & \ddots & \\ & & & Z_{NN} \end{pmatrix} \tag{16}$$

generally approximates the impendance matrix pretty well, as far as the mutual interaction of the bodies isn't too strong. This fact implies to use M as a preconditioner, the single blocks of the preconditioner then result from the physical significance of the block matrices. M^{-1} follows from a simple LU decomposition of the single diagonal blocks

$$M = \begin{pmatrix} L_1U_1 & & & \\ & L_2U_2 & & \\ & & \ddots & \\ & & & L_NU_N \end{pmatrix}. \tag{17}$$

The block Jacobi preconditioning method has the advantage of not requiring any additional storage, as the diagonal blocks are already existing in the impendance matrix, moreover they are easily implemented and parallelized. Furthermore, the method is extremely efficient, as the following examples may demonstrate.

5 Numerical Experiments

We have tested the method by some examples. In these examples the structures are designed in such a way that galvanically not connected parts establish an overall configuration. Then the resulting equation system has the form as in eq. (6) (arrays of PEC cubes, ex. 3 and 4, Fig. 3). Moreover, some configurations have been tested that have a not completely filled system matrix (concentric dielectric spheres, ex. 2) and configurations, whose analysis requires in addition to a single–layer current distribution according to the EFIE also a double–layer current distribution. Treating these kinds of problems one has to apply also the magnetic field integral equation (MFIE), which has not been explicitely introduced here (model of a human being close to a car, ex. 5 (Fig. 2), and dielectric body, ex. 1). For details see [2].

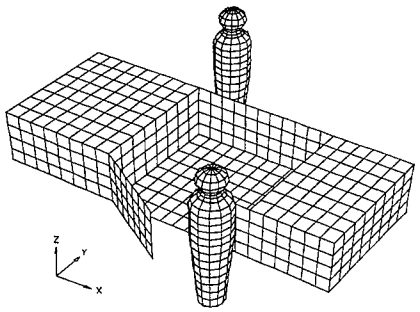

Figure 2: Simple model of two humans being close to a car

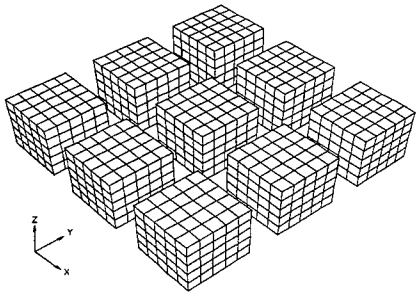

Figure 3: Array of nine PEC cube scatterers

Each of these examples can be treated with a field calculation program (CONCEPT). Here is applied a special version of the LU decomposition, which partly takes advantage of the population structure (zero blocks) for solving the equation system. The arithmetic times of the direct method are compared with those of the iterative methods in conjunction with the preconditioning time. The following table shows that in every case the iterative method is superior to the direct one. All examples were calculated on an IBM RS6000–580. Stopping criterion for all problems is $||r_k|| < \varepsilon$, with $\varepsilon = 10^{-6}$.

Ex.	$n(n_1,\ldots,n_N)$	t_{LU}	t_{PC}	t_{GMRES}	t_{it}	its.	δ
1	1056 (528,528)	66.45	17.40	3.96	21.36	11	0.06
2	1248 (528,360,360)	56.13	14.10	2.26	16.36	6	0.02
3	1500 (5×300)	188.33	8.01	2.32	10.33	4	0.02
4	2700 (9×300)	1145.68	14.41	7.45	21.86	3	0.04
5	3386 (1056,1056,1274)	1035.99	248.57	10.85	259.42	2	0.02

Table 1: n number of unknowns, n_i number of unknows of subproblem i; t_{LU} arithmetic time for LU decomposition of the system matrix, t_{PC} arithmetic time to build up the preconditioner M resp. M^{-1}, t_{GMRES} arithmetic time for GMRES, t_{it} overall time of the iterative method; all times in CPU seconds; its. number of iterations, δ maximal error in percent in comparison to the solution vector of the LU decomposition.

One has to consider that the huge numerical effort is caused by the LU decomposition of the preconditioner. The effort is reduced, if a great number of partial problems has to be solved (see the PEC cube array example with five, ex. 3, and nine substructures, ex. 4). In addition to that it will be advantageous, if all partial problems have about the same size. It makes no sense to try to solve a problem by this method, if the number of unknowns in the partial problem is only little smaller than the overall number of unknowns. Remarkable is the little number of required iterations of GMRES. This number is also reduced if the number of unknowns rises. This effect has a positive impact on the arithmetic time, as then a lower number of matrix–vector multiplications and vector–vector operations is required. Moreover, the storage effort is limited, because the number of basis vectors that have to be stored is limited, so that the parameter m can be chosen very small.

The results show that if a problem satisfies all preconditions (a number of galvanically not connected substructures of almost the same size) this method is evidently superior to the direct method, even when some of the the zero blocks are utilized.

References

[1] R.F. Harrington, *Field Computation by Moment Methods*, New York: IEEE Press, 1993.

[2] Th. Mader, *Berechnung elektromagnetischer Felderscheinungen in abschnittsweise homogenen Medien mit Oberflächenstromsimulation*, Doct. Thesis, TU Hamburg–Harburg, 1992.

[3] Y. Saad and M.H. Schultz, "GMRES: a generalized minimal residual algorithm for solving nonsymmetric linear systems", *SIAM J. Sci. Stat. Comput.*, **7**, pp. 856–869, 1986.

VI = Volume I
VII = Volume II

AUTHOR INDEX